

37th European Conference
on Solid-State Transducers

EUROSENSORS 2025

Wrocław, Poland - September 7th - 10th, 2025

Book of abstracts

EUROSENSORS

Wrocław University
of Science and Technology

Faculty of Electronics,
Photonics and Microsystems

Proceedings

EUROSENSORS XXXVII

Wroclaw, Poland - Sept. 7th - 10th 2025

These proceedings cover the short papers of the lectures of the EUROSENSORS XXXVII Conference.

The authors are responsible for form and content of the papers.

AMA Service GmbH accepts no responsibility for the correctness and completeness of the details and the consideration of private rights of third parties.

Herausgeber / Publisher:

AMA Service GmbH
Von-Münchhausen-Str. 49
31515 Wunstorf / Germany
Tel. +49 5033 9639-0
info@ama-service.com
www.ama-service.com / www.sensor-test.com
www.ama-science.org / www.smsi-conference.com

ISBN 978-3-910600-07-2

© AMA Service GmbH, 2025

Preface

On behalf of the Chairs of the Conference we welcome you to the 37th European Conference on Solid-State Transducers Eurosensors 2025 in Wrocław, Poland.

Eurosensors, a highly successful series of conferences, has become the leading European forum to cover the entire field of sensors, actuators, microsystems and nanosystems. Today, Eurosensors provides an excellent opportunity to bring together scientists and engineers from academia, research centres, national research institutes and companies, to present and discuss the latest results in these fields.

Eurosensors attracts hundreds of participants every year, mainly from Europe but also from other countries. As mentioned, Eurosensors asks for contributions describing the latest results on solid state-based sensors, actuators, micro and nanosystems as well as the emerging and related technologies, application areas and new sensors concepts involving quantum sensors and instruments for space exploration.

This year's conference program includes six plenary presentations, including those by the 2023 Nobel Prize winner, Prof. Anne L'Hullier (organized in collaboration with the cademia Europaea Wrocław Hub), nearly 100 oral presentations across three plenary sessions, two satellite events related to the implementation of European projects – AMUSENS and INTAKE, and over 140 poster presentations during two sessions at the end of the first two days of the conference.

The social events on Monday and Tuesday, located near Wrocław's cultural and entertainment center – the Market Square – will hopefully allow you to relax, engage in informal discussions, and network after a day of scientific discussions.

The abstract book of EUROSENSORS 2025 is published by AMA Association for Sensors and Measurement. All the abstracts receive individual DOI number. The authors are asked to submit their full-length paper to Journal of Sensors and Sensor Systems (JSSS). After peer reviewing process, the full-length papers are published in a EUROSENSORS 2025 special issue.

We want to thank you all for attending the Conference. It is the quality of your presentations and your passion to communicate with the others participants that really makes this conference success. We wish you a fruitful conference and a pleasant stay in Wrocław.



Prof. Rafał Walczak
Conference Chair



PhD Patrycja Śniadek
Organizing Committee Chair

PT: Plenary Talk II

Chair: Rafał Walczak, Jean-Paul Viricelle

PT2 **AI and other Trends in MEMS Industry change Foundry Models 22**
S. Majoni, Bosch, Reutlingen (Germany)

Special Session: INTAKE 1 - Integrated Nanocomposites for Thermal and Kinetic Energy Harvesting

Chair: Karolina Laszczyk

SP1.2 **Molecular Dynamics Analysis of Virus-Induced Vibrational Changes in Single-layer Graphene 24**
Z. Wang, H. Kurita, F. Narita, Tohoku University, Sendai (Japan)

SP1.3 **Planar Coils Made in the Thick-Film and LTCC Technology For the Electromagnetic Microgenerator 26**
M. Gierczak. A. Dziedzic. Wrocław University of Science and Technology, Wrocław (Poland)

SP1.4 **Laser Etching Effects on the Electrical and Mechanical Properties of Barium Titanate Thick Films 28**
Y. Matsui, K. Maruyama, Z. Wang, H. Kurita, F. Narita, Tohoku University, Sendai (Japan), Y. Kawakami, Research Institute for Electromagnetic Materials, Tomiya (Japan)

Special Session: INTAKE 2 - Integrated Nanocomposites for Thermal and Kinetic Energy Harvesting

Chair: Zhejin Wang

SP2.1 **One-Step Fabrication of Piezoelectric Ceramics/Carbon Fiber Reinforced Polymer Composites with Enhanced Performance 30**
Z. Lin, Z. Wang, H. Kurita, F. Narita, Tohoku University, Sendai (Japan)

SP2.2 **Broadband Rotational Energy Harvesting Using Upward and Downward Piezoelectric Cantilevers under Aerospace-Induced Vibrations 32**
M. S. Ahmed, Y. Jia, Aston University, Birmingham (UK)

SP2.3 **The Impact of Elementary Cell Topology on the Bending Tests of 3D Printed Sandwich Beams 34**
R. Pawlowski, R. Trzeciakowski, K. Laszczyk, P. Piórkowski, Wroclaw University of Science and Technology, Wroclaw (Poland), H. Kurita, F. Narita, Tohoku University, Sendai (Japan)

SP2.4 **Real-Time Monitoring of Cracks in Carbon Fiber-reinforced Polymers under Bending Vibrations with Piezoelectric Composite Sensors 36**
Y. Sueda, Z. Wang, H. Kurita, F. Narita, Tohoku University, Sendai (Japan), Y. Watanabe, H. Sato, R. Ohiwa, Nikkiso Co., Ltd., Tokyo (Japan)

M1.1: Gas Sensors 1

Chair: Donatella Puglisi

M1.1.1 **A Screen-Printed and Light-Activated Copper Oxide Sensor for Acetone Detection 38**
A. Chatterjee, J Zikulnig, J. Kosel, M. T. Vijjapu, Silicon Austria Labs GmbH, Villach (Austria), B. Jakoby, Johannes Kepler University, Linz (Austria)

M1.1.2 **Simultaneous Thermal and Optical (De-)Activation of Microhotplate-Based CMOS-Integrated SnO2 + Ag NPs Gas Sensors 40**
F. Sosada-Ludwikowska, A. Köck, L. Egger, Materials Center Leoben Forschung GmbH, Leoben (Austria), O. Casals, Universitat de Barcelona, Barcelona (Spain), J. D. Prades, Universitat de Barcelona, Barcelona (Spain), Technische Universität Braunschweig, Braunschweig (Germany)

M1.1.3 Active Colorimetric Sensor for real-time detection of gas mask filter saturation 42
R. Rousier, R. Anciant, S. Donet, H. Fontaine, Univ. Grenoble Alpes CEA, Grenoble (France)

M1.1.4 MOF-199 as a Colorimetric Sensor for Trace Humidity Detection. 44
M. González-Gómez, O. Casals, C. Fàbrega, University of Barcelona, Barcelona (Spain), J. D. Prades, Technische Universität Braunschweig, Braunschweig (Germany), E. M. Medina, M. M. López, E. X. Martín, University of Barcelona, Barcelona (Spain), J. Kovac, Jozef Stefan Institute, Ljubljana (Slovenia)

M1.2: Sensors for Space Exploration

Chair: Jan A. Dziuban

M1.2.1 Lab-on-chip systems – new perspectives for microgravitional biomedical research in space 46
A. Krakos, Wroclaw University of Science and Technology, Wrocław (Poland)

M1.2.2 A Novel Concept for a Hanle Vector Magnetometer for Space Application 48
S. Laddha, A. Betzler, R. Lammegger, Graz University of Technology, Graz (Austria), C. Amtmann, A. Pollinger, I. Jernej, W. Magnes, Austrian Academy of Sciences, Vienna (Austria)

M1.2.3 Towards Miniaturized XRF Systems: A MEMS X-ray Source for Space Exploration 50
P. Urbanski, P. Szyszka, T. Grzebyk

M1.3: Physical Sensors

Chair: Christos Tsamis

M1.3.1 "Matching" of Photodetectors Integrated in a 0.18 µm Modular CMOS Foundry Technology 52
D. Gaebler, F. Fischer, R. Roesch, P. F. Siles, X-FAB Global Services GmbH, Erfurt (Germany)

M1.3.2 Thin – Film Thermocouple Sensor Development for Smart Battery Cells 54
H.Y.C. Altintas, E. Guk, J. Marco, T. Vincent, University of Warwick, Coventry (United Kingdom)

M1.3.3 Vapor-Channeled Porous Pressure Sensors 56
N.T. Beigh, N. Alcheikh, Khalifa University, Abu Dhabi (United Arab Emirates)

M1.3.4 Miniaturized Electric Field Mill based on Lorentz Force Actuation 58
F. Keplinger, Technical University of Vienna, Vienna (Austria), W. Hortschitz, G. Kovac, University for Continuing Education Krems, Wiener Neustadt (Austria)

M2.1: Quantum Sensors

Chair: Anton Köck

M2.1.1 Simultaneous Magnetic Field and Temperature Measurements on a Battery with a Fiber-Coupled Quantum Sensor 60
T. van Ree, H. Bartling, C. Osorio Tamayo, Netherlands Organisation for Applied Scientific Research (TNO), Delft (The Netherlands), V. Place, L. Castro, S. Kinge, Toyota Motor Europe (TME), Zaventem (Belgium)

M2.1.2 Development of Glass-Based Atomchip 62
F. Pöpsel, A. Kassner, H. Heine, F. Dencker, M. C. Wurz, Leibniz University, Hannover (Germany), J. Heinz, LPKF Laser, Electronics SE, Garbsen (Germany)

M2.1.3 SILICON CARBIDE ON INSULATOR (SiCOI) MATERIALS FOR MEMS AND QUANTUM APPLICATIONS USING WAFER BONDING METHODS 64
H. D. Ngo, B. Wang, T. Weiland, O. Pohl, University of Applied Sciences Berlin, Berlin (Germany), B. Naydenov, Helmholtz Centre Berlin for Material Research and Energy, Berlin (Germany), T. S. Nguyen, Linköping University, Linköping (Sweden), Y. Akabane, TDC Corporation, Rifucho Miyagi (Japan)

M2.2: MEMS

Chair: Stefan Majoni

M2.2.1 **A novel piezoelectric MEMS speaker with push-pull actuation for in-ear applications....66**
F. Cerini, S. Adorno, STMicroelectronics, Cornaredo (Italy), C. Gazzola, F. P. Perli, M. Rosso, A. Corigliano, Politecnico di Milano, Milano (Italy)

M2.2.2 **Advancing On-Chip Micromotor Fabrication Through Electrochemical Micromachining of Silicon....68**
F. Abazar, S. Surdo, C. Cozzi, G. Polito, G. Barillaro, University of Pisa, Pisa (Italy)

M2.2.3 **High-resolution laser ablation of a copper layer for the fabrication of 3D-printed MEMS and microsensors....70**
M. Roig, D. Bourrier, P.-F. Calmon, C. Arvanitis, C. Bergaud, V. Mansard, LAAS-CNRS, Toulouse (France)

M2.2.4 **Impact of Nitrogen Doping on the Q-Factor of Polycrystalline 3C-SiC MEMS Resonators....72**
D. Huber, P. Jurekovic, C. Schallert, G. Pfusterschmied, U. Schmid, TU Wien, Vienna (Austria)

M2.3: 3D Printed Microfluidics

Chair: Péter Fürjes

M2.3.1 **A 3D printed microfluidic device for droplet-based cell encapsulation and study....74**
D. Mazur, W. Kubicki, Wroclaw University of Science and Technology, Wroclaw (Poland)

M2.3.2 **3D-Printed Hollow Microneedles on Si Microfluidics for Healthcare....76**
T. E. Abi-Ramia Silva, S. Kohler, N. Bartzsch, A. T. Güntner, ETH Zürich, Zurich (Switzerland), F. Beuschlein, University Hospital Zurich, Zurich (Switzerland)

M2.3.3 **3D-Printed Flow Cells with Piezoelectric Resonators and Machine Learning for Biofuel Characterization....78**
V. Corsino, V. Ruiz-Díez, A. Braic, J. L. Sánchez-Rojas, Universidad de Castilla La-Mancha, Toledo (Spain)

M2.3.4 **3D-Printed µ-GC Integrated with an E-Nose System for Enhanced Plant Health Prediction....80**
U. Yaqoob, D. Limbani, S. Esfahani, M. Cole, J. W. Gardner, University of Warwick, Coventry (United Kingdom)

M3.1: Gas Sensors 2

Chair: Michał Mazur

M3.1.1 **Novel corrole-based e-nose for methanol detection in wine....82**
F. Pizzoli, G. Magna, S. Nardis, C. Di Natale, R. Paolesse, University of Rome Tor Vergata, Rome (Italy)

M3.1.2 **Fabrication and Chracterization of Polymer-Based Ethanol Gas Sensor....84**
M. M. Uddin, M. A. Islam Bhuyan, H. C. Kim, University of Ulsan, Ulsan (South Korea)

M3.1.3 **CO2 Sensor based on Au functionalised CuO thin films....86**
C. Maier, F. Sosada-Ludwikowska, L. Egger, A. Köck, Materials Center Leoben Forschung GmbH, Leoben (Austria), S. Becker, J. S. Niehaus, Fraunhofer Center for Applied Nanotechnology CAN, Hamburg (Germany), K. Reichmann, Institute for Chemistry and Technology of Materials, TU Graz, Graz (Austria)

M3.1.4 **Toluene Sensing at Room Temperature using SnO2 Quantum Dot Decorated rGO Aerogel....88**
P. K. Kannan, J. W. Gardner, University of Warwick, Coventry (United Kingdom), Z. Chen, T. Bhowmick, T. Hasan, University of Cambridge, Cambridge (United Kingdom)

M3.2: MOEMS

Chair: Tomasz Grzebyk

M3.2.1 **KNN Lead-free MEMS Mirror: Thermal behavior....90**
L. Mollard, C. Dieppedale, A. Hamelin, G. Le Rhun, University Grenoble Alpes, Grenoble (France)

M3.2.2 Characterization of Sensor Responses in 1D and 2D Scan Patterns Via AlScN-Based MEMS Mirrors....92
J. -Y. Hwang, M. Shuvho, E. Yarar, G. Wille, F. Lofink, S. Gu-Stoppel, Fraunhofer Institute for Silicon Technology, Itzehoe (Germany), M. Shuvho, F. Lofink, Christian-Albrecht-University Kiel, Kiel (Germany), F. Lofink, Kiel Nano, Surface and Interface Science KiNSIS, Kiel (Germany)

M3.2.3 Hybrid Photonic-Plasmonic Waveguides (HPWG) for Hydrogen Sensing....94
R. Gremaud, ABB Switzerland Ltd, Baden-Dättwil, (Switzerland)

M3.3: Novel Technologies and Applications of Sensors 1

Chair: Jean-Philippe Polizzi

M3.3.1 Cutting-edge healthcare technologies for monitoring, care and coaching in elderly residential facilities: the perspec-tive of the Italian project "Age-it"....96
G. Rescio, A. M. Carluccio, A. Manni, A. Caroppo, Z. Romeo, E. Macchia, A. Bobbo, M. Noale, R. De Benedictis, G. Cortellesa, P. Siciliano, A. Leone, National Research Council of Italy, Rome (Italy)

M3.3.2 Lock and Key Interconnects for Modular Flexible and Printed Electronics....98
P. G. Perez, E. B. Alexandre, M. Bleidy, S. Lengger, J. Kosel, M. T. Vijjapu, Silicon Austria Labs GmbH, Villach (Austria)

M3.3.3 Capacitive Excitation of Out-of-Plane Modes in MEMS Resonators with a Planar Electrode Design....100
D. Huber, M. Gülly, G. Pfusterschmied, U. Schmid, TU Wien, Vienna (Austria)

M3.3.4 Reduction of an Irregular Sensor Network for Continuous Humidity Monitoring in Wood Structures....102
M. Bankwitz, C. Engel, K. Giske, R. Bendyk, S. Hirsch, University of Applied Sciences, Brandenburg (Germany), F.E. Schmid-Bonde, J. Röder, University of Applied Sciences, Potsdam (Germany)

T4.1: MEMS Gas Sensors

Chair: Andreas Güntner

T4.1.1 Ultra-compact MEMS gas analyzer based on ion-optical spectrometry....104
P. Szyszka, K. Stambulskyi, T. Grzebyk, Wroclaw University of Science and Technology, Wrocław (Poland)

T4.1.2 MEMS-based microplasma sources for gas analysis....106
E. Vereshchagina, E. Escobedo-Cousin, K. Milenko, S. Zonetti, A. Ellingsen, D. C. H. Hoang, SINTEF Digital, Oslo (Norway), S. Dutta, T.-A. Nguyen-Le, C. D'Alessandro, Respiro B.V., Leiden (The Netherlands)

T4.1.4 Ceramic MEMS Platforms for Metal Oxide Gas Sensors: Compatibility of Sensing Layers with Thick Film Materials....108
A. Vasiliev, Dubna State University, Dubna (Russia), O. Kul, A. Bolshakov, LLC "C-Component", Moscow (Russia), A. Mokrushin, Kurnakov Institute of Inorganic Chemistry, Moscow (Russia), A. Shaposhnik, Voronezh State Agrarian University, Voronezh (Russia)

T4.2: AI for Sensors

Chair: Vincent Ch. Lee

T4.2.1 Short-Term Pollution Prediction Using Personal Environmental Monitoring and Machine Learning....110
F. Pan, J.A. Covington, University of Warwick United Kingdom)

T4.2.2 Portable AI-Assisted System for Real-Time Dust Exposure Monitoring in Working and Occupational Environments....112
I. Romanytsia, ELLONA SAS (France)

T4.2.3 Correlation of gaseous emissions with phenological phases in tomato crops....114
M. Tamisari, E. Tavaglione, F. Tralli, B. Fabbri, University of Ferrara, Ferrara (Italy), M. Valt, Bruno Kessler Foundation, Trento (Italy)

T4.3: Novel Technologies and Applicatons of Sensors 2

Chair: Julian Gardner

T4.3.1 **Free Chlorine Digitization Using Colorimetric Barcodes and Machine-Leaning Models 116**
M. González-Gómez, I. Benito-Altamirano, H. Lizarzaburu-Aguilar, D. Martínez-Carpena, C. Fàbrega, J. D. Prades, Universitat de Barcelona, Barcelona (Spain), I. Benito-Altamirano, Universitat Oberta de Catalunya, Barcelona (Spain), J. D. Prades, Technische Universität Braunschweig, Braunschweig (Germany)

T4.3.2 **A low-power wireless sensor platform for real-time monitoring of pH and nitrate in the soil 494**
C.Boko, E Saoutieff, P Fourcade, V. Elhorga, A. Ohl, Univ Grenoble Alpes, Grenoble (France), I.Vogeler, H. Smit, Christian-Albrechts-Universität, Kiel (Germany), N. Surendran, A. Wille, Fraunhofer EMFT, Munich (Germany), H. Shao, A. O'Riordan, Tyndall National Institute, Cork (Ireland), L. Kulas, P. Kalkowski, Gdansk University of Technology, Gdansk (Poland), H.Trindade, University of Trás os Montes e Alto Douro, Quinta de Prados (Portugal), L. Kohl, S.Ullah, University of Eastern Finland, Kupio (Finland)

T4.3.3 **Development and Characterization of Tribotronic Transistor based on ZnO thin film..... 118**
M. Moustaka, C. Tsamis, National Center for Scientific Research "Demokritos", Athens (Greece), E. Hourdakis, National Technical University of Athens, Athens (Greece)

T4.3.4 **Machine Learning-Enhanced Odor Detection System as Next-Generation Forensic Technology..... 120**
D. Puglisi, J. Eriksson, I. Shtepliuk, R. Stenberg, Linköping University (Sweden), K. Montelius, National Board of Forensic Medicine, Linköping (Sweden), E. Tavaglione3, B. Fabbri, University of Ferrara, Ferrara (Italy)

T5.1: Gas Sensors 3

Chair: Renaud Leturcq

T5.1.1 **Activated Carbon in Focus: Is It the Key to Better NO? Gas Sensors? 122**
P. Kyokunzire, J. Zaraket, V. Fierro, A. Celzard, University of Lorraine, Epinal (France)

T5.1.2 **Ammonia flue gas sensors for SCR applications: A comparison between zeolite-based capacitive sensors and mixed-potential sensors utilizing vanadia-based electrodes 124**
R. Moos, T. Wöhrl, N. Donker, D. Schönauer-Kamin, G. Hagen, University of Bayreuth, Bayreuth (Germany)

T5.1.3 **Enhanced Hydrogen Sensing Using Palladium-Functionalized MoO3-x Nanosheets Synthesized via Anodic Oxidation..... 126**
S. Shahabadi, M. Ranjbar, A. Tavallaei, Isfahan University of Technology, Isfahan (Iran), V. Salari, University of Calgary, Calgary (Canada)

T5.1.4 **Room Temperature CO2 Gas Sensor Based on Carbon Polymer Dots - PEDOT: PSS Composite Thin Film 128**
A. M. Laera, G. Cassano, M. Penza, ENEA - Italian National Agency for New Technologies, Energy and Sustainable Economic Development, Brindisi (Italy)

T5.2: Sensors for Medicine and Life-Sciences 1

Chair: Wojciech Kubicki

T5.2.1 **Early-stage Detection of Ovarian Cancer through E-nose Odor Profile Determination 130**
J. Eriksson, I. Shtepliuk, L. Meng, D. Puglisi, C. Borgfeldt, Linköping University, Linköping (Sweden)

T5.2.2 **An Optically-Induced Dielectrophoresis-Based Platform for Enhanced Identification of Prostate Cancer Cells with Different Grades of Malignancy..... 132**
J. Filippi, P. Casti, F. Corsi, G. Antonelli, G. Curci, M. D'Orazio, A. Riccardi, E. Debbi, A. Mencattini, E. Martinelli, University of Rome Tor Vergata, Rome (Italy), A. Pelliccia, Fondazione PTV - Policlinico Tor Vergata, Rome (Italy), M. Scagliotti, L. Mariucci, Italian Nation Research Council (CNR), Rome (Italy), S. L. Neale, University of Glasgow, Glasgow (United Kingdom)

T5.2.3 **Signal Averaging with Heartbeat Envelope for Non-Contact Heart Sound Measurement..... 134**
S. Muramatsu, J. W. Fastier-Wooller, M. Yamamoto, T. Itoh, The University of Tokyo, Tokyo (Japan)

T5.3: Biochemicaland Environmental Sensors 1

Chair: Dorota Pijanowska

T5.3.1 **AlN piezoelectric micromachined ultrasound transducer (pMUT) for E. Coli detection.....136**
V. Fabre, G. Daufouy, Romain Liechti, B. Fain, J. Bastien, T. Alava, S. Giroud, Univ. Grenoble Alpes, CEA, Grenoble (France), A. Laborde, F. Mathieu, Université de Toulouse, Toulouse (France)

T5.3.2 **Fiber optic sensors based on Mach-Zehnder Interferometer for the detection of bacterial biofilms 138**
A. Rashidi, F. Esposito, A. Srivastava, S. Campopiano, A. Iadicicco, University of Naples "Parthenope", Naples (Italy), A. Sacco, G. Di Prisco, Institute for Composites and Biomaterials-CNR, Portici (Italy) Sustainable Plant Protection-CNR, Portici (Italy)

T5.3.3 **Development of Wearable Lactate Sensors with Dynamic Visual Pattern Responses.....140**
Y. Kanekiyo, E. Sakai, Kitami Institute of Technology, Kitami (Japan)

T5.3.4 **A Flexible Glucose Electrochemical Sensor for Textile Integration 142**
M. Martínez-Estrada, I. Gil, R. Fernández-García, Universitat Politècnica de Catalunya, Terrassa(Spain)

T6.1: Gas Sensors 4

Chair: Eduard Llobet

T6.1.1 **Development of Piezoelectric Micro-Cantilever Gas Sensor.....144**
J. Moore, A. Michael, The University of New South Wales Sydney, Sydney (Australia)

T6.1.2 **Rapid Detection of Linalool Using Solidly Mounted Resonators for Plant Health Monitoring 146**
U. Yaqoob, S. Esfahani, M. Cole, J. W. Gardner, University of Warwick, Coventry (United Kingdom), B. Urasinska-Wojcik, Sorex Sensors Ltd, Cambridge (United Kingdom)

T6.1.3 **Metal-Organic Framework (MOF)-based Materials for Electrochemical Sensing.....148**
C. Clemente, V. Gargiulo, L. Cimino, M. Alfè, National Research Council of Italy, Naples (Italy), C. Clemente, G. P. Pepe, G. Ausanio, University of Naples Federico II, Naples (Italy)

T6.1.4 **Frequency Multiplexing Method for Implementing a Reference Channel in Resonator-enhanced Direct Photoa-coustic Setups 150**
D.Sieg, V. Kuczius, G. Rodríguez Gutiérrez, S. Palzer, Technical University Dortmund, Dortmund (Germany)

T6.2: Sensors for Medicine and Life-Sciences 2

Chair: Małgorzata Szczerska

T6.2.1 **Impedance Spectroscopy Based Flow Rate Monitoring in Autonomous Cell Analytical Micro-Capillary Systems.....152**
P. Fürjes, D. Bereczki, L. Bató, Zs. Szomor, J. M. Bozorádi, O. Hakkel, E. L. Tóth, HUN-REN Centre for Energy Research, Budapest (Hungary), K. Papp, Eötvös Loránd University, Budapest (Hungary), J. Prechl, Diagnosticum Zrt, Budapest (Hungary)

T6.2.2 **A Microfluidic Platform based on LIG Electrodes and Machine learning for Real-Time Skeletal Muscle Analysis 154**
G. Curci, M. Marini, J. Filippi, G. Antonelli, P. Casti, M. D'Orazio, A. Riccardi, E. Debbi, S. Pescetelli, A. Agresti, A. Mencattini, E. Martinelli, University of Rome Tor Vergata, Rome (Italy)

T6.2.3 **Method for the Detection of Blood Perfusion in Intracranial Tissues with Optical Fiber Sensor.....156**
V. R. Marrazzo, M. A. Cutolo, F. Fienga, M. Riccio, A. Irace, G. Breglio, University of Naples Federico II (Italy)

T6.3: Biochemical and Environmental Sensors 2

Chair: Marcin Urbanowicz

T6.3.1 Flexible surface-enhanced Raman spectroscopy sensor for wearable devices 158
K. Milenko, E. Vereshchagina, A. Ellingsen, K. Milenko, E. Escobedo-Cousin, C. Hoang, S. Zonetti, A. Liberale, E. Vereshchagina, SINTEF Digital, Oslo (Norway)

T6.3.2 DNA-scaffold biosensors for real-time pH tracking in dynamic environments 160
G. Antonelli, A. Mencattini, G. Curci, J. Filippi, A. Riccardi, P. Casti, E. Debbi, M. D'Orazio, E. Martinelli, Department of Electronic Engineering, University of Rome Tor Vergata, Rome (Italy), A. Chamorro-Garcia, A. Idili, University of Rome Tor Vergata, Rome (Italy)

T6.3.3 Modelling and Design of a Microfluidic Platform for Precision Exposure to Environmental Samples of Surface-Enhanced Raman Scattering Sensors 162
S. Zonetti, E. Vereshchagina, K. Milenko, SINTEF Digital, Oslo (Norway)

W7.1: Gas Sensors 5

Chair: Barbara Fabbri

W7.1.1 Electropolymerization of Amino-Derived Silicon Phthalocyanines for Chemical Sensing Applications 164
M. Cyr, B. H. Lessard, J. L. Brusso, University of Ottawa, Ottawa (Canada), G. Magna, F. Pizzoli, A. Mita, L. Di Zazzo, R. Paolesse, University of Rome Tor Vergata, Rome (Italy)

W7.1.2 WO3/ SnS2 Hybrid Material for ppb-level NO2 Detection 166
A. Fdhila, F.E. Annanouch, E. Llobet, University Rovira i Virgili, Tarragona (Spain), A. Fdhila, Z. Haddi, NVISION Systems and Technologies, Barcelona (Spain)

W7.1.3 Morphological Control of ZnO and ZnO@NiO Heterojunctions: Improving Sensitivity, Selectivity, and Humidity Resistance for Gas Sensing Applications 168
P. P. Ortega, E. Longo, Federal University of São Carlos, São Carlos (Brazil), S. Gherardi, M. Astolfi, G. Zonta, SCENT S.r.l., Ferrara (Italy), E. Spagnoli, G. Cruciani, C. Malagù, University of Ferrara, Ferrara, (Italy)

W7.1.4 Ultrafast Recovery and Humidity Effect in a MoS2-ZnO functionalized CNTs Array driven as an e-nose 170
M. Galvani, L. Sangaletti, Surface Science and Spectroscopy Lab at I-Lamp, Department of Mathematics and Physics, Università Cattolica del Sacro Cuore, Brescia (Italy)

W7.2: Theory, Design and Testing

Chair: Ulrich Schmidt

W7.2.1 The Need for Fast Olfactory Sensing in Turbulent Environments 172
N. Dennler. A. Güntner. ETH Zurich. Zurich (Switzerland)

W7.2.2 Improving Computational Efficiency of Finite Element MEMS Transducer Models by Fine-Tuned Homogenization 174
S. Bielefeldt, F. Püntener, C. Rüttimann, C. Roman, ETH Zurich, Zurich (Switzerland)

W7.2.3 Toward Digital Twins in Orthopedic Implants: Finite Element Analysis of Malalignment Effects in Instrumented Tibial Trays 176
L. Merzak, C. Ott, E. Saoutieff, P. Gasnier, V. Elhorga, S. Boisseau, CEA Leti, Grenoble (France)

W7.2.4 Finite-Element Analysis of Nodus-Driven Flexibility in Dragonfly Wings for Micro-Air Vehicles 178
M. U. Yousaf, R. Gaidys, Kaunas University of Technology, Kaunas (Lithuania)

W7.3: Novel Technologies and Applications of Sensors 3

Chair: Karolina Laszczyk

W7.3.1 **Smart Wastewater Surveillance of Viral Antibodies via Real-Time Optical Fiber Sensing 181**
M. Szczerska, F. Janiak, K. Cierpiak, P. Wityk, P. Sokolowski,), S. Fudala-Ksiazek, A. Luczkiewicz, Gdansk University of Technology, Gdansk (Poland), University of Sussex, Brighton (United Kingdom), , M. Kosowska, Bydgoszcz University of Science and Technology, Bydgoszcz (Poland), S. Garcia-Galan, Jean Universitety, Lineares (Spain)

W7.3.2 **A 3D printed RT-LAMP microdevice for the detection of feline calicivirus 183**
W. Kubicki, J. Kornicka, R. Walczak, Wroclaw University of Science and Technology, Wroclaw (Poland)

W7.3.3 **PCB-Based Electrochemical Electrodes with Self-temperature Regulation Functionality for Electrochemical Studies at Target Temperatures 185**
M. Derakhshani, T. Posnicek, M. Brandl, University for Continuing Education, Krems (Austria), W. Hilber, S. Mirsian, B. Jakoby, Johannes Kepler University, Linz (Austria)

W7.3.4 **Sensitivity Tuning and ON/OFF Switching in a Resonant Micro-accelerometer 187**
A. Zobova, M. Drizovsky, S. Krylov, Tel Aviv University, Tel Aviv (Israel)

W8.1: Gas Sensors 6

Chair: Michał Krysztof

W8.1.1 **Gasochromic Tungsten Oxide Thin Films for Hydrogen Monitoring in Natural Gas 189**
A. Longato, Pietro Fiorentini SpA, Arcugnano (Italy), E. Colusso, A. Martucci, University of Padova, Padova (Italy)

W8.1.2 **Optical Response to Hydrogen of WO3 Thin Films Pre-pared by Magnetron Sputtering 191**
W. Weichbrodt, J. Domaradzki, M. Mazur, Wroclaw University of Science and Technology, Wroclaw (Poland)

W8.2: Biochemical and Life-Science Sensors

Chair: Elizaveta Vereshchagina

W8.2.1 **A field-effect device for specific and label-free biosensing 193**
G. Shalev, Ben-Gurion University of the Negev, Beer Sheva (Israel)

W8.2.2 **The Art of Building a Good Chemiresistive Sensor Based on AC: Tips and Tricks for Better Detection Performance 194**
J. Zaraket, P. Kyokunzire, V. Fierro, A. Celzard, Université de Lorraine, Épinal (France)

W8.2.3 **Selective Optical and Chemoresistive H2 Sensors by Nanosecond Pulsed Laser Annealing of Sol?Gel VO2 Films 196**
M. Basso, E. Colusso, M. Cattelan, E. Napolitani, A. Martucci, University of Padova and INSTM, Padova (Italy), V. Paolucci, V. Ricci, C. Cantalini, University of L'Aquila, L'Aquila (Italy)

W8.3: Biochemical and Phyxical Sensors

Chair: Agnieszka Krakos

W8.3.1 **Strain Sensors Based on Hybrid Electronics with Flexible Packaging 198**
D. Zymelka, Y. Takei, National Institute of Advanced Industrial Science and Technology, Tsukuba (Japan)

W8.3.2 **Analyzing Electrochemiluminescence Signal and Detection Limits Through Device-Independent Color Space Mapping 200**
S. R. Muiña, R. K. R. Gajjala, E. F. Martín, F. J. del Campo, UPV/EHU Parque Científico, Leioa (Spain)

W8.3.3 **High-Performance and Low-Cost Microfluidic-Electrohemical Biosensors 202**
Z. Zhang, National Research Council Canada, Ottawa (Canada), Z. Wang, C. Xu, McMaster University, Hamilton (Canada)

MP: Poster Session I

3D Printed Sensors and AI for Sensors

MP1 **A 3D Printed Strain Sensor Employing Conductive TPU for Marine Applications** **204**
D.N. Pagonis, A. Stavros, I. Iakovidis, S. Dimitrellou, G. Kaltsas, University of West Attica, Athens (Greece)

MP2 **Bayesian Inference for Reliable Gas Sensing with Metal-Oxide Sensors** **206**
S. Pültz, Saarland University, Saarbrucken (Germany)

Bio/chemical and Environmental Sensors

MP3 **Selective Formaldehyde Sensing: Unraveling Metal–Support Interaction Effects in Single-Atom Cu Catalysts** **208**
H. Shin, A. Güntner, ETH Zürich, Zurich (Switzerland)

MP4 **PEDOT: PSS gated field-effect transistor for ion sensing applications** **210**
X. T. Vu, Y. Zhang, S. Ingebrandt, RWTH Aachen University, Aachen (Germany)

MP5 **(MgCoNiCuZn)O High-Entropy Oxide as Novel Gas Sensing Material** **212**
I. Vergés Gazulla, P. Pellegrino, G. Domenech Gil, A. Romano Rodriguez, Universitat de Barcelona, Barcelona (Spain)

MP6 **Dependence of the Determination of Refractive Index Sensitivity of Plasmonic Sensors on the Calibration Method** **214**
N. Tarpataki, A. Bonyár, Budapest University of Technology and Economics, Budapest (Hungary), T. Lednický, Leibniz Institute of Photonic Technology, Jena (Germany)

MP7 **Metal Organic Frameworks Based Quartz Microbalance for Ammonia Detection** **216**
C. Clemente, V. Gargiulo, L. Cimino, M. Alfè, National Research Council of Italy, Naples (Italy), C. Clemente, G. P. Pepe, G. Ausanio, University of Naples Federico II, Naples (Italy)

MP8 **Dual-Channel Fluorescence Optical Sensor for Microplastic Detection and Polymer Classification** **218**
Y. Li, V. Allegra, R. Pizzoferrato, C. Di Natale, A. Catini, University of Rome Tor Vergata, Rome (Italy), E. Nicolai, Saint Camillus International University of Health Sciences, Rome (Italy)

MP9 **A microfluidic system with integrated inkjet-printed capacitive sensors for biosensing applications** **220**
B. Andò, D. Greco, S. Castorina, University of Catania, Catania (Italy), C. Trono, S. Tombelli, N. Marcucci, M. Fytory, Consiglio nazionale delle Ricerche Istituto di Fisica Applicata;Nello Carrara, Firenze (Italy), M. R. Guascito, G. Lamberti, L. Martina, University of Salento, Lecce (Italy), N. Cennamo, University of Campania "Luigi Vanvitelli", Aversa (Italy)

MP10 **Application of ZnO–Imine Nanocomposites for Optical Detection of Metal Ions in Water** **222**
I. Tepliakova, M.M. Drava, R. Viter, University of Latvia, Riga (Latvia), G. Zvirgzdine, Center for Physical Sciences and Technology, MB "SensoGrafa", Vilnius (Lithuania)

MP11 **Detection of Cerium(III) by Optimized Adsorption Stripping Voltammetry Using a New Electrochemical Sensor** **224**
M. Grabarczyk, E. Wlazlowska (Poland)

MP12 **Copper film electrode as an electrochemical sensor for the determination of trace concentrations of lead ions in envi-ronmental waters by anodic stripping voltammetry** **226**
M. Grabarczyk, A.Wawruch (Poland)

MP13 **Impedimetric Detection of COVID Proteins on Functionalized Boron Doped Diamond Electrodes – is the Redox Marker Necessary?** **228**
A. Olejnik, R. Bogdanowicz, Gdansk University of Technology. Gdansk (Poland)

MP14 **The Effect of Perinone Polymer Potential Polymerization Range on its Effectiveness as a Solid Contact in Ion-Selective Electrodes** **230**
C. Wardak, K. Morawska, University of Maria Curie-Sklodowska, Lublin (Poland)

MP15 **Improving Analytical Parameters of Ammonium Potenti-ometric Sensors Using Carbon Nanocomposite** **232**
C. Wardak, K. Morawska, University of Maria Curie-Sklodowska, Lublin (Poland)

MP16 **Highly Sensitive Biosensor Platform Based on Substrate Bias Extended-Gate Field-Effect Transistor 234**
F. Ughi, Chang Gung University, Taoyuan (Taiwan), E. Remiszewska, D. G. Pijanowska, Polish Academy of Sciences, Warsaw (Poland), C.-S. Lai, National Yang Ming Chiao Tung University, Hsinchu (Taiwan), C.-M. Yang Chang Gung University, Taoyuan (Taiwan)

MP17 **Study Modification Parameters for Electrochemical Detection of Benzotriazole 236**
J. Vujančević, N. Sodnik, M. Hadolin, Z. Samardžija, K. Žagar Soderžnik, Jožef Stefan Institute, Ljubljana (Slovenia)

MP18 **Towards Polyamine Biosensors: Stabilizing Prussian Blue Electrodes with Polymers for Sensitive H?O? Detection....238**
N. Sodnik, G. Della Pelle: K. Žagar Soderžnik, Jožef Stefan Institute, Ljubljana (Slovenia), Jožef Stefan International Postgraduate School, Ljubljana (Slovenia)

MP19 **Sensitivity Enhancement of LSPR Sensors on Flexible Glass Substrates through Bending-Induced Deformation....240**
J. Vujancevic, N. Sodnik, M. Hadolin, Z. Samardžija, K. Žagar Soderžnik, Jožef Stefan Institute, Ljubljana (Slovenia), N. Sodnik, K. Žagar Soderžnik, Jožef Stefan International Postgraduate School, Ljubljana (Slovenia), M. Hadolin, K. Žagar Soderžni

MP20 **A photoelectrochemical electrode of electrodeposited cuprous oxide on ITO/glass with deposition time adjustment....242**
L. Sze Tsui, C.-M. Yang, I. Shaheen, Chang Gung University, Taoyuan (Taiwan), M. Urbanowicz, A. Paziewska-Nowak, D. G. Pijanowska, Polish Academy of Sciences, Warsaw (Poland)

Energy Harvesting for Sensors

MP21 **Lead-Free Piezoelectric Vibration Energy Harvesters: Spark Plasma Sintered KNN compared with commercial KNN 244**
G. Forges, N. Bencharef, H. Debéda, Univ. Bordeaux, Talence Cedex (France), U.-C. Chung, C. Elissalde, Univ. Bordeaux, Pessac (France), D. Gibus, Univ. Savoie Mont Blanc, Annecy (France)

MP22 **Optimal Design of Cantilever-type Vibro Harvester Working at Second Eigenfrequency....246**
P. Skerys, R. Gaidys, B. Narijauskaite, Kaunas University of Technology, Kaunas (Lithuania)

MP23 **Design of a set-up for Measuring Magnetostrictive Materials without Strain Gauges to assess the magnitude of Villari Effect....248**
W. Pałka, K. Laszczyk, Wrocław University of Science and Technology, Wrocław (Poland)

Gas Sensors

MP24 **Nanoporous Materials for Light and Heat Activated Gas Sensing 251**
L. Egger, F. Sosada-Ludwikowska: A. Köck, Materials Center Leoben Forschung GmbH (Austria), N. Rising, L. Sacco, VSParticle B.V. (The Netherlands)

MP25 **Bi2O2CO3/CuO Micro-flowers with Abundant Oxygen Vacancies for Enhanced VOC Detection....253**
Z. Zheng, K. Liu, Y. Zhou, Yangzhou University, Yangzhou (PR China), C. Bittencourt, University of Mons, Mons (Belgium), C. Zhang, Yangzhou University, Yangzhou (PR China)

MP26 **Selective Benzene Sensing Enabled by Catalytically-Active Metastable Nanoparticles....255**
M. D'Andria, T. E. Abi-Ramia Silva, A. T. Güntner, ETH Zürich, Zurich (Switzerland)

MP27 **Single-Atom Metal Catalysts on Flame-Made Oxide Supports for Gas Sensing....257**
H. Shin, A. Güntner, ETH Zürich, Zurich (Switzerland)

MP28 **Enhancing Selectivity Through Fast Heater Cycles with MOx Sensors....259**
N. Dennler. J. Sommerhäuser. A. Güntner. ETH Zurich. Zurich (Switzerland)

MP29 **Evaluation of a MEMS-based Absolute Humidity Sensor using Thermal Conductivity 261**
S. Emperhoff, J. Wöllenstein, Albert-Ludwigs-Universität, Freiburg (Germany), M. Eberl, Infineon Technologies AG, Neubiberg (Germany)

MP30 **Electro-Optical Gas Sensing Characteristics of PEDOT:PSS Thin Films 263**
Z. Hamzei, I. Gràcia, E. Figueras, S. Vallejos, Institute of Microelectronics of Barcelona (IMB-CNM, CSIC), Barcelona, (Spain)

MP31 **Ethanol sensing at room temperature via ZnS nanostructure-based optical approach.....265**
H. Trabelsi, I. Gràcia, C. Cané, S. Vallejos, Institute of Microelectronics of Barcelona (IMB-CNM, CSIC), Barcelona (Spain), H. Trabelsi, K. Alouani, University of Tunis El Manar, Tunis, (Tunisia)

MP32 **MoS2-InSe heterostructure synthesized via Liquid Phase Exfoliation for NO2 sensing 267**
J. Sharma, D. Fadil, E. Llobet, Universitat Rovira i Virgili, Tarragona (Spain)

MP33 **In-depth Characterisation of a Colorimetric Label for Formaldehyde Monitoring. 269**
M. González-Gómez, A. Zymohliad, I. Benito-Altamirano, O. Casals, C. Fàbrega, M. i Franqués, University of Barcelona, Barcelona (Spain), J. D. Prades, Technische Universität Braunschweig, Braunschweig (Germany)

MP34 **Palladium Doped WSe2 for Gas Sensing Applications 271**
M. I. Rizu, F. E. Annanouch, J. Sharma, D. Fadil, E. Llobet, Universitat Rovira i Virgili, Tarragona (Spain)

MP35 **Development of Metallic inks for the Fabrication of a Flex-ible Metal Oxide Gas Sensors by Inkjet Printing Process.....273**
B. Le Porcher, M. Rieu, J.-P. Viricelle, University Lyon, Saint-Etienne (France)

MP36 **Hexagonal WO3 nanorods for Selective H2S Detection: Synthesis, Characterization, and Gas Sensing Properties. 275**
S. B. Haj Fraj, G. Neri, University of Messina, Messina (Italy), V. Zabolotnii, R. Viter, University of Latvia, Riga, (Latvia), M. Sahul, Slovak University of Technology in Bratislava, Trnava (Slovakia), A. Fioravanti, National Research Council (CNR), Ferrara (Italy)

MP37 **Comparative analysis of WO^3 nanostructures for chemoresistive ammonia sensing 277**
D. Ahmed, E. Spagnoli, G. Cruciani, V. Guidi, B. Fabbri, University of Ferrara, Ferrara (Italy), M. Ferroni, University of Brescia, Brescia (Italy), M. Ferroni, CNR-ISMN, Bologna (Italy)

MP38 **Impedance Spectroscopy: A Key to More Selective and Reliable Chemoresistive Gas Sensors.....279**
M. Magoni, Eurac Research, Bolzano (Italy), G. Andrea, M. Valt, P. Tosato, A. Orlando, R. Furlan, Fondazione Bruno Kessler, Trento (Italy)

MP39 **Novel multi pixel-based gas sensor fabricated by local Inkjet printing of metal-oxides structures 281**
A. Debot, V. Rogé, S. Glinsek, S. Girod, N. Adjeroud, R. Leturcq, Luxembourg Institute of Science and Technology, Belvaux (Luxembourg), H. Pakdel, D. Zappa, University of Brescia, Brescia (Italy), I. Boehme, Sciosense Germany GmbH, Reutlingen (Germany)

MP40 **Novel pyridinium luminophores as optical gas sensors for detection of volatile acids 283**
R. Viter, V. Zabolotnii, M. M. Drava, A. Kinens, University of Latvia, Riga (Latvia)

MP41 **H2S Sensor Studied by Electrochemical Impedance Spectroscopy 285**
K. Schneider, B. Dziurdzia, K. Zakrzewska, AGH University of Krakow, Krakow (Poland)

MP42 **Selectivity Acetone Detection by Spinel MnxOy Sensor.....287**
R. Theodoro, D. P. Volanti, São Paulo State University (UNESP), São José do Rio Preto (Brazil), T. E. A. Silva, M. D'Andria, A. T. Güntner, ETH Zurich, Zurich (Switzerland)

MP43 **Sub-ppm Methane Sensing by Spark-Ablation-Synthesized SnO2 Nanoparticle-based Materials 289**
D. Gounaris, S. E. Pratsinis, G. Biskos, Climate and Atmosphere Research Center, Nicosia (Cyprus), A. Baut, A. Güntner, Human-centered Sensing Laboratory, ETH Zürich, Zürich (Switzerland)

MP44 **The Dimensionality of MOX Sensors in Air Quality assessment 291**
L. Miranda, B. Dorizzi, M. Hariz, D. Petrovska, J. Boudy, Télécom SudParis, Palaiseau (France), N. Redon, C. Duc, M. Verriele, IMT Nord Europe, Douai (France), J. Montalvão, Universidade Federal de Sergipe, São Cristóvão (Brazil)

MP45 **Experimental Characterization of Negative Temperature Coefficient Resistor Noise Depending on Polarization Voltage 293**
A. Riaud, ABB Corporate Research, Baden-Dättwil (Switzerland)

MP46 **Investigations on Ammonia Using Resistive and Photoa-coustic Sensor Elements 295**
H. Wünscher, C. Heinze, S. Herbst, T. Schildhauer, CiS Forschungsinstitut für Mikrosensorik, Erfurt (Germany)

MP47 **Integration of MEMS-based plasma emission sources in a a low volume flow cell.....297**
A. Ellingsen, K. Milenko, E. Escobedo-Cousin, C. Hoang, S. Zonetti, A. Liberale, E. Vereshchagina, SINTEF Digital, Oslo (Norway)

MP48 **Morphology Dependent Response of SnO2 Gas Sensors from Spark Ablation, Spray Pyrolysis, and Sputter Coating Techniques** **299**
N. Rising, L.Sacco, VSParticle, Delft (Netherlands), L. Eggers, A. Köck, Material Center Leoben Forschung GmbH, Leoben (Austria), C. Mitterer, Montanuniversität Leoben, Leoben (Austria)

Microfluidics

MP49 **Voltage-Triggered Wetting in Bio-Inspired Microfluidic Channels** **301**
M. Weiß, W. Baumgartner, B. Heise, E. Leiss-Holzinger, M. Kaltenbrunner, S. Puttinger, G. Buchberger, Johannes Kepler University Linz, Linz (Austria)

MP50 **Numerical Investigation of Microfluidics Micromixer Integrated with Screw Element and Complex Micropillar Structure for Enhanced Mixing** **303**
M. Waqas, A. Palevicius, Kaunas University of Technology, Kaunas (Lithuania)

MP51 **Microgravity-induced wet chemical etching of borosilicate glass – towards enhanced microfabrication methods** **305**
K. Baranowski, M. Białas, A. Krakos, Wroclaw University of Science and Technology, Wrocław (Poland)

MP52 **Rapid microfluidic hydrogel imprint based on CNT-induced thermoresponsive effect** **307**
M. Zóltowski, A. Cieslak, A. Krakos, J. Detyna, R. Walczak, Wroclaw University of Science and Technology, Wroclaw (Polska)

Novel Technologies and Applicatons of Sensors

MP53 **Plant Growth Monitoring Using Electromechanical Sensors** **309**
B. Lehner, A. Stoiber, F. Bauernfeind, F. Stöger, G. Buchberger, Johannes Kepler University Linz, Linz (Austria)

MP54 **Energy-Efficient Sensor System for Structural Wear Detection in Building Envelopes for Digital Twin and Predictive Analytics** **311**
K. Giske, S. Hirsch, Brandenburg University of Applied Sciences, Brandenburg (Germany)

MP55 **C-V measurement of Schottky Barrier LSMO/Nb:STO heter-ostructure dedicated to optoelectronic devices** **313**
F. Gning, J. Blond, V. Pierron, L. Méchin, B. Guillet, Caen Normandy University, Caen (France)

MP56 **Inkjet-Printed PEDOT:PSS/ZnO Diodes on a Flexible Polyi-mide Substrate** **315**
A. Apostolakis, D. Barmpakos, D.-N. Pagonis, G. Kaltsas, University of West Attica, Athens (Greece), F. Jaber, K. Aidinis, Ajman University, Ajman (United Arab Emirates)

MP57 **Study of the material variability and processing tech-niques on white light photoluminescence sensors based on porous Si, ZnO and carbon dots** **317**
S. Kiniklis, N. Chouchoumi, S. N. Katsantonis, N. Ganotis, C. Tsamis, National Center for Scientific Research “Demokritos”, Athens (Greece), S. Gardelis, National and Kapodistrian University of Athens, Athens (Greece), N. Kagiara, K. V. Kordatos, E. Hourdakis, National Technical University of Athens, Athens (Greece)

MP58 **Power consumption analysis of an OpenThread border router in a Wireless Sensor Network for Precision Agriculture** **319**
A. Buratti, A. Checco, University of Rome, La Sapienza, Rome (Italy), D. Polese, Consiglio Nazionale delle Ricerche, Italy, Rome (Italy)

MP59 **UV-sensitive Hydrogel GelMA Filled with FeCo-PET Particles** **321**
W. Chuda, Wroclaw University of Science and Technology (Poland), M. Kobayashi, Tohoku University (Japan), K. Laszczyk, Wroclaw University of Science and Technology (Poland), M. Yamamoto, Tohoku University (Japan)

MP60 **Thin-Film Strain Gauge Sensor to determine the difference between infill cell designs for the sandwich beams** **323**
R. Trzeciakowski, R. Pawlowski, K. Laszczyk, P. Piórkowski, Wroclaw University of Science and Technology, Wroclaw (Poland)

MP61 **Detection of Electron Beam in Atmospheric Pressure Using CMOS Image Sensor** **325**
M. Krysztof, K. Baranowski, M. Zychla, Wroclaw University of Science and Technology, Wroclaw (Poland), M. Hausladen, R. Schreiner, Ostbayerische Technische Hochschule, Regensburg (Germany), A. Knápek, Institute of Scientific Instruments of the Czech Academy of Sciences, Brno (Czech Republic)

Physical Sensors

MP62 **Piezoresistive Pressure Sensors Based on ZrO? Substrate Fabricated by Photolithography and Inkjet Printing** **327**
V. Povolny, A. Laposa, J. Kroutil, Czech Technical University in Prague, Prague (Czech Republic)

MP63 **Elastomer-based flexible THz metasurfaces for sensing applications** **329**
A. Kovacs, J. Petit, B. Sittkus, V. Bucher, U. Mescheder, Furtwangen University, Furtwangen (Germany), P. Lopato, M. Herbko, West Pomeranian University of Technology, Szczecin (Poland)

MP64 **GNPs-Based Strain Sensors Derived from Recycled Cellulose Acetate: Fabrication and Analysis** **331**
P. Zarafshani, F. Esposito, S. Campopiano, A. Iadicicco, University of Naples Parthenope, Naples (Italy), M. Zahid, A. Kumar, Leonardo SPA, Rome (Italy), F. Cilento, L. Sansone, M. Giordano, National Research Council of Italy, Portici (Italy)

MP65 **Development of a Ferrofluidic Inclinometer exploiting a Vision-based Readout Strategy** **333**
B. Andò, D. Greco, S. Castorina, A. Campisi, University of Catania, DIEEI, Catania (Italy)

Quantum Sensors

MP66 **A Calibration Method for Spatial Localization of OPM Sen-sors Based on a Rigid Coil Array Framework** **335**
W. Xu, F. Cao, Y. Li, C. Wang, X. Ning, Beihang University, Beijing (China)

MP67 **Removal method of correlation artifact based on reference magnetic signal** **337**
Y. Li, H. Lu, F. Cao, C. Wang, X. Ning, Beihang University (Beijing), D. Wang, Beijing Microelectronics Technology Institute, Beijing (China)

Theory, Modelling, Design and Testing

MP68 **Comprehensive Mass Resolution Model for 2D Nanomechanical Resonant Sensors** **339**
T. Platten, P. Zhang, C. Hierold, ETH Zurich, Zurich (Switzerland)

MP69 **Simulation and Optimization of Magnetic Field Actuated MEMS-Based Metasurface for Terahertz Applications** **341**
B. Szymanik, P. Lopato, G. Psuj, M. Herbko, M. Maciusowicz, West Pomeranian University of Technology, Szczecin (Poland), P. Kondamarri, J. Petit, A. Kovacs, U. Mescheder, Furtwangen University, Furtwangen im Schwarzwald (Germany)

MP70 **Simulation Environment for Optimized Grating-Based Plasmon Couplers** **343**
P. Sarapukdee, C. Spenner, D. Schulz, S. Palzer, Technical University Dortmund, Dortmund (Germany)

MP71 **Time-integrated Sensing to Study Extreme Weather Events in Pulsed Pesticide Contamination** **345**
N. Tariq, C. Martin, F. Regan, Dublin City University, Dublin (Ireland), H. J. Albrechtsen, Technical University of Denmark, Lyngby (Denmark), K. B. M. Kuszewska, SINTEF, Oslo (Norway)

MP72 **Establishing a Raman spectra database for the detection of Terbuthylazine metabolites using SERS-based optical sensors** **347**
I.-A. Baragau, O. Rasoga, A. Costas, National Institute of Materials Physics, Magurele (Romania), H.-J. Albrechtsen, Technical University of Denmark, Lyngby (Denmark), K.Gizynski, Polish Academy of Sciences, Warsaw (Poland), K. Milenko, E. Vereshchagina, J. Jose, SINTEF, Oslo (Norway), F. Regan, Dublin City University, Dublin (Ireland)

MP73 **Optimization of Ultrasound Coupling for Clamp-On Flowmeters Using FEM Tools** **349**
M. Schackmar, A. Bittner, A. Dehé, P. Selle, Axel Sikora, Hahn-Schickard-Gesellschaft für angewandte Forschung e.V., Villingen-Schwenningen (Germany), Thilo Engel, Thomas Hahn-Jose, inoson GmbH, St. Ingbert (Germany)

TP: Poster Session II

Bio/chemical and Environmental Sensors

TP1 **Nanowire Array Biosensor** **351**
A. Yesayan, Swiss Federal Institute of Technology in Lausanne, Lausanne (Switzerland), A. Grabski, Paris-Saclay University, Gif-sur-Yvette (France)

TP2 **Dopamine assessment on conductive polymers/gold NPs with appended metalloporphyrins composites** **353**
T. R. Bastami, F. Pizzoli, F. Caroleo, S. Nardis, R. Paolesse, L. Lvova, University of Rome "Tor Vergata", Rome (Italy)

TP3 **Benchmarking surface sensitivity of LSPR sensors: com-parison of experimental methods** **355**
R. Kovács, A. Bonyár, Budapest University of Technology and Economics, Budapest (Hungary), T. Lednický, M. Ziegler, Leibniz Institute of Photonic Technology, Jena (Germany)

TP4 **The Importance of Surface Sensitivity in the Optimization of Plasmonic Sensors** **357**
A. Bonyár, R. Kovács, N. Tarpataki, Budapest University of Technology and Economics, Budapest (Hungary), T. Lednický, Leibniz Institute of Photonic Technology, Jena (Germany)

TP5 **Metal Oxide – Schiff Base Nanofibers as Novel Optical Sensors for Different Metal Ion Detection in Aquatic Environment** **359**
D. Mandal, M. Barwiolek1, D. Jankowska, A. Kaczmarek-Kędziera, T. M. Muzioł, Nicolaus Copernicus University in Torun, Torun (Poland), I. Tepliakova, R. Viter, University of Latvia, Riga, (Latvia)

TP6 **Two-Step Nanostructuring of Carbon Electrodes for Multiplexed Electrochemical Sensing Using Off-Axis MPECVD and Laser Micropatterning** **361**
M. Pierpaoli, I. Kaczmarzyk, A. Olejnik, R. Bogdanowicz, Gdansk University of Technology (Poland)

TP7 **Metasurface development for SERS-based optical sensors** **363**
A. M. Baracu, A. Dinescu, National Institute for Research and Development in Microtechnologies-IMT Bucharest, Voluntari (Romania), K. Milenko-Kuszewska, SINTEF Microsystems and Nanotechnology, Oslo (Norway), O. Rasoga, I.-A. Baragau, National Institute of Materials Physics, Magurele (Romania)

TP8 **Hydrogen Sensors for Oxygen-Free Ambient** **365**
N. Ma, Z. Liu, Y. Li, Shanghai Institute of Ceramics, Shanghai (China), A. Vasiliev, Dubna State University, Dubna (Russia), O. Kul,LLC "C-Component", Moscow (Russia), A. Shaposhnik, Voronezh State Agrarian University, Voronezh (Russia), M. Yablokov, Enikolopov Institute of Synthetic Polymeric Materia, Moscow (Russia)

TP9 **Electronic Circuit for Temperature and Humidity measurements for the purpose of the Mini Robot Caterpillar** **367**
K. Wilczewska, A. Musiał, M. Flak, K. Laszczyk, Politechnika Wrocławska, Wrocław (Poland)

TP10 **Colorimetric Detection of Cortisol Using an Alginate-Based Biosystem** **369**
S. Izaddoust, University of the Basque Country UPV/EHU, Leioa (Spain), L. Basabe-Desmonts, Fernando Benito-Lopez, University of the Basque Country UPV/EHU, Vitoria-Gasteiz (Spain)

TP11 **Direct-printed amiodarone electrochemical sensor. Identi-fication of DNA based bioreceptor** **371**
M. Urbanowicz, A. Paziewska-Nowak, K. Bobrowska, A. Sołdatowska, M. Dawgul, D. G. Pijanowska, Polish Academy of Sciences, Warsaw (Poland)

TP12 **Sensitive cell identification in impedance flow cytometry using optimized dielectric buffer properties and low cost microchannels** **373**
M. Favrod-Coune, O. Guenat, University of Bern, Bern (Switzerland), P. Eberle, Lucerne University of Applied Sciences, Lucerne (Switzerland)

TP13 **Lens-free Microscope for Portable Pollen Grains Imaging System** **375**
A. B. Dharmawan, G. Schöttler, A. Waag, J. D. Prades, Technische Universität Braunschweig, Braunschweig (Germany)

TP14 **Recent Advances in Multiparameter 2D Chemical Imaging of Environmental Samples with Optical Sensors (Optodes)** **377**
A. V. Kalinichev, M. R. Rasmussen, K. Koren, Aarhus University, Aarhus (Denmark)

TP15 **Fabrication of modified á-Fe2O3 NPs on ZnO NRs/Ni-foam nanocomposite as electrode for electrochemical detection of arsenic in drinking water 379**
S. Ngok, R. Yann, X. Liu, M. Willander, O. Nur, Linköping University, Norrköping (Sweden), C. O. Chey, Royal University of Phnom Penh, Phnom Penh (Cambodia)

TP16 **Influences on the Sensitivity of Camera-Based Colorimetric Gas Sensors Systems..... 381**
S. Hoffmann, Fraunhofer EMFT, Munich (Germany), S. Trupp, Bundeswehr University Munich, Neubiberg (Germany)

TP17 **Noble Metal Decorated Graphene Sensor for Detecting Hydrogen at Room Temperature..... 383**
P. K. Kannan, J. W. Gardner, University of Warwick, Coventry (United Kingdom), M. Tyler, Paragraf Ltd, Somersham (United Kingdom)

TP18 **Al-doped ZnO Gas Sensors Toward Safe and Effective Monitoring in Protected Environments..... 385**
E. Tavaglione, A. Rossi, V. Guidi, B. Fabbri, University of Ferrara, Ferrara (Italy), M. Ferroni, Institute for Microelectronics and Microsystems IMM-CNR, Bologna (Italy)

TP19 **Field Calibration Strategies for Methane Monitoring with Electronic Noses..... 387**
G. Domènech-Gil, K. Munnuru Singamshetty, D. Bastviken, Linköping University, Linköping (Sweden), D. Montecinos, Swedish Meteorological, Hydrological Institute SMHI (Sweden)

TP20 **Rapid detection of olive oil markers using a gas chromatography sensor system..... 389**
O. T. Penagos Carrascal. M. Czerny. T. Sauerwald. G. Zeh. Fraunhofer Institute for Process Engineering and Packaging IVV. Freising (Germany). J. Bröckelmann. M. Bücking. Fraunhofer Institute for Molecular Biology and Applied Ecology IME. Schmallenberg (Germany)

TP21 **Optimizing AC Excitation Frequency for Linear Complex Impedance Response in Metal Oxide Semiconductor Gas Sensing..... 391**
H. A. Imran, O. Brieger, C. Bur, A. Schütze, Lab for Measurement Technology Saarland University, Saarbruecken (Germany)

TP22 **Novel Pyridinium Luminophores for Optical Ammonia Detection..... 393**
V. Zabolotnii, R. Viter, M. M. Drava, A. Kinens, University of Latvia, Riga (Latvia)

TP23 **A Novel IoT System for Highly-specific Gas Sensing Applied to Health Monitoring at Home 395**
I. Benito-Altamirano, O. Romera-Aller, M. González-Gómez, C. Fàbrega, Universitat de Barcelona, Barcelona (Spain), I. Benito-Altamirano, Universitat Oberta de Catalunya, Barcelona (Spain), M. Alfaras, Z. Haddi, A. Espinoso, NVISION Systems and Technologies SL, Barcelona (Spain), J. A. Sáez, Sensing&Control SL, Barcelona (Spain)

TP24 **Development of wafer singulation technique for MEMS and MOX gas sensors using 355 nm UV laser ablation process..... 397**
S. Stoukatch, F. Dupont, J.-M. Redouté, Liege University, Liège (Belgium)

TP25 **Response of Silicon Nanowire Arrays to Humidity and Ammonia 399**
M.T. Sultan, E. Fakhri, A. Manolescu, H.G. Svavarsson, Reykjavik University, Reykjavik (Iceland), P. Powroznik, A. Kazmierczak-Balata, W. Jakubik, Silesian University of Technology;Gliwice (Poland)

TP26 **Vacancy-Engineered MoS2 for Selective CO Sensing: A DFT Perspective on Intercalation 401**
D. Florjan, P. Radomski, M. J. Szary, Poznan University of Technology (Poznan, Poland)

MEMS and MOEMS

TP27 **On the design of a magnetically driven quasi-static MEMS micromirror..... 403**
P. Malagò, C. Fleury, S. Lumetti, L. Enger, S. Guerreiro, A. Piot, A. Lagosh, Silicon Austria Labs GmbH, Villach (Austria)

TP28 **Design and Fabrication of Carbon Black Polymer Composite Based Pressure Sensor Array..... 405**
M. A. I. Bhuyan, M. M. Uddin, H. C. Kim, University of Ulsan, Ulsan (South Korea)

TP29 **Comprehensive correlative study of post-treated vertically grown ZnO nanowires 407**
T. Bhadauria, N. Guillaume, G. Ardila, C. Ternon, Univ. Grenoble Alpes, Grenoble (France)

TP30 **Sputter deposited aluminum nitride for an efficient manufacturing of piezoelectric folded MEMS membranes..... 409**
M. T. Becker, D. Becker, A. Bittner, A. Dehé, Hahn-Schickard-Gesellschaft für angewandte Forschung e.V., Villingen-Schwenningen (Germany), A. Dehé, Albert-Ludwigs-Universität, Freiburg (Germany)

TP31 **Modelling and Characterization of PZT-based High Performance PMUTs for In-Air Applications 411**
A.Vogl, G.Sordo, SINTEF Digital, Oslo (Norway), L. Lidicky, Elliptic Laboratories ASA, Oslo (Norway)

TP32 **Study of the possibility to add piezoelectric sensors on boat hulls and investigation of shear stress caused by drag 413**
G. Cayla, P. D. Folkow, Chalmers University of Technology, Göteborg (Sweden), C. Rusu, E. Staaf, V. Udén, Research Institute of Sweden, Göteborg (Sweden), A. A. Shiri, M. Leer-Andersen, SSPA Sweden AB, Göteborg (Sweden)

Polymer MEMS Microcantilever-Integrated Microfluidic System for Biochemical Sensing 415
P. P. Kanade, Robert M. Bowman, P. T. Baine, Queen's University Belfast, Belfast (United Kingdom)

TP33 **Snap-through Mode Shape Reconstruction of Bistable PiezoMEMS Membranes through Parametric Exploration 417**
M. Mortada, M. Schlögl, U. Schmid, M. Schneider, TU Wien, Vienna (Austria)

Novel Technologies and Applications of Sensors

TP34 **Ultra-Stable Few-Layer Black Phosphorus UV Detector En-capsulated in Nitrocellulose 419**
M. Suplewski, M. Szczerska, P. Jakóbczyk, Gdansk University of Technology, Gdansk (Poland)

TP35 **Orthogonality characterization of 3D Helmholtz coil fields 421**
P. Leitner, F. Slanovc, L. Enger, M. Ortner, Silicon Austria Labs GmbH, Graz (Austria), S. Leisenheimer, Infineon Technologies AG, Neubiberg (Germany), C.-G. Iot, C.-P. Juglan, M. Iatco, M. Muntean, Infineon Technologies Romania, Bucure?ti (Romania)

TP36 **A lightweight Method for Interconnecting Sensors via Power Line Communication 423**
M. Brandl, K. Kellner, University for Continuing Education Krems, Krems (Austria)

TP37 **Tracking Fish Trajectories through Dynamic Pressure Signals: A Dual-Sensor System for Hydrodynamic Cues Monitoring 425**
C. Porcon, B. Lagneaux, G. Jodin, F. Razan, IETR - UMR 6164 / ENS Rennes, Rennes (France)

Modelling and Experimental Validation of Pzt-based Spring Terminated Micro-Actuator 427
I. Shah, A. Michael, UNSW, Kensington (Australia)

TP38 **Enhancing Stability of Few-Layer Black Phosphorus via Nitrocellulose Encapsulation for Optoelectronic Applications 430**
J. Gierowski, M. Suplewski, M. Szczerska, P. Jakóbczyk, Gdansk University of Technology, Gdansk (Poland)

TP39 **Nanoimprint lithography for multiple cavity height Fabry-Perrot filter array from two-level master 432**
C. Fleury, B. Kalas, B. Realista-Ferreira, R. Nallagatla, M. Azeem, M. Garg, B. Mareddi, T. D. Dao, Silicon Austria Labs GmbH, Graz (Austria), P. Schuster, M. Preuß, V. Lingel, EV Group E. Thallner GmbH, St. Florian am Inn (Austria)

Printed Paper-Based Thermal Devices Using a Custom CB/rGO Ink for Sensing and Heating 434
D. Barmpakos, A. Apostolakis, G. Kaltsas, V. Belessi, University of West Attica, Athens (Greece), V. Georgakilas, University of Patras, Rio (Greece)

Physical Sensors

TP40 **Detection of Butyric Acid Concentration in Aqueous Solu-tion Towards Intraruminal Volatile Fatty Acid Measurement 436**
J. Fastier-Wooller, D. Yamaguchi, S. Muramatsu, M. Yamamoto, T. Itoh, The University of Tokyo, Tokyo (Japan)

TP41 **Flip Chip bonding of bare die on a flexible PET substrate with ablated copper. 438**
M.H. Malik, M.T. Vijjapu, E. Bezerra, S.L. Thomas, Silicon Austria Labs, Villach (Austria), E. Bezerra, École Polytechnique Fédérale de Lausanne (EPFL) (Switzerland), C. Kollegger, T. Herndl, Infineon Technologies Austria AG, Graz (Austria), A. Levy, E. Dvash, KLA Corporation, Yavna (Israel)

TP42 **Biological transistor (bioFET) for the specific and label-free sensing of CRP in unprocessed blood"" and ""Specific and label-free bioFET sensing of the interaction between the electrically neutral small estriol molecule and its antibody in a microliter d 440**
S. Babbar, I. Ron, G. Shalev, M. Y. Bashouti, B. Akabayov, G. Hazan, Ben-Gurion University of the Negev, Beer-Sheva (Israel), A. Eisenberg-Lerner, Z. Rotfogel, Kaplan Medical Center, Rehovot (Israel), E. Pikhay, I. Shehter, A. Elkayam, Y. Roizin, Tower Semiconductor, Migdal Haemek (Israel)

TP43 **Novel gating mechanism employed on nano bio-FET towards real-time, point-of-care diagnostics in human whole blood..... 441**
V. Garika, I. Ron, G. Shalev, S. Harilal, M. Y. Bashouti, B. Akabayov, Ben-Gurion University of the Negev, (Israel), A. Eisenberg-Lerner, Z. Rotfogel, Kaplan Medical Center, Rehovot (Israel), E. Pikhay, I. Shehter, A. Elkayam, Y. Roizin, Tower Semiconductor, Migdal Haemek (Israel), S. Bhattarai, V. Bamm, M. Wills, University of Guelph, Guelph, Ontario (Canada)

TP44 **Approximation of temperature characteristics of Seebeck coefficients for CuNi-Ag and Ca3Co4O9-Ag thermopiles 442**
S. Wójcik, A. Dziedzic, Wroclaw University of Science and Technology, Wroclaw (Poland)

TP45 **MEMS Based Field Mill for Measuring Hybrid Electric Fields..... 444**
W. Hortschitz, G. Kovacs, F. Keplinger, University for Continuing Education Krems, Wiener Neustadt, (Austria)

TP46 **A High-Sensitivity Co-Oscillating Electrochemical Vector Hydrophone Based on Micron-Scale Controllable Microelectrodes..... 446**
H. Zhang, J. Wang, D. chen, Y. Lu, Aerospace Information Research Institute of Chinese Academy of Sciences(Beijing CHINA), University of Chinese Academy of Sciences, Beijing (China)

TP47 **Performance Improvement of Resonant Absolute Pressure Sensors Based on Topology Optimization and Suspension Design 448**
X.H. Liu, B. Xie, J. B. Wang, D. Y. Chen, Y. L. Lu, B. W. Tan, X. Y. Li, Z. Y. Tan, Aerospace Information Research Institute, Chinese Academy of Sciences, School of lectronic, Electrical and Communication Engineering, University of Chinese Academy of Sciences, Beijing (China)

TP48 **Novel Acoustic Method for Detecting Fluid Phase Boundaries 450**
M. Kamrad, L. Reindl, K. Schmitt, J. Wöllenstein, University of Freiburg, Freiburg (Germany), J. Rautenberg, Endress+Hauser Flow Deutschland GmbH, Coburg (Germany)

TP49 **Measurement of Vacuum Pressure with Resonators in the Closed-Loop Configuration..... 452**
J. Qin, X. Liu, J. Wang, D. Chen, B. Xie, Y. Lu, X. Huo, Aerospace Information Research Institute, Chinese Academy of Sciences, Beijing (China), J. Qin, X. Liu, J. Wang, D. Chen, B. Xie, Y. Lu, X. Huo, University of Chinese Academy of Sciences, Beijing (China)

TP50 **Wearable Multi-Modal Sensor Array with Wireless Communication for Monitoring Medical Bandage Condition 454**
I. Bársony, J. M. Bozorádi, F. Braun, G. Battistig, P. Fu¨rjes, HUN-REN Centre for Energy Research, Budapest (Hungary), P. Földesy, HUN-REN SZTAKI, Budapest (Hungary)

TP51 **Integrating Carbon Nanotube Strain Gauges onto Stretchable PDMS Patches for Respiration Activity Sensing 456**
S. Jucker, M. Vollmann, C. Roman, S. L. Vehusheia, M. Basu, C. Hierold, ETH Zurich, Zurich (Switzerland)

TP52 **Dielectric Mass Concentration and Moisture Sensing of Organic Powders in Industrial Sensors 458**
T. Schwar, M. Neumayer. T. Suppan, J. Dornhofer, T. Bretterklieber, H. Wegleiter, Institute of Electrical Measurement and Sensor Systems, Graz (Austria), C. Feilmayr, S. Schuster, voestalpine Stahl GmbH, Linz, (Austria)

A New Sensor Effect for Nuclear Process Control 460
S. Lozanova, A. Ivanov, C. Roumenin, Instutute of Robotics at Bulgarian Academy of Sciences, Sofia (Bulgaria)

Sensors for Automation and Industry

TP53 **A Shunt Based Low Frequency Current Sensing Approach at an Earthing Switch for Power Grid Applications 462**
A. Elsässer, M. Neumayer, B. Schweighofer, T. Bretterklieber, F. Grubinger, H. Wegleiter, Institute of Electrical Measurement and Sensor Systems, Graz (Austria), P. Schachinger, Austrian Power Grid AG, Vienna (Austria)

TP54 **Low Cost Level Sensing for Receivers in Small Sized Refrigeration Systems with Natural Refrigerants** **464**
M. Neumayer, G. Pertiller, F. Eder, R. Rieberer, Graz University of Technology, Graz (Austria)

TP55 **Limitations of LWIR Cameras for Industrial Air Leak Detection** **466**
K. Lex, T. Sauterm, H. Brückl, University of Continuing Education Krems, Wiener Neustadt (Austria)

TP56 **Experimental Analysis of Flat Spot-Induced Vibrations Using Piezoelectric IEPE-Accelerometers** **468**
P. Kersten, C. Engel, S. Hirsch, University of Applied Sciences Brandenburg, Brandenburg an der Havel (Germany)

TP57 **Blind Prediction of Odor Concentration in Deodorization Process in Wastewater Treatment Plant Using E-nose and Dynamic Olfactometry** **470**
I. Crosnier, A. Nevers, F. Maalem, M. Diallo, F. Siinoa, V. Bourges, SIAAP Direction des Laboratoires et de l'Environnement, Service Environnement, F. Ayouni, J.-C. Mifsud, I. Romanytsia, ELLONA SAS, Toulouse (France)

TP58 **A Novel Surface Recognition System Using an Artificial Finger** **471**
A. Abbasimoshaei, A. M. H. Osman, F. Youssef, T. A. Kern, Hamburg University of Technology, Hamburg (Germany)

TP59 **Adaptive algorithm for microsensor in sustainable environmental monitoring** **473**
N. Daupayev, C. Engel, R. Bendyk, S. Hirsch, Brandenburg University of Applied Science, Brandenburg (Germany)

TP60 **Sensor Density Optimization of Active Magnetic Shielding System based on Monte Carlo Simulation** **475**
H. Wang, Y. Wu, R. Feng, B. Han, Beihang University, Beijing (China), D. Chen, Beihang University, Beijing (China)

TP61 **Selective Breath Acetone Detection for Metabolic Health Monitoring** **477**
J. Ko, A. Güntner, ETH Zürich, Zurich (Switzerland)

TP62 **Rapid and Sensitive MiRNA Detection in Biofluids Using Ultra Microelectrode Sensors.** **478**
M. Valente, M. A. Ridwan, A. O'Riordan, J. H. Marques, Tyndall National institute, UCC, Cork (Ireland), J. Browne, K. G. Meade, University College Dublin, Dublin (Ireland)

TP63 **Direct-printed, solid-contact pH sensor for clinical applications: Challenges of non-specific adsorption** **480**
M. Urbanowicz, A. Paziewska-Nowak, K. Bobrowska, A. Sołdatowska, M. Dawgul, D. G. Pijanowska, Polish Academy of Sciences, Warsaw (Poland), M. Ekman, Medical University of Gdańsk, Gdańsk (Poland)

TP64 **DNA-6MP interactions for electrochemical biosensor development** **482**
A. Sołdatowska, M. Urbanowicz, K. Sadowska, D. G. Pijanowska, Polish Academy of Sciences, Warsaw (Poland), M. Urbanowicz, National Medicines Institute, Warsaw (Poland)

TP65 **Electrochemical detection of cortisol using carbon nano-tubes (CNT) modified with a pyrene derivative** **484**
A. R. Santos, B. Faria, M. C. Paiva, J. C. Viana, A. F. Silva, University of Minho, Guimarães (Portugal), F. Bento, Chemistry Research Centre of the University of Minho, Braga (Portugal)

TP66 **Force measurement in Laparoscopic Stapler for Ex-Vivo Tissue Characterization** **486**
J. M. Bozorádi, Zs. Sz. Bérces, P. Fürjes, HUN-REN Centre for Energy Research, Budapest (Hungary), M. B. Maros, Óbuda University, Budapest (Hungary), G. Papp, Uzsoki Hospital, Budapest (Hungary)

TP67 **Design of Soft and Fast Nanocantilever for High-Speed Atomic Force Microscopy** **488**
E. S. Wong, A. Michael, C. Y. Kwok, UNSW Sydney, Sydney (Australia), H. Pota, UNSW Canberra, Campbell (Australia)

TP68 **Microphysiological analytical chip with non-invasive Raman microspectroscopy analysis of epithelial permeability and inflammatory biomarkers** **490**
A. Calogiuri, D. Bellisario, E. Sciurti, L. Blasi, V. Esposito, F. Casino, P. Siciliano, L. Francioso, Institute for Microelectronics and Microsystems IMM-CNR, Lecce (Italy)

TP69 **Fully Integrated Sensor Platform for Remote Respiratory Biomarker Monitoring** **492**
S. Schlapansky, F. Burisch, R. Rusch, A. Güntner, ETH Zürich (Switzerland)

DOI 10.5162/EUROSENSORS2025/PT2

AI and other Trends in MEMS Industry Change the Foundry Models

Dr. Stefan Majoni
Robert Bosch GmbH
Stefan.Majoni@Bosch.com

Summary:
AI requires drastically increase in computing power, which is not primary limited by the processors, but two other factors:
1.) Core to core communication, which will switch from electronic to optical data transfer to overcome current issues. Here a fundamental change from silicon- and silicon nitride-photonic to lithium niobate and similar is happening. The later one is incompatible with CMOS technology, shifting photonic from ASIC to MEMS foundries. The according customers request design- and product-support, increasing the foundry responsibility beyond pure wafer processing, which is a significant step for MEMS foundries.
2.) Computing power is throttled due to overheating, requiring new cooling concepts. Beside water cooling of the racks, decentralized local cooling will be necessary. Here MEMS will play a key role due to low cost, power consumption and size, resulting in a multitude of designs and process flows for individual solution per processor as discrete element or integrated with the µprocessors. Here and in many other cases, it is obvious, that the standardized process approach as copied from ASIC foundries is not successful. The wafer process reflects the mutual optimum of customers-design and -requirements and foundry capabilities. The trend for integrated MEMS-cooling, inertials with an ASIC cap, pMUT and medical fluidics on ASIC, etc reflects the merge of CMOS, MEMS and assembly processing [1]. This drives pure-play MEMS foundries to extend their scope. Additionally, MEMS-on-ASIC accelerates the 300mm transition of MEMS to be compatible with the advanced CMOS nodes.

Keywords: AI, MEMS foundry, medicals, TFLN photonic, CMOS compatibility, 300mm.

Introduction

In the early days of MEMS it became obvious, that the ASIC foundry approach of pre-defined and standardized processes is not useful in MEMS industry, resulting in one-product-one-process methodology. With pMUT technology, the standardized MEMS process flow had a short revival, which now again disappears. So, today the typical approach is the cooperation of a fabless customer with a specialized MEMS foundry for a tailor-made process on 150 or 200mm wafers [2], where the foundry is only responsible for the wafer processing. All of that is subject to change due to recent industry trends.

Photonic

Silicon- and silicon nitride-photonics are CMOS compatible and require tight CD control. Consequently, they are fabricated primarily in CMOS foundries using high end lithography. The upcoming thin film lithium niobate TFLN [3] and similar materials do not comply with CMOS wafer processing, they will be produced in MEMS foundries. But the according customers expect design support or predefined design libraries, a PDK and a standardized process flow. The design ownership let the clear separation of foundry (only process-responsibility) and a device supplier vanish, because the design & process ownership results in a product performance responsibility. The foundry must extend its scope or partner with a design house and share the responsibility.

Medicals

Fluidic devices and probe holder for medicals are not real MEMS, since no mechanical-electrical functionality is given. However, as specialty semiconductors they are produced in MEMS foundries, because those are used to tailormade solutions. But medical devices bring their own and very specific requirements to the MEMS fab. Biological compatibility drives new contamination monitoring concepts as well as unusual materials and coatings.

DNA sequencing is a challenge by itself, since very small line width may be combined with materials, which are not CMOS-compatible. Here a drive to 300mm may occur to get access to ArF lithography for the required CDs despite relatively low volume [4].

MEMS with ASIC as cap, ultrasound-transducers- and other MEMS-on-ASIC

Several companies with different devices evaluate an ultrasound transducer to be built on the CMOS on wafer level. Another approach uses the ASIC as a cap for the MEMS [5]. We see for many more cases a strong tendency to MEMS-on-ASIC technology. In all those cases, beside alignment, chip size and chemical compatibility, the wafer size of ASIC and MEMS must match. Switching to a smaller ASIC node drives the need for 300mm MEMS processing also for device types, where the wafer volume doesn't justify such leap. For many customers / devices, the generation 1 is a discrete element, whereas the later generations are MEMS-on-ASIC. This factor has increasing importance for the foundry choice.

MEMS Cooling

The µprocessor calculation power is more and more limited by overheating. The current macroscoping cooling solutions will be extended or replaced by MEMS cooling [6]. Those technologies may drive stacking of the actor wafer with interposers for in- and outlet of air, generating chaotic turbulences, etc.. Integration of cooling MEMS on CMOS or system in package solutions may be the subsequent step. This is another factor of merging MEMS-, CMOS- and assembly processing.

Extended defect monitoring and full or partial wafer level test at the foundry

Defect sensitive devices drive extended monitoring. But on one hand it is not commercially useful to scrap all wafers with a defect; on the other hand, it is too expensive to install an additional defect monitoring at the customer to fish dies with killing defects. Therefore, it is useful to 1.) adapt the defect monitoring to the specific product requirements and 2.) transfer the available defect information per wafer to the customer, like position and criticality based on defect type and size as inkmap. Consequently, 1.) foundry and customer have to partner openly and 2.) the foundry takes over responsibility for the functionality of single devices on the wafer. Similar is valid, when the foundry does apply electrical wafer test of the devices.

References

[1] *Combining MEMS with ASIC and raw wafer production*; H. Stahl et al.; MikroSystemTechnik Congress 2021; VDE: (see https://ieeexplore.ieee.org/document/9698288)

[2] *MEMS Product Development*; A.M. Fitzgerald et al.; Springer Int. Publ.; 03/2022

[3] *Lithium niobate on insulator (LNOI) for micro-photonic devices*; G. Poberaj et al.; Laser & Photonics Reviews; Special Issue: Integrated Optics; Vol. 28, Issue 17, pp. 24452-24458; (2012)

[4] *Innovative technologies crowd the short-*read sequencing market; M. Eisenstein; Nature 614, 798-800 (2023)

[5] *Method of fabrication of Al/Ge bonding in a wafer packaging environment and a product produced therefrom*; S. Nasari et al. (2008); United States Patent and Trademark Office (USPTO) patent no. 7442570.

[6] *Meet xMEMS, a challenger to AirJet`s radical solid-steate chop cooling*; M. Hachmann; PCWorld 2024, (see https://www.pcworld.com/article/2430971/meet-xmems-a-challenger-to-airjets-radical-solid-state-chip-cooling.html)

DOI 10.5162/EUROSENSORS2025/SP1.2

Molecular Dynamics Analysis of Virus-Induced Vibrational Changes in Single-layer Graphene

Zhenjin Wang[1], *Hiroki Kurita*[1], *Fumio Narita*[1]

[1]*Department of Frontier Sciences for Advanced Environment, Graduate School of Environmental Studies, Tohoku University, Sendai, Japan.*
Zhenjin.wang.d6@tohoku.ac.jp

Summary:
In the past serval years, the COVID-19 pandemic has significantly impacted people's lives, raising concerns about how to effectively mitigate pandemic-related panic. Early detection of airborne viruses could serve as an important means of triggering timely alarms and preventing further spread. Therefore, the development of highly sensitive virus detection technologies is essential. In this work, a novel concept for virus detection using single-layer graphene (SLG) is proposed. The influence of virus attachment on the vibrational behavior of SLG was investigated through molecular dynamics (MD) simulations.

Keywords: single-layer graphene, molecular dynamics simulation, vibrational analysis, mass sensing, virus detection

Background, Motivation an Objective

The COVID-19 pandemic has drastically transformed human life across the globe over the past several years. Although its direct impact has largely diminished, the challenge of preventing future large-scale epidemics remains a pressing concern. One promising strategy is to detect airborne viruses in real time and integrate the information with Internet of Things (IoT) systems, enabling early warnings and helping people avoid contaminated environments. Therefore, the development of rapid and reliable airborne virus detection technologies has become critical [1]. Conventional virus detection methods, such as polymerase chain reaction (PCR), although accurate, are time-consuming, require specialized equipment, and depend heavily on professional expertise. More importantly, traditional PCR methods do not provide real-time data, making them unsuitable for continuous, on-site virus monitoring. This highlights the urgent need for novel, real-time virus detection approaches. In recent years, the emergence of two-dimensional (2D) materials—materials composed of only one or a few atomic layers—has opened up new possibilities in sensing technologies due to their unique physical and chemical properties. Among them, SLG has attracted particular attention [2]. SLG is a one-atom-thick sheet of carbon atoms arranged in a hexagonal lattice, renowned for its exceptional mechanical strength, high electrical and thermal conductivity, and distinctive quantum behaviors. These properties make it highly sensitive to external perturbation, including mass changes caused by adsorbed particles.

Recent studies have demonstrated the potential of SLG in mass sensing applications. For instance, M. Mirakhorya et al. [3] employed MD simulations to investigate the vibrational characteristics of triangular graphene sheets with various geometries, showing that equilateral configurations exhibit the highest resonance frequencies. Similarly, S. Ahmad Fazelzadeh et al. [4] proposed a novel vibration-based mass sensing model for orthotropic SLG with multiple attached nanoparticles, emphasizing the influence of temperature variation, nanoparticle mass and location, and nonlocal effects on the sensor's vibrational response. Given that viruses typically have masses on the order of several attograms, even a single virus adsorbed on an SLG surface may cause detectable shifts in its vibrational behavior. This suggests a new opportunity for highly sensitive virus detection based on monitoring the vibrational response of graphene.

In this work, we propose a novel virus detection technique that utilizes the change in vibrational characteristics of SLG before and after virus attachment. MD simulations were conducted to analyze these vibrational differences, with a focus on the effect of COVID-19 virus attachment on the graphene's dynamic behavior.

Description of the Method

MD simulations were conducted using LAMMPS to investigate the vibrational behavior of SLG before and after the adsorption of the SARS-CoV-

2 main protease [5]. For the initial vibration analysis, a pristine graphene sheet was constructed with its edge atoms fixed to simulate a clamped boundary condition. A pulsed force was applied to the sheet to excite vibrations, and the atomic trajectories were recorded to extract vibrational modes and frequencies (see in Fig. 1).

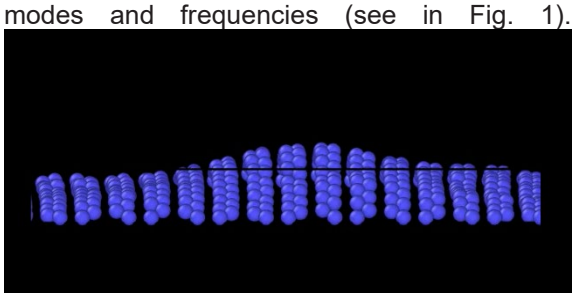


Fig. 1 Schematic of the vibration of SLG.

Prior to the adsorption simulations, the SARS-CoV-2 main protease was coarse-grained to reduce computational complexity while preserving its essential mass distribution and structural integrity. Coarse-graining allows for efficient simulation of large biomolecules, enabling longer simulation times and larger system sizes without significantly compromising the accuracy of mechanical interactions.

Subsequently, the coarse-grained protease was positioned on the central region of the graphene surface. The same fixed boundary conditions were applied, and vibrational excitation was introduced as before. The trajectories of graphene atoms were analyzed to assess changes in vibrational behavior caused by virus adsorption.

Results

The MD simulations showed clear differences in the vibrational behavior of SLG before and after the adsorption of the SARS-CoV-2 main protease. The model used for the simulation is illustrated in Fig. 2. In the pristine state, the graphene sheet exhibited distinct and stable vibrational modes. After virus adsorption, the overall vibrational response changed, with shifts observed in the natural frequencies and slight modifications in the vibration patterns. These changes suggest that the mass and interaction of the adsorbed virus significantly affect the dynamic characteristics of the graphene sheet. The results indicate that monitoring variations in vibrational behavior could serve as an effective approach for detecting the presence of virus particles on graphene surfaces.

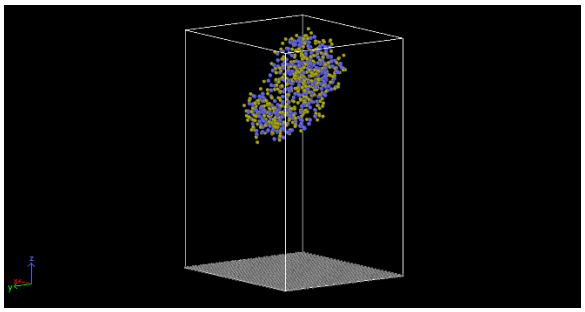


Fig. 2 Model of the SLG and coarse-grained protease.

Conclusion

This study employed MD simulations to investigate the vibrational behavior of SLG before and after virus adsorption. The results showed that virus attachment leads to changes in vibrational behavious, demonstrating the potential of MD-based methods for developing real-time, ultra-sensitive virus detection systems.

References

[1] F. Narita, Z. Wang, H. Kurita, Z. Li, Y. Shi, Y. Jia, C. Soutis, A Review of Piezoelectric and Magnetostrictive Biosensor Materials for Detection of COVID-19 and Other Viruses, Advanced Materials 33, 2005448 (2021); doi:10.1002/adma.202005448

[2] E. Singh, M. Meyyappan, H.S. Nalwa, Flexible Graphene-Based Wearable Gas and Chemical Sensors, ACS Applied Materials & Interfaces 9, 34544–34586 (2017); doi: 10.1021/acsami.7b07063

[3] M. Mirakhory, M.M. Khatibi, S. Sadeghzadeh, Vibration analysis of defected and pristine triangular single-layer graphene nanosheets, Current Applied Physics 18, 1327–1337 (2018); doi: 10.1016/j.cap.2018.07.014

[4] S.A. Fazelzadeh, E. Ghavanloo, Nanoscale mass sensing based on vibration of single-layered graphene sheet in thermal environments, Acta Mechanica Sinica 30, 84–91 (2014); doi: 10.1007/s10409-013-0102-6References (style "EUS_Conferences _RefText"): please use the style shown for Ref. [2] and provide the DOI of the articles

[5] A. Douangamath, D. Fearon, P. Gehrtz, et al., Crystallographic and electrophilic fragment screening of the SARS-CoV-2 main protease, Nature Communications 11, 5047 (2020); doi: 10.1038/s41467-020-18709-w

Acknowledgements

This work was supported by the JSPS KAKENHI Grant-in-Aid for Early-Career Scientists (Grant Number: 23K13213). The authors also acknowledge the developers of the open-source MD software LAMMPS.

DOI 10.5162/EUROSENSORS2025/SP1.3

Planar Coils Made in the Thick-Film and LTCC Technology For the Electromagnetic Microgenerator

Mirosław Gierczak, Andrzej Dziedzic
Wrocław University of Science and Technology,
27 Wybrzeże Stanisława Wyspiańskiego st.
50-370 Wrocław

Summary:

This study presents the structure of silver planar coils made by thick-film and LTCC technology. These coils were used along with magnets as the basic elements included in a rotary electromagnetic microgenerator. The fabricated microgenerator has been fully characterized. Results and conclusions will be presented in the paper, along with the further research direction.

Keywords: coils, thick-film, LTCC, electromagnetic microgenerator, 3D printing

Background, Motivation an Objective

Developments in electronics are driving electronic devices into more areas of our lives. In recent years, for example, rapidly developing industrial automation (Industry 4.0), wearable electronics, or the Internet of Things (IoT) are generating increased demand for electricity for mobile devices. With the miniaturization of circuits, there is a need to miniaturize their power sources while deviating from conventional solutions. Typical means of power supply, such as commonly used batteries, have finite energy resources, limited lifespans and contain environmentally dangerous chemicals. In addition, they are characterized by their significant size relative to currently manufactured devices. Conventional batteries are being replaced by autonomous, miniature systems that enable the extraction of electricity from the environment [1], such as from wind, hydropower, solar energy, electromagnetic waves, vibration or heat.

Technological progress has reduced the power consumption of sensors, actuators and other components of microcircuits and microsystems. As a result, such low-power systems have become potential consumers of energy recovered from the environment. Therefore, the devices become maintenance-free, which benefits the environment due to the reduction of chemical waste from batteries. Various methods of energy harvesting have been studied for many years [2, 3]. The research focuses on reducing size and weight, increasing the surface or volume power density, and reducing environmental harm.

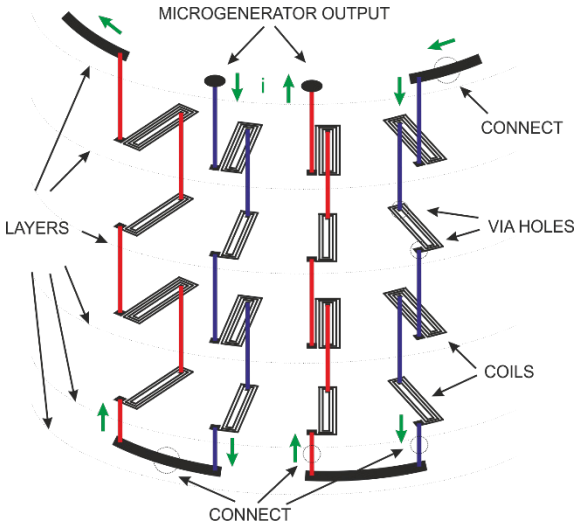


Fig. 1. Connection method.

Description of the Methodology

Electromagnetic microgenerators consisting of a disc with magnets and a coil structure with an outer diameter of 50 mm were designed and fabricated. The magnets disc that was placed on the rotating element and the disc was realized using 3D printing technology. This made it possible to place magnets with different geometric dimensions in it. The coil structure was made using Low-Temperature Co-Fired Ceramic technology. As a result, miniaturization of the spatially connected planar coil system was carried out. Twelve 2-, 8-, 10- and 12-layer structures were fabricated using two different sets of coil patterns. The first coil patterns were rectangular in shape, with external dimensions matching those of the magnets. The second designs were more

trapezoidal, allowing for better space management on the substrate. There were 28 coils on each layer, the same number as the magnets on the rotor disc. Thus, the total number of coils in each structure was 56, 224, 280 and 336, respectively. To determine the properties of single coils, single layers with printed inductors were also realized.

A series of calculations, simulations and measurements of electrical properties and parameters were carried out. The geometric properties of the single coils were investigated. The obtained results were then compared with calculated values as well as with the results of computer simulations. Electrical measurements were carried out using a self-designed and partly fabricated measuring system.

Results

The measurement system for the characterization of electromagnetic microgenerators made it possible to generate an alternating magnetic field and to measure the rotational speed of the disc with magnets that generate it. Using an electronic system, electrical measurements of coil structures were carried out. For an 8-layer structure with this particular pattern of coils, printed with DuPont silver paste, the best output performance was obtained: for 11620 rpm, the microgenerator generated 589.91 mW (for a load resistance of 167 Ω). The best solution was found to be a configuration with trapezoidal magnets. The maximum value of the obtained volume power density is 23.13 mW/cm^3.

Conclusions

Based on the study, it can be concluded that the optimization of electromagnetic microgenerators should first include the design of a miniature coil structure due to geometric constraints. In the design, special attention should be given to the number of turns of individual coils and their total number in the planned structure. Equally important is their arrangement, i.e. choosing their shape in such a way that they cover as much as possible of the substrate that will be under the influence of an alternating magnetic field. The next element of the microgenerator, the disc with magnets, should be designed with regard to the geometry of the coils so that the surface of the magnets covers as much as possible of a single coil. The last very important parameter is the distance between the two elements - the disc with magnets and the structure of the integrated coils.

With LTCC technology, rotary electromagnetic microgenerators were made, the output parameters of which depend most on the rotational speed of the element generating the alternating magnetic field.

References

[1] J. Pei, F. Guo, J. Zhang, B. Zhou, Y. Bi, R. Li; Review and analysis of energy harvesting technologies in roadway transportation, Journal of Cleaner Production, vol. 288 (2021), art. 125338, 17 s.

[2] K.V. Selvan, M.S.M. Ali; Micro-scale energy harvesting devices: Review of methodological performances in the last decade, Renewable and Sustainable Energy Reviews, vol. 54 (2016), s. 1035-1047.

[3] H. Pan, L. Qi, Z. Zhang, J. Yan; Kinetic energy harvesting technologies for applications in land transportation: A comprehensive review, Applied Energy, vol. 286 (2021), art. 116518, 22 s.

Acknowledgements

This project has received funding from the European Union's Horizon 2020 research and innovation programme under the Marie Skłodowska-Curie grant agreement No 101007429. Project co-financed by the Polish Ministry of Education and Science under the program called International Co-financed Projects.

Co-funded by the European Union

DOI 10.5162/EUROSENSORS2025/SP1.4

Laser Etching Effects on the Electrical and Mechanical Properties of Barium Titanate Thick Films

Yuto MATSUI[1], Kohei MARUYAMA[1], Yoshihiro KAWAKAMI[2], Zhenjin WANG[1], Hiroki KURITA[1], Fumio NARITA[1]
[1] Department of Frontier Sciences for Advanced Environment, Graduate school of Environmental Studies, Tohoku University, Sendai, Miyagi 980-8579, Japan
[2] Research Institute for Electromagnetic Materials, Tomiya, Miyagi 981-3341, Japan
[1] E-mail: matsui.yuto.s6@dc.tohoku.ac.jp

Summary:
The rapid spread of the Internet of Things (IoT) has increased demand for compact, high-capacity capacitors. In this study, barium titanate ($BaTiO_3$, BTO) thick films were fabricated by aerosol deposition (AD) and etched by laser. Electrical and mechanical evaluations revealed that laser etching enhanced the relative permittivity and Young's modulus of the films. These findings indicate that laser etching has strong potential as a processing technique for BTO thick films used in compact capacitors.

Keywords: barium titanate, aerosol deposition method, laser etching, dielectric properties, ceramic capacitors

Background

The Internet of Things (IoT) has rapidly spread in recent years. These IoT devices and sensor systems are all connected through the Internet, so a stable energy supply is essential. Therefore, the demand for capacitors is growing because of their ability to store and release electrical energy at high speeds. However, capacitors have limited capacity and space issues, so thick film capacitors are effective.
Barium titanate ($BaTiO_3$, BTO) is widely used as a capacitor due to its excellent relative permittivity and temperature stability. Moreover, the aerosol deposition (AD) method can improve brittleness by compositing with metal plates. The AD method is a deposition method in which raw material powders are mixed with gas and impacted onto a substrate. It can deposit dense films on any substrate at room temperature and high speed [1]. However, heat treatment is necessary to improve the low crystallinity and low relative permittivity of AD films [2]. So, in this study, we focused on laser etching as a new approach that can both process and anneal the films at the same time. Therefore, the objective is to investigate the effect on the electrical and mechanical properties of laser-etched BTO thick films.

Specimens' preparation

0.2 mm thick stainless steel and Fe-Co/Ni clad materials were used as substrates, and the AD method formed BTO thick films. The deposition was performed at room temperature using N_2 as the carrier gas at a flow rate of 15 L min^{-1}, with a nozzle measuring 0.5 × 30 mm^2 positioned 15 mm from the substrate and a scanning speed of 1 mm s^{-1}. The film thickness was set to 20 μm, and Au electrodes were formed on the surface using a sputtering system.

Experimental method

The fabricated specimens were etched using a laser cutting machine varying the laser power from 1 W to 10 W under fixed conditions of 1 mm s^{-1} etching speed and one processing cycle. During laser processing, the substrate temperature was recorded. Subsequently, the processing width was measured using a scanning electron microscope (SEM). Next, Young's modulus and relative permittivity were measured under various laser powers, etching cycles, and etching speeds to understand the influence of laser etching on the mechanical and electrical properties of the BTO film. The heat-affected zone (HAZ) was then estimated by evaluating the relative permittivity of samples etched with different gaps between the laser lines. Finally, X-ray diffraction (XRD) analysis was performed on both the laser-etched and as-deposited films to investigate changes in crystallinity induced by laser etching.

Results

Measurement results of substrate temperature showed a positive correlation between laser power and temperature, with the temperature rising from about 80°C at 1 W to nearly 400°C at 10 W. Similarly, the process width measurement showed a positive correlation between laser power and process width, ranging from 147 μm at 1 W to 238 μm at 10 W.

Fig. 1 gives the evaluation results of Young's modulus and relative permittivity. The numbers in the legend represent the laser power (W), etching cycles (times), and etching speed (mm s^{-1}) used in the laser etching process. Fig. 1 (a) shows that Young's modulus of the laser-etched film ranges from 120 to 140 GPa, which is higher than that of the as-deposited film, which is around 100 GPa, especially under the conditions of 7 W laser power, 2 times of etching cycle, and 4 mm s^{-1} etching speed (7-2-4). Similarly, Fig. 1 (b) shows that the relative permittivity of the laser-etched film became larger than the as-deposited film, and the 7-2-4 condition showed the highest relative permittivity, increasing from 75 to about 180. Frequency sweep measurement of the relative permittivity showed that relative permittivity decreased as the frequency increased, and this is typical ferroelectric behavior. It is evident that laser etching increases both Young's modulus and the relative permittivity of the AD-fabricated BTO thick films, and the laser etching parameters influence these enhancements.

Therefore, the condition labeled 7-2-4 was selected to etch the BTO thick film with varying gapping distances ranging from 0.5 mm to 2.0 mm in 0.25 mm intervals. The relative permittivity in each etched area was then measured to understand the HAZ of the laser etching better. As a result, the relative permittivity of the film reaches its highest value when the gap between the laser etching lines is 1.0 mm. It is assumed that a too-small gap causes the HAZs to overlap, leading to damage in the film and a decrease in relative permittivity. In contrast, a too-large gap results in some areas of the film not being affected by the laser, leading to a lower relative permittivity. Therefore, the width of the HAZ under the laser etching condition labeled 7-2-4 is estimated to be approximately 1.0 mm.

The XRD patterns of the as-deposited and laser-etched BTO films are presented in Fig. 2. The results show that laser etching enhanced the intensity and sharpness of the diffraction peaks, accompanied by a shift toward higher angles. These changes indicate improved crystallinity, which suggests that laser etching may have helped relieve residual compressive stress. These structural modifications may explain the film's relative permittivity and Young's modulus enhancement.

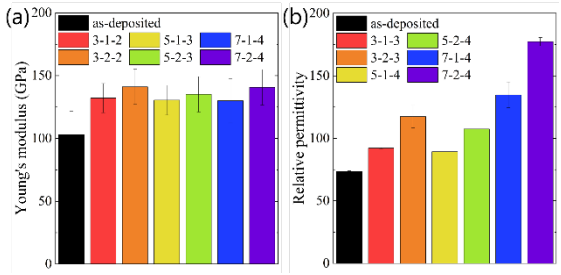


Fig. 1. (a) Young's modulus and (b) relative permittivity measurement at 1 kHz. Legend: laser power (W) – etching cycles (times) – etching speed (mm s^{-1})

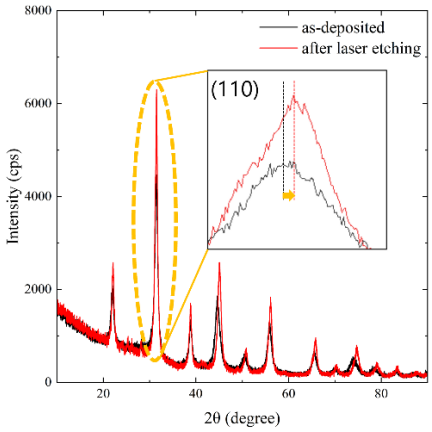


Fig. 2. XRD patterns for as-deposited and after laser etching film.

Conclusion

In this study, BTO thick films fabricated by the AD method were successfully etched by laser processing, and this laser etching improved Young's modulus and relative permittivity of the BTO thick films. It was also found that the increased crystallinity of the BTO thick film due to laser etching was one of the factors that improved Young's modulus and relative permittivity. These results demonstrate the potential of laser etching for processing in thick-film capacitors.

References

[1] R. Moos, An Overview of the Aerosol Deposition Method: Process Fundamentals and New Trends in Materials Applications, *J. Ceram. Sci. Tech. 6, 147-182 (2015)*; doi: 10.4416/JCST2015-00018

[2] Chrir, A., Rojas, O., Boyer, L., Durand-Panteix, O., Marchet, P., Effect of post-annealing on microstructure and electrical properties of BaTiO3 thick films grown by aerosol deposition (AD), *Journal of the European Ceramic Society*. 44, 3965-3984 (2024); doi: 10.1016/j01.073

DOI 10.5162/EUROSENSORS2025/SP2.1

One-Step Fabrication of Piezoelectric Ceramics/Carbon Fiber Reinforced Polymer Composites with Enhanced Performance

Zhengxiao Lin[1], *Zhenjin Wang*[1], *Hiroki Kurita*[1], *Fumio Narita*[1]
[1]*Department of Frontier Sciences for Advanced Environment, Graduate School of Environmental Studies, Tohoku University, Sendai, Japan.*
lin.zhengxiao.p8@dc.tohoku.ac.jp

Summary:
Recently, a composite combining $K_xNa_{1-x}NbO_3$ nanoparticle-filled epoxy with carbon fiber-reinforced polymer (CFRP) electrodes has been developed, showing enhanced mechanical and piezoelectric properties. However, the fabrication process is time-consuming, and the incorporation of resin may weaken the material's piezoelectric properties. In this work, we proposed a new strategy for combining piezoelectric material and CFRP, which reduces the time and effort required and improves the piezoelectric performance of the material.

Keywords: Piezoelectric composite, Carbon fiber-reinforced polymer, One-step fabrication, Corona-poling, Mechanical property

Background

Carbon fiber reinforced polymer (CFRP) is widely used in aerospace and construction due to its lightweight, high strength, and stability. However, its complex structure and the use of thermoset resins make it difficult to detect and repair once it is broken. Structural health monitoring (SHM) is essential for real-time crack detection. Traditional SHM methods like ultrasound and thermal imaging are costly and complex. Sensor-based approaches have gained attention, but external power remains a challenge. Piezoelectric materials offer a self-powered solution by converting mechanical stress into electrical signals and work as self-powdered sensors [1]. While lead zirconate titanate (PZT) is widely used for its excellent properties, its lead content raises environmental concerns. In contrast, lead-free sodium potassium niobate ($K_xNa_{1-x}NbO_3$ (KNN)) has emerged as a promising lead-free alternative, featuring good piezoelectric performance and high Curie temperature [2]. However, as ceramics, KNN suffers from inherent brittleness and poor fatigue resistance, which limits its durability. Recently, a composite combing KNN nanoparticle-filled epoxy (Ep) with twill weave (TW) CFRP electrodes has been developed, showing enhanced mechanical and piezoelectric properties [3]. This composite has high sensing sensitivity for damage detection, indicating potential applications in SHM. However, the fabrication process is time-consuming, and the incorporation of resin may weaken the material's piezoelectric properties. Besides, TW-KNN-Ep must be polarized by direct poling in silicon oil. If there are any weak points within the composites, they will break during the fabrication process, resulting in a low yield rate. Additionally, as the KNN content in the composites increases, weak points increase, limiting the KNN content to under 40 vol. %. This constraint has become a significant barrier to the CFRP-KNN-Ep composite. To reduce the time and effort required and improve the piezoelectric performance, in this study, a one-step molding method for ceramics/CFRP piezoelectric composites and a new piezoelectric CFRP structure was proposed, where micro-sized KNN layers were sandwiched between CFRP layers. The fabrication conditions were examined, and the performance of the KNN-CFRP composites was investigated. The cross-section of the fabricated composites was observed using scanning electron microscopy (SEM). The piezoelectric, electric, and mechanical properties were measured by a d_{33}-meter, an impedance analyzer, and a 3-point bending test on a universal machine, respectively.

Experimental Procedure

Unlike previous studies, we eliminated adding resin or hardener in this work. Instead, the composites were manufactured by directly combining piezoelectric material powder with CFRP. KNN powder was uniformly distributed onto the surface of the CFRP and then sandwiched by (0/90/KNN/0) CFRP prepregs. The unidirectional

(UD) CFRP and TW CFRP were used. A hot press was used to apply high pressure to the CFRP and KNN powder, ensuring a strong bond between the two materials while the heating process solidified the CFRP. After curing, the UD-KNN and TW-KNN were polished to prepare the specimens with a length of L=55 mm, a width of W=10 mm, and a thickness of H=1.3 mm (KNN h=0.5 mm). Next, corona-poling poled the specimens under 16 kV/mm at 105 °C for 60 min along the thickness direction. Then, a d_{33}-meter was used to measure the piezoelectric coefficient d_{33} of the composite, and a 3-point bending test measured the mechanical properties of the composite.

Results and Discussion

The SEM micrograph of the cross-section of the composites indicated that the KNN powder in the composites prepared by one-step molding is tightly bound compared to the TW-KNN-Ep in previous work (see Fig. 1). However, there are still some micro-sized voids between the particles in the TW-KNN composite.

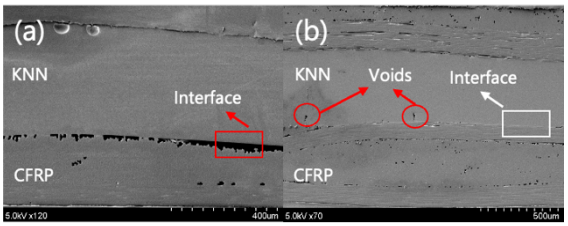


Fig. 1. SEM micrograph of the cross-section of the KNN composites.

The piezoelectric coefficient d_{33} of the composites was measured by d_{33}-meter after corona-poling along the thickness direction. As expected, the incorporation of resin affected the piezoelectric performance of the composite. The piezoelectric coefficient d_{33} of the TW-KNN composites prepared by one-step molding reached values twice (~9 pC/N) as high as those of TW-KNN-Ep in previous work (~4 pC/N), and the UD-KNN composites reached six times (~25 pC/N). The piezoelectric layer of the composites in this work is almost composed of KNN powder, resulting in a significant enhancement in piezoelectric properties. Impedance analysis was also conducted to investigate further resin's influence on the composites' piezoelectric properties. The results indicate that the TW-KNN-Ep composite exhibited the lowest relative permittivity (ε_r= 21) and electrical conductivity (G= 5×10^{-6} S, at 1MHz), due to the incorporation of resin. Besides, the UD-KNN and TW-KNN showed a higher dielectric loss, which can be attributed to the micro-sized voids in the KNN layer, which is consistent with the SEM results. The results of the 3-point bending test of the composites are shown in Fig. 2. Compared to the TW-KNN-Ep composite (E= 3.8 GPa, σ_b= 170 MPa), the TW-KNN and UD-KNN composites exhibited a significant improvement in both Young's modulus and bending strength (E= 46.4 GPa, σ_b= 700 MPa, E= 6.4 GPa, σ_b= 323 MPa, respectively). However, the toughness of the TW-KNN composite was substantially reduced. It is primarily because the KNN in the TW-KNN sample existed in a ceramic state, leading to greater brittleness and reduced composite toughness.

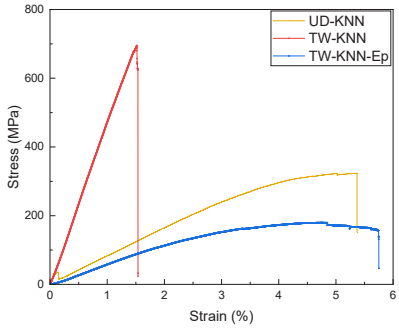


Fig. 2. Bending strain-stress curve of the KNN composites.

Conclusion

In this work, we proposed a new strategy for combining piezoelectric material and carbon fiber reinforcement, which reduces the time and effort required and improves the material's piezoelectric and mechanical properties compared to previous research. The piezoelectric coefficient d_{33} of the TW-KNN composites prepared by one-step molding reached values twice as high as those of TW-KNN-Ep in previous work, and the UD-KNN composites reached six times. Besides, the composites in this work showed a significantly higher Young's modulus and greater bending strength than the TW-KNN-Ep in previous work, although the toughness of TW-KNN was reduced.

References

[1] N. Rubab, S. Kim, Self-powered Sensors based on Piezoelectric Nanogenerators, *Journal of Sensor Science and Technology*, *31*(5), 293–300 (2022); doi: 10.46670/JSST.2022.31.5.293

[2] Y. Saito, H. Takao, T. Tani, *et al.,* Lead-free piezoceramics, *Nature* 432, 84–87 (2004); doi: 10.1038/nature03028

[3] Y. Yu, C. Luo, H. Chiba, Y. Shi, F. Narita, Energy harvesting and wireless communication by carbon fiber-reinforced polymer-enhanced piezoelectric nanocomposites, *Nano Energy*, *113 (2023)*; doi: 10.1016/j.nanoen.2023.108588

Acknowledgements

The authors would like to acknowledge the support of this work by Nikkiso Co. Ltd. The research was also supported by the Japan Science and Technology Agency (JST).

DOI 10.5162/EUROSENSORS2025/SP2.2

Broadband Rotational Energy Harvesting Using Upward and Downward Piezoelectric Cantilevers under Aerospace-Induced Vibrations

Md Shamim Ahmed[1], *Yu Jia*[1]
[1] *Aston University, Birmingham, United Kingdom*
md.shamim.ahmed@ieee.org ; y.jia1@ason.ac.uk

Summary:
A broadband piezoelectric rotational energy harvester with upward and downward cantilevers was developed. The system captures energy from both directions of rotation using PVDF materials. It was tested under two aerospace vibration profiles with distinct frequency content. The downward cantilever produced a peak average power of 57.8 µW. The upward cantilever reached 33.5 µW under different excitation. Results confirm broadband rotational energy harvesting capability for aerospace vibration environments.

Keywords: REH, bi-stability, nonlinear, Cantilever upward, cantilever downward.

Introduction

Energy harvesting from vibration in aerospace platforms presents an attractive solution for powering distributed sensor nodes in locations where battery replacement is impractical. Rotational energy harvesters (REHs) that use piezoelectric materials offer a compact and passive approach. However, one challenge is capturing energy across a broad frequency spectrum, especially under variable aerospace operating conditions. This study evaluates a broadband REH design that employs both upward and downward cantilever configurations to extract energy from rotation-induced vibrations in aerospace environments.

Background, Motivation an Objective

The harvester design is based on two flexible PVDF cantilevers mounted on a rotating structure—one directed upward and the other downward and one free moving magnet. These orientations leverage both gravitational and inertial (centrifugal) forces causes bi-stability to generate alternating strain during rotation [1]. This study focuses on representative aerospace vibration environments, specifically Aerospace in Flight which characterizes typical engine and aerodynamic vibrations during cruise and Aerospace in Elevation represents vibration during altitude change and maneuver [2].

The objective is to assess the broadband harvesting performance of each cantilever configuration under these two vibration sources and analyze their rms voltage and average power output as well as input acceleration for both sources.

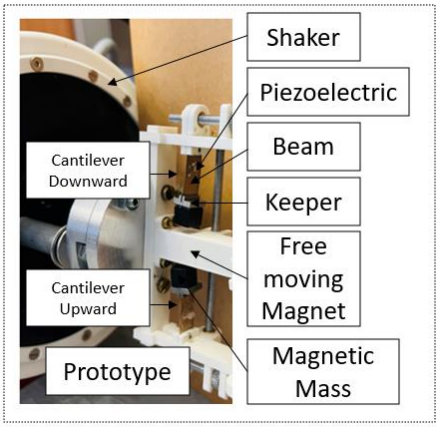


Fig. 1. Experimental Setup of proposed rotational energy harvester.

Methodology

The proposed system (Figure 1) employs two PVDF piezoelectric cantilevers mounted in upward and downward orientations on a rotating disc. This dual setup captures inertial strain during both upward and downward motion, enabling broadband energy harvesting without active tuning. A levitated magnet introduces nonlinear dynamics, enhancing sensitivity to a wider frequency range. The system is tested on a vibration shaker replicating aerospace noise. Output voltage is measured across resistive loads, and power is calculated from RMS voltage, demonstrating efficient passive harvesting under realistic flight conditions.

Results

Voltage and power outputs were measured from both cantilever configurations under two aerospace-specific vibration profiles: Aerospace in Flight and Aerospace in Elevation. The experiments used a vibration shaker system replicating real-world flight data setup with PVDF piezoelectric cantilevers.

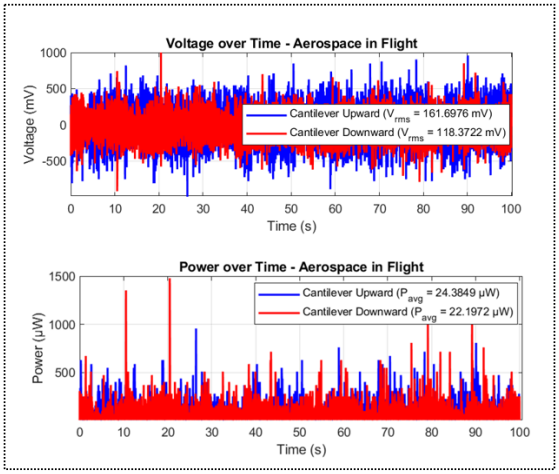


Fig. 2. Experimental results of voltage over time and Power over time for Aerospace in Flight.

Figures 2 and 3 present time-domain voltage and power plots over 100 seconds of vibration exposure. Under Aerospace in Flight, the upward cantilever produced slightly higher power than the downward. In contrast, under Aerospace in Elevation, the downward cantilever significantly outperformed the upward one, indicating stronger response to higher amplitude and more broadband frequency content.

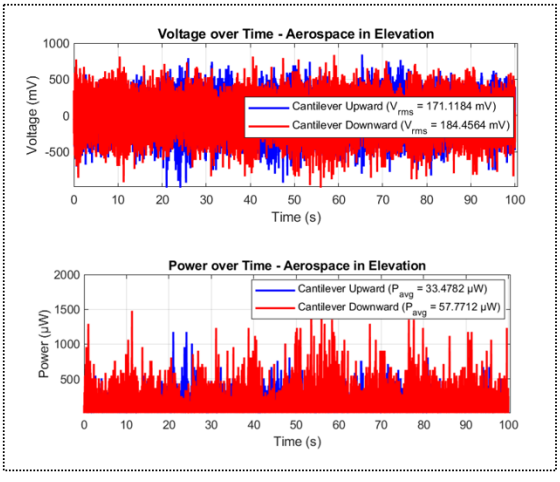


Fig. 3. Experimental results of voltage over time and Power over time for Aerospace in Elevation.

Conclusion

These results confirm that the dual-orientation configuration enables broadband energy harvesting by capturing complementary motion patterns. The upward cantilever performs well under stable, low-amplitude vibrations, while the downward configuration excels in dynamic, high-energy environments, enhancing total power extraction across varying aerospace conditions.

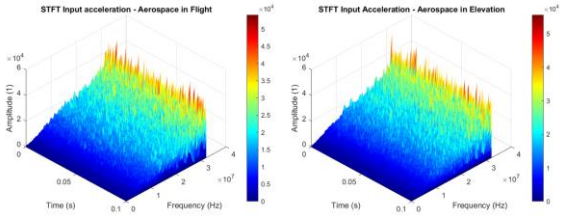


Fig. 4. STFT Input acceleration for Aerospace in Flight and Aerospace in Elevation.

Measured root mean square (RMS) voltage and average power output of upward and downward piezoelectric cantilevers under two distinct aerospace vibration environments: Aerospace in Flight and Aerospace in Elevation. Data were collected over 100 seconds using a resistive load of 50 kΩ. The upward cantilever showed higher performance in the flight condition due to better alignment with mid-frequency content, while the downward cantilever yielded higher power in elevation due to stronger broadband excitations.

Tab. 1: RMS voltage and average power output for upward and downward cantilevers under aerospace-induced vibration environments.

Cantilever Orientation	Noise Source	V_{rms} (mV)	P_{avg} (μW)
Upward	In Flight	161.7	24.4
Downward	In Flight	118.4	22.2
Upward	In Elevation	171.1	33.5
Downward	In Elevation	184.5	57.8

References

[1] M.S. Ahmed, M. Longden, X. Ma, Y. Jia, Gravity and Magnet-Induced Bi-Stability For Broadband Rotational Energy Harvesting, Proc. 2024 IEEE 23rd Int. Conf. on Micro and Miniature Power Systems, Self-Powered Sensors and Energy Autonomous Devices (PowerMEMS), 223–226 (2024); doi: 10.1109/PowerMEMS63147.2024.10814242

[2] Y. Jia, X. Wei, L. Xu, C. Wang, P. Lian, S. Xue, A. Al-Saadi, Y. Shi, Multiphysics vibration FE model of piezoelectric macro fibre composite on carbon fibre composite structures, Composites Part B: Engineering 161, 376–385 (2019); doi: 10.1016/j.compositesb.2018.12.081

Acknowledgements

This work was supported by EPSRC PhD studentship at Aston University, Birmingham, UK and Marie Skłodowska-Curie grant agreement No 101007429 (INTAKE).

DOI 10.5162/EUROSENSORS2025/SP2.3

The Impact of Elementary Cell Topology on the Bending Tests of 3D Printed Sandwich Beams

Rafał Pawłowski[1], Rafał Trzeciakowski[1], Karolina Laszczyk[1], Paweł Piórkowski[1], Hiroki Kurita[2], Fumio Narita[2]*

1) Wroclaw University of Science and Technology, 27 Wybrzeże Stanisława Wyspiańskiego st. 50-370 Wrocław, Poland;

2) Tohoku University, Graduate School of Environmental Studies Department of Frontier Sciences for Advanced Environment, 468-1 Aramaki Aza Aoba, Aoba-ku Sendai, 980-8572, Miyagi, Japan.

**contact: karolina.laszczyk@pwr.edu.pl*

Summary:

This study investigates the influence of elementary cell topology on the bending behaviour of the 3D printed sandwich beams. Three distinct designs for the cell topologies (Schwarz P, Star and Octet) were fabricated using UV-curable resin and tested under three-point bending conditions. The results indicated that the use of the cell topology Schwarz P gave the highest force resistance and bending stiffness, while the Star design provided a balanced compromise between strength and deformation. In contrast, the Octet-based beam exhibited gradual failure, suggesting its potential for the vibration energy harvesting in micro- and meso-scale.

Keywords: 3D printing, sandwich beam, cell topology, bending tests, UV-vat-photopolymerization

Background, Motivation an Objective

Advances in 3D printing have enabled the production of complex structures that can yield lightweight yet mechanically robust components. Previous studies have highlighted the benefits of using unconventional geometries to optimize properties such as stiffness, strength to weight ratio, vibration damping, as well as energy absorption [1-2]. Although mechanical properties of cell topologies has been explored, there are no results reported for the vat photopolymerization (known commonly as stereolithography, SLA or Digital Light processing, DLP), It is especially demanded, as this technique can downsize the structures to tens micrometers comparing to the Filament Deposition Modelling (FDM) techniques reported in such case [3]. The primary objective of this work was to analyse how three distinct elementary cell designs affect the bending performance of 3D printed structures using UV-curable resins as a building material. By comparing the selected cell topologies (Fig. 1), the research aimed to determine which design offers optimal balance between high load-bearing capacity and ductility. Such comparative analysis was expected to provide valuable insights for designing components where mechanical integrity and controlled deformation are essential, for example in energy harvesting systems.

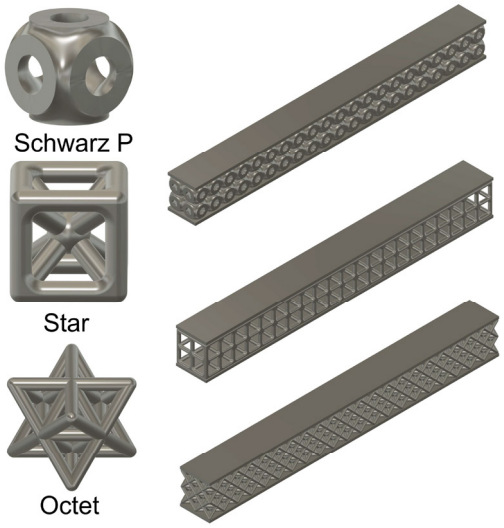


Fig. 1. A schematic illustrations of the cell topologies (left) and their use for filling the sandwiched beams (right)- a screen views from Autodesk Fusion (Autodesk, US).

Description of the Methodology

Based on [1-2], there were three cell topologies selected: Schwarz P, Star and Octet, due to their superior mechanical properties regarding strength, load capacity, deflection under bending loads and stiffness. To isolate the influence of elementary cell topology on bending performance, a controlled comparative experiment was designed. All specimens were fabricated using the same 3D printer ASIGA MAX X35 (ASIGA, AU),

with the identical photopolymer resin DentaStudy (ASIGA, AU) and printing parameters. Each printed sample had the same external dimensions (63,2 × 6,3 × 6,6 mm^3) and internal cell count (21×2×2). This methodological consistency means that any differences in mechanical behavior can be attributed solely to the cell geometry itself. Seven identical samples of each topology were produced and subjected to a standard three-point bending test, using the Chatillon CS2-1100 force tester (AMETEK, US), under identical conditions (span length, support placement, and loading rate held constant). Force-deflection curves were recorded for all tests, and the bending stiffness, strength (peak load) and failure mode were evaluated for each design.

Results

The bending tests revealed distinct mechanical behaviours for each elementary cell topology. The Schwarz P-based sandwich beam demonstrated the highest average bending force (approximately 63 N) and maximum displacement (about 8,35 mm), with a bending stiffness near 19,58 N/m (Fig. 2). These results confirmed that the continuous minimal surface design of the Schwarz P topology provided superior load-bearing capability and resistance to bending deformation. In contrast, the Star topology-based beam delivered intermediate performance, with an average bending force around 41 N and maximum displacement close to 7 mm, accompanied by a stiffness of approximately 15,64 N/m (Fig. 2). Although not the strongest among the tested geometries, the Star-based beam offered a balanced compromise between strength and flexibility, suggesting its potential suitability in applications requiring moderate deformation. The Octet-based beam exhibited the lowest average bending force (approximately 17 N) and the smallest stiffness (roughly 11,58 N/m) (Fig. 2).

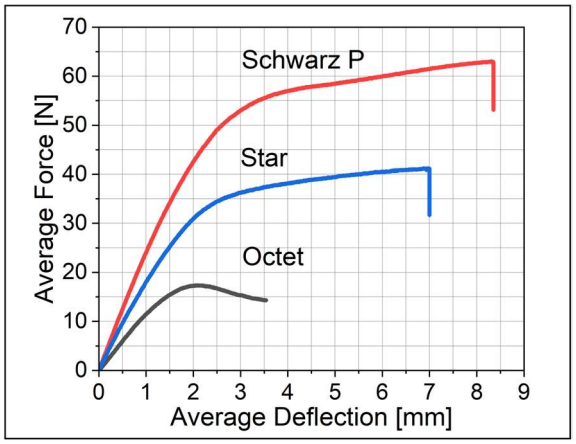


Fig. 2. Graphs of the averaged force values as a function of the averaged deflection values for sandwich structures with the following elementary cell geometries: Schwarz P, Star and Octet.

Notably, the Octet samples displayed a gradual failure mechanism- characterized by progressive cell crushing rather than abrupt fracture. This implied enhanced energy absorption capabilities.

Conclusions

The experimental investigation confirmed that the topology of the elementary cells in 3D printed sandwich beams significantly impacted their bending behaviour. The obtained distinct responses suggested that design optimization should consider trade-offs beyond mere strength. Future research should explore additional cell geometries, a wider range of material systems, and advanced post-processing techniques to further optimize the mechanical performance of 3D printed structures. Such studies will contribute to the development of tailored components with specific performance characteristics, expanding the application potential of advanced additive manufacturing techniques and may be particularly effective in energy harvesting applications, where controlled deformation and energy dissipation are advantageous.

References

[1] S.A.M. Ghannadpour, M. Mahmoudi, K. Hossein Nedjad, Structural behavior of 3D-printed sandwich beams with strut-based lattice core: Experimental and numerical study, Composite Structures 281 (2022); doi: 10.1016/j.compstruct.2021.115113

[2] N. Iranmanesh, H. Yazdani Sarvestani, B. Ashrafi, M. Hojjati, Beyond honeycombs: Core topology's role in 3D-printed sandwich panels, Materials Today Communications 37 (2023); doi: 10.1016/j.mtcomm.2023.107548

[3] Q. Ge, Z. Li, Z. Wang, K. Kowsari, W. Zhang, X. He, J. Zhou, N.X. Fang, Projection micro stereolithography based 3D printing and its applications, International Journal of Extreme Manufacturing 2 (2020); doi: 10.1088/2631-7990/ab8d9a

Acknowledgements

This project has received funding from the European Union's Horizon 2020 research and innovation programme under the Marie Skłodowska-Curie grant agreement No 101007429. Project co-financed by the Polish Ministry of Education and Science under the program called International Co-financed Projects.

Co-funded by the European Union

DOI 10.5162/EUROSENSORS2025/SP2.4

Real-Time Monitoring of Cracks in Carbon Fiber-reinforced Polymers under Bending Vibrations with Piezoelectric Composite Sensors

Yuki SUEDA[1], Zhenjin WANG[1], Yusuke Watanabe[2], Hoshiki Sato[2], Ryozo Ohiwa[2], Hiroki KURITA[1], Fumio NARITA[1]
[1]Department of Frontier Sciences for Advanced Environment
Graduate School of Environment Studies, Tohoku University, Sendai 980-8579, Japan
[2]Research & Development Section, Engineering Department 1, Aerospace Research and Technology Center, Aerospace Division, Nikkiso Co., Ltd., *Higashimurayama-shi, Tokyo 189-8520, Japan*
E-mail: sueda.yuki.r7@dc.tohoku.ac.jp

Summary:
Detecting defects in carbon fiber reinforced polymers (CFRP) used in aircraft is time-consuming and costly, increasing maintenance burdens and affecting safety. This study proposes a real-time crack detection method by laminating KNN-epoxy composite onto CFRP and analyzing its electrical response during bending vibration. Vibration tests revealed that cracks cause a decrease in resonance frequency and output voltage, while rectified AC voltage stored in a capacitor enabled wireless transmission for crack detection via time delay, demonstrating the system's potential for real-time CFRP monitoring to improve safety and efficiency.

Keywords: Structural Health Monitoring, Carbon fiber-reinforced polymer, Piezoelectric composites, Potassium sodium niobate, Crack detection sensors

Background

In recent years, as the cruising range of aircraft has increased, there has been an increasing demand for improved fuel efficiency and safety. Carbon fiber-reinforced polymers (CFRP), which have a high specific strength [1], are attracting attention as a material for aircraft bodies. However, detecting internal defects in CFRP is difficult, causing problems such as reduced safety and increased maintenance burdens.
This study proposes a method for real-time defect detection in CFRP using piezoelectric composite materials. The aim was to detect internal cracks using the electrical signals generated by piezoelectric materials, using vibrations during aircraft operation. In particular, we focused on potassium sodium niobate (KNN), which can be used over a wide temperature range [2], and created a piezoelectric composite material with improved flexibility by mixing it with epoxy resin [3]. Furthermore, a bending vibration test was conducted using samples in which the length of the interlayer cracks was varied by laminating this material onto CFRP. Its power generation performance was evaluated, and it confirmed that the power generated could be used as a power source for data transmission. Based on the above, we showed that the CFRP and KNN-epoxy specimen (CFRP/KNN-epoxy) is a promising self-powering defect detection sensor.

Preparation of specimens

KNN particles were mixed with epoxy resin at a volume fraction of 30% to create a composite material (KNN-epoxy) with an optimized balance of piezoelectricity and flexibility. Furthermore, this material was laminated with two sheets of CFRP prepreg to create four types of specimens with cracks of 0, 5, 10, and 15 mm between the CFRP and KNN-epoxy layers [4].

Experimental method

One end of CFRP/KNN-epoxy was fixed and attached to a vibration machine to apply bending vibration in the thick direction. The voltage generated at that time was recorded, and the relationship between the length of the interlayer crack, resonant frequency, and output voltage was investigated. Furthermore, the alternating current (AC) voltage generated was connected to an Internet of Things (IoT) kit, which includes a rectifier and a capacitor for wireless communication, and the transmission interval was measured.

Results and Discussion

Using a vibration machine, we applied vibrations of 150 to 350 Hz to four types of CFRP/KNN-

epoxy specimens and measured the amplitude of the generated voltage (Fig. 1). As a result, the CFRP/KNN-epoxy without a crack resonated at 262 Hz, and a maximum voltage of 13.6 V was recorded. On the other hand, as the length of the interlaminar crack increased, the resonance frequency decreased, and a trend of accompanying voltage amplitude decreasing was confirmed. In the specimen with a crack length of 15 mm, the resonance frequency decreased by 8 Hz, and the voltage amplitude decreased by approximately 6 V at maximum. In addition, when comparing specimens with different crack lengths, a certain relationship was observed between the change in resonance frequency and the decrease in voltage output. It suggests that by analyzing the resonance characteristics of CFRP/KNN-epoxy, it is possible to quantitatively evaluate the presence of interlaminar cracks and their length.

Furthermore, to evaluate the power generation characteristics and energy storage performance of CFRP/KNN-epoxy, an experiment was conducted to utilize the generated power by connecting it to the IoT kit. The capacitor built into the transmitter charges over time, and when the voltage reaches 1.4 V, radio waves are transmitted (Fig. 2). As a result of the measurements, it was found that in the crack-free specimen, the first transmission was confirmed after 3059 s, but in the specimen with an interlayer crack, as the crack length increased, the charging rate of the capacitor decreased. It became clear that the interval between wireless communication increased. In particular, the transmission interval increased significantly in the specimen with a 15 mm crack, confirming that the effect of interlaminar cracks on energy conversion efficiency is significant. In addition, the observed correlation between the change in transmission interval and crack length demonstrates that real-time monitoring of interlaminar cracks in CFRP is feasible by utilizing the energy harvested from the CFRP/KNN-epoxy.

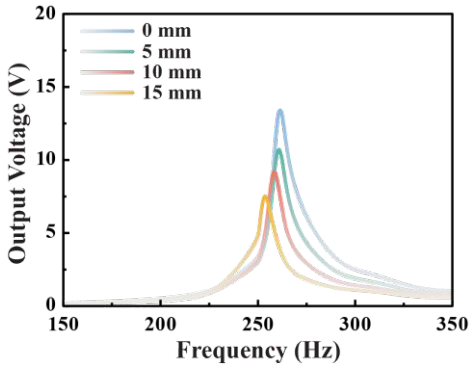


Fig. 1. Impact of different crack lengths on the output voltage and resonance frequency.

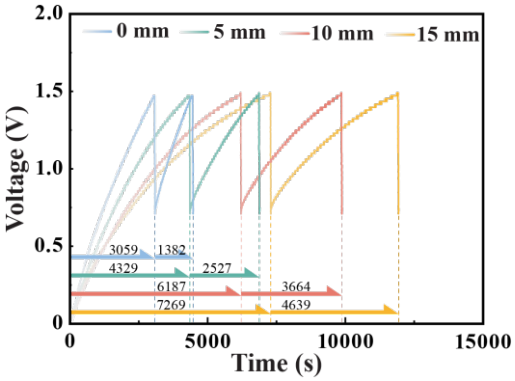


Fig. 2. Transmission interval of the IoT kit's radio waves.

Conclusion

In this study, a CFRP/KNN-epoxy laminate was fabricated, and its piezoelectric properties and defect detection performance were evaluated. The CFRP/KNN-epoxy showed high piezoelectric performance, and an output voltage of 13.6 V was obtained at a resonance frequency of 262 Hz. Furthermore, the effect of interlayer cracks on the resonance frequency and voltage amplitude was analyzed, and a decrease in frequency and voltage corresponding to the length of the crack was confirmed. In addition, the energy storage performance of CFRP/KNN-epoxy was evaluated, and it was shown that it was possible to supply sufficient power for LED lighting and wireless communication. From the above, this material can be expected to be applied as a defective detection sensor that does not require an external power supply.

References

[1] C. Li, L. Ke, J. He, Z. Chen, Y. Jiao. Effects of mechanical properties of adhesive and CFRP on the bond behavior in CFRP-strengthened steel structures. *Composites Structures* 221, 163-174 (2019); doi: 10.1016/j.compstruct.2018.12.020.

[2] L. Wang, C. Su, Y. Liao, H. Hao, H. Liu. Phase tuning on $BiCoO_3$ modified KNN ceramics with increased overall pyroelectric properties and high Curie temperature. *Journal of the European Ceramic Society* 45, (11) (2025) ;doi: 10.1016/j.jeurceramsoc.2025.117372.

[3] G. D'Ambrogio, O. Zahhaf, Y. Hebrard, M. Q. Le, P-J. Cottinet, J-F. Capsal. Micro-Structuration of Piezoelectric Composites Using Dielectrophoresis: Toward Application in Condition Monitoring of Bearings. *Advanced Engineering Materials* 23, (1), (2021); doi: 10. 1002/ adem.202000773.

[4] Y. Yu, C. Luo, H. Chiba, Y. Shi, F. Narita, Energy harvesting and wireless communication by carbon fiber-reinforced polymer-enhanced piezoelectric nanocomposites, *Nano Energy* 113 (2023); doi: 10.1016/j108588.

DOI 10.5162/EUROSENSORS2025/M1.1.1

A Screen-Printed and Light-Activated Copper Oxide Sensor for Acetone Detection

Amit Chatterjee[1,2], Johanna Zikulnig[1,3], Bernhard Jakoby[2], Jürgen Kosel[1], Mani Teja Vijjapu[1]
[1] Sensor Systems Division, Silicon Austria Labs GmbH, Europastraße 12, Villach 9524 Austria
[2] Institute for Microelectronics and Microsensors, Johannes Kepler University Linz Austria
[3]École Polytechnique Fédérale de Lausanne, EPFL, Bio/CMOS Interfaces Lab, CH-2000 Neuchâtel, Switzerland
Correspondence: amit.chatterjee@silicon-austria.com

Abstract:

In this work, we report on the design, fabrication, and investigation of a low-power screen-printed Cu_2O/CuO chemiresistive sensor. Typically, copper oxide sensors are fabricated either using microfabrication technologies or by directly depositing copper oxide through solution processes. In contrast, we thermally oxidized commercially available copper ink to develop chemiresistive sensors. This process paves the way for an additive and scalable production of copper oxide-based gas sensors. The sensors were activated with a blue light emitting diode and tested with acetone vapor at room temperature. Based on the evaluated repeatability and linearity, we consider this sensor to be a promising candidate for use in power efficient chemical sensing applications like breath analyzers.

Keywords: Printed gas sensor, Acetone sensor, Metal oxide semiconductor (MOS) sensor, Light-activated sensors, Room temperature sensor

Introduction

Chemiresistive gas sensors based on metal oxide semiconductors (e.g., ZnO, CuO, Cu_2O, SnO_2) can detect various harmful volatile organic compounds (VOCs, e.g., acetone, methanol, ethanol) by monitoring changes in electrical resistance upon interaction with the analyte gases [1 - 3]. These MOS sensors require high temperature for activation which leads to elevated power consumption [4]. Light activation offers a viable alternative, not only addressing this issue but also potentially enhancing sensor sensitivity and selectivity, as studies suggest [5].

Screen printing has been widely used for fabricating sensors, enabling additive manufacturing, and the use of various substrates, such as PET, glass, and paper [6]. In this work, we present a fully screen-printed Cu_2O/CuO-based chemiresistive sensor, activated by blue light, for acetone detection operable at room temperature.

Materials and methods

Regular microscopic glass slides were used to provide mechanical stability for the sensors. The Loctite ECI 1006 E&C silver ink was used for printing interdigitated electrodes (IDEs, 14.8 mm long, 300 μm wide, and 500 μm spacing) on the glass substrates followed by curing at 120 °C for 15 minutes in the regular oven. Saral Copper 200 screen printable ink was mixed with Saral curing agent A and curing agent B (in the specific ratio) and a blanket layer of copper was screen printed on top of the silver IDEs followed by curing in an oven at 150 °C temperature for 5 minutes. The entire printed structures were thermally oxidized at 450 °C for 1 hour on a hot plate under ambient conditions.

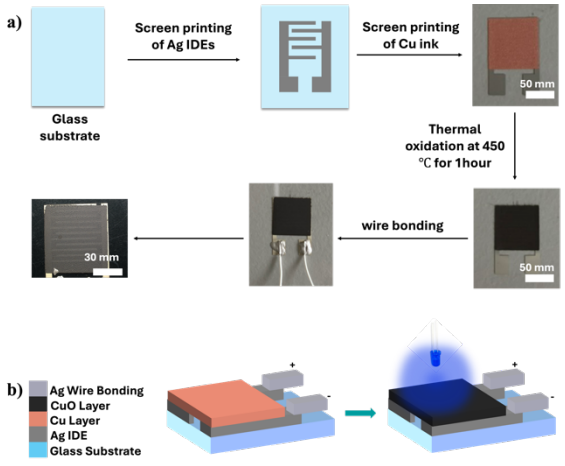


Fig. 1 a) A schematic diagram of the process flow for the sensor fabrication including images of the fabricated devices. b) Cross-section schematics of the fabricated sensors.

The sensor was tested with acetone in a VOC gas testing chamber [7] at room temperature. The sensor was activated with a commercially available blue LED which remained on

throughout the entire experiment. For a p-type semiconductor, like copper oxide, an increase in resistance indicates a response to acetone (reducing gas) [8] and the relative response was calculated by

$$S = \frac{R_g - R_0}{R_0} \times 100\%, \quad (1)$$

where R_g represents the sensor resistance in the presence of acetone and R_0 represents the sensor resistance in air.

Results

The XRD patterns (Fig. 2a) confirmed that the screen-printed copper layer has been oxidized leading to the formation of both phases of copper oxides, i.e., cuprous oxide (Cu_2O) and cupric oxide (CuO). It can also be qualitatively said that Cu_2O is present in a higher proportion than CuO along with a trace of unoxidized copper. Fig. 2b demonstrates the sensor's response to repeated cycles of exposure to acetone vapor, in the fixed time range of 5000 seconds for each cycle.

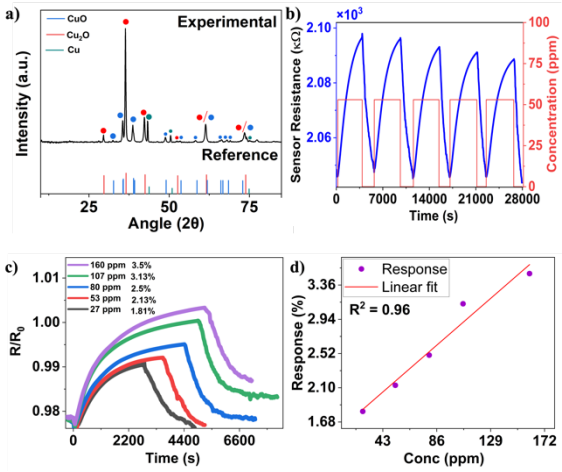


Fig. 2 a) XRD result of screen-printed and thermally oxidized copper oxide b) Sensor response to cyclic acetone exposure c) Normalized response towards different concentrations of acetone d) Response vs. concentration.

This copper oxide-based chemiresistive sensor detects acetone through surface adsorption and desorption that modulate the hole concentration, altering the resistance of copper oxide. The slight drift (Fig. 2b) in response may be due to the irreversibility during surface adsorption and desorption. Fig. 2c presents the normalized sensor's response to different concentrations of acetone, showing that the responsivity increases with increasing acetone concentration and from Fig. 2d, a sensitivity of 5% per 100 ppm of acetone was estimated.

Conclusion

In this work, we have introduced a copper oxide-based acetone sensor by screen printing copper ink and converting it to copper oxide by thermal oxidation. XRD confirmed the formation of copper oxide, and the sensor responded to acetone under blue light activation at room temperature. This method is suitable for large-scale production of copper oxide sensors for power-efficient acetone detection.

Acknowledgements

This work has been jointly supported by the European Union under the MSCA COFUND project CRYSTALLINE, grant agreement no. 101126571 and Silicon Austria Labs (SAL). SAL is owned by the Republic of Austria, the Styrian Business Promotion Agency (SFG), the federal state of Carinthia, the Upper Austrian Research (UAR), and the Austrian Association for the Electric and Electronics Industry (FEEI).

References

[1] Drmosh QA, Olanrewaju Alade I, Qamar M, Akbar S. Zinc Oxide-Based Acetone Gas Sensors for Breath Analysis: A Review. *Chemistry – An Asian Journal*. 2021;16(12):1519-1538. doi:10.1002/asia.202100303

[2] Yang F, Guo J, Liu M, et al. Design and understanding of a high-performance gas sensing material based on copper oxide nanowires exfoliated from a copper mesh substrate. *J Mater Chem A*. 2015;3:20477-20481. doi:10.1039/C5TA06806A

[3] Li Z, Zeng W, Li Q. SnO2 as a gas sensor in detection of volatile organic compounds: A review. *Sensors and Actuators A: Physical*. 2022;346:113845. doi:10.1016/j.sna.2022.113845

[4] Nasriddinov A, Zairov R, Rumyantseva M. Light-activated semiconductor gas sensors: pathways to improve sensitivity and reduce energy consumption. *Frontiers in Chemistry*. 2025;13. doi:10.3389/fchem.2025.1538217

[5] Xu F, HO H-P. Light-Activated Metal Oxide Gas Sensors: A Review. *Micromachines*. 2017; 8(11):333. https://doi.org/10.3390/mi8110333

[6] Simonenko NP, Fisenko NA, Fedorov FS, Simonenko TL, Mokrushin AS, Simonenko EP, Korotcenkov G, Sysoev VV, Sevastyanov VG, Kuznetsov NT. Printing Technologies as an Emerging Approach in Gas Sensors: Survey of Literature. *Sensors*. 2022; 22(9):3473. https://doi.org/10.3390/s22093473

[7] Zikulnig J, Lengger S, Rauter L, Carrara S, Kosel J. A Sustainable Printed Chitosan-Based Sensor for Acetone Detection. In: *2023 18th Conference on Ph.D Research in Microelectronics and Electronics (PRIME)*. ; 2023:121-124. doi:10.1109/PRIME58259.2023.10161879

[8] Barsan, N., Simion, C., Heine, T. *et al.* Modeling of sensing and transduction for p-type semiconducting metal oxide based gas sensors. *J Electroceram* **25**, 11–19 (2010). https://doi.org/10.1007/s10832-009-9583-x

DOI 10.5162/EUROSENSORS2025/M1.1.2

Simultaneous Thermal and Optical (De-)Activation of Microhotplate-Based CMOS-Integrated SnO_2 + Ag NPs Gas Sensors

Florentyna Sosada-Ludwikowska[1], Anton Köck[1], Larissa Egger[1],
Olga Casals[2], J. Daniel Prades[2,3]
Clement Fleury[4], Ali Roshanghias[4],
Andreas Tekautz[5], Michael Donnelly[5]
[1] Materials Center Leoben Forschung GmbH, Vordernberger Straße 12, 8700 Leoben, Austria,
[2] Universitat de Barcelona, Gran Via De Les Corts Catalanes 585, Barcelona 08007, Spain
[3] Institute of Semiconductor Technology (IHT) & Laboratory for Emerging Nanometrology (LENA) Technische Universität Braunschweig, 38106 Braunschweig, Germany
[4] Silicon Austria Labs GmbH, 8010 Graz, Austria
[5] UnraveITEC OG, 8010 Graz, Austria

Corresponding Author's e-mail address: florentyna.sosada-ludwikowska@mcl.at

Summary:
In this paper, we report on the light activation of SnO_2-based gas sensing films decorated with Ag nanoparticles (NPs). The sensing layers were deposited by spray pyrolysis, and the metallic NPs were sputter-deposited on CMOS-integrated microhotplate-based gas sensor devices. The response towards the target gas CO can be tuned by different LED wavelengths. From the results achieved, we conclude that the combined thermal-optical excitation of the gas sensing materials can make a significant contribution to optimizing chemo-resistive MOx-based gas sensor devices.

Keywords: metal oxide, optical activation, gas sensing, metallic nanoparticles, CMOS technology

Background

Air quality control has become a critical global issue due to pollution from fine particulate matter and hazardous gases [1]. Conductometric chemical sensors based on metal oxides offer a practical approach for detecting these harmful species, as their operation relies on changes in electrical resistance in the presence of specific target gases. [2] This principle provides a significant advantage in terms of measurement simplicity. While metal oxide gas sensors demonstrate high sensitivity to various gases, they are often affected by cross-sensitivity. To address this limitation, LED light has been successfully employed to activate or deactivate the response of thin film metal oxide-based gas sensors. In this study, we report the performance of SnO_2 thin films integrated on CMOS-based micro-hotplate (µhp) devices, functionalized with silver nanoparticles, and activated under light illumination at 395 nm and 270 nm.

Description of the System

The CMOS-integrated µhp chips have been fabricated by ams AG. This is a unique device where a single chip contains 8 µhps. Each µhp contains 2 single sensing layers suitable for 4-point measurement. The SnO_2 sensing layer was deposited by spray pyrolysis with a thickness of 50 nm and functionalized with Ag nanoparticles by magnetron sputtering. The chip was then glued and contacted on a specific PCB (sensing-PCB) and mounted in the gas measurement chamber face-to-face to a PCB with LEDs (LED-PCB).

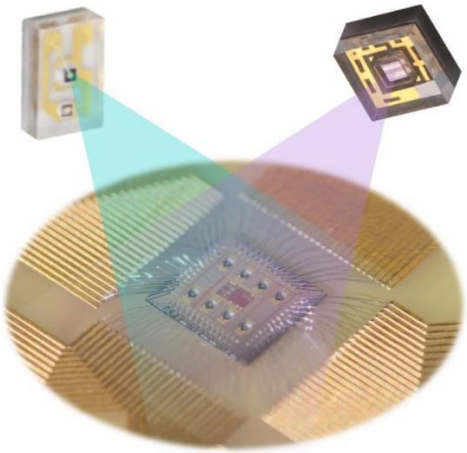


Fig. 1. Scheme of LED radiation on the CMOS-based gas sensing device.

Gas measurements were performed by an automatized setup with synthetic air (80% N_2, 20% O_2) as a background gas and a constant flow rate of 1000 sccm. The humidity level of 50% was kept constant for all measurements and the gas concentration of carbon monoxide was 50 ppm. The temperatures of the µhp were in the range of 100-200°C. The response was calculated as follows:

$$Response = \frac{R_{air}-R_{gas}}{R_{air}} * 100\% \quad (1)$$

where R_{air} is the resistance of the sensor in synthetic air (50% rH) before each gas pulse and R_{gas} is the resistance of the sensor in the presence of the test gas.

Results

Responses of the SnO_2 sensor functionalized with Ag NPs towards a concentration of 50 ppm carbon monoxide are shown in Fig. 2. Without illumination the sensor shows 10% response at 100°C, which increases to 53% at 200°C. With 270 nm illumination, the response can be deactivated/decreased to 2% at 100°C, and 30% at 200°C. With 395 nm radiation, the response can be activated/increased up to 37% at 100°C, and up to 71% at 200°C. This means that the optical and thermal excitation can both be used to optimize the sensing system and work as a switch (ON/OFF) of the sensor response.

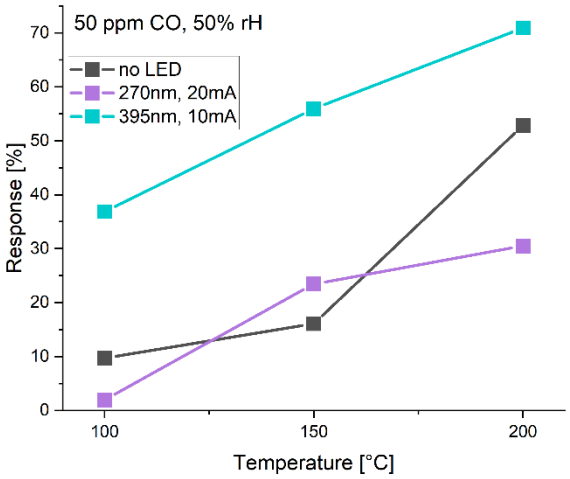


Fig. 2. Response of the SnO_2-sensor functionalized with Ag NPs towards 50 ppm of CO in 50% rH, at 100-150-200°C.

The sensor behaviour can be attributed to two primary phenomena. The first is the photoconductivity of the sensing layer under optical illumination [3], which is evidenced by a decrease in the resistance of the metal oxide layer. This effect results in an increased availability of surface electrons, thereby enhancing the number of active sites for gas detection [4] (see Fig. 2 – 395 nm). The second phenomenon involves the increased desorption rate of gas molecules under higher energy radiation (270 nm, UV range), which leads to a reduced interaction between the gas and the sensing layer, and consequently, a lower sensor response. [5]

These results clearly demonstrate the potential of combining thermal and optical excitation to tune the response behaviour of metal oxide sensors. The ability to activate and deactivate the sensor response through light illumination offers a promising strategy for enhancing selectivity toward specific target gases.

References

[1] T. Feng, Y. Sun, Y. Shi, J. Ma, C. Feng, and Z. Chen, “Air pollution control policies and impacts: A review,” *Renew. Sustain. Energy Rev.*, vol. 191, p. 114071, 2024, doi: 10.1016/j.rser.2023.114071.

[2] G. Korotcenkov, “Gas response control through structural and chemical modification of metal oxide films: state of the art and approaches,” *Sensors Actuators B Chem.*, vol. 107, no. 1, pp. 209–232, 2005, doi: 10.1016/j.snb.2004.10.006.

[3] H. K. Hassun, B. H. Hussein, E. M. T. Salman, and A. H. Shaban, “Photoelectric properties of SnO2: Ag/P–Si heterojunction photodetector,” *Energy Reports*, vol. 6, pp. 46–54, 2020, doi: https://doi.org/10.1016/j.egyr.2019.10.017.

[4] I. Sayago, C. Sánchez-Vicente, and J. P. Santos, “Highly Sensitive and Selective SnO2-Gr Sensor Photoactivated for Detection of Low NO2 Concentrations at Room Temperature,” *Nanomaterials*, vol. 14, no. 24. 2024. doi: 10.3390/nano14241994.

[5] E. Espid and F. Taghipour, “UV-LED Photoactivated Chemical Gas Sensors: A Review,” *Crit. Rev. Solid State Mater. Sci.*, vol. 42, no. 5, pp. 416–432, Sep. 2017, doi: 10.1080/10408436.2016.1226161.

Acknowledgements

The work has been performed within the project “Nano4E - Integrated thermo-optically activated Nanosensors for environmental monitoring”, which receives funding from the Austrian Funding Agency FFG (project No: FO999899024).

JDP is supported by the Alexander von Humboldt Professorship of the Humboldt Foundation and the Federal Ministry for Education and Research (Germany), and the Zukunft Niedersachsen program of the Lower Saxony Ministry for Science and Culture and the Volkswagen Foundation (Germany).

DOI 10.5162/EUROSENSORS2025/M1.1.3

Active Colorimetric Sensor for Real-Time Detection of Gas Mask Filter Saturation

Rodrigue Rousier[1], Romain Anciant[1], Sébastien Donet[2], Hervé Fontaine[2]
[1] Univ. Grenoble Alpes, CEA, LETI, Minatec Campus, F-38054 Grenoble Cedex, France
[2] Univ. Grenoble Alpes, CEA, LITEN, Minatec Campus, F-38054 Grenoble Cedex, France
rodrigue.rousier@cea.fr

Summary:
The respiratory filter cartridge ensures the wearer's safety in toxic environments, provided the cartridge remains unsaturated. To address the challenge of monitoring this saturation to alert the wearer, we present an active colorimetric detection system, which is evaluated with ammonia using a sensitive chromogenic dye. The influence of humidity is also investigated.

Keywords: Chemical warfare agents, toxic industrial chemicals, end-of-service life indicator, colorimetric sensors

Background, Motivation and Objective

Terrorist attacks or industrial disasters can release toxic gases, creating an invisible and often lethal threat to affected areas. In these situations, rescue teams must be deployed to locate and assist victims, requiring them to use personal protective equipment such as gas masks with filter cartridges to mitigate the risk of inhaling harmful substances. However, the efficiency of these filters is influenced by factors including the type of gas, its concentration, and environmental variables such as temperature and humidity. The lifespan of the filter is typically limited by the saturation of its active materials, which decreases its ability to adsorb harmful gases. Therefore, a system capable of detecting filter saturation is crucial to ensure the safety and effectiveness of rescue operations [1,2].

In this study, we present a novel approach for detecting filter saturation using an active colorimetric system, which enables real-time monitoring of filter saturation. The study focuses on the system and a specific chromophore dye, chosen for its sensitivity to both organosphosphorus compounds and ammonia.

Description of the New Method or System

The filter cartridge saturation detection device consists of a sensor module array connected to an electronic board interface via flexible data cables. Each sensor module (see Fig. 1), measuring 12 mm x 10 mm, includes a colorimetric sensor and a commercial air quality gas sensor, the BEM680 from Bosch. The colorimetric sensor is made up of two white LEDs (L130-4070002011001 from LUMILEDS) and a photodetector (VEML3328SL from VISHAY) providing a R, G, B ,C (Red, Green Blue and Clear without filter) optical signals. It operates based on reflection detection. Colorimetric sensor is designed to detect only one specific chemical compound. Therefore, the use of an array of sensors is more effective for detecting saturation caused by a wider range of toxic molecules, and could also be used to provide redundancy and thus improve reliability. The BEM680 sensor measures ambient temperature, barometric pressure, and relative humidity (RH), while also detecting a broad range of gases such as volatile organic compounds (VOC). Subsequently the BEM680 will be able to compensate from drifts in the ambient environment and to take into account saturation due to gases not detected by the colorimetric sensors.

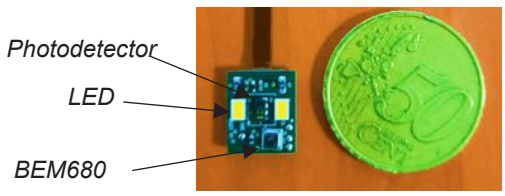


Fig. 1. Module sensor composed of colorimetric sensor and the Bosch BEM680 sensor.

An experimental dedicated filter cartridge integrates 8 sensor modules to be tested on gas test bench (see Fig. 2), this cartridge is the same size as commercial one but it includes flanges for connecting to the gas test bench. A USB wire connection between the electronic board and the computer allows power-up and real-time data ac-

quisition. During experimental evaluation, activated charcoal is replaced by some piece of PTFE to avoid adsorption. The sensor array is integrated into the cartridge between two layers of PTFE chunks. In line with the direction of air flow, the first layer serves as the primary filtration, while the second layer is designed to provide enough time to replace the cartridge after the saturation alarm is triggered by the sensors.

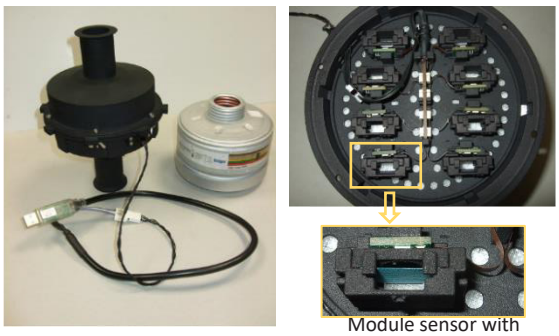


Fig. 2. On the left, the dedicated instrumented filter cartridge is compared to a commercial filter. On the right, the module sensor array inside the dedicated cartridge.

Results

The colorimetric sensor performances were evaluated with gas test bench on ammonia. The gas bench test provides a flow rate range from 6 l/min to 85 l/min, closely matching dynamic respiration range. The carrier gas is synthetic air with RH ranging from 0% to 75%. Ammonia is supplied from a diluted gas bottle with a concentration of 15 ppm. The colorimetric substrate consists of a rectangular piece of paper with a circular area, 8 mm diameter, containing chromogenic dye diluted in dimethyl sulfoxide (DMSO) at a concentration of 10 mM. The remaining area of the paper is black to minimize optical noise.

Experiments were conducted at flow rates of 6 l/min, 33 l/min and 85 l/min with RH set at 0%, 25%, 50%, and 75%, all at room temperature. The system was initially flushed with synthetic air at the desired RH and flow rate. The cartridge was then isolated by closing the valves before and after it. During this isolation, synthetic air mixed with ammonia, maintained at the same RH and flow rate, was stabilized on an independent line until equilibrium was reached. Once stabilized was achieved, the ammonia mixture was switched onto the cartridge. Throughout this entire procedure, measurements were continuously taken for the all eight module sensors. To clarify further, the Figure 3 presents the results of an experiment for only one module sensor, at a flow rate of 85 L/min and 25% RH. The other module sensors showed a similar response. The Green colorimetric signal is not shown due to its high correlation (approximately 0.99) with the Red signal.

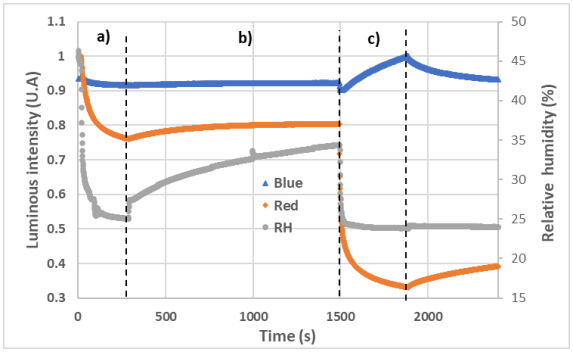


Fig. 3. RH and optical signal responses (Red and Blue signals) under different conditions. a) flow rate of 85 l/min with 25% RH, b) isolation (no flow), c) flow rate of 85 l/min with ammonia and 25% RH.

The results reveal that the colorimetric sensor is able to detect a concentration of 15 ppm ammonia; however; relative humidity interferes with the optical signal. Variations in humidity and ammonia reduce the light intensity of the Red and Green responses, while the Blue response appears less affected by relative humidity, showing an inverse variation with ammonia. As the humidity increases, the magnitude of the variation with NH_3 become more pronounced. For this chromophore, the Blue signal is a key factor to consider when accounting for variations in humidity. However, further investigation and a more in-depth analysis of all the signals are needed to identify the most relevant approach to compensate for humidity.

All the results will be synthesized and presented at the conference related to the final application.

References

[1] G. Favas, End of Service Life Indicator (ESLI) for Respirator Cartridges, Part I: Literature Review, Defence Science and Technology Organisation, 2005, p. 49.

[2] A. Trinchi, I. L. Kyratzis, J. Oestreich, R. Wild, et M. R. Hill, Residual Lifetime Indicators for Respiratory Cartridges and Canisters: Challenges and Opportunities for Sensing, Advanced Sensor Research, vol. 4, nº 2, p. 2400029, 2025, doi: 10.1002/adsr.202400029.

Acknowledgements

The authors thank the French trans-governmental CBRN-E R&D program for its financial support.

DOI 10.5162/EUROSENSORS2025/M1.1.4

MOF-199 as a Colorimetric Sensor for Trace Humidity Detection.

María González-Gómez[1,2], Elizabeth Martínez Medina[3], Janez Kovač[4], Olga Casals[1], J. Daniel Prades[2], Mónica Martínez López[3], Elena Xuriguera Martín[3], Cristian Fàbrega[1].

[1] *MIND/IN2UB, Dept. of Electronics and Biomedical Engineering, University of Barcelona, Marti i Franqués 1, Barcelona, ES08028, Spain.*
[2] *Institute of Semiconductor Technology (IHT), Laboratory for Emerging Nanometrology (LENA), Technische Universität Braunschweig, 38106 Braunschweig, Germany.*
[3]*Dept. of Materials Science and Physical Chemistry, University of Barcelona, Marti i Franqués 1, Barcelona, ES08028, Spain.*
[4]*Jozef Stefan Institute, Department of Surface Engineering, Jamova 39, SI-1000 Ljubljana, Slovenia.*
lugosagonzalez@ub.edu

Summary:

This work presents a low-cost, portable, colorimetric sensor based on the metal-organic framework MOF-199 ($Cu_3(BTC)_2$) for trace humidity detection across a wide range (0–80% RH). The MOF's color transition, from dark blue to turquoise, enables detection down to 18 ppm H_2O (<0.1% RH). The sensor was fabricated by spraying MOF-199 onto polyester and integrating it with a commercial LED-photodiode module. Interferent studies showed strong selectivity for H_2O over CO_2, CH_4, and N_2O with good reversibility and stability over one week.

Keywords: colorimetric sensing, MOF-199, $Cu_3(BTC)_2$, metal-organic frameworks, humidity detection, optical sensors

Background, Motivation an Objective

Low relative humidity (ppm) sensors are vital in industries such as microelectronics and petrochemicals, where even trace amounts of moisture can compromise safety or efficiency [1]. Most portable monitoring solutions rely on electrical sensors [2,3], which are less sensitive than optical methods, particularly in the ppb–ppm detection range [4]. Applications like transformer oil monitoring, cooling gas purity, or radioactive material handling demand sensors with ultra-low detection limits that also withstand harsh conditions.

Metal-Organic Frameworks (MOFs) are crystalline porous structures made by coordinating metal ions with organic ligands. Their tunable pore size, chemical functionality, and structural diversity make them promising for gas sensing. While MOFs are well-studied for their stability and reactivity, their colorimetric potential has been underexplored. MOF-199 ($Cu_3(BTC)_2$), one of the most studied MOFs, is unique for its visible and reversible color transition upon moisture exposure—dark blue to turquoise—without any added dye [5].

Description of the New Method or System

A novel sensor was developed by spray-coating MOF-199 on polyester films and mounting them onto a holder aligned with a commercially available LED-photodiode pair. The system detects reflected color changes caused by the interaction between water molecules and the copper paddle-wheel units of $Cu_3(BTC)_2$. The design is user-friendly and cost-effective, relying on common materials and scalable manufacturing techniques.

The detection limit was estimated at 18 ppm H_2O (below 0.1% RH). This platform requires no external heating or activation and operates at room temperature. The colour change is fully reversible upon drying with clean air. The sensor's performance is not only sensitive in the low humidity regime but also spans a broad range up to 80% RH.

Results

The sensor demonstrated strong and reproducible colour transitions across the entire tested humidity range. Figure 1 illustrates the relationship between analyte concentration and the optical

signal at various ppm humidity concentrations. For humidity levels greater than 1% RH, the sensor exhibited different linearity ranges, which we compared to the sensor's behaviour during humidity adsorption. These similarities enabled us to link the color transition to the interaction between the gas and the active sites in the MOF, revealing an adsorption isotherm profile for humidity that closely mirrored the color variation.

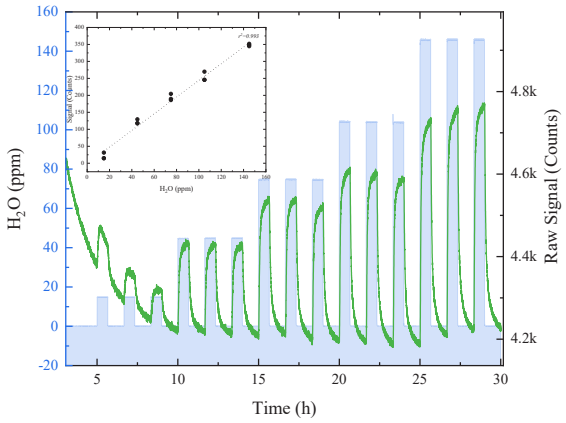


Fig. 1. Signal obtained from MOF-199 exposed to 15-150 ppm of H_2O (<1%RH, 25ºC,1atm).

Interferent gas studies revealed significant changes in presence of NH_3, CO, and ethanol, while gases like CO_2, CH_4, and N_2O showed negligible effects. Some analyte interactions were irreversible, suggesting different binding strengths and affinities. Despite this, the moisture signal remained dominant and distinguishable.

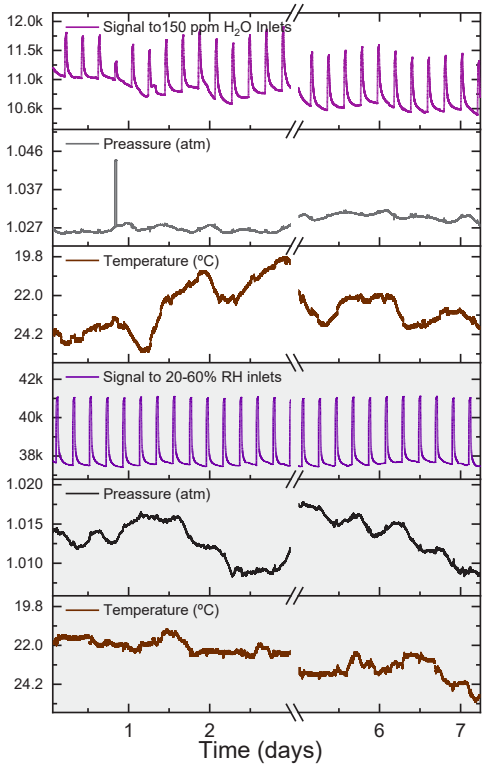


Fig. 2. Signals collected from MOF-199 during humidity inlets every 5 hours over a 7-day period. The input ranged from 0-150 ppm (top) and 20 to 60% RH (bottom). Pressure and temperature measurements were taken simultaneously using commercial BME280 sensor.

A long-term experiment conducted over one week demonstrated excellent repeatability and full reversibility of the sensor's response after drying. The stability of the MOF-199 layer was maintained without performance degradation. However, temperature variation is correlated with variation of the signal demonstrating a strong dependency.

References

[1] Domènech-Gil, G.; Puglisi, D. Benefits of Virtual Sensors for Air Quality Monitoring in Humid Conditions. *Sens Actuators B Chem* **2021**, *344*, 130294, doi:10.1016/J.SNB.2021.130294.

[2] Kumar, L.; Islam, T.; Mukhopadhyay, S.C. Sensitivity Enhancement of a PPM Level Capacitive Moisture Sensor. *Electronics 2017, Vol. 6, Page 41* **2017**, *6*, 41, doi:10.3390/ELECTRONICS6020041.

[3] Li, Y.; Deng, C.; Yang, M. Facilely Prepared Composites of Polyelectrolytes and Graphene as the Sensing Materials for the Detection of Very Low Humidity. *Sens Actuators B Chem* **2014**, *194*, 51–58, doi:10.1016/J.SNB.2013.12.080.

[4] Ma, Z.; Fei, T.; Zhang, T. An Overview: Sensors for Low Humidity Detection. *Sens Actuators B Chem* **2023**, *376*, 133039, doi:10.1016/J.SNB.2022.133039.

[5] Ullman, A.M.; Jones, C.G.; Doty, F.P.; Stavila, V.; Talin, A.A.; Allendorf, M.D. Hybrid Polymer/Metal-Organic Framework Films for Colorimetric Water Sensing over a Wide Concentration Range. *ACS Appl Mater Interfaces* **2018**, *10*, 24201–24208, doi:10.1021/acsami.8b07377

DOI 10.5162/EUROSENSORS2025/M1.2.1

Lab-on-chip systems – new perspectives for microgravitional biomedical research in space

Agnieszka Krakos[1]
[1]Faculty of Electronics, Photonics and Microsystems, Wroclaw University of Science and Technology, Wrocław 27 Wybrzeże Stanisława Wyspiańskiego st., Poland
agnieszka.krakos@pwr.edu.pl

Summary:
The investigation of the microgravity influence onto different biochemical and biomedical samples is the new research subject discussed in the literature widely. Especially interesting is the opportunity to use small scale, low-weight and fully autonomous lab-on-chip instrumentation to provide comprehensive research in space. According to the current NASA and ESA roadmaps, microfluidic and MEMS-based tools are more and more common, since apart from the ISS research conducted with an astronaut assistance, they can be successfully utilized for the autonomous, unmanned, and highly expertized astrobiological missions. In the paper, the overview of microfluidic technologies developed for space research will be discussed (nanosatellites missions, ISS investigation). Opportunities for microgravity simulation in Earth laboratories conditions with the use of lab-on-chip systems will also be described. The paper ends with a conclusion regarding the perspectives for microgravitional biomedical research.

Keywords: MEMS, microfluidics, microgravitional research, space science,

Background and Objective

Lab-on-Chip (LOC) technologies are pushing boundaries far beyond Earth's labs, with their applications in space research showing limitless potential. There's been a surge of interest in conducting research in the unique microgravity and radiation environments of space, showing atypical behavior of living specimens. Cutting-edge technologies are paving the way for a new generation of miniature instruments for what's called space biomedicine. The compact size of these devices offers significant advantages for space exploration, i.e. reduced launch costs and autonomous operation. This evolution in LOC applications is revolutionizing how we approach scientific research in the challenging conditions of space.

Biological nanosatellites

Though few biological nanosatellite projects have been launched, we've already seen that microgravity significantly impacts living organisms' development. NASA, for example, pioneered missions like GeneSat-1 (2006) and EcAMSat (2017), Fig. 1. These labs were equipped with Lab-on-Chip (LOC) structures, microfluidic components, and optical components, allowing for precise sample dosing, management, and analysis. The focus of both missions was to study *E. coli* bacteria. Researchers simultaneously assessed changes in their metabolism and proliferation using excited fluorescence techniques showing inhibited growth of E. coli colonies in a microgravity environment [1].

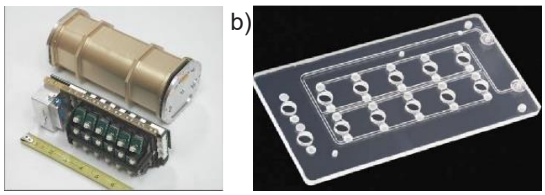


Fig. 1. Gene-Sat laboratory: a) payload, b) lab-chip.

Interesting mission strategies were provided with NASA's O/OREOS (2010) and LabSat (2022, Wrocław University of Science and Technology and SatRev, Poland). Both missions shared a key characteristic: they simultaneously ran two distinct experiments using a Lab-on-Chip (LOC) microfluidic laboratory. The O/OREOS mission used an LOC platform paired with an optical spectrometer to analyze changes in organic compounds like polycyclic aromatic hydrocarbons, amino acids, and quinones in space. Concurrently, O/OREOS investigated the "on-chip" development of *B. subtilis* and *H. chaoviatoris* bacteria. For both strains, researchers noted inhibited colony growth compared to how they grow on Earth [2].

The LabSat mission in turn aimed to study how microgravity affects the cultivation of *F. culmorum* fungi and *L. sativum* seeds. The microlaboratory integrated various microfluidic and optical components to enable direct examination of

biological samples in orbit. Both fungal spores and cress seeds were loaded into lab-chips in a "dry" state. The cultivation process began once the nanosatellite reached its designated altitude and established radio communication. A vision system within the payload was programmed to capture images of the cultures multiple times daily. As a result of the mission, the images showing the germination of cress seed in Low Earth Orbit (LEO) could be captured.

Currently, no biological nanosatellite missions have experimented with more complex biosamples, such as human-derived ones. This limitation stems from the significant challenges in protecting these cells during rocket launches. Thus, stem and cancer cell research in microgravity primarily remains within projects conducted on the International Space Station (ISS).

ISS research

The International Space Station (ISS) offers numerous biomedical testing facilities, e.g. KUBIK, ABRS, EMCS, Bioculture System Facility (Fig. 2), and TangoLab-1. ISS is currently a home to several groundbreaking projects investigating how microgravity affects human cells. In a microgravity environment, cell cultures naturally form spheroids, mimicking how they appear in the human body. ESA's ESA-SPHEROIDS campaign and M4PM (Microgravity for Personalized Medicine) initiative are actively pursuing this research. So far, studies have revealed several significant changes in cancer cells exposed to microgravity. These include reduced proliferation, altered differentiation, changes in cell morphology, and the ability to form aggregations. These aggregations can minimize the impact of shear forces and stresses present in the extracorporeal environment, offering a unique perspective on cancer cell behavior.



Fig. 2. Bioculture System Facility.

NASA in collaboration with US institutions has also been driving the "Tissue Chips" project. This initiative leverages ISS facilities to study cell cultures, focusing on areas like cancer cells, drug resistance mechanisms (especially in kidney and heart tissue dysfunction), immunological changes, and musculoskeletal deconditioning. In 2023, the latest "Tissue Chips" campaign on the ISS, led by a consortium from Stanford University and Johns Hopkins Medicine, featured the Engineered Heart Tissues Chip (EHTs chip). This innovative chip allowed researchers to investigate the function of heart cells, model diseases, and determine the drug resistance of cardiomyocytes [3].

Microgravity simulation in Earth's labs

Beyond the ISS, academic communities are driving significant efforts in microgravity biomedical research. Given the limited capacity of the ISS and the complexities of constructing dedicated research nanosatellites, microgravity simulators are becoming the preferred initial tool for understanding phenomena caused by a quasi-microgravity environment. Instruments like the Random Position Machine (RPM), Rotating Wall Vessel (RWV), and Rotating Cell Culture System (RCCS) are widely used for studying biological samples. A more recent and interesting approach is diamagnetic levitation. Unlike the rotation-based simulators, diamagnetic levitation achieves limited graviperception through the use of magnetic force, offering a unique way to simulate microgravity conditions [4].

Conclusion

Microgravity biomedicine is a fascinating and rapidly evolving field that demands collaboration across numerous scientific disciplines. To create instruments capable of operating in the harsh environment of space, it's essential to leverage extreme technologies, including microelectronics, innovative materials, and intelligent, fully integrated autonomous computer systems. Further miniaturization of analytical devices, despite the inherent construction challenges and unique microscale phenomena, appears to be the most effective way to make microgravity biomedical research more accessible. Microfluidic lab-on-a-chip devices are increasingly being proposed for use in ISS projects, biological nanosatellite missions, and future research initiatives by NASA and ESA—even those extending beyond Low Earth Orbit (LEO).

References

[1] M.R. Padgen, et al., The EcAMSat fluidic system to study antibiotic resistance in low earth orbit: Development and lessons learned from space flight, *Acta Astronautica* 173, 449-459 (2020)

[2] P. Ehrenfreund, et al., The O/OREOS mission—Astrobiology in low Earth orbit, *Acta Astronautica*, 93, 501-508 (2014)

[3] A. Krakos, Lab-on-chip technologies for space research — current trends and prospects. *Microchim Acta* 191 (2024)

[4] A. Vashi, et al., Lab-on-a-Chip Technologies for Microgravity Simulation and Space Applications, *Micromachines* 14, 116 (2023)

DOI 10.5162/EUROSENSORS2025/M1.2.2

A Novel Concept for a Hanle Vector Magnetometer for Space Application

Sunny Laddha[1,2], Christoph Amtmann[1,2], Andreas Pollinger[2], Alexander Betzler[1,2], Irmgard Jernej[2], Roland Lammegger[1] and Werner Magnes[2]
[1] Institute of Experimental Physics, Graz University of Technology, Graz, Austria
[2] Space Research Institute, Austrian Academy of Sciences, Graz, Austria
Corresponding author e-mail: laddha@tugraz.at

Summary:
A novel sensor design for a Hanle vector magnetometer is presented. Linearly and circularly polarized light beams are used in parallel to enable magnetic field measurements with an isotropic noise floor that is stable down to 10^{-1} Hz. The level is three times lower compared to a state-of-the-art fluxgate magnetometer at 1 Hz. The first functional test shows no intrinsic crosstalk between the sensor axes. With the possibility to add an absolute scalar measurement mode, this sensor has the potential to replace the combination of a fluxgate and absolute reference magnetometer on space missions.

Keywords: space, quantum, optical, zero-field, magnetometer

Introduction

Magnetic field measurements in space have advanced the knowledge in various space sciences, such as plasma, Helio- and planetary physics. Therefore, magnetometers are part of many scientific space missions. Fluxgate magnetometers (FGMs) are the preferred technology, due to their low size, weight and power requirements as well as high reliability. However, their systematic offset drifts necessitate in-flight calibration using for example spacecraft roll maneuvers or an additional onboard absolute reference sensor. For the latter, quantum magnetometers are used, as they derive the magnetic field measurement from fundamental atomic properties [1]. A recent example is the scalar instrument on board ESA's Jupiter Icy Moons Explorer mission. This optically pumped magnetometer (OPM) is based on the 'Coupled Dark State Magnetometer' (CDSM) design and provides dead-zone-free reference values of the absolute magnetic field strength to calibrate the accompanying FGMs [2]. In order to reduce the need for in-flight calibration altogether and to improve the sensitivity of vector measurements, Hanle effect based zero-field magnetometers are a potential replacement for FGMs. Here, we present a proof-of-concept laboratory model for a novel sensor design, with the main goal of enabling vector measurements with isotropic sensitivity and outperforming FGMs in terms of long-term stability.

Method

The Hanle effect describes resonances in the absorption of laser light by an atomic species, as the ambient magnetic field components of either of two principal axes are scanned through zero. The orientation of the third 'insensitive' axis with respect to the optical axis depends on the light polarization state (see [3]). Most Hanle magnetometers favor a single-beam setup for its mechanical simplicity and extract the third vector component with lower sensitivity through a special lock-in detection scheme [4]. Our setup uses two beams in parallel configuration, one linearly polarized, the other circularly (see Fig. 1). This avoids the mutually exclusive insensitive axes and enables isotropic measurement sensitivity. The linearly polarized beam yields the magnetic field component parallel to the beam direction and the circular beam detects the transverse components.

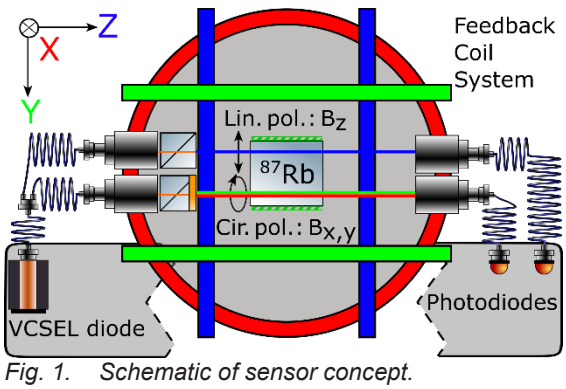


Fig. 1. Schematic of sensor concept.

For the laboratory setup, the feedback current source (design from [5]) and two external photodiodes are realized as separate units. Closed-loop operation is initialized through iterative magnetic field scans, with superimposed AC-fields with a distinct frequency for each axis. This enables the use of phase sensitive lock-in detection for increased signal to noise ratio.

First Results

The functionality and sensitivity of the sensor were tested within a µ-metal shielding with a residual ambient magnetic field of less than 5 nT. Fig. 2 shows the triaxial sensor response to a sinusoidal test field applied along the Z-axis. The amplitude of <0.2% (of the applied test field) in the X- and Y-axes indicates a misalignment between sensor and test coil, rather than a systematic measurement error.

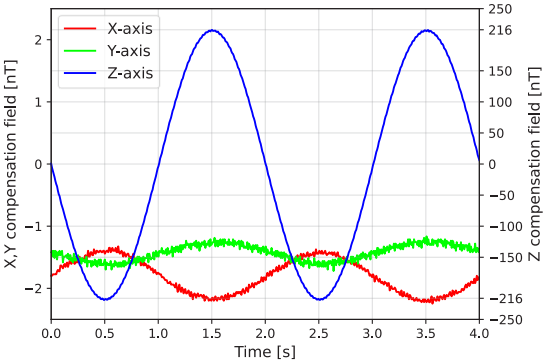


Fig. 2. Time domain instrument response to a sinusoidal test signal applied along the sensor Z-axis, with 216 nT amplitude and 0.5 Hz frequency.

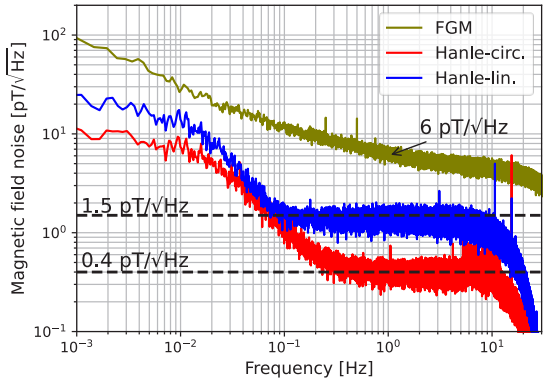


Fig. 3. Noise spectral density of a representative FGM axis and both optical paths of the Hanle magnetometer.

Fig. 3 compares the sensitivity performance between both polarization paths of the Hanle setup (circular pol=X; linear pol.=Z) and a representative axis of an FGM. The used FGM is one of the flight models for ESA's Comet Interceptor mission. The Hanle sensor achieves a noise floor at least four times lower than the FGM at 1 Hz and maintains a stable level down to ca. 0.5 Hz. The different noise levels in both polarization paths are likely due to the choice of frequencies for lock-in detection. In principle, a sensitivity of less than 20 pT/√Hz at 1 mHz has been achieved for both polarization states in all axes when operated individually.

Discussion and Outlook

The initial results obtained with this laboratory setup demonstrate the capability of this novel sensor concept to measure the full magnetic field vector with a near isotropic sensitivity that is higher than from a state-of-the art FGM. Due to the multidimensional parameter space, such as the three different lock-in detection frequencies, there is still room for improvement for lowering the 1/f noise below 10^{-1} Hz. The next development step for this setup is to demonstrate operation in a dynamic range of ±5000 nT. With the addition of a single hardware component (microwave oscillator), the current setup could technically also be operated as a CDSM. The combination of a vector and absolute scalar measurement mode would enable the use of a single, self-calibrating magnetometer instead of two separate instruments on future space missions.

References

[1] D. Budker, D.F.J. Kimball, Eds., Optical Magnetometry, *Cambridge University Press*, (2013); doi: 10.1017/CBO9780511846380

[2] C. Amtmann et al., Accuracy of the scalar magnetometer aboard ESA's JUICE mission, *Geoscientific Instrumentation, Methods and Data Systems* 13, 177-191 (2024); doi: 10.5194/gi-13-177-2024

[3] A. Grosz et al. (eds), High Sensitivity Magnetometers, *Smart Sensors, Measurement and Instrumentation* 19, 361-424 (2017); doi: 10.1007/978-3-319-34070-8_13

[4] R. E. Slocum and F.N. Reilly, Low field Helium Magnetometer for Space Applications, *IEEE Transactions on Nuclear Science* vol. 10 no. 1, 165-171 (1963); doi: 10.1109/TNS.1963.4323257

[5] M. S. Mrozowski et al., Ultra-low noise, bi-polar, programmable current sources, *Rev. Sci. Instrum.* 94, 014701 (2023); doi: 10.1063/5.0114760

Acknowledgements

This work is enabled through the "Young Researcher Program at Graz" as well as the ESA technology development project "Optical Vector Magnetometer based on the HANLE Effect" (contract no. 4000145027/24/NL/AR/ahhhe). Furthermore, we sincerely thank our colleagues M. Agú, G. Fremuth, F. Giner, M. Leichtfried, R. Steinhöfler, A. Ullmann, A. Valavanoglou and J. Wilfinger for their support in this project.

DOI 10.5162/EUROSENSORS2025/M1.2.3

Towards Miniaturized XRF Systems: A MEMS X-ray Source for Space Exploration

Paweł Urbański, Piotr Szyszka, Tomasz Grzebyk
Faculty of Electronics, Photonics and Microsystems, Wroclaw University of Science and Technology, Wrocław 27 Wybrzeże Stanisława Wyspiańskiego st., Poland
pawel.urbanski@pwr.edu.pl

Summary:
The analysis of planetary surfaces composition using X-ray fluorescence (XRF) is essential for understanding geological processes and resource potential. Traditional XRF systems are based on bulky X-ray tubes or radioisotopes, limiting their use in space missions. This work presents a MEMS-based miniature X-ray source integrating a field emission electron source and a transmission target within a miniature silicon-glass structure. The source operates at low power (<0.1 W), while efficiently generating X-rays. By combining it with a small X-ray detector one obtains lightweight, energy-efficient planetary exploration instrument.

Keywords: MEMS, lunar regolith, space, XRF, X-ray source

Introduction

X-ray fluorescence (XRF) spectrometry is one of the most effective, and at the same time nondestructive, methods for analyzing the elemental composition of any materials. In space explorations it perfectly suits for analyzing lunar regolith and other planetary surfaces. Previous space missions have used mainly radioisotope radiation sources and conventional X-ray tubes [1-3]. While effective, these solutions have significant limitations: they are relatively large, heavy, and require significant amounts of energy, which creates a challenge to the miniaturization of scientific instruments for planetary missions. Consequently, there is a need for developing alternative X-ray sources that are compact, energy-efficient, and suitable for autonomous measurement systems.

Microelectromechanical systems (MEMS) technology opens up new possibilities for miniaturization of X-ray sources. By integrating functional components at the micrometer scale, compact and efficient X-ray generation systems can be created [4]. This paper presents a novel MEMS X-ray source that uses a field emitter as an electron source and a transmission target for X-ray generation [Fig. 1]. The silicon-glass structure of the device allows for reduced system weight and dimensions, and the use of a combination of magnetic and electrostatic focusing of the electron beam enables high efficiency. In addition, the source offers the possibility to control emission intensity, energy, and electron beam size. The source enables efficient XRF operation at very low power consumption (<0.1 W).

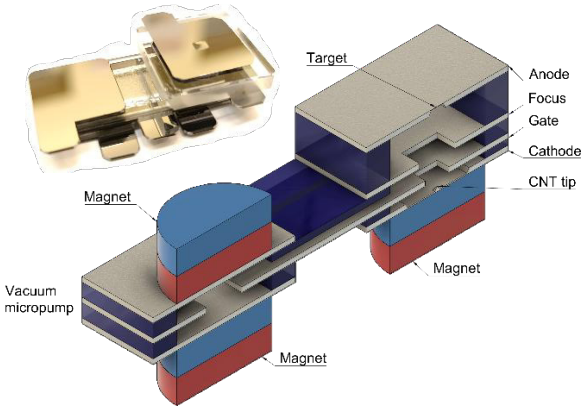


Figure 1. Structure of the MEMS X-ray source

In this article the basic characterization of the X-ray source as well as the analysis of its potential for XRF studies of planetary and lunar surfaces has been carried out.

Device characterization

The X-ray sources for XRF systems must provide sufficient intensity while being compact, energy-efficient, and lightweight.

The developed MEMS X-ray source represents a significant advancement, offering a compact design with high radiation intensity and low power consumption. Unlike X-ray tubes, MEMS source generates intense radiation at low energies [Fig. 2], improving the excitation efficiency for light elements such as oxygen, sodium, or magnesium. The design of electron-optics column allows for precise control over the electron beam, and tailoring radiation characteristics for specific analyses. Operating at lower voltages

(from a few to 30 kV), MEMS source requires only 0.1 W, making it energy efficient for planetary missions. With a mass of just 3.7 g for the MEMS structure and 3.4 g for magnets, it is significantly lighter than traditional X-ray tubes.

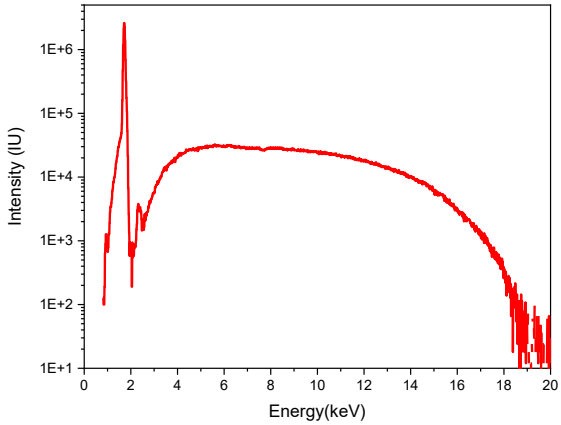


Figure 2. X-ray spectrum emitted by a MEMS source in vacuum

XRF analysis of lunar regoliths

This study investigates the use of a MEMS X-ray source together with compact Ketek X-ray detector to analyze the chemical composition of lunar regolith simulants under vacuum conditions (5E-5 hPa). XRF measurements were performed on four simulants and the results showed a clear and intense signal, particularly for light elements such as sodium (Na), magnesium (Mg), and aluminum (Al). A total of 20 characteristic peaks were identified, highlighting the presence of elements commonly found in lunar basalts and anorthosites, including sodium (Na), magnesium (Mg), aluminum (Al), silicon (Si), phosphorus (P), sulfur (S), chlorine (Cl), potassium (K), calcium (Ca), scandium (Sc), titanium (Ti), neodymium (Nd), iron (Fe), nickel (Ni) and copper (Cu). In addition, a small argon (Ar) peak was detected, indicating the presence of residual amounts of argon in the vacuum [Fig. 3]. The detected elements align with the manufacturer's data for the simulants (except manganese) [5].

Conclusions

This study demonstrates that the developed MEMS X-ray source, with its high intensity in the low-energy range, significantly enhances the efficiency of lunar regolith analysis, particularly for detecting light elements essential for lunar resource exploration and future In situ resource utilization (ISRU) missions.

The presented solution may find application in future planetary missions, offering a lightweight and energy-efficient alternative to traditional sources used for XRF, significantly expanding the possibilities for autonomous analysis of regoliths and other extraterrestrial surfaces.

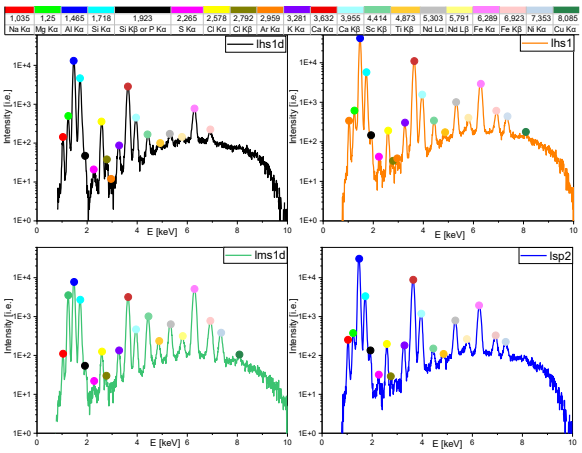


Figure 3. XRF analysis of lunar regolith simulants under vacuum conditions

References

[1] A. Allwood et al., Texture-specific elemental analysis of rocks and soils with PIXL: The Planetary Instrument for X-ray Lithochemistry on Mars 2020, in 2015 IEEE Aerospace Conference, IEEE, 1-13 (2015), doi: 10.1109/AERO.2015.7119099.

[2] J. L. Campbell et al., A fundamental parameters approach to calibration of the Mars Exploration Rover Alpha Particle X-ray Spectrometer, J Geophys Res Planets, 114(E4) (2009), doi: 10.1029/2008JE003272.

[3] I. Adler *et al.*, Apollo 16 Geochemical X-ray Fluorescence Experiment: Preliminary Report, *Science*, 177(4045), 256–259 (1972), doi: 10.1126/science.177.4045.256.

[4] P. Urbański and T. Grzebyk, MEMS-Compatible X-Ray Source, *Journal of Microelectromechanical Systems*, 33(5), 508–510 (2024), doi: 10.1109/JMEMS.2024.3426111.

[5] Lunar Regolith Simulants, Space Resource Technologies. Access: 03.04.2025, https://space-resourcetech.com/collections/lunar-simulants

Acknowledgments

The work was financed by the project 2021/41/B/ST7/01615 of Polish National Science Centre.

DOI 10.5162/EUROSENSORS2025/M1.3.1

"Matching" of Photodetectors Integrated in a 0.18 µm Modular CMOS Foundry Technology

Daniel Gäbler[1], Frank Fischer[1], Roland Rösch[1], Pablo F. Siles[1]
[1] X-FAB Global Services GmbH, Haarbergstraße 67, 99097 Erfurt, Germany
daniel.gaebler@xfab.com

Summary:
Matching is a design parameter for analog CMOS applications which describes the statistical device differences between pairs of identical designed and used devices [1]. This is common for transistors but not (yet) for photodiodes. Its significant impact on common optical detection tasks is explained related to extracted values from three photodiodes manufactured in the XS018 CMOS technology.

Keywords: Matching, Photodiodes, CMOS, Spectral Response, Dark Current, Capacitance

The Hidden Power

Matching or the synchroneity of devices has the power to make or break the function of an integrated circuit. People carefully check performance parameters but often forget to think about the limitations in the system aspect that are caused by asynchrony of variations between parts. In sensor technology, the most important thing is to extract the signal in the noise. Improved matching is reducing the noise, increasing the working range, the sensitivity and last but not least the yield.

Description of the Devices and the Test

Exemplary three typical junction diodes are used for the investigations. *doa* is a deep n-well in p-epi (substrate) with a broad-spectrum response, *dob* is adding an electrically shorted p-well into the deep n-well resulting in a cutoff for the short wavelength. *doa* and *dob* are preferably used as pair when two distinct spectral functions are needed, with little as possible other differences in the device behavior (see Fig. 1 & 2). Finally, *doe* is an n-well in p-epi (substrate) diode with a broad-spectrum response, like *doa*, but with less process effort and the potential of higher fill factor due to simpler layout and tighter design rules.

To cover several use cases three major layout options have been investigated for each diode.

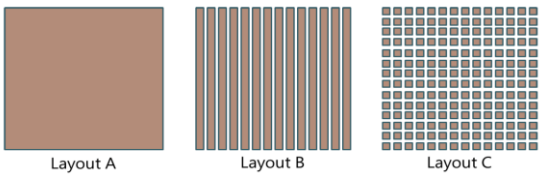


Fig. 1. Investigated layouts. A is a single device, B and C are arrays of devices connected in parallel.

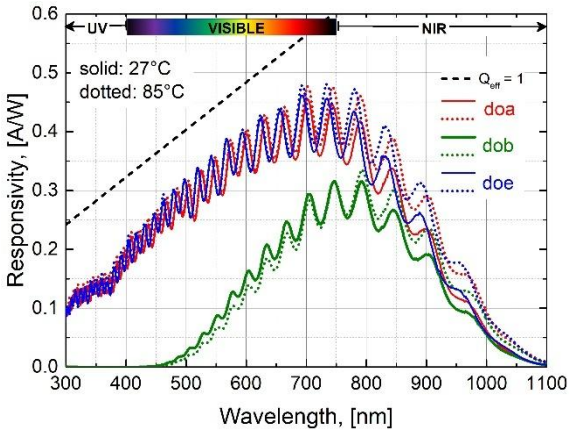


Fig. 2. Spectral response of the devices investigated.

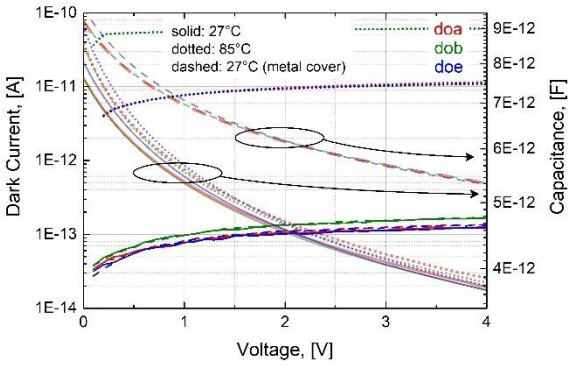


Fig. 3. Dark current and capacitance behavior of 250x250 µm² optical active area devices (Layout A).

For the matching investigations 174 elements from 3 wafers for each diode pair respectively layout options (see Fig. 1) were tested on two temperatures (27°C and 85°C) for dark current, capacitance and photocurrent at two wavelengths (420 nm & 850 nm) altogether about 50k measurements. This was done using a Keithley S600 with a specialized optical probe card to enable the photocurrent test. The photodiodes

were biased at 0.9 V in reverse and the capacitance was measured at 100 kHz. All photodiodes had a 3.3 V reverse biased guard ring. Parasitic effects of the system and the layout (PAD, wiring) until the DUT (photodiode) have been subtracted using dummy layout elements.

Results and Discussion

The light insensitive (metal covered, here called "blind") photodiodes have a systematic offset of the capacitance caused by the metal plate used to shield the light, which can be compensated. The sigma is excellent.

Tab. 1: doa dark current and capacitance matching.

Parameter /Layout		*open/open*		*blind/blind*		*open/blind*	
		sigma	mean	sigma	mean	sigma	mean
Dark Current @ 85°C	A	0.82	0.74	0.51	0.08	1.06	-1.10
	B	0.79	-0.01	0.63	-0.37	1.97	-4.79
	C	0.77	-0.02	0.47	0.11	1.27	-4.02
Capacitance @ 27°C	A	0.19	0.05	0.13	-0.03	0.38	29.27
	B	0.18	0.12	0.16	-0.01	0.20	-3.51
	C	0.19	0.06	0.16	-0.02	0.22	-9.52
Capacitance @ 85°C	A	0.47	0.02	0.40	-0.04	0.51	-28.48
	B	0.48	0.15	0.51	-0.08	0.48	-3.44
	C	0.64	0.09	0.64	-0.04	0.67	-9.47

Dark current measurements require a perfectly dark environment. The noise limit of the measurement equipment and the imperfect darkness require elevated temperatures for reliable results, therefore only the 85°C results are used. The offset (mean) is small, and the sigma are well below 2.5 even for the combination of light sensitive (open) and dark reference (blind) which showcase the significant improvement achieved by [2].

Tab. 2: dob dark current and capacitance matching.

Parameter /Layout		*open/open*		*blind/blind*		*open/blind*	
		sigma	mean	sigma	mean	sigma	mean
Dark Current @ 85°C	A	1.91	-0.11	1.51	0.03	1.45	-0.59
	B	0.62	0.02	0.47	-0.05	1.45	-1.91
	C	0.69	0.37	0.44	0.24	1.29	-0.34
Capacitance @ 27°C	A	0.16	0.05	0.14	-0.03	0.40	-29.20
	B	0.18	0.06	0.17	-0.01	0.20	-3.59
	C	0.19	0.02	0.16	-0.03	0.22	-9.51

Such small sigma for the open to blind pair enables to expand the sensitivity range by 1.5 orders of magnitude. Alternatively, it maintains the sensitivity for up to 50 K higher temperature.

This is due to the usage of the blind device for dark current subtraction which cuts away the noise. It allows omitting cooling measures which are costly, bulky and consume energy. Additionally, the sensor devices can be made smaller because of the higher sensitivity, which saves chip area, improves yield, allows for smaller form factors and most importantly lowers the cost.

Tab. 3: doe dark current and capacitance matching.

Parameter /Layout		*open/open*		*blind/blind*		*open/blind*	
		sigma	mean	sigma	mean	sigma	mean
Dark Current @ 85°C	A	2.06	1.73	2.08	0.27	2.31	-0.88
	B	0.74	0.12	0.57	-0.23	1.91	-4.63
	C	0.70	0.01	0.59	-0.03	1.44	-4.07
Capacitance @ 27°C	A	0.17	-0.01	0.14	-0.03	0.35	-28.77
	B	0.15	0.07	0.18	-0.02	0.22	-3.88
	C	0.20	0.05	0.19	-0.01	0.24	-10.34

The capacitance matching values for 85°C have been left out for dob and doe, as they are redundant information.

Tab. 4: Photocurrent matching at 420 nm.

Parameter /Layout		*doa*		*dob*		*doe*	
		sigma	mean	sigma	mean	sigma	mean
Photocurrent @ 27°C	A	0.29	1.52	-	-	0.27	1.27
	B	0.30	2.24	-	-	0.21	1.13
	C	0.16	1.07	-	-	0.18	0.41
Photocurrent @ 85°C	A	0.23	-0.46	-	-	0.22	-0.66
	B	0.16	0.53	-	-	0.17	-0.56
	C	0.15	0.45	-	-	0.13	-0.76

DOI 10.5162/EUROSENSORS2025/M1.3.1

The photocurrent needs light, thus only the combination open-open makes sense to look at. The photodiode *dob* is insensitive to short wavelength light (see Fig. 2). These values are left blank in table 4 by intention.

Overall, the photocurrent offset is small and the sigma superb with a value below 0.3, enabling high precision multi-channel sensors.

Tab. 5: Photocurrent matching at 850 nm.

Parameter /Layout		*doa*		*dob*		*doe*	
		sigma	mean	sigma	mean	sigma	mean
Photocurrent @ 27°C	A	0.20	0.25	0.23	0.40	0.24	1.23
	B	0.29	2.18	0.25	0.74	0.26	1.23
	C	0.21	0.18	0.26	1.07	0.23	0.07
Photocurrent @ 85°C	A	0.15	-1.43	0.21	-0.04	0.24	-0.47
	B	0.17	-0.61	0.24	0.78	0.22	-0.09
	C	0.19	0.03	0.20	0.48	0.20	-0.64

Conclusion and Summary

There is little improvement potential on the signal strength of a silicon photodetector. In contrast lowering the noise level has huge potential. Good matching photodetectors allow pushing the limits by ~1.5 orders of magnitude towards lower light levels or 50 K in temperature, which is a huge step with a lot of practical benefits.

References

[1] Marcel J.M. Pelgrom, Hans P. Tuinhout and Maarten Vertregt, "Transistor matching in analog CMOS applications", IEDM 1998, pp 915-918

[2] Daniel Gäbler, Pablo F. Siles, "Dark reference device for improved dark current matching", Patent GB 2596122 B, 18.06.2020

DOI 10.5162/EUROSENSORS2025/M1.3.2

Thin – Film Thermocouple Sensor Development for Smart Battery Cells

Huseyin Yigit Cem Altintas[1], Dr. Erdogan Guk[1], Prof. James Marco[1], Dr. Timothy Vincent[1]
[1] WMG, University of Warwick, Coventry, CV4 7AL, United Kingdom

Summary:
Smart battery cell concept, cells with integrated sensors, becomes more important as battery manufacturer tend to manufacture larger capacity packs to meet electrification demand. In order to accomplish smart cell concept in battery cells first step is accurate perception of battery states. However, conventional sensors are not able to measure parameters precisely. Furthermore, these bulky conventional sensors add significant weight resulting in significant loss in energy/kg density, thereby limiting the feasible quantity and therefore spatial coverage. This study presents a thin-film temperature sensor designed for battery monitoring. A thin layer (total <150 nm) of Alumel & Cromel (K-type thermocouple) are sputtered onto a newly developed TECASUB PEEK LDS (Polyether ether ketone). The sensor was tested externally on cylindrical cell and successfully capture temperature gradients with 1C cycling test.

Keywords: Thin – film, Flexible Sensors, Sputtering, Temperature Sensing, Smart Batteries

Background, Motivation an Objective

Batteries are being pivotal part of net-zero society. However, increasing prevalence of batteries highlights their safety problem for example China experienced an average of seven EV fire incidents per day in the first half of 2022 [1]. Moreover, this trend is likely to increase as vehicle manufacturers move towards longer range, larger vehicles, requiring higher capacity packs. Early fault detection mechanisms are essential to prevent cell failures becoming catastrophic. Current pack topologies, trade-off sensor deployment with cost, typically resulting in one or two temperature sensors per module (12 – 16 cells). This sparse configuration causes inefficient management of battery cell resulting with premature degradation & safety issues.

To minimise potential safety hazards and increasing efficiency of batteries, we propose smart cell, cells integrated with sensors and circuitry. At laboratory scale, integrating sensors within a cell has been demonstrated [2], its practical application is hindered by conventional, bulky sensors, which significantly increase the weight of the battery pack & inability to be implanted within the construction of the cell for more fast and accurate measurement.

Thin – film sensor technology offers promising solution for this field – principally films can be deposited on a range of substrates, including flexible materials. Their minimal size, high precision and fast responses make them ideal candidate for battery applications. Current state-of-art blends flexible substrates with off-the-shelf sensors, for example Vincent et al. embedded a thermistor film array inside a cylindrical cell to measure core temperature [3]. Challenges such as corrosive environment, potential negative effect on battery performance (capacity loss, necessity of cell modification post-manufacture).

In this study, a novel thin – film temperature sensor was developed with Polyether ether ketone substrate and manufactured by DC sputtering. The sensor was wrapped around cylindrical cell (Molicel P45B 21700, 4.5 Ah) for preliminary testing to verify sensor and concept design for further sensor implantation into cell.

Materials & Method

Due to its application requirements temperature sensor must be resilient & fast. The sensor will be placed into a cell to observe the gradient between core and external; minimal fluctuations in temperature may help identify degradation, critical to provide an early indicator of failure. Fundamentally, thin-film thermocouples are fast response, reliable and present minimal electrical interference compared to alternative options (thermistors, RTDs etc.). As a passive component, thermocouples which do not need any external excitation to measure temperature, which is crucial to ease applications in batteries.

Sensor Fabrication & Testing

The sensor was fabricated using DC magnetron sputtering (Korvus HEX Magnetron Sputtering System) onto a TECASUB LDS film (Ensinger GmbH, 0.1 mm). A three leg thermocouple

design (3 sensing points, located 15mm apart) was selected to observe axial thermal gradient.

Prior to sputtering active materials, a 30 nm thin layer of titanium was sputtered onto substrate to enhance bonding between sensor and polyimide. Then, 90 nm cromel and 100 nm alumel layers were sputtered respectively to build sensor, following by annealing at 200 °C for 6 hours to strengten bonding.

Subsequent fabrication, sensor was wrapped around the external of a cylindrical cell with K-Type reference thermocouples (RS 363 - 0250) for proof of concept. Shown in Figure – 2.

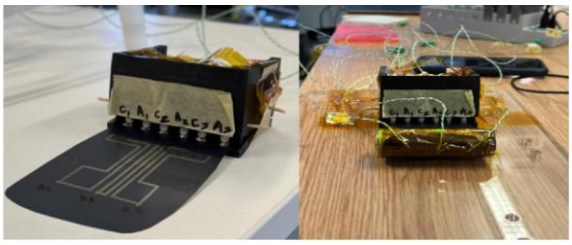


Figure 2 Thin-film sensor and experiment setup on cylindrical cell with reference thermocouples

Post instrumentation, the cell was tested under various battery cycling regimes (housed within a climate chamber at 25°C) to observe sensor reliability and response magnitude. Commercial thermocouples were placed on cell surface to validate temperature reading, Figure – 3.

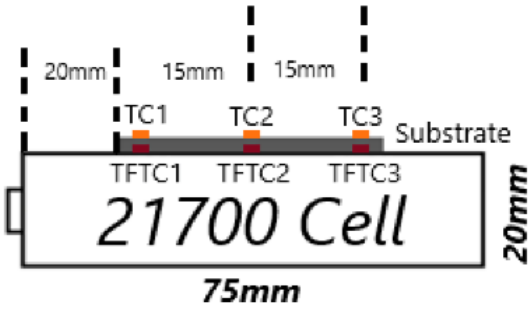


Figure 3 - Layout of thermocouple sensing points.

Measurement was conducted by using data acquisition system (NI 9212 DAQ and 9718 Chassis) configured to record voltage output with acquisition rate of 1s and 1ms respectively. The voltage values were converted to temperature via thermocouple table lookup interpolation.

Results and Discussion

The thin-film sensor successfully tracked temperature during two cycling regimes (firstly 1C with 30-min rest, Figure 4, and secondly 1C with 2-hr rest, Figure 5). The fabricated sensors typically demonstrated good performance (TFTC1 shown here), within +/- 0.5 °C of the reference thermocouples, considering manual sensor alignment. Peak temperature of ~11°C above baseline was recorded at the end of each discharge cycle, aligning with values recorded in prior studies [2]. Baseline drift was observed highlighting the necessity of improved cold junction compensation (CJC) in the aquistion system. Nevertheless, thin – film sensor prominent candiates for smart cell concept.

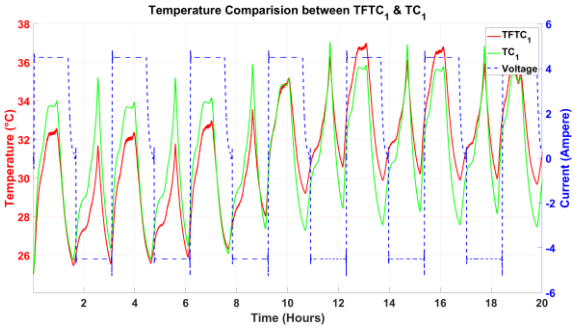


Figure 4 Temperature Value of First Cycling (Red: Thin-Film Thermocouple, Green: Reference)

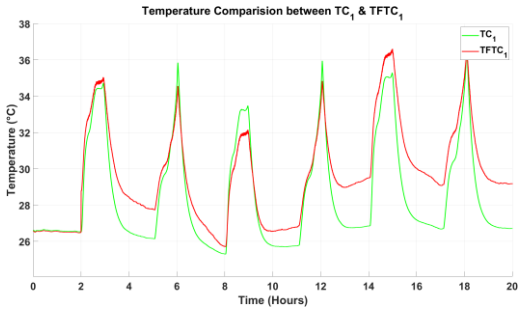


Figure 5 Temperature Value of Second Cycling (Red: Thin-Film Thermocouple, Green:Reference

Future work will involve optimising measurement setup accounting for CJC, and sputtering a novel ceramic coating onto the sensor to prepare the sensor for direct insertion into the cell, to achieve fast and reliable temperature data acquisition. Overall, this study successfully developed a thin-film thermocouple on a novel substrate with an integrated connection mechanism.

Acknowledgements

Thanks to Calum Briggs and Ensinger GmbH.

References

[1] W. Wang, et al., “Advancing Smart Lithium-Ion Batteries: A Review on Multi-Physical Sensing Technologies for Lithium-Ion Batteries,” *Energies*, vol. 17, no. 10, pp. 2273–2273, May 2024, doi: https://doi.org/10.3390/en17102273.

[2] T. A. Vincent, et al., “In-situ instrumentation of cells and power line communication data acquisition towards smart cell development,” *Journal of Energy Storage*, vol. 50, p. 104218, Jun. 2022, doi: https://doi.org/10.1016/j.est.2022.104218.

[3] C. M. Jones, et al., “Direct measurement of internal temperatures of commercially-available 18650 lithium-ion batteries,” *Sci. rep.*, 13, 1, Sep. 2023, doi: https://doi.org/10.1038/s41598-023-41718-w.

DOI 10.5162/EUROSENSORS2025/M1.3.3

Vapor-Channeled Porous Pressure Sensors

Nadeem Tariq Beigh[1*] *and Nouha Alcheikh*[1*]
[1]Khalifa University, Abu Dhabi, United Arab Emirates
[*]nadeem.beigh@ku.ac.ae;[*]nouha.alcheikh@ku.ac.ae

Summary: The superior performance of porous thin-film sensors over the bulk counterparts is constrained by the current porosity induction technology. The state-of-the-art porous sensors are expensive, time and energy intensive, and require high temperature etching steps. In this work, we overcome this issue by realizing a novel mechanism of porosity induction in 2D nanoparticle infused flexible, polymer nanocomposites. Thereby, giving a new direction to low-cost, rapid design, scalable porous nanocomposite design for pressure sensing applications.

Keywords: Porous nanocomposites, pressure sensor, tactile sensing, micro-channels, piezoresistive.

Introduction, Background and Motivation

Porous thin films have been explored for their superior mechanical deformability, higher strain transduction, and high sensitivity in applications involving multi-axis strain/pressure stimulus[1, 2]. However, the fabrication of porous thin films, particularly 2D-material infused nanocomposites has been challenging; owing to the complex, chemically intensive, and energy-inefficient processing[3]. This has severely restricted the projected potential of porous sensors in applications such as robotics, tactile sensing, smart automation, healthcare, sports science, etc.

Embedding porosity is a key method for achieving near-ideal flexible pressure sensors from conventional nanocomposites. These pores act as zero-stiffness dopants, lowering the matrix modulus and thus boosting flexibility, pressure sensitivity, and dynamic sensing range. Recently, various methods such as scaffolding, templating, 3D molds, have been employed to fabricate porous pressure sensors. These methods are passive in terms of transporting the active 2D nanoparticles to regions of maximum strain translation. They follow a bake-first approach, in which the pores are formed after the polymer has solidified. This prevents the dynamics re-adjustment of 2D nanoparticles into microchannel or region of maximum strain[4].

We introduce a novel, easily fabricated porous nanocomposite of vapor-channeled PDMS and graphene nanoplatelets that dramatically enhances pressure sensing. Our optimized ”parallel bake” process creates tunable porosity, yielding a 7-fold increase in pressure sensitivity and a 2.25-fold wider sensing range compared to non-porous counterparts. This technology enables integrated pressure sensors for applications in smart healthcare, sports science, and gait assessment.

Description of Porosity Introduction

The porous structure for our pressure sensor leverages a novel, vapor-induced pore/channel formation within the GNP/PDMS nanocomposite (Process flow shown in Fig. 1). This method employs a two-stage bake cycle: a brief, intense hot-bake (140^{o}C-45 seconds) followed by a prolonged, low-temperature open bake (60^{o}C-4 hours). Initially, high-temperature curing of ethanol-mixed GNP/PDMS triggers bubble nucleation. As these bubbles ascend, they strategically redistribute GNPs into the resulting micro-channels via capillary action. This continuous bubble movement, coupled with the high curing temperature, ensures robust channel formation, which is subsequently stabilized by extended open bake. The final product is a porous thin film with a high concentration of GNPs precisely located within the micro-channels.

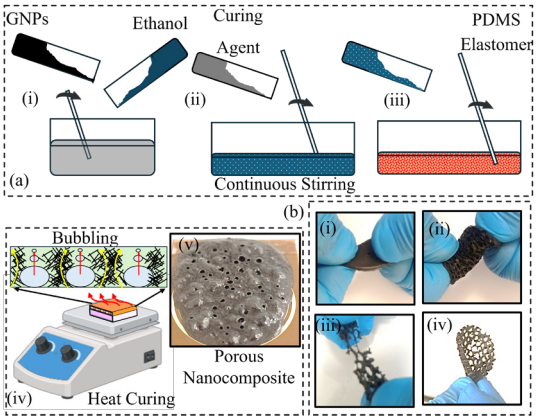


Fig. 1: a) Process flow for porous piezoresistive nanocomposite;i) ethanol/GNP mix ii) mixing the curing agent; iii) PDMS elastomer mixing; iv) 2-step baking; v) final porous film. b) The flexibility of porous nanocomposite as i) compressed; ii) twistable; iii stretchable; iv) bendable.

Results and Discussions

The porosity of the nanocomposite is primarily determined by the initial volume of ethanol and the hot baking temperature. Our work uti-

DOI 10.5162/EUROSENSORS2025/M1.3.3

lizes only 5% GNP/PDMS and demonstrates that hot bake temperatures of 100^{o}C and above are crucial for reliable ethanol bubbling and channel formation; lower temperatures resulted in prolonged saturation times and inconsistent channel development. The hot bake saturation time and temperature define our innovative bake cycle.

Fig. 2a reveals that for a 5% GNP/PDMS nanocomposite, saturation time increases linearly with ethanol volume at a constant hot bake temperature. Notably, at higher temperatures ($>$120^{o}C), lower ethanol volumes lead to smaller pores and lower pore density with scattered distribution, while higher ethanol volumes result in larger pores (implied). Therefore, achieving a specific pore size and density necessitates an optimized ethanol volume. The increase in pore density drastically reduces the initial resistance of the nanocomposite pressure sensor by forming denser micro-channels (Fig. 2 b. Crucially, pore size dictates the GNP concentration and stiffness of these channels. Larger pores create thinner, higher-GNP channels with lower resistance but increased stiffness. This requires a trade-off: optimizing the pore size balances strainability, initial resistance, and pore density to maximize sensor sensitivity.

Mechanical and Electrical Characterization

The mechanical and electrical characterization of the fabricated porous 5% GNP/PDMS nanocomposite is performed with a universal testing machine (UTM−X350−20) using a 2000 Kgf load cell and integrated with Keithley 2450 source−meter. The peak loading and peak %stress varies is obtained as ∼487 N and 68.97% (Fig. 2 c. Furthermore, the initial(unloaded) resistance R_o is calculated as 2.5 K. The force is applied from 0−700 N (corresponding to applied pressure of 0−3 MPa) with a speed of 1mm/min. The % relative resistance change (%RRC) shows a conventional "linear−saturation" trend over the applied forcing range. The linear region extends to 2.5 MPa and the corresponding pressure sensitivity of 33.2% MPa^1 is achieved (Fig. 2 c). Piezoresistive sensitivity, quantified by the gauge factor (GF). Porous GNP/PDMS demonstrated significantly enhanced sensitivity with two distinct linear regions; GF = 0.66 (0−45% strain) and GF = 1.72 ($>$45%). This substantial improvement in sensitivity and sensing range is attributed to the enhanced deformation limit and the formation of high−concentration GNP micro−channels, enabling intricate sensing via GNP tunneling, overlapping, and disconnection.

Application: Tactile Pressure Sensor

Finally, the vapor channeled porous GNP/PDMS is is fabricated on a flexible polyamide substrate (1.5cm $\times$ 1.5cm) with copper/gold interdigitated electrodes. The fabricated piezoresistive sensor is deployed as a tactile pressure sensor to detect varying finger taps as shown in Fig. 2d. The

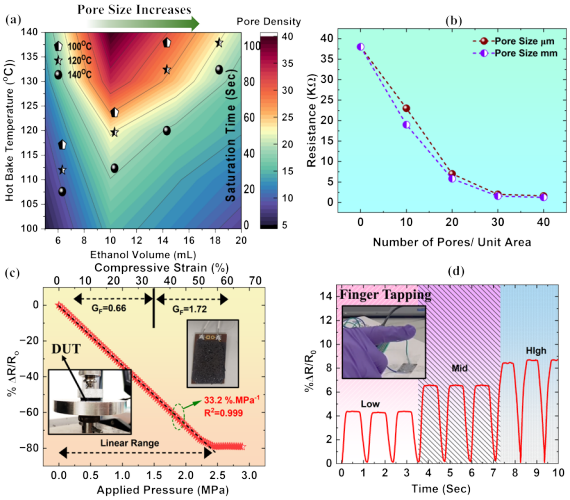


Fig. 2: a) 2D-map showing dependence of hot-bake pore size, pore density, saturation time on initial ethanol volume. b) Corelation between pore density at different pore sizes on initial nanocomposite resistance. c) Sensitivity and GF calculation of the porous nanocomposite. d) A finger tap response of the prepared porous pressure sensor.

sensor reliably detects a wide range of finger tap strengths (low, mid, high), exhibiting a stable and repeatable response, even for forces as low as 0.12 MPa (%RRC=4.2).

Nonetheless, this work can be extended to any flexible polymer nanocomposite irrespective of the transduction mechanism and therefore offers a new direction in porous sensors.

Acknowledgment

We acknowledge Khalifa University of Science and Technology (KU) and RiC2D. This work is under KU Award No. FSU-2023-028.

References

[1] J. Yan, K. Dong, Y. Zhang, X. Wang, A. A. Aboalhassan, J. Yu, and B. Ding, "Multifunctional flexible membranes from sponge-like porous carbon nanofibers with high conductivity," *Nature communications*, vol. 10, no. 1, p. 5584, 2019.

[2] N. T. Beigh, F. T. Beigh, and D. Mallick, "Machine learning assisted hybrid transduction nanocomposite based flexible pressure sensor matrix for human gait analysis," *Nano Energy*, vol. 116, p. 108824, 2023.

[3] I. Barbaros, Y. Yang, B. Safaei, Z. Yang, Z. Qin, and M. Asmael, "State-of-the-art review of fabrication, application, and mechanical properties of functionally graded porous nanocomposite materials," *Nanotechnology Reviews*, vol. 11, no. 1, pp. 321–371, 2022.

[4] S. Wu, J. Zhang, R. B. Ladani, A. R. Ravindran, A. P. Mouritz, A. J. Kinloch, and C. H. Wang, "Novel electrically conductive porous pdms/carbon nanofiber composites for deformable strain sensors and conductors," *ACS applied materials & interfaces*, vol. 9, no. 16, pp. 14207–14215, 2017.

DOI 10.5162/EUROSENSORS2025/M1.3.4

Miniaturized Electric Field Mill based on Lorentz Force Actuation

Franz Keplinger[1], *Wilfried Hortschitz*[2] *and Gabor Kovac*[2]
[1] Institute of Sensor and Actuator Systems, Technical University of Vienna, Austria, Gusshausstrasse 27-29, 1040 Vienna, Austria
[2] Department for Integrated Sensor Systems, University for Continuing Education Krems, Viktor Kaplan Strasse 2E, 2700 Wiener Neustadt, Austria
Franz.Keplinger@tuwien.ac.at

Summary: In this paper we report on electric field sensors based on MEMS technology and the field mill concept with interdigitated combs. To achieve high sensitivity, the movable comb is excited by the Lorentz force in the out-of-plane direction. The sensor can be supplied with voltages below 1 V, resulting in a low internal crosstalk.

Keywords: MEMS, electric field mill, Lorentz force, sensor, simulation

Introduction

Although the strength of an electric field is one of the fundamental physical quantities, it is very difficult to measure, despite a long history of knowledge. This applies mainly to DC fields or low-frequency AC fields. The typical measuring device, the electric field mill, chops the field to be measured with a mechanical shutter. This creates varying charges on the electrodes below the shutter. By measuring the currents to the electrodes, the electric field strength can be calculated. However, these sensitive devices are quite bulky and require rotating parts that are prone to wear.

The corresponding miniaturized concept is based on shutters that move back and forth. The most common variant uses interdigital combs, one stationary and one grounded, which vibrates in the plane of the combs. The vibration in the electric field changes the charges on the combs and the current to the electrodes (combs) is in turn measured ([1, 2, 3]). Since the active area of the sensor is in the square millimeter range, the current is only a few pA. Therefore, noise is a common limitation.

The shutter is driven by an electrostatic actuator at half the frequency of the mechanical resonance f_r with relatively high voltages U of several tens of volts, resulting in high crosstalk. Since the excitation force is proportional to U^2, the frequency of the crosstalk is $f_r/2$, while the useful signal is at f_r. However, remaining relevant drawbacks of in-plane vibration are the squeeze film damping between the fingers, which limits the quality factor of the vibration, and the vibration amplitude, which directly affects the size of the output signal.

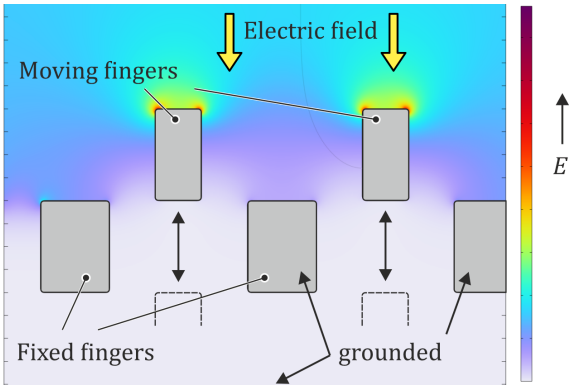


Fig. 1: The electric field sensor consists of two combs, fixed fingers and moving fingers that vibrate out of the comb plane.

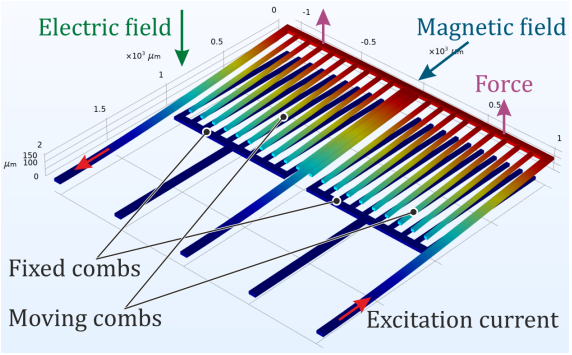


Fig. 2: Excitation and deflection of the moving structure by the Lorentz force due to the electric current and the magnetic field.

Sensor Concept

The structure studied in this work overcomes these disadvantages by vibrating the movable comb out of the plane (Fig. 1) and by using the Lorentz force for actuation (Fig. 2 and 3). Here, the mechanical amplitude is no longer limited by the distance between the fingers, and squeeze film damping is not relevant as long as there is a sufficiently large air gap under the structure. In addition, the density of the fingers is greater than for in-plane vibration sensors. Lorentz force ex-

citation was achieved by applying an alternating current to the line on the moving structure at the frequency of mechanical resonance and by applying a magnetic field from a permanent magnet under the chip.

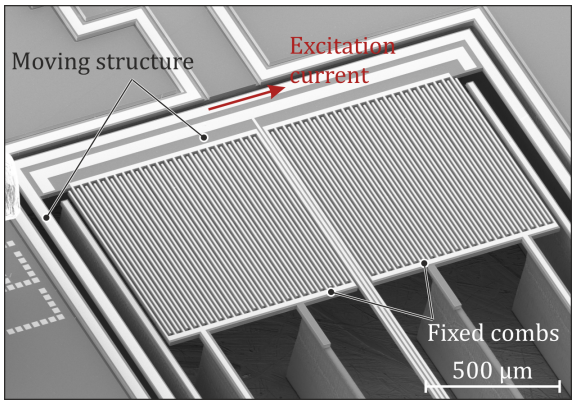


Fig. 3: Scanning electron microscope image of the MEMS electric field sensor. The moving structure is E-shaped with an array of fingers on the inside. The outer bars of the E carry the excitation current and the middle bar is for the signal paths.

Chip fabrication

The devices have been fabricated on 100 mm SOI wafers with a 20 µm thick device layer. The structures have been defined by deep reactive ion etching (DRIE) from the front and back, creating a gap of 8 µm between the combs. The buried oxide was removed by wet etching. The lines for the excitation current and the signal paths are made of 20 nm chromium and 250 nm gold.

Measurement Setup and Results

The sensor chip and permanent magnet are bonded and grounded in a DIL28 package. This part forms the bottom electrode of a parallel plate capacitor to generate the measurement field.

The moving structure was driven with a current of 2 mA in a field of about 200 mT at the resonant frequency of 2.03 kHz, resulting in a mechanical amplitude of about 20 µm and a quality factor of 40. The currents to the fixed and moving combs are converted to voltages using transimpedance amplifiers with a feedback resistance of 100 MΩ. The two signals are then added and measured at the excitation frequency by a lock-in amplifier. Figure 4 shows an offset-corrected sensor characteristic.

Conclusion

MEMS electric field mills with out-of-plane vibration, excited by the Lorentz force, present a promising alternative to in-plane devices with electrostatic actuators. A salient benefit of these devices is that, due to the low excitation voltage, internal crosstalk is negligible, thereby enabling high-resolution measurements. The substantial size of the sensitive area and vibration amplitude has enabled a sensitivity level that exceeds 70 fA/V/m. It must be noted that further development is still feasible.

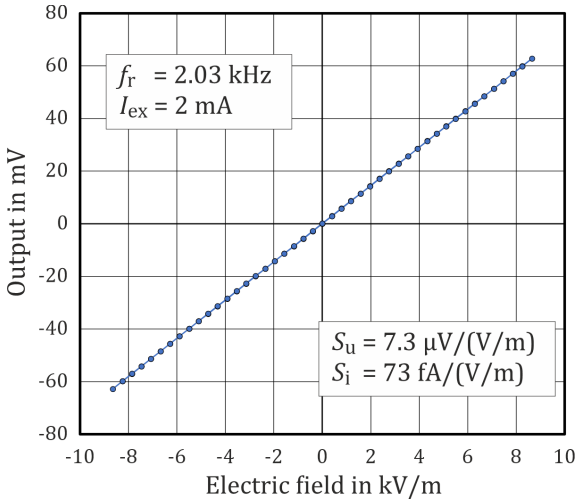


Fig. 4: Cyclic measurement starting and ending at 0 V/m. Each point is the average of 50 readings, the standard deviation for all points is less than 50 µV.

References

[1] M. Horenstein, and P. Stone, *Journal of Electrostatics*, 50–51, 515, (2001), Elsevier; doi: 10.1016/S0304-3886(01)00048-1

[2] W. Hortschitz, and A. Kainz, and R. Beigelbeck, and G. Schmid, and F. Keplinger, *Measurement Science and Technology*, 35, 5, 052001, (2024), IOP Publishing; doi: 10.1088/1361-6501/ad243a

[3] Wang, G., Yang, P., Chu, Z., Ran, L., Li, J., Zhang, B., Wen, X. (2024). A Review on Resonant MEMS Electric Field Sensors. *Micromachines*, 15(11), 1333.; doi: 10.3390/mi15111333

DOI 10.5162/EUROSENSORS2025/M2.1.1

Simultaneous Magnetic Field and Temperature Measurements on a Battery with a Fiber-Coupled Quantum Sensor

Tijmen van Ree[1], Hans Bartling[1], Vadim Place[2], Laurent Castro[2], Sachin Kinge[2], and Clara Osorio Tamayo[1]

[1] Netherlands Organisation for Applied Scientific Research (TNO), Stieltjesweg 1, Delft, 2628CK, The Netherlands.

[2] Toyota Motor Europe (TME), Hoge Wei 33, Zaventem, 1930, Belgium.

tijmen.vanree@tno.nl, sachin.kinge@toyota-europe.com

Summary: This work describes a proof-of-principle for simultaneous measurements of the temperature and current of a battery with the use of a single fiber-coupled nitrogen-vacancy-based sensor. These parameters can be used to obtain information about the State of Health of a battery device. Tracking the State of Health is important for maximizing the life cycle of a battery, and also for monitoring its safety.

Keywords: Quantum sensor, nitrogen vacancy centers, temperature sensor, magnetic field sensor, batteries

Background, Motivation and Objective

Long-lasting and reliable battery devices are a requirement for various applications in electric mobility as well as stationary energy storage. For such applications, it is important to monitor the battery's State of Health (SoH), which gauges the degradation of a battery over time. A deteriorated SoH can be observed empirically by measuring physical parameters of the battery such as the temperature and localized currents [1]. Monitoring the SoH is not only important for maximizing the duration of a device's life-cycle, but also for ensuring the safety of the device. In this talk, we will report on the use of a fiber-coupled nitrogen-vacancy-center-based sensor to simultaneously measure the magnetic field and temperature of different types of batteries. By leveraging the unique properties of nitrogen-vacancy (NV) centers, we aim to enhance the precision and reliability of battery monitoring systems.

Description of the New Method or System

The basic elements of the sensor are shown in the schematic in figure 1. The main element of the NV sensor is a 3x3x0.5 mm^3 diamond, with a NV-concetration of 4.5 ppm, glued onto the ferrule of an optical fiber. Wrapped around the ferrule is a copper coil that acts as an antenna for microwave driving of the NV centers. A 515 nm laser is used for optical excitation and a splitter is used to split of 1% of the green light. The light from the 1% arm of the splitter is attenuated and led unto the other arm of the balanced photo-detector. The remaining 99% proceeds to a circulator, after which it is sent to the diamond-containing fiber. The red light emitted from the diamond is collected by the same fiber and enters back into the circulator. Thereafter, excess green light is filtered out and red fluorescence is guided to one of the ports of a balanced photo-detector.

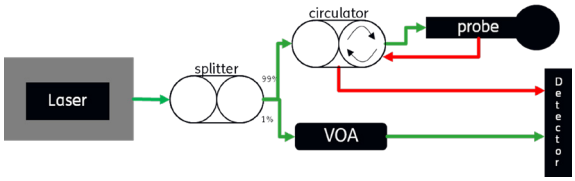


Fig. 1: Schematic of the optical elements of the sensor. The probe consists of an NV-containing diamond glued to an optical fiber. A copper wire is wound around the ferrule of this fiber for microwave driving of the NV-centers.

A continuous-wave optically detected magnetic resonance (CW-ODMR) measurement consists of the continuous application of green laser light and microwaves of varying frequency. Firstly, both are turned on for a set duration (typically 10-30 seconds) in order to let the system (temperature) stabilize. Next, the microwave frequency is increased periodically, and the fluorescence light intensity is recorded. In the resulting spectrum, eight resonances can be observed. Since the NV electron-spin ground state is spin-1, two transitions can be driven directly with microwaves (m_s = 0 to m_s = -1 and m_s = 0 to m_s = +1). Due to four possible orientations of the NV center in the diamond lattice, we then observe a total of eight transitions. Note that it is necessary to observe multiple NV orientations in order to extract the magnetic field vector (three variables) and the temperature (one additional variable) [2][3].

Measurements and Results

We start by calibrating the sensor for temperature. We use an external heater to control the diamond temperature and use a thermocouple to measure its temperature. For varying temperatures, we then measure the zero-field splitting ($\mathbf{D}$). We obtain a relation of $\mathbf{D}(\mathbf{T}) = 2.8728 *$

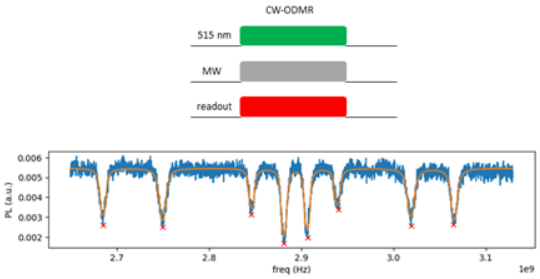


Fig. 2: (top) Measurement sequence to perform a continuous-wave optically detected magnetic resonance (CW-ODMR) measurement. The green laser and microwaves are turned on simultaneously and the resulting counts are recorded. (bottom) Photoluminescence (PL) plotted against the applied microwave frequency plotted in blue, the Lorentzian fit in orange, and red indicates the initial guesses for the fit.

$10^9 - 6.55 * 10^4 * \mathbf{T} - 162.0 * \mathbf{T}^2$, where $\mathbf{T}$ is the temperature of the diamond in degrees Celsius and $\mathbf{T}$ is the zero-field splitting in Hz.

Current and temperature measurements were performed on different batteries with different geometries and capacities: a pouch cell with a capacity of 3150 mAh, a cylindrical cell with a 2400 mAh capacity, and a coin cell of 200 mAh capacity. For the pouch cell, measurements were taken with the probe at different locations. Figure 3 shows the results of the two measurements on the pouch cell. A clear correlation between the measured magnetic field magnitude and the current in the battery can be observed.

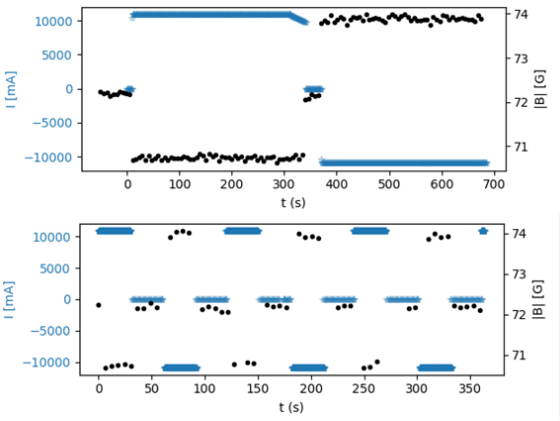


Fig. 3: Results for two measurements on the pouch cell. In the top image, the battery was charging for 5 minutes, followed by 30 seconds of resting, and 5 minutes of discharging. In the bottom image, the battery was cycled through 30 seconds of charging, resting, discharging, resting. For both measurements, the charging C-rate was 3.5C. The blue data points indicate the current that is running through the battery, and the black data points denote the magnetic field magnitude picked up by the NV sensor.

A clear distinction between measurements at the different locations on the pouch cell can be observed. On the contact of the battery, the magnitude of the changes in the measured magnetic field were almost a factor 10 bigger than on the center of the pouch cell. At the edge of the battery measured values were about 5 times bigger than at the center. For the measurements on the pouch cell, the temperature changes on the outside were not significant enough to be measured. In order to show the capability of our sensor to measure temperature, we additionally perform measurements on a cylindrical cell (Fig. 4).

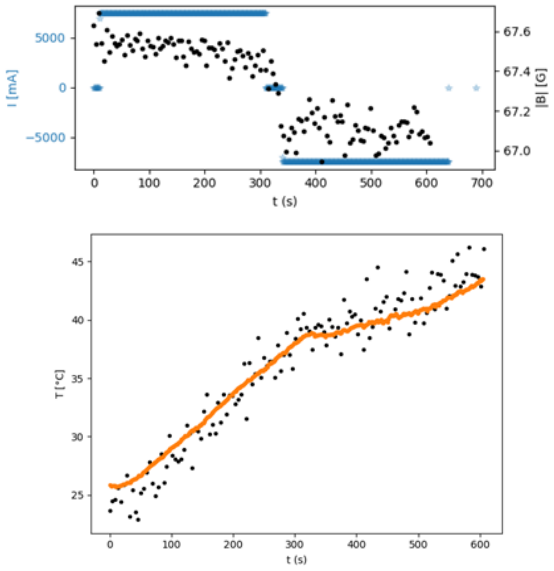


Fig. 4: Magnetic field (top) and temperature (bottom) data for a measurement on the cylindrical cell. (top) The blue points indicate the current on the battery, while the black points denote the measured magnetic field. (bottom) The orange data points indicate the temperature measured by the thermocouple and the black data points are the temperature as determined by the NV sensor.

Outlook

We showed proof-of-principle measurements for simultaneously measuring the temperature and current on the surface of a set of batteries with a fiber-coupled nitrogen-vacancy-center-based sensor. A next step is to perform such measurements on battery devices with different SoHs to determine how the physical parameters of the battery reflect the SoH. Eventually, the sensor could be used as a continuous monitor of the SoH of an arbitrary battery device.

References

[1] S. K. Pradhan and B. Chakraborty, "Battery management strategies: An essential review for battery state of health monitoring techniques," Journal of Energy Storage, vol. 51, p. 104427, Jul. 2022, doi: 10.1016/j.est.2022.104427.

[2] Doherty, Marcus W., et al. "The nitrogen-vacancy colour centre in diamond." Physics Reports 528.1: 1-45, jul. 2013, doi: 10.1016/j.physrep.2013.02.001

[3] Chipaux, Mayeul, et al. "Magnetic imaging with an ensemble of nitrogen-vacancy centers in diamond." The European Physical Journal D 69 1-10, mayy 2015 10.1140/epjd/e2015-60080-1

DOI 10.5162/EUROSENSORS2025/M2.1.2

Development of Glass-Based Atomchip

Frederik Pöpsel[1], Alexander Kassner[1], Jannis Heinz[2], Hendrik Heine[3], Folke Dencker[1], Marc C. Wurz[1]
[1] Leibniz University Hannover, Institute for Micro Production Technology, An der Universität 2, 30823 Garbsen, Germany
[2] LPKF Laser & Electronics SE, Osteriede 7, 30827 Garbsen, Germany
[3] Leibniz University Hannover, Institute of Quantumoptics, Welfengarten 1, 30167 Hannover, Germany
Corresponding Author's e-mail address: poepsel@impt.uni-hannover.de

Summary:
In this work, we present the design and fabrication of a novel glass-based atom chip optimized for quantum applications. Atomchips are key components in quantum optics and technology, as they enable the control and manipulation of ultracold atoms on microscopic scales. Traditionally, atom chips have been based on aluminum nitride or silicon substrates; however, glass-based substrates offer significant advantages in terms of faster fabrication, optical transparency and electrical insulation.

Keywords: atomchip, glass-substrate, quantum technology, Laser-induced deep etching, quantum sensing

Introduction

The development of compact and efficient atom chips is becoming increasingly important for a wide range of applications in the fields of quantum measurement, atomic interferometry and quantum information processing. These chips use microscale conductor tracks on substrate materials to create magnetic micro traps for ultracold atoms [1]. Silicon substrates are commonly used for conventional atom chips [2]. During fabrication, these chips undergo a series of multi-step micro-engineering fabrication processes [3]. A significant disadvantage of using silicon as a substrate material is its opacity to the wavelengths used by the lasers. The use of glass as a transparent substrate offers completely new design possibilities. One notable advantage is the ability to introduce laser beams from the back of the chip. Furthermore, glass is an electrical insulator at the targeted temperature ranges. This has two advantages: First, it suppresses eddy currents that could otherwise affect chip functionality, and second, it eliminates the need for additional, potentially defect-prone insulation layers. These properties make glass an attractive substrate material for advanced atom chips. An additional advantage arises from the use of laser-induced-deep-etching process (LIDE). These can significantly reduce the total number of process steps, resulting in faster and potentially more cost-effective production [4]. Therefore, the development and production of a process chain for the production of a glass-based atom chips is investigated.

Methods

In the present work, a 500 µm thick BF33-wafer is structured using the LIDE process. This process enables the three-dimensional structuring of glass components without the use of masks, making it an extremely flexible tool for microstructuring. A flat surface is required for interferometry, which is why the cavities for the conductor tracks are embedded in the glass using LIDE.

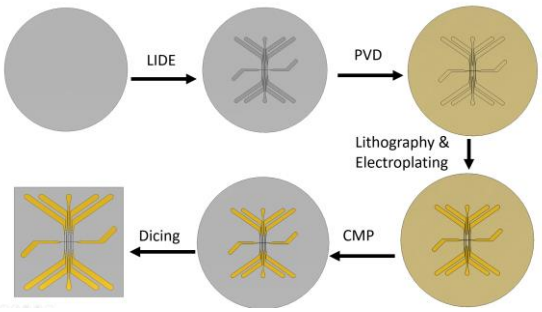


Fig. 1. Process plan of the glass-based atomchip

The LIDE process is divided into two steps. First, the glass is modified using a pulsed laser in a high-speed direct writing process. In this step, the glass structure is locally modified to increase the selectivity in the subsequent etching process. In the second step, wet chemical etching is carried out with a hydrofluoric acid (HF)-based solution. It can be seen that the areas previously modified by the laser are etched at a higher rate than the unmodified areas. This selective etching process enables the precise implementation of cavities that act as receptacles for conductor tracks. After structuring the glass wafer, a seed layer for electroplating is applied by physical

vapour deposition (PVD). First, a sputter etch step is performed to achieve a clean surface pre-treatment. Then, a titanium (Ti) adhesion promoter is applied, followed by a copper (Cu) layer as a seed layer. These layers serve to prepare the electrolytic deposition in the subsequent process. A photoresist is homogeneously applied to the substrate using a spin-coating process. This is then structured and developed using photolithography to expose the desired conductor track geometries. The previously created cavities are then filled by gold electroplating. This step ensures excellent electrical conductivity of the structures introduced. To ensure a flat and smooth chip surface, planarization by chemical-mechanical polishing is carried out in the penultimate step. Finally, the chip is diced into its final shape. The complete process (see figure 1) demonstrates an efficient and precise method for fabricating micro-structured glass components for use in microelectronics.

Results

The cavities after the LIDE process are shown in Figure 2. By optimizing the parameters such as pitch and etching time, the average roughness depth (R_z) and the arithmetic mean roughness (R_a) of the cavities for the conductor tracks could be reduced to a range that allows electrical applications (see table 1).

Tab. 1: Roughness values cavities

parameter	standard	optimized
Ra [µm]	0.65 ± 0.01	0.16 ± 0.02
Rz [µm]	3.25 ± 0.13	1.19 ± 0.25

The conductive tracks have been planarized after galvanic filling by using CMP. They have a depth of 14 µm. A greater depth would favor delamination of the conductor tracks during operation due to the layer stresses. After passing through the process plan, the diced atom chip (see figure 3) has a size of 30 x 30 mm and can be used for further experiments.

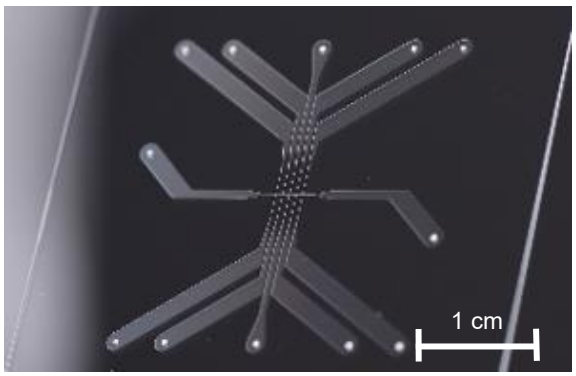


Fig. 2. BF 33 after LIDE process

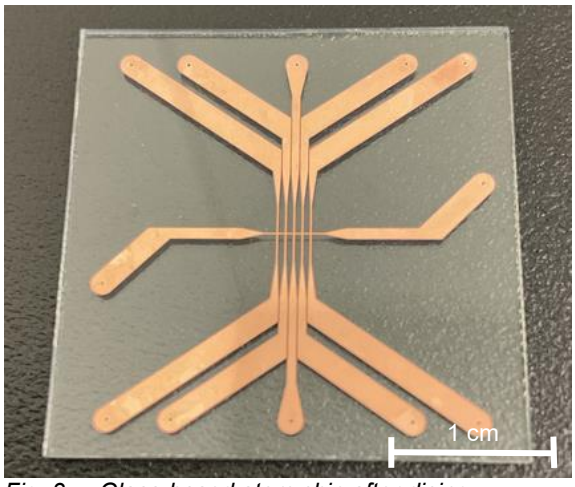


Fig. 3. Glass-based atom chip after dicing

Conclusion

By utilizing established manufacturing methods, we were able to develop a process plan for the production of a novel glass-based atom chip. Compared to the silicon-based standard, it can be produced faster and does not require any isolation layers, which are often prone to defects. In initial tests at atmospheric pressure, the lower thermal conductivity does not show any significant disadvantage. However, tests under vacuum are required and planned here.

References

[1] Keil, M. et al., Fifteen years of cold matter on the atom chip: promise, realizations, and prospects. *Journal of Modern Optics*, *63*(18), 1840–1885 (2016). https://doi.org/10.1080/09500340.2016.1178820

[2] Vivek Singh, V. B. et al., Development and characterization of atom chip for magnetic trapping of atoms. *J. Appl. Phys.* 28 February 2023; 133 (8): 084402. https://doi.org/10.1063/5.0130749

[3] A. Kassner et al., Atom Chip technology for use under UHV conditions, *Smart Systems Integration; 13th International Conference and Exhibition on Integration Issues of Miniaturized Systems*, Barcelona, Spain, 2019, pp. 1-7.

[4] R. Santos et al., Processing Glass Substrate for Advanced Packaging using Laser Induced Deep Etching, *2020 IEEE 70th Electronic Components and Technology Conference (ECTC)*, Orlando, FL, USA, 2020, pp. 1922-1927, doi: 10.1109/ECTC32862.2020.00300

Acknowledgements

This work has been carried out as a part of the joint project “Quantum Gravimeter with advanced LIDE-based Atomchip” (Q-GALA, funding code 03ZU1209KB) funded by the German Federal Ministry of Education and Research (BMBF) as part of the funding program QVLS-iLabs.

DOI 10.5162/EUROSENSORS2025/M2.1.3

SILICON CARBIDE ON INSULATOR (SiCOI) MATERIALS FOR MEMS AND QUANTUM APPLICATIONS USING WAFER BONDING METHODS

Ha Duong Ngo[1], Bei Wang[1], Thomas Weiland[1], Olaf Pohl[1], Boris Naydenov[2], Tien Son Nguyen[3]
[1]University of Applied Sciences Berlin, Wilhelminenhofstr. 75A, 12459 Berlin, Germany
[2]Helmholtz-Zentrum Berlin für Materialien und Energie, Albert Einstein Strasse 16, D-12489 Berlin, Germany
[3]Linköping University, SE-581 83 Linköping, Sweden
Corresponding Author's e-mail address: haduong.ngo@htw-berlin.de

Summary:
This paper reports two novel process flows to fabricate SiCOI (Silicon Carbide on Insulator) with very high purity for use in MEMS and quantum applications using anodic bonding. 100mm SiCOI wafers with different over layer thicknesses have been fabricated using semi insulating 4HSiC material from Cree. Samples with color centers (SiV) ensemble have been fabricated and verified using EPR (Electron Paramagnetic Resonance) and ODMR (Optically Detected Magnetic Resonance). EPR-results show the feasibility of this technology and the potential of this material for MEMS and quantum applications. The coherence time in RT is in hundred ms range similar to the one from NV diamond.

Keywords: SiC, SiCOI, Point defects, SiV in SiC, SiC MEMS, quantum sensor

Background

Single photon sources (SPSs) are essential for a wide range of quantum applications, including quantum communication, quantum cryptography, quantum computing, quantum sensing and quantum metrology. In these applications, single photons are used as fundamental building blocks to encode and transmit quantum information (figure 1). Differences in fundamental properties of single photons over attenuated coherent states will lead to quantum applications mostly based on their interference properties for single-photons. Scalability to more complex set-ups combining multiple indistinguishable photons generated by independent sources will be essential in future.

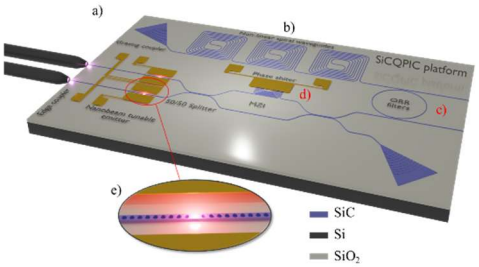


Fig. 1: Schematic of a PIC (Photonic Integrated Circuit) circuit and building blocks in SiCOI material.

SiC is a robust and versatile material that is widely used in the semiconductor industry. It has a wide bandgap and high thermal conductivity, making it suitable for high-temperature and high-power applications. SiC also has a high concentration of defects (figure 2, [2]), including silicon vacancy (VSi), divacancy (VSiVC) and many other defects in the O-band (NCVSi and Vanadium), which can act as single photon emitters.

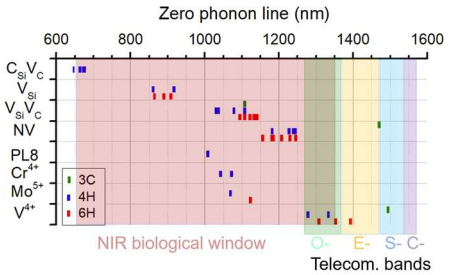


Fig. 2: Summary of the SiC colour centres versus zero-phonon line emission wavelength in different polytypes of SiC. Blue lines, green lines, and red lines represent the 4H, 3C and 6H SiC polytypes respectively. The NIR biological windows and the telecommunication band.

Color centers in SiC exhibit several desirable properties for single photon sources. One example is the VSi defect, which has a strong optical transition at around 917 nm. This transition can be frequency converted to the telecom wavelength range using nonlinear optical techniques, making VSi a promising candidate for on-chip

single photon sources that can emit at telecom wavelengths. Additionally, VSi defects can operate at room temperature, which is crucial for practical quantum technologies. Furthermore, the VSi defects in SiC have a long coherence time, allowing them to maintain their quantum state over longer times being essential for matching requirements to future quantum memories. SiC is compatible with existing semiconductor fabrication technologies, which allows for the development of integrated photonic devices that are scalable and compatible with existing optical communication infrastructure. This enables the development of compact, scalable, and reliable quantum devices based on SiC.

Novel Process Flow to Manufacture SiCOI

We used anodic bonding and gluing to bond high purity 100mm 4H SiC wafers [1] onto silicon wafers as carrier. After bonding, the SiC has been thinned and polished to get the final thickness. Both methods have been successfully implemented to fabricate SiCOI substrates with very high purity, as the process temperatures are very low. The developed technology here is compatible to other material systems without any issues. For the anodic bonding material, we have used a bondable glass of about 3-5µm [3] deposited using plasma method on the SiC-surface. For gluing method, a very thin glue (mrI9020) of 200nm has been used. We used electron irradiation with a dose of ($1x10^{18}cm^{-2}$, 2 MeV) and annealed the samples at an appropriate temperature to get desired concentration of color centers. Figure 3 and 4 show the two process flows to fabricate SiCOI materials in thisproject.

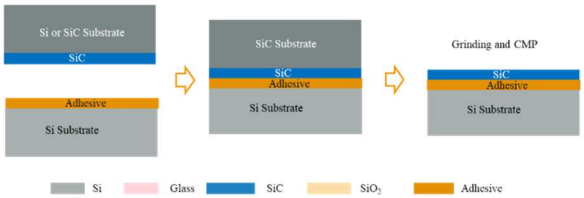


Fig. 3: Process flow for fabrication of SiCOI using gluing, grinding and polishing techniques.

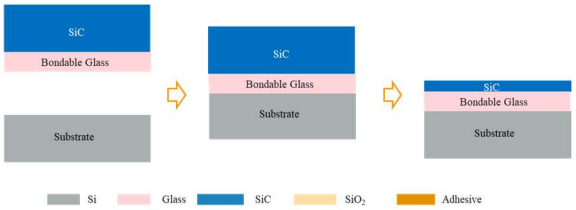


Fig. 4: Process flow for fabrication of SiCOI using anodic bonding, grinding and polishing techniques.

Results

The SiCOI (100mm, different over layers – figure 5) wafers have been fabricated and tested regarding mechanical stability using crack test, regarding surface quality and quantum performance using EPR. ODMR measurement is still ongoing. Crack test shows similar stability as bulk anodic bonding near 40MPa. EPR setup at RT with 9.8 GHz, power 0.1438 mW, modulation amplitude 0.12G, modulation frequency 100kHz and conversion time 20ms and 150 scans. The spins concentration of $1.8x10^{10}cm^{-3}$ has been confirmed and coherence time in ms range.

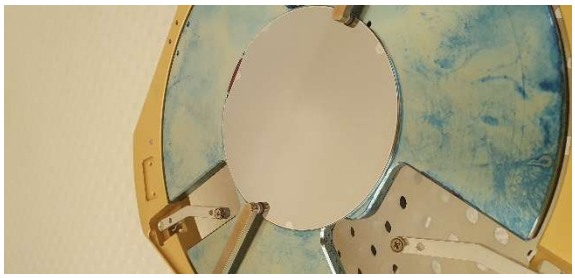


Fig. 5: 100mm SiC-Insulator-Silicon carrier after bonding.

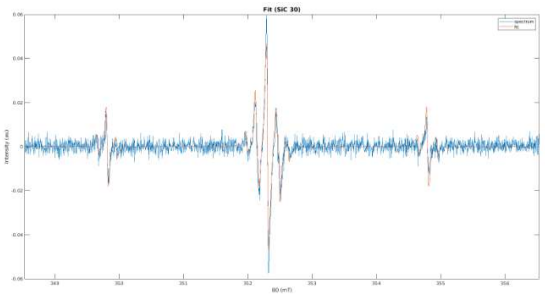


*Fig. 6. EPR spectrum of a SiC sample with 1,8*1010 spins. EPR setup with 9.8 GHz, power 0.1438 mW, modulation amplitude 0.12G, modulation frequency 100kHz and conversion tome 20ms and 150 scans..*

References

[1] HPIS 4H-SiC substrates from Wolfspeed. https://assets.wolfspeed.com/uploads/2020/12/materials_catalog.pdf.

[2] N. T. Son et al. “Development silicon carbide for quantum spintronics”, Appl. Phys. Lett. 116, 190501 (2020).

[3] X. Hu et al., Stress-free bonding technology with bondable thin glass layer for MEMS based pressure sensor“, 2017 IEEE 19th Electronics Packaging Technology Conference (EPTC). 10.1109/eptc.2017.8277550

Acknowledgements

Authors thank IBB (Investitionsbank Berlin) for funding the work.

DOI 10.5162/EUROSENSORS2025/M2.2.1

A novel piezoelectric MEMS speaker with push-pull actuation for in-ear applications

Fabrizio Cerini[1], Chiara Gazzola[2], Filippo P. Perli[2], Michele Rosso[2], Silvia Adorno[1], Alberto Corigliano[2]
[1] STMicroelectronics, Via Tolomeo 1, 20007 Cornaredo Mi, Italy
[2] Politecnico di Milano, Piazza Leonardo da Vinci 32, 20133 Milano MI, Italy
filippopietro.perli@polimi.it

Summary:
This work introduces an innovative high-performance push-pull piezoelectric Micro-Electro-Mechanical System (MEMS) loudspeaker for in-ear applications. It consists of a diaphragm featuring narrow slits and covered with two distinct piezoelectric patches that are actuated with a 180° out-of-phase sinusoidal signals to increase its maximum displacement. The device delivers a Sound Pressure Level (SPL) of up to 109.5 dB SPL from 100 Hz onward with an excitation of 30 Vpp, shows a Total Harmonic Distortion (THD) of 0.8% at 1 kHz and at 94 dB SPL, and maintains a compact square footprint of 4.5 x 4.5 mm².

Keywords: Push-pull actuation, Piezoelectric thin film, Micro-speaker, IEC 60318-4 coupler.

Introduction

Loudspeakers are key components of modern audio systems, with MEMS variants offering compact, low-power solutions ideal for devices such as smartphones, wearables, and hearing aids.

Piezoelectric MEMS speakers stand out for their high driving forces achievable at low voltages, attracting growing scientific interest. These devices generally consist of a suspended diaphragm actuated exploiting the inverse piezoelectric effect and various methods have been explored to further improve their mechanical and acoustic performance. A key example is the mechanically open, acoustically closed (MOAC) design principle [1], which adds openings to the diaphragm to lower stiffness and increase elongation, while narrow gaps retain enough air resistance to prevent acoustic leakage.

Another recent advancement is the out-of-phase activation of separate piezoelectric patches [2]. Despite requiring more complex wiring, these patches can be positioned strategically to increase the diaphragm total displacement while keeping the same piezoelectric capacitance.

Both these concepts are applied for the design of a new high-performance prototype that was numerically simulated, fabricated and tested. The speaker of this work achieves a SPL greater than 109.5 dB SPL from 100 Hz onward with a bias voltage of 15 V_{dc} and two alternate voltages of 30 V_{pp} and opposite phase, and a THD of 0.8% at 1 kHz and 94 dB SPL.

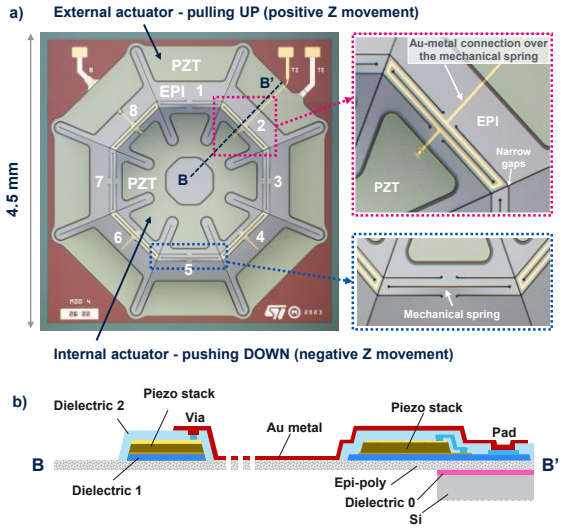


Fig. 1. a) Optical microscope view of the MEMS speaker with details of the Au-metal connection and mechanical springs, b) Schematic of its cross section.

Working principle

The MEMS loudspeaker is shown in Fig. 1a, while a schematic of its cross section is reported in Fig. 1b. The design features eight trapezoidal plates fabricated from a 13 µm thick layer of Epi-Poly, separated by 5 µm narrow slits to reduce acoustic short-circuits [3], and partially coated with a 2 µm thick film of Lead Zirconate Titanate (PZT) with a piezoelectric capacitance of 35 nF, forming the external actuator. These plates are attached to the device's central portion via mechanical springs and secured to an external, fixed frame, resulting in a total footprint of 4.5 x 4.5 mm².

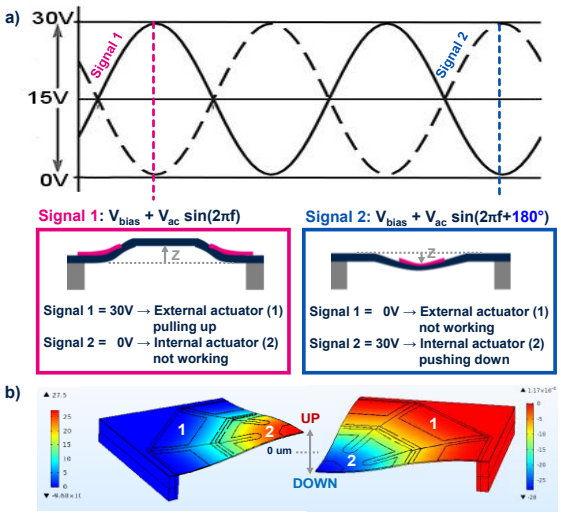


Fig. 2. a) Schematic of both pulling up and pushing down actuations represented with the relative electric signals in opposition of phase. b) Finite Element Method (FEM) simulations of the resulting static displacements considering an excitation of 30 V.

An additional 2 µm thick PZT patch covers the central portion as well and forms the internal actuator, with a lower capacitance of 15 nF, and a dedicated Au-metal electrical connection integrated along the mechanical spring. As shown in Fig. 2, this structure allows a bidirectional movement: actuating the external patch causes the trapezoidal plates to bend upward (pulling up), while actuating the central patch causes the central portion to bend downward (pushing down). The independent electrical connections allow to excite the two actuators with a 180° phase difference, resulting in alternating upward and downward movements in a push-pull actuation. The resulting maximum deflection is the sum of the two modes actuated separately, and as shown in Fig. 3 it surpasses the deflection achievable with a standard single-patch actuation. Moreover, the total piezoelectric capacitance is kept lower or equal to 35 nF during the whole actuation as the maximum excitation voltage is never applied contemporary to both patches.

Results

The device was numerically modeled through the FE software COMSOL Multiphysics, fabricated and tested with the experimental setup reported in [3]. The result in terms of SPL is reported in Fig. 4 together with another our MEMS speaker used as reference with piezoelectric capacitance of 35 nF and same footprint of 4.5 x 4.5 mm² but actuated by a single PZT patch. The new push-pull design was actuated with a bias voltage of 15 V_{dc} and two alternate voltages of 30 V_{pp} and opposite phase, applied separately to the two patches. The speaker reaches up to 109.5 dB SPL from 100 Hz onward, with a THD of 0.8% at 1 kHz and at 94 dB SPL.

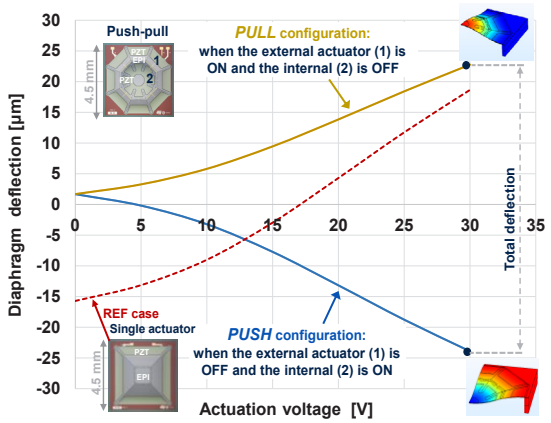


Fig. 3. FEM estimation of the static displacement from pulling up and pushing down actuations, compared with a standard single piezoelectric actuator with equivalent piezoelectric capacitance of 35 nF.

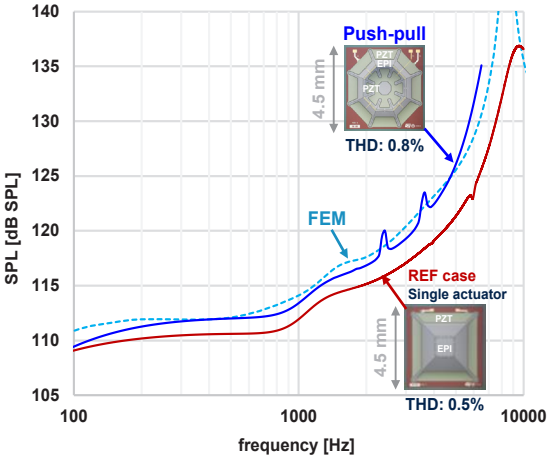


Fig. 4. Comparison of the experimental (solid lines) and numerical (dotted line) SPL measured in-ear conditions between the piezoelectric speaker with push-pull actuation and a traditional speaker with a single PZT patch, for a bias voltage of 15 V_{DC} plus an alternate voltage of 30 V_{pp}. THD of 0.8% measured at 1 kHz and at 94 dB SPL.

The SPL is incremented by 0.4 dB SPL at 100 Hz and by 1.5 dB SPL at 1 kHz with respect to the compared device.

References

[1] F. Stoppel, A. Männchen, F. Niekiel, D. Beer, T. Giese, B. Wagner, New integrated full-range mems speaker for in-ear applications, *2018 IEEE MEMS,* 1068-1071, (2018); doi: 10.1109/MEMSYS.2018.8346744

[2] N. Deng, X. Ma, X. Ding, Q. Zheng, K. Cao, H. Shang, H. Xie, Y. Lu, Optimization of dual-electrode ratio and driving phase of piezoelectric MEMS speakers for improving sound pressure level, Sensors and Actuators: A. Physical 382, 116109 (2025); doi: 10.1016/j.sna.2024.116109

[3] C. Gazzola, V. Zega, A. Corigliano, P. Lotton, M. Melon, A reduced-order-model-based equivalent circuit for piezoelectric micro-electro-mechanical-system loudspeakers modeling, J. Acoust. Soc. Am. 155, 1503-1514 (2024); doi: 10.1121/10.0024939

DOI 10.5162/EUROSENSORS2025/M2.2.2

Advancing On-Chip Micromotor Fabrication Through Electrochemical Micromachining of Silicon

*Farbod Abazar[1], Salvatore Surdo[1], Chiara Cozzi[1], Giovanni Polito[1], Giuseppe Barillaro[1]**
[1] Department of Information Engineering, University of Pisa, via G. Caruso 16, 56122, Pisa, Italy
**Corresponding Author's e-mail address: giuseppe.barillaro@unipi.it*

Summary:
This paper presents the first fabrication of interlocked microgears etched in silicon chips using electrochemical micromachining (ECM). These microgears represent a major step toward the development of fully integrated silicon-based micromotors. The ability to fabricate freestanding rotors around stationary stators with sub-micrometric precision with a single-step ethching surpasses the capabilities of existing micromachining technologies. As proof of concept, we demonstrate the integration these microgears within a microfluidic channel designed for transduction of flow motion into rotational speed.

Keywords: MEMS, Electrochemical micromachining (ECM), Silicon micromachining, Microgears, Micromotors

Introduction

Silicon micromachining tools have enabled disruptive technologies like micro-accelerometers, pressure sensors, and inkjet heads. However, deep etching of silicon has yet to demonstrate rotating structures like microgears. The most advanced fabrication method remains the LIGA process [1], which relies on metal electrodeposition within patterned polymers. Meanwhile, micromotors powered by chemical reactions hold promise for power-free lab-on-chip devices [2].

ECM has recently demonstrated its capability for etching complex, freestanding microstructures at high aspect ratios (AR>100) and ultra-smooth surfaces (roughness<10 nm) [3,4]. Here, we extend ECM to the fabrication of free-standing silicon microgears (rotors) around anchored shafts (stators) for integrated micromotors. As a case study, we integrate interlocked microgears with involute teeth into a microfluidic channel, suitable for future fluidic-to-mechanical energy conversion.

Results and discussion

The fabrication process involves three main steps (Figure 1): (1) surface patterning of a silicon substrate, (2) nucleation seed formation for ECM, (3) anisotropic ECM phase to define deep features, and (4) isotropic ECM phase to release the freestanding microgear. By dynamically switching between anisotropic and isotropic etching phases, ECM allows achieving movable Si micro-rotors, using sacrificial support structures for precise large-area fabrication.

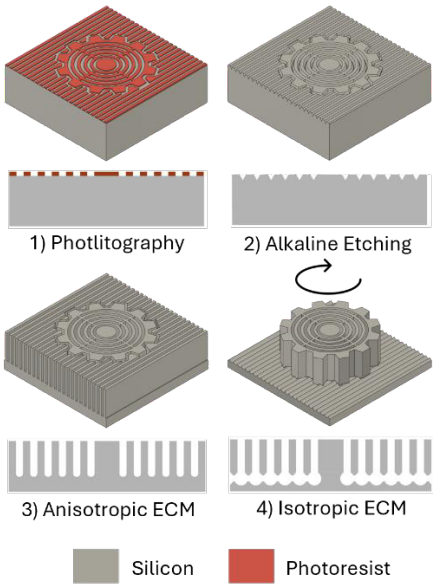


Fig. 1. Schematic of the fabrication steps used for silicon microgear electrochemical machining

Figures 2A and 2B present a representative example of an array of two interlocked freestanding microgears etched in silicon. Each gear is ~50 µm tall and is free to rotate around a cylindrical shaft anchored to the Si substrate. The gear structure consists of periodic parallel circular silicon walls (~1 µm thick, AR ~50) acting as distributed Bragg reflectors, enabling optical monitoring of rotation speed. The smaller gear, 68 µm in diameter with 20 teeth, interlocks with a larger 136 µm gear with 40 teeth, providing a 1:2 gear ratio. This ensures that one gear rotates at twice the speed of the other, demonstrating precise mechanical transmission.

A major advantage of ECM is the superior surface quality and precision achieved. The gear teeth exhibit a smooth surface roughness (~10 nm) and an involute profile, critical for smooth rotational power transmission. Unlike conventional deep silicon etching (e.g., DRIE), which suffers from scalloping effects and requires additional post-processing, ECM directly yields high-aspect-ratio structures with ultra-smooth surfaces. This advantage minimizes speed or torque variations during gear interlocking, improving efficiency and durability.

Figures 2C and 2D illustrate the integration of these interlocked microgears within a microfluidic system, demonstrating their potential for fluid-to-mechanical actuation. The system consists of two large reservoirs (mm² scale) connected via a microfluidic channel, where one of the microgears partially extends into the channel with paddle-like teeth. This design enables transduction of flow motion into rotational speed, presenting a viable path toward electric-free micromotors.

Conclusion

Our study successfully extends ECM technology to fabricate interlocked silicon microgears and integrate them into a microfluidic system for transduction of flow motion into rotational speed. The key advantages of ECM include high aspect-ratio ething, sub-micrometric precision, ultra-smooth surface finishing, anisotropic-to-isortropic etching switching. These results open new possibilities for the fabrication of on-chip micromotors, particularly for applications in power-free lab-on-chip devices with microfluidic-driven actuation. Future work will focus on optimizing gear geometries for improved efficiency and demonstrating practical applications in integrated micro-electromechanical systems (MEMS).

References

[1] M. S. Huang, C. J. Li, J. C. Yu, Y. M. Huang, L. C. Hsieh, Robust parameter design of micro-injection molded gears using a LIGA-like fabricated mold insert, *J Mater Process Technol*, vol. 209, no. 15–16, pp. 5690–5701, 2009; doi: https://doi.org/10.1016/j.jmatprotec.2009.05.032

[2] G. Vizsnyiczai, G. Frangipane, C. Maggi, F. Saglimbeni, S. Bianchi, R. Di Leonardo, Light controlled 3D micromotors powered by bacteria, *Nat Commun*, vol. 8, 2017; doi: https://doi.org/10.1038/ncomms15974

[3] M. Bassu, S. Surdo, L. M. Strambini, G. Barillaro, Electrochemical micromachining as an enabling technology for advanced silicon microstructuring, *Adv Funct Mater*, vol. 22, no. 6, pp. 1222–1228, 2012; doi: https://doi.org/10.1002/adfm.201102124

[4] S. Surdo et al., Optofluidic microsystems with integrated vertical one-dimensional photonic crystals for chemical analysis, *Lab Chip*, vol. 12, no. 21, pp. 4403–4415, 2012; doi: https://doi.org/10.1039/C2LC40613F

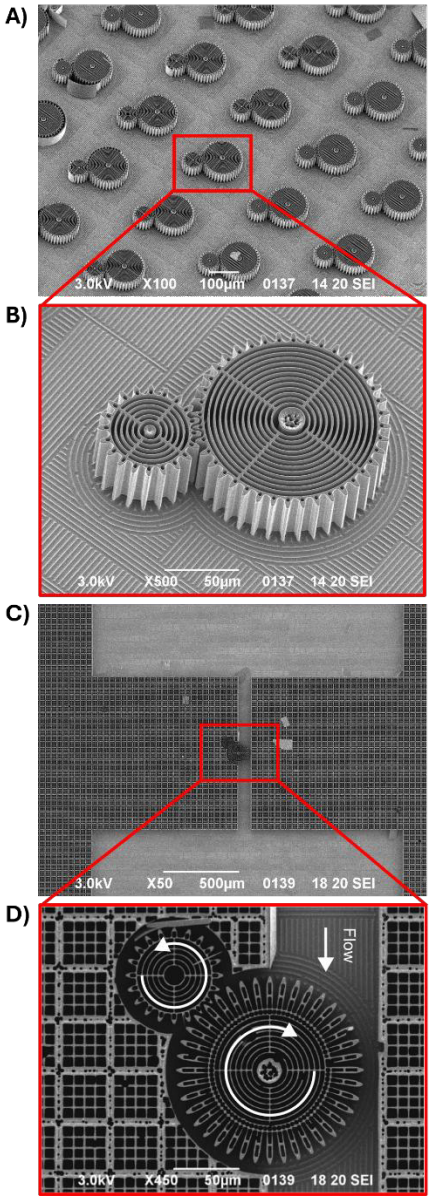


Fig. 2. A) Scanning electron microscopy (SEM) images of an array of interlocked microgears. B) Magnified image of one of the microgear pair in the array. C) SEM (top view) image of a silicon microfluidic system integrating two freestanding interlocked microgears integrated with a microfluidic channel. D) Magnification of the microgears integrated into the microchannel for fluid-mechanical actuation

DOI 10.5162/EUROSENSORS2025/M2.2.3

High-resolution laser ablation of a copper layer for the fabrication of 3D-printed MEMS and microsensors

Mathilde Roig[1], David Bourrier[1], Pierre-François Calmon[1], Constandina Arvanitis[1], Christian Bergaud[1], Vincent Mansard[1]
[1] LAAS-CNRS, 7 av. Du Colonel Roche, F-31400 Toulouse, France
vincent.mansard@laas.fr

Summary :
This paper presents a novel method for structuring metallized layers on a polymer layer using laser ablation. The technique enables the fabrication of metallic tracks with a resolution of about 1 µm with minimal or no damage to the underlying polymer layer. It offers the flexibility required for complex 3D-printed structures and overcomes the limitations of conventional approaches. It will provide an efficient alternative for MEMS fabrication.

Keywords: MEMS, 3D Printing, Laser etching, additive manufacturing, multi-material technology.

Background, Motivation and Objective

3D printing is now established as a key manufacturing technology. Today high-resolution 3D printing produces objects with resolutions down to 1µm [1]. This new capability seems particularly well suited for the design of MicroElectro-Mechanical Systems (MEMS) –devices such as sensors or actuators– that combine mechanical and electrical components at the microscale and require three-dimensional shaping. Traditional cleanroom processes, like photolithography, heavily rely on planar techniques. In contrast, stereolithography, enables to create complex 3D structures. However, surprisingly only a few studies have explored the potential of 3D-printed MEMS [2].

One major challenge lies in the need to integrate both 3D-shaped mechanical structures and electrical circuits for actuation and sensing. It requires the integration of different materials (conducting and non-conducting) in the same structure. Currently, additive manufacturing technologies of multi-materials do not seem mature enough to produce objects at high resolution.

The main strategy involves depositing a metallic layer after printing the mechanical structure. The Deposition of metal in 3D-printing is relatively straightforward using physical vapor deposition (PVD) or wet metallization. Consequently, the present challenge is to pattern the metallic layer into a complex electrical circuit. Traditional processes (e.g. photolithography coupled with lift-off) are poorly adapted for 3D-printing. Recently, alternative techniques have been explored, including laser-activated metallization [3] or shadow masking[4], [5].

We propose a novel strategy for structuring metallized layers on laser ablation to address these challenges. Laser ablation [6] involves locally etching metal by irradiating it with a high-intensity laser beam, resulting in vaporization or plasma formation. Our method enables the rapid structuring of metallic tracks with resolutions of a few microns. Furthermore, it offers the flexibility and versatility of CAD technology compatible with 3D printing.

Description of the Method

Our method has been demonstrated on a 5µm-thick layer of SU-8 photoresist. The SU-8 6005 resist was spin-coated at 950rpm followed by pre-bake, UV-curing and post-bake.

Before metallization, the samples underwent oxygen plasma treatment at 200W for two minutes. Metallization was performed using cathodic sputtering, where a 1µm thick copper layer was deposited onto a 100nm thick titanium adhesion layer.

The metal layers were then patterned using laser etching with the Femtika Nanofactory system. The pulsed laser (wavelength of 515nm) has a beam diameter of approximately 1 µm. We tested the influence of the laser power (ranging from 1mW to 50mW) and the hatching distance (distance between successive ablation lines). The writing speed is set to 10mm/s. Finally, the samples were washed with a mixture of hydrogen peroxide and hydrochloric acid solution for 2’45’’ to complete the process.

Results

Our high-resolution method enables to pattern 10µm wide metallic tracks with great precision [Fig. 1]. The typical processing time is about 5

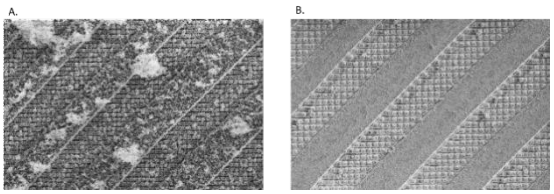


Fig. 1 Two images of the same pattern before (A) and after wet etching (B). Before wet etching, dust particles from the ablation process are visible both on the ablated surfaces and on the copper spirals. After wet etching, a reduction in the amount of dust can be observed.

min to create a square pattern of 500µm side length. Immediately after ablation, we observe the presence of dust deposited on the ablated areas and on the metallic tracks [Fig. 1a]. It consists of copper and resin debris. To address this issue, we subjected the system to a wet etching process using a solution of hydrochloric acid and hydrogen peroxide. This etching effectively removes the dust particles of copper. However, it also results in the etching of ~100 nm of copper.

We investigated the influence of ablation parameters on the ablation depth. Particularly we focused on the laser power and hatching distance to ensure complete removal of the copper layer while minimizing damage to the underlying polymer layer. Once the cleaning process is completed, the surface condition is analyzed [Fig. 2] using SEM imaging and Energy-Dispersive X-ray Spectroscopy (EDX) to confirm the presence of residual copper on the surface.

The hatching distance must be sufficiently small to ensure that no copper remains between adjacent tracks. For large hatching distances [Fig. 2c-d], the laser path is visible. It forms a square grid with the presence of copper between the lines confirmed by EDX analysis. A hatching distance of 0.5µm [Fig. 2a-b] appears optimal, as

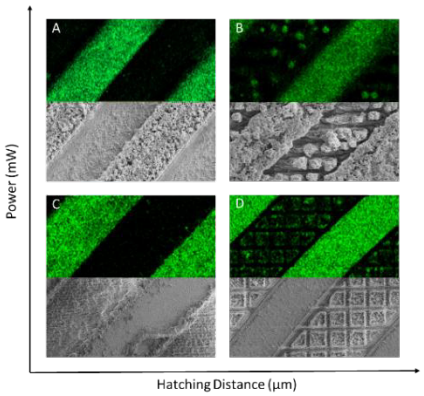


Fig. 2 SEM (bottom) and EDX (top) images of copper tracks created by laser ablation, varying the hatching distance (0.5µm for A and C, 3µm for B and D) and laser power (3mW for C and D, 19mW for A and B). The green dots represent areas where there is copper detected by EDX.

the grid disappears, indicating the absence of residual copper.

The writing power was also fine-tuned. At 19mW, the polymer is also ablated [Fig. 2c] leaving resin debris on the copper tracks that cannot be removed by the cleaning solution. A lower power between 3 to 5mW yields optimal results [Fig. 2a], with no residual copper between the tracks and minimal etching of the resin. Moreover, EDX analysis confirms that the absence of carbon deposition on the tracks.

In conclusion, we successfully developed a process for structuring metallization onto a resin layer. This method enables high-precision hatching with a relatively thick layer of copper of 1µm, and could be adapted for other metals such as gold. An optimization of the ablation parameters (especially laser power and hatching distance) is essential to ensure efficient removal of the metal with minimal damage to the underlying polymer layer. Future work will focus on extending this method onto photoresin 3D-printed parts.

References

[1] C. N. LaFratta and T. Baldacchini, “Two-photon polymerization metrology: Characterization methods of mechanisms and microstructures,” *Micromachines*, vol. 8, no. 4, 2017, doi: 10.3390/mi8040101.

[2] M. R. Khosravani and T. Reinicke, “3D-printed sensors: Current progress and future challenges,” *Sensors Actuators, A Phys.*, vol. 305, p. 111916, 2020, doi: 10.1016/j.sna.2020.111916.

[3] J. Li *et al.*, “Selectively Metalizable Stereolithography Resin for Three-Dimensional DC and High-Frequency Electronics via Hybrid Additive Manufacturing,” *ACS Appl. Mater. Interfaces*, vol. 13, no. 19, pp. 22891–22901, 2021, doi: 10.1021/acsami.1c01199.

[4] S. Pagliano *et al.*, “Micro 3D printing of a functional MEMS accelerometer,” *Microsystems Nanoeng.*, vol. 8, no. 1, 2022, doi: 10.1038/s41378-022-00440-9.

[5] S. Kim, C. Velez, R. S. Pierre, G. L. Smith, and S. Bergbreiter, “A Two-Step Fabrication Method for 3D Printed Microactuators: Characterization and Actuated Mechanisms,” *J. Microelectromechanical Syst.*, vol. 29, no. 4, pp. 544–552, 2020, doi: 10.1109/JMEMS.2020.2992367.

[6] N. Bellini, R. Geremia, S. Norval, G. Fichet, and D. Karnakis, “Laser thin film patterning for rapid prototyping and customised production of flexible electronics devices,” *J. Laser Micro Nanoeng.*, vol. 11, no. 3, pp. 388–394, 2016, doi: 10.2961/jlmn.2016.03.0019.

Acknowledgements

This work was supported by LAAS-CNRS micro and nanotechnologies platform, a member of the Renatech french national network. This work was funded by ANR – FRANCE (French National Research Agency) under grant ANR-23-CE19-0014 (project WISPERS) and ANR-21-ESRE-001 (project Nanofutur Equipex+).

DOI 10.5162/EUROSENSORS2025/M2.2.4

Impact of Nitrogen Doping on the Q-Factor of Polycrystalline 3C-SiC MEMS Resonators

Dominik Huber[1], *Patricia Jurekovic*[1], *Christoph Schallert*[1], *Georg Pfusterschmied*[1], *Ulrich Schmid*[1]
[1] *TU Wien, Institute of Sensor and Actuator Systems, Gußhausstraße 27-29, 1040, Vienna, Austria*
Dominik.Huber@tuwien.ac.at

Summary:
This paper reports on the impact of nitrogen doping on the quality factor (*Q*) of polycrystalline 3C-SiC MEMS resonators. The resonance characteristics of mechanical beam resonators fabricated from an unintentionally and an intentionally doped 3C-SiC thin film were measured with laser Doppler vibrometry. We find a reduction of *Q* of 28% and 39% for the first and second out-of-plane modes when comparing the unintentionally with the intentionally doped thin film. The difference in *Q* is attributed to a modification of Young's modulus (*E*), due to a change in microstructure and/or the average bond strength.

Keywords: MEMS resonators, SiC, doping, Q-factor, LPCVD

Background, Motivation, and Objective

For more than 30 years, SiC has been intensively studied for MEMS applications. In contrast to silicon, it has superior mechanical properties, like hardness, Young's modulus, and thermal stability for high-temperature applications [1]. SiC is also a promising candidate for RF applications like filters and timing devices [2]. Capacitive actuation of these devices is very common, due to a straightforward realization of the transducer elements and fast response times. However, a sufficient conductivity of the electrodes is necessary to support high resonance amplitudes. In-situ doping of polycrystalline 3C-SiC thin films is a well-known approach to reach this goal [3].

Our research adopted the LPCVD growth of polycrystalline 3C-SiC on SiO_2/Si substrates and extended the characterization tools on static cantilevered MEMS resonators as stated by Trevino et al. [4] to evaluate the resonance properties of cantilevered MEMS resonators, as well as the thin films microstructure for different thicknesses.

Description of the New Method or System

Alternating supply deposition (ASD) is used in an LPCVD process to grow polycrystalline 3C-SiC on silicon dioxide layers of 4"-silicon wafers [5]. Within 2000 cycles of ASD, a flow of 2.5 sccm ammonia is used simultaneously with silane and propane for the synthetization of an n-type doped thin film. Cantilevered MEMS resonators shown in Figure 1 are fabricated from both unintentionally and intentionally doped thin films. In the same step, multiple trenches are etched into the thin films close to the anchor regions of the resonators to determine with white light interferometry (WLI) the local value of the film thickness (*h*), as shown in Figure 2. The frequency response of photo-thermally actuated resonators is measured with laser Doppler vibrometry under vacuum, and a Lorentzian fit is performed to extract *Q* and the resonance frequency (*f*).

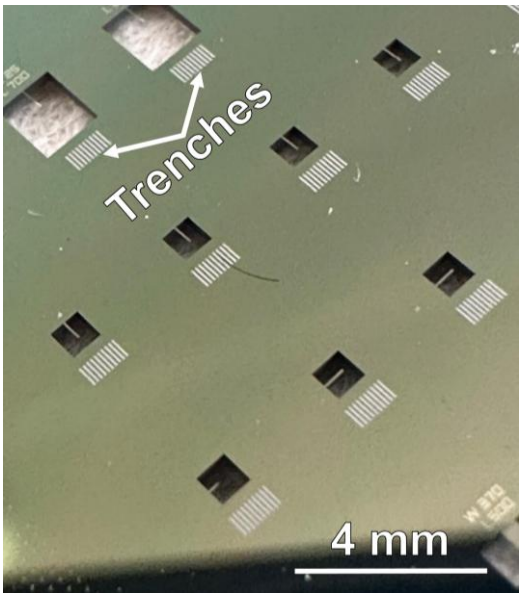


Figure 1: Optical photograph of cantilevered MEMS resonators with a length of 500 µm and a width (w) of 50 µm. Next to each resonator trench-type test structures are etched into the device layer and down to the buried silicon dioxide for a precise local thickness measurement with WLI. A variation in h across the wafer is expected due to the gas flow parallel to the substrate surface in the LPCVD process.

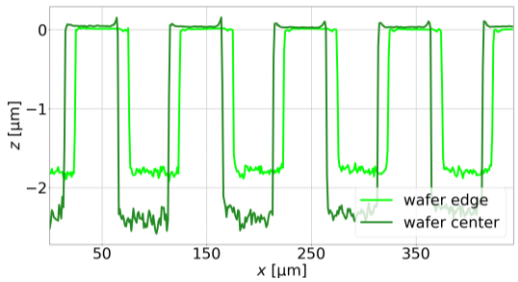


Figure 2: The device layer thickness equals the device height and is measured with WLI via trench-type test structures etched through the device layer. Two typical examples illustrate the local variation in device height from the wafer edge to the wafer center, due to the horizontal arrangement of the wafers during the LPCVD process. Postprocessing is performed on the measured data and the actual height is extracted automatically.

Results

WLI measurements of the trench-type test structure next to 40 different device positions across the wafer show a comparable mean value of *h* of the unintentionally and intentionally doped thin films of 2.17±0.17 µm and 2.36±0.24 µm, whereas mean *f* values of 11 739±963 Hz and 12 526±1441 Hz were measured. However, there is a significant drop in mean *Q* of the first and second Euler-Bernoulli modes of 28% and 39% from the unintentionally to the intentionally doped thin film, as shown in Figure 3.

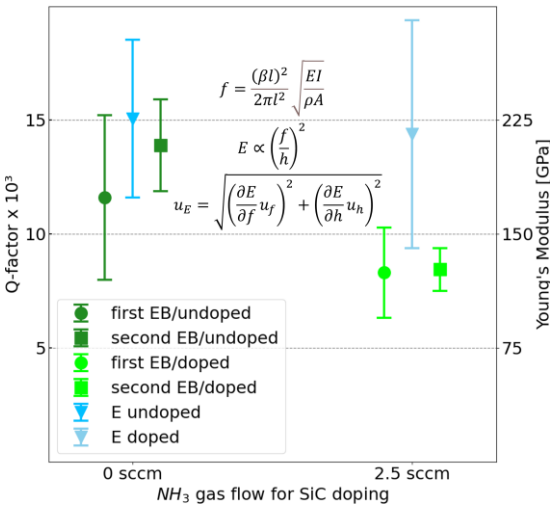


Figure 3: Statistical analysis of the measured Q is performed for 40 resonators, each fabricated from the unintentionally and intentionally doped thin film.

The measured resonance frequencies and device heights were used to calculate *E* from the Euler-Bernoulli beam theory. Here the density ρ = 3210 kg/m^3 is used from literature, while the cross-section $A = w \cdot h$ and area moment of inertia $I = wh^3/12$ are calculated from measured *h* and known width *w*. The error propagation on *E*, (u_E), is calculated according to the formula in Figure 3 with the standard deviations of frequency and thickness, u_f and u_h, respectively. A reduction of *E* from 226±52 GPa to 216±75 GPa is the first indication of the effect of nitrogen doping on the microstructure as well as on the mean bond strength, which decreases due to the presence of nitrogen atoms in the crystal lattice. Similar electronic effects in the elastic constants of doped silicon were described by Hall [6]. Additional SEM images in Figure 4 show a change of the fine-grained microstructure to larger grains with nitrogen doping, while the RMS roughness (S_q) decreases from 16 nm to 10 nm. These results need to be supported and extended by XRD and XPS measurements to get deeper insights, as the microstructure strongly influences the Q-factor of MEMS resonators.

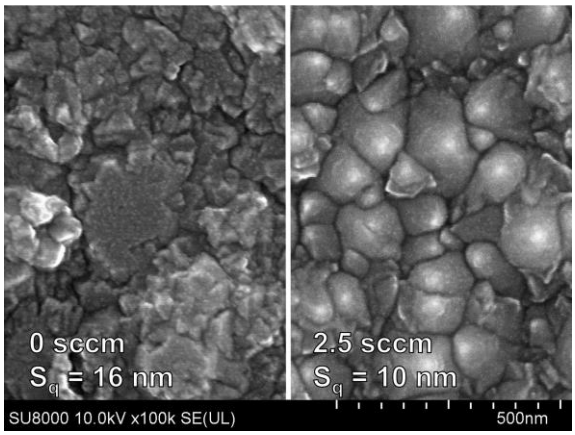


Figure 4: SEM image of polycrystalline 3C-SiC thin films demonstrating that the grainy microstructure of the unintentionally (0 sccm, left) differs from that of the intentionally (2.5 sccm, right) doped thin film. This top view analysis shows that the grains of the intentionally doped thin film are larger, while due to doping AFM measurements show a reduction of S_q from 16 nm to 10 nm.

References

1. La Via, F., et al., *Emerging SiC Applications beyond Power Electronic Devices.* Micromachines, 2023. **14**(6): p. 1200.
2. Melzak, J.M. *Silicon carbide for RF MEMS*. in *IEEE MTT-S International Microwave Symposium Digest, 2003*. 2003.
3. Zhao, Y.-M., et al., *Doped Polycrystalline 3C-SiC Films Deposited by LPCVD for Radio-Frequency MEMS Applications.* Chinese Physics Letters, 2008. **25**(6): p. 2269.
4. Trevino, J., et al., *Doped polycrystalline 3C-SiC films with low stress for MEMS: part II. Characterization using micromachined structures.* Journal of Micromechanics and Microengineering, 2014. **24**(6): p. 065001.
5. Moll, P., et al., *Impact of alternating precursor supply and gas flow on the LPCVD growth behavior of polycrystalline 3C-SiC thin films on Si.* Sensors and Actuators A: Physical, 2024. **372**: p. 115376.
6. Hall, J.J., *Electronic Effects in the Elastic Constants of n-Type Silicon.* Physical Review, 1967. **161**(3): p. 756-761.

DOI 10.5162/EUROSENSORS2025/M2.3.1

A 3D printed microfluidic device for droplet-based cell encapsulation and study

Dagmara Mazur, Wojciech Kubicki
Wrocław University of Science and Technology, Faculty of Electronics, Photonics and Microsystems, Department of Microsystems, Janiszewskiego Street 11/17, 50-372 Wrocław, Poland
Contact: dagmara.mazur@pwr.edu.pl

Summary:
This paper presents a 3D printed microfluidic chip for the encapsulation of biological cells in micro-droplets. The chip is capable of generating and trapping nanolitre-sized droplets of water-based cell culturing medium in the surrounding oil phase. Each droplet serves as an individual microincubator for cell culture study. The chip was fabricated using DLP 3D printing technology with a biocompatible GR-10 resin. The chip has successfully enabled the generation of droplets, the encapsulation of yeast cells and the real-time observation of their proliferation.

Keywords: microfluidics, cell encapsulation, droplet microfluidics, 3D printing, DLP, cell culture

Introduction

Miniaturization is a significant trend not only in technology but also in life science, where the development of miniature cell research devices is gaining prominence. Traditional cell culture on a static surface is laborious, time-consuming and often fails to replicate the dynamic *in vivo* conditions [1]. To address such limitations, microfluidic devices offer accurate control of proliferation environment, enable single-cell research and provide integration of various laboratory processes on a miniature lab-on-a-chip (LOC). Recently, many LOCs have been created using additive manufacturing with biocompatible resins. These 3D printed devices are a promising approach for life science applications, providing many benefits, such as rapid prototyping and cost-effectiveness [2]. The droplet-based cell culture method also offers many advantages, such as undisturbed and uniform culturing conditions, accurate flow control, easy parametrization of the experiment, and minimization of human error [3]. In this work, we present a fully 3D printed microfluidic device which enables the generation and trapping of droplets for cell encapsulation and culture.

Materials and Methods

The device was fabricated using the additive technology of Digital Light Processing (DLP) using Asiga MAX 3D printer. A biocompatible Printodent GR-10 resin (Pro3dure) was used due to its biocompatibility, high transparency, and mechanical stability. The microfluidic chip contains a flow-focusing droplet generator and a long main meandering channel with multiple droplet traps and perpendicularly connected bypass channels (Fig. 1). The operation principle is based on encapsulation of yeast cells in the generated water-in-oil droplets, which here play a role of miniature incubators for easy observation of the proliferation process.

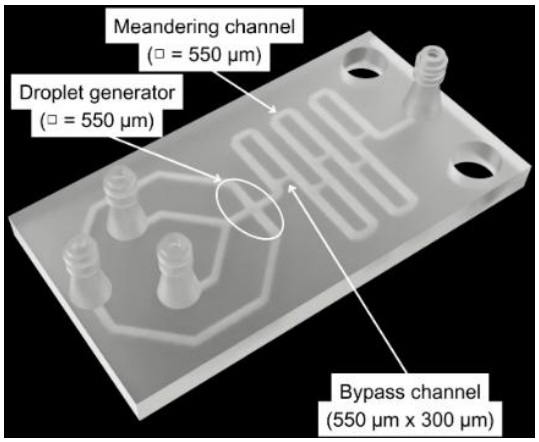


Fig. 1. 3D model of a microfluidic chip for cell encapsulation in water-based droplets

Cell encapsulation experiments were carried out with commercially available baker's yeast (*Saccharomyces cerevisiae*), as the model organism. Cells were suspended in yeast extract peptone dextrose broth medium (YPD) at a 1% w/v ratio and then incubated at 37°C for 10 minutes. The pressure-driven method was applied to control the flow of the yeast cell solution in the microfluidic device. The droplets were distributed in the meandering channel with controlled pressure of water (p_w = 9 mbar) and oil (p_o = 13 mbar). Next,

the pressure ratio p_w/p_o was adjusted to 0.42 to redirect the flow through the bypass channels and effectively immobilize the droplets in the traps (Fig. 2).

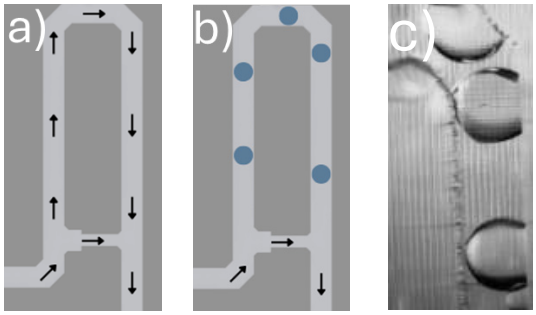


Fig. 2. Droplet flow control in the microfluidic device: a) droplets flowing alternately through the meandering and bypass channels, b) droplets trapped in the meandering channel while the flow is driven through the bypass channels, c) photo of trapped droplets with encapsulated yeast cells

Results

Experiments of encapsulating yeast cells in microdroplets with YPD medium showed successful cell proliferation within the controlled environment. Over a 2-hour observation period, cell proliferation was proven through visible budding over time, an increased number of cells, and noticeable gas production by yeasts, with bubbles forming within the droplets (Fig. 3). The number of yeast cells in the observation area increased by 75% (start: 797 cells, 2h: 1396 cells; Fig. 4).

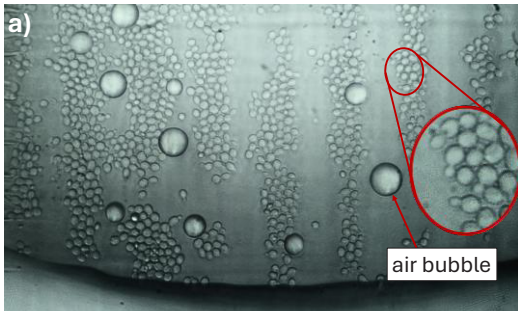


Fig. 3. Proliferation of yeast cells in droplet; red oval – yeast cells budding

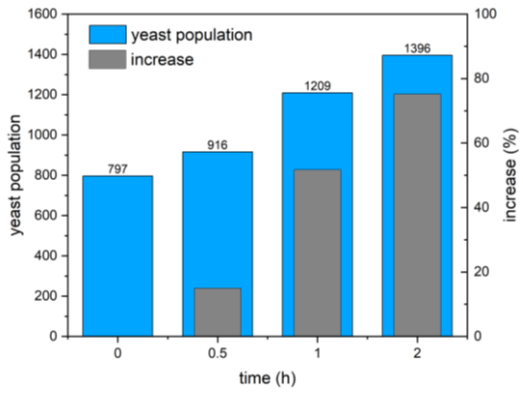


Fig. 4. Growth of the yeast population in droplets

Statistical analysis of droplet volume repeatability was also performed. For a group of 25 droplets, the measured volumes ranged from 71.5 to 129.1 nL, with a mean value of 92.3 nL (Fig. 5).

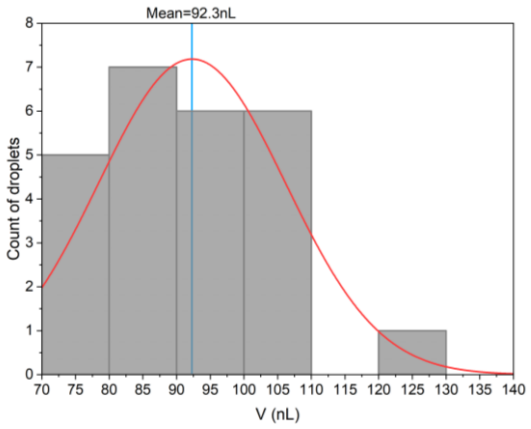


Fig. 5. Statistical analysis of droplet volume

Summary

The development of a 3D printed microfluidic device for droplet-based yeast cell encapsulation has demonstrated significant potential in cell culture research. The chip, fabricated using 3D printing technology with biocompatible resin, enabled generation and trapping of water-in-oil droplets that served as individual microincubators. The experiments confirmed the encapsulation of yeast cells in such droplets, with visible proliferation confirmed by budding, noticeable gas production, and increased cell number. The study demonstrated the potential of the combined 3D printing technology and droplet generation technique to enable controllable cell culture research in the microfluidic device.

References

[1] A. Podwin, D. Lizanets, D. Przystupski, W. Kubicki, P. Śniadek, J. Kulbacka, A. Wymysłowski, R. Walczak, J. A. Dziuban, “Lab-on-Chip Platform for Culturing and Dynamic Evaluation of Cells Development,” *Micromachines*, vol. 11, no. 2, p. 196, Feb. 2020, doi: 10.3390/mi11020196.

[2] A. V. Nielsen, M. J. Beauchamp, G. P. Nordin, and A. T. Woolley, “3D Printed Microfluidics,” *Annu. Rev. Anal. Chem.*, vol. 13, no. 1, pp. 45–65, Jun. 2020, doi: 10.1146/annurev-anchem-091619-102649.

[3] P. K. Periyannan Rajeswari, H. N. Joensson, and H. Andersson-Svahn, “Droplet size influences division of mammalian cell factories in droplet microfluidic cultivation,” *ELECTROPHORESIS*, vol. 38, no. 2, pp. 305–310, Jan. 2017, doi: 10.1002/elps.201600316.

DOI 10.5162/EUROSENSORS2025/M2.3.2

3D-Printed Hollow Microneedles on Si Microfluidics for Healthcare

Tiago Elias Abi-Ramia Silva[1], Stephan Kohler[1], Nicolas Bartzsch[1], Felix Beuschlein[2], Andreas T. Güntner[1,2]
[1] Human-centered Sensing Laboratory, Department of Mechanical and Process Engineering, ETH Zürich
[2] Department of Endocrinology, Diabetology and Clinical Nutrition, University Hospital Zurich and University of Zurich
andregue@ethz.ch

Summary:

Hollow polymer microneedles (MNs), fabricated using two-photon polymerization (TPP), offer a painless means of penetrating the skin for interstitial fluid (ISF) extraction, enabling next-generation health monitoring. Integrated with a silicon-based microfluidic chip, the resulting wearable patch ensures consistent ISF sampling, mechanical durability, and biocompatibility—confirmed through both in vivo studies and surrogate testing. The system enables continuous biomarker monitoring for up to 72 hours without causing skin irritation or damage, highlighting its suitability for minimally invasive health applications.

Keywords: 3D printing, microfabricated hollow needles, wearables, microfluidics, silicon

Dermal ISF presents a promising alternative to traditional biomarker sampling methods [1], with MNs emerging as a minimally invasive solution for both ISF extraction and biomarker sensing due to their painless application [2]. However, the biocompatibility of sensing materials often limits the effectiveness of traditional MNs. Hollow MNs enhance versatility by separating the processes of sampling and sensing, enabling more advanced, real-time health monitoring and drug delivery systems. Recent advances in TPP have made it possible to fabricate hollow polymer MNs with complex, biocompatible geometries.

This work presents a wearable patch designed for skin penetration and ISF extraction, which integrates 18 polymer-based hollow MNs with a silicon microfluidic platform via additive manufacturing (Figure 1) [3]. The MNs are optimized for mechanical stability and minimized flow resistance, while the microfluidic chip ensures uniform ISF extraction through an equal-length arrangement, preventing temporal averaging. A clean-room fabrication process, combining micromachining and 3D printing, guarantees high precision with minimal variation in MN height and alignment, surpassing traditional manufacturing methods. FEM simulations and experimental tests confirm the MNs' resilience to compressive and shearing loads during skin penetration (Figures 2a and 2b). Despite the hollow design's inherent stress concentration, the MNs exhibit mechanical strength – approximately 400 mN per MN to induce failure – comparable to non-hollow designs [4], with negligible risk of fragmentation or detachment under real-world conditions.

The penetration capability and biocompatibility of the 3D-printed polymer MNs were evaluated through both skin surrogate and in vivo testing. The MN array showed consistent force-displacement behavior during ten repeated insertions and removals, with no performance degradation or damage (Figure 3), confirming its mechanical robustness and secure attachment to the microfluidic platform. In vivo tests conducted with the wearable (Figure 4) demonstrated painless insertion and rapid recovery, with minimal skin irritation and no adverse effects, highlighting the biocompatibility of the MN material. After 72 hours of continuous wear, the device showed no biofouling or MN degradation. Moreover, successful ISF extraction yielded approximately 1 µl of fluid within one hour, validating the device's functionality for continuous biomarker monitoring.

This adaptable platform, enabled by TPP, offers design flexibility for diverse skin conditions and analytes. Decoupling sampling from sensing provides a foundation for integrating novel sensing materials into a biocompatible platform with promising medical applications, such as continuously monitoring yet explored biomarkers.

References

[1] J. Madden, C. O'Mahony, M. Thompson, A. O'Riordan, P. Galvin, Biosensing in dermal interstitial fluid using microneedle based electrochemical devices, *Sensing and Bio-Sensing Research* 29 100348 (2020); doi: 10.1016/j.sbsr.2020.100348

[2] S. Kaushik, A.H. Hord, D.D. Denson, D.V. McAllister, S. Smitra, M.G. Allen, M.R. Prausnitz, Lack of Pain Associated with Microfabricated Microneedles, *Anesthesia & Analgesia* 92(2) 502-504 (2001); doi: 10.1213/00000539-200102000-00041

[3] T. Elias Abi-Ramia Silva, S. Kohler, N. Bartzsch, F. Beuschlein, A. T. Güntner, 3D-printed polymer hollow microneedles on microfluidic platforms for minimally invasive interstitial fluid extraction, *Cell Biomaterials* 1(1) 100008 (2025); doi: 10.1016/j.celbio.2024.100008

[4] Z. Faraji Rad, R.E. Nordon, C.J. Anthony, L. Bilston, P.D. Prewett, J.-Y. Arns, C.H. Arns, L. Zhang, G.J. Davies, High-fidelity replication of thermoplastic microneedles with open microfluidic channels, *Microsystems & Nanoengineering* 3(1) 17034 (2017); doi: 10.1038/micronano.2017.34

Acknowledgements

This study was primarily funded by the Swiss State Secretariat for Education, Research, and Innovation (SERI) under contract number MB22.00041 (ERC-STG-21 "HEALTHSENSE") and the Swiss National Science Foundation (grant #228864).

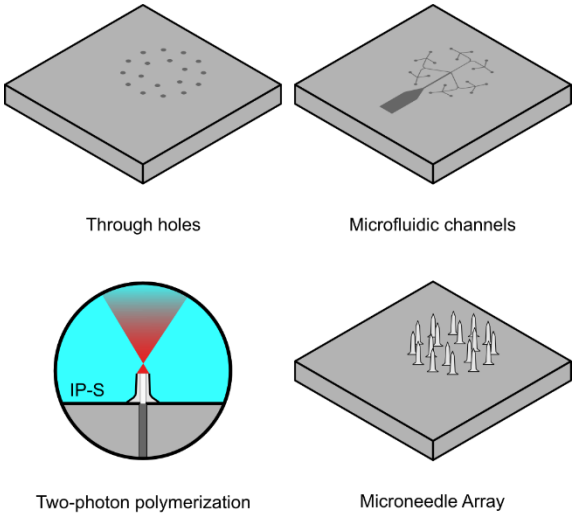


Fig 1. Fabrication process of the microfluidic chip and TPP printing of the 18-MN array. Adapted from [3].

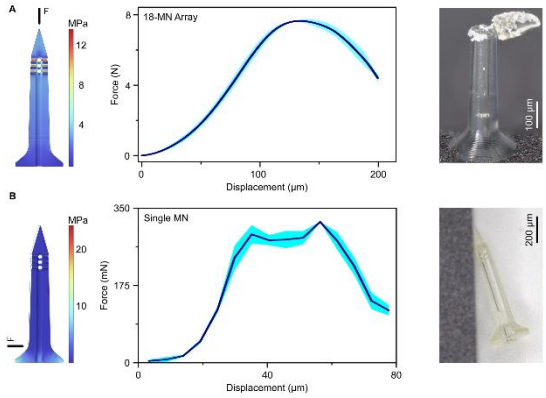


Fig. 2 ***(a)*** *FEM simulation and experimental mechanical testing under compressive load.* ***(b)*** *FEM simulation and mechanical testing under shear load; micrograph shows a representative MN after mechanical failure. Adapted from [3].*

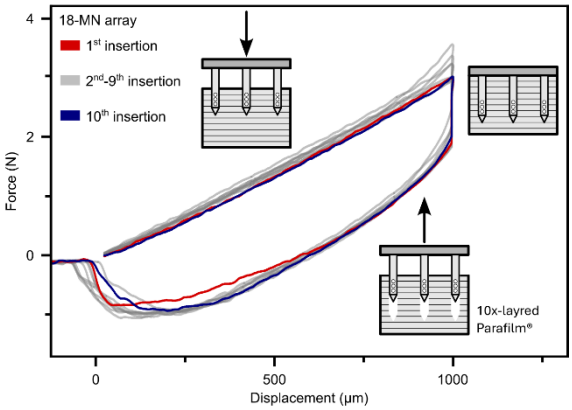


Fig 3. Repeated insertion test performed ten consecutive times on a skin surrogate to assess durability and performance. Adapted from [3].

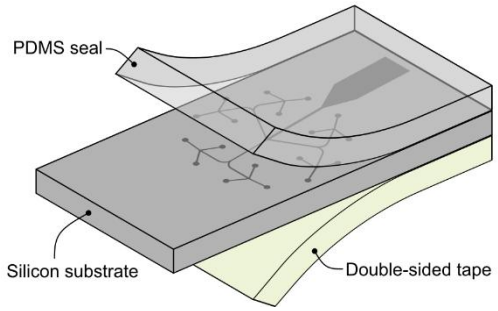


Fig 4. Wearable patch produced from the MN array. Adapted from [3].

DOI 10.5162/EUROSENSORS2025/M2.3.3

3D-Printed Flow Cells with Piezoelectric Resonators and Machine Learning for Biofuel Characterization

Víctor Corsino[1], Víctor Ruiz-Díez[1], Andrei Braic[1], José Luis Sánchez-Rojas[1]
[1] Microsystems, Actuators and Sensors Group, INAMOL-Universidad de Castilla La-Mancha, 45004, Toledo, Spain,
Victor.Corsino@uclm.es

Summary:
Biodiesels serve as a greener alternative to conventional fossil fuels. Typically produced from vegetable oils, these fuels tend to have higher viscosity, which, if excessive, can result in reduced engine efficiency. Existing methods for analyzing these properties require expensive equipment, limiting practicality. To address these challenges, we propose multi-resonant 3D-printed sensors integrated with simple electronics and machine learning algorithms, offering a portable and cost-effective solution for precise biofuel property evaluation.

Keywords: 3D printing, resonances, machine learning, viscosity, biofuel.

Background, Motivation and Objective

Biofuels have gained popularity in recent years due to depletion of fossil fuel reserves, increasing energy demand, and the need to reduce emissions. Monitoring their physical properties is essential, as biodiesels, characterized by higher density and viscosity, can lead to injector deposits and interfere with the atomization process during combustion These issues may result in reduced engine performance and increased emissions [1,2]. Piezoelectric sensors have previously demonstrated the effectiveness to monitor diesel mixtures with lubricants [3], and there are established methods in the literature for measuring these properties in biofuels [4,5]. However, these methods often require expensive laboratory equipment and complex electronics, limiting their practical applicability. To overcome these challenges, we propose 3D-printed sensors capable of operating in multiple vibration modes, integrated into a microcontroller system equipped with deep learning algorithms for enhanced functionality.

Description of the New System

Resonators were developed using 3D-printed cells equipped with vibrating membranes activated by piezoelectric plates—one for actuation and the other for detection. The cells, fabricated in Rigid10K material, incorporated a cavity designed to connect the fluid with the vibrating membrane and facilitate liquid flow. Earlier research [6] explored similar cells, focusing on designs that resonate in a specific mode. The present work introduces a novel approach aimed at maximizing vibrational freedom to facilitate the emergence of multiple vibration modes. This was achieved by modifying membrane dimensions and geometry, incorporating pillars to increase the contact surface with the fluid and enable multiple interrogation points. Additionally, the influence of cavity height on sensing was examined to boost acoustic phenomena participation. Adjustments to plate size, geometry, and quantity were also examined to achieve a broader range of resonance peaks in the fluid. Figure 1 shows several examples of the resonators produced through this study process.

This methodology represents a significant departure from traditional research, which primarily focuses on analyzing properties through the quality factor and frequency of a single resonance. The use of advanced machine learning techniques enables comprehensive analysis across a broad spectrum of vibrations. This proves advantageous, as resonance peaks exhibit different variations depending on the fluid under examination, amplifying differentiation between liquids and providing enriched datasets for AI algorithm processing. Furthermore, this approach simplifies control electronics by incorporating a microcontroller that integrates data acquisition and processing. This results in a compact, portable, cost-effective, and highly precise device capable of monitoring the physical properties of fluids.

Results

The sensors were evaluated using two types of biofuel: pure diesel (DS0) with a viscosity of 2.35 mPa·s and density of 0.821 g/mL, and a mixture

containing 90% diesel and 10% sunflower oil (DS10), with a viscosity of 3.011 mPa·s and a density of 0.829 g/mL. Different sensor geometries were tested by introducing the fluids sequentially without cleaning and recording spectra within the 1 kHz to 1 MHz frequency range at regular intervals to assess sensitivity and resolution. Selected results, presented in Figure 2, highlight the potential of these sensors for determining the physical properties of biofuels. The spectra were obtained using an Analog Discovery Digilent instrument, which will be replaced by a microcontroller-based system with transistorized circuits (illustrated in Figure 3) and integrated convolutional networks for direct fluid property estimation. The effectiveness of this system was previously validated using MEMS sensors [7]. Furthermore, the device will be tested with larger biofuel mixtures conforming to European regulatory limits to confirm its performance across the range of permissible viscosities.

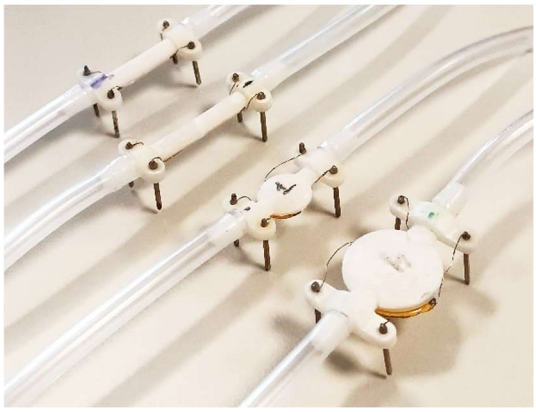


Fig. 1. Sensors with different membrane sizes and geometries.

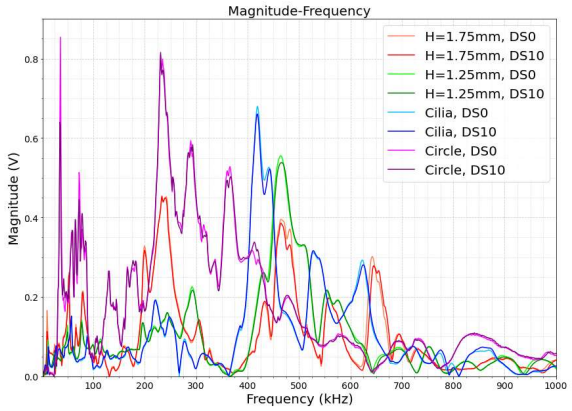


Fig. 2: Spectra for two biofuels obtained using sensors with varying cavity heights (H), membrane embeddings (Cilia), and geometries (Circle or Rectangle).

Acknowledgements

This work was supported by Universidad de Castilla-La Mancha, Spain, through Grant PID2023-146163OB-I00 by MCIN/AEI and FEDER ‘ERDF A way of making Europe’.

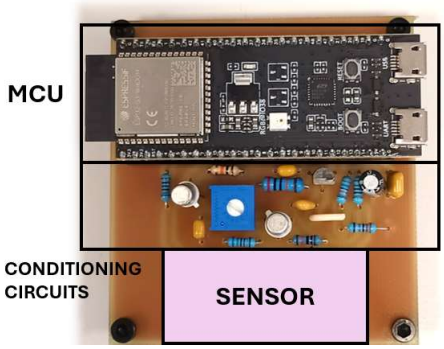


Fig. 3: Complete sensor system.

References

[1] L. Razzaq, M. Farooq, M.A. Mujtaba, F. Sher, M. Farhan, M.T. Hassan, M.E.M. Soudagar, A. E. Atabani, M.A. Kalam, M. Imran, Modeling viscosity and density of ethanol-diesel-biodiesel ternary blends for sustainable environment, *Sustainability*, 12(12), 5186 (2020); doi: 10.3390/su12125186.

[2] R. Estevez, L. Aguado-Deblas, A. Posadillo, B. Hurtado, F.M. Bautista, J.M. Hidalgo, C. Luna, J. Calero, A.A. Romero, D. Luna, Performance and emission quality assessment in a diesel engine of straight castor and sunflower vegetable oils, in diesel/gasoline/oil triple blends, *Energies*, 12(11), 2181 (2019); doi: 10.3390/en12112181.

[3] J. Toledo, T. Manzaneque, J. Hernando-García, J. Vázquez, A. Ababneh, H. Seidel, M. Lapuerta, J. L. Sánchez-Rojas, Application of quartz tuning forks and extensional microresonators for viscosity and density measurements in oil/fuel mixtures, *Microsystem technologies*, 20, 945–953 (2014); doi: 10.1007/s00542-014-2095-x.

[4] S. Goel, P.S. Venkateswaran, R. Prajesh, A. Agarwal, Rapid and automated measurement of biofuel blending using a microfluidic viscometer, *Fuel*, 139, 213-219 (2015); doi: 10.1016/j.fuel.2014.08.053.

[5] J. L. Camas-Anzueto, J. Gómez-Pérez, R. Meza-Gordillo, G. Anzueto-Sánchez, M. Pérez-Patricio, F.R. López-Estrada, M. Abud-Archila, C. Ríos-Rojas, Measurement of the viscosity of biodiesel by using an optical viscometer, *Flow measurement and instrumentation*, 54, 82-87 (2017); doi: 10.1016/j.flowmeasinst.2016.12.004.

[6] J. Toledo, V. Ruiz-Díez, J. Velasco, J. Hernando-García, J.L. Sánchez-Rojas, 3D-printed liquid cell resonator with piezoelectric actuation for in-line density-viscosity measurements, *Sensors*, 21 (22), 7654 (2021); doi: 10.3390/s21227654.

[7] V. Corsino, V. Ruiz-Díez, J. L. Sánchez-Rojas, Smart density and viscosity sensing based on edge machine learning and piezoelectric MEMS for edible oil monitoring, *Sensors and Actuators A: Physical*, 385, 116258 (2025); doi: 10.1016/j.sna.2025.116258.

DOI 10.5162/EUROSENSORS2025/M2.3.4

3D-Printed µ-GC Integrated with an E-Nose System for Enhanced Plant Health Prediction

Usman Yaqoob[1], *Dylan Limbani*[1], *Siavash Esfahani*[1], *Marina Cole*[1], *Julian W. Gardner*[1]
[1] *School of Engineering, University of Warwick, Coventry CV4 7AL, UK*
J.W.Gardner@warwick.ac.uk

Summary:
This work integrates a low-cost 3D-printed µ-GC with an e-nose system for improved plant health prediction. Metal oxide sensors are placed before and after the µ-GC column and show that ethanol elutes first, followed by trans-2-hexenal with a 1 s and linalool with a 2.5 s delays; demonstrating the column's ability to separate out these pest plant biomarkers. Features are extracted from the sensor time-dependent responses and analysed using partial least squares (PLS) method. They accurately predict the VOC type and concentration. This simple e-nose system may offer a cost-effective solution for real-time plant health monitoring with enhanced prediction capabilities of harmful pests.

Keywords: plant health, micro gas chromatography, VOCs, metal oxide sensors, 3D printing

Background, Motivation and Objective

Several crop plants, including maize (*Zea mays*), release volatile organic compounds (VOCs) such as ethanol, trans-2-hexenal, and linalool in response to herbivore attacks from pests like the fall armyworm (FAW), brown marmorated stink bug (BMSB), and European corn borer (ECB). Ethanol emissions in maize occur due to tissue damage and stress, while trans-2-hexenal, produced by wounded leaves, serves both defensive and communicative roles. Linalool, emitted by plants like *Nicotiana attenuata*, attracts natural predators of herbivorous insects, thereby enhancing indirect defense [1, 2]. VOCs released after pest attacks often form complex mixtures, making it crucial to separate and detect them accurately using systems like e-noses to assess plant health.

Conventional gas chromatography (GC) is accurate and versatile for analyzing complex mixtures, but its high cost, bulk, and power consumption make it impractical for practical field applications. Recent efforts have focused on fabricating µ-GCs on Si substrates using a Lift-off process, which offers precise control over column dimensions for efficient separation. However, this microsystem approach is costly and time-consuming for low-volume applications. In contrast, we use a low-cost 3D printer (Elegoo Mars 4 Ultra) to quickly create micro-channels in plastic resin, providing a faster and more affordable solution. Our apporach is to integrate a low-cost 3D-printed µ-GC column with simple metal oxide gas sensors to seperate and detect different concentrations of three componds including ethanol, trans-2-hexenal, and linalool.

Design, Fabrication and Methodology

Fig. 1 illustrates the overall setup (MOX-µGC-MOX), which includes two sensor chambers containing metal oxide sensors, a sealed µ-GC column, and a microcontroller (Arduino Feather TFT: ESP32-S3). In this configuration, target VOCs flow through the first chamber A, then the µ-GC column, and finally the second chamber B, while the microcontroller monitors the sensor resistances over time. (Nb: an SMR sensor is included by reported elsewhere).

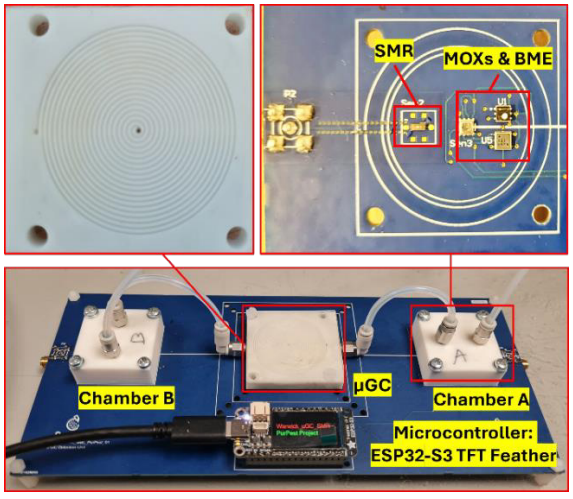


Fig. 1. µ-GC based e-nose. Top shows µ-GC column, commercial MOX gas sensor and Bosch BME280 for ambient temperature and RH.

The µ-GC column was printed using commercial Composite-X UV resin, with overall dimensions

of 40mm × 40mm × 5mm (length, width, and height). The channel measures ca. 1.2 m in length, 0.5 mm in width, and 0.4 mm in depth. The channel was then coated with OV-1 stationary phase (SP). To ensure a uniform SP coating, the column was first functionalized with Polymethylhydrosiloxane (PMHS) and dried at 200°C, followed by the injection of the prepared OV-1 solution. Finally, the column was sealed using UV resin spun coated on the 1.0 mm thick polyethylene terephthalate glycol (PETG) sheet.

Results and Discussions

The MOX-μGC-MOX system was tested with three compounds: ethanol, trans-2-hexenal, and linalool, each at two different concentrations. Due to space constraints, this abstract presents results for one concentration of each VOC, both before and after the μ-GC column. As a proof of concept, two sets of data were collected for each VOC and its concentration, which were used to train and test a partial least squares (PLS) model to predict the VOC class and concentration.

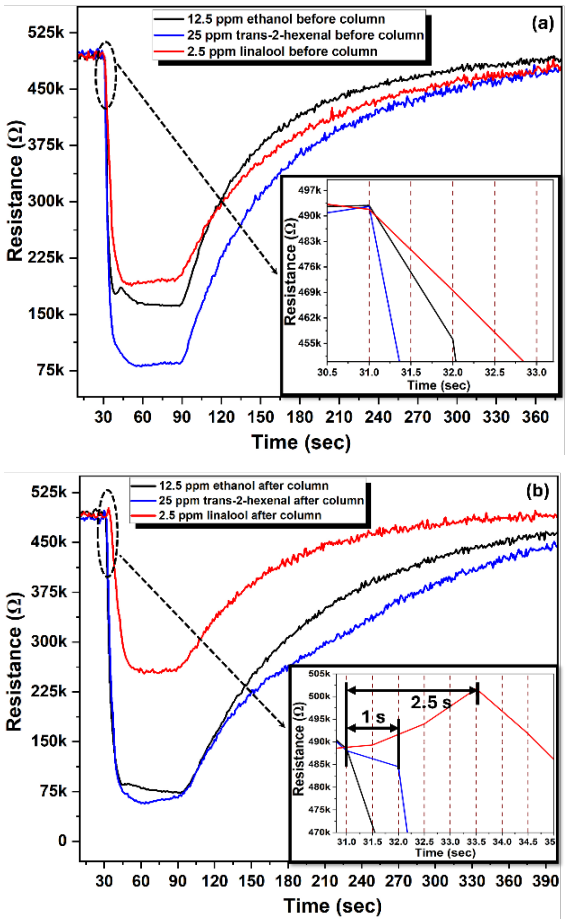


Fig. 2. MOX sensors response, (a) before μ-GC, and (b) after μ-GC.

Fig. 2(a) shows the response of MOX sensor (before column) for all three VOCs, with an inset displaying a magnified view of the initial response curve of MOX to each VOC. The results demonstrate that MOX responds to all three VOCs simultaneously, but with varying curve slopes depending on the concentration and molecular properties of the compound.

Fig. 2(b) presents the response of MOX sensor (after column) response, revealing delays of 1 s and 2.5 s for trans-2-hexenal and linalool, respectively, compared to ethanol (see inset in Fig. 2(b)). These delays were expected due to the differences in molecular size, with lighter molecules eluting first.

Finally, features were extracted from the time-dependent sensor responses (e.g. change in resistance, response time) and used to train and test a PLS model for the prediction of VOC class and concentration levels. Fig. 3 shows confusion matrix for the trained model showed 100% accuracy in predicting unknown ethanol, trans-2-hexenal, and linalool concentrations. Further investigations are needed to control more accurately the inlet velocities of the target VOCs and life of the columns.

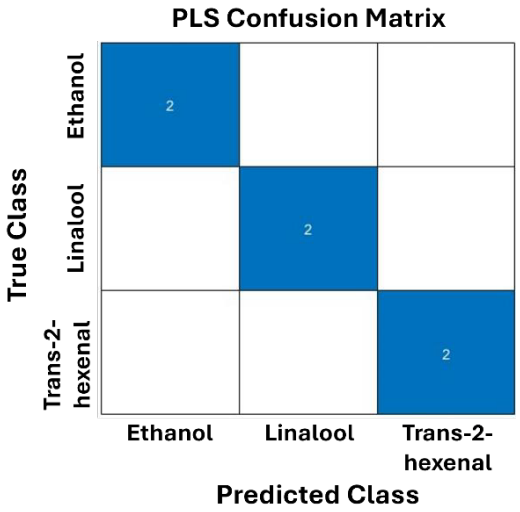


Fig. 3. Confusion matrix for trained PLS model.

References

[1] J.H. Christensen, M V. Kolomiets, The lipid signaling and volatile oxylipin pathways are integrated in maize. Plant, Cell & Environment, 34(10), 1630-1641 (2011). https://doi.org/10.1111/j.1365-3040.2011.02356.x

[2] A. Kessler, I.T. Baldwin, Defensive function of herbivore-induced plant volatile emissions in nature. Science, 291, 2141–2144 (2001). https://doi.org/10.1126/science.1057083.

Acknowledgements

This work is supported by the project "PurPest under Horizon Europe Program (grant #101060634), the Horizon Research and Innovation Action from European Research Executive Agency.

DOI 10.5162/EUROSENSORS2025/M3.1.1

Novel corrole-based e-nose for methanol detection in wine

Francesco Pizzoli[1], Gabriele Magna[1], Sara Nardis[1], Corrado Di Natale[2] and Roberto Paolesse[1]
[1] Department of Chemical Science and Technology, University of Rome Tor Vergata, 00133 Roma, Italy
[2] Department of Electronic Engineering, University of Rome Tor Vergata, 00133 Roma, Italy

Summary:

Corrole derivatives are a versatile class of coordination complexes successfully exploited in different applications, ranging from medical to environmental fields, due to their peculiar tunable properties. Herein, we report novel N-alkyl corroles-based gravimetric sensors obtained by the deposition of twelve different macrocycles on quartz microbalances (QMBs). Sensors were tested against 17 VOCs and 4 gases, showing notable sensitivities, particularly to CO, NO, and ethanolamine. Data analysis revealed clear trends related to the alkyl chain structure, confirmed through correlations with linear solvation equation relationship (LSER) parameters. Principal Component Analysis enabled the clustering of compound families and discrimination along homologous series (e.g. class of alcohols). The sensors demonstrated strong potential for analyte differentiation in complex mixtures as demonstrated by a study cases where methanol content was estimated in both real and synthetic wine samples.

Keywords: Quartz Microbalances, porphyrinoids, e-nose, array, VOCs, gas, methanol, wine

1. Introduction

Corroles and related macrocycles are widely employed in the field of chemical sensors, where they are used as sensing materials for optical, electrochemical, gravimetric and conductometric transducers [1]. Specifically, porphyrinoid-based Thickness Shear Mode Resonating sensors (TSMRs) have been widely studied and used with excellent results on different analytes and real samples [2]. An interesting attempt to increase the selectivity towards different analytes was proposed by our group in the past, exploiting a series of porphyrins having different chain lengths covalently linked in the peripheral positions [3]. However, the presence of the alkyl chains improves the metalloporphyrin thin film permeability but at the same time increases the magnitude of non-specific interactions, reducing the influence of the intrinsic metalloporphyrin selectivity. To address this issue, a novel class of N- alkylated free-base corroles is proposed here to be used as sensing material, in order to obtain more homogeneous and selective sensing layers [4]. The insertion of chains with different lengths and numbers in the core of the macrocycle would allow, at the same time, to obtain homogeneous films and an increase in selectivity. Here, we have composed an e-nose using an array of twelve different N-alkyl corroles deposited on QMB, and we have tested it towards different VOCs and gases in order to study the different responses and sensitivities. Thus, we have performed tests on six samples of Italian wines and artificial wines to verify the possible use of our platform for methanol detection.

2. Materials and methods

Free-base N-alkyl corroles are synthesized according to literature methods [5]. Thin layer films are prepared by drop-casting a chloroform solution of porphyrinoids directly onto quartz microbalances (QMBs). The covered QMB were allocated in a plastic chamber, where each sensor was connected to an individual oscillator circuit and frequency variations were measured by means of an integrated frequency counter and then stored on a computer. Organic vapors of the different analytes were generated by bubbling an N_2 stream into a liquid sample of the compound. The saturated vapor concentration of the volatile organic compound was calculated using Antoine's law. Different concentrations of nitric oxide (NO), carbon monoxide (CO), molecular hydrogen (H_2), and carbon dioxide (CO_2) were also tested. The six samples of wine were purchased in local stores. Relative changes in responses have been considered as features, and data analysis is performed in Matlab®.

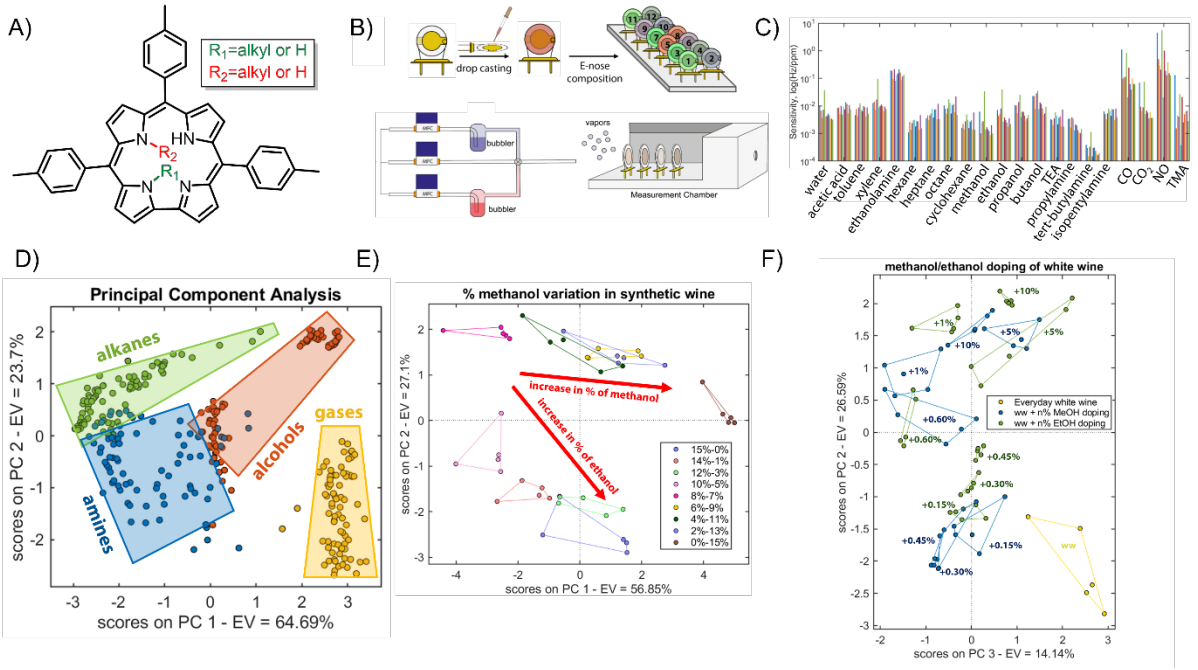


Fig. 1. A) Structure of an N-alkyl corrole B) Set-up for sensor fabrication, the e-nose arrangement and the functioning of the measure. B) Typical sensor response to an analyte. C) Sensitivity of the sensors based on the selected N-alkyl corroles. *D) PCA of experimental data considering responses from a QMB selection towards the classes of gases, alkanes, alcohols and amines. E) PCA of experimental data of methanol percentage variation in synthetic wine.F) PCA of experimental data of different solutions of methanol/ethanol doped white wine.*

3. Result and discussion:

Data analysis allowed the evaluation of sensor sensitivities, revealing strong responses, especially toward CO, NO, and ethanolamine. To understand the influence of the alkyl substituent on sensing performance, the sensors were grouped into series and correlated with LSER parameters of selected analytes. Pearson correlation matrices revealed differences according to the position and length of alkyl chains. Principal Component Analysis (PCA) showed a clear separation of the four main classes of compounds: gases, alkanes, alcohols, and amines. Moreover, a separation along the homologous series of alcohols and alkanes was observed based on the length of the analyte's alkyl chain. These findings confirm the ability of N-alkyl corroles to discriminate among different analytes and support the potentially useful presence of the alkyl chain. Following these results, we finally explored the possibility of using this array for the discrimination of methanol in wine, essential for regulatory compliance and product quality assurance. We first performed tests on six different varieties of Italian wines, obtaining a good separation based on the alcohol content and on the white and red varieties. Finally, two different studies were performed, the first testing wine samples doped with increasing concentrations of methanol and ethanol, the second on synthetic wine samples prepared using different ethanol/methanol ratios. Both studies confirmed the effectiveness of the array to discriminate between the two alcohols in different conditions, paving the way for several possible applications in environmental and agri-food monitoring.

References

[1] R. Paolesse, S. Nardis, D. Monti, M. Stefanelli, and C. Di Natale. *Chemical reviews,* 2017, *117*(4), 2517-2583. doi.org/10.1021/acs.chemrev.6b00361.

[2] Di Natale, C.; Salimbeni, D.; Paolesse, R.; Macagnano, A.; D'Amico. *Sensors Actuators, B Chem.* 2000, *65* (1), 220– 226.

[3] Di Natale, C., Paolesse, R., Macagnano, A., Nardis, S., Martinelli, E., Dalcanale, E., Costa, M., D'Amico, A., *J. Mater. Chem.*, 2004, 14, 1281.

[4] Barata, J. F. B., Neves, M. G., Faustino, M. A. F., Tomé , A. C., Cavaleiro, J. A. S., *Chem. Rev.*, 2017, 117, 3192.

[5] Pizzoli F., Nardis, S., Fata A., Marsotto M., Petrella G., Fronczek F.R., Smith K.M., Paolesse R., *N*-Alkylcorroles, *J. Porph. Phthaloc.*, 2024, 28, 06, 358-369.

DOI 10.5162/EUROSENSORS2025/M3.1.2

Fabrication and Chracterization of Polymer-Based Ethanol Gas Sensor

Md Mayen Uddin[1], Mohammad Ariful Islam Bhuyan[1], Hyeon Cheol Kim[1]
[1] Department of Electrical, Electronic and Computer Engineering, University of Ulsan, 93 Daehak-ro, Nam-gu, Ulsan 680-749, South Korea
hckim08@mail.ulsan.ac.kr

Abstract:

In this study, we present the fabrication and characterization of polymer-based ethanol gas sensors developed for environmental ethanol detection. The sensors were fabricated using MEMS process. A protective SU-8 film was applied to the sensing area, followed by the deposition of various polymer films, including PNPD, to enhance gas-sensing performance. The base resistance was measured to evaluate the sensor's stability. Ethanol gas responses were evaluated at 3000 ppm, 5000 ppm, and 10,000 ppm. The results confirm the potential of the fabricated sensors for reliable and effective environmental ethanol detection.

Keywords: Gas sensor, Ethanol sensor, SU-8, PNPD polymer, Response-recovery

Background, Motivation and Objective

Ethanol is widely used in industrial, biomedical, and domestic settings, making its detection and monitoring increasingly important for safety and environmental management. Prolonged exposure to ethanol vapors poses health risks and fire hazards, especially in confined spaces. Therefore, reliable ethanol gas sensors with high sensitivity, stability, and fast response times are essential. Among various sensing technologies, polymer-based gas sensors have garnered attention due to their low cost, ease of fabrication, and tunable sensitivity through polymer functionalization [1][2]. Integration with microfabrication techniques, such as photolithography and RF sputtering, further enhances the precision and reproducibility of sensor devices.

Traditional metal oxide-based sensors often require high operating temperatures, which limit their use in low-power or wearable applications. In contrast, polymer-based sensors can operate effectively at room temperature, offering a safer and more energy-efficient alternative. By incorporating functional polymers like PNPD, it is possible to tailor the sensor's selectivity and sensitivity toward ethanol gas [3]. The use of SU8 as a passivation layer also improves mechanical stability and surface protection during operation. A need remains for fabricating and testing such sensors with well-defined structures and reliable response characteristics to varying ethanol concentrations.

The primary objective of this work is to design and fabricate ethanol gas sensors using a polymer-based approach supported by microfabrication processes. This study aims to demonstrate the potential of such polymer-based sensors for use in practical environmental ethanol monitoring applications.

Materials and Methods

The fabrication process began with the preparation of a clean substrate suitable for photolithographic processing. A photoresist layer was deposited onto the substrate using a spin coater to ensure uniform coverage and desired film thickness. Fig 1. shows the schematic diagram of the sensor.

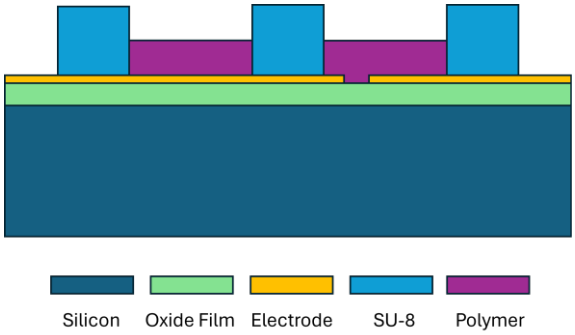


Fig. 1. Schematic diagram of ethanol sensor

Ti/Au electrodes were patterned on oxidized silicon wafers via the lift-off porcess with RF sputtering. An SU-8 photoresist was patterned to act as a containment barrier for the polymer during

subsequent processing. Following dicing into individual sensor chips, functional polymer layers were deposited onto the sensing area. Poly (N-phenyl diaminopyridine) (PNPD) polymer was selected as the active material due to its strong chemical affinity for ethanol vapors and its stable electrical properties. The Polymer was appled using drop-casting technique, with the the deposition parameters adjusted based on the desired film morphology and thickness. The fabricated sensors were susbsequently dried at room temperature. A shematic illustration of the sensor structure is provided in Fig. 2.

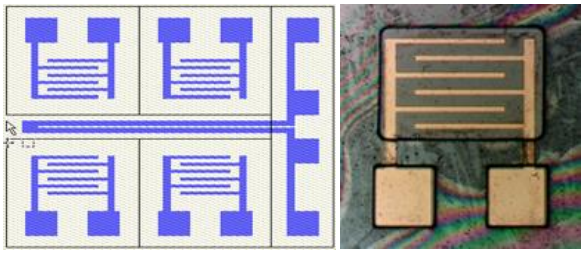


Fig. 2. Electrode layout(left) and the fabricated picture(right) of ethanol sensor

Results and Discussion

Fig. 3 illustrates the resistance response of the fabricated polymer-based ethanol gas sensor when exposed to ethanol concentrations of 3000 ppm and 10,000 ppm over time. In both cases, a sharp decrease in resistance is observed upon ethanol exposure, indicating good sensitivity and prompt response to the gas. After each exposure cycle, the resistance returns close to its baseline, confirming the sensor's repeatability and recovery behavior. The response magnitude is more pronounced at 10,000 ppm, showing that higher ethanol concentration leads to a larger resistance change.

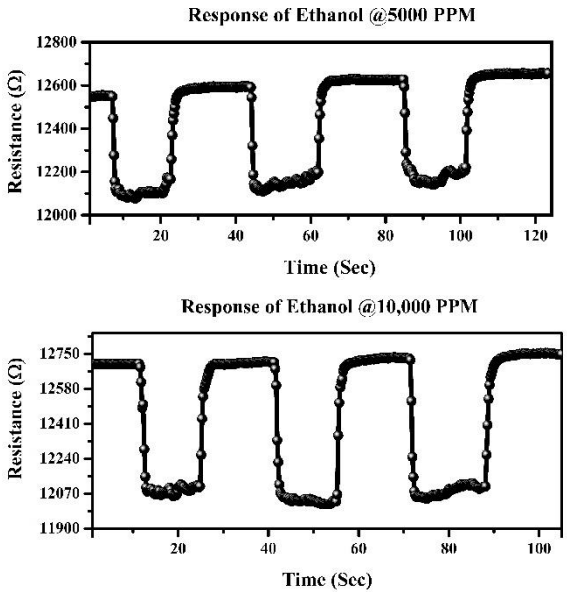


Fig. 3. Response characteristics of ethanol sensor

These results confirm that the sensor is capable of detecting ethanol at various concentrations with consistent performance.as the ratio of resistance change upon gas exposure to the baseline resistance.

Fig. 4 shows the relationship between the resistance change rate (%) of the sensor and the square root of ethanol gas concentration. A strong linear correlation is observed, with a correlation coefficient R^2 = 0.9992, indicating excellent sensor response predictability. The linear trend (slope = 0.0507) confirms that the sensor's response increases proportionally with higher ethanol concentrations. This result validates the sensor's capability for quantitative ethanol detection with high sensitivity and reliability.

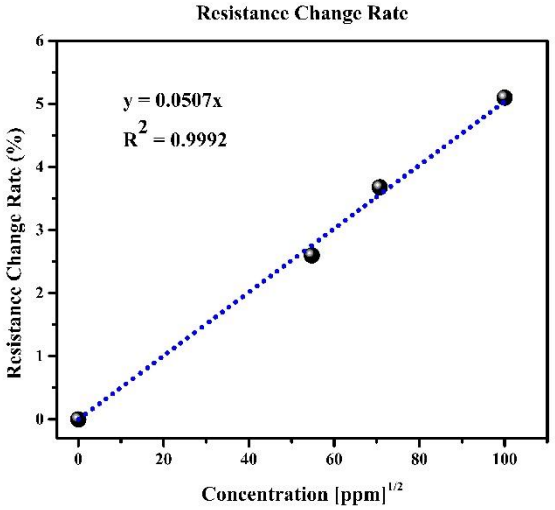


Fig. 4. Resistance change ratio for PNPD polymer

Conclusions

To address the need for low-cost, room-temperature ethanol sensing, a PNPD-baed polymer gas sensor was fabricated using microfabrication techniques. The sensor exhibited high sensitivity, repeatability, and fast reponse.

Acknowledgements

This study was confucted with the support of TAESUNG ENVIRONMENT.

References

[1] R.K. Gupta, A. Verma, S. Sharma, Polymers for gas sensing applications, Progress in Polymer Science 37, 595–625 (2012); doi: 10.1016/j.progpolymsci.2011.09.003

[2] A. Bai, H. Shi, Review of polymer-based gas sensors, Sensors 17, 1091 (2017); doi: 10.3390/s17051091

[3] M. Penza, G. Cassano, A. Tortorella, Chemical sensing with functionalized conducting polymers, Sensors and Actuators B: Chemical 50, 9–18 (1998); doi: 10.1016/S0925-4005(98)00123-8

DOI 10.5162/EUROSENSORS2025/M3.1.3

CO_2 Sensor based on Au functionalised CuO thin films

Christian Maier[1], Florentyna Sosada-Ludwikowska[1], Larissa Egger[1], Anton Köck[1], Soeren Becker[2], Jan Steffen Niehaus[2], Klaus Reichmann[3]

[1] Materials Center Leoben Forschung GmbH, Roseggerstraße 12, 8700 Leoben, Austria

[2] Fraunhofer Center for Applied Nanotechnology CAN, Grindelallee 117, 20146 Hamburg, Germany

[3] Institute for Chemistry and Technology of Materials, TU Graz, Stremayrgasse 9, 8010 Graz, Austria

Correspondence: christian.maier@mcl.at; +43-3842-45922-550

Summary:

In this work, we present chemical nanosensors based on ultrathin CuO/Cu_2O films, which are fabricated by thermal evaporation and subsequent oxidation on SiN-based micro-hotplate chips. The sensors are tested against target gas carbon dioxide (CO_2). The CuO/Cu_2O films are functionalized with Au nanoparticles (Au-NPs) stabilized with citrate. The Au-NPs clearly increase the sensor response in particular for CO_2 up to 310%.

Keywords: metal oxide, CuO, Cu_2O, nanomaterials, nanoparticles, gas sensors

Introduction

Detecting harmful or toxic gases such as Volatile Organic Compounds (VOCs), carbon dioxide (CO_2), and carbon monoxide (CO) is increasingly important for monitoring air quality both indoors and outdoors, due to their detrimental effects on human health. Conductometric gas sensors are commonly used for this purpose; they work by measuring changes in the electrical conductance of a gas-sensitive material when exposed to different gases. Metal oxides like tin oxide (SnO_2), zinc oxide (ZnO), and copper oxide (CuO) are widely used in these sensors because of their high sensitivity to a broad range of gases [1]. The performance of these sensors, particularly their selectivity, can be significantly enhanced through surface functionalization with metallic nanoparticles (such as gold, palladium, or platinum) [2, 3]. Recently, we have successfully used gold nanoparticle (Au-NP) solutions to functionalize Cu_xO-based sensors, resulting in improved CO_2 detection performance [4]. In this study, we investigate the functionalization with Au-NPs of different diameters and how they influence the sensor performance towards CO_2.

Sensor Fabrication

The sensing material is composed of ultrathin CuO/Cu_2O films, which are fabricated by thermal evaporation 50nm Cu and subsequent thermal oxidation. These are used on a silicon nitride (Si_3N_4) micro hotplate (µhp) chip with Pt electrodes and heaters. The structuring was done by e-beam lithography, resulting in a circularly shaped (450 µm) sensor structure.

Au-NP Functionalisation

The sensors were functionalised using the drop coating technique with gold nanoparticles (Au-NPs) stabilized in citrate of 20, and 40 nm in diameter. Thus, a drop of 0.2 µL is placed on the sensitive layer and dried for 10 minutes. This process is repeated twice to ensure sufficient Au-NPs coverage of the sensitive layer. In Figure 1, the functionalised sensor is displayed.

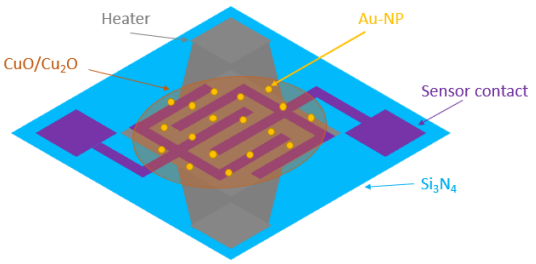


Fig. 1 Illustration of an Au-NP functionalised Cu_xO film-based gas sensor [5]

Sensor Characterization & Results

The sensor devices have been operated at 300°C and tested against CO_2. Synthetic air with 50 % relative humidity level (r.h.) has been employed as a background gas. Cu_xO sensors functionalised with Au-NPs of different diameter have been compared. Fig.2 shows the electrical resistance behavior of all sensors when exposed to 1000, and 2000 ppm CO_2. The sensors are heated for 45 min before the measurement to ensure a stable resistance baseline.

Fig.3 compares the responses of the sensors towards 1000 ppm and 2000 ppm of CO_2. While

pure Cu_xO has no response towards CO_2 (not shown here), the response to CO_2 is highly increased with Au-NPs. Cu_xO sensor functionalized with citrate stabilized Au-NPs exhibits the highest response (310 %) towards CO_2.

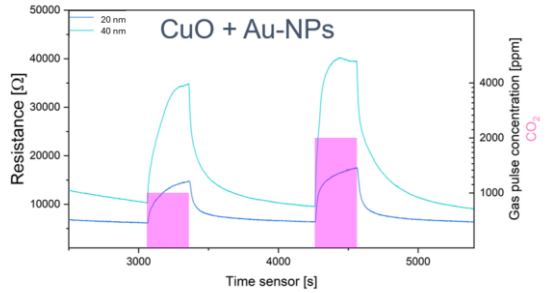


Fig. 2 Resistance measurement during exposure to 1000 / 2000 ppm CO_2 at 300 °C operation temperature and 50% r.h for sensors functionalised with 20nm and 40nm sized Au-NPs.

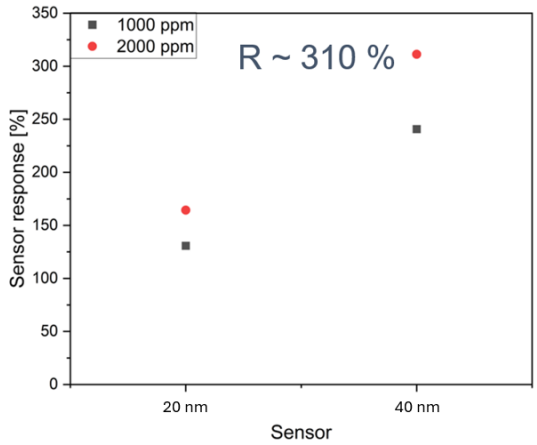


Fig. 3 Sensor response towards 1000 ppm and 2000 ppm CO_2 at 300 °C operation temperature and 50% r.h for sensors functionalised with 20nm and 40nm sized Au-NPs.

Conclusion & Outlook

We have shown that the Au-NPs clearly increase the response towards CO_2. For an Au-NP size of 40nm we have achieved the highest response up to 310% towards 2000ppm CO_2.

We are convinced that the presented pathway for improving the sensitivity towards CO_2 is a very promising approach for realisation of the first conductometric CO_2 sensor on the market.

References

[1] M. V. Nikolic, V. Milovanovic, Z. Z. Vasiljevic, Z. Stamenkovic, Semiconductor Gas Sensors: Materials, Technology, Design, and Application. *Sensors* 2020, 20 (22) https://doi.org/10.3390/s20226694.

[2] C. Maier, L. Egger, A. Köck, K. Reichmann, A Review of Gas Sensors for CO_2 Based on Copper Oxides and Their Derivatives, *Sensors* 24 (17). https://doi.org/10.3390/s24175469

[3] F. Sosada-Ludwikowska, L. Reiner, L. Egger, E. Lackner, J. Krainer, R. Wimmer-Teubenbacher, V. Singh, S. Steinhauer, P. Grammatikopoulos, Anton Koeck, Adjusting surface coverage of Pt nanocatalyst decoration for selectivity control in CMOS-integrated SnO_2 thin film gas sensors", *Nanoscale Adv.*, 2024, https://doi.org/10.1039/D3NA00552F

[4] R. Wimmer-Teubenbacher, F. Sosada-Ludwikowska, B. Travieso, S. Defregger, O. Tokmak, J. S. Niehaus, M. Deluca, A. Köck, CuO Thin Films Functionalized with Gold Nanoparticles for Conductometric Carbon Dioxide Gas Sensing, *Chemosensors* 2018, 6 (4), 56 https://doi.org/10.3390/chemosensors6040056.

[5] C. Maier, L. Egger, A. Köck, K. Reichmann, S. Becker, J. S. Niehaus, K. Reichmann, Investigation of the gas-sensing performance of CuO sensors functionalized with different stabilized Au nanoparticles, *J. Sens. Sens. Syst. 2025* 14 (1), S. 55–65. DOI: 10.5194/jsss-14-55-2025.

Funding

The authors gratefully acknowledge the financial support under the scope of the COMET program within the K2 Center "Integrated Computational Material, Process and Product Engineering (IC-MPPE)" (Project No 886385). This program is supported by the Austrian Federal Ministries for Climate Action, Environment, Energy, Mobility, Innovation and Technology (BMK) and for Labour and Economy (BMAW), represented by the Austrian Research Promotion Agency (FFG), and the federal states of Styria, Upper Austria and Tyrol.

DOI 10.5162/EUROSENSORS2025/M3.1.4

Toluene Sensing at Room Temperature using SnO_2 Quantum Dot Decorated rGO Aerogel

Padmanathan Karthick Kannan[1], Zhuo Chen[2], Tynee Bhowmick[2], Tawfique Hasan[2] and Julian W. Gardner[1]
[1] School of Engineering, University of Warwick, Coventry CV4 7AL, United Kingdom
[2] Cambridge Graphene Centre, University of Cambridge, Cambridge CB3 0FA, United Kingdom
Corresponding Author's e-mail address: J.W.Gardner@warwick.ac.uk

Summary:
This work reports on the fabrication of a reduced graphene oxide (rGO)/tin oxide (SnO_2) aerogel-based sensor for the detection of toluene at room temperature. Unlike conventional high-temperature metal oxide gas sensors, this low-power, cost-effective sensor enables efficient toluene detection under ambient conditions. Our preliminary data clearly show that the rGO/SnO_2 sensor can detect toluene at concentrations as low as 100 parts per billion (ppb); highlighting its potential for the development of practical VOC sensors with enhanced sensitivity.

Keywords: Reduced graphene oxide, tin oxide, aerogel, toluene sensor, chemical sensor

Background, Motivation an Objective

One of the most hazardous volatile organic compounds (VOC) released by automobiles is toluene. It is also extensively used as a solvent in a variety of industries, including paints, glues and cosmetics. Despite its widespread usage in numerous commercial applications, prolonged exposure to toluene can cause major health problems for humans, including damage to the central nervous systems and other important organs [1]. The Health and Safety Executive (HSE) suggests an exposure limit of 100 ppm for a 15 min short-term exposure limit (STEL) and 20 ppm for an 8 hr time-weighted average (TWA) [2]. Therefore, it is crucial to detect toluene at low ppm concentrations for both environmental monitoring and human safety. There have been many articles on the development of highly sensitive toluene sensors based on metal oxide semiconductors (MOS) [3]. Despite showing high sensitivity, their main drawbacks are high operating temperature and power consumption, which limit their practical use in in detecting toluene. Taking this into careful consideration, the current work aims to develop a room-temperature operable sensor for detecting very low concentrations of toluene using SnO_2 quantum dot (QD)-decorated rGO aerogel .

Description of the New Method or System

A surfactant-assisted hydrothermal growth method was employed for the synthesis of rGO/SnO_2 hybrid material. Subsequently, copper chloride and ascorbic acid were added to initiate the gelation and surface doping process, resulting in a highly crosslinked rGO-SnO_2 ink. One layer of the hybrid ink was first spin-coated on a gold interdigitated electrode (IDE) with 10 µm gap substrate at 5000 rpm for 60 s, followed by 60°C annealing for 5 min. Once the substrates had cooled down, a second layer was spin-coated at 2500 rpm for 15 s. The samples were immediately frozen in liquid nitrogen for 10 min and transferred to a freeze dryer (LyoQuest, Telstar) for overnight freeze-drying. The freeze-dried sample was washed with acetone twice and dried in the air (sample denoted as NC2), whereas NC1 refers to the sample that did not undergo the washing step. Both the samples were then annealed at 160°C for 3 h to further reduce the GO before being ready for gas sensing measurements. Fig. 1a shows the image of the uncoated IDE substrates used in the present study. Top-view SEM images (Figs. 1b and 1c) show a uniform, 5nm thick porous aerogel on the sensor substrate. The film bridges a 10 µm gap between two sensor electrode pads. The high porosity of hybrid aerogel with rGO as the skeleton and QDs for sensitisation facilitates efficient gas diffusion and reaction, thus enhancing sensor response and kinetics.

The coated aerogel device was mounted on a PCB and electrical contacts were made using the wire-bonding technique. The fabricated aerogel sensor was placed in a customized sensor chamber connected to the automated gas testing bench, where gas flow rates were controlled by a National Instruments LabVIEW program. The sensor parameters were extracted using NI USB

6343 data acquisition system (DAQ) using an indigenously developed LabVIEW module.

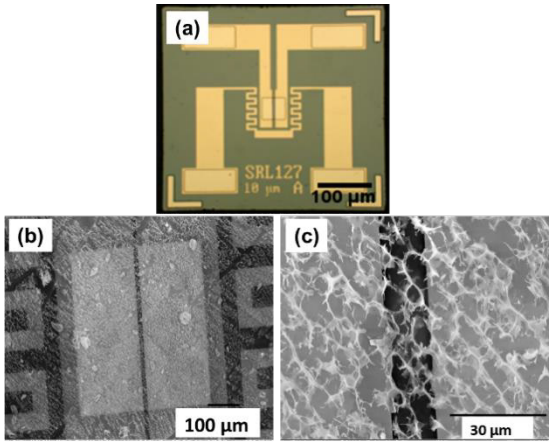


Fig. 1 (a) Photograph of uncoated IDE substrate. SEM images of rGO/SnO_2 aerogel sample with (b) low and (c) high magnifications.

Results

The electrical resistance of both the samples was measured at room temperature after exposure to different toluene concentrations in the range 0.1 - 5 ppm. Figs. 1a and 1b show the sensor responses for both NC1 and NC2 samples. Each toluene exposure time lasted for 5 minutes, followed by a 25 min recovery period under dry air.

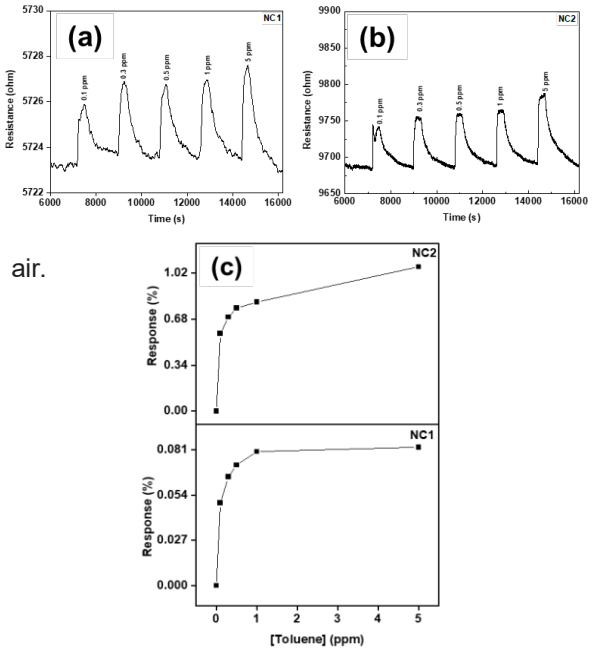


Fig. 1. Dynamic response plots of rGO/SnO_2 aerogel samples (a) NC1 (b) NC2 at different concentrations of toluene. Plot between sensor response % and concentration of toluene.

The sensor response is defined using the following equation.

$$Response\ (\%) = \frac{R_g - R_a}{R_a} * 100 \qquad (1)$$

Where R_a is the stable resistance value measured in ambient air and R_g is the resistance measured in the target gas, toluene.

The testing results showed that the resistance of both samples increased with rising toluene concentrations, indicating the overall p-type semiconducting nature of the samples with surface doping. Between the two samples, NC2 exhibited a higher response % to toluene than NC1 across the measured concentration range and the respective values are given in Table 1.

Tab. 1: Calculated sensor response % values for both the samples at diff. concentrations of toluene

PPM	Response (%) NC1	Response (%) NC2
0.1	0.04942	0.57302
0.3	0.06488	0.69578
0.5	0.07186	0.76117
1	0.07991	0.80682
5	0.08256	1.06806

The better response of NC2 than NC1 is attributed to the washing process that removes residual precursors and crosslinking agents that negatively impact sensitivity. Further investigations into the effects of humidity and temperature on the aerogel sensor response, along with studies on cross-sensitivity and long-term stability, are currently underway. The complete results will be presented at the conference.

References

[1] M. Saeedi, B. Malekmohammadi, S. Tajalli, Interaction of benzene, toluene, ethylbenzene, and xylene with human's body: Insights into characteristics, sources and health risks, *Journal of Hazardous Materials Advances* 16, 100459-17 (2024); 10.1016/j.hazadv.2024.100459

[2] M. Rooseboom, N.A. Kocabas, C. North, R.J. Radcliffe, L. Segal, Recommendation for an occupational exposure limit for toluene, *Regulatory Toxicology and Pharmacology* 141, 105387-9 (2023); 10.1016/j.yrtph.2023.105387

[3] Y. Chen, J. Xu, Y. Pan, Q. Cao. K. Yuan, Trace detection of benzene, toluene and xylene (BTX) by chemiresistive metal oxide-based gas sensors: Recent advances in heterojunction materials design, *Chinese Chemical Letters* 110606 (2024); 10.1016/j.cclet.2024.110606.Acknowledgements

Acknowledgements

This research was supported by the Engineering and Physical Sciences Research Council grant EP/W024284/1

DOI 10.5162/EUROSENSORS2025/M3.2.1

KNN Lead-free MEMS Mirror: Thermal behavior

L.Mollard[1], C.Dieppedale[1], A.Hamelin[1], G.Le Rhun[1]
[1] Univ. Grenoble Alpes, CEA, Leti, F-38000 Grenoble, France.

laurent.mollard@cea.fr

Summary:

This paper presents the thermal behavior of KNN-based quasi-static biaxial piezoelectric MEMS mirrors. These mirrors achieved state-of-the-art performance at ambient temperature across different MEMS mirror sizes. Specially, they reach an optical angle of up to 8.5° at 40V with a 2×2 mm² mirror. These mirrors were initially designed for LIDAR (Light Detection and Ranging) applications, using a 1550 nm pulsed laser with high incident power. This paper presents a series of experimental results on the thermal behavior of such KNN mirrors, which could be affected by high incident power or high ambient temperature. It shows that the mirror and KNN actuator thermal deformations are consistent with a first-order model, without any detrimental effects up to 100°C. It also demonstrates that the mirror remains operational at this temperature, with 2D beam scanning behavior consistent with previous study and no significant deviation of the spot during a 30-minutes period. These results enables a better prediction of the evolution of the KNN-mirror and 2D scanning when temperature increases for LIDAR systems or new application domains.

Keywords: MEMS mirror, Piezoelectric, KNN, Lead-free, Actuator.

Due to their compact size, affordability, and low power consumption compared to conventional mechanical scanning systems, MEMS mirrors [1] are widely used in various applications. These include projection display systems for augmented reality (AR) and virtual reality (VR) smart glasses, biological imaging**,** and Light Detection And Ranging (LIDAR) system [2], among others.

Piezoelectric actuation emerges as a promising choice, offering notable advantages such as high force generation, low voltage requirements, high frequency capability, and rapid response times. For a long time, lead Zirconate Titanate (PZT) has been the dominant piezoelectric material thanks to its competitive electromechanical coupling and high piezoelectric coefficient. However, the presence of lead in PZT raise significant concerns regarding the practical application of piezoelectric MEMS mirrors. The release of lead and its associated compounds poses a substantial threat to both the environment and human health [3]**.**

To replace PZT actuators, sodium potassium niobate (KNN) emerges as particularly promising due to its high Curie temperature and strong piezoelectric coefficient [4]. The integration of lead-free KNN material integrated into actuators offers potential applications in various fields, from Light Detection And Ranging (LIDAR) systems to biomedical applications, thanks to its full biocompatibility [5].

This work presents the thermal behavior of biaxial piezoelectric MEMS mirror with 2×2 mm² diameters, as presented in Tab. 1, featuring a gold reflector. The performance of such mirrors at ambient temperature was presented previously in [6] [7]. The studied mirrors incorporate a 1.5 µm sputtered $(K_{0.3}Na_{0.7})$ NbO_3 thin film from Sumitomo Chemicals [8].

This paper demonstrates that the 2×2 mm² KNN mirror remains functional as the temperature increases and undergoes no detrimental deformation even when heated to 100 °C. The deformation of the KNN actuators based tends to shift downward, with a 40 µm decrease in the mirror's Z-position when heated to 100°C. This result is consistent with a first-order model. The mirror's planarity under temperature increase is also studied and potential optimization strategies for improving planarity are presented. In addition, the 2D-projection model under increasing temperature revealed no variation in optical angle at 50°C and a 5% increase at 100°C. This result is also consistent with previous studies [9]. Finally, the stability of 2D scanning during continuous use, at 100 °C was investigated. The finding demonstrate that a KNN

MEMS scanner can operate at a temperature of at least 100 °C for 30 minutes without significant deviation.

The authors thanks Sumitomo Chemical for depositing KNN films with electrodes on the SOI wafers. This work is part of the IPCEI Microelectronics and Connectivity and was supported by the French Public Authorities within the frame of France 2030.

Tab. 1: KNN MEMS mirror described in this work

Reflector	Mirror Size (mm^2)	MEMS Footprint (mm^2)	f_x (kHz)
Au	2×2	≈8×8	1.92

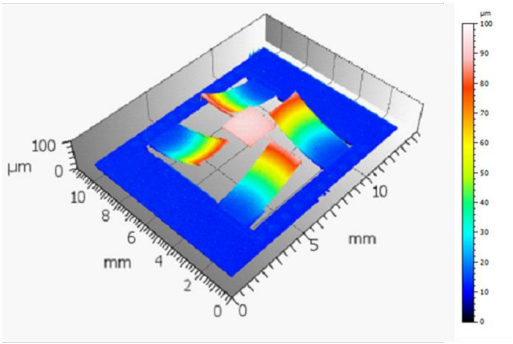


Fig. 2. Scanner deformation along Z-axis with Gold reflector at ambient (25°C).

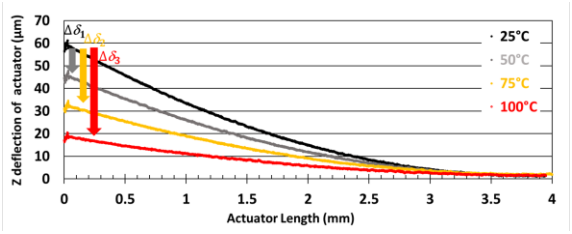


Fig. 3. Evolution of the Z-deflection of the KNN arms as a function of temperature

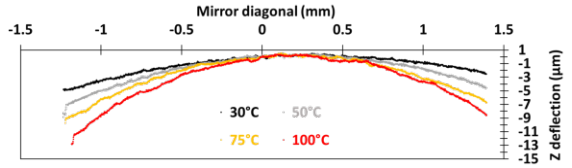


Fig. 3. Evolution of mirror deformation as a function of temperature from 25°C to 100°C.

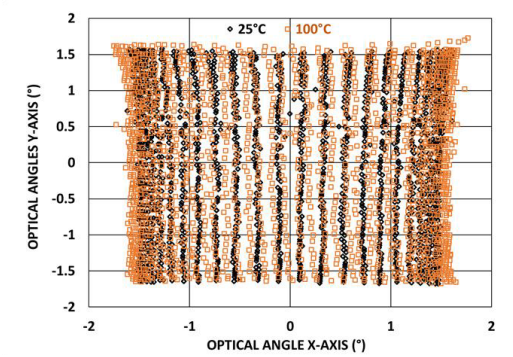


Fig. 3. 2D beam scanning at 25°C and 100°C

References

[1] Holmstrom, S.T.S.; Baran, U.; Urey, H. MEMS Laser Scanners: A Review. *J. Microelectromech. Syst.* **2014**, *23*, 259–275. doi:10.1109/JMEMS.2013.2295470.

[2] Yoo, H.W.; Druml, N.; Brunner, D.; Schwarzl, C.; Thurner, T.; Hennecke, M.; Schitter, G. MEMS-Based Lidar for Autonomous Driving. *e & i Elektrotechnik und Informationstechnik* **2018**, doi:10.1007/s00502-018-0635-2.

[3] Panda, P.K. Review: Environmental Friendly Lead-Free Piezoelectric Materials. *Journal of Materials Science* **2009**, *44*, 5049–5062, doi:10.1007/s10853-009-3643-0.

[4] Aspe, B.; Cissé, F.; Castel, X.; Demange, V.; Députier, S.; Ollivier, S.; Bouquet, V.; Joanny, L.; Sauleau, R.; Guilloux-Viry, M. K x Na1−xNbO3 Perovskite Thin Films Grown by Pulsed Laser Deposition on R-Plane Sapphire for Tunable Microwave Devices. *Journal of Materials Science* **2018**, *53*, 13042–13052, doi:10.1007/s10853-018-2593-9.

[5] Gaukås, N.H.; Huynh, Q.-S.; Pratap, A.A.; Einarsrud, M.-A.; Grande, T.; Holsinger, R.M.D.; Glaum, J. *In Vitro* Biocompatibility of Piezoelectric $K_{0.5}Na_{0.5}NbO_3$ Thin Films on Platinized Silicon Substrates. *ACS Applied Bio Materials* **2020**, *3*, 8714–8721, doi:10.1021/acsabm.0c01111.

[6] Kuentz H.; le Rhun G.. KNN lead-free technology on 200 mm Si wafer for piezoelectric actuator applications. Sensors and actuators A:Physical, 2024, submitted.

[7] Mollard, L., Dieppedale, C., Hamelin, A., Liechti, R., and Le Rhun, G.: Effects of potassium sodium niobate (KNN) thickness on biaxial non-resonant microelectromechanical systems (MEMS) mirror performance, Journal of Sensors and Sensor Systems, 14, 27–35, https://doi.org/10.5194/jsss-14-27-2025, 2025.

[8] Shibata, K.; Watanabe, K.; Kuroda, T.; Osada, T. KNN Lead-Free Piezoelectric Films Grown by Sputtering. *Applied Physics Letters* **2022**, *121*, doi:10.1063/5.0104583.

[9] Dahl-Hansen, R. P., Tybell, T., and Tyholdt, F.: Performance and reliability of PZT-based piezoelectric micromirrors operated in realistic environments, in: 2018 IEEE ISAF-FMA-AMF-AMEC-PFM Joint Conference (IFAAP), 2018 IEEE ISAF-FMA-AMF-AMEC-PFM Joint Conference (IFAAP), Hiroshima, 1–4, https://doi.org/10.1109/ISAF.2018.8463243, 2018.

DOI 10.5162/EUROSENSORS2025/M3.2.2

Characterization of Sensor Responses in 1D and 2D Scan Patterns Via AlScN-Based MEMS Mirrors

Jeong-Yeon Hwang[1], Md Golam Mehdy Hassan Shuvho[1,2], Erdem Yarar[1], Gunnar Wille[1], Fabian Lofink[1,2,3] and Shanshan Gu-Stoppel[1]
[1] Fraunhofer Institute for Silicon Technology (ISIT), Fraunhoferstraße 1, 25524 Itzehoe, Germany
[2] Christian-Albrecht-University Kiel, Christian-Albrechts-Platz 4, 24118 Kiel, Germany
[3] Kiel Nano, Surface and Interface Science KiNSIS, Christian-Albrechts-Platz 4, 24118 Kiel, Germany
Corresponding author: shanshan.gu-stoppel@isit.fraunhofer.de

Summary: This paper presents an in-depth characterization of sensing capabilities using AlScN-based 3D-constructed MEMS mirror device. Generating 1D line scan or 2D Lissajous scan patterns while acquiring sensor signals simultaneously, this research investigated the correlation between scan angle and sensor output, as well as the potential applications in feedback control.

Keywords: MEMS Mirror, Piezoelectric, Aluminum Scandium Nitride (AlScN), Sensor

Introduction

Quasi-static MEMS mirror is primarily responsible for quasi-static actuation, tilting and holding the mirror plate at a specific scan angle under DC voltage. However, by utilizing resonant driving, the actuation efficiency can be improved, allowing for larger scan angles even under low voltage levels. Especially, this device has the potential to implement various scanning patterns including Lissajous, circular, and spiral scans [1]. In this research, the sensing capabilities of the device shown in Figure 1 have been investigated in depth.

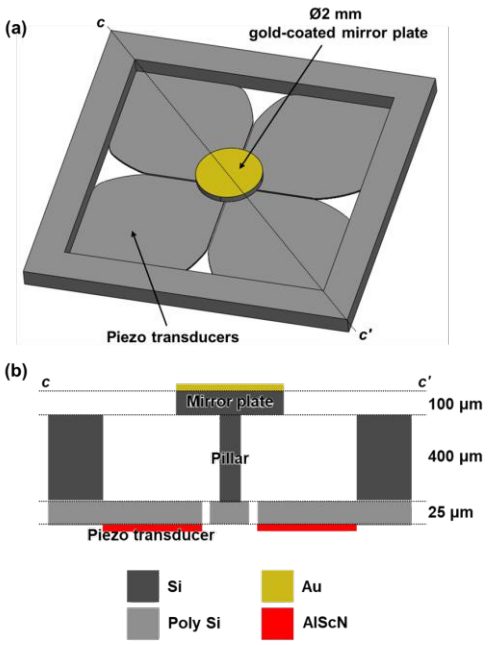


Fig. 1. (a) 3D schematic and (b) cross-sectional view of the analyzed MEMS mirror device.

Characterization of Sensing Capabilities

The photo of the MEMS mirror device and the schematic diagrams of the four independent piezoelectric transducers (P_1, P_2, P_3 and P_4) are shown in Figure 2(a). Figure 2(b) illustrates examples for simultaneous 1D or 2D scanning and sensing. For example, if P_1 is utilized as an actuator to generate 1D diagonal line scan, P_3 can be used as a sensor to detect the deflection angle level. This concept can also be applied in 2D Lissajous scan. P_1 and P_2 are driven at different frequencies, and P_3 ad P_4, located diagonally opposite, can be used as sensors.

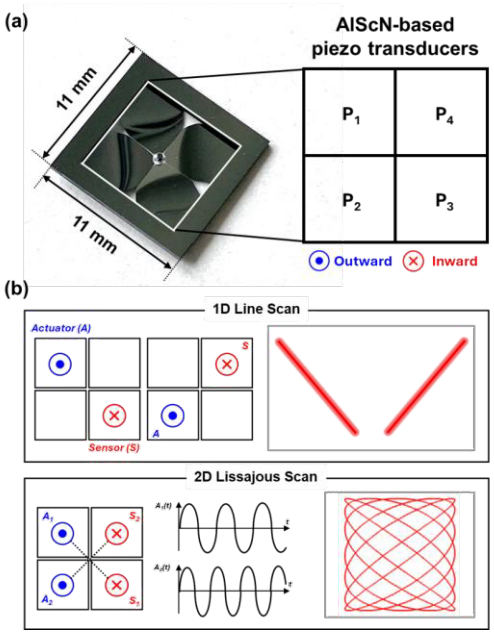


Fig. 2. (a) Overview of AlScN-based piezo transducers and (b) examples of implementation for 1D and 2D scanning.

Experimental Results

Figure 3(a) shows the resultant 1D laser scan trajectories under different voltage levels of 0.1 V_{pp} and 0.5 V_{pp}. The utilized actuator-sensor combinations are inserted in the top-right corner of the Figure 3(a). The frequency response result and corresponding senor output are shown in Figure 3(b). The results show that as the frequency increases, the total optical scan angle (TOSA) also increases, and the deflection level of the sensor located at the diagonal opposite increases, leading to an increment in the sensor output. The Figure 3(c) shows the linear increase in sensor output with increase in TOSA.

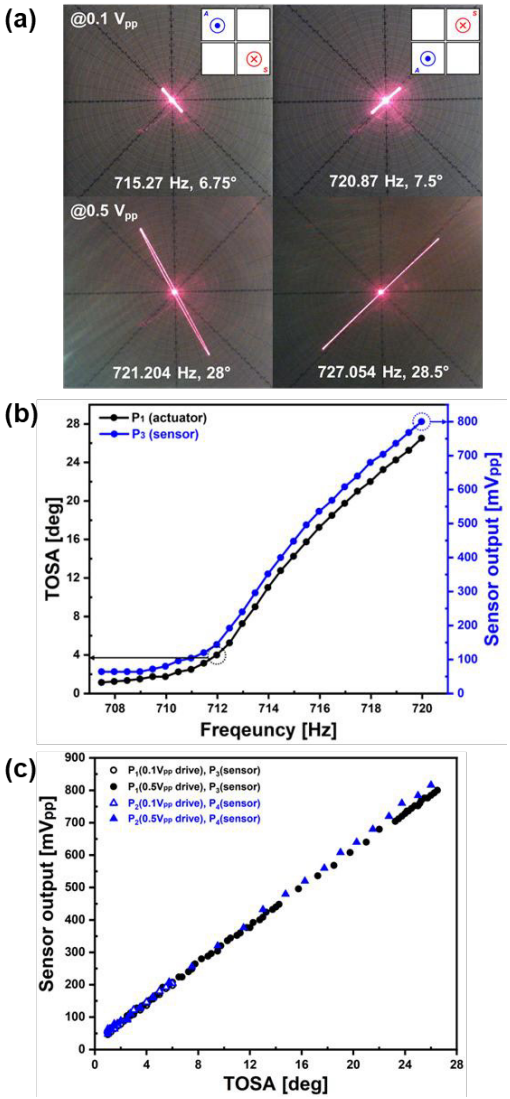


Fig. 3. (a) Resultant laser beam trajectories of 1D line scan under different voltage levels, (b) frequency response result and corresponding sensor output, (c) plot of the generated sensor output vs. total optical scan angle.

In addition, the 2D sensing capability was analyzed. The resultant Lissajous scan pattern is shown in Figure 4(a) and acquired sensor signals are presented in Figure 4(b). The sinusoidal signals extracted from the sensors (P_3 and P_4) can be used to predict the TOSA by utilizing the linear relationship between the TOSA and sensor output level presented in Figure 3(c). Subsequent studies on reconstruction of scan pattern and feedback control are ongoing. In addition to the characterization presented in this paper, further research leveraging the sensing capability-such as Q-factor estimation-is currently under investigation.

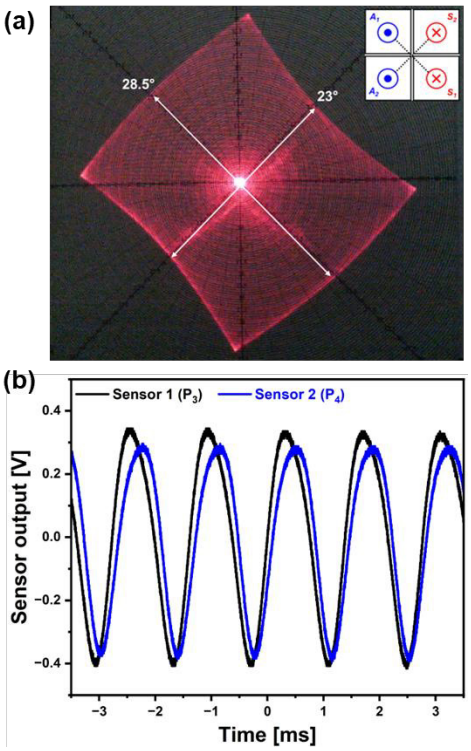


Fig. 4. (a) Generated 2D Lissajous scan pattern and (b) acquired sensor signals.

References

[1] J.-Y. Hwang et al., Low Power Compact 3D-Constructed AlScN Piezoelectric MEMS Mirrors for Various Scanning Strategies, *Micromachines* 14, 1789 (2023); doi: 10.3390/mi14091789.

Acknowledgements

This research was supported in part by the framework of the Fraunhofer Cluster of Excellence Advanced Photon Sources-CAPS funded by Fraunhofer Gesellschaft and in part (Investigation on piezoelectric material-based sensing) funded by the Ministry of Trade, Industry, and Energy (MOTIE), Korea, under the “Global Industrial Technology Cooperation Center (GITCC) program” supervised by the Korea Institute for Advancement of Technology (KIAT). (Task No. P0028389)

DOI 10.5162/EUROSENSORS2025/M3.2.3

Hybrid Photonic-Plasmonic Waveguides (HPWG) for Hydrogen Sensing

Robin Gremaud
[1] ABB Research, ABB Switzerland Ltd, Baden-Dättwil, Switzerland
robin.gremaud@ch.abb.com

Summary:

This contribution describes an HPWG structure, comprising a dielectric waveguide, a buffer layer and a metallic or semi-metallic sensing layer stack (metallic waveguide). By using the HPWG as a polarization selector, this layer stack works as a chemical sensor whose signal is independent of intensity variations of the incoming light and is therefore optically self-calibrated. Hydrogenation of the sensing layer stack changes its effective light absorption coefficient and/or refractive index upon changes of the hydrogen partial pressure in the environment. We demonstrate by modeling the optical response of the HPWG that, by tuning the thickness of the buffer layer and the respective layers (materials composition, thickness) of the sensor stack, it is possible to build optically self-calibrated HPWG structures to be used as sensors for hydrogen.

Keywords: hydrogen sensing, waveguide, photonics, plasmonics, HPWG

Background, Motivation and Objective

Dielectric (or photonic) waveguides are microstructures used in photonics to guide light by total internal reflection, similarly to optical fibers. In contrast to optical fibers, dielectric waveguide do not generally have a circular cross-section, and are deposited, machined, or ion-implanted in/on a substrate. Prominent examples of such waveguide are Silicon-on-a-substrate (SOI) waveguide, i.e. a –comparatively high refractive index- Si waveguide of rectangular cross-section obtained by lithography on a –comparatively lower refractive index- SiO_2 substrate.

Metallic (or plasmonic) waveguides are metallic microstructures on a dielectrics. In this case, light propagates near the metal surface, either at the metal-dielectric interface, or in a gap of the metal. Typical metal used is silver. Losses for metallic waveguides are usually much higher than for dielectric waveguides, but the higher confinement allows smaller structures (rings, sharp turns). Hybrid (photonic-) plasmonic waveguides (HPWG) are structures that use a combination of both structures introduced above.[1]

The materials used in most reported hydrogen sensors is Palladium (Pd).[2] If an optical readout scheme is used, Magnesium (Mg) alloyed with transition metals offers a higher optical contrast between the metallic and hydride states,[3] and also allow to decrease the lowest detection level (LOD).[4] The sensing layer can be e.g. deposited at the tip of an optical fiber and operated in reflection mode.[5] This design relies on the change of light amplitude induced by hydrogen absorption. Any other variation of the light intensity, such as from the light source or change in optical coupling could therefore induce errors in the hydrogen reading if not properly addressed. In this contribution, we propose to use HPWG waveguide structures for optical hydrogen sensing, providing an intrinsic referencing of the light intensity.

General Principle of Operation

As shown in Figure 1, the TE mode is guided by the dielectric waveguide and its intensity is relatively insensitive to the sensor stack.

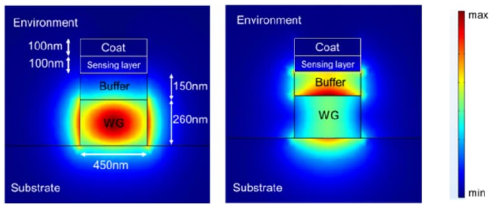


Figure 1. Cross-section of proposed sensor structure. Color code: Electric field magnitude for the HPWG (COMSOL, RF module). left, transverse magnetic (TE) mode, right, transverse electric (TM) mode. Substrate and Buffer: SiO_2 (n = 1.5), WG = Waveguide: Si (n = 3.44), Sensor stack: Sensor = $Mg_{70}Ti30H_x$ and Coat: Pd (n = 3.2, k = 8.15). Environment: air (n = 1).

The TM mode is mostly guided within the buffer region and is therefore in first order sensitive to

variation of absorption coefficient of the sensor stack. The attenuation per HPWM length of the TM mode can be tuned by changing the thickness of the buffer layer. The TM mode is also sensitive to the refractive index of the sensor stack. The attenuation per HPWG length is lower for the transverse electric (TE) propagation mode than for the transverse magnetic propagation mode, and this for all values of the absorption coefficient of the sensor stack. Hence the transmission of the TE mode may be used as an internal light intensity reference, and the transmission of the TM as the sensing signal.

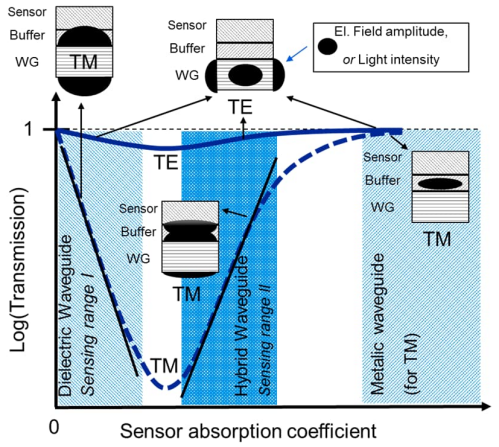


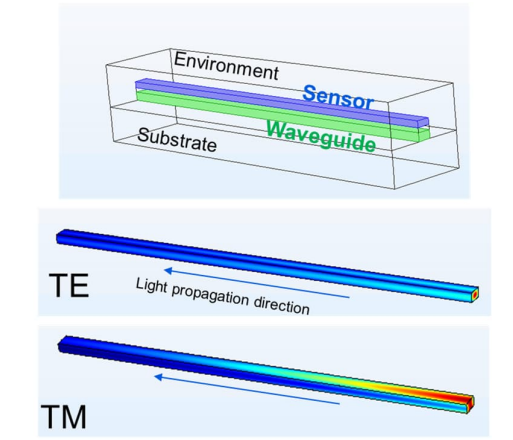
Figure 2. Principle of operation and sensing ranges of proposed HPWG sensor. Transmitted light intensity as a function of optical absorption coefficient of the sensor stack (for constant refractive index) WG: dielectric waveguide, TE: transverse Electric mode, TM: transverse magnetic mode.

Results

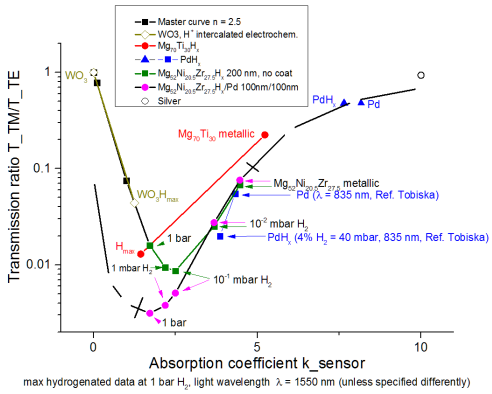
Figure 3 shows the ratio of the light intensities TM/TE for a simple linear waveguide geometry. We take a few hydrogen absorbing materials as examples to exemplify the sensing range I (dielectric waveguide) with proton-intercalated tungsten trioxide (WO_3), or sensing range II (HPWG) with Pd-coated Mg-Ni-Zr or Pd-coated Mg-Ti layers, covering a range of H_2 pressures from 10^{-3} to 10^2 mbar (not shown here).

Summary

We presented a HPWG readout concept for optical hydrogen sensing that is independent of the light source intensity. It is compatible with protection layers on top of the sensor stack to ensure sensitivity only to the desired species (H_2) and resistant to adverse species (H_2O, O_2). It is also cost-effective, as it works at a telecom wavelength of 1550 nm, for which low-cost components are available.



(a)



(b)

Figure 3. (a) 3D view of the HPWG structure with (color code) light intensity for TE and TM mode through waveguide. (b) Ratio of the transmission of TM and TE modes for various hybrid waveguide structures as a function of the absorption coefficient of the sensing layer. Refs. for optical properties: Pd [6], WO_3[7], Mg-Ti, Mg-Ni-Zr: own measurements as in [3],[4]. Silver: http://refractiveindex.info/

References

[1] M. Z. Alam, *et al.*, *Laser & Photonics Rev,* vol. 8, pp. 394-408, 2014. DOI: 10.1002/lpor.201300168

[2] P. Tobiška, *et al.*, *Sensors and Actuators B: Chemical,* vol. 74, pp. 168-172, 2001. DOI: 10.1016/S0925-4005(00)00728-0

[3] M. Slaman, et al, Sens. Actuators B 123, 538 2007. DOI: 10.1016/j.snb.2006.09.058

[4] M. Victoria, *et al.*, *American Chemical Society Sensors, vol. 1, pp 222-226*, 2016. DOI:10.1021/acssensors.5b00265

[5] T. Mak, *et al.*, *Sensors and Actuators B: Chemical,* vol. 190, p. 8, 26 September 2013 2013. DOI: 10.1016/j.snb.2013.09.080

[6] K. v. Rottkay, et al, Electrochimica Acta, vol. 44, p. 8, 1998. DOI:10.1016/S0013-4686(99)00025-0

[7] M. J. DeVries, *et al.*, J. Vac. Sci. Technol. A, vol. 17, p. 5, 1999 1999. DOI : 10.1116/1.581958

DOI 10.5162/EUROSENSORS2025/M3.3.1

Cutting-edge healthcare technologies for monitoring, care and coaching in elderly residential facilities: the perspective of the Italian project "Age-it"

Gabriele Rescio[1], Anna Maria Carluccio[1], Andrea Manni[1], Andrea Caroppo[1], Zaira Romeo[2], Eleonora Macchia[2], Alvise Bobbo[2], Marianna Noale[2], Riccardo De Benedictis[3], Gabriella Cortellesa[3], Pietro Siciliano[1], Alessandro Leone[1]

[1] National Research Council of Italy, Institute for Microelectronics and Microsystems, Lecce, Italy

[2] National Research Council of Italy, Neuroscience Institute, Padua, Italy

[3] National Research Council of Italy, Institute of Cognitive Sciences and Technologies, Rome, Italy

Corresponding Author's e-mail address: gabriele.rescio@cnr.it

Summary:

An innovative healthcare ecosystem was developed to enhance care and coaching in elderly residential facilities. It integrates minimally invasive sensors, AI-based analysis and adaptive decision-making for continuous health tracking and early detection of conditions like falls or sarcopenia. Through vital signs monitoring and surface electromyography, the system enables personalized care, while high detection accuracy and Transfer Learning schemes ensure robust generalization in real-world settings. Scalable and workflow-compatible, it lays the groundwork for next-generation data-driven models in residential care facilities.

Keywords: healthcare, wearable sensors, transfer learning, fall detection, sarcopenia.

Motivation

Wearable and portable technologies enable continuous, non-invasive monitoring of physiological parameters, providing real-time health data such as heart rate (HR), respiratory rate (BR) and physical activity. When integrated into a connected ecosystem, this data benefits patients, healthcare professionals, caregivers and institutions. The work addresses the need to improve healthcare models in residential care facilities, where the aging population poses challenges in resource allocation and timely intervention. Traditional monitoring relies on manual data collection and reactive approaches, delaying interventions and increasing costs. A scalable cloud platform has been developed to collect and analyze data from heterogeneous wearable devices, offering real-time actionable insights. The platform supports timely interventions, reduces healthcare staff workload and promotes a proactive, data-driven approach to elderly care, improving diagnostic accuracy and optimizing healthcare resources.

Healthcare Ecosystem Overview

The proposed system (Fig.1) is a modular, cloud-based healthcare platform designed for continuous health monitoring. It integrates minimally invasive, wireless and low-power wearable devices, including the surface EMG device (FREEMG1000, BTS Bioengineering [1]), the Fitbit Versa 4 [2] for fall detection and the Samsung Galaxy A35 [3] for both vital signs estimation through remote photoplethysmographic paradigm (rPPG) and gateway capabilities.

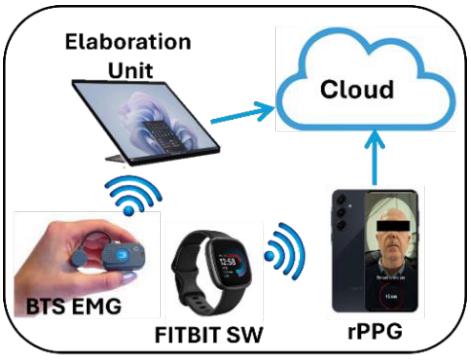


Fig. 1. Overview of the proposed healthcare ecosystem.

The platform aims to improve usability and efficiency compared to existing smart monitoring systems through a hardware-software-services ecosystem tailored for real-world deployment. Intelligent data fusion and hybrid edge/cloud processing ensure high-accuracy monitoring and early detection of health anomalies, even with consumer-grade sensors. The system focuses on detecting falls, anomalies in vital signs, postural imbalances, and early signs of sarcopenia. User-centered design guided the development of intuitive interfaces for both healthcare staff and caregivers. The system automatically generates alerts, daily summaries, and long-term

trend reports, enhancing responsiveness and overall care quality. High detection accuracy is achieved through an AI architecture with strong generalization capabilities via Transfer Learning (TL). Then, an intelligent decision support system (Combined deductiOn and abduCtiOn (COCO)) inspired by the cognitive theories of dual process was integrated into the platform, which, using automatic planning, generates personalised intervention plans based on expert knowledge and predefined objectives, while a reactive rules-based engine continuously adapts actions in response to real-time data. This dynamic feedback loop supports informed, flexible decision-making and personalized care strategies. Designed for scalability and seamless workflow integration, the system (see Fig. 2) offers a forward-looking, data-driven approach to elderly care enhancing monitoring, reducing staff burden and improving residents' well-being.

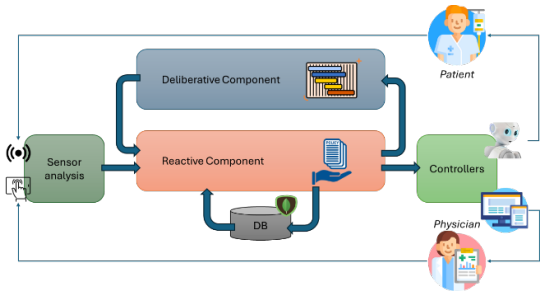


Fig. 2. Overview of the reasoning system.

Moreover, a field trial in a residential care facilities has recently been launched to evaluate the system's performance in a real-world elderly care setting. This study named "Multidomain Interventions to Improve the COgnitive and FUNctional Well-being of Elderly Individuals in Residential Structures" aims to evaluate the feasibility, acceptability and effects of a multidomain intervention for older adults in Long-Term Care Facilities. The intervention includes cognitive stimulation, physical activity, a Mediterranean diet enriched with functional foods, and vaccination recommendations. The sEMG protocol is validated against EWGSOP2 standards, including bioelectrical impedance analysis (BIA) and handgrip strength testing.

Results

This section briefly reports the performance of the three previously introduced technologies in controlled laboratory environments. Specifically, 20 participants were involved in rPPG. Each was equipped with ground truth instruments, allowing comparison with estimated HR, BR and SpO2 values from our system. To evaluate the performance of the system, Mean Absolute Error (MAE) and Root Mean Squared Error (RMSE) were used as metrics and, the obtained results are shown in Table 1, fixing the ambient light intensity (51-100 Lux) and the distance (20 cm) between the user and the smartphone camera.

Tab. 1: MAE and RMSE for rPPG system.

Metrics	HR	BR	SpO2
MAE	4.47	2.4	0.57
RMSE	7.83	4.11	0.95

Finally, for the sEMG platform, analyses were carried out on gait monitoring, for the early detection of abnormalities, such as toe walking. Different TL architectures were used to limit the problem of large training data for the CNN architecture. For brevity, the achieved results with the best tested architectures for fall detection (DenseNet201 (DN201)) and sEMG platform (InceptionResNetV2(IRNV2)) are reported in Table 2 considering Accuracy (Acc), Precision (Pr), Recall (Re) and F1-score (F1) as metrics.

Tab. 2: Performance of the fall detection (DN121) and normal/toe walking classification (IRNV2).

Model	Acc	Pr	Re	F1
DNet201	0.9756	0.9743	0.9674	0.9741
IRNV2	0.9525	0.9519	0.9440	0.9519

The achieved accuracies are comparable to the literature [4,5] for both fall detection and normal/toe walking classification, but with the advantage of a greater degree of generalization of the approach due to the use of TL and, consequently, greater adaptability in real-world contexts and without supervised learning technique that requires a large amount of labelled training data with the complexity to classify new data.

References

[1] https://www.btsbioengineering.com/it/products/freeemg/. Accessed April 9, 2025.

[2] https://store.google.com/it/product/fitbit_versa_4?hl=it. Accessed April 9, 2025.

[3] https://www.samsung.com/it/smartphones/galaxy-a/galaxy-a35-5g-awesome-iceblue-128gb-sm-a356blbbeue/. Accessed April 9, 2025.

[4] J. Marques, P. Moreno, Online fall detection using wrist devices, Sensors, 23, 1146, (2023); doi: 10.3390/s23031146.

[5] D. Borzelli, M. Morano, S. Fioretti, F. Di Nardo, The pooled scalogram: A wavelet-based approach to detect the co-activation of several muscles in the time-frequency domain. Biomedical Signal Processing and Control, 99, 106802, (2025); doi: 10.1016/j.bspc.2024.106802.

Acknowledgements

This paper was developed within the project funded by Next Generation EU-"Age-It-Ageing well in an ageing society" project (PE0000015), National Recovery and Resilience Plan (NRRP)-PE8-Mission 4, C2, Intervention 1.3.

DOI 10.5162/EUROSENSORS2025/M3.3.2

Lock and Key Interconnects for Modular Flexible and Printed Electronics

Paulina Gallego Perez[1], Emily Bezerra Alexandre[1,2], Majd Bleidy[1], Sabine Lengger[1], Jürgen Kosel[1], Mani Teja Vijjapu[1].
[1]Sensor Systems Division, Silicon Austria Labs GmbH, Europastraße 12, Villach, 9524 Austria
[2]Laboratory of Bio/CMOS Interfaces, École Polytechnique Fédérale de Lausanne (EPFL), Neuchâtel, Switzerland
mani.vijjapu@silicon-austria.com

Summary:
In rigid electronic systems, various methods such as USB connectors and pin headers enable temporary electrical and mechanical connections between components. Conversely, such solutions are still lacking in the flexible electronics landscape. This work introduces a novel interconnection method for flexible and printed electronics, using mechanically defined grooves in the encapsulation layer to align with contact pads on detachable modules, enabling robust and reliable connections between flexible electronic segments. Inspired by a lock-and-key mechanism, it enhances modularity without requiring additional materials or components, preserving system design while supporting reconfigurable integration, mechanical flexibility, and reduced material usage—a scalable and sustainable solution for next-generation electronics.

Keywords: printed electronics, modular electronics, flexible interconnects, biomedical devices.

Background, Motivation and Objective

The evolution of Modular Biomedical Electronics has significantly advanced the development of lightweight, adaptable, and high-performance devices for applications such as wearable technology and medical sensors [1]. These systems are increasingly gaining attention in the biomedical field due to their flexibility, repairability, and sustainability [2].

A key design strategy is using interchangeable components, enabling upgrades or repairs without replacing the entire device. Modular designs support adding new functions or replacing worn parts, enhancing adaptability and longevity, which is useful in health monitoring, where sensors degrade faster than electronics [3].

However, the modular nature of these systems introduces a significant challenge: ensuring reliable electrical and mechanical interconnection between different counterparts—such as sensors, chips, and circuit segments, especially in wearable biomedical devices due to several interrelated factors. Material mismatches between substrates can cause delamination [4], while the flexibility needed for wearables leads to mechanical fatigue from repeated motion, compromising connection integrity over time [5].

Traditional interconnection methods like soldering, mechanical crimping or conductive adhesives add material, require extra materials and complex processing, reducing flexibility, raising costs, and causing environmental concerns, making them unsuitable for the specific demands of wearable biomedical applications.

To address these challenges, a novel interconnection technique inspired by lock-and-key-inspired is proposed, mimicking male-female connectors to ensure reliable electrical and mechanical contact without extra materials or complex manufacturing. It supports repeated replacements with minimal wear, improving modularity and sustainability. Notably, the connection resistance increases by no more than 10% over 20 insertion cycles—markedly outperforming conventional solutions such as anisotropic conductive films, which show an immediate resistance increase of approximately 30% upon application due to poor compliance with flexible substrates and a tendency to delaminate under stress [6].

Materials and Methods

A modular interconnection system was developed to achieve simple and sustainable device assembly, with electrical contact established through mechanical insertion. Fig. 1 shows the structure of a printed circuit using conductive silver ink on a polyethylene terephthalate (PET) substrate, which was then encapsulated through a lamination process at 120 °C using an anisotropic non-conductive film (ANCF) as an intermediate layer, followed by an additional PET sheet as the top layer. This lamination not only protects the printed structures from environmental

exposure but also enhances the overall robustness and durability of the system.

The ANCF layer was patterned with small grooves, forming recessed pockets that act as connection points for external components—creating a female-type connector.

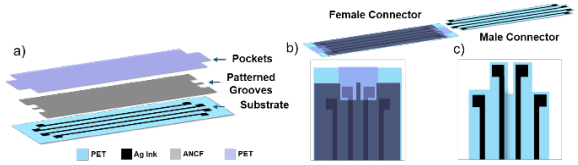


Fig. 1. (a) Exploded view of the female connector, Schematics of (b) Female connector (c) Male connector .

The male counterpart, shown in Fig. 2 (a) is fabricated from the same silver-ink-on-PET material but precisely cut to match the geometry of the female pockets. It is designed to be inserted into the grooved regions of the female connector, shown in Fig. 2 (b), enabling direct electrical contact through mechanical insertion.

When the male and female parts are joined, the embedded pockets in the ANCF guide and hold the male contacts in place, establishing a reliable and reusable plug-in style connection. This modular interconnection approach allows for repeated use, mechanical stability, and electrical continuity even under deformation, as demonstrated in Fig. 2 (c) & (d).

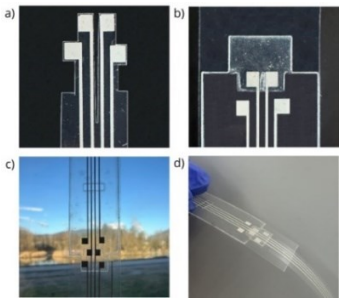


Fig. 2. (a) Male connector with printed structures on PET, cut to fit grooves (b) Female connector with Ag ink circuit on encapsulated PET.(c–d) Interconnection under bending, showing flexible and robust contact.

Results

Electrical performance was assessed by first measuring the resistance between two fixed points on the male part of the modular structure to establish a baseline. The male and female components were cycled through repeated attachments. Resistance was recorded every 5 cycles over a total of 50 repetitions in three different samples, generating a curve (Fig. 3) that illustrates how resistance changed relative to the baseline.

Results show stable electrical performance up to approximately 15–20 cycles, making the connector suitable for point-of-care (PoC) diagnostic systems, where limited sensor replacements are typically sufficient during a device's operational life and can be improved with additional coatings.

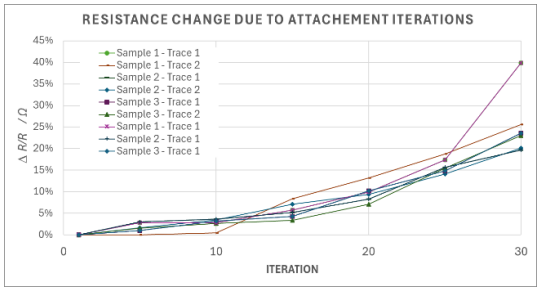


Fig. 3. Resistance variation over 30 attachment cycles across three samples and two circuit traces.

Our connector concept offers a practical solution for modular and disposable sensing elements, ideal for PoC applications where rapid sensor interchangeability, mechanical reliability, and electrical consistency are essential. The fabrication process is compatible with various substrates, including flexible and biodegradable materials, expanding the potential of the system toward sustainable, next-generation sensor platforms in wearable, portable, and eco-friendly medical technologies.

References

[1] X. Nan, Y. Zhang, et. Al, Review of Flexible Wearable Sensor Devices for Biomedical Application, *Micromachines* 13, 1395 (2022); doi: 10.3390/mi13091395.

[2] M. Keil, T. Viere, et. Al, The impact of switching from single-use to reusable healthcare products: A transparency checklist and systematic review of life-cycle assessments, *Eur. J. Public Health* 33, 50–56 (2023); doi: 10.1093/eurpub/ckac174.

[3] S. Y. Yang, K. J. Yu, et. Al, Powering Implantable and Ingestible Electronics, *Adv. Funct. Mater*. 31, 2009289 (2021); doi: 10.1002/adfm.202009289.

[4] Y. Liu, M. Pharr, G., et. Al, Lab-on-skin: A review of flexible and stretchable electronics for wearable health monitoring, *ACS Nano* 11, 9614–9635 (2017); doi: 10.1021/acsnano.7b04898.

[5] T. Q. Trung, N. E. Lee, Flexible and stretchable physical sensor integrated platforms for wearable human-activity monitoring and personal healthcare, *Adv. Mater.* 28, 4338–4372 (2016); doi: 10.1002/adma.201504244.

[6] J. W. Kim, S. H. Cho, et. Al., Characterization of failure behaviors in anisotropic conductive interconnection, *Mater. Trans.* 48, 1070–1078 (2007); doi: 10.2320/matertrans.48.1070.

Acknowledgements

This work has been jointly funded by the EECONE project, supported by the Chips Joint Undertaking and its members, including the top-up funding by National Funding Authorities under grant agreement no. 101112065 and by Silicon Austria Labs (SAL), owned by the Republic of Austria, the Styrian Business Promotion Agency (SFG), the federal state of Carinthia, the Upper Austrian Research (UAR), and the Austrian Association for the Electric and Electronics Industry (FEEI).

DOI 10.5162/EUROSENSORS2025/M3.3.3

Capacitive Excitation of Out-of-Plane Modes in MEMS Resonators with a Planar Electrode Design

Dominik Huber[1], *Michael Guelly*[1], *Georg Pfusterschmied*[1], *Ulrich Schmid*[1]
[1] *TU Wien, Institute of Sensor and Actuator Systems, Gußhausstraße 27-29, 1040, Vienna, Austria*
Dominik.Huber@tuwien.ac.at

Summary:
This paper reports on a novel planar electrode design for the capacitive excitation of out-of-plane (OOP) resonance modes in MEMS test structures to study local material parameters. A simple device fabrication process is developed consisting of 4 process steps only. As a straightforward result, the fabricated plate resonator bends in the OOP directions due to a release of the intrinsic thin film stress. The planar electrodes and the bent resonator feature electrostatic forces in the OOP direction, thus actuating the OOP vibrational modes of the resonator.

Keywords: MEMS resonators, capacitive excitation, planar electrode, out-of-plane modes

Background, Motivation, and Objective

MEMS resonators are relevant for measuring non-electrical signals, such as rotation rate with gyroscopes [1], the viscosity of liquids [2, 3], and time [4]. Typical actuator principles for MEMS resonators are based on thermal, magnetic, piezoelectric, and electrostatic effects [5]. A relevant drawback of thermal and magnetic actuation is the high power consumption due to Joule losses. Piezoelectric, in contrast to capacitive actuation, covers the resonator with a piezoelectric layer, thus reducing the Q-factor. Despite their widespread use, the fabrication of electrostatic actuators is not straightforward since considerations on sticking and the pull-in effect must be taken into account. An external electrode configuration to handle the pull-in effect was demonstrated by Rosa et al. [6]. However, the wafer needs to be patterned before the thin film deposition for the stepwise deposition of electrode and cantilever material with a sacrificial layer in between.

This paper reports on a novel electrode design using electrostatic forces to actuate Euler-Bernoulli (EB), torsional (T), roof-tile-shaped (RTS) [7], and higher order plate (HOP) modes in single-side clamped plate-shaped (SSCP) MEMS resonators. Since resonators fabricated from any conducting material can be actuated, the presented devices can be used as a test structure to study local and device-relevant material parameters. The advantage of the simple fabrication process is described, and the application of a polycrystalline silicon (PCSi) MEMS resonator with several resonance modes in the range of up to 220 kHz is demonstrated.

Description of the New Method or System

At 600 °C, a 2 µm thick PCSi thin film is deposited within a low-pressure chemical vapor deposition (LPVCD) process on a 4-inch <100>-silicon wafer with a wet thermal oxide of 500 nm on its top surface.

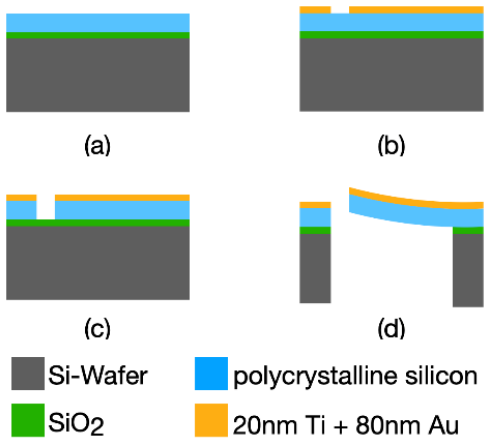


Figure 1: Fabrication process of SSCP MEMS resonators with a planar electrode arrangement.

Subsequently, titanium-gold contacts are evaporated and the device and the handle layer are etched with a Bosch process. The buried oxide is removed in the last step releasing the resonator structure. Consequently, the thin resonator releases intrinsic stress from the thin film fabrication while bending in the OOP direction. The fabrication steps are shown schematically in Figure 1 and an SEM image of a MEMS resonator with the novel arrangement of the electrodes in Figure 2. The asymmetric arrangement of the small and large static

electrodes allows the excitation of T and especially RTS modes. The gap size between the resonator and the static electrodes is set to 5 µm as a tradeoff between reliable dry etching results and high electric fields, thus high actuation forces.

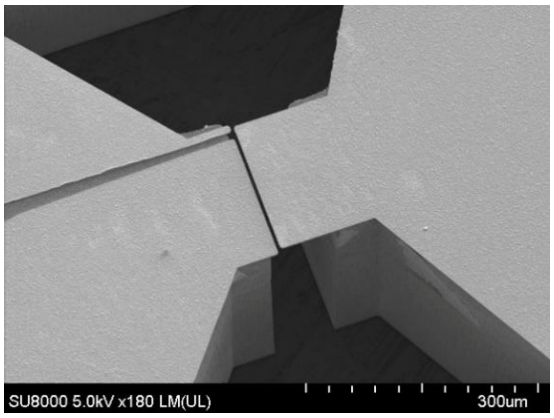


Figure 2: SEM image of a 100 µm long and 220 µm wide SSCP MEMS resonator.

Results

Intrinsic stress in the device layer causes the fabricated MEMS resonators to bend out of the horizontal position. Figure 3 shows a representative topography measurement with white light interferometry (WLI), demonstrating the OOP bending of the resonator with a typical maximum deflection of 3 µm at the tip region.

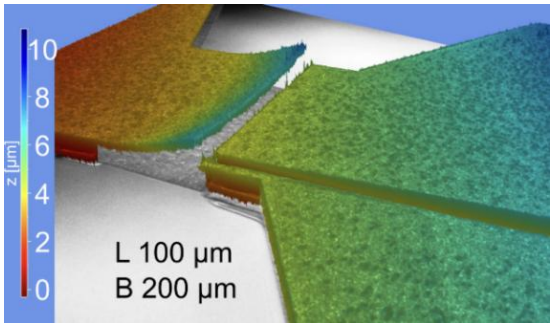


Figure 3: Topography measurement of a fabricated SSCP MEMS device.

The device is operated under vacuum conditions with a pressure level of 10^{-5} mbar. The actuation is done with a sinusoidal signal with an amplitude of 5 V and a constant offset of 5 V. The offset is necessary to mechanically pre-stress the resonator to maximize the amplitude. The vibrational response characteristics are measured with laser Doppler vibrometry (LDV) at the edge of the SSCP MEMS resonator to cover all possible OOP modes. A frequency sweep from 10 to 220 kHz demonstrates the ability of the electrode design to actuate seven OOP and one in-plane resonance modes within this frequency range, as shown in Figure 4. The measured vibrational amplitudes range from 0.02 nm to 50 nm and, hence, are small compared to the static deflection.

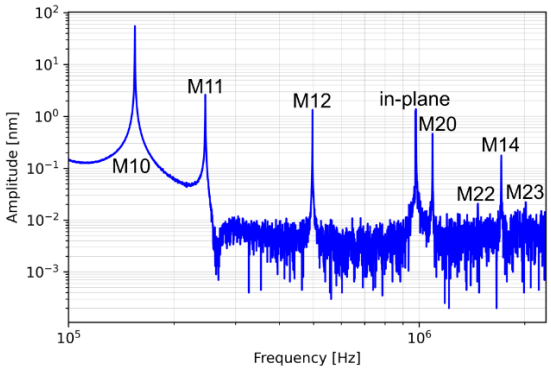


Figure 4: Frequency sweep of the capacitively actuated wide SSCP MEMS resonator from 10 to 220 kHz.

The few standard steps of device fabrication, inherent to many MEMS fabrication processes, and the prevention of sticking and pull-in effects are clear benefits of the presented design. In future studies, doped device layers will be investigated since the metallic electrode material must not cover the MEMS resonator's surface so that the bare device layer can be studied. In the near future, this test structure concept will be exploited for Q-factor analysis of different MEMS materials.

References

1. Kulygin, A., U. Schmid, and H. Seidel, *Characterization of a novel micromachined gyroscope under varying ambient pressure conditions.* Sensors and Actuators A: Physical, 2008. **145-146**: p. 52-58.
2. Pfusterschmied, G., et al., *Responsivity and sensitivity of piezoelectric MEMS resonators at higher order modes in liquids.* Sensors and Actuators A: Physical, 2019. **295**: p. 84-92.
3. Saba, N., N. Soin, and K.N. Khamil. *Simulation and analysis of actuation voltage of electrostatically actuated RF MEMS cantilever switch*. in *2015 International Conference on Smart Sensors and Application (ICSSA)*. 2015.
4. Nguyen, C.T., *MEMS technology for timing and frequency control.* IEEE Transactions on Ultrasonics, Ferroelectrics, and Frequency Control, 2007. **54**(2): p. 251-270.
5. Algamili, A.S., et al., *A Review of Actuation and Sensing Mechanisms in MEMS-Based Sensor Devices.* Nanoscale Research Letters, 2021. **16**(1): p. 16.
6. Michel, A.R., et al., *A novel external electrode configuration for the electrostatic actuation of MEMS based devices.* Journal of Micromechanics and Microengineering, 2004. **14**(4): p. 446.
7. Kucera, M., et al., *Characterization of a roof tile-shaped out-of-plane vibrational mode in aluminum-nitride-actuated self-sensing micro-resonators for liquid monitoring purposes.* Applied Physics Letters, 2014. **104**(23).

DOI 10.5162/EUROSENSORS2025/M3.3.4

Reduction of an Irregular Sensor Network for Continuous Humidity Monitoring in Wood Structures

Madeleine Bankwitz[1], Christian Engel[1], Finn Esben Schmid-Bonde[2], Karl Giske[1], Ricky Bendyk[1], Jörg Röder[2], Sören Hirsch[1]

[1] Brandenburg University of Applied Science, Department of Engineering, Magdeburger Str. 50, 14770 Brandenburg/Havel, Germany

[2] University of Applied Sciences, Civil Engineering Department, Kiepenheuerallee 5, 14469 Potsdam, Germany

madeleine.bankwitz@th-brandenburg.de

Summary:

This work demonstrates a sensor network that regulates the temperature of heating bands to reduce the moisture content within the wood structures of existing buildings. The system is designed to monitor the condition of the walls and determine the appropriate level of activation of the heating bands. To find the characteristic points for identifying the moisture behavior, a cluster analysis was carried out on the irregular network.

Keywords: Sensor Network, Cluster Analysis, Wood Structures, Reduction, Climate Monitoring

Background

In the past, it has been shown that the ability to effectively monitor complex systems in a safety-relevant way is significantly limited, e.g. the unexpected collapse of bridges [1]. This is mainly due to the considerable number of influencing factors that are not yet continuously and digitally monitored. Buildings are subject to physical processes within the walls during their design, construction and use. The external climatic environment influences the type, intensity and extent of chemical and biological corrosion in the structures [2]. One major issue is mold, which is caused by excessive humidity. Heat and humidity have a strong indirect proportional relationship, so trying to increase temperature causes humidity to decrease [3]. However, there are climate targets in Europe to keep CO2 emissions low and therefore there are limits to the continuous supply of heat [4]. To provide heat only at certain times, a monitoring system is required which provides information about the moisture content and its location. Sensor networks are already being used in various areas, including structural monitoring. They are suitable for monitoring different parameters at different locations, but have significantly limited resources in terms of energy, bandwidth, storage space and more. Cluster technologies are used to efficiently increase the service life [5]. The measured data from the sensor network is used to control heat bands in the insulated walls and thus reduce the moisture content.

Method

In a house built in 1872, a network of 30 multimodal sensor nodes was installed during the latest renovation process. The sensor nodes were placed due to power supply possibilities over three floors and were provided with an index based on their location, as illustrated in Table 1. To ensure the successful activation of the heating bands at the intended time and location, it is essential to obtain comprehensive location and time data.

Tab. 1: Position of Sensors

Floor	Sensor index
Ground floor	5,6,7,13
First Floor	1,2,3,4,16,18,20,21,22,23
Top Floor	8,9,10,11,12,14,15,17,19

Figure 1 shows the sensor head (diameter: 1cm) with the sensors for acceleration, ambient light, temperature and humidity. The sensor system combining six channels of analog-to-digital conversion, complemented by a high bandwidth preprocessing stage used for filtering and signal conditioning. Following data processing, analysis and compression performed by the microcontroller, data is sent via standard UART interface to the communications module which allows both, wired as well as wireless communication.

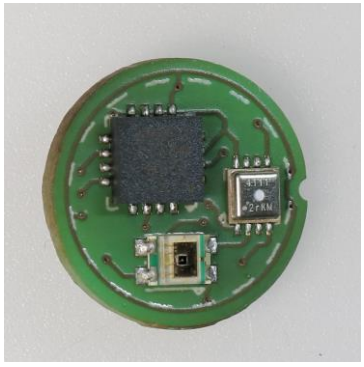


Fig. 1. Multimodal sensor node with 3 axis accelerometer sensor (top left), ambient light sensor (bottom left) and relative humidity and temperature sensor (right).

Results

To further develop a resource-efficient sensor network, it is grouped using cluster analysis (Fig. 2), where the temperature data is plotted over the humidity data. The next step is to determine the similarity of the measurement points. To ensure comparability, the temperature and humidity values are standardized with the z-score (fig 2, Step 1). On this basis, a similarity matrix is created showing the distances between all the points (fig. 2, Step 2). The shortest distance is determined, and the two points are grouped together (fig. 2, Step 3). Depending on the degree of clustering, the distance matrix is updated repeatedly until only two groups remain.

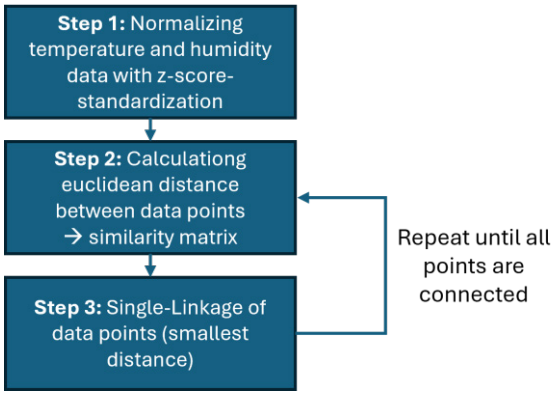


Fig. 2. Procedure of Cluster-Analysis

As illustrated in Figure 3, the cluster analysis of the temperature-humidity behavior of the sensors on March 1, 2025, demonstrates clear distinctions in the data. The similarity is illustrated on the y-axis, while the indices of the sensors are represented on the x-axis.

In general, the dendrogram has a flat structure with similarity values below 1. The highest similarity is shown by sensors 8 (top floor) and 20 (first floor), with the last sensor placed between the outer wall and the inner insulation of the first floor. Sensor 23, which represents the closest connection to the first cluster, has a similar position. Sensors 3 and 4 are also very similar (S=0.114). Both are in rooms on the first floor on the east side. Sensors 5, 6 and 7 are grouped at a level of 0.5-0.6. All three sensors are in rooms on the ground floor. The sensor with the least similarity is sensor 2, which is in a room on the first floor.

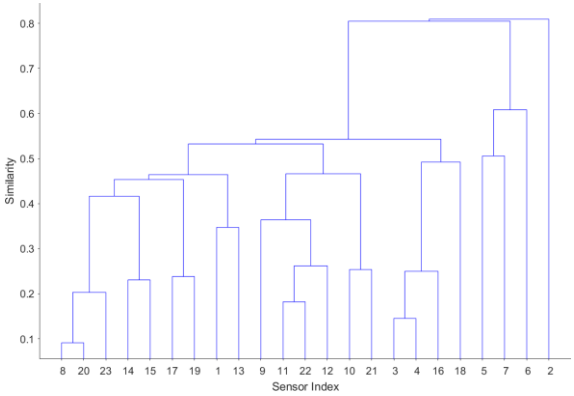


Fig. 3. Cluster analysis for temperature-humidity relation over sensor index

Conclusions

In summary, the results of the cluster analysis show a tendency towards different behavior depending on the floor of the building, especially on the first floor compared to the other floors. It can also be seen that the sensors between the outer walls and the insulation on the same floor show similar behavior (S<0.6). Therefore, in the next step, the room sensors from the ground floor and within the external walls on the first floor can be grouped together.

References

[1] Deng, L., Wang, W., & Yu., Y. (2016). State-of-the-art review on the causes and mechanisms of bridge collapse. *J. Perform. Constr. Facil.*, Bd. 30, Nr. 2. https://doi.org/10.1061/(asce)cf.1943-5509.0000731

[2] Bajno, D., Grzybowska, A., & Bednarz, Ł. (2021). Old and modern wooden buildings in the context of sustainable development. *Energies*, Bd. 14, Nr. 18, S. 5975. https://doi.org/10.3390/en14185975

[3] Bylund Melin, C., Hagentoft, C. E., Holl, K., Nik, V. M., & Kilian, R. (2018). Simulations of moisture gradients in wood subjected to changes in relative humidity and temperature due to climate change. *Geosciences*, *8*(10), 378.

[4] Congedo, P.M., Baglivo, C., D'Agostino, D., & Albanese, P.M. (2024). Overview of EU building envelope energy requirement for climate neutrality. *Renewable and Sustainable Energy Reviews,* 202(114712), S. 114712. https://doi.org/10.1016/j.rser.2024.114712

[5] Hutkai, K., & Katunský, D. (2021). Insulation of historic buildings and case study simulation. *IOP Conf. Ser.*: Mater. Sci. Eng. 1209 012003.

DOI 10.5162/EUROSENSORS2025/T4.1.1

Ultra-compact MEMS gas analyzer based on ion-optical spectrometry

Piotr Szyszka, Kostiantyn Stambulskyi, Tomasz Grzebyk
Wroclaw University of Science and Technology, 11/17 Janiszewskiego Str., 50-370 Wrocław
piotr.szyszka@pwr.edu.pl

Summary:
Here, we present handheld gas analyzer based on ion optical emission spectrometry (OES) applied in a miniature MEMS (micro-electro-mechanical system) structure. The instrument consists of in-house developed gas ionizer, playing simultaneously a role of high vacuum micropump which provides background pressure of 1e-7 hPa, integrated with a needle type gas dosing valve and a compact optical spectrometer necessary to analyze optical emission of molecules ionized inside the chip. The total mass of all components (including electronics is 350 grams and can be assembled into instrument with volume of 0.2 U.

Keywords: Gas analysis, ion optical emission, MEMS, microsystems, on-chip integration

Introduction

Ion optical emission spectrometry is a technique that utilizes the spectral measurement of light emitted by ionized molecules. However, ionization at near-atmospheric pressure is challenging, as it requires very high voltages and leads to a rapid degradation of electrodes. Therefore, this technique is primarily applied in the analysis of solid or liquid samples, often using laser ablation [1] or plasma-based methods, either in vacuum systems [2] or in space applications [3], where pressure is already reduced. The method itself appears promising also for gas analysis in Earth conditions, including industrial applications. However, in such situations the problem of reducing operational pressure needs to be solved.

This is where our instrument offers a breakthrough—it works with atmospheric gases by the analysis process is performed in vacuum.

Device construction

The instrument that is proposed in this paper, despite being miniature, incorporates MEMS gas ionizer, high vacuum pump and gas dosing valve which can introduce external atmosphere into the chip. The ionization occurs under reduced pressure in a Penning-like discharge cell. The ion-sorption mechanism is responsible for maintaining vacuum [4], and leak valve gives opportunity of exchange the residual gas composition inside the chip. By analysis of optical spectrum it is possible to determine the composition of gases in a mixture by comparing the heights of their characteristic peaks.

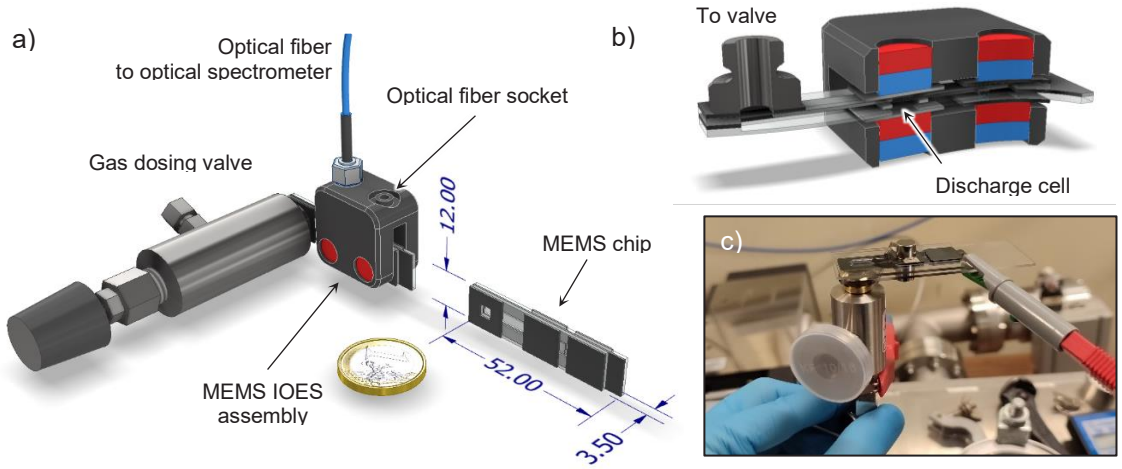


Fig. 1. MEMS ion optical emission spectrometer: a) device construction, b) MEMS cross section and c) device photography

Measurement methodology

The experiments were performed on a laboratory desk. The structure was pre-pumped to a background level of 1e-7 hPa by igniting a discharge inside it. While this pressure was reached, the measurement could be conducted by opening a gas dosing valve (Chell Instruments, CMV-VFM-1-P) and introducing gas mixture inside the chip. The gas mixture (N_2:He) was prepared using mass-flow-meter-based gas mixing station. The glow from the chip was collected using optical fiber connected with optical spectrometer (Ibsen Photonics, FREEDOM HR-VIS / C-VIS).

Initial experiments allowed to distinguish two measurement modes:

1. Continuous mode – where the gas dosing and analysis is performed simultaneously (leak valve is open and the discharge cell is turned on all the time),
2. Impulsive mode – where the gas dosing and analysis is performed separately – in the first stage gas is dosed to reach a certain pressure inside the MEMS device, then the discharge cell is turned on resulting in obtaining a bright glow. In the same time the gas valve is turned off. Next measurement can be performed, when the structure is evacuated to high vacuum level once again.

Those two approaches gave different results. In the first case mostly peaks of helium were visible in the spectrum (Fig, 2a), and nitrogen was barely detectable. In the second mode both gases were clearly visible (Fig. 2b).

Such situation is caused by the fact that the discharge cell acts simultaneously as a pumping cell, and this affects the measurement. In the first case the more reactive gases are pumped down more rapidly, thus they are visible in the spectrum in a lesser degree. In the second case when the spectrum is measured at the beginning of the discharge process, the proportions of gases in the plasma are the same as in the mixture.

Both modes can be utilized interchangeably depending on the type of gas mixture being analyzed and the required sensitivity of the analysis. In the case of impulsive mode, the sensitivity is estimated at 0.1%, and in continuous mode, when measuring passive gases such as Helium or Argon, it is possible to obtain a sensitivity of the ppm level.

Conclusions

To conclude, the elaborated MEMS gas analyzer is a very promising, easy to use instrument for fast, and reliable gas measurements. However, much attention should be paid to the choice of a proper measurement method. The first approach is simpler, but gives accurate results not for all gas mixtures. The second approach is universal, but it is not adequate for continuous analysis. Thus, the method should be adjusted for a certain application.

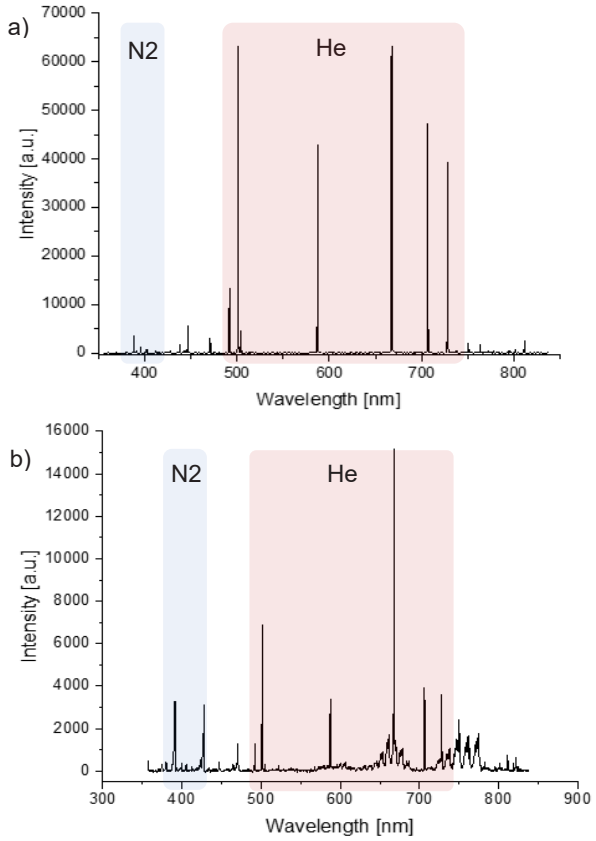


Fig. 2. Experimental results of 1:1 mix of N2:He analysis: a) continuous mode, b) impulsive mode.

References

[1] N. K. Abdalameer, S. N. Mazhir, and S. N. Mazhir, “Laser-Induced Plasma Atomic and Ionic Emission During Target Ablation,”, vol. 20, no. 5, Nov. 2021, doi: 10.1142/S0219581X21500447.

[2] S. P. Koirala, M. H. Gordon, L. Cai, S. L. Burkett, and L. W. Schaper, “Optical emission spectroscopy in a reactive ion etching system,” *2007 IEEE Region 5 Technical Conference, TPS*, pp. 189–193, 2007, doi: 10.1109/TPSD.2007.4380379.

[3] R. C. Wiens, X. Wan, J. Lasue, and S. Maurice, “Laser-induced breakdown spectroscopy in planetary science,” *Laser-Induced Breakdown Spectroscopy, Second Edition*, pp. 441–471, Jan. 2020, doi: 10.1016/B978-0-12-818829-3.00020-4.

[4] J. A. Dziuban, P. Knapkiewicz, T. Grzebyk, and P. Chen, “MEMS Ion Optical Spectrometer for Methane Detection on Mars,” *2022 21st International Conference on Micro and Nanotechnology for Power Generation and Energy Conversion Applications, PowerMEMS 2022*, pp. 219–222, 2022, doi: 10.1109/POWERMEMS56853.2022.10007595.

DOI 10.5162/EUROSENSORS2025/T4.1.2

MEMS-based microplasma sources for gas analysis

Elizaveta Vereshchagina[1], Enrique Escobedo-Cousin[1], Karolina Milenko[1], Simone Zonetti[1], Abélia Ellingsen[1], Do Chi Huong Hoang[1], Satadal Dutta[2], Trang-Anh Nguyen-Le[2], Cristian D'Alessandro[2]
[1] SINTEF Digital, Gaustadalléen 23C, Oslo, Norway,
[2] RespiQ, Respiro B.V., Langegracht 70, Leiden, The Netherlands
Elizaveta.Vereshchagina@sintef.no

Summary:
This paper presents the development of miniaturized microplasma sources for gas analysis based on micro-electromechanical systems (MEMS) technology. We discuss critical device design aspects, from FEM modeling and device concept to fabrication and experimental validation. A functional demonstrator was fabricated, and successful plasma ignition was achieved under controlled conditions. The results suggest that the developed microplasma sources hold strong potential as compact, integrable components for gas analysis systems in various industrial applications.

Keywords: MEMS, microplasma, plasma emission spectroscopy, gas sensor, gas analysis

Introduction

Chemical detection using plasma optical emissions has found multiple applications across environmental and medical fields. Building on earlier work [1-3], we explore three types of microplasma device configurations based on dielectric barrier discharge (DBD). Although interest in this technology dates back two decades, progress has been limited likely due to early challenges in integration and a lack of compelling applications. Recent advances in microfabrication and optical detection techniques now make MEMS-based microplasma devices a promising platform, offering scalability, reproducibility and integration for gas analysis. Miniaturizing this approach enables compact, portable systems capable of real-time gas detection in remote or point-of-need settings.

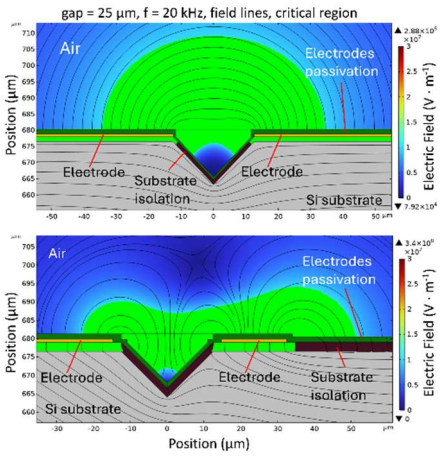


Fig. 1. Electric field norm in air and field lines for the two of the three geometries studied, and the case study with a cavity size of 25 µm.

Modeling

To optimize the design, three FEM models were developed in COMSOL® to investigate electric fields and estimate critical field values for device materials and the surrounding gas, without explicitly simulating generation of species and plasma chemistry. The models focus on identifying conditions favorable for plasma ignition in: (i) flat metal electrodes on an insulated substrate, (ii) a similar setup with a microcavity, and (iii) a setup with a microcavity and substrate electrode. Due to computational constraints, a 3D electric field approximation is used. Parametric sweeps of layer thickness and cavity geometry were performed, driven by sinusoidal voltage excitation. The simulations revealed the regions where plasma is likely to ignite and where insulator breakdown may occur, with examples showing plasma confinement and critical field zones (Fig.1). This approach provides valuable insight into the design parameters and material selection while avoiding complex plasma modeling.

Design

Several design variants, both as single microplasma and arrays of microplasma sources, were adapted. The most critical design parameters are the microcavity size (10, 25, 50, 100 µm), the distance between the microcavities, and the distance between the electrodes, which define the area of plasma ignition, as well as operating parameters at which plasma would ignite. Fig. 2 shows two examples of implemented designs and HRSEM images, close up on the device active area where the ignition occurs, and plasma confinement is desired.

Device fabrication

Fabrication was performed in an ISO-certified cleanroom for CMOS / MEMS components on 150 mm Si wafers. The devices were fabricated in 4 and 5 masks processes. The substrate isolation is a dielectric material (e.g. SiO_2 or Si_3N_4) to minimize leakage currents into the substrate. Thin film aluminum (Al) was used as electrode material, patterned using wet etching, and was protected with another dielectric layer (e.g. SiO_2 or Si_3N_4) to prevent re-sputtering of the metal. A combination of RIE and wet etching techniques were used for opening contacts to substrate and electrodes. The total chip size is 8 x 8 mm², and the electrical contacts are exposed from passivation for wire-bonding from the outer edges of the chip to a printed circuit board (PCB). Fig.3. (top) shows a testing ready, packaged device.

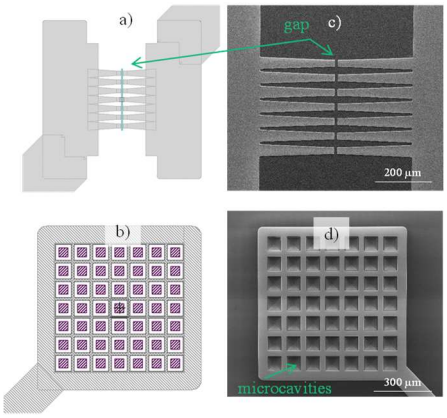


Fig. 2. Examples of CAD designs and HRSEM images of active device areas: an array of surface metal electrodes only (a and c), and the configuration with a microcavity array with metal and substrate electrodes (b and d).

Device characterization

The wafers were electrically characterized (I-V and C-V measurements) prior to dicing. Leakage currents were in the range 10–60 pA. Measured capacitances were in the range 5-20 pF, with higher capacitance observed in arrays compared with single devices with electrodes of equivalent geometry. The plasma was monitored via a microscope connected to a digital camera at peak-to-peak excitation voltages in the range of 0.9-1.4 kV, frequencies in the range of 3-10 kHz and pressures in the range of 100-500 mbar. Fig.3 shows examples of successful plasma ignition tests from two device configurations. We observed stable, continuous plasma for up to 20 min. Efforts to optimize design and fabrication parameters are ongoing and expected to extend device lifetime significantly. Optical emission spectra (OES) were collected using an Ocean-Optics 2000+ spectrometer showing the characteristic wavelength peaks of molecules present in air (Fig. 3). As a reference, a larger-scale, not chip-based prototype using the same detection principle was previously used to obtain data for several VOCs. Fig.4 shows an example of OES for methane in air, highlighting its characteristic peak at 431 nm.

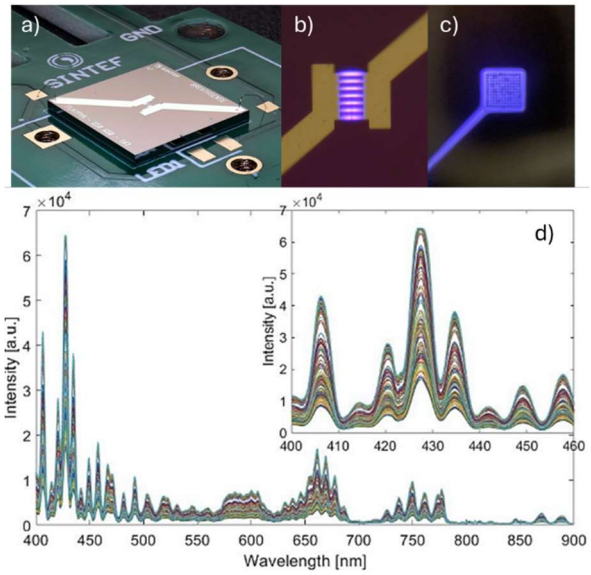


Fig. 3. A packaged device on a custom-made PCB (a), plasma experiments observed (in air) with array of 7 sources (b), and 13 x 13 array sources (c), example of optical emission spectra collected (d).

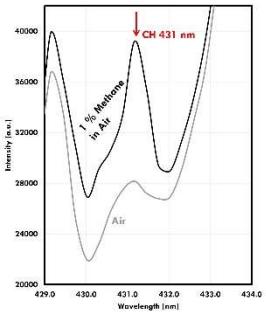


Fig.4 Example of optical emission spectra collected for methane in air using a reference larger scale plasma emission spectroscopy system (CH peak at 431 nm).

Conclusions

The data collected suggests that the developed miniaturized microplasma sources are promising as components of gas analysis systems.

References

[1] Kogelschatz, U. (2007), Applications of Microplasmas and Microreactor Technology. Contrib. Plasma Phys., 47: 80-88.

[2] Park S.J. et al. (2005), 40000-pixel arrays of ac-excited silicon microcavity plasma devices, Appl. Phys. Lett. 86, 111501.

[3] R. Brandenburg et al., Barrier Discharges in Science and Technology Since 2003. *Plasma Chem. Plasma Process*. 43 (2023), 1303–1334.

Acknowledgements

The work in this project is financed by Horizon Europe (grant agreement number 101115028).

DOI 10.5162/EUROSENSORS2025/T4.1.4

Ceramic MEMS Platforms for Metal Oxide Gas Sensors: Compatibility of Sensing Layers with Thick Film Materials

Alexey Vasiliev[1,2], Oleg Kul[2], Alexander Bolshakov[2], Artem Mokrushin[3], Alexey Shaposhnik[4]
[1] Dubna State University, Universitetskaya str,19, Dubna, 141980, Russia
[2] LLC "C-Component", Tushinskaya str., 17, 125362, Moscow, Russia
[3] Kurnakov Institute of Inorganic Chemistry, RAS, Leninskiy prosp, 31, 119991, Moscow, Russia
[4] Voronezh State Agrarian University, Michurin str., 1, 394087, Voronezh, Russia
Corresponding Author's e-mail address: A-A-Vasiliev@yandex.ru

Summary:
The problem of the compatibility of the glass ceramic materials used in thick film technology and, in particular, in ceramic MEMS technology, with sensing layers (SnO_2, TiO_2, In_2O_3, ZnO) was studied in detail. It was demonstrated that long term operation at high working temperature (up to 450ºC) and, especially, technological annealing of the sensing element at temperature up to 750ºC leads to the dissolution of the glass components in the sensing layer. The application of such elements as Bi and Pb in the glass leads to the dramatic poisoning of the sensing layers.

Keywords: gas sensors, thick films, screen printing, glass ceramics, sensing layers, compatibility of materials.

Introduction

The thick film technology is widely used for the fabrication of both experimental and commercial gas sensors. Glass binder is an element of all parts of the sensor made by screen printing: microheaters, substrates, insulation layers, etc. Glass is also a component of the LTCC (low temperature co-fired ceramics) used in gas sensor technology. Therefore, a possible poisoning of the sensing material of gas sensor with glass components is a very important issue for long-term stability of gas sensors.

Our very early results showed that, solid state interaction of RuO_2 with PbO in commercial thick film inks used as a material for the heaters leads to the formation of lead ruthenates and to the drift of the microheater resistance. Another example of the importance of this problem is the strong difference in the stability of thermocatalytic sensors made using uncoated and glass coated Pt wire: slow reaction between Al_2O_3/Pt/Pd catalyst and SiO_2 of Pt wire shell leads to the formation of alumosilicates and, respectively, to much stronger drift of the sensor signal compared to uncoated Pt wire at working temperature of 450ºC.

In numerous publications about thick film and LTCC platforms for semiconductor gas sensors, the influence of the composition of platform materials to the properties of gas sensor is not considered as a rule, although this role is really important. At least, we did not meet such publications touching specially this issue.

In our research of the ceramic MEMS devices [1], we met a problem of dramatic drop of the SnO_2-sensor response in the case of the application of inadequate glass for the fabrication of the elements of the cantilever: cantilever body, Pt leads to the sensing material, insulation, etc. This was a reason to start this research.

Experiment

In the experiment we used two types of substrates. The first one was described in [1], photo of the substrate is presented in Fig. 1.



Fig. 1. Photo of the screen-printed cantilever type ceramic MEMS with Pt microheater, Pt contacts, glass-ceramic insulation between microheater and contacts. The chip is to be packaged in TO-5 holder.

Another substrate was used for the investigation of the dissolution of glass components in sensing layers. We used alumina ceramic substrates (30x16 mm^2) screen printing coated with glass under investigation. The glass layer was

fired at 850ºC for 15 min. The glasses studied in this work are listed in Table 1. After this, the sensing layers consisting of ZnO, SnO_2, In_2O_3, or TiO_2 nanoparticles (~ 10 nm) made by sol-gel technology were deposited using screen printing as ink in mixture with terpineol on whole surface of the glass layer.

Tab. 1: Composition of glasses used in the experiments as a coating of alumina substrate.

Glass type	Glass composition, wt. %
PD-Sn	BaO — 30-45%, SiO_2 — 20-30%, B_2O_3 — 20-30%, CaO — 8-12%, SnO_2 — 5-12%, MnO_2 — 0,1-3%, CuO — 0,1-3%
PD-HS	SiO_2 — 42%, B_2O_3 — 4,5%, CaO — 3,5%, MgO — 1,5%, BaO — 31%, Al_2O_3 — 16%
PPL	Bi_2O_3 — 66%, PbO — 18,5%, SiO_2 — 7,5%, B_2O_3 and ZnO — 8%

To simulate the typical process of the sensing layer firing, the layer of oxide on the glass surface was heated from room temperature to final temperature of 720 ºC for 15 min, then was kept at 720ºC for 15 min, and finally the plate was cooled during 15 min. Earlier [2], we found this procedure to be optimal for the fabrication of SnO_2 based gas sensing layers. The thickness of metal oxide layer after firing was equal to 12 μm. Then, the sensing material was removed from the glass coated alumina with plastic squeeze, which doesn't damage glass sublayer. The sensing material powder was collected for further study at the Laboratory of chemical analysis of the NRC Kurchatov Institute (ICP-AES) and at the Kurnakov Institute of general and inorganic chemistry (ICP-MS). For comparison, we studied in the same way the sensing layers deposited onto uncoated alumina substrates. To study the influence of the glass composition onto sensing properties we used sensor microheaters with different glasses; the sensing layers were ZnO and SnO_2.

Results and discussion

The powder obtained from the substrate coated with PPL glass (Table 1) was strongly contaminated by Bi and Pb diffusing from the glass to the sensing layer. Only 15 min at 720ºC of the contact between two layer was sufficient to change completely the composition of the sensing layer. On the other hand, the composition of the oxide layers deposited onto the surface of the glasses without Bi and Pb were not changed significantly. An example of the results obtained using ICP-AES is presented in Tab. 2.

Similar results were obtained as well with other sensing materials investigated in this work. All of them are strongly contaminated by Pb and Bi after annealing at 720 ºC for 15 min.

Tab. 1: Contaminants (in wt. %) of SnO_2 after deposition and firing on the surface of glasses mentioned in Table 1.

	PPL	PD-Sn	PD-HS
Ca	0.056	0.042	0.061
Mg	0.060	0.047	0.060
Ba	0.034	0.0066	0.0065
Fe	0.039	0.040	0.085
Ni	0.0071	0.0076	0.0069
Cr	0.0014	<0.0020	<0.0020
Cu	0.0028	0.0028	0.0027
Sb	<0.005	<0.005	<0.005
Pb	3.8	0.0089	0.012
Bi	14.8	<0.0050	0.015

The results obtained with the application of ICP-AES and ICP-MS strongly correlate with the gas sensitivity of the sensors fabricated using the substrate shown in Fig. 1. Typical value of the bare SnO_2 sensing layer response is of factor of 10 at the H_2 concentration equal to 200 ppm. The sensing layer deposited onto substrate with Pt leads made with PPL glass has a response of about factor of 2 under the same conditions. Both SnO_2 and ZnO based sensors on substrates with Bi and Pb containing glasses in contrast to substrates with PD-HS and PD-Sn glasses demonstrate dramatic decrease in gas response to NO_2. This sensitivity drop can be related with a change in acidic and basic properties and with the re-crystallization of the material due to the incorporation of Bi and Pb.

Conclusion

Important role of the thick film substrates and microhotplates in the sensing properties of semiconductor layers was demonstrated. The application of Bi and Pb containing glasses in all elements of microhotplates should be excluded. The sensing layers and glass components used in gas sensors should be tested for their compatibility regarding a possible dissolution of glass components in the sensing layer material and its influence onto both chemical stability and recrystallization of the last one.

Acknowledgement

The research was supported by the Russian Science Foundation grant № 24-13-00254, (https://rscf.ru/project/24-13-00254/)

References

[1] O.Kul, A.Vasiliev, A.Shaposhnik, A.Nikitin, A.Dmitrieva, et al. Novel screen-printed ceramic MEMS microhotplate for MOS sensors. *Sensors & Actuators: A.* 379, 115907(2024). https://doi.org/10.1016/j.sna.2024.115907.

[2] J.H.Kim, J.S.Sung, Yu.M.Son, A.A.Vasiliev, et al. Propane/butane semiconductor gas sensor with low power consumption. *Sensors and Actuators, B,* 1997, V. 44, P. 452-457. doi:10.1016/s0925-4005(97)00237-2

DOI 10.5162/EUROSENSORS2025/T4.2.1

Short-Term Pollution Prediction Using Personal Environmental Monitoring and Machine Learning

Feiling Pan[1], J.A. Covington[1]
[1] School of Engineering, University of Warwick, Coventry, CV4 7AL, UK
Feiling.Pan@warwick.ac.uk

Summary:

Due to increasing global concerns around air pollution, research on portable environmental monitoring has become an expanding area of research. This study used an in-house developed personal environment monitor, coupled to machine learning, to identify scene switch recognition and short-term pollution prediction. Here, decision trees excelled in environmental identification (97% accuracy), while XGBoost performed best in pollution prediction (R^2 = 0.93). This study provides an effective scheme for short-term pollution warnings, which in the future could be used to warn users of potential harm.

Keywords: Personal environment monitoring, machine learning, short-term pollution prediction, environmental identification, Wearable device

Introduction

As environmental challenges become increasingly complex, personal environmental monitoring equipment has emerged as an important area of research. Unlike traditional environmental monitoring methods, these personal devices offer a significant advantage - the ability to provide precise, real-time ambient data about an individual's immediate environment. Current research on portable monitoring devices covers a range of temporal predictions, from hourly short-term forecasts to longer-term trend analyses. However, the existing prediction models face challenges, particularly when dealing with rapidly changing environments and quick scenario transitions. The current prediction ranges often fall short of meeting the risk assessment needs of personal monitoring devices. This limitation is especially pronounced in short-term prediction research, where the ability to anticipate environmental changes within brief time frames remains a significant challenge [1].

To address this issue, we have divided this task into two stages. First, we attempt to identify a change in the user's environment, which could lead to new pollution risks. This includes identifying the likely location (e.g. outside, coffee shop etc.) the user is in. With this information, we then use machine learning to predict future pollution levels based on the changing levels in that location, therefore providing a targeted warning to the user. We believe that this approach will allow users to make decisions before being exposed to high levels of pollution and make an intervention, such as walking in a different direction.

Material and Methods

This study used an internally developed personal sensing device [2], which can monitor 10 environmental pollution indicators, such as temperature and humidity, CO_2, light intensity, ultraviolet, volatile organic compounds (VOC), NO_X and noise. Using this multi-dimensional environmental data, it uses an in-house developed scoring system to provide an overall environmental score. Fig.1 shows the design of the device and its accompanying APP.



Fig. 1. Design of Monitor unit and App

The environmental score (S), range 0 (risk) to 100 (comfort), is determined based on an assessment of the ten environmental parameters. For each parameter reading, it considers whether it is within a comfort range, discomfort range, or risk range. These individual sensor values are then combined to create a final "environmental score", which is displayed to the user.

This study conducted field testing in the city of Coventry, UK, using the device described above, covering various scenarios and a range of different environments. 1,178 environmental data points were collected and annotated for the specific environment. Using this data, machine learning models were created and compared in their performance in short-term pollution prediction. These models included Long Short-Term Memory (LSTM), Extreme Gradient Boosting (XGBoost), and Convolutional Neural Networks (CNN). The study employed a sliding window mechanism and set time steps to achieve environmental risk prediction approximately 30 seconds in advance.

Result and Discussion

Fig. 1 shows some environmental score data for different locations within Coventry, including restaurants, bus, train station, coffee shops, etc. Tab. 1 shows the results of the machine learning models used to identify the location of the user.

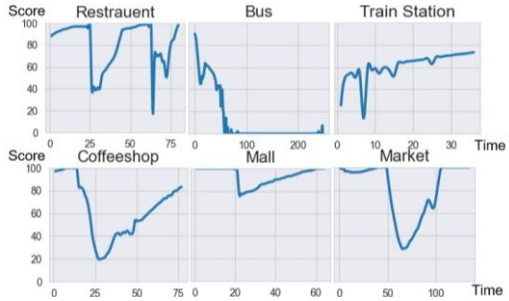


Fig.1. Score changes for typical environments

Tab.1 summarises the performance of each model in identifying the type of environment.

Tab. 1: Environmental identification performance

Model	Accuracy
Decision Tree	97.03%
Random Forest	96.61%
SVM	93.22%
Naive Bayes	89.83%

As can be seen from the table, the decision tree and random forest have the highest accuracy in environmental scene classification.

In addition, this study used a variety of models for short-term (30 seconds in advance) pollution score prediction. Score prediction combines data from multiple pollutants into a simple single predictive value to make it easier for the user. This not only adapts to changes in different environments, but also improves the accuracy of forecasting, helping users make faster decisions.Tab.2 shows some results from three models.

Tab. 2: Short-term pollution warning performance

Model	R^2	MAE	RMSE
XGBoost	0.93	4.96	10.66
CNN	0.91	5.79	12.02
LSTM	0.89	7.89	13.57

According to Tab.2, XGBoost performs best, followed by CNN and LSTM. Fig.2(a), (b) and (c) respectively show the training performance of models. XGBoost performs best at contamination risk (0 value), with concentrated residuals, minimal errors, and stable predictions. CNN is second, there is still some deviation in the low pollution risk area, but the overall stability.

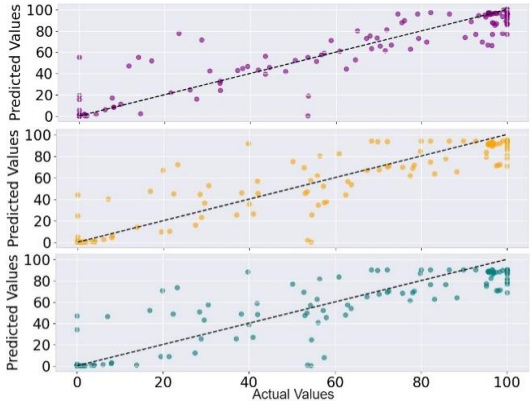


Fig.2. Prediction Accuracy Scatter Plot for Environmental Score: XGBoost (purple), CNN (orange), LSTM (teal)

Conclusions

This study demonstrates the effect of improving short-term pollution prediction and environmental identification through personal environmental sensor data. In terms of environment recognition, the decision tree and random forest model perform well. For short-term pollution prediction, XGBoost has the best effect, followed by CNN and LSTM, which can effectively capture the nonlinear change of environmental pollution. In the future, optimised models can provide more accurate warning and personalised environmental assessment. This may, for example, allow users to adjust their trips, making such environmental predictions closer to their needs.

References

[1] Feng, Y., Liu, S., Wang, J., Yang, J., Jao, Y. L., & Wang, N., Data-driven personal thermal comfort prediction: A literature review, *Renewable and Sustainable Energy Reviews*, 161 (2022) 112357.doi: 10.1016/j.rser.2022.112357

[2] F. Pan, J. A. Covington, A Portable Personalized Environmental Quality Monitoring System (PONG) Version 3, *IEEE Sensors Journal* (2024); doi: 10.1109/JSEN.2024.3405858

DOI 10.5162/EUROSENSORS2025/T4.2.2

Portable AI-Assisted System for Real-Time Dust Exposure Monitoring in Working and Occupational Environments

Ivan ROMANYTSIA
ELLONA SAS, 3 Avenue Didier DAURAT, 31400 Toulouse, FRANCE,
ivan.romanytsia@ellona.io

Summary:
Despite improved workplace exposure limits regulations, many workers remain at risk from airborne particulate matter with lasting health effects. To address this, we developed a portable device that measures dust concentration, identifies chemical composition, and calculates individual exposure in real time. The system combines sensor-based measurements with an AI model trained to classify particulate types, offering a compact, efficient tool for occupational exposure assessment. This approach enhances early detection of hazardous conditions and supports more responsive workplace safety management.

Keywords: respirable fraction, personal exposure, dust identification, trained model, portable sensor

Background, Motivation an Objective

Recent studies in toxicology and regular updates of regulation policy allows to reduce risks of personal exposure to widely used or new hazardous materials. However, more than 1 billion workers are exposed to dangerous substances and factors, like chemicals, fumes, vapors and airborne particulate matter, with long-term impacts on health and quality of life [1]. Majority of the rules are based on average 8-hour total weight average (TWA) permissible exposure limit (PEL), which requires, by definition, a long term monitoring and averaging of data. In case of particulate matter exposure, the collection time and further chemical analysis could take from few hours to few days, and short term exposure limits (STELs) or peaks are not detected and evaluates for adequate protection of workers. To address this, we have developed a portable device capable of measuring dust concentration, identifying the chemical nature of dust particles, and calculating individual exposure in real time.

Description of the New Method

Method is based on few following facts. The granulometric signature of particulate matter generated by same tool but on different materials (wood, plastics, concrete, metal, etc.) is different. The different tool or activity (drilling, polishing, cutting, etc.) produce different granulometric distribution, as well [2, 3]. The individual worker with his personal tool is near to the source. Sensor collection head is near to respiratory tract, so it corresponds to inhaled air.

The system integrates multiparameter sensor-based measurements with an AI model trained to classify particulate types. Data used for model training consist real time measurement and previously collected data completed by chemical analysis according to regulation policy. Its allow to create a database with different sources/tool/material combination and select most probable sources according to working environment.

During operation sensor collect and transfer to server data in almost real time, with 10 seconds interval. Then data are evaluated by server based trained model to calculate dust concentration of respirable or thoracic fraction of dust, identifies chemical composition according to saved database and calculates individual exposure to hazardous substance, like hard wood, crystalline silica, black carbon, oil droplets, etc.

Results

In the development stage multiple candidates of low cost particle counter are tested. In-vitro conditions were realized in 250L test bench, where sensors are placed and exposed by commercially available powders samples: alumina, carbon black, graphite, moondust, quartz in ranges from 1 to 50 mg/m^3. Following data treatment with principal component analysis and linear discriminant analysis were used to identify most promising low cost particle counter (see Fig. 1) The 2 dimensional linear discriminant analysis is showed for finally selected sensor.

In industrialization phase the capacity for measurement of respirable fraction were evaluated. As reference instrument a device called CIP-10 were used [4]. Multiple simultaneous test (see Fig 2) shows very good correlation between

approved dust collection device with developed sensor based on particle counter.

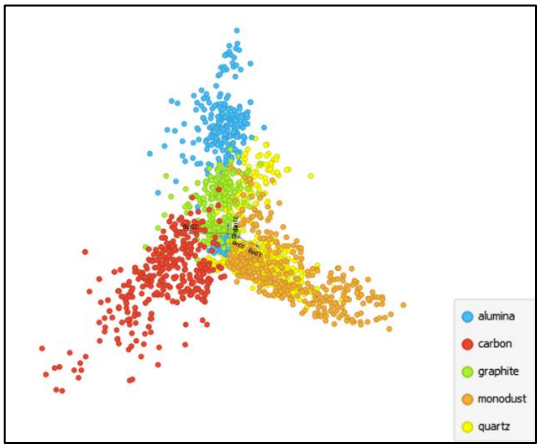


Fig. 1. LDA visualization of discrimination capacity of low cost particle counter

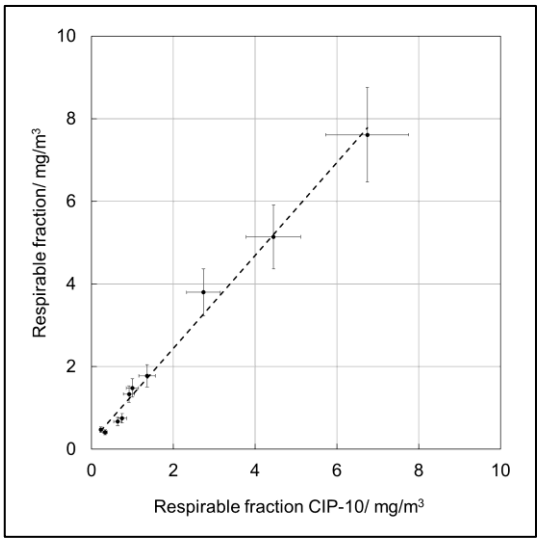


Fig. 2. Graph of respirable fraction collected by CIP-10 vs respirable fraction measured by sensor in 10 different campaign.

Final device, (see Fig.3), has two main parts: sensor head and data collection and treatment module with battery for more than 10h of autonomous work. Sensor head could be easily replaced by new one or different, according to working condition and particulate type.



Fig. 3. Sensor used by worker consist A – sensor head, B – electronic board with battery.

References

[1] Exposure to hazardous chemicals at work and resulting health impacts: *A global review International Labour Office* – Geneva: ILO, 2021, ISBN:978-9-22-034219-0

[2] Kminiak, R.; Kučerka, M.; Kristak, L.; Reh, R.; Antov, P.; Očkajová, A.; Rogoziński, T.; Pędzik, M. Granulometric Characterization of Wood Dust Emission from CNC Machining of Natural Wood and Medium Density Fiberboard. *Forests*, 12, 1039. (2021) doi:10.3390/f12081039

[3] Qi C, Echt A, Gressel MG. On the Characterization of the Generation Rate and Size-Dependent Crystalline Silica Content of the Dust from Cutting Fiber Cement Siding. *The Annals of Occupational Hygiene* 60(2), 220-230, (2016); doi:10.1093/annhyg/mev066

[4] Prélèvement des aérosols par le dispositive CIP 10 Version 3 – janvier 2022 © INRS https://www.inrs.fr/dms/inrs/PDF/metropol-prelevement-cip10/metropol-prelevement-cip10.pdf

DOI 10.5162/EUROSENSORS2025/T4.2.3

Correlation of gaseous emissions with phenological phases in tomato crops

Tamisari Melissa[1], *Tavaglione Emanuela*[2], *Francesco Tralli*[2], *Matteo Valt*[3], *Barbara Fabbri*[2]
[1] *Department of Neuroscience and Rehabilitation, University of Ferrara, Via Luigi Borsari 46, 44121 Ferrara, Italy*
[2] *Department of Physics and Earth Science, University of Ferrara, Via Giuseppe Saragat 1/C, 44122 Ferrara, Italy*
[3] *Sensors and Devices Center, Bruno Kessler Foundation, Via Santa Croce 77, 38123 Trento, Italy*

Corresponding Author's e-mail address: melissa.tamisari@unife.it

Summary:
Currently, plant phenological phases are determined through models based on historical data series and advanced measurement tools such as satellite imaging, which are not always accurate. This study explores innovatively the relationship between Volatile Organic Compounds emitted by tomato plants and their phenological phases using machine learning algorithms. Supervised models, particularly k-NN, achieved an accuracy of 96.8% in identifying phases. These results highlight the potential of sensors and AI to accurately monitor crop development.

Keywords: Machine Learning, Phenological Phases, Precision agriculture, Volatile organic compounds, MOX gas sensors.

Introduction

Precision agriculture represents a strategic approach aimed at improving agricultural productivity while simultaneously reducing resource use and maintaining high-quality standards. At the same time, it serves as a fundamental tool for climate adaptation, addressing the growing environmental challenges faced by modern agricultural systems. Indeed, rising temperatures and prolonged periods of drought are causing serious issues, including shifts in crop phenological cycles, leading to a decline in both the quantity and quality of yields. The aim of this study is to identify a relationship between Volatile Organic Compounds (VOCs) secreted by tomato crop, and empirically derived agronomic parameters — in particular, the phenological phase (PPhases)— via supervised machine learning algorithms [1]. PPhases are currently complemented by more sophisticated estimates obtained through models based on historical data series and measurement tools such which are not always accurate. The Growing Degree Days (GDD) index, which measures the accumulation of heat useful for plant growth during the crop cycle, is used to mark the transition from one PPhase to another. Since each phenological stage requires a specific amount of thermal energy to be completed, knowing a plant's thermal requirements allows for reasonably accurate estimates of the duration of its developmental stages. PPhases represent the main stages of the crop's growth cycle, marking key moments in plant development. The PPhases are: (1) pre-emergence, (2) sowing/transplanting (3) fruit set – first truss (4) veraison – first truss (5) veraison – second truss, (6) ripening: 50% of berries fully colored and (7) ripening: 100% of berries fully colored.

Method

From 2020 to 2022, we carried out industrial tomato monitoring campaigns lasting three to four months (typically from early June to early September). As part of the project, a multifunctional station was installed in tomato crop field, equipped with: a relative humidity (RH%) and temperature sensor (Sensirion SHT11); a small camera with a removable infrared filter, used to monitor the plants' radiation absorption; four metal oxide (MOX)-based gas sensors to monitor plant gas emissions during their phenological development [3]. In particular, the sensors used were SnO_2/Au, SnO_2/Pt, SnO_2/Pd, WO_3; monitoring of VOCs emitted by plants is primarily aimed at assessing their health status, which can be affected by insects or diseases [4]. Classification may be defined as a supervised learning method in which machine learning (ML) algorithms are trained to assign

DOI 10.5162/EUROSENSORS2025/T4.2.3

labels to input data based on patterns learned from a labeled training dataset [1]. The main goal of these algorithms is generalizing from the training examples in order to enable the model to correctly predict the label of unseen data. In light of this, applying ML techniques to a wide range of sensor signals, makes it possible to train a model able to identify the phenological phase. In this work, a model capable of doing this type of classification was trained due to the vast amount of data acquired during the years.

Results

A signal was recorded approximately every 14 seconds during the data acquisition period. The datasets we obtained generally cover phenophases from 2 to 6, which have been assigned to classification labels ranging from 1 to 5.

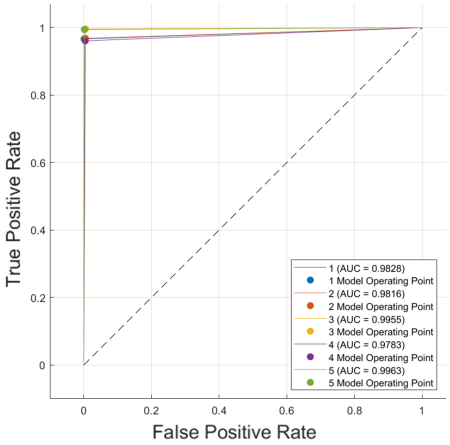


Fig. 1. ROC curves and AUC values for the k-NN algorithm (validation).

As an initial investigation, the 2020 dataset presented here was analyzed using several supervised machine learning methods, using a dataset split of 90% training and 10% testing, with 5-fold cross-validation. Even with relatively simple algorithms, the results proved to be promising. Among these, the k-nearest neighbors (k-NN) algorithm emerged as the best-performing method, achieving an accuracy of 96.8%, along with a high Receiver Operating Characteristic (ROC) curve score (Fig. 1), implying significant discriminatory power. The confusion matrix for this model is shown in Fig. 2. These promising results suggest that training the model on multi-year datasets at disposal could lead to a robust method for determining phenophases based on the signals acquired from an array of four chemoresistive gas sensors. A model of this kind could be integrated into decision support systems in agriculture, helping to improve the identification of phenophases and, consequently, to optimize agronomic strategies, making farming practices more efficient and sustainable.

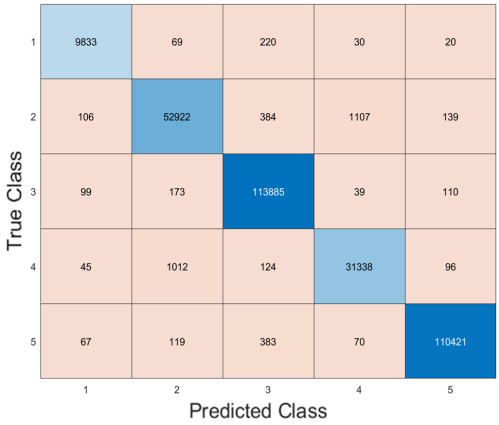


Fig. 2. Confusion matrix for the k-NN algorithm (validation).

References

[1] S. L. Stevan Jr., A. F. C. Garcia, B. A. Menegotto, J. C. Ferreira Da Rocha, H. V. Siqueira, R. A. Ayub, "Phenological stages analysis in peach trees using electronic nose" *Open Agriculture*,9, (2024), 20220337. doi: 10.1515/opag-2022-0337

[2] L. S. Pereira, R. G. Allen, M. Smith, D. Raes, Crop evapotranspiration estimation with FAO56: Past and future, Agricultural Water Management, 147, 4 (2015) doi: 10.1016/j.agwat.2014.07.031

[3] B. Fabbri, M. Valt, C. Parretta, S. Gherardi, A. Gaiardo, C. Malagù, F. Mantovani, V. Strati, V. Guidi, Correlation of gaseous emissions to water stress in tomato and maize crops: From field to laboratory and back, Sensors and Actuators B: Chemical, 303, 127227 (2020) doi: 10.1016/j.snb.2019.127227

[4] K. Takayama, R.M.C. Jansen, E.J. van Henten, F.W.A. Verstappen, H. J. Bouwmeester, H. Nishina, Emission index for evaluation of volatile organic compounds emitted from tomato plants in greenhouses, Biosystems Engineering, 113, 220 (2012) doi:10.1016/j.biosystemseng.2012.08.004

Acknowledgements

This work is done in collaboration with CER Consortium (Consorzio di Bonifica Canale Emiliano Romagnolo) and the Emilia-Romagna Region, as part of the POSITIVE project (Scalable Operational Protocols for Precision Agriculture).

DOI 10.5162/EUROSENSORS2025/T4.3.1

Free Chlorine Digitization Using Colorimetric Barcodes and Machine-Leaning Models

María González-Gómez[1], Ismael Benito-Altamirano[1,2,], Hanna Lizarzaburu-Aguilar[1,3], David Martínez-Carpena[1,3], J. Daniel Prades[1,4] and Cristian Fàbrega[1]*

[1] IN2UB, Department of Electronic and Biomedical Engineering, Universitat de Barcelona, Martí i Franquès 1, 08028 Barcelona, Spain

[2] eHealth Center, Faculty of Computer Science, Multimedia and Telecommunications, Universitat Oberta de Catalunya, Rambla del Poblenou, 156, Sant Martí, 08018 Barcelona, Spain

[3] Department of Mathematics and Computer Science, Universitat de Barcelona, Gran Via de les Corts Catalanes, 585, Barcelona, 08007, Barcelona, Spain

[4] Institute of Semiconductor Technology (IHT) and Laboratory for Emerging Nanometrology (LENA), Technische Universität Braunschweig, Hans-Sommer Str. 66, D-38106 Braunschweig, Germany

ismael.benito@ub.edu, ibenitoal@uoc.edu

Summary:

The introduction of colorimetric barcodes, this is a 2D barcode which embeds a color chart, has enabled the digitization of colorimetric chemical sensors using smartphones. We applied this concept to free chlorine monitoring in water using commercial BTB and DPD reagents.Color QR Codes acted as both localization and color correction references. Images were processed through geometric normalization and nonlinear color correction. Machine-learning models achieved high accuracy under real-world conditions. This approach enables low-cost, hardware-free chlorine monitoring for on-site applications.

Keywords: colorimetric sensing, QR Code, chlorine detection, computer vision, smartphone analysis

Introduction

Ensuring the safety of drinking or pool water requires regular monitoring of free chlorine (FC), a commonly used disinfectant. Traditional colorimetric tests like BTB strip and DPD powder methods —gold standard in the HORECA sector— are cost-effective but rely on subjective visual interpretation[1]. Recent advances in computer vision and mobile imaging have enabled the digitization of colorimetric indicators, by introducing machine-readable patterns like barcodes embedded with several color references[2]. Our work builds on this idea by integrating color reference patterns into QR Codes, creating compact, printable, and robust calibration charts for smartphone-based sensing, while improving accuracy and enabling traceability.

Methodology

We present a novel method for FC detection using 'colorimetric QR Codes'—barcodes that include embedded color references for calibration—. Each QR Code corresponds to a specific test type (BTB strip or DPD powder) and includes color patches aligned with the test's color response curve. These codes are placed next to the test during imaging, enabling geometric correction and color calibration using thin plate spline warping. Smartphone images are processed using OpenCV to detect the QR Code, extract the region of interest (ROI), correct for lighting conditions, and feed color features into machine-learning models trained for FC classification and regression. Fig. 1, shows these color QR Codes alongside each of the test.

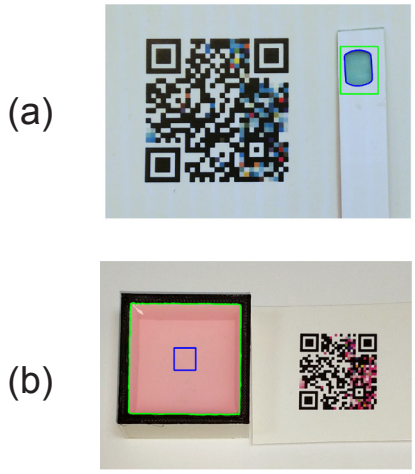


Fig. 1. (a) ROI detection on BTB strip test with adjacent colorimetric QR Code; (b) color extraction from DPD cuvette using contour-based segmentation. Both setups illustrate the use of QR Codes for geometric alignment and color correction under uncontrolled lighting.

Free chlorine solutions from 0.1 to 8.4 ppm were prepared by stepwise dilution of a 100 ppm sodium hypochlorite stock. Concentrations up to 2.2 ppm were measured directly using a Hach DR300 colorimeter (±0.02 ppm), while higher values were extrapolated from diluted samples. These tagged concentrations served as ground truth for evaluating both BTB and DPD tests.

Results

A supervised machine-learning pipeline was implemented to quantify free chlorine from smartphone-acquired images of colorimetric tests. For each sensor (BTB strip and DPD powder), mean RGB and HLS features were extracted from the region of interest after applying geometric normalization and thin plate spline color correction. A two-stage analysis was done: (1) a Support Vector Classifier (SVC) was trained to categorize free chlorine concentration into three regulatory classes—*low*, *middle*, and *high*; and (2) a regression model was applied only to the *middle* class to refine concentration estimates. Models were trained using data from a Huawei P20 and tested over an iPhone SE, a Morotorola G6 and a Xiaomi A2.

For the BTB test, all six color features (R, G, B, H, L, S) were used as input to the SVC after dimensionality reduction via Principal Component Analysis (PCA), which preserved over 97% of the variance in two components. Regression in the acceptable range used the logarithm of the corrected red channel, which exhibited the strongest monotonic decay.

Tab. 1: Evaluation results for BTB strip and DPD powder methods. All models were trained using the Fixed Setup and tested in Room Setup conditions. Classification accuracy and regression performance (R^2) are reported for each smartphone. For BTB, flash and no-flash conditions are compared; for DPD, only no-flash results are included due to reflection artifacts.

Smartphone	Flash	Method	Classification (Accuracy %)	Regression (R^2)
Huawei P20	No	BTB	88.1	0.88
	Yes	BTB	92.5	0.82
	No	DPD	88.1	0.94
iPhone SE	No	BTB	91.3	0.87
	Yes	BTB	95.8	0.79
Motorola G6	No	BTB	87.0	0.78
	Yes	BTB	96.6	0.80
	No	DPD	100.0	0.82
Xiaomi A2	No	BTB	100.0	0.96
	Yes	BTB	94.7	0.79
	No	DPD	90.0	0.91

For the DPD test, classification was performed using the green and blue channels as raw inputs, while regression employed a PCA-based projection of their logarithmic values. This hybrid approach improved both robustness and accuracy across lighting conditions and smartphone models. The best performance was achieved by the Xiaomi A2 in the BTB test without flash, reaching 100% classification accuracy and a regression R^2 of 0.96 against the actual concentration values (Tab. 1). An application was developed for a potential client named *Selfytest* (Fig. 2.).

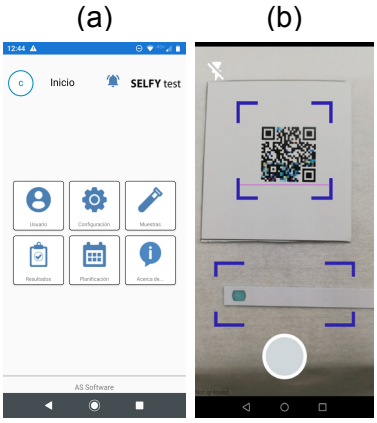


Fig. 2. Application for free chlorine measurements using colorimetric test and Color QR Codes as helper. (a) a view of the user data; (b) the scanner view.

References

[1] Shang J. et al., On Site Determination of Free Chlorine in Water Samples by a Smartphone Based Colorimetric Device, New J. Chem. 2019

[2] Benito Altamirano I. et al., Back Compatible Color QR Codes for Colorimetric Applications, Pattern Recognition 2023, doi:10.1016/j.patcog.2022.108981

[3] Benito Altamirano I. et al., Image Color Consis tency in Datasets: The Smooth TPS3D Method, arXiv:2409.05159

Acknowledgements

This work was supported by Agència per la Competitivitat de l'Empresa (ACCIO, INNOTECRD19-1-0002). I. Benito-Altamirano acknowledges the support from project PID2022-138721NB-I00, funded by MCIN (Spain). J.D. Prades acknowledges the support from the sponsorship of the Alexander von Humboldt Professorship of the Humboldt Foundation and the Federal Ministry for Education and Research (Germany) and the H2020 Framework Program with the ERC Grant Agreement no. 957527. and EIC Grant Agreement no. 951774. I.Benito-Altamirano acknowledges the support from MCIN (PID2022-138721NB-I00) Spain.

DOI 10.5162/EUROSENSORS2025/T4.3.3

Development and Characterization of Tribotronic Transistor based on ZnO thin film

Maria-Anna Moustaka[1], Emmanouel Hourdakis[1,2], Christos Tsamis[1]
[1]Institute of Nanoscience and Nanotechnology / NCSR Demokritos, Patr. Grigoriou E' & 27 Neapoleos Str., Aghia Paraskevi, 15341, Athens, Greece
[2] School of Electrical and Computer Engineering, National Technical University of Athens, 15772 Athens, Greece
c.tsamis@inn.demokritos.gr

Summary:
In this work, we present a tribotronic field effect transistor (T-FET) composed of a ZnO active layer and Al interdigitated electrodes (IDEs). Integrating the gate dielectric with one of the triboelectric surfaces, we demonstrate the modulation of carrier transport by the triboelectric potential generated during contact separation cycles. The electrical characterization of the T-FET is carried out measuring the output voltage of the device under varying contact forces and distances for different triboelectric materials. The resulting modulation proposes a promising device for self-powered interactive electronics.

Keywords: tribotronics, T-FET, ZnO, self-powered electronics, interdigitated electrodes

Introduction

The growing demand for sustainable electronics and intelligent sensing systems has led to the development of a new field of tribotronics [1]. The merging of semiconductors and triboelectric devices can result in direct modulation of conventional electronics using mechanical triggers such as human touch or ambient motion.

Typical tribotronic transistors operate by replacing the traditional gate electrode with a triboelectric material that can also be utilized as the gate dielectric. The charge transport in the semiconductor channel is modulated by the electrostatic potential induced during the contact-separation cycle of the triboelectric surfaces. Several tribotronic devices have demonstrated promising results and applications [2].

This work focuses on the fabrication and electrical characterization of a Triboelectric FET (T-FET) based on a ZnO thin film as an active channel. This device demonstrates the feasibility of a mechanically controlled ZnO FET while also exploring low complexity fabrication methods and material versatility.

Materials and Methods

Figure 1a shows a schematic representation of the T-FET. The device is fabricated using standard microelectronic techniques offering minimal and scalable device architecture. Several dielectrics were evaluated as the triboelectric gate including FEP, PET and Kapton. The interdigitated source and drain aluminum electrodes were patterned on an oxidized silicon wafer, following a lift-off process. Various device geometries were evaluated with the distance between the electrodes, that corresponds to the channel length of the T-FET, ranging from 55μm to 405μm.

A thick (300nm) ZnO active layer was patterned and deposited by RF magnetron sputtering. Following the same process, a 200nm SiO_2 layer was deposited for device passivation. To create a smooth dielectric top surface suitable for triboelectric gating, 1.5 μm of AZ5214E photoresist was spin-coated and hard-baked onto the device. The final device is shown in Figure 1b.

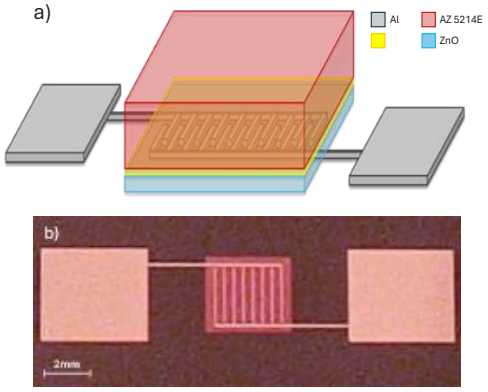


Fig. 1. (a) Schematic representation and (b) photograph of the T-FET.

All measurements were performed under ambient conditions using an in-house system for the periodic linear motion of the dielectric surfaces

(Fig 2). The T-FET was mounted onto a stationary stage while the triboelectric films were attached to a 3D printed base. Subsequently, they were mounted onto the movable stage of a linear motor and carefully aligned with the active area of the T-FET. The source-drain voltage (V_{SD}) was measured using a Keithley 2400 Source Measure Unit (SMU). The transient voltage measurements were realized using varying contact forces and separation distances while a constant current was applied.

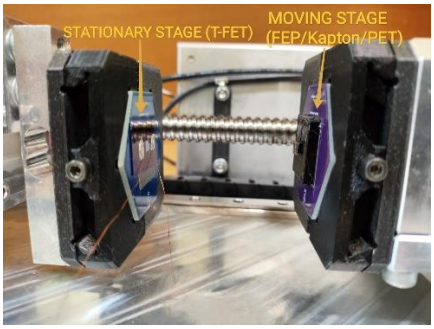


Fig. 2. Setup for the characterization of the T-FET

Results

The triboelectric modulation of the ZnO channel is achieved through controlled contact-separation with precise tuning of the spacing between the triboelectric surfaces and the force applied during contact. During contact there is a charge exchange between the photoresist deposited on the T-FET and the triboelectric material. The surface charge density depends on the relative electron affinities of the materials. The accumulated surface charges remain localized on the dielectric surfaces, when they are separated, inducing an electrostatic potential to the gate.

Figure 3 shows the source-drain voltage (V_{SD}) response as a function of time and in terms of the relative displacement of the T-FET and the triboelectric surface, following an original contact between the two surfaces.

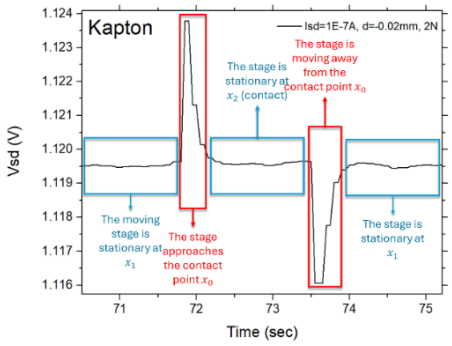


Fig. 3. Change of the source-drain voltage as a function of the relative motion between the T-FET and the triboelectric surface.

A signal change is observed in the source-drain voltage when the two surfaces are in relative motion due to the potential difference that is induced and modulates the carrier concentration in the ZnO channel.

Figure 4 shows the change of the source-drain voltage as a function of the distance of the triboelectric surface from the T-FET for different triboelectric materials. At a fixed distance, the output signal depends on the material of the triboelectric gate. This behavior is expected since the amount of charge that is exchanged between the two surfaces depends on the relative position of the materials in the triboelectric series, which is a manifestation of their respective electron affinities. From the analysis of the results, optimal material combinations can be identified to maximize the influence of the triboelectric gate on the transistor channel. The initial contact force between the two surfaces plays also an important role and will be further analyzed in subsequent work.

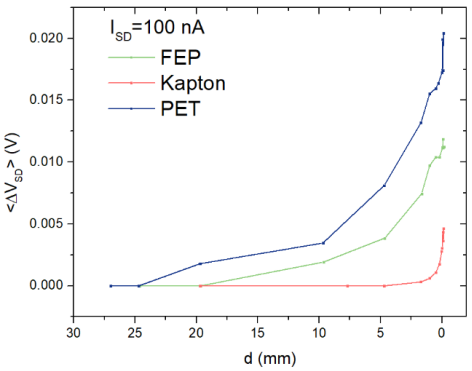


Fig. 4. Change of the source-drain voltage as a function of the distance of the triboelectric surface from the T-FET for various triboelectric surfaces.

Our work demonstrated that IDE based triboelectric FET can be utilized as mechanically-gated electronic components that could be exploited for sensing and logic applications.

References

[1] C. Zhang, W. Tang, L. Zhang, C. Han, and Z. L. Wang, "Contact Electrification Field-Effect Transistor," *ACS Nano*, vol. 8, no. 8, pp. 8702–8709, Aug. 2014, doi: 10.1021/nn5039806.

[2] J. Zhao *et al.*, "Flexible Organic Tribotronic Transistor for Pressure and Magnetic Sensing," *ACS Nano*, vol. 11, no. 11, pp. 11566–11573, Nov. 2017, doi: 10.1021/acsnano.7b06480.

Acknowledgements

The authors acknowledge the technical support from the Nanotechnology and Microsystems Laboratory of the Institute of Nanoscience and Nanotechnology (INN) at NCSR "Demokritos"

DOI 10.5162/EUROSENSORS2025/T4.3.4

Machine Learning-Enhanced Odor Detection System as Next-Generation Forensic Technology

Donatella Puglisi[1], Jens Eriksson[1], Kerstin Montelius[2], Emanuela Tavaglione[3], Barbara Fabbri[3], Rebecca Stenberg[4], Ivan Shtepliuk[1]

[1] Department of Physics, Chemistry and Biology, Linköping University, 58183 Linköping, Sweden

[2] Department of Forensic Genetics and Forensic Toxicology, National Board of Forensic Medicine, 58758 Linköping, Sweden

[3] Department of Physics and Earth Sciences, University of Ferrara, 44122 Ferrara, Italy

[4] Department of Management and Engineering, Linköping University, 58183 Linköping, Sweden

donatella.puglisi@liu.se

Summary:

In this work, we present an innovative scent-based detection system able to rapidly detect and correctly classify unique odor signatures released by biological materials from deceased humans as a revolutionizing form of forensic evidence. Our device, equipped with 32 metal oxide semiconductor (MOS) chemiresistive sensor elements and integrated with machine learning algorithms, was applied to different scenarios, demonstrating the potential of its application in forensic investigations.

Keywords: novel forensic technology, electronic nose, machine learning, volatile organic compounds, MOS sensors

Background, Motivation and Objective

Understanding the volatile organic compound (VOC) profile released during the early post-mortem period (0-72 h interval) is essential for applications in search and rescue operations to rapidly locate victims and survivors [1]. Gas chromatography-mass spectrometry (GC-MS), commonly used to analyze odor profiles in the laboratory, requires multiple data processing steps and is not suitable for *in situ* use and rapid response [1,2]. Specially trained dogs, so called cadaver detection dogs (CDDs), have been successfully used in forensic investigations since 1888 [3] to locate missing people, identify human remains or even detect traces of human decomposition odors. However, although CDDs are considered the most rapid and efficient tool for the search and detection of human remains, from a juridical perspective, their results cannot be used as physical evidence in court.

Here, we demonstrate that our proposed machine learning (ML)-enhanced gas sensor technology is a promising solution that can help investigators overcome current limitations in the use of CDDs, thus advancing forensic practices and outcomes [4-6].

Description of the New Method or System

Blood, putrefaction fluids, and muscle tissue samples were collected from the National Board of Forensic Medicine, Department of Forensic Medicine in Gothenburg, Sweden, during forensic autopsies of four individuals of different age and gender. The samples were stored in aliquots of 1 mL or approximately 1.5 g at -20°C ±1°C and defrosted immediately before VOC measurements. All ethical aspects of handling biological materials from deceased humans were carefully considered and appropriate Ethical Committee approval was obtained from the Swedish Ethical Review Authority in accordance with ethical review legislation, Act (SFS 2003:460), Reg. No. 2023-05783-01. Measurements were carried out using an electronic nose (e-nose) prototype consisting of 32 commercially available metal oxide semiconductor (MOS) gas sensors from the Figaro TGS2X product line [7]. Each measurement lasted 10 min including exposure to the target sample (5 min) and recovery to the baseline (5 min). The measurement sampling rate was set to 0.1 s, meaning that, for each individual measurement, we obtained 32 voltage-time signals, resulting in a dataset with dimensions of 32 × 6000. The obtained sensor signals were smoothed using a Savitzky-Golay filter and then normalized. Before developing the ML models, standard PCA was performed to investigate the primary sources of variance in the data and to identify any underlying patterns or clusters that may distinguish between classes. We then extracted 85 features from each signal to ensure a detailed representation of the signals across both time and frequency domains, and developed a sensor utility evaluation algorithm based

on Pearsson correlation coefficients for binary classification tasks.

We studied the e-nose response to VOCs in three different forensic scenarios. In the first case (see Fig. 1), we analyzed samples from deceased and living individuals to demonstrate the ability of our model to distinguish between *post-mortem* and *ante-mortem* samples as a critical factor in determining the time and circumstances of death. In the second case, we compared animal and human tissue samples as a key discriminant in complex forensic scenarios, particularly in the detection and identification of human remains. In the third case, we studied the aging process of pig meat to understand the dynamics of organic tissue decomposition over time.

Results

The Optimizable Ensemble was found to be the most effective model for all classification tasks. The obtained results showed that our model was able to distinguish between *post-mortem* and *ante-mortem* human biosamples with highest accuracy of 98.1%, sensitivity of 98.4 %, and specificity of 97.9%. A majority-voting mechanism was implemented to finalize classifier decisions on the status of samples. Furthermore, our model, based on a smartly designed feature matrix, was capable of accurately classifying animal and human samples, achieving 97.2% accuracy. Finally, using pig meat samples as a model, we demonstrated the capacity for precise post-mortem interval estimation down to a single day in the early stages of decomposition (1, 2, 3 days).

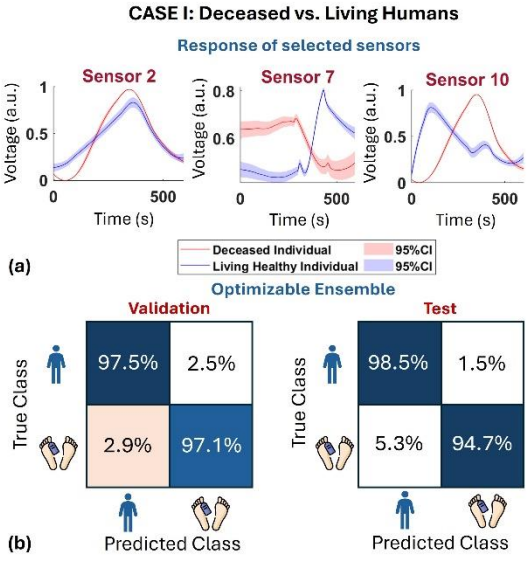


Fig. 1. Performance of the e-nose in one of the three forensic scenarios studied. CASE I: Discrimination between post-mortem and ante-mortem samples. (a) Averaged signals with confidence intervals from selected sensors for deceased and living humans. (b) Validation and test confusion matrix showing classification performance.

Acknowledgements

This work was supported by the Swedish Police Authority, Dnr. A170.261/2024, the Strategic Research Area in Forensic Sciences (SOFO), Dnr. IFM-2023-00208, the Faculty of Science and Engineering (LiTH) at Linköping University, Dnr. LiU-2025-00019, the National Board of Forensic Medicine (ethical application), and the Swedish Research Council, grant No. 2023-07219. The computations and data handling were enabled by resources provided by the National Academic Infrastructure for Supercomputing in Sweden (NAISS), partially funded by the Swedish Research Council through grant agreement no. 2022-06725. The authors would like to thank VOC Diagnostics AB for providing the instrument, Angelica Johansson and Carl Winskog for collecting the autopsy samples, Bo Lundqvist, Gunilla Inger Nilsson, Christer Lindvall, Magnus Stenlilja, and Linda Kvist from the Swedish Police for their valuable support and advice, as well as students and colleagues who contributed to sampling and measurements.

References

[1] D. Patel, R. Dargan, W.S. Burr, B. Daoust, S. Forbes, Identifying the Early Post-Mortem VOC Profile from Cadavers in a Morgue Environment Using Comprehensive Two-Dimensional Gas Chromatography, *Separations* 10(11), 566 (2023); doi: 10.3390/separations10110566

[2] C.J.G. Frazier, V.A. Gokool, H.K. Holness, D.K. Mills, K.G. Furton, Multivariate Regression Modelling for Gender Prediction Using Volatile Organic Compounds from Hand Odor Profiles via HS-SPME-GC-MS, *PLoS ONE* 18(7), e0286452 (2023); doi: 10.1371/journal.pone.0286452

[3] B. Blum, The Hounds of Empire: Forensic Dog Tracking in Britain and its Colonies, 1888-1953, *Law and History Review* 35(3), 621-665 (2017); doi: 10.1017/S0738248017000232

[4] K.G. Furton, N.I. Caraballo, M.M. Cerreta, H.K. Holness, Advances in the Use of Odour as Forensic Evidence Through Optimizing and Standardizing Instruments and Canines, *Philosophical Transactions of the Royal Society B: Biological Sciences* 370(1674), 20140262 (2015); doi: 10.1098/rstb.2014.0262

[5] W. Zhang, T. Liu, M. Ueland, S.L. Forbes, R.X. Wang, S.W. Su, Design of an Efficient Electronic Nose System for Odour Analysis and Assessment, *Measurements* 165, 1, 108089 (2020); doi: 10.1016/j.measurement.2020.108089

[6] A. Törneholm, Electronic Nose May Help in Court, *Linköping University News*, 22 Aug. 2022, available at https://liu.se/en/news-item/elektronisk-nos-kan-pa-sikt-sakra-rattsfallen

[7] J. Eriksson, D. Puglisi, C. Borgfeldt, Electronic Nose for Early Diagnosis of Ovarian Cancer, *Proceedings* 97, 145 (2024); doi: 10.3390/proceedings2024097145

DOI 10.5162/EUROSENSORS2025/T5.1.1

Activated Carbon in Focus: Is It the Key to Better NO_2 Gas Sensors?

Proscovia Kyokunzire[1], Jean Zaraket[1], Vanessa Fierro[1], Alain Celzard[1,2]
[1]Université de Lorraine, Centre National de la Recherche Scientifique (CNRS), Institut Jean Lamour (IJL), F-88000, Épinal, France
[2]Institut Universitaire de France (IUF), 75231 Paris, France

Corresponding Author's e-mail address: proscovia.kyokunzire@univ-lorraine.fr

Summary:
Gas sensors play a crucial role in detecting harmful environmental gases. This work therefore gives an insight into the sensing performance of a commercial Activated Carbon (AC) for NO_2 detection at room temperature. NO_2 sensing was assessed over a dynamic concentration range from 1 to 20 ppm and 20 to 1 ppm. The impact of increasing and decreasing NO_2 concentration, and saturation on sensor response was examined. NO_2 sensing proceeded by adsorption, facilitated by the porosity and high surface area of AC, and a response limit close to 65% was observed at sensor saturation.

Keywords: *Resistive gas sensor, Activated carbon, Adsorption, Saturation, Response*

Background, Motivation an Objective

Air pollutants cause significant adverse effects on the natural environment and human health, and are presently considered to be one of the main drivers of climate change [1]. Among these pollutants, NO_2 plays an important role in the deterioration of air quality [2]. Current health regulations set by the US Environmental Protection Agency (EPA) define an annual standard level of 53 parts per billion (ppb) NO_2, with a one-hour daily maximum concentration of 100 ppb [3]. It is therefore necessary to develop new, more efficient, real-time sensors to monitor NO_2 accurately.

The potential of ACs as sensitive layers for gas sensors has been explored due to their well-developed internal porous structure, high specific surface area, rich surface chemistry, ability to tailor their structure to specific applications, chemical stability and ease of preparation [4]. These features greatly enhance the adsorption and retention of gas molecules in the carbon matrix, thus improving sensor response. Our previous meticulous review of the literature revealed that only one article had explored the use of AC for the detection of NO_2 gas [5].This limited research represents a significant gap in understanding the overall operation and sensing performance of AC in the detection of NO_2, which is considered a major environmental pollutant.

Therefore, the objective of this work is to examine the NO_2 gas sensing capability of unmodified AC used as a sensitive layer at 25 °C, with particular emphasis on the influence of various parameters on sensor response and to optimize the operation of NO_2 gas sensors based on AC.

Experimental details

Commercial AC (Norit® A Supra) and Nafion® used as the binder were supplied by Norit, Netherlands and Sigma Aldrich, respectively. Interdigitated electrodes (IDEs) were purchased from Nano SPR, USA.

AC was dispersed in an isopropanol/water solution (20/80, v/v) containing 0.2 wt.% Nafion® binder. The mixture was sonicated for 1 hour to obtain a uniform dispersion. Four 2-µL drops of the resulting ink were drop-cast onto pre-cleaned gold-plated IDEs, followed by drying under an infrared lamp, and then placed in a vacuum oven at 80 °C for 12 hours for complete drying.

The obtained sensing layers were tested at various NO_2 concentrations (1-20 ppm) at 25 °C. Relative responses were calculated as a function of resistance in NO_2 gas (R_{GAS}) and dry synthetic air (R_{AIR}) in two distinct ways: (i) fixing the initial or baseline resistance (R_{AIR_i}) of the sensors; (ii) using each new cycle's resistance ($R_{AIR_{ci}}$) as the initial resistance to calculate the responses.

$$Response,\ R_i\ (\%) = \frac{R_{AIR_i} - R_{GAS}}{R_{GAS}} \times 100\% \qquad \text{(i)}$$

$$Response, R_{ci}\ (\%) = \frac{R_{AIR_{ci}} - R_{GAS}}{R_{GAS}} \times 100\% \qquad \text{(ii)}$$

Results

Fig. 1(a, b) shows real-time dynamic response curves of sensors exposed to 1-20 ppm and 20-1 ppm NO_2 gas concentrations. The responses R_i (%) increased with increasing and decreasing NO_2 concentration, whereas R_{ci} (%) decreased with decreasing concentration. Since this specific AC is characterized by a high degree of microporosity and a large surface area with a multitude of adsorption sites, a greater number of NO_2 molecules at high concentration interact with the available sites, resulting in a higher degree of adsorption. This increased adsorption is directly correlated with a higher sensor response, indicating that a greater number of molecules are detected. The increase in R_i (%) at decreasing concentration can be attributed to an enhanced response resulting from the formula $R = (R_{air\ (initial)} - R_{gas})/R_{gas}$.

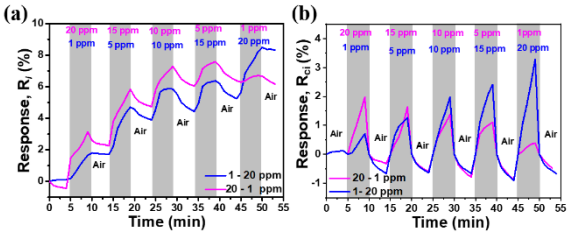


Fig. 1. Real-time dynamic responses of the AC-based sensor:; (a) R_i and (b) R_{ci} exposed to 1-20 ppm (blue) and 20 -1 ppm (pink) of NO_2 gas at 25 °C

As shown in Figs. 2(a, b) a limit in the response of our AC-based sensors was reached after 5.5 hours of exposure to 20 ppm NO_2 gas, with a constant response (R_i and R_{ci}) of 64.7%. The observed response limit is linked to the fact that a greater number of NO_2 gas molecules are physically adsorbed in the micropores via the pore-filling mechanism.

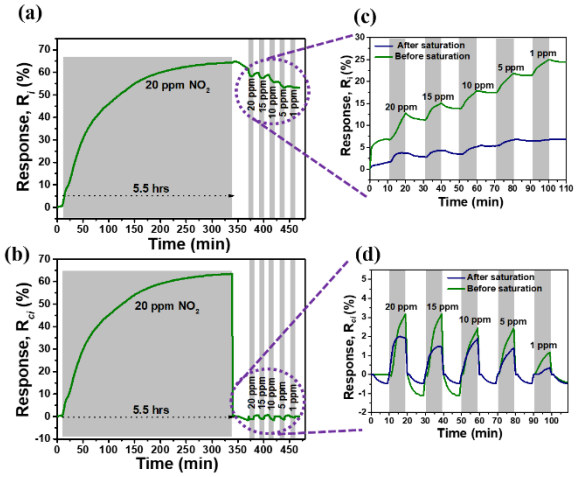


Fig.2 Response (a) R_i (%) and (b) R_{ci} (%) curves for saturation under 20 ppm NO_2 and dynamic response from 20 to 1 ppm. Responses (c) R_i (%) and (d) R_{ci} (%) curves showing the dynamic responses of the sensors for a new unsaturated sample (in green) and after saturation (blue, zoomed in from (a, b) when exposed to 20 ppm to 1 ppm of NO_2 gas after 5.5 hours at 25 °C.

When the adsorption/desorption cycles were repeated for decreasing NO_2 gas concentrations after saturation, a change in resistance could be observed, as illustrated in Figs. 2(a, b). The magnitude of the post-saturation response was weaker compared with a fresh new sample shown in green in Figs. 2(c, d). This can be attributed to high-energy binding sites on the AC that were tightly occupied by NO_2 molecules during saturation, resulting in an unrecoverable response. The saturation response (64.7%) remained higher than that of the fresh AC-based sensor at 20 ppm NO_2 gas, indicating that the charge transfer of previously strongly adsorbed NO_2 molecules significantly improves the overall response.

Conclusion

This work reports the capability of ACs to detect NO_2 gas at 25 °C and contributes to a deeper understanding of the performance of AC-based NO_2 gas sensors that are currently less studied.

References

[1] G. Jeong, H.J. Cheon, S.Y. Shin, E. Wi, P. Kyokunzire, H. Cheon, V. Van Tran, T.T. Vu, M. Chang, Improved NO_2 gas sensing performance of nanoporous conjugated polymer (CP) thin films by incorporating preformed CP nanowires, Dye. Pigment. 214 (2023)111235.https://doi.org/10.1016/j.dyepig.2023.111235.

[2] J.Y. Kim, A. Mirzaei, J.H. Kim, SnO_2 Nanowire/MoS_2 Nanosheet Composite Gas Sensor in Self-Heating Mode for Selective and ppb-Level Detection of NO_2 Gas, Chemosensors.12(2024)107.https://doi.org/10.3390/chemosensors12060107.

[3] US EPA, Primary National Ambient Air Quality Standards (NAAQS) for Nitrogen Dioxide | US EPA,(n.d.).https://www.epa.gov/NO_2 pollution/primary-national-ambient-air-quality-standards-naaqs-nitrogen-dioxide (accessed September 16, 2024).

[4] R. Pietrzak, T.J. Bandosz, Activated carbons modified with sewage sludge derived phase and their application in the process of NO_2 removal, Carbon N. Y. 45 (2007) 2537–2546. https://doi.org/10.1016/j.carbon.2007.08.030.

[5] P. Kyokunzire, J. Zaraket, V. Fierro, A. Celzard, Recent developments in the use of activated carbon-based materials for gas sensing applications, J. Environ. Chem. Eng. 12(2024)113702.https://doi.org/10.1016/j.jece.2024.113702.

Acknowledgements

P.K. is grateful to the French Ministry of Higher Education for funding this research.

DOI 10.5162/EUROSENSORS2025/T5.1.2

Ammonia flue gas sensors for SCR applications: A comparison between zeolite-based capacitive sensors and mixed-potential sensors utilizing vanadia-based electrodes

Ralf Moos[1,2], *Thomas Wöhrl*[1,2], *Nils Donker*[1], *Daniela Schönauer-Kamin*[1], *Gunter Hagen*[1,2]
[1] *Department of Functional Materials, University of Bayreuth, 95447 Bayreuth, Germany,*
[2] *Center of Energy Technology (ZET), University of Bayreuth, Germany*
Functional.Materials@Uni-Bayreuth.de

Summary:
Two different, planar, and very selective ammonia sensor types are compared in this study with regard to their applicability in flue gas from biomass combustion processes: a YSZ-based mixed potential sensor and a zeolite-based capacitive sensor. Both are operated at several hundred °C. The zeolite sensor shows a small cross-sensitivity to water vapor, whereas the signal of the mixed-potential sensor depends on O_2, especially at lower oxygen concentrations. In both cases the signal can be corrected by a lambda-probe. Both sensors behave well in real exhausts, both in flue gas and in real engine exhausts.

Keywords: Sensors for selective catalytic reduction (SCR), biomass combustion, zeolite-based sensors, mixed-potential sensors, high-temperature sensors

Background, Motivation and Objective

Biogenic materials are often used for CO_2-neutral energy production. For the combustion of biomass, limits for nitrogen oxide emissions (NOx) have to be met as well. Therefore, SCR (Selective Catalytic Reduction) systems are required. Here, ammonia (NH_3) or NH_3-forming substances (like liquid urea-water solutions) are added to the flue gas. NH_3 serves as a reducing agent for NOx. In order to control SCR-systems and/or to monitor their functionality, NH_3 sensors are required. Besides, NH_3 is seen as a CO_2-free energy carrier that can be shipped worldwide and that can even be burned directly in NH_3 combustion engines. Therefore, there is a need for selective and reliable NH_3 sensors, too.

This contribution compares two recently in our group developed sensor types for flue gas application: a capacitive zeolite-based and a YSZ-based NH_3 sensor.

Principles and Technology

The basic technological setup of both sensor types is similar. They are made in planar ceramic thick-film technology, which is well-established for years. On the lower side of the alumina substrate, there is a covered heater structure that also serves as a temperature sensor (Fig. 1a). On the upper side of the sensor tip, either planar interdigital electrodes covered by a zeolite functional film (Fig. 1c) or a YSZ film and two gold electrodes are applied. As a process simplification, the dense YSZ film was made by the recently developed powder aerosol deposition method (PAD or ADM) [1,2]. One electrode is covered with an SCR-active porous layer (Fig. 1b) that is responsible for the difference in the potential (U) between both electrodes in the presence of NH_3. It consisted of a commercial formulation based on vanadia, tungsten oxide, and titania (abbr. VWT) supplied by Johnson Matthey.

The sensor readout for the zeolite sensor is either impedimetric, or, if one stays at a defined frequency, here 700 kHz, the capacitance change can be used as the signal. As a remarkable feature, the interdigital electrode (IDE) structure was patterned to a line width and spacing of 20 µm [3,4]. The gas sensitive layer was a commercial H-ZSM5 zeolite with a module of 27 from ALSI Penta Zeolite GmbH.

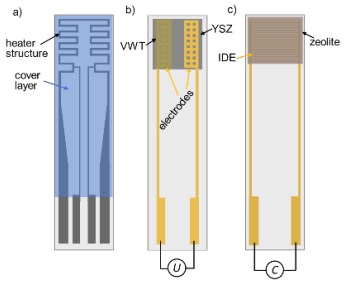


Fig. 1. Setup of the two sensors types.

YSZ-based NH_3 Mixed-Potential Sensor

The sensors were exposed to a synthetic exhaust containing water vapor, O_2, and N_2, as well as NH_3, NO and/or NO_2 as indicated. First of all, an optimum sensor temperature was looked for and 550 °C turned out to be a good compromise between sensitivity and noise. CO_2, and C_3H_8 were also added to the base gas and the sensors did not show any response to them.

A variation in the water vapor concentration did not affect the sensor signal *U*, too. At 550°C, the effect of varying O_2 concentrations, as it occurs in flue gas and the effect of NO, and NO_2 were studied. The results are shown in Fig. 2. Obviously, only at low O_2 concentrations in the exhaust, there is a dependency on NOx, with NO and NO_2 showing opposite signals.

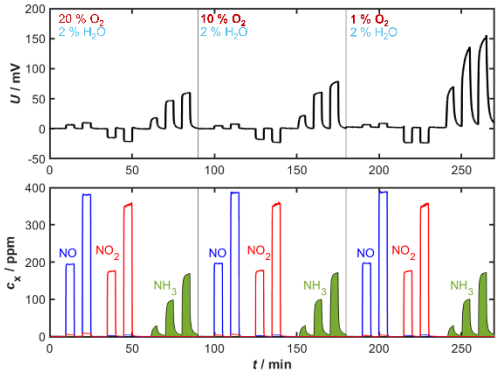


Fig. 2. Response of the mixed-potential NH_3 sensor.

Capacitive Zeolite-based NH_3 Sensor

Similar tests have been performed with the capacitive zeolite-based sensors. Here, 400 °C turned out to be the optimum temperature. The base gas consisted of O_2, CO_2, water vapor, and N_2 (as a balance). NO, NO2 and NH_3 were added as indicated. The results are shown in Fig. 3. Obviously, O_2 variations and additional tests with C_3H_8, CO, or H_2 do not affect the sensor response. However, the influence of water vapor on the sensor signal becomes noticeable.

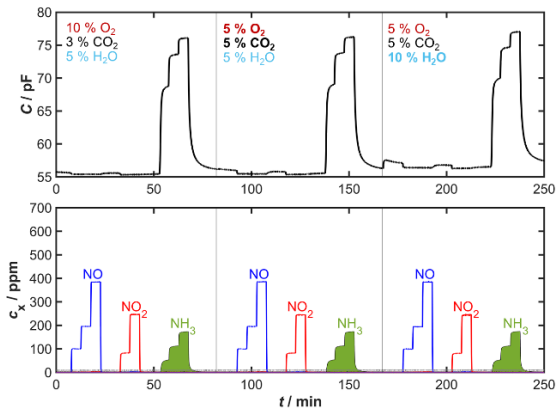


Fig. 3. Response of the zeolite-based NH_3 sensor.

Results and Discussion

Since the materials that are used for the sensor are well-known for harsh exhaust applications, long-term stability can be expected and has also been observed. Both sensors are very selective towards other components that may be present in flue gas exhausts. The mixed-potential sensor is operated at around 550°C. As a result, it requires slightly higher power than the zeolite sensor (400°C). However, it is better protected against soot deposits, as soot already burns off at this temperature. The zeolite sensor shows a small cross-sensitivity to water vapor (due to the sensor principle). This can be eliminated using an additional lambda probe or a humidity sensor. The mixed-potential sensor, however, is not sensitive to water vapor, but (also owing to the mixed-potential sensing mechanism) its signal depends on O_2, especially at lower oxygen concentrations. The signal can be corrected by a lambda-probe, too.

When NH_3 and NOx are simultaneously present in the flue gas, one has to consider that both gas sensitive materials, zeolite H-ZSM5 and VWT catalyze the SCR reaction. Therefore, there is some cross-sensitivity towards NOx if NH_3 is present, which has been very recently investigated in detail [4]. Especially NO_2 that is more SCR-active than NO is responsible for this interfering effect (so-called fast SCR reaction).

Further tests showed that both sensors behave well in real exhausts, both in flue gas and in real engine exhausts. These data will be presented in the conference as well.

References

[1] M. Schubert, et al., Powder aerosol deposition method — novel applications in the field of sensing and energy technology, *Functional Materials Letters*, 12, 1930005 (2019); doi: 10.1142/S1793604719300056

[2] N. Donker, D. Schönauer-Kamin, R. Moos, Mixed-Potential Ammonia Sensor Based on a Dense Yttria-Stabilized Zirconia Film Manufactured at Room Temperature by Powder Aerosol Deposition, *Sensors*, 24, 811 (2024), doi: 10.3390/s24030811

[3] T. Wöhrl, J. Kita, R. Moos, G. Hagen, Capacitive, Highly Selective Zeolite-Based Ammonia Sensor for Flue Gas Applications, *Chemosensors*, 11, 413 (2023), doi: 10.3390/chemosensors11070413

[4] T. Wöhrl, R. Moos, G. Hagen, Analyzing the cross-sensitivities of a zeolite-based ammonia sensor for SCR systems for application in the flue gas of biogenic waste combustion, *Sensors and Actuators B: Chemical*, 436, 137727 (2025); doi: 10.1016/j.snb.2025.137727.

DOI 10.5162/EUROSENSORS2025/T5.1.3

Enhanced Hydrogen Sensing Using Palladium-Functionalized MoO3-x Nanosheets Synthesized via Anodic Oxidation

Shohreh Shahabadi[1], Mehdi Ranjbar[1], Vahid Salari[2], AmirHossein Tavallaei[1]
1 Department of Physics, Isfahan University of Technology, Isfahan, 841568311, Iran,
2 Quantum cloud lab, University of Calgary, Calgary, Canada.
Corresponding Author: s.shahabadi@ph.iut.ac.ir

Summary:
Defective metal oxides are promising for gas sensing due to enhanced free carrier concentrations. In this work, reduced molybdenum oxide nanosheets (MoO_{3-x} NSs) were synthesized on alumina substrates using a fast electrochemical method and decorated with palladium chloride. Structural and morphological analysis confirmed temperature-dependent properties. Hydrogen sensing tests showed that operating temperature significantly affects response and recovery times, demonstrating the material's potential for efficient gas sensor applications.

Keywords: hydrogen sensing, reduced MoO3 nanosheets, Metal oxide, Palladium, Response time.

Background

Hydrogen, a clean and efficient energy carrier, is used in fuel cells, electric vehicles, and power systems. However, its wide flammability range (4–75%), low ignition energy, and invisibility pose significant safety risks, making hydrogen sensors crucial for early leak detection in industrial settings at low concentrations [1,2]. Effective sensors must offer high sensitivity and selectivity under real-world conditions. Resistive sensors based on semiconductor metal oxides are preferred due to their stability, simplicity, and scalability. Molybdenum trioxide (MoO_3), with its unique layered structure and high electron mobility, shows promise, especially in its substoichiometric form (MoO_{3-x}), which exhibits enhanced conductivity and gas-sensing performance due to oxygen vacancies [3]. This study focuses on synthesizing MoO_{3-x} nanosheets via anodic oxidation and functionalizing them with $PdCl_2$ to improve hydrogen sensitivity, aiming to develop a cost-effective, fast-response sensor.

Description of the New Method and system

MoO_{3-x} nanosheets were synthesized through anodic oxidation of high-purity molybdenum in 0.02 M HCl at 30 V for 15 minutes, yielding oxygen vacancy-rich structures with enhanced conductivity. The nanosheets were drop-cast onto Al_2O_3 substrates with gold electrodes and functionalized with $PdCl_2$ to boost hydrogen adsorption. Hydrogen sensing was evaluated in a custom chamber using static H_2 injection (10% H_2/Ar, diluted), alternating 210 s exposure and 180 s recovery under vacuum at 150–300 °C. Ar served as the carrier gas, ambient air enabled recovery, and RH was kept at ~30%. Electrical signals were recorded via IVIUMSTAT potentiostat, with sensor response calculated as:

$$\mathrm{Re}sponce = \frac{R_{air} - R_{gas}}{R_{gas}} \qquad (1)$$

Where R_{air} and R_{gas} are the resistances in air and hydrogen, respectively.

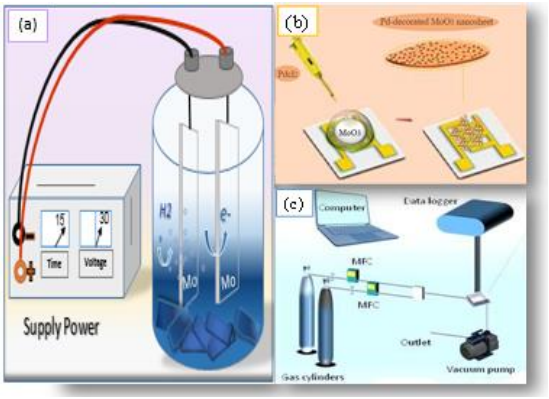


Figure 1 *Schematic of (a) anodic synthesis of MoO_{3-x} nanosheets, (b) Pd functionalization on gold electrodes, and (c) hydrogen gas sensing system.*

Results and Discussion

The structural and morphological properties of MoO_{3-x} nanosheets (NSs) were analyzed using XRD, Raman spectroscopy, FESEM, and TEM. XRD (Fig. 2a) revealed a nanocrystalline structure with broad peaks, indicating partial disorder.

Raman spectroscopy (Fig. 2b) identified characteristic O–Mo–O and Mo=O vibrations, suggesting oxygen vacancies. FESEM (Fig. 2c) showed a wrinkled, layered structure, while TEM (Fig. 2d) confirmed stacked nanosheets with dispersed nanoparticles, enhancing the surface area for gas sensing. XPS analysis (inset of Fig. 2d) confirmed the presence of molybdenum, oxygen, and residual carbon.

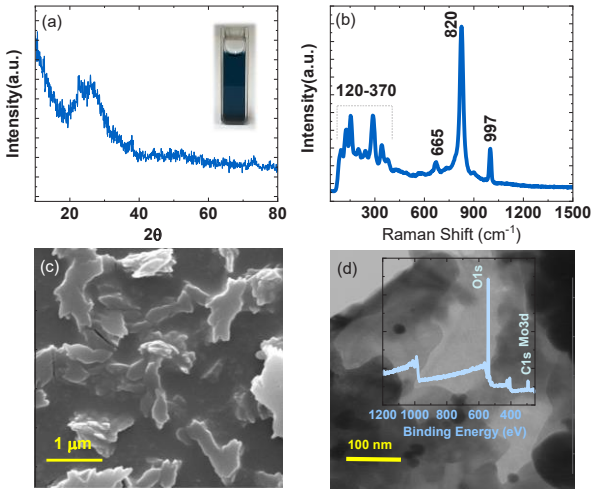


Figure 2 *MoO_{3-x} NSs charecterization, (a) XRD, (b) Raman spectroscopy, (c) SEM, (d) TEM(inside: XPS survey scan).*

Hydrogen sensing performance of the MoO_{3-x} NSs was assessed by monitoring the variation in electrical resistance under controlled gas exposure at different operating temperatures (Fig. 3a). When 10% H_2 gas was injected for 210 seconds, a notable increase in electrical current (decrease in resistance) was observed, especially at elevated temperatures. This behavior aligns with the n-type semiconducting nature of molybdenum oxide, where hydrogen exposure donates electrons and enhances conductivity. As shown in Fig. 3b, the sensor response significantly increased with temperature, peaking at 300 °C. The response was reversible upon returning to air, demonstrating excellent repeatability and stability. Figure 3c highlights the response after 210 seconds of hydrogen exposure, with negligible sensitivity at 150 °C and sharp increases above 250 °C, reaching maximum values exceeding 22200(222/%, in diagram). This temperature dependence emphasizes the importance of high temperatures for sensor performance. Figure 3d shows the response and recovery times, with response times under 210 seconds and recovery times under 8 seconds, demonstrating fast kinetics. This combination of high response, rapid recovery, and stability makes Pd-decorated MoO_{3-x} NSs promising for efficient, low-cost hydrogen sensing, particularly in high-temperature environments.

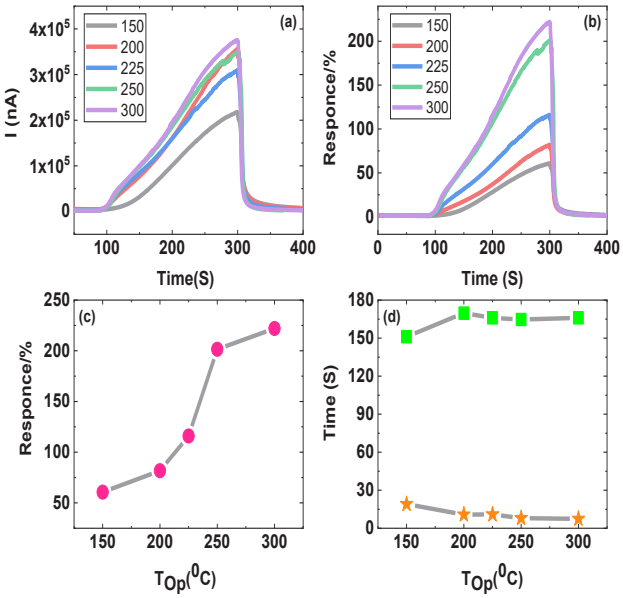


Figure 3 *(a) Current variation of MoO_{3-x} NSs during H_2 exposure; (b) dynamic response of Pd-functionalized NSs at different temperatures; (c) response at 210 s; (d) response/recovery times vs. temperature.*

The MoO_3 NSs demonstrated high selectivity for hydrogen at 300 °C, showing significantly higher response to H_2 than to CO_2, NO_2, CH_4, and ethanol, confirming their specificity and suitability for reliable gas sensing applications.

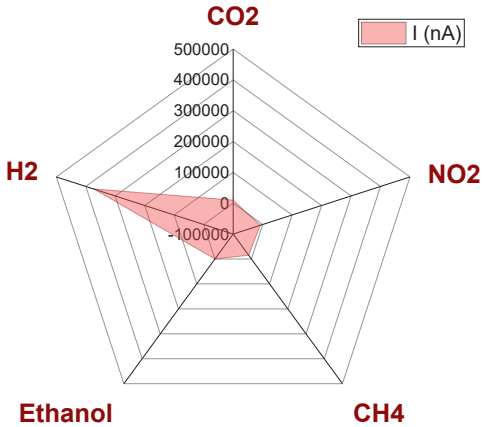


Figure 4 *Hydrogen selectivity of sample at the operation temperature of 300 °C.*

References

[1] M. Yue, H. Lambert, E. Pahon, R. Roche, S. Jemei, D. Hissel, Hydrogen energy systems: A critical review of technologies, applications, trends and challenges, Renew. Sustain. Energy Rev. 146 (2021).

[2] S.H. Kim, K.S. Yun, Room-temperature hydrogen gas sensor composed of palladium thin film deposited on NiCo2O4 nanoneedle forest, Sensors Actuators B Chem. 376 (2023).

[3] Q. Li, L. Wang, A. Xiao, L. Zhu, Z. Yang, Hydrogen sensing towards palladium-based nanocomposites: A review, Int. J. Hydrogen Energy. (2024).

DOI 10.5162/EUROSENSORS2025/T5.1.4

Room Temperature CO_2 Gas Sensor Based on Carbon Polymer Dots - PEDOT:PSS Composite Thin Film

Anna Maria Laera[1], *Gennaro Cassano*[1], *Michele Penza*[1]
[1] *ENEA-Italian National Agency for New Technologies, Energy and Sustainable Economic Development, Brindisi Research Centre, S.S. 7, Km 706, 72100, Brindisi, Italy.*
Corresponding Author's: annamaria.laera@enea.it

Summary

A green synthetic method was developed to produce carbon polymer dots with a high content of amino groups. A composite material, obtained dispersing the synthetized dots in the conductive polymer matrix PEDOT:PSS (Poly(3,4-EthyleneDiOxyThiophene) PolyStyrene Sulfonate), was used to fabricate a low-cost, flexible chemiresistive gas sensor for CO_2 detection in the concentration range 150-3000 ppm. The sensor device showed high response and good repeatability upon CO_2 exposure at room temperature with negligible responses towards CO. Being a stronger Lewis acid, the CO_2 can accept lone pairs of electrons from amino groups on carbon dots surface.

Keywords: carbon polymer dots, gas sensors, chemiresistive sensors, interdigitated electrodes, flexible electronics.

Introduction

The monitoring of CO_2 has great relevance for environmental protection and global warming control. Being the combustion product of fossil fuel, solid waste and other biologic materials, CO_2 is considered the main greenhouse gas responsible for climate change. The CO_2 measurements also play a crucial role for many industrial uses such as food packaging, carbonation of beverages, and fertilizer production. In addition, to ensure safety in workplaces and in all confined indoor spaces the maximum amount of CO_2 should be in the range 350-800 ppm. Higher concentrations can induce headaches, sore throat and nasal irritation [1]. Currently, CO_2 sensors are mostly based on rigid ceramic materials that require a high operating temperature. In present study a composite material, obtained dispersing Carbon Polymer Dots (CPDs) in the conductive polymer matrix PEDOT:PSS, was used to fabricate a low-cost, flexible chemiresistive gas sensor for CO_2 detection at room temperature. CPDs are promising low-cost materials, generally produced with simple synthesis methods, and results superior to traditional semiconductor quantum dots for robustness, chemical inertness, and biocompatibility, being non-toxic compounds that do not contain metals [2]. The proposed sensor, based on CPDs - PEDOT:PSS composite, showed high responses and good repeatability upon CO_2 exposure with negligible responses towards interfering CO molecules.

Materials and methods

The dipicolinic acid, chosen as precursor for CPDs, was mixed to an excess of freshly distilled ethylenediamine without solvent addition. The CPDs were obtained by applying a steady temperature of 300°C for 30 minutes in a microwave reactor. Finally, ethanol was added on the crude reaction mixture and the solid carbon nanoparticles were separated through centrifugation for 5 min at 1000 rpm. The carbon dots were recovered by water dissolution. To fabricate the sensor device, a water solution of CPDs and PEDOT:PSS with weight ratio 1:1 was dropped on flexible substrate made by PolyEthylene Terephthalate (PET), previously coated with inkjet-printed interdigitated electrodes in silver (Ag). The chemiresistive sensor was located in a sealed stainless cell and exposed to synthetic air (reference gas) and to several dilutions of CO_2 in dry air keeping the flow rate constant as 1000 sccm.

Results

With the aim to produce nitrogen rich CPDs, a precursor containing a pyridinic nitrogen moiety, as the dipicolinic acid, and an excess of ethylenediamine were selected as starting reagents. A composite material, obtained dispersing the synthetized CPDs in the conductive polymer matrix PEDOT:PSS, was used to fabricate a chemiresistive gas sensor for CO_2 detection in the concentration range 150-3000 ppm at room temperature. Typical gas detecting curves, reported in Figure 1, put in evidence an increase

of electrical resistance upon exposure to 1000, 500 and 250 ppm of CO_2. Being a Lewis acid, the chemisorbed CO_2 can accept lone pairs of electrons from nitrogen atoms on CPDs surface, reducing the number of major charge carriers, and consequently increasing the electrical resistance.

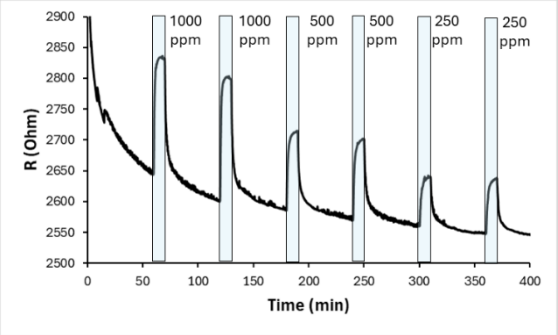


Fig. 1. Sensor resistance versus time upon exposure of decreasing CO_2 concentrations of 1000, 500 and 250 ppm at room temperature.

The sensor response (SR%) was calculated by the following relationship:

$$SR\% = \left(\frac{Rg-Ra}{Ra}\right) * 100 \qquad (1)$$

where R_g and R_a are the electrical resistance measured with exposure to gas and air, respectively. The logarithmic fitting curve of SR% versus CO_2 concentration was reported in Figure 2. The sensor response versus the logarithm of concentration can well fitted by a straight line in the investigated concentration range 150-3000 ppm (inset of Fig. 2). No sensor responses were recorded in an analogous device fabricated with pure PEDOT:PSS films.

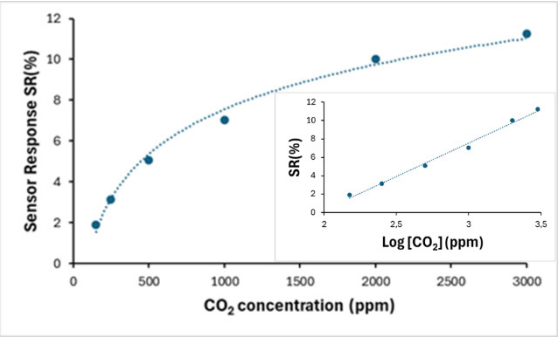


Fig. 2. Sensor response versus gas concentration and sensor responses versus the logarithm of concentration in the inset.

As additional relevant indicators of device performances, the response time and the recovery time were calculated considering the required time to reach 90% of the maximum response under CO_2 exposure and the 10% under reference gas exposure, respectively. An average value of 160 sec was calculated as response time, while the recovery time was almost double. No significant responses were obtained exposing the same sensor to several CO concentrations. The amino groups on CPDs surface selectively interact with CO_2 that is a stronger Lewis acid. The acid-base reactions between the amino groups and CO_2 promote the formation of ions such as carbamates and bicarbonates, which in turn, contribute to change in the resistance of the sensor active layer. Repeated exposure test at 2000 ppm of CO_2, showed in Figure 3, demonstrated the good stability of the baseline resistance and the good reproducibility of measurements.

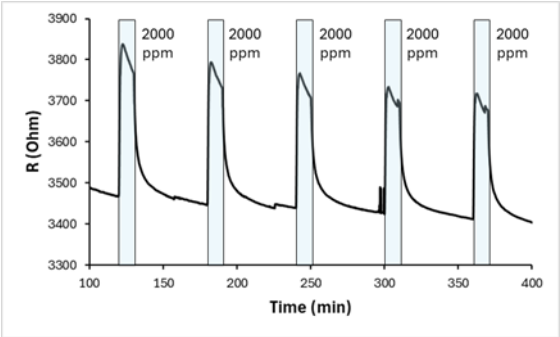


Fig. 3. Five repeated exposure tests at 2000 ppm of CO_2.

Conclusions

In summary, a green synthetic method was developed to produce nitrogen rich CPDs and a chemiresistive flexible sensor to monitor CO_2 at room temperature was fabricated by using a CPDs - PEDOT:PSS composite material. The sensor device showed high responses and repeatability upon CO_2 exposure in the large concentration range 150-3000 ppm with negligible sensitivity towards CO. The presented data highlighted the CPDs potential in sensing applications. Due to the simple design and fabrication process, the described sensor could lead to the implementation of flexible wearable devices suitable for air quality monitoring in confined workspaces such as mines and manufacturing facilities including indoor monitoring.

References

[1] A. Molina, V. Escobar-Barrios, J. Oliva, A review on hybrid and flexible CO_2 gas sensors, *Synthetic Metals* 270, 116602 (2020); doi: 10.1016/j.synthmeth.2020.116602.

[2] C. Xia, S. Zhu, T. feng, M. Yang, B. Yang, Evolution and synthesis of carbon dots: from carbon dots to carbonized polymer dots, *Advanced Science* 6, 1901316 (2019); doi: 10.1002/advs.201901316.

Acknowledgements

This study was funded by project SENSAIR (*Gas SENSing solutions for smart AIR monitoring applications)* granted by Italian PNRR cascade call SAMOTHRACE - Next Generation EU.

DOI 10.5162/EUROSENSORS2025/T5.2.1

Early-stage Detection of Ovarian Cancer through E-nose Odor Profile Determination

Jens Eriksson[1,2] *Ivan Shtepliuk*[1], *Lingyin Meng*[1], *Christer Borgfeldt*[3], *Donatella Puglisi*[1]
[1] *Department of Physics, Chemistry and Biology, Linköping University, 58183 Linköping, Sweden,*
[2] *VOC Diagnostics AB, LEAD Linköping AB Teknikringen 7, Sweden*
[3] *Department of Obstetrics and Gynecology, and Department of Biomedical and Clinical Sciences, Linköping University, Linköping, Sweden*
jens.eriksson@liu.se

Summary:
Endogenous volatile organic compounds (VOCs) are products of metabolic activity. Metabolite concentrations are affected by tumor necrosis, resulting in cancer-specific VOC patterns. Here we introduce an e-nose for use in cancer diagnostics based on odor detection from 1 ml of blood plasma. Based on measurements of 169 samples from cancer patients (124 ovarian cancer patients and 45 endometrial cancer patients in stages I – IV) along with 161 negative controls, our machine-learning model can distinguish between cancer and healthy samples with a sensitivity of 96.9%**,** and a specificity of 97.1%.

Keywords: Cancer, diagnostics, electronic nose, machine learning, early detection, ovarian cancer

Background, Motivation and Objective

While the risk of dying from cancer has steadily declined over the last 30 years, global annual cancer incidences are around 19.3 million, with nearly 10 million people dying from cancer each year [1]. Many of them would not need to if the condition had been detected at an early stage. A subcategory of cancers known as the silent killers are characterized by being asymptomatic until late stages, resulting in bleaker prognosis upon diagnosis. Ovarian cancer (OC) is often asymptomatic with 60-75% of patients diagnosed at late stages [2]. To exacerbate the problem, there are also no viable screening tests available for this silent killer, meaning that early-stage detection is rare.

Description of the New Method or System

Here we introduce an electronic nose that allows shining a light on these wannabe killers while they are immature, thereby enabling their removal before they grow into killers. The primary target is early detection of OC using an approach based on condition-specific odor patterns resulting from metabolites found in blood. Endogenous volatile organic compounds (VOCs) are products of metabolic activity whose concentrations in blood are affected by tumor necrosis, resulting in VOC patterns that are specific to cancer type, subtype, and stage. The results discussed here come from measurements of 169 blood samples from cancer patients (124 OC- and 45 endometrial cancer patients in stages I – IV) together with 161 healthy controls.

The specific electronic nose [3] comprises 4 × 8 chemiresistive sensors (TGS2X series, FIGARO INC. IL, USA) designed towards interaction with different classes of molecules, arranged in four banks operating at different temperatures. Samples (blood plasma) are placed in a holder which is inserted into the instrument at the start of a measurement. After an equilibration step where VOCs are emitted into the instrument-headspace, a fan moves the VOCs over the sensors. The signals from 32 sensors upon interaction with the sample-specific VOCs are recorded for ten minutes at 10 Hz during a measurement and are used to train offline machine learning (ML) models that are used for stepwise binary classification based on 85 features extracted from preprocessed sensor data (see Fig. 1). Each classifier pertains to an ML model trained on known (labeled) data and is used to determine the class (cancer/no cancer, cancer type, and cancer stage) of blind samples. The final classification algorithm is transferred to the instrument and allows a diagnostic prediction on unknown blood samples immediately after the 10 min measurement.

Results

Signal preprocessing, feature extraction, classifier training and testing, performed using three independent approaches, all show overall accuracy higher than 98%. For the best model, binary classification as either “cancer” or “healthy” based on 85 features and a random forest

classifier resulted in sensitivity = 96.9%, specificity = 97.1%, and an ROC-AUC of 0.995 using a 10/90 train/test split. Additional classifiers were implemented sequentially for further division into cancer type and stage, allowing identifying OC and endometrial cancers with sensitivities of 94.8% and 93.1%.

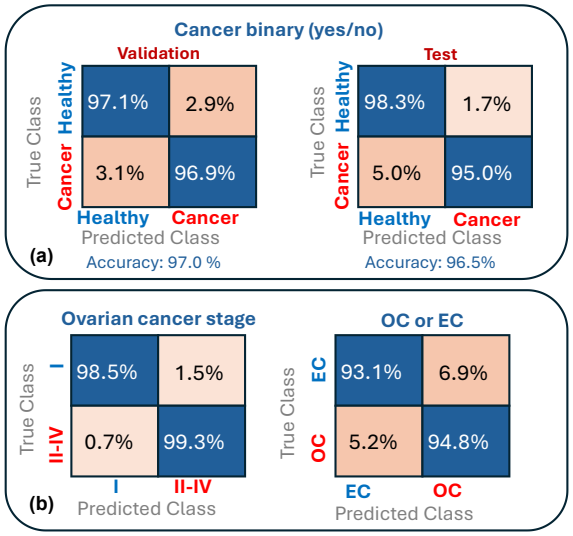


Fig. 1. Confusion matrices showing the classification at (a) validation and test stages for binary classification between healthy controls and the two studied cancer types grouped together as just one class, and (b) validation confusion matrices for classification of ovarian cancer stage I or II – IV (left panel) and distinction between ovarian- (OC) and endometrial cancer (EC) (right panel).

References

[1] Sung H, Ferlay J, Siegel RL, Laversanne M, Soerjomatram I, Jemal A, Bray F. Global cancer statistics 2020: GLOBOCAN estimates of incidence and mortality worldwide for 36 cancers in 185 countries. *CA Cancer J Clin*. 2021: 71: 209 – 249, https://doi.org/10.3322/caac.21660

[2] Leandersson P, Hogberg T, Dickman PW, Malander S, Borgfeldt C. Incidence and survival of epithelial ovarian, fallopian tube, peritoneal, and undesignated abdominal/pelvic cancers in Sweden 1960–2014: A population-based cohort study. BMC Cancer. 2021;21(1):465)

[3] J. Eriksson, D. Puglisi, C. Borgfeldt, Electronic Nose for Early Diagnosis of Ovarian Cancer, *Proceedings* 97, 145 (2024); doi: 10.3390/proceedings2024097145

Acknowledgements

The work was carried out within the Strategic Innovation Programs Swelife and MedTech4Health, a joint venture of Vinnova, Formas and the Energy Agency, grant No. 2022-03464 and grant No. 2023-03874, and within the Convergence Accelerator Program (Track L – Real-World Chemical Sensing Applications), funded by the Swedish Research Council, Vetenskapsrådet, grant No. 2023-07219, and Sweden's Innovation Agency, Vinnova, grant No. 2023-04186, in collaboration with the US National Science Foundation (NSF).

DOI 10.5162/EUROSENSORS2025/T5.2.2

An Optically-Induced Dielectrophoresis-Based Platform for Enhanced Identification of Prostate Cancer Cells with Different Grades of Malignancy

J. Filippi[1,2], P. Casti[1,2], F. Corsi[3], A. Pelliccia[4], G. Antonelli[1,2], G. Curci[1,2], M. D'Orazio[1,2], A. Riccardi[1,2], E. Debbi[1,2], M. Scagliotti [5], L. Mariucci[5], A. Mencattini[1,2], S. L. Neale[6], E. Martinelli[1,2]

[1]Department of Electronic Engineering, University of Rome Tor Vergata, Via del Politecnico 1, 00133 Rome, Italy
[2]Interdisciplinary Center for Advanced Studies on Lab-on-Chip and Organ-on-Chip (ICLOC), Via del Politecnico 1, 00133 Rome, Italy
[3]Department of Chemical Sciences and Technologies, University of Rome Tor Vergata, 00133 Rome, Italy
[4]U.O.S.D. Medical Oncology, Fondazione PTV - Policlinico Tor Vergata, 00133 Rome, Italy
[5]Italian Nation Research Council (CNR), Rome, Italy
[6]James Watt School of Engineering, University of Glasgow, Glasgow, UK
Corresponding Author's e-mail address: filippi@ing.uniroma2.it

Summary:

Understanding phenotypic heterogeneity at the single-cell level is essential for precise diagnosis and treatment evaluation. The integration of optically-induced dielectrophoresis (ODEP) with microfluidics, live-cell imaging, and machine learning offers a rapid, label-free, and non-invasive method for cell manipulation and analysis. By studying the defocusing dynamics of individual cells under varying DEP-induced frequencies, this platform generates unique phenotypic signatures to distinguish between cell types presenting different tumorigenicity levels.

Keywords: optically-induced dielectrophoresis, lab-on-chip, machine learning, single-cell analysis, prostate cancer

Background, Motivation an Objective

The ability to distinguish and classify individual cells within a heterogeneous population remains a major technological bottleneck in biomedical research, especially in cancer diagnostics [1]. Conventional cell classification methods often rely on biochemical markers or morphological features, which can be invasive, time-consuming, or limited in sensitivity. In this context, we propose a novel platform based on defocused optical analysis integrated with optically-induced dielectrophoresis (ODEP) [2] to stratify cancer cell types in a label-free and high-throughput manner. This approach exploits the subtle phase and contrast changes observed when cells are slightly out of focus, providing a unique optical fingerprint that can be used to differentiate subpopulations at the single-cell level. This technological innovation holds particular relevance for prostate cancer (PCa), the second most common malignancy among men worldwide. The disease is characterized by extreme phenotypic and molecular heterogeneity, complicating diagnosis, prognosis, and therapy selection [1]. Addressing this complexity requires tools capable of resolving single-cell variability efficiently and cost-effectively. In previous works, ODEP has been revealed to be a powerful method for single-cell dielectric characterization by evaluating individual cell responses across a frequency spectrum [3,4,5]. Here, we introduce a novel platform that integrates ODEP with microfluidics, live-cell imaging, and machine learning to extract dynamic information along the z-axis, a dimension typically overlooked in cell classification. By analyzing the depth-dependent optical signatures generated during DEP-induced motion, the system captures previously untapped features that reveal intrinsic phenotypic differences.

Description of the Method

The proposed approach exploits a novel DEP-induced dynamic to extract novel information content for better single-cell stratification. In detail, PCa cells were suspended in a low-conductivity buffer, loaded into a lab-on-chip device,

trapped, and measured with the ODEP-based platform, as shown in Figure 1. In particular, we considered hundreds of PC3 (human prostate cancer) cells, representative of castration-resistant cancer with high tumorigenicity, and LNCaP (Lymph Node Carcinoma of the Prostate) as androgen-sensitive cancer with low tumorigenicity (see Fig. 1a).

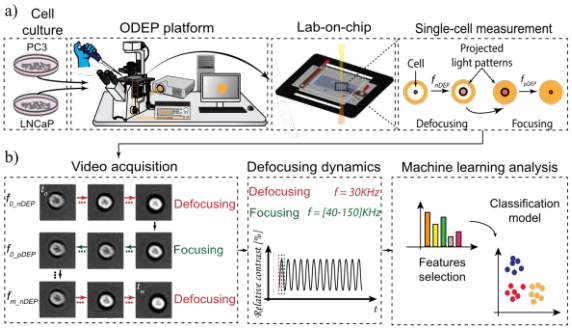


Fig. 1. General overview of the platform for the single-cell analysis. a) Measurement procedure. Cells were loaded into the LOC device for measurement. b) Analysis. TLM videos were acquired and analyzed. The features extracted and selected from the defocusing dynamic allow to build the classification model.

An AC signal was applied to the device, and light patterns were projected on the photosensitive substrate (amorphous silicon). The novel measurement approach involves multiple stimulation cycles to induce defocusing dynamics on the single cell. We considered an amplitude of 7 Vpp and varying frequencies, producing two different cell motions induced by the dielectrophoretic (DEP) force: attractive (pDEP) and repulsive (nDEP). A doughnut shape pattern was projected at 30 kHz to induce nDEP along the z-axis, alternating with a circular pattern at different attractive frequencies in range [40-150] kHz with step 10 kHz (see Fig. 1a). We acquired videos of cell responses recorded via time-lapse microscopy (TLM) (see Fig. 1b). For each video, a region of interest including the dynamic responses of a single cell was automatically extracted, after appropriate normalizations. The contrast was evaluated frame by frame with the Michelson formula (see Eq. (1)).

$$\boldsymbol{contrast(t)} = \frac{\max_{x,y}[I(x,y,t)] - \min_{x,y}[I(x,y,t)]}{\max_{x,y}[I(x,y,t)] + \min_{x,y}[I(x,y,t)]} \qquad (1)$$

A smoothed signal of the defocusing dynamic, in terms of variations relative to the first frame, was obtained for each cell as a unique signature of each cell type. After performing feature extraction and selection, an LDA classification model was built using the most automatically selected features (see Fig.1b).

Results

The stimulation cycles change the relative contrast of the single cell (with respect to the first frame). For example, Figures 2a and 2b show signals representing the percentage of relative contrast for a PC3 and a LNCaP cell, respectively. A number of 24 descriptors were extracted from the smoothed signals. The selected features were used to build an LDA classification model. The average accuracy, obtained with 10-fold cross-validation, increases with the number of considered stimulation cycles, as shown in Figure 2c. On average, the maximum value is 88.2%, with a standard deviation of 7.6% in correspondence of the 9th cycle. Figure 2d shows the confusion matrix of the classification model.

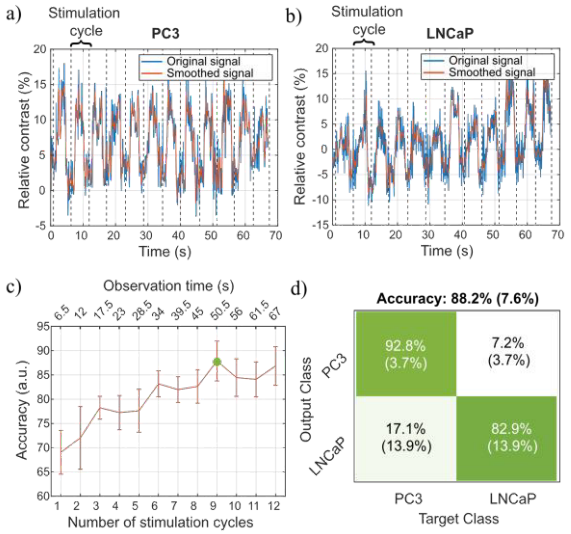


Fig. 2. a) Percentage of relative contrast for PC3 and (b) LNCaP cells. c) Classification accuracy as a function of the number of stimulation cycles. The green dot identifies the maximum value corresponding to the 9th cycle. d) Confusion matrix of the LDA classification model.

References

[1] M.C. Haffner, et al., Framework for the pathology workup of metastatic castration-resistant prostate cancer biopsies, *Clinical Cancer Research* 31.3, 466-478 (2025); doi: 10.1158/1078-0432.CCR-24-2061.

[2] P. Y. Chiou, et al., Massively parallel manipulation of single cells and microparticles using optical images, *Nature* 436.7049: 370-372 (2005); doi: 10.1038/nature03831.

[3] J. Filippi, et al., Exploiting spectral information in Opto-Electronic Tweezers for cell classification and drug response evaluation, *Sensors and Actuators B: Chemical*, 368, n.132200 (2022); doi: 10.1016/j.snb.2022.132200.

[4] J. Filippi, P. Casti, et al., Cell Electrokinetic Fingerprint: A Novel Approach Based on Optically Induced Dielectrophoresis (ODEP) for In-Flow Identification of Single Cells, *Small Methods*, 8(8), n. 2300923 (2024); doi: 10.1002/smtd.202300923.

[5] J. Filippi, P. Casti, et al., ODEP-based Robotic System for Micro-Manipulation and In-Flow Analysis of Primary Cells, *Cyborg and Bionic Systems* 6, 0234 (2025); doi: 10.34133/cbsystems.0234.

DOI 10.5162/EUROSENSORS2025/T5.2.3

Signal Averaging with Heartbeat Envelope for Non-Contact Heart Sound Measurement

Shun Muramatsu[1], Jarred W. Fastier-Wooller[1], Michitaka Yamamoto[1], Toshihiro Itoh[1]
[1] Dept. Precision Engineering, Graduate School of Engineering, The University of Tokyo, 7-3-1 Hongo, Bunkyo-ku, 113-8656, Tokyo, Japan
smuramatsu@g.ecc.u-tokyo.ac.jp

Summary:
We propose a non-contact heart sound measurement method using signal averaging in conjunction with the heartbeat envelope as a trigger. The performance of the heartbeat envelope was 0.01 s as the standard deviation of the R-R interval estimation error, meeting the trigger requirement for our signal averaging method. The main component of the heart sound was extracted from a sound signal measured 40 mm away from the chest wall.

Keywords: heart sound, non-contact measurement, signal averaging, heartbeat, microphone

Introduction

Cardiovascular disease (CVD) is the most common causes of death worldwide [1]. Heart sound monitoring is a popular approach to early detection of these diseases. There have been many studies to measure heart sounds using wearable devices [2]. However, these devices are not yet widely used in the world. One of the reasons for this is that these wearable devices have disadvantages such as discomfort due to constant wear and the need for intermittent charging. Therefore, a non-invasive and user-friendly heart sound monitoring method is desirable.

Previously, we have attempted to measure heart sound without contact [3,4]. In particular, we have proposed an approach using signal averaging, and reported that signal averaging with an appropriate trigger, e.g., an electrocardiogram (ECG), can extract the heart sound from the non-contact measured sound [4]. However, because ECG measurement requires contact, a method is required to acquire the appropriate trigger without contact.

In this study, we propose to use the heartbeat envelope instead of the ECG as the trigger, and the performance of this trigger is clarified.

Materials and Methods

The outline of our method is illustrated in Fig. 1. Heart sound is extracted from a non-contact measured sound through signal averaging using heartbeat envelope as the trigger. The heartbeat envelope is the power variability of the heart sound and was extracted from non-contact measured sound using independent component analysis (2-ch), full-wave rectification, and low-pass filtering (5 Hz, 1st order, Butterworth).

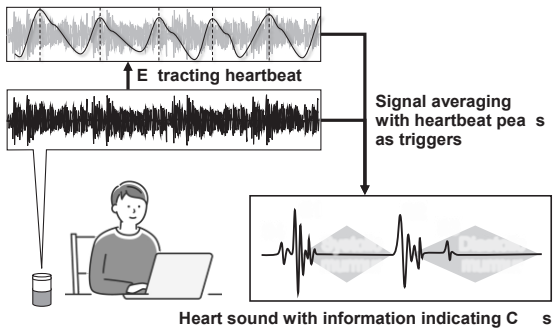


Fig. 1. Outline of our signal averaging method for non-contact heart sound measurement.

The sound was measured using two sets of a microphone and preamplifier (MI-1235 and IM-3111, Ono Sokki Co., Ltd.) in a quiet conference room. The front of the microphone was positioned at a distance of 40 mm from the chest wall. The measurement duration was 180 seconds. During the measurement, the subject (the first author) was shirtless, sat motionless in a chair, and breathed slowly. The sampling frequency and quantization resolution are 48 kHz and 16 bits, respectively. The measured sound was preprocessed using a bandpass filter (10 Hz to 1000 Hz, 1st order Butterworth) to extract the frequency range of the heart sound.

ECG readings were acquired simultaneously with the heart sound to use as a reference for the appropriate trigger. It was measured using a 3-point induction method with an ECG monitor (AD8232 SparkFun Single Lead Heart Rate Monitor, SparkFun Electronics).

Results and Discussion

Figure 2 shows an example of the synchronized ECG and the heartbeat envelope. This indicates that the heartbeat envelope was successfully extracted to sufficiently detect the peaks. Specifically, the peaks of the ECG and the heartbeat appear alternately, and there are near-constant delays between the two of approx. 64 ms.

Figure 3 shows the error of the R-R interval (RRI) estimated by the heartbeat, compared to the reference RRI. The mean ± standard deviation is – 0.0004 ± 0.01 s. This value meets the trigger accuracy (below 0.04 s [4]) for our signal averaging method. On the other hand, the errors are in three clusters. This is because the envelope consists of two small peaks instead of one. We believe that this variance can be reduced by using cross-correlation functions.

Figure 4 (a) shows the raw sound. This represents the difficulty of non-contact heart sound measurement due to the low power of the heart sound. Figure 4 (b) shows the sound extracted by the signal averaging with the ECG trigger. The number of detected peaks was 220. This sound has both S1 and S2, which are the main components of the heart sound. It indicates that signal averaging with an appropriate trigger is effective for non-contact heart sound measurement. Figure 4 (c) shows the sound extracted by signal averaging with the heartbeat envelope trigger. The number of detected peaks was 207. The resulting sound has S1, which means that the heartbeat envelope trigger works properly. In other words, this demonstrates the feasibility of complete non-contact heart sound measurement. On the other hand, the waveform remains noisy even from a distance as short as 40 mm. Therefore, the proposed method shows promise in non-contact heart sound monitoring. However, further improvements are necessary.

Conclusion

We proposed using heartbeat envelope instead of ECG as the trigger for our non-contact signal averaging heart sound measurement method. The trigger accuracy of the heartbeat envelope was 0.01 s as a standard deviation of the RRI estimation error. This value met the requirement of our signal averaging method. This method demonstrated that the S1 can be extracted from the sound measured 40 mm away from the chest wall. The next step is to improve signal noise and extend the measurement distance.

References

[1] World Health Organization, Cardiovascular diseases (CVDs), https://www.who.int/news-room/fact-sheets/detail/cardiovascular-diseases-(cvds) (accessed April 10th, 2025).

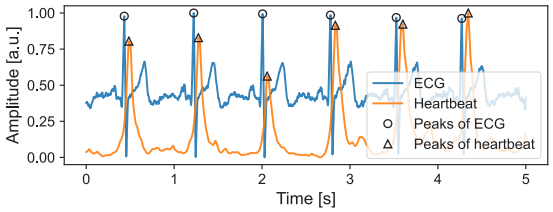


Fig. 2. Synchronized ECG and heartbeat envelope. Circles and triangles represent detected peaks.

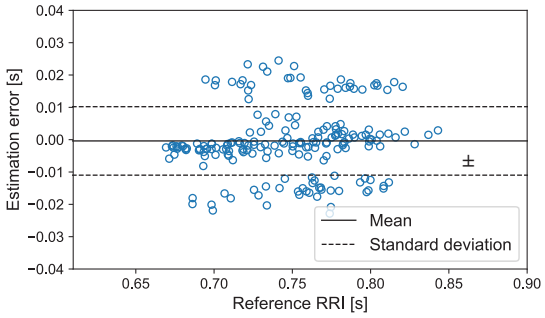


Fig. 3. Error of RRI estimated by the heartbeat envelope, against the reference RRI.

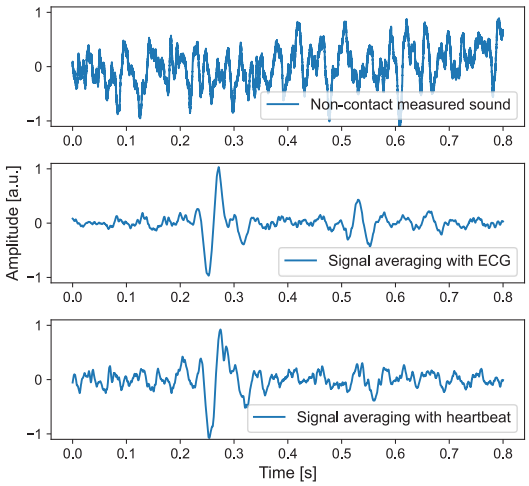


Fig. 4. (a) Raw sound. (b) Output using the ECG trigger. (c) Output using the heartbeat envelope trigger.

[2] A. R. u Shan *et al*, Advancements in wearable heart sounds devices for the monitoring of cardiovascular diseases, *SmartMat* 6, e1311 (2025); doi: 10.1002/smm2.1311

[3] S. Muramatsu, M. Yamamoto, S. Takamatsu, T. Itoh, Non-contact heart sound measurement using independent component analysis, *IEEE Access* 10, 98625-98632 (2022); doi: 10.1109/ACCESS.2022.3206467

[4] S. Muramatsu, K. Kurihara, Remote photoplethysmography-triggered signal averaging for non-contact heart sound measurement, *Proc. EMBC 2025*, in press.

Acknowledgements

This work was supported by JSPS KAKENHI Grant Number JP24K23901 and the Precise Measurement Technology Promotion Foundation (PMTP-F).

DOI 10.5162/EUROSENSORS2025/T5.3.1

AlN piezoelectric micromachined ultrasound transducer (pMUT) for E. Coli detection

Victor Fabre[1], Adrian Laborde[2], Fabrice Mathieu[2], Guillaume Daufouy[1], Romain Liechti[1], Bruno Fain[1], Jean-Claude Bastien[1], Thomas Alava[1], Sophie Giroud[1]
[1] Univ. Grenoble Alpes, CEA, Leti, F-38000 Grenoble, France
[2] LAAS-CNRS, Université de Toulouse, CNRS, INSA, 31400 Toulouse, France
victor.fabre@cea.fr

Summary: This work presents the fabrication process and characterization of a pMUT intended for the detection of E. Coli in liquid samples. A piezoelectric transducer in aluminium nitride is integrated in a CMOS-based process and later functionalized with specific antibodies to achieve E.Coli detection through resonance frequency tracking in air using a Vector Network Analyser.

Keywords: pMUT, AlN, Biosensing, E. Coli

Introduction

E. Coli presence in surface water and drinking water is a global health and economic issue worldwide. Rapid and advanced biosensor are needed as, tests, currently available on the market based on PCR or bacterial culture, have response time far away from real-time detection. Real-time detection can be achieved using Micro-electromechanical systems (MEMS) which have proven their efficacity for mass sensing application [1]. However, mechanical biosensor have yet failed to provide market-ready solution [2]. To bring mechanical biosensor ready for on field application, we think that in the wide range of MEMS systems, pMUT using AlN is the most promising technology. Indeed the physical properties of AlN such as a low permittivity dielectric couple with pMUT advantages i.e no cavity structure, electrical sensing method, no voltage bias [3] make it a good choice for biosensing. This contribution presents a fabrication process of a membrane-based pMUT and dedicated experiments to detect E. coli based on mass sensing through microgravimetry.

Experimental details

The pMUT is a circular membrane of 75µm radii. This design is the result of a study to detect a few bacteria (at least one) on its surface. Figure 1 shows the process flow to make the device. The device is made using 4 inches of SOI wafers (with 3µm thick buried oxide and 1.5µm thick top silicon). On top of the SOI a stack of 200 nm of Mo, 1µm of AlN, and 200nm of Mo has been deposited. This stack is then processed to build the pMUT layout with the Mo as top and bottom electrodes of the AlN piezoelectrical layer. The first steps consists in patterning the top elctrode, the AlN and the bottom electrod as descibed in picture Fig1 a) to d). A lift-off of Ti/Ni/Au is then done to generate bond pads and a gold disk of 30 nm (made also by lift-off) is deposited on top of the membrane (Fig 1e) 1f)). This gold disk will be used for future specific functionalization of the pMUT. To get a fully functional device a backside deep reactive ion etching followed by an RIE is done to etch first silicon and then the SiO_2 buried oxide. Figure 2a) shows an optical micrograph of the pMUT sensor.The left pMUT is used for the detection meanwhile the right pMUT is used as an electrical reference (this pMUT is not open).

To detect E.coli, a two-step functionalization protocol is implemented. First, the device is incubated in a Phosphate Buffer Saline (PBS 1X) solution containing anti-Ecoli antibodies at 10µg/mL for 60 minutes. The device is then rinsed using PBS 1 X and incubated for 30 min with a solution of Bovine Serum Albumin (BSA) at 2% (w/w) in order to passivate non specific binding sites. The device is here again rinsed using PBS 1X and then in de-ionized water. Finally, the device is immersed in a suspension of E.coli (O157H7 strain with Syto-9, stained to be observed in green fluorescence) at 10^8 CFU/mL for 60 min at 300 RPM. The protocole is presented in Figure 2b). To avoid frequency fluctuation due to environement changes, a resonant frequency tracking was used in between each step for at least 5 minutes at room temperature : before the

functionalization step, between the functionalization and E. Coli incubation, and finally after this incubation.

Results and discussion

Figure 3 shows the COMSOL simulation for the membrane and the capacitance measurement using a vector network analyzer. The fundamental mode of resonance can be found at 986 kHz. At this frequency, the pMUT shows a capacitance of 1.2 pF. Although FEM simulations and experimental data are similar, there is a slight difference in the resonance frequency as well as the width of the resonance. These difference have been explained by a mismatch in the value of the silicon nitride layer stress between the actual deposited film and the parameters used in FEM computing. A second factor can be a variability in the membrane thickness due to deterioration during the buried oxide etching step.

The added mass resulting of the fonctionnalization step is shown in Figure 4a), this step results in a mean resonance frequency shift of -978 Hz. After E. coli incubation the mean resonance frequency shifts of -100 Hz. This result has been coupled with fluorescence microscopy images (Fig 4b) which clearly show two E. Coli on top of the membrane. The theorytical mass sensitiviy calculated of our pMUT is -20Hz/pg. As a bacteria weight arround 1pg we should get -40Hz instead of -100Hz after the incubation which means that others compounds have been deposited. The work paves the way for the detection of E.Coli directly in aqueous media. Additional experiments are being conducted in aqueous media and supplementary data will be presented during the conference.

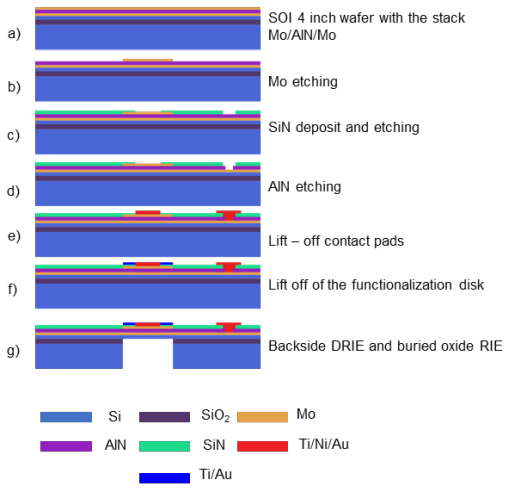


Figure 1: Process flow Description of the main technological steps of the micro- fabrication process used to fabricate the proposed pMUTs

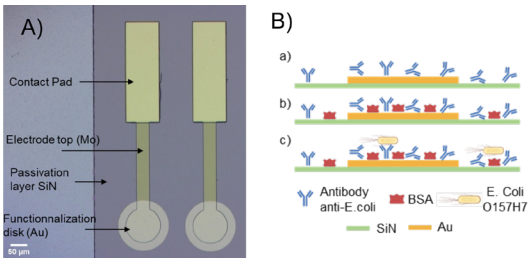


Figure 2: A) Optical micrograph of a two pMUT. The left one is used for the detection meanwhile the right one is used for electrical reference. B) Functionnalization steps : a) antibodies anti-E. coli b) BSA. c) Incubation of E. Coli prior detection

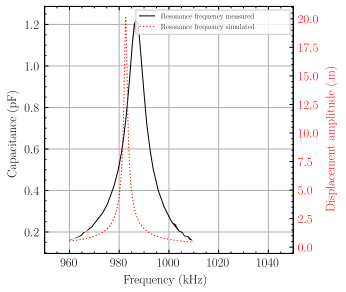


Figure 3: Resonance frequency measured (black curve) vs resonance frequency simulated using COMSOL (red dotted curve)

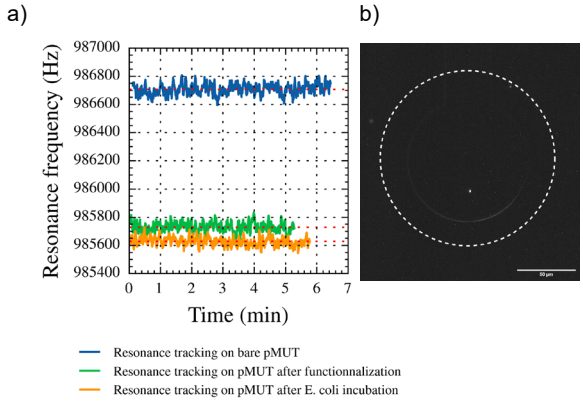


Figure 4 a) Real-time measurement of the frequency resonance: bare pMUT (blue curve), after functionalization (green curve) and after E. coli incubation(yellow curve). b) Fluorescence micrograph of the pMUT after E. coli incubation, the white dotted circle delimits the perimeter of the membrane.

References

[1] I.-B. Baek *et al.*, « Attogram mass sensing based on silicon microbeam resonators », *Sci. Rep.*, vol. 7, nº 1, p. 46660, avr. 2017, doi: 10.1038/srep46660.

[2] T. Leïchlé, L. Nicu, et T. Alava, « MEMS Biosensors and COVID-19: Missed Opportunity », *ACS Sens.*, vol. 5, nº 11, p. 3297-3305, nov. 2020, doi: 10.1021/acssensors.0c01463.

[3] H. Nazemi *et al.*, « Mass Sensors Based on Capacitive and Piezoelectric Micromachined Ultrasonic Transducers—CMUT and PMUT », *Sensors*, vol. 20, nº 7, Art. nº 7, janv. 2020, doi: 10.3390/s20072010.

DOI 10.5162/EUROSENSORS2025/T5.3.2

Fiber optic sensors based on Mach-Zehnder Interferometer for the detection of bacterial biofilms

Attena Rashidi[1], Flavio Esposito[1], Adriana Sacco[2], Federica Granata[3], Anubhav Srivastava[1], Carmine Vitagliano[4], Stefania Campopiano[1], Michele Giordano[4], Giuseppe Coppola[3,], Gennaro Di Prisco[2,*], Lucia Sansone[4,*], Agostino Iadicicco[1,*]*

[1] Department of Engineering, University of Naples "Parthenope", 80143 Naples, Italy

[2] Institute for Sustainable Plant Protection (IPSP), CNR, 80055 Portici, Italy

[3] Institute of Applied Science and Intelligent Systems (ISASI), CNR, 80128 Naples, Italy

[4] Institute for Polymers, Composites, and Biomaterials (IPCB), CNR, 80055 Portici, Italy

**giuseppe.coppola@cnr.it (G.C.), gennaro.diprisco@cnr.it (G.D.P.), lucia.sansone@ipcb.cnr.it (L.S.), agostino.iadicicco@uniparthenope.it (A.I.)*

Summary:

In this work, a chemical sensor based on an In-fiber optic Mach-Zehnder Interferometer (MZI) is reported. The MZI is fabricated using standard single-mode fiber with a waist-enlarged splicing method, where the spliced point acts as a coupling and re-coupling element for cladding modes and core mode. Unlike conventional transmission based MZIs, a reflective configuration is prepared by coating the fiber tip with silver developing a convenient fiber optic probe. A sensitivity of about 125 nm/RIU to the surrounding medium refractive index is obtained. As an application, the biofilm growth of a Gram-negative aerobic bacterium, i.e. *Pseudomonas alcaligenes*, is observed by monitoring the resonance wavelength shifts in real-time over three days. Biofilm thickness is further analyzed by using Atomic Force Microscopy technique demonstrating the effectiveness of fiber optic technology for real time continuous monitoring of biofilm growth.

Keywords: Mach-Zender interferometer, fiber optic sensors, biofilms, environmental monitoring.

Introduction

Biofilms are microbial communities found on various surfaces, impacting ecosystems, health, and industry. They serve as environmental indicators, capturing data on nutrients, pollutants, and microbial dynamics. Effective monitoring enables early detection of contamination and supports sustainability efforts [1]. Optical fiber sensing technology offers advantages for biofilm monitoring, providing high sensitivity, real-time monitoring, and data deployment in complex environments while minimizing manual sampling [2]. Despite the increased importance of biofilm monitoring, there are only few researches available where it is performed using fiber optic technology [3], [4]. In this work, we develop and test a fiber optic sensing probe based on Mach-Zehnder Interferometer (MZI) achieved by overlap splicing of standard single-mode fibers. After refractometric characterization, the sensor was tested for *Pseudomonas alcaligenes* biofilm detection. This study is a part of the Italian MoBeeFO project, which will further apply the probe for real-time monitoring of honeybee immune responses.

Development of the sensor

The proposed MZI based fiber optic probe is fabricated using a simple and cost-effective approach with commercially available components, as schematically reported in Fig. 1(a).

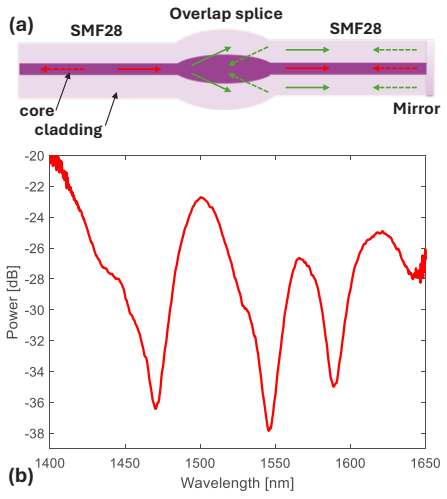


Fig. 1. MZI fiber optic sensing probe: (a) schematic view; (b) reflected optical spectrum.

It consists of two spliced single-mode fibers (Corning SMF28) with an overlap/waist-enlarged region to excite cladding modes. A silver mirror

is integrated at the fiber tip to enable reflection-based operation. The interference spectrum is generated as the overlap spliced region re-couples cladding and core modes [5], [6].Fabrication was performed using a Fujikura 62S+ fusion splicer with specific parameters (arc time: 700 ms, overlap: 150 µm), resulting in a 6 mm-long MZI device. The reflected spectrum showed three main interference peaks in the 1400–1650 nm range as shown in Fig. 1(b). Sensitivity testing involved immersing the probe in calibrated refractive index (RI) solutions (within 1.33-1.39), showing a wavelength shift at 1550 nm with a sensitivity of about 125 nm/RIU. This range is relevant for subsequent biofilm experiments.

Results for biofilm monitoring

To monitor biofilm growth experiment, a *P. alcaligenes* biofilm was selected as a case study. A bacterial culture of *P. alcaligenes* was prepared by inoculating a single colony into a growth medium and incubating overnight at 30 °C. The MZI-based fiber optic probe was then immersed in the solution, and resonance wavelength shifts of the device were monitored in real-time for 60 hours using an HBM FiberSensing FS22 interrogator. The solution was continuously stirred at 100 rpm throughout the experiment. Additionally, the Atomic Force Microscopy (AFM) has been used to measure biofilm thickness.

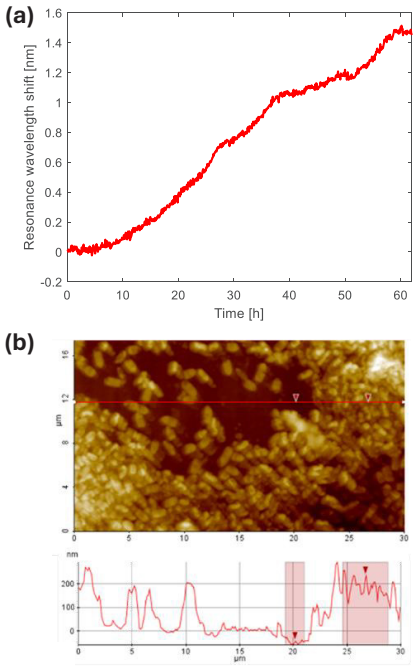


Fig. 2. (a) Sensor response in terms of resonant wavelength shift during bacterial biofilm growth. (b) AFM measurement of biofilm on optical fiber with map view and height profile.

Fig. 2(a) shows the resonance wavelength shift of the MZI peak located at 1550 nm during the biofilm growth experiment, indicating a shift of up to 1.5 nm after 60 hours. The red shifts indicate the increase in surrounding RI and the biofilm formation by a new layer around the fiber. AFM imaging reported in Fig. 2(b) confirmed biofilm formation, revealing typical bacterial morphology and granular structure. A biofilm thickness of about 250 nm and granular surface (avg. roughness: 50 nm) were found, validating the fiber optic probe's capability for real-time detection via wavelength-encoded measurements.

Conclusions

In this work, we designed and fabricated a cost-effective fiber optic probe using an MZI overlap configuration on a single-mode fiber tip for chemical sensing. The probe was successfully tested for detecting *P. alcaligenes* biofilm growth, demonstrating advantages in simplicity, compactness, and robust wavelength-encoded measurements. Future research will focus on comprehensive sensing characterization and biofilm response analysis. Additionally, within the MoBeeFO project, the transducer will be explored for real-time monitoring of honeybee innate immunity dynamics.

Acknowledgements

This work was performed within the project "Monitoring of Honeybee Immunomodulation and Resilience to Stress Factors by Fiber Optic Technology" (MoBeeFO) CUP I53D23000390006 under PRIN 2022 grant financed by the European Union – Next Generation EU, Mission 4 Component 1 and Italian Ministry of University and Research.

References

[1] R. Funari, A. Q. Shen, Detection and Characterization of Bacterial Biofilms and Biofilm-Based Sensors, ACS Sensors 7, 347–357 (2022); doi: 10.1021/acssensors.1c02722.

[2] S. Soares et al., Cortisol detection using a Long Period Fiber Grating Immunosensor coated with Graphene Oxide, Sensors and Actuators Reports 9, 100279 (2025); doi: 10.1016/j.snr.2024.100279.

[3] A. Rakhimbekova et al., Biofilm Detection by a Fiber-Tip Ball Resonator Optical Fiber Sensor, Biosensors 12, 481 (2022); doi: 10.3390/bios12070481.

[4] N. Zhong, M. Zhao, Y. Li, U-shaped, double-tapered, fiber-optic sensor for effective biofilm growth monitoring, Biomed. Opt. Express 7, 335 (2016); doi: 10.1364/BOE.7.000335.

[5] D. Aydin, J. A. Barnes, H.-P. Loock, In-fiber interferometry sensors for refractive index, Appl. Phys. Rev. 10, (2023); doi: 10.1063/5.0105147.

[6] A. Srivastava, F. Esposito, S. Campopiano, A. Iadicicco, Mode transition phenomena into an in-fiber Mach-Zehnder interferometer, Opt. Fiber Technol. 80, 103481 (2023); doi: 10.1016/j.yofte.2023.103481.

DOI 10.5162/EUROSENSORS2025/T5.3.3

Development of Wearable Lactate Sensors with Dynamic Visual Pattern Responses

Yasumasa Kanekiyo, Emi Sakai
Kitami Institute of Technology, 165 Koen-cho, Kitami, Hokkaido 090-8507, Japan
e-mail: kanekiyo@mail.kitami-it.ac.jp

Summary:
This study explored the responses of cotton fabrics functionalized with lactateresponsive and non-responsive polymers, focusing on color and pattern changes. Facial pattern samples were created using two monomer solutions and stained with anionic dyes. When immersed in 100 mM lactate, smiling faces gradually turned into crying faces. Pattern changes correlated with lactate concentration and response time, with full transformation observed after 120 min at 100 mM lactate. These findings suggest dye desorption from responsive areas enables visual, concentration-dependent lactate sensing.

Keywords: lactate, colorimetric, pattern change, boronic acid, smart textile

Introduction

Since lactate is a substance that serves as an indicator of physical fatigue and exercise intensity, easy measurement of lactate concentration in body fluids would be useful for not only top athletes but also for the general public to improve their competitive performance and health. Conventional lactate measurement methods require blood sampling, which imposes a heavy workload on athletes and related personnel (trainers and coaches), and does not allow continuous measurement, so improvements are needed. In recent years, methods for measuring lactic acid in sweat using wearable sensors have been developed. However, there are still many problems to be overcome, such as the large measuring device that interferes with the wearer's movement and the high cost and instability of the device.

In our laboratory, we are developing sportswears that changes its design in response to lactate using boronic acid as a lactate interface. Boronic acids are known to reversibly form negatively-charged complexes with *cis*-diol compounds such as saccharides. It is also known that boronic acids can interact with *α*-hydroxy acids in which a hydroxyl group binds to the *α*-carbon adjacent to the carboxyl group. By utilizing the characteristics of boronic acid, our group have succeeded in developing thin films that exhibit colorful responses against lactic acid. In the present study, we combined the above–mentioned lactic acid-responsive thin film with cotton fabric to develop sports wears that change their patterns in response to the lactic acid concentration in sweat. This is a completely different approach from conventional methods using enzymatic or electrochemical reactions. The wearer does not have to bear any extra burden such as sensing units and data transmitters, and the design changes in response to the lactate concentration in sweat simply by wearing the garment (Fig. 1). If such a wearable sensor that doesn't feel like wearing at all is put to practical use, it will enable anyone to easily determine the degree of physical fatigue and exercise intensity.

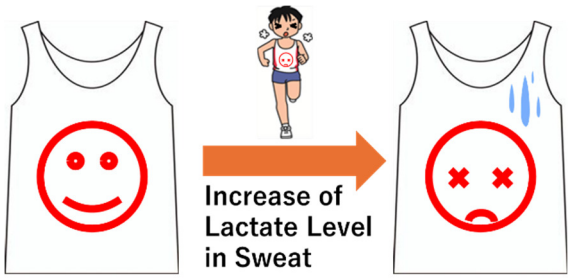


Fig. 1 Concept of our wearable lactate sensor with dynamic visual pattern responses

Experimental

An outline of the sample preparation is shown in Fig. 2. The cotton fabric was cut into 6 cm × 6 cm pieces, washed with water and acetone, and dried with cold air from a hair dryer. In a glove box replaced with nitrogen to reduce the oxygen concentration to about 1.0%, 0.15 mL of the monomer solution for non-responsive area (Table 1) was dropped onto the cotton fabric with photomask 1 attached. After irradiation with UV light (365 nm) through a photomask for 19 h, the cotton fabric was immersed in 100 mL of distilled water and stirred in an incubator at 25 °C for 1 h. The washed cotton fabric was then immersed in an anionic dye solution ([dye] = 1 mM, pH 7.4 by 10 mM HEPES) and stirred in an incubator at 25 °C for

10 min. The colored cotton fabric was then immersed in distilled water, washed, and dried in cold air using a hair dryer. After trimming the edges of the cotton fabric by 5 mm, the process was repeated with the monomer solution for the lactate-responsive area (Table 1) and photomask 2.

Table 1. Monomer compositions[a)]

Pattern area	[Monomer] / mM			
	1	2	3	4
Lactate-responsive	800	200	0	400
Non-responsive	0	50	950	400

[a)]Initiator: AAPH (90 mM), Solvent: MeOH:H_2O = 3:2 (v/v).

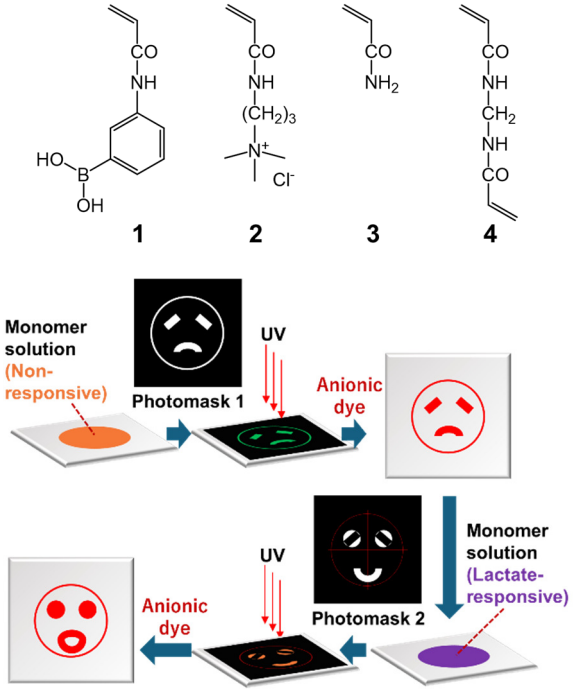


Fig. 2. Fabrication process of the facial pattern sample.

Results and Discussion

Facial pattern samples were prepared by using two different monomer solutions and their corresponding photomasks. Two anionic dyes, Indigo (Indigotrisulfonate) and AR18 (Acid Red 18), were used for coloring. When these samples were immersed in a 100 mM lactate solution, the smiling pattern changed over time and transformed into a crying face (Fig. 3). No major differences in response behavior were observed between the dyes. To numerically evaluate these pattern changes, the RGB values of the lactate-responsive and non-responsive areas in the sample photographs were determined. In the case of the Indigo-colored samples, the R and G values increased significantly in the lactate-responsive area, whereas the increase in the B value was relatively small. In contrast, in the non-responsive area, the R and B values showed only slight changes, and the increase in the G value was small compared to that in the lactate-responsive area. For the AR18-colored samples, the G and B values increased significantly in the lactate-responsive area, whereas the R value decreased slightly. In contrast, in the non-responsive area, the increases in the R and B values were small compared to those in the lactate-responsive area, and the G value showed virtually no change.

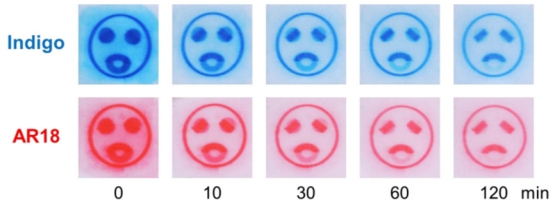


Fig. 3. Lactate-responsive changes in the facial pattern samples immersed in 100 mM lactate solutions.

Next, we examined changes in the pattern as a function of lactate concentration in samples colored with AR18. As shown in Fig. 4, changes in the pattern in response to lactate appeared as the response time increased. When the response time was 120 min, the pattern completely changed from a smiling face to a crying face as the lactate concentration increased from 0 to 100 mM. These results indicated that the dye preferentially desorbed from the lactate-responsive areas in the pattern and changed to a different pattern based on the dye remaining in the non-responsive areas.

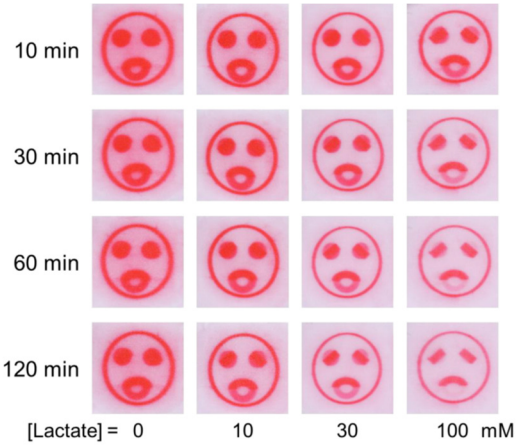


Fig. 4. Pattern changes of the facial pattern samples stained with AR18 after immersion in aqueous lactate solutions.

Acknowledgements

This research was financially supported by the Descente and Ishimoto Memorial Foundation for the Promotion of Sports Science.

DOI 10.5162/EUROSENSORS2025/T5.3.4

A Flexible Glucose Electrochemical Sensor for Textile Integration

Marc Martínez-Estrada[1], *Ignacio Gil*[1], *Raúl Fernández-García*[1]
[1] *Department of Electronical Engineering, Universitat Politecnica de Catalunya; Terrassa, Spain,*
Emails: marc.martinez.estrada@upc.edu, ignasi.gil@upc.edu and raul.fernandez-garcia@upc.edu

Summary:
A printed electrochemical sensor based on Ag flexible ink is presented to determine chemical substances concentrations. The sensor consists of 3-electrodes structure with different thickness and distances. This design permits to measure by chronoamperometry different glucose concentrations and compare the responses obtained by the different geometries presented. The decrease of the current measured between the sensor electrodes provides enough information to identify the increase of the glucose concentration along the solutions.

Keywords: printing, textile, chemical, sensor, flexible

Background, Motivation an Objective

Electrochemical sensors have been centered the focus of numerous researchers who work on developing new opportunities to integrate sensors on flexible substrate[1], [2], [3]. The integration of electrochemical sensors over flexible substrates could lead to the appearance of new healthcare control applications.

One of the biomarkers which has attracted the interest of the researchers over the last years is the glucose. The importance to control the concentration in blood with direct measuring or indirect measuring (sweat) is very important to predict hypoglycemia or hyperglycemia from diabetic people. Flexible technologies have proved the possibility to integrate or built electrochemical sensor to measure the glucose concentration over textile or flexible substrates [1], [4]. Several of the electrochemical sensors developed use chemical treatments over the conductive materials to obtain sensitivity to chemical substances. These treatments could be chemical coatings or enzymatic treatments which are placed over the sensors to improve their functionality.

A flexible electrochemical sensor has been designed to detect different concentrations of glucose. The sensor has been built using commercially available silver ink (Ag) without additional chemical or enzymatic treatments.

Description of the New Method or System

The printed electrochemical sensor has been built following the 3-electrodes sensor design, where the longest electrode is the counter electrode (CE) the center electrode is the working electrode (WE) and the right electrode is the reference electrode (RE). Three different geometries have been prepared to analyze the impact of the different sizes and distance of the electrodes. Figure 1 shows the printed electrochemical sensors.



Fig 1. Printed electrochemical sensor with 3 electrodes. From left to right the parameters for the electrodes changed are: 2mm of thickness and 1 mm distance (d1t2), 1mm thickness and 2mm distance(d2t1) and 1mm thickness distance(d1t1)

To print the sensor a flexible silver ink (FS0142), which is produced by ACI Materials company, is used. The ink is used with a *Voltera Nova* drop casting printing machine to manufacture each of the sensor over a flexible thin film (Fig 2). The printed sensor is connected to a Keithley Source Measurement unit SMU2636B (SMU) by pairs, CE and WE will be fed with a constant 400mV. Meanwhile, the current generated between WE and RE is measured.

To test the response of the sensor to a chemical substance, three glucose solutions are prepared. The glucose concentrations present in the solutions are 90, 180 and 900 mg/dL

Results

Sensor values are obtained performing a chronoamperometry with different glucose concentrations. Each measurement is performed during 30 seconds. After the initial 5 seconds, 10uL of solution is dropped.

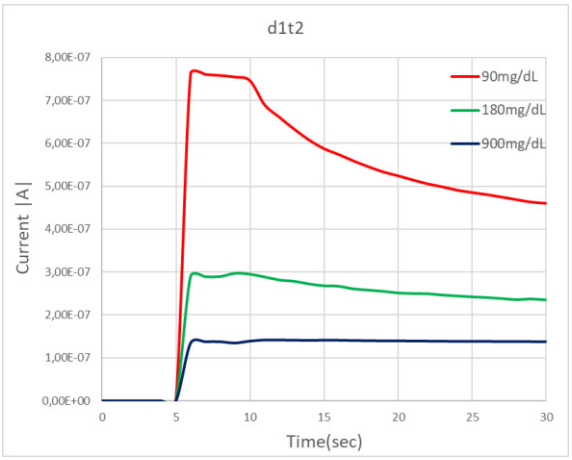


Fig 2. Chronoamperometry for the sensor 2mm thickness and 1mm distance.

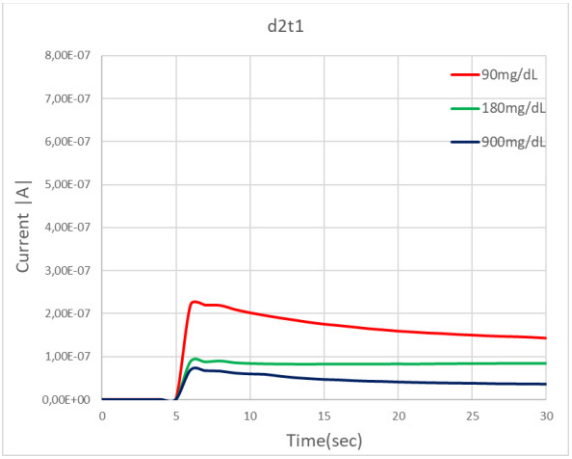


Fig 3. Chronoamperometry for the sensor 1mm thickness and 2mm distance.

It is observed in Figures 2, 3 and 4 how the lower concentration 90 mg/dL obtain the highest current measured. As the concentration increases, the current measured on the electrochemical flexible sensor decreases. The flexible sensor response for the 90 mg/dL also shows a higher instantaneous peak compared with the other solutions.

The printed sensor with both characteristics equal has a more stable and similar distributed data, meanwhile, the sensors with 2mm distance (Fig 2) or 2 mm thickness (Fig 3) shows a wider step from 90 mg/dL to 180 mg/dL.

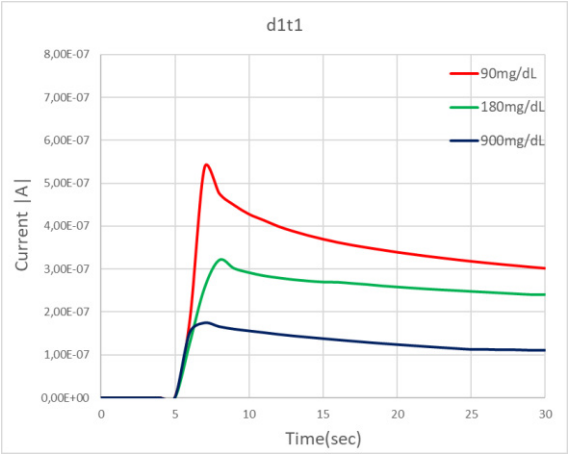


Fig 4. Chronoamperometry for the sensor 1mm thickness and 1mm distance.

Specially the sensor response observed in Fig 2 shows how the current value for 90 mg/dL is almost 2 times the current measured of 180 mg/dL and 4 times the current value of 900 mg/dL, which could be interesting for future applications and characterizations.

Overall, the printed flexible sensor presented demonstrate the ability to detect chemical substance concentration in solutions and also how the geometry could affect the behavior of the sensor. The flexible printed sensor could be integrated over textile or flexible substrate by direct drop printing or iron fixing to provide new possibilities of applications from textile substrates.

Acknowledgements

This work was supported by the Agencia Estatal de Investigación under project PID2021124288OB-I00

References

[1] S. Khosravi, S. Soltanian, A. Servati, A. Khademhosseini, Y. Zhu, and P. Servati, “Screen-Printed Textile-Based Electrochemical Biosensor for Noninvasive Monitoring of Glucose in Sweat,” *Biosensors*, vol. 13, no. 7, Art. no. 7, Jul. 2023, doi: 10.3390/bios13070684.

[2] W. Pan *et al.*, “An Integrated Stretchable Sensing Patch for Simultaneously Monitoring of Physiological and Biochemical Parameters,” in *2021 IEEE 16th International Conference on Nano/Micro Engineered and Molecular Systems (NEMS)*, Apr. 2021, pp. 762–767. doi: 10.1109/NEMS51815.2021.9451353.

[3] G. Polidori, S. Tonello, M. Serpelloni, M. Giamberini, X. Montané, and J. A. Reina, “Preliminary Study on Printed Membrane by Aerosol Jet for Ion Detection in Industrial Field,” in *2024 IEEE International Workshop on Metrology for Industry 4.0 & IoT (MetroInd4.0 & IoT)*, May 2024, pp. 1–6. doi: 10.1109/MetroInd4.0IoT61288.2024.10584232.

[4] A. Sinha, null Dhanjai, A. K. Stavrakis, and G. M. Stojanović, “Textile-based electrochemical sensors and their applications,” *Talanta*, vol. 244, p. 123425, Jul. 2022, doi: 10.1016/j.talanta.2022.123425.

DOI 10.5162/EUROSENSORS2025/T6.1.1

Development of Piezoelectric Micro-Cantilever Gas Sensor

Jayden Moore[1], Aron Michael[1],
[1] UNSW, High St Kensington Sydney Australia,
jayden.moore@unsw.edu.au

Summary:

This paper presents the development of on-chip dynamic functionalized PZT based piezoelectric cantilever with self-sensing read-out circuit. The cantilever consists of Pd layer acting as a top electrode and functional layer, with the PZT grown on the bottom Pt/Ti electrode. The cantilever has been fabricated using surface micro-machining and characterized. It demonstrated 0.1 % shift in resonant frequency per 12 MPa stress change in the functional layer and 1.125 µ*m* change in displacement at resonance frequency per 1 MPa stress change in the functional layer.

Keywords: MEMS Cantilever, Hydrogen Sensing, Gas Sensing, Self-Sensing, Piezoelectric

Motivation

As the world transitions to renewable energy, hydrogen is anticipated to play a significant role. However, hydrogen is a colorless odorless and explosive gas, that requires sensitive sensors to detect leaks and ensure safety. In addition to the safety aspect, the environmental monitoring of fugitive hydrogen emissions is of interest to track changes in background hydrogen concentration. Currently there are a range of hydrogen sensors such as semiconductor metal oxides, optical and passive mems cantilevers, these however suffer from either a lack of selectivity, limited operational temperatures or the need for large bulky external equipment. Gurusamy et. al reported a static MEMS based PPB cantilever sensor [1] however, this method used an optical readout which required bulky external equipment. Li et al describes a static cantilever that uses a piezoresistive sensor to detect the changes in Hydrogen concentration [2] while their method is sensitive it requires relatively large millimeter scale cantilevers. Boon-Brett et al discussed the performance of commercially available hydrogen sensors [3]. These sensors operated using a wide range of methods such as catalytic, semiconductor metal oxide and electrochemical sensors. However, these sensors suffered from drawbacks such as low detection limit and high cross sensitivity with carbon monoxide, susceptibility to environmental conditions such as temperature and humidity and variability from sensor to senor. In this work, piezoelectric microcantilever with self-readout circuit that utilizes a highly absorbent functional layer to reduce cross sensitivity and operates in dynamic mode optimized to enhance sensitivity is reported.

Fabrication Process

A surface micro-machined piezoelectric cantilever with a Palladium (Pd) functionalization layer has been fabricated. The fabrication process is illustrated in Figure 1. It starts with an SOI wafer which is oxidized to grow 1 μm thick SiO_2 (Figure 1(a)). The bottom Pt/Ti electrode is then sputtered on the oxidized surface followed by Sol-gel PZT deposition (Figure 1(a)). The SOI/SiO_2/Pt/Ti/PZT (1um) sample is patterned with a Pd thin film acting as both the hydrogen sensing layer and the top electrode (Figure 1(a)). The PZT piezoelectric layer is then etched using photoresist as a mask in an ICP RIE followed by RIE etching of bottom Pt/Ti electrode and silicon oxide layers (Figure 1(a). A SiO_2/Pt/Ti/PZT/Pd cantilever is released by performing SF_6 isotropic silicon etch (Figure 1(a)). The SEM images of the released PZT cantilevers are shown in Figures 1(b) and (c).

Experimental Results

The dynamic behaviors of the released PZT cantilevers have been characterized and presented in Fig. 2. As can be seen from Fig. 2(a), the PZT cantilevers measured 5.85 kHz resonant frequency, quality factor (Q) of 25 dB. The frequency response of the cantilever shifts when the cantilever is biased at different DC voltages. The shift in resonance frequency due to the DC biasing is plotted in Fig. 2(b), showing 5 Hz shift per volt. Translating the biasing DC voltage to stress change in the Pd layer, the shift corresponds to 0.1 % frequency shift per 12 MPa stress change. The tip deflection of the cantilever at the various DC biasing is measured and shown in Fig. 3, exhibiting a sensitivity of 13.5 μm/V or 1.125 μm/MPa. It has been reported that the stress in Pd changes by as much as 200 MPa when in an environment of 5 % hydrogen concentration [5]. This either causes the resonance frequency to shift or tip deflection to change. The shift in resonance frequency and change in tip deflection is captured by a readout circuit which is shown in Fig, 4. The resonance frequency captured by the readout circuit is presented in Fig. 5.

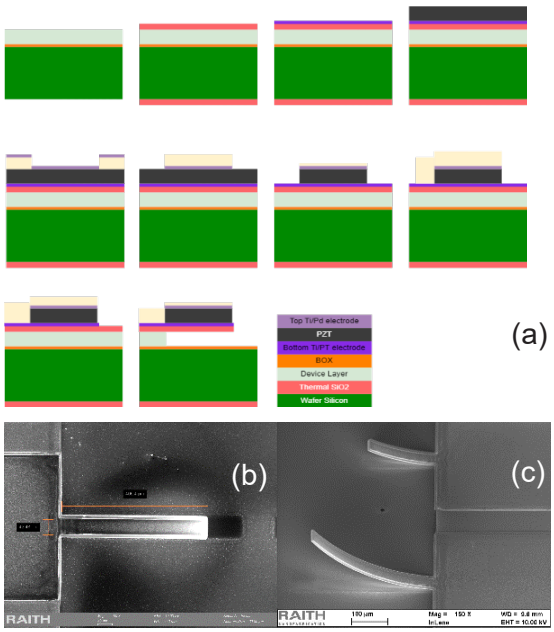


Fig. 1. (a) Fabrication steps for piezoelectric cantilever (b) SEM top view of released cantilever (c) SEM side view of released cantilevers.

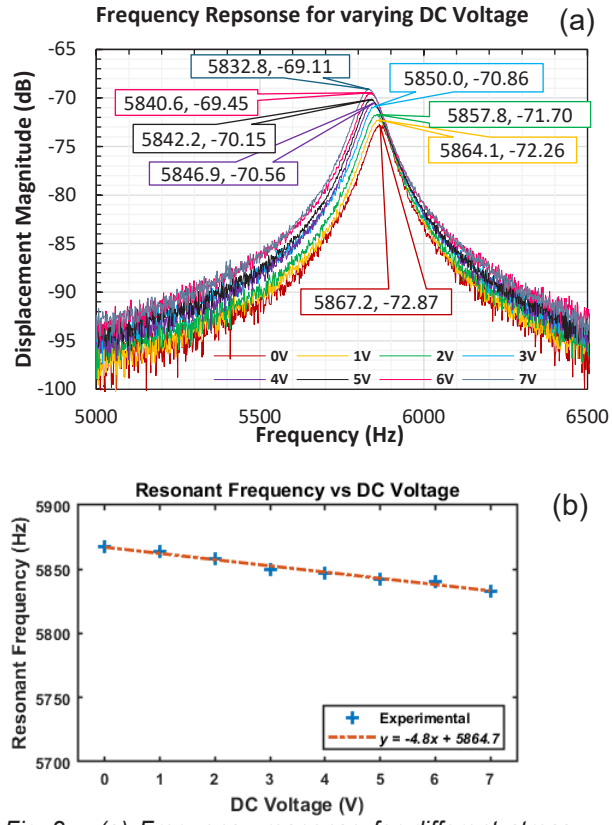


Fig. 2. (a) Frequency response for different stress (applied DC voltage on PZT layer) (b) Shift in resonant frequency due to applied voltage.

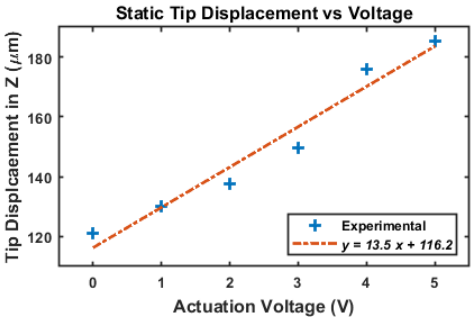


Fig. 3. Tip deflection of cantilever for various DC voltage

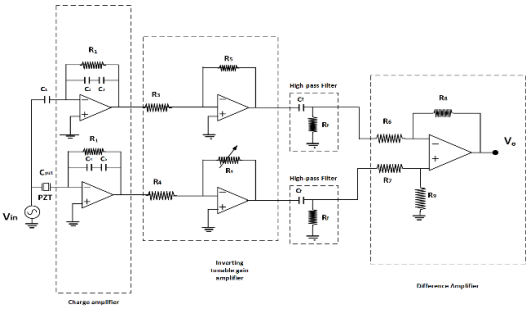


Fig. 4. Self-sensing readout circuit.

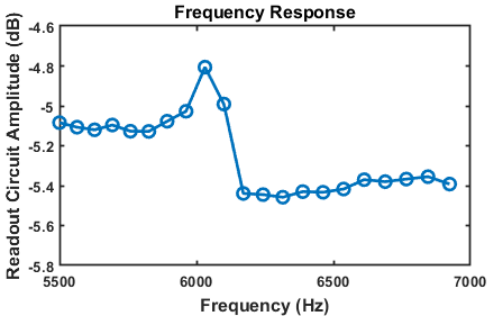


Fig. 5. Measurement of resonant frequency using self-sensing readout circuit.

References

[1] J. Gurusamy, G. Putrino, R. D. Jeffery, K. D. Silva, M. Martyniuk, A. Keating, L. Faraone, Mems based hydrogen sensing with parts-per-billion resolution, Sensors and Actuators B: Chemical 281, (2019); doi: 10.1016/j.snb.2018.07.118

[2] H. Li, Y. Li, K. Wang, L. Lai, X. Xu, B. Sun, Z. Yang, G. Ding, Ultra-high sensitive micro-chemo-mechanical hydrogen sensor integrated by palladium-based driver and high-performance piezoresistor, International Journal of Hydrogen Energy 46, (2021); doi: 10.1016/j.ijhydene.2020.10.013

[3] L. Boon-Brett, J. Bousek, P. Moretto, Reliability of commercially available hydrogen sensors for detection of hydrogen at critical concentrations: Part ii – selected sensor test results, International Journal of Hydrogen Energy 34, (2009); doi: 10.1016/j.ijhydene.2008.10.033

[4] S. M. R. Rasid, A. Michael, H. R. Pota, On-chip self-sensing piezoelectric micro-lens actuator with feedback control, IEEE Sensors Journal, vol. 23, no. 10, pp., 2023 doi: 10.1109/JSEN.2023.3261965

[5] Neha Verma, Rob Delhez, Niek M. van der Pers, R.W.A. Hendrikx, R.M. Huizenga, Amarante J. Böttger, Dislocations, texture and stress development in hydrogen-cycled Pd thin films: An in-situ X-ray diffraction study, International Journal of Hydrogen Energy, 47, Issue 24, 2022, Pages 12119-12134; doi: 10.1016/j.ijhydene.2022.01.233.

DOI 10.5162/EUROSENSORS2025/T6.1.2

Rapid Detection of Linalool Using Solidly Mounted Resonators for Plant Health Monitoring

Usman Yaqoob[1], Barbara Urasinska-Wojcik[2], Siavash Esfahani[1], Marina Cole[1], Julian W. Gardner[1]
[1] School of Engineering, University of Warwick, Coventry CV4 7AL, UK
[2] Sorex Sensors Ltd, New Cambridge House, Bassingbourn Road, Litlington, SG8 0SS, UK
J.W.Gardner@warwick.ac.uk

Summary:
This paper presents the detection of VOCs by functionalised solidly mounted resonators (SMRs) for plant health monitoring. Two designs of SMRs have been developed, one by the University of Warwick (UWAR) and the other by Sorex Sensors Ltd. These were coated with ethyl cellulose and tested for a response to linalool – a plant pest biomarker. Both sensors show strong responses, with sensitivities of 1.03 kHz/ppm (UWAR) and 15 kHz/ppm (Sorex). While the Sorex sensor exhibited higher sensitivity, it had a slower response time. In contrast, UWAR SMR responded within 6 sec and showed higher resolution. Results highlight the potential of SMR sensors for rapid and accurate plant health monitoring.

Keywords: piezoelectric sensor, VOC detection, plant health, SMRs

Background, Motivation and Objective

Plants emit different volatile organic compounds (VOCs) as part of their defense response to insect herbivory, i.e. pests. One such compound, linalool, is a widely occurring monoterpene known for its ecological role in both repelling herbivores and attracting natural enemies of pests. Its emission is often triggered or elevated during pest attacks, suggesting the potential as a biomarker for early pest detection.

Conventional pest monitoring methods are labour intensive and often fail to detect infestations in their early stages. In contrast, monitoring VOCs through cost-effective, and compact smart sensors offer a non-invasive, real-time approach to crop health monitoring. Various crops, such as maize (*Zea mays*), tea (*Camellia sinensis*), tobacco (*Nicotiana tabacum*), and chrysanthemum (*Chrysanthemum morifolium*), are known to release linalool when attacked by herbivorous insects. However, achieving fast, accurate, and selective detection of emitted linalool traces remains a significant challenge [1, 2].

This work introduces a custom 3D-printed chamber designed for the simultaneous detection of linalool using two SMRs (UWAR and Sorex), integrated with a commercial temperature and humidity sensor (Bosch BME280). Both SMRs were functionalised with ethyl cellulose, were tested in the presence of linalool diluted in air and exhibited a rapid, strong, and selective response.

Materials and methods

The UWAR and Sorex SMR devices used in this study are shown in Figures 1(a) and 1(b), respectively. The UWAR device was designed in the laboratory and fabricated at SilTerra (Malaysia) using a combined CMOS-MEMS 180 nm process. The fabricated SMR has overall dimensions of 1.0 mm × 2.5 mm, with a VOC sensing area of 500 µm × 351 µm. A solution of ethyl was spin-coated onto the top surface of both SMRs to form a sensing layer.

Fig. 1 shows microscopic images of the EC-coated SMRs. Although the deposited layer is very thin (<100nm) and transparent, making it difficult to observe directly, the light reflections produce varying colours on the surface, confirming successful deposition of the thin film.

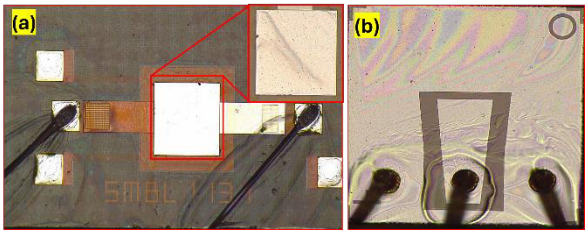


Fig. 1. EC coated SMRs, (a) UWAR SMR, inset show the magnified image of the sensing area, and (b) Sorex SMR.

After depositing the sensing film, both SMRs were installed in the 3D-printed chamber, as shown in Fig. 2. This chamber was designed to enable simultaneous monitoring of both SMRs in the presence of linalool, while continuously

tracking ambient temperature and humidity levels using the BME280 sensor.

A Keysight VNA, integrated with a customized NI LabVIEW program, was used to monitor frequency shifts over time. The VOC flow through the sensing chamber was precisely regulated using fully automated mass flow control system.

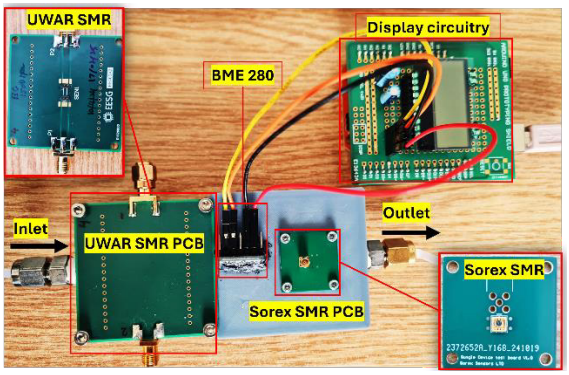


Fig. 2. 3D printed chamber (grey) with both SMRs, inset shows the front side of UWAR and Sorex sensors.

Results and Discussions

The SMR devices are highly sensitive to environmental changes, particularly temperature and humidity. To account for this, a BME280 sensor was installed inside the chamber to monitor both parameters throughout the experiment. It was observed that the frequency of the UWAR SMR decreases with increasing temperature, whereas the frequency of the Sorex SMR increases under the same conditions. Significant baseline drift was observed in both sensors. To compensate for this, a linear temperature compensation model was applied:

$$f_{(t,c)} = f_m + k_T\ (\Delta T) \qquad (1)$$

Where $f_{(t,c)}$ is temperature compensated frequency, f_m is measured frequency, k_T is a constant, and ΔT is temperature change.

Figures 3(a) & 3(b) display the temperature-compensated responses of the UWAR and Sorex SMRs, respectively. The insets in each figure show the sensor responses before compensation, with arrows indicating the direction of baseline drift due to temperature fluctuations. The SMRs were tested with linalool at concentrations of 10, 5, and 1 ppm in dry air conditions. The UWAR SMR exhibited a faster response with higher resolution, while the Sorex sensor showed a stronger overall response but with a longer response time. Testing with higher concentrations of potentially intefering other plant biomarkers, namely trans-2-hexenal and ethanol, confirmed excellent selectivity to linalool. The UWAR SMR includes an integrated micro-heater and is undergoing further investigations to assess response at higher temperatures. This low-cost MEMS-based SMR technology has great potential as a non-invasive, real-time solution for plant health monitoring.

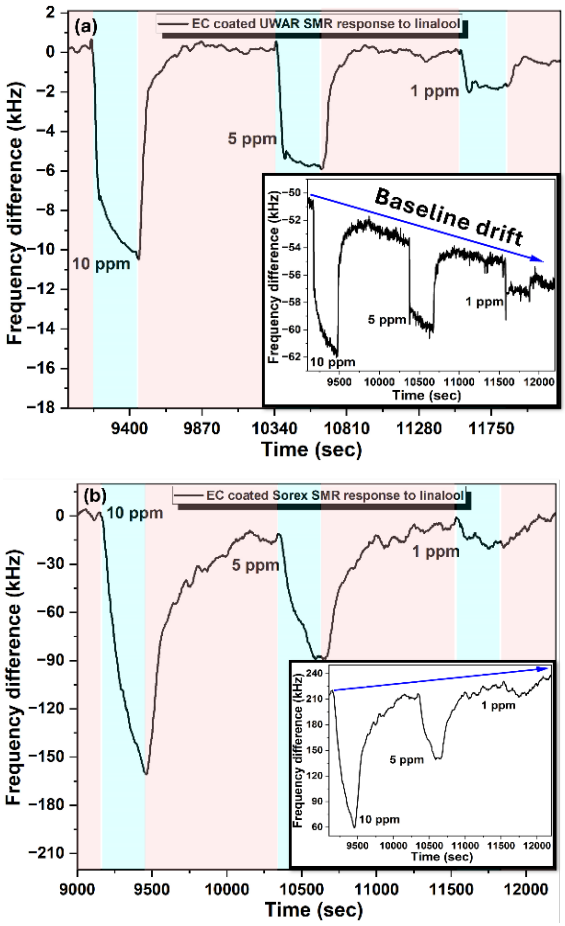


Fig. 3. Temperature compensated frequency shift vs. time responses of SMRs to PPM levels (a) UWAR SMR, and (b) Sorex SMR.

References

[1] A. Kessler, I.T. Baldwin, Defensive function of herbivore-induced plant volatile emissions in nature. Science, 291, 2141–2144 (2001). https://doi.org/10.1126/science.1057083.

[2] T.C.J. Turlings, M. Erb, Tritrophic interactions mediated by herbivore-induced plant volatiles: Mechanisms, ecological significance, and application potential. Annual Review of Entomology, 63, 433–452 (2018). https://doi.org/10.1146/annurev-ento-031616-035059.

Acknowledgements

This work is supported by the project "PurPest under Horizon Europe Program (grant #101060634), the Horizon Research and Innovation Action from European Research Executive Agency.

DOI 10.5162/EUROSENSORS2025/T6.1.3

Metal-Organic Framework (MOF)-based Materials for Electrochemical Sensing

C. Clemente[12], V. Gargiulo[2], L. Cimino[2], G.P. Pepe[1], G. Ausanio[1], M. Alfè[2]
[1] Department of Physics of the University of Naples "Federico II", Italy, 80125 Naples, Italy
[2] Institute STEMS of the National Research Council of Italy (CNR), 80125 Naples, Italy

Corresponding Author's e-mail address: claudio.clemente@unina.it

Summary:
Metal-Organic Frameworks (MOFs) are widely explored in electrochemical sensing due to their high surface area, tunable porosity, and structural versatility. In this work, MOF-derived hybrid materials were investigated for their potential in electrochemical applications. These materials preserve the hierarchical framework of the precursor MOFs while exhibiting enhanced electrical conductivity, making them promising candidates for the development of highly sensitive electrochemical sensors. Their performance in detecting target analytes in aqueous media, including heavy metal ions, was assessed using differential pulse anodic stripping voltammetry (DPASV), demonstrating their potential for environmental monitoring.

Keywords: Electrochemical sensors, MOFs, MOF-derived hybrid materials, Heavy metals.

Background, Motivation and Objective

Metal-Organic Frameworks (MOFs) are a class of hybrid organic-inorganic crystalline materials characterized by a periodic arrangement of metal clusters interconnected by organic linkers [1]. This highly tunable structure results in materials with exceptionally high surface area, well-defined porosity, and diverse chemical functionalities, making them ideal candidates for applications ranging from gas storage and catalysis to drug delivery and chemical sensing [2]. The ability to control their composition at the molecular level enables the design of MOFs with tailored adsorption properties and specific interactions with target analytes. However, their low conductivity limits direct electrochemical applications. A possible strategy to overcome this limitation is the pyrolysis of MOFs to obtain carbon-derived materials, which preserve the porous structure of the original MOFs while enhancing electrical conductivity and stability in aqueous environments [3]. These features make them ideal for electrochemical sensing. For example, carbon-based ZIF-8 modified with bismuth has been successfully employed for the detection of Cd(II) and Pb(II), owing to their hierarchical porosity and high surface area [4]. Electrochemical techniques are widely employed for the sensitive and selective detection of metal ions in solutions [5]. In this study, differential pulse anodic striping voltammetry (DPASV), known for its low detection limits and high sensitivity [6], is used to evaluate the sensing performance of MOF-derived hybrid materials, with a particular focus on detecting cadmium and lead in aqueous solutions. The conductive properties of these materials enhance charge transfer, while their porous structure facilitates analyte diffusion, resulting in improved detection limits. ZIF-8 was selected as the MOF precursor due to its high surface area and porosity, which contribute to its effectiveness in sensing applications. This approach, however, can be extended to other MOFs, which will be explored in future work.

Method

ZIF-8 was synthesized using a hydrothermal approach, with Zn^{2+} as the metal and 2-methylimidazole as the ligand, using water as the solvent. ZIF-8 was subjected to a pyrolysis process in a nitrogen atmosphere for one hour to obtain the corresponding carbon-based hybrid material. This material was characterized using X-ray diffraction, and electrochemical techniques including cyclic voltammetry (CV), differential pulse voltammetry (DPV), and electrochemical impedance spectroscopy (EIS). For sensor fabrication, a suspension of the corresponding MOF-derived hybrid material in Nafion solution was drop-casted onto the working electrode surface of a screen-printed electrode (SPE) producing a uniform coating of the sensitive material. To evaluate the sensing performance, DPASV was performed in a buffer solution containing 20 mM H_2SO_4 and 30 mM KCl.

Results

The electrochemical analysis of ZIF-8-derived carbon-based material performed by DPASV technique aimed to the quantitative determination of cadmium and lead ions in model solutions. From Figure 1 can be seen that as the concentration increases, the intensity of the oxidation peak current signal continuously increases. The corresponding calibration curve was constructed to assess the sensor response across a concentration range of 2 to 10 µM, as shown in Figure 2. The sensor demonstrated a reliable linear relationship between analyte concentration and its corresponding signal, enabling accurate detection within this range.

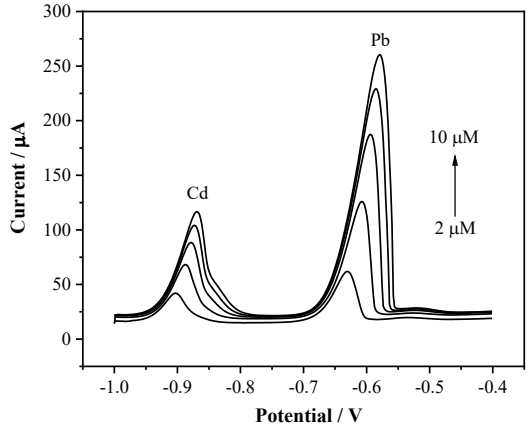


Fig. 1. DPASV response of ZIF-8-derived carbon-based material for detection of Cd(II) and Pb(II).

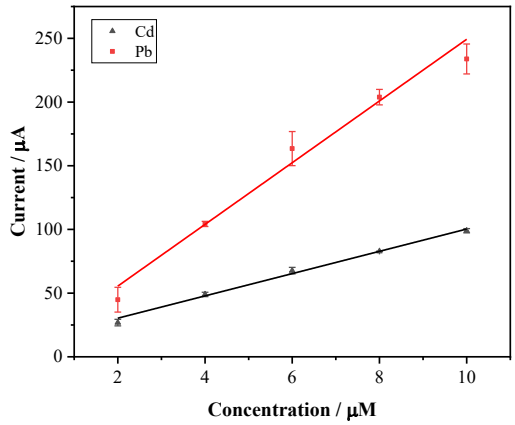


Fig. 2. The corresponding linear plots of Cd(II) and Pb(II).

The formula for the calculation of the limit of detection (LOD) from a calibration curve is as follows:

$$LOD = \frac{3.3\sigma_{blank}}{m} \quad (1)$$

Where σ_{blank} is the standard deviation of the blank, representing the variability in measurements of a sample with no analyte, indicating the background noise. The slope of the calibration curve is the rate of change in the current (I) with respect to the analyte concentration (C), obtained from the linear regression of the calibration data. The detection limits (LOD) for Cd(II) and Pb(II) obtained from the electrochemical analysis DPASV using the ZIF-8-derived carbon-based material were below 0.05 µM and 0.007 µM, respectively. These values are comparable and, in some cases, lower than those estimated implementing classical carbon-based materials. These preliminary results demonstrate the suitability of the MOF-derived hybrid materials in the development of sensors for the determination of heavy metals in aqueous solutions, with potential applications in environmental monitoring.

References

[1] L. Jiao, J. Y. R. Seow, W. S. Skinner, Z. U. Wang, H.-L. Jiang, Metal–organic frameworks: Structures and functional applications, *Materials Today* 27, 43-68 (2019); doi: 10.1016/j.mattod.2018.10.038

[2] B. Li, H.-M. Wen, Y. Cui, W. Zhou, G. Qian, B. Chen, Emerging Multifunctional Metal–Organic Framework Materials, *Adv. Mater.* 28, 8819-8860 (2016); doi: 10.1002/adma.201601133

[3] J. M. Gonçalves, P. R. Martins, D. P. Rocha, T. A. Matias, M. S. S. Julião, R. A. A. Munoz, L. Angnes, Recent trends and perspectives in electrochemical sensors based on MOF-derived materials, *J. Mater. Chem. C* 9, 8718–8745 (2021); doi: 10.1039/d1tc02025k

[4] L. Xiao, H. Xu, S. Zhou, et al., Simultaneous detection of Cd(II) and Pb(II) by DPASV at a nitrogen-doped microporous carbon/Nafion/bismuth-film electrode *Electrochim. Acta*, 143, 143-151 (2014); doi: 10.1016/j.electacta.2014.08.021

[5] D. Shi, W. Wu, X. Li, Multiplexed detection of aqueous Cd2+, Pb2+ and Cu2+ ions at mercury-on-graphene film modified electrode by DPASV, *Sens Biosensing Res* 34 100464 (2021); doi: 10.1016/j.sbsr.2021.100464

[6] F.R. Simões, M.G. Xavier, Electrochemical Sensors, *Nanoscience Appl., Micro Nano Technol.* 6 155–178 (2017); doi: 10.1016/B978-0-323-49780-0.00006-5.

Acknowledgements

This work was supported by the Project 'EMBRC UP'—EMBRC Unlocking the Potential for health and food from the seas, CUP: C63C22000570001—Project code IR0000035 for PhD fellowship founding. The projects "ECCSELLENT - Development of ECCSEL R. I. ItaLian facilities: usEr access, services and loNg-Term sustainability" Code: IR0000020 – CUP F53C22000560006 and iENTRANCE@ENL "The Infrastructure for Energy TRAnsition aNd Circular Economy @ EuroNanoLab" - IR0000027 - CUP:B33C22000710006) were also acknowledged.

DOI 10.5162/EUROSENSORS2025/T6.1.4

Frequency Multiplexing Method for Implementing a Reference Channel in resonator-enhanced direct photoacoustic setups

Daniel Sieg[1], Vincent Kuczius[1], Gabriel Rodríguez Gutiérrez[1], Stefan Palzer[1]
[1]Department of Electrical Engineering and Information Technology, Technical University Dortmund, Otto-Hahn-Straße 8, 44227 Dortmund, Germany
stefan.palzer@tu-dortmund.de

Summary:
Direct photoacoustic setups offer means for selective and sensitive detection of trace gases, particularly when using light sources with emission profiles smaller that the absorption features of target molecules and acoustic resonators to enhance the acoustic signal. However, those setups still require the measurement of the exciting light source's intensity, which to date is achieved using photodiodes. Here a method relying on the position-dependent excitation of acoustic modes is proposed to determine light intensity and number density independently, which may be used to calibrate the signal's dependence on light intensity without using additional components.

Keywords: photoacoustics, acoustic resonator, frequency multiplexing

Introduction

Optical gas sensors enable the selective detection of trace gases and the miniaturization of setups is crucial to enable scalable, widespread use at low cost. Photoacoustic approaches are particularly suited to achieve this. In direct photoacoustic spectroscopy setups, the signal strength depends on the light intensity as well as the particle density [1]. Consequently, sensor setups based on this principle will suffer from signal changes if the light source intensity changes [2], e.g. by aging or staining. This causes distorted gas measurement result and therefore this effect must be compensated for. At the same time, acoustic resonators feature a rich mode spectrum [3], where different resonance frequencies correspond to spatially varying pressure changes inside the resonator. In turn, the different spatial mode distributions result in coupling efficiencies that depend on the position of the sound source. Hence different resonance frequencies may be used to couple in photoacoustic signals from different position in the vicinity of the acoustic resonator. This may be used to establish a reference channel for direct photoacoustic setups.

Typically, the resonance frequencies for different resonant modes are different, as is the spatial distribution of the associated vibrations coupled into the resonator. To this end, an acoustic resonator may be designed such that, in addition to longitudinal modes, at least one azimuthal or radial mode can be excited. To establish means to udetermine the light intensity, the coupling of the photoacoustic signal generated by a metallic reflector may be adjusted so that the associated signal is coupled into an azimuthal mode, while photoacoustic signals resulting from gas absorption is coupled into a second mode.

In this contribution a moveable light emitting diode (LED) exciting nitrogen dioxide (NO_2) at 400 nm is employed in an acoustic resonator enhanced setup to test the viability of the approach and probe the influence of the coupling efficiency on the sound source position. Simultaneously, the influence of the microphone position inside the resonator is determined.

Experimental

An ultraviolet LED (UV-LED LHUV-0415-A070, Lumileds Holding B.V.) emitting light at 415 nm is modulated at frequencies in the range between 500 Hz – 30 kHz and two microphones (ICS-40619, InvenSense) inside a cylindrial acoustic resonator with inner diameter and length of 11.4 mm and 54.5 mm, respectively, determine the sound wave amplitudes resulting from exciting photoacoustic signals at different positions. One microphone is placed on the symmetry axis of the resonator, while the second microphone is placed at the wall. After amplification of the microphone signals a Lockin amplifier (204, Anfatec Instruments AG) is used to analyze their signals. The resonator may be rotated

such that the standing wave distribution may be probed. The setup is depicted in Figure 1.

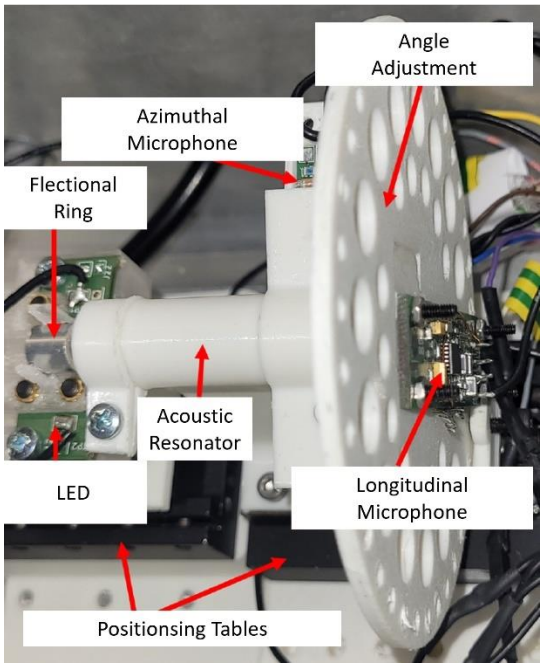


Figure 1: The experimental setup to probe coupling efficiency in the vicinity of the acoustic resonator opening as well as the spatial distribution of the standing wave inside the resonator.

Results

The influence of the position of the photoacoustic source has been determined for various resonator modes and an exemplary result is shown in Figure 2. This highlights the possibility of adjustable the coupling efficiency for different resonance modes. In particular, the most efficient coupling position for the azimuthal mode differs considerably from that for longitudinal modes.

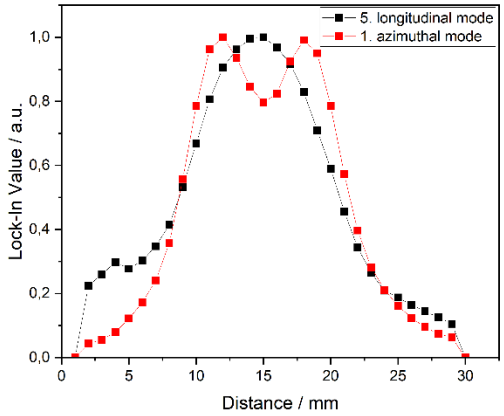


Figure 2: Normalized lock-in values of the radial microphone for two types of modes. The ideal coupling position for longitudinal modes is on the symmetry axis of the resonator, while azimuthal modes show an offset.

The relevance of the placing of microphones for detecting the azimuthal mode is highlighted by the results shown in Figure 3. While the amplitude of longitudinal modes is independent on the rotation, azimuthal modes may only be efficiently detected if the photoacoustic source and the microphone are at suitable angles with respect to each other.

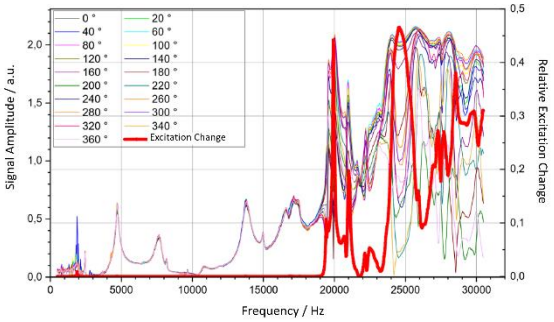


Figure 3: Several resonance frequencies may be excited in the frequency range to 30 kHz. The azimuthal modes spatial distribution makes the positioning the microphone crucial.

Conclusion

The results demonstrate that the relative position of the photoacoustic sound source with respect to the acoustic resonator may be used to tune the coupling efficiency. Since azimuthal and longitudinal modes are also separated in frequency, multiplexing may be used to simultaneously determined photoacoustic signals originating from different locations, which in turn may be used to establish a reference channel.

References

[1] S. Palzer, "Photoacoustic-Based Gas Sensing: A Review," *Sensors (Basel, Switzerland)*, vol. 20, no. 9, 2020, doi: 10.3390/s20092745.

[2] T. Rück, R. Bierl, and F.-M. Matysik, "Low-cost photoacoustic NO2 trace gas monitoring at the pptV-level," *Sensors and Actuators A: Physical*, vol. 263, pp. 501–509, 2017, doi: 10.1016/j.sna.2017.06.036.

[3] K. Schmitt, M. Sendelbach, C. Weber, J. Wöllenstein, and T. Strahl, "Resonant photoacoustic cells for laser-based methane detection," *Journal of Sensors and Sensor Systems*, vol. 12, no. 1, pp. 37–44, 2023, doi: 10.5194/jsss-12-37-2023.

DOI 10.5162/EUROSENSORS2025/T6.2.1

Impedance Spectroscopy Based Flow Rate Monitoring in Autonomous Cell Analytical Micro-Capillary Systems

Péter Fürjes[1], *Dóra Bereczki*[1], *Lilia Bató*[1], *Zsombor Szomor*[1], *János Bozorádi*[1], *Orsolya Hakkel*[1], *Eszter L. Tóth*[1], *Krisztián Papp*[2], *József Prechl*[3]
[1] *HUN-REN Centre for Energy Research, Konkoly-Thege str. 29-33., H-1121 Budapest, Hungary,*
[2] *Eötvös Loránd University, Pázmány Péter prom. 1/c., H-1117 Budapest, Hungary,*
[3] *Diagnosticum Zrt, Attila str. 126., H-1047 Budapest, Hungary*
furjes.peter@ek.hun-ren.hu

Summary:
A hybrid polymer and silicon based, modular, autonomous microfluidic device was designed and fabricated with integrated electrode system to enable simple, robust detection of the interactions between particulate elements of cellular samples as blood and the functionalized capillary wall. The sequential filling of the specially designed capillary system can be monitored by measuring directly the electrical impedance between the integrated parallel electrode lines, thus the cell-surface interaction affected flow characteristics can be quantified. This method enables the fast and easy-to-use detection of disease specific cells from whole blood samples or screening the blood type and coagulation process in the microfluidic system.

Keywords: autonomous microfluidics, impedance spectroscopy, blood screening, coagulation

Introduction

Actual goal regarding the development of Point-of-Care (POC) diagnostic devices is to design complex biosensing solutions integrated with microfluidic systems, which are capable of extracting biomedical information immediately. The passive microfluidic systems utilizing label-free sensing principles and combined with integrated signal detection, processing and communication capabilities can revolutionize the medical diagnostic conceptions. Accordingly, a polymer based, autonomous microfluidic system was designed and fabricated to enable simple monitoring the binding of cells and other particulate elements of blood on the adequately functionalized channel walls or directly the fluidmechnical properties of the sample through the flowrate variation. Previous studies demonstrated that the fast analysis of the AB0 blood group system is feasible in a passive microfluidic system, applying respective antibody reagents and capillary blood samples with different blood groups, as the interaction between the cells and the reagents changes the local hydrodynamic resistance of the microfluidic channels [1].

Materials and Methods

The characteristics of sample flow can be examined in a specially designed, autonomous microfluidic devices. The microfluidic systems have dedicated sequential geometric structure and adequate material composition to define suitable conditions for sensitive detection of individual flow rates. The fluidic channels were fabricated by soft lithography using SU8 molding pattern with adequate heights compatible with cell sizes. Surface modified polydimethylsiloxane (PDMS) was chosen as the structural material of the microfluidic chip to solve the autonomous sample transport. The PDMS was modified by embedding amphiphilic PDMS-b-PEO molecules to achieve adequate hydrophilic behavior of the channels [2].

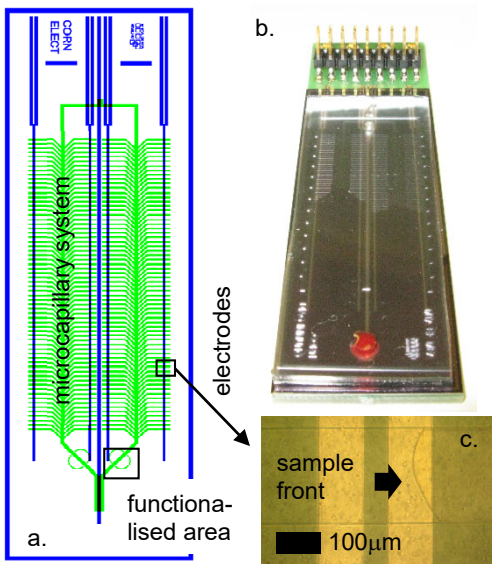


Fig. 1: Schematic architecture of the sequential micro-capillary system (a) and the assembled device during sample loading (b). The sequential resistance change measured between the parallel electrodes (c).

To monitor the sequential filling of the capillaries electrode array was designed and fabricated by micromachining technology on silicon substrate and integrated with the PDMS microfluidic system. The impedance monitoring microsystem contains parallel gold electrodes perpendicularly crossing the microfluidic side channels (Fig. 1). In this work we have demonstrated that the capillary flow in the microfluidic system can be precisely monitored by real-time impedance measurement. As analytical signal the electrical resistance changes of parallel connected fluidic channels was detected to determine fluid movement and sequential channel filling.

Results

As a preliminary functional validation the resistance of the parallel electrode pairs were monitored during capillary filling up the microfluidic system by phosphate buffer solution (PBS) as Fig. 2 demonstrates. The impedance was decreased in quantified steps as the conducting sample shunting the parallel electrodes after reaching the first side channel. Although the step time (time to fill an individual channel) was not changed significantly (Fig. 3).

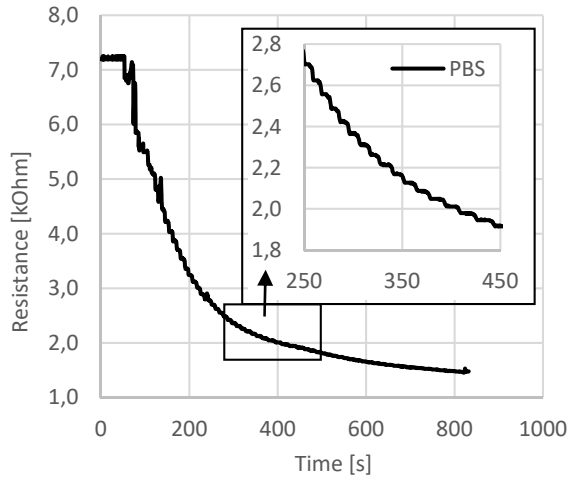


Fig. 2: Time dependent decreasing of electrode resistance clearly demonstrates the sequential filling of individual channels (by PBS).

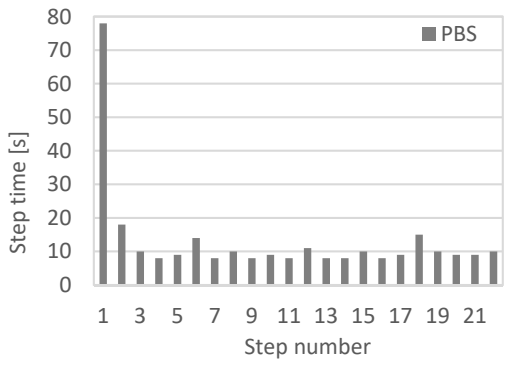


Fig. 3. The filling time of the individual side channels.

The time dependent signal clearly refers the change in sample flow rate, and can quantify the interactions between the blood cells (e.g. coagulation) or between the functionalised channel walls and the specific cells. To demonstrate its feability to quantify interaction-triggered cell binding assay, the blood flow in coagulant modified system was analysed. One of the channel was modified by $CaCl_2$ to significantly change the coagulation behavior of the injected EDTA treated blood sample. The flow characteristics were significantly different in the individual channels, and the coagulant caused flow rate deterioration and clogging as shown in Fig. 4.

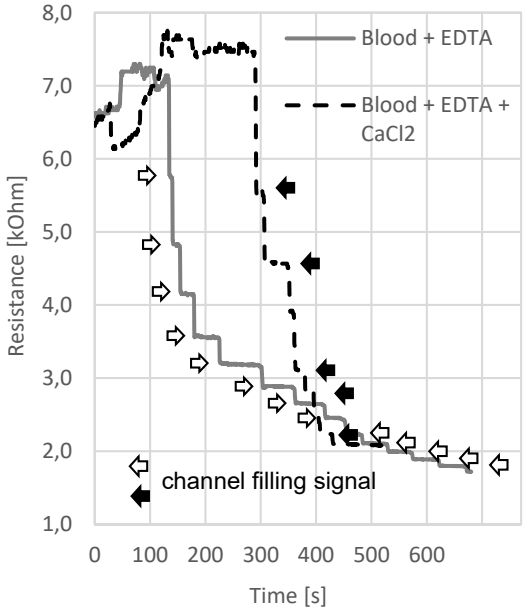


Fig. 4. The sensor signal refers to sample flow rate (step length) and the number of filled channel (step number): the $CaCl_2$ covered surface triggering the coagulation of the blood sample causing slower filling and faster clogging of channel system.

Our proof-of-concept results can provide basis for construction simple quantitative device for blood screening for different diseases.

References

[1] É. Sautner et al., Detection of red blood cell surface antigens by probe-triggered cell collision and flow retardation in an autonomous microfluidic system, Scientific Reports 7, Article number: 1008, 2017

[2] E. Holczer, P. Fürjes, Effects of embedded surfactants on the surface properties of PDMS; applicability for autonomous microfluidic systems, Microfluidics and Nanofluidics 21: 81, 2017

Acknowledgements

The work was supported by the National Research, Development and Innovation Fund (NKFIA) via INBIOM TKP2021-EGA-04 grant.

DOI 10.5162/EUROSENSORS2025/T6.2.2

A Microfluidic Platform based on LIG Electrodes and Machine learning for Real-Time Skeletal Muscle Analysis

Giorgia Curci[1], Mario Marini[2], Joanna Filippi[1], Gianni Antonelli[1], Paola Casti[1], Michele D'Orazio[1], Alessia Riccardi[1], Erica Debbi[1], Sara Pescetelli[1], Antonio Agresti[1], Arianna Mencattini[1], Eugenio Martinelli[1]
[1] Department of Electronic Engineering, University of Rome Tor Vergata, Via del Politecnico 1, 00133 Rome Italy
[2] Department of Systems Medicine, University of Rome Tor Vergata, Via Montpellier 1, Rome 00133, Italy
Corresponding Author's e-mail address: giorgia.curci@uniroma2.it

Summary:

Lab-on-chip technologies offer powerful tools for studying biological processes in physiologically relevant microenvironments. We present a microfluidic platform for real-time analysis of muscle contraction, uniquely integrating Laser-Induced Graphene electrodes fabricated via direct CO_2 laser engraving on polyimide tape adhered to polystyrene. This rapid, low-cost method enables precise electrical stimulation of muscle tissues. Time-lapse microscopy captured the resulting contractions, which were quantitatively analysed using machine learning algorithms to extract contractile features.

Keywords: Laser Induced Graphene, Time-lapse Microscopy, Lan-On-Chip, Skeletal Muscle Contraction.

Background, Motivation and Objective

Lab-on-chip (LoC) platforms are increasingly adopted for in vitro modeling of physiological processes, offering fine control over microenvironments and enabling high-throughput analysis. In particular, LoC systems are well-suited for studying muscle tissue contraction dynamics, a process that requires precise stimulation and real-time monitoring [1]. Electrical stimulation is commonly used in microfluidic devices to induce action potentials in excitable cells, typically implemented via integrated electrodes. These electrodes are often fabricated from metals such as gold or platinum, which require complex microfabrication steps and may pose biocompatibility challenges [2]. Laser-induced graphene (LIG) has emerged as a promising alternative for bioelectronic interfaces due to its excellent electrical conductivity, cytocompatibility, and ease of fabrication [3]. Our approach integrates LIG electrodes directly onto the LoC polystyrene substrate. Starting from commercial polyimide tape (PI), we pattern LIG via laser engraving and peel off the residuals. This technique avoids chemical etching or metal deposition steps and allows the electrodes to be easily and precisely positioned only at the extremities of the microfluidic chamber. This fabrication method ensures compatibility with cell cultures and offers a straightforward path to customization and miniaturization. As a result, the central culture area remains untouched and fully transparent, enabling high-quality optical monitoring. Unlike approaches where the LIG remains on the polyimide substrate, resulting in an opaque surface [4], our transfer technique preserves transparency in the culture zone, which is crucial for real-time optical inspection and imaging. Indeed, we integrate time-lapse microscopy to capture contraction events at high temporal resolution, allowing for direct, video-based quantification of cell activity. To extract meaningful metrics from the time-lapse videos, we employ machine learning techniques to perform motion quantification [5]. This automated image processing pipeline enhances the precision and throughput of contraction analysis.

Methods description

The lab-on-chip device was fabricated using laser cutting techniques on sheets of Polystyrene (PS) from Petri dishes, Polymethyl Methacrylate (PMMA) and Cyclic Olefin Polymer (COP). LIG was synthesized on commercial PI tape, which was directly bonded onto PS substrates. After the laser processing, the non-functionalized residual portions of the tape were carefully peeled off, leaving only the patterned conductive regions adhered to the substrate, as in Fig.1. Electrodes were characterized both electrically with

four probe measurements on 8x8 mm^2 squares and morphologically at Scanning Electron Microscopy (SEM), evaluating the effects of laser processing parameters such as power and speed. C2C12 murine myoblasts were cultured and differentiated on the chip for approximately 20 days, with daily medium refill. At the end of the differentiation period, mature myotubes were obtained, forming skeletal muscle fibers capable of responding to electrical stimulation. Stimulation was delivered using an arbitrary waveform generator, applying square wave signals at a frequency of 0.5 Hz with varying duty cycles. Contractions were recorded via time-lapse video microscopy through an inverted optical microscope at a temporal resolution of ~10 frames per second. The videos were analyzed using machine learning algorithms to identify contraction centers and quantify displacement and contraction velocity.

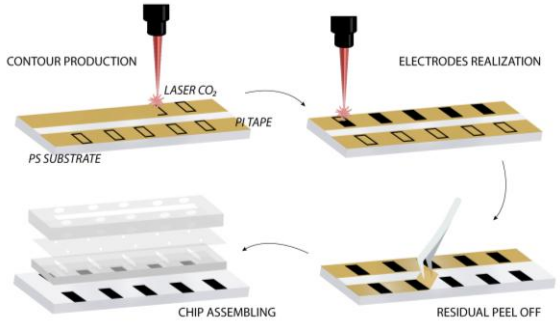


Fig. 1. Scheme of the LIG on PI tape production process and subsequent chip assembling.

Results

The electrical characterization of the LIG electrodes enabled the optimization of the fabrication parameters. Both electrical and morphological analyses revealed directional structure. SEM imaging highlights how the directionality of the laser pattern applied to the polyimide is imprinted onto the plastic substrate, resulting in a well-defined microstructure morphology (Fig. 2). This structural anisotropy is also reflected in the electrical measurements, as resistance values differ significantly depending on the direction of interrogation. Once assembled, the chip supports the replication of skeletal muscle cells, which, upon maturation, form elongated fibers, myotubes, as shown in Fig. 2. Electrical stimulation, optimized at 0.5 Hz with a 100 ms pulse duration, induced muscle contractions that were frequency-aligned. The contraction velocity quantified through an image velocimetry analysis is also reported in Fig. 2.

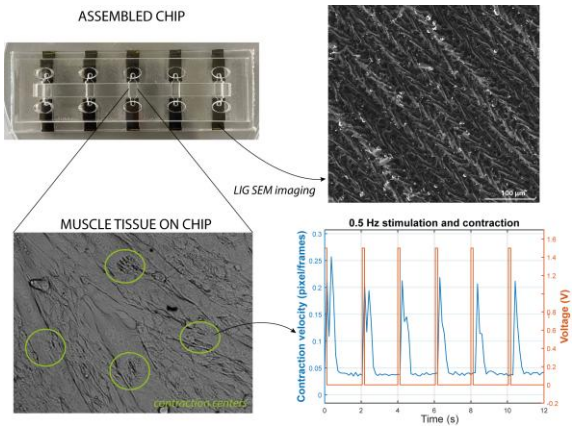


Fig. 2. Assembled chip, SEM images (scale bar 100 µm), muscle tissue in lab-on-chip chamber, stimulation and relative contraction velocity trends.

The resulting device with the integration of LIG electrodes allows for efficient electrical stimulation and real-time monitoring of muscle contraction dynamics, highlighting the platform's potential for customizable bioelectronic assays.

References

[1] J. M. Fernández-Costa et al., Training-on-a-Chip: A Multi-Organ Device to Study the Effect of Muscle Exercise on Insulin Secretion in Vitro, *Advanced Materials Technologies*, (2022), doi:10.1002/admt.202200873

[2] S. Ahadian et al., Interdigitated array of Pt electrodes for electrical stimulation and engineering of aligned muscle, *Lab on a Chip* (2012) 12(18) 3491, doi:10.1039/c2lc40479f

[3] J. Lin et al., Laser-induced porous graphene films from commercial polymers, *Nature Communications (2014) 5(1) 5714,* doi:10.1038/ncomms6714

[4] A. Svetlova et al., Benchtop Fabrication and Integration of Laser-Induced Graphene Strain Gauges and Stimulation Electrodes in Muscle on a Chip Devices, *Advanced Functional Materials* 35(13) (2025); doi:10.1002/adfm.202417184

[5] W. Thielicke, R. Sonntag, Particle Image Velocimetry for MATLAB: Accuracy and enhanced algorithms in PIVlab. *Journal of Open Research Software*, 2021, 9(1), 12., doi: 10.5334/jors.334

Acknowledgements

This work was supported by Italian Minister MUR, PRIN-2022 project "SELENE", grant number 2022RWYH2K_001.

DOI 10.5162/EUROSENSORS2025/T6.2.3

Method for the Detection of Blood Perfusion in Intracranial Tissues with Optical Fiber Sensor

Vincenzo Romano Marrazzo, Maria Alessandra Cutolo, Francesco Fienga, Michele Riccio, Andrea Irace, Giovanni Breglio
Department of Electrical Engineering and Information Technology, University of Naples Federico II, Naples, Italy
vincenzoromano.marrazzo@unina.it

Summary:
The proposed method integrates an optical probe to detect blood and prevent internal bleeding during biopsy, by acquiring reflected signals to identify the presence of blood in real time. This approach is validated using a modulated peristaltic pump that simulates blood flow in an artificial vein. During testing, the phantom is illuminated while a spectrometer collects the reflected light. To enhance detection, a lock-in technique tracks heartbeat-related light variations. Results confirm reliable blood detection, using a biopsy-compatible probe and a prism that replicates the lateral aperture of a typical biopsy needle.

Keywords: Optical Fiber Sensor, Blood Perfusion Detection, Lock-In Detection, Non-Invasive Detection, Optoelectronic System.

Introduction

In brain biopsies, detecting blood flow in real time is vital to prevent serious complications [1]. Usually this type of procedure is guided by imaging tests, such as computer tomography and magnetic resonance, which often run into problems of misalignment between preoperative images and the actual brain anatomy [2]. Optical techniques offer minimally invasive, high-resolution tools to assess tissue health and vessel location [3]. Technologies like laser Doppler [4] allow detailed hemodynamic monitoring. In this work, an optical fiber sensor to detect blood perfusion using a lock-in method is proposed. The system employs a probe to illuminate a silicone vein model perfused with synthetic blood via a modulated peristaltic motor. The lock-in approach enhances the signal-to-noise ratio, enabling precise detection of blood flow and estimation of vein distance.

Methods

The proposed concept aims to associate the blood flow within a vein with the light it reflects, using a distinct modulation signal. By demodulating the acquired optical signal at the modulation frequency, the presence of blood perfusion can be accurately detected. To validate this approach, the experimental setup shown in Figure 1 was implemented. Here, synthetic blood circulates through the test vein, driven by a peristaltic pump operating at 500 rpm. A square wave generator simulates the heartbeat by toggling the pump on and off at a frequency of 1 Hz. The optical part comprises of an optical fiber probe from AVANTES designed with six fibers arranged circularly for illumination and one in the center for reception, with a total diameter of 1.5 mm. The illumination is provided by the AVANTES Avalight-HAL, in the spectrum range of 200-1100 nm. The light illuminates the vein under test, providing a reflected signal addressed to a spectrometer, via a splitter. The employed spectrometer matches the spectral range of the light source and includes dedicated software for light acquisition, allowing for adjustable integration time and data plotting in either time or frequency domain. The reflected signal was acquired from the same probe and processed in MATLAB environment. The vein under test was manufactured using a medium-hard silicone rubber, consisting of an empty internal channel parallel to the working surface, which serves both to pass the synthetic blood and to simulate a vein. Due to its consistency, the flowing synthetic blood caused the external walls to expand at its passage.

Results

Tests were performed measuring the reflected light from a lateral illumination by means of a 45° prism. The light is irradiated inside a drill performed in the phantom at 1 mm of distance from the vein for a time window of 1 and 10 seconds with 100 ms of integration time, and a frequency sampling of 10 Hz.

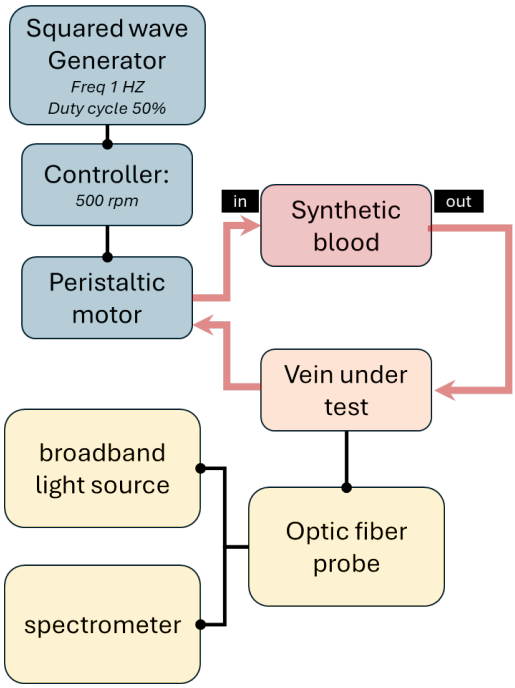


Fig. 1. Block scheme describing the experimental setup.

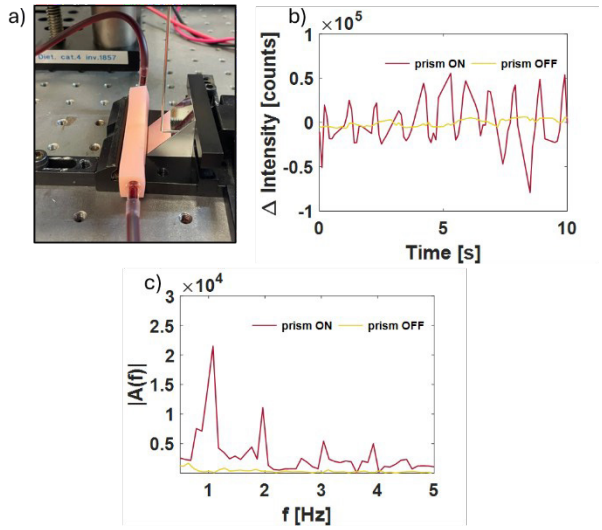


Fig. 2. Illustration of the probe and the phantom under test (a) with relative results in time domani (b) and in frequency (c)

Moreover, data were processed in time and in frequency domain, comparing the results obtained when the motor was in ON state (blood flowing) and in OFF state (blood static). In Figure 2 results are shown: the illustration of the phantom under test subjected to lateral illumination is reported in (a); the time domain variation of the acquired signals is reported in (b). It can be noted the difference between the presence of flow due to the motor, (prism ON and OFF in the plot) since a modulation can be observed. Moreover, to further validate the result, a Fast Fourier Transform (FFT) was performed (c), processing the signal with a Hammington window showing a difference in the 1 Hz harmonic magnitude (modulating frequency) between the signals acquired when the motor was in ON and OFF state. What is worth noting is that the 1 Hz modulation is significant compared to the different condition of motor on/off in time and in frequency domain. Finally, the modulation amplitude was calculated for the position previously described, following the method described in [5], comparing the results in case of blood flowing and in case of static blood. The results in Tab 1 show that the signal amplitude differs by approximately two orders of magnitude between the ON and OFF states. This confirms that when the fundamental harmonic of the reflected light aligns with the modulation signal, the lock-in technique successfully detects the presence of blood flow. Finally, it was demonstrated that the system can reliably detect blood perfusion in the artificial vein using a probe compatible with standard biopsy needles, typically designed with lateral aperture.

Tab. 1: Results on the amplitude calculated in static and dynamic blood flowing in different time intervals

Time interval	Blood flowing (motor ON)	Blood not flowing (motor OFF)
10 sec	9.44 x10^3	0.15 x10^3
1 sec	8.22 x10^3	0.23 x10^3

References

[1] Azagury, D. E., et al., (2015). Image-guided surgery. Curr Probl Surg, 52(12), 476-520.

[2] Bucholz, R. D. (1995). Introduction to journal of image guided surgery. Journal of image guided surgery, 1(1), 1-3.

[3] Valdes, C. P., et al., (2014). Speckle contrast optical spectroscopy, a non-invasive, diffuse optical method for measuring microvascular blood flow in tissue. Biomedical optics express, 5(8), 2769-2784.

[4] Wardell, K., et al., (2007). A laser Doppler system for intracerebral measurements during stereotactic neurosurgery. 29th Annual International Conference of the IEEE Engineering in Medicine and Biology Society (pp. 4083-4086).

[5] Zhang, S., et al. (2016). Optimization of a digital lock-in algorithm with a square-wave reference for frequency-divided multi-channel sensor signal detection. Review of Scientific Instruments, 87(8).

Acknowledgements

This work was supported by the MISE Project F/310089/01-05/X56, submitted under the Decree of March 18, 2022, as part of the Innovation Agreements Ministerial Decree of December 31, 2021, titled “PROTECH - Robotic Teleoperation Platform for Minimally Invasive Surgery” (CUP: B89J23000930005 – COR: 10820791).

DOI 10.5162/EUROSENSORS2025/T6.3.1

Flexible surface-enhanced Raman spectroscopy sensor for wearable devices

Karolina Milenko, Elizaveta Vereshchagina, Abelia Ellingsen
SINTEF Microsystems and Nanotechnology, Gaustadalleen 23C, 0737 Oslo, Norway,
karolina.milenko@sintef.no

Summary:
We report the fabrication and characterization of a flexible, nanostructured surface-enhanced Raman spectroscopy sensor designed for integration in wearable optical devices. This sensor utilizes the biocompatible material FlexDym®, which offers excellent flexibility and advantages in manufacturing. The nanostructures are embossed through a temperature and pressure-assisted molding process using a silicon master. The fabricated SERS structures exhibit significant enhancement in Raman signal detection. This work advances state-of-the-art in flexible SERS and wearables.

Keywords: SERS, wearable sensors, biosensors, nanofabrication, Raman spectroscopy

Background

Raman spectroscopy provides a molecular fingerprint signal that corresponds to the specific structural vibrations of molecules, enabling label-free detection. Surface-enhanced Raman Spectroscopy (SERS) amplifies the Raman signal by 10^{10} to 10^{11}-fold using nanostructured metallic surfaces, thereby achieving very high sensitivity [1]. Recently, flexible SERS has garnered significant interest due to its potential in a wide range of applications, particularly for detecting molecules on irregularly shaped objects [2]. These applications include non-invasive detection of biomarkers in biological tissues, food safety monitoring for pesticides and contaminants in fruits, vegetables, and other food items, textile analysis for dyes and chemicals on fabrics, forensic science for trace detection of drugs and explosives on various surfaces, and environmental monitoring. FlexDym® used in this work is the first prototyping material specifically designed for microfluidics community as an alternative to PDMS, offering flexibility, mouldability, scalability, transparency and resistance to molecules adsorption. It also has been shown to have no harmful effects to the human body when in contact for a prolong amount of time (ISO certified for interaction with blood, in vitro cytotoxicity, systemic toxicity, etc. [3]). To leverage these advantages, we developed a novel fabrication process for flexible SERS sensors using FlexDym®.

Methods

The nanostructured masters for molding SERS (various periodic patterns with characteristic dimensions in the range of 170–330nm, and depth 200-600nm) were fabricated in a cleanroom using a combination of UV-Nanoimprint Lithography (UV-NIL) and Dry Reactive Ion Etching (DRIE) [4] (Fig. 1 A-D). For the molding process, FlexDym® sheets are placed over the Si masters, with controlled temperature and pressure conditions using a portable embossing setup. This ensures the accurate transfer of nanostructures from the Si master to the FlexDym® sheets. The molded FlexDym® sheets are then separated from the master, resulting in flexible SERS substrates with the desired nanostructures. The final step involves coating the FlexDym® substrates with a layer of gold (60 nm) using a sputter tool (Q150R ES, Quorum Technologies, UK) (Fig.1 E-H). This gold coating enhances the SERS effect by providing the necessary metallic surface for signal amplification.

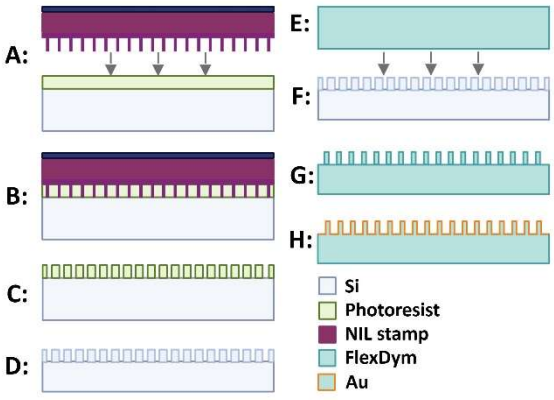


Fig. 1. A simplified schematic of the fabrication flow of a mold in Si (A to D) and the flexible SERS device (E to H).

The fabricated sensor consists of 4 active SERS areas 1mmx1mm each, with periodic, rectangular nanostructures, coated with 60nm Au (Fig 2).

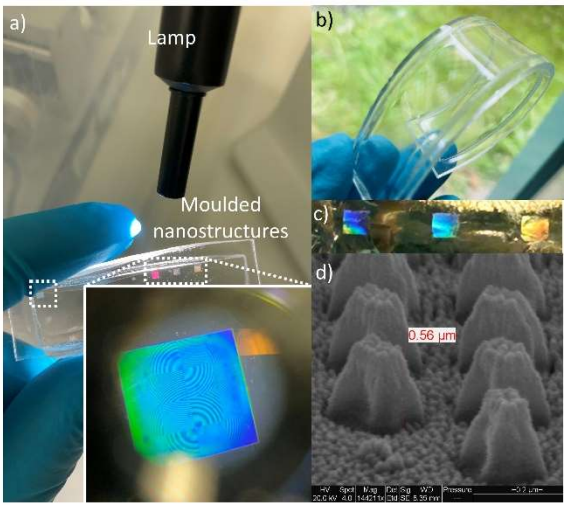


Fig. 2.a) A photograph of molded substrate with four SERS areas 1mm x 1mm each, and an optical microscopy image of the molded SERS in FlexDym® showing characteristic diffraction pattern; b) A photograph of; c) Molded SERS coated with 60nm of gold; d) SEM of the metasurface master used for molding.

Results

For the SERS measurements a BWS465-785S i-Raman Plus spectrometer with a fiber probe and 785nm excitation wavelength was used. Rhodamine 6G (R6G, Merck KGaA) which was diluted in water and used as a sample for benchmarking and comparison with other published works. 6 µL of R6G was pipet onto SERS chips and left to dry. The measured Raman intensity shows excellent enhancement of the fabricated nanostructures and a different level of enhancement depending on the nanostructures shape (Fig. 3a). To evaluate the performance of the flexible SERS sensors, three different FlexDym® material thicknesses were tested: 250, 750, and 1200 µm. The Raman spectra obtained from different thicknesses showed similar SERS responses, indicating that the thickness of the FlexDym® material does not affect the enhancement of the Raman signal (Fig. 3b).

Conclusions

We presented a flexible SERS sensor fabricated using novel and biocompatible material FlexDym®. The nanostructured SERS chips are molded and replicated, allowing for efficient fabrication with high accuracy possible for mass production. Moreover, the approach allows for a straightforward integration with other Si- or glass-based components and supports innovations requiring molding of ultra-small structures. Future work will include combining the SERS sensor with flexible microfluidic chip with a sub-microliter chamber with inlets for passive sample collection.

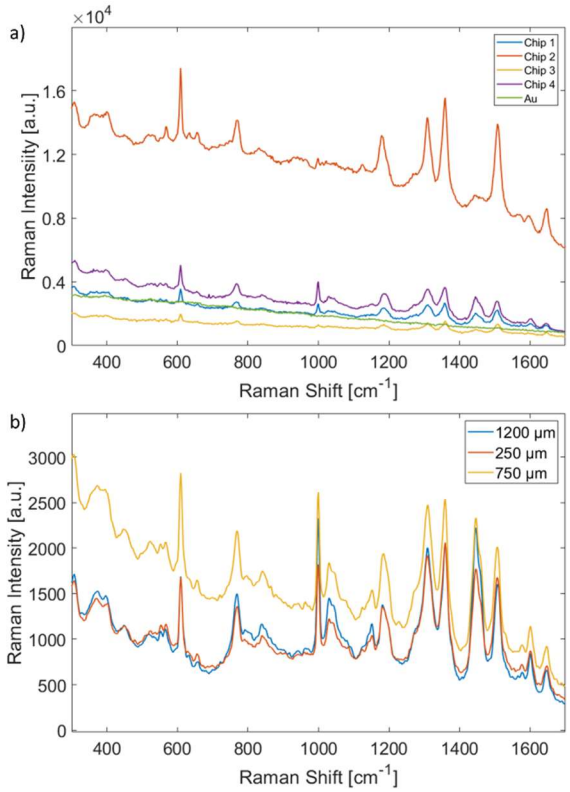


Fig. 3. Measured Raman spectra of a) 1mM R6G dried on 250µm FlexDym® SERS and on gold for comparison; b) R6G on SERS in molded in three thicknesses 250, 750 and 1200µm of FlexDym® material.

References

[1] E.C. Le Ru et al. Enhancement Factors: A Central Concept during 50 Years of Surface-Enhanced Raman Spectroscopy, ACS Nano 18(14), 9773-9783 (2024); doi:10.1021/acsnano.4c01474

[2] K. Xu et al., Toward Flexible Surface-Enhanced Raman Scattering (SERS) Sensors for Point-of-Care Diagnostics. Adv. Sci. 6, 1900925 (2019); doi:10.1002/advs.201900925

[3] https://eden-microfluidics.com/flexdym-microfluidic-chips/

[4] C.A. Dirdal et al. UV-Nanoimprint and Deep Reactive Ion Etching of High Efficiency Silicon Metalenses: High Throughput at Low Cost with Excellent Resolution and Repeatability, *Nanomaterials* 13, 3 (2023); doi:10.3390/nano13030436

Acknowledgements

This research was partially funded by the Research Council of Norway, project number 194068/F40. The authors would like to thank the European Commission and the Research Council of Norway for funding in the frame of the collaborative international consortium STARDUST financed under the 2022 Joint call of the European Partnership 101060874 - Water4All.

DOI 10.5162/EUROSENSORS2025/T6.3.2

DNA-scaffold biosensors for real-time pH tracking in dynamic environments

Gianni Antonelli[1], Alejandro Chamorro-Garcia[2], Paola Spitalieri[3], Arianna Mencattini[1], Giorgia Curci[1], Joanna Filippi[1], Alessia Riccardi[1], Paola Casti[1], Erica Debbi[1], Michele D'Orazio[1], Federica Sangiuolo[3], Andrea Idili[2], Eugenio Martinelli[1]

[1] Department of Electronic Engineering, University of Rome Tor Vergata, Via del Politecnico 1, 00133 Rome Italy
[2] Department of Chemical Sciences and Technologies, University of Rome Tor Vergata, Via della Ricerca Scientifica, Rome 00133, Italy
[3] Department of Biomedicine and Prevention, University of Rome Tor Vergata, Via Montpellier 1, Rome, 00133, Italy
Corresponding Author's e-mail address: g.antonelli@ing.uniroma2.it

Summary:
Lab-on-chips have transformed the approach to studying biological models for drug discovery. However, some information could be misinterpreted without knowing the chemical information near the biological entity. In this work, we exploited DNA scaffolds to realise fluorescent hydrogel pH microsensors that can be easily integrated into lab-on-chips. A machine learning model was trained to read the biosensors' response and predict pH in a dynamic microfluidic environment. The proposed system is highly biocompatible and can be used in many biological applications, such as monitoring organoids' metabolism.

Keywords: DNA scaffold sensors, real-time monitoring, pH sensing, lab-on-chip, machine learning

Background, Motivation, and Objective

In recent years, biological research has advanced significantly, driven by breakthroughs in bioengineering and microfabrication [1]. Organoids and lab-on-chip technologies have enabled researchers to investigate biological mechanisms at unprecedented levels, accurately replicating tissue and organ functions within microscale environments. However, integrating real-time monitoring with high spatiotemporal resolution into these platforms remains a considerable challenge, limiting the ability to capture the intricate dynamics of biological activities, which are fundamental to uncovering new insights into human physiology [2].

Optical sensors play a pivotal role in detecting subtle biological dynamics by translating them into variations in optical properties, offering a powerful approach for real-time analysis near living systems [3]. The data collected from optical biosensors is typically embedded in complex signals (such as spectra or images) and often requires advanced processing to extract meaningful information [4].

This work presents an integrated platform that leverages DNA scaffolding technology to develop hydrogel fluorescent biosensors, combined with computer vision and machine learning, for real-time detection of the target compound. The sensors have been integrated into a lab-on-chip using a custom stereolithographic technique, and a machine learning algorithm was designed to analyse the hydrogel images. To further enhance sensor performance, the system was calibrated for pH monitoring using a ratiometric approach, enabling real-time measurements [5].

We validated this platform by monitoring the pH changes in a microfluidic system. We dynamically imposed the pH using a syringe pump and different buffer solutions, recording real-time fluorescent images while predicting the local pH with the machine learning algorithm. We believe this system can be easily integrated to monitor biological dynamic applications, particularly organoids.

Methods

Lab-on-chips were fabricated using laser ablation of Poly Methyl MethAcrylate and Cyclic Olefin Polymer slabs, making them adhere using adhesives and a hydraulic press.

After that, the biosensors prepolymer was prepared by mixing Poly Ethylene Glycol DiAcrylate, LAP photoinitiator and the DNA scaffold sensing molecule. The solution was introduced in the lab-on-chip chamber and crosslinked using a custom

stereolithographic setup. This optical system uses a commercial projector to permit UV light patterning in the lab-on-chip. After rinsing in distilled water, the biosensors were ready for use (see Fig. 1).

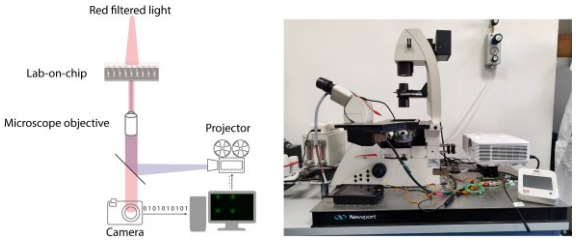


Fig.1: A scheme and a picture of the stereolithographic optical setup used to grow hydrogel biosensors.

Subsequently, fluorescence microscopy was used to capture images of the biosensors at different pH levels. This image dataset was then processed and utilised to train a custom machine-learning algorithm.

After the training, the lab-on-chips were connected to a microfluidic setup to impose the flow of different buffer solutions in the chambers. In the meanwhile, the device was monitored using fluorescent time lapse microscopy.

Results

The proposed system was calibrated using a series of buffer solutions, enabling the integrated machine-learning algorithm to estimate pH values based on fluorescence images. The platform demonstrated a rapid response time, making it suitable for integration into dynamic microfluidic environments.

To assess its performance under changing conditions, we used a syringe pump connected to a microfluidic setup to modulate the pH in real time while continuously acquiring fluorescence images of the hydrogel-based biosensors. This approach allowed for continuous monitoring and estimation of local pH within the microfluidic chamber throughout the whole experiment. An example of pH estimation under dynamic conditions is shown in Figure 2, where changes in pH were precisely tracked within the microfluidic system.

As an additional validation step, the Lab-on-Chip device was tested using embryoid bodies, one of several possible biological models such as organoids or microtissues, that can be monitored during experiments. In this case, we observed that biosensors positioned closer to the biological structures exhibited greater sensitivity, detecting localised decreases in pH associated with cellular metabolism (detailed data will be shown at the conference).

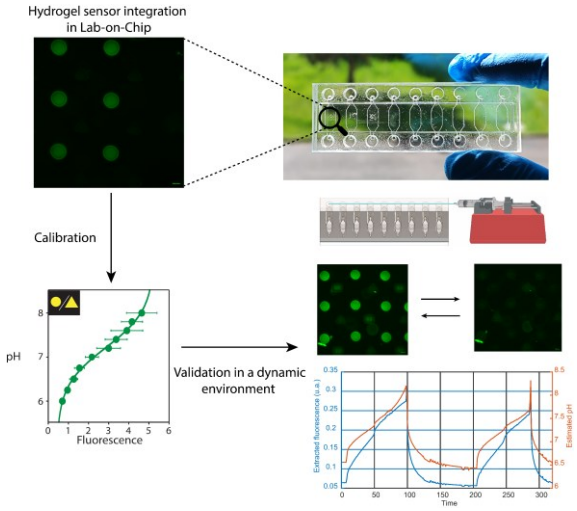


Fig 2: pH hydrogel biosensors are integrated into Lab-on-Chip, and a machine learning algorithm is calibrated to predict pH. This platform is then validated in different dynamic environments.

Ultimately, the system provides a straightforward and efficient method for real-time pH measurement in Lab-on-Chip environments. Furthermore, the platform can be extended with appropriate modifications to accommodate multiple hydrogel-based sensors, allowing simultaneous detection of various analytes within a single experiment.

References

[1] S. E. Park, et al., “Organoids-on-a-chip”, *Science* 634, 960-965 (2019); doi: 10.1126/science.aaw7894

[2] E. Gayibov et al., “The use of patient-derived xenografts and patient-derived organoids in the search for new therapeutic regimens for pancreatic carcinoma. A review”, *Biomedicine & Pharmacotherapy* 182 (2025), 182, 117750; doi: 10.1016/j.biopha.2024.117750.

[3] Z. Liao et al., “Microfluidic chip coupled with optical biosensors for simultaneous detection of multiple analytes: A review”, *Biosensors and Bioelectronics* 126 (2019), 697-706, doi: 10.1016/j.bios.2018.11.032

[4] G. Antonelli et al., “Integrating machine learning and biosensors in microfluidic devices: A review”, *Biosensors and Bioelectronics* 263 (2024), 116632, doi: 10.1016/j.bios.2024.116632

[5] G. Antonelli et al., “Continuous pH Monitoring in Organ-on-Chip devices with Single-step Fabricated DNA Scaffold Sensors Conjugated Hydrogels and Machine learning”, *Submitted*

DOI 10.5162/EUROSENSORS2025/T6.3.3

Modelling and Design of a Microfluidic Platform for Precision Exposure to Environmental Samples of Surface-Enhanced Raman Scattering Sensors

Simone Zonetti, Elizaveta Vereshchagina, Karolina Milenko
SINTEF Digital, Gaustadalléen 23C, Oslo, Norway
Simone.Zonetti@sintef.no

Summary:

SERS sensors offer high sensitivity for real-time molecular detection but face limitations due to sample drying and reproducibility in exposure to samples. Integrating SERS with microfluidics addresses these issues. Here, we discuss microfluidic designs and material selection to enhance SERS sensitivity and minimize background interference. Using Finite Element Method (FEM) simulations and experimental optical characterization, we systematically optimized designs for uniform SERS sensors exposure to liquid samples. The manufacturability of microfluidics in glass and wafer-level anodic bonding for integration were considered.

Keywords: Surface-enhanced Raman spectroscopy, microfluidics, water analysis, optical sensor

Background

Microfluidic SERS sensors are promising for real-time field monitoring of emerging contaminants in water, addressing public health, and climate change concerns (Fig.1) [1-3]. SERS excels in obtaining molecular "fingerprints" without labeling, detecting complex matrices, and being miniaturized for portable monitoring [4]. Sampling reliability and sensor-flow interaction are crucial [5]. Integrating SERS with microfluidics was shown to enhance detection [2,3].

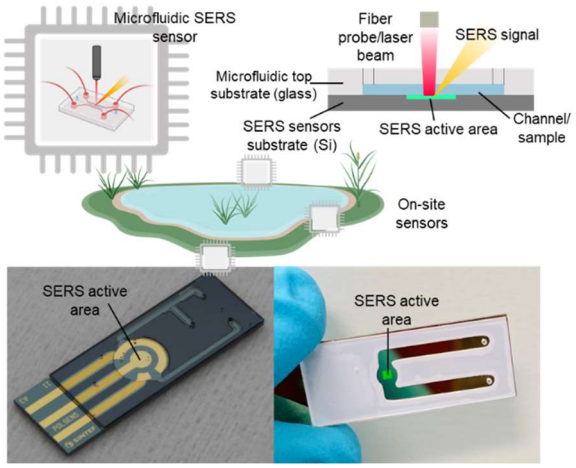


Fig. 1. Concept and examples of fabricated microfluidic SERS sensors [1-4] (part of the image is created with BioRender.com).

Reported microfluidic systems often lack a systematic approach to microfluidics design and material selection, as well as a manufacturability perspective. This publication addresses this gap.

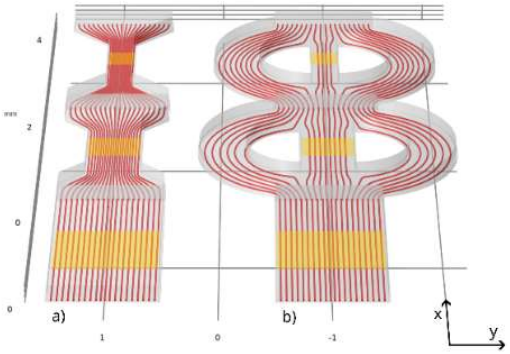


Fig. 2: Microfluidic channel designs, including flow lines, consisting of 3 consecutive SERS elements spaced by 2 mm. a) Tapered channel design, b) Side channel design. The location of the SERS areas is highlighted in yellow. The flow is along the x axis.

Description of the FEM model and aims

The main goal is to optimize the design of microfluidic channels to ensure uniform flow conditions across the entire SERS active area and at the interface with the liquid sample, preferring lower flow velocities that lead to longer interaction with the SERS surface. We aim at designs offering comparable performance for different SERS area sizes, which are combined within a single channel (Fig.2). We consider as baseline a channel with a cross-section of 1000x50 µm, optimizing the design while addressing

technological and experimental issues. We aim for larger channel depths above SERS areas, as it has been experimentally observed that the optical detection through shallower channels can be compromised both due to high background reducing the SERS signal (Fig.3) and material properties generating additional Raman peaks (Fig.4). Considering the laser spot size of 84 µm, and need for alignment, it is desirable to have a channel not wider than the SERS area itself. With a straight channel design tapering to the SERS sizes, velocities would vary between designs and therefore require compensation. To address these issues, we consider two main additions to baseline design: 1) extra depth; 2) side channels, redirecting part of the flow from the SERS. The 3D model consists of a 2 mm long section of the channel, centered in the middle of the SERS area, which is also the middle of the channel. We model each design independently, to reduce computational load, assuming the flow returns to an unperturbed, fully formed creeping flow after each section. The model is symmetrical and solved for half the geometry (Fig.5a).

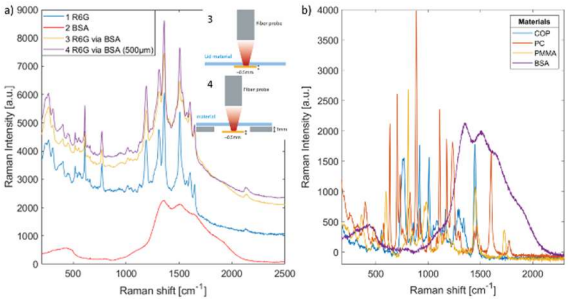


Fig. 3: Raman spectra of a) (1) Rhodamine 6G (R6G), (2) Borosilicate (BSA) fluidic substrate, (3) R6G measured via BSA in proximity, (4) R6G via BSA in a 0.5mm distance; b) Raman spectra of different microfluidic substrate materials

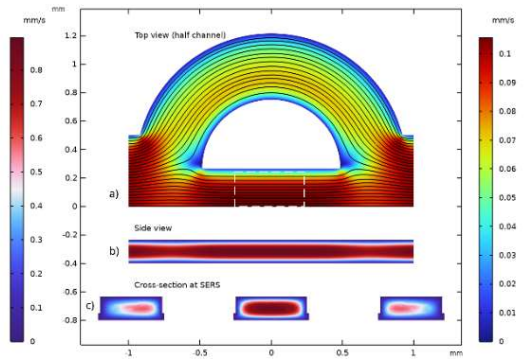


Fig. 5: Flow velocity norm for a proposed design with 500 µm SERS side length, 450 µm wide side channels, and extra channel depth. Velocities are uniform towards the center of the SERS area, inside the dashed line in a) and in the cross-section c).

Results and conclusions

Based on the FEM results (Fig.5, Table 1), while a 1 mm SERS area with extra depth† is the simplest and best performing design, cost and alignment issues suggest the need for a better solution. A 250 µm SERS area‡ could suffer from non-uniform and relatively larger flow velocities, affecting measurement quality. A 500 µm SERS area*, with extra channel depth and side channels, offers a good compromise between the two, with only 1/4 of the surface, flow velocities (v_{max}) comparable to the straight channel and relatively low transversal velocity falloff (δ_v^T).

Tab. 1: Main designs and flow characteristics.

SERS	Type	v_{max}	δ_v^T
1000	baseline	100%	0%
1000†	+depth	11%	0%
500	tapered, +depth	24%	2%
500*	side chan., +depth	12%	2%
250	tapered, +depth	56%	26%
250‡	side chan., +depth	14%	26%

References

[1] R. Moldovan et al., Anal. Chim. Acta, 1209 (2022), 339250.

[2] R. Moldovan et al., Food Chem., 405 (2023), 134713.

[3] E. Vereshchagina et al., IEEE SENSORS 2023; doi: 10.1109/SENSORS56945.2023.10324970.

[4] K. Milenko et al., Nanomater., 13 (2023), 10, 1598.

[5] S. Lian et al., ACS Appl. Mater. Interfaces, 17 (2025), 10193-10230.

Acknowledgements

The authors would like to thank the European Commission and the Research Council of Norway for funding in the frame of the collaborative international consortium STARDUST financed under the 2022 Joint call of the European Partnership 101060874 - Water4All.

DOI 10.5162/EUROSENSORS2025/W7.1.1

Electropolymerization of Amino-Derived Silicon Phthalocyanines for Chemical Sensing Applications

Mélanie Cyr[1,2], *Gabriele Magna*[3], *Francesco Pizzoli*[3], *Alessandro Mita*[3], *Lorena Di Zazzo*[3], *Roberto Paolesse*[3], *Benoît Lessard*[2], *Jaclyn Brusso*[1]

[1] *Department of Chemistry and Biomolecular Sciences, University of Ottawa, Ottawa, ON K1N 6N5, Canada*

[2] *Department of Chemical and Biological Engineering, University of Ottawa, Ottawa, ON K1N 6N5, Canada*

[3] *Department of Chemical Sciences and Technology, University of Rome Tor Vergata, 00133 Rome, Italy*

Corresponding Author's e-mail address: roberto.paolesse@uniroma2.it

Summary:

Silicon phthalocyanines (SiPcs) are a versatile class of organic semiconductors for applications in organic thin film transistors (OTFTs) and organic photovoltaics (OPVs) due to their simple synthesis, easy tunability and high charge transport characteristics. Herein, a novel class of electropolymerized SiPcs have been synthesized and incorporated in both mass-based and conductometric sensors. The results indicated that not only were both sensor types successful in recognizing various gases and volatile organic compounds, but partial selectivity was also achieved in the conductometric sensors with high sensitivity for CO_2 and trimethylamine gases.

Keywords: Electropolymerization, phthalocyanines, electronic nose, quartz microbalance, interdigitated electrode

Introduction:

Organic sensors provide a cost-effective alternative to conventional inorganic sensors for analyte detection with low temperature manufacturing and simple operation, with small form factor.[1] Phthalocyanines is an exciting class of small molecules organic semiconductor with high thermal and chemical stability that can be synthesized in a few high yielding steps. Phthalocyanines can also interact with redox active species through electron transfer, making them great candidates for various sensing applications. Silicon Phthalocyanines (SiPc) are tetravalent molecules which can be easily functionalized through axial coupling leading to changes in solubility, solid state packing and tuning frontier molecular orbital energy levels.[2]

Electropolymerization of amino-derived porphyrin and corrole materials via cyclic voltammetry is a facile and effective method in fabricating polymeric films onto conductometric sensors, for gas sensing and electronic nose applications.[3] The polymer forms via a phenazine bridge catalyzed by aminophenyl groups on the materials. The work presented herein looks at the electropolymerization of novel *para*, *meta* and *ortho* oriented bis(aminophenoxy) silicon phthalocyanines (SiPcs), where the formation of the phenazine linkers occurs at the axial position rather than the periphery of the phthalocyanine. This will create a linear polymer where the SiPc cores will be parallel to one another, which can be ideal for charge transfer within the polymer material. The SiPc polymers (poly-SiPc) were polymerized and characterized on both quartz microbalances (QMBs) for mass-based sensing and interdigitated electrodes (IDEs) for conductometric sensing against gases and volatile organic compounds (VOCs) for the very first time.

Materials and methods:

The synthesis of the amino-derived silicon phthalocyanines (SiPcs) was done using a similar synthetic pathway for other previously synthesized SiPc derivates.[4] The poly-SiPcs are produced via electropolymerization using either cyclic voltammetry (CV) or chronoamperometry (CA) techniques. Polymers were deposited firstly on indium tin oxide (ITO) glass to characterize the optoelectronic properties of the polymer films, followed by deposition on QMB and IDE (Figure 1A). During the deposition, the ITO glass or electrodes were immersed in a 1 mM monomeric solution of the amino-derived SiPc in dichlorobenzene (DCB)

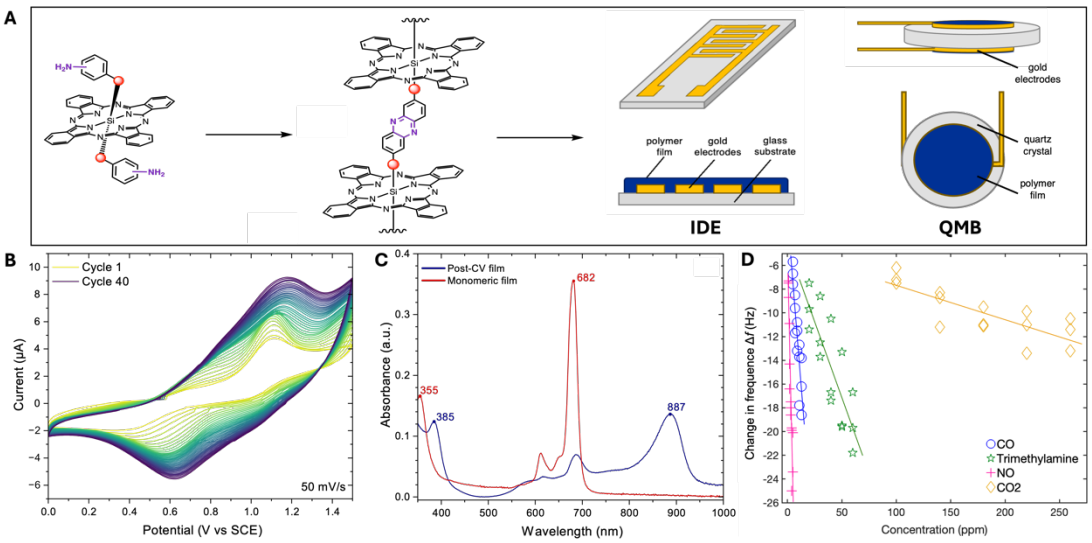


Figure 1. A) Polymerization process of amino-derived SiPc and visual representation of the film growth onto QMB and IDE electrodes. B) Typical cyclic voltammogram upon polymer formation. C) UV-vis-NIR characterization of the polymer film on ITO glass versus the starting monomer. D) Characteristic curves of para-SiPc polymer to CO, TMA, NO and CO_2.

containing 0.1 M of tetrabutylammonium perchlorate (TBAP) as the supporting electrolyte. For the testing of the sensors, QMBs and IDEs are enclosed in a chamber connected to a mass flow controller regulated to deliver specific gas concentrations blended with N_2. The QMB and IDEs are tested against carbon monoxide (CO), carbon dioxide (CO_2), nitric oxide (NO), trimethylamine (TMA), H_2O, toluene, hexane, ethanol, pentanol, triethylamine (TEA), and acetic acid (AcOH). The fundamental oscillation frequency (for QMB) and resistances (for IDE) of the sensors are measured at 1 sample/s with a proper electronics or multichannel multimeter connected to a computer; delta frequencies or relative resistance changes in responses have been considered as features, and data analysis is performed in Matlab®.

Results and discussion:

Three amino-derived SiPc monomers were synthesized, where the amino groups vary from the *para, meta* and *ortho* positions, to further evaluate the ease with which the material polymerizes depending on its positioning. The materials were characterized via UV-vis-NIR spectroscopy and spectroelectrochemistry which confirmed successful polymerization of the *para* and *ortho* derivatives only (CV and UV-vis spectra seen in Figures 1B and 1C).

The sensing performances of the polymer films formed via CV and CA on QMBs were investigated by testing gases (CO, CO_2, NO, TMA) and VOCs (H_2O, Toluene, Hexane, EtOH, PentOH, TEA, AcOH). Results showed that although all QMBs were successful in sensing all analytes, slight differences in the selectivity can be observed when comparing polymers from the *para* and *ortho* derivatives (an example of the response curve for a QMB sensor against gases can be seen in Figure 1D). Furthermore, when tested as an array, the principal component analysis (PCA) demonstrates that the films formed from either CV or CA will also have some difference in the correlation of their detection, thus allowing for the sensors to work together and gain selectivity as an electronic nose.

For the IDE sensors, the sensitivity of each poly-SiPc IDE has been shown to vary when tested under darkness and under light, with an increased signal response when subjected to analytes under visible light (white LED). The IDEs were tested firstly against varying concentrations of gases (CO, CO_2, NO, TMA) mixed with N_2, from which selectivity for CO_2 and TMA gases was apparent. Further ongoing testing is being conducted with this series of sensors under synthetic air and at varying humidity levels to evaluate their responding potential under realistic environmental conditions.

References

[1] R. Paolesse, S. Nardis, D. Monti, M. Stefanelli, C. Di Natale. *Chem. Rev.* 117, 2517–2583 (2017); DOI: 10.1021/acs.chemrev.6b00361

[2] B. H. Lessard. *ACS Appl. Mater. Interfaces.* 2021, 13, 27, 31321–31330; DOI : 10.1021/acsami.1c06060

[3] L. Zazzo, I. di Filippo, L. Guido, G. Magna, L. Lvova, F. Caroleo, M. Stefanelli, L. Duranti, S. Nardis, C. Di Natale, R. Paolesse. *Adv. Sens. Res.* 3, 2400005 (2024); DOI: 10.1002/adsr.202400005

[4] B. H. Lessard, R. T. White, M. AL-Amar, T. Plint, J. S. Castrucci, D. S. Josey, Z.-H. Lu, T. P. Bender. *ACS Appl. Mater. Interfaces.* 7, 5076−5088 (2015); DOI: 10.1021/am508491v

DOI 10.5162/EUROSENSORS2025/W7.1.2

WO_3/ SnS_2 Hybrid Material for ppb-level NO_2 Detection

Aladine Fdhila[1,2], Fatima Ezahra Annanouch[1], Zouhair Haddi[2], Eduard Llobet[1]
[1] Departament d'Enginyeria Electronica, Universitat Rovira i Virgili, Països Catalans 26, 43007 Tarragona, Spain,
[2] NVISION Systems and Technologies, Avenida de Barcelona 105, 08700 Igualada, Barcelona, Spain

Corresponding Author: fatimaezahra.annanouch@urv.cat

Summary:

Heterostructures exhibit superior performance, due to strong interfacial interactions, compared to their single-component structures. Herein, we demonstrate the effectiveness of a hybrid structure of tungsten trioxide (WO_3) nanoneedles loaded tin disulfide (SnS_2) nanosheets, for NO_2 detection at law temperature. The co-existence of both materials is confirmed by FESEM and EDX. Furthermore, the impact of SnS_2 material on the WO_3 gas-sensing performance was demonstrated by the sensor's response to 800 ppb of NO_2 at law temperature, where the response of WO_3/SnS_2 was amelioration by 5 folders compared to bare WO_3. Notably, the WO_3/SnS_2 heterostructure exhibited high sensitivity toward NO_2 at the ppb level, operating efficiently at room temperature.

Keywords: Gas sensors; TMDs; SnS_2; WO_3; AACVD; APCVD; nanomaterials.

Background, Motivation and Objective

Tungsten oxide (WO_3) is a versatile n-type semiconductor with a band gap of 2.6–2.8 eV, which is a conventional type of gas-sensing material. Its wide band gap and excellent gas-sensing properties make it a strong candidate for detecting various gases such as NO_2, H_2S, acetone, NH_3, CO, and others [1]. Nonetheless, its high operating temperature, high power requirements, and lack of selectivity have triggered a hunt for new gas-sensing materials or structures with better response and selectivity at room temperature. Transition metal dichalcogenides (TMDs) nanostructured materials possess unique physical and chemical properties, making them promising candidates for electrically transduced gas sensors. Among TMDs, tin disulfide (SnS_2) nanostructure demonstrates excellent characteristics for gas sensing applications, such as a large surface area, abundant active sites, high selectivity, as well as long-term stability [2]. In an attempt to address the shortcoming observer in WO_3 and inherent its limitations for gas sensors, scientists have focused on creating hybrid nanocomposites of metal oxides and Transition metal dichalcogenides (TMDs) nanomaterials in order to produce heterojunctions and attain enhanced gas-sensing performance with tunable electronic properties that surpass the capabilities of a single material. NO_2 is one of the most hazardous air pollutants, that poses serious risks to soil, water, and the atmosphere. It plays a significant role in the production of ozone layers, acid rain, and photochemical smog. Extended exposure to NO_2 concentrations above 3 ppm can lead to severe respiratory illnesses and even death. Therefore, it is crucial to monitor NO_2. Here, we report the successful synthesis of WO_3\SnS_2 heterostructure using the combination of aerosol assisted and atmospheric pressure chemical vapor deposition methods, (AACVD and APCVD), for ppb traces level detection of NO2 at temperatures near the one of the ambient.

Description of the New Method or System

The first step is the direct growth of WO_3 nanoneedles onto alumina substrate via aerosol-assisted chemical vapor deposition (AACVD) of 50 mg tungsten hexacarbonyl ($W(CO)_6$) dissolved in a mixture of 20 mL of acetone and methanol, at temperature of 400ºC. Herein, 0.5 L/min of nitrogen was used as a carrier gas. Subsequently, SnS_2 nanosheets were synthesized via an ambient-pressure chemical vapor deposition (APCVD) sulfurization process, using SnO_2 and sulfur powders as precursors, with argon as a carrier gas. In the final step, the SnS_2 nanosheets are airbrushed onto the surface of the pre-grown WO_3 nanoneedles to form the hybrid heterostructure.

Results

First, we investigated the morphology of the WO_3 nanoneedles, grown directly on top of the alumina substrate with AACVD, displayed in Fig. 1(a). The results prove the formation of WO_3 nanoneedles, with a regular morphology and uniform size, distributed homogenously over the

electrode area. Fig. 1(b) represents the FESEM image of the structure WO_3\SnS_2 which confirmed the successful growth of SnS_2 nanosheets, with a good hexagonal shape, on top of WO_3.

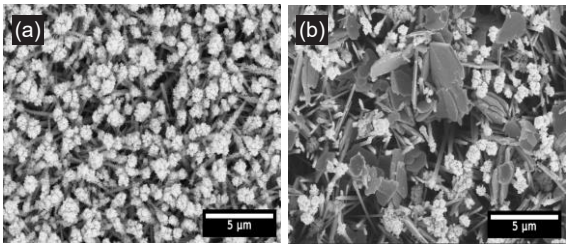


Fig. 1. FESEM images of (a) WO_3, (c) WO_3/SnS_2 nanostructures.

In order to verify the composition and the structure of our materials we examined our samples using energy-dispersive spectroscopy (EDX) techniques. WO_3 spectra is represented in Fig.2(a) and WO_3\SnS_2 spectra is represented in Fig.2(b). The results confirm the growth of WO_3 in the first stage, then the simultaneous presence of multilayers of WO_3 and SnS_2 materials proven the formation of the WO3/SnS2 heterostructure.

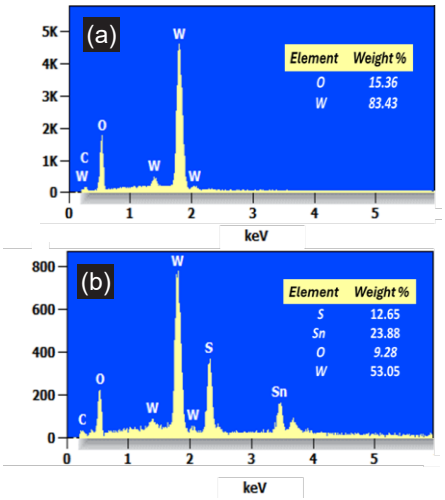


Fig. 2. EDX spectra of (a) WO_3, (b) WO_3/SnS_2 nanostructures.

For gas sensing measurement, we tested bare WO_3 and hybrid WO_3\$SnS_2$ sensors towards 800 ppb of NO_2, at different operating temperatures (RT, 100, and 150ºC). At low operating temperatures, bare WO_3 exhibited significant baseline resistance drift, and even at 150 °C, its sensitivity remained insufficient, as illustrated in Fig. 3. In contrast, the hybrid WO_3\$SnS_2$ sensor demonstrated improved stability and significantly higher sensitivity at low temperatures, achieving its optimal response at 150 °C. Moreover, at room temperature, WO_3\$SnS_2$ was able to detect the target gas at ppb-level, with enough sensitivity. Fig. 4 shows the real sensors responses as a function of time toward 800 ppb of NO_2 at 150ºC. Both sensors exhibited an n-type semiconductor behavior, increasing resistance upon exposure to oxidizing gas and decreasing it upon exposure to dry air.

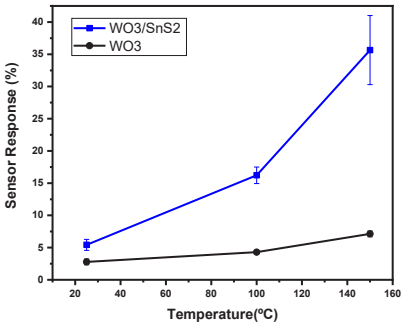


Fig. 1. Sensors responses toward 800 ppb of NO_2 as a function of temperature.

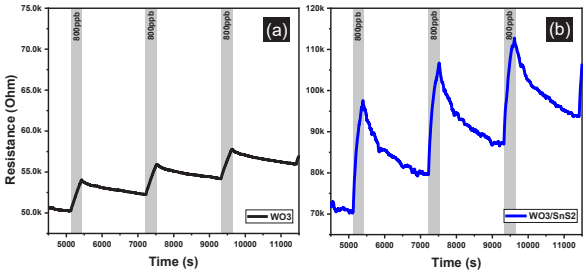


Fig. 2. Responses of sensors (a) WO_3, and (b) WO_3\SnS_2 at 150ºC toward 800 ppb of NO_2.

At low temperatures, the bare WO_3 sensor showed two primary limitations which are poor response and slow recovery. The sensitivity of the sensor was greatly increased by the addition of SnS_2 nanosheets. The WO_3\SnS_2 hybrid sensor's response was five times greater than that of pristine WO_3, as seen in Fig. 4. Efforts are ongoing to further improve the recovery characteristics through extended recovery times and the application of UV illumination. Investigations into humidity cross-reactivity are also in progress; more information will be provided at the conference.

Conclusions

This study presents a facile and scalable method for synthesising a WO_3\SnS_2 heterostructure, demonstrating its enhanced selectivity, response speed, and stability for ppb-level NO_2 detection at low operating temperatures.

References

[1] W. Song, R. Zhang, X. Bai, Q. Jia, H. Ji, Exposed crystal facets of WO3 nanosheets by phase control on NO2-sensing performance. J Mater Sci: Mater Electron 31, 610–620 (2020); doi: 10.1007/s10854-019-02565-6

[2] Wu, J. et al. Flexible, 3D SnS2/Reduced graphene oxide heterostructured NO2 sensor. Sensors and Actuators B: Chemical 305, 127445 (2020); doi: 10.1016/j.snb.2019.127445

DOI 10.5162/EUROSENSORS2025/W7.1.3

Morphological Control of ZnO and ZnO@NiO Heterojunctions: Improving Sensitivity, Selectivity, and Humidity Resistance for Gas Sensing Applications

Pedro P. Ortega[1], Sandro Gherardi[2], Elena Spagnoli[3], Michele Astolfi[2,3], Giulia Zonta[2,3], Giuseppe Cruciani[3], Cesare Malagù[3], Elson Longo[1]
[1] Federal University of São Carlos, São Carlos, Brazil,
[2] SCENT S.r.l., Via Quadrifoglio 11, 44124, Ferrara, Italy.
[3] University of Ferrara (UNIFE), Via Saragat 1, 44122, Ferrara, Italy.
pedro.ortega@ufscar.br

Summary:
ZnO samples with distinct morphologies and ZnO@NiO heterostructures were synthesized via a microwave-assisted hydrothermal method. Structural characterization confirmed crystalline phases without impurities. Plate- and rod-like ZnO morphologies were obtained, each decorated with NiO in two concentrations. Gas sensing tests showed that ZnO plates had higher ethanol sensitivity, selectivity, and better humidity resistance than rods. ZnO@NiO heterostructures based on plates lowered the operating temperature and improved sensitivity and humidity resistance, despite reducing selectivity.

Keywords: zinc oxide, nickel oxide, heterostructure, chemical synthesis, gas sensor

Introduction

Metal oxide semiconductors (MOSs) are widely used in gas sensing applications due to their high sensitivity, low cost, and simple fabrication. However, challenges such as poor selectivity and humidity cross-interference limit their performance, thus reducing sensing accuracy. Some strategies to enhance selectivity and sensitivity include doping, morphological control, and the formation of heterostructures [1]. Among these, morphological control and heterojunctions are promising due to their ability to engineer surface properties, band structures, and to create preferential adsorption sites. In this work, we synthesized sub-micron zinc oxide (ZnO) structures with rod and plate morphologies, and we also combined them with nickel oxide (NiO) to form heterostructures via a single and a two-step microwave-assisted hydrothermal (MAH) method, respectively. The MAH approach allowed precise control over particle morphology. Thick films of the as-synthesized materials were fabricated using screen-printing method and evaluated as gas sensors for carbon monoxide, carbon dioxide, ethanol, benzene, hydrogen, and humidity.

Materials and Methods

The pure ZnO and ZnO@NiO heterostructures were synthesized via a single- and a two-step MAH method. The first step consisted in the synthesis of the ZnO morphologies. For such, analytical grade zinc acetate dihydrate and sodium hydroxide were used as precursors. Each precursor was separately dissolved in 40 mL of deionized water. Then, the sodium hydroxide solution was slowly added to zinc acetate dihydrate one. The mixture was poured into a PTFE autoclave and placed inside a microwave oven. The syntheses were performed at 130°C for 8 minutes. Two solutions with Zn^{2+} to OH^- molar ratios of 1:5 and 1:10 were used (1). The synthesis of the standard NiO sample followed a similar procedure. In this case, nickel nitrate hexahydrate was dissolved in 80 mL of deionized water (2), followed by an adjustment of the pH to 11 by adding a 2 M solution of sodium hydroxide. The synthesis was carried out at 140°C for 8 minutes, and the resultant product was calcined at 400°C for 1 hour. The synthesis of the heterostructures were performed by adding 600 mg of the as-synthesized ZnO samples in (1) to the Ni solution in (2), thereafter following the exact same steps of the NiO synthesis.

The as-synthesized powders were then used to fabricate the sensing films via the screen-printing method. The powders were mixed with alfa-terpineol and ethyl cellulose to prepare a paste and then printed onto alumina substrates with gold electrodes. The samples were calcined at 400°C for 1 hour to eliminate the organic compounds.

Results

X-ray diffractometry revealed crystalline samples free from phases other than wurtzite ZnO

and fluorite-type NiO. For the ZnO@NiO heterostructures, both phases were detected. Rietveld analysis confirmed the increase in the NiO wt%, revealing samples with 24.30% and 41.80% for ZnO plates and 24.82% and 37.86% for ZnO rods.

The different Zn^{2+}/OH^- ratios resulted in two different ZnO morphologies, plates and rods, for 1:5 and 1:10 molar ratios, respectively. For the heterostructures shown in Fig. 1, it is possible to notice that the synthesis did not alter the morphology of the base ZnO sample. Also, the porous NiO nanosheets appear distributed on the surface of ZnO. The estimated band gaps were ~3.3 eV for ZnO and ~3.5 eV for NiO, consistent with literature. In the heterostructures, the absorbance edge of ZnO and NiO remained mostly unchanged.

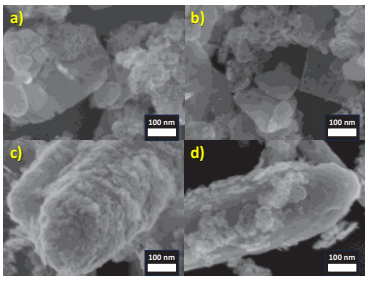


Fig. 1. Field-emission scanning electron microscopy of the heterostructures representing the base ZnO morphology, plates (a) and (b), and rods (c) and (d) decorated with NiO porous nanosheets.

Carbon monoxide was used to determine the working temperature of the sensors. As shown in Fig. 2, the ZnO plates with ~24% NiO showed the highest response to CO across all temperatures, with the best at 300°C, which is lower compared to the pure ZnO samples.

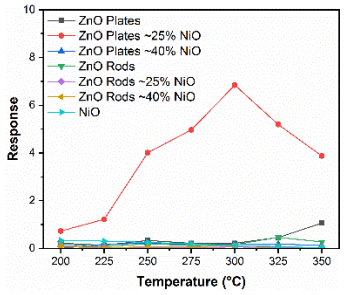


Fig. 2. Working temperature for the pure ZnO and ZnO@NiO heterostructures toward CO.

As shown in Fig. 3, the ZnO plates presented an improved humidity resistivity compared with ZnO rods, and a higher selectivity to ethanol, being able to detect it in the sub-ppm range. The heterostructure composed of ZnO plates and ~24% NiO showed an increased sensitivity compared to the pure ZnO samples and a significantly reduced cross-sensitivity to humidity, despite also presenting a decreased selectivity toward the tested gases. The other heterostructures did not present significant responses.

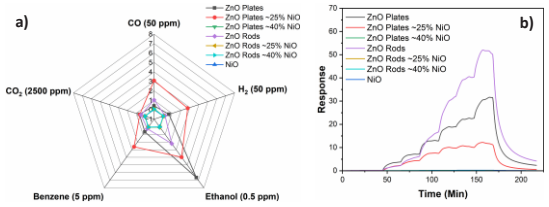


Fig. 3. Selectivity tests and dynamic response to different relative humidity levels, from ~0% to ~55% RH.

The morphological effect on the sensing results from the surface characteristics of each sample. The ZnO plates display polar surfaces with higher surface energy compared to rods, which changes their interaction with the different gaseous molecules, in this case increasing ethanol selectivity and humidity resistivity. The formation of heterostructures increases charge separation at the heterojunction, altering the depletion layer properties, which can increase the sensor sensitivity [1], as shown in Fig. 3. The improved humidity resistive of the heterostructures can be assigned to NiO on the surface since it is considered a humidity resistive material [2].

Conclusions

In this work, different ZnO morphologies were synthesized and used to prepared ZnO@NiO heterostructures. ZnO morphology improved ethanol sensitivity and decreased humidity cross-sensitivity compared with rod-shaped ZnO. The heterostructure consisting of ZnO plates and NiO improved sensitivity and humidity resistiveness but decreased selectivity. Thus, this work showed that morphological control and surface modification with other metal oxides can be a promising alternative to modify the semiconductor properties, design sensors with increased sensitivity and selectivity.

Acknowledgements

This work was founded by the São Paulo Research Foundation (FAPESP), Grant Number #2024/08759-0 and #2023/07486-8.

References

[1] F. Meng, R. Xin, S. Li, Metal Oxide Heterostructures for Improving Gas Sensing Properties: A Review, *Materials* 16(1), 263 (2023); doi: 10.3390/ma16010263

[2] C.E. Simion, C. Ghica, C.G. Mihalcea, D. Ghica, I. Mercioniu, S. Somacescu, O.G. Florea, A. Stanoiu, Insights about CO Gas-Sensing Mechanism with NiO-Based Gas Sensors—The Influence of Humidity, *Chemosensors* 9, 244 (2021) doi: 10.3390/chemosensors9090244.

DOI 10.5162/EUROSENSORS2025/W7.1.4

Ultrafast Recovery and Humidity Effect in a MoS_2-ZnO functionalized CNTs Array driven as an e-nose

Michele Galvani[1], *Luigi Sangaletti*[1]
[1] *Surface Science and Spectroscopy Lab at I-Lamp, Department of Mathematics and Physics, Via della Garzetta 48, 25133 Brescia, Italy.*

Summary:
Gas sensors are essential in various fields, and high chemical selectivity and fast response/recovery times are usually crucially important. Chemiresistors based on nanomaterials are still a central sensors category due to ease of fabrication, which allows for an easy prototyping of novel architecture, especially when sensor arrays are operated as e-noses. Here, we present an array of ultrafast, highly selective gas sensors using CNTs layers decorated with ZnO and MoS_2. The sensors exhibit strong NH_3 selectivity, with recovery times below 10 seconds. Lastly, the array can be operated as an electronic nose, successfully discriminating the different target gas molecules using both scatter plots and PCA analysis.

Keywords: chemiresistors, carbon nanotubes, response-recovery times, electronic nose, PCA.

Background and Motivation

Gas sensors represent an extremely active field of research. New devices play a fundamental role in various sectors, including industry (food and beverage, automotive, etc.) and air quality monitoring. Sensors need to be chemically selective, meaning they should react only to the chosen target gases, and fast, then capable of responding and recovering from gas exposure quickly enough to be suitable for industrial applications.

There are several types of gas sensors, each based on different working principles. Among them, chemiresistors still represent an opportunity to develop and prototype novel architectures, due to their low production cost, compact size, and ease of implementation. Additionally, the use of machine learning algorithms and approaches for data analysis have shown to be able to expand the sensors performances when used in e-noses.

Regarding nanostructured carbon based chemiresistors, the fastest ones, in terms of response and recovery time, have t_{res} and t_{rec} of the order of 5-10 seconds [1].

Within this context, an array of ultrafast and highly selective gas sensors based on zinc oxide nanoparticles (ZnO NPs), and molybdenum disulfide nanoflakes (MoS_2 NFs)-functionalized carbon nanotubes (CNTs) is presented. Both the functionalization strategies are widely used in chemiresistors and are often combined with nanostructured carbon to achieve fast and responsive NH_3 sensors (see e.g. [2] and [3]).

Materials and methods

Four samples were prepared: pristine CNTs, (without functionalization), CNTs decorated with MoS_2 NFs (CNT + MoS_2), with ZnO NPs (CNT + ZnO), and with a combination of both (CNT + MoS_2 + ZnO). The solutions, along with the functionalizations, have been dropcasted onto 13.4x7 mm^2 interdigitated electrodes (IDEs), composed of an insulating alumina substrate and a conducting silver pathway. The sensors were then characterized using an inVia^{TM} Raman microscope, to check also possible doping effects induced by the functionalization.

All samples were tested in a chemiresistor configuration, using a custom-developed control setup, consisting of an electronic breadboard for resistance measurements and a dedicated LabView procedure. The sensors were exposed to various contaminants, particularly ammonia and water. The resulting responses were then analyzed using appropriate Python procedures to assess the array's discriminating capabilities.

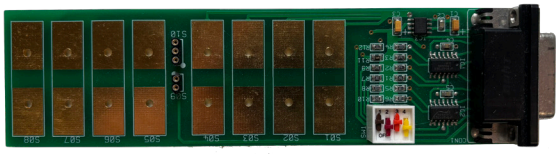


Fig. 1. Chemiresistors controlling breadboard.

Results

All four samples exhibit different responses to ammonia and water. The results are reproducible. Figure 2 shows their dynamical responses while exposed to different ammonia

concentrations and RH variations. RH and NH_3 were measured with properly calibrated commercial sensors. RH baseline value was set at 70%.

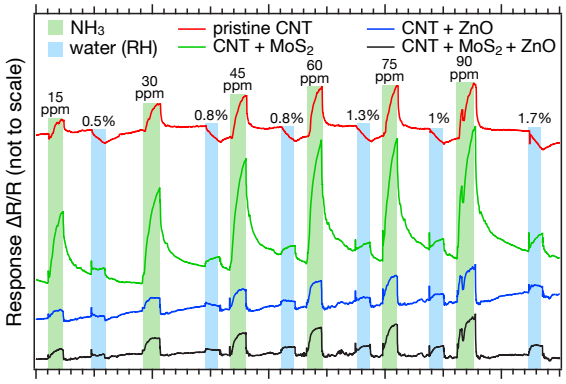


Fig. 2. Top: Chemiresistors dynamical responses to an ammonia-water concentration ramp. Bottom: relative humidity (RH) trend during the exposures.

Response and recovery times have been calculated. Notably, despite the sensors operating in a static regime [4], the recovery time remains well below 10 seconds. The t_{res} and t_{rec} values for ammonia and water exposures, measured for the CNT + ZnO sensor, are presented in Figure 3.

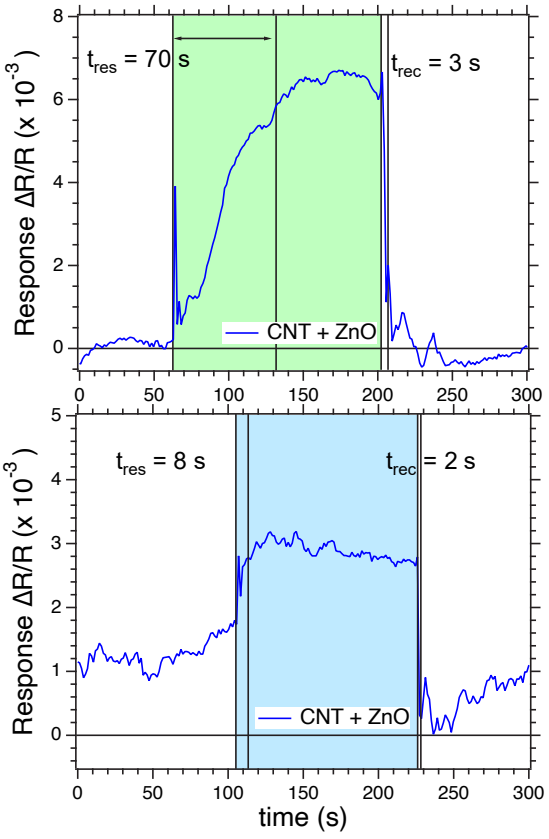


Fig. 3. CNT + ZnO sensor velocity to ammonia (top panel) and water (bottom panel).

Additionally, the sensor array was tested with other target gases, including some volatile organic compounds (VOCs), such as acetone, ethanol, and isopropyl alcohol (IPA), and nitrogen dioxide. We observed that different contaminants produce distinct response patterns in the array, enabling their complete discrimination. Responses scatter plots and PCA analysis are presented in Figure 4. It is possible to notice that with both techniques a complete separation of the target gas is obtained. However, PCA offers a better clustering of the points, due to the collective contribution of all sensors. Clustering algorithms, such as DBSCAN, and indicators like silhouette score were be used to quantify the mentioned results.

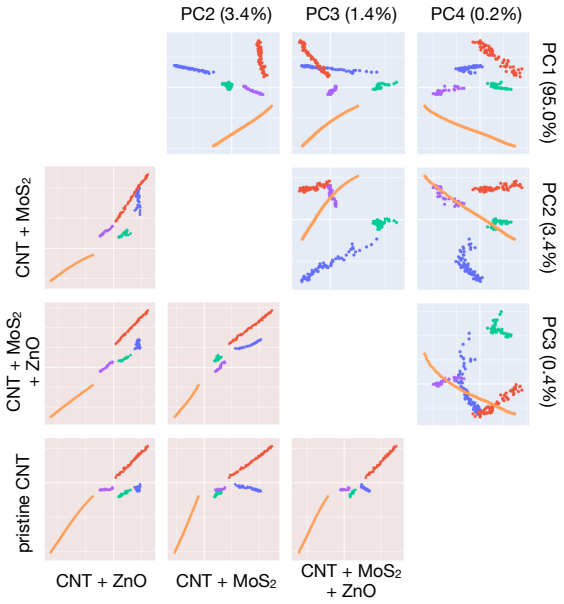


Fig. 4. Responses scatter plot and PCA.

References

[1] M. Galvani, S. Freddi, L. Sangaletti, Disclosing fast detection opportunities with nanostructured chemiresistor gas sensors based on metal oxides, carbon, and transition metal dichalcogenides, *Sensors* 24.2, 584 (2024); doi: https://doi.org/10.3390/s24020584

[2] M. Abniel, et al. Sensitive and reversible ammonia gas sensor based on single-walled carbon nanotubes, *Chemosensors* 11.4, 247 (2023); doi: https://doi.org/10.3390/chemosensors11040247

[3] M. Morsy, et al. Portable and battery operated ammonia gas sensor based on CNTs/rGO/ZnO nanocomposite, *Journal of Electronic Materials* 48, 7328-7335 (2019); doi: https://doi.org/10.1007/s11664-019-07550-7

[4] A. Ponzoni, A statistical analysis of response and recovery times: the case of ethanol chemiresistors based on pure SnO2, *Sensors* 22.17, 6346 (2022); doi: https://doi.org/10.3390/s22176346

DOI 10.5162/EUROSENSORS2025/W7.2.1

The Need for Fast Olfactory Sensing in Turbulent Environments

Nik Dennler[1] and Andreas Güntner[1]
[1]Human-centered Sensing Lab, ETH Zurich, Sonneggstrasse 3 8092 Zürich, Switzerland
dennlern@ethz.ch

Summary: Odour signals in natural environments are shaped by turbulence, resulting in intermittent, rapidly fluctuating plumes. These fluctuations carry essential environmental information, but are only accessible to sensors with sufficiently fast response times. Most conventional sensors are too slow, acting as low-pass filters that obscure many of the plume's informative features. Here we present a physics-informed perspective on why fast sensing is necessary in turbulent environments, and offer a combined approach of fast sensing, plume imaging, and signal processing to translate between controlled experiments and real-world deployment.

Keywords: turbulent odour plumes, high-speed gas sensing, MOx sensors, olfactory robotics

Introduction

Chemical sensing in turbulent environments is increasingly relevant for applications in agriculture, ecology, and autonomous robotics. While many of these are satisfied by static implementations of relatively slow sensors, other would benefit from more dynamic solutions.

Information in Turbulent Odour Plumes

In natural environments, airborne odour signals are transported by turbulent advection rather than smooth diffusion. Turbulence introduces structure across multiple scales, resulting in odour plumes that are intermittent and filamentous, composed of sharp concentration bursts ("bouts") interspersed with clean-air gaps ("blanks"). These features arise from the turbulent energy cascade, in which large eddies break into smaller ones, stretching and folding odour filaments across a wide range of temporal and spatial scales.

Consequentially, turbulent odour signals are neither bandlimited nor continuous. Power spectral analyses often reveal a log-log-linear decaying power-law distribution [1], indicating that significant information resides in high-frequency componentsSimultaneously, odour encounters are sparse in time: bouts and inter-bout intervals follow heavy-tailed statistics [2]. This dual character—broadband and sparse—presents a unique challenge for sensing systems.

While turbulent odour plumes may appear chaotic, their statistical structure encodes meaningful spatial information. Features such as amplitude, intermittency, and encounter frequency of bouts correlate with plume dimensions and distance to source [3, 4]. Temporal correlations between odour encounters—either at a single point or across multiple sensors—can reveal source separation or localisation cues [5, 6].

Notably, many of these features are accessible only through fast sensing. Odour concentration fluctuations can exceed $100\,\mathrm{Hz}$ [7], with exposure times down to a few milliseconds [2]. Insects, for example, exhibit olfactory receptor neuron latencies below $2\,\mathrm{ms}$ and resolve odour dynamics well beyond $100\,\mathrm{Hz}$ [8], enabling them to track fast-varying signals [9] and perform complex tasks such as source localisation [10]. Sensors with insufficient temporal resolution fail to resolve these features. Acting as low-pass filters, they smooth rapid fluctuations into slow signals and often erase information on plume structure and source configuration.

Sensor Constraints and Implications

Photoionisation detectors (PIDs) and planar laser-induced fluorescence (PLIF) can resolve odour dynamics at millisecond timescales; however their size, power requirements, and operational complexity make them impractical for most field applications. Among compact and low-cost alternatives, metal-oxide (MOx) gas sensors are the most widely used due to their robustness, sensitivity, and ease of integration. Yet, their response and recovery times often span several seconds to minutes. While these suffice a vast range of applications, they severely constrain the operation of more dynamic solutions, in particular olfactory robotics.

Our recent work [11] demonstrates that MOx sensors, when paired with fast thermal control and high-rate acquisition, can resolve odour dynamics on millisecond timescales—unlocking a new regime of high-speed chemical sensing with compact, low-power hardware. While these results were obtained under highly controlled laboratory conditions, they offer a compelling proof of principle for extending MOx-based sensing to turbulent, real-world environments.

DOI 10.5162/EUROSENSORS2025/W7.2.1

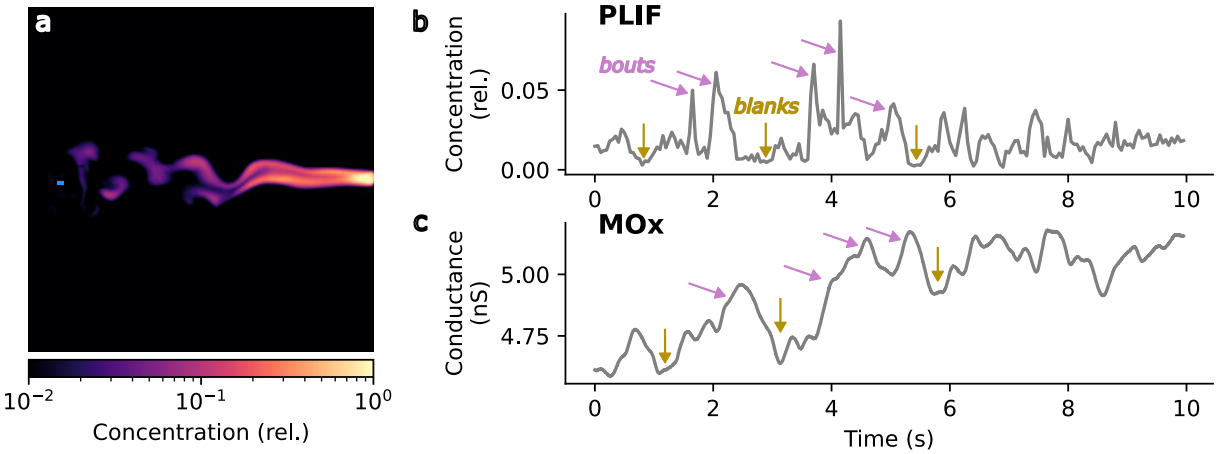


*Fig. 1: **a** Turbulent odour imaging using Planar laser induced fluorescence (PLIF). Blue rectangle denotes sensor location. **b** PLIF time series data extracted from sensor location, illustrating "bouts" and "blanks". **c** Raw MOx sensor data, co-localised and synchronised with point-source PLIF data.*

MOx Sensors in Turbulent Environments

Achieving this transition requires not only continued optimisation of hardware, but also advanced post-processing algorithms capable of deconvolving the sensor's response [12]. For this, it is critical to use reliable and non-invasive ground-truth measurements [13].

We collected a comprehensive dataset combining high-resolution imaging with fast gas sensing. In a custom-built wind tunnel, we used a PLIF setup to visualise the turbulent transport of acetone vapour [14]. The vapour was excited using a multi-head, pulsed UV laser, and recorded with a high-speed camera, enabling spatially and temporally resolved plume imaging (see Fig. 1a&b). Simultaneously, we acquired co-localised sensor data using a high-speed e-nose [11] (see Fig. 1c). Different plume structures and flow regimes were tested, for probing the relationship between environmental signal features and sensor performance.

The direct comparison between sensor output and PLIF measurements provides an unique opportunity to evaluate the fidelity with which MOx sensors captures turbulent gas dynamics, enabling qualitative assessment and quantitative modelling of temporal filtering characteristics. Notably, even in the raw data, sub-second plume features are preserved and readily identifiable in the MOx response (see Fig. 1c). Thus, this work forms a valuable testbed for developing and validating model-based and data-driven signal reconstruction algorithms, aiming to recover true concentration signals from the sensors.

Conclusion and Outlook

We argue for a system-level approach where sensor dynamics match environmental bandwidths. Combining fast sensors with signal reconstruction methods offers a practical path toward robust chemical sensing in turbulent, real-world conditions.

References

[1] K. R. Mylne and P. J. Mason, "Concentration fluctuation measurements in a dispersing plume at a range of up to 1000 m," *Quarterly Journal of the Royal Meteorological Society*, vol. 117, no. 497, pp. 177–206, 1991.

[2] A. Celani, E. Villermaux, and M. Vergassola, "Odor Landscapes in Turbulent Environments," *Physical Review X*, vol. 4, p. 041015, Oct. 2014.

[3] J. E. Fackrell and A. G. Robins, "The effects of source size on concentration fluctuations in plumes," *Boundary-Layer Meteorology*, vol. 22, pp. 335–350, Mar. 1982.

[4] M. Schmuker, V. Bahr, and R. Huerta, "Exploiting plume structure to decode gas source distance using metal-oxide gas sensors," *Sensors and Actuators, B: Chemical*, vol. 235, pp. 636–646, 2016.

[5] M. J. Weissburg, D. B. Dusenbery, H. Ishida, J. Janata, P. J. W. Roberts, and D. R. Webster, "A Multidisciplinary Study of Spatial and Temporal Scales Containing Information in Turbulent Chemical Plume Tracking," *Environmental Fluid Mechanics*, vol. 2, pp. 65–94, 2002.

[6] T. Ackels, A. Erskine, D. Dasgupta, A. C. Marin, T. P. Warner, S. Tootoonian, I. Fukunaga, J. J. Harris, and A. T. Schaefer, "Fast odour dynamics are encoded in the olfactory system and guide behaviour," *Nature*, vol. 593, no. 7860, pp. 558–563, 2021.

[7] E. Yee, R. Chan, P. R. Kosteniuk, G. M. Chandler, C. A. Biltoft, and J. F. Bowers, "The vertical structure of concentration fluctuation statistics in plumes dispersing in the atmospheric surface layer," *Boundary-Layer Meteorology*, vol. 76, pp. 41–67, Oct. 1995.

[8] P. Szyszka, R. C. Gerkin, C. G. Galizia, and B. H. Smith, "High-speed odor transduction and pulse tracking by insect olfactory receptor neurons," *Proceedings of the National Academy of Sciences*, vol. 111, pp. 16925–16930, Nov. 2014.

[9] J. Crimaldi, H. Lei, A. Schaefer, M. Schmuker, B. H. Smith, A. C. True, J. V. Verhagen, and J. D. Victor, "Active sensing in a dynamic olfactory world," *Journal of Computational Neuroscience*, vol. 50, pp. 1–6, Feb. 2022.

[10] P. Szyszka, T. Emonet, and T. L. Edwards, "Extracting spatial information from temporal odor patterns: insights from insects," *Current Opinion in Insect Science*, vol. 59, p. 101082, Oct. 2023.

[11] N. Dennler, D. Drix, T. P. Warner, S. Rastogi, C. D. Casa, T. Ackels, A. T. Schaefer, A. van Schaik, and M. Schmuker, "High-speed odor sensing using miniaturized electronic nose," *Science Advances*, vol. 10, no. 45, p. eadp1764, 2024.

[12] D. Martinez, J. Burgués, and S. Marco, "Fast measurements with mox sensors: a least-squares approach to blind deconvolution," *Sensors*, vol. 19, no. 18, p. 4029, 2019.

[13] A. C. True and J. P. Crimaldi, "Distortion of passive scalar structure during suction-based plume sampling," *Sensors and Actuators B: Chemical*, vol. 367, p. 132018, 2022.

[14] E. G. Connor, M. K. McHugh, and J. P. Crimaldi, "Quantification of airborne odor plumes using planar laser-induced fluorescence," *Experiments in Fluids*, vol. 59, p. 137, Sept. 2018.

DOI 10.5162/EUROSENSORS2025/W7.2.2

Improving Computational Efficiency of Finite Element MEMS Transducer Models by Fine-Tuned Homogenization

Sira Bielefeldt[1], *Florin Püntener*[1], *Chris Rüttimann*[1], *Cosmin Roman*[1]
[1]*ETH Zurich, Rämistrasse 101, 8092 Zurich, Switzerland*
croman@ethz.ch

Summary:
We present a top-down homogenization approach for simplifying the finite element (FE) model of a complex MEMS transducer, here a capacitive tactile sensor (taxel). This method addresses the challenge of high computational costs in modeling MEMS devices. The number of degrees of freedom (NDOF) of the homogenized model is reduced by a factor of 34.6. The model achieves a normalized root mean squared error (NRMSE) with respect to the measurement data of 5.5±0.5% for force- and of 9.4±1.5% for capacitance-displacement characteristics. Our method thereby achieves significant computational savings while maintaining accuracy of a non-homogenized model.

Keywords: model simplification, homogenization, finite elements, MEMS transducers, tactile sensors

Background

Finite element (FE) models have become a cornerstone of MEMS transducer design, offering accurate multiphysics simulations and device optimization. In spite their success, FE models require significant computational resources. To reduce their complexity, approaches based on projection [1] or homogenization [2] have been proposed. While the former is commonly used by the MEMS community, the latter is more familiar to the multiscale material modeling community.

Description of the New Method

In this work, we explore the potential of homogenization for reducing the complexity of finite element (FE) models of MEMS transducers. Our approach follows a top-down strategy, starting with a detailed 3D FE model and simplifying both its geometry and materials through homogenization. To refine the effective material parameters, we employ targeted 3D simulations of individual sub-parts of the device. We refer to this approach as *fine-tuned homogenization* (FTH). Key parameters of the homogenized model are extracted using experimental measurements. The computational efficiency of the homogenized model makes it suitable for numerical optimization, thus expediting both fine-tuning and model calibration.

We showcase the FTH method on a MEMS capacitive tactile sensor (taxel). In our previous work we demonstrated a soft artificial finger featuring 144 taxels (Fig. 1B) [3]. Each micro taxel comprises a circular suspended membrane stabilized by a solder ball, with peripheral spring structures (Fig. 1A). A thin polyimide grid on the bottom electrode acts as stoppers, preventing membrane pull-in [4].

Integrating tactile sensing into robotic grippers is aiming to improve their dexterity and automation. An accurate model of the taxel array is crucial for training a robotic hand [5] equipped with tactile artificial fingers. Due to multiple scales, layers, materials, and complex topography, modelling even one taxel, let alone an array, has been challenging.

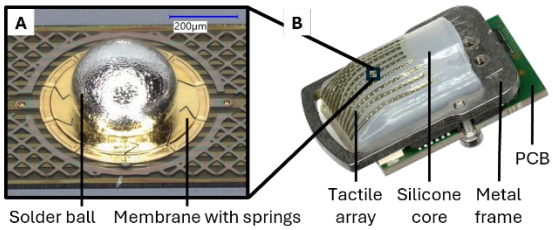


Figure 1: Tactile sensing technology. (A) Close-up of a tactile sensor (taxel) on an (B) artificial silicone finger containing an array of 144 taxels.

Individual taxels have been characterized electro-mechanically, with the setup shown in Fig. 2, using a flat-tip aluminum needle mounted on a force sensor (Novatech F329) on a stepper motor (step size: 0.31 µm, max. reaction *F*=15 mN).

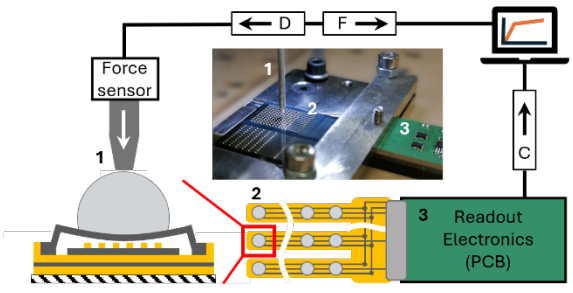


Figure 2: Experimental taxel characterization setup. A force sensor (1) with flat tip needle actuates a taxel in the array (2). The applied displacement D, measured force F, capacitance C are recorded simultaneously.

An axisymmetric taxel model (NDOF 2D:32.6K, 3D:465K) was set up in COMSOL Multiphysics (Fig. 3 top), using the parameters in Tab. 1. Geometrical features of the taxels have been extracted from FIB-SEM cross-sections (Fig. 3 bottom), focusing on layer

thickness, stopper region and membrane shape in the spring region.

In our FTH approach, first, all subdomains of each region (Fig. 3, excl. the solder ball) were merged into one domain with effective material parameters given by volumetric weighting. For example, in the spring region the Youngs moduli E of 4 thin-film layers and the spring cutouts were homogenized into $E_{sp,init}$. Second, separate unit-cell simulations were utilized to fine-tune the effective material parameters, where needed. For example, $E_{sp,init}$ was fine-tuned into $E_{sp,corr.}$ by fitting the 2D axisymmetric to a 3D taxel model of a 36° sector unit-cell containing one spring (NDOF: 16.1M).

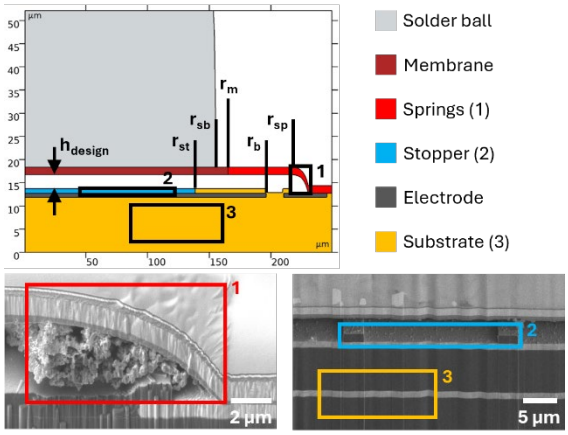


Figure 3: The 2D axisymmetric COMSOL model (top) parameterized based on FIB-SEM cross sections of selected regions (bottom).

Initial simulations assumed an initial gap of h_{design}=3 µm. Subsequently, to calibrate the model, a taxel-specific initial gap (see Tab. 1) was determined from the experimental F-D data, as the point where stiffness changes, i.e. where the membrane hits the stoppers.

*Tab. 1: Geometrical and material model parameters utilized in COMSOL simulation (r: x-y dim.; h: z dim.). Values shown in blue are the final parameters obtained through our FTH method. (*electrical ε_{r_st}: 1.51)*

Region	Geometry [µm]	E [GPa]
Solder ball	r_{sb}: 147 ± 1	E_{sb}: 50
Substrate	h: 11.9	E_s: 12.7
Electrode	r_b: 196, h_b: 0.9	E_b: 107
Membrane	r_m: 115, h_m: 1.3	E_m: 109
Stopper*	r_{st}: 138, h_{st}: 1	$E_{st,\ corr}$: 2.67
Springs	r_{sp}: 250, h_{sp}: 1.3	$E_{sp,\ init}$: 106 $E_{sp,\ corr.}$: 90
Initial gap	h_{design}: 3	-
	h_1: 2.27, h_2: 1.54, h_3: 1.95	

Results

Fig. 4. shows a comparison of the simulations to the experimental data for three selected typical taxels. The model parameters in Tab. 1 result in a very good agreement (see Fig. 4 NRMSE values), both in the mechanical D-F (top) and the electric D-C domain (bottom). Our proposed FTH approach to simplify FE models can be transferred to other complex MEMS transducers.

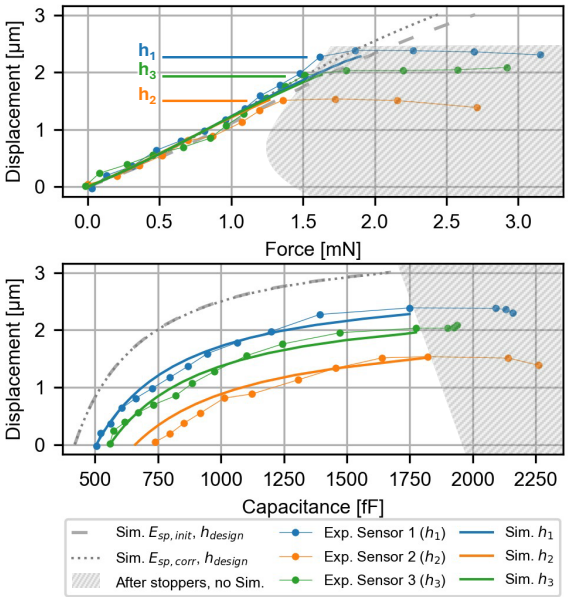


Figure 4: Experiments vs. simulation. D-F (top) and D-C (bottom) for 3 typical taxels. Initial simulation parameter values before (gray) and after tuning the initial gap (color) are given in Tab. 1. The average NRMSE of measured vs simulated values (normalized for F/C exp. range) is 6.1% (initial) and 5.5% (tuned) for D-F, and 48.5% (initial) and 9.3% (tuned) for D-C.

References

[1] R. Kumar et al., A state-of-the-art survey of model order reduction techniques for large-scale coupled dynamical systems, *Int J Dynam Control* 11, 900-916 (2023), doi: 10.1007/s40435-022-00985-7

[2] S. Firooz et al., Homogenization of Composites With Extended Generel Interfaces: Comprehensive Review and Unified Modeling, *App Mech Rev* 73 (2021), doi: 10.1115/1.4051481

[3] J. Weichart et al., Artificial Fingertip with Embedded Fiber-Shaped Sensing Arrays for High Resolution Tactile Sensing, *Soft Robot.* 11 4, 573–584 (2024), doi: 10.1089/soro.2022.0238

[4] J. Weichart et al., Tactile Sensing with Scalable Capacitive Sensor Arrays on Flexible Substrates, *J. Microelectromechanical Syst.* 30 6, 915–929 (2021), doi: 10.1109/JMEMS.2021.3104352.

[5] W. Zhao et al., Sim-to-Real Transfer in Deep Reinforcement Learning for Robotics: a Survey, *IEEE SSCI*, 737-744 (2020), doi: 10.1109/SSCI47803.2020.9308468

Acknowledgements

We gratefully acknowledge Prof. Christofer Hierold for his invaluable support. This work was supported by ETH Zurich Research Grant No. 22-2 ETH-047.

DOI 10.5162/EUROSENSORS2025/W7.2.3

Toward Digital Twins in Orthopedic Implants: Finite Element Analysis of Malalignment Effects in Instrumented Tibial Trays

Leila Merzak[1], Célestin Ott[1], Elise Saoutieff[1], Pierre Gasnier[1], Vincent Elhorga[1], Sébastien Boisseau[1],
[1] Univ. Grenoble Alpes, CEA, Leti, F-38000 Grenoble, France
leila.merzak@cea.fr

Summary

This study investigates the impact of knee prosthesis malalignment on the strain distribution in the tibial tray. A 3D finite element model was developed to simulate all prosthetic components. Simulations showed that malalignment leads to detectable strain patterns. These findings highlight the potential to detect malalignment using a sensor-enhanced tray previously developed, which includes an integrated sensor based on a “tray–pillar–membrane” structure. These preliminary results will serve as a foundation for the implementation of a digital twin framework dedicated to alignment assessment of knee implants.

Keywords: Total Knee Arthroplasty (TKA), Finite Element Analysis (FEA), Prosthetic Malalignment, Aseptic Loosening, Digital Twin

Introduction

Total Knee Arthroplasty (TKA) is a common orthopedic procedure, aiming to restore joint function and reduce pain in patients suffering from severe knee osteoarthritis. Despite its clinical success, TKA is still associated with various complications, among which aseptic loosening being one of the primary causes of implant failure [1]. Prosthesis malalignment is one of several mechanical factors that may contribute to aseptic loosening [1]. In a recent study, Gasnier et al. [2] proposed an instrumented knee prosthesis that enables the measurement of forces and moments applied on the tibial component. However, their simulations and experimental tests were limited to idealized loading conditions involving a single, localized point load. In this study, we extend the previous work by simulating the mechanical behavior of the complete prosthetic system, with a more realistic force transmission through the femur. We first analyze the strain response of the tibial membrane under aligned conditions, and then introduce a malalignment between the femoral and tibial components to observe its effect on strain distribution.

Materials and Methods

A full 3D model of the knee prosthesis was developed, as shown in Fig 1. It includes the femur, femoral component, polyethylene spacer, tibial component, and the tibial bone. The tibial component includes an integrated sensor based on the “tray–pillar–membrane” architecture, as proposed in [2]. In this design, mechanical loads applied to the tibial tray are transmitted through a central pillar to a deformable membrane located within the tray. Strain gauges bonded to the membrane surface measure the resulting longitudinal strain.

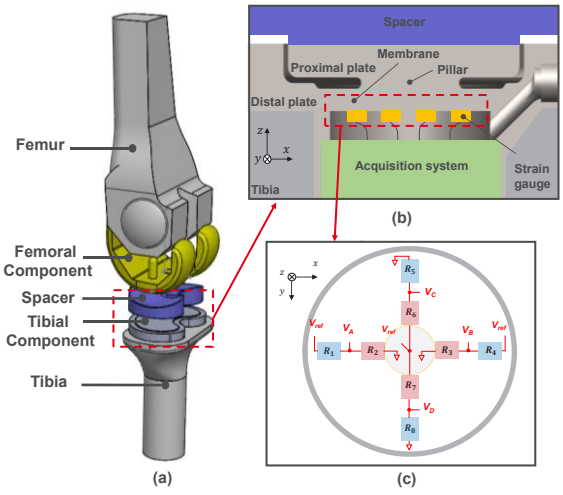


Fig. 1. (a) 3D model of the knee prosthesis. (b) Schematic cross section of the “tray–pillar–membrane” configuration. (c) Bottom view of the membrane with sensor placement.

To evaluate the strain behavior of the tibial membrane under both aligned and malaligned conditions, a finite element analysis (FEA) was performed using the prosthetic knee assembly in COMSOL Multiphysics®. Each component was assigned appropriate mechanical properties from literature as presented in Tab 1. In the

model, the connections between the femur/femoral component and the tibia/tibial component were considered fully bonded, reflecting realistic implant fixation conditions. Specifically, the lower surface of the spacer was bonded to the tibial tray, the upper surface of the femoral component was bonded to the femur, and the lower surface of the femoral component was set in contact with the tibial component under a frictionless condition due to the static conditions considered in this analysis. The bottom of the tibial bone was fixed. A refined mesh was applied around the membrane to accurately capture strain gradients.

Tab. 1: Material properties of the knee prosthetic components.

Component / Material	Young's Modulus	Poisson's ratio
Femur: Bone	20 GPa	0.45
Femoral component: Ti6A14V, grade 23	110 GPa	0.34
Spacer: UHMWPE	0.8 GPa	0.45
Tibial Component: Ti6A14V, grade 23	110 GPa	0.34
Tibia: Bone	20 GPa	0.45

Results

To investigate the impact of prosthesis alignment on strain distribution in the tibial membrane, three simulation scenarios were performed: a neutrally aligned configuration, a 5° valgus malalignment, and a 5° varus malalignment. These configurations are illustrated in Fig 2, representing the coronal plane alignment between the femoral and tibial components.

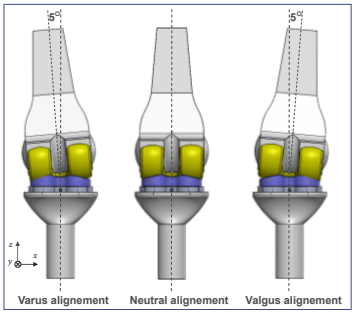


Fig. 2. Simulated alignment conditions: 5° varus, neutral and 5° valgus in the coronal plane.

In the neutral alignment configuration, the strain distribution across the membrane is symmetrical, with two balanced peaks located medially and laterally as it is shown in Fig 3. In the 5° varus configuration, the strain profile shifts toward the medial side. Conversely, in the 5° valgus configuration, the peak strain shifts laterally. These asymmetries illustrated in Fig 4

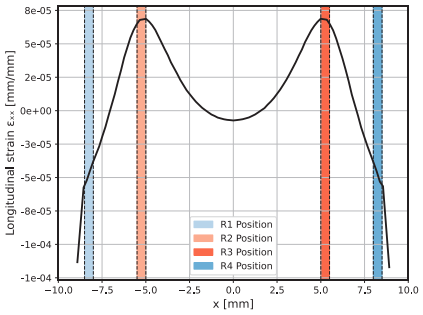


Fig. 3. FEM modeling (COMSOL) showing longitudinal strain distribution at the membrane in the neutral alignment configuration for Fz = 180N.

are directly reflected in the strain levels measured at the sensor locations on the membrane. This highlights the potential of the instrumented membrane, equipped with strain gauges, not only to measure the magnitude of the load [1] but also to detect prosthetic malalignment using strain data.

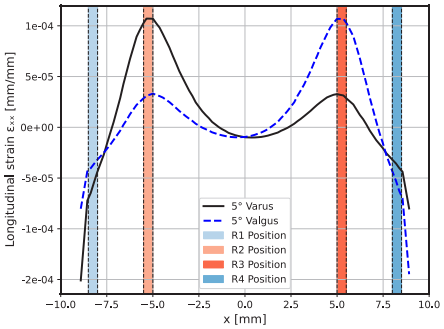


Fig. 4. FEM modeling showing the longitudinal strain distribution at the membrane under malalignment conditions for F_z = 180N.

These results will be further exploited within a digital twin framework developed in [3], which combine physics-based models, data-driven approaches, and real-time sensor data to detect and predict malalignment angles in knee prostheses. The simulation outputs generated in this study will serve as a training dataset for neural network models within that framework.

References

[1] Baek, Ji-Hoon *et al*. Early aseptic loosening of primary total knee arthroplasty in patients with osteonecrosis of the knee: A case series. *Clinical case reports* (2022); doi:10.1002/ccr3.6773

[2] Gasnier, Pierre *et al.* Design, Simulations and Tests of a Novel Force and Moments Sensor for Instrumented Knee Implants, *IEEE transactions on bio-medical engineering* (2023); doi:10.1109/TBME.2023.3289623

[3] Merzak, Leila *et al.* "Virtual sensor" approach for damage localization in mechanical structures – methodology and experimental validation, *Engineering Research Express* (2025); doi:10.1088/2631-8695/adb6f0

DOI 10.5162/EUROSENSORS2025/W7.2.4

Finite-Element Analysis of Nodus-Driven Flexibility in Dragonfly Wings for Micro-Air Vehicles

Muhammad Usman Yousaf[1], Prof. Dr. Rimvydas Gaidys[2],
[1]Department of Mechanical Engineering, Kaunas University of Technology, Kaunas, Lithuania
muhammad.yousaf@ktu.edu

Summary:
We investigate how the stiffness of the nodus joint affects deformation of a dragonfly forewing under a static distributed pressure load, using a full-wing finite element model in COMSOL Multiphysics. A simplified triangular model was initially used for calibration. In the final model the forewing is represented by shell/beam elements with material properties of insect cuticle and a spring at the nodus to simulate the hinge stiffness. Under uniform pressure the tip deflection is highly sensitive to the nodus rotational stiffness: lower stiffness yields larger deflections. Results are quantified by a deflection–stiffness curve. Our findings indicate that a more compliant nodus markedly increases wing flexibility, whereas a rigid nodus limits deflection, consistent with insect wing biomechanics in the literature.

Keywords: dragonfly wing, nodus joint, finite element model, beam–shell coupling, rotational spring, wing deformation, MAVs

Introduction

Dragonfly wings exhibit complex venation and specialized joints (e.g. nodus) that modulate flexibility. Prior work has shown that insect wing stiffness depends strongly on venation pattern and scale[1]. In particular, the dragonfly wing nodus is a vein discontinuity containing soft (resilin) and hard cuticle that acts like a one-way hinge [2]. Experimental studies report that the nodus greatly influences wing compliance: a flexible ("open") nodus increases bending flexibility, whereas a stiffened ("closed") nodus maintains rigidity [3]. Similarly, it was found that fliers tend to have less soft resilin at the nodus, implying a stiffer joint to avoid excessive wing deflections [4]. Finite-element modeling of insect wings has been used to probe these effects: for example, [5] constructed a 3D dragonfly wing FEM (beams and shells) to predict deformation under loads and included soft vein joints in a 3D wing model to study passive deformation. In this work we extend such analysis [6]by systematically varying the nodus rotational stiffness and quantifying the resulting wing deflection under static pressure.

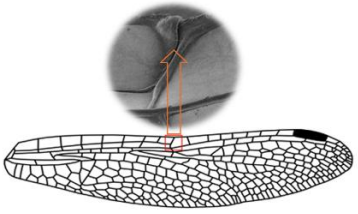


Fig. 1. Nodus Joint Highlighted in Dragonfly Wing

Materials and Methods

The dragonfly forewing geometry (planform and vein layout) was taken from published measurements and digitized for modeling [7]. The wing is modeled as a thin corrugated shell with embedded beam elements for major veins, following [5].

A rotational spring at the nodus enforces a moment rotation relation denoted by eq. (1) where K_{nodus} is varied as a parameter. The wing root is clamped at four points near the base fig.1, and a uniform static pressure load is applied on the wing surfaces to simulate aerodynamic loading. Material properties for cuticle and resilin are based on insect wing literature [5]. A representative set of mechanical properties is given in Table 1. All simulations were performed in COMSOL Multiphysics using linear elasticity (small deflection) assumptions.

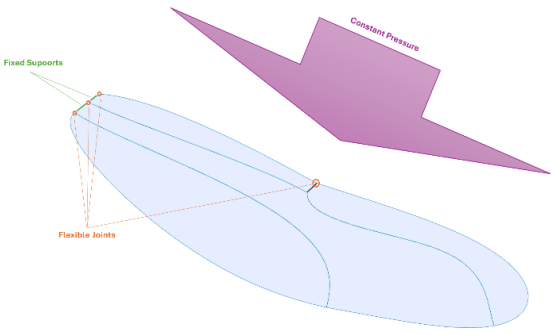


Fig. 2. Wing Model illustrating Boundary conditions

Tab. 1: Material properties used in the wing model.

Material	Elastic Modulus (GPa)	Poison Ratio	Density (kg/m^3)
Membrane	2.0	0.3	1200
Veins	5.0	0.3	1200
Nodus	0.002	0.49	1200

These material properties were adapted by a thorough literature review especially from [8]

Equations

The structural response is governed by linear elasticity. For bending dominated deformation of wing veins/shells, a one-dimensional approximation (Euler–Bernoulli beam) can be expressed as:

$$EI\frac{d^4w}{dx^4} = q(x) \quad (1)$$

where E is Young's modulus, I the second moment of area, w(x) the deflection, and q(x) the distributed load. In our FEM implementation the equivalent plate/shell equations are solved in COMSOL. The nodus is idealized as a hinge with torsional stiffness, i.e. the bending moment at the joint is proportional to the angular deflection

$$M_{nodus} = K_{nodus} \cdot \Delta\theta \quad (2)$$

This rotational spring eq (2) is key to assessing how variation in K_{nodus} alters the global wing compliance. The COMSOL model solves the full 3D elasticity equations subject to these boundary and joint conditions.

Results and Discussion

The tip deflection under a uniform pressure load was found to vary strongly with K_{nodus}. Fig. 3 shows the calculated wing tip deflection (mm) as nodus stiffness is increased.

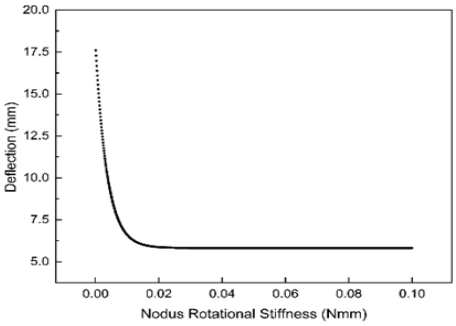


Fig. 2 illustrates the relationship between Nodus stiffness and max deflection at tip

A sharp decrease in deflection occurs for small value of rotational stiffness, a completely floppy nodus yields ~18 mm tip deflection, while a very stiff nodus limits deflection to ~5.5 mm. This nonlinear trend reflects the coupling of wing sections at the nodus: as reported experimentally, making the nodus stiffer greatly reduces overall wing bendability [1] In fact, the deflection–stiffness curve is qualitatively consistent with beam theory (inverse relation) and supports the idea that the nodus acts as a compliance regulator.

Under load, wing model exhibits camber and twist phenomenon as shown in Fig. 3. The red and black outline curves highlight the induced spanwise twist and chordwise chamber of the wing. The wing twists along its span and develops camber, as is typical in real dragonfly wings; here the nodus stiffness was set to an intermediate value. Most bending occurs toward the tip (where the red line deviates most), while the proximal wing remains relatively rigid. Such coupled bending-twist behavior is characteristic of insect wings under pressure and was noted in earlier structural analyses.

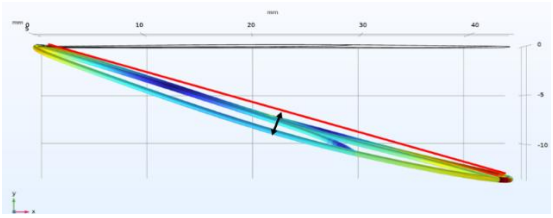


Fig. 3 Red & Black lines illustrate the spanwise twist and chordwise camber.

The displacement field (magnitude in mm) is shown in Fig. 4 for a representative case. Maximal displacement (red) occurs at the wing tip and leading edge, tapering to near zero at the fixed root. This pattern is expected for a cantilevered wing and indicates that much of the wing stiffness is concentrated near the root. Gradual gradient also shows that the membrane and vein stiffness was smoothly distributed in the model. A stiffer nodus shifts more load toward the root, reducing tip motion, Fig. 2, whereas a floppy nodus yields larger tip deflection as seen here.

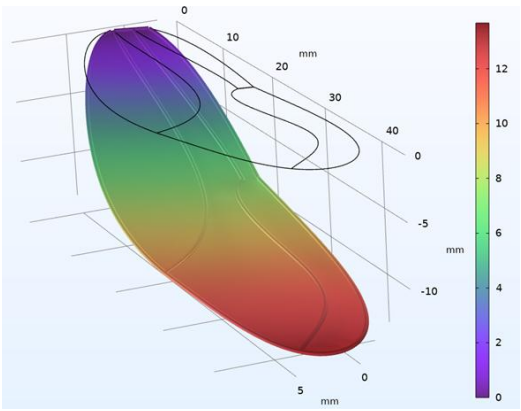


Fig. 4 Distribution of Displacements in Beam & Shell Elements Combined

The von Mises stress distribution is plotted in Fig. 5. Stress concentrates strongly at the nodus joint and at the wing root (dark red regions), while mid-span veins carry moderate stress (green blue). Notably, the nodus sees a stress peak due to the bending moment it transmits, consistent with prior findings that the nodus and pterostigma are mechanical hotspots [5] Insects may mitigate such stress by local material adaptations; for example, the presence of a nodus protrusion (knot) was hypothesized to limit rotation and protect against overload. In our model, as K_{nodus} increases, the stress at the nodus rises further, reflecting the stiffer joint transmitting more moments.

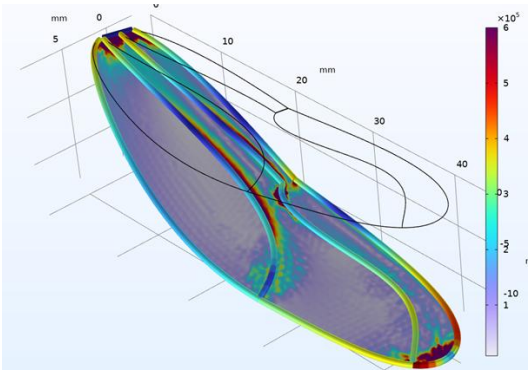


Fig. 5 Distribution of Stresses in Beam & Shell Elements Combined

Conclusion

A full-wing finite-element model in COMSOL was used to quantify the effect of nodus rotational stiffness on dragonfly wing bending. The simulations show that tip deflection under a given load decrease sharply as the nodus stiffness increases. In other words, a flexible nodus greatly enhances wing flexibility, whereas a rigid nodus maintains wing rigidity. Stress analysis reveals the nodus as a stress concentrator, explaining why insects often reinforce or limit motion there. These findings provide insight into how nodus mechanics influence overall wing behavior, with implications for the design of adaptive flapping wings.

References

[1] S. A. Combes and T. L. Daniel, “Flexural stiffness in insect wings I. Scaling and the influence of wing venation,” *Journal of Experimental Biology*, vol. 206, no. 17, pp. 2979–2987, Sep. 2003, doi: 10.1242/jeb.00523.

[2] D. Hou, Z. Zhong, Y. Yin, Y. Pan, and H. Zhao, “The Role of Soft Vein Joints in Dragonfly Flight,” *J Bionic Eng*, vol. 14, no. 4, pp. 738–745, Dec. 2017, doi: 10.1016/S1672-6529(16)60439-0.

[3] S. Zhang, Y. Sunami, and H. Hashimoto, “Deformation behavior of dragonfly-inspired nodus structured wing in gliding flight through experimental visualization approach,” *Sci Rep*, vol. 8, no. 1, p. 5751, Apr. 2018, doi: 10.1038/s41598-018-24237-x.

[4] H. Rajabi, N. Ghoroubi, K. Stamm, E. Appel, and S. N. Gorb, “Dragonfly wing nodus: A one-way hinge contributing to the asymmetric wing deformation,” *Acta Biomater*, vol. 60, pp. 330–338, Sep. 2017, doi: 10.1016/j.actbio.2017.07.034.

[5] S. R. Jongerius and D. Lentink, “Structural Analysis of a Dragonfly Wing,” *Exp Mech*, vol. 50, no. 9, pp. 1323–1334, Nov. 2010, doi: 10.1007/s11340-010-9411-x.

[6] H. Rajabi, K. Stamm, E. Appel, and S. N. Gorb, “Micro-morphological adaptations of the wing nodus to flight behaviour in four dragonfly species from the family Libellulidae (Odonata: Anisoptera),” *Arthropod Struct Dev*, vol. 47, no. 4, pp. 442–448, Jul. 2018, doi: 10.1016/j.asd.2018.01.003.

[7] K. G. ZURLYTĖ, R. GAIDYS, and B. NARIJAUSKAITE, “Biomechanical Study of the Wing of the Dragonfly Aeshna Cyanea,” *Mechanics*, vol. 30, no. 3, pp. 270–278, Jun. 2024, doi: 10.5755/j02.mech.36178.

[8] J. Sun and B. Bhushan, “The structure and mechanical properties of dragonfly wings and their role on flyability,” *Comptes Rendus. Mécanique*, vol. 340, no. 1–2, pp. 3–17, Dec. 2011, doi: 10.1016/j.crme.2011.11.003.

Acknowledgements

This research has received funding from the Research Council of Lithuania (LMTLT), agreement No S-MIP-24-46, “Intelligent micro sensor array for physical environmental monitoring based on the mechanisms of the behavior of insect mechanoreceptors”

DOI 10.5162/EUROSENSORS2025/W7.3.1

Smart Wastewater Surveillance of Viral Antibodies via Real-Time Optical Fiber Sensing

Małgorzata Szczerska[1,], Filip Janiak[1,6], Kacper Cierpiak[1], Monika Kosowska[2], Paweł Wityk[3], Patryk Sokołowski[1], Sebastián García-Galán[4], Sylwia Fudala-Książek[5], Aneta Łuczkiewicz[5]*

1 Faculty of Electronics, Telecommunications and Informatics, Gdańsk University of Technology, 11/12 Narutowicza Street, 80-233 Gdansk, Poland

2 Faculty of Telecommunications, Computer Science and Electrical Engineering, Bydgoszcz University of Science and Technology, Al. Prof. S. Kaliskiego 7, 85-796 Bydgoszcz, Poland

3 Department of Biotechnology and Microbiology , Faculty of Chemistry, Gdańsk University of Technology, 11/12 Narutowicza Street, 80-233 Gdansk, Poland

4 Telecommunications Engineering Department, Linares Higher Polytechnic School, Jaén University, Avenida de la Universidad S/N, 23700, Linares, Spain

5 Department of Water and Wastewater Technology, Faculty of Civil and Environmental Engineering, Gdańsk University of Technology, 11/12 Narutowicza Street, 80-233 Gdańsk, Poland

6 Sussex Neuroscience, School of Life Sciences, University of Sussex, Brighton, UK

malgorzata.szczerska@pg.edu.pl

Summary:

We present a remote, real-time wastewater monitoring system using a fiber-optic biosensor combined with machine learning to detect SARS-CoV-2-specific antibodies in untreated wastewater. The system is autonomous, requires no sample transport or preparation, and shows strong classification accuracy even in a complex matrix. The solution supports the early detection of epidemic outbreaks and aligns with current European directives on urban wastewater surveillance

Keywords: wastewater monitoring, SARS-CoV-2, fiber-optic sensor, machine learning, biosensing

1. Background, Motivation and Objective

Wastewater-based epidemiology (WBE) has emerged as a critical tool for public health monitoring. It enables early detection of viral outbreaks, including COVID-19, by assessing markers shed by both symptomatic and asymptomatic individuals. During the pandemic, WBE was utilized across EU member states to track SARS-CoV-2 activity [1]. As of April 2024, the revised Urban Wastewater Treatment Directive mandates real-time surveillance of public health markers—including SARS-CoV-2, influenza, and antimicrobial resistance—in municipal sewage systems [2].

However, conventional WBE depends on point sampling and laboratory analysis, typically involving time-consuming RT-qPCR methods [3]. These limitations inhibit continuous and automated monitoring. Our objective is to overcome these challenges by implementing a remote, label-free sensor system based on a biofunctionalized fiber-optic probe and supported by AI-driven signal classification. The system can detect SARS-CoV-2 IgG antibodies directly in raw sewage without sample preparation or transport, operating autonomously and in real time.

2. Description of the New Method or System

The core sensing element is a standard telecommunication-grade optical fiber with a microsphere tip, biofunctionalized to specifically bind SARS-CoV-2 antibodies. The functional layer was prepared using silanization, biotin-streptavidin coupling, and immobilization of spike S1 protein conjugates [4]. This sensor is capable of operating at 1310 nm, a wavelength compatible with current optical infrastructure.

Samples of untreated wastewater were collected and spiked with known concentrations of IgG (10^{-6} to 10^{-1} mg/mL). The probe was immersed in the samples, and signal variations were monitored using an optical spectrum analyzer. Key features were extracted from the resulting interferograms to create a numerical representation of each measurement.

157 signals were collected and processed. Machine learning models were trained to distinguish “positive” samples (IgG ≥ 10^{-4} mg/mL) from “negative” ones. Feature vectors were generated using three engineered parameters—peak

prominence variance, maximum peak width, and peak width standard deviation—and evaluated across a suite of algorithms for classification performance.

3. Results

The fiber-optic sensor system showed a strong, concentration-dependent response to IgG antibodies spiked into real, untreated wastewater. The design allowed signal modulation to be detected directly from the probe immersed in wastewater, without any need for sample filtration, concentration, or chemical labeling. The operational mechanism relies on the refractive index shift and light absorption changes caused by specific antigen-antibody interactions occurring at the surface of the microsphere sensor head.

When exposed to increasing IgG concentrations (10^{-6}-10^{-1} mg/mL), the reflected optical power recorded by the sensor exhibited a consistent and quantifiable decrease. In the lower concentration rangethe sensor response was linear, with a characteristic sigmoidal shape appearing at higher concentrations due to surface saturation. This response confirms the sensor's high sensitivity and specificity to the SARS-CoV-2 antibody-antigen binding reaction. The fast interaction kinetics, attributed to the biofunctionalized microsphere's high surface activity, supported real-time signal acquisition every 2 seconds with no signal lag.

Given the optical complexity of wastewater as a biological matrix—containing suspended solids, organic matter, and potential chemical interferents—signal interpretation based on raw optical intensity was insufficient. Traditional thresholding methods resulted in a low classification accuracy of only 38.9%. This performance was hampered by the signal variability caused by matrix noise, lighting fluctuations, and refractive interferences unrelated to specific binding.

To address this limitation, a machine learning pipeline was implemented. From collected interferogram, three engineered features were extracted: peak prominence variance, maximum peak width height, and standard deviation of peak widths. It was chosen based on their relevance to the expected spectral modulation during antigen-antibody interactions and their robustness to background interference. The dataset, was split into "positive" and "negative" classes using a 10^{-4} mg/mL IgG concentration threshold.

Multiple classification algorithms were trained and evaluated. The best-performing model, the KNeighborsClassifier, achieved an overall accuracy of 94.23%, a balanced accuracy of 92.97%, and an F1 score of 94.19%. These metrics reflect the model's ability to both correctly identify true positives and avoid false classifications. Compared to other models tested—such as ExtraTrees, GaussianNB, and LGBM—KNeighbors offered the best balance of accuracy, sensitivity, and computation time.

Additional validation of the sensor system was performed through repeatability testing. The probe was subjected to multiple cycles of antibody exposure and rinsing. The sensor response remained consistent across repeated measurements, with no evidence of hysteresis or sensor drift. No degradation of the biofunctionalized surface was observed.

The sensing system required no auxiliary reagents, labelling compounds, or pre-filtration steps, allowing real-time deployment directly in wastewater inflow channels. The ability to detect target biomolecules autonomously and continuously in situ makes this approach fundamentally different from conventional SARS-CoV-2 wastewater surveillance methods based on RT-qPCR.

In comparison to electrochemical sensors and surface-enhanced Raman scattering (SERS)-based approaches, which rely on pre-processed samples or high-cost instruments [5–7], the fiber-optic sensor system described here uniquely combines simplicity, scalability, and compatibility with existing optical fiber networks. This positions the system as a viable candidate for future implementation in smart urban infrastructure, enabling real-time health surveillance at the scale of cities, campuses, airports, and high-density public spaces.

4. References

[1] Singer AC et al., *A world of wastewater-based epidemiology*, Nat Water 2023;1:408–15.
[2] European Parliament, *New EU rules to improve urban wastewater treatment*, 2024.
[3] Ahmed W et al., *First confirmed detection of SARS-CoV-2 in untreated wastewater in Australia*, Sci Total Environ 2020;728:138764.
[4] Szczerska M et al., *The SARS-CoV-2 specific IgG antibodies biophotonic sensor*, J Biophotonics 2023;16(1):e202200172.
[5] Kumar MS et al., *Electrochemical sensing of SARS-CoV-2 amplicons with PCB electrodes*, Sens Actuators B 2021;343:130169.
[6] Sen P et al., *Detecting SARS-CoV-2 in wastewater using electrochemical aptamer sensors*, ACS Sens 2023;8:1558–67.
[7] Tian C et al., *SERS-based aptasensor for rapid detection of SARS-CoV-2 viral particles*, Sens Actuators B 2022;371:132445.

DOI 10.5162/EUROSENSORS2025/W7.3.2

A 3D printed RT-LAMP microdevice for the detection of feline calicivirus

Wojciech Kubicki, Justyna Kornicka, Rafał Walczak
Wrocław University of Science and Technology, Faculty of Electronics, Photonics and Microsystems, Department of Microsystems, Janiszewskiego Street 11/17, 50-372 Wrocław, Poland
wojciech.kubicki@pwr.edu.pl

Summary:
This study presents preliminary results of the development and characterization of a 3D-printed microfluidic lab-on-a-chip (LOC) device for rapid molecular diagnostics of feline calicivirus (FCV). The device was fabricated using digital light processing (DLP) technology and printed with biocompatible GR-10 photopolymer resin. The LOC was successfully applied to perform a reverse transcription loop-mediated isothermal amplification (RT-LAMP) assay for the detection of FCV, a common pathogen in cats. The results of the RNA amplification reactions confirmed the high potential of 3D printing technology and the applied UV-curable resin with isothermal enzymatic reactions for prospective use in veterinary medicine.

Keywords: LAMP, lab-chip, RNA, 3D printing, DLP, FCV.

Introduction

Lab-on-a-chip technology enables the integration of sample preparation, chemical reactions, separation, detection and many other processes within a single miniaturized device. In recent years, additive manufacturing methods have emerged as a powerful alternative that offers fast, low-cost, and customizable manufacturing of microfluidic chips, especially for research and small-batch production. 3D printing technology allows direct translation of virtual models into functional prototypes without the need for master molds or cleanroom facilities [1]. In this work, a microdevice (LOC, chip) for rapid molecular diagnostics using LAMP method was fabricated using 3D printing DLP technology with biocompatible resin. The chip was applied for RT-LAMP detection of FCV, which is a common and highly contagious pathogen that affects cats, particularly in shelters and multi-cat environments.

Materials and methods

The RT-LAMP chip was designed with CAD software and fabricated using a DLP 3D printer (ASIGA MAX, Asiga) with biocompatible photopolymer resin (GR-10, Pro3dure). The microdevice has dimensions of 50 mm x 25 mm x 2.2 mm and contains four microreactors (25 µL capacity each), which allow simultaneous amplifications, for example, one negative and one positive control, and two DNA/RNA samples (Figure 1). Each microreactor contains an inlet and an outlet for sample introduction and pressure distribution. The fabrication time of a single 3D printed chip is approximately 1 hour, including post-processing.

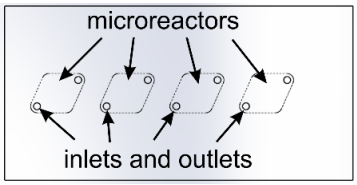


Fig. 1. Layout of the 3D printed LAMP microdevice

A similar device with identical dimensions of the microreactors, but arranged in different locations (Figure 2), was fabricated with borosilicate glass [2], using wet etching and fusion bonding processes (described elsewhere [3]). Here, a glass chip was used as a reference device, which was manufactured using verified glass technology.

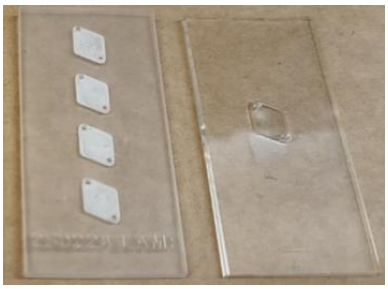


Fig. 2. Ready-to-use chips for RT-LAMP: 3D printed (on the left) and all-glass (on the right)

The microreactors of both devices were loaded with the same volume of LAMP solution, comprising SuperScript™ IV RT-LAMP Master Mix, FIP/BIP, F3/B3 and LoopF/LoopB primers and target RNA. The chips were sealed with PCR adhesive foil and placed on a laboratory hotplate (SD162, Stuart). The amplification reaction was carried out for 30 min at 67°C. Subsequently, the

sealing was removed and 1 µL of SYBR Green fluorescence dye was added to each reaction microchamber. The fluorometric signal was measured using a laser-induced fluorescence setup (Figure 3), containing a laser diode (490 nm, 350 mW, Thorlabs) with planoconvex lenses and optical bandpass filter (497 nm, Thorlabs), a CCD board camera with optical long-pass filter (525 nm, Thorlabs), video grabber, a computer with custom detection software (LabVIEW), and a set of 3D printed or commercially available mechanical stages for proper arrangement of the chip.

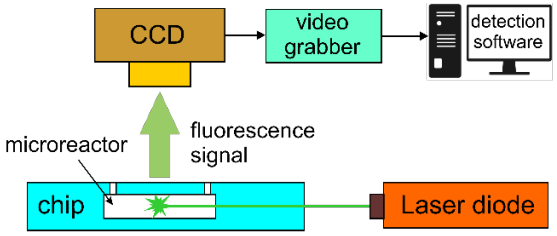


Fig. 3. Scheme of the fluorometric detection setup.

Results

Exemplary images captured by the CCD camera are presented in Figure 4. The software enables image analysis in the selected regions of interest (ROI) to calculate the intensity of the fluorescence signal. For all images, the same location and ROI area were applied to provide comparative results of LAMP output signal detection.

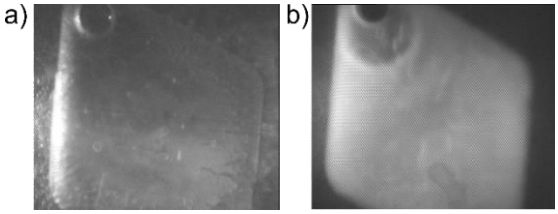


Fig. 4. Images of the 3D printed microreactors after LAMP: a) negative control, b) sample analyzed

The RT-LAMP process was performed for three samples: negative control (NEG) – equine RNA, positive control (POS) – *Feline Calicivirus* (M86379.1) RNA genome fragment 5179-5369 (191 bp), and tested sample (SAM). The RNA of the SAM sample was isolated from FCV-positive feline gingival swabs. The results of the analysis confirmed that a similar fluorescence intensity was obtained for the same sample type, regardless of the chip construction material (Figure 5). In the case of the 3D printed chip, the NEG value is slightly higher, while the POS and SAM values are a little lower in comparison to the glass device. Such differences can be explained by the observed increased intensity of background signal, probably invoked by a higher autofluorescence of the resin. This effect has already been investigated for other polymers [4], but more studies are required for the resin used here.

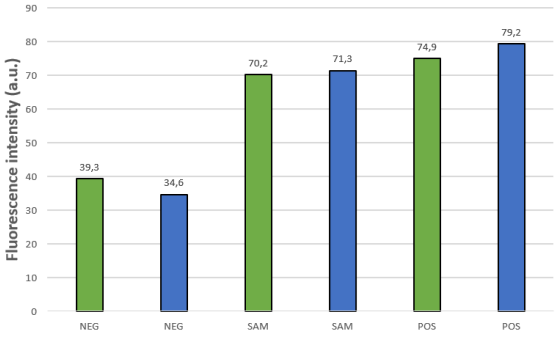


Fig. 5. Results of FCV RT-LAMP performed on the 3D printed device (green bars) and on the all-glass device (blue bars). Abbreviations: NEG/POS – negative/positive control, SAM – sample analyzed

Summary

This study successfully demonstrated the development of a 3D printed microfluidic chip for the application of RT-LAMP in veterinary diagnostics. The device was manufactured using digital light processing technology and printed with biocompatible GR-10 photopolymer resin. The primary objective was to use this device to perform a reverse transcription loop-mediated isothermal amplification assay to detect feline calicivirus, a contagious pathogen that affects cats. To conclude, this study confirms a promising future for the use of 3D printing technology to develop microfluidic devices for molecular diagnostics, offering fast, low-cost, and customizable solutions for veterinary applications. Nevertheless, more studies and optimizations are required to fully harness the potential of this technology.

References

[1] M. Sharafeldin, A. Jones, J.F. Rusling, 3D-Printed Biosensor Arrays for Medical Diagnostics, *Micromachines* 9, 394 (2018); doi: 10.3390/mi9080394

[2] R. Walczak, W. Kubicki, P. Śniadek, W. Kosek, A. Górecka-Drzazga, J. Dziuban, Portable Laboratories in Suitcases Utilizing Microfluidic Chips for Identification of Bacteria and Virus Pathogens as a New tool of EU Countries Biological Threats Defense Strategy, *Procedia Engineering* 168, 163-167 (2016); doi: 10.1016/j.proeng.2016.11.196

[3] W. Kubicki, B. Pająk, K. Kucharczyk, R. Walczak, J. Dziuban, Rapid detection of highly pathogenic A(H7N7) avian influenza virus genetic markers in heterogenic samples utilizing on-chip SSCP-CE method, *Sensors and Actuators B* 236, 926-936 (2016); doi: 10.1016/j.snb.2016.03.083

[4] A. Piruska, I. Nikcevic, S.H. Lee, C. Ahn, W.R. Heineman, P.A. Limbach, C.J. Seliskar, The autofluorescence of plastic materials and chips measured under laser irradiation, *Lab on a Chip* 5, 1348-1354 (2005); doi: 10.1039/B508288A

Acknowledgements

The Polish Ministry of Science and Higher Education financed this work as part of the Implementation Doctorate **DWD/5/0305/2021.**

DOI 10.5162/EUROSENSORS2025/W7.3.3

PCB-Based Electrochemical Electrodes with Self-temperature Regulation Functionality for Electrochemical Studies at Target Temperatures

Mohammad Derakhshani[1,2], Wolfgang Hilber[2], Samaneh Mirsian[2], Thomas Posnicek[1], Bernhard Jakoby[2], Martin Brandl[1]

[1] Center for Water and Environmental Sensors, Department for Integrated Sensor Systems, University for Continuing Education Krems, Dr.-Karl-Dorrek-Strasse 30, 3500 Krems an der Donau, Austria,

[2] Institute for Microelectronics and Microsensors, Johannes Kepler University Linz, 4040 Linz, Austria

Corresponding Author's e-mail address: mohammad.derakhshani@donau-uni.ac.at

Summary:

Electrochemical electrodes with self-temperature regulation functionality developed by PCB technology are reported. A two-layer PCB on which electrochemical electrodes in a three-electrode configuration on the top layer and a heater on the bottom layer are designed. The heater warms up the electrochemical electrodes and the sample on them, and a controller switching circuit is designed to turn on/off the heater sequentially in order to keep the sample temperature constant at the target value. Cyclic voltammetry represents the stable performance of PCB-based electrochemical electrodes with both electroplated gold and ENIG surface finishes at different temperatures. The presented platform has a great potential for developing temperature-sensitive chemical/biochemical sensors.

Keywords: PCB technology, temperature regulation, electrochemical electrodes, sensors

Background, Motivation an Objective

Printed Circuit Board (PCB) technology has recently been a popular approach for developing electrochemical sensors [1]. Specifically, PCB technology is exploited for fabricating electrodes of electrochemical sensors. However, beyond fabricating electrochemical electrodes, PCB technology has still significant potential for developing more advanced electrochemical sensors.

Temperature plays a key role in the performance of biochemical and chemical sensors. Temperature variation can influence the chemical and biochemical reaction rates, especially for biochemical sensors that usually contain enzymes or antibodies, whose activity is highly sensitive to temperature variations [2]. However, this important factor is usually neglected in sensor developments, and the sensor functionality is merely investigated at room temperature.

In this work, we present electrochemical electrodes and an integrated heater on a single board made by PCB technology for electrochemical analysis at target temperatures. The heater warms up the electrodes and the sample to a chosen temperature, and the reached temperature is kept constant by a designed controller circuit. The developed PCB-based platform offers a promising solution for temperature-sensitive chemical and biochemical sensors, due to its ability to maintain stable electrochemical functionality across varying temperatures and ensures precise temperature control.

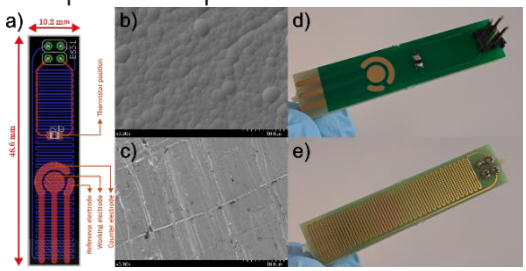


Fig. 1. a) Layout of the designed PCB. b, c) SEM image of ENIG and electroplated PCBs, respectively. d, e) Pictures from the top and bottom layer of the fabricated PCB, respectively.

Description of the New Method or System

The designed PCB layout (Fig. 1a) was produced by a commercial PCB company (https://www.multi-circuit-boards.eu/) on FR-4 boards with two different surface finishes, electroplated gold and Electroless Nickel Immersion Gold (ENIG). While both offer gold surfaces, the electroplated surface offers thicker gold layer and a flatter surface. Scanning Electron Microscopy (SEM) images of ENIG and electroplated gold electrodes are shown in Fig. 1b and 1c, respectively. The top layer of the PCBs contains electrochemical electrodes in a three-electrode

configuration and a position on which an SMD NTC thermistor (Vishay, NTCS0805E3472FMT, 4.7K) is soldered (Fig. 1d), while a heater is designed on the bottom layer (Fig. 1e). The heater was biased by a DC power supply with I = 1.2 A. A switching circuit powered by an Arduino Uno was designed to turn on/off the heater at a target temperature in order to keep the temperature constant over the sample on top of the electrodes (Fig. 2). Different temperatures can be achieved by modifying V_t in the Arduino code. Cyclic voltammetry (CV) was used to study the electrochemical properties of electrodes at different temperatures with a well-known reversible electrochemical reaction $[K_4[Fe(CN)_6]/K_3[Fe(CN)_6]$ (5mM in KCl 0.1M).

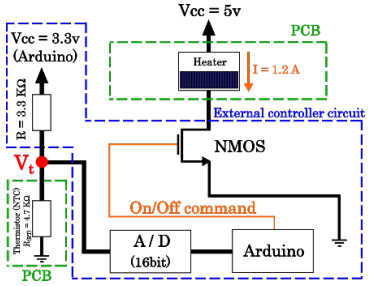


Fig. 2. Schematic diagram of the controller switching circuit.

Results

The sample is dropped over the electrochemical electrodes on the PCB top layer, and the heater on the PCB bottom layer is turned on subsequently. Based on the designed controller circuit, the PCB reaches higher temperatures by setting V_t at lower values, and the generated heat is transferred to the sample over the electrochemical electrodes. A commercial needle tip digital thermometer was used to precisely measure the sample temperature independently. Fig. 3 shows the temperature evolution of both the thermistor on the PCB and the sample at different V_t values. After a short transient state, both the thermistor and sample temperatures reach a stabilized value, which is kept constant using the controller circuit. The transient state duration and the stabilized temperature value depend on the chosen V_t value.

It should be noted that the thermistor temperature reflects only the temperature of the location on the PCB at which the thermistor is positioned, while the sample is located at a different location on the PCB. However, since the thermistor temperature uniformly follows the sample temperature in the designed PCB (Fig. 4a), V_t can be used as a parameter to set the sample temperature (Fig. 4b).

After reaching the stabilized temperature, CV was performed to conduct the electrochemical reaction $[K_4[Fe(CN)_6]/K_3[Fe(CN)_6]$. CV plots show the stable electrochemical performance of

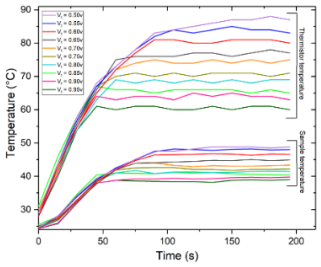


Fig. 3. Temperature evolution of the thermistor and the sample at different V_t values.

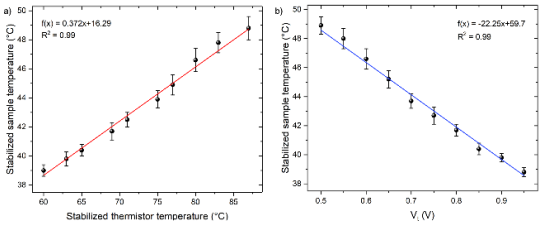


Fig. 4. a) Stabilized thermistor temperature vs, stabilized sample temperature. b) V_t can be used as a variable to set the sample temperature.

PCB-based electrodes at different temperatures for both ENIG and electroplated surface finishes (Fig. 5). The observed shifts in the peak voltages are likely caused by using a pseudo reference electrode. Also, a slight difference in the peak currents observed at different temperatures is probably due to a change in the reaction rate and diffusion coefficient at different temperatures.

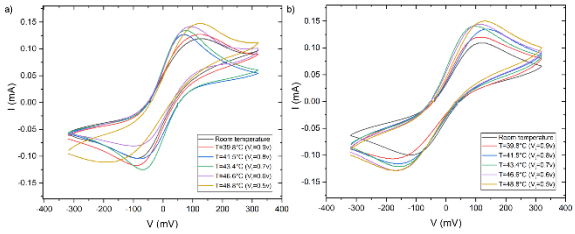


Fig. 5. CV plots at different temperatures for a) ENIG and b) electroplated electrodes.

Acknowledgements

This work is part of the European Marie Skłodowska-Curie network MiEl. The MiEl project received funding by the European Union under the Grant Agreement no. 101073003. Views and opinions expressed are however those of the author(s) only and do not necessarily reflect those of the European Union. Neither the European Union nor the granting authority can be held responsible for them.

References

[1] H. Shamkhalichenar, C. J. Bueche, and J. W. Choi, “Printed Circuit Board (PCB) Technology for Electrochemical Sensors and Sensing Platforms,” Oct. 30, 2020, *NLM (Medline)*. doi: 10.3390/bios10110159.

[2] A. Singh, S. K. Pasha, P. Manickam, and S. Bhansali, “Single-domain antibody based thermally stable electrochemical immunosensor,” *Biosens Bioelectron*, vol. 83, pp. 162–168, Sep. 2016, doi: 10.1016/j.bios.2016.04.054.kh

DOI 10.5162/EUROSENSORS2025/W7.3.4

Sensitivity Tuning and ON/OFF Switching in a Resonant Micro-accelerometer

Alexandra Zobova,[1], *Maxim Drizovsky* [1], *and Slava Krylov*[1]
[1] Faculty of Engineering, School of Mechanical Engineering, Tel Aviv University, Ramat Aviv, Israel
alexzobova@tauex.tau.ac.il

Summary: We report on a differential resonant accelerometer with electrostatically tunable and switchable transmission of the inertial load from the proof mass to the vibrating sensing beam. The device consists of a proof mass (PM) and two frames, interacting with the PM only electrostatically and connected through a compliant amplification pseudo-mechanism to the sensing beams. Displacement of the PM due to inertial forces affects the electrostatic coupling, the axial tension and the frequency of the sensing beams. ON/OFF switchable and tunable by voltage scale factors registered in the experiments are consistent with the model predictions.

Keywords: vibrating beam accelerometer, switchable sensitivity, electrostatic interaction, lumped model, SOI

Introduction

Microelectromechanical systems (MEMS) resonant accelerometers are widely used in various applications due to their small size, low cost, low power consumption, and better noise characteristics compared to their static counterparts [1]. These devices performance is affected by the trade-off between sensitivity and dynamic range, scale factors (SF), temperature dependency, and drifts [2]. The possibility to actively tune and switch OFF the device sensitivity may open the possibility of in situ self-calibration and therefore could be essential for further improvement of the high-end inertial sensors' performance.

Architecture and operational principle

We introduce a novel resonant accelerometer architecture with tunable and switchable force transmission from the PM to the vibrating sensing beams (resonators), Fig. 1. The device consists of a PM moving along the (sensing) y-axis and two force-transmitting frames moving along the x-axis, all suspended by flexible beams. Each resonator is anchored at one end and is attached to a corresponding frame through a compliant force amplification mechanism at the other end. Non-interdigitated comb-like electrodes attached to the mass and the frames operate in both gap-closing and area-changing modes. There is no mechanical interaction between the PM and the frames/resonators. When the frames are grounded and a steady voltage V is applied to the PM, the resulting electrostatic (ES) forces lead to the axial tension of both resonators. Acceleration-induced displacement of the PM alters the ES forces and, therefore, the resonators' tension and frequency. The acceleration is extracted by measuring the frequency shifts between the resonators.

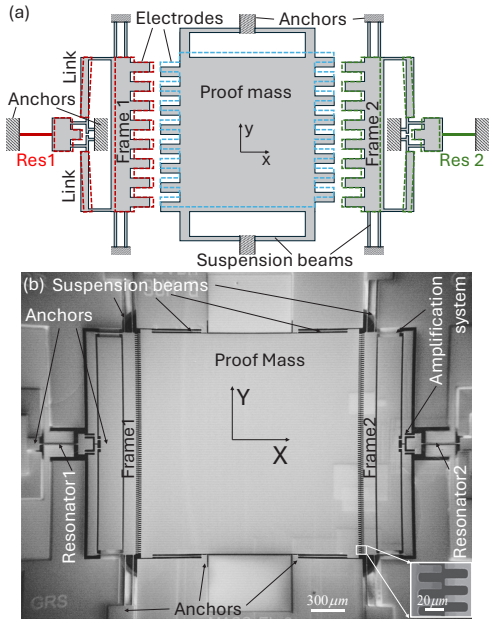


Fig. 1: (a) Schematics of the device; colored dash lines depict the deformed configuration. (b) The scanning electron microscope image of the device. The comb-like electrodes are shown in the inset.

Model

The lumped model of the device was built under common assumptions of perfectly rigid proof mass, links, and frames, along with massless suspension beams, compliant mechanism pseudo-hinges, and resonators [3]. The device is considered as a three-degree-of-freedom (DOF) system, with the displacements of the PM and each of the two frames (in the y and x directions, respectively) as the generalized coordi-

DOI 10.5162/EUROSENSORS2025/W7.3.4

nates. From equilibrium equations of the system, for the applied voltage V and the inertial load, we determine the resulting axial forces, which shift the resonant frequencies according to the double-clamped stretched beam model. Thus, for each resonator's frequency, we get:

$$f_i(V, \hat{a}_x, \hat{a}_y) = f_0 \Big[1 + \mathrm{SF}^V V^2 + (-1)^{i-1} \mathrm{SF}^x(V)\hat{a}_x + (-1)^i \mathrm{SF}^y(V)\hat{a}_y\Big].$$

Here $i = 1, 2$ refers to the left and right resonator, respectively, $f_{0,i}$ is the frequency of the unstretched resonator, SF^V is a relative voltage scale factor — a coefficient defining the tunability of the resonant frequency of the correspondent resonator only by the voltage, without inertial input; $\mathrm{SF}^x(V)$ and $\mathrm{SF}^y(V)$ are non-differential relative sensitivity (relative scale factor) of the frequency to the acceleration in the x and y-direction respectively; $\hat{a}_{x,y} = a_{x,y}/g$ is non-dimensional acceleration, and $g = 9.81$ m/s^2 is the acceleration of gravity. Both relative scale factors depend on the applied voltage:

$$\mathrm{SF}^x = \mathrm{SF}^x_0(1 + C^x V^2), \quad \mathrm{SF}^y = C^y V^2$$

Experiment

The device was fabricated from a highly doped device layer of an SOI wafer with (100) upper surface orientation using the SOI MUMPS process.The device was wire-bonded to a printed circuit board (PCB) and mounted in a custom vacuum chamber (VC), operating at a stabilized room temperature and pressure between 2.9 and 4 mTorr (Fig. 2(a)). The capacitive sensing was adopted to measure the resonators' frequencies in open and close loop modes [4]. In the zero inertial load experiment, the resonators' frequencies were measured in open-loop mode for a range of voltages; the sensing plane (x, y) of the device mounted in the VC was horizontal. In the turn-table experiment, the VC with the device inside was mounted on a dividing head, allowing angular rotation of the vertical sensing (x, y) plane about the z-axis.

The tunability of the frequencies due to an inertial input in the x and y directions and by voltage was shown in the experiment. The results of the experiments are shown in Fig. 2. By analyzing the data, the following figures of merit were obtained: the baseline resonator frequency $f_0 = 292.5$ kHz (an average for two resonators), the sensitivities $\mathrm{SF}^V = 8.6$ ppm/V^2, $\mathrm{SF}^x_0 = 235$ ppm/g, $C^x = 25$ ppm/V^2, $C^y = 0.075$ ppm/(g·V^2). Differential electro-statically tuned sensitivity along the y-axis reaches 86.6 Hz/g at $V = 45$ V.

Conclusion

We propose a novel vibrating beam accelerometer with a controllable electrostatic transmission of inertial input from the PM to the sensing elements. The device demonstrates tunable resonator frequencies and switchable sensitivity. The results lay the groundwork for optimizing electrode and frame designs, with potential applications in online calibration and noise reduction in MEMS inertial sensors.

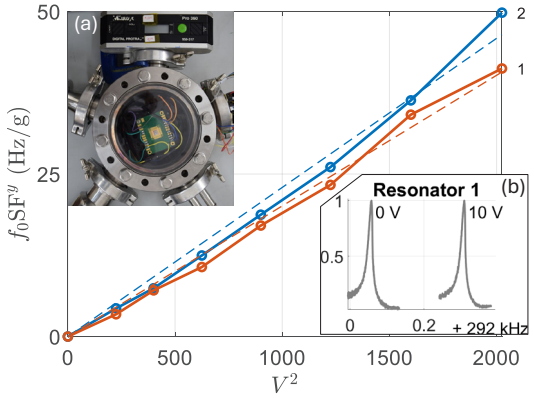


Fig. 2: Tunability of the scale factor in y-direction by applied voltage; solid lines correspond to the experimental data for Resonators 1 and 2 (numbers), dashed lines depict linear fit. Insets: (a) fabricated device on the PCB inside the vacuum chamber; (b) open-loop frequency response curves of Resonator 1 for $V = 0, 10$ (V) in the zero inertial load experiment.

Acknowledgements. This work was supported by The Israeli Ministry of Innovation, Science and Technology, grant no. 1001818762. AZ was supported by the Center for Integration in Science of the Israeli Ministry of Aliyah and Integration, SK was supported by the Henry and Dinah Krongold Chair of Microelectronics.

References

[1] C. Wang, F. Chen, Y. Wang, S. Sadeghpour, C. Wang, M. Baijot, R. Esteves, C. Zhao, J. Bai, H. Liu, *et al.*, "Micromachined accelerometers with sub-μg/$\sqrt{HZ}$hz noise floor: a review," *Sensors*, vol. 20, no. 14, p. 4054, 2020.

[2] W. Babatain, S. Bhattacharjee, A. M. Hussain, and M. M. Hussain, "Acceleration sensors: Sensing mechanisms, emerging fabrication strategies, materials, and applications," *ACS Applied Electronic Materials*, vol. 3, no. 2, pp. 504–531, 2021.

[3] A. Zobova and S. Krylov, "Self calibration by on/off sensitivity switching-feasibility study of a resonant accelerometer," *Sensors and Actuators, A: Physics*. Submitted for publication, arXiv preprint arXiv:2409.15839.

[4] A. Zobova, M. Drizovsky, O. HaLevy, N. Melech, S. Livne, and S. Krylov, "Single proof mass resonant mems accelerometer with parallel motion linkage amplifier," *IEEE Sensors Letters*, 2024.

DOI 10.5162/EUROSENSORS2025/W8.1.1

Gasochromic Tungsten Oxide Thin films for Hydrogen Monitoring in Natural Gas

Alessandro Longato[1], Elena Colusso[2], Alessandro Martucci[2]
[1] Pietro Fiorentini SpA, Via E. Fermi 8/10, Arcugnano (VI) 36057, Italy
[2] Industrial Engineering Department, University of Padova, Via Marzolo 9, Padova 35131, Italy

Corresponding e-mail: elena.colusso@unipd.it

Summary:
In this study we reported a gasochromic sensor for detecting hydrogen in natural gas, utilizing a tungsten oxide thin film coated with platinum nanoparticles. The sensor demonstrated excellent accuracy and repeatability in hydrogen detection within a methane environment, along with significant long-term stability. This advancement enhances the reliability of gas detection technologies for improved safety and efficiency.

Keywords: natural gas, methane, hydrogen, optical sensor, gasochromism, tungsten oxide, platinum nanoparticles, sol-gel

Background, Motivation an Objective

Natural gas represents a crucial element in the global energy supply; however, there is an increasing attention on renewable energy sources, particularly hydrogen, to mitigate climate change impacts. Blending hydrogen into existing natural gas pipelines is regarded as one of the most cost-effective approaches to reduce carbon emissions without requiring substantial changes for consumers [1]. To ensure precision in hydrogen dosing and to maintain the quality of the gas, it is essential to accurately measure hydrogen concentrations in natural gas. Several types of hydrogen sensors have been developed, including gas chromatographs and thermal conductivity detectors. However, these technologies often present challenges, such as high costs or operational limitations. Considering that natural gas is a complex mixture composed of components such as methane, ethane, and non-combustible gases like carbon dioxide and nitrogen, there is a pressing need for advancements in detection methods.
In this contest, we have developed a gasochromic sensor for hydrogen detection in natural gas using tungsten oxide (WO_3) thin films. When these films are coated with a metal catalyst like platinum, palladium, or gold, they undergo a color change from transparent to blue upon exposure to hydrogen. This change occurs as molecular hydrogen dissociates and alters the valence state of tungsten, resulting in the formation of tungsten bronze (HxWO3), which leads to the color shift [2]. This material serves as an effective optical transducer for hydrogen sensing. Previous research has shown that platinum-coated tungsten oxide demonstrates excellent performance in detecting hydrogen in air, nitrogen and in argon [3], making it a promising candidate for applications in hydrogen detection within natural gas systems.

Description of the New Method or System

WO_3 thin films were prepared using a sol-gel synthesis method with peroxotungstic acid as the precursor [3]. The sol-gel solution was spin-coated onto fused silica substrates at 2000 rpm for 30 seconds and then annealed at 550°C for 2 hours in air. Platinum (Pt) nanoparticles, synthesized using the polyol method, were deposited onto the WO_3 thin film through spin coating, followed by a treatment at 250°C for 10 minutes. X-ray diffraction (XRD) and scanning electron microscopy (SEM) characterizations confirmed the crystallization of the films. Pt nanoparticles uniformly covered the entire film, with an estimated surface coverage of 37% and an average diameter of 11 nm. (Figure 1).
Gas sensing tests were conducted by analyzing the absorbance changes induced by hydrogen in the 350-900 nm range. A Harrick gas flow cell was used in conjunction with a spectrophotometer at an operative temperature of 200°C. Time-resolved optical responses were recorded at a fixed wavelength of 850 nm. Preliminary investigations were performed with hydrogen balanced in methane to demonstrate the effective response in a reducing atmosphere.

DOI 10.5162/EUROSENSORS2025/W8.1.1

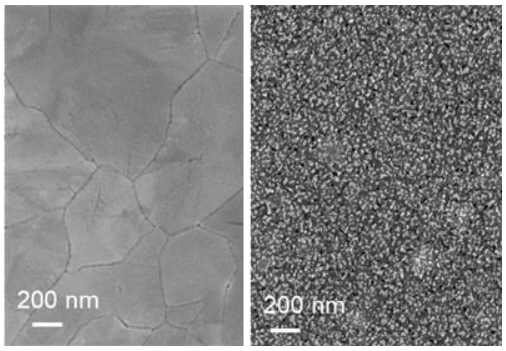


Fig. 1. SEM images of pristine WO_3 film (left) and Pt-coated WO_3 film (right).

Results

When exposed to hydrogen, the Pt-coated WO3 sample turns from transparent to blue, indicating an increase in absorbance at the edge of the visible spectrum. By monitoring the changes at 850 nm, we were able to evaluate the sensing performance of the films. We first investigated the optical response to 5% (v/v) hydrogen in methane, increasing the operating temperature (OT) from 100 °C to 200 °C. As reported in Figure 2, the best response and recovery times (1 second and 58 seconds, respectively) were achieved at 200 °C. This suggests that the bleaching mechanism in the absence of air is the decomposition of tungsten bronze, which can only occur at temperatures above 176 °C [2].

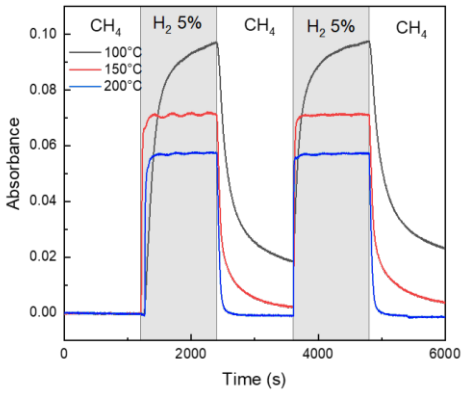


Fig. 2. Dynamic response at 850 nm Pt-coated WO3 sample collected at various temperatures under cycles methane – 5% H2 in methane.

The sensor's response exhibited a linear correlation with hydrogen concentrations ranging from 1% to 20% v/v (maximum concentration allowed in the pipeline), with a coefficient of determination (R^2) of 99.6%. We also tested the repeatability and long-term stability of the sensor. The sample was subjected to 5% and 10% (v/v) concentrations of hydrogen in methane over more than ten cycles, demonstrating excellent signal repeatability with variations in absorbance of less than 1% for all tested concentrations. Additionally, the dynamic response of the sample was maintained even after being stored for one month in a simulated pipeline environment containing hydrogen in methane.

As previously mentioned, natural gas consists not only of methane but also of other hydrocarbons, diluents, and inert gases. Therefore, the sensor was also tested with natural gas. **T**he sensor performs similarly in both methane and natural gas, with comparable response times and maximum absorbance changes. However, the recovery time increases due to the slower bleaching kinetics in the presence of other natural gas components. No cross-sensitivity was observed with any components of natural gas.

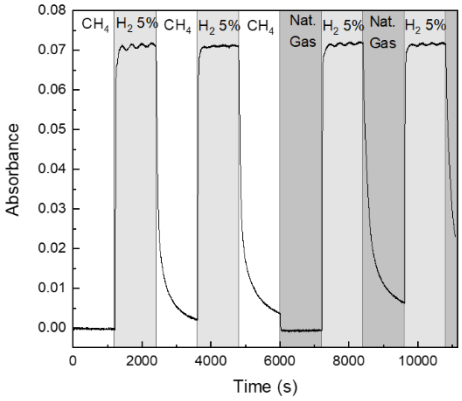


Fig. 3. Dynamic response for Pt-WO3 collected at 200°C under two cycles methane – 5% H2 in methane – methane and two cycles natural gas – 5% H2 in natural gas – natural gas.

The sensor's performance was found to be relatively independent of gas flow.

References

[1] B. C. Erdener, B. Sergi, O. J. Guerra, A. L. Chueca, K. Pambour, C. Brancucci, B.M Hodge, A review of technical and regulatory limits for hydrogen blending in natural gas pipelines, *Int. J. Hydrogen Energy* 48, 5595–5617 (2023); doi: 10.1016/j.ijhydene.2022.10.254.

[2] S. Amrehn, X. Wu, and T. Wagner, Tungsten Oxide Photonic Crystals as Optical Transducer for Gas Sensing, *ACS Sensors*, 3, 191–199, (2018), doi: 10.1021/acssensors.7b00845.

[3] A. Longato, M. Vanzan, E. Colusso, S. Corni, and A. Martucci, Enhancing Tungsten Oxide Gasochromism with Noble Metal Nanoparticles: The Importance of the Interface, *Small*, 2205522, (2022); doi: 10.1002/smll.202205522.

Acknowledgements

The authors acknowledge financial support from Pietro Fiorentini SpA.

DOI 10.5162/EUROSENSORS2025/W8.1.2

Optical Response to Hydrogen of WO_3 Thin Films Prepared by Magnetron Sputtering

Wiktoria Weichbrodt[1], Jarosław Domaradzki[1], Michał Mazur[1]
[1] Wroclaw University of Science and Technology, Faculty of Electronics, Photonics and Microsystems, Janiszewskiego 11/17, 50-372 Wroclaw, Poland
Corresponding Author's e-mail address: michal.mazur@pwr.edu.pl

Summary:
Tungsten oxide thin films were prepared using gas impulse magnetron sputtering and as-deposited samples were additionally annealed at 400°C to obtain nanocrystalline structure. Surface studies revealed good homogeneity of the prepared coatings. Thin films were exposed to hydrogen with different concentrations and their optical response, that is the decrease of transmission coefficient, was measured in the spectral range from 200 to 1000 nm. The change of resistance upon exposure to hydrogen, was also measured to compare optical and electrical reponse.

Keywords: WO_3, thin film, magnetron sputtering, gasochromic properties, hydrogen gas sensor

Introduction

Gasochromic WO_3 thin film sensors typically require noble metal nanoparticles as catalysts to facilitate the absorption and dissociation of H_2 molecules. One proposed mechanism, known as the "generation of oxygen vacancies" model, suggests that H^+ ions reduce W^{6+} on the WO_3 surface, forming oxygen vacancies that lead to colouration process [1,3]. Bleaching occurs via the re-oxidation of W^{5+} to W^{6+} by atmospheric oxygen, restoring transparency [1,3]. WO_3 thin films can be prepared using many various methods, including sol-gel, electron beam evaporation, thermal evaporation and magnetron sputtering. Noble metals like Pd, Pt, or Au can be applied as very thin adlayers at the top of thin films or used as dopants to improve sensing response. Nishizawa et al. [15] showed that Pt-doped WO_3 films respond faster to 4% H_2 than Pd-doped ones, and both showed high repeatability. Garavand et al. [8] reported that Pt/WO_3 coatings had higher coloration efficiency at 90–200 °C, while Pd/WO_3 performed better below this range. Lee et al. [10] deposited Pd on amorphous WO_3 by e-beam evaporation, which resulted in a 50% transmittance decrease as a response to 1% H_2.

In this work we show the gasochromic properties of nanocrystalline tungsten oxide thin films prepared by gas impulse magnetron sputtering. We compared optical and electrical response of this thin films to hydrogen exposure with different concentrations, up to 2.5%. The highest optical response was nearly twenty, while electrical resistance changed by several orders of magnitude.

Experimental methods

Tungsten oxide thin films were deposited using the gas impulse magnetron sputtering process with. The deposition process was conducted for 45 minutes with the average pressure of around $5 \cdot 10^{-3}$ mbar. Metallic tungsten target (purity of 99.95%) was sputtered with a mixture of argon and oxygen with a ratio of 7:1. The gas impulses were injected directly above the target surface with a frequency of 10 Hz, while the powering cycles were synchronized with gas pulses and lasted for 30 ms. Thin films were deposited at various substrates including fused silica for X-ray diffraction (XRD) and optical studies including gasochromic measurements, silicon for scanning electron microscope (SEM) investigations and alundum with interdigitated electrodes for determination of electrical response to hydrogen. Moreover, a very thin Pt catalyst with a thickness of ca. 2 nm was deposited at the top of WO_3 thin films using electron beam evaporation. Directly after deposition thin films were annealed in a tubular quartz furnace in an ambient air and pressure for 4 hours at 400°C.

SEM studies were performed with the aid of high-resolution field-emission scanning electron microscope FE-SEM (FEI Helios Xe-PFIB). XRD investigations were done with the use of Empyrean PANalytical X-ray diffractometer containing a PIXel3D detector and Cu$K\alpha_1$ radiation.

Transmission coefficient measurements were performed in the wavelength range of 300 to

1000 nm with the use of an Ocean Optics QE65000 spectrophotometer and a coupled deuterium-halogen light source. Gasochromic investigations were done at a temperature of 150°C using Janis ST-100H optical cryostat. Gas flow of hydrogen mixed with air was controlled MKS mass flow controllers. Measurement cycles consisted of coloring in diluted hydrogen with concentrations up to 2.5% and bleaching in pure air. Each cycle lasted for 30 minutes. The optical response (OR) was calculated according to the eq. (1):

$$OR = \frac{T_{air}}{T_{H2}} \quad (1)$$

where: T_{air} – transmission coefficient in air, T_{H2} – transmission coefficient in H_2 with specific concentration.

Furthermore, studies of sensor response (SR) in terms of resistance change upon exposure to hydrogen were conducted.

Results

WO_3 thin films directly after deposition had uniform surface with low roughness and were amorphous. After post-process annealing, a phase transition to WO_3-monoclinic occurred, and the average crystallite size was about 23 nm.

Figure 1 shows the optical response of annealed tungsten oxide thin films exposed to hydrogen concentrations from 0.5 to 2.5%. As can be seen from the transmission coefficient spectra, increasing the hydrogen concentration to 1% resulted in a significant decrease of the transparency of the thin films in the near-infrared wavelength region. Moreover, for a concentration of 2.5% and a wavelength of 900 nm, the transmission decreased from 84.6% to 4.5%, which gives the optical response of 18.9.

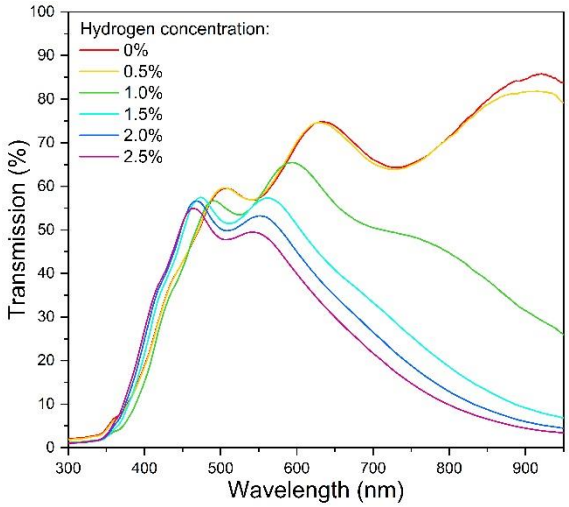


Fig. 1. Optical transmission spectra change upon exposure to hydrogen (in air) with various concentrations.

The sensor response of these thin films in terms of resistance change was over 6 orders of magnitude, i.e. it changed from 10^8 Ω to a value well below 10^2 Ω.

Summary

Tungsten oxide thin films revealed very good gasochromic properties as the optical response for the highest concentration was almost 19. It is also worth to emphasize that the resistance of the same thin films measured at the same conditions was decreased of several orders of magnitude. This means there was a significant change from dielectric to conducting behavior of the tested thin films. The in-situ studies of X-ray photoelectron spectroscopy and Raman spectroscopy will be performed in the future to determine changes in the surface and structural properties of WO_3 thin films exposed to hydrogen.

References

[1] A. Mirzaei, J.H. Kim, H.W. Kim, S.S. Kim, Gasochromic WO_3 nanostructures for the detection of hydrogen gas: An overview. *Applied Sciences 9, 9, (2019);* doi: 10.3390/app9091775

[2] C. Gao, X. Guo, L. Nie, X. Wu, L. Peng, J. Chen, A review on WO_3 gasochromic film: Mechanism, preparation and properties. *International Journal of Hydrogen Energy 48,* 2442–2465, (2023); doi: 10.1016/j.ijhydene.2022.10.100.

[3] K. Nishizawa, Y. Yamada, K. Yoshimura, Low-temperature chemical fabrication of WO_3 gasochromic switchable films: A comparative study of Pd and Pt nanoparticles dispersed WO_3 films based on their structural and chemical properties. *Thin Solid Films* 709, 138201, (2020); doi: 10.1016/j.tsf.2020.138201.

[4] N. T. Garavand, S. M. Mahdavi, A.I. Zad, Pt and Pd as catalyst deposited by hydrogen reduction of metal salts on WO_3 films for gasochromic application. *Applied Surface Sciemce* 273, 261-267, (2013); doi: 10.1016/j.apsusc.2013.02.027.

[5] Y. A. Lee, S.S. Kalanur, G. Shim, J. Park, H. Seo, Highly sensitive gasochromic H_2 sensing by nanocolumnar WO_3-Pd films with surface moisture. *Sensors and Actuators B: Chemical* 238, 111-119, (2017); doi: 10.1016/j.snb.2016.07.058.

Acknowledgements

This work was co-funded from the sources given by the Polish National Science Centre (NCN) as a Sonata research project No UMO-2020/39/D/ST5/00424 in the years 2021–2024 and under the OPUS call in the Weave programme, grant No 2023/51/I/ST11/02195.

DOI 10.5162/EUROSENSORS2025/W8.2.1

A field-effect device for specific and label-free biosensing

Gil Shalev
Ben-Gurion University of the Negev, Beer Sheva, Israel
glshalev@bgu.ac.il

Transistor-based biosensing is the holy grail of medical diagnostics as it supports low-cost self-use and point-of-care tests in a multiplexed manner from ultra-small physiological samples. Still, transistor-based specific and label-free sensing technology is not available today despite continuous efforts during the last several decades. We recently developed and introduced the Meta-Nano-Channel (MNC) field-effect biosensor for specific and label-free sensing of diverse molecular interactions. The MNC biosensor addresses solid-solution interface challenges related to the demand for electrochemical equilibrium of solution and molecular species during measurements, and the localization challenge of molecular gating. The MNC chip is fabricated exclusively for us in a large-scale chip factory (Tower Semiconductor) providing stability, robustness, and excellent electronic grade inherent to the CMOS (complementary metal-oxide semiconductor) process. Moreover, the extreme miniaturization of CMOS technology provides the infrastructure for unparalleled multiplexed sensing from ultra-small samples, as well enabling embedded chip configurations comprising additional circuitry related to logic, switching, memory, antennas, etc. The MNC biosensor has been demonstrated for sensing in neutral solutions, diluted serum, diluted plasma, and milk samples with typical limit-of-detection (LOD) in the range of fg/mL, with about 10 orders of magnitude in dynamic range and with excellent sensitivity and linearity[1–5]. In the talk I will present the underlying methodology of the MNC biosensor. Also, I will present direct MNC biosensor measurements of several molecular interactions in 0.5 μL samples of blood and sweat samples. The measurements are performed without any sample preprocessing and without premeasurement washing steps for the removal of the non-specific species. The sensing is quantitative and performed in real-time. We believe the MNC biosensor method provides real opportunities for the utilization of FET devices towards diverse applications concerning molecular sensing.

References

1 P. Verma, Y. Ben-Shahar, S. Samanta, V. Garika, S. Babbar, S. Bhattarai, S. Harilal, G. Feldheim, A. Pevzner, I. Columbus, H. Prihed, E. Pikhay, I. Shehter, A. Elkayam, M. Y. Bashouti, B. Akabayov, A. Weissberg, Y. Roizin, I. Ron and G. Shalev, *ACS Appl Mater Interfaces*, 2025, 17, 19165–19174.

2 V. Garika, S. Babbar, S. Samanta, S. Harilal, A. Eisenberg-Lerner, Z. Rotfogel, E. Pikhay, I. Shehter, A. Elkayam, M. Y. Bashouti, B. Akabayov, I. Ron, G. Hazan, Y. Roizin and G. Shalev, *Biosens Bioelectron*, 2024, 265, 116689.

3 I. Ron, I. M. Bhattacharyya, S. Samanta, V. S. Tiwari, D. Greental, R. Shima-Edelstein, E. Pikhay, Y. Roizin, B. Akabayov and G. Shalev, *Sens Actuators B Chem*, 2023, 393, 134171.

4 S. Samanta, I. M. Bhattacharyya, A. Prajapati, I. Ron, R. Shima-Edelstein, E. Pikhay, D. Greental, A. Eisenberg-Lerner, Z. Rotfogel, Y. Roizin, B. Akabayov and G. Shalev, *Adv Mater Technol*, DOI:10.1002/admt.202202200.

5 S. Samanta, S. Babbar, B. Chen, M. Muppidathi, S. Bhattarai, S. Harilal, E. Pikhay, I. Shehter, A. Elkayam, M. Y. Bashouti, B. Akabayov, I. Ron, Y. Roizin and G. Shalev, *Biosens Bioelectron*, 2024, 258, 116368.

DOI 10.5162/EUROSENSORS2025/W8.2.2

The Art of Building a Good Chemiresistive Sensor Based on AC: Tips and Tricks for Better Detection Performance

Jean Zaraket[1], Proscovia Kyokunzire[1], Vanessa Fierro[1], Alain Celzard[1,2]
[1]Université de Lorraine, Centre National de la Recherche Scientifique (CNRS), Institut Jean Lamour (IJL), F-88000, Épinal, France
[2]Institut Universitaire de France (IUF), 75231 Paris, France

Corresponding Author's e-mail address: jean.zaraket@univ-lorraine.fr

Summary:
Due to rising air pollution, gas sensors have become essential in fields such as industry, medicine and environmental monitoring. This work presents advancements in gas-sensing technologies, emphasizing the role of activated carbons (ACs) and their hybrids. ACs are gaining interest thanks to their high surface area and porous structure, which enhance gas adsorption. Their surfaces can be modified with additives or combined with other materials to improve sensor performance. The present communication highlights the sensing performance of AC-based gas sensors, and future challenges in this field.

Keywords: Activated carbon (AC), Gas sensors, Hybrids, Porosity, Surface area

Background, Motivation and Objective

Figs. 1 and 2 illustrate the number of publications from 2000 to 2024, based on the literature reviewed. From the data presented in these figures, it is evident that research on the development of AC-based materials for chemical gas sensing, particularly for air pollution monitoring, has remained relatively limited attention until recent years. Given the growing focus on developing chemical gas sensors with highly porous, sensitive and highly selective sensing layers, with a fast gas detection rate, operating at room temperature and inexpensive, a comprehensive review of AC-based sensors is both timely and necessary. Such a review can help to identify the challenges associated with the application in gas sensing.

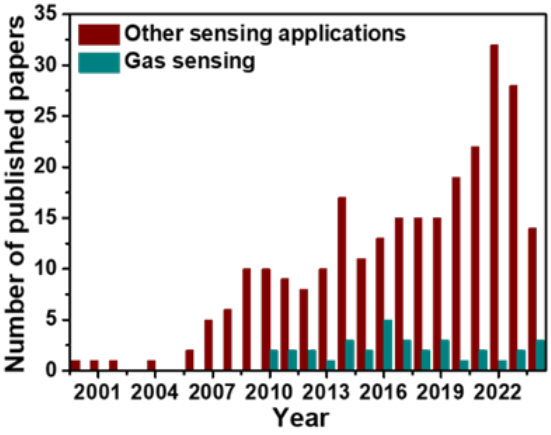


Fig. 1. Number of articles published on AC-based materials for sensing since 2000, obtained from the SCOPUS database.

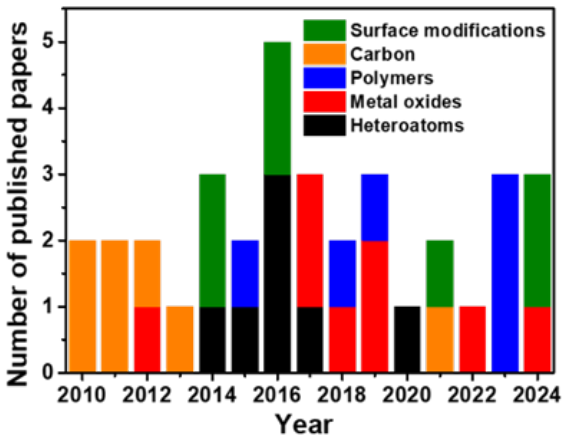


Fig. 2. Number of papers reviewed in which AC was combined with various materials for gas sensing applications.

The objective of this work is to examine the latest progress in gas sensors based on AC used as sensitive layers, with particular focus on hybrid composites formed by combining AC with other materials, to improve sensor performance.

About AC-based gas sensors in general

AC is characterized by a complex 3D network of aromatic nano-domains (2–3 nm in size) [1], comprising narrow pores. Each nano-domain typically consists of a stack of 3–4 graphene-like sheets, each measuring approximately 3 nm or less [2]. This structural characteristic provides an exceptionally high surface area (up to 3000 $m^2.g^{-1}$), which offers numerous active sites for the adsorption of large quantities of gas molecules [3]. Despite these advantages, AC has certain

limitations, including low recovery and recyclability, as well as moderate electrical conductivity. In comparison, graphene-based materials can exhibit electrical conductivities on the order of 10^4 $S.cm^{-1}$ [4], whereas AC typically shows a lower conductivity in the range of 20–50 $S.cm^{-1}$ [5], leading to limited charge transfer at the carbon surface [6]. To overcome these drawbacks, it is critical to modify the AC surface with other materials such as metal oxides, conducting polymers, heteroatoms or other carbons. These modifications enhance critical properties such as conductivity and recoverability, which are essential parameters for gas sensor applications [7].

a) AC doped with heteroatoms

The enhanced gas sensing performance of heteroatom-modified activated carbons can be primarily attributed to changes in their surface chemistry. The incorporation of heteroatoms such as boron (B), nitrogen (N), oxygen (O) and sulfur (S) can: ***(1)*** improve the electrical properties of AC; ***(2)*** facilitate more efficient charge transfer interactions between ACs and target gases; ***(3)*** improve the surface reactivity by providing more active sites for gas adsorption; and ***(4)*** introduce various functional groups on the AC surface, which significantly enhance selectivity and sensitivity toward specific gases.

b) AC-metal oxide hybrid materials

The combination of AC and metal oxides takes advantage of: ***(1)*** the high surface area and adsorption capacity of AC; and ***(2)*** the excellent gas-sensing properties of metal oxides. Many metals oxides function as semiconductors and exhibit changes in their electrical properties upon gas exposure. When integrated with AC, the formation of heterojunctions between these material interfaces act as electron transfer pathways, thereby improving charge carrier mobility. Additionally, the porous structure and high surface area of AC provide an ideal support matrix for the uniform dispersion of metal oxide, further enhancing the overall sensing performance.

c) AC-polymer composites

AC enhances the performance of polymer-based gas sensors by increasing surface area, thereby offering numerous adsorption sites for gas molecules. The porous structure of AC helps trapping gas molecules, allowing the polymer matrix to interact with a higher density of analytes. These characteristics make AC–polymer composites highly effective for a broad range of gas-sensing applications.

d) Composites of AC with other carbon materials

The detection performance of AC-based composites combined with other carbonaceous materials is generally attributed to the high specific surface area and porous structure of AC, which significantly enhance the overall adsorption capacity of the composites. Moreover, when AC is combined with highly conductive carbon materials such as carbon black, graphene or carbon nanotubes, efficient conductive networks are formed. These networks can: ***(1)*** increase the overall electrical conductivity of the composites; and ***(2)*** improve their response to gas adsorption.

Conclusion

This work summarizes AC-based gas sensors and explores their integration with various other sensing materials, including heteroatom-doping, metal oxides, alternative carbon materials and polymers, which contribute to enhanced gas sensing performance.

References

[1] N. Kobayashi, T. Enoki, C. Ishii, K. Kaneko, M. Endo, N. Kobayashi, T. Enoki, 1998, Gas adsorption effects on structural and electrical properties of activated carbon fibers Gas adsorption effects on structural and electrical properties of activated carbon fibers 198310.1063/1.476774.

[2] R. Paul, B. Das, R. Ghosh, Novel approaches towards design of metal oxide based hetero-structures for room temperature gas sensor and its sensing mechanism: a recent progress, J. Alloy. Compd. 941 (2023) 168943, https://doi.org/10.1016/j.jallcom.2023.168943.

[3] A.A. Khaleed, A. Bello, J.K. Dangbegnon, D.Y. Momodu, M.J. Madito, F.U. Ugbo, A.A. Akande, B.P. Dhonge, F. Barzegar, O. Olaniyan, B.W. Mwakikunga, N. Manyala, Effect of activated carbon on the enhancement of CO sensing performance of NiO, J. Alloy. Compd. 694 (2017) 155–162, https://doi.org/10.1016/j.jallcom.2016.09.310

[4] X. Liu, W. Wu, B. Guo, M. Cui, H. Ma, Z. Zhang, R. Zhang, Facile fabrication of ultrathin gr phene film with ultrahigh electrical conductivity an superb electromagnetic interference shielding effective ness, J. Mater. Chem. C. 9 (2021) 214–222, https://doi.org/10.1039/d0tc04576d.

[5] A. Celzard, J.F. Marêché, F. Payot, G. Furdin, Electrical conductivity of carbonaceous powders, Carbon N. Y 40 (2002) 2801–2815, https://doi.org/10.1016/S0008-6223(02)00196-3.

[6] P. Ndagijimana, H. Rong, P. Ndokoye, J.P. Mwi erwa, F. Nkinahamira, S. Luo, D. Guo, B. Cui, A r view on activated carbon/ graphene composite-based materials: synthesis and applications, J. Clean. Prod. 417 (2023), https://doi.org/10.1016/j.jclepro.2023.138006.

[7] J. Pierre, C. Liu, K. Xu, N. Zhao, Y. Li, P. Ndag jimana, Z. Chen, J. Shen, AC / reduced graphene oxide wrapped LiFePO 4 cathode for Li-ion batteries with ultrahigh capacities and high specific energy density, FlatChem 34 (2022) 100393, https://doi.org/10.1016/j.flatc.2022.100393.

DOI 10.5162/EUROSENSORS2025/W8.2.3

Selective Optical and Chemoresistive H_2 Sensors by Nanosecond Pulsed Laser Annealing of Sol−Gel VO_2 Films

Maria Basso[1], Valentina Paolucci[2], Vittorio Ricci[2], Elena Colusso[1], Mattia Cattelan[3], Enrico Napolitani[4], Carlo Cantalini[2], Alessandro Martucci[1]

[1]*Industrial Engineering Department, University of Padova and INSTM, Via Marzolo 9, Padova 35131, Italy.*

[2]*Industrial Engineering Department, University of L'Aquila, Roio 67100 L'Aquila, Italy.*

[3]*Chemical Sciences Department, University of Padova and INSTM, Padova 35131, Italy.*

[4]*Physics and Astronomy Department and LNL-INFN, University of Padova and INSTM, Padova 35131, Italy.*

Corresponding email: maria.basso@unipd.it

Summary:

Nanosecond Pulsed Laser Annealing (ns-PLA) is a promising technique to simultaneously crystallize and nanostructure metal oxides films. Here, high nanostructured surface area was achieved on sol-gel VO_2 thin films by ns-PLA. The gas sensing tests showed excellent selectivity toward H_2, low operating temperatures of 150°C, detection limit as low as 2 ppm, and long-term stability over 500 h. Advanced in-operando GIXRD and in-situ XPS proved that the sensing mechanism involves reversible structural and chemical changes, based on reversible variations of V oxidation state and H_xVO_2 bronze formation.

Keywords: vanadium oxide, chemoresistive sensor, optical sensor, hydrogen, laser annealing

Background, Motivation an Objective

Nanosecond Pulsed Laser Annealing (ns-PLA) offers notable advantages for the fabrication of functional thin films, enabling ultrafast and localized heating that promotes crystallization and nanostructuring within a few seconds. Unlike conventional thermal treatments, ns-PLA is energy-efficient, compatible with temperature-sensitive substrates, and can significantly reduce process times and emissions. These features make it a compelling method for scalable and sustainable material processing. In this work, we employed ns-PLA to fabricate nanostructured thin films of vanadium dioxide (VO_2), a transition metal oxide known for its thermally induced, reversible metal-insulator transition (MIT) near 68°C. This phase transition results in abrupt changes in VO_2's optical and electrical properties, which can also be modulated by electric fields or strain.[1] Among its various polymorphs, the monoclinic/tetragonal VO_2 (M1/R) phases are particularly interesting for sensing applications but remain less explored than the VO_2 (B) phase.[2] Using a simple and environmentally-friendly sol-gel approach, we prepared VO_2 (M1/R) films by either ns-PLA or traditional furnace-annealing (FA), to assess the impact of crystallinity and nanostructuring on hydrogen (H_2) sensing performance. Dual-mode optical and chemoresistive sensors offer great advantages for cross-validation, versatility in application to multiple platforms, and better understanding of sensing mechanisms. Therefore, the optical and chemoresistive response to H_2 of the VO_2-based sensors was tested in concentrations ranging from a few ppm up to 50,000 ppm. The films were functionalized with Pt nanoparticles to exploit their catalytic activity in enhancing surface reactions. Selectivity tests were performed to verify NO_2 and humidity cross-sensitivity. The sensing mechanism was investigated through in-operando and in-situ techniques, including grazing-incidence X-ray diffraction (GIXRD) and X-ray photoelectron spectroscopy (XPS).

Description of the New Method or System

Sol-gel VO_2 films were crystallized by either ns-PLA or FA. The ns-PLA was performed in air, by irradiating the samples with a KrF excimer laser system for 1 min, while FA was performed under a N_2 flux at 550°C for 1 h.[3] Ellipsometry analysis revealed an average thickness of ~30 and 50 nm, respectively.

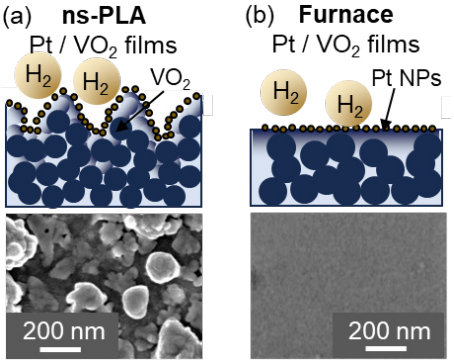


Figure 1. Schematic and SEM images of sol-gel VO_2 films crystallized by (a) ns-PLA or (b) furnace annealing, and decorated by Pt nanoparticles.

Scanning electron microscopy (SEM) revealed the spontaneous formation of nanostructures after ns-PLA (Figure 1a), compared to a smooth flat morphology for FA (Figure 1b). GIXRD and Raman confirmed the successful crystallization into VO_2 (M1) for both samples. The optical transmittance, measured at low (20°C) and high (90-150°C) temperatures, proved the presence of a reversible MIT (Figure 2, black/blue lines).

Results

Initially, we investigated the chemoresistive response of both ns-PLA and FA samples to H_2 (5−500 ppm) at 150°C operating temperature (OT) in dry air background. Both samples show an *n*-type behavior, with the electrical resistivity decreasing upon H_2 exposure, coupled with an excellent recovery of the baseline resistance. A good relative response (RR=R_{air}/R_{gas}) of 1.4±0.1 and 1.7±0.1 is found for ns-PLA and FA, respectively, along with a theoretical limit of detection (LOD) of 2.9 and 2.0 ppm, respectively. Both samples sustained over 3 months (~500 h) under working conditions, confirming an excellent long-term stability, and were highly selective towards H_2, as no response was shown upon exposure to NO_2 (400 ppb-2 ppm) or humidity (20-80% at 25°C).

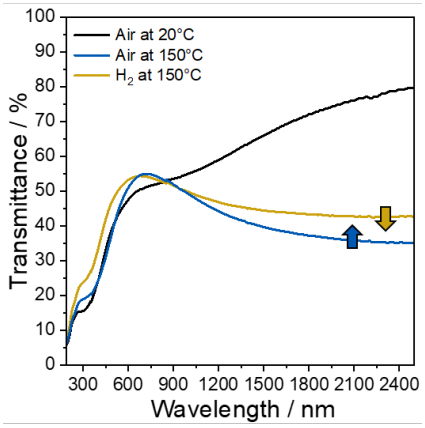


Figure 2. Optical transmittance of the FA sample in air at 20°C (black line) and 150°C (blue line). Gas sensing response of the FA sample to 5% H_2 at 150°C OT with dry air background (yellow line).

In addition, both ns-PLA and FA samples show a fully reversible modulation of the optical properties upon H_2 exposure within the entire UV-vis-NIR range (Figure 2). In the UV, the ns-PLA sensor shows a remarkably higher H_2 response (RR=3.8), with respect to RR=1.2 of FA. Both sensors display an H_2 response at OTs below 150°C, down to room temperature (30°C).

The overall gas sensing mechanism is explained by considering the concurrent role of both Pt nanoparticles (NPs) and VO_2 films. Pt NPs favorably induce the catalytic dissociation of molecular H_2 into atomic H on the surface of VO_2. The H spillover leads to its diffusion within the bulk of the VO_2 films, and results in the formation of the H_xVO_2 bronze (Eq. 1). The latter reacts with adsorbed oxygen, which results in a decrease in resistance due to the electron release (Eq. 2):

$$VO_2 + H \rightleftharpoons H_xVO_2 \quad (1)$$

$$4H_xVO_2 + O_2^- \rightleftharpoons 4VO_2 + 2H_2O + e^- \quad (2)$$

The reversible bronze formation, coupled with the reversible variations in the V oxidation states, were proved by in-operando GIXRD and in-situ XPS. As shown in Figure 3, the appearance of the H_xVO_2 diffraction (yellow pattern) can be seen upon sample exposure to H_2, which is found to be fully reversible, confirming the chemoresistive and optical gas sensing tests.

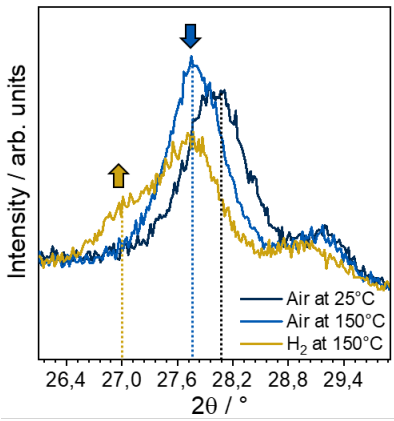


Figure 3. GIXRD of the FA sample in air at 20°C (black pattern), showing the principal monoclinic M1 diffraction, and 150°C (blue pattern), showing the rutile diffraction. GIXRD of the FA sample upon exposure to 5% H_2 at 150°C (yellow pattern), showing the formation of the H_xVO_2 bronze.

Coherently, in-situ XPS highlights the changes in V oxidation state upon H_2 exposure, with the V^{4+} state reversibly decreasing from ~53% to ~43%.

In conclusion, we successfully fabricated H_2 sensors via ns-PLA, offering a dual chemoresistive and optical mode, selectivity towards H_2, excellent baseline recovery, and long-term stability.

References

[1] Zhang, Y. et al. Recent Progress on Vanadium Dioxide Nanostructures and Devices: Fabrication, Properties, Applications and Perspectives. *Nanomaterials* 2021, 11, 338. doi.org/10.3390/nano11020338.

[2] Liang, J. et al. High-Sensitivity NH3 Gas Detection at Room Temperature Using In2O3 Nanoparticles-Modified VO2(B) Nanorods Heterojunction. *Appl Surf Sci* 2024, *649*, 159170. doi.org/10.1016/j.apsusc.2023.159170.

[3] Basso, M., et al. Sol-gel Pt-VO_2 films as selective chemoresistive and optical H_2 gas sensors. *ACS Appl. Mater. Interfaces* 2024, 16, 42, 57558–57570. doi.org/10.1021/acsami.4c13003.

DOI 10.5162/EUROSENSORS2025/W8.3.1

Strain Sensors Based on Hybrid Electronics with Flexible Packaging

Daniel Zymelka[1] *and Yusuke Takei*[1]
[1]National Institute of Advanced Industrial Science and Technology
1-2-1 Namiki, Tsukuba 305-8564, Japan
daniel.zymelka@aist.go.jp

Summary: Flexible printed strain sensors have a broad range of applications, primarily in wearable technologies, but they are also being explored in less conventional areas, such as strain measurement on engineering structures - the main target application of the sensors investigated in this work. In response to the global challenge posed by the rapidly aging road and bridge infrastructure, this study focuses on the development of large-area, flexible strain sensors intended for civil infrastructure monitoring. The fabrication process and sensor design are based on a multilayered construction and hybrid electronics, combining printed electronics with conventional components. Sensor evaluation demonstrates good strain sensitivity and a linear output signal, indicating potential for practical applications in local strain distribution analysis.

Keywords: hybrid electronics, additive manufacturing, screen printing, strain sensors, strain mapping.

Introduction

Flexible strain sensors have a broad range of applications, primarily due to their ability to conform to diverse surfaces and their relatively low cost. The most common applications include wearable devices and robotics, but they are also increasingly being investigated for use in structural health monitoring (SHM) of civil engineering structures. In recent years, SHM has become a significant challenge for infrastructure administrators and an important concern.

The condition of infrastructure and the associated maintenance requirements, particularly for road bridges, are raising growing global concerns. For instance, Japan's road network includes over 700,000 bridges [1]. By the late 2020s, nearly 50% of these bridges will be over 50 years old, the typical lifespan after which deterioration accelerates and major renewal is generally required. Europe's bridge infrastructure is also extensive and rapidly aging.

In response to the global challenge posed by the aging bridge infrastructure, there has been growing interest in recent years in developing sensor systems for civil infrastructure monitoring using various technologies. Printed strain sensors, have shown great promise for monitoring local strain distribution around crack tips in concrete and steel structural elements [2], [3].

In this study, the fabrication process and design of a new strain sensor concept are presented. In contrast to the previously reported sensor design [2], this work introduces a multilayered construction based on hybrid electronics, combining printed electronics with conventional components. The wiring system, contact pads, and sensors were screen printed onto thin polyimide substrates using silver and carbon conductive pastes. The sensors were then evaluated through bending tests to assess their strain sensitivity. The results demonstrate that the fabrication process enables the production of large-area, flexible sensor clusters with good strain sensitivity and a linear output signal within the strain range relevant to the target SHM application.

Materials and Methods

In the first step, the contact pads with wires were screen printed onto a 25 μm polyimide substrate using a silver paste (Toyobo DW-440L-29C). The printed patterns were then dried in a convection oven at 90℃ for 30 minutes. Next, three sensors were printed on top of the contact pads using a carbon paste (Toyobo DY-200L-2) and cured at 130℃ for 60 minutes. This polyimide sheet with the printed sensors served as the bottom layer of the complete sensor array structure. The contact pads were designed to transmit electrical signals

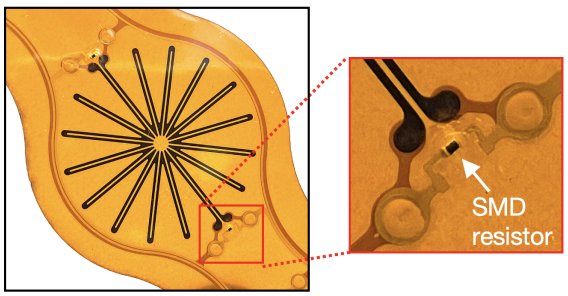


Fig. 1: Three polyimide layers incorporating printed layers of wires, contact pads, and sensing elements, integrated with SMD resistors, together comprise the structure of the sensors.

DOI 10.5162/EUROSENSORS2025/W8.3.1

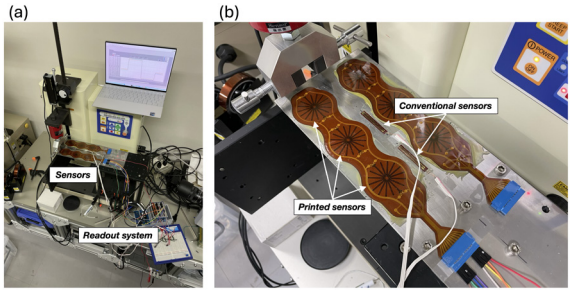


Fig. 2: a) Experimental setup used for the evaluation of the sensors. b) The array of three printed sensors was bonded to the metal plate, along with two conventional strain sensors used as references for the calibration process.

from the sensors, while the main wiring system was located on the top layer of the sensor construction.

The main wiring system was screen printed on a separate polyimide sheet using the same silver paste as used for the electrodes and cured at 130 °C for 60 minutes. The sensors were designed in a half-Wheatstone-bridge configuration, incorporating two active gauges made from the carbon paste. To complete the Wheatstone bridge, two SMD resistors were added for each individual sensor. These resistors were bonded at specific locations on the top layer, while the carbon-based sensing elements were located on the bottom layer (Fig. 1).

The top and bottom layers were bonded using a hot-melt adhesive. Prior to bonding, a laser was used to create vias at designated locations on the top layer. To establish electrical contact between the layers, the vias were filled with silver paste using a dispenser and subsequently cured in the oven. In the final step, a third polyimide layer (a cover layer) was bonded to the top layer to protect the printed wiring. The sensor array was then cut from the stacked layers into the desired shape. For evaluation, the sensors were bonded to a metal plate, as shown in Figure 2.

Results

During the analysis, the plate with the sensors was subjected to bending deformations, generating various levels of strain. As demonstrated in Figure 2, two conventional sensors were installed alongside the printed sensors, one in the middle and the other near the edge of the metal plate support, where larger strains were expected. The output signals from all printed sensors (Fig. 3a) and conventional sensors were measured simultaneously. Using specially developed software, the measured output voltage was converted into resistance changes, and the results were compared, as shown in Figure 3b.

The collected data demonstrate a uniform output signal from both printed sensors within the investigated strain range. This range corresponds to the typical strains encountered in practical structural health monitoring applications when no damage occurs. The output signal was linear and exhibited no hysteresis. The calculated gauge factor (GF), which specifies strain sensitivity, was approximately 6.1. For comparison, the GF of the conventional sensors was about 2. These results are promising for the practical implementation of the demonstrated printed sensors in monitoring engineering structures, particularly in applications requiring local strain distribution analysis, such as early crack detection or monitoring crack propagation.

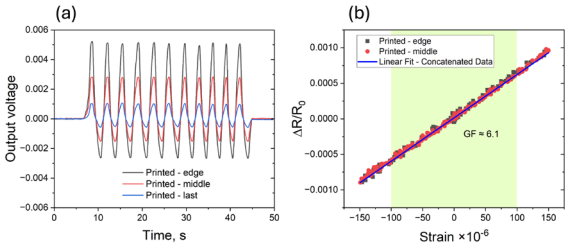


Fig. 3: a) Output signals from the printed sensors. b) Comparative analysis of resistance changes in the printed sensors and strain measured by conventional sensors.

Conclusion

This study demonstrates the fabrication and evaluation of flexible strain sensors with an original multilayered hybrid electronics design, specifically developed for structural health monitoring of engineering structures. The sensors exhibit good strain sensitivity and a linear output signal with no hysteresis, highlighting the potential of the printed sensors. The fabrication methods employed enable scaling up the construction to larger sensor arrays, thus increasing the sensing area. These promising results suggest that the developed sensor arrays are well suited for practical implementation in civil infrastructure monitoring.

References

[1] `https://www.mlit.go.jp/road/road_e/s3_maintenance.html`

[2] D. Zymelka, K. Togashi, T. Kobayashi, Carbon-based printed strain sensor array for remote and automated structural health monitoring, *Smart Mater. Struct.* 29, 105022 (2020); doi: 10.1088/1361-665X/aba81c

[3] D. Zymelka, K. Togashi, T. Kobayashi, Concentric Array of Printed Strain Sensors for Structural Health Monitoring, *Sensors*, 20, 1997 (2020); doi: 10.3390/s20071997

Acknoledment

This work was supported by the JSPS KAKENHI Grant JP 22K18421.

DOI 10.5162/EUROSENSORS2025/W8.3.2

Analyzing Electrochemiluminescence Signal and Detection Limits Through Device-Independent Color Space Mapping

Stephania Rodríguez Muiña[1], Rajendra Kumar Reddy Gajjala[1], Eduardo Fernández Martín[1], F. Javier del Campo[1,2]*
[1] BCMaterials, Basque Center for Materials, Applications and Nanostructures. UPV/EHU Parque Científico, E-48940 Leioa, Bizkaia, Spain.
[2] IKERBASQUE, Basque Foundation for Science, 48009 Bilbao, Spain.
**javier.delcampo@bcmaterials.net*

Summary:
Luminance quantification with consumer cameras becomes reliable through color space transformations, including gamma correction and conversion to device-independent spaces. This study offers an in-depth analysis of inter-channel relationships using the $Ru(bpy)_3^{2+}$/TPrA system as a model, demonstrating how distinct color dimensions reveal unique signal features. This approach improves noise assessment, detection limits, and overall robustness of smartphone-based ECL measurements, advancing their applicability in biosensing and diagnostics.

Keywords: Gamma correction, smartphone camera, image analysis, electrochemiluminescence (ECL), color spaces.

Background, Motivation and Objective

Smartphone cameras have become increasingly popular in analytical chemistry. Their portability, affordability, and advanced imaging capabilities have enabled widespread application in colorimetric, fluorescence, and chemiluminescence assays, particularly for point-of-care diagnostics [1-4].

Electrochemiluminescence (ECL), a light-emitting process initiated by electrochemical reactions, is especially well-suited for camera-based detection due to its high sensitivity, lack of background interference, and independence from external light sources [2]. However, the transition from traditional photodetectors to consumer-grade CMOS smartphone sensors presents new challenges. Mayor challenges are the nonlinear transformations introduced by the image signal processing pipeline—especially gamma correction—which distort the true relationship between recorded intensity values and analyte concentration [3,4].

Many studies still assume a linear response between RGB values and concentration, often neglecting the impact of device-specific encoding and perceptual distortions. This leads to significant errors in quantification, limiting the reproducibility and accuracy of such approaches [1-3].

This study evaluates how different device-independent color spaces (CIEXYZ, CIExyY, CIELAB) impact ECL quantification from smartphone images. By analyzing inter-channel relationships, signal variability, and detection limits, it shows that each color space reveals distinct signal characteristics. This multidimensional analysis improves accuracy and robustness for biosensing applications.

Description of the New Method or System

A smartphone-potentiostat-based ECL assay was combined with a standardized image processing workflow to quantify $Ru(bpy)_3^{2+}$/TPrA emission using RGB data transformed into CIEXYZ, CIExyY, and CIELAB color spaces. Beyond simple intensity measurements, the analysis explored inter-channel relationships such as a* vs. b*, hue angle, luminance (Y, L*), and chromaticity (xy), offering a multidimensional perspective.

Results

ECL emission, triggered by applying 1.2 V vs. Ag/AgCl, peaked around 5 s, marking the frame selected for analysis. RGB data were converted into device-independent color spaces (CIEXYZ, CIExyY, and CIELAB), enabling robust assessment beyond device limitations.

Quantification can be focused on red-sensitive channels—R (BT709), X (CIEXYZ), and a* (CIELAB)—using both linear (eq.1) and piecewise nonlinear models (eq.2) to capture signal response across concentrations (see Fig.1) [3].

$$Intensity = mC \quad (1)$$

$$Intensity = \begin{cases} b \cdot C, & C < T \\ c \cdot C^a - d, & C \geq T \end{cases} \quad (2)$$
$$with\ c = (b \cdot C\ + d)\ /\ (C^a)$$

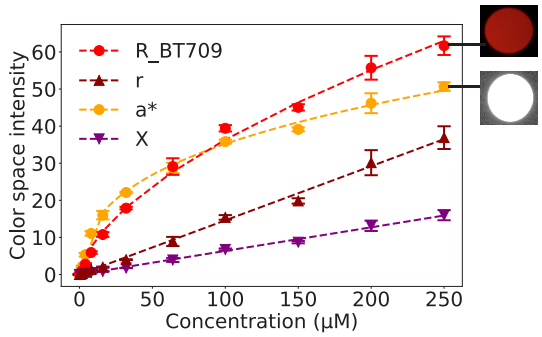


Fig. 1. Color space transformations of background-subtracted ECL intensity values from wavelength-selected channels relevant to the red-emitting ECL system, including R from BT709, linearized r, X from CIEXYZ, and a from CIELAB color space transformations.*

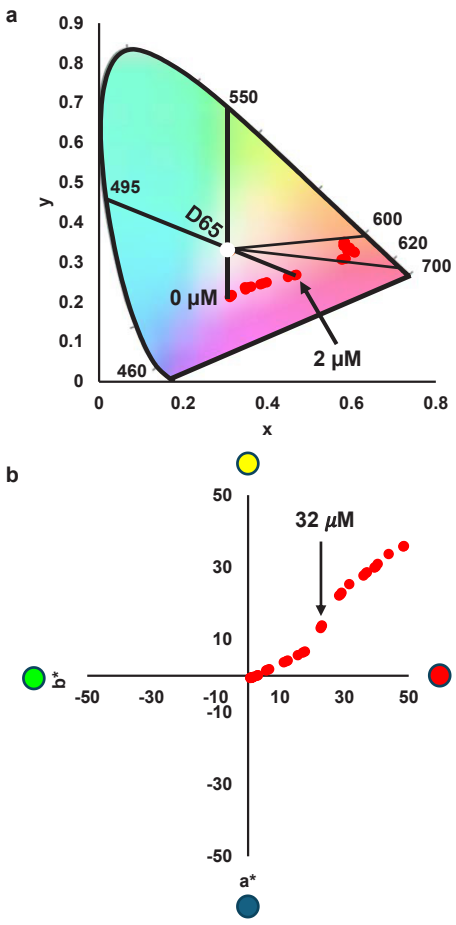


Fig. 2. a) CIExy chromaticity diagram showing ECL emission coordinates across concentrations, overlaid on the spectral locus, illustrating wavelength-related color shifts. b) CIELAB a vs. b* plot revealing chromaticity clustering behavior as a function of ECL intensity.*

Nevertheless, inter-channel studies revealed unique insights beyond intensity-based quantification. In the CIExy chromaticity plot (Fig. 2a), signal points below ~2 µM deviated from the expected chromatic locus red area, suggesting that the smartphone sensor lacks the resolution to reliably detect ultra-low concentrations without additional signal enhancement. Signal-to-noise ratio (SNR) and detection limit assessments across different color spaces confirmed ~2 µM as the practical threshold for reliable detection.

Meanwhile, the a* vs. b* plot (Fig. 2b) revealed two distinct signal regimes above and below ~30 µM, suggesting underlying shifts in emission characteristics that were not evident from intensity-only models

This multidimensional approach—combining color theory, inter-channel behavior, and perceptually relevant metrics—proves essential to capture both physical and visual attributes of ECL, supporting more accurate and interpretable quantification in biosensing applications.

References

[1] A. Priye, C. S. Ball, R. J. Meagher, Colorimetric-Luminance Readout for Quantitative Analysis of Fluorescence Signals with a Smartphone CMOS Sensor, *Anal. Chem.* 90 (21), 12385–12389 (2018); doi: 10.1021/acs.analchem.8b03521

[2] C. Meng, S. Knežević, F. Du, Y. Guan, F. Kanoufi, N. Sojic, G. Xu, Recent Advances in Electrochemiluminescence Imaging Analysis, *eScience* 2 (6), 591–605 (2022); doi: 10.1016/j.esci.2022.10.004

[3] S. Rodríguez Muiña, R. Gajjala, E. Fernández, F. J. del Campo, Gamma Correction and Color Space Transformations for Quantitative Analysis of Electrochemiluminescence Images Using Smartphone Cameras, submitted for publication.

[4] J. Velasco, P. Galán, R. K. R. Gajjala, E. Fernández, J. Trimaille, J.-Y. Hihn, B. Lakard, A. Álvarez-Gila, A. Picón, F. J. del Campo, Image-Based Analysis of Electrochromic Materials: Gamma Correction with a LEGO Luminance Checker, *Electrochim. Acta* 525, 146062 (2025); doi: 10.1016/j.electacta.2025.146062

Acknowledgements

This work was supported by the ECLectic project, which has received funding from the European Union´s MSCA Doctoral Network Horizon Europe programme (Grant Agreement No. 101119951).

DOI 10.5162/EUROSENSORS2025/W8.3.3

High-Performance and Low-Cost Microfluidic-Electrohemical Biosensors

Zhiyi Zhang[1], Zexi Wang[2] and Changqing Xu[2]
[1] Quantum and Nanotechnologies Research Center, National Research Council Canada, 1200 Montreal Road, Ottawa, ON K1A 0R6, Canada
[2] Department of Engineering Physics, McMaster University, 1280 Main St W, Hamilton, ON L8S 4L8, Canada
Zhiyi.zhang@nrc-cnrc.gc.ca

Summary:
Microfluidic-electrochemical biosensors were fabricated by printing capillary microfluidic channels over printed electrodes using a functional material. The printed sensors without electrode modification were tested with a limit of detection (LOD) of 7 μM on glucose detection. This work has demonstrated the possibility of achieving high sensing performance with low-cost sensors, and reported how the printed microfluidic channels bring the performance to this level.

Keywords: Biosensors, microfluidic, electrochemical, printing.

Introduction

Microfluidic-electrochemical biosensors are normally fabricated by integrating microfluidic hollow channels with electrodes [1] or printing electrodes on paper-based microfluidic channels [2]. Both of them are not suitable for fabricating high-performance devices at low cost. Our invented capillary microfluidic technology [3] makes it possible to print the devices in volume at low cost. More importantly, the printed sensors are characterized with very high sensitivity without any surface modification of electrodes using expensive materials and processes. This paper presents the method of printing the sensors, the application of the sensors in glucose detection, and the effects of the microfluidic channels on sensing performance.

Experiment

Commercial Ag/AgCl inks (Kayaku Advanced Materials) and carbon inks (Loctite) were used to print reference, working and countering electrodes on transparent PET films, followed by the printing of microfluidic channels on their top using a functional material. The functional materials were formulated in house by mixing alumina particles, silica particles, polyvinyl alcohol and dimethyl sulfoxide (Millipore Sigma). An ASYS EKRA X1-SL semi-automatic screen printer (ASYS Group was used for the printing.

For the glucose detection using the printed electrochemical biosensors, a Princeton Applied Research PARSTAT 2263 potentiostat (AMETEK Scientific Instrument) was used for both cyclic voltammetry and chronoamperometry measurement. In In the analysis, 1 μL of enzyme (glucose oxidase) solution containing 100 mM potassium ferricyanide and 1 M KCl in 0.1 M PBS at pH 7.4 was first added onto each microfluidic channel over the working electrode and was allowed to dry at room temperature. Then, 6 μL of the glucose sample was added to the channel inlet and allowed to travel through the whole channel (within 1 minute). The experiments were performed between a potential of −0.3V and 1V and at scan rates ranging from 25 to 400 mV/s.

Results

Fig. 1 illustrates the process of printing microfluidic-electrochemical sensors using the method and materials. The obtained microfluidic channels are characterized with standalone structure and can transport fluid through capillary action in the similar fashion as the paper-based microfluidic channels do (Fig. 2).

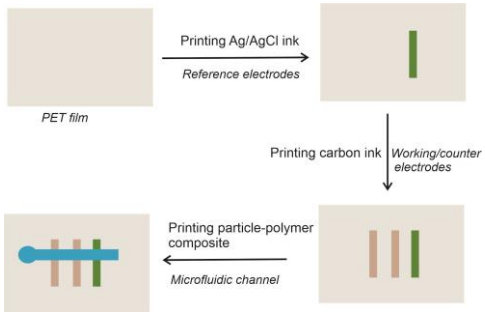


Fig. 1. Process flow of printing microfluidic-electrochemical biosensors.



Fig. 2. Photograph of printed straight capillary microfluidic channels. 2 seconds after a diluted inkjet ink was dropped onto the inlet of the central channel, and a colored paper was placed underneath for photo taking.

Fig. 3 shows the printed sensors with a single testing channel and multiple testing channels for enzymatic detection. After an enzyme solution is dopped onto the microfluidic section over the electrodes, testing samples can be dropped onto the circular inlets of the microfluidic channels for the detection. Many sensors can be printed on a transparent PET film with a high yield using a pilot-scaled screen printer, and the process can be implemented in sheet-to-sheet and even roll-to-roll for volume production.

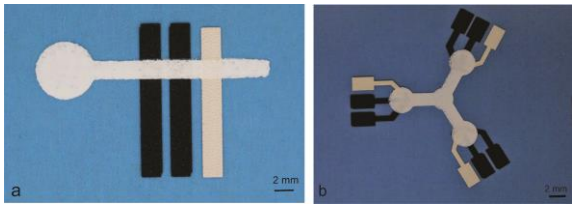


Fig. 3. Photographs of printed microfluidic-electrochemical biosensors for enzymatic detection. a, device for single reaction detection; b, device for simultaneous detection of three types of enzymatic reactions. The devices were printed with a screen printer, and colored papers were placed underneath for photo taking.

The printed microfluidic channels play a vital role in sensing performance through their porous structure. The interconnected pores, that are formed from the packing voids of the inorganic particles in the particle-polymer composite (Fig. 4), can substantially enhance the sensitivity while transporting testing samples to electrode surfaces through capillary action. This type of enhancement was not reported in any electrochemical sensors. A very lower polymer concentration in the composite was found in favor of the enhancement effect but mechanically weakening the printed structure. A two-layer microfluidic channel structure was thus developed by first printing the composite with 3% polymer on the electrodes for high sensing performance and then printing the composite with 8% polymer on top to provide mechanical protection. As such, sensors with high sensing performance and sufficient mechanical strength can be printed in large quantity.

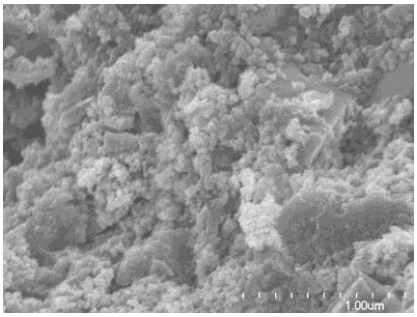


Fig.4. SEM image of the microfluidic channel of one printed biosensor. The particle-polymer composite composing of 97% alumina and silica particles, and 3% polyvinyl alcohol was printed with a screen printer.

The printed biosensors were tested in glucose detection (Fig. 5) with a limit of detection (LOD) at 7 μM obtained, due to the powerful sensitivity enhancement by the pores in microfluidic channels. A LOD in such low level was only reported when expensive nano materials with complicated processes were used in fabricating electrochemical biosensors. This work has demonstrated the possibility of fabricating high-performance biosensors at low cost.

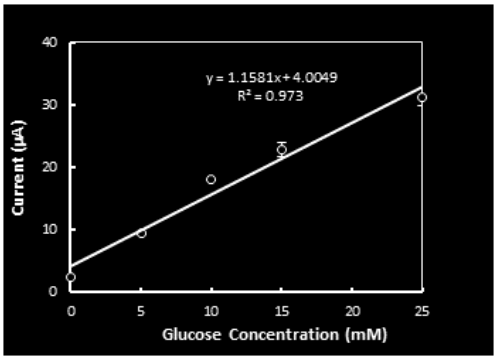


Fig. 5. Chronoamperometric calibration curve for glucose concentration as a function of current at 30 s. The biosensors with a structure in Figure 3a were printed with the composite with 3% PVA on bottom and the composite with 8% PVA on top.

References

[1] A. S. Ghrera, C. M. Pandey, M. A. Ali, B. D. Malhotra, Electrochemical studies of lateral flow assay test results for procalcitonin detection, Appl. Phys. Lett. 106, 193703 (2015).

[2] E. Noviana, C.P. Mccord, K. C. Clark, I. Jang, C. S. Henry, Electrochemical paper-based devices: sensing approaches and progress toward practical applications, Lab. Chip. 20, 9(2020).

[3] Z. Zhang, Y. Tao, J. Lu, G. Xiao, Raised fluidic channels and methods of manufacture, US patent, US20240342703A1.

DOI 10.5162/EUROSENSORS2025/MP1

A 3D Printed Strain Sensor Employing Conductive TPU for Marine Applications

D.N. Pagonis[1,2], A. Stavros[1], I. Iakovidis[1], S. Dimitrellou[1], G. Kaltsas[2]
[1] Department of Naval Architecture, University of West Attica, Egaleo 122 43, Athens, Greece
[2]microSENSES Laboratory, Department of Electrical and Electronics Engineering, University of West Attica, Egaleo 122 44, Athens, Greece
email: D.N.Pagonis@uniwa.gr

Summary:
This work investigates the development of a fully 3D printed strain sensor using conductive Thermoplastic Polyurethane elastomer (TPU) and Polylactic Acid (PLA) filaments. The sensor is produced solely through additive manufacturing Fused Deposition Modeling (FDM) technology. This process is particularly beneficial in maritime environments as it enables remote production, thereby reducing downtime, minimizing inventory demands, and lowering environmental impact. The use of conductive TPU compared to previously performed research employing CNT-enriched PLA filament results in expanded measuring range and reduced hysteresis, mainly attributed to the elasticity of the building material. The developed sensor maintains the key advantages of a fully 3D printed device, including robustness, a straightforward design, and a single-step manufacturing process, while offering a reliable electrical interface through standard soldering. These combined features enhance its reliability, durability, and overall suitability for structural monitoring applications in marine environments.

Keywords: Additive manufacturing, conductive TPU, strain sensor, structural health monitoring, marine engineering.

Background, Motivation and Objective

The application of 3D printed sensors in the marine industry can provide substantial benefits such as cost-effectiveness, minimal downtime, and circular economy compliance. Prior work by our research group demonstrated the feasibility of using Carbon Nanotube (CNT) enriched filaments as piezoresistive elements for FDM-printed strain sensors, which showed adequate and promising performance when subjected to bending with consecutive compression and elongation steps [1]. However, hysteresis and non-linearity were recorded especially at displacements larger than 0.6 mm, possibly attributed to the fracture of the conductive paths within the polymer matrix.

To address this challenge, the present work investigates the employment of a conductive Thermoplastic Polyurethane elastomer (TPU) filament -a composite material characterized by intrinsic elasticity and resilience- for the sensing element. The goal was to develop a fully printed sensor with improved repeatability, lower hysteresis, and better long-term reliability in strain detection applications relevant to structural monitoring of marine components. The proposed sensor consists of a monolithic body comprising of two layers: a non-conductive layer acting as a substrate, and a piezoresistive layer on top as the sensing element. The device can be attached to a structural component to monitor mechanical stress and can be easily connected to the appropriate measurement electronics via integrated solder pads, enabling straightforward interconnection.

Description of the Developed Process

The device was fabricated exclusively using FDM additive manufacturing technology, employing a dual-material strategy; the sensing element is fabricated from a commercially available conductive TPU filament enriched with lamp black (approx. 10% w/w, Recreus Industries S.L.) while the mechanical supporting frame is printed using standard Polylactic Acid (PLA) building material (Ultimaker B.V.).

Due to the inherent elasticity of TPU, the sensor is expected to exhibit higher durability under cyclic loading conditions, along with reduced hysteresis. This improvement is attributed to TPU's ability to accommodate strain through reversible deformation and facilitate a more stable balance between the disruption and reformation of the conductive network (percolation pathways) within the piezoresistive element. In contrast, CNT-enriched PLA filament employed in previous research leads to a more rigid polymer

matrix which may result to conductive network fragmentation under strain, therefore enhancing hysteresis. All process steps, from CAD design to print parameters, including extrusion temperature, building plate temperature, print speed, layer thickness and infill pattern, were optimized for consistent extrusion and interlayer bonding within the conductive piezoresistive path and between the two structural layers. These optimizations aimed to ensure uniform electrical conductivity and enhanced mechanical stability of the device. The application of an appropriate thermal treatment step on the printed device was also investigated to enhance its sensing characteristics, in accordance with previous research results [2,3]. In brief, annealing alters the polymer microstructure, which changes from an amorphous state to a semi-crystalline state, affecting its viscoelastic behaviour; this leads to a lower and more stable resistance when no strain is applied and improved hysteresis [1].

Results

Compared to previous CNT-based printed sensors, the TPU-based prototype demonstrated a significantly expanded measuring range and noticeably improved hysteresis. It can accurately detect displacements up to 5 mm, which is more than a ninefold increase compared to the previous 0.6 mm limit. The average recorded hysteresis as a percentage of the maximum resistance variation (ΔR_{max}) for each step of the compression-decompression cycle is reduced by approximately two thirds. Figure 1 illustrates the corresponding resistance variation (ΔR) as a percentage of the initial resistance (R_0) for each deformation step−applied for a duration of one minute−and the corresponding calculated hysteresis. The resistance variation value represents the mean value of ten consecutive measurements. The deduced mean hysteresis value (excluding the zero and maximum deformation points) is calculated at 15.9%, which is significantly lower than the 46% observed for the PLA-based piezoresistive element. Stability under cyclic loading was also investigated, as illustrated in Figure 2, with baseline drift mainly observed during the initial strain cycles. Additionally, the significant effect of thermal treatment in reducing the initial resistance of the device is highlighted, as reported in the case of CNT-enriched PLA [1], inkjet printing and screen-printing technologies [4,5].

The results indicate that elastic conductive polymer composite filaments, such as TPU, can be used effectively in single-step, 3D-printed strain sensors where resilience and consistent behavior are essential. Consequently, the previously developed process for fabricating cost-effective strain sensors using additive manufacturing technology has been significantly improved, making remote on-site fabrication with readily available equipment more feasible. This advancement aims to reduce the need for extensive inventories and long supply chains, which is crucial for practical marine applications. Ongoing work focuses on optimizing the geometry of the strain sensor and embedding it within Glass Fiber Reinforced Polymer (GFRP) composites for structural health monitoring and maintenance purposes.

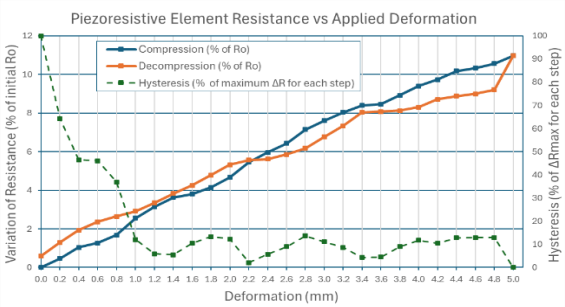


Fig. 1. Calculated hysteresis and resistance variation (ΔR) as a percentage of the initial resistance (R_0) recorded for each step of deformation.

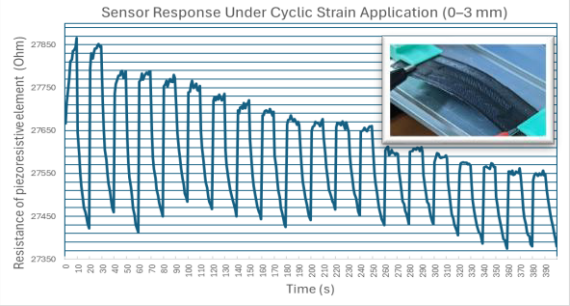


Fig. 2. Sensor response under twenty consecutive cyclic strain applications (3 mm of displacement).

References

[1] T. Kouvatsos, D. N. Pagonis, I. Iakovidis, G. Kaltsas, *Towards a 3D Printed Strain Sensor Employing Additive Manufacturing Technology for the Marine Industry*, Appl. Sc. 14, 6490 (2024); doi: 10.3390/app14156490

[2] M. Amjadi, A. Pichitpajongkit, S. Lee, S. Ryu, I. Park, *Highly Stretchable and Sensitive Strain Sensor Based on Silver Nanowire–Elastomer Nanocomposite,* ACS Nano 8, 5154 (2014); doi:10.1021/nn501204t

[3] Hu N. Alamusi, H. Fukunaga, S. Atobe, Y. Liu, J. Li, *Piezoresistive Strain Sensors Made from Carbon Nanotubes Based Polymer Nanocomposites*, Sensors 11, 10691–10723 (2011); doi:10.3390/s111110691

[4] A. Kamyshny, S. Magdassi, *Conductive Nanomaterials for Printed Electronics*, Small 10, 3515–3535 (2014); doi:10.1002/smll.201303000

[5] S. Magdassi, The chemistry of inkjet inks. *In The Chemistry of Inkjet Inks*, World Scientific Pub Co., Pte Ltd.: Singapore, (2009); doi: 10.1142/6869

Acknowledgment: This work has been partially funded by University of West Attica (Research Project: 80713)

DOI 10.5162/EUROSENSORS2025/MP2

Bayesian Inference for Reliable Gas Sensing with Metal-Oxide Sensors

Sebastian Pültz[1]
[1] *Lab for Measurement Technology, Saarland University, 66123 Saarbrucken, Germany, s.pueltz@uni-saarland.de*

Summary:
In this study, a probabilistic regression approach for the quantification and separation of epistemic and aleatoric uncertainties in gas measurement with temperature-modulated MOS sensors is presented. The uncertainty of feature extraction is analyzed using Monte Carlo simulations. The subsequent regression modeling is based on Partial Least Squares Regression (PLSR) combined with Hamiltonian Monte Carlo (HMC) to capture uncertainties in the parameter estimator. The evaluation shows that most of the uncertainty is due to feature extraction, while epistemic uncertainties remain comparatively small.

Keywords: MOS sensors, TCO, Markov Chain Monte Carlo, Uncertainty

Introduction

MOS gas sensors (metal-oxide semiconductors) provide a viable basis for cost-effective and miniaturizable gas sensors. In order to improve their selectivity despite limited chemical specificity, temperature-cyclic operation has established itself as an effective method [1]. By systematically varying the surface temperature of the sensors, characteristic dynamic response patterns are generated, which are used to quantify gas concentrations by frequently extracting features [2].

This is prone to aleatoric uncertainties due to sensor noise and feature computations. At the same time, epistemic uncertainties are introduced due to limited model knowledge and training data. Classical methods such as PLSR ignore these aspects. This paper therefore presents a Bayesian regression approach with Hamiltonian Monte Carlo (HMC), which quantifies both types of uncertainties separately. In addition, the often neglected uncertainty of the extracted features relevant in temperature-cyclic operation is addressed.

This approach enables a probabilistic assessment of the prediction quality and provides uncertainty measures that go beyond standard errors, providing a crucial step towards more robust and reliable gas sensor systems.

Demonstration data set

The Dataset used for demonstration can be found in [3]. It was collected using two SGP30 gas sensors, each coated with four different MOS sensor layers. The aim is to quantify the concentrations of various gases in complex mixtures. The sensors were operated under temperature-cyclic operating conditions, with each cycle comprising several defined heating and cooling phases. The resulting time-varying response patterns enable the extraction of relevant features for regression analysis.

The complete data set contains several phases. In this work, only data collected with layer 2 of sensor 0 during the initial calibration, i.e. the first series of measurements under controlled laboratory conditions was used. This reduces complexity to validate the proposed Bayesian approach for separating epistemic and aleatoric uncertainty and ensures that external influencing factors such as ageing, or environmental changes are excluded.

Methodes

First, relevant features were extracted by segmenting the temperature-cyclic sensor signals. The mean value and the slope within certain time periods (0.5 s) are extracted as features from each cycle. This extraction reduces data dimensionality while preserving the relevant information about the gas concentrations.

A feature selection is then carried out based on the Pearson correlation to the target value. Then, a partial least squares regression (PLSR), particularly suitable for highly correlated and high-dimensional input data, is used for modeling.

Bayesian inference is applied to the PLSR to quantify the epistemic uncertainty. For this purpose, a Hamiltonian Monte Carlo (HMC) sampler is used, sampling from the posterior distribution of the model parameters and the measurement variance (σ^2), representing the aleatoric uncertainty.

A Monte Carlo simulation was performed to estimate the aleatoric uncertainty due to feature extraction. The initially extracted features were perturbed with random, normally distributed noise corresponding to the empirically estimated standard deviation per feature. For each perturbed feature matrix, a prediction was then calculated using the means of the regression coefficients from the HMC sampling distribution. The standard deviation of these predictions per data point quantifies the uncertainty resulting solely from the variances in feature extraction.

Results

Fig 1 shows the prediction of the hydrogen concentration based on MOS gas sensor data, considering the determined uncertainty components. The mean prediction (black line) closely follows the true curve, with the colored areas visualizing the uncertainty. The dark blue area represents epistemic uncertainty, caused by limited training data and model uncertainty. The light blue area shows the total uncertainty including epistemic and aleatoric components. The latter result from random influences, especially in feature extraction and the residuals. The red dots represent individual prediction samples derived from MCMC sampling. The diagram illustrates the model's ability to quantify and separate uncertainty in a structured manner.

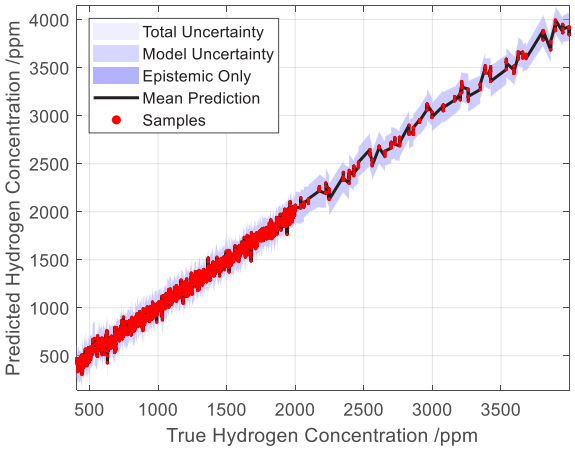


Fig. 1. Prediction of the hydrogen concentration with uncertainty quantification. Shown are the mean prediction (black), epistemic uncertainty (shaded blue), model-induced uncertainty (light blue) and the total bounds (gray). The red dots mark observed calibration values. The uncertainties result from Hamiltonian Monte Carlo (epistemic), feature Monte Carlo (aleatory, sensor-related) and residual model uncertainty.

Fig 2 provides the relative contributions of the different uncertainty components to the overall uncertainty of the predicted hydrogen concentration. The epistemic uncertainty (blue), the aleatoric uncertainty from the feature extraction (red) and the aleatoric uncertainty from the model residuals (yellow) are shown separately. It can be clearly seen that most of the uncertainty is caused by the feature extraction, while the epistemic uncertainty only accounts for a small part. The residual uncertainty is constantly in the lower range. This illustration demonstrates that sensor operation and feature calculation are significant factors influencing the reliability of the prediction.

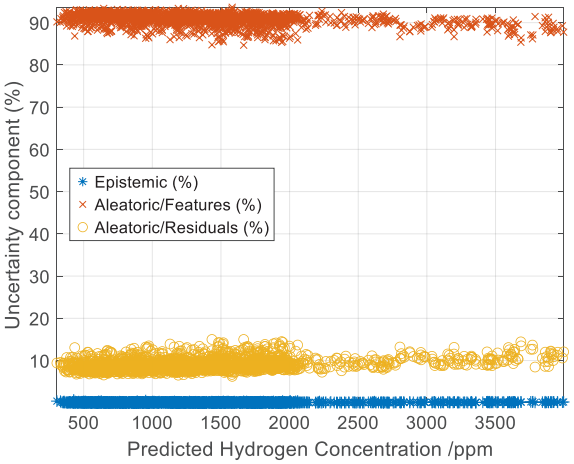


Fig. 2. Prediction of the hydrogen concentration with uncertainty quantification. Shown are the mean prediction (black), epistemic uncertainty (shaded blue), model-induced

Discussion

The presented method successfully separates epistemic and aleatoric uncertainties in gas measurement with temperature-modulated MOS sensors. The analysis shows: The main cause of the overall uncertainty is the feature extraction and to a lesser extent the inherent uncertainty of the raw data. Subsequent work will therefore also deal with more advanced feature extraction, for example within the framework of a convolutional neural network.

References

[1] C. Schultealbert, T. Baur, A. Schütze, and T. Sauerwald, 'Facile Quantification and Identification Techniques for Reducing Gases over a Wide Concentration Range Using a MOS Sensor in Temperature-Cycled Operation', *Sensors*, vol. 18, no. 3, Art. no. 3, Mar. 2018, doi: 10.3390/s18030744.

[2] T. Baur, A. Schütze, and T. Sauerwald, 'Detektion von kurzen Gaspulsen für die Spurengasanalytik: Detection of short gas pulses for trace gas analysis', *tm - Technisches Messen*, vol. 84, no. s1, pp. 88–92, Sep. 2017, doi: 10.1515/teme-2017-0035.

[3] J. Amann, T. Baur, and C. Schultealbert, 'Measuring Hydrogen in Indoor Air with a Selective Metal Oxide Semiconductor Sensor: Dataset'. Zenodo, Mar. 10, 2021. doi: 10.5281/zenodo.4593853.

DOI 10.5162/EUROSENSORS2025/MP3

Selective Formaldehyde Sensing: Unraveling Metal–Support Interaction Effects in Single-Atom Cu Catalysts

Hamin Shin[1]*, *Andreas Güntner*[1]
[1]*Human-centered Sensing Laboratory, Department of Mechanical and Process Engineering, ETH Zürich, CH-8092, Zürich, Switzerland,*
hashin@ethz.ch

Summary:
The selective detection of air pollutants remains a critical challenge. Here, we investigate the role of metal–support interaction in determining gas sensing behavior using single-atom Cu catalysts anchored on Co_3O_4 for formaldehyde vapor. Strong interfacial coupling modulates the redox properties of the support, enhancing sensitivity, selectivity, and low-temperature operation toward formaldehyde. This work provides mechanistic insights into how atomic-level catalyst–support integration governs environmental sensing performance.

Keywords: formaldehyde sensing, single-atom catalyst, Co_3O_4, metal–support interaction, gas sensor mechanism

Background, Motivation an Objective

Detecting formaldehyde at trace concentrations is critical for indoor air quality monitoring. Chemoresistive gas sensors relying on semiconductive nanoparticles[1] are promising due to their compact size, low power and high sensitivity. While Co_3O_4 is a promising oxide for chemoresistive sensors, its performance is limited by poor low-temperature reactivity and selectivity.[2] Single-atom catalysts (SACs), when electronically coupled to the support, can modulate surface redox properties and enable more efficient gas-solid interactions.[3] Here, we investigate Cu-based SACs on flame-made[4-6] Co_3O_4 and directly compare them with nanoparticle-decorated counterparts. Our objective is to reveal how metal–support interaction (SMSI) at the atomic scale governs sensitivity, humidity stability, and gas selectivity in formaldehyde sensing.

Description of the New Method or System

Atomically dispersed Cu^{2+} species were stabilized on Co_3O_4 nanoparticles through a post-synthetic incorporation route, facilitated by intrinsic surface defects introduced during the oxide fabrication process. Spectroscopic analyses confirmed the formation of well-defined metal–oxygen–support interfacial motifs, accompanied by enhanced surface redox reactivity. This engineered interface led to a notable improvement in sensing performance under low-temperature and humid conditions, outperforming systems based on aggregated Cu species or unmodified supports.

Results

H_2-TPR analysis (Fig. 1) revealed a distinct low-temperature reduction peak in the Cu SAC system, indicating enhanced lattice oxygen activation due to strong metal-support interaction. Under 50% relative humidity, the Cu SAC sensor maintained the highest absolute response to 1 ppm formaldehyde among all samples (Fig. 2), demonstrating superior low-temperature activity and robustness under realistic environmental conditions

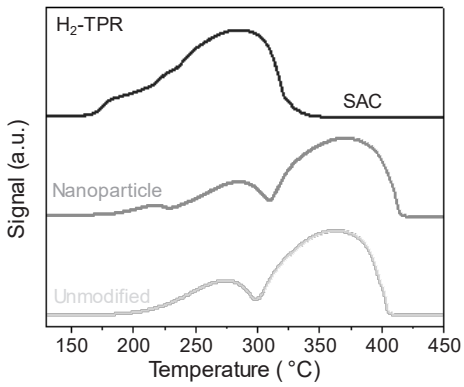


Fig. 1. H_2-TPR profiles of pure Co_3O_4, Cu_{NP}-Co_3O_4 and Cu_1-Co_3O_4 under 5 vol% H_2/Ar.

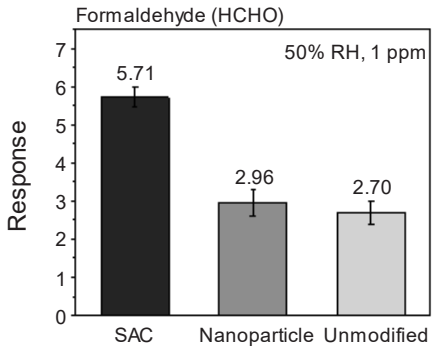


Fig. 2. Response of Cu_1-Co_3O_4 toward 1 ppm formaldehyde in comparison to reference samples at 50% RH and 75 °C.

References

[1] P. M. Bulemo, D.-H. Kim, H. Shin, et al., Selectivitiy in Chemiresistive Gas Sensors: Strategies and Challenges, *Chemical Reviews* (2025); doi: 10.1021/acs.chemrev.4c00592

[2] M. D'Andria, F. Krumeich, Z. Yao, et al., Structure-Function Relationship of Highly Reactive CuO_x Clusters on Co_3O_4 for Selective Formaldehyde Sensing at Low Temperatures, *Advanced Science* 11, 2308224 (2024); doi: 10.1002/advs.202308224

[3] G. Lei, H. Pan, H. Mei, et al., Emerging Single Atom Catalysts in Gas Sensors, *Chemical Society Reviews* 51, 7260-7280 (2022); doi: 10.1039/D2CS00257D

[4] A. T. Güntner, N. J. Pineau, S. E. Pratsinis, Flame-Made Chemoresistive Gas Sensors and Devices, *Progress in Energy and Combustion Science* 90, 100992 (2022); doi: 10.1016/j.pecs.2022.100992

[5] M. D'Andria, T. E. A.-R. Silva, E. Consogno, et al., Metastable $CoCu_2O_3$ Nanocrystals from Combustion-Aerosols for Molecular Sensing and Catalysts, *Advanced Materials* 36, 2408888 (2024); doi: 10.1002/adma.202408888

[6] A. Baut, M. P. Martins, A. T. Güntner, Template-Free Synthesis of Highly Porous Metal Nitride Architectures for Electronics and Molecular Sensing, *Small Structures,* 2500044 (2025); doi: 10.1002/sstr.202500044

Acknowledgements

A.T.G. and H.S. acknowledge financial support by the Swiss State Secretariat for Education, Research, and Innovation (SERI) under contract number MB22.00041 (ERC-STG-21 "HEALTHSENSE") and by the Swiss National Science Foundation (grant 10001714).

DOI 10.5162/EUROSENSORS2025/MP4

PEDOT: PSS gated field-effect transistor for ion sensing applications

Xuan Thang Vu[1], Yiqian Zhang[1], Sven Ingebrandt[1]
[1] Institute of Materials in Electrical Engineering 1 (IWE1), RWTH Aachen University, Sommerfeldstr. 24, 52074 Aachen, Germany,
vu@iwe1.rwth-aachen.de

Summary:
This paper introduces a new approach utilizing poly(3,4-ethylenedioxythiophene): poly(styrene sulfonate) (PEDOT: PSS) as the gate electrode of an ion-sensitive field-effect transistor (ISFET) in a configuration similar to a metal oxide semiconductor field-effect transistor (MOSFET) for ion sensing applications. The transistor exhibited the capability to operate effectively in both dry and aqueous environments. In the latter case, the aqueous solution is in direct contact with the PEDOT:PSS while the gate voltage is applied to the PEDOT:PSS gate. Experimental results demonstrated significant sensitivity to the conductivity of the solution and stable performance of the device over many cycles.

Keywords: ISFET, PEDOT:PSS, Ion sensor, Biochemical sensing

Background and Motivation

Ion-sensitive field-effect transistors (ISFETs) are well-established sensors that have been used to detect ions, pH value or biomolecules, through the gate oxide surface potential changes [1]. To be used as an ion-sensitive sensor, the gate oxide of the ISFET must be functionalized with an ion-sensitive layer that is in direct contact with the electrolyte. Furthermore, the ISFET requires a reference electrode to provide a known, stable potential to the electrolyte during the measurements, which brings challenges when compact encapsulations are needed in practical applications. PEDOT: PSS is a widely used conductive polymer in the field of bioelectronics because of its high conductivity, biocompatibility and processability [2]. The applications of PEDOT:PSS as an organic electrochemical transistor (OECT) channel material and the electrode coating material indicate its ability as an ionic-to-electronic transducer [3,4]. This work introduces an approach that allows for ion detection without a reference electrode by reconfiguring an ISFET into a MOSFET configuration, utilizing PEDOT:PSS as the gate electrode material. We present the fabrication methods and key characteristics of these transistors, specifically their stability and response to solution conductivity.

Materials and Methods

The p-type enhancement ISFET was fabricated using standard microfabrication techniques on a 4-inch wafer scale as described previously [5]. 4x4 arrays of ISFET were fabricated on an n-type silicon substrate. The conducting line was highly implanted with boron to decrease the serial resistance and passivated with 200 nm thermal-grown SiO_2. A high-quality 8 nm thermal-grown SiO_2 gate insulator was used for the ISFET operation. An Au ring microelectrode was fabricated around the gate of the ISFET while the contact line of the ring electrode was passivated with 300 nm PECVD SiO_2.

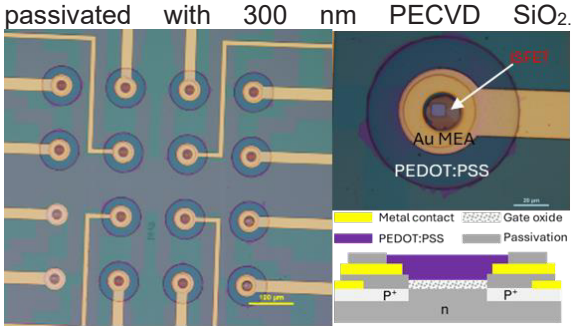


Fig. 1 Left: light microscope images of a 4x4 array of PEDOT:PSS gated FET. Right: optical image of a device in the arrays and a schematic representation of the cross-section view of the device

Aqueous PEDOT:PSS dispersion was modified by ethylene glycol (EG) to enhance the conductivity, and (3-glycidyloxypropyl) trimethoxysilane (GOPS) was used as a crosslinker to enhance the stability of PEDOT: PSS film in electrolyte. The deposition of PEDOT: PSS on the gate of the ISFET was accomplished using laser lithography, followed by spin-coating of the mixture solution and a subsequent lift-off process in acetone and isopropanol to remove the unwanted PEDOT: PSS. [4]. Figure 1 shows the top view of a 4x4 array ISFET-MEA coated with PEDOT: PSS along with its cross-sectional view. Electrical

measurements were performed using a Keithley 4200-SCS semiconductor analyzer. The transfer characteristics of the transistors were investigated in air and under NaCl solutions with varying concentrations.

Results

Figure 2 illustrates the transfer characteristics of the transistor measured in air and with a liquid (DI water) in contact with PEDOT: PSS. Under dry conditions, the transistor operates similarly to a MOSFET device. However, when DI water was introduced to the chip surface, there was a significant change in the threshold voltage as well as in the transconductance of the transistor.

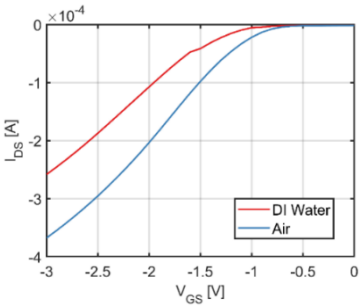


Fig. 2 Transfer characteristics of the transistor in air and aqueous environments, with V_{DS} = -1V.

Figure 3a shows the transfer characteristics of the devices measured in NaCl solutions with concentrations of 1 mM, 10 mM, and 100 mM, corresponding to the conductivities of these solutions at 96.2 µS/cm, 918.7 µS/cm, and 8937.9 µS/cm, respectively. A clear shift in the threshold voltage was observed. As the concentration of NaCl increases, the absolute value of the threshold voltage decreases. The shift in threshold voltage was extracted from the transfer characteristic curves, as shown in Figure 3b. A linear dependence was observed between the change in threshold voltage and the logarithm of the NaCl concentration, or conductivity. The shift in threshold voltage yielded a sensitivity of approximately 90.7 mV/decade.

The durability tests on the transistor in an electrolyte solution showed reliable transfer characteristics with a shift of the threshold voltage of around 2 mV after 350 measurements.

The proposed system can be used as a reliable ion-sensitive sensor compared to our previous work using OECT [4], demonstrating potential for miniaturization by excluding the reference electrode. Further experiments are being conducted to evaluate the system with different ions and enhance the selectivity of the sensor.

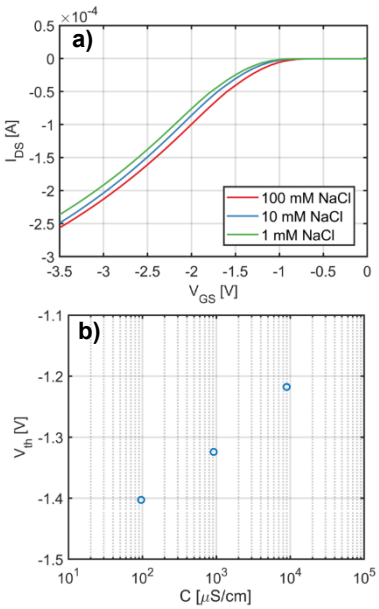


Fig. 3 (a)Transistor's responses to different NaCl solution concentrations, V_{DS} = -1V. (b)Threshold voltages shift according to the corresponding solution conductivity

References

[1] P. Bergveld, Development of an ion-sensitive solid-state device for neuro-physiological measurements, *IEEE transactions on bio-medical engineering* 17 70–71 (1970); doi: 10.1109/tbme.1970.4502688.

[2] A. Benoudjit, M.M. Bader, W.W.A. Wan Salim, Study of electropolymerized PEDOT:PSS transducers for application as electrochemical sensors in aqueous media, *Sensing and Bio-Sensing Research* 17 18–24 (2018); doi: 10.1016/j.sbsr.2018.01.001.

[3] J. Rivnay, S. Inal, A. Salleo, R.M. Owens, M. Berggren, G.G. Malliaras, Organic electrochemical transistors, *Nat Rev Mater* 3 (2018); doi: 10.1038/natrevmats.2017.86.

[4] C. Li, Z. Li, T. D. D. Nguyen, S. Ingebrandt, X. T. Vu, Real-time and multiplexed detection of sodium and potassium ions using PEDOT:PSS OECT microarrays integrated with ion-selective membranes, Electrochimica Acta,507(2024); doi:10.1016/j.electacta.2024.145111

[5] A. Susloparova, X.T. Vu, D. Koppenhöfer, J.K.-Y. Law, S. Ingebrandt, Investigation of ISFET device parameters to optimize for impedimetric sensing of cellular adhesion. Phys. Status Solidi A, 211 (2014); doi: 10.1002/pssa.201330636

Acknowledgements

We sincerely acknowledge the technical support provided by the Micro- and Nanotechnology (ZMNT) staff at RWTH Aachen University. The financial support for this project was received from RWTH Aachen University.

DOI 10.5162/EUROSENSORS2025/MP5

(MgCoNiCuZn)O High-Entropy Oxide as Novel Gas Sensing Material

Iván Vergés Gazulla[1,2], Paolo Pellegrino[1,2], Guillem Domenech Gil[1,2,3], Albert Romano Rodriguez[1,2]
[1] Department of Electronic and Biomedical Engineering, University of Barcelona (UB), 08028 Barcelona, Spain,
[2] Institute of Nanoscience and Nanotechnology (IN2UB), University of Barcelona (UB), 08028 Barcelona, Spain
[3] Department of Thematic Studies and Environmental Change, TEMA M, Linköping University, Sweden
Corresponding Author's e-mail address: pellegrino@ub.edu, guillem.domenech-gil@liu.se

Summary:
We report the performance of (MgCoNiCuZn)O material as chemoresistive gas sensor, both against reducing and oxidizing agents at different temperatures. The active material has been synthetized by mixing the different oxides in the form of nanopowers and applying a thermal treatment at 1000 ºC for several hours, quenching the resulting rock-salt compound by a rapid cooling. The structural characterization confirms the formation of a uniform elemental distribution and single-phase formation. The chemoresistive response of the material has been assessed against several gases, such as humidity, sulfur dioxide and methane. We determined the p-type semiconductor character of the material and get first insights of its temperature behavior and its sensing mechanisms.

Keywords: high entropy oxide, chemoresistor, gas sensing, humidity sensor, sulfur dioxide.

Headlines

We are exploring the gas sensing performance of (MgCoNiCuZn)O material, belonging to the so-called High Entropy Oxides category, a novel class of materials that owns a wide range of interesting properties and behaviors.

We demonstrate the semiconducting and chemoresistive nature of this material via its optical and electrical properties as well as characterizing its gas sensing behavior when working at different temperatures.

Background, Motivation and Objective

Since 2015 (MgCoNiCuZn)O has been synthesized as a rock salt belonging to the so-called High Entropy Oxides (HEO). This class of materials can present a stable single phase, despite the variety of crystalline structures of the individual binary oxides which are composing it [1]. Their complex composition gives rise to enhanced functional properties, such as outstanding thermal stability, low thermal conductivity and tunable electronic, magnetic, and catalytic properties [2].

We are interested in exploring the performance of this material as a gas sensor. Similarly to other HEOs with a different composition, the chosen multicomponent oxide is thought to behave as an improved gas sensor due to its peculiar properties. Among the features that would enhance its sensing ability, one would include the large variety of sites at the surface for absorption of gas molecules and the strong thermal endurance at high temperatures and under extreme conditions such as resilience to harsh gas species [3]. One can foresee a large flexibility in tailoring the composition of the material to adapt it to a specific sensing application.

We aim at fabricating dedicated test samples of this material to convert them into the active region of a gas sensor. A comprehensive structural analysis is mandatory in order to fully assess the actual composition and crystalline status of the fabricated compound. Finally, a set of dedicated experiments are able to provide the chemoresistive response towards reducing and oxidizing gases, enabling us to assess the quality of the material as gas sensor.

Methodology

Starting from a homogenous mixing of the single oxide components in the form of nanopowders, the resulting mixture was annealed at 1000 ºC for several hours and then rapidly cooled in order to stabilize the material to the desired structure.

X-ray diffraction confirmed the rock-salt crystalline structure, and at the same time allowed to

discard the presence of secondary phases. Additionally, the lattice parameters are in agreement with the ones reported in literature within a range of 2%.

Elemental mapping by Energy Dispersive X-Ray Spectroscopy confirms the homogeneous distribution of all the metallic components in the resulting powder, with an average grain size of few micrometers, while from optical transmission measurements we estimated a direct optical bandgap of 1.4 eV.

In order to perform the gas measurements, the fabricated powder was dispersed onto an interdigitated metallic pattern engraved on a silica slab, mounted on a TO8 support together with a micro-heater and a temperature sensor. The resulting sensor is shown in Figure 1.

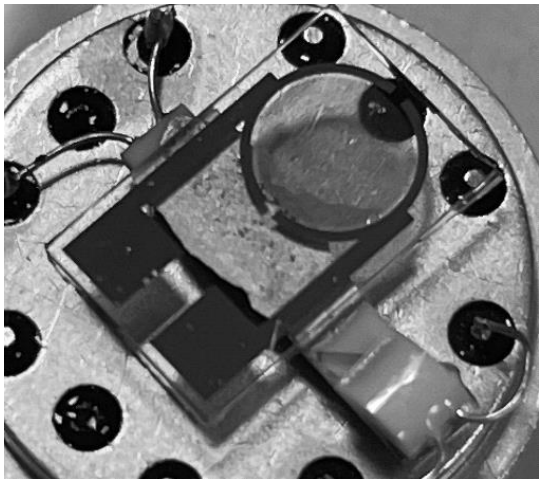


Fig. 1. Picture of one the fabricated gas sensors based on the synthetized (MgCoNiCuZn)O powder acting as active media.

Results

We will present and discuss the gas sensing behavior observed for the fabricated structures when exposed to humidity, CH_4, and SO_2, in a wide range of temperatures and gas concentrations. The temperature behavior of the device resistance and the rectifying characteristics of the electrical contacts point to the semiconducting character of the active synthetized material. A typical example of the recorded chemoresistive change under the flow of a train of gas pulses is depicted in Figure 2. The tracking of the relative response of the sensor as a function of temperature enables us to single out the optimal operation temperature. A value of 140 ºC was attained, which corresponds to a maximum response of 60% towards a humidity pulse of 80%. A complete analysis of the interaction and recovery time allows us to get insight on the detection mechanisms. The demonstration of the chemoresistive character of such novel material paves the way to further studies and applications in the field of the chemical resistive sensors.

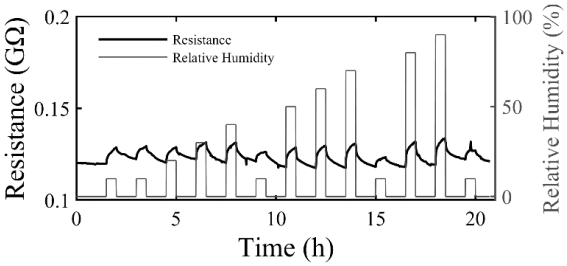


Fig. 2. Typical response trace of the fabricated sensor towards a train of relative humidity pulses.

References

[1] A. Salian and S. Mandal, *Crit. Rev. Solid State Mater. Sci.* 47, 142–193 (2022); doi: 10.1080 / 10408436.2021.1886047.

[2] R. Z. Zhang and M. J. Reece, *J. Mater. Chem. A* 7, 22148–22162 (2019); doi: 10.1039 / C9TA05698J

[3] H. Chen et al., *J. Mater. Chem. A* 6, 11129–11133 (2018); doi: 10.1039 / C8TA01772G

Acknowledgements

This work has been financially supported by the MICIU/AEI/10.13039/501100011033 and ERDF, EU under project PID2023-151565OB-C44 and by the Horizon Europe's Marie Skłodowska-Curie grant agreement No 101109501.

DOI 10.5162/EUROSENSORS2025/MP6

Dependence of the Determination of Refractive Index Sensitivity of Plasmonic Sensors on the Calibration Method

Nóra Tarpataki[1,2], Tomáš Lednický[3], Attila Bonyár[1,2]
[1] Department of Electronics Technology, Faculty of Electrical Engineering and Informatics, Budapest University of Technology and Economics, Egry József street 18, H-1111, Budapest, Hungary
[2] Wigner Research Centre for Physics, Konkoly-Thege Miklós way 29-33, H-1121, Budapest, Hungary
[3] Leibniz Institute of Photonic Technology, Albert-Einstein-Str. 9, 07745 Jena, Germany
tarpatakin@edu.bme.hu

Summary:
Among label-free biosensors, plasmonic sensors are a growing area of interest for various applications. One of the most important and widespread parameters to characterize and compare them is bulk refractive index sensitivity (*RIS*). However, most of the researchers use different methods (solutions) to determine this value. In this work, various methods were tested on a single sensor element to investigate whether the different characterizing methods and used calibration solutions affect the obtained results.

Keywords: Localized surface plasmon resonance (LSPR), refractive index sensitivity (RIS), gold nanoparticles, microfluidics.

Background, Motivation and Objective

Localized surface plasmon resonance (LSPR) is a phenomenon that occurs when the incident light (i.e. electromagnetic radiation) interacts with the electron cloud of metallic nanoparticles, causing an oscillation of the electrons [1]. This happens at a specific frequency, the resonance frequency, which appears as an absorption peak in the optical spectrum.

The frequency – and thus wavelength – of the resonance is determined by numerous different factors, such as the size, shape, and material of the nanoparticles, as well as the refractive index of the surrounding medium. This last parameter is the one that enables the usage of nanoparticles as sensor elements: an increase in the concentration of the target molecule increases the refractive index, resulting in a shift of the absorbance peak that can be detected.[2]

The most common metric used to characterize these sensors is the refractive index sensitivity (*RIS*), which can be defined by eq. (1):

$$RIS = \frac{\Delta\lambda_p}{\Delta n} \qquad (1)$$

where $\Delta\lambda_p$ is the shift of the spectral peak, and Δn is the change of the refractive index of the surrounding medium [1].

Different studies employ different methods to determine the sensitivity of their sensor. Most commonly, a dilution series of test solutions is used to measure the plasmonic response of the nanoparticles in the function of a changing refractive index. The aim of this work was to investigate whether these various approaches and calibration solutions lead to the same result.

Description of the Method

The nanostructures used for the experiments are hexagonally arranged ellipsoidal gold nanoparticles. The fabrication process included the use of a porous alumina template, deposition, and then dewetting – as described in an earlier work [3].

Three different sets of solutions – sodium chloride, glucose and glycerol – were prepared and used for the experiments.

The optical spectroscopy measurements were performed using polydimethyl siloxane (PDMS) microfluidic cells.

Results

The raw data are presented in Fig. 1. Time is shown on the x-axis, whilst the changes in the peak's wavelength can be observed on the y-axis. These changes are caused by the different media (in order: air, water, NaCl: 5, 10, 15, 20, 25 w/w%, water, glycerol: 10, 20, 30, 40, 50, 60 w/w%, water, glucose: 10, 20, 30, 40 w/w%, water) surrounding the sensor in the microfluidic cell. As can be seen, solutions with increasing concentrations – and thus increasing refractive indices – resulted in increasing peak wavelengths.

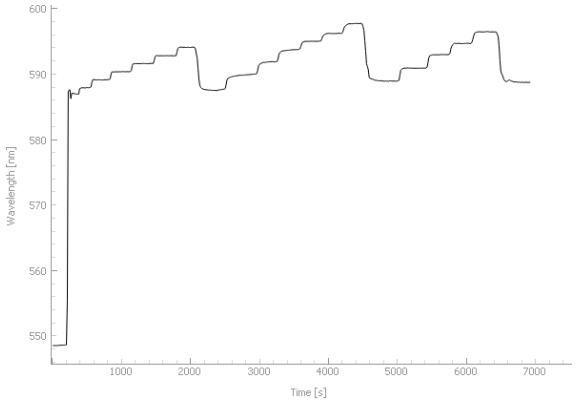


Fig. 1. Measurement results: shifts in peak wavelength vs time, caused by refractive index differences.

The results of the measurement are summarized in Table 1. After the evaluation of the obtained data, bulk refractive index sensitivities were calculated, taking into account the results of only one type of solution at a time.

Tab. 1: Refractive indices of the solutions and corresponding peak positions.

	c [w/w%]	n [-]	Peak [nm]
Sodium chloride	0	1.333	588.3
	5	1.342	589.6
	10	1.350	591.0
	15	1.359	592.4
	20	1.368	593.8
	25	1.378	595.3
Glycerol	0	1.333	587.7
	10	1.345	590.1
	20	1.357	592.4
	30	1.371	594.5
	40	1.384	596.1
	50	1.398	597.6
	60	1.413	599.5
Glucose	0	1.333	589.2
	10	1.348	591.4
	20	1.364	593.9
	30	1.381	596.0
	40	1.399	598.1

The bulk refractive index sensitivities for sodium chloride, glycerol and glucose were found to be 157.2 nm/RIU, 134.4 nm/RIU and 137.2 nm/RIU, respectively. This suggests that the RIS depends not only on the specific sensor but also on the calibration solution used to determine its value. Further investigation is needed to better understand the reasons behind this phenomenon. In our work we will present detailed data obtained on various calibration scenarios aimed at systematically testing this behaviour, and an explanation for the observed differences will be given in the form of a model, that can be generally used for the reproducable and comparable calibration of plasmonic sensors.

References

[1] K. M. Mayer and J. H. Hafner, “Localized surface plasmon resonance sensors,” Jun. 08, 2011. doi: 10.1021/cr100313v.

[2] J. L. Hammond, N. Bhalla, S. D. Rafiee, and P. Estrela, “Localized surface plasmon resonance as a biosensing platform for developing countries,” 2014, *MDPI*. doi: 10.3390/bios4020172.

[3] T. Lednický and A. Bonyár, “Large Scale Fabrication of Ordered Gold Nanoparticle-Epoxy Surface Nanocomposites and Their Application as Label-Free Plasmonic DNA Biosensors,” *ACS Appl Mater Interfaces*, vol. 12, no. 4, pp. 4804–4814, Jan. 2020, doi: 10.1021/acsami.9b20907.

Acknowledgements

The research was supported by the National Research and Innovation Office under project number 2020-1.2.3-EUREKA-2022-00030 and by the Nanoplasmonic Laser Fusion Research Laboratory project (2022-2.1.1-NL-2022-00002). Tomáš Lednický acknowledges CzechNanoLab Research Infra-structure supported by MEYS CR (LM2023051) and funding from the European Union’s Horizon Europe research and innovation programme under grant agreement No 101109232).

DOI 10.5162/EUROSENSORS2025/MP7

Metal Organic Frameworks Based Quartz Microbalance for Ammonia Detection

Sujitha Murugaiyan[1], Rosamaria Capuano[1], Gabriele Magna[2], Manuela Stefanelli[2], Alexandro Catini[1], Kishore Pushparaj[1], Valerio Allegra[1], Roberto Paolesse[2], Corrado Di Natale[1]

[1] Department of Electronic Engineering, University of Rome Tor Vergata, Via del Politecnico 1, 00133 Roma; Italy

[2] Department of Chemical Science and Technologies, University of Rome Tor Vergata, Via della Ricerca Scientifica, 00133 Roma; Italy

dinatale@uniroma2.it

Summary:

Nanoporous materials are highly required for efficient gas sensing. Here, we explore the sensing properties of a set of metal-organic frameworks as sensitive materials of quartz microbalances. The sensors have been shown to be very sensitive to ammonia with a sub-ppm estimated limit of detection compatible with the resolution necessary in industrial and clinical applications.

Keywords: Quartz Microbalance, Metal Organic Frameworks, Ammonia

Introduction

In recent years, the accurate sensing of ammonia gas has obtained great attraction due to its usage in diverse industrial sectors [1]. Furthermore, ammonia is a product of human metabolism, and anomalous concentrations in breath are associated with kidney diseases. The average concentration of ammonia in breath is found to be above 30 ppm in individuals affected by chronic kidney diseases respect to 3 ppm in healthy controls [2]. For these reasons, the development of sensitive and selective ammonia sensors is highly pursued.

In this paper, we investigate the sensitivity to ammonia of three metal organic frameworks (MOFs). MOFs are characterized by high porosity and large internal surface area. This results in a large number of adsorption sites compared to other sensing materials; owing to this property, MOFs have been the object of interest in the field of gas sensors.

However, in spite of the supposed sensitivity, their lack of conductivity may limit their practical use in sensors. Mass sensitive devices are a good opportunity to exploit the sensitivity of MOFs. To this regard, the detection of carbon dioxide and methane was demonstrated with MOF functionalized surface acoustic wave and quartz microbalance [3]. In this paper we investigated the sensitivity to ammonia of MOFs coated quartz microbalance (QMB) sensors.

Experimental

QMBs have been functionalized with three different MOFs: Cu-BTC, Ni doped ZIF-67, Fe-BDC.

The octahedral shaped Cu-BTC MOF was prepared using copper ions as the metal nodes and the 1,3,5-Benzenetricarboxylic acid (BTC) as the organic linker. The hexagonal micro spindle shaped Fe-BDC MOF was prepared using the terephthalic acid (BDC) as a linker. The Cu-BTC MOF and Fe-BDC MOF were synthesized using the hydrothermal technique. The bimetallic rhombic dodecahedral shaped nickel doped ZIF-67 was prepared using the nickel and cobalt metals salts with 2-methylimidazole as the organic linker through sonochemical synthesis. The structural and morphological characteristics of the materials were studied using XRD, FTIR, RAMAN spectra, and SEM (data not shown here). MOFs were coated by drop-casting onto the surface of 20 MHz (KVG Gmbh, Germany) QMB. Ammonia was provided in a certified bottle. The concentration was adjusted by mixing ammonia with the carrier gas (nitrogen) using a set of mass flow controllers (CMA 10B, MKS Instruments, Inc.). The gaseous mixture was delivered at 100 sccm into a Teflon-sealed sensors cell.

Results

Figure 1 shows the evolution of the frequency of the QMB sensors during the sequence of exposures to ammonia. For simplicity, frequencies

have been shifted with respect to the first recorded frequency.

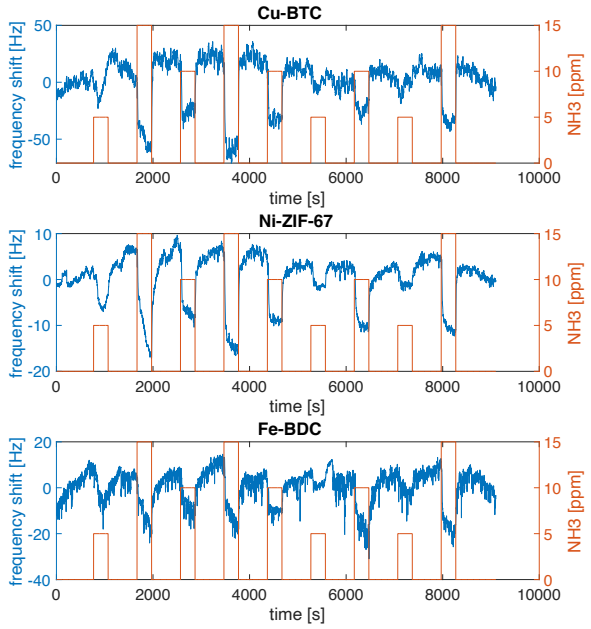


Figure 1. Time evolution of sensor response to the sequential exposure to ammonia concentrations.

Sensor responses are reversible and clearly proportional to the concentration of ammonia.

For each exposure, a synthetic feature has been calculated as the difference between the frequencies measured before and at the end of the exposure.

Figure 2 shows the response curve of the three sensors fitted with a linear function.

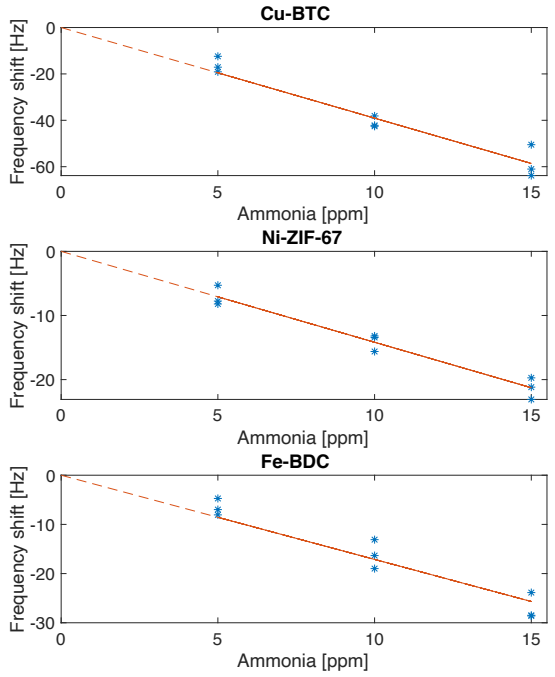


Figure 2. Response curve of sensors with the linear fit.

The sensitivity of the sensors is evaluated as the slope of the linear fit in Figure 2. The sensitivities are compared in Figure 3. Error bars correspond to the slope uncertainty as retrieved in the minimum least squares fit in Figure 2.

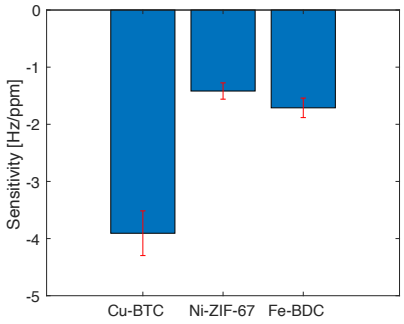


Figure 3. Sensitivity to ammonia.

The detection limit can be evaluated as the ratio between the noise of the sensor signal and the sensitivity [4].

Sensors are characterized by a different amount of noise. The reasons for this difference are under study; a probable origin of the fluctuation could be the non-uniform distribution of the MOFs onto the sensor surface and defects in the interface between the gold surface of the QMB and the layer of MOFs. Sensitivity, noise, and estimated limit of detection (LOD) are given in Table 1.

Tab. 1: Sensitivity, noise, and LOD of the three sensors

Sensor	Sensitivity [Hz/ppm]	Noise [Hz]	LOD [ppm]
Cu-BTC	-3.9	2.7	0.7
Ni-ZIF-67	-1.4	0.4	0.3
Fe-BDC	-1.7	1.3	0.7

References

[1] D. Kwak et al. Ammonia gas sensors: a comprehensive review, *Talanta* 204 (2019) 713-730

[2] A. Romani et al. Utility of SIFT-MS to Evaluate Volatile Organic Compounds in Nephropathic Patients' Breath. *Sci. Rep.12 (2022) 10413*

[3] J. Devkota et al. Zeolitic imidazolate framework-coated acoustic sensors for room temperature detection of carbon dioxide and methane, *Nanoscale* 10 (2018) 8075

[4] C. Di Natale and A. D'Amico, A contribution on some basic definition of sensors properties, *IEEE Sens. J.* 1 (2001) 183-190.

DOI 10.5162/EUROSENSORS2025/MP8

Dual-Channel Fluorescence Optical Sensor for Microplastic Detection and Polymer Classification

Yuliu Li[1], Valerio Allegra[1], Eleonora Nicolai[2], Roberto Pizzoferrato[3], Corrado Di Natale[1], Alexandro Catini[1]

[1] Department of Electronic Engineering, University of Rome Tor Vergata, Via del Politecnico 1, 00133 Rome, Italy,

[2] Departmental Faculty of Medicine, UniCamillus-Saint Camillus International University of Health Sciences, Via di Sant'Alessandro 8, Rome, Italy,

[3] Department of Industrial Engineering, University of Rome Tor Vergata, Via del Politecnico 1, 00133 Rome, Italy

catini@ing.uniroma2.it

Summary:

Microplastic pollution in aquatic systems poses ecological and health risks. However, current detection methods (e.g., FTIR, Raman spectroscopy) are time-consuming, costly, require skilled personnel and lack field applicability. We present a dual-channel fluorescence-based optical sensor for rapid detection and classification of microplastics dispersed in water. The detection is accomplished by exploiting the affinity of fluorescent solvatochromic dye DANS with plastic microparticles. A dual-channel pulse intensity spectral analysis of fluorescence emission enables the identification of at least three different microplastics: polypropylene (PP), polystyrene (PS) and polyethylene terephthalate (PET).

Keywords: optical sensor, microplastic, fluorescence, water contaminants, environmental monitoring

Introduction

Microplastic pollution is a critical environmental and health concern, with particles detected in drinking water, marine ecosystems, and even human blood. Conventional detections are laboratory methods, such as Fourier-transform infrared spectroscopy and Raman microscopy, that are accurate but costly and time-consuming. Meanwhile, field-applicable alternatives like Nile Red staining suffer from low specificity and interference from organic matter [1]. To improve the performance of dyes, we developed a fluorescence sensor that combines dye-enhanced selectivity and dual-channel detection, in order to design a low-cost and portable device. The system is based on the chemical and optical properties of DANS (4-dimethylamino- 4'-nitrostilbene), where the selective binding of microplastics is signaled by a change in the fluorescence emission spectra [2]. Simultaneous dual-channel fluorescence measurement in the spectral ranges of 450–550 nm (nonpolar dominant) and >550 nm (polar dominant) enables the identification of plastics by peak intensity spectral analysis.

Methodology

The optical sensor used in this work is an upgraded version of our previous single-channel optical device [3]. The experimental setup includes three main parts: fluorescence labeling and excitation, dual-channel optical detection, and signal processing. Three microplastics with different polarities were used: nonpolar PP (25-45 µm fragments), PS (30 µm beads) with moderate polarity and polar PET (1-49 µm fragments). The fluorescence labeling was performed with 1 mg/mL DANS dye stock solution prepared in acetone to achieve a concentration of 1 mg/L in prefiltered water with 0.22 µm Nylon filters. The experimental setup is shown in Fig. 1.

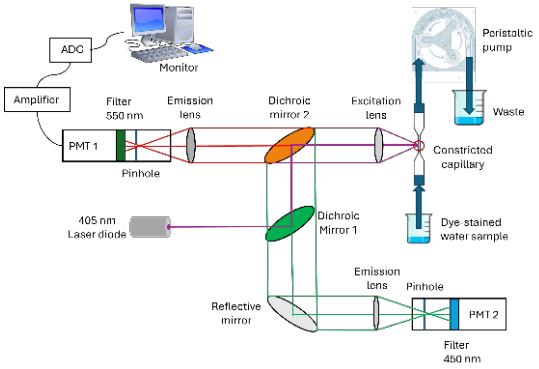


Fig. 1. Experimental setup of the Dual-channel optical sensor for microplastic detection.

A 405 nm laser diode (CW output power of 4.5 mW) is used to excite the DANS-labeled microplastics in liquid samples flowing through a glass

capillary with a constriction part of 200 µm. The dual-channel detection system captures emitted light pulses at 450–550 nm and wavelengths longer than 550 nm by using two dichroic mirrors and optical filters. A MATLAB-based script has been developed to acquire the signals and perform peak detection, pulse duration analysis, and peak area calculation. For comparison, fluorescence microscopy observation and spectroscopy measurements were also performed to characterize the fluorescence properties of the DANS-labeled microplastics.

Results

The fluorescent and solvatochromic dye DANS exhibits a strong binding to PET via sulfonamide-polar interactions and hydrophobic affinity for PP. Both the fluorescence spectra (see Fig.2) and the microscopy images (see Fig. 3) show the shift towards longer wavelengths of the more polar polymer PS and PET, while PP emits fluorescence mainly in the green/blue region.

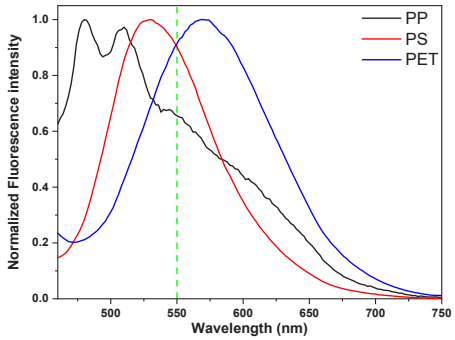


Fig. 2. Normalized fluorescence spectra of DANS-labeled plastics under 405 nm excitation. The green dashed line at 550 nm is the separation wavelength of the two channels.

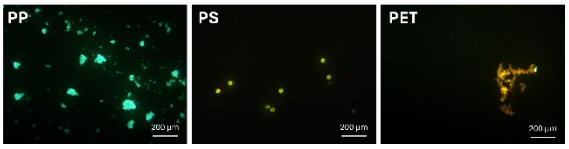


Fig. 3 Fluorescence microscopy of DANS-labeled PP, PS and PET under excitation of 405 nm laser and with 450 nm optical filter.

The system employs 405 nm excitation and two synchronized detection channels, Channel 1 (λ>550 nm) for yellow/red emission (indicative of polar polymers) and Channel 2 (λ>450 and <550 nm) for blue/green emission (dominant for non-polar polymers). By analyzing the intensity of each fluorescence pulse (area under peak) and its ratio (P_1/P_2) between channels, we achieved the identification of the polymers, while particle counting is performed via thresholding the combined fluorescence signal. As shown in Fig. 4, the angular direction calculated as the ratio of the peak area of the two channels are specific for each microplastic, enables the identification of the plastics (see Tab. 1). The peak area ratio decreases from 18.98 to 1.15 as microplastic polarity increases, with polymers fluorescing more strongly in the yellow/red region. This suggests a method to predict system behavior for other polymers.

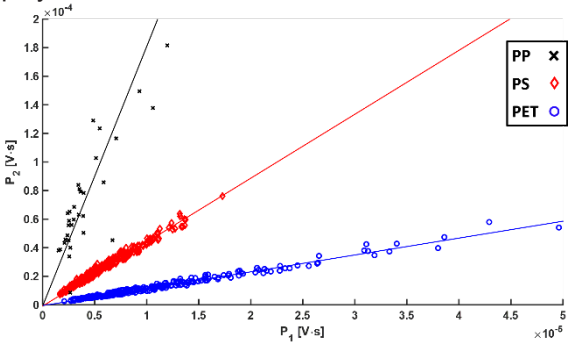


Fig. 4. Intensity of fluorescence pulses of the two spectral channels for three DANS-labeled polymers.

Tab. 1: Fluorescence peak, dielectric constant and channel intensity ratio of the three microplastics.

Microplastic	Fluorescence peak (Exc. 405 nm)	Peak area ratio (P_1/P_2)
PP	480 nm	18.98±5.41
PS	530 nm	4.51±0.31
PET	568 nm	1.15±0.11

In conclusion, the dual-channel system provides information on the interaction of DANS with microplastic, providing not only the evaluation of the particle density but also the polymer identification. This low-cost, field-portable system offers a practical solution for environmental microplastic monitoring.

References

[1] C.B.B. Alvim et al., Identification of Microfibers in Drinking Water with Nile Red. Limitations and Strengths, *J. Environ. Chem. Eng.* 11, 109697 (2023); doi:10.1016/j.jece.2023.109697.

[2] G. Sancataldo et al., Identification of Microplastics Using 4-Dimethylamino-4 ′ -Nitrostilbene Solvatochromic Fluorescence, *Microsc. Res. Tech.* *84*, 2820–2831 (2021); doi:10.1002/jemt.23841.

[3] E. Nicolai et al., Quantitative Detection of Microplastics in Water Through Real-Time Analysis of Fluorescence Signal, In Engineering Methodologies for Medicine and Sports EMMS 2024; *Springer Nature Switzerland*, 162, 216–228 (2024); doi:10.1007/978-3-031-63755-1_17.

Acknowledgements

We gratefully acknowledge the support of Cinzia Colagrossi (Resind S.r.l., Rome) throughout the early stages and development of this project.

DOI 10.5162/EUROSENSORS2025/MP9

A microfluidic system with integrated inkjet-printed capacitive sensors for biosensing applications

Bruno Andò[1], Danilo Greco[1], Salvatore Castorina[1], Cosimo Trono[2], Sara Tombelli[2], Niccolò Marcucci[2], Mostafa Fytory[2], Maria Rachele Guascito[3], Giuseppe Lamberti[3], Laura Martina[3], Nunzio Cennamo[4]
[1] University of Catania (DIEEI), Catania, Italy;
[2] Consiglio nazionale delle Ricerche (Istituto di Fisica Applicata "Nello Carrara"), Firenze, Italy;
[3]University of Salento (DiSTeBA), Lecce, Italy;
[4]University of Campania "Luigi Vanvitelli" (Department of Engineering), Aversa, Italy
danilo.greco@phd.unict.it

Summary:
This paper presents a novel microfluidic system integrating an inkjet-printed interdigitated capacitive biosensor, specifically targeting Tumor Necrosis Factor alpha. The system exploits an aptamer-based functional layer whose dielectric permittivity is affected by the target analyte. Low-cost, rapid prototyping technologies have been exploited for the device fabrication. Experimental results demonstrate good sensor performances, especially within the low detection range of TNFα. In particular, a sensor responsivity of 15.291 fF/pM in the range [0-1] pM has been estimated.

Keywords: biosensing, IDC sensor, microfluidic, InkJet Printing, optimal design.

Background, Motivation and Objective

Advanced biochemical sensing techniques are crucial in many fields, such as food, environment and healthcare [1]. The quantification of biomarkers for the diagnosis of many diseases, typically requires expensive equipment and trained personnel. Thus, there is an increasing interest in the development of low-cost Point of Care system for the rapid detection of biomarkers [2]. To this aim, rapid prototyping technologies, such as InkJet Printing (IJP), exploiting suitable functional materials, inks and substrates, represent viable solutions to the affordable development of disposable biosensors [3] and chemical sensors [4].

In this work a microfluidic biosensing system, for the detection of Tumor Necrosis Factor alpha (TNFα) is investigated. In particular, the design, the realization (by IJP technology) and the experimental behavior of the InterDigitated Capacitive (IDC) sensing element is addressed. Main novelties and advantages of the proposed approach are: i) the implemented architecture, exploiting a dedicated multi-layer stack for the realization of the IDC based readout sensing strategy; ii) the integration of the multi-layer IDC sensor within the microfluidic system, thanks to the thin film technology adopted for the realization of the sensor; iii) features offered by the sensor, especially at low target concentrations, including fast and reliable detection; iv) the low-cost of the sensing architecture, mainly supported by the adopted rapid prototyping technology; v) the use of transparent layers allowing for future potential development of electrical/optical multi-sensing approach.

Description of the New Method and System

The adopted measurement principle is based on the variations in the dielectric permittivity of a functional material, due to the trapping mechanism fixing the target analyte over the sensing surface. The fabricated IDC sensor has a multilayer dielectric structure: i) an inert, 140 µm-thick, Polyethylene terephthalate (PET) substrate supporting the IDC structure; ii) a 46 µm-thick, polypropylene insulation layer bonded over the IDC sensor; iii) a Polydopamine (PDA) film realized by chemical deposition: a 50 mM Dopamine solution in 0.5 M Phosphate Buffer Solution (PBS) was casted on the insulation layer, up to full coverage of the support. The PDA film was left to deposit for 5 h in air and then left to dry up; iv) an aptamer-based functional layer: after washing with water, the PDA-coated sensor was left in contact overnight with a solution 1 microM of the aptamer specific for Tumor Necrosis Factor alpha (TNFa); the sensor was then washed with PBS and the surface was passivated with ethanolamine (1 mM in PBS, 15 minutes).

The sensor, whose structure is schematized in Fig. 1a, is embedded in a sealed microfluidic cell to convey the target analyte. The microfluidic cell, shown in Fig. 2a, is composed of a rigid

plastic substrate and a soft Polydimethylsiloxane sealing layer.

To optimize the design of the IDC, a dedicated approach aimed at maximizing the device response against the analyte concentration has been adopted, by applying both the partial capacitance method and the conformal mapping transformation [5,6]. Given a sensing area of $7.0 \times 6.9\ mm^2$, fingers spacing has been fixed to 300 µm (constrained by the technology), fingers length to 7.0 mm (compliant with the device dimension). The adopted analytical model has been used to simulate the responsivity of the sensor to the dielectric permittivity of the functional layer, ϵ_3, as a function of the finger width, w, and functional layer thickness, h_3. Simulation results are shown in Fig. 1b, which demonstrates that the maximum responsivity is achieved for $w = 300\ \mu m$, regardless to h_3. The IDC is realized by InkJet printing a Metalon® JS-A102A silver nanoparticle ink on a Novele™ IJ-220 substrate, through a Dimatix® Printer DMP-2850. Developed electronic exploits the capacitance to digital converter AD7746, handled by a microcontroller (Arduino UNO) to perform data acquisition with a sampling frequency of 1 Hz. A peristaltic pump has been used to convey solutions to the sensing chamber.

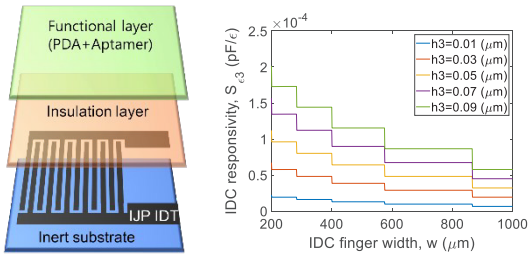


Fig. 1. a) Multilayer IDC structure; b) Simulated sensor responsivity vs track width, for different values of the functional layer thickness.

Results

To assess the behavior of the sensor, a dedicated measurement protocol has been adopted. The sensor output has been recorded during the following steps:(a) as first the microfluidic chamber has been filled with 40 mM of PBS (zero-target condition);(b) a solution of TNFα and 40 mM of PBS has been then injected in the microfluidic chamber for 10 min; (c) a flushing cycle of the functional layer with PBS, aimed at removing any exogenous compound, has been performed for 2.5 min; (d) successively, the sensor output has been acquired for at least 120 s; (e) above steps have been repeated for different analyte concentrations (1, 10, 100 and 1000 pM).

After the flushing cycle, followed by an idle 15 s time window, the average capacitance value, C_{av}, over an observation time window of 15 s has been estimated. The observation time interval has been selected as the minimum duration providing a stable averaged output.

The system response, reported in Fig. 2b, shows the mean values of the sensor output estimated through 5 consecutive observation intervals and their distribution (standard deviation), as a function of different target concentrations. The sensor responsivity estimated at [0, 1, 10, 100] pM are [15.291, 0.345, 0.038, 0.005] fF/pM, which offers suitable values, especially in the low detection range.

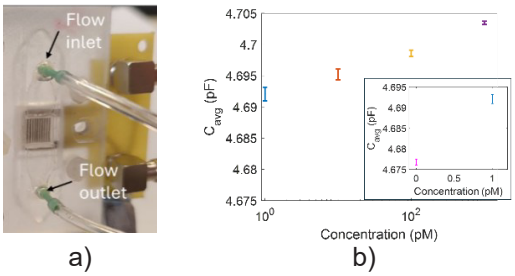


Fig. 2. a) Real view of the microfluidic chamber b) Transduction diagram (the point at 0 pM is not shown due to the adopted scale). The inset shows the sensor behavior in the range [0, 1] pM.

References

[1] S. Givanoudi, et al. A Review on Bio- and Chemosensors for the Detection of Biogenic Amines in Food Safety Applications: The Status in 2022" Sensors 23, no. 2: 613 (2023). doi: 10.3390/s23020613

[2] F. Piorino, et al. Low-cost, point-of-care biomarker quantification. Curr Opin Biotechnol. 76:102738 (2022). doi: 10.1016/j.copbio.2022.102738.

[3] M. Hartwig, et al. Inkjet-Printed Wireless Chemiresistive Sensors—A Review. Chemosensors, 6, 66. (2018), doi: 10.3390/chemosensors6040066

[4] B. Andò et al., A Capacitive Sensor, Exploiting a YSZ Functional Layer, for Ammonia Detection, in IEEE TIM, 71, 1-11, 2022 doi: 10.1109/TIM.2022.3167766.

[5] R. Igreja et al, Analytical evaluation of the interdigital electrodes capacitance for a multi-layered structure, Sensors and Actuators A: Physical, Vol. 112, No. 2–3, 2004, pp. 291-301, doi: 10.1016/j.sna.2004.01.040.

[6] B. Ando, S et al. A Capacitive Readout Strategy for Ammonia Detection: Design Flow, Modeling and Simulation. 1-6. Proceedings of SAS 2021, 2021, doi: 10.1109/SAS51076.2021.9530059

Acknowledgements

We acknowledge the support of the European Union by the Next Generation EU project PRIN2022 – 2022JRKETK_PE7 - Versatile hybrid in-fiBer Optical-electrocHemical systEMs for wIdely Applicable bioseNsing – BOHEMIAN.

DOI 10.5162/EUROSENSORS2025/MP10

Application of ZnO–Imine Nanocomposites for Optical Detection of Metal Ions in Water

Iryna Tepliakova[1], Matiss Drava[1], Greta Zvirgzdine[2,3], Roman Viter[1]
[1] Institute of Atomic Physics and Spectroscopy, University of Latvia, Jelgavas Str.3, Riga, Latvia
[2] Center for Physical Sciences and Technology, Savanorių Ave. 231, Vilnius, Lithuania
[3] MB „SensoGrafa", Kiparisu G. 29, Didžiosios Riešės k, Lithuania
iryna.tepliakova@lu.lv

Summary:

This work presents a study of nanocomposites based on organic imine-type ligands and ZnO tetrapods, and their application as sensors for photochemical detection of metal ions. Structural and electronic properties of the obtained nanocomposite were investigated by SEM, XRD, DLS, photoluminescence, and diffuse reflectance spectroscopy. A hydrophilic sensor platform was developed to detect metal cations in water. The selectivity of the nanocomposite was significantly improved compared to the pure ligand. Main sensor parameters, such as limit of detection and sensor response time, were calculated.

Keywords: ZnO tetrapod, imines, photochemical sensors, detection of metal ions, water pollution.

Introduction

The detection of metal ions in water is important in various fields such as agriculture, medicine, biology, and environmental protection[1]. Many accurate methods exist for deter-mining ion concentrations in aqueous media, but most are expensive, time-consuming, and require laboratory conditions. Thus, the industry seeks low-cost, portable, and sufficiently accurate optical sensors for metal ions that can operate in real-world conditions.

Schiff bases, imines, salens, and related organic ligands show promise due to their room-temperature photoluminescence and chelation abilities. These ligands are easily modifiable for industrial applications but have limitations: they typically work only in solution, undergo photobleaching, and some are not selective[2].

To overcome these challenges, attaching the chelating ligand to a nanostructured template is proposed. This work presents nanocomposites based on ZnO tetrapods and a symmetric imine ligand.

Experimental

In this research, we used commercially produced ZnO tetrapods (**ZnO**) and the imine ligand (**L1**), whose chemical structure is shown in Fig. 1. First, 5 mg of **L1** were dissolved in 15 mL of ethanol (99.8%), followed by the addition of 50 mg of **ZnO**. The mixture was stirred at room temperature for 72 hours. The resulting solids were filtered, washed with ethanol, and freeze-dried.

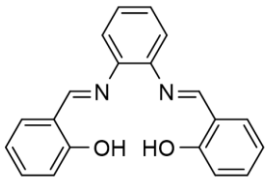


*Fig. 1. Chemical structure of **L1***

The structural properties of the ZnO-L1 nanostructures were investigated using XRD, SEM, FTIR, diffuse reflectance (300–800 nm), and photoluminescence (350–800 nm). Contact angle measurements were conducted to assess the chip's suitability for aqueous environments.

For sensor testing, samples were transferred to glass substrates. To enhance wettability and prevent sample washout, a protective hydrophilic layer was applied using a nafion dispersion solution (an ionomer and perfluorinated copolymer). The samples were coated with Nafion and dried overnight at 70°C to stabilize the polymer.

Results

The formation of the **ZnO-L1** composite was confirmed by XRD and FTIR analysis. XRD indicates that the ligand is amorphous on the ZnO surface, with no crystal planes from **L1**. FTIR confirmed the presence of **L1**-specific chemical bonds between 1750 and 700 cm^{-1}(**Fig. 3**).

The contact angle of the composite was 150°, indicating near-superhydrophobicity. The contact angle of the Nafion-coated **ZnO-L1** samples (**ZnO-L1-Naf**) was 70°, indicating hydrophilicity.

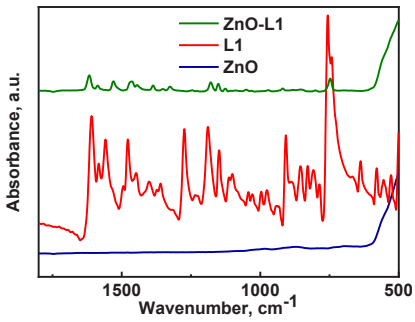


*Fig. 3. FTIR spectra of **ZnO-L1** composite, **L1, ZnO***

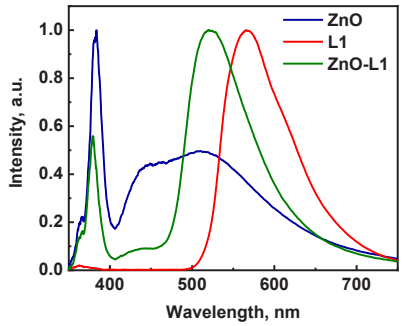


*Fig.4. PL spectra of **ZnO, L1, ZnO-L1***

The PL spectrum of the composite shows a strong emission peak at 520 nm, corresponding to L1, with a 40 nm blue shift (**Fig. 4**).

Sensitivity and selectivity were evaluated using steady-state and time-resolved PL measurements. As an example, the changing of **ZnO-L1-Naf** PL after interaction with Cd^{2+} ions are shown in **Fig.5**

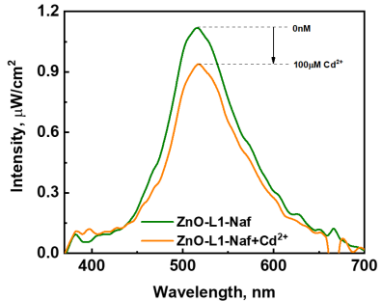


*Figure 5. PL spectra of **ZnO-L1-Naf** before and and after interaction with Cd^{2+} ions*

A rapid selectivity test was performed with 100 μM metal ion water solutions.

Sensor signal was evaluated using equation (1):

$$S = \left|1 - \frac{I(C_n)}{I_0}\right| \times 100\% \quad (1)$$

Results for L1 and **ZnO-L1-Naf** samples are shown in **Fig. 6**. While L1 responded strongly to most ions, the **ZnO-L1-Naf** composite demonstrated improved selectivity with a comparable sensing response.

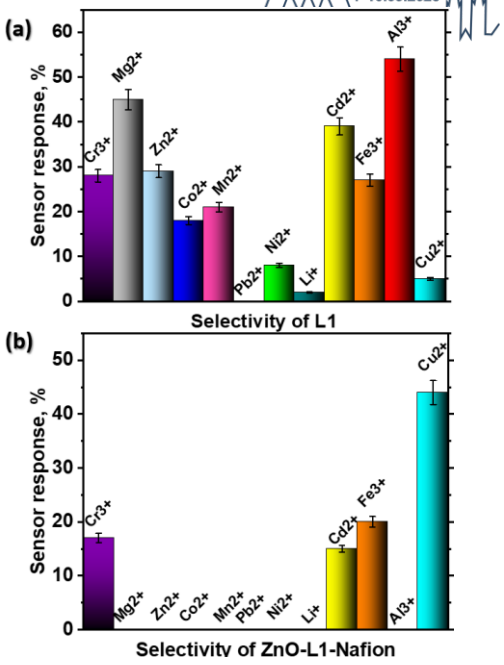


*Fig.6. Selectivity test of **L1(a), ZnO-L1-Naf (b)***

Conclusions

ZnO and **L1**-based composites have been successfully obtained. The hydrophilicity problem was addressed by incorporating Nafion ionomer. It is well established that perfluorinated copolymers possess a negative surface charge, which enhances the interaction of the chip with metal cations. The establishment of an innovative sensor platform for metal ion detection in water, based on ZnO and imine ligand composite, was achieved. Sensing layer can be further modified to improve the selectivity of sensor. Nevertheless, chips, based on metal oxides and chelating ligands composites, covered with ionomer layer are emerging as novel sensors with potential to implement optical detection of metal ions in aqueous media.

References

[1] Omar Dagdag, Taiwo W. Quadri, Rajesh Haldhar, Seong-Cheol Kim, Walid Daoudi, Elyor Berdimurodov, Ekemini D. Akpan, and Eno E. Ebenso, Heavy Metals in the Environment: Management Strategies for Global Pollution., 3-24, *ACS Symposium Series* (2023); DOI:10.1021/bk-2023-1456.ch001.

[2] Saima Q. Memon, Najma Memon, Arfana Mallah, Rubina Soomro, M. Y. Khuhawar, Schiff Bases as Chelating Reagents for Metal Ions Analysis, *Current Analytical Chemistry, 10*-3; (2014); DOI: 10.2174/15734110100314052111373l

Acknowledgements

This research was funded by HE-MCSA-RISE-2022, Sens4Corn, grant number 101086364.

DOI 10.5162/EUROSENSORS2025/MP11

Detection of Cerium(III) by Optimized Adsorption Stripping Voltammetry Using a New Electrochemical Sensor

Malgorzata Grabarczyk[1], Edyta Wlazlowska[1]
[1] Department of Analytical Chemistry, Institute of Chemical Sciences, Faculty of Chemistry, Maria Curie–Skłodowska University, Maria Curie–Skłodowska Sq. 3, 20–031 Lublin, Poland, malgorzata.grabarczyk@umcs.mail.pl

Summary:
A simple and rapid method for determining cerium was developed using an electrochemical sensor based on a mixture of multi-walled carbon nanotubes (MWCNTs), spherical glassy carbon powder (SGC), and epoxy resin. The adsorptive stripping voltammetric procedure was optimized by analyzing factors affecting the cerium signal. Experimental parameters, such as the composition and concentration of the supporting electrolyte, the concentration of the complexing agent (Alizarin S), as well as the accumulation potential and time, were carefully selected based on conducted experiments.

Keywords: cerium, adsorptive stripping voltammetry, electrochemical sensor, carbon nanomaterials

Introduction

Cerium is a rare earth element of significant industrial and environmental importance, what makes developing of effective methods for its determination crucial [1]. A modern approach to trace metal analysis is adsorptive stripping voltammetry (AdSV), which combines the process of analyte adsorption on the surface of a working electrode with its electrochemical oxidation or reduction what effectively improves the sensitivity of the determination [2]. To increase the efficiency of this method, modern electrodes are being introduced, the surface area of which has a key influence on the adsorption capacity of metal ions. In the present study, an electrode based on a mixture of multi-walled carbon nanotubes (MWCNTs) and spherical glassy carbon powder (SGC) was used to improve conductivity and increase the active surface area [3]. Alizarin S was used to complex Ce(III) ions, allowing their selective accumulation on the electrode surface [4]. The developed method, carried out in acetate buffer, showed high sensitivity and repeatability of measurements, confirming its potential for the precise determination of cerium.

Measurement Procedure

The analyzed solution was placed in a classic three-electrode quartz cell. Measurements were conducted in a 0.1 mol L^{-1} acetate buffer solution (pH = 5.3) containing 5 × 10^{-5} mol L^{-1} Alizarin S, which acted as a complexing agent. The experiments were performed in deaerated solutions at room temperature. The voltammetric procedure consisted of the following steps:

1. Adsorption of Ce(III)-Alizarin S complexes onto the MWCNTs/SGC electrode at a constant potential of -0.6 V for 65 s.
2. Voltammetric scan – the potential of the MWCNTs/SGC electrode was swept from 0.55 V to 1.2 V, recording the voltammogram and obtaining the analytical signal in the form of a oxidation peak of the accumulated Ce(III)-Alizarin S complexes.

On the recorded voltammogram, the cerium peak appeared at a potential of 0.85 V. After each measurement cycle, the electrode was electrochemically cleaned by applying a potential of -1.3 V for 10 s, followed by 0.2 V for 10 s.

Results and Discussion

Optimization of the composition of the supporting electrolyte: The effect of the composition of the supporting electrolyte on the peak current of cerium required precise selection, as the electrolyte ensures appropriate conductivity and conditions for effective oxidation of cerium ions. Acetate buffer with a concentration of 0.1 mol L^{-1} was chosen as the electrolyte, and the effect of pH on the peak corresponding to the concentration of cerium ions in the solution was investigated, as pH can influence the dissociation degree and chemical activity of cerium ions. The experiments were conducted in the pH range from 3.5 to 5.5, using a solution containing a constant concentration of Alizarin S (1 µmol L^{-1}) and Ce(III) ions. The best signal was obtained at pH 5.3, which was chosen for further measurements. The next parameter investigated

was the concentration of the acetate buffer. Its effect on the intensity of the cerium signal was examined by using a solution containing constant concentrations of Ce(III) and Alizarin S while varying the concentration of the acetate buffer at pH 5.3 in the range from 0.03 to 0.2 mol L^{-1}. The peak current of Ce(III) increased with rising buffer concentration until the current stabilized at a concentration of 0.1 mol L^{-1}. After analyzing the results, it was concluded that the optimal concentration of the acetate buffer is 0.1 mol L^{-1}.

Optimization of the concentration of the complexing agent: To determine Ce(III) ions using the adsorptive stripping voltammetry method, a complexing agent is necessary to form electrochemically active complexes that effectively accumulate on the working electrode. In the proposed procedure, the complexing agent is Alizarin S, and the accumulation process occurs on the electrode surface through the adsorption of the Ce(III)-Alizarin S complex. The effect of the complexing agent concentration on the peak current visible on the voltammogram was investigated by conducting experiments at different concentrations of Alizarin S. The studies were carried out for a solution containing a constant concentration of Ce(III) ions, and the accumulation of the complexes was performed at a potential of -0.3 V for 40 s. The tested solution had a volume of 10 mL and contained, in addition to Ce(III) ions, a constant concentration of acetate buffer (pH 5.3) equal to 0.1 mol L^{-1}, with varying concentrations of Alizarin S. Analysis of the results showed that the Ce(III) peak current increased with the concentration of Alizarin S, reaching the maximum current at a concentration of 1 µmol L^{-1}. At higher concentrations, a decrease in peak current was observed.

Effect of Accumulation Potential and Time: The value of the accumulation potential has a significant impact on the sensitivity of the method, which directly influences the recorded current values. The accumulation potential was varied in the range from -1.0 V to -0.3 V, with steps of 0.1 V. For each potential, a voltammogram was recorded, and the peak current of cerium was measured. The peak current increased as the accumulation potential value rose in the range from -1.0 V to -0.6 V. After reaching an accumulation potential higher than -0.5 V, the peak current decreased. The optimal accumulation potential was found to be -0.6 V. Another important parameter in adsorptive stripping voltammetry is the accumulation time of the Ce(III)-Alizarin S complex on the working electrode. The effect of the accumulation time was studied in the presence of 0.1 mol L^{-1} acetate buffer at pH 5.3, a 1 µmol L^{-1} concentration of Alizarin S as the complexing agent, and a constant concentration of Ce(III) ions. The accumulation potential was maintained at a constant value of -0.6 V, and the accumulation time was varied in the range from 0 to 80 s, with intervals of 5 s. The intensity of the cerium peak current increased with the accumulation time until it reached 65 s. After further extending the accumulation time, the peak current intensity started to decrease slightly.

Using a solution with an optimized composition, a low detection limit for cerium of 5×10^{-9} mol L^{-1} was achieved. Optimization of parameters such as buffer concentration, pH, accumulation time and potential significantly improved the sensitivity of the method. It was observed that, with appropriate parameter values, the method provides high precision and reproducibility of measurements. The results obtained demonstrate the great potential of the proposed method for the analysis of trace cerium concentrations in various samples.

References

[1] S.A. Abdelnour, M.E. Abd El-Hack, A.F. Khafaga, A.E., Noreldin, M. Arif, M.T. Chaudhry, et al., Impacts of rare earth elements on animal health and production: Highlights of cerium and lanthanum. *Science of The Total Environment* 672, 1021–1032 (2019); doi: 10.1016/j.scitotenv.2019.02.270

[2] Y. Wang, A.K.S. Kumar, R.G. Compton, Optimising adsorptive stripping voltammetry: strategies and limitations. *ChemElectroChem* 8, 2343–2352 (2021); doi: 10.1002/celc.202100679

[3] M. Grabarczyk, C. Wardak, R. Piech, A. Wawruch, An electrochemical sensor for the determination of trace concentrations of cadmium, based on spherical glassy carbon and nanotubes. *Materials* 16, 3252 (2023); doi: 10.3390/ma16083252

[4] M. Grabarczyk. M. Fialek, E. Wlazlowska A Convenient Strategy for the Voltammetric Direct Determination of Ce(III) in Environmental Waters Using a Multi-Walled Carbon Nanotubes Modified Screen-Printed Carbon Electrode. *Molecules* 29,1198 (2024); doi: 10.3390/molecules29061198

DOI 10.5162/EUROSENSORS2025/MP12

Copper film electrode as an electrochemical sensor for the determination of trace concentrations of lead ions in environmental waters by anodic stripping voltammetry

Malgorzata Grabarczyk[1], Agnieszka Wawruch[1]
[1]Department of Analytical Chemistry, Institute of Chemical Sciences, Faculty of Chemistry, Maria Curie-Sklodowska University, Maria Curie-Skłodowska Sq. 5, 20-031 Lublin, Poland
Corresponding Author e-mail: malgorzata.grabarczyk@mail.umcs.pl

Summary:
Metallic film electrodes are currently experiencing a major development as environmentally friendly electrochemical sensors used in stripping voltammetry. Their development began when attention was drawn to the toxicity of mercury electrodes commonly used as working electrodes in voltammetric procedures. Some of the first non-mercury metallic film electrodes to be developed since 2000, when they were introduced by Wang's team, were bismuth electrodes [1]. The next ones of great interest were lead film electrodes introduced by Korolczuk's team [2]. We wish to propose in this work the use of a film copper electrode for the determination of trace concentrations of lead ions in natural waters. The aim of this work was to optimize the conditions for generating a copper film electrode on glassy carbon as a substrate and then to optimize the conditions for concentrating the analyte, which was lead in metallic form, and then to obtain an analytical signal by anodic stripping voltammetry.

Keywords: electrochemical sensor, copper film electrode, anodic stripping voltammetry, Pb(II) determination, environmental waters

Introduction

Lead is one of the elements that is enjoying constantly growing interest. Lead is toxic and has the property of accumulating in the human body, mainly in bones. Its sources are food, air and water, into which lead gets, among other things, through industrial effluents. Therefore a constant need for simple, rapid and sensitive procedures for the determination of lead ions in environmental water emerges. One method ideally suited for this purpose is stripping voltammetry, which is why there are numerous voltammetric procedures for the determination of Pb(II) using various non-mercury working electrodes, such as bismuth–nafion film screen-printed gold electrode [3], carbon rod electrode [4], modified screen-printed electrode [5], boron-doped nanocrystalline diamond electrode [6]. We proposed using a film-generated copper electrode on glassy carbon in combination with anodic stripping voltammetry for the determination of low Pb(II) concentrations as a working electrode.

Measurement procedure

The glassy carbon electrode on which the film copper electrode was generated was cleaned at the beginning of each measurement day by polishing with alumina, and between measurements the electrode was electrochemically cleaned by applying to it a potential of -1.25 V for 5 s initially and then +0.4 V for 15 s. The copper film electrode was generated in situ by applying a potential of -0.8 V to the glassy carbon (GC) electrode for 80 s. During this time, copper ions introduced into the test solution were simultaneously reduced to form a metallic film, and lead ions present in the water sample analysed were reduced to metallic form. After this step, the potential was changed to a more positive value, producing a voltammetric signal with a well-formed lead peak at a potential of -0.5 V.

Optimisation of measurement conditions

Optimization of the proposed procedure involved the selection of a number of parameters, such as the type and concentration of the supporting electrolyte and the concentration of Cu(II) ions introduced into the analyzed sample. The results obtained are presented in Fig. 1 and Fig. 2. Based on these results, the following optimum solution composition was selected: analyzed sample + 0.5 M HCl + 5 10^{-5} M Cu(II). ASV measurement parameters, such as copper film formation potential and time and metallic lead accumulation potential and time and signal re-registration potential range, were also selected. The

results obtained confirmed that the copper film formation step can take place simultaneously with lead accumulation I finally both processes occurred at a constant accumulation potential of -0.8 V for 80 s and then the voltammetry was recorded as the potential changed from -0.8 V to -0.4 V.

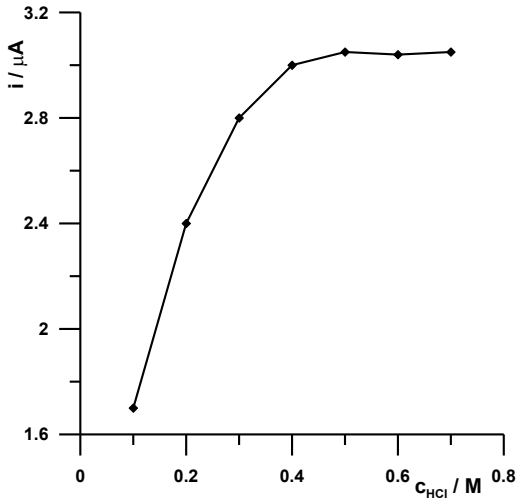


Fig. 1. Influence of supporting electrolyte HCl concentration on lead peak current. Concentration of Pb(II) 5 × 10^{-8} M.

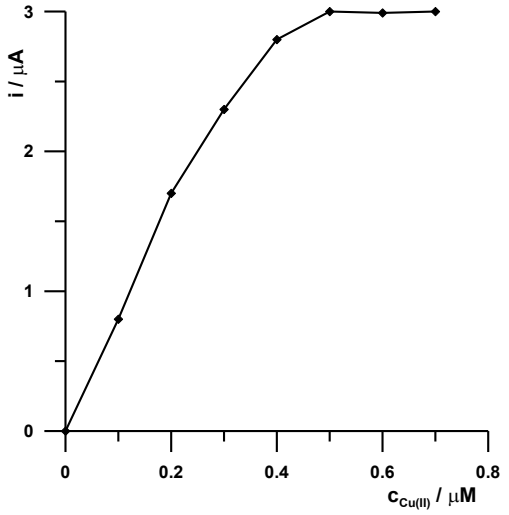


Fig. 2. Influence of Cu(II) concentration on lead peak current. Concentration of Pb(II) 5 × 10^{-8} M.

Analytical Characteristics

Using the previously optimized parameters such as supporting electrolyte concentration, copper concentration, accumulation potential and time measurements were carried out to obtain a calibration curve. The calibration plot was linear in the range from 3 × 10^{-9} mol L^{-1} to 3 × 10^{-7} mol L^{-1} with linear correlation coefficient r = 0.994. For the developed procedure, the detection limit was found to be 1 × 10^{-9} mol L^{-1} estimated from three times the standard deviation for the lowest studied Pb(III) concentration.

Conclusion

Based on the experiments discussed above, general observations and conclusions can be made:
- the copper film electrode can be a good alternative to mercury electrodes for the determination of Pb(II) by anodic stripping voltammetry;
- the formation of a copper film on the GC by the in situ method and the simultaneous accumulation of lead in metallic form allows a significant reduction in measurement time;
- the developed procedure for the determination of lead is simple and does not require expensive equipment.

References

[1] J. Wang, J. Lu, S.B. Hocevar, P.A.M. Farias, Bismuth-Coated Carbon Electrodes for Anodic Stripping Voltammetry, *Analytical Chemistry* 72, 3218-3222 (2000); doi: 10.1021/ac000108x

[2] M. Korolczuk, K. Tyszczuk, M. Grabarczyk, Adsorptive stripping voltammetry of nickel and cobalt at in situ plated lead film electrode, *Electrochemistry Communications*, 7, 1185-1189 (2005); doi: 10.1016/j.elecom.2005.08.022

[3] I. Albalawi, A. Hogan, H. Alatawi, E.A. Moore, A sensitive electrochemical analysis for cadmium and lead based on NafionBismuth film in a water sample, *Sensing and Bio-Sensing Research* 34, 100454 (2021); doi: 10.1016/j.sbsr.2021.100454

[4] K. Honeychurch, Trace Voltammetric Determination of Lead at a Recycled Battery Carbon Rod Electrode, *Sensors* 19, 770 (2019); doi: 10.3390/s19040770

[5] N. Żurga, D. Majer,M. Finsgar, Pb(II) Determination in a Single Drop Using a Modi-fied Screen-Printed Electrode, *Chemosensors* 9, 38 (2021); doi: 10.3390/chemosensors9020038

[6] T.M. Arantes, A. Sardinha, M.R. Baldan, F.H. Cristovan, N.G. Ferreira, Lead detection using micro/nanocrystalline boron-doped diamond by square-wave anodic stripping voltammetry, *Talanta* 128, 132–140 (2014); doi: 10.1016/j.talanta.2014.04.074

DOI 10.5162/EUROSENSORS2025/MP13

Impedimetric Detection of COVID Proteins on Functionalized Boron Doped Diamond Electrodes – is the Redox Marker Necessary?

Adrian Olejnik[1], *Robert Bogdanowicz*[1]
[1] *Department of Metrology and Optoelectronics; Faculty of Electronics, Telecommunications, and Informatics; Gdansk University of Technology; Narutowicza 11/12 St., Gdansk, Poland*
adrian.olejnik@pg.edu.pl

Summary:
Boron doped diamond (BDD) electrodes were functionalized with receptors specific to COVID-19 viral proteins. It was shown that the concentration of the protein can be quantitatively estimated using electrochemical impedance spectroscopy (EIS). Detection was successful using the standard methodology with external redox marker, as well as without the marker. Pros and cons of both strategies are discussed, emphasizing the differences in measurements protocols, electrode stability, and reliability of the results.

Keywords: Boron Doped Diamond, Biosensor, COVID, Electrochemical Impedance Spectroscopy,

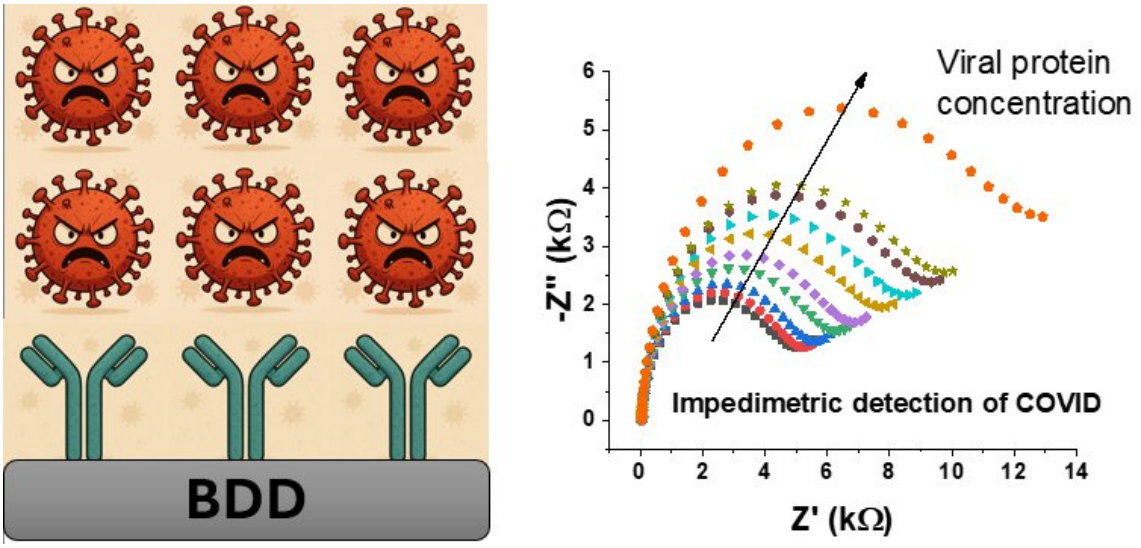


Fig. 1 Cartoon of receptor-functionalized boron doped diamond (BDD) electrode and application of electrochemical impedance spectroscopy (EIS) for quantitative detection of COVID viral proteins.

Background, Motivation an Objective

Detection of viral proteins is essential for quick and reliable diagnostics. COVID-19 and Influenza still remain the most abundant causes of viral infections. There is a variety of approached including optical, spectroscopic, colorimetric, and electrochemical. Despite a substantial effort in recent decades, reliability and cost-efficiency of viral sensors is still to be improved.

Electrochemical methods offer the possibility of cheap and fast detection of viral proteins, provided the electrodes are functionalized with specific receptors, and the measurement protocol is properly optimized (Fig. 1). Typically, to realize such experiments redox-active compounds (such as hexaferrocyanides (II/III) or hexaamineruhenium (II/III)) are added to the analyte solutions prior the measurement serving as amplifiers of the chemical signal. According to this approach, receptor-antigen binding event is reflected as an increase in the charge transfer resistance of the modified electrode, which can be converted to the protein concentration by linear function [1].

Although this method is well-established and gives decent results, it possesses intrinsic drawbacks, which might affect the quality of measurement and make detection unreliable. Besides on obvious inconvenience of adding external compound, redox marker can interact with both the receptor and target protein. Therefore, changes in the impedance might originate not only in the receptor-antigen binding event, but also those unintended interactions. Moreover, stability of the electrode can be compromised by those interaction. This work discusses pros and cons of using the external redox marker in electrochemical biosensing research on the example case of COVID-19 protein detection using boron doped diamond (BDD) functionalized with angiotensin convertase enzyme (ACE2).

Methods

Boron doped diamond electrodes are prepared using microwave-assisted chemical vapor deposition process and functionalized with ACE2 receptors against COVID proteins according to the methods elaborated in the work [2]. The successful formation of nanostructured boron doped diamond and biomolecules functionalization of receptors are confirmed accordingly.

Detection of the receptor binding domain (RBD) protein of COVID-19 is realized by electrochemical impedance spectroscopy in neutral aqueous solution with or without external hexaferrocyanide (II/III) redox couple in 1 mM concentration. For simplicity, detection signal is assumed to be the imaginary part of the impedance at 1 Hz frequency. Fitting of equivalent circuit is not necessary.

Limit of detection was calculated according to the approach advised in the work [3]:

$$LOD = \frac{3.3\,SD}{a} \quad (1)$$

Where the slope a is taken from three first points of the low concentration edge of the linear range, and the standard deviation SD is the sum of squared errors from the linear fit of these three points.

Results

The BDD-ACE2 sensor response covers several orders of magnitude of the RBD concentration from 1 pg/L to 1 mg/L. The linear range spans from 0.05 µg/L to 1 mg/L regardless whether the external redox marker is used. However, LOD value is significantly lower (Figure 2.) for the non-marker case, and the slope is greater – these two factors are beneficial for sensor performance.

Disadvantage of the non-marker approach is larger initial impedance of the electrode and higher deviation from the response linearity, which originates from 1/f noises. Moreover, stability and repeatability of the response is higher compared to the standard protocol.

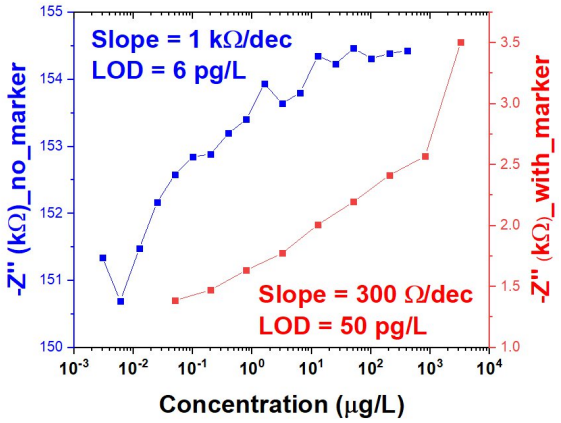


Fig. 2. Dependence of imaginary part of the impedance for RBD protein detection in the variants with or without the redox couple. Electrolyte is 1 X Tris buffered saline (pH = 7.2).

References

[1] J. Wu, H. Liu, W. Chen, B. Ma, H. Ju, Device Integration of Electrochemical Biosensors, Nature Reviews Bioengineering, 1, 346-360 (2023); doi: 10.1038/s44222-023-00032-w

[2] M. Brodowski, M. Pierpaoli, M. Janik, M. Kowalski, M. Ficek, P. Ślepski, B. Trzaskowski, G. Swain, J. Ryl, R. Bogdanowicz, Enhanced susceptibility of SARS-CoV-2 spike RBD protein assay targeted by cellular receptors ACE2 and CD147: Multivariate data analysis of multisine impedimetric response, Sensors and Actuators B: Chemical 370, 132427-132441 (2022); doi: 10.1016/j.snb.2022.132427

[3] P. Konieczka, J. Namieśnik, Quality Assurance and Quality Control in the Analytical Chemical Laboratory: a Practical Approach, CRC Press (2016);

Acknowledgements

This research was funded by National Science Center of Poland OPUS LAP UMO-2021/43/I/ST7/03205 and National Centre of Research and Development HYDROSTRATEG1/0006/2022

DOI 10.5162/EUROSENSORS2025/MP14

The Effect of Perinone Polymer Potential Polymerization Range on its Effectiveness as a Solid Contact in Ion-Selective Electrodes

Cecylia Wardak[1], Klaudia Morawska[1]
[1] University of Maria Curie-Skłodowska, Faculty of Chemistry, Institute of Chemical Sciences, Department of Analytical Chemistry, Maria Curie-Sklodowska Sq. 3, 20-031 Lublin, Poland
cecylia.wardak@mail.umcs.pl

Summary:
Perinone polymer is the latest type of conductive polymer used in solid contact ion-selective electrodes. This paper presents the application of the above-mentioned perinone polymer in two different potential ranges (-1.3 – 1.45 V and 0 – 1.45V) in potassium-selective electrodes, and the effect of the polymerization range on the basic analytical parameters was determined. The use of the conductive medium applied in both polymerization ranges significantly improved the characteristics of the electrode (higher slope), stability, and reversibility of the electrode.

Keywords: perinone polymer, solid contact, potentiodynamic polymerization, potassium ion-selective electrode

Introduction

Ion-selective electrodes (ISEs) have been developing very rapidly for many decades. Nowadays, the scientific market is dominated by those of the solid contact type (SC-ISEs). Unfortunately, along with the construction of these types of sensors, work began on their improvement – which was and is necessary. This is due to the elimination of the internal solution. For this reason, unmodified SC-ISEs are characterized by poor stability and potential reversibility due to the lack of a medium that acts as a carrier and converter of ions to charge (in the classical liquid-contact version, this role was played by the internal electrolyte). To prevent these disadvantages, an intermediate layer (solid contact) is introduced, which exhibits good ion-to-electron conductivity. Among the materials that are used for this purpose, we can mention carbon derivatives, conducting polymers, or combinations of different materials, so-called composite or hybrid materials[1]. In the present work, perinone polymer (PP) was used as a conducting medium – it belongs to the group of organic conductors. It has all the characteristics that a solid contact should have and performs very well in this role. The effect of the range of potentiodynamic polymerization on the parameters of potassium ion-selective electrodes was compared.

Methods and ISEs preparation

To apply a layer of perinone polymer, pre-prepared glassy carbon electrodes (GCE) were placed in a three-electrode system, where GCE – working electrode, platinum wire – auxiliary electrode, and silver wire – reference electrode were used. Potentiodynamic polymerization was carried out in a saturated solution of perinone polymer (dispersed in 0.1 M solution of tetrabutylammonium hexafluorophosphate in dichloromethane)[2]. Polymerization was carried out in the shorter potential range (0 – 1.45V) for 10 (GCE/10c_PP-SR) and 30 (GCE/30c_PP-SR) cycles and in the wider range (-1.3 – 1.45V) for 10 (GCE/10c_PP-WR) and 30 (GCE/30c_PP-WR) cycles. Electrodes prepared in this way were coated with potassium membrane in three series of 50 µL, every 30 minutes. The control electrode was GCE covered only with the membrane (GCE).

Results and discussion

After the electrodes were conditioned in $1x10^{-3}$ M KNO_3 solution, potentiometric tests were started. To determine whether the electrodes were working properly, calibration was performed using KNO_3 solutions of different concentrations, and calibration curves were plotted for the range of C= $1x10^{-1}$ – $1x10^{-7}$ M. The dependence is shown in Figure 1 for each of the studied electrodes. Based on the responses, the basic parameters were determined (Table 1), which turned out to be the most favorable for GCE/10c_PP-SR – slope 58.51, detection limit – $1.6x10^{-6}$ M. Polymer applied in a narrower potential range in both cases gave us better results

(mainly concerning electrode sensitivity). The presence of PP improved the linearity range for the modified ISEs.

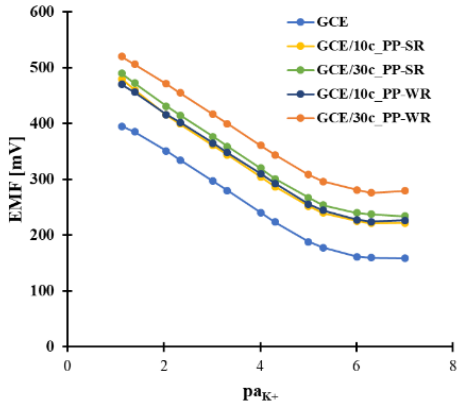


Fig. 1. Calibration curves obtained for each electrode.

Tab. 1: Basic parameters characterizing ion-selective electrodes.

ISE	Slope [mV/dec]	Detection limit [M]	Linearity range [M]
GCE	54.48	2.9×10^{-6}	5×10^{-2} – 5×10^{-6}
GCE/10c_PP-SR	58.51	1.5×10^{-6}	1×10^{-1} – 5×10^{-6}
GCE/30c_PP-SR	57.21	1.7×10^{-6}	1×10^{-1} – 5×10^{-6}
GCE/10c_PP-WR	55.32	2.4×10^{-6}	1×10^{-1} – 5×10^{-6}
GCE/30c_PP-WR	55.29	2.1×10^{-6}	1×10^{-1} – 5×10^{-6}

In addition to calibration, short-term stability was also determined (potential was measured for 2h in 1×10^{-3} M KNO_3, and then potential drift values were calculated). The drift values are 2.74, 0.16, 0.59, 0.47, and 0.67 μV/s for GCE, GCE/10c_PP-SR, GCE/30c_PP-SR, GCE/10c_PP-WR, and GCE/30c_PP-WR, respectively. Remarkably, stability improvements were observed for PP-modified electrodes applied in both modes. However, the best values were obtained for PP-modified ISE applied in 10 cycles in the narrow range. Subsequently, the potential reversibility was determined by measuring the EMF alternately at 1×10^{-4} and 1×10^{-3} M. The curves showing this relation can be found in Figure 2, and the results (standard deviations from the mean value of the potential for 5 measurements, for a certain concentration) are given in Table 2. Similarly, as in the case of potential stability, a significant improvement in this parameter was obtained for electrodes modified with perinone polymer compared to unmodified GCE. Again, the best performing electrode was GCE/10c_PP-SR.

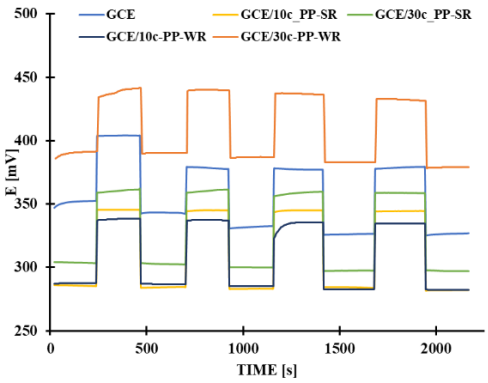


Fig. 1. Reversibility of the potential.

Tab. 2: Standard deviation from mean values for each concentration (n=4) – reversibility of the potential.

ISE	Standard deviation for 10^{-4} M K^+ (n=4)	Standard deviation for 10^{-3} M K^+ (n=4)
GCE	11.06	11.52
GCE/10c_PP-SR	1.01	0.32
GCE/30c_PP-SR	2.72	1.30
GCE/10c_PP-WR	2.90	1.80
GCE/30c_PP-WR	4.97	4.36

As we can assess, the presence of perinone polymer alone (no matter in what number of cycles and in what range of polymerization) contributed to improving the basic parameters of SC-ISEs. However, it should be emphasized that the polymerization range and the number of cycles had a major impact on the quality of the results obtained. The best response, short-term stability and potential reversibility were obtained for GCE/10c_PP-SR. Using a wider range (for 10 and 30 cycles) proved to be a poorer option.

References

[1] Y. Shao, Y. Ying, J. Ping, Recent advances in solid-contact ion-selective electrodes: functional materials, transduction mechanisms, and development trends, *Chemical Society Reviews* 49, 4405-4465 (2020); doi: 10.1039/C9CS00587K

[2] K. Morawska, M. Czichy, P. Janasik, M. Łapkowski, C. Wardak, Novel usage of perinone polymer as solid contact in ion-selective electrodes, *Sensors and Actuators B: Chemical* 422, 136662 (2025); doi: 10.1016/j.snb.2024.136662.

DOI 10.5162/EUROSENSORS2025/MP15

Improving Analytical Parameters of Ammonium Potentiometric Sensors Using Carbon Nanocomposite

Cecylia Wardak[1], Klaudia Morawska[1]
[1] University of Maria Curie-Skłodowska, Faculty of Chemistry, Institute of Chemical Sciences, Department of Analytical Chemistry, Maria Curie-Sklodowska Sq. 3, 20-031 Lublin, Poland
cecylia.wardak@mail.umcs.pl

Summary:
The main goal of this work was to optimize and, at the same time, improve the analytical performance of ammonium ion-selective electrodes with a solid contact. A carbon nanocomposite consisting of multiwalled carbon nanotubes and carbon nanofibers was used as the mediation layer. The results obtained for the modified working electrode were compared with the unmodified (control) electrode. The incorporation of transducer media (carbon nanocomposite) not only improved the response of the electrodes but also favorably affected the stability and reversibility of the potential.

Keywords: ion-selective electrodes, nanocomposite, solid contact, ammonium, carbon

Introduction

With the development of industry and global progress, not only is our civilization evolving, but in many ways this is leading to massive destruction and pollution of the ecosystem. As Paracelsus said “All things are poison, and nothing is without poison; the dosage alone makes it so a thing is not a poison”. This is why monitoring the levels of particular elements and compounds in the soil is so important, and to guard ourselves and our surroundings from exposure to excess levels of different compounds. Ammonium ions are one of the ions to which we should pay particular attention (especially in agricultural areas). Among other things, their excess causes eutrophication of waters, which leads to the destruction of aquatic environments, but is also unhealthy for humans [1]. One of the methods used to monitor NH_4^+ ion levels is potentiometry, in which we use sensors – ion-selective electrodes (ISEs). Our team is engaged in the development of new potentiometric sensors with the type of solid contact, which, due to their imperfection resulting from poor transduction and charge transfer (the result of the inefficiency of this process is poor reversibility and stability of the potential), must be modified by introducing a material that exhibits ion-to-electron conductivity[2]. In this case, our team used a carbon nanocomposite as a solid contact, which significantly improved the performance of the electrode.

Methods and Electrode Preparation

To develop a new type of sensor, ISEs with an inner electrode made of glassy carbon (GCE) were used. Before modification, the GCEs were cleaned on wetted alumina, on felt, and then cleaned in an ultrasonic bath and rinsed with distilled water. Two sets of electrodes were prepared: (1) a control electrode coated with an ion-sensitive membrane (GCE/ISM) and (2) an electrode coated with a solid contact consisting of carbon nanocomposite and an ion-sensitive membrane (GCE/CNC/ISM). The nanocomposite was created by mixing in a 1:1 ratio multiwalled carbon nanotubes (1.5 mg) and carbon nanofibers (1.5 mg), which were dispersed in 3 ml of tetrahydrofuran. The mixture of nanocomposite was then homogenized by placing it in an ultrasonic bath for 2h. The mixture prepared in this way was spotted onto the GCE surface in a volume of 15 µL. After two hours, a membrane with a total volume of 150 µL was spotted in three series (every 30 minutes). The membrane consisted of 3% nonactin, 0.86% potassium tetrakis(4-chlorophenyl) borate, 30% polyvinyl chloride, and 66.14% bis(1-butylpentyl) adipate. After 24 hours, the electrodes were placed in $1x10^{-3}$ M NH_4NO_3 to perform conditioning.

Results and Discussion

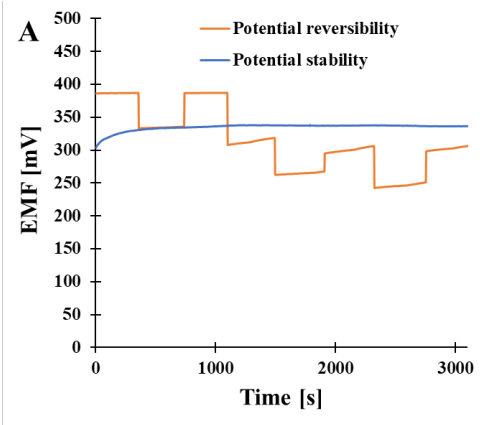
As a preliminary step, the responses of the tested electrodes were determined by measuring the potential in the concentration range of 10^{-1} – 10^{-7} M (the specified concentrations were obtained using the standard addition method). Based on the obtained values, the dependence of the electromotive force (EMF) on the negative logarithm of the activity of the main ion was determined. Based on the results, the electrodes were characterized by determining the sensitivity (slope) (S), limit of detection (LOD), and range of

linearity (LR) - the results are placed in Table 1. The use of carbon nanocomposite increased the sensitivity (almost Nernst response – 58.41 mV/decade), gently decreased the limit of detection but did not affect the range of linearity.

Tab. 1: Basic parameters determined from the characteristics of the electrodes.

Parameter	GCE/ISM	GCE/CNC/ISM
S [mv/decade]	55.84	58.41
LOD [M]	$6.3x10^{-6}$	$3.9x10^{-6}$
LR [M]	10^{-5}-10^{-1}	10^{-5}-10^{-1}

Subsequently, the stability of the potential (measurement of EMF in $1x10^{-3}$ NH_4NO_3 for 1h) and the reversibility of the potential (alternate measurement of EMF in solutions of $1x10^{-2}$, $1x10^{-3}$, $1x10^{-4}$ M NH_4NO_3 successively) were determined. Graphs showing these two parameters for both ISEs are presented in Figure 1. Based on the obtained results, the potential drift (determining stability) and the average potential values with standard deviations for each concentration (describing reversibility) were calculated – Table 2. By introducing a mediation layer in the form of a MWCNTs:CNFs composite, almost 50 times better stability was obtained relative to the nonmiodified electrode, and an improvement in reversibility was attained. This proves that the use of the above-mentioned composite as a solid contact was a good solution. This proves that the material has excellent ion-to-electron conductivity, as evidenced by the test results obtained.



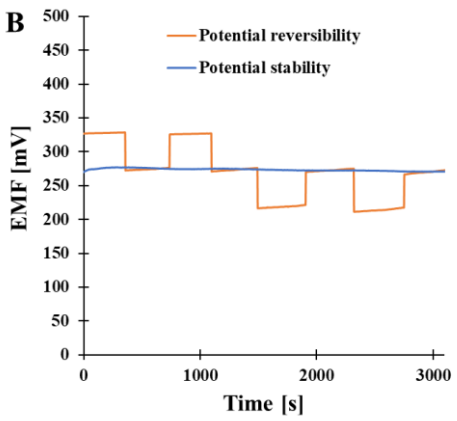


Fig. 1. Potential stability and reversibility for GCE/ISM (A) and GCE/CNC/ISM (B).

Tab. 2: Calculated results for stability and reversibility of the potential.

Parameter	GCE/ISM	GCE/CNC/ISM
Potential drift [μV/s]	2.20	0.05
Mean potential value for 10^{-2} M NH_4^+	387.29±0.70	327.67±0.11
Mean potential value for 10^{-3} M NH_4^+	327.14±8.59	276.24±0.18
Mean potential value for 10^{-4} M NH_4^+	258.99±8.34	219.89±1.61

The effect of external conditions, i.e., different illumination of the sample, the presence of oxygen and carbon dioxide in the sample, as well as sensitivity to changes in the redox potential, were also investigated. The electrode modified with the nanocomposite showed an unchanged potential under all the mentioned conditions, while for GCE/ISM, not only a drift of the potential was noted but also a variation. Modification with the carbon nanocomposite had the intended effect – it was possible to improve the parameters of ISEs.

References

[1] R. Esteban, I. Ariz, C. Cruz, J.F. Moran, Review: Mechanism of ammonium toxicity and the quest for tolerance, *Plant Science* 248, 92-101 (2016); doi: 10.1016/j.plantsci.2016.04.008.

[2] C. Wardak, K. Pietrzak, K. Morawska, M. Grabarczyk, Ion-Selective Electrodes with Solid Contact Based on Composite Materials: A Review, *Sensors* 23, 5839 (2023); doi: 10.3390/s23135839.

DOI 10.5162/EUROSENSORS2025/MP16

Highly Sensitive Biosensor Platform Based on Substrate Bias Extended-Gate Field-Effect Transistor

Fuad Ughi[1], Elżbieta Remiszewska[2], Dorota G. Pijanowska[2], Chao-Sung Lai[3*], Chia-Ming Yang[4,5,6*]*
[1] Graduate Institute of Biomedical Engineering, Chang Gung University, Taoyuan, Taiwan,
[2] Institute of Biocybernetics & Biomedical Engineering, Polish Academy of Sciences, Warsaw, Poland,
[3] Institute of Pioneer Semiconductor Innovation, National Yang Ming Chiao Tung University, Hsinchu, Taiwan,
[4] Institute of Electro-Optical Engineering, Chang Gung University, Taoyuan, Taiwan,
[5] Department of Materials Engineering, Ming Chi University of Technology, New Taipei, Taiwan,
[6] Department of Neurosurgery, Chang Gung Memorial Hospital, New Taipei, Taiwan,
dpijanowska@ibib.waw.pl, cslai@nycu.edu.tw, cmyang@mail.cgu.edu.tw

Summary:
A novel electrical protocol featuring substrate bias modification is applied to extended-gate field-effect transistors (EGFETs) to enhance the pH sensitivity beyond the Nernst limit. The sensitivity enhancement driven by the body effect characteristics of the p-channel metal-oxide-semiconductor field-effect transistor (MOSFET), which serves as the transducer. As proof-of-concept in the biosensor application, the proposed method achieved sensitivity around 320 mV/dec for DNA detection, 16 times higher than the conventional gate-bias configuration which yielded sensitivity around 20 mV/dec.

Keywords: Biosensor, EGFET, DNA, body effect, sensitivity

Introduction

Theoretically, field-effect transistor-based (FET-based) sensors obey the Nernst equation which shows that the maximum pH sensitivity that can be achieved is around 59 mV/pH at room temperature [1]. However, sensitivity enhancement of pH sensors to surpass the Nernst limit is possible on the transducer side, which is important in biosensor that requires detection of small potential changes.

A different structure of FET such as tunnel FET (TFET) is reported by Dwivedi et al. to enhance the sensitivity which utilizes the property of band-to-band tunneling phenomenon in the TFET to yield sensitivity up to 180 mV/pH [2]. Another method that has been reported by several researchers is the use of double-gates FET or even multiple-gates FET. This method was first reported by Spijkman et al. in 2010 that shows the possibility of sensitivity that could be achieved up to 2.25 V/pH [3]. In this type of method, the key to sensitivity enhancement is the ratio of the capacitive coupling between the top oxide and the bottom oxide of each gate, respectively. With the same concept, Cho et al. reported the use of triple-gates FET sensor could reach 2.36 V/pH [4]. These reported methods are effective to enhance the sensitivity of FET-based sensors from the transducer side, with the requirement of a customized transducer. However, the complex fabrication of the customized transducer and the requirement of a semiconductor development facility could hinder the replication of similar methods in a limited environment.

Substrate bias EGFET

In this study, we utilized body effect characteristics of the commercial p-channel MOSFET (PMOS) that is used as transducer in an extended-gate field-effect transistor (EGFET) configuration. The extended gate was fabricated by sputtered TiN on indium tin oxide (ITO)/glass substrate. In a long channel device, typically, the body effect of PMOS is smaller than that of the n-channel MOSFET (NMOS) counterpart. Smaller body effect means higher V_{BS} is required to get a significant deviation of threshold voltage (V_{th}). Since V_{th} determines the activation of the channel of the MOSFET, the shifting of V_{th} by the body effect can be understood as the effect of V_B on the channel activation. The small body effect means the less effectiveness of V_B to control the channel activation.

Unlike conventional EGFET that uses gate voltage (V_G) to control the channel, in this proposed method, V_B is used to control the activation of the channel. The sensing membrane is still connected to the gate terminal of the MOSFET; thus, the surface potential still follows the Nernst limit. The reference electrode is then biased with a

constant voltage that exceeds the initial V_{th} to induce an initial generation of the channel. The V_B is then used to turn off the channel utilizing the body effect, since at one point the V_G will be lower than the shifted-V_{th}. Owing to the small body effect of PMOS, high V_B is required to completely close the channel of the MOSFET, which leads to high sensitivity enhancement.

Results

Fig. 1 shows a quick pH measurement test to ensure the sensor worked properly prior to the biosensor functionalization. Both substrate bias and gate bias configurations used the same PMOS transistor. Our preliminary study showed that biosensor application is feasible with a DNA hybridization technique that yielded sensitivity around 320 mV/dec compared to the sensitivity around 20 mV/dec of the conventional EGFET, as can be seen in Fig. 2. Both pH measurement and DNA detection showed the substrate bias is much more sensitive, more than 16 times that of the conventional gate bias. Fig. 3 and Fig. 4 show the I-V curves of DNA detection using substrate bias and gate bias, respectively.

The proposed method offers an efficient sensitivity enhancement method for FET-based sensors as the enhancement can be made even with the available commercial MOSFETs.

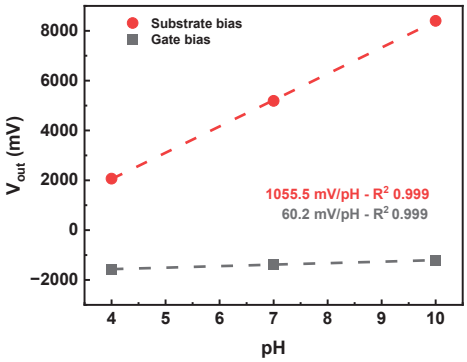


Fig. 1. pH measurements of TiN EGFET with gate bias or substrate bias configuration.

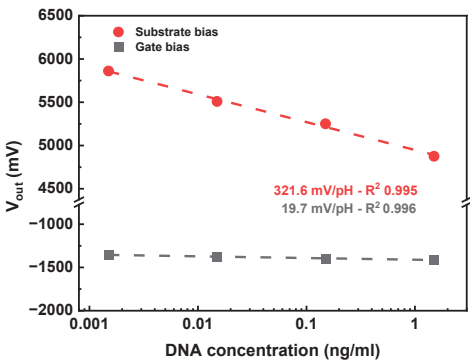


Fig. 2. DNA detection test of TiN EGFET with gate bias or substrate bias configuration.

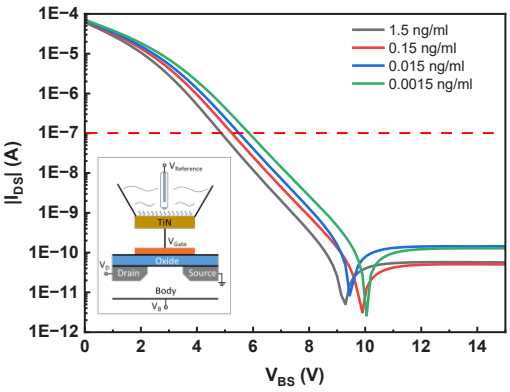


Fig. 3. I-V curve of DNA detection with substrate bias configuration of TiN EGFET.

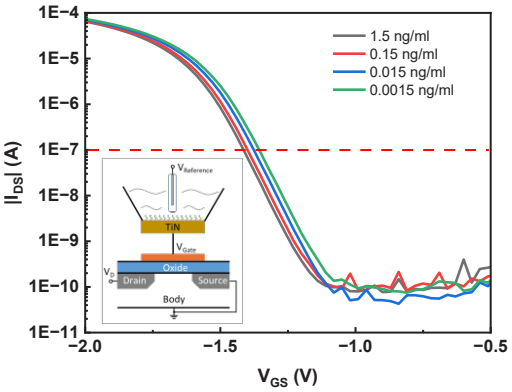


Fig. 4. I-V curve of DNA detection with gate bias configuration of TiN EGFET.

References

[1] P. Bergveld, Thirty years of ISFETOLOGY: What happened in the past 30 years and what may happen in the next 30 years, *Sensors and Actuators B: Chemical* 88, 1-20 (2003); doi: 10.1016/S0925-4005(02)00301-5

[2] Z. Rasool, S.I. Amin, L. Majeed, I. Bashir, A. Seraj, S. Anand, Simulation-based Study of Super-Nernstian pH Sensor Based on Doping-less Tunnel-field Effect Transistor, *Silicon* 15, 4285-4296 (2023); doi: 10.1007/s12633-023-02329-2

[3] M-J. Spijkman, J.J. Brondijk, T.C.T. Geuns, et al., Dual-Gate Organic Field-Effect Transistors as Potentiometric Sensors in Aqueous Solution, *Advanced Functional Materials* 20, 898-905 (2010); doi: 10.1002/adfm.200901830

[4] J.-H. Jeon, W-J. Cho, High-performance extended-gate ion-sensitive field-effect transistors with multi-gate structure for transparent, flexible, and wearable biosensors, *Science and Technology of Advanced Materials* 21, 371-378 (2020); doi: 10.1080/14686996.2020.1775477

DOI 10.5162/EUROSENSORS2025/MP17

Study Modification Parameters for Electrochemical Detection of Benzotriazole

Jelena Vujančević[1], Neža Sodnik[1,2], Melanija Hadolin[1,3], Zoran Samardžija[1], Kristina Žagar Soderžnik[1,2,3]

[1] Department for Nanostructured Materials, Jožef Stefan Institute, Jamova cesta 39, SI-1000 Ljubljana, Slovenia

[2] Jožef Stefan International Postgraduate School, Jamova cesta 39, SI-1000 Ljubljana, Slovenia

[3] Faculty of Chemistry and Chemical Technology, Večna pot 113, SI-1000 Ljubljana, Slovenia

Corresponding Author's e-mail address: jelena.vujancevic@ijs.si

Summary:

Benzotriazole (BZT), a widely used corrosion inhibitor, poses environmental and health risks. In this study, we developed an electrochemical sensor based on screen-printed electrodes modified with a Vulcan–polymer composite for detecting BZT. The influence of synthesis parameters, including sulfonation time of the polymer, concentrations of Vulcan and sulfonated poly(ether ether ketone), and suspension volume for electrode modification, was investigated. The Vulcan nanoparticles enhanced electron transfer, while the sulfonated polymer provided a stable matrix for better adsorption of BZT.

Keywords: Benzotriazole, screen-printed electrode, Vulcan XC-72-R, polyether ether ketone, electrochemical sensor.

Background, Motivation an Objective

Benzotriazole (BZT) is a polar chemical extensively utilized as a corrosion inhibitor for copper and its alloys, forming a protective layer that prevents undesirable surface reactions. It is also found in applications in household dishwashing products as a protection agent for silver [1]. Its applications span various industries, including aerospace, automotive, and oil and gas, due to that it discharges into receiving waters or is run-off from roads due to tire abrasion [2]. The widespread use of BZT has raised environmental concerns, as it is highly water-soluble and not readily biodegradable. It is classified as harmful for aquatic life and is under assessment as an endocrine disruptor, meaning that it influences hormonal status [3]. Therefore, the development of sensitive and reliable electrochemical sensors for BZT detection is essential for environmental monitoring. Screen-printed electrodes (SPEs) offer a promising, cost-effective, and portable alternative to conventional electrochemical systems. Their sensitivity can be significantly enhanced through surface modification using materials that improve the conductivity of the working electrode. In this study, we investigate the effect of synthesis parameters of Vulcan–polymer composite materials used to modify SPEs for the electrochemical detection of BZT.

Description of the New Method or System

A screen-printed electrode (SPE) comprising a carbon working electrode, a platinum counter electrode, and a silver reference electrode was used for sensor fabrication. The working electrode was modified with a composite of Vulcan XC-72-R and sulfonated poly(ether ether ketone) (SPEEK). Vulcan was first functionalized using nitric acid (HNO_3), while poly(ether ether ketone) (PEEK) was sulfonated in sulfuric acid (H_2SO_4), following the procedure reported by Kuila et al [4]. The effects of sulfonation duration and polymer concentration on sensor performance were systematically investigated. The Vulcan-SPEEK composites were prepared by mixing the components and sonicating the dispersions until fully homogenized. Modification of the working electrode was performed by drop-casting various volumes of the prepared dispersion (ranging from 2 µL to 10 µL) onto the electrode surface, followed by drying at room temperature overnight. BZT solutions were prepared in 0.1 M H_2SO_4. Electrochemical measurements were conducted using cyclic voltammetry (CV) and square wave voltammetry (SWV) with a PalmSens4 potentiostat.

Results

The synthesized Vulcan–SPEEK composite particles are shown in *Fig. 1*. Transmission electron microscopy (TEM) images reveal that the Vulcan

XC-72R nanoparticles exhibit an average size of approximately 100 nm.

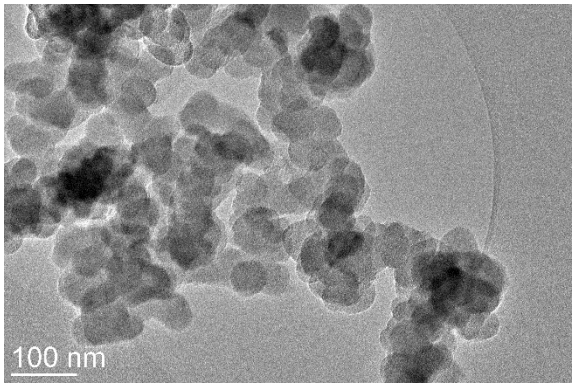


Fig. 1. TEM image of the Vulcan nanoparticles modified with polymer.

The electrochemical behavior of BZT on the modified screen-printed electrode (SPE-V-SPEEK) was evaluated using CV and SWV. A distinct reduction peak was observed at approximately -1.4 V vs quasi-Ag electrode, indicating the electrochemical activity of BZT at the modified electrode surface. The effect of synthesis parameters on the electrochemical reduction of BZT was systematically investigated, as shown in *Fig. 2*.

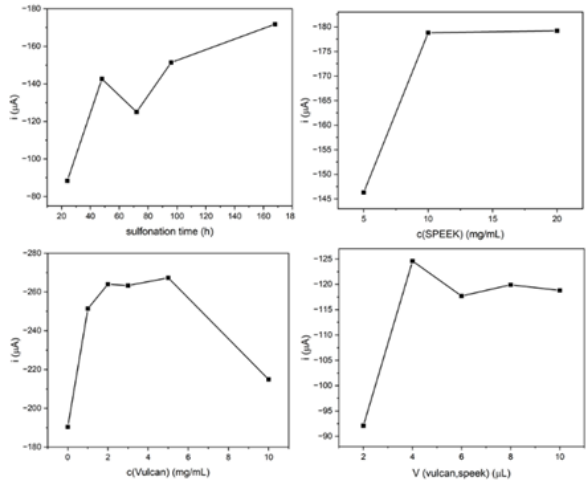


Fig. 2. Influence of the modification parameters on the maximum peak current of the reduction of BZT: sulfonation time, concentration of SPEEK, concentration of Vulcan, and volume of drop-casted dispersion on the working electrode.

The degree of sulfonation of the polymer significantly influenced the electrochemical response. With increased sulfonation time, a higher reduction peak current was observed, suggesting improved adsorption of BZT on he surface of the electrode by adding sulfonate groups. The concentration of sulfonated poly(ether ether ketone) also affected sensor performance. Peak current increased with SPEEK concentration from 5 to 10 mg/mL, after which further increases had no significant effect, indicating a saturation point. Similarly, optimization of Vulcan content showed that concentrations between 2 and 6 mg/mL provided the highest current response. Higher concentrations led to a decrease in current, likely due to nanoparticle agglomeration, which can hinder electron transfer. The volume of suspension used for electrode modification was also optimized. The best electrochemical response was obtained with a 4 µL volume, suggesting an optimal coating thickness that balances conductivity and surface coverage. Overall, the careful adjustment of Vulcan and polymer content, as well as sulfonation degree, enabled the development of a sensor with a low limit of detection (LOD) of 1.4 µM. The Vulcan particles enhance electron transfer during the redox reaction, while the sulfonated polymer provides a stable matrix for electrode modification and better adsorption of the BZT on the surface of the electrode. These features make the proposed SPE-based sensor a promising platform for reliable BZT detection in real environmental samples.

References

[1] S. Weiss, T. Reemtsma, Determination of Benzotriazole Corrosion Inhibitors from Aqueous Environmental Samples by Liquid Chromatography-Electrospray Ionization-Tandem Mass Spectrometry, *Analytical Chemistry* 77, 7415–7420, (2005); https://doi.org/10.1021/ac051203e.

[2] A. Kloepfer, M. Jekel, T. Reemtsma, Occurrence, Sources, and Fate of Benzothiazoles in Municipal Wastewater Treatment Plants, *Environmental Science and Technology* 39, 3792–3798 (2005); https://doi.org/10.1021/es048141e.

[3] Y. Sakuragi, H. Takada, H. Sato, A. Kubota, M. Terasaki, S. Takeuchi, A. Ikeda-Araki, Y. Watanabe, S. Kitamura, H. Kojima, An analytical survey of benzotriazole UV stabilizers in plastic products and their endocrine-disrupting potential via human estrogen and androgen receptors, *Science of The Total Environmen*t 800, 149374 (2021); https://doi.org/10.1016/j.scitotenv.2021.149374.

[4] T. Kuila, A.K. Mishra, P. Khanra, N.H. Kim, Md.E. Uddin, J.H. Lee, Facile Method for the Preparation of Water Dispersible Graphene using Sulfonated Poly(ether–ether–ketone) and Its Application as Energy Storage Materials, *Langmuir* 28, 9825–9833 (2012); https://doi.org/10.1021/la301469u.

Acknowledgements

The authors acknowledge that the ARIS funded our research activities through projects and programmes P2-0084 and J2-3051.

DOI 10.5162/EUROSENSORS2025/MP18

Towards Polyamine Biosensors: Stabilizing Prussian Blue Electrodes with Polymers for Sensitive H_2O_2 Detection

Neža Sodnik[1,2], Giulia Della Pelle[1,2] and Kristina Žagar Soderžnik[1,2]
[1]Department for Nanostructured Materials, Jožef Stefan Institute, Jamova cesta 39, SI-1000 Ljubljana, Slovenia,
[2]Jožef Stefan International Postgraduate School, Jamova cesta 39, SI-1000 Ljubljana, Slovenia

Corresponding Author's e-mail address: neza.sodnik@ijs.si

Summary:
Polyamines (PAs) are critical biomolecules linked to various diseases, yet their detection remains challenging due to limited electrochemical activity. Enzymatic biosensors enable indirect detection via hydrogen peroxide (H_2O_2), measured using Prussian Blue (PB) electrodes. However, PB's poor stability in neutral media limits performance. This study investigates the use of polymers (chitosan and PDDA) to enhance the stability and sensitivity of PB-modified screen-printed electrodes for H_2O_2 detection, laying the groundwork for future polyamine biosensors.

Keywords: Prussian blue, hydrogen peroxide, polyamines, screen-printed electrodes, enzymatic biosensors.

Background, Motivation and Objective

Polyamines (PAs), such as spermine and spermidine, are essential biomolecules involved in various physiological processes, including cell cycle regulation, gene expression, and membrane stability. Their concentrations in biological fluids like urine and blood are tightly regulated, and deviations from normal levels are associated with various health conditions, including neurodegenerative diseases and multiple types of cancer. Therefore, the ability to monitor PAs in biological samples is critical for the future development of diagnostic and therapeutic tools. [1]

Despite their known biological importance, real-time detection of PAs remains challenging. Conventional chromatography-based methods often lack portability and are cost- and labour-intensive. In response, electrochemical sensors have emerged as a promising alternative, offering rapid detection with minimal sample preparation and without the need for highly trained personnel. These sensors utilise bio- and nanomaterials to sensitively and selectively detect PAs in complex matrices such as urine and saliva. [1, 2]

Because PAs possess limited electrochemical activity, only oxidising at high working potentials around 1 V vs. Ag/AgCl, indirect detection using enzymatic biosensors is a more viable approach. These sensors utilise enzymes (polyamine oxidase) to catalyse PA oxidation, generating hydrogen peroxide (H_2O_2) as a by-product, which is then detected electrochemically. To enhance selectivity and minimize interferences, redox mediators like Prussian blue (PB) are used to detect H_2O_2 at lower potentials (~0 V vs. Ag/AgCl). However, the main limitation of PB lies in its reduced electrochemical stability in neutral media, which is essential for maintaining enzyme activity. [2, 3]

Different approaches have been proposed to stabilize the PB layer. Numerous studies have shown that combining PB NPs with polymers and nanomaterials generally improves the stability of the layer. [3] In this work, we investigate the binding interactions of common polymers with PB and evaluate their effect on the sensor's sensitivity toward H_2O_2. The sensors are based on screen-printed electrodes (SPEs) for enhanced portability and ease of use.

Materials and Methods

PB nanoparticles were synthesized via a polyvinylpyrrolidone-assisted crystallization method, following the procedure reported in the literature. [4]

Suspensions were prepared containing 1 mg/mL PB and 10 mg/mL of the selected polymer. For electrode modification, 4 µL of the PB/polymer suspension was drop-cast onto the carbon working electrode of an SPE (DRP-150, Dropsens, Metrohm). The modified electrodes were dried at 70 °C for 2 hours.

Chronoamperometric measurements were performed using a PalmSens potentiostat at a fixed potential of 0 V vs. Ag/AgCl in phosphate-buffered saline (PBS, pH 7.4).

Results and Discussion

The electrochemical performance of PB-modified electrodes with or without polymer (PDDA or chitosan) integration was evaluated for H_2O_2 detection. As shown in Fig. 1, all three sensors responded to stepwise additions of H_2O_2 with a proportional increase in cathodic current, confirming successful detection. The electrodes modified with chitosan (SPEC-PB/CHIT) and Poly(diallyldimethylammonium chloride) (SPEC-PB/PDDA) showed significantly higher current response than the unmodified PB electrode (SPEC-PB). However, while the PDDA-modified sensor maintained suitable stability, the addition of chitosan led to increased signal noise and reduced stability, indicating the need for further optimization of this formulation.

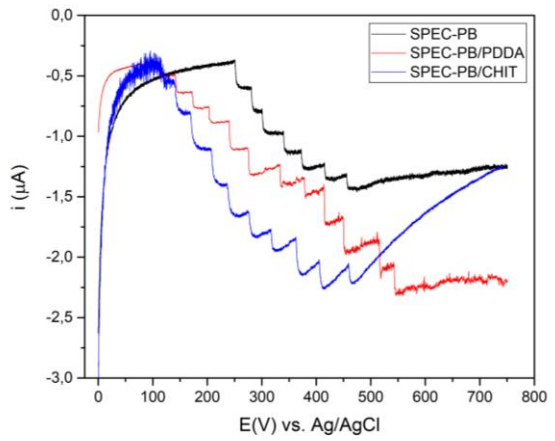


Fig. 1: Chronoamperometric response SPEC-PB electrodes to stepwise additions of hydrogen peroxide (H_2O_2) in PBS (pH 7.4) at 0 V vs. Ag/AgCl. Sensors were modified with either no polymer (black), PDDA (red), or chitosan (blue).

Fig. 2. shows the calibration curves for all three sensors, with the slope reflecting the sensitivity towards H_2O_2. The unmodified PB sensor showed the lowest sensitivity but maintained the widest linear range. In contrast, both polymer-modified sensors demonstrated significantly higher sensitivity in the low to mid-micromolar range, making them more suitable for real-life applications. Overall, these preliminary results suggest that incorporating polymers into the PB layer enhances the sensing performance. This lays the groundwork for further investigations using alternative polymers, such as polydopamine, poly(caffeic acid), and Nafion, to further optimize sensor characteristics, and serve as a support for enzyme immobilization.

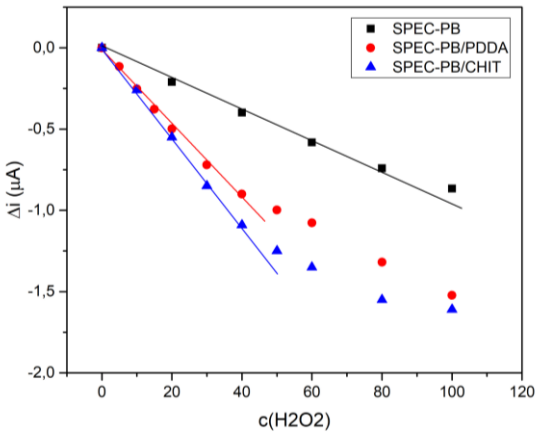


Fig. 2: Calibration curves showing the change in current (Δi) as a function of H_2O_2concentration for SPEC-PB, SPEC-PB/PDDA, and SPEC-PB/CHIT sensors.

References

[1] S. K. Kannan, B. Ambrose, S. Sudalaimani, M. Pandiaraj, K. Giribabu, M. Kathiresan, “A review on chemical and electrochemical methodologies for the sensing of biogenic amines,” *Analytical Methods,* vol 12, no. 27, 3438–3453, (2020); doi: 10.1039/d0ay00358a.

[2] W. Henao-Escobar, O. Domínguez-Renedo, M. A. Alonso-Lomillo, M. J. Arcos-Martínez, “A screen-printed disposable biosensor for selective determination of putrescine,” *Microchimica Acta*, vol. 180, no. 7–8, 687–693 (2013); doi: 10.1007/s00604-013-0989-4.

[3] A. A. Karyakin, “Advances of Prussian blue and its analogues in (bio)sensors,” *Curr Opin Electrochem*, vol. 5, no. 1, 92–98 (2017); doi: 10.1016/j.coelec.2017.07.006.

[4] H. Ming, N. L. K. Torad, Y. D. Chiang, K. C. W. Wu, Y. Yamauchi, “Size- and shape-controlled synthesis of Prussian Blue nanoparticles by a polyvinylpyrrolidone-assisted crystallization process,” *CrystEngComm*, vol. 14, no. 10, 3387–3396 (2012); doi: 10.1039/c2ce25040c.

Acknowledgements

The authors acknowledge the funding of our research activities by the ARIS through the projects PR-13411 and P2-0084.

DOI 10.5162/EUROSENSORS2025/MP19

Sensitivity Enhancement of LSPR Sensors on Flexible Glass Substrates through Bending-Induced Deformation

Chih-Ching Ho[1], Chia-Ming Yang[1,2,3,*], Nikhil Bhalla[4]
[1] Institute of Electro-Optical Engineering, Chang Gung University, Taoyuan, Taiwan
[2] Department of Electronic Engineering, Chang Gung University, Taoyuan, Taiwan
[3]Department of Materials Engineering, Ming-Chi University of Technology, New Taipei City 243, Taiwan
[4]Nanotechnology and Integrated Bioengineering Centre (NIBEC), School of Engineering, Ulster University, Shore Road, Jordanstown BT37 0QB, Northern Ireland, UK
cmyang@mail.cgu.edu.tw

Summary:
This study presents a flexible LSPR sensor based on gold nanoislands on a flexible glass substrate. Upon mechanical bending, the sensor exhibited a two-fold increase in refractive index sensitivity (from 96 to 205 nm/RIU), while maintaining stable extinction spectra. The enhancement may attributed to reduced interparticle spacing and increased near-field coupling. This bending-induced effect provides a simple yet effective strategy for sensitivity tuning in wearable plasmonic sensors.

Keywords: LSPR, Au, Biosensing, Flexible, Wearable

Introduction

Localized surface plasmon resonance (LSPR) refers to the collective oscillation of conduction electrons in metallic nanoparticles when excited by incident light, typically occurs when the particle dimensions are smaller than the wavelength of light [1]. LSPR-based sensors can detect shifts in extinction or absorbance spectra upon analyte binding, allowing for label-free and real-time biosensing with high sensitivity [2]. Unlike conventional rigid glass or silicon wafers, flexible materials can conform to curved and dynamic surfaces, making them suitable for on-skin or in vivo biosensing, which is particularly valuable for wearable technologies, where sustained contact with soft biological surfaces is required [3]. Furthermore, flexible plasmonic substrates offer mechanical tunability, which may influence sensor performance or integrate with stretchable electronics. This study investigates the use of a flexible glass-based LSPR sensor and demonstrates the performance enhancement achieved through mechanical bending of the substrate.

Materials and Methods

A flexible glass with length/width/thickness as 3 cm/2 cm/50 μm was used for the substrate, an 8 nm of gold thin film was deposited on the flexible glass via thermal evaporation and followed by rapid thermal annealing (RTA) at 450 °C for 60 seconds, resulted in the formation of randomly distributed gold nano-islands as shown in Fig. 1(a). The LSPR characterization was carried out using extinction spectra with measurement system as schematical plot shown in Fig. 1(b). Broadband illumination was provided by a halogen light source (HL-2000, Ocean Optics, U.S.), captured through a spectrometer (USB 4000, Ocean Optics, U.S.). The sensor was mounted on a motorized stage equipped with a custom-designed 3D-printed holder that enabled measurements under bending *configuration*. The substrate was deformed with a specified curvature to provide a mechanical stress condition.

For refractive index sensing, extinction spectra were performed with different refractive indices solutions, in the range of approximately 1.33 to 1.40. Multi-points measurements were conducted for bending *configuration* for determining error bars, proving the overall reliability of the results. All extinction spectra and LSPR peak positions were determined by Gaussian fitting using Origin software.

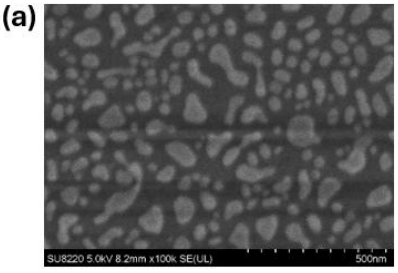


Fig. 2. (a) SEM images of Au nano-islands,

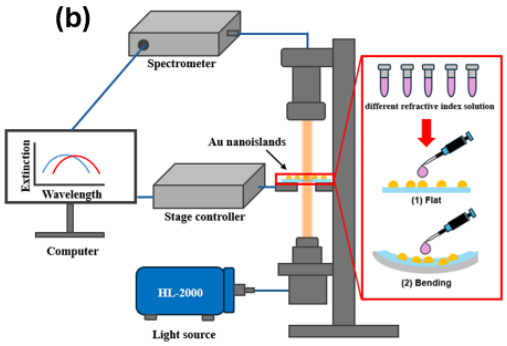


Fig. 2. (b)LSPR setup with flexible glass under flat and bending configurations.

Results and Discussion

The extinction spectra for flat and bending *configuration* showed negligible differences in the overall peak shape and position, indicates that the nano-islands maintained their structural integrity despite mechanical deformation. Such robustness is essential for potential integration into wearable or dynamic sensing systems [4].

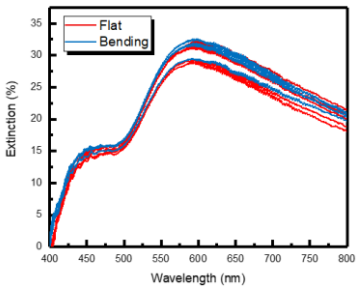


Fig. 3. Extinction spectra of flexible LSPR sensor under flat and bending configurations.

However, a notable distinction emerged when comparing refractive index sensitivity between the two conditions. The flat *configuration* has a sensitivity of approximately 96 nm/RIU. In contrast, the bending *configuration* showed a significantly higher sensitivity of about 205 nm/RIU, which is more than two-fold increase in sensitivity suggests that mechanical bending introduces beneficial changes at the nanoscale level.

The observed enhancement in sensitivity is likely due to several mechanisms. First, Bending may reduce nano-island spacing then enhance plasmonic coupling, leading to stronger near-field effects and improved sensitivity [5]. Substrate curvature could also modulate light scattering or alter resonance conditions slightly, contribute to heightened refractive index responsiveness.

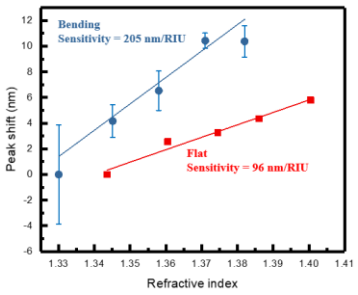


Fig. 4. Refractive index sensitivity of the LSPR sensor under (a) flat and (b) bending configurations, showing sensitivities of 96 nm/RIU and 205 nm/RIU, respectively.

Conclusion

This study demonstrates that LSPR sensors fabricated on the flexible glass substrate with an enhanced sensitivity through mechanical bending. While the extinction spectra remain stable across deformation states, the refractive index sensitivity increases from 96 nm/RIU to 205 nm/RIU. Nonetheless, adhesion issues were observed as repeated measurements after bending introduced variability. Future efforts should improve nanoisland stability via adhesion layers or embedding, and enhance packaging to protect the sensing layer, enabling robust, flexible plasmonic sensors.

References

[1] M. Li, S. K. Cushing, and N. Wu, "Plasmon-enhanced optical sensors: a review," *Analyst,* vol. 140, no. 2, pp. 386-406, 2015.

[2] F. Arefnia, M. I. Zibaii, A. Layeghi, S. Rostami, M.-M. Babakhani-Fard, and F. M. Moghadam, "Citrate polymer optical fiber for measuring refractive index based on LSPR sensor," *Scientific Reports,* vol. 14, no. 1, p. 18637, 2024.

[3] B. Miranda, I. Rea, P. Dardano, L. De Stefano, and C. Forestiere, "Recent advances in the fabrication and functionalization of flexible optical biosensors: Toward smart life-sciences applications," *Biosensors,* vol. 11, no. 4, p. 107, 2021.

[4] M. Nan *et al.*, "Wearable localized surface plasmon resonance-based biosensor with highly sensitive and direct detection of cortisol in human sweat," *Biosensors,* vol. 13, no. 2, p. 184, 2023.

[5] A. Bonyár, "Maximizing the surface sensitivity of LSPR biosensors through plasmon coupling—Interparticle gap optimization for dimers using computational simulations," *Biosensors,* vol. 11, no. 12, p. 527, 2021.

DOI 10.5162/EUROSENSORS2025/MP20

A photoelectrochemical electrode of electrodeposited cuprous oxide on ITO/glass with deposition time adjustment

Leung Sze Tsui[1], Iqra Shaheen[2], Marcin Urbanowicz[3], Agnieszka Paziewska-Nowak[3], Dorota G. Pijanowska[3], Chia-Ming Yang[1,2,4,5,6]
[1] Institute of Electro-Optical Engineering, Chang Gung University, Taoyuan, Taiwan
[2] Department of Electronic Engineering, Chang-Gung University, Taoyuan, Taiwan
[3] Institute of Biocybernetics & Biomedical Engineering, Polish Academy of Sciences, Warsaw, Poland
[4] Department of Neurosurgery, Chang Gung Memorial Hospital Linkou, Taoyuan, Taiwan
[5] Department of Materials Engineering, Ming-Chi University New Taipei City 243, Taiwan
[6] Department of Electronics Engineering, Ming-Chi University New Taipei City 243, Taiwan
cmyang@mail.cgu.edu.tw

Summary:
Electrodeposition of Cu_2O on ITO glass at 50°C was carried out at various time with studies on their morphological and photoelectrochemical properties. AFM analysis exhibits a clear correlation between electrodeposition time and the average surface roughness. The electrochemical performance evaluated by cyclic voltammetry (CV) demonstrates the excellent conductivity of Cu_2O fabricated at 120s for photocurrent generation. A proper Cu_2O film exhibits a high photocurrent generation, highlighting the significance of controlled film thickness in optimizing device performance, which can be applied in photoelectrochemical applications.

Keywords: cyclic voltammetry, Electrodeposition, Photoelectrochemical, photoelectron conduction

INTRODUCTION

With the continuous advancement in technology, health and environmental protection gain attention. Therefore, green energy production and highly selective detection methods have attracted great interest. Photoelectrochemical (PEC) methods are involved in a photo-enhancement to drive electrochemical reactions at the interface of a photoactive material and an electrolyte [1]. Furthermore, the design of PEC devices can be optimized by illumination management, ensure electrochemical stability, and be compatible with mass production for widespread deployment [2]. The most important component of PEC device is the photoactive material which determine performances including photo-electron transfer efficiency and stability. Among Several metal-oxide based materials, Cu_2O has been obtained significant interests for PEC systems, as its advantages of proper band gap (2.3 eV) matched to visible light adsorption, low cost, easy availability and eco-friendliness. Electrodeposition does not require specialized vacuum system and can be conveniently implemented under standard laboratory conditions. Operational flexibility make electrodeposition an attractive method to generate Cu_2O films. Therefore, photoelectrochemical characterization of Cu_2O prepared by temperature-dependent electrodeposition is proposed in this study.

MATERIALS AND METHODS

The fabrication flow and setup of electrodeposited Cu_2O layer on indium tin oxide (ITO)/glass (RLO35SD, Ruilong, Taiwan) is shown in Fig. 1(a). ITO/glass was cleaned by acetone, methanol and distill water sequentially for 10 min in each step. 0.4 M copper sulfate and 3 M lactic acid (Sigma, U.S.) solution were prepared for electrodeposition. A constant bias voltage at -0.4 V was provided by a potentiostat (PalmSens4, PalmSens BV, Netherlands) via 3-electrode setup with working electrode, counter electrode made of ITO/glass and a commercial Ag/AgCl as reference electrode, respectively. The deposition temperature was controlled for 50°C at different time from 600 to 30s as various experimental groups. 4-well encapsulation with Polydimethylsiloxane (PDMS) was attached on the surface of fabricated Cu_2O samples with a fixed area of 3x3 mm^2 of each well used as working electrode. Cyclic voltammetry (CV) measurement was performed using the potentiostat with the 3-electrode setup. The measurement setup with a counter and reference electrode are platinum plate and commercial Ag/AgCl reference electrode (RE-1B, ALS Co. LTD., Japan) as shown in Fig. 2, respectively. To evaluate the photoelectrochemical response, an LED illumination system with multiwavelength (pE-4000, CoolLED, UK) was used to provide the fixed

power intensity of 1 mW/cm^2 of a LED with wavelength of 525 nm through an optical fiber to fabricated Cu_2O samples.

RESULTS AND DISCUSSION

Morphology of all Cu_2O layers were investigated by atomic force spectroscopy (AFM) (NanoView1000, FSM-Precision, China) as shown in Fig. 3(a)-(e) for Cu_2O deposition time from 600s to 30s, respectively. These images show unique surface features with orientated crystalline resulting that the increase in deposition time is directly proportional to the average surface roughness. Cross-sectional SEM images of different groups present the thickness reduction with deposition time. To know their basic electrochemical response, a standard cyclic voltammetry (CV) measurement is performed to Cu_2O films with and without illumination of 525 nm LED as shown in Fig. 4(a)-(e). Highest enhancement was observed in both (cathodic and anodic) for the Cu_2O electrodeposited for 120s. Excellent electrical conductivity and greater photoactivity, supporting its suitability for photocurrent generation [3]. The enhancement rate of the 50°C-120s sample is higher than that of the 50°C-600s, 240s, 120s and 60s sample. This supports the idea that thinner Cu_2O films can efficiently amplify electrical signals in response to illumination.

CONCLUSION

The photoelectrochemical characteristics of the Cu_2O thin films revealed the influence of deposition time on their electrochemical performance. The surface roughness and thickness of Cu_2O crystals is directly affected by the process time. Electrochemical studies prove the excellent electrical conductivity and photoactivity of an electrodeposition time of 120s. A thinner film benefits to enhance photoelectron conduction, demonstrating a direct relationship between film thickness and photoelectrochemical signal strength. A high efficiency achieved for the Cu_2O deposited at 50°C for 120 sec, which can be applied in PEC relative applications. Altogether, these findings highlight the critical role of controlled electrodeposition in tailoring the properties of Cu_2O/ITO thin films, providing valuable insights for optimizing their performance in different applications.

References

[1] M.A. Soldatov, et. al., Nanomaterials. 12 (2022), 839.

[2] Y.H. Chiu, et. al., APL Materials, 7 (2019). 080901.

[3] J.Y. Huang, et. al., Journal of Physical Chemistry C. 122 (2018) 13027–13033.

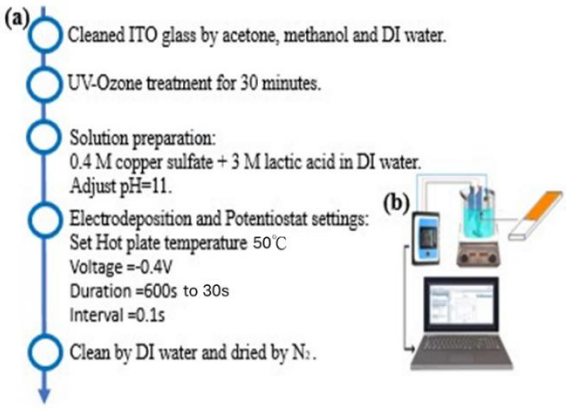


Fig. 1. (a) Process flow and (b) experimental setup of electrochemical deposition of Cu_2O.

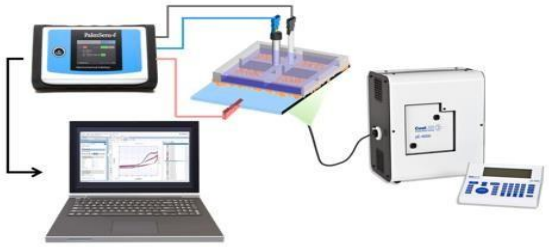


Fig. 2. CV measurement setup with illumination setup.

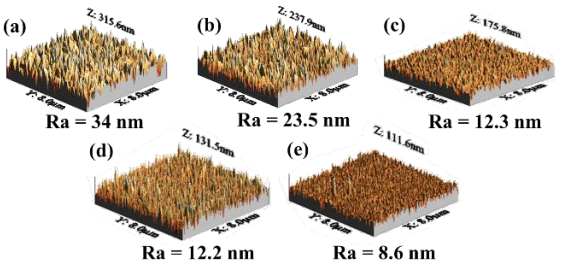


Fig. 3. Surface morphology of Cu_2O samples electrodeposited at different process time: (a) 600s, (b) 240s, (c) 120s, (d) 60s and (e) 30s collected by AFM with its average roughness (Ra).

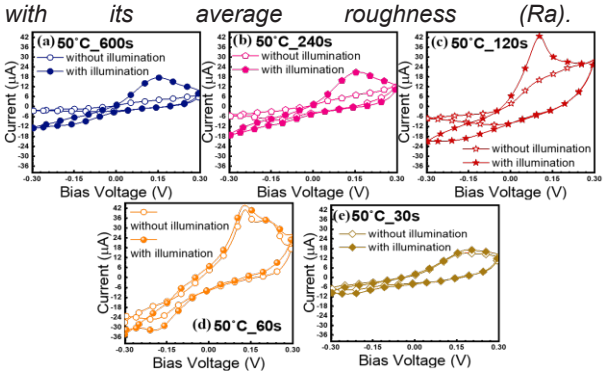


Fig. 4. CV curves of Cu_2O samples electrodeposited at different process time: (a) 600s, (b) 240s, (c) 120s, (d) 60s and (e) 30s measured in 0.1X PBS solution with and without illumination.

.

DOI 10.5162/EUROSENSORS2025/MP21

Lead-Free Piezoelectric Vibration Energy Harvesters: Spark Plasma Sintered KNN compared with commercial KNN

Grégoire Forges[1,3], Nadia Bencharef [1,2], U-Chan Chung[2], Catherine Elissalde[2], David Gibus[3], Hélène Debéda[1]
[1]Univ. Bordeaux, CNRS, Bordeaux INP, IMS, UMR 5218 F-33405 Talence Cedex, France,
[2]Univ. Bordeaux, CNRS, Bordeaux INP, ICMCB, UMR 5026, F-33600 Pessac, France
[3]SYMME, Univ. Savoie Mont Blanc, F74000 Annecy, France
gregoire.forges@univ-smb.fr

Summary:
This work presents the use of lead-free piezoelectric material, pure KNN sintered by spark plasma sintering, for applications in vibration energy harvesting. KNN ceramics of dimensions 1 × 2 × 8 mm3 were densified at 1000°C and thinned to 0.5mm before electromechanical characterizations. The deduced parameters were used for the design of piezoelectric bimorph cantilever. A power of 115 µW at 1m/s² and a normalized power of $6.75\ \mu W.g^{-2}.mm^{-3}$ are expected from FEM simulations. Such results are similar as those of commercial KNN ceramics, showing the potentialities of the process.

Keywords: Piezoelectric cantilever, SPS, KNN, FEM

Introduction

Considering the piezoelectric material in piezoelectric vibration energy harvesters (VEH), the community is looking for alternatives to lead-based perovskites. Lead-free piezoelectric perovskites, like (K,Na)NbO3 (KNN), are not only promising in both film or ceramic form but also challenging in the context of VEH [1]. Also, to reduce the cost of Silicon cantilevers a focus on the replacement of the Si substrate by metallic or polymer substrate [1-3] is done and thicker films (>10µm) may also help to maximize powered energy. However, the thermal budget of processes in literature is quite high with a firing step of hours at 900°C for example [4]. Hence, an original processing route combining screen-printing technology with Spark Plasma Sintering (SPS) process allowing sintering at lower temperature for short periods of time [5]. Here, the objective is to use pure KNN commercial nanoparticles to efficiently sinter bulk ceramic by SPS, before moving to the screen-printing/SPS combination to sinter a KNN screen-printed thick film printed on a StSt. For this process, controlling grains size and their distribution after SPS sintering will be the key to achieve characterizations similar than those of commercial KNN. After SPS sintering of the KNN, the electromechanical characterizations led on the fabricated KNN ceramics will be used to conduct FEM modelling and predict the harvested energy for bimorph cantilevers integrating KNN thinned ceramics.

Ceramic Process

Two dense (98 %) pellets of diameter 10 mm and 1 mm (D1) and 2 mm (D2) thick, were produced from a commercial KNN (K0.5Na0.5NbO3) nanopowder. The SPS equipment is Syntex Dr. Sinter Lab Model SPS-515S (Fig.1). The sintering process was led under vacuum at 1000°C for 15 min, with a pressure of 100 MPa and a heating rate of 100°C/min. Following sintering, an annealing treatment 2 hours at 1000°C was carried out to recover the oxygen stoichiometry [6]. The two pellets were initially coated with a thin layer of sputtered gold, then poled and characterized before being sectioned into bars (B1 and B2). Dimensions of 1 × 2 × 8 mm3 were prepared using a wire saw and subsequently polished to achieve a final thickness of 0.5 mm. As illustrated in Fig. 2, the bars were cut in two different orientations to assess the influence of the electric field direction during poling versus the pressure applied during SPS sintering, on the electromechanical properties. Subsequently, the bars underwent the same processing steps as the pellets, including metallization, poling, and characterization. The dielectric properties were led using a HP-4194 impedance/gain-phase analyzer. Poling was performed at room temperature in a silicone oil bath under an electric field of 3 kV/mm for 5 min. The piezoelectric coefficient d_{33} was then measured using a Berlincourt-type piezometer (frequency: 110 Hz, applied force: 0.25 N). Following sample preparation, structural and microstructural characterizations were performed. The X-ray diffraction pattern confirms an orthorhombic perovskite structure with no detectable secondary phases. At the microstructural level, the grains exhibit a cubic morphology with an average size of approximately 10µm (Fig. 3). Table I summarizes the values from dielectric and

piezoelectric characterization for each configuration. After cutting, a difference was observed between the properties of the ceramic bars and the original disks. Dielectric loss increased by 2 to 6% and the d_{33} value decreased. This degradation may be attributed to mechanical stresses introduced during the cutting process, which can generate surface defects and cause partial depolarization of the already-poled ceramics. The effect is particularly pronounced in the 2 mm samples (B2), where the larger surface area exposed to mechanical stress leads to greater losses and more significant depolarization.

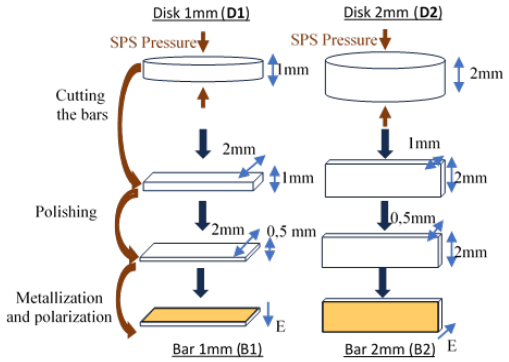


Fig.2 Ceramic process from SPS pellets to bars

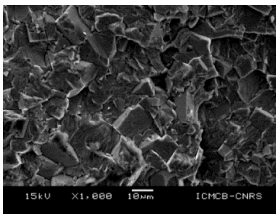


Fig.3 Scanning electron microscopy of the SPS ceramic fired at 1000°C

Tab 1: Dielectric and piezoelectric coefficients

	Disks		***Bars***	
	D_1	D_2	B_1	B_2
ε_r **(1kHz, 25°C)**	*380*		*350*	*400*
Dielectric losses (1kHz, 25°C)	*2 %*		*5 %*	*6 %*
d_{33} ***(pC/N)***	*110*		*100*	*70*

31-Mode Characterization of bars

The KNN bars (B1) were assessed by impedance analysis to study the 31 piezoelectric mode, that is exploited in cantilevers. Mechanical and electrical material parameters were extrapolated using method from [7] (Tab. 2).

Tab. 2: Characteristics of assessed KNN bars

$f_0\,(kHz)$	k^2	Q_m	C_0 (pF)	$s_{11}^E(m^2.N^{-1})$	$d_{31}(pC.N^{-1})$	ϵ_{33}
343	0,048	133	57	$7{,}69.10^{-12}$	-35	324

Finite Elements Modeling

FEM on COMSOL Multiphysics was conducted to investigate the performance of KNN bars for energy harvesting in a bimorph cantilever with a steel substrate. The prototype dimensions are given in Tab. 3 and the harvested power is represented in fig.4. At 302 Hz, the power is 115 µW as shown on fig. 6. The normalized power to the acceleration and volume is $6.75\ \mu W.g^{-2}.mm^{-3}$. When compared to industrial LF02B KNN [9], which is, commonly, not pure KNN with doping elements [9], the delivered power is comparable (Fig. 4). The resistive load for the LF02B was set to $940\ k\Omega$ to achieve optimal power output.

Tab. 3: Geometric parameters and optimal resistive load

Length	**Width**	**Sub thick.**	**Piezo thick.**	R_{Load}	**Volume**
7,9 mm	1,95 mm	0,6 mm	*0,6 mm*	3,56 MΩ	1,64 cm^3

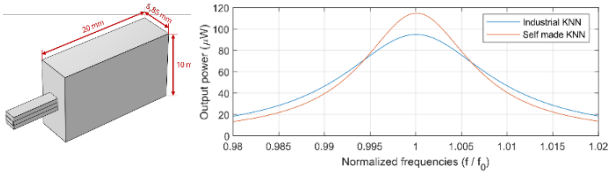


Fig. 4. Left : Prototype investigated in finite element simulation, Right : Harvested power for a pure optimal resistive load under the resonance frequency and an acceleration of $1 m/s^2$

Conclusion

SPS KNN bars were presented in this work. Pure KNN nanopowder was used to fabricate the ceramics and compare their properties to commercial doped KNN. Thanks to electromechanical characterization good piezoelectric properties were assessed and the simulation show that interesting harvested power can be expected from a bimorph cantilever under vibration. Work is on progress to validate experimentally these results with a prototype further tested under vibration with several resistive loads.

References

[1] M. Safaei, et al. Smart Mater. Struct. (2019) DOI 10.1088/1361-665X/ab36e4
[2] T. DUFAY ET AL. ENERGY TECHNOLOGY 6, 5, (2017) DOI 10.1002/ENTE.201700732
[3] L Van Minh et al 2016 J. Phys.: Conf. Ser. 773 012003, doi:10.1088/1742-6596/773/1/012003
[4] E.Fernandes et al. Smart Mater. Struct 27(3) DOI: 10.1088/1361-665X/aaaba5
[5] H. Debéda et al., Ceramics 2020, 3(4) DOI: /10.3390/ceramics3040038
[6] R. Pinho et al., Applied Materials Today 2020, DOI: 10.1016/j.apmt.2020.100566
[7] Y. Zhuang, et al. "Derivation of piezoelectric losses from admittance spectra." Japanese Journal of Applied Physics 48.4R (2009)
[8] https://www.niterragroup.com/resource/pdf/product_piezoelectric-ceramics_characteristic_j.pdf
[9] Y. Liao et al., Ceramics International, vol. 45, no. 2, Part A, pp. 2644–2652, Feb. 2019, doi: 10.1016/j.ceramint.2018.10.211.

Acknowledgements

French National Research Agency ANR for its financial support of the PLAYER-ONE project n°ANR-22-CE51-0030.

DOI 10.5162/EUROSENSORS2025/MP22

Optimal Design of Cantilever-type Vibro Harvester Working at Second Eigenfrequency

Paulius Skėrys[1], Dr. Rimvydas Gaidys[1], Dr. Birutė Narijauskaitė[1]
[1] Kaunas University of Technology, Studentų g. 56-344, Kaunas, Lithuania
paulius.skerys@ktu.lt

Summary:
The research presents an optimization procedure for the thickness of the active element in a piezoelectric energy harvester for the fixed second eigenfrequency to enhance electrical output. The cantilever beam is modelled as a two degree of freedom Bernoulli-Euler element. The optimal design cantilever achieves a 70% efficiency of generated strain compared to the uniform cantilever, with experimental results confirming the mathematical model.

Keywords: shape optimization, sensitivity analysis, vibration energy harvesting.

Background, Motivation, and Objective

Recent advancements in energy harvesting technologies have garnered significant attention, particularly in piezoelectric energy harvesters (PEHs) [1]. A notable challenge in enhancing the efficiency of PEHs is the strain distribution in cantilever designs. While much of the existing beam shape optimization focuses on width [2-4], this study introduces an approach that optimizes the thickness of piezoelectric cantilevers for fixed second eigen frequency, allowing for strain maximization at the upper layer of the active element.

Methodology

When a piezoelectric material is mechanically strained, electric polarization that is proportional to the applied strain is produced [5]. This means that if the strain is maximized, the electric polarization will be maximum too.
The optimization problem is to maximize the strain of the upper layer of the cantilever (Fig. 1) by varying its thickness for fixed second eigenfrequency. The design variable was the thickness of the cantilever, state variable - eigenfrequency.

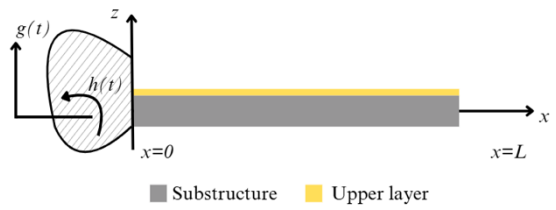


Fig. 1. Active element of the cantilever type vibration energy harvester

Optimization problem now can be formulated: maximize the objective function

$$Max\ \Psi_0(b) = \sum_{i=1}^{m} \left| -\frac{b_i}{2} \frac{d^2 v(x)}{dx^2} \right| = \sum_{i=1}^{m} |[B_i]\{u_i^e\}| = \sum_{i=1}^{m} \left| -\frac{b_i}{2} \left[-\frac{6}{l^2} + \frac{12x}{l^3} \quad \frac{6}{l^2} - \frac{12x}{l^3} \quad -\frac{4}{l} + \frac{6x}{l^2} \quad -\frac{2}{l} + \frac{6x}{l^2} \right] \begin{Bmatrix} v_1^i \\ \theta_1^i \\ v_2^i \\ \theta_2^i \end{Bmatrix} \right| \quad (1)$$

subject to the state equation

$$K(b)\varphi = \zeta M(b)\varphi \quad (2)$$

and constraints

$$\Psi(\zeta, b) \geq 0. \quad (3)$$

Where: i – finite element number, $v(\mathrm{x})$ – bending beam shape function vector, $\{u_i^e\}$ – element nodal displacement vector, $[B_i]$ - the strain-displacement matrix, l – finite element length (the same for all $i = 1, m$), b_i – thickness of element, $K(b)$ - is the stiffness matrix, $M(b)$ - is the inertia matrix, φ - is the eigenvector of a given vibration mode, ζ is the corresponding eigenvalue.
The gradient projection method with sensitivity analysis was used to solve this optimization problem. Initial geometry was a uniform cantilever with a second bending eigen frequency equal to the target value.

Results

Design variables, the thickness of the beam, were constrained to minimum thickness. The state variable, second eigen frequency, was constrained to be the same ($w_2 = 267\ Hz$), as of the initial uniform cantilever. Optimization was simulated in MATLAB®, optimal shape cantilever was then imported into COMSOL Multiphysics ® for transient analysis.
The optimal design cantilever is presented in Fig. 2. Fig. 3 depicts a bending second eigenform of the cantilever with a normalized normal strain field. Some region of maximum strain occurs at the clamped end of the cantilever, however, a second range of strain is observed in the middle

section. The third part of the cantilever exhibits negligible strain and is an inertial mass.

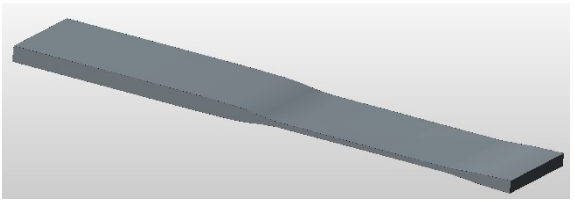


Fig. 2. Optimal shape cantilever for the fixed second eigenfrequency

Normal strain distribution along the cantilever during transient analysis is presented in Fig. 4. The total strain amount of the optimal design cantilever was around 70% higher compared to the uniform cantilever.

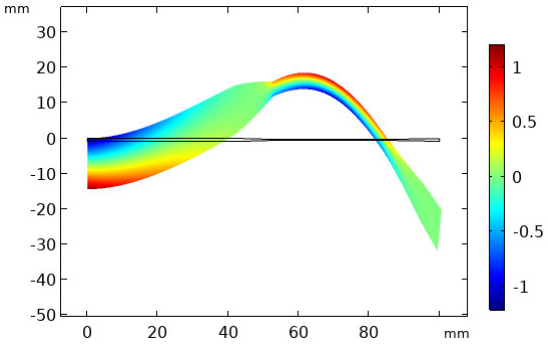


Fig. 3. Second bending eigenform of the optimal design cantilever. Normalized normal strain field.

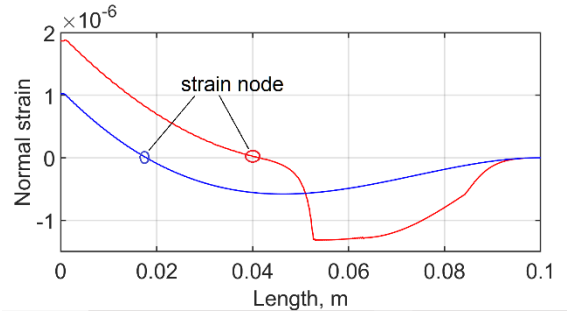


Fig. 4. Normal strain distribution at the upper layer of the cantilever, kinematically excited by second eigen frequency $w_2 = 267\ Hz$, during transient analysis at the time moment of the max strain. Blue - uniform cantilever, red – optimal design cantilever.

Simulation results were verified experimentally. Specimens were manufactured using additive manufacturing technology with photopolymer Tough 2000 and featured a PVDF DT1-028K/L piezoelectric sensors to generate electrical signals which were recorded by a digital oscillometer while the cantilever was excited by a vibrational plate to its second eigen frequency. In Fig. 5 the result of the experiment is presented. Maximum peak-to-peak values were compared of uniform and optimal design cantilevers.

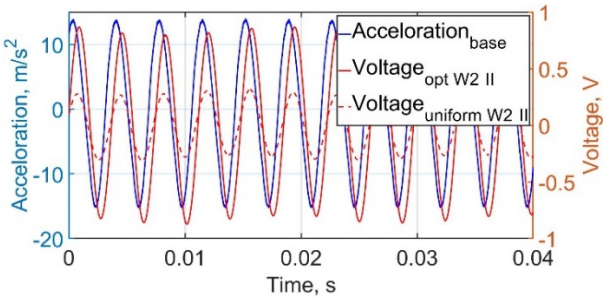


Fig. 5. Experimental results graph. Blue line - accelerometer signal, red solid – optimal cantilevers output, red dashed – initial cantilevers output.

In Fig. 5, the cantilevers were excited by a 14 m/s^2 acceleration. The uniform cantilever output is a 0.31V, optimal design - 0.8V, in cantilever's interval from strain node to tip.

Conclusion

The optimal design cantilever for the second eigenfrequency was found, which generates a 70% more normal strain amount along the cantilever length with the fixed eigenfrequency. The simulation results were validated experimentally, confirming the generation of normal strain.

References

[1] Li, Y., Yu, J., Wei, Y., Wang, Y., Feng, Z., Cheng, L., Huo, Z., Lei, Y., & Sun, Q. (2023). Recent progress in self-powered wireless sensors and systems based on TENG. Sensors, 23(3), 1329. https://doi.org/10.3390/s23031329

[2] Karadag, C.V., Ertarla, S., Topaloglu, N., et al. (2021). Optimization of beam profiles for improved piezoelectric energy harvesting efficiency. Struct Multidisc Optim, 63, 631–643. https://doi.org/10.1007/s00158-020-02714-0

[3] Wang L, Tong X, Yang H, Wei Y, Miao Y (2019) Design and analysis of a hollow triangular piezoelectric cantilever beam harvester for vibration energy collection. Int J Pavement Res Technol 12(3):259–268. ISSN 1997-1400 https://doi.org/10.1007/s42947- 019-0032-1

[4] Hashim, A. A., Mahmoud, K. I., & Ridha, H. M. (2021). Geometry and shape optimization of piezoelectric cantilever energy harvester using COMSOL multiphysics software. International Review of Applied Sciences and Engineering, 12(2), 103-110. https://doi.org/10.1556/1848.2021.00170

[5] Erturk, A., & Inman, D. J. (2011). Piezoelectric energy harvesting (1st ed.). John Wiley & Sons, Ltd. ISBN: 978-0-470-68254-8.

Acknowledgments

This research has received funding from the Research Council of Lithuania (LMTLT), agreement No S-MIP-24-46, "Intelligent micro sensor array for physical environmental monitoring based on the mechanisms of the behavior of insect mechanoreceptors".

DOI 10.5162/EUROSENSORS2025/MP23

Design of a set-up for Measuring Magnetostrictive Materials without Strain Gauges to assess the magnitude of Villari Effect

*Wojciech Pałka, Karolina Laszczyk**
Wrocław University of Science and Technology, Poland, Wrocław, Wybrzeże Stanisława Wyspiańskiego 27,
**Corresponding Author's e-mail address: karolina.laszczyk@pwr.edu.pl*

Summary:

This paper presents the set-up design for measuring the properties of magnetostrictive materials to assess the magnitude of the Villari effect. For this, the method to do measurements was developed and described, further the set-up was designed. A significant advantage of this method is the elimination of the need for additional consumable materials, such as strain gauges.

Keywords: Magnetostrictive materials, Villari effect, energy harvesting, strain gauges

Background, Motivation and Objective

Magnetostriction refers to the ability of a material to undergo mechanical strain in response to the magnetic field. It is the phenomenon observed in almost all ferromagnetic materials. It couples elastic, electric, magnetic, and in some situations also thermal fields [1]. The magnetostrictive phenomenon is reversible, i.e. a mechanical impact on these materials results in their magnetic properties modification. This is a direct analogy to the piezoelectric case, where the elastic and dielectric properties are involved as well as the piezoelectric. In the magnetostrictive case a reverse phenomenon is known as the Villari effect [1]. Therefore, it is considered to be used for sensors, actuators or power scavenging, where electric power could be harvested due to a vibrated structure with magnetostrictive properties, e.g. piezomagnetic coefficient. Such a typical vibration energy harvester (EH) set-up then consists of a cantilever that produces an oscillating magnetic field wound with a coil. The cantilever experiences a time-varying compressive mechanical stress, inducing the current in the coil that is connected to a resistive load.

Low level vibrations are ubiquitous: they are present in buildings, automobiles, aircraft, ships, trains, industrial and home machines. A combination of theory and experiment shows that from vibrations about 300 μWcm^{-3} could be generated [2]. This makes it a potential reliable remote energy source to replace batteries for low power demand components, e.g. for IoT sensors [2]. Today, the magnetostrictive materials are present in a form of solid blocks, fibers, powders [3], To make the use of such forms of magnetostrictive materials for small type energy harvesters, it must be possible to adapt them to fabrication techniques available for a micro- or meso-scale, including 3D printing. This is achievable by developing new composite materials possessing magneto-strictive properties [4]. However, a new issue is arising, how to check their properties in order to confirm their utility and further to improve these composites to achieve higher conversion efficiency [5]. In the magnetostrictive EHs, output energy depends on the coupling of magnetic susceptibility, mechanical stresses, strains and magnetic field strength. Additionally, the output power is not uniform across the frequency spectrum [8, 9]. Although, there are a lot of challenges and parameters to be confirmed, the magnetoelastic coupling coefficient is the primary to be investigated. Commonly, the magnetostrictive materials are characterized by static measurements; the sample is placed in the tuned DC magnetic field, meanwhile the compressive stresses of a sample are obtained using the strain gauge [8]. However, aside from the nonlinearity, the issue is the thermal effect that is inevitable when the investigated materials are combined with the strain gauges; in [9] it was reported that the reduction of the temperature effect of the substrate on the measurements is of high importance and can be achieved by the integration of microfabricated strain gauges directly on the sample. This raises challenges

DOI 10.5162/EUROSENSORS2025/MP23

about the additional time to spend on the design, fabrication and measurement calibration.

The objective of this work was to design a setup for measuring the coupling between excitation from the impact on the sample r and the generated magnetic field in an alternative way, i.e dynamic, based on the Villari effect, without the necessity to use the strain gauges.

The set-up design

The set-up design implementations encompassed following assumptions:
1) to create an impact to transform stress to magnetic field, 2) to measure the magnitude of the generated magnetic field in a simple way and 3) to minimize measurement errors between different samples. These requirements were achieved respectively by: ad 1. including a dedicated vibrating electromechanically controlled carrier for the measured samples, ad 2. a magnetometer, whose magnetic bias is negligible, and ad. 3 to use of the carrier's holder that enables in the ease and repeatable manner to mount samples.

On the other hand, it is necessary to establish the method, based on the theory, how to transition the obtained data to make them useful to estimate the magnitude of the Villari effect from the investigated samples. In the context of energy scavenging, precise knowledge of the piezomagnetic coupling is not required: the energy harvesters are matched to the frequency spectrum associated with the presence of mechanical vibrations [2]. Therefore, it is more important to know the function of the generated magnetic field for the selected frequencies. This can be achieved by measuring the magnetic field of a sample in regards to the sample's position, specifically described as a function of displacement in time.

In the proposed set-up the sample vibrates in one direction. Hence, the displacement of the sample is considered as a 1D wave vector (ψ(r,t); Eq. 1) for a selected frequency, in the form of a wave number k, amplitude a and wave position r. Consequently, the magneto--mechanical coupling becomes the conversion of a wave vector (ψ(r,t)) into the corresponding magnetic field.

$$\psi(\mathbf{r}, t) = A\cos(\mathbf{k} \cdot \mathbf{r}) \quad \text{(Eq. 1.)}$$

Based on the present assumptions and relations a dedicated experimental set-up was designed (Fig. 1). It comprises a vibration table as a carrier with a sample holder. All this serves as the excitation base. Additionally the set-up has a magnetometer AK09918 (AKM, JP) and an accelerometer ICM20600 (InvenSense, US). The vibration table is driven by a DC motor Pololu 2214 (Wagney, PL). The whole set-up is controlled by an ESP-32 microcontroller (Espressif, PRC). The motor speed controller was created using the regulator LM2596 (Texas Instruments, US) with a digital potentiometer connected to its feedback loop and the microcontroller.

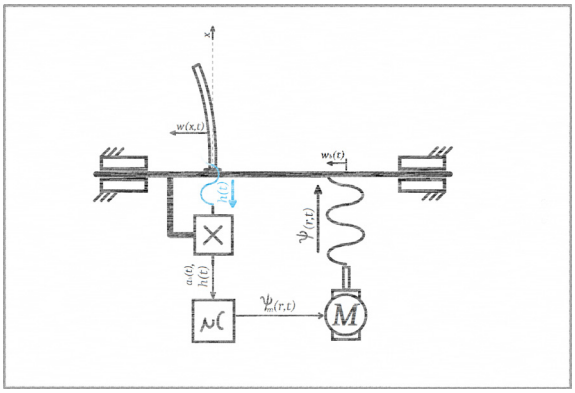


Fig. 1. Schematic picture of a proposed measurement set-up.

When the sample is mounted to the vibration table, the displacement at w(0,t), remains identical to the displacement of wb(t) - at the base. . The displacement at wb(t) is controlled by a microcontroller. a frequency and amplitude sweep are obtained from… and contribute to the frequency-based characteristics. As the result, in a mapping of a 2d plane of frequencies and magnitudes (wave vectors) into a generated magnetic field by the sample. To minimize noise, the data gathered from an accelerometer are useful to further post into the wave vector. Additionally, the corresponding values of the generated magnetic field are recorded. . The acquired data are processed in real time using algorithms designed to filter out external noises (e.g. mechanical disturbance).

Conclusions

The proposed set-up can be utilized in the initial iteration phase of designing magnetostrictive samples. For example, by comparing the results of each iteration it is possible to determine the highest magnetic field output. t This enables a basic optimization process for samples intended for micro-scale energy harvesting applications. Furthermore, based on the frequency response of a given sample, a more

suitable load circuit can be subsequently designed.

Based on the change in output power concerning the resistive load and Faraday's coupling, a new measuring setup was developed to minimize measurement errors between different samples. This was achieved by replacing the pickup coil with a magnetometer, whose magnetic bias is negligible. In addition the developed setup eliminates the need for specialized laboratory equipment and consumables, making the measurement process more efficient and accessible..

[1] "Ieee standard on magnetostrictive materials: Piezomagnetic nomenclature," IEEE Std 319-1990, pp. 1–, 1991, doi: 10.1109/IEEESTD.1991.101048

[2] S. Roundy, P. K. Wright, and J. M. Rabaey, Energy Scavenging for Wireless Sensor Networks. Springer Book Archive, Springer New York, NY, 1 ed., 2003, doi: 10.1007/978-1-4615-0485-6

[3] L.A. Dobrzański, A. Tomiczek, B. Tomiczek, A. Ślawska-Waniewska, O. Iesenchuk, "Polymer matrix composite materials reinforced by $Tb_{0.3}Dy_{0.7}Fe_{1.9}$ magnetostrictive particles", Journal of Achievements in Materials and Manufacturing Engineering, vol. 37 no. 1, 16--23, 11 2009,

[4] A. A. Paul, Q. H. Nguyen, W. Shen, "3D printed magnetostrictive polymer composites (MPCs) for wireless stress sensing," Materials & Design, vol. 247, 2024, doi: 10.1016/j.matdes.2024.113402

[5] L. Wei, H. Liu, L. Shu, L. Zhao, Z. Liu, and Y. Chang, "Study of a magnetostrictive energy harvester for harvesting transient shock vibration," Sensors and Actuators A: Physical, vol. 361, p. 114577, 2023, doi: 10.1016/j.sna.2023.114577

[6] D. Davino, A. Giustiniani, and C. Visone, "Effects of hysteresis and eddy currents in magnetostrictive harvesting devices," Physica B: Condensed Matter, vol. 407, no. 9, pp. 1433–1437, 2012, doi: 10.1016/j.physb.2011.07.038

[7] L. Wang and F. G. Yuan, "Vibration energy harvesting by magnetostrictive material," Smart Materials and Structures, vol. 17, p. 045009, jun 2008, doi: 10.1088/0964-1726/17/4/045009

[8] A. Bieńkowski, R. Szewczyk, and R. Kolano, "Influence of thermal treatment on magnetoelastic villari effect in fe78si13b9 amorphous alloy," Materials Science and Engineering: A, vol. 375-377, pp. 1024–1026, 2004, doi: 10.1016/j.msea.2003.10.045

[9] M. Li, Z. Hu, B. Yan, J. Wang, H. Zhang, F. Ye, B. Sun, J. Liu, Y. Li, G. Ding, F. Zang, and Z. Yang, "A flexible resistive strain gauge with reduced temperature effect via thermal expansion anisotropic composite substrate,"Microsystems nanoengineering, vol. 10,p. 129, 09 2024, doi: 10.1038/s41378-024-00762-w

Acknowledgment

This project has received funding from the European Union's Horizon 2020 research and innovation programme under the Marie Skłodowska-Curie grant agreement No 101007429.

Project co-financed by the Polish Ministry of Education and Science under the program titled International Co-financed Projects.

DOI 10.5162/EUROSENSORS2025/MP24

Nanoporous Materials for Light and Heat Activated Gas Sensing

Larissa Egger[1], Florentyna Sosada-Ludwikowska[1], Nigel Rising[2], Leandro Sacco[2], Anton Köck[1]
[1] Materials Center Leoben Forschung GmbH, Roseggerstrasse 12, 8700, Leoben, Austria
[2] VSParticle, Oostsingel 209, 2612 HL, Delft, The Netherlands
larissa.egger@mcl.at

Summary:
In this work, we investigate the influence of optical and thermal activation of metal oxides on the gas sensing performance. This has been achieved by combining micro-hotplate-based gas sensor devices with UV-LEDs emitting at different wavelengths. Nanoporous films of nickel oxide and tin oxide were printed by spark ablation and the gas sensing performance was investigated towards 5 ppm toluene.

Keywords: gas sensing, nanoporous structures, thermal and optical excitation

Introduction

Indoor air quality (IAQ) monitoring plays an important role in public health and well-being, Poor IAQ has been linked to a variety of health issues ranging from transient discomfort and headache, to respiratory diseases and cardiovascular problems. In particular in harsh environment, such as industrial settings or mines, AQ monitoring is key to maintain a safe working environment.

Conductometric gas sensors, which detect changes in the electrical conductance of gas-sensitive materials in response to the surrounding gas, are very good candidates for IAQ. Mostly, metal oxides (MOx) like SnO_2, ZnO, NiO or CuO are used because of their high sensitivity to a large variety of gases [1]. For effective air quality monitoring, selectivity—the ability to accurately detect a specific target gas within a complex mixture—is a critical challenge.

A very promising approach to achieve a high degree of selectivity is using optical (light) and thermal activation (heat) of the gas sensitive materials. Since photons can also supply the energy needed to exploit the surface ionization scheme [2], which opens an entirely new parameter space for chemical sensing. Moreover, this approach promises a lower power consumption [3] of the sensor device compared to the just heated one.

Sensor and Materials

In this work, SiN-based micro-hotplate chips with integrated heating structure (up to 500°C) and Pt electrodes was used. The materials were printed on the micro-hotplates using a spark ablation generator VSP-G1 (VSParticle B.V.). For the deposition of NiOx and SnOx, two pairs of 6 mm Ni and Sn rods (99.99 % purity) were used. Argon was used as a carrier gas with a 1 l/min flow, and in both cases the sparkling potential and current were set at 1 kV and 10 mA, respectively. The generator was connected to an impaction printer VSP-P1 (VSParticle B.V.) that operated at 0.15 mbar and room temperature. The nozzle diameter was 100 µm. The substrate was placed in a holder that can be moved in the XYZ directions allowing prints without the requirement of lithography technology. A 500 µm long line was printed between the electrodes. The substrate-nozzle distance was fixed at 300 µm. The printing speed (100-1000 µm/s) and the number of passes (2-18) were varied to adjust the nanoparticle layer (NPL) thickness. To stabilize and oxidize the NPL, the chips were annealed at 400°C in flowing synthetic air for 10 minutes. The micro-hotplates were mounted on a Kyocera socket and wire bonded.

Measurement setup

All sensors have been measured simultaneously in an automated gas measurement setup. As background gas synthetic air with tunable humidity level was chosen. In this work the humidity was set at 50%. The operation of the temperature is kept constant during a measurement (25°C, 150°C and 300°C). The target gases are subsequently introduced into the setup for 5 min with flow meters. Presently commercial LEDs are employed, which are mounted on a PCB in two groups of 4 LEDs opposite of 2 sensor sockets. The LED chips emitting at 4 different emission wavelengths (415, 385, 365, and 270 nm) which are employed to screen the impact of optical excitation on the sensor response.

The relative resistance changes due to the interaction with the test gas, i.e. the sensor response S, has been calculated according to:

$$S = \frac{R_{air} - R_{gas}}{R_{air}} \quad (1)$$

where R_{gas} is the sensor resistance in the presence of the test gas and R_{air} is the sensor resistance in pure synthetic air.

Results

We investigated the gas properties of Ni- oxide (Figure 1) and Sn- oxide (Figure 2) nanoporous films towards 5 ppm toluene for different operation temperatures (25°C, 150°C and 300°C). As shown in Figures 1 and 2, without illumination, the response of the metal oxides towards toluene is increasing with increasing operation temperature. Afterwards we have investigated the influence of optical excitation - illuminating the samples with LEDs with different wavelengths – on the responses. In case of the Ni oxides the illumination shows very low to none effect on the responses (Figure 1).

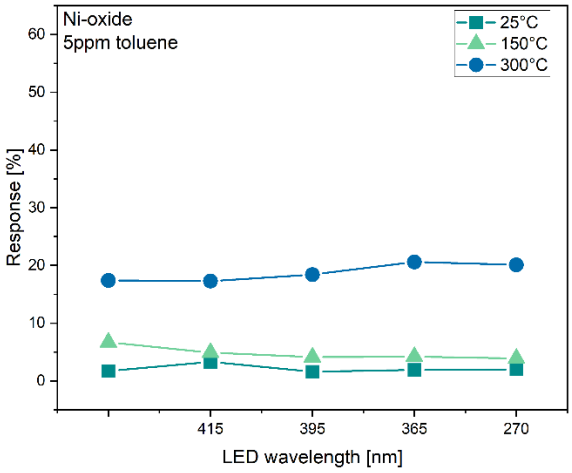


Fig. 1. Response Ni- oxides sensor towards 5 ppm toluene at 25°C/ 150°C/300°C operation temperature without and with 415nm/ 395nm/ 365nm/ 270 nm LED exposure.

However, this is not the case for the Sn- oxides. For lower operation temperatures the optical excitation increases the response except for the LED with a wavelength of 270nm (Figure 2). At an operation temperature of 300°C the optical excitation reduces the responses. This effect can mean that the optical and thermal excitation start to interfere with each other at a certain temperature. A maximum response was reached for the LED with a wavelength of 395nm at room temperature.

In the present work, it is evidenced that combining optical/thermal excitation on nanoporous layers, is a suitable approach to increase sensor selectivity.

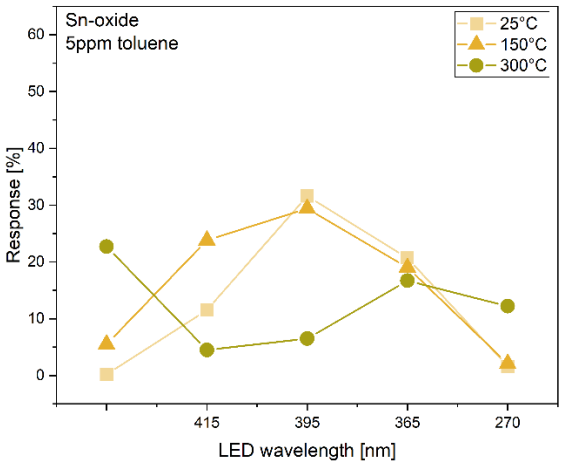


Fig. 2. Response Sn- oxides sensor towards 5 ppm toluene at 25°C/ 150°C/300°C operation temperature without and with 415nm/ 395nm/ 365nm/ 270 nm LED exposure.

References

[1] N. Barsan, D. Koziej, U. Weimar, Metal oxide-based gas sensor research: How to? Sensors Actuators, B Chem., vol. 121, no. 1, pp. 18–35, 2007, https://doi.org/10.1016/j.snb.2006.09.047

[2] O. Casals, N. Markiewicz, C. Fabrega, I. Gràcia, C. Cané, H. S. Wasisto, A. Waag, J. D. Prades, “A Parts Per Billion (ppb) Sensor for NO2 with Microwatt (μW) Power Requirements Based on Micro Light Plates”, ACS Sens. 2019, 4, 4, 822–826, https://doi.org/10.1021/acssensors.9b00150

[3] E. Comini, A. Cristalli, G. Faglia, G. Sberveglieri, “Light Enhanced Gas Sensing Properties of Indium Oxide and Tin Dioxide Sensors”, Sensors and Actuators B: Chemical, 65, 260-263 (2000) https://doi.org/10.1016/S0925-4005(99)00350-0

Acknowledgements

The work has been performed within the projects “Nano4E - Nano4E - Integrated thermo-optically activated Nanosensors for environmental monitoring” (project No: FO999899024), and “RealSens - Advanced Nanomaterials for Real-time Environmental Monitoring Sensor System (project No 922632), which receive funding from the Austrian Funding Agency FFG.

The authors gratefully acknowledge the financial support under the scope of the COMET program within the K2 Center “Integrated Computational Material, Process and Product Engineering (IC-MPPE)” (Project No 886385). This program is supported by the Austrian Federal Ministries for Climate Action, Environment, Energy, Mobility, Innovation and Technology (BMK) and for Labour and Economy (BMAW), represented by the Austrian Research Promotion Agency (FFG), and the federal states of Styria, Upper Austria, and Tyrol.

DOI 10.5162/EUROSENSORS2025/MP25

$Bi_2O_2CO_3$/CuO Micro-flowers with Abundant Oxygen Vacancies for Enhanced VOC Detection

Zichen Zheng[1,2], Kewei Liu[1], Yiwen Zhou[1], Carla Bittencourt[2], Chao Zhang[1]
[1] College of Mechanical Engineering, Yangzhou University, Yangzhou 225127, PR China
[2] Chimie des Interactions Plasma-Surface, University of Mons, 7000 Mons, Belgium
Corresponding Author's e-mail address: zhangc@yzu.edu.cn

Summary:
This study introduces a cutting-edge sensor for nonanal, using a bismuth subcarbonate/copper oxide ($Bi_2O_2CO_3$/CuO) heterojunction. The sensor exhibits exceptional responsiveness to nonanal concentrations from 10-90 ppm, characterized by high sensitivity and excellent linearity. The enhanced sensing performance is attributed to the presence of oxygen vacancies and improved charge separation mechanisms within the heterojunction. Furthermore, we demonstrate the sensor's practical application in evaluating the quality of cooked rice through the detection of volatile organic compounds (VOCs). This research highlights the potential of this sensor as a valuable tool for agricultural product quality evaluation and food safety monitoring.

Keywords: gas sensor, room temperature, hetorojunction, high sensitivity, nonanal

Background

$Bi_2O_2CO_3$ (BOC), an n-type semiconductor with a characteristic Aurivillius structure, comprises alternating $Bi_2O_2^{2+}$ and CO_3^{2-} layers [1] and has been extensively used in gas sensors [2]. However, BOC-based sensors often struggle to achieve high sensitivity, stability, and selective detection simultaneously. Recent advancements in the fabrication of p-n heterostructures within ternary metal oxides offers significant potential for enhancing gas sensing performance [3]. By strategically combining different metal oxides, their electronic properties can be tailored, leading to enhanced charge carrier mobility [4]. This results in a more sensitive and selective response to target gases. Such innovations hold promises for advancing gas sensors in various applications, including environmental monitoring and industrial safety, leading to more reliable and efficient detection systems.

Nonanal is a volatile organic compound (VOC) produced during the deterioration of cooked rice quality [5]. The amount of nonanal increases with the duration of cooked rice storage, providing a valuable reference for assessing the freshness and quality of agricultural products.

Description of the New Method or System

Here, a facile one-step hydrothermal approach was used to synthesize $Bi_2O_2CO_3$/CuO hetorojunction with varying CuO loading amounts, designated as BOC, BOC@10Cu, BOC@20Cu, BOC@30Cu, and BOC@40Cu, respectively, where the mass ratios of $CuCl_2$ to $Bi(NO_3)_3 \cdot 5H_2O$ were adjusted to around 0%, 10%, 20%, 30%, and 40%. Gas-sensing tests were conducted using a four-channel gas sensing testing instrument, which measures electrical resistance signals in highly pure air and target gas.

Results

Due to limited space, we will focus our discussion on the sensor that yielded the best sensing results i.e., the BOC@20Cu (see Fig. 3). The structure of the samples was analyzed using electron microscopy. As shown in Fig. 1a-1c, BOC@20Cu exhibits a micro-flower structure with semi-hollow characteristics. The selected area electron diffraction pattern (Fig. 1d) confirms the single crystalline nature of BOC@20Cu. The energy-dispersive X-ray spectroscopy elemental mapping in Fig. 2e-2i reveals a uniform distribution of Bi, C, O, and Cu elements throughout the BOC@20Cu micro-flower.

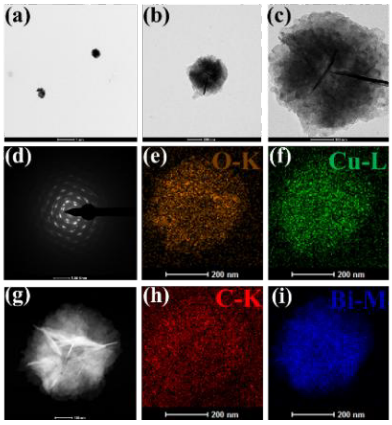


Fig. 1. (a-c) TEM images of BOC@20Cu, (d) SAED pattern of BOC@20Cu, (e-f, h-i) EDS elemental mapping images of O, Cu, C and Bi of BOC@20Cu, (g) HAADF-STEM image of BOC@20Cu.

The XPS O 1s spectra recorded in the different samples can be deconvolved into three components: lattice oxygen, oxygen vacancies (O_V), and surface-chemisorbed oxygen. Comparing the pristine BOC and the BOC@20Cu and samples, it becomes clear that the BOC@20Cu sample has a higher relative amount of quantity of O_V (53.8%) than in the pristine (42.3%) (Fig. 2). This increase in O_V suggests that lattice mismatch induces changes in the positions of electrons or ions within BOC@20Cu, leading to the formation of excess O_V.

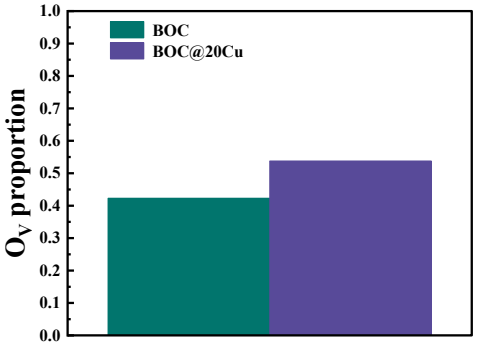


Fig. 2. The percentage of O_V in XPS results.

Fig. 3 shows that BOC@20Cu exhibits the highest response to nonanal molecules compared to the other three sensors at room temperature. The order of response values is: BOC@20Cu > BOC@30Cu > BOC@10Cu > BOC@40Cu. The enhanced gas-sensing performance of BOC@20Cu can be attributed to the creation of a p-n heterojunction, which increases the number of O_V in the material. This heterojunction alters the energy band structure and electric field distribution, leading to improved surface reactivity and facilitating the formation of additional O_V. Moreover, the defect energy levels associated with these O_V was reported to enhance electron capture, resulting in heightened sensitivity [1].

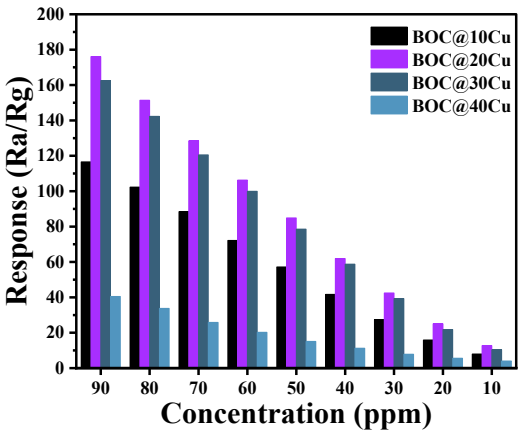


Fig. 3. The response values of BOC@xCu (x = 10, 20, 30, and 40) film to nonanal (10-90 ppm) at room temperature.

As shown in Tab. 1, the good linear correlation between the sensor response and the concentration of the detected gas has also been obtained, demonstrating its potential for practical application.

Tab. 1: Concentration (X)-dependent response curves (Y) of the fabricated sensors for nonanal.

Sensor	Relationship	R^2
BOC@10Cu	Y=1.41X-11.48	0.9954
BOC@20Cu	Y=2.09X-17.06	0.9947
BOC@30Cu	Y=1.97X-16.03	0.9950
BOC@40Cu	Y=0.47X-5.19	0.9600

This study successfully synthesized $Bi_2O_2CO_3$/CuO hetorojunctions using a controlled hydrothermal reaction. The obtained micro-flowers exhibit abundant O_V from CuO loading. The BOC@20Cu sensor shows a strong response to 10-90 ppm nonanal at room temperature, providing valuable insights for Bi-based semiconductor applications.

References

[1] X.Y. Huang, K. Chen, W. Xie, Y. Li, F. Yang, Y. Deng, J. Li, F. Jiang, Y. Shu, L. Wu, W.F. Xie, Y. Deng, Chemiresistive Gas Sensors Based on Highly Permeable Sn-Doped Bismuth Subcarbonate Microspheres: Facile Synthesis, Sensing Performance, and Mechanism Study, Advanced Functional Materials, 33 (2023) 2304718; doi: 10.1002/adfm.202304718.

[2] X.Y. Huang, Z.T. Chi, W. Yang, Y. Deng, W.F. Xie, Synthesis of $Bi_2O_2CO_3$/$In(OH)_3$·xH_2O nanocomposites for isopropanol sensor with excellent performances at low temperature, Sensors and Actuators B: Chemical, 361 (2022) 131715; doi: 10.1016/j.snb.2022.131715.

[3] D.R. Miller, S.A. Akbar, P.A. Morris, Nanoscale metal oxide-based heterojunctions for gas sensing: A review, Sensors and Actuators B: Chemical, 204 (2014) 250-272; doi: 10.1016/j.snb.2014.07.074.

[4] L.Y. Zhu, X.Y. Miao, L.X. Ou, L.W. Mao, K. Yuan, S. Sun, A. Devi, H.L. Lu, Heterostructured α-Fe_2O_3@ZnO@ZIF-8 Core–Shell Nanowires for a Highly Selective MEMS-Based ppb-Level H_2S Gas Sensor System, Small, 18 (2022) 2204828; doi: 10.1002/smll.202204828.

[5] Q. Zhao, J. Xi, D. Xu, Y. Jin, F. Wu, Q. Tong, Y. Yin, X. Xu, A comparative HS-SPME/GC-MS-based metabolomics approach for discriminating selected japonica rice varieties from different regions of China in raw and cooked form, Food Chem. 385 (2022) 132701; doi: 10.1016/j.foodchem.2022.132701.

DOI 10.5162/EUROSENSORS2025/MP26

Selective Benzene Sensing Enabled by Catalytically-Active Metastable Nanoparticles

Matteo D'Andria[1], Tiago Elias Abi-Ramia Silva[1], Andreas T. Güntner[1]
[1] Human-centered Sensing Laboratory, Department of Mechanical and Process Engineering, ETH Zürich
andregue@ethz.ch

Summary:

Prolonged exposure to volatile organic compounds (VOCs), especially benzene, poses serious health risks due to their toxic nature. However, detecting benzene at parts-per-billion (ppb) concentrations is challenging, as it often coexists with chemically similar compounds like toluene and xylene. A catalytic packed-bed system using $CoCu_2O_3$, combined with a Pd/SnO_2 chemoresistive sensor, successfully detected benzene concentrations down to 15 ppb, even in the presence of high levels of confounders.

Keywords: benzene, chemoresistive, nanotechnology, gas sensor, aromatic volatile compounds

Prolonged exposure to VOCs remains a major occupational health risk [1]. Among them, benzene is particularly concerning due to its high biotoxicity, prompting the World Health Organization to impose stringent exposure limits [2]. Accurately detecting benzene at ppb levels is especially challenging in environments where chemically similar compounds like toluene and xylene are also present.

In this work, we introduce a sensing system capable of detecting benzene from 15 to 1000 ppm, even when toluene and xylene are present at concentrations up to 100 times higher (Figures 1a and 1b). The $CoCu_2O_3$-based catalytic packed-bed system [3] was evaluated under varying relative humidity (RH) conditions from 40% to 90% yet maintained a stable benzene response and effectively eliminated toluene and xylene with only 16 mg (Figure 1c).

Notably, tests over six months confirmed the system's operational stability, which was further supported by XRD analysis after continuous exposure to operating temperatures for over a week (Figure 1d). The system utilized a packed-bed loading optimized to remove high toluene concentrations while preserving benzene detection capability [3].

This packed bed was then integrated it with a Pd/SnO_2 [4] chemoresistive sensor – known for its sensitivity but limited selectivity. Through a combination of flow-bench experiments and catalytic performance assessments, the engineered system successfully detected down to 15 ppb benzene in the presence of 2 ppm each toluene and xylene. Furthermore, it demonstrated the ability to quantify benzene in real-world samples collected from gas stations. Overall, this strategy offers a promising pathway for miniaturized sensor platforms that comply with evolving exposure regulations.

References

[1] Dick, F. D., Solvent neurotoxicity, *Occupational and Environmental Medicine* 63, 221-226 (2006); doi: 10.1136/oem.2005.022400

[2] Yardley-Jones, A., Anderson, D. & Parke, D. V., The toxicity of benzene and its metabolism and molecular pathology in human risk assessment, *British Journal of Industrial Medicine* 48, 437-444 (1991); doi: 10.1136/oem.48.7.437

[3] M. D'Andria, T. Elias Abi-Ramia Silva, E. Consogno, F. Krumeich, A. T. Güntner, Metastable $CoCu_2O_3$ Nanocrystals from Combustion-Aerosols for Molecular Sensing and Catalysis, *Advanced Materials* 36, 2408888 (2024); doi: 10.1002/adma.202408888

[4] A. T. Güntner, V. Korenm, K. Chikkadi, M. Righettoni, S. E. Pratsinis, E-nose sensing of low-ppb formaldehyde in gas mixtures at high relative humidity for breath screening of lung cancer?, *ACS Sensors* 1 (5), 528-535 (2016); doi: 10.1021/acssensors.6b00008

Acknowledgements

This study was financially supported by the Swiss State Secretariat for Education, Research, and Innovation (SERI) under contract number MB22.00041 (ERC-STG-21 "HEALTHSENSE").

DOI 10.5162/EUROSENSORS2025/MP26

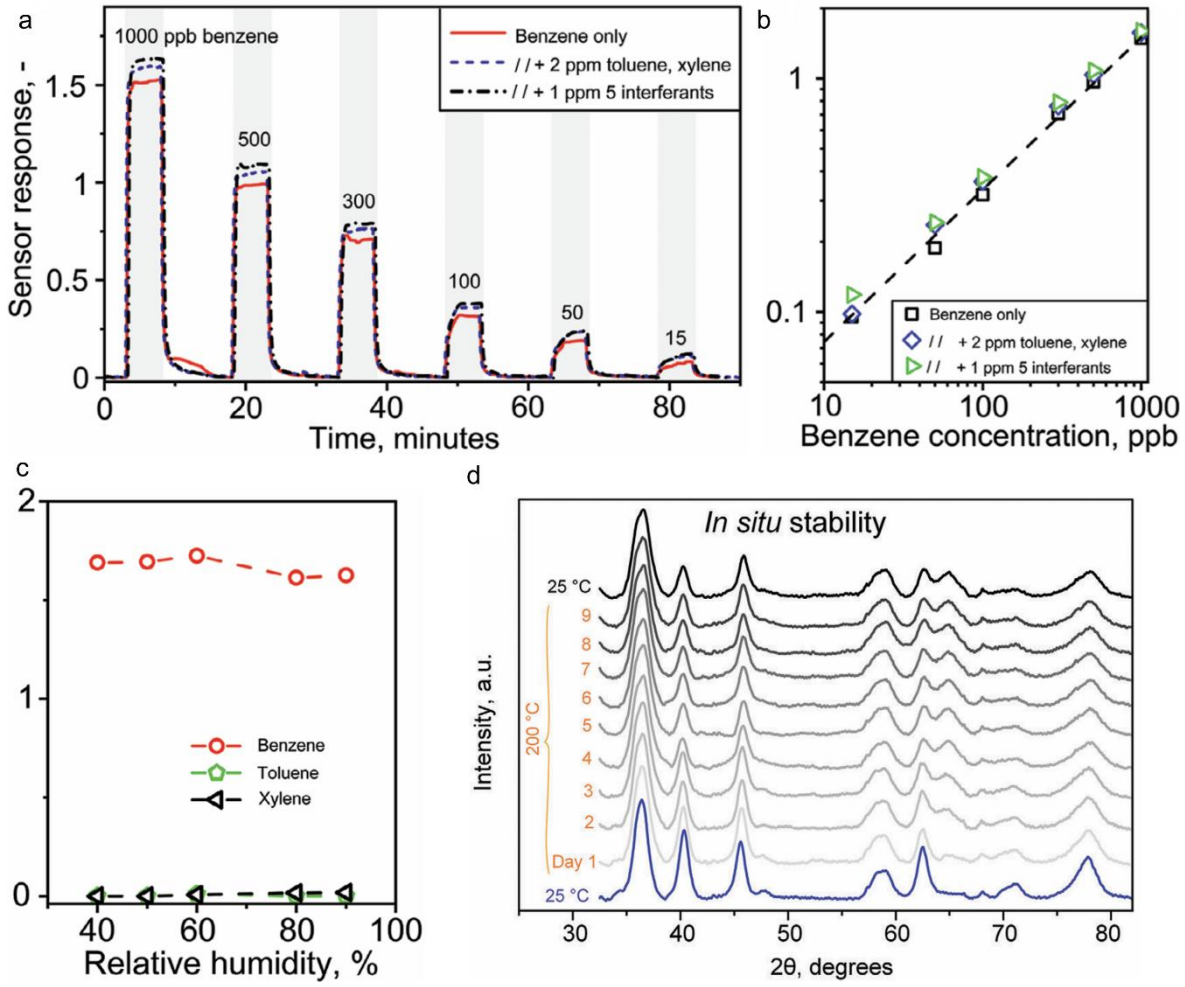


Fig 1. (a) Transient sensor response to benzene exposure (solid red line) at 50% relative humidity (RH). System robustness was assessed by co-feeding 2 ppm of toluene and xylene (dashed lines), along with 1 ppm of up to five interfering compounds (dash-dotted lines): toluene, xylene, methanol, ethanol, and acetone. (b) Corresponding sensor responses as a function of benzene concentration. (c) Sensor response to benzene, toluene, and xylene across a humidity range of 40–90% RH. (d) XRD patterns of $CoCu_2O_3$ recorded at 200 °C over a period of 9 days, demonstrating material stability. Adapted from [3].

DOI 10.5162/EUROSENSORS2025/MP27

Single-Atom Metal Catalysts on Flame-Made Oxide Supports for Gas Sensing

Hamin Shin[1]*, *Andreas Güntner*[1]
[1]*Human-centered Sensing Laboratory, Department of Mechanical and Process Engineering, ETH Zürich, CH-8092, Zürich, Switzerland,*
hashin@ethz.ch

Summary:
We demonstrate a generalizable approach for synthesizing single-atom metal catalysts (SACs) on flame-made oxide supports by leveraging high densities of oxygen vacancies. Using Co_3O_4 as a model system, atomically dispersed Cu^{2+} species were stabilized without aggregation. This strategy is being extended to other support–metal combinations, offering a versatile materials design platform for gas sensing applications.

Keywords: single-atom catalysts, oxygen vacancies, flame spray pyrolysis, metal–support interaction, gas sensor materials

Background, Motivation and Objective

Single-atom catalysts (SACs) represent a frontier of gas sensor material design due to their unparalleled surface control and maximum atom utilization.[1] However, scalable synthesis of non-noble metal SACs remains challenging, especially under high-temperature conditions typical of sensor fabrication. In this work, we use flame spray pyrolysis (FSP) to synthesize oxide supports[2-4] with abundant surface oxygen vacancies[5]—thermodynamically favorable anchoring sites for SACs. Our goal is to establish a modular synthesis platform for various SAC-support systems beyond Cu-Co_3O_4, ultimately enabling tailored redox interfaces for improved gas sensing performances such as selectivity.[6]

Description of the New Method or System

The FSP process yields nanocrystalline oxide particles with high surface defect densities, particularly oxygen vacancies, which are exploited to immobilize transition metal atoms via post-synthetic wet impregnation and annealing. We demonstrate this approach using Cu on Co_3O_4 as a model, achieving 1.42 wt% loading of atomically dispersed Cu^{2+} without aggregation. EXAFS and XANES confirm the isolated, oxidized nature of Cu in square-planar coordination. The same methodology is being extended to alternative oxides and metal precursors to create a library of SAC-functionalized sensing materials. This work establishes a scalable and tunable pathway toward next-generation gas sensing platforms via vacancy-assisted SAC design.

Results

Elemental mapping (Fig. 1) revealed a homogeneous distribution of Cu atoms across the Co_3O_4 surface, with no evidence of clustering. EXAFS analysis (Fig. 2) confirmed the absence of Cu–Cu coordination, supporting the atomic dispersion of Cu^{2+} species. Together, these results validate the successful synthesis of stable, single-atom Cu catalysts on flame-made Co_3O_4 nanoparticles. These atomically dispersed sites translated into superior formaldehyde sensing performance, enabling high sensitivity at low operating temperature and enhanced selectivity under humid conditions.

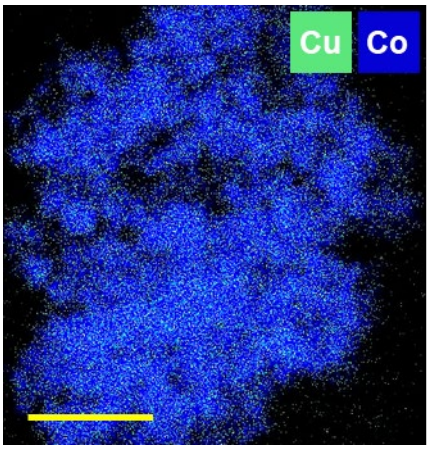


Fig. 1. EDS mapping on Co and Cu for Cu SAC-anchored Co_3O_4 (scale bar: 250 nm)

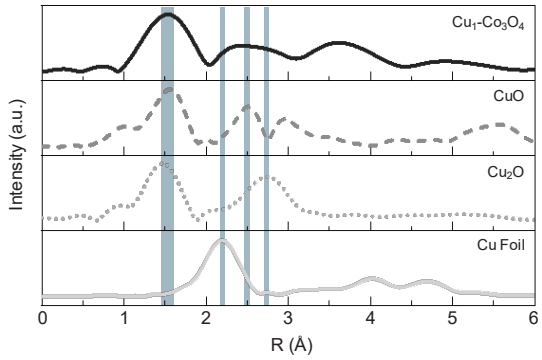


Fig. 2. Fourier transform radial distribution function of the Cu K-edge EXAFS spectra of Cu SAC-anchored Co_3O_4 and reference samples.

References

[1] G. Lei, H. Pan, H. Mei, et al., Emerging Single Atom Catalysts in Gas Sensors, *Chemical Society Reviews* 51, 7260-7280 (2022); doi: 10.1039/D2CS00257D

[2] A. T. Güntner, N. J. Pineau, S. E. Pratsinis, Flame-Made Chemoresistive Gas Sensors and Devices, *Progress in Energy and Combustion Science* 90, 100992 (2022); doi: 10.1016/j.pecs.2022.100992

[3] M. D'Andria, T. E. A.-R. Silva, E. Consogno, et al., Metastable $CoCu_2O_3$ Nanocrystals from Combustion-Aerosols for Molecular Sensing and Catalysts, *Advanced Materials* 36, 2408888 (2024); doi: 10.1002/adma.202408888

[4] M. D'Andria, F. Krumeich, Z. Yao, et al., Structure-Function Relationship of Highly Reactive CuO_x Clusters on Co_3O_4 for Selective Formaldehyde Sensing at Low Temperatures, *Advanced Science* 11, 2308224 (2024); doi: 10.1002/advs.202308224

[5] S. Liu, C. Dun, Q. Jiang et al. Challenging Thermodynamics: Combining Immiscible Elements in a Single-Phase Nano-Ceramic, *Nature Communications* 15, 1167 (2024); doi: 10.1038/s41467-024-45413-w

[6] P. M. Bulemo, D.-H. Kim, H. Shin, et al., Selectivitiy in Chemiresistive Gas Sensors: Strategies and Challenges, *Chemical Reviews* (2025); doi: 10.1021/acs.chemrev.4c00592

Acknowledgements

A.T.G. and H.S. acknowledge financial support by the Swiss State Secretariat for Education, Research, and Innovation (SERI) under contract number MB22.00041 (ERC-STG-21 "HEALTHSENSE") and by the Swiss National Science Foundation (grant 10001714).

DOI 10.5162/EUROSENSORS2025/MP28

Enhancing Selectivity Through Fast Heater Cycles with MOx Sensors

Nik Dennler[1] and Andreas Güntner[1]
[1]Human-centered Sensing Lab, ETH Zurich, Sonneggstrasse 3 8092 Zürich, Switzerland
dennlern@ethz.ch

Summary: Recent advances in MEMS-based metal-oxide (MOx) gas sensors offer new opportunities for high-speed sensing. Here we demonstrate that ultrafast heater cycling, achieved via precision hardware and feedback regulation, enables robust classification of odours on sub-second timescales. Phase-aligned feature extraction from heater-modulated sensor responses yields high classification accuracy, even for brief (20 ms) odour pulses. Beyond generic sensing, we propose that pairing this thermal modulation scheme with selectively engineered MOx films may enable compact, low-power gas sensors that combine temporal acuity with molecular selectivity.

Keywords: Fast heater cycling, MOx sensors, Odour classification, Electronic nose, Selective sensing

Introduction and Motivation

Sensing and interpreting volatile compounds in real time is critical for autonomous agents operating in complex and dynamic environments. While animals demonstrate olfactory processing on millisecond timescales [1, 2, 3], robotic olfactory systems based on metal-oxide (MOx) gas sensors often remain constrained by slow sensor dynamics and limited temporal resolution, rendering them suboptimal for tasks such as odour plume tracking or source localisation [4].

Recent advances in MEMS-based MOx sensor fabrication have enabled substantial reductions in thermal mass, offering the hardware foundation for faster operation [5]. However, most prior work has either relied on isothermal operation or employed slow heater modulation cycles (typically $> 1\,\mathrm{s}$), which limits the temporal fidelity of the recorded sensor response [6, 7].

Here we demonstrate a system for *ultrafast heater cycling*, achieving precise and reproducible temperature transitions on the order of tens of milliseconds [8]. We discuss that this not only improves responsiveness but also unlocks temporally structured sensor features suitable for robust and fast odour classification.

System Design for Fast-Cycled Heater Modulation

Our electronic nose system (Fig. 1a) employs MEMS-based MOx sensors, allowing for rapid thermal transitions when paired with appropriately tuned electronic control. Each sensor is coupled to an independent heater control loop, enabling dynamic temperature modulation at a resolution of $1\,\mathrm{kHz}$. Sensor resistance and heater current are sampled using simultaneous-sampling, 24-bit ADCs, while heater voltages are driven via high-linearity 12-bit DACs, minimising quantisation noise and transient artefacts [8].

We implement both *open-loop feedforward* and *adaptive closed-loop* control strategies to manage hotplate temperatures during fast cycling. A linearised model of the hotplate's thermal response is used for initial control, which is then refined by proportional correction in response to environmental perturbations such as airflow fluctuations. This hybrid control architecture maintains precise target temperatures during rapid transitions between 150 °C and 400 °C, with cycle durations as short as 50 ms (Fig. 1b).

Signal Processing and Classification

We extract discriminative features from rapidly cycled sensor data by segmenting the sensor output into windows aligned with the heater phase. Each window captures the transient resistance trajectory as the sensor transitions between two temperature setpoints. These segments are then baseline-normalised using a prestimulus reference and log-scaled to mitigate sensor-to-sensor variability and drift effects (Fig. 1c).

The resulting features represent short, high-dimensional trajectories in sensor space that are well-suited to data-driven classification. Classifiers trained only on long pulses ($1\,\mathrm{s}$) retained high performance when tested on much shorter pulses (e.g. $20\,\mathrm{ms}$), and accuracy remained robust even down to 20% of the trained odour concentration [8]. This suggests that heater-synchronised transients encode odour identity more effectively than steady-state signals.

Further, preliminary results suggest that the resulting data features may be subsampled without substantial loss in classification performance. On the mentioned odour discrimination tasks, we observed that downsampling the phase-aligned features by a factor of five—effectively reducing the temporal resolution from $1\,\mathrm{kHz}$ to $200\,\mathrm{Hz}$—led

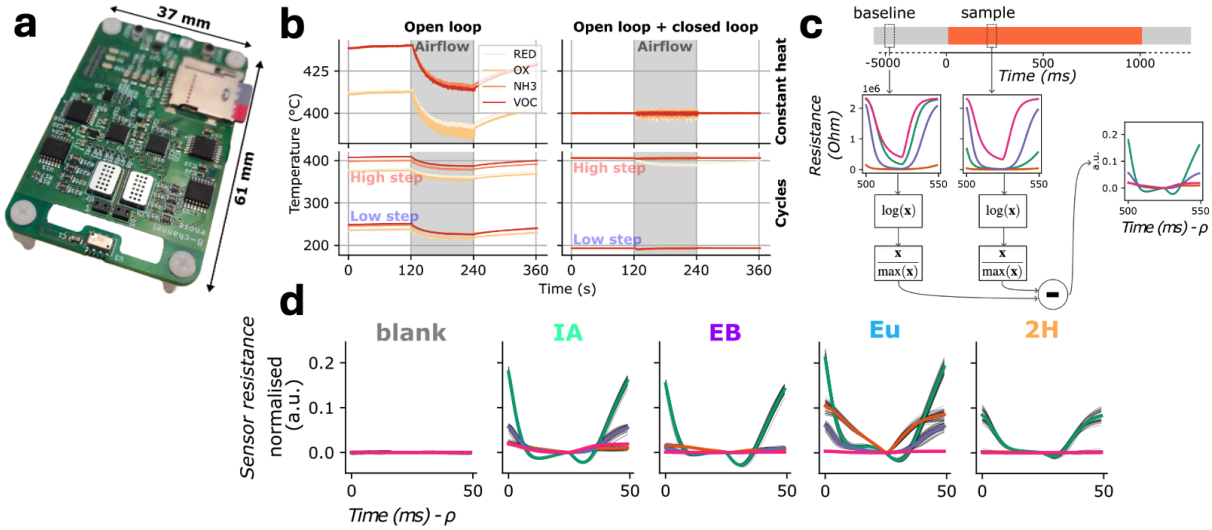


*Fig. 1: **a** Electronic nose circuitry. **b** Open-loop vs. open-loop + closed-loop control of sensor heaters, for constant heat and cycles. **c** Normalisation procedure for the heater modulation data feature. **d** Fifty-millisecond normalised data feature for different gases. Odorants abbreviations: IA, isoamyl acetate; EB, ethyl butyrate; EU, cineol; 2H, 2-heptanone; blank, odorless control. Figure panels and captions adapted from Dennler et al. [8] CC-BY.*

to an accuracy drop of less than one percentage point. This indicates that the most informative components of the transient response are preserved at lower sampling rates, opening possibilities for further reductions in data bandwidth, energy consumption, and computational load in embedded or low-power applications.

Extensions to Selective MOx Sensor Design

The fast cycling approach is broadly compatible with structurally and chemically tailored MOx sensing films. Selectivity enhancements achieved via nanoparticle size, film thickness, porosity, or dopant type [9, 10] could be harnessed by pairing them with rapid temperature modulation. This may enable time-resolved gas fingerprints unique to both analyte and material.

In particular, the combination of engineered film properties with heater-driven transient responses could form the basis of compact selective sensors operating at high temporal resolution—suitable for mobile or embedded deployments in robotics, environmental sensing, or health diagnostics.

Conclusion and Outlook

Fast heater cycling dramatically enhances the temporal resolution of MOx-based electronic noses, enabling robust classification of odours on sub-second timescales. Our system achieves millisecond-scale odour recognition through a combination of high-bandwidth sensor interfacing, rapid thermal control, and phase-locked feature extraction. These results demonstrate that even commercially available MOx sensors, when modulated at high speed, can rival the temporal performance previously thought exclusive to biological systems.

Looking ahead, this sensing paradigm invites new directions in sensor material design, where selective MOx films engineered for transient response can be matched with fast modulation schemes. Such integration could pave the way for compact, field-deployable systems capable of disentangling complex odour scenes with high specificity and temporal fidelity.

References

[1] P. Szyszka, R. C. Gerkin, C. G. Galizia, and B. H. Smith, “High-speed odor transduction and pulse tracking by insect olfactory receptor neurons,” *Proceedings of the National Academy of Sciences*, vol. 111, no. 47, pp. 16925–16930, 2014.

[2] S. Krofczik, “Rapid odor processing in the honeybee antennal lobe network,” *Frontiers in Computational Neuroscience*, vol. 2, 2008.

[3] T. Dekker and R. T. Cardé, “Moment-to-moment flight manoeuvres of the female yellow fever mosquito (*Aedes aegypti* L.) in response to plumes of carbon dioxide and human skin odour,” *Journal of Experimental Biology*, vol. 214, pp. 3480–3494, Oct. 2011.

[4] A. J. Lilienthal, A. Loutfi, and T. Duckett, “Airborne chemical sensing with mobile robots,” *Sensors*, vol. 6, no. 11, pp. 1616–1678, 2006.

[5] E. L. W. Gardner, J. W. Gardner, and F. Udrea, “Micromachined Thermal Gas Sensors—A Review,” *Sensors*, vol. 23, p. 681, Jan. 2023.

[6] Y. Xing, T. A. Vincent, M. Cole, and J. W. Gardner, “Real-time thermal modulation of high bandwidth MOX gas sensors for mobile robot applications,” *Sensors*, vol. 19, no. 5, p. 1180, 2019.

[7] S. Nakata and N. Takahara, “Characteristic nonlinear responses of a semiconductor gas sensor to hydrocarbons and alcohols under the combination of cyclic temperature and continuous flow,” *Sensors and Actuators B: Chemical*, vol. 307, p. 127635, 2020.

[8] N. Dennler, D. Drix, T. P. Warner, S. Rastogi, C. D. Casa, T. Ackels, A. T. Schaefer, A. van Schaik, and M. Schmuker, “High-speed odor sensing using miniaturized electronic nose,” *Science Advances*, vol. 10, no. 45, p. eadp1764, 2024.

[9] J. van den Broek, S. Abegg, S. E. Pratsinis, and A. T. Güntner, “Highly selective detection of methanol over ethanol by a handheld gas sensor,” *Nature communications*, vol. 10, no. 1, p. 4220, 2019.

[10] I. C. Weber, P. Rüedi, P. Šot, A. T. Güntner, and S. E. Pratsinis, “Handheld device for selective benzene sensing over toluene and xylene,” *Advanced Science*, vol. 9, no. 4, p. 2103853, 2022.

DOI 10.5162/EUROSENSORS2025/MP29

Evaluation of a MEMS-based Absolute Humidity Sensor using Thermal Conductivity

Sophie Emperhoff [1,2], *Matthias Eberl*[2] *and Jürgen Wöllenstein*[1,3]
[1] Department of Microsystems Engineering (IMTEK), Albert-Ludwigs-Universität Freiburg, 79110 Freiburg im Breisgau, Germany
[2] Infineon Technologies AG, 81549 Neubiberg, Germany
[3] Fraunhofer Institute for Physical Measurement Techniques, 79110 Freiburg im Breisgau, Germany
sophie.emperhoff@infineon.com

Summary: Thermal conductivity sensors, which are often used to measure gases such as hydrogen, are influenced by humidity changes. While this usually leads to challenges in compensating these effects, we are investigating the potential of thermal conductivity sensors as humidity sensors. Using a gas mixing model from Melling, it is shown that thermal conductivity sensors have limitations at low to medium humidity levels. In environments with high temperatures and humidity, where common relative humidity sensors often have problems, thermal conductivity sensors offer a significant potential for accurate measurements.

Keywords: thermal conductivity, absolute humidity, MEMS, humidity sensor

Background

In our previous work, we investigated the impact of humidity on a thermal conductivity sensor for the detection of hydrogen [1, 2]. This measurement principle is particularly well-suited for hydrogen detection due to its high thermal conductivity. Humidity usually poses challenges for thermal conductivity gas sensors as it affects the resulting thermal conductivity of the gas mixture. Nevertheless, this sensitivity to humidity can also be utilized.
Okcan and Akin e.g. demonstrated the use of a thermal conductivity sensor to measure the relative humidity at $20°C$, $30°C$ and $40°C$. They observed a nearly linear response of the sensor [3]. Essing et al. used the thermal conductivity changes caused by humidity to compensate for humidity influences in their photoacoustic sensor [4]. Kimura introduces a method to measure absolute humidity changes using a single micro-air-bridge heater while compensating for the ambient temperature [5].
In this short paper, we want to evaluate whether a MEMS-based thermal conductivity sensor such as the one used in prior investigations can also be used as a low-cost absolute humidity sensor for specific applications.

Materials and Methods

In this study, we employ an adapted model provided by Melling et al. [6] which is based on a gas mixing equation introduced by Mason and Saxena [7]. We have previously validated this model using our thermal conductivity sensor and two other commercially available thermal conductivity sensors, demonstrating that it can describe the behavior of thermal conductivity sensors towards absolute humidity [2]. The thermal conductivity as a function of absolute humidity, as predicted by Melling's model, is illustrated in figure 1. The graph displays the thermal conductivity of a gas mixture containing air and water vapor in the range of 0 to 100% relative humidity at the respective temperature.

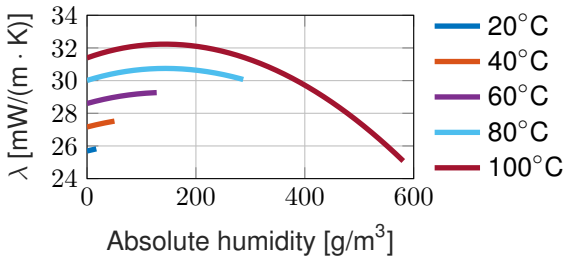


Fig. 1: Thermal conductivity of humid air across absolute humidity according to Melling et al. [6]

Results

A limiting factor of thermal conductivity humidity sensors is notable in figure 1. The parabolic shape of the function indicates that a single thermal conductivity value can correspond to two distinct humidity values. To avoid ambiguity, the measurement environment must be constrained to a specific range of humidity.
We can estimate the performance of our thermal conductivity sensor towards sensing humidity by determining the humidity resolution of the sensor using the derivative of thermal conductivity with respect to the absolute humidity and the noise level of the sensor.

$$resolution = \frac{3 \cdot \lambda_{rms}}{\frac{d\lambda}{dAH}} \tag{1}$$

Figure 2 illustrates the derivative of the thermal conductivity with respect to absolute humidity

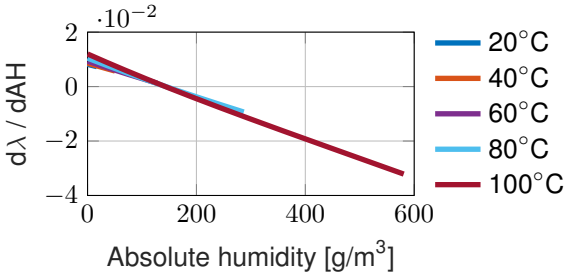


Fig. 2: Derivative of the thermal conductivity with respect to the absolute humidity (AH) according to simulation over the absolute humidity range.

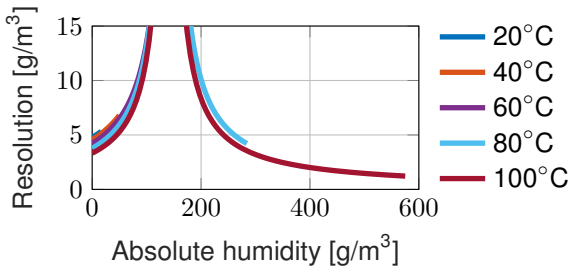


Fig. 3: Resolution according to simulation over the absolute humidity range assuming a rms noise of $0.013\ mW/(m \cdot K)$.

(AH). It shows that the sensitivity of the sensor varies substantially across the evaluated range. The highest sensitivity can be reached at higher temperatures. At the peak point of the humidity dependence, the sensitivity has a zero crossing. Assuming a root mean square (rms) noise λ_{rms} of approximately $0.013\ mW/(m \cdot K)$, we can estimate the resolution using equation 1. The resulting resolution is displayed in figure 3, demonstrating that it is influenced by both temperature and humidity level. As expected, the resolution improves at higher temperatures. Between 100 to $200\ g/m^3$, the resolution undergoes a significant increase due to the zero crossing, after which it decreases with increasing humidity and approaches zero.

Tab. 1: Estimated resolution of a humidity sensor based on thermal conductivity assuming a rms noise level of $0.013 mW/(m \cdot K)$*. The resolution is given in %RH dependent on the relative humidity level and the temperature.*

RH [%]	20°C	40°C	60°C	80°C	100°C
0	28.0	9.0	3.3	1.3	0.6
20	28.6	9.7	4.0	2.3	3.5
40	29.2	10.5	5.1	7.1	0.9
60	29.9	11.3	7.1	6.8	0.4
80	30.5	12.4	11.1	2.3	0.3
100	31.2	13.5	23.9	1.5	0.2

To allow a comparison with standard relative humidity sensors, we calculated the estimated resolution as a function of relative humidity level and temperature, expressed in %RH (see table 1). The results indicate that a thermal conductivity sensor is outperformed by standard relative humidity sensors below $100°C$. However, at higher temperatures and high humidities, relative humidity sensors often experience limitations whereas the estimated resolution for a thermal conductivity sensor significantly improves. This suggests that a thermal conductivity sensor has significant potential for applications requiring the measurement of small changes in humidity at high temperatures and absolute humidities. Furthermore, a physical measurement principle like thermal conductivity, leads to a very stable sensor and is less prone to aging and drifting. Averaging and data processing can further increase the performance of the sensor.

References

[1] S. Emperhoff, M. Eberl, T. Dwertmann, and J. Wöllenstein, “Humidity Impact on Thermal Conductivity Sensors,” in *MDPI Proceedings*, (Lecce, Italy), 2023.

[2] S. Emperhoff, M. Eberl, T. Dwertmann, and J. Wöllenstein, “On the Influence of Humidity on a Thermal Conductivity Sensor for the Detection of Hydrogen,” *Sensors*, vol. 24, no. 9, p. 2697, 2024.

[3] B. Okcan and T. Akin, “A thermal conductivity based humidity sensor in a standard CMOS process,” in *17th IEEE International Conference on Micro Electro Mechanical Systems. Maastricht MEMS 2004 Technical Digest*, (Maastricht, Netherlands), pp. 552–555, IEEE, 2004.

[4] S. Essing, M. Trautmann, D. Tumpold, and G. Schrag, “Humidity Sensing for free—advanced thermoacoustic signal models in miniaturized photoacoustic gas sensors,” in *2023 24th International Conference on Thermal, Mechanical and Multi-Physics Simulation and Experiments in Microelectronics and Microsystems (EuroSimE)*, (Graz, Austria), pp. 1–4, IEEE, Apr. 2023.

[5] M. Kimura, “Absolute-humidity sensing independent of the ambient temperature,” *Sensors and Actuators A: Physical*, vol. 55, no. 1, 1996.

[6] A. Melling, S. Noppenberger, M. Still, and H. Venzke, “Interpolation Correlations for Fluid Properties of Humid Air in the Temperature Range 100 ℃ to 200 ℃,” *Journal of Physical and Chemical Reference Data*, vol. 26, pp. 1111–1123, July 1997.

[7] E. A. Mason and S. C. Saxena, “Approximate Formula for the Thermal Conductivity of Gas Mixtures,” *Physics of Fluids*, vol. 1, no. 5, p. 361, 1958.

DOI 10.5162/EUROSENSORS2025/MP30

Electro-Optical Gas Sensing Characteristics of PEDOT:PSS Thin Films

*Z. Hamzei [1], I. Gràcia[1], E. Figueras[1], S. Vallejos[1]**
[1]Institute of Microelectronics of Barcelona (IMB-CNM, CSIC), Campus UAB, Barcelona
** Stella.Vallejos@imb-cnm.csic.es*

Summary:
A gas sensor was developed by depositing a PEDOT: PSS thin film onto glass-based platforms with interdigitated electrodes. Its properties were evaluated at room temperature (24 °C) using UV-Vis spectroscopy and electrical measurements towards various gases at a fixed concentration of 40 ppm. The sensor exhibited promising optical and electrical responses to hydrogen and acetone, while ethanol and ethylene showed weaker responses. These findings demonstrate the potential of PEDOT: PSS-based sensors for electro-optical gas sensing and improved selectivity.

Keywords: PEDOT: PSS, Optical gas sensing, Resistive gas sensing

Background, Motivation and Objective

Poly(3,4-ethylenedioxythiophene) polystyrene sulfonate (PEDOT: PSS) is a conductive polymer known for its unique electrical and optical properties, including sensitivity to various gases. However, its inherently low conductivity limits its sensing performance, necessitating modifications through solvent treatment. In this study, dimethyl sulfoxide (DMSO) was used to enhance the electrical and optical properties of PEDOT: PSS by influencing its structure and conductivity [1]. PEDOT: PSS holds considerable promise for gas sensing applications in diverse fields, including environmental monitoring, agriculture, and chemical detection. Improving its electrical and optical properties is key to enhancing its sensitivity and selectivity, especially for detecting specific volatile organic compounds (VOCs) such as alcohols, aldehydes, and isoprene [2]. This work presents the fabrication of a microsensor by depositing a PEDOT: PSS thin film onto a glass-based platform with interdigitated electrodes. The sensor operates at room temperature and demonstrates promising electrical and optical responses to gases/vapors such as hydrogen, ethanol, acetone, and ethylene, highlighting its potential for practical gas sensing applications.

Results

The SEM image of the PEDOT: PSS film (Figure 1-A), deposited via drop-coating on a silicon substrate using DMSO as the solvent, reveals a uniform film with excellent substrate coverage. The UV-Vis analysis of the PEDOT: PSS film (Figure 1-B) showed a sharp peak at 303 nm, corresponding to the PSS component, indicating well-defined absorption characteristics. Additionally, the PEDOT component exhibited a broad absorption spanning the visible to near-infrared range (400–1200 nm), reflecting its delocalized charge carriers and conductive nature.

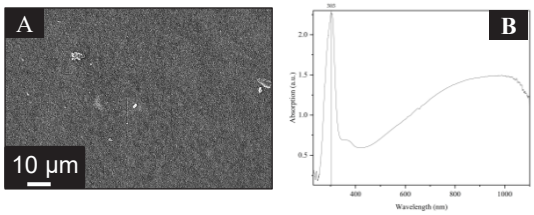


Figure 1. A- SEM image of PEDOT: PSS film deposited by drop-coating on a silicon substrate, with a scale bar of 10 µm. The image reveals a uniform film with excellent substrate coverage, indicative of successful deposition and film integrity. B- UV-Vis absorption spectrum of PEDOT: PSS film showing a sharp peak at 303 nm corresponding to the PSS component and a broad absorption band in the 400–1200 nm range attributed to the PEDOT component.

The surface of the PEDOT film was analyzed using X-ray photoelectron spectroscopy (XPS). The survey scan identified the primary elements in the film, including carbon (C), oxygen (O), and sulfur (S), with minor peaks for silicon (Si) and sodium (Na). The presence of Si is attributed to the silicon substrate, while Na is a result of its use in the PEDOT synthesis process. This analysis provides valuable insight into the film's elemental composition and the contributions of both the PEDOT material and the substrate.

For gas sensing applications, PEDOT: PSS was drop-coated onto a glass-based platform with conductive ITO electrodes. Electrical and optical

measurements were conducted at room temperature under a fixed gas concentration of 40 ppm. Optical measurements were performed at two key wavelengths: 299 nm, corresponding to the PSS component, and 1002 nm, corresponding to the PEDOT component. The film was exposed to hydrogen, ethanol, acetone, and ethylene gases. As shown in Figure 2, hydrogen and acetone elicit the strongest electrical and optical responses, with lower responses observed for ethanol and ethylene.

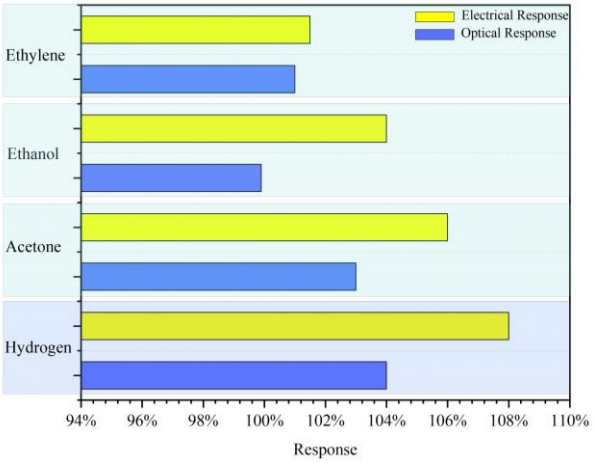


Figure 2- Electrical and optical responses of PEDOT:PSS film exposed to hydrogen, ethanol, acetone, and ethylene gases at a fixed concentration of 40 ppm. The results indicate that hydrogen and acetone elicit the strongest electrical and optical responses, with ethanol and ethylene showing comparatively lower signals.

In the electro-optical diagrams for hydrogen (H_2) and acetone (Ac), both the optical and electrical responses are shown together in a single plot (Fig. 3). The X-axis represents time, illustrating the progression of optical and electrical changes (Y-axis) during gas exposure. The sections corresponding to the presence of each gas are highlighted, facilitating easier comparison of the optical and electrical responses.

This presentation enables a clear comparison of the film's behavior under hydrogen and acetone exposure. The stronger sensor response to hydrogen is attributed to its higher polarity compared to ethanol, which enhances its interaction with the PEDOT: PSS film. Likewise, the smaller molecular size of acetone relative to ethylene allows for easier diffusion into the film, resulting in greater charge transfer and enhanced sensor responses. The results demonstrate significant potential by integrating two distinct response outputs—electrical and optical—within a single device. This dual-mode sensing approach could offer key advantages, such as enhanced gas discrimination and improved selectivity. By combining these outputs, the need for large sensor arrays typically used in electronic noses can be reduced, simplifying system design while maintaining or even increasing performance.

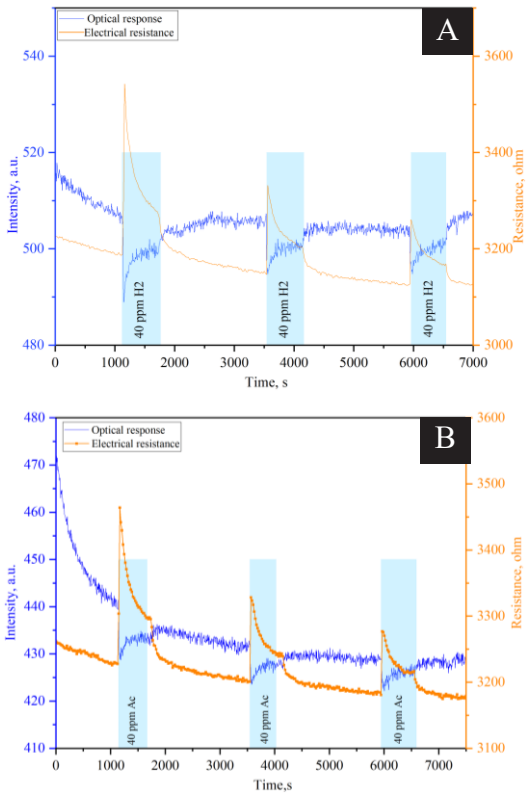


Figure 3- *Electro-optical response of the PEDOT: PSS film upon exposure to 40 ppm hydrogen (A) and 40 ppm acetone (B) at 299 nm. The plots illustrate simultaneous optical and electrical measurements over time, with highlighted sections indicating gas presence.*

References

[1] Lin, Y. J., Lee, J. Y., & Chen, S. M. (2016). Changing electrical properties of PEDOT: PSS by incorporating with dimethyl sulfoxide. Chemical Physics Letters, 664, 213-218.

[2] Bai, H., & Shi, G. (2007). Gas sensors based on conducting polymers. Sensors, 7(3), 267-307.

Acknowledgements

This work has been realized in the framework of the AGRARSENSE project supported by the Chips JU and the European Union (Grant agreement No. 101095835).

DOI 10.5162/EUROSENSORS2025/MP31

Ethanol sensing at room temperature via ZnS nanostructure-based optical approach

Houyem Trabelsi[1,2], Isabel Gràcia[1], Khaled Alouani[2], Carles Cané[1], Stella Vallejos[*,1]

[1] Institute of Microelectronics of Barcelona (IMB-CNM, CSIC), Barcelona, Spain

[2] University of Tunis El Manar, Faculty of Science, Tunis, Tunisia

* stella.vallejos@imb-cnm.csic.es

1. Summary

A novel approach for synthesizing zinc sulfide (ZnS) nanostructures via aerosol-assisted chemical vapor deposition (AACVD) technique is developed. These ZnS structures are characterized and tested upon a series of gases, demonstrating optical responses to ethanol at room temperature (RT).

Keywords: Optical sensor, ZnS nanostructures, Ethanol, AACVD

2. Background and motivation

Metal sulfide (MS) materials have gained significant attention for gas sensing applications due to their tunable optoelectronic properties, high surface reactivity, and capability to function at room temperature [1,2]. Among these materials, zinc sulfide (ZnS) stands out with its wide bandgap (3.5 - 3.7 eV), chemical stability, and exceptional optical properties [3]. These characteristics make ZnS not only an excellent candidate for conventional resistive gas sensors but also a promising material for alternative optical sensing techniques, particularly due to its potential to operate effectively at room temperature (RT). Despite these advantages the use of ZnS in optical gas sensors has been scarcely reported in the literature. Additionally, the synthesis of ZnS structures via AACVD remains largely unexplored. To address these gaps, this study presents a novel route for synthesizing ZnS structures using the AACVD technique, and evaluates their performance as optical gas sensors at RT.

3. Results and discussion

3.1. Films characterization

ZnS nanostructures were successfully deposited on silicon substrates at 450 ºC using a mixture of $ZnCl_2$ and $Et_4P_2S_2$ ligands via the AACVD technique.

X-ray diffraction (XRD) analysis confirmed the crystalline nature of the material, with diffraction peaks corresponding to the cubic phase (ICDD card no. 01-086-8934) and a preferred orientation along the [111] direction (Figure 1).

Top-view and cross-sectional SEM images of the ZnS nanostructures revealed leaf-like morphology with an approximate length of 600 nm (Figure 2).

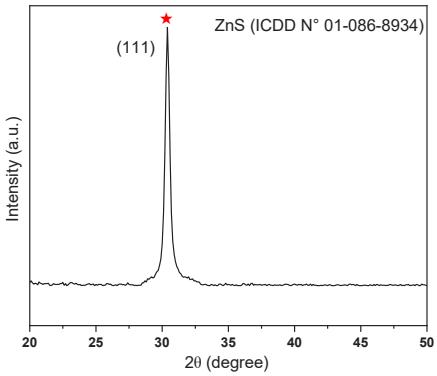


Figure 1. *XRD pattern of ZnS deposited on Si substrates by AACVD at 450 ºC.*

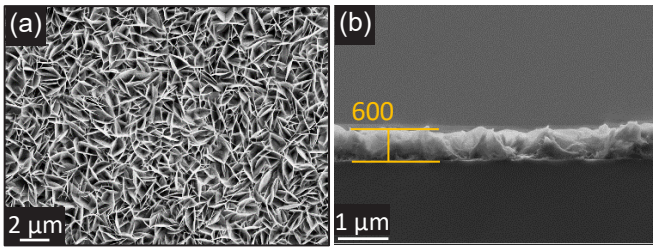


Figure 2. *(a) Top view and (b) cross-sectional SEM images of ZnS structures deposited on Si substrates by AACVD at 450 ºC.*

The surface of the nanostructures was examined using XPS analysis, as shown in Figure 3. The survey scan of the ZnS films identifies the main elements (Zn 2p and S 2p) present in the film, with minor phosphorus contamination attributed to the ligand $Et_4P_2S_2$.

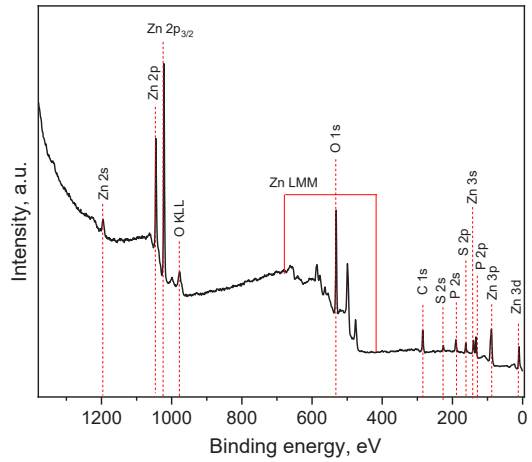


Figure 3. *XPS survey scan of ZnS structures deposited on Si substrates by AACVD at 450 ºC.*

3.2. Gas sensing test

ZnS structures were deposited onto ITO/glass substrates and evaluated as gas-sensors towards ethanol, acetone, and ethylene at room temperature in dry air. The measurements were performed under illumination from a light source covering a wavelength range of 200–1100 nm, and the response was recorded as the transmittance intensity.

The sensor demonstrated a significant response in the 355–380 nm wavelength range, showing a noticeable change in intensity upon exposure to 60 ppm of ethanol (Figure 4.a)., while displaying negligible sensitivity to acetone (Figure 4.b). Moreover, no detectable response was observed for 20 ppm of ethylene (Figure 4.c). These findings highlight the sensor's sensitivity and selectivity toward ethanol.

This study demonstrate that ZnS can optically sense ethanol at RT offering a significant advantage in terms of power consumption. Unlike earlier approaches that relied on electrical resistance measurements, which required high operating temperatures or additional functionalization with catalytic nanoparticles like gold [4].

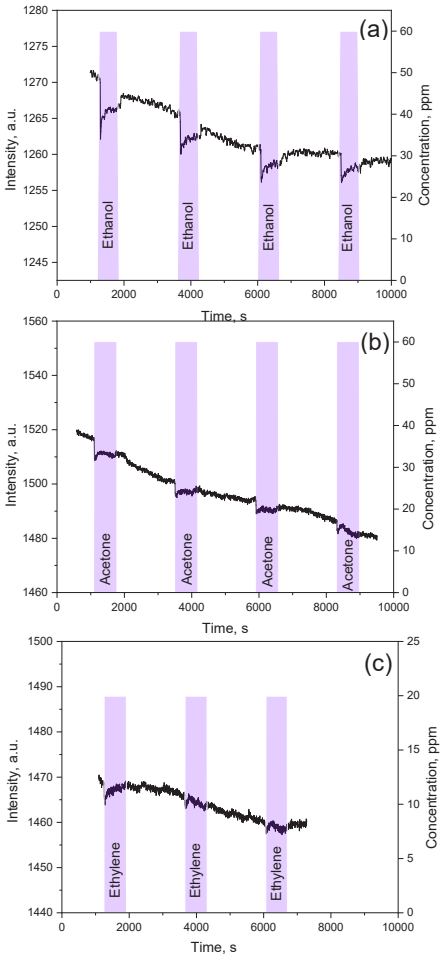


Figure 4. *Typical optical responses recorded on the ZnS nanostructure to (a) ethanol, (b) acetone, and (c) ethylene at RT. The purple bars represent the periods of gas injection and its concentration.*

References

[1] B. Chatterjee y A. Bandyopadhyay, *Materials Science and Engineering: B*, vol. 297, p. 116781, nov. 2023, doi: 10.1016/j.mseb.2023.116781.

[2] H. Tang, L. N. Sacco, S. Vollebregt, H. Ye, X. Fan, y G. Zhang, *J. Mater. Chem. A*, vol. 8, n.º 47, pp. 24943-24976, 2020, doi: 10.1039/D0TA08190F.

[3] M. Alzaid, W. S. Mohamed, M. El-Hagary, E. R. Shaaban, y N. M. A. Hadia, *Optical Materials*, vol. 118, p. 111228, ago. 2021, doi: 10.1016/j.optmat.2021.111228.

[4] L. Zhang, R. Dong, Z. Zhu, y S. Wang, *Sensors and Actuators B: Chemical*, vol. 245, pp. 112-121, jun. 2017, doi: 10.1016/j.snb.2017.01.179.

Acknowlegements

This work was carried out under the AGRARSENSE project, funded by the Chips JU and its members via Grant Agreement No. 101095835, the MCIN/AEI/10.13039/501100011033 via Grant PCI2022-135006-2, and the European Union Next Generation EU/PRTR. Support through the María de Maeztu grant CEX2023-001397-M, funded by MICIU/AEI/10.13039/501100011033, is also acknowledged.

DOI 10.5162/EUROSENSORS2025/MP32

MoS_2-InSe heterostructure synthesized via Liquid Phase Exfoliation for NO_2 sensing

Jyayasi Sharma[1], Dalal Fadil[1] , Eduard Llobet[1]
[1] Departament d'Enginyeria Electronica, Universitat Rovira i Virgili, Països Catalans 26, 43007 Tarragona, Spain.

Corresponding Author's e-mail address: eduard.llobet@urv.cat

Summary:

Designing sensitive NO_2 gas sensors is essential for detecting and mitigating hazardous effects on health and the environment, such as respiratory difficulties, acid rains, and industrial pollution. Conventional metal oxide based NO_2 sensors exhibit low selectivity and high operating temperatures. Two-dimensional materials are now the focus. Meanwhile, bare TMD sensors have shortcomings such as high LOD and poor response in humid conditions. This study presents a highly sensitive InSe-MoS_2 heterostructure based NO_2 sensor, with remarkable responses, even in the presence of ambient moisture (50% RH).

Keywords: Gas sensor, TMDs, NO_2, LPE, nanomaterials

Background, Motivation and Objective

Nitrogen dioxide (NO_2) is a major air pollutant caused by combustion activities, including automobile emissions and industrial activity. Accurate and prompt NO_2 detection is crucial because of its detrimental impacts on the environment and human health, including respiratory problems and its part in the emission of pollution such as acid rain and smog. Metal oxide gas sensors (MOX) have been utilized extensively in the past, however they have limitations such as high operating temperatures and low selectivity. For enhanced sensing capabilities, two-dimensional (2D) materials like graphene and transition metal dichalcogenides (TMDs) like Indium selenide (InSe) and Molybdenum disulfide (MoS_2) have recently drawn interest.
InSe and MoS_2 have garnered significant interest due to their exceptional properties. Various research works have demonstrated the potential of InSe and MoS_2-based sensors for detecting gases including NO_2. However, bare InSe and bare MoS_2 sensors face challenges like sluggish responses in presence of ambient humidity. Producing heterostructures from TMD materials can actually improve the sensing performance[1,2]. In this study, a highly sensitive InSe-MoS_2 heterostructure for NO_2 sensing is presented with superior performance with anti-humidity capabilities, exhibiting high responses.

Materials and Methods

InSe and MoS_2 are obtained using the liquid phase exfoliation (LPE) process, which involves exfoliating 10 mg of InSe and 10 mg of MoS_2 in IPA solution, respectively. The resulting exfoliated solutions were drop casted onto three silicon substrates with gold interdigitated electrodes. The Pristine MoS_2 sensor is made using a first substrate coated with an exfoliated MoS_2 solution. The second substrate was coated with an exfoliated InSe solution, resulting in a pristine InSe sensor, while the third is a hybrid sensor composed of a InSe-MoS_2 heterostructure coated with the two previous solutions layer by layer forming heterojunction of InSe and MoS_2.

Results

Fig. 1 (a,b and c) illustrates morphology of InSe, MoS_2 and heterostructure respectively. As seen from the Field Emission Scanning Electron Microscopy (FESEM) images, the deposited sensors depict flaky morphology and heterostructure shows the complete covering of the substrate layer by layer. Also, the InSe nanoflakes can be seen in the form of flower-like structures (in red circles) (Fig. 1 (a)). The samples were further characterized using Scanning Electron Microscopy (ESEM). Color mapping of the samples show successful layering of InSe with MoS_2 nanoflakes as shown in Fig. 2 (a). Fig. 2 shows EDX spectrum of the InSe-MoS_2. We tested Pristine InSe, Pristine MoS2 and InSe-MoS_2 Heterostructure sensors towards 1 ppm of NO_2 at different operating temperatures - (RT), 100°C,150°C, 200°C and 250°C in presence of 50% R.H. The sensor based on InSe-MoS_2 heterostructure exhibited

the highest response of 48% compared to Pristine sensors.

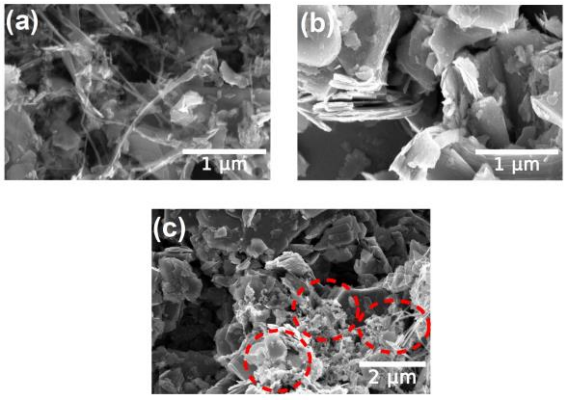


Fig. 1. FSESM images of (a) Pristine InSe, (b) Pristine MoS_2, (c) InSe-MoS_2 (Red circles indicate InSe nanoflakes).

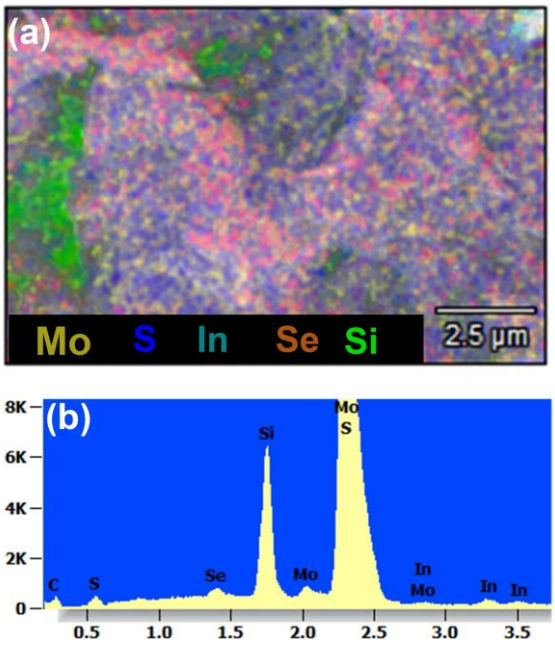


Fig. 2. (a) Color mapping of MoS_2-InSe heterostructure (b) EDS spectrum of MoS_2-InSe heterostructure

The optimum temperature came out to be 200°C. Fig. 3 (a) illustrates the sensor resistance dynamics towards 1 ppm of NO_2 at 200°C (50% of R.H.). The pristine InSe sensor showed 6% response and pristine MoS_2 sensor showed 41% response to 1 ppm of NO_2, very less than the responses shown by the best sensor at all temperatures. The sensor responses are stable and repeatable. Fig. 3 (b) demonstrates the sensor response for lower concentrations of NO_2 at optimum temperature of 200°C with 50% R.H. A detailed selectivity and operating temperature study will be presented at the conference.

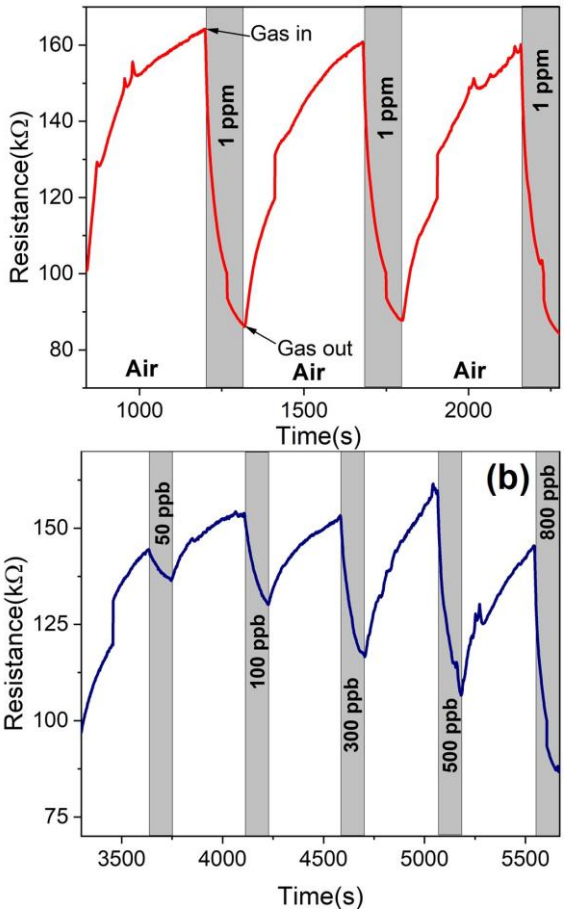


Fig. 3. (a) Resistance dynamics of InSe-MoS_2 sensor towards 1 ppm of NO_2 (50% of R.H.) at optimum temperature (b) InSe-MoS_2 sensor response towards lower concentrations of NO_2 (50% of R.H.).

Conclusions

This study presents a highly sensitive InSe-MoS_2 heterostructure for NO_2 sensing, achieving a remarkable 48% response under 50% R.H.

References

[1] W. Li, M. Shahbazi, K. Xing, T. Tesfamichael, N. Motta, D.C. Qi, Highly Sensitive NO2 Gas Sensors Based on MoS2@MoO3 Magnetic Heterostructure, Nanomaterials 12 (2022). https://doi.org/10.3390/nano12081303.

[2] J. Le Fan, X.F. Hu, W.W. Qin, Z.Y. Liu, Y.S. Liu, S.J. Gao, L.P. Tan, J.L. Yang, L.B. Luo, W. Zhang, UV-light-assisted gas sensor based on PdSe2/InSe heterojunction for ppb-level NO2 sensing at room temperature, Nanoscale 14 (2022). https://doi.org/10.1039/d2nr03881a.

Acknowledgements

J.S. is supported by the predoctoral program AGAUR-FI SDUR under grant no. 2022 FI SDUR 00307 of the Department of Research and Universities of the Government of Catalonia and the European Social Plus Fund.

DOI 10.5162/EUROSENSORS2025/MP33

In-depth Characterisation of a Colorimetric Label for Formaldehyde Monitoring.

María González-Gómez[1,2], Anna Zymohliad[1], Ismael Benito-Altamirano[1,3], Olga Casals[1], J. Daniel Prades[2], Cristian Fàbrega[1].

[1] MIND/IN2UB, Dept. of Electronics and Biomedical Engineering, University of Barcelona, Marti i Franqués 1, Barcelona, ES08028, Spain.

[2] Institute of Semiconductor Technology (IHT), Laboratory for Emerging Nanometrology (LENA), Technische Universität Braunschweig, 38106 Braunschweig, Germany.

[3] eHealth Center, Faculty of Computer Science, Multimedia and Telecommunications, Universitat Oberta de Catalunya, Rambla del Poblenou 156, Barcelona, ES08018, Spain

lugosagonzalez@ub.edu

Summary:

A simple, easy-to-maintain colorimetric label has been developed to monitor formaldehyde at ppb levels, designed for cost-effective large-scale production. The detection of gaseous formaldehyde occurs through a specific chemical reaction which ensures selectivity. This reaction increases the acidity, leading to the protonation of a pH indicator that causes a color change from green to yellow. The colorimetric label is incorporated into a commercial readout chip, which measures both reflected and transmitted light. The sensor can instantly monitor formaldehyde concentrations between 100 and 600 ppb with excellent repeatability across devices.

Keywords: formaldehyde, colorimetric sensor, gas detection, pH indicator, dosimeter

Background, Motivation and Objective

The reliability of formaldehyde sensors is often questioned due to issues such as cross-sensitivity to interfering gases, degradation of sensing materials, and insufficient sensitivity in the ppb range [1]. Formaldehyde is a challenging analyte, as its detection is only relevant around strict exposure thresholds—such as those established by the European Union and OSHA—typically between 60 and 100 ppb. In this context, even minimal interaction with external factors may compromise the accuracy and reliability of the sensor.

Colorimetric sensors have historically demonstrated the best performance in terms of selectivity and sensitivity for formaldehyde detection [2], [3]. However, most reported systems exhibit irreversible responses, behaving as dosimeters without the capability to provide real-time or continuous readings. Despite their promising characteristics for short-term or point measurements, this sensing approach has been underexplored for monitoring purposes. Consequently, a detailed investigation into the limits and capabilities of colorimetric sensors as monitoring devices is lacking. This study addresses this gap by developing and characterizing a robust colorimetric sensor capable of low-level formaldehyde detection with high reproducibility and stability under varying environmental conditions.

Description of the New Method or System

The proposed sensor consists of a replaceable colorimetric label impregnated with an optimized sensitive substance, engineered to maintain a stable and reliable response to formaldehyde for at least one week. This advancement introduces a paradigm shift: despite the irreversible nature of the underlying chemical reaction, it becomes possible to correlate the optical response of the sensor—such as intensity and kinetics—with the gas concentration. As a result, the system enables quantitative monitoring without the need for individual pre-configuration of the colorimetric element (understood as setting a zero-reference point).

The label is integrated into a cost-effective commercial readout chip equipped with multiple LEDs and a broadband photodetector, allowing measurement of both reflected and transmitted light during gas exposure. The interaction between formaldehyde and the sensing material triggers a nucleophilic addition reaction with a primary amine, forming an imine. This reaction increases the local acidity and leads to the protonation of a pH indicator, causing a visible color change from green to yellow. While the reaction is irreversible and the sensor is not intended for long-term reuse, the device is ideally suited for personal exposure monitoring—particularly in occupational environments—over extended periods such as an 8-hour work shift or longer.

Results

In the first stage, several components of the formulated ink were evaluated and varied to extend the lifetime and stability of the sensitive element. Once the formulation exhibited optimal performance in terms of reactivity and stability, a comprehensive calibration procedure was carried out. This involved exposing the sensor to a range of formaldehyde concentrations under varying humidity conditions to assess the consistency and reliability of the optical response (Figure 1).

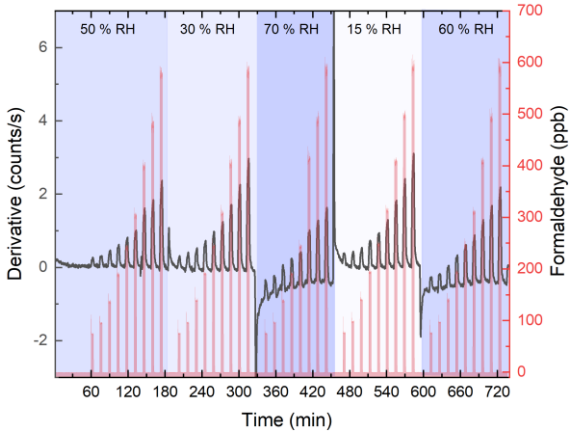


Fig. 1. Response of the sensor to 100 – 600 ppb formaldehyde range in varying humidity conditions.

It was observed that humidity plays a significant role in the sensor signal, requiring the development of a multivariate calibration model to accurately relate the optical response to the formaldehyde concentration (Figure 2). By using parameters such as signal intensity and its temporal derivative, a robust model was built that accounts for environmental fluctuations while preserving the dosimeter behaviour.

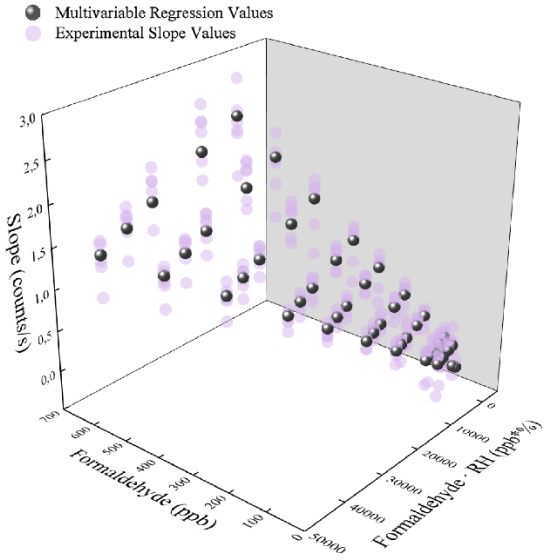


Fig. 2. Multivariable Model proposed for correlating signal response to formaldehyde in varying humidity scenarios.

Potential interferents, including common indoor gases such as carbon monoxide (CO), carbon dioxide (CO_2), and ethanol (EtOH), were also tested. The sensor demonstrated excellent selectivity toward formaldehyde, with minimal cross-sensitivity to these compounds. Furthermore, tests showed high reproducibility across different batches of the colorimetric label and consistent behavior among replicate sensors, confirming the robustness of the fabrication method and the reliability of the sensing mechanism.

References

[1] P. R. Chung, C. T. Tzeng, M. T. Ke, and C. Y. Lee, “Formaldehyde gas sensors: A review,” *Sensors (Switzerland)*, vol. 13, no. 4, pp. 4468–4484, Apr. 2013, doi: 10.3390/S130404468.

[2] L. Feng, C. J. Musto, and K. S. Suslick, “A simple and highly sensitive colorimetric detection method for gaseous formaldehyde,” *J Am Chem Soc*, vol. 132, no. 12, pp. 4046–4047, 2010, doi: 10.1021/ja910366p.

[3] S. Zhao, J. Lei, C. Hou, J. Huang, J. Hou, and X. Luo, “An optoelectronic detector for aldehydes discrimination applications based on CD-like colorimetric chip,” *Microchemical Journal*, vol. 149, no. June, p. 103979, 2019, doi: 10.1016/j.microc.2019.103979.

Acknowledgements

The authors would like to thank Dr. Guillem Domènech-Gil for generously sharing his insights and best practices regarding gas characterization of sensors, which significantly contributed to the quality and rigor of this work.

.

DOI 10.5162/EUROSENSORS2025/MP34

Palladium Doped WSe_2 for Gas Sensing Applications

Mubdiul Islam Rizu[1], Fatima Ezahra Annanouch[1], Jyayasi Sharma[1], Dalal Fadil[1], Eduard Llobet[1]*
[1] Departament d'Enginyeria Electronica, Universitat Rovira i Virgili, Avinguda Països Catalans 26, 43007 Tarragona, Spain.
**Corresponding Author's e-mail address: fatimaezahra.annanouch@urv.cat*

Summary:
In the concurrent research era, doping transition metal dichalcogenides (TMDCs) with noble metals has drawn significant attention to enhance gas sensing performance. In this regard, we report for the first time a highly sensitive palladium doped WSe_2 (Pd-WSe_2) sensor for trace level detection of NO_2 gas at room temperature. The Pd-WSe_2 was synthesized by the combination of aerosol assisted chemical vapor deposition (AACVD) and hydrogen free simple atmospheric pressure chemical vapor deposition (APCVD) methods. Morphological and compositional analysis have revealed good yield for adsorbing the target gas. The sensor exhibited remarkable response towards 800 ppb NO_2 at room temperature even in the presence of humidity without applying any external stimuli. This finding will surely have high impact towards ongoing TMDCs based gas sensor research as well as environmental sustainability.

Keywords: APCVD, gas sensor, NO_2, TMDCs, nanomaterials

Background, Motivation and Objective

The explicit detection of NO_2, a greenhouse gas emitted from the vehicular exhaust and industrial pollution, has become one of the prime concerns in order to ensure public health safety as well as environmental conservation. In this regard, Metal Oxide (MOX) based gas sensors have been widely used but they suffer from long recovery time, poor selectivity and high operational temperature. Alternatively, some low dimensional materials e.g. carbon nanotube, black phosphorous, conductive polymer, graphene have been explored, however they are affected by humidity, deterioration and complex manufacturing process. Researchers have found 2D semiconducting TMDCs as potential substitutes because of their unprecedented physical, chemical and electronic properties. In particular, WSe_2 exhibiting p-type semiconductive behavior has large surface area, tunable electronic properties and excellent chemical stability [1]. Nevertheless, pristine WSe_2 often exhibits limited sensitivity and slow responses at room temperature. Doping with noble metal like Pd is a possible solution to address this limitation. Pd atoms acts as catalytic sites facilitating charge transfers between NO_2 molecules and enhancing overall gas sensing performance [2]. In this study, Pd doped WSe_2 sensor has outperformed for the trace level detection of NO_2 at room temperature under stimulus-free conditions.

Materials and Methods

The sensing film was deposited on SiO_2/Si substrate in two steps. First, Pd-WO_3 was deposited using AACVD technique. In this aspect, 25 mg tungsten hexacarbonyl and 5 mg palladium acetylacetonate were dissolved in 9 ml acetone and

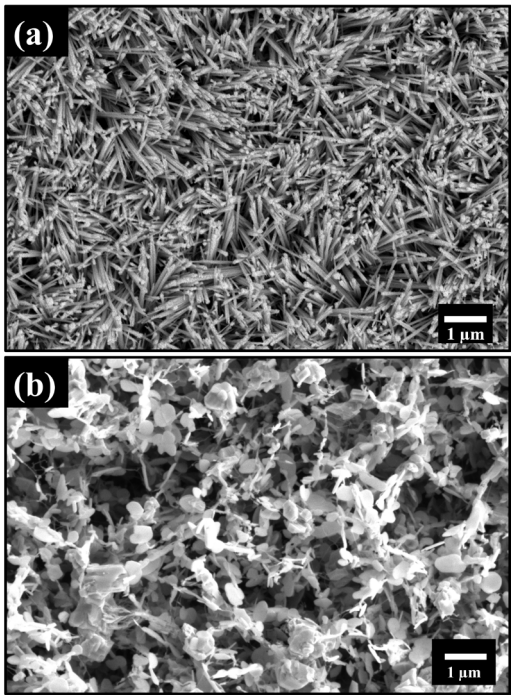


Fig. 1. FESEM images of (a) Pd-WO_3 and (b) Pd-WSe_2.

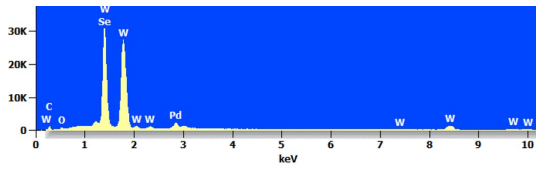


Fig. 2. EDX analysis of Pd-WSe_2.

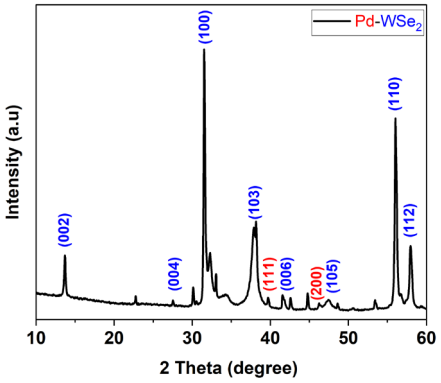


Fig. 3. XRD diffractogram of as grown Pd-WSe_2.

5 ml methanol respectively. These two solutions were then mixed in a glass flask, sonicated for 20 minutes and placed in an ultrasonic humidifier to create aerosol. Nitrogen (0.5 L/min) was used to carry this aerosol to the substrate placed inside the hot wall reactor. The deposition temperature was maintained 350°C. Then the as grown Pd-WO_3 was selenized with hydrogen free simple APCVD method using argon as a carrier gas and Se powder as precursor.

Results

The morphology illustrated in Fig. 1(a) indicates the as-grown Pd doped WO_3 nano needles. These nano needles were converted to edge enriched nano sheets of Pd-WSe_2 as shown in Fig. 1(b) having distinct porosity which is effective for trapping the target gas molecules. Fig. 2 shows the EDX analysis indicating a strong presence of W, Se and Pd with minimal impurities. The XRD pattern exhibited in Fig. 3 reveals the intense peaks at 13.6°, 27.5°, 31.4°, 37.8°, 41.7°, 47.4°, 55.9° and 57.9° corresponding to the (002), (004), (100), (103), (006), (105), (110) and (112) crystal planes (marked blue) of 2H-WSe_2. Two distinct peaks at 39.7° and 46.2° ascribe to the (111) and (200) crystal planes (marked red) of Pd, respectively.

For gas sensing measurements, first the Pd-WSe_2 sensor was tested towards 800 ppb NO_2 at room temperature. A decrease of the resistance was observed when the sensor was exposed to the oxidizing gas NO_2, indicating p-type semiconducting behaviour. In Fig. 4(a) the sensor exhibited a 26% response having complete recovery to the baseline. The sensor took 3

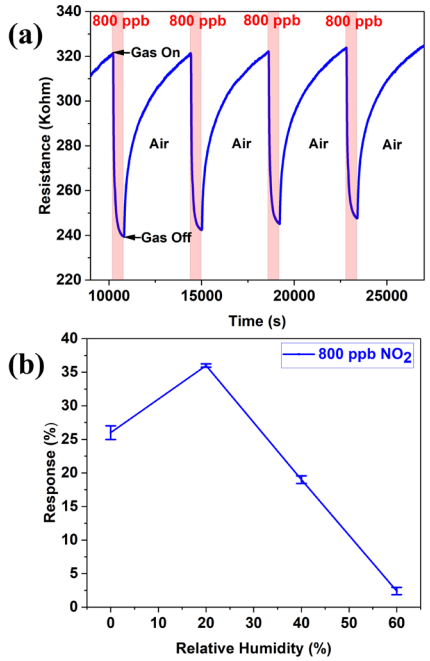


Fig. 4. (a) Pd-WSe_2 sensor resistance dynamic towards 800 ppb NO_2 at room temperature, and (b) its response in different relative humidity levels.

minutes to reach its 90% of the response. Meanwhile, the recovery time was found around 40 minutes which is noteworthy for room temperature gas sensing. Moreover, the sensor showed excellent cyclic repeatability over the long tenure.

The sensor was also tested under the presence of different relative humidity (RH) levels in room temperature to verify its feasibility in real world applications. For 800 ppb NO_2 exposure, the sensor responses 36%, 19% and 2.4% were recorded for 20%, 40% and 60% RH respectively. From these results we can conclude that, the sensor provided with its optimal performance while it was under 20% RH.

Conclusions

In this work, we have proposed a highly sensitive Pd doped WSe_2 gas sensor for detecting trace levels of NO_2 at room temperature without any external influence. Thus, our sensor holds great potential for next-generation IoT compatible gas sensing applications.

References

[1] A. Alagh et al., Three-Dimensional Assemblies of Edge-Enriched WSe2 Nanoflowers for Selectively Detecting Ammonia or Nitrogen Dioxide, *ACS Applied Materials & Interfaces* 14, 54946–54960 (2022); doi: 10.1021/acsami.2c16299.

[2] J. Ni, W. Wang, M. Quintana, F. Jia, S. Song, Adsorption of small gas molecules on strained monolayer WSe_2 doped with Pd, Ag, Au, and Pt: A computational investigation, Applied Surface Science 54, 145911 (2020); doi: 10.1016/j.apsusc.2020.145911.

DOI 10.5162/EUROSENSORS2025/MP35

Development of Metallic inks for the Fabrication of a Flexible Metal Oxide Gas Sensors by Inkjet Printing Process

Le Porcher Bastien[1], *Rieu Mathilde*[1], *Viricelle Jean-Paul*[1]
[1] *Mines Saint-Etienne, Univ Lyon, CNRS, UMR 5307 LGF, Centre SPIN, F-42023 Saint-Etienne, France*

Corresponding Author: rieu@emse.fr

Summary:
This study focuses on developing homemade inks in order to prepare inkjet-printed gas sensor on a flexible substrate. The primary challenge lies in formulating metallic inks with long term stability, high concentration, and inkjet compatible properties. Two distinct methodologies were explored: one centered around nanoparticle-based synthesis, while the other one was particle-free. To achieve an operational sensor, numerous layers were deposited, ranging from gold electrodes to platinum resistance and a SnO_2 sensing layer. Every stage of the manufacturing process has been optimized, allowing to obtain a functional device.

Keywords: Nanoparticles synthesis, Metallic inks, Inkjet printing, Flexible electronic, SnO_2 sensing layer

Introduction

The context of this study is the preparation of a flexible gas sensor onto a plastic substrate, by inkjet printing. In order to get a full sensor, as shown in Fig. 1, semi-conductive metal oxide gas sensors are composed by a sensing material, here, tin dioxide. This layer allows the detection of different type of gas by measuring the resistance change of the semiconductor layer. This semiconductor layer is bridging two gold electrodes that are needed to acquire all the electrical measurement. Electrode are typically made of conductive material such as metals. Gold is frequently used in sensor fabrication field due to is low reactivity with gases. A heater is also printed on the back side of the heater. In this case, this heater can be made of platinum layers connected to gold tracks and it is heating the sensor by using Joule effect.

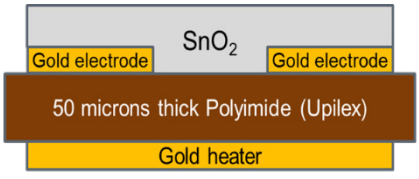


Fig. 1. Scheme of metal oxide gas sensor compositive layers [1]

In this work, homemade metallic inks have been developed. The advantages of homemade inks comparing to commercial one's is that the compositions are controlled and no additives or pollutants are added.

All the intermediate steps of the metallic ink development involving particles synthesis, ink formulation, printing process, deposition, thermal treatment and coating characterization, will be discussed. At the end of the day, a fully inkjet printed sensor will be characterized.

Materials & methods

Gold nanoparticles (AuNPs) solutions have been made by an optimized Turkevich method [1] using Tanique Acid (TA) and Sodium Citrate (SC) in aqueous medium allowing to obtain 3.9mM solutions. Platinum nanoparticles (PtNPs) solutions have been synthesized by reduction of a platinum salt by polyols reaction triggered by the presence of a 150°C ethylene glycol (EG) solution. Both of these nanoparticles solutions have been formulated depending on their own properties (surface tension and viscosity) in order to obtain suitable ink for inkjet process. This was done by adding mixture of solvents to modify these initial values. Particles free inks have also been developed based on metallic salt solvation in solvents mix, resulting in obtaining a concentrated gold ink and a concentrated platinum ink. Finally, SnO_2 ink and deposition have been developed by a sol-gel process in presence of ethylene glycol that is allowing to obtain a ready to print tin dioxide ink [2].

All these steps were merged together to obtain a complete and functional gas sensor.

Results

The gold nanoparticles solution was composed by a 5 to 15nm gold particles as shown by the particle distribution. Addition of glycerol and isopropanol to the AuNPs solution led to decrease the surface tension from 73 mN/m to 31.7 mN/m and to increase the viscosity from 1mPa.s to 14mPa.s. This ink was correctly printed after optimizing the waveform, the tension applied, the nozzle and platen temperatures and the wettability of the substrate. A total number of layers of 100 was printed on PI foil and then dried at 110°C and then thermally treated at 350°C for 2 hours. Finally, coating was not continuous as shown by SEM image presented in Fig. 2. [3]

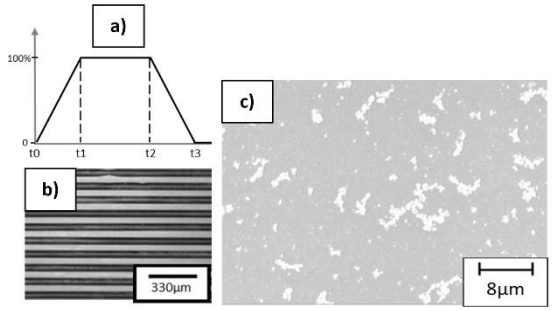


Fig. 2. a) waveform used for inkjet printing of AuNPs ink b) 1D lines obtained after deposition optimization and c) SEM image of 100 layers deposited AuNPs coating

A second goal ink was studied. Particle free ink was composed by $HAuCl_4$ directly dissolved in a mixture water, ethylene glycol and isopropanol. The viscosity and surface tension of this ink were measured and are 32 mN/m and 14 mPa.s. All the printing parameters were also optimized and then “60 layers” were deposited. Coating obtained after thermal treatment at 350°C, shown on the Fig. 3., is conductive. The measured resistivity is about $1.0x10^{-7}$ Ω.m.

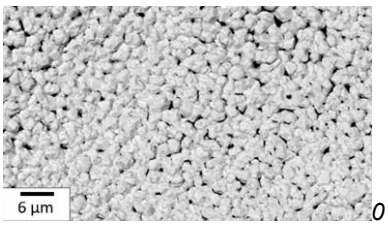


Fig. 3. SEM image of the deposit of 60 layers of particle free gold ink after thermal treatment at 350°C for 2 hours

Combination of AuNPs made ink and precursor made ink make possible to deposit homogeneous, high resolution, and conductive gold electrodes onto polyimide foils [3].

On the other side, platinum ink is developed. Polyvinylpyrrolidone (PVP) stabilized platinum nanoparticles has been synthesized by reduction of H_2PtCl_6 salt in near boiling point ethylene glycol solution [4]. Optimized synthesis led to obtaining concentrated EG-PtNPs solutions. This platinum nanoparticles solution was mixed isopropanol and different solvents in order to reach a suitable surface tension and viscosity for the inkjet printing process.

The SnO_2 material was prepared using sol-gel process, the $SnCl_2$ was dissolved in pure ethanol and the mixture was stirred and kept at 80 ◦C for 5 h in a closed vessel to form a transparent tin ethoxide solution ($Sn(OEt)_2$) [2].

All these layers were cured at a maximum temperature of 350°C in order to not degrade the PI substrate. This complete device was characterized under reducing and oxidizing gases.

Before evaluation of the responses under gases, the sensor was heated up at 350°C for 3 hours which was the working temperature. It was then exposed to reductive gas (CO) and oxidizing gas (NO_2), for 20 minutes and then a stabilizing time of 30 minutes between each gas injection. Gas concentrations were varied from 100 to 300 ppm. Absolute humidity, oxygen percentage and total gas flow were fixed at 1%, 20% and 30L/h respectively. After a short stabilization time, the sensor shows a rapid response to 100 ppm injection of CO. The same behavior is observed for 200 and 300 ppm of CO which mean the sensor is suitable for CO detection. For the NO_2, the response was observable for 200 and 300 ppm injection of NO_2.

Discussion on these homemade sensors will conclude this work.

References

[1] J. Turkevich, Discuss. Faraday Soc., 11 1951, 55, DOI.org/10.1039/DF9511100055

[2] Rieu M, Camara M, Tournier G, et al (2016) Fully inkjet printed SnO2 gas sensor on plastic substrate. Sensors and Actuators B: Chemical 236:1091–1097. https://doi.org/10.1016/j.snb.2016.06.042

[3] Kassem O, Saadaoui M, Rieu M, Viricelle J-P (2017) Synthesis and Inkjet Printing of SnO2 Ink on a Flexible Substrate for Gas Sensor Application. In: Proceedings of Eurosensors 2017, Paris, France, 3–6 September 2017. MDPI, p 622

[4] Le Porcher B, Rieu M, Viricelle J-P (2024) Development of Gold Inks for Inkjet Printing of Gas Sensors Electrodes on Plastic Support. Electronics 13:2110. https://doi.org/10.3390/electronics13112110

[5] Bonet F, Delmas V, Grugeon S, et al (1999) Synthesis of monodisperse Au, Pt, Pd, Ru and Ir nanoparticles in ethylene glycol. Nanostructured Materials 11:1277–1284. https://doi.org/10.1016/S0965-9773(99)00419-5

DOI 10.5162/EUROSENSORS2025/MP36

Hexagonal WO_3 nanorods for Selective H_2S Detection: Synthesis, Characterization, and Gas Sensing Properties.

Sarah Ben Haj Fraj[1], *Viktor Zabolotnii[2], Martyn Sahul[3], and Roman Viter[2] Ambra Fioravanti[4], Giovanni Neri[1]*

[1] Department of Engineering, University of Messina, C.da Di Dio, I-98166 Messina, Italy.

[2] Institute of Atomic Physics and Spectroscopy, University of Latvia, 19 Raina Blvd., Riga, LV 1586, Latvia

[3] Slovak University of Technology in Bratislava, Faculty of Materials Science and Technology in Trnava, J. Bottu 25, 917 24 Trnava, Slovakia

[4] Institute of Sciences and Technologies for Sustainable Energy and Mobility (STEMS), National Research Council (CNR), Via Canal Bianco, 28, 44124, Ferrara, Italy

gneri@unime.it

Summary:

Hydrogen sulfide (H_2S) is a hazardous gas that necessitates reliable detection in industrial and environmental settings. Hexagonal tungsten oxide (h-WO_3) has gained attention as a promising sensing material due to its high surface reactivity and structural stability. This study presents the hydrothermal synthesis of h-WO_3, characterized by XRD, Raman spectroscopy, and SEM. The material exhibited outstanding selectivity and sensitivity toward H_2S, attributed to its porous structure and surface chemistry. These findings underscore the potential of h-WO_3 for effective H_2S gas sensing applications.

Keywords: Hydrogen sulfide (H_2S), Hexagonal tungsten oxide (h-WO_3), Metal oxide semiconductors (MOS), gas sensor.

Hydrogen sulfide (H_2S) is one of the most common highly toxic, flammable, and corrosive gas emitted from industrial processes, natural gas production, and wastewater treatment, posing severe risks to human health and the environment **[1]**. Effective detection of trace amount H_2S is crucial for workplace safety and environmental monitoring. Metal oxide semiconductors (MOS), such as WO_3, have gained attention as gas-sensing materials due to their structural defects, high sensitivity, stability, oxygen vacancies **[2]**. Among various WO_3 phases, hexagonal tungsten oxide (h-WO_3) exhibits superior gas-sensing performance compared to m monoclinic (m-WO_3). While m-WO_3 has been widely studied due to its high stability, bulk m-WO_3 exhibits poor gas sensitivity at 25–500°C, particularly toward gases like CO and H_2S. This limitation has driven the need to enhance WO_3's gas-sensing performance. Szilágyi et al. demonstrated that h-WO_3 outperforms m-WO_3 in detecting low concentrations (10 ppm) of H_2S **[3]**. The unique structural advantages of h-WO_3 such as its large hexagonal and trigonal tunnels contribute to a high specific surface area, facilitating superior gas adsorption and reactivity. In the current research, h-WO_3 was synthesized by a hydrothermal process and carefully examined by X-ray diffraction (XRD), Raman spectroscopy, and scanning electron microscopy (SEM) and transmission electron microscopy (TEM) to define its structural and morphological features against sensing performance.

Synthesis of pure h-WO_3

For synthesis of pure h-WO_3 285 mg of ammonium metatungstate hydrate (AMT) were dissolved in 10ml of water. The pH of the final solution was kept in the range of pH=1.8-2.0 by adding nitric acid. The prepared solutions have been transferred into Teflon lined autoclaves and kept in a furnace at 180°C for 24 hours. The autoclaves were cooled down to the room temperature. The obtained product was rinsed by water and ethanol 3 times and freeze dried.

Gas sensor preparation

The fabrication procedure for the solid-state gas sensor electrode was as follows: First, the powder material was dispersed in distilled water to form a paste, which was then deposited onto an alumina ceramic substrate with interdigitated Pt electrodes and heating elements. The deposited layer was dried on a hotplate at 100°C for 5 min to evaporate water.

Results and discussion

SEM image of the h-WO_3 nanorods is reported in Fig.1. In the inset is also reported TEM image shows the nanoscale dimension of the nanorods,

consisting of one-dimensional needle-like structures. Linear dimensions of the h-WO_3 rods were 406±100 nm in length and 38±14 nm in diameter.

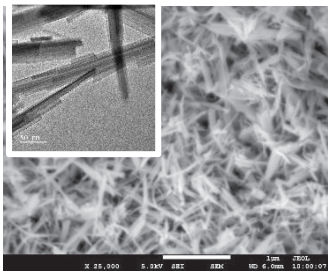


Fig. 1. *SEM and TEM images of h-WO_3 sample.*

The microstructural characterization by XRD (Fig. 2) and Raman (Fig. 3) measurements, confirmed that nanorods display the hexagonal WO_3 phase.

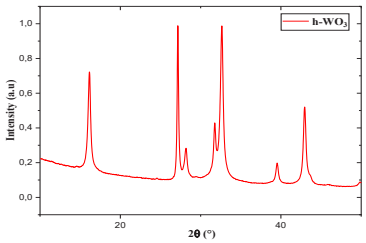


Fig. 2*. XRD pattern of h-WO_3 sample.*

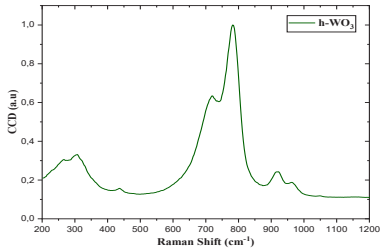


Fig. 3*. Raman spectra of h-WO_3 sample.*

Gas-Sensing Measurements

Preliminary gas sensing measurements indicated that the h-WO_3 rods based sensor is highly sensitive to H_2S. At the optimal operating temperature of 250 °C, the sensor exhibited a gradual decrease in resistance upon H_2S exposure, followed by a rapid recovery to its baseline resistance (Fig- 4). This behavior confirms the sensor's fast and fully reversible response and recovery to H_2S. Additionally, since the baseline resistance decreased upon H_2S exposure, the sensing mechanism was attributed to n-type semiconductor behavior. Figure 4 presents the calibration curve, where the response (Ra/Rg) is plotted against H_2S concentration (ppm). Based on this curve, the sensor demonstrated a detection limit (LOD) of 11.1 ppb, highlighting its high sensitivity.

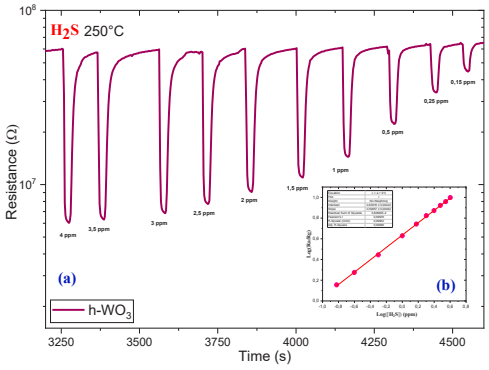


Fig. 4. *a) Response of h-WO_3 sensor at the operating temperature of 250°C as a function of H_2S concentration. Inset in b) shows the calibration curve.*

.

Conclusion

h-WO_3 particles were synthesized using an hydrothermal method. Characterization data confirms the hexagonal phase of tungsten trioxide. This material shows promising p-type behavior for detecting reducing gas H_2S with fast response/recovery, making it suitable for environmental and industrial gas sensors. Further studies are finalized to the optimization of sensor performances (sensitivity, selectivity, stability).

References

[1] Z. Li, Y. Huang, S. Zhang, W. Chen, Z. Kuang, D. Ao, W. Liu, Y. Fu, A fast response & recovery H2S gas sensor based on α-Fe2O3 nanoparticles with ppb level detection limit, *Journal of Hazardous Materials* 300,167–174 (2015). https://doi.org/10.1016/j.jhazmat.2015.07.003.

[2] Q. Zhang, Q. Ma, X. Wang, Y. Wang, D. Zhao, Surface double oxygen defect engineering in button-shaped porous CeO2/WO2.9 heterostructures for excellent n-butanol detection at room temperature, *Applied Surface Science* 616, 156536 (2023). https://doi.org/10.1016/j.apsusc.2023.156536.

[3] I.M. Szilágyi, S. Saukko, J. Mizsei, A.L. Tóth, J. Madarász, G. Pokol, Gas sensing selectivity of hexagonal and monoclinic WO3 to H2S, *Solid State Sciences* 12,1857–1860 (2010). https://doi.org/10.1016/j.solidstatesciences.2010.01.019.

Acknowledgements

This work has been partially funded by the European Union (Next Generation EU), through the MUR-PNRR project SAMOTHRACE (ECS00000022) and by HORIZON-MSCA-2021-SE-01-01, SENS4CORN, No 101086364.

DOI 10.5162/EUROSENSORS2025/MP37

Comparative analysis of WO_3 nanostructures for chemoresistive ammonia sensing

Danial Ahmed [1], Elena Spagnoli [1], Matteo Ferroni [2,3], Giuseppe Cruciani [1], Vincenzo Guidi [1], and Barbara Fabbri [1]

[1] Department of Physics and Earth Sciences, University of Ferrara, Ferrara, via Giuseppe Saragat 1/C, 44122, Italy

[2] Department of Civil, Environmental, Architectural Engineering and Mathematics (DICATAM) – University of Brescia - Via Branze, 43 - 25123 Brescia, Italy

[3] Institute for the Study of Nanostructured Materials - National Research Council (CNR-ISMN) Bologna - Via Gobetti, 101 - 40129 Bologna, Italy

Corresponding Author's e-mail: hmddnl@unife.it

Summary:

The study compares three metal oxide semiconductor (MOS) sensors based on diverse WO_3 nanostructures for ammonia detection: nanoparticles, nanoflakes, and WO_3-x nanoflowers. Among them, WO_3-x nanoflowers exhibited the highest response and low-power operation (300°C). The results highlight the crucial role of nanostructure morphology and lead to further optimization to enhance response in humid environments for selective ammonia sensor.

Keywords: MOS sensors, chemoresistive sensor, ammonia detection, WO_3 nanostructures, gas sensing

Background, Motivation, and Objective

Despite being a common industrial gas, ammonia (NH_3) is extremely hazardous to human health and the environment because of its high reactivity and toxicity. Even at low concentrations (≥50 ppm), NH_3 can cause irritation to the skin, eyes, and respiratory system [1]. Furthermore, it contributes to air pollution by producing fine particulate matter (PM 2.5), which leads to respiratory and cardiovascular problems [2]. Therefore, the development of highly sensitive and selective NH_3 sensors is essential for use in environmental monitoring, healthcare, and industrial safety applications.

The extensive research into gas sensing applications selects metal-oxide semiconductors (MOS), especially tungsten trioxide (WO_3), because of their high sensitivity and stability, together with their user-friendly manufacturing process. After Shaver first discovered a WO_3-based gas sensor for hydrogen detection [3], a lot of research was done to determine whether WO_3 might be used to detect additional gases such NO_2, NH_3, CO, CH_4, and H_2S. The gas-sensing ability of WO_3 is heavily influenced by its morphology, crystal structure, and synthesis process, which affect critical characteristics as surface area, porosity, and oxygen vacancies [4]. Modifying WO_3 nanostructures enhances NH_3 sensing capability by optimizing response, operating temperature, and humidity interference. However, conventional WO_3-based sensors often operate at high temperatures, resulting in high power consumption and limiting their integration into portable or wearable devices. Despite extensive research on WO_3-based NH_3 sensors, a direct comparison of different WO_3 nanostructures synthesized via various techniques remains limited.

This study compares three WO_3 nanostructures through morphology analysis to enhance NH_3 sensing performance, aiming to develop next generation ammonia sensor with enhanced sensitivity, reduced operating temperature and improved stability under humid conditions.

Materials and methods

WO_3-nanoparticles (WO_3 NPs) were synthesized using sol-gel method. WO_3 nanoflakes (NFs) [5], and reduced tungsten oxide (WO_{3-x} NFLs) nanoflowers were achieved via solvothermal approach followed by washing and drying. The resulting powder was then calcined and characterized by morphological, structural and electrical point of view. The powders were combined with α-terpineol, and ethyl cellulose to form a homogeneous sensing paste. The final paste was screen-printed onto alumina substrates with gold interdigitated electrodes on the front side and a platinum heater on the rear side. The films were sintered at 450°C for 2 hours to increase adhesion, structural stability, and electrical performance.

Results

The scanning electron microscopy (SEM) analysis of three WO_3-based materials demonstrated

unique morphological features as shown in Fig. 1. The WO_3 NPs existed as spherical structures, whereas WO_3 NFs displayed a flake morphology. The nanoflower morphology of WO_{3-x} NFLs presented itself as a unique flower-like shape. X-ray diffraction (XRD) analysis of WO_{3-x} NFLs confirms the monoclinic $W_{18}O_{49}$ phase formation.

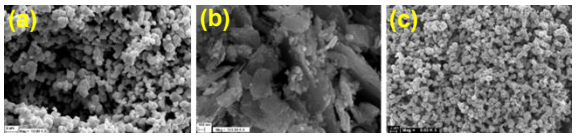


Fig. 1. SEM images of (a) WO_3 NPs, (b) WO_3 NFs, (c) WO_{3-x} NFLs.

The optimal operating temperature was determined by exposing the sensors to 25 ppm of ammonia at various temperatures. The sensitivity measurements were performed at 300 °C while detecting 5, 10, 20, and 50 ppm ammonia concentrations. The dynamic response of NH_3 at varying concentrations is depicted in Fig. 2a, where $W_{18}O_{49}$ nanoflowers outperform WO_3 NPs and NFs in terms of sensing performance and response. This highlights the enhanced performance of the $W_{18}O_{49}$ NFLs across all concentrations.

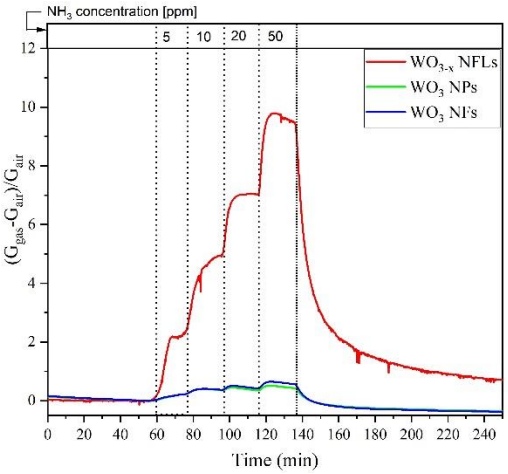


Fig. 2a. Dynamic responses at NH_3 concentration varying from 5-50 ppm.

As seen in Fig. 2b, the sensing performance were also evaluated at 30% of relative humidity (RH%). Sensitivity calibration curves for each of the three samples were displayed under both dry and humid conditions. As expected, humidity reduced responses of all samples, but $W_{18}O_{49}$ NFLs retained the better response, surpassing both WO_3 NPs and NFs. Humidity, however, negatively impacted each sample's response. About the selectivity, 25 ppm of CO and 100 ppm of H_2 were tested. $W_{18}O_{49}$ NFLs-based sensor exhibited a ten-times higher response to NH_3 than these interferents.

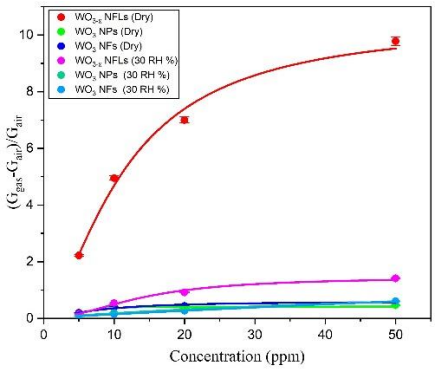


Fig. 2b. Response calibration in dry air and 30 RH%.

Conclusion

The study presents a highly sensitive $W_{18}O_{49}$ NFLs-based sensor for ammonia detection, achieving a remarkable response of at a quite low operating temperature of 300°C. Their improved responsiveness could be attributed to their distinct morphology and oxygen vacancies, showing promise for ammonia sensing applications. However, proper functionalization with Pt and Pd are ongoing to improve performance in humid environments.

Acknowledgement

This work was carried out during the Ph.D. program in Physics 39th-cycle at the University of Ferrara, with support from a scholarship funded by the Italian PNRR (Next Generation-EU), Mission 4, Component 1, Investment 3.3, under Ministerial Decree No. 117/2023. The scholarship is co-funded by SACMI Imola S.C. and the Ministry of University and Research (MUR).

References

[1] Reis, T., et al., *Ammonia Detection by Electronic Noses for a Safer Work Environment.* Sensors, 2024. 24(10): p. 3152. doi: 10.3390/s24103152

[2] Kim, K.-H., E. Kabir, and S. Kabir, *A review on the human health impact of airborne particulate matter.* Environment international, 2015. **74**: p. 136-143. doi: 10.1016/j.envint.2014.10.005

[3] Shaver, P., *Activated tungsten oxide gas detectors.* Applied Physics Letters, 1967. **11**(8): p. 255-257. doi: 10.1063/1.1755123

[4] Zeb, S., et al., *Controllable synthesis of ultrathin WO_3 nanotubes and nanowires with excellent gas sensing performance.* Sensors and Actuators B: Chemical, 2020. **305**: p. 127435. doi: 10.1016/j.snb.2019.127435

[5] Spagnoli, E., et al. *WO_3 Nanoparticles and Nanoflakes Based Sensors for Selective Detection of Alcohols*. in *Electrochemical Society Meeting Abstracts 239*. 2021. The Electrochemical Society, Inc. doi: 10.1149/MA2021-01561437mtgabs

DOI 10.5162/EUROSENSORS2025/MP38

Impedance Spectroscopy: A Key to More Selective and Reliable Chemoresistive Gas Sensors

Magoni Marco [1], *Gaiardo Andrea* [1], *Matteo Valt* [1], *Pietro Tosato* [1], *Antonio Orlando* [1] *and Riccardo Furlan* [1]
[1] Sensors and Devices, Bruno Kessler Foundation, Via Sommarive 18, Povo (TN), Italy
Corresponding Author's e-mail address: mmagoni@fbk.eu

Summary: This proceeding explores the usage of impedance spectroscopy to enhance the performance of chemoresistive gas sensors. By employing and studying a frequency dependent response across various concentration of two gases, Hydrogen and Methane, we were able to identify distinct impedance signatures. Preliminary results suggest improvement regarding the time of response, limit of detection, sensitivity and selectivity compared to a more conventional approach by using the resistive readouts. Moreover, impedance leads into a richer dataset for sensor characterization integrating data analysis techniques to support both gas classification and quantification.

Keywords: Impedance Spectroscopy, Chemoresistive Gas Sensor, Selectivity, Reliability, Electrical Characterization

Introduction

The increasing interest in hydrogen as a clean energy carrier brings new challenges related to its safe distribution and monitoring. Hydrogen, while versatile and sustainable, is highly flammable and difficult to detect at low concentrations, especially when mixed with methane in existing natural gas infrastructures. Methane itself is a potent greenhouse gas, and even minor leaks in the distribution system have significant environmental implications.

To address these challenges, we propose a novel sensing approach based on impedance spectroscopy applied to metal oxide (MOX) gas sensors. Traditional chemoresistive sensors often struggle to distinguish between hydrogen and methane due to their similar interaction mechanisms at the sensor surface. By leveraging the frequency-dependent electrical response of the sensors, impedance spectroscopy provides a richer set of information, potentially allowing both enhanced sensitivity and selectivity [1]. This work aims to enable accurate detection and quantification of hydrogen and methane leaks, supporting a safer and more sustainable energy transition. The study leverages known information about the potential of impedance spectroscopy for enhancing the performance of chemoresistive gas sensor [2].

Materials & Methods

A custom test bench was developed to evaluate the performance of various MOX-based sensors under controlled gas exposure. The sensors were exposed to different concentrations of hydrogen and methane, both separately and in mixture, within a gas mixing chamber equipped with calibrated mass flow controllers. The impedance spectra were measured using a Keysight E4990A impedance analyzer over a defined frequency range (200 Hz to 500 kHz).

The sensing elements included lab-fabricated MOX sensors, based on SnO_2:Pd materials. The impedance was recorded in dry air conditions.

Preliminary Results

This study examines the relationship between the imaginary part of the impedance and the concentration of gases, specifically hydrogen and methane, at varying frequencies. The impedance measurements reveal a clear correlation with gas concentration, indicating the potential use of impedance spectroscopy for gas sensing applications.

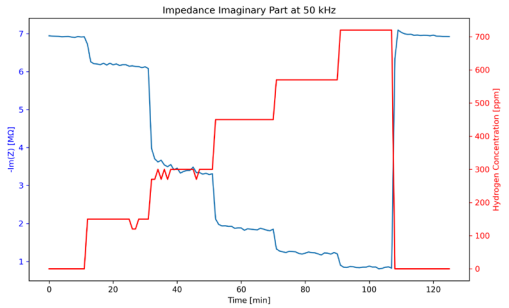


Fig. 1: Imaginary part of the sensor impedance at various concentration of Hydrogen fluxed inside the test chamber.

In presence of Hydrogen at a frequency of 50 kHz, the data demonstrate a stepwise increase in the imaginary part of the impedance as it can be seen in Figure 1. This behavior suggests a strong and reliable relationship between

the impedance response and the gas concentration with a time of response that is close to one minute. A similar trend is observed for Methane at 300 kHz in Figure 2; however, at this higher frequency, the fluctuations in the impedance data become more pronounced. In this case the results obtained are also closer to a linear trend between the imaginary part of the impedance of the sensor and the concentration of the gas. For Methane the preliminary results mimic the one obtained and presented in literature [2].

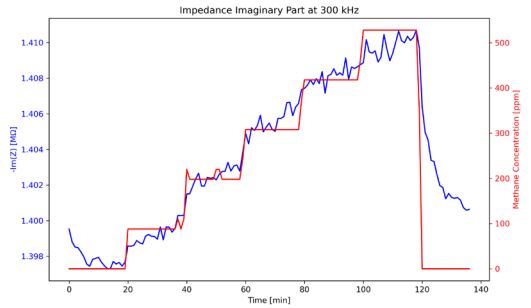


Fig. 2: Imaginary part of the sensor impedance at various concentration of Methane fluxed inside the test chamber.

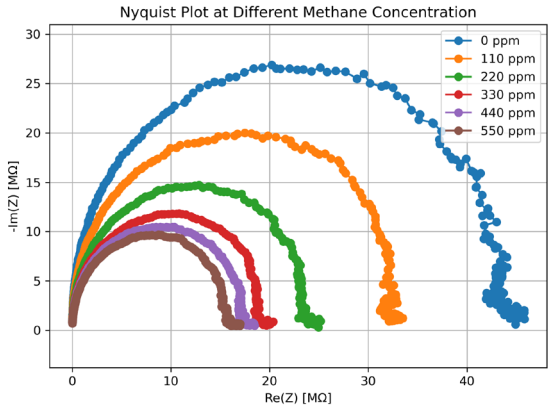


Fig. 3: Nyquist Plot of the SnO_2:Pd sensor at different concentrations of Methane.

Moreover the Nyquist plots in Figure 3 obtained in the different conditions further support these findings, displaying the characteristic semicircular arcs typically observed in impedance spectroscopy. These arcs shift in response to changes in gas concentration, providing visual evidence of the impact of the gas. This observation underscores the utility of impedance-based measurements for distinguishing between different gas concentrations, which is essential for applications in environmental monitoring and industrial processes.

In conclusion, the preliminary results highlight the strong potential of impedance spectroscopy for gas detection, with both the imaginary part of the impedance and the Nyquist plot providing valuable information on gas concentration and composition.

References

[1] V. Balasubramani, S. Chandraleka, T. S. Rao, R. Sasikumar, M. Kuppusamy, and T. Sridhar, “Recent advances in electrochemical impedance spectroscopy based toxic gas sensors using semiconducting metal oxides,” *Journal of The Electrochemical Society*, vol. 167, no. 3, p. 037572, 2020.

[2] R. A. Potyrailo, S. Go, D. Sexton, X. Li, N. Alkadi, A. Kolmakov, B. Amm, R. St-Pierre, B. Scherer, M. Nayeri, *et al.*, “Extraordinary performance of semiconducting metal oxide gas sensors using dielectric excitation,” *Nature Electronics*, vol. 3, no. 5, pp. 280–289, 2020.

DOI 10.5162/EUROSENSORS2025/MP39

Novel multi pixel-based gas sensor fabricated by local Inkjet printing of metal-oxides structures

Alice Debot[1], Vincent Rogé[1], Hakimeh Pakdel[2], Dario Zappa[2], Sebastjan Glinsek[1], Stephanie Girod[1], Noureddine Adjeroud[1], Inci Boehme[3], Renaud Leturcq[1]
[1] Luxembourg Institute of Science and Technology, 41 rue du Brill, L4422, Belvaux, Luxembourg,
[2] University of Brescia, Sensor lab, Department of Information Engineering, 38 Via Branze, 25123 Brescia, Italy
[3]Sciosense Germany GmbH, Gerhard-Kindler-Straße 8, 72770 Reutlingen, Germany
Corresponding Author: vincent.roge@list.lu

Summary:
This paper highlights the development of a novel multi pixel-based gas sensor fabricated by local Inkjet printing of metal-oxides structures. Multiple metal-oxide particles have been printed on a four-pixel micro-hotplate platform (from Sciosense) already available on the market for low power applications. With this approach we hope to drastically improve the lack of selectivity of standard chemiresistive detectors using a fabrication process applicable at the industrial level.

Keywords: Inkjet printing, metal oxides, multi pixels, gas sensing.

Introduction

Chemiresistive gas sensors based on the metal-oxides technology are widely used for gas detection due to their high sensitivity and fast response time. These sensors function by altering the electrical resistance of metal-oxides when exposed to a gas. The change in resistance is directly related to the concentration of the gas, allowing for precise monitoring [1]. They are cost-effective, robust, and capable of detecting low concentrations of gases, making them ideal for multiple applications like environmental monitoring and industrial safety. The limitation of metal-oxide based gas sensors lies in a relatively low gas selectivity, as they can respond to multiple gases simultaneously, making the identification of a specific one very complicated or even impossible [2].

An alternative to circumvent the selectivity restrictions of metal-oxides gas sensors is the designing of multi-pixel ones, with different materials on each pixel. The concept of multi-pixel gas sensors has been widely studied at the laboratory scale [3], but their commercialisation suffers from several challenges, particularly the lack of industrial method for depositing efficiently several metal-oxides materials on a single chip. Currently, commercial products based on the multi-pixel approach do not show selectivity improvement as compared to single sensors because they are produced with a single identical material on each different pixel.

In this work, we propose an innovative approach to manufacture multi-pixel gas sensors, fabricated with four different metal-oxide materials for four pixels, by using a localized Inkjet printing technic. To reach this goal, four metal-oxides materials known for their gas sensing properties (CuO, SnO_2, Co_3O_4 and In_2O_3) have been synthesized in liquid phase and processed into four stable printable inks. The local printing of the formulated inks has been performed with a high droplet resolution compatible with interdigitated electrodes of less than 100 μm x100 μm.

Materials and methods

All metal-oxides materials have been synthesized in liquid phase, using Cobalt nitrate, Copper chloride, Tin chloride and Indium nitrate as metal source. A cobalt oxalate complex has been prepared in a water/dimethylacetamide solvent mix before to be annealed into Co_3O_4, while CuO, In_2O_3 and SnO_2 have been prepared using water as solvent. For the ink formulation, the protocol described in the work of J.S. Gebauer *et al.* [4] has been followed. The Inkjet printing of inks has been performed using a Ceraprint X-serie printer from the Ceradrop company. Morphological characterizations have been realized with an optical microscope MX-61 from the Olympus company and a SEM Helios Nanolab 650 from the FEI company.

Discussion

Spherical SnO_2 and anisotropic Co_3O_4, In_2O_3 and CuO have been synthesized for their

chemiresistive sensing properties. The morphology of cobalt oxide particles and the printability of its ink are presented herein as an example. The typical morphology obtained for Co_3O_4 is presented on the SEM images on the Figure 1, where one can observe homogeneous anisotropic nanorods of widths below 50 nm and an aspect ratio around six. Those nanorods been suspended in a slightly acidified H_2O/Ethylene glycol solvent mix at 0.4_{wt}% to form a printable ink.

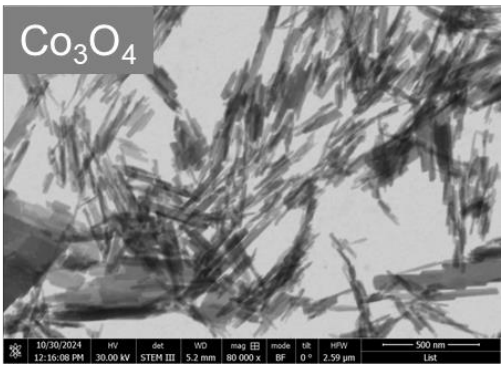


Fig. 1. SEM images of cobalt oxide nanorods.

The jetting properties of the formulated ink are presented on the Figure 2. On this image, recorded with a high framerate CCD camera, we can see that droplets ejected from the cartridge form single drops with no tails, which is evidencing an appropriate printability behavior. At 200 μs after jetting, most of the droplets are beyond 400 μm, except for the nozzle 6. It indicates that the jetting of this ink is a little bit to fast, as the targeted value is usually $2m.s^{-1}$. Also, it points out some instability of the jetting that must be further improved.

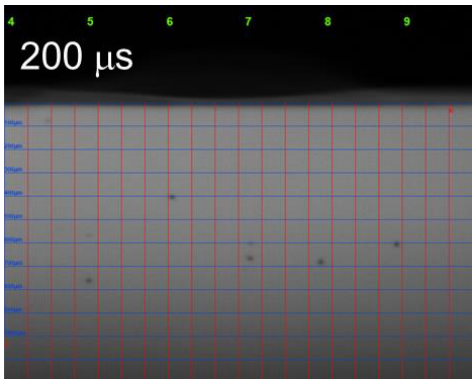


Fig. 2. Optical image of droplets formed at 200μs after jetting for five ejection nozzles.

Drawing from the results obtained for the Co_3O_4 ink, the three other metal-oxide materials have been formulated into processable inks and tested alongside with the Co_3O_4 one for the local printing on the Sciosense commercial micro-hotplate platform. Printing results are presented on the Figure 3where three out of the four inks that have been printed on each pixel can be observed. For each case, 15 drops have been performed on top of the interdigitated electrodes. It is clear from this picture that the local printing of each material is successful, even if the particles density must drastically be improved to form a homogeneous layer on top of the metallic fingers.

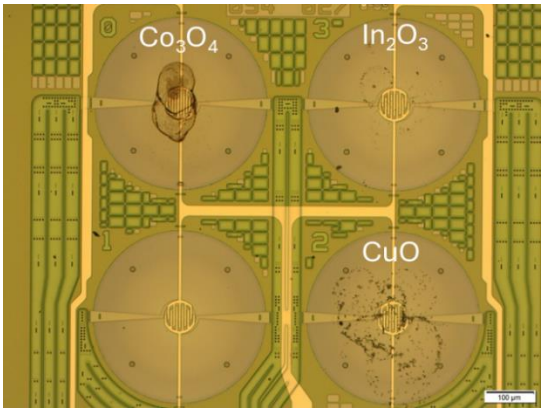


Fig. 3. Optical microscope image of a multi pixel sensor. Three materials out of four have been printed by the Inkjet technic.

This last aspect is already under consideration. We envisage to increase the concentration of materials in the ink, or we foresee multiple pass with the printing head.

Acknowledgements

The authors would like to thank the European Union for the founding of the AMUSENS project under grant agreement no. 101130159. Views and opinions expressed are however those of the authors only and do not necessarily reflect those of the European Union. Neither the European Union nor the granting authority can be held responsible for them.

Bibliography

[1] Pegah N, Ahad G. Chemiresistor gas sensors: Design, Challenges, and Strategies: A comprehensive review. Chemical Engineering Journal. 2024;498:154999.

[2] Turlybekuly A, Shynybekov Y, Soltabayev B, Yergaliuly G, Mentbayeva A. The Cross-Sensitivity of Chemiresistive Gas Sensors: Nature, Methods, and Peculiarities: A Systematic Review. ACS Sensors. 2024;9(12):6358-71.

[3] Bae G, Kim M, Song W, Myung S, Lee SS, An KS. Impact of a Diverse Combination of Metal Oxide Gas Sensors on Machine Learning-Based Gas Recognition in Mixed Gases. ACS Omega. 2021;6(36):23155-62.

[4] Gebauer JS, Mackert V, Ognjanovic S, Winterer M. Tailoring metal oxide nanoparticle dispersions for inkjet printing. J Colloid Interface Sci. 2018;526:400-9.

DOI 10.5162/EUROSENSORS2025/MP40

Novel pyridinium luminophores as optical gas sensors for detection of volatile acids

Roman Viter[1], Viktor Zabolotnii[1], Matis Martins Drava[1] and Artis Kinens[1]

[1] University of Latvia, 19 Raina Blvd., Riga, LV 1586, Latvia
Corresponding Author's e-mail roman.viter@lu.lv

Summary:
Detection of volatile acids (VA), such as HCl, TFA, etc., in industrial processes and biological reactions is an actual problem. Pyridinium luminophores is a new class of materials with tunable chemical structure and optical properties. Sensor properties of these materials have not been explored yet. This study presents fabrication of pyridinium luminophores and characterization by XRD, FTIR and photoluminescence (PL) spectroscopy. The material, tested PL spectroscopy at room temperature, exhibited outstanding sensitivity towards VA, attributed to its chemical structure. These findings underscore the potential of pyridinium luminophores for effective detection of VA in hazardous environments.

Keywords: Volatile acids, Optical gas sensors, Pyridinium luminophores, Photoluminescence.

Introduction

Volatile acids (VA) such as HCl, TFA, etc., are common by products in industrial processes and biological reactions [1]. Effective and low-cost detection of is crucial for environmental monitoring and human health. Recent approaches show significant progress in VA detection by using resistive sensors [1]. The sensors, constructed from metal oxides, metal alloys and conductive polymers showed high sensitivity and selectivity towards VA at room temperatures [1]. Organic compounds with advanced optical and structure properties are efficient alternatives for VA detection [2]. VA vapors have been detected by metal organic compound (MOF) sensors using photoluminescence spectroscopy at room temperature [2]. Despite the reversible signal, the concentration range of the MOF sensor and optical detection units are to be optimized [2]. Pyridinium luminophores are novel organic semiconductors with high quantum yield, mainly used in light emission diodes [3]. Their unique properties exhibit high potential for photoluminescence gas sensor applications. In the present research we report on novel pyridinium luminophores have been synthesized and studied by X-ray diffraction (XRD), FTIR spectroscopy, and photoluminescence spectroscopy (PL). PL spectroscopy has been used to examine sensor properties of the luminophores to vapors of HCl, TFA and acetic acids at room temperature.

Synthesis of pyridinium luminophores

The luminophores have been prepared as described in [3]. In the final step, the reaction with HCl at 70 ^{0}C has been performed. The precipitated powder was dried in vacuum and analysed by NMR. The structure of the obtained luminophore is shown in Figure 1.

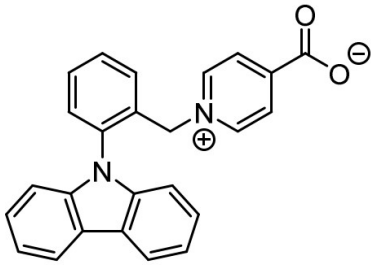


Fig. 1. Chemical structure of pyridinium luminophore.

Gas sensor testing

Gas sensor testing to HCl, TFA and acetic acid was performed in home made gas chamber. The gas chamber (V_c=7.7 l) was equipped with a ventilator, inlet and outlet, sample holder and quartz window. Saturated vapor with precise volume V_s (V_s<<V_c) was injected into the chamber. Photoluminescence (PL) was excited by UV LED (325 nm, 0.05 mW) and the optical sensor signal has been measured by fiber optic spectrometer (Ocean Optics HR2000). During the sensor tests, the full PL spectrum was recorded before and after adsorption equilibrium. Kinetic measurements have been performed at the pre-selected wavelengths.

Results and discussion

Sensor response of the pyridinium luminophore to HCL and TFA is presented in Figure 2 and 3, respectively. The PL intensity of the luminophore decreased upon interaction with acidic vapors. The sensor showed significant response to HCl in the range of 90-360 ppm, whereas sensor range towards TFA vapors was at 350-1400

ppm. Kinetic response to volatile acids was recorded at fixed wavelength of 520 nm (Figure 4). The sensor response was about 250 seconds for HCl and 1000 seconds for TFA.

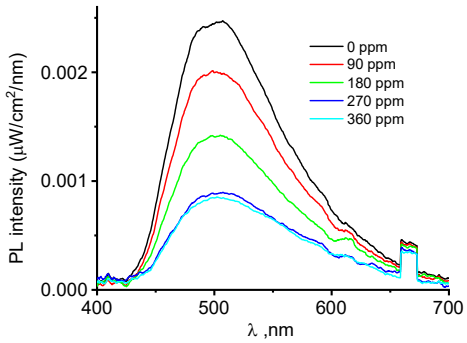


Fig. 2. Sensor response of pyridinium luminophore to HCl vapors measured by photoluminescence spectroscopy

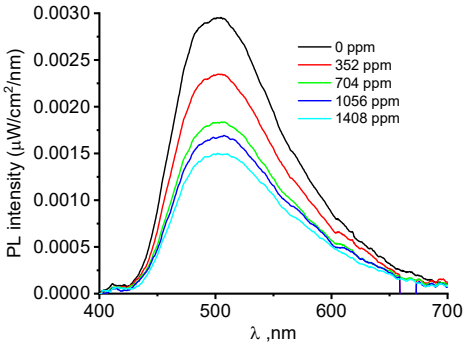


Fig. 3. Sensor response of pyridinium luminophore to TFA vapors measured by photoluminescence spectroscopy

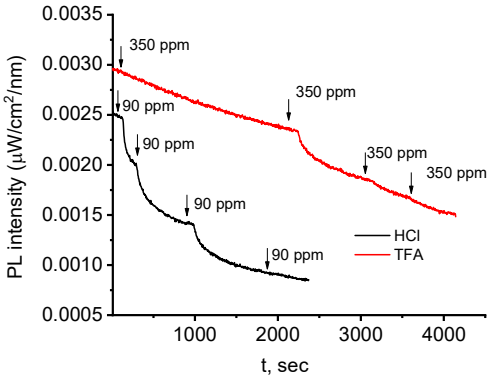


Fig. 4. The Kinetic response of the pyridinium luminophore to HCl and TFA vapors were recorded at fixed wavelength of 520 nm.

FTIR spectra of the pyridinium luminophore before and after are shown in Figure 5. Peak shift from 1630 cm^{-1} to 1703 and 1730 cm^{-1} suggest on protonation of the luminophore and forming of carboxylic groups as result of interaction with volatile acids. The observed changes in the chemical structure of the luminophore depend on the acidic strength of the volatile acids.

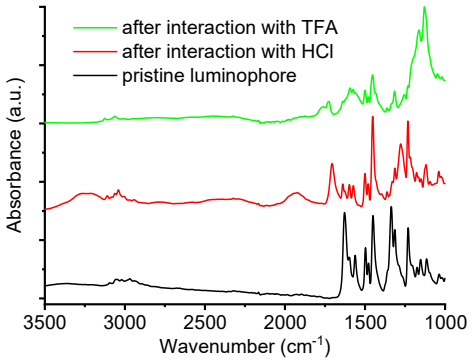


Fig. 5. Sensor response to HCl vapors measured by photoluminescence spectroscopy

Conclusion

The synthesized pyridinium luminophore has shown chemical interaction with volatile acids. Sensor range, senor response time and interaction mechanism were the function of the acidic strength of the volatile acid compounds. This material shows promising behavior for detection of volatile acids at room temperature, what is applicable for environmental and industrial gas sensors. Further studies are finalized to optimize the sensor performances (sensitivity, selectivity, limit of detection).

References

[1] A. Verma, R. Gupta, A. Singh Verma, T. Kumar, A review of composite conducting polymer-based sensors for detection of industrial waste gases, *Sensors and Actuators Reports* 5, 100143 (2023) https://doi.org/10.1016/j.snr.2023.100143

[2] Z. Zhu, Z. Ni, H. Zou, G.Feng, B. Tang, Smart Metal–Organic Frameworks with Reversible Luminescence/Magnetic Switch Behavior for HCl Vapor Detection, *Advanced Functional Materials* 31, 2106925 (2021) https://doi.org/10.1002/adfm.202106925

[3] K. Leduskrasts, A. Kinens, E. Suna, The emission efficiency of cationic solid state luminophores is directly proportional to the intermolecular charge transfer intensity, *Chemical Communications* 59, 6905–6908 (2023) https://doi.org/10.1039/D3CC01674A

Acknowledgements

We acknowledge the project *Atveseļošanas un noturības mehānisma projekts "Latvijas Universitātes iekšējā un ārējā konsolidācija" (Nr. 5.2.1.1.i.0/2/24/I/CFLA/007)*
Piridīnija luminofora strukturālo un optisko īpašību projektēšana pielāgotai sensora reakcijai for support of the research.

DOI 10.5162/EUROSENSORS2025/MP41

H_2S Sensor Studied by Electrochemical Impedance Spectroscopy

Krystyna Schneider, Barbara Dziurdzia, Katarzyna Zakrzewska
Faculty of Computer Science, Electronics and Telecommunications, AGH University of Krakow, 30-059 Krakow, Poland

Corresponding Author's e-mail kryschna@agh.edu.pl

Summary:
In the present work we studied by an electrochemical impedance spectroscopy, EIS, of the SnO_2 thin films as a hydrogen sulphide sensor. It was found that EIS is a useful technique for characterization of metal oxide sensos based on nanostructural materials.

Keywords: Thin films, reactive sputtering, tin dioxide, electrochemical impedance spectroscopy, sulphide gas sensor.

Background, Motivation an Objective

Hydrogen sulphide (H_2S) is a flammable, corrosive and lethal gas even at low concentrations (ppm levels). It is produced by various emitting sources (such as oil and gas processing facilities, natural emissions, sewage treatment plants, landfills and other industrial plants) [1]. Its limit of exposure of humans of concentration ranges from 10-100 ppm at time of exposure from 1-10 min. Therefore, there is an urgent need to develop some devices that allow fast, portable and low-cost monitoring of the H_2S responsible for air pollution and danger to human health [1,2].
Successful development of H_2S gas sensors for commercialization requires achieving three 'S': sensitivity, selectivity and stability Recently, metal oxide semiconductor thin films of H_2S gas sensors have been studied extensively because of their simple fabrication process and low cost [2]. Commonly, direct current measurements have been used for determination of the sensor properties, such as three 'S'. Impedance spectroscopy, however, in addition to the same information, can also determine of individual properties of the sensing mterials such as grain boundary, grain bulk and interface between electrode contact and senising material [2-6]. In this work we describe impedance spectra of SnO_2 thin films recorded on air and H_2S gas atmospheres.

Experimental

Sample preparation

The thin films SnO_2 thin films were deposited by rf reactive sputtering from a metallic Sn target in a Ar-O_2 gas flow-controlled atmosphere. Corundum CC2 type supports (BVT Technologies, Czech Republic) were used as a target.

Impedance measurements

Impedance spectra were taken by two-probe technique with FRA Solatron 1260 using the Solatron Dielectric Interface1296. Frequency range was from 1 Hz to 1 MHz. Amplitude of sinusoidal disturbance was 10 mV. Measurements were carried out in dry air - H_2S of the concentration range between: 0, 0.75, 1.5, 2.25, 3 ppm at 347°C.

Results

Figure 1 shows an example of the impedance spectra of the sensor SnO_2 thin film plotted as Nyquist form, at 374°C, under air and H_2S gas. The diameter of the semicircles decreases drastically with the increase in the concentration of H_2S.

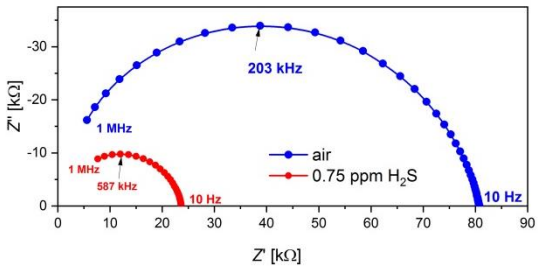


Fig. 1 Experimental impedance spectra of SnO_2 thin film at 347°C under air and 0.75 ppm H_2S.

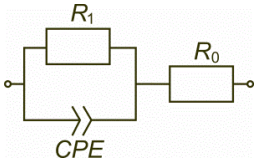


Fig. 2 Equivalent circuit used for the analysis of the impedance spectra.

The simplest equivalent circuit for measured spectra is presented in Fig. 2. It is composed of the resistor R_0 connected in series with the element composed from resistor R_1 and a constant phase element, *CPE* connected parallel. The impedance Z_{CPE} is given by the formulas [8]:

$$Z_{CPE} = A(2\mathrm{p}\, fj)^{-\frac{1}{n}} \quad (1)$$

Where: *A*, *n* – constants, *f* - frequency [Hz], *j* - imaginary unit.

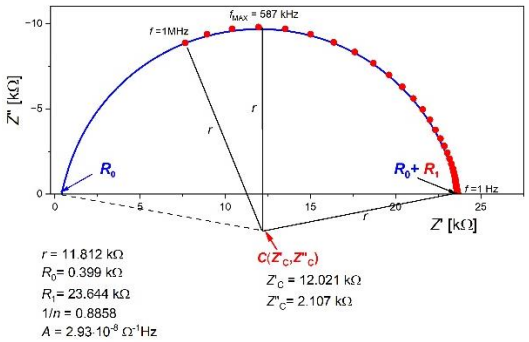


Fig. 3 *Determination parameters of the equivalent circuit for* SnO_2 *thin film at* 347°*C under* 0.75 *ppm* H_2S.

Figure 3 illustrates experimental points (red symbols) and fitted curve obtained based on the hypothetical equivalent circuit. The agreement is quite good. The method for determining the parameters of the equivalent circuit as well as their values are depicted in Fig. 3.

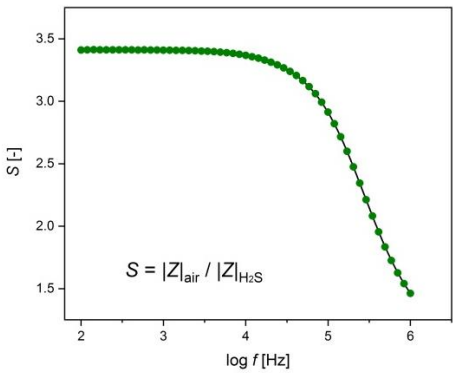


Fig. 4 *Sensor signal, S of* SnO_2 *thin film at* 347°*C under* 0.75 *ppm* H_2S.

The sensor signal *S* is done by the following equation:

$$S = \frac{|Z|_{AIR}}{|Z|_{H2S}} \quad (2)$$

Were |*Z*| is a modulus of impedance at air and H_2S, respectively. Fig. 4 illustrates sensor signal as a function of frequency.

Conclusions

In the present work we studied by an electrochemical impedance spectroscopy, EIS of the SnO_2 thin films as a hydrogen sulphide sensor. It was found that the EIS is a useful technique for characterization of metal oxide gas sensors based on nanostructural materials.

References

[1] Y.C Chan, S.S. Mun Lock , M. K. Wong , C. L. Yiin, A. C. Minh Loy, K. W. Wai Cheah, S. Y.Wang Chai, C. Li , B. S. How , B. L.Fui Chin, Z. P. Chan, S. S. Lam, A state-of-the-art review on capture and separation of hazardous hydrogen sulfide (H_2S), Env. Pol. 314 (2022)120219, doi.org/10.1016/j.envpol 2022/20219.

[2] V. Balaubramant, S. Chandraleka, T. Subba Rao, R. Sasikumar, M.R. Kuppusamy, T.M. Sridhar, Review- Recent advances in electrochemical impedance spectroscopy based toxic gas sensors using semiconducting metal oxides,*J. Electrochem. Soc.* 167 *Semiconductor* (2020) 037572, doi:10.1149/1945-7111/ab77a0.

[3] F. Vyslouzil, V. Myslik, M. Kovanda, R. Frycek, M. Jelinek, Impedance measurements of chemical gas sensors, *The Forth International Conference on Advanced Devices and Microsystem,* Slomenice, Slovaka 2002 pp 317-320: doi.10.1109/ASDAM 2002.1088532.

[4] S. Luo, G. Fu, H. Chen, Y. Zhang, Gas sensing properties and complex impedance analysis of La_2O_3 -added WO_3 nanoparticles to VOC gases, *Materials Chemistry and Physics* 109 *(* 2008) 541-546, doi. 10.1016j.matchemphys2008.01.015.

[5] J.M. Rheaume, A.P. Pisano, A review of recent progress in sensing of gas concentrations by impedance change, *Ionics* (2011) 17:99-108, doi 10.1007/s11581-010-0515-1.

[6] T. Tasaki, S. Takase, Y. Shimizu, Impedancemetric acytylene gas sensing properties of Sm-Fe based perovskite-type oxide-based thick-film device, *Sensors and Actuators B:Chemical* B 187 (2013) 128-134, http:/dx.doi.org/10.1016/s.snb.2012.09.086.

[7] S.N. Shkerin, A.S. Tolkacheva, A.V. Nikonov, N.B. Pavzderin, Impedance spectroscopy of cell with Pt electrodes on oxygen-conducting material with matenite-related structure, *Ionics* (2016) 0593.

[8] J. Ross, in *Impedance spectroscopy*, John Wiley & Sons 1987.

Acknowledgements

The Statutory Project for Science for 2025 at the Institute of Electronics, Faculty of Computer Science, Electronics and Telecommunications AGH UST is greatly acknowledged.

DOI 10.5162/EUROSENSORS2025/MP42

Selectivity Acetone Detection by Spinel Mn_xO_y Sensor

Reinaldo dos Santos Theodoro[1,2], Tiago Elias Abi-Ramia Silva[2], Matteo D'Andria[2], Diogo Paschoalini Volanti[1], Andreas T. Güntner[2]
[1] São Paulo State University (UNESP), Rua Cristóvão Colombo 2265, 15054-000 São José do Rio Preto, Brazil,
[2] ETH Zurich, CH-8092 Zurich, Switzerland
andreas.guentner@hsl.ethz.ch

Summary:
The accurate detection of volatile organic compounds such as acetone has drawn great attention. We present manganese oxide films fabricated via flame spray pyrolysis as acetone sensor with humidity enhanced sensitivity.

Keywords: Chemoresistor, Nanotechnology, Gas sensors, Breath Analysis

Background

In recent years, the precise detection of Volatile Organic Compounds (VOCs) has attracted the attention of the scientific community, mainly because these VOCs can be used to evaluate indoor air quality, as well as for health monitoring [1].

Therefore, developing sensor materials capable of selectively detecting acetone at ppb-level in high relative humidity is essential for practical applications. This work presents a chemoresistor acetone sensor based on semiconductor metal oxide nanoparticles, specifically manganese oxide. Sensor films composed of the Mn_xO_y were fabricated using flame spray pyrolysis (FSP) [2] with varying thicknesses.

Experimental

Mn_xO_y-based sensing films were prepared using flame spray pyrolysis (FSP) [3]. A precursor solution based on Mn (II) 2-ethylhexanoate in xylene was atomized, and combusted. Nanoparticles were collected on a filter positioned above the flame. The Mn_xO_y nanoparticles were directly deposited onto Al_2O_3 substrates with interdigitated Pt electrodes and a resistance temperature detector (RTD). The thickness of the film was adjusted according to the deposition time. Finally, the Mn_xO_y films was annealed at 500 °C for 5 h. Fig. 1 illustrates the fabrication of sensor films. The sensors were mounted on specific holders and connected to a gas mixing system for analysis, using hydrocarbon-free synthetic air and calibrated mass flow controllers to create the desired gas mixture composition [4]. The sensor response (S) was determined as:

$$S = \frac{Ra}{Rg} - 1$$

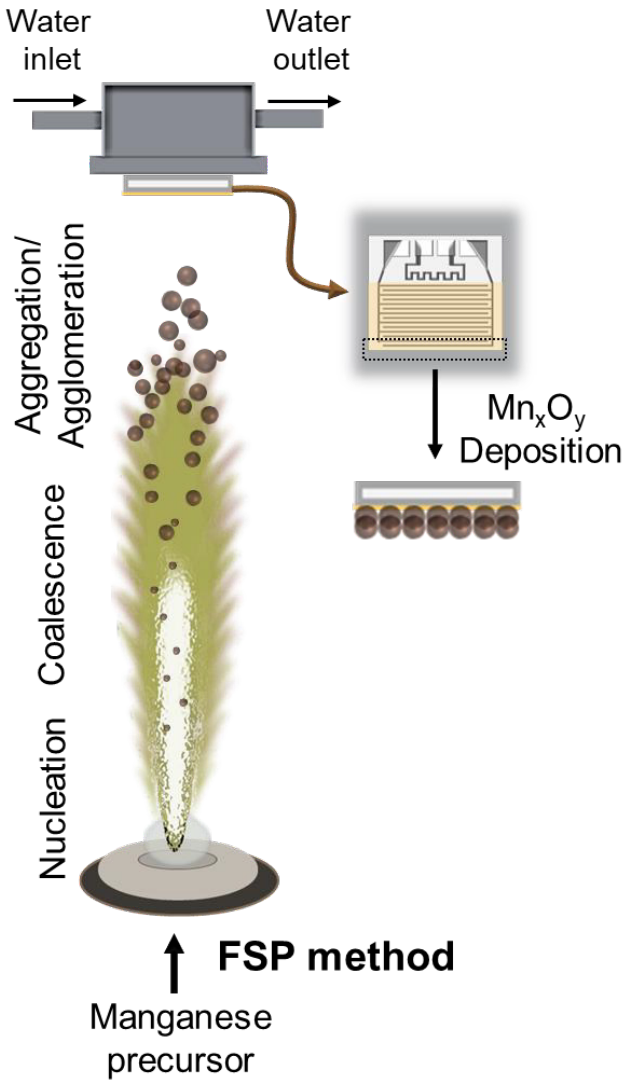


Fig. 1. Schematic illustration of sensor films fabrication.

Results

Sensor was tested for acetone detection. The initial results showed that MnxOy-based sensors exhibited significant sensing performance for acetone, with good selectivity against major interfering gases, as shown in Fig. 2.

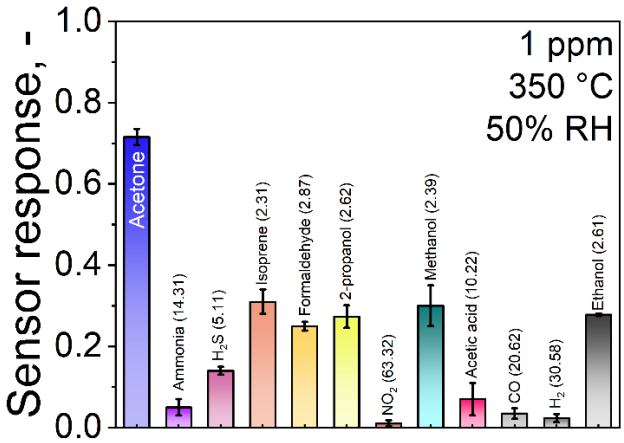


Fig. 2. Selectivity graphs for acetone detection against interfering gas at 350 °C and 50% RH.

The Mn_xO_y sensor was tested under different relative humidity (RH) conditions and various acetone concentrations (in ppm) to evaluate its humidity robustness, as shown in Fig. 3. As can be seen, the sensor demonstrates enhanced sensitivity under different RH conditions. These findings suggest that the sensor can be used in various application fields, such as breath analysis, where acetone is a marker of fat metabolism during dieting [5] and exercising [6].

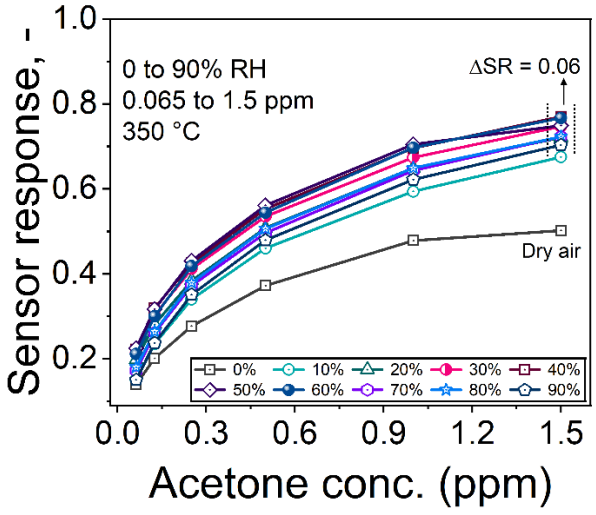


Fig. 3. Sensing performance under different RH (0 – 90%) in different acetone configurations at 350 °C.

Our analysis will be complemented by crystallographic analysis by X-ray diffraction, surface area measurement by N_2 adsorption as well as electron microscopic characterization.

References

[1] Elias Abi-Ramia Silva, T., Burisch, F., Güntner, A. T. Gas sensing for space: Health and environmental monitoring. TrAC Trends in Analytical Chemistry, 177, 117790, (2024); doi.org/10.1016/J.TRAC.2024.117790

[2] Güntner, A. T., Pineau, N. J., & Pratsinis, S. E. Flame-made chemoresistive gas sensors and devices. Progress in Energy and Combustion Science, 90, 100992, (2022); doi.org/https://doi.org/10.1016/j.pecs.2022.100992

[3] D'Andria, M., Krumeich, F., Yao, Z., Wang, F. R., Güntner, A. T. (2024). Structure-Function Relationship of Highly Reactive CuO_x Clusters on Co_3O_4 for Selective Formaldehyde Sensing at Low Temperatures. Advanced Science, 11(10), 2308224, (2024); doi.org/10.1002/ADVS.202308224

[4] Güntner, A. T., Righettoni, M., & Pratsinis, S. E. Selective sensing of NH_3 by Si-doped α-MoO_3 for breath analysis. Sensors and Actuators B: Chemical, 223, 266–273, (2016); doi.org/10.1016/J.SNB.2015.09.094

[5] Güntner, A. T., Sievi, N. A., Theodore, S. J., Gulich, T., Kohler, M. & Pratsinis, S. E. Noninvasive Body Fat Burn Monitoring from Exhaled Acetone with Si-doped WO_3-sensing Nanoparticles. Anal. Chem. 89, 10578-10584, (2017); doi.org/10.1021/acs.analchem.7b02843

[6] Güntner, A. T., Kompalla, J. F., Landis, H., Theodore, S. J., Geidl, B., Sievi, N. A., Kohler, M., Pratsinis, S. E. & Gerber, P. A. Guiding Ketogenic Diet with Breath Acetone Sensors. Sensors 18, 3655 (2018); doi.org/10.3390/s18113655

Acknowledgements

This work was sponsored by São Paulo Research Foundation (FAPESP); Process numbers: 2020/06421-1 and 2022/05381-1.

DOI 10.5162/EUROSENSORS2025/MP43

Sub-ppm Methane Sensing by Spark-Ablation-Synthesized SnO_2 Nanoparticle-based Materials

D. Gounaris[1], A. Baut[2], S. E. Pratsinis[1], A. Güntner[2] and G. Biskos[1,3,4]
[1]Climate and Atmosphere Research Center, The Cyprus Institute, Nicosia, 2121, Cyprus
[2] Human-centered Sensing Laboratory, Department of Mechanical and Process Engineering, ETH Zürich, 8092, Zürich, Switzerland
[3]Faculty of Applied Sciences, Delft University, 2629 HZ Delft, the Netherlands
[4]Faculty of Civil Engineering and Geosciences, Delft University of Technology, Delft, 2628-CN, the Netherlands
d.gounaris@cyi.ac.cy

We demonstrate a simple and scalable method to synthesize Sn nanoparticles via spark ablation using nitrogen at atmospheric pressure. Post-annealing, the particles convert to SnO_2, as confirmed by X-ray diffraction and Transmission Electron Microscopy (TEM), and processed into gas sensing materials for methane detection. The sensors respond to concentrations as low as 0.2 ppm with high sensitivity and repeatability. Performance remained stable over repeated cycles. Our results demonstrate that spark ablation provides a promising route for fabricating reliable low-level methane sensors.

Keywords: Spark Ablation, Methane Detection, MOx Gas sensor, SnO_2 NPs

Metal oxide gas sensors play a crucial role in a number of applications. Despite their advantages such as high sensitivity, stability, low cost, small size and low power consumption, however, we currently lack sensors that are sensitive and selective enough for applications in environmental monitoring[1], underlining an important need for further efforts to improve their performance.

Metal oxide nanoparticles are predominantly synthesized using wet chemical methods for instance sol-gel or hydrothermal techniques[2]. However, emerging dry methods, including flame spray pyrolysis and spark ablation offer distinct advantages, such as improved contamination control, single-step synthesis and the ability to directly deposit porous films[3]. Spark ablation, which is an environmentally friendly technique that produces high-purity nanoparticles with controlled size and composition, provides also a very good alternative. The technique, initially introduced by Schwyn et al.[4], produces nanoparticles via repeated spark discharges between two conductive electrodes, evaporating small amounts of material from their heated surface, and forming nanoparticles upon quenching. To date, it has been successfully employed for the synthesis of catalytic, sensing and photovoltaic nanomaterials among others[5].

Here we employ atmospheric-pressure spark ablation, using N_2 as a carrier/quenching gas and two Sn electrodes (2 mm in diameter), to produce Sn nanoparticles. The particles produced are agglomerates, with an average mobility diameter of approximately 80 nm and a geometric standard deviation (GSD) of 1.57. BET measurements of the collected nanoparticle powders have a specific surface area of 105.5 m^2/g for the as-prepared Sn nanoparticles, which decreases to 45 m^2/g after thermal annealing. Upon annealing the pure Sn nanoparticles also convert to SnO_2. The crystallite size of the SnO_2 in the annealed samples was determined to be 15 nm. The sensing film, fabricated via doctor blading, was further characterized using scanning electron microscopy (SEM), which revealed a highly porous and uniform network with pore sizes ranging from the nanometer to micrometer scale (cf. Figure 1). This porous structure is expected to enhance gas diffusion, making it well-suited for sensing applications[6].

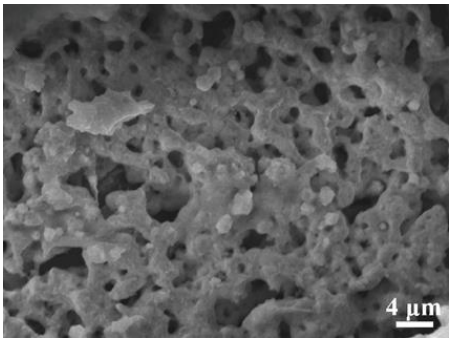


Figure 1. SEM image of the porous sensing film comprised by annealed SnO_2 nanoparticles.

The resulting sensors, designed for methane detection and operating at 275 °C, successfully detected concentrations ranging from 0.2 ppm to 10 ppm at 20% relative humidity (cf. Figures 2 & 3). In addition, they demonstrated excellent response and repeatability over more than 10 cycles at a constant methane concentration of 5 ppm.

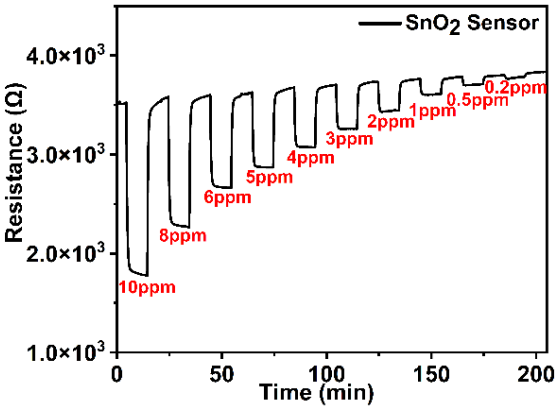


Figure 2. Resistance of the sensor as a function of time, while the concentration of methane in the overlaying gas ranged from 0.5 to 10ppm.

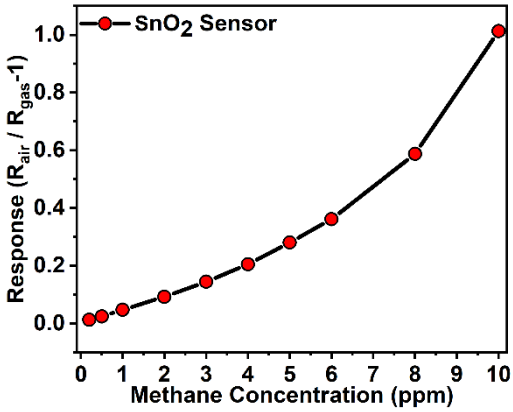


Figure 3. Response of the sensor as a function of methane concentration.

The performance of the sensor was evaluated in the presence of water vapor and interfering gases including acetone, ethanol, hydrogen, carbon monoxide and ammonia. Its response to a constant methane concentration of 10 ppm remained stable across relative humidity (RH) levels ranging from 20 to 80%. Variations in response were consistently below 10%, indicating that the sensor operates reliably under different humidity conditions, ensuring its suitability for diverse environmental applications.

Our results show the potential of spark ablation for synthesizing high-performance methane sensors, addressing the critical need for reliable sub-10 ppm detection. The approach is simple, scalable and well-suited for real-world environmental and industrial monitoring applications.

References

[1] N. A. Isaac, I. Pikaar, and G. Biskos, “Metal oxide semiconducting nanomaterials for air quality gas sensors: operating principles, performance, and synthesis techniques,” *Microchim Acta*, vol. 189, no. 5, p. 196, May 2022, doi: 10.1007/s00604-022-05254-0.

[2] A. M. Negrescu, M. S. Killian, S. N. V. Raghu, P. Schmuki, A. Mazare, and A. Cimpean, “Metal Oxide Nanoparticles: Review of Synthesis, Characterization and Biological Effects,” *Journal of Functional Biomaterials*, vol. 13, no. 4, Art. no. 4, Dec. 2022, doi: 10.3390/jfb13040274.

[3] A. T. Güntner, N. J. Pineau, and S. E. Pratsinis, “Flame-made chemoresistive gas sensors and devices,” *Progress in Energy and Combustion Science*, vol. 90, p. 100992, May 2022, doi: 10.1016/j.pecs.2022.100992.

[4] S. Schwyn, E. Garwin, and A. Schmidt-Ott, “Aerosol generation by spark discharge,” *Journal of Aerosol Science*, vol. 19, no. 5, pp. 639–642, Oct. 1988, doi: 10.1016/0021-8502(88)90215-7.

[5] D. P. Debecker *et al.*, “Spark ablation: a dry, physical, and continuous method to prepare powdery metal nanoparticle-based catalysts,” *Chem. Commun.*, vol. 60, no. 79, pp. 11076–11079, Oct. 2024, doi: 10.1039/D4CC03469D.

[6] A. T. Güntner, M. Wied, N. J. Pineau, and S. E. Pratsinis, “Rapid and Selective NH3 Sensing by Porous CuBr,” *Advanced Science*, vol. 7, no. 7, p. 1903390, 2020, doi: 10.1002/advs.201903390.

Acknowledgements

This work was supported by the Research & Innovation Foundation (Cyprus) under grant CODEVELOP-AG-SH-HE/0823/00164 (DANTE Project).

DOI 10.5162/EUROSENSORS2025/MP44

The Dimensionality of MOX Sensors in Air Quality assessment

Luiz Miranda[1], Nathalie Redon[2], Caroline Duc[2], Marie Verriele[2] Jugurta Montalvão[3], Bernadette Dorizzi[1]
, Mossaab Hariz[1], Dijana Petrovska[1], Jerome Boudy[1]
[1] Samovar, Télécom SudParis, Institut Polytechnique de Paris, Palaiseau, France
[2] IMT Nord Europe, Institut Mines-Télécom, Univ. Lille, Center for Energy and Environment, Douai, France
[3] Universidade Federal de Sergipe, UFS, São Cristóvão, Brazil
Corresponding Author's e-mail address: luiz.miranda_cavalcante_neto@telecom-sudparis.eu

Summary: This paper investigates why air quality applications using MOX gas sensors typically rely on sensor arrays with limited number of sensors. Despite their high sensitivity, MOX sensors suffer from low selectivity, and practical constraints like power and processing capability limit the array size. By analyzing two datasets with different complexities, in terms of monitored pollutants, using three intrinsic dimensionality (ID) estimators, the study shows that the effective dimensionality of sensor data is often much lower than the total number of sensors. This suggests redundancy in sensor responses and supports the common use of 2 to 4 MOX sensors. Results also highlight that features that include some dynamic information, like relative response, yield higher information.

Keywords: Metal-oxide gas sensors, intrinsic dimensionality, air quality, sensor arrays, feature selection

Introduction

Metal oxide (MOX) gas sensors are widely used due to their low cost, high sensitivity, and long lifespan compared to technologies like electrochemical and polymer sensors [1]. However, their low selectivity makes that several sensors are often combined into arrays (electronic noses) to distinguish between gases. Applications such as breath analysis may use up to 19 sensors, but air quality monitoring typically uses fewer than 10 due to power and size constraints, especially in portable devices where each MOX sensor's micro-heater impacts battery life [2].

To address these constraints, studies often seek to optimize sensor selection, with numbers between 2 and 4 MOX sensors frequently found to be sufficient depending on the target gases [2]. In this work, we try to give a theoretical justification of these numbers by analyzing the intrinsic dimensionality (ID) of data from air quality experiments. The following sections define dimensionality in this context, introduce the ID concept, describe the datasets used, and discuss our results.

Intrinsic Dimensionality for MOX sensors

The apparent dimensionality D of multivariate signals from array of MOX sensors is determined by the number of sensors or features used to process their data. For example, a 5-sensor system is 5-dimensional with raw data, or 10-dimensional if features like relative response (R_s) and the average sensor response are used. As dimensionality increases, data visualization and computation become more challenging. However, high-dimensional data can usually be described with fewer variables, known as latent variables, the quantity of which is given by the Intrinsic Dimensionality (ID) of the underlying phenomenon, thus, the minimum number of variables needed to describe the data without loss of information [3].

ID can also be seen as the perceived dimensionality of data, indicating redundancy when ID is lower than the apparent dimensionality. Given that the sensitivity profiles of MOX sensors often overlap, systems with multiple sensors are expected to exhibit some level of redundancy.

Material and methods

Datasets

Tests were performed in two datasets, in which result from commercially available MOX sensors. Dataset 1 is an indoor activity dataset in which 10 different daily household activities were performed in a room monitored by 21 distinct MOX sensors [1]. Dataset 2 is a qualification dataset in which 4 unique MOX sensors are exposed to a fixed concentration (600 ppb) of formaldehyde and toluene injected in a 36 liters chamber. The sensors used in Dataset 1 include the sensors used in Dataset 2.

Features for both datasets were considered as the average value and the normalized relative response (NRR) during the execution of the activities, for Dataset 1, and injection of the target gases, for Dataset 2. The NRR is calculated as $R_s = (R_g - R_0)/R_0$, where R_0 and R_g are the sensors' responses at the beginning and end of activity or injection, respectively. Both datasets are available upon request.

ID estimators

ID can be estimated in several ways, here we implemented three different methods to perform this estimation. The first is based on PCA in which the ID is given by the number of eigenvectors representing more than 90 % of the data

variance. The second is an adaptation [4] of the Grassberger and Procaccia (GP) correlation dimension [5]. And the third is the Maximum Likelihood Estimator (MLE) from Levina and Bickel (2004) using the parameter $k = 20$ [6].

Results and discussion

Table 1 summarizes the results of the tests performed. The GP method sometimes provides two values, as it estimates the ID in several scales of signal intensity (multiscale analysis). Thus, when two stable estimates are observed, for two different signaling scales, the method reports two numbers. For both datasets, most resulting intrinsic dimensionalities (d) are smaller than the original dimensionality (D), indicating redundancy, which is typical in multidimensional experimental data. The experiment for Dataset 1, which involves multiple volatile compounds, results in a higher ID compared to the experiment that generated Dataset 2, which only tests two gases. This shows that more complex experiments tend to generate data with a higher degree of freedom, reflected in the higher ID values.

Although providing different results, the different ID estimators provide mostly agreeing values, with the exception of PCA. We believe that it comes from the linear nature of the PCA method, which is not able to estimate the local dimension of curved structures suggested by observations, thus, causing an overestimation [3].

The different features tested also give clues of which one can provide most information about the phenomenon behind observations. While the average measurement from the sensors can be useful for some application, the relative response introduces an idea of time progression which is often more important to characterize the phenomenon. This is reflected in the resulting ID of these features. Therefore, as higher ID represents a higher complexity (degrees of freedom), more information can be extracted from the features.

Finally, to try to understand why the number of sensors in air quality applications are often limited to 4, as previously mentioned, we can go back to the richness of the experiment. As air quality applications using these sensors often try to identify and quantify concentration of a handful of target gases, the complexity of these applications is closer to the experiment for Dataset 2 than for Dataset 1. As ID is the lower bound of the number of "ideal" sensors, we see that this low number of sensors (and ID) is reflected in these types of experiments.

Tab. 1: Comparison of dimensionality estimation methods across two datasets.

Estimator	**Dataset 1** ($D = 21$)		**Dataset 2** ($D = 4$)	
	Mean	R_s	Mean	R_s
PCA	6	5	3	4
MLE	4.4	6.5	1.9	2.8
GP	3.2	3.5 or 5.8	1.4 or 2.4	2.5

Conclusion

This study investigated the intrinsic dimensionality (ID) of data from MOX gas sensor arrays using three estimation methods across two datasets of differing richness. Results showed that the effective dimensionality is significantly lower than the total number of sensors, confirming that only a few ideal sensors (or very diverse actual ones) would be enough to capture the essential information in air quality monitoring applications.

These findings give a new perspective for most practical systems that use 2 to 4 MOX sensors, especially under power and processing constraints. Additionally, the use of relative response as a feature yielded higher IDs than the average response of the sensors, suggesting that some idea of time progression can provide more useful information for measuring relevant gases in air quality applications.

References

[1] L. Miranda, C. Duc, N. Redon, J. Pinheiro, B. Dorizzi, J. Montalvão, M. Verriele, and J. Boudy, "Automatic detection of indoor air pollution-related activities using metal-oxide gas sensors and the temporal intrinsic dimensionality estimation of data," *Indoor Environments*, vol. 1, no. 3, 2024.

[2] Z. Yuan, X. Luo, and F. Meng, "Machine Learning-Assisted Research and Development of Chemiresistive Gas Sensors," *Advanced Engineering Materials*, vol. 26, no. 20, p. 2400782, 2024.

[3] F. Camastra and A. Staiano, "Intrinsic dimension estimation: Advances and open problems," *Information Sciences*, vol. 328, pp. 26–41, 2016.

[4] J. Montalvão, J. Canuto, and L. Miranda, "Bias-Compensated Estimator for Intrinsic Dimension and Differential Entropy," *Journal of Communication and Information Systems*, vol. 35, pp. 300–310, Dec. 2020.

[5] P. Grassberger and I. Procaccia, "Characterization of Strange Attractors," *Physical Review Letters*, vol. 50, pp. 346–349, Jan. 1983.

[6] E. Levina and P. Bickel, "Maximum likelihood estimation of intrinsic dimension," in *Advances in Neural Information Processing Systems*, vol. 17, MIT Press, 2004.

Acknowledgments

The authors gratefully acknowledge the support of ADEME and the Hauts-de-France Region for funding the extraction and processing of the datasets as part of the doctoral work of the first author. This work is currently supported by the European Union through the HORIZON-CL4-2023-RESILIENCE-01-33 project "Smart sensors for the Electronic Appliances market (RIA)," grant number 101130159 – AMUSENS.

DOI 10.5162/EUROSENSORS2025/MP45

Experimental Characterization of Negative Temperature Coefficient Resistor Noise Depending on Polarization Voltage

Antoine Riaud[1]
[1] ABB Corporate Research, Baden-Dättwil, Switzerland,
antoine.riaud@ch.abb.com

Summary:
Negative Temperature Coefficient Resistors (NTC) are a workhorse of temperature measurement when sensitivity is the primary concern. NTC are semicrystalline semiconductor blends and exhibit flicker noise. We report here experiments showing that the NTC noise depends heavily on the polarization voltage.

Keywords: negative temperature coefficient resistor, noise, voltage

Introduction

Resistive temperature sensors are chosen according to a trade-off between low drift and high linearity (resistive temperature detectors - RTD) and high sensitivity (thermistors). While the noise of RTD is the well-known Johnson-Nyquist noise, the noise of thermistors, like most semiconductors, arises from several processes [1] and often must be determined empirically. Many of these phenomena are well-described by Hooge's law, which postulates that the resistivity of the material not only varies due to actual temperature drift (phonon noise) but also because of random fluctuations in carrier density and/or mobility.

The noise in PTC has been connected to carrier mobility fluctuations in the depletion region near the grain interface [2]. Ralph and Schofield have proposed a model without adjustable parameters to predict the noise. However, unlike PTC, the conductivity of NTC is not determined at the grain boundary but by bulk properties [3]. Therefore, the noise generation process is not well understood .

Ryger et al. [4] have measured the noise of negative temperature coefficient resistors and shown that physically smaller devices were noisier than larger ones, in agreement with the empirical Hooge's law. However, these results did not predict well the noise of an NTC used in ABB instruments. The NTC is thermalized at higher temperature (87°C) and voltage (10 V) than the ones used in Ryger's study [4]. Furthermore, the NTC is polarized at constant voltage, as opposed to the 1 kHz in the previous study. Therefore, we investigated the effect of those operating parameters on the NTC noise. Most parameters were found to have a small effect and therefore we report mainly on the voltage that had by far the largest effect on noise.

Method

Four detector beads were assembled in Wheatstone bridge configuration and immersed in colza oil. The oil provided a higher thermal inertia than in air, and reduced convective currents, which allowed testing the NTC at higher voltage. Extra resistors were added in series with individual beads to balance the bridge and maximize the power supply rejection. The bridge was placed in a Faraday cage and supplied either by an ultra-low-noise voltage source or a battery.

To ensure that the noise was coming from the circuit and not from the amplifier, the signal was recorded via two independent channels. Each channel included a low-noise instrumentation amplifiers (SR 560) with a bandwidth of 0,03 Hz to 100 Hz, and a gain of 50,000. The signal from each amplifier was then digitized by an oscilloscope.

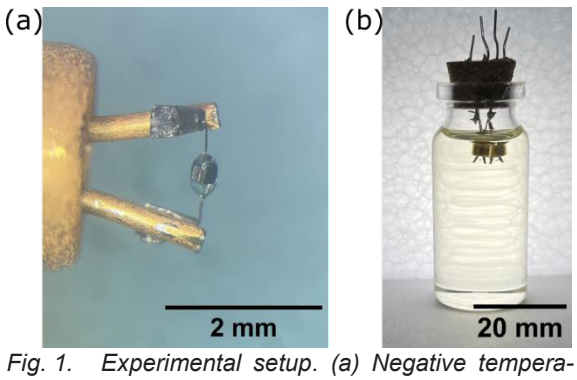


Fig. 1. Experimental setup. (a) Negative temperature coefficient (NTC) resistor, protected by a glass shell. (b) two NTC immersed in an oil bath. Two of these bottles were used to build the Wheatstone bridge.

Signal processing

Assuming the resistance of each NTC is given by $R_0(1+\epsilon_i)$, with the power spectrum density of ϵ_i given by S_{RR}, we can show that the voltage noise density S_{VV} at the bridge reads:

$$\frac{S_{VV}}{V_b^2} \approx \frac{S_{RR}}{R^2}, \qquad (1)$$

with $V_b = \frac{1}{2}U_0$ the voltage on the half bridge. To distinguish between amplifier noise and circuit noise, the cross-spectral density (CSD) from the output of the two amplifiers was used as a proxy of the circuit noise. We note that in all our experiments, the CSD was very similar to the power spectral density the amplified signals, showing that the amplifier noise is negligible. Furthermore, accounting for the PSR offered by the bridge, the voltage source noise was estimated to be of the order of 1 nV/$\sqrt{Hz}$, much smaller than the recorded noise (132 nV/$\sqrt{Hz}$).

Results & discussion

The noise density of the NTC was found to be insensitive to the medium temperature. However, we observed that the noise depends on the excitation voltage, as shown in Fig 1:

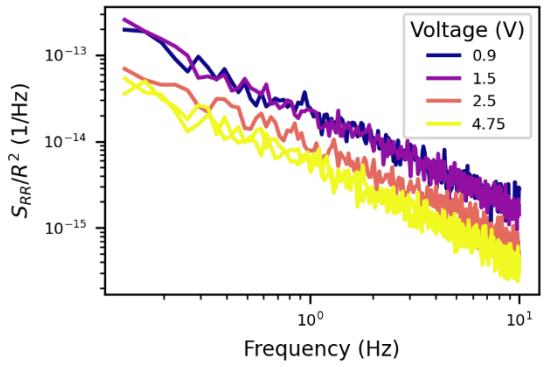


Fig. 2. NTC noise spectral density at various polarization voltages.

The variation of noise density with polarization voltage is shown in Fig. 2:

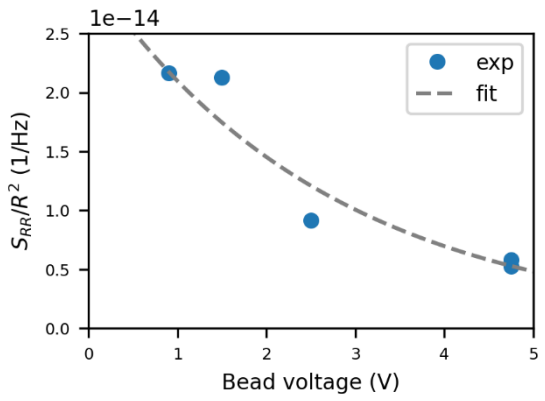


Fig. 3. NTC noise at 1 Hz vs polarization voltage.

Experimental noise levels are well described using the following model:

$$\frac{S_{RR}}{R^2} \approx \frac{A}{f} e^{-\frac{V_b}{V_0}}, \qquad (2)$$

with $A = 3 \times 10^{-14}$ and $V_0 = 2.7$ V. The value of V_0 suggest that a bandgap mechanism may be at the origin of the noise.

Despite extensive literature review, the authors have not found reports that NTC noise depends on the excitation voltage. Our study suggests that the signal to noise ratio of NTC exponentially increases with the voltage as follows:

$$SNR \approx \sqrt{\frac{A}{f}\frac{\beta^2 S_{\theta\theta}}{T_0^4} e^{\frac{V_b}{V_0}}}, \qquad (2)$$

With $S_{\theta\theta}$ the power spectrum density of the temperature signal, T_0 the average temperature of the sensor, and β its temperature coefficient ($R(T) = R_0 e^{\beta/T}$ with R_0 a fictive resistance at infinite temperature). While using elevated voltages can bias the measurement by heating up the medium, and even add noise, for instance due to convection, our study highlights that there is some trade-off in increasing the voltage that might be worth considering for high precision applications.

References

[1] M.B. Weissman 1/f noise and other slow, nonexponential kinetics in condensed matter, Rev. Mod. Phys. 60, 537 (1988); doi: 10.1103/RevModPhys.60.537

[2] J.E. Ralph, J.M.S. Schoefield, 1/f noise in positive temperature coefficient thermistors, *Physica* 115B, 35-40 (1982); doi: 10.1016/0378-4363(82)90053-5

[3] S.G. Song, Z. Ling, F. Placido, impedance analysis of MnCoCuO NTC ceramic, *Materials Research Bulletin* 40(7), 1081-1093 (2005); doi: 10.1016/j.materresbull.2005.04.001

[4] I. Ryger et al. Noise characteristics of thermistors: Measurement methods and results of selected devices, Review of Scientific Instruments 88, 024707 (2017); doi: 10.1063/1.4976029

Acknowledgements

We gratefully acknowledge Kai Hencken and Yannick Maret for the discussions and advice when conducting this research and preparing this manuscript.

DOI 10.5162/EUROSENSORS2025/MP46

Investigations on Ammonia Using Resistive and Photoacoustic Sensor Elements

Heike Wünscher, Christoph Heinze, Steffen Herbst, Toni Schildhauer
CiS Forschungsintitut für Mikrosensorik GmbH
Konrad-Zuse-Straße 14, 99099 Erfurt, Germany
e-mail address: hwuenscher@cismst.de

Summary:
Two different ammonia sensors are introduced which are designed for the measurement of residual ammonia traces in a pipe of an ammonia cracker. The resistive sensor enables a continuous monitoring by an impedance measurement of the gas in a condensate, and allows the detection especially of low ammonia levels. The photoacoustic sensor operates in the gas phase directly.

Keywords: ammonia, condensate, impedance, absorption, microphone

Motivation

Ammonia can be used in energy storage [1]. It can be transported much easier than hydrogen and represents a conceivable fuel [2]. After releasing from an ammonia cracker, the gas mixture from hydrogen and nitrogen can be fed into a fuel cell. Due to the limited durability of the materials against ammonia residues, the gas quality must meet the specific requirements [3-5]. An ammonia sensor is, therefore necessary to ensure the gas quality (Fig.1).

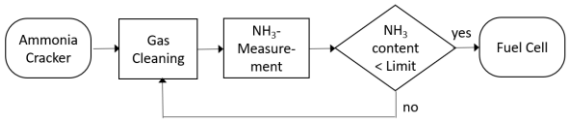


Fig.1 Sensor application field

For this purpose, the sensor should be suitable for the installation in a pipe and low maintainance. In this paper two different approaches are studied: the resistive and the photoacoustic sensor principle.

Sensor Principles and Description

A) Resistive sensor

The resistive gas sensor is based on the impedance measurement of an aqueous condensate of the ammonia. The gaseous sample is fed into alkaline water. According to Henry´s law all gas components are distributed between the liquid phase in the tank and the gas phase above the liquid. On cooling an interdigital structure above the liquid, a waterdrop arises which contains dissolved gas. Ammonia is the only component of this gas mixture which dissociates in the waterdrop, i.e. the electrical impedance of the drop decreases with increasing ammonia content. It can therefore, be used for concentration measurement. It has been shown that the chemical resistance is sufficient [6].

B) Photoacoustic sensor

The photoacoustic sensor is based on the effect of absorbed electromagnetic energy on the gas by means of acoustic detection. The absorption causes local heating, generating a thermal expansion which creates a pressure wave (Fig. 2).

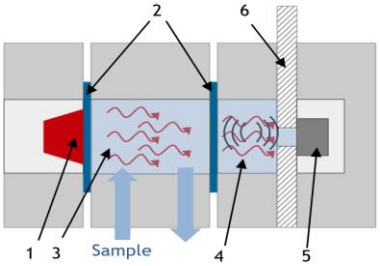


Fig. 2. Photoacoustic sensor principle

The gaseous sample from the ammonia cracker is introduced in the sample room (3). The sample is irradiated with infrared (IR) light coming from a thermal emitter which is operated in pulsed mode (1). Passing through both windows (2) and the sample room, the light reaches the reference chamber (4) which is filled with highly concentrated ammonia. Therein the sound is generated which is detected by a MEMS microphone (5). The latter one is mounted on a PCB with a hole (6). In the gas mixture coming from the cracker, ammonia alone absorbs the infrared light. With increasing ammonia concentration in the sample, the incoming light in the reference chamber decreases and thus the microphone signal decreases Due to the low radiation intensity in the long-wavelength region an innovative array from

16 MEMS-IR-emitter with a nominal power of 1600 mW has been prepared for ammonia detection.

Measurements

The resistive measurement system was prepared using a silicon sensor including an interdigital structure and a temperature diode which were mounted on a sealed tank. The interdigital electrode was directed to the bottom side so that the condensate could drop down into the liquid sample again. The condensate was formed by cooling the interdigital electrode using a peltier element. After equilibration a stable impedance was obtained. This process took at least several minutes. Low ammonia levels can be sensitively detected (see Fig. 3).

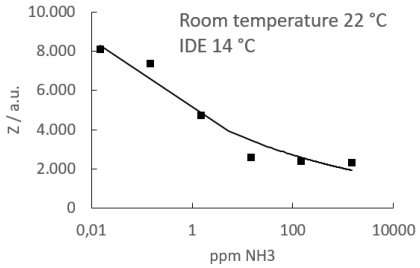


Fig. 3. Impedance of the condensate obtained at 50 kHz vs. ammonia content

For photoacoustic measurements a modular system has been created. The system is designed for IR emitter in a TO-39 housing. The emitter and the MEMS microphone are mounted at opposite ends (Fig. 4).

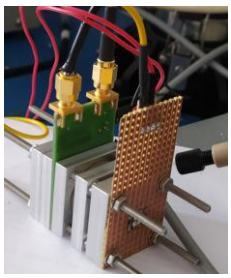


Fig. 4. Detection unit of the photoacoustic sensor

The mentioned IR radiator array was applied. The first functional tests were performed using the surrounding air. This one contains carbon dioxide and humidity which absorb IR light. Thus, it can act as a test medium. The detection unit consists of the reference chamber and the MEMS microphone. It was studied regarding its behavior towards broadband IR radiation when filled with air, pure nitrogen and after evacuation up to 200 ... 300 mbar. The sealing of the housing was checked. For this purpose, the chamber was evacuated and the subsequent penetration of the air into the sealed apparatus was recorded (see Fig. 5). With increasing observation time, the microphone signal grows due to increasing concentrations of carbon dioxide and water vapour in the chamber. It can be concluded that the system works as expected, although it is not completely hermetic.

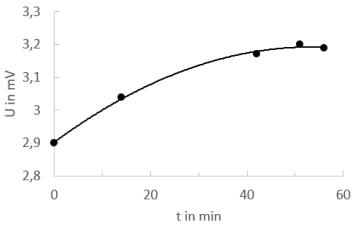


Fig. 5. Microphone signal in sealing test

Results

Both sensoric systems are designed to measure ammonia continuously in the special gaseous environment. The resistive system allows the sensitive detection low ammonia levels. A clearly nonlinear relationschip between impedance and ammonia content is obtained. Due to the need for equalization the response time is rather long. An alternative might be a photoacoustic system which is still in progress.

References

[1] https://www.elektroniknet.de/power/erneuerbare-energien/weltweit-erste-brennstoffzelle-mit-ammoniak-im-einsatz.184180.html, status 22.6.22

[2] https://analytik.news/presse/2022/568.html?mtm_campaign=newsflash&mtm_cid=2239&mtm_medium=email&mtm_source=newsletter, status 4.10.2022

[3] Florian Ernst Nigbur: *Ammoniak-Cracker zur Brenngasversorgung von Brennstoffzellen - Experimentelle und simulative Untersuchungen*. 1. Auflage. Cuvillier-Verlag, Göttingen 2021, ISBN 978-3-7369-7497-5.

[4] C. Xu, G. Xu, Analysis Technology of Trace Impurities in Hydrogen for Hydrogen Fuel Cell Vehicles. *Chemical Industry and Engineering Progress,* 40(2), 688-702 (2021); doi: 10.16085/j.issn.1000-6613.2020-0690

[5] https://www.agilent.com/cs/library/applications/an-ammonia-hydrogen-fuel-cell-vehicles-5994-7439en-agilent.pdf, status 24.4.25

[6] H. Wünscher, T. Frank, I. Tobehn-Steinhäuser, A. Cyriax, T. Ortlepp, T. Kirner, Monitoring of Ammonia in Biogas, IV. CMP International conference on Monitoring & Process Control of Anaerobic Digestion Plants, Leipzig, Deutschland, 26.-27.03.2019

Acknowledgements

Financial support of the German Federal Ministry for Economic Affairs and Climate Action (BMWK), for the projects NH3-BZ (49MF220229) and AmmoniaSens (KK 5085701CS0 Z) are gratefully acknowledged.

DOI 10.5162/EUROSENSORS2025/MP47

Integration of MEMS-based plasma emission sources in a low volume flow cell

Abélia Ellingsen, Karolina Milenko, Enrique Escobedo-Cousin, Do Chi Huong Hoang, Simone Zonetti, Alessandro Liberale and Elizaveta Vereshchagina
SINTEF Digital, Gaustadalléen 23C, Oslo, Norway
abeliaellingsen@gmail.com

Summary:
This paper discusses the integration and testing of micro-electro-mechanical systems (MEMS)-based microplasma devices with low-volume flow cells at the PCB level for emission spectroscopy of volatile organic compounds (VOCs). We introduced a novel bonding process that ensures a tight gas seal, stable pressure control down to 150 mbar, and the exchange of top fluidic glass substrates to assess their influence on the emission spectrum. The bonding process facilitates the assembly of pre-packaged MEMS components for reconfigurable and repeatable gas exposure experiments.

Keywords: MEMS, microplasma, plasma emission spectroscopy, microfluidics, bonding, packaging

Introduction

MEMS-based plasma emission sources based on dielectric-barrier discharges can serve as components in systems for the analysis of VOCs [1]. Integrating microplasmas with low-volume chambers is a logical step towards compact, portable analysis systems. Before proceeding with wafer-level integration of miniaturized chambers, a low-cost prototyping phase is often useful for screening of chamber materials and designs, as well as prototypes testing. Here, we report a demonstrator assembled using a straightforward and novel bonding method and testing approach.

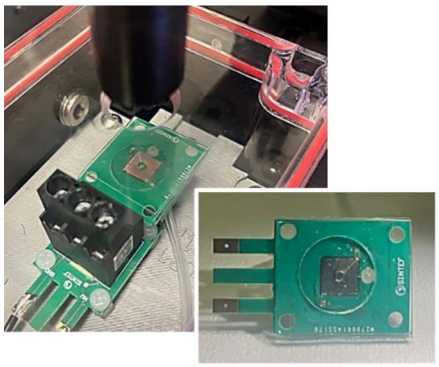


Fig. 1. Photographs of the device assembled with a low volume chamber and vacuum tube. The device is fixed in a mount connected to a voltage amplifier below a spectrometer.

Experimental

A microplasma source pre-packaged on a custom-made PCB was integrated into a low-volume chamber (241 mm³) using Flexdym™ as a sealing material [2]. The chamber consisted of the 1200 µm sealing layer and top glass substrate. The method provides a sufficiently strong bond to enable plasma ignition experiments at pressures down to 150 mbar, while permitting exchange of the glass chamber top to study the effects of material properties and chamber volume on optical detection.

All tests were conducted using the same microplasma chip tested in two chamber configurations: a compact, low-volume chamber (Compact) and a larger chamber (Box), each fitted with different types of top glass substrates through which detection occurs. Flexdym™ (Eden Microfluidics, available in 250 µm – 2 mm thickness) was thermally bonded to the PCB with an already wire-bonded chip at 120 °C for 180 seconds. Switching between chambers in different materials involved exchanging glass on the unbonded side of the FlexDym and adjusting the vacuum tubing. The pressure was initially set to either 150 mbar or atmospheric pressure. The voltage was then gradually increased until a stable plasma glow was achieved and maintained for 2 minutes. Optical emission spectra (OES) from the plasma were recorded using OceanOptics 2000+ spectrometer and a multimode fiber. The data was used to evaluate stability of intensity signal and to compare emission profiles.

Results and Discussion

Stable plasma was consistently obtained for all tests. The intensity of the OES at 434.875 nm - corresponding to the nitrogen (N_2) emission peak – was monitored over time to assess plasma stability after re-ignition during tests with different glass types. The stable plasma observed at 150 mbar in the compact chamber

(Fig. 2) indicates sealing allowing consistent pressure. The fact that the same ignition voltage (920 Vpp at 10 kHz) was required in both the compact and the large chambers further supports that the pressure was comparable, and that the small chamber reliably maintained the 150 mbar setpoint. A quantitative assessment of plasma stability was performed using the coefficient of variation (CV) of emission intensity at 434.875 nm.

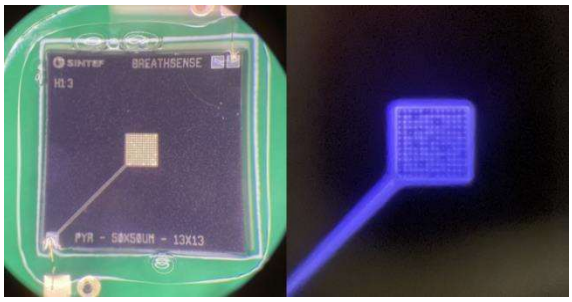


Fig. 2. An optical microscope image of the tested devices before and during operation.

Tab. 1: Overview of experiments. G1 : Borofloat (300 µm), G2: Borofloat (525 µm), G3: Fused silica (500 µm), G4: Borosilicate (500 µm), PN: Polycarbonate (3 mm).

#	Chamber type	Pressure/ Voltage	Glass type
1	Box	150 mbar/ 920 Vpp	G1, G2, G3, G4, PN
2	Compact	150 mbar/ 920 Vpp	G1, G2, G3, G4
3	Box	Atm/ 1040 Vpp	G1, G2, G3, G4, Air
4	Compact	Atm/1060-1070 Vpp	G1, G2, G3, G4

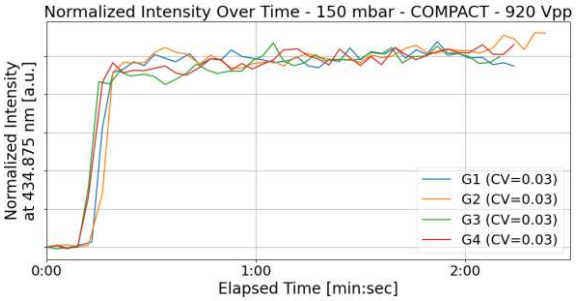


Fig. 3. Comparison of stability of emission intensity at 434.875 nm following plasma re-ignition through glass types G1 to G4 in the compact chamber at 150 mbar. Intensities are normalized to the mean between 1 and 2 minutes. The coefficient of variation, calculated as the standard deviation in this interval, was 0.03 for all glass types.

As shown in Fig. 3, CV values between 1-2 minutes of emission were identical (0.03) for all glass types, indicating consistent performance across materials. As shown in Fig. 4, spectral profiles were consistent across all glass types except for PN, which attenuates transmission and blocks UV below 400 nm completely. The shape of the spectra (normalised for intensity) remained constant and closely matched these profiles, regardless of the chamber configuration, pressure, or applied voltage. Therefore, the choice among G1-G4 should prioritise practical factors such as future manufacturability of design of interest and costs, as all tested glass materials exhibit comparable and satisfactory optical transmission.

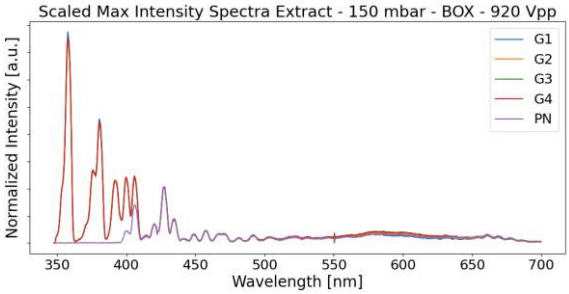


Fig. 4. Comparison of optical emission spectra collected from larger gas volume chamber (Box) at 150 mbar and 920 Vpp. The spectra have been scaled to the maximum intensity peak of PN. Glass types G1 to G4 have minimal impact on spectra, while PN blocks UV transmission.

Conclusions

The integration and testing of MEMS-based microplasma devices with low-volume flow cells at the PCB level represents a significant advancement towards emission spectroscopy platforms for gas analysis, including VOCs. The presented bonding and testing methodology based on Flexdym™ sealing to PCB ensures a reliable seal and stable pressure. This approach is well suited for the prototyping and troubleshooting of materials and designs during the development phase of MEMS-based gas sensing components.

References

[1] R. Brandenburg et al., Barrier Discharges in Science and Technology Since 2003: A Tribute and Update. *Plasma Chem. Plasma Process*. 43 (2023), 1303–1334.

[2] J. Lachaux et al., Thermoplastic elastomer with advanced hydrophilization and bonding performances for rapid (30 s) and easy molding of microfluidic devices, *Lab Chip* (2017), 17, 2581-2594.

Acknowledgements

The work in this project is financed by Horizon Europe (grant agreement number 101115028).

DOI 10.5162/EUROSENSORS2025/MP48

Morphology Dependent Response of SnO_2 Gas Sensors from Spark Ablation, Spray Pyrolysis, and Sputter Coating Techniques

Nigel Rising,[1] Larissa Eggers,[2] Leandro Sacco,[1] Anton Köck,[2] and C. Mitterer,[3]
[1] VSParticle, Oostsingel 209, 2612 HL, Delft, The Netherlands
[2] Materials Center Leoben Forschung GmbH, Roseggerstrasse 12, 8700, Leoben, Austria
[3] Department of Materials Science, Montanuniversität Leoben, Franz-Josef-Straße 18, 8700 Leoben, Austria
n.rising@vsparticle.com

Summary: In this work, the response of SnO_2 gas sensing layers manufactured via spark-ablated nanoparticle impaction printing, spray pyrolysis, and sputter coating is tested for acetone, NH_3, and CO_2. The spark-ablation-based layers show a higher response to all test gases. This is due to the high surface-area-to-volume ratio of nanoporous layers, a morphology inherent to spark ablation-made layers. Dry-printing layers via spark ablation is an attractive technique for responsive SnO_2 gas sensors, fabricated in one step without the need for solvents or complicated post-processing. These benefits can help drive innovation in gas sensing layers.

Keywords: MO_x gas sensors, spark ablation, nanoporous layers, sputter coating, spray pyrolysis

Introduction

CO_2, NH_3, and acetone are all pollutants that can harm the environment in small concentrations, and an increasing demand in environmental monitoring, especially in the EU, requires innovation in cheap and mass-producible gas sensors [1][2]. Metal oxide semiconductors (MO_x) gas sensing devices fit this requirement; however tend to suffer from low selectivity, short lifetimes, and high power consumption [3].

In order to alleviate these negatives, the layers need to be engineered on the nanoscale to increase the gas-sensing surface area, and decrease the particle size [4]. Often, fabricating MO_x layers that fulfill these requirements takes multiple, complicated steps both before and after deposition [5].

While still requiring multiple steps, sputter coating and spray pyrolysis are simple techniques that can be used to deposit MO_x layers. Spark ablation is also a simple method, but only requires one step for layer deposition. This work seeks to investigate the effect that these different deposition methods have on the gas sensing response towards NH_3, acetone, and CO_2.

Experimental

Device Fabrication

In this work, SiN-based micro-hotplate chips with integrated heating structure (up to 500 °C) and Pt electrodes were used as substrates to deposit SnO_2 layers using different techniques [6].

Spray Pyrolysis The precursor solution was a tin chloride pentahydrate ($SnCl_4 \cdot 5H_2O$) in ethyl acetate. The solution was sprayed with an N_2 carrier gas on the chips, which were kept at 400 °C during the spraying process. The sensing film was structured by a photolithography process and dry Ar ion etching.

Sputter Coating: An oxygen partial pressure ratio of 40 % at a working pressure of 1 Pa was used. The Sn target was pre-sputtered for 5 min to remove surface contaminants. During thin film deposition, the Sn target was operated at an average power of 50 W, and the deposition time was adjusted to achieve a film thickness of 50 nm. Neither external heating nor bias voltage was applied to the substrate during the deposition process. The sensing film was structured by a lift- off process.

Spark Ablation: SnO_2 spark ablation devices were deposited using the VSP-P1 nanoprinter. Nanoparticles are first generated via spark ablation in the VSP-G1 creating an aerosol in argon (Ar), and then accelerated due to the pressure difference in the generator (ambient) and the print chamber (0.2 mbar). This creates a network of sintered nanoparticles forming a highly porous thin film. 6 mm diameter Sn (99.99%) electrodes were used with spark current of 10 mA and potential of 1.3 kV. The nanoparticles were transported using 1 l/m 99.999% Ar gas to the 0.1 mm nozzle which is fixed 300 μm from the substrate. A snaked-rectangle pattern was used with a stitch size of 75 μm and a print speed of 100 μm/s.

To stabilize and oxidize the films, the chips were annealed at 400 °C in flowing synthetic air for 10 minutes. The micro- hotplates were mounted on a Kyocera socket and wire bonded.

Device Characterization

All sensors have been measured simultaneously in an automated gas measurement setup. As background gas synthetic air with tunable humidity level was chosen. In this work the humidity was set at 50 %. The operation of the temperature is kept constant during a measurement (25 °C, 150 °C and 300 °C). The target gases are

subsequently introduced into the setup for 5 min with flow meters.

The relative resistance changes due to the interaction with the test gas, i.e. the sensor response *S*, has been calculated according to:

$$S(\%) = \frac{R_{gas} - R_{air}}{R_{air}} * 100\%$$

where R_{gas} is the sensor resistance in the presence of the test gas and R_{air} is the sensor resistance in pure synthetic air.

The average response of the last 30 seconds of the gas pulse was used for R_{gas} and a 30 second average around 500 seconds after the end of the gas pulse was used for R_{air}.

Results and Discussion

Sensors fabricated with spark ablation show a greater response to NH_3, CO_2, and acetone. Sensors manufactured with spray pyrolysis and sputter coating show no response to NH_3 or acetone at all, while spark ablation devices show a 12.3 % response and a 7.6 % response toward 0.5 ppm of the gases respectively. Figure 1 shows the response of all the sensors to each test gas.

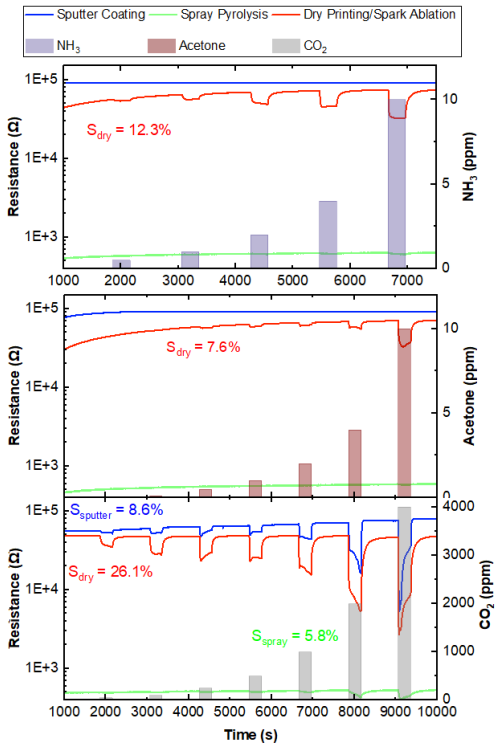


Fig. 1: Gas sensing response of SnO_2 based devices fabricated via sputter coating (blue), spray pyrolysis (green), and spark ablation(red) towards CO_2 (grey bars), NH_3 (purple bars), and Acetone (burgundy bars). Text inset gives the response to the lowest concentration that shows one.

Of the three techniques investigated in this work, sensors fabricated with spark ablation show a superior response for all target gasses. The layers produced through spark ablation are highly porous, and consist of agglomerates of nanocrystals which creates a much larger sensing surface area than the other techniques. This explains the response at much lower concentrations of test gas. Furthermore, the high surface free energy of SnO_2 nanocrystals allows spark ablation based sensors to detect gasses that other fabrication techniques cannot [7].

In addition to the superior performance, spark ablation is also a fully dry, one-step technique for layer deposition, reducing the number of steps and therefore time required for gas sensor production. By reducing the number of steps involved in the deposition, there is less room for defects or other faults that can occur during fabrication and handling [3].

References

[1] P. Nakhle, I. Stamos, P. Proietti, and A. Siragusa, "Environmental monitoring in european regions using the sustainable development goals (sdg) framework," *Environmental and Sustainability Indicators*, vol. 21, p. 100 332, Feb. 2024, ISSN: 2665-9727. DOI: 10.1016/J.INDIC.2023.100332.

[2] B. Tao, J. Bai, F. Miao, and M. Zhao, "Passive rfid integrated acetone sensor and ammonia sensor based on lafeo3/zno/rgo composites," *Microchemical Journal*, vol. 207, p. 112 122, Dec. 2024, ISSN: 0026-265X. DOI: 10.1016/J.MICROC.2024.112122.

[3] L. N. Sacco, N. Schouten, L. Egger, *et al.*, "Multiarray gas sensors based on nanoporous layers produced à la carte by spark ablation using metal oxides, binary and ternary alloys," *Proceedings of IEEE Sensors*, 2024, ISSN: 21689229. DOI: 10.1109/SENSORS60989.2024.10785068.

[4] N. Yamazoe and K. Shimanoe, "Fundamentals of semiconductor gas sensors," *Semiconductor Gas Sensors*, pp. 3–34, Jan. 2013. DOI: 10.1533/9780857098665.1.3.

[5] Y. Masuda, "Recent advances in sno2 nanostructure based gas sensors," *Sensors and Actuators B: Chemical*, vol. 364, p. 131 876, Aug. 2022, ISSN: 0925-4005. DOI: 10.1016/J.SNB.2022.131876.

[6] L. Egger, L. Reiner, F. Sosada-Ludwikowska, *et al.*, "Development of a screening platform for optimizing chemical nanosensor materials," *Sensors 2024, Vol. 24, Page 5565*, vol. 24, p. 5565, 17 Aug. 2024, ISSN: 1424-8220. DOI: 10.3390/S24175565.

[7] X. Gao and T. Zhang, "An overview: Facet-dependent metal oxide semiconductor gas sensors," *Sensors and Actuators B: Chemical*, vol. 277, pp. 604–633, Dec. 2018, ISSN: 0925-4005. DOI: 10.1016/J.SNB.2018.08.129.

DOI 10.5162/EUROSENSORS2025/MP49

Voltage-Triggered Wetting in Bio-Inspired Microfluidic Channels

Michael Weiß[1,2], Werner Baumgartner[1], Bettina Heise[3], Elisabeth Leiss-Holzinger[3], Martin Kaltenbrunner[4], Stefan Puttinger[2], and Gerda Buchberger[1]

[1] Institute of Biomedical Mechatronics, Johannes Kepler University Linz, Altenberger Str. 69, 4040 Linz, Austria,

[2] Department of Particulate Flow Modelling, Johannes Kepler University Linz, Altenberger Str. 69, 4040 Linz, Austria,

[3] Research Center for Non-Destructive Testing GmbH (RECENDT), Altenberger Strasse 69, 4040 Linz, Austria,

[4] Department of Soft Matter Physics, Johannes Kepler University Linz, Altenberger Str. 69, 4040 Linz, Austria

gerda.buchberger@jku.at

Summary:

This work presents bio-inspired microfluidic channels that form liquid diodes and are then equipped with a needle-like electrode to create "liquid triodes," analogous to electronic triodes. The devices transport liquid uni- or (bi)directionally over centimeters at velocities in the range of mm/s in response to high-voltage signals. Fabrication involves laser ablation. The topography of the microfluidic channels was analyzed by optical coherence tomography (OCT). The components have potential applications in biomedical microfluidics, labs-on-a-chip, lubrication, filtration, and electronics cooling.

Keywords: EWOD, fluid diode, directional, capillary, wetting

Background, Motivation and Objective

Devices for directional liquid transport are known as liquid diodes [1], fluid diodes [2], or (micro)fluidic diodes [3–5]. Some are based on bio-inspired designs from animals [4,6,7]. They have gained attention because they are capable of unidirectional liquid transport without requiring external energy input. Lizard- [3,7] and flea-inspired devices [4,8] use asymmetric capillary channels for directional transport. Fabrication techniques include laser ablation [3,4,7], and three-dimensional (3D) printing [8]. Material combinations vary, such as oil on elastomer [6] and soapy water on poly(methylmethacrylate) (PMMA) [4,7]. Inspired by the structures on the integument of Texas horned lizards [3,7] we apply electrowetting to create liquid triodes capable of changing their wetting state. We envision applications such as the transport of cooling lubricants, water-oil separation, and drug coating.

Description of the New Method or System

We succeeded in the fabrication of liquid triodes based on microfluidic channels bioinspired by Texas horned lizards [3,7] (Fig. 1), revealing three wetting states: non-wetting, unidirectional, and (bi)directional liquid transport. To this end, we applied electrowetting [9] to reduce the pristine contact angle to force the liquid into open capillary channels even in the backward direction. A CO_2 laser (Speedy 300 TM laser cutter/engraver from Trotec Produktions- und Vertriebs GmbH, Machtrenk, Austria) was applied to engrave the bio-inspired capillary channels in 3 mm thick PMMA plates. Several of the unit cells shown in Figure 1 were placed consecutively. Capillary channels were fabricated using a Trotec lens with a focal length of 1.5 inches and five cycles with an average power of 95 W, a velocity of 106.5 cm/s, a pulse repetition rate of 42 kHz, and a pulse energy of 2.3 mJ. Nitrogen was used for flushing to prevent burning. OCT with a center wavelength of 1.3 μm served for topography assessment (MEMS-VCSEL Swept Source Laser and a Vega Serie SS-OCT system from Thorlabs, Bergkirchen, Germany).

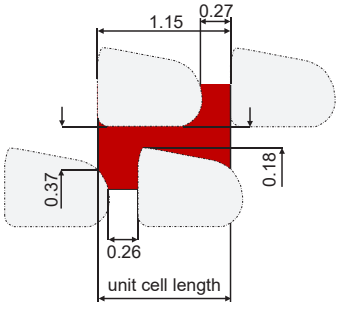


Fig. 1. Bio-inspired capillary channel design. All dimensions are given in mm.

The open-source software Fiji (version 1.53q; ImageJ2 distribution developed by Wayne Rasband and coworkers, National Institutes of Health, Bethesda, MD, USA) was used for OCT data processing, including image filtering and computing the topography with the TopoJ-plugin (quadratic window of 20). For device testing, 0.2 % w/w of the red dye "Ponceau S" (article number: 5938.1, CAS number: 6226-79-5; Carl Roth GmbH + Co. KG, D-76185 Karlsruhe, Germany) was added to distilled water.

Results

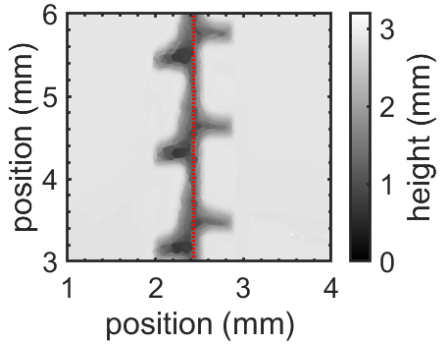


Fig. 2. Topography section of the bioinspired capillary channel. The axis of the capillary channel is highlighted with a dashed red line.

The topography data of the structure reveals maximal capillary channel depths of approx. 2.2 mm (Fig. 2). We dispensed 100 µl of test liquid onto the sample and put the needle-like electrode into it (Fig. 3). Increasing and decreasing the applied voltage in a ramp (from 0 kV to 8 kV in 200 s, plateau of 8 kV for 10 s, from 8 kV to 0 kV in 20 s), the wetting states were switched from non-wetting over unidirectional wetting to bidirectional wetting. The unidirectional wetting started at a threshold voltage of ~1.58 kV.

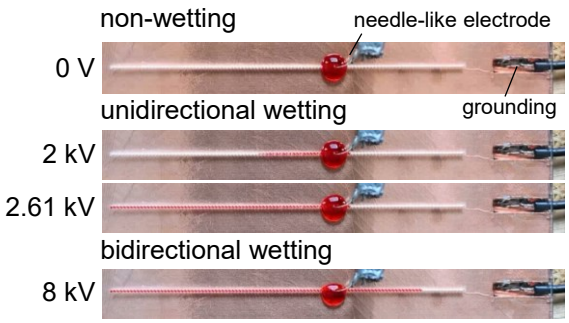


Fig. 3. Increasing the applied voltage, the wetting states were switched from non-wetting over unidirectional wetting to (bi)directional wetting. The capillary channel is 12 cm long.

References

[1] J. Li, X. Zhou, J. Li, L. Che, J. Yao, G. McHale, M.K. Chaudhury, Z. Wang, Topological Liquid Diode, *Science Advances* 3, eaao3530 (2017); doi: 10.1126/sciadv.aao3530

[2] D. Shou, J. Fan, An All Hydrophilic Fluid Diode for Unidirectional Flow in Porous Systems, *Advanced Functional Materials* 28, 1800269 (2018); doi: 10.1002/adfm.201800269

[3] G. Buchberger, R. Baumgartner, A. Kogler, T. Fritz, S. Bauer, W. Baumgartner, Bio-Inspired "Fluidic Diode" for Large-Area Unidirectional Passive Water Transport Even Against Gravity, *Sensors and Actuators A: Physical* 283, 375–385 (2018); doi: 10.1016/j.sna.2018.09.070

[4] G. Buchberger, A. Kogler, A. Weth, R. Baumgartner, P. Comanns, S. Bauer, W. Baumgartner, "Fluidic Diode" for Passive Unidirectional Liquid Transport Bioinspired by the Spermathecae of Fleas, *Journal of Bionic Engineering* 15, 42–56 (2018); doi: 10.1007/s42235-017-0003-7

[5] R.D. Sochol, C.C. Glick, A. Lu, M. Wah, T. Brubaker, K.Y. Lee, K. Iwai, L.P. Lee, L. Lin, Single-Layer Microfluidic Diodes via Optofluidic Lithography for Ultra-Low Reynolds Number Applications, in: Transducers & Eurosensors XXVII: 2201–2204 (2013); doi: 10.1109/Transducers.2013.6627240

[6] F. Hischen, G. Buchberger, C. Plamadeala, O. Armbruster, E. Heiss, K. Winands, M. Schwarz, B. Jüttler, J. Heitz, W. Baumgartner, The External Scent Efferent System of Selected European True Bugs (Heteroptera): a Biomimetic Inspiration for Passive, Unidirectional Fluid Transport, *Journal of the Royal Society Interface* 15, 20170975 (2018); doi: 10.1098/rsif.2017.0975

[7] G. Buchberger, F. Hischen, P. Comanns, R. Baumgartner, A. Kogler, A. Buchsbaum, S. Bauer, W. Baumgartner, Bio-Inspired Microfluidic Devices for Passive, Directional Liquid Transport: Model-based Adaption for Different Materials, in: *Procedia Engineering*: 106–111 (2015); doi: 10.1016/j.proeng.2015.08.576

[8] C. Sammartino, M. Rennick, H. Kusumaatmaja, B. El Pinchasik, Three-Dimensional Printed Liquid Diodes with Tunable Velocity: Design Guidelines and Applications for Liquid Collection and Transport, *Physics of Fluids* 34 (2022); doi: 10.1063/5.0122281

[9] F. Mugele, J.C. Baret, Electrowetting: From Basics to Applications, *Journal of Physics Condensed Matter* 17 (2005); doi: 10.1088/0953-8984/17/28/R01

Acknowledgements

The research was funded by the Austrian Science Fund (FWF) [10.55776/T1270] during the project "Functional Surfaces with Liquid Diode Characteristics". B.H. and E.L. acknowledge the co-financing by the project "HyperMAT" by the federal government of Upper Austria and the European Regional Development Fund (EFRE) in the framework of the EU-program IBW/EFRE & JTF 2021-2027.

DOI 10.5162/EUROSENSORS2025/MP50

Numerical Investigation of Microfluidics Micromixer Integrated with Screw Element and Complex Micropillar Structure for Enhanced Mixing

Muhammad Waqas[1], Arvydas Palevicius[1]
[1] Faculty of Mechanical Engineering and Design
Kaunas University of Technology
Kaunas, Lithuania
Corresponding Author's muhammad.waqas@ktu.edu, arvydas.palevicius@ktu.lt

Summary:

This work presents the numerical investigation of three different microfluidics micromixer designs integrated with screw element and complex shape micropillar structure as a passive element. For this purpose, COMSOL Multiphysics with two physics such as laminar flow and transport diluted species to examine the fluid flow and mixing behavior inside a microchannel. The results revealed that the third micromixer design integrated with screw element and complex shape micropillar structures deliver a best mixing efficiency of 99.95% at Reynold numbers 1. In addition, the pressure drop from inlet to outlet is also examined that is 31.26502 Pa. The findings obtained from this study provide deep insights to examine the optimal micromixer design with larger mixing performance and lower pressure drop.

Keywords: micromixer, screw element, micropillars, mixing index, pressure drop

Introduction

Microfluidics technology has rapidly expanded into a vigorous interdisciplinary topic with considerable attention in a wide range of biomedical applications such as mixing, sorting and separation [1, 2]. The fluid flow through a microchannel is considered as a challenging task to control efficiently due to its tiny amount of sample. Mixing is one of the crucial processes for mixing various biofluids and chemicals [3]. Microfluidics micromixers are widely used for mixing purposes under laminar flow conditions. Annan Xia et al. [4] proposed a novel micromixer with "Tai Chi" structure with enhanced performance and low pressure drop. They examined mixing performance more than 50% and pressure drop less than 18000 Pa for all Reynolds number. A. Farahinia et al. [5] investigated a passive T shape micromixer with different geometrical configurations. They revealed the improved mixing efficiency up to 25%. Muhammad Waqas et al. [6] proposed a novel kind micromixer integrated with screw element. They optimized the optimal design with 98.47% mixing index. According to current literature, most of the researchers explored various kinds of micromixer with different geometrical configurations such as T-shape with zigzag pattern, Tai Chi shape etc. using active as well as passive approach but there is limited work has been explored by combining the different geometrical configurations such as integration of screw element and complex shape micropillar structures. The main objective is to design and perform numerical simulations of microfluidics micromixer integrated with and without screw element and complex shape micropillar structure for enhanced mixing at various Reynolds numbers. In addition, comparison study is also carried out to evaluate the optimal micromixer design with enhanced mixing performance. The findings from this research work have meaningful practical and theoretical worth in biomedical field.

Microfluidics Micromixer Design

Three different microfluidics micromixer desigs such as plane micromixer, integrated with screw element generates the rotational flow for better mixing and integrated with complex shape micropillar structures creates vertexes which increase the mixing. Figure 1 illustrates the optimal design of micromixer with geometrical dimensions.

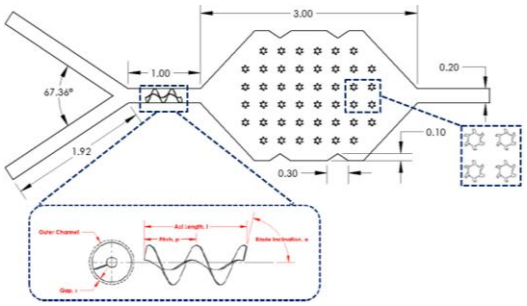


Fig. 1. Microfluidics micromixer design

Computational domain and Meshing

Figure 2 shows the computational domain with two inlets and one outlet where water and ethanol are injected and mixed solution is collected respectively. In addition, tetrahedral mesh elements are used for meshing due to the channel's complex geometry.

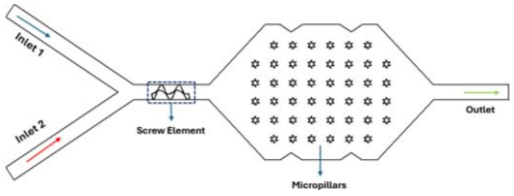


Fig. 2. Computational domain

Physics and Performance Parameters

Two physics such as laminar flow and transport of diluted species are used to model fluid flow and mixing of reactive species. Mixing index and pressure drop serve as performance parameters, with the mixing index calculated using the following equation.

$$MI = 1 - \sqrt{\frac{\sigma^2}{\sigma^2_{\max}}} \quad (1)$$

Results

Figure 3 shows the variation of mixing index with Reynolds numbers (1, 10, 50, 100) for three designs. Design 3 achieves the highest efficiency (99.95%) at Re = 1, while the plane micromixer shows the lowest (68.57%) at Re = 100.

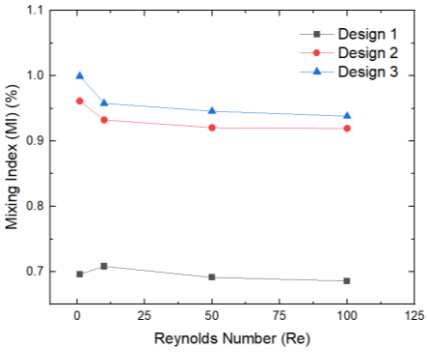


Fig. 3. Variation of mixing index with different Re

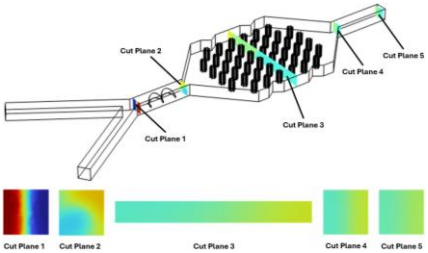


Fig. 4. Mixing concentration at five different cut planes

The screw and micropillar structures induce rotational flow and micro-vortices, enhancing diffusion at low Reynolds numbers. Figure 4 illustrates mixing concentration at five cut planes along the channel, highlighting mixing before and after passive elements, with green indicating optimal mixing (0.5 concentration). Figure 5 shows the pressure drop along the channel, caused by passive elements like screws and micropillars. The highest pressure drop, 31.27 Pa, occurs in design 2 at Re = 100.

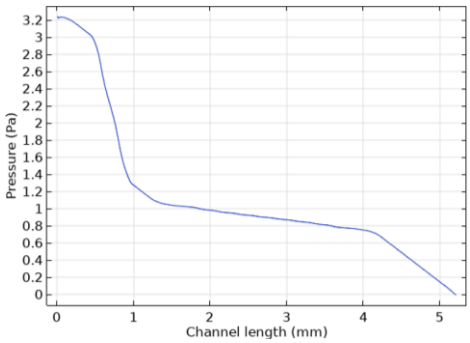


Fig. 5. Pressure drops along the channel length

Conclusion

Numerical simulations of three different micromixer designs are carried out using to investigate the mixing performance at different Reynolds numbers. Third, micromixer design delivers the best mixing performance compared to other designs. The findings can be beneficial for researchers to design optimal micromixers with enhanced mixing efficiency and lower pressure drop.

References

[1] Z. Li, B. Zhang, D. Dang, X. Yang, W. Yang, and W. Liang, "A review of microfluidic-based mixing methods," Sensors Actuators A Phys., vol. 344, no. June, p. 113757, 2022, doi: 10.1016/j.sna.2022.113757.

[2] M. Waqas and V. Naginevicius, "Numerical Investigation of Micromixer Using Hybrid Actuation Approach," Int. Conf. Perspect. Technol. Methods MEMS Des., no. May, pp. 108–112, 2024, doi: 10.1109/MEMSTECH63437.2024.10620043.

[3] M. Juraeva and D. Kang, "Mixing Performance of the Modified Tesla Micromixer with Tip Clearance," 2022.

[4] A. Xia et al., "Numerical and Experimental Investigation on a 'Tai Chi'-Shaped Planar Passive Micromixer," Micromachines, vol. 14, no. 7, 2023, doi: 10.3390/mi14071414.

[5] A. Farahinia and W. J. Zhang, "Numerical investigation into the mixing performance of micro T-mixers with different patterns of obstacles," J. Brazilian Soc. Mech. Sci. Eng., vol. 41, no. 11, 2019, doi: 10.1007/s40430-019-2015-1.

[6] M. Waqas, A. Palevicius, V. Jurenas, K. Pilkauskas, and G. Janusas, "Design and Investigation of a Passive-Type Microfluidics Micromixer Integrated with an Archimedes Screw for Enhanced Mixing Performance," Micromachines, vol. 16, no. 1, 2025, doi: 10.3390/mi16010082.

DOI 10.5162/EUROSENSORS2025/MP51

Microgravity-induced wet chemical etching of borosilicate glass – towards enhanced microfabrication methods

Kamil Baranowski[1], *Marcin Białas*[1], *Agnieszka Krakos*[1*]

[1]*Faculty of Electronics, Photonics and Microsystems, Wroclaw University of Science and Technology, Wrocław 27 Wybrzeże Stanisława Wyspiańskiego st., Poland*

[*]*agnieszka.krakos@pwr.edu.pl*

Summary:
This study investigates the impact of simulated microgravity on wet chemical etching of borosilicate glass to identify the potential microfabrication efficiency. For the first time, straight microchannels were etched in HF-based solutions using microgravity simulators (RWV, RPM). In result, with RPM the highest etching rate could be achieved (3.06 μm/min), showcasing a novel approach to chemical processing. Moreover, the structures formed under microgravity were found to be of high-quality—RPM gave the deepest, and most uniform channels, while RWV ensured the best reproducibility. These findings offer a strong basis for further research in microgravity conditions, especially in the context of reaction kinetics.

Keywords: microgravity simulators, lab-on-a-chip, microfluidics, wet chemical etching, etching rate

Introduction

The growing interest in space science and human space exploration has triggered a wave of innovation in materials processing, experimental techniques, and autonomous manufacturing systems [1]. One of the most prominent technological directions in this area is miniaturization [1]. Devices are being scaled down to reduce weight, energy consumption, and spatial footprint—making them ideal for integration into spacecraft environments.

To explore space environments without the need for spaceflight, microgravity simulators have emerged as powerful research tools. Devices like the Random Positioning Machine (RPM) and Rotating Wall Vessel (RWV) allow scientists to mimic the effects of weightlessness in Earth-based labs, enabling them to study reaction kinetics, material behaviors, and biological systems in controlled quasi-zero gravity conditions [2].
This paper is a response to current space-related scientific trends and contributes to the ongoing effort by investigating how simulated microgravity influences microfabrication processes, specifically wet chemical etching in borosilicate glass—widely used in microelectronics, MEMS, and lab-on-chip technologies.

Materials and methods

In the studies, borosilicate glass substrates with dimensions of 76 × 26 × 1.1 mm were used (BOROFLOAT® 33 Schott, Mainz, Germany). As the research is fundamental, the typical microfluidic patterns, i.e. microchannels, were prepared for the microgravity-induced microfabrication (Fig. 1).

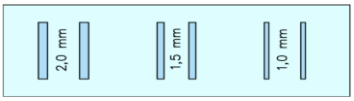


Fig. 1. Mask designed for wet chemical etching of glass substrates with straight microchannels of different widths (1.0, 1.5 and 2.0 mm).

A dedicated experimental setup was developed to safely perform wet chemical etching in hydrofluoric acid under simulated microgravity conditions (Fig. 2). The core of the setup was a custom 3D-printed stand designed to securely hold two glass substrates while allowing easy placement and removal with standard laboratory tweezers. To ensure safety during the process, the stand was positioned inside a PTFE container containing the etching solution, which was further secured within an external container acting as a leak barrier.

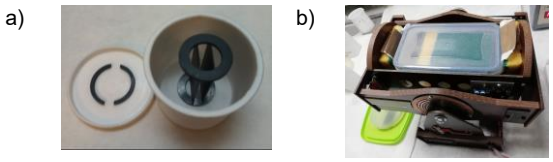


Fig. 2. Stand designed for the etching on RPM and RWV: a) stand at a glance, b) set-up for wet chemical etching of the glass substrate.

Results and discussion

To evaluate changes in etching effectiveness, etching rates were determined for all samples using a micrometer screw gauge, followed by statistical analysis including mean, standard deviation, and minimum/maximum values (Tab. 1, Fig. 3). As the same etching solution was reused for all samples, a gradual decrease in etching rate was noted, suggesting potential aging of the solution. The experiment was carried out using a 40% HF : 65% HNO_3 solution (10:1, v/v) at room temperature. Rotation speeds were set to 10 RPM for both RPM and RWV simulators, and 1000 RPM for the magnetic stirrer [4].

Tab. 1: Wet chemical etching of glass substrates in RPM and RWV compared with reference.

	RPM etching rate [µm/min]	RWV etching rate [µm/min]	Reference etching rate (no stirrer) [µm/min]	Reference etching rate (with stirrer) [µm/min]
Mean value	2.85	1.54	1.26	1.69
Standard deviation	0.13	0.14	0.09	0.21
Maximum value	3.06	1.71	1.39	2.01
Minimum value	2.74	1.52	1.18	1.52
Min/max × 100%	89.54	88.89	84.89	75.62

The results clearly indicate that the use of the RPM simulator led to the highest etching rates among all tested methods. The average etching rate achieved with RPM was 2.85 µm/min, which is approximately 40% higher than that of the reference process using a magnetic stirrer. The RWV simulator showed a slightly lower etching rate than the stirred reference (by about 9%) but still outperformed the unstirred reference by around 18%.

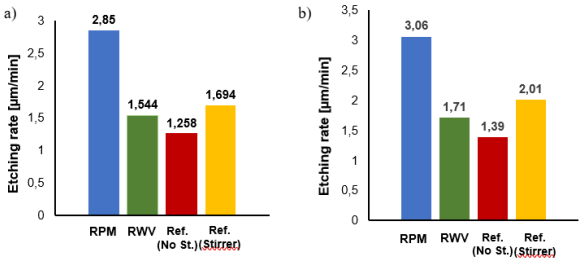


Fig. 3. Graph representing etching rates of the samples depending on the etching method: a) mean values, b) maximum values.

Microscopic inspection of the etched microchannels showed isotropic etching across all samples, with the best surface quality observed for RPM, RWV, and the reference with stirring. The deepest and most uniform channels were achieved using RPM, while RWV produced the sharpest edges—valuable for precise microstructures. SEM analysis showed no significant surface defects in any microgravity-processed samples (Fig. 4).

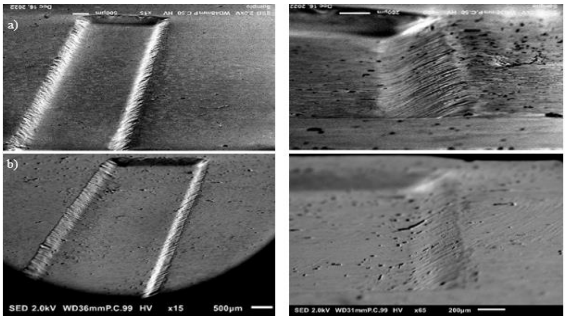


Fig. 4. SEM images of the etched microchannels with the use of: a) RPM, b) RWV. On the left – microchannel view, on the right – magnified edge profile.

Conclusion

In conclusion, results presented in these studies have showed that microgravity environment provided by microgravity simulators can constitute interesting research tools. Further investigation in this field, especially in the area of chemical reaction dynamics could be done to verify other application ideas.

References

[1] Kuang S et al (2022) Role of microfluidics in accelerating new space missions. Biomicrofluidics 16:021503. doi:10.1063/5.0079819

[2] Krakos, A. Correction to: Lab-on-chip technologies for space research — current trends and prospects. Microchim Acta 191, 86 (2024). doi:10.1007/s00604-023-06170-7

DOI 10.5162/EUROSENSORS2025/MP52

Rapid microfluidic hydrogel imprint based on CNT-induced thermoresponsive effect

Michał Żółtowski[1], Adrianna Cieślak[2], Agnieszka Krakos[1], Jerzy Detyna[2], Rafał Walczak[1]*
[1] Department of Microsystems, Faculty of Electronics, Photonics and Microsystems, Wrocław University of Science and Technology, Wrocław, Poland,
[2] Department of Mechanics, Materials and Biomedical Engineering, Faculty of Mechanical Engineering, Wrocław University of Science and Technology, Wrocław, Poland
Corresponding Author's e-mail address: adrianna.cieslak@pwr.edu.pl

Summary:
The study concerns the rapid development of precise, diverse-shaped hydrogel microfluidic structures utilizing CNT-based thermoresponsive effect. Biocompatible self-developed polymer compositions were prepared for the additive manufacturing of hydrogel matrices. Concurrently, 3D-printed structures covered with CNTs were fabricated in the form of heaters to imprint microfluidic channels into the hydrogel matrices. The experiments resulted in the precise formation of channels within the hydrogels, which is essential for further research in microfluidics and biomedical studies.

Keywords: microfluidics, hydrogel matrix, additive manufacturing, carbon nanotubes, imprinting

Background, Motivation, and Objective

Hydrogels made from natural polymers, such as sodium alginate or methylcellulose, are interesting solutions for diverse biomedical research, as they have unique properties. Hydrogel matrices equipped with microfluidic structures can create a specific environment for cellular research at the microscale, imitating the natural cell environment, i.e., ECM. On the other hand, CNTs are increasingly gaining popularity in microfluidic applications, mainly thanks to their high thermal and electric conductivity, chemical resistance, and biocompatibility. Moreover, the incorporation of CNTs into hydrogels can improve their mechanical strength, which expands their application fields significantly [1]. In this particular research, for the first time, CNTs-coated structures were used to obtain spatial microfluidic structures in hydrogel matrices, thanks to the thermoresponsive effect and utilizing the latest technological achievements of a 3D printing technique.

Description of the New Method or System

Our research was mainly focused on the fabrication of 1 W resistive heaters that serve as punches that can melt and form microchannels in a hydrogel matrix at high temperatures (approximately 140 °C). The stamps were 3D printed utilizing the DLP technique (Asiga printer, DentaStudy resin). The conductive elements of the heater were made of SWCNT (OCSiAl's Tuball Batt with 0.4% SWCNT and 0.8% poly(vinylpyrrolidone) (PVP) in H_2O), and the leads were made of silver-coated wire.

Hydrogel matrices fabrication proceeds as follows. Appropriate amounts of natural polymer powders, such as sodium alginate and methylcellulose (different concentrations), were weighed as shown in Tab. 1. A 0.9 % saline solution (NaCl) was then added as a solvent. The mixture was stirred at room temperature for 20 h on a magnetic stirrer. This allowed the obtainment of a homogeneous polymer solution - ink. The extrusion process was performed to obtain the designed matrix (nozzle type: 22G, process temperature: 25 ºC, printing speed: 5 mm/s). The structure was then stabilized using a calcium chloride solution (CaCl2, 1 M) as a crosslinking agent (t = 20 minutes).

Tab. 1: Different hydrogel compositions used for imprinting procedures

Hydrogel symbol	*Hydrogels ingredients*
1	*3% Sodium alginate + 2% Methylcellulose + NaCl*
2	*5% Sodium alginate + 3% Methylcellulose + NaCl*
3	*3% Sodium alginate + 2% Methylcellulose + 0.1% CNT + NaCl*

Results

The following 300 Ω resistance heaters were used to provide different patterns in the hydrogel structures, as shown in Fig. 1. The procedure for fabricating an imprint takes about 5 seconds, regardless of the sample. The conductive layer made of SWCNT is applied manually over the 3D-printed pattern. Each heater consists of 30 layers of SWCNTs, which corresponds to a total thickness of SWCNT layers of about 15 µm. Example results are shown in Figs. 2, 3, and 4. The results obtained for all the samples allow us to confirm that it is possible to obtain complex shapes in the hydrogel structures.

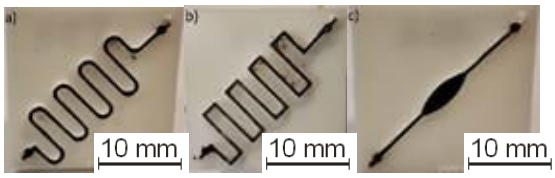


Fig. 1. Heaters with: a) meander rounded microchannel, b) meander right-angled microchannel, c) straight microchannel with widening. The width of the path of the heating element is 0.5 mm, the length of the heaters is 30 mm, and the depth of the pattern is 2 mm. The widening of the pattern from Fig. 1c) is 3 mm at the widest point.

In the case of samples defined as “1” hydrogel symbol, some inconvenience was the uneven surface of the sample, and the bubbles present inside, which deformed the imprinted pattern (Fig. 2).

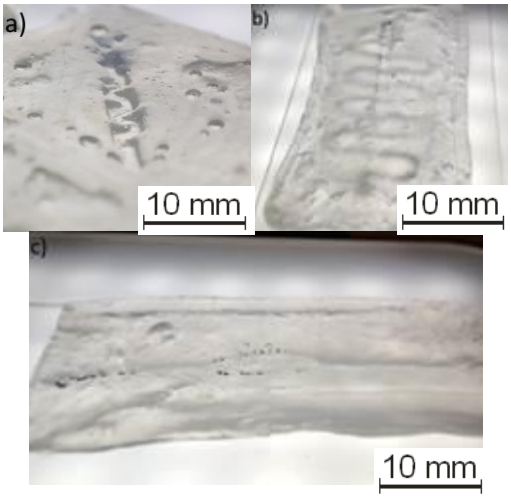


Fig. 2. Hydrogel patterns at a glance (“1” hydrogel symbol): a) meander heater with rounded edges, b) pattern laid on a glass substrate forming a microfluidic channel, c) straight microchannel with widening.

On the other hand, samples titled as “2” hydrogel symbol allow the best results in terms of pattern reproduction quality (Fig. 3). Thanks to the use of a hydrogel substrate, it was possible to create an even channel along its entire length. The only disadvantage of these samples is that making a deeper channel requires a longer annealing time, which causes boiling and consequent burning of the hydrogel.

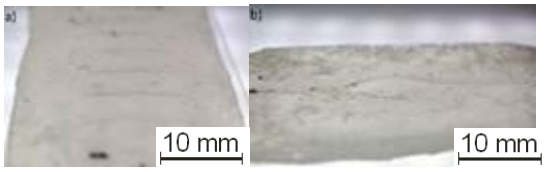


Fig. 3. Hydrogel patterns at a glance: a) meander heater with rounded edges, b) heater with widening.

In the case of the “3” hydrogel symbol, the patterns reproduce best in terms of depth but at the expense of hydrogel dissolution. It is worth mentioning that these samples are characterized by a very uniform structure and surface, which allows obtaining patterns of satisfactory quality, probably due to the addition of CNTs (Fig. 4).

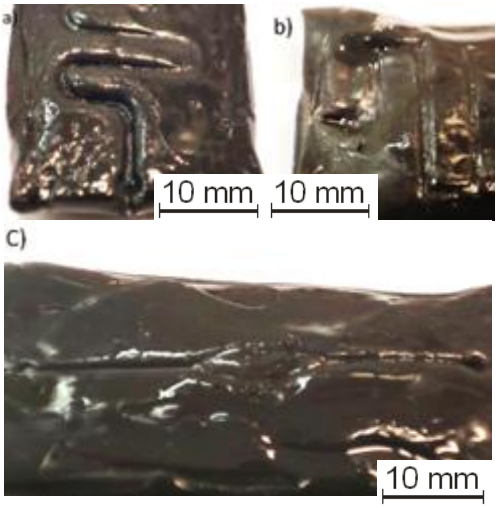


Fig. 4. Hydrogel patterns at a glance: a) meander heater with rounded edges, b) meander heater with right-angled edges, c) heater with widening.

In summary, a simple and easy-to-follow method of stamping patterns with SWCNT-layer resistive heaters makes it possible to swiftly produce microfluidic channels of versatile and complex shapes in hydrogel materials. This innovative idea could be the basis for further development of precise hydrogel structures on a microscale.

References

[1] Cieślak A. *et al., Microchimica Acta*, vol. 191, no. 10, p. 608, 2024.

DOI 10.5162/EUROSENSORS2025/MP53

Plant Growth Monitoring Using Electromechanical Sensors

Benjamin Lehner[1], Alexander Stoiber[1], Florian Bauernfeind[1], Florian Stöger[1], and Gerda Buchberger[1]
[1] Institute of Biomedical Mechatronics, Johannes Kepler University (JKU) Linz, Altenberger Str. 69, 4040 Linz, Austria
gerda.buchberger@jku.at

Summary:
This work presents proof-of-concepts (POCs) of two types of electromechanical sensors that record changes in plant length. The first one consists of an extensible solenoid with a cast iron core and possesses a length-dependent inductance. The second one is a highly stretchable resistor made from an elastomer and compliant electrodes. Both sensor principles were applied successfully to pea plants. They have potential applications in agriculture, market gardening, forestry, and vertical farming.

Keywords: plant growth monitoring, wearable, electromechanical sensor, stretchable sensor, extensible solenoid

Background, Motivation, and Objective

Flexible plant-wearable sensors show great potential for precise and intelligent monitoring of real-time physical and chemical signals in forestry seedlings [1]. They are also an emerging data collection tool for plant phenotyping in general [2].

Description of the New Method or System

We present two types of electromechanical sensor proof-of-concepts (POCs) for plant growth monitoring in the millimeter range. The first one consists of a solenoid with a core of cast iron that changes its inductance when extended (Fig. 1a). The second type of POCs was manufactured from an elastomer and compliant electrodes of carbon black particles. The resistances of these POCs change with elongation (Fig. 1b).

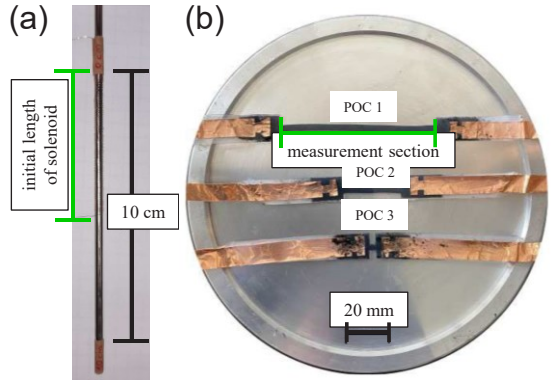


Fig. 1. Proof-of-concepts of electromechanical sensors. (a) Self-wound extensible solenoid. (b) Stretchable resistors made from silicone rubber with compliant carbon black particle electrodes.

The extensible solenoid was manufactured using a Ni/Fe 60/40 core with a diameter of 3.2 mm (VDB-Schweißtechnik NIFE 60/40 WIG Schweißstäbe Gußeisen) and enamelled copper wire with a diameter of 0.1 mm (Block-Trafo Dreifach isolierter Kupferdraht, FA-Nr.: 310863) by chucking the cylindrical core into a handheld drill and simultaneously guiding the wire by hand. It possessed approximately 80 windings. For the stretchable resistors, an Ecoflex/carbon black/Ecoflex sandwich structure was employed. To this end, part A and part B from the silicone rubber Ecoflex 0035/1 from Smooth-on were mixed in a 1:1 weight ratio. The entrapped air bubbles were removed using a vacuum chamber. The silicone mixture was cast onto an aluminium plate, and then carbon black particles (Carbon black ≥99%, metals basis, Super P® Conductive from Thermo Fisher Scientific) were applied using brushes and paper templates. At the ends, adhesive copper tape was placed on top of the carbon black. T*o protect the electrodes,* a second layer of Ecoflex was poured onto the configuration. Last, the POCs were cut out using a scalpel, and the widths of the measurement sections were reduced during this processing step.

Results

The solenoid was characterized by measuring the root-mean-square voltage signals versus the length of the (extended) solenoid (Fig. 2); the measurement data were fitted using a 4th-degree polynomial function. The measurements were conducted using a peak-peak supply voltage of 5 V with a frequency of 5 MHz and a resistor of 38.3 Ω in a high-pass configuration.

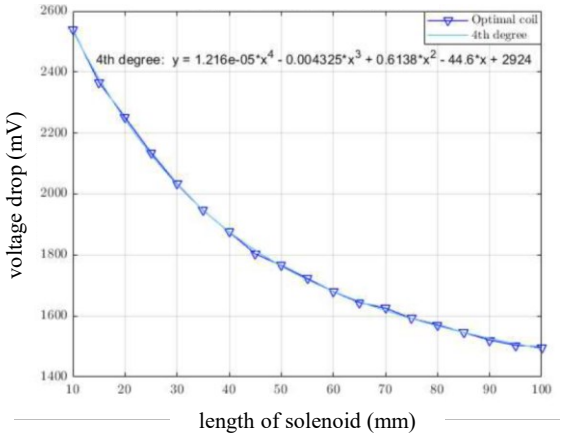


Fig. 2. Characterization of the extensible solenoid. The graph shows the voltage drop at the solenoid versus the length of the solenoid.

Furthermore, the resistances of the POCs made from silicone rubber and carbon black electrodes were recorded under elongation using a digital multimeter.

For growth monitoring of pea plants, the iron core was stuck into the earth next to the plant and the top of the extensible solenoid was wound around the top of the plant (Fig. 3a). The stretchable resistor was plugged through the holes at the bottom of the pot and clamped between the two bifurcating top twigs of the pea plant (Fig. 3b).

Using the manufactured POCs, the heights of pea plants were measured over a time period of one week (Fig. 4). For the extensible solenoid, the measured and calculated heights were in good agreement (Fig. 4a). The measurement section of the stretchable resistor (Fig. 1b) had an initial length of 50 mm, an initial width of 1 mm, and an initial thickness of 2 mm. The outer sections at the ends of the sensor were 10 mm wide.

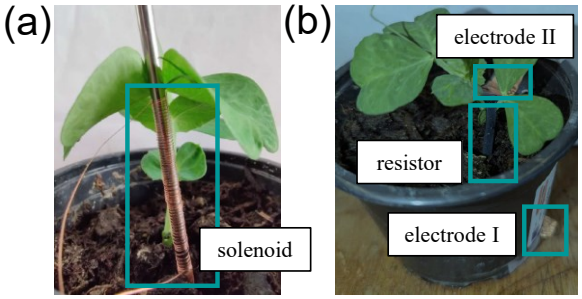


Fig. 3. Attachment of the POCs for plant growth monitoring. (a) Extensible solenoid with iron core. (b) Stretchable resistor. The electromechanical sensor POCs are highlighted with green rectangles.

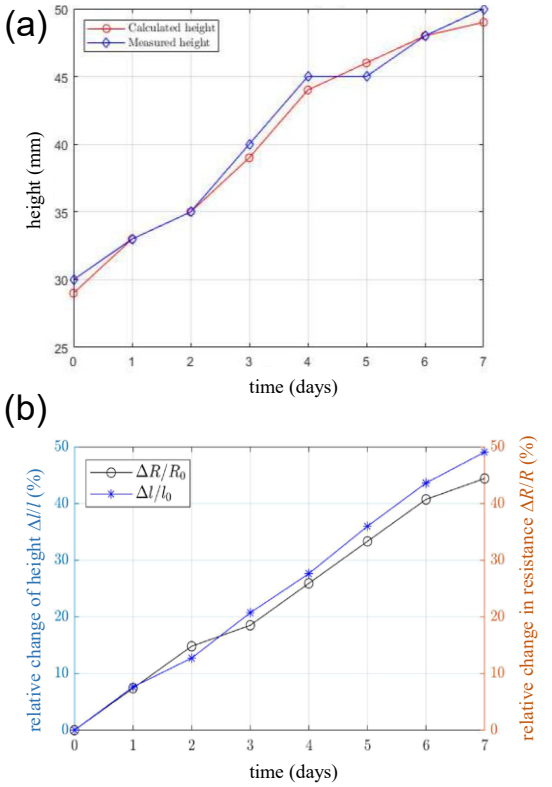


Fig. 4. The electromechanical sensors were applied to pea plants for growth monitoring. (a) The height calculated from the measured voltage drop at the solenoid is in good agreement with the measured height of the pea plant. (b) The relative change in resistance of the silicone rubber–carbon black sandwich sensor correlates well with the relative change in pea plant height.

The stretchable resistor had a resistance of 136 kΩ in the unmounted configuration. In the pre-stretched mounted configuration on a plant with an initial height of 27 mm, the resistance was 275 kΩ. The relative resistance changed approximately linearly with the relative change of plant height (Fig. 4b).

References

[1] Y. Li, H. Xu, C. Han, Y. Bai, Y. Wang, H. Yu, W. Song, Z. Sun, Plant-Wearable Sensors for Intelligent Forestry Monitoring, *Advanced Sustainable Systems* 7, paper ref.: 2200333, 23 pp. (2023); doi: 10.1002/adsu.202200333

[2] C. Zhang, J. Kong, D. Wu, Z. Guan, B. Ding, F. Chen, Wearable Sensor: An Emerging Data Collection Tool for Plant Phenotyping, *Plant Phenomics* 5, paper ref.: 0051, 19 pp. (2023); doi: 10.34133/plantphenomics.0051

Acknowledgements

The research was funded by the Austrian Science Fund (FWF) [10.55776/T1270] during the project “Functional Surfaces with Liquid Diode Characteristics”. We thank Werner Baumgartner for providing resources.

DOI 10.5162/EUROSENSORS2025/MP54

Energy-Efficient Sensor System for Structural Wear Detection in Building Envelopes for Digital Twin and Predictive Analytics

Karl Giske [1], *Soeren Hirsch* [1]
[1] Brandenburg University of Applied Sciences, Magdeburger Straße 50, 14770 Brandenburg/Havel, Germany
Corresponding Authorś e-mail address: karl.giske@th-brandenburg.de

Summary: This paper presents the development of an energy-efficient sensor node designed for predictive maintenance in building infrastructure. By continuously monitoring temperature, humidity, pressure, and acceleration, the system detects mechanical wear in doors and windows. The intelligent combination of sensor data and low-power operation enables real-time maintenance recommendations, reducing costs and optimizing energy efficiency.

Keywords: Predictive maintenance, Sensor nodes, Energy efficiency, Building monitoring, Digital twin

Maintenance of windows and doors in buildings is often resource-intensive and time-consuming, especially when relying on fixed inspection intervals [1]. Such routines can overlook early wear, while reactive maintenance may lead to unexpected failures and increased energy loss [2].

This work introduces an energy-efficient sensor node for predictive maintenance. By continuously monitoring environmental and structural parameters, the system enables early detection of wear, reducing manual inspections and enabling targeted, data-driven interventions [3]. This approach enhances operational efficiency and supports long-term sustainability goals.

Method

Sensor Selection and Microstructure Design

The selection of sensors was guided by the need to capture high-resolution physical changes linked to structural wear while minimizing energy consumption and hardware complexity. The sensor node integrates analog-output components to monitor ambient pressure, humidity, temperature, and motion along three spatial axes. To enable meaningful interpretation, the sensors are combined with a microcontroller that performs local preprocessing, including offset correction and noise filtering. This ensures that only high-fidelity data contributes to downstream analytics. By embedding this preprocessed data into a predictive maintenance workflow, it becomes possible to replace manual inspection routines with real-time, sensor-driven diagnostics. This transformation not only lowers the frequency of physical maintenance but also enables early intervention before irreversible damage occurs.

Hardware Implementation

Two main circuit configurations were developed: a baseline model and an optimized energy-efficient variant. The baseline model provided the initial system architecture, facilitating comparative analysis. The optimized variant included enhancements such as the selective activation of sensors through an enable-pin on the voltage regulator and improved sensor layout to minimize power consumption and size. Energy consumption was significantly reduced from an initial 69.6mW to 16.6mW during active operation, and further minimized to 0.9 mW in sleep mode.

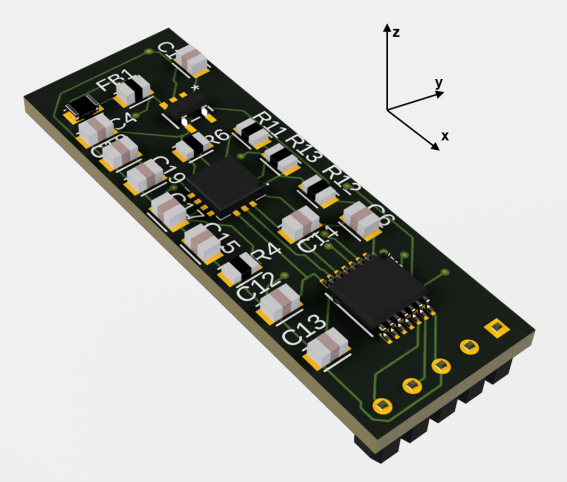


Fig. 1: 3D-Rendering of the sensor system

Figure 1 provides a 3D rendering of the final miniaturized sensor node. With dimensions of 14 mm × 40 mm, the compact form factor supports integration into space-constrained environments such as window or door frames. The layout includes a low-power microcontroller, dual voltage regulation with enable-pin control, and analog-output sensors. Components are densely placed to optimize PCB footprint while ensuring signal integrity through proximity-based placement of passive filtering elements. The design supports

dynamic sensor activation to minimize energy usage. Additionally, the figure indicates the sensor's orientation axes for motion detection, aiding interpretation of measured accelerations in real-world applications.

Embedded Firmware, Signal Preprocessing, and Data Handling

The firmware manages sensor operation, data acquisition, and adaptive power control. Measurement intervals are dynamically triggered based on detected motion using a tri-axial accelerometer, reducing energy consumption during inactive periods.

Signal preprocessing includes offset correction, smoothing, and low-pass filtering to suppress noise and transient effects. Implausible values are filtered through statistical outlier detection without compromising trend fidelity. Time-synchronized and normalized sensor data ensures robust feature extraction.

Processed data is evaluated via a hybrid system: edge-level analytics detect immediate anomalies, while cloud-based analysis supports long-term trend evaluation.

Validation and Performance Analysis

The sensor node was validated by mounting it onto window frames and monitoring both environmental and mechanical influences under real-world conditions. Distinct acceleration peaks were consistently recorded during closure events, indicating structural impacts relevant for early-stage wear detection.

Beyond dynamic events, the system captured sustained shifts in Z-axis acceleration when the window was left in a tilted-open position. These deviations allowed differentiation between closed, open, and ventilated states. A tilt-angle estimation algorithm, based on gravitational offset, indicated a deviation of approximately 5.7° along the Z-axis—consistent with the physical tilt geometry of the test window.

To evaluate long-term performance, over 19 million raw sensor samples were recorded across multiple days. The data shown in Figure 2 represents unfiltered raw data and illustrates the correlation between acceleration events and window usage. These findings confirm that the sensor node reliably detects both transient mechanical shocks and static positional changes, supporting predictive maintenance strategies in building applications.

Outlook: Digital Twin Expansion and Predictive Intelligence

Future work will focus on deepening integration with digital twin platforms to model wear progression and environmental effects over time. High-resolution sensor data will support real-time monitoring and long-term simulations within Building Information Modeling (BIM) environments. The predictive framework will be enhanced by AI-based analytics for fault detection and lifetime estimation. Wireless communication (e.g., Zigbee, BLE) and energy harvesting (e.g., photovoltaic, thermoelectric) will be added to support autonomous, maintenance-free operation. In future developments, MEMS-based sensors will be increasingly investigated for applications in jointed or flexibly mounted structures. [4]

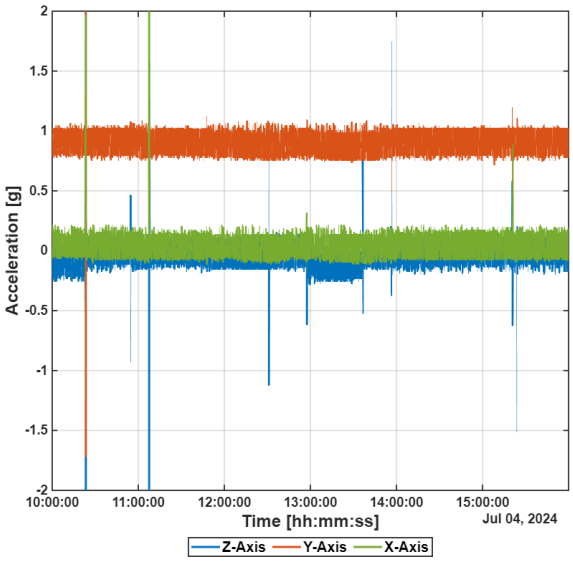


Fig. 2: Measured acceleration over time

References

[1] A. Rasheed, O. San, and T. Kvamsdal, "Predictive maintenance using digital twins: a systematic literature review," *Information and Software Technology*, vol. 151, p. 107008, 2022. doi: 10.1016/j.infsof.2022.107008.

[2] Y. Himeur, K. Ghanem, A. Alsalemi, F. Bensaali, and A. Amira, "Artificial intelligence based anomaly detection of energy consumption in buildings: A review, current trends and new perspectives," *arXiv preprint arXiv:2010.04560*, 2020. doi: 10.48550/arXiv.2010.04560.

[3] Z. Liu, E. Blasch, M. Liao, C. Yang, K. Tsukada, and N. Meyendorf, "Digital twin for predictive maintenance," in *Digital Twin for Predictive Maintenance*, SPIE, 2023.

[4] S. Majcherek and S. Hirsch, "A mems based measurement system for structure health monitoring applications," in *Smart Sensor Phenomena, Technology, Networks, and Systems 2009*, vol. 7316, p. 73160L, SPIE, 2009.

DOI 10.5162/EUROSENSORS2025/MP55

C-V measurement of Schottky Barrier LSMO/Nb:STO heterostructure dedicated to optoelectronic devices

Fallou Gning[1], Jeremy Blond[1], Victor Pierron[1], Laurence Méchin[1], Bruno Guillet[1]
[1] Caen Normandy University, ENSICAEN, CNRS, Normandy Univ., GREYC, UMR6072, F-14000 Caen, France
fallou.gning@unicaen.fr, bruno.guillet@unicaen.fr

Summary:
This study investigates the electrical properties of the Schottky diode based on the heterostructure formed by the association of a $La_{2/3}Sr_{1/3}MnO_3$ (LSMO) thin film with a 0.01 %wt Nb-doped $SrTiO_3$ (Nb:STO) substrate. Capacitance-voltage (C–V) measurements in reverse bias were carried out at 100 kHz from 300 K to 380 K. The dopant concentration of substrate and the Schottky Barrier Height were extracted from the $1/C^2$–V curve fit. The results show a systematic increase in both parameters with temperature, affecting the space-charge region and shifting the spectral response from near-infrared to visible. These results highlight the importance of a good knowledge of oxide interface electrical properties and also the potential of oxide thickness engineering for improving diode photodetection efficiency.

Keywords : Oxide heterostructure, Schottky diode, C-V characteristics, Nb:STO, LSMO

Motivation

Oxide-based heterostructures have emerged as a promising platform to explore novel electronic phenomena at interfaces due to their distinctive electrical properties and multifunctional potential [1]. In particular, the nobium-doped $SrTiO_3$ (Nb:STO), with a bandgap of 3.25 eV [2], is a suitable candidate for ultraviolet (UV) photodetection, while the Schottky Barrier Height (SBH) Φ_{Bf} of approximately 0.92 eV at the LSMO/Nb:STO interface [3] is appropriate for visible and near-infrared sensing. This work aims to provide a detailed understanding of the junction characteristics by extracting the doping level and SBH from C–V measurement under various temperatures. This constitutes the baseline for a future design of an optoelectronic sensing device.

Heterostructure Fabrication

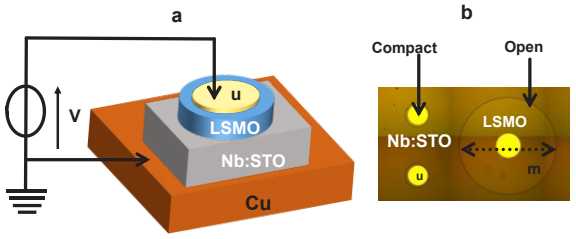


Figure 1 : (a) Cross-section diagram of the LSMO/Nb:STO heterojunction b) Examples of different heterojunction geometries

The studied samples were fabricated on lightly-doped single-crystal STO substrates at 0.01 wt% Nb content with two different thin LSMO films 10 nm and 20 nm epitaxially grown using Pulsed Laser Deposition (PLD) at 730°C. A 130 nm gold top electrode (Au) was also deposited at room temperature by Ion Beam Deposition (IBD), defining the contact on LSMO anode. The cathode was contacted using a copper plate (Cu) bonded to the back of the substrate with silver-paste. Circular heterostructures compact and open as on Figure 1 were defined on each sample by UV photolithography and chemical/ion etching. The open was used just to identify the effective surface area, enabling measurements to be normalized.

Results

C–V characteristics were measured under dark conditions using a Keithley 590 CV analyzer at 100 kHz over the temperature range of 300 K to 380 K, in steps of 20 K on the compact LSMO/Nb:STO heterojunction for each sample.

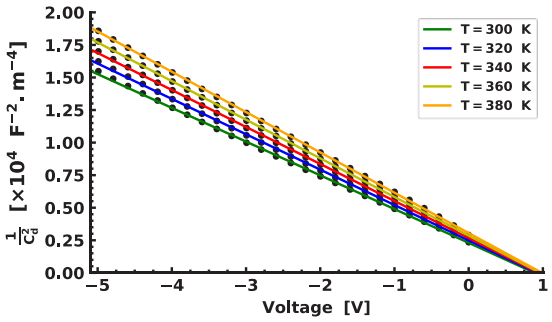


Figure 2 : Evolution of $1/C^2$ with voltage of the compact LSMO/Nb:STO heterojunction for 20 nm thick

As shown in Figure 2, linear 1/C²-V characteristics between -5 V and 0 V were revealed. This behavior is consistent with the independence of the relative permittivity ε_r of lightly doped Nb:STO from the electric field [4]. The latter decreases between 300 K and 400 K, according to Figure 3 plotted using Barrett's formula [5] where b(T) was assumed to be linearly dependent upon temperature. In this case, the N_d doping concentration and Φ_{Bf} will be extracted by linear fitting using eq.(1) [5]. As illustrated in Figures 4a and 4b, an increase in Schottky Barrier Height and doping concentration as a function of temperature was observed. The Nb doping concentrations are of the same order as the theoretical value of 3.1×10^{18} cm^{-3} expected for 0.01 wt% doped Nb:STO substrates. This evolution has an impact on the expected width of the Space Charge Region (SCR) eq.(2) [5] (see Figure 5), which broadens with reverse bias and constricts with temperature (relative permittivity decrease). These variations impact the spectral response of the devices, as the SBH value is determining the absorption cut-off wavelength of the Schottky diode for the internal photoemission process [6]. Higher barriers 1.21–1.36 eV for the 10 nm thick LSMO anode shorten the cut-off slightly wavelength to 0.91–1.02 µm, while lower barriers 0.89–0.99 eV for the 20 nm thick anode extend the cut-off wavelength 1.25–1.40 µm in the Near-InfraRed (NIR) band. This demonstrates ability to target specific spectral regions by adjusting only LSMO thickness.

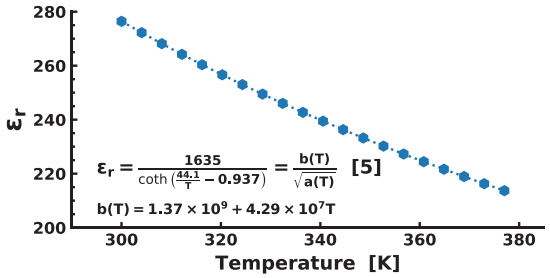


Figure 3 : Variation of relative permittivity for 0.01%wt doped Nb:STO with temperature, with zero electric field

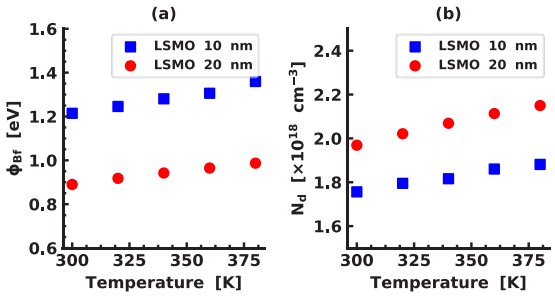


Figure 4 : Temperature dependence of (a) Schottky Barrier Height and (b) doping concentration N_d.

$$\frac{1}{C_d^2} = \underbrace{\frac{2\sqrt{a(T)}}{b(T)\varepsilon_0 q N_d}}_{\alpha}\underbrace{\phi_{Bf}}_{} - \underbrace{\frac{2\sqrt{a(T)}}{b(T)\varepsilon_0 q N_d}}_{\beta} V = \alpha + \beta V \qquad (1)$$

$$W_{SCR_{max}} = \frac{b(T)\varepsilon_0}{q(T)N_d} cosh^{-1}\left[1 + \frac{qN_d}{\sqrt{a(T)}b(T)\varepsilon_0}(\phi_{Bf} - V)\right] (2)$$

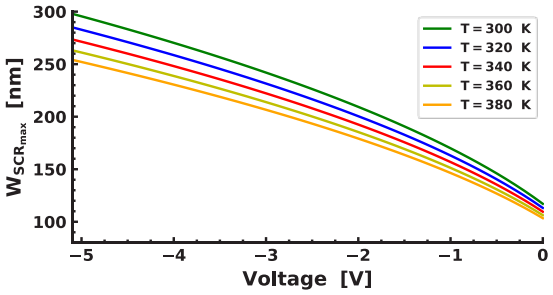


Figure 5 : Evolution of the expected Space Charge Region width versus applied reverse voltage of the compact LSMO/Nb:STO heterojunction for 20 nm thick

Conclusion

The results of this study highlight the sensitivity of oxide junctions to temperature and design parameters, which is crucial for developing performant optoelectronics devices. The observed modification of the Schottky Barrier Height versus the LSMO thickness could be interesting in developing wavelength-selective optoelectronic oxide devices. A study taking into account the frequency-dependent behavior of this to better understand the interface physics and transport mechanisms in such LSMO/Nb:STO heterostructure will be part of a future work.

References

[1] C. A. F. Vaz et al. *J. Phys. Condens. Matter* 27 123001 (2015); doi: 10.1088/0953-8984/27/12/123001

[2] S. Ramanathan, Thin Film Metal-Oxides, Chap. 5 (2010); doi: 10.1007/978-1-4419-0664-9

[3] K. G. Rana, et al., Phys. Rev. B 87 (2013); doi: 10.1103/PhysRevB.87.085116

[4] S. Suzuki et al., J. App. Phys., 81, 6830 (1997); doi: 10.1063/1.365242

[5] T. Yamamoto et al., J. App. Phys., 37, 4737 (1998); doi: 10.1143/JJAP.37.4737

[6] S. M. Sze, *Physics of Semiconductor Devices*, Ed. 3 (2007); doi: 10.1002/0470068329

DOI 10.5162/EUROSENSORS2025/MP56

Inkjet-Printed PEDOT:PSS/ZnO Diodes on a Flexible Polyimide Substrate

Apostolos Apostolakis[1], Dimitris Barmpakos[1], Fadi Jaber[3,5], Konstantinos Aidinis[4,5], Dimitrios-Nikolaos Pagonis[1,2], Grigoris Kaltsas[1]

[1] microSENSES Laboratory, Department of Electrical and Electronics Engineering, University of West Attica, Athens, Greece,

[2] Department of Naval Architecture, University of West Attica, Egaleo 122 44, Athens, Greece,

[3] Department of Biomedical Engineering, Ajman University, P.O. Box 346, Ajman, United Arab Emirates,

[4] Department of Electrical and Computer Engineering, Ajman University, P.O. Box 346, Ajman, United Arab Emirates,

[5] Center of Medical and Bio-allied Health Sciences Research, Ajman University, P.O. Box 346, Ajman, United Arab Emirates

apapostolakis@uniwa.gr

Summary:

Printing techniques offer an innovative and cost-effective approach to fabricating large amounts of flexible and lightweight electronic devices. However, developing a multilayered device such as a diode, which requires precise layer-to-layer alignment, remains a challenge. In this work, we present a fully printed approach for fabricating inkjet-printed pn-diodes on metalized polyimide substrates. The device consists of a pn junction formed by two inkjet-printed layers, namely a n-type zinc oxide (ZnO) and a p-type (PEDOT:PSS), while the bottom copper (Cu) electrode is pre-patterned onto the substrate. The device demonstrated stable rectifying behavior and exhibited promising electrical performance.

Keywords: Printed Electronics, Inkjet printing, pn-diode, Zinc oxide (ZnO), PEDOT:PSS.

Background, Motivation and Objective

Driven by growing research interest in IoT applications and the industry's shift toward greener solutions, the consumer electronics market has seen an increasing demand for flexible electronic circuits [1]. Printed and hybrid electronics have attracted significant attention as cost-effective and high-efficiency manufacturing approaches, well-suited for large-area manufacturing. Inkjet printing technique has emerged as a promising technique due to its key advantages including low-temperature processing, maskless and non-contact deposition, digitally programmable patterning, compatibility with a wide range of rigid/flexible substrates and minimal material waste. Advances in material development and the formulation of functional inks with high-performance properties—such as high mobility—have enabled the inkjet printing of advanced electronic devices, including transistors [2], diodes [3], capacitors [4], and nanoparticle-based microelectromechanical systems (MEMS) [5].

Considering these advancements, research on printed pn-diodes has gained attention due to the ability of printing techniques to selectively deposit a wide range of functional materials, enabling the formation of junctions with diverse material combinations. Among these, oxide semiconductors have shown significant potential to enhance the performance of these structures. In particular, n-type metal oxides are advantageous due to their conduction bands being derived from extended metal s-orbitals, which results in high electron mobility [6]. Consequently, materials such as ZnO, NiO, SnO_2, TiO_2, and In_2O_3 have been employed as n-type layers in printed diode structures for a variety of applications. ZnO, has emerged as a favorable candidate as it combines high carrier mobility, excellent optical transparency, and compatibility with low-temperature processing. Moreover, ZnO has demonstrated reliable performance in inkjet-printed devices and has been successfully integrated with various flexible substrates. However, metal oxides typically exhibit poor performance as p-type semiconductors. To address this challenge, hybrid diode structures have been developed, in which an organic semiconductor serves as the p-type layer. One of the most widely used

materials is PEDOT:PSS. Due to the presence of polystyrene sulfonate (PSS), PEDOT:PSS is identified as a stable p-type polymer. As a result, PEDOT:PSS is considered a solution-processable p-type polymer, highly compatible with various substrates making it an ideal candidate for multilayer heterojunction structures.

Description of the Device Fabrication

Here, we present the fabrication of inkjet-printed ZnO/PEDOT:PSS diodes on a polyimide substrate. The device consists of two printed layers and a metal layer acting as a contact. Both printed layers were designed using CAD software, in order to be aligned accurately and were printed in sequence. A low-temperature sintering process at approximately 140°C, was employed after printing each layer. A commercial polyimide (Kapton) substrate, 25μm thick with 9μm copper tracks, served as the base and the bottom electrode after the selective CU patterning. A commercially available ZnO ink was used as the n-type semiconductor while a commercial PEDOT:PSS ink served as the p-type layer. Printing was carried out using a semi-custom Drop-on-Demand (DOD) inkjet printer. Optimal printing parameters for the two inks were determined experimentally, with a droplet spacing of 65μm in both axes to ensure consistent droplet overlap. The final devices—Cu/PEDOT:PSS/ZnO—are shown in Fig. 1a, while Fig. 1b presents detail at the edge of the structure from the optical microscope.

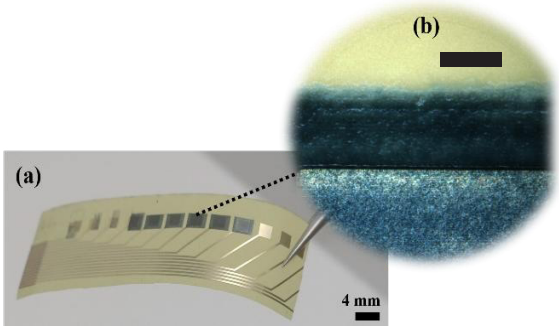


Fig.1 Inkjet-printed PEDOT:PSS/ZnO diode photographs (a); top view (scale bar is 500 μm) (b).

Results

Preliminary electrical characterization was conducted on all printed samples to validate the diode-like behavior of the fabricated ZnO/PEDOT:PSS structures. The measurements were performed using a typical probe station, connected to a Keithley 2612 source meter controlled via a custom LabVIEW interface. All characterizations were carried out at room temperature, and under dark conditions.

Fig. 2 shows three representative I–V curves (1st, 50th, and 100th) from a single ZnO/PEDOT:PSS diode using a double-staircase sweep (+0.2 → +3 V and –0.2 → –3 V) at a constant rate of 0.59 V s^{-1} for 100 measurement loops. The curves exhibit a rectifying behavior characteristic of pn-junction diodes with a low reverse leakage current. A slight hysteresis is indicated, which may be caused by charge trapping. The good overlap of the 1st, 50th, and 100th curves validates device operational stability, which is a major issue in printed electronic components.

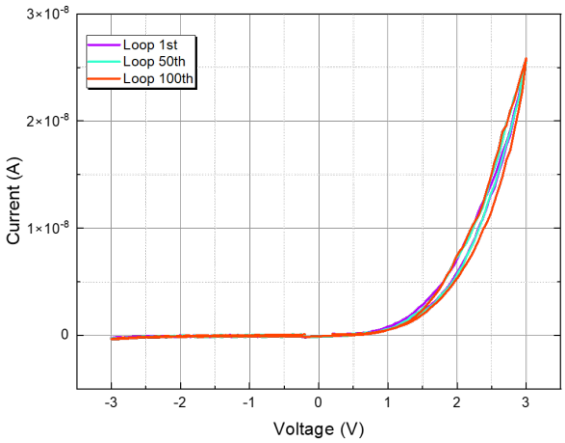


Fig. 2. I–V curves of the printed diode. The curves shown correspond to the 1st, 50th, and 100th measurement loops.

References

[1] Kim, M.S.; Almuslem, A.S.; Babatain, W.; Bahabry, R.R.; Das, U.K.; El-Atab, N.; Ghoneim, M.; Hussain, A.M.; Kutbee, A.T.; Nassar, J.; et al. Beyond Flexible: Unveiling the Next Era of Flexible Electronic Systems. *Advanced Materials* **2024**, *36*, 2406424, doi:10.1002/adma.202406424.

[2] Chung, S.; Cho, K.; Lee, T. Recent Progress in Inkjet-Printed Thin-Film Transistors. *Advanced Science* **2019**, *6*, 1801445, doi:10.1002/advs.201801445.

[3] Chu, Y.; Qian, C.; Chahal, P.; Cao, C. Printed Diodes: Materials Processing, Fabrication, and Applications. *Advanced Science* **2019**, *6*, 1801653, doi:10.1002/advs.201801653.

[4] Liu, Y.; Cui, T.; Varahramyan, K. All-Polymer Capacitor Fabricated with Inkjet Printing Technique. *Solid-State Electronics* **2003**, *47*, 1543–1548, doi:10.1016/S0038-1101(03)00082-0.

[5] Lau, G.-K.; Shrestha, M. Ink-Jet Printing of Micro-Electro-Mechanical Systems (MEMS). *Micromachines* **2017**, *8*, 194, doi:10.3390/mi8060194.

[6] Al-Jawhari, H.A. A Review of Recent Advances in Transparent P-Type Cu2O-Based Thin Film Transistors. *Materials Science in Semiconductor Processing* **2015**, *40*, 241–252, doi:10.1016/j.mssp.2015.06.063.

Acknowledgements

This work was supported by Ajman University (grant agreement 2023-IRG-1003 ENIT-12) and by the Special Account for Research Grants - University of West Attica

DOI 10.5162/EUROSENSORS2025/MP57

Study of the material variability and processing techniques on white light photoluminescence sensors based on porous Si, ZnO and carbon dots

Stavros Kiniklis[1,2], Nikoleta Chouchoumi[1,2], Niki Kagiara[1,2], Spyridon N. Katsantonis[1,3], Nikolaos Ganotis[1], Spiros Gardelis[4], Konstantinos V. Kordatos[3], Emmanouel Hourdakis[1,2], Christos Tsamis[1]

[1] Institute of Nanoscience and Nanotechnology / NCSR Demokritos, Patr. Grigoriou E' & 27 Neapoleos Str., Aghia Paraskevi, 15341, Athens, Greece,

[2] School of Electrical and Computer Engineering, National Technical University of Athens, 9 Iroon Polytechniou Str., 15772 Athens, Greece

[3] Department of Chemical Sciences, School of Chemical Engineering, National Technical University of Athens, 9 Iroon Polytechniou Str., 15772 Athens, Greece

[4] Condensed Matter Physics Section, Physics Department, National and Kapodistrian University of Athens (NKUA), Panepistimioupolis Zografos, 15784 Athens, Greece

c.tsamis@inn.demokritos.gr

Summary:

This study presents an investigation of the photoluminescence (PL) intensity and peak position of 3 different materials based on their fabrication conditions. These materials are porous Si, ZnO and carbon dots. Combinations of these materials have been shown to produce white light by a single wavelength excitation. Herein, the variability of the PL of each individual material is demonstrated, enabling the design of the combined PL characteristics. Moreover, the patterning of the materials using standard Si processing is demonstrated. The results show the applicability of the presented materials and methods for the development of integrated, PL-based devices.

Keywords: photoluminescence, porous Si, zinc oxide, carbon dots, photodetectors

Introduction

The motivation behind this work is to create pixel-type photoluminescence (PL) based devices, whose emission covers the entire visible spectrum (White Light Emission), using a single wavelength excitation. These devices can be used in multi-analyte sensing schemes based on color changes within the visible spectrum, aiming towards the fabrication sensors [1] as well as optical devices [2].

Recently, we have shown that it is possible to create PL emissions that cover the entire visible spectrum using layered structures of porous Si (pSi), ZnO and carbon q dots (CDs) [3]. These materials are known to be bio-compatible, batch-Si processing compatible and environmentally friendly. They are known to emit within different spectral ranges, specifically in red, blue and green, respectively.

In this work, we advance beyond our previous publication, studying the variability of the 3 materials' PL properties according to their fabrication conditions. This variability will be necessary in creating sensor devices with application-tailored properties. Moreover, we demonstrate the ability to process these materials in CMOS-compatible manner, creating simple structures and devices on Si substrates. The achievements described herein constitute a significant step beyond the state-of-the art and allow the creation of property-tailored sensor devices.

Materials and Methods

Porous Si (pSi) layers were formed by anodization of p-type Si substrates, of different conductivities. Conductivities ranging from a few Ωcm to a few mΩcm were used. Oxidation in different conditions was used to increase the variability of samples. ZnO films were grown on the surface of the different pSi substrates by a two-step process. Finally, different types of CDs were synthesized via a hydrothermal method by varying the type of precursor materials and the type of doping (i.e. N-doping, P-doping etc.).

PL characterization of the samples was performed by two different excitation lasers, namely one at 337nm and one at 532nm. The influence of the processing conditions on the PL signal was evaluated both independently for each

material (pSi, ZnO, CDs) as well as for combinations of them. The definition of patterns using the above materials was performed using standard Si processing photolithography and etching techniques.

Results

The effects of oxidation conditions on the PL intensity and peak position for pSi samples on p+ Si substrates (0.001 Ωcm) are presented in figure 1. It can be clearly seen that the oxidation conditions can be used to effectively control the PL emission characteristics very effectively. This allows for tailoring the emission of this material in the red part of the visible spectrum or even for the complete removal of PL signal.

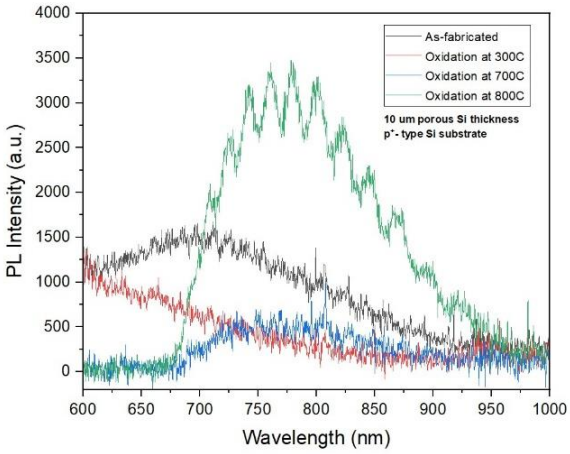


Fig. 1. Graph of PL spectrum of porous Si samples with 10µm thickness on p⁺- type Si, for different oxidation conditions.

The PL intensities of two different kinds of CDs on Si substrate are presented in Fig. 2. The N,P-co-doped CDs exhibit peak PL at around 450 nm, while P-doped CDs exhibit two PL peaks at around 450 nm and 550 nm.

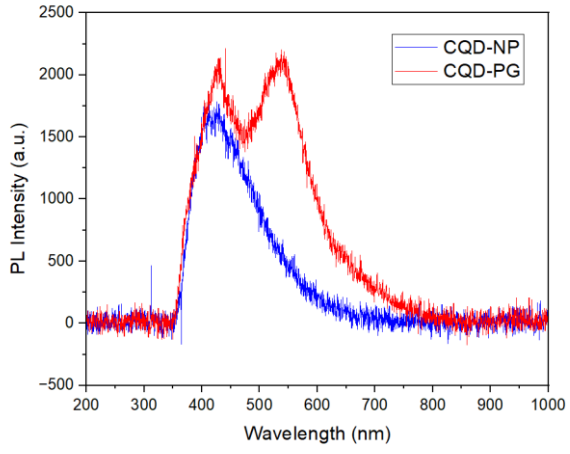


Fig. 2. Graph of PL spectrum of different CDs. NP refers to N,P-co-doped CDs and PG refers to P-doped CDs.

So, as in the case of PSi the tunability of the PL intensity as a function of fabrication conditions is demonstrated for this material.

The advantage of the proposed approach is that all materials can be either patterned (ZnO, CDs) or locally formed (pSi) using standard microelectronics processing. Figure 3 is an SEM image of a patterned ZnO layer on top of a pSi layer on a Si substrate using photolithography and etching. This enables the development of devices with precisely engineered PL properties tailored to the specific application. Results will be presented at the conference.

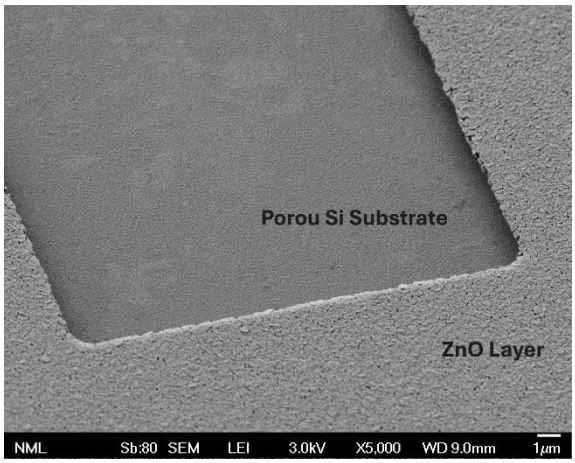


Fig. 3. Representative 45°-angle SEM image of a ZnO film grown on a porous Si substrate

References

[1] H. Zhang, D. Chen, H. Ma, and P. Cheng, 'Real-Time Detection of Traces of Benzaldehyde in Benzyl Alcohol as a Solvent by a Flexible Lanthanide Microporous Metal–Organic Framework', Chemistry A, 21, 44, 15854 (2015), doi: 10.1002/chem.201502033

[2] Islam N U, Usman M, Rasheed S and Jamil T 2021 Review— white light-emitting diodes: past, present, and future. ECS J. Solid State Sci. Technol. 10 106004

[3] E. Hourdakis, A. Bardakas, A. Segkos, S. Tsilivaki, S. Gardelis and C. Tsamis, 'Tunable and white light photoluminescence from ZnO on porous Si with the addition of carbon quantum dots', Nanotechnology, 34, 45, 455202 (2023), doi:10.1088/1361-6528/aced0f

Acknowledgements

This research was sponsored by the NATO Science for Peace and Security Programme under grant id. [G7264]."

DOI 10.5162/EUROSENSORS2025/MP58

Power consumption analysis of an OpenThread border router in a Wireless Sensor Network for Precision Agriculture

Andrea Buratti [1], Davide Polese[2] and Alessandro Checco[1]
[1] Computer Science Department, University of Rome "La Sapienza", Italy
[2] Istituto per la Microelettronica e Microsistemi (IMM) Consiglio Nazionale delle Ricerche, Italy

Summary: We performed an energy consumption analysis of a Wireless Sensor Network (WSN) for precision agriculture using the OpenThread protocol. Focusing on the Raspberry Pi as a border router, we examine strategies for optimizing power usage through peripheral deactivation and CPU frequency adjustments. A custom real-time monitoring system based on an Arduino board and Hall-effect sensor measures power consumption under varying network loads. Experimental results show that lower CPU frequencies do not necessarily reduce power draw and that increased network size raises energy demands. Findings support energy-aware configurations that prioritize sleep scheduling and optimized CPU usage for long-term WSN deployment.

Keywords: Precision Agriculture, OpenThread, energy management.

Introduction

Wireless Sensor Networks (WSNs) represent an efficient and low-cost technology for the monitoring of environmental parameters in agronomical applications and environmental monitoring [1]. Minimizing the power draw of embedded systems is critical, as these architectures are typically intended to operate using renewable energy sources and potentially in remote areas. Effective energy management is particularly critical in battery-powered contexts, where even modest consumption can significantly affect system performance and longevity. The analysis focused on the Raspberry Pi configured as a border router, which accounts for a disproportionately high share of total system energy usage. While identifying power-consuming components is relatively straightforward, developing energy-efficient strategies that preserve system performance is considerably more complex. In this work, we will investigate the energy consumption performance of a WSN based on the OpenThread networking protocol for short-range wireless communication, which claims to provide lower latency, more efficient routing algorithms, and easier interconnectivity with other IP-based networks than other protocols [2].

Experimental setup

Our WSN based on the OpenThread networking protocol is composed by one border router that acts as a bridge between the WSN and the external world and collect all sensor data in a local database, and an increasing number of sensor nodes that can act as router-nodes, i. e. nodes that collect sensor data and route the network messages and end-nodes i. e. nodes that just send their sensor data to the border router by the router-nodes. Router and end nodes are implemented by custom hardware [2], whereas the border router is implemented using a Raspberry Pi with Raspbian OS. This configuration without any optimization will be referred as "baseline".

Peripheral Management

To optimize energy consumption, a targeted strategy was adopted to deactivate all non-essential components required for the operation of the OpenThread daemon. Specifically, the HDMI ports were disabled, given their redundancy in a headless setup, alongside the Wi-Fi interface, which was used solely during the development phase for SSH access.

CPU Configuration and Energy Dynamics

Besides to deactivate unused board peripherals, the optimization of the CPU loads can improve the power consumption. It is generally assumed that higher clock frequencies lead to increased power consumption, empirical evidence suggests that this relationship is not strictly linear. However, Kaup, Gottschling, and Hausheer [3] suggest that reducing CPU frequency may, in some scenarios, results in a greater overall energy usage. To this purpose, we analyzed two power configuration "baseline" and "low-power" in the first configuration we disable all unused peripheral but we do not modify the CPU clock (1.5 GHz) and governor; in the second configuration, we set CPU clock at 600 MHz, the CPU governor has be modified to energy saving mode, and the arm_boost parameter of the boot file has be set to avoid the automatic overclock of CPU and GPU as usual in the Raspberry Pi models.

Profiling Tools and Methodology

A custom monitoring system was developed, comprising an Arduino board and a Hall-effect

sensor that allows high-resolution real-time profiling of absorbed power and current (with a resolution of 0.01 W and 0.01 A respectively), and CPU load percentage on a per-second basis. This solution enables direct, real-time measurement of the Raspberry Pi's current consumption and generates corresponding visualizations, with the capability for live display.

Two scripts were developed to manage the Raspberry Pi's power-saving configuration. The first script reduces CPU frequency and disables all non-critical interfaces, while the second restores the system's default behavior. Additional optimizations at boot include disabling the *arm_boost* parameter, onboard LEDs, and the *hdmi_blanking* option, which otherwise persistently attempts to detect a display interface.

Increasing network configuration

To evaluate the power consumption as function of the number of the nodes composing the network, a profiling script was initiated, and sensors were added incrementally. After the arrival of the first CoAP packet from each newly added sensor, a waiting period of approximately one minute was used to ensure system stabilization. This setup allows us to analyze power consumption as a function of both time and network size.

Results

In the "baseline" configuration, the Raspberry Pi consumes 4.4 W on average (σ = 0.01 W), while "low-power" mode slightly increases usage to 4.46 W (σ = 0.01 W). As shown in Fig. 1, lower CPU frequencies demand more current for equivalent workloads, highlighting the need for sleep-optimized CPU scheduling.

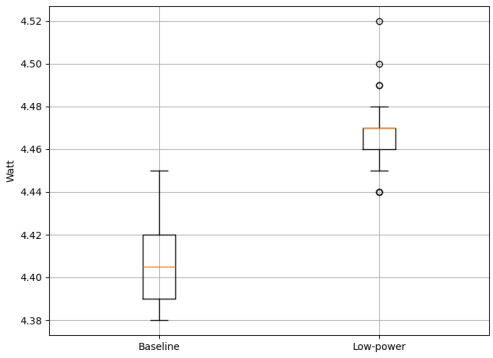


Fig. 1: Power consumption of two energy profiles.

After establishing this baseline and confirming better efficiency at higher frequencies, we evaluated power use as the network size increased. Each sensor sends a CoAP request every 2–3 s. Fig. 2 shows power varying from 4.9 W to 5.10 W with six sensors, and standard deviation rising from 0.04 W to 0.11 W, reflecting, as expected, the router's growing workload in terms of data collection and network management.

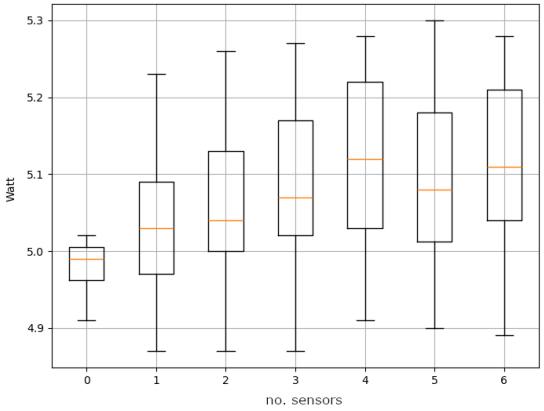


Fig. 2: Power consumption vs number of nodes.

Conclusions

Contrary to common assumptions, operating the Raspberry Pi border router at lower CPU frequencies does not necessarily yield energy savings. In fact, higher frequencies offered better energy efficiency. Additionally, power consumption scaled with network size, as increased communication demands from additional sensors led to measurable current fluctuations. Future work will focus on profiling the energy consumption of individual sensor nodes and comparing the Raspberry Pi's performance with alternative hardware platforms for the border router, as well as further investigating optimized peripheral management and CPU sleep strategies, aiming to identify more power-efficient solutions for long-term WSN deployment in agriculture.

Acknowledgments

We thank the PlumJuice team and Vladimiro Paschali for their invaluable help. This work has been partially funded by the European Union, Next Generation EU programme, PRIN project 202293CWWS.

References

[1] D. Thakur, Y. Kumar, A. Kumar, and P. K. Singh, *Applicability of Wireless Sensor Networks in Precision Agriculture: A Review*, vol. 107. Springer US, 2019.

[2] A. Checco, V. Fabiani, M. Palmisano, and D. Polese, "Network connectivity and sensor response of an openthread wsn platform for crop monitoring," *IEEE Transactions on AgriFood Electronics*, 2024.

[3] F. Kaup, P. Gottschling, and D. Hausheer, "Powerpi: Measuring and modeling the power consumption of the raspberry pi," in *39th Annual IEEE Conference on Local Computer Networks*, pp. 236–243, IEEE, 2014.

DOI 10.5162/EUROSENSORS2025/MP59

UV- sensitive Hydrogel GelMA Filled with FeCo-PET Particles

Weronika Chuda[1*], Mako Kobayashi[2], Karolina Laszczyk[1], Masaya Yamamoto[2],
[1] Wrocław University of Science and Technology -27 Wybrzeże Stanisława Wyspiańskiego st. 50-370 Wrocław, Poland
[2] Tohoku University, 2-1-1 Katahira, Aoba-ku, Sendai, Miyagi 980-8577, Japan
*contact: weronika.chuda@pwr.edu.pl.

Summary:
The purpose of this study was the preliminary development of a biocompatible material suitable for soft actuating. In this paper we present the process and results of UV-sensitive GelMA synthesis, which has an addition of FeCo particles, and we confirm its responsibility to the magnetic field. The development of soft biocompatible materials could lead to the creation of new applications in biomedicine through controlled actuation, for example, for precise drug delivery.

Keywords: hydrogels, soft actuation, magnetic particles, ultra violet, biocompatibility

Background, Motivation and Objective

Since the development of a biocompatible 3D-printable hydrogel, its function tuning has been of significant importance in research. Among these developments, the increasing interest in remotely stimuli-responsive and biocompatible components to the magnetic field could lead to new applications in various fields [1]. With its 3D-printable properties, it can be considered as a component for miniaturised devices in the form of soft microactuators or active microvalves. So far, such soft actuators have been made of conventional thermoresponsive hydrogel materials such as PEGDA, PNIPAM [2]. However, their fabrication often relies on traditional, less scalable methods. Meanwhile, these materials have limited mechanical strength and slow response. In this paper we present the preliminary study of the development of a UV-sensitive hydrogel mixed with magnetic particles and the simple result of its response to the magnetic field.

Materials and Methods

For hydrogel synthesis, we chose gelatin methacryloyl (GelMA). To determine the degree of substitution (DS) of amide groups with methacryloyl in GelMA, we used the 2,4,6-trinitrobenzenesulfonic acid (TNBS)-based assay. To make the hydrogel structures harden, we used a UV exposure. For this we incorporated photosensitive agents (lithium phenyl-2,4,6-trimethylbenzoylphosphinate (LAP; Sigma Aldrich, US). Furthermore, we added the magnetic particles (MPs) (FeCo or SmFeN) whose size was determined by SEM microscopy. However, these MPs in an aqueous environment are unstable. This can be prevented with the surface coating of the particles that makes them hydrophilic. For the coating, polyethylene terephthalate (PET) was used. To make the PET coating, the MPs were ultrasonicated in PET/hexafluoro-2-propanol (HFLP, Sigma-Aldrich, US). Then the MPs were released from solution, washed in ethanol, and dried. To confirm the coating, we used SEM and Fourier Transform Infrared (FT-IR) analyses. Furthermore, the MPs were placed in the synthesised hydrogel, the channel was formed aside MPs and UV-cured (Fig. 1). To confirm the responsiveness of the hydrogels with MPs to the magnetic field, a commercial magnet (~ 100 mT) was used. As a liquid, to be guided through the channel, we chose blue-coloured water.

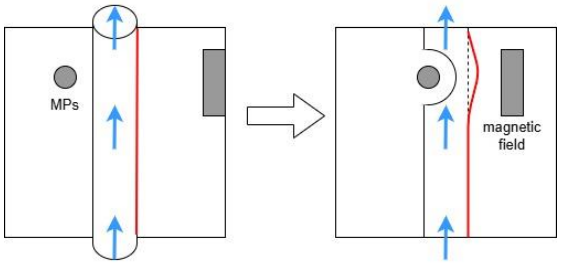


Fig. 1. A scheme to confirm if the liquid in the tunnel can be controlled.

Results

We confirmed the particles' surface was successfully coated with the PET (Fig. 2 a-d). The evidence is the black contrast on the photodiode-backscattered electron (PDBSE) image; the particle appeared black (PET presence), while the white areas represent uncoated FeCo (Fig. 2d).

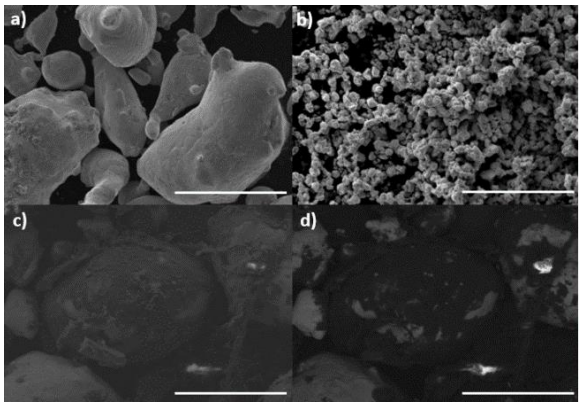


Fig. 2. SEM images of magnetic particles a and b) without coating, for FeCo (a) and SmFeN (b); c and d) with the PET coating, only FeCo covered by PET is seen in the usual image (c) and the photo diode-backscattered electron detector image (d). The scale bar was equal to 40 µm.

In the FT-IR analysis, a characteristic peak (1725 cm−1) was observed indicating C = O ester that is related to the presence of PET (Fig. 3). The coating for the SmFeN particles was not observed; hence, those particles were excluded from further research.

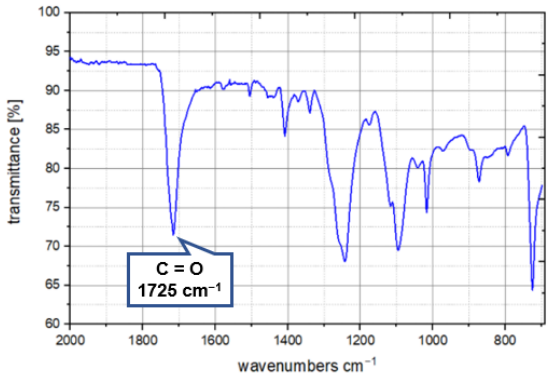


Fig. 3. The graph of the FTIR analysis for FeCo particles covered by PET.

In the hydrogel, the channel was formed with a dia ~ 1 mm along which the FeCo-PET were placed. As the water was introduced into the channel, the influence of the magnetic field presence on the hydrogel with particles was observed (Fig. 4). As a consequence, the blue line was moved (~ 0,7 mm) due to the channel wall bending toward the magnet. Meanwhile, the blue line returned to its original state as the magnet was away.

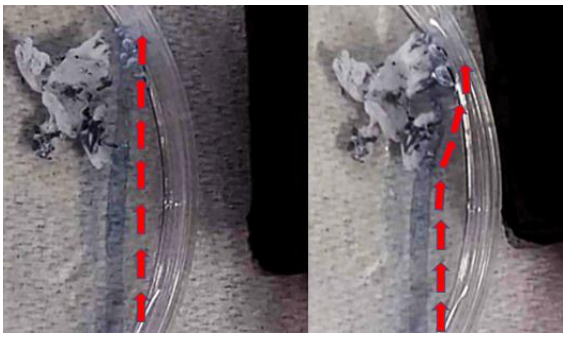


Fig. 4. The effect of the magnetic field on the flow channel with the blue coloured water line, without the presence of the magnet (left) and with the magnet in its proximity (right).

Discussion

The process of synthesis of a UV-sensitive GelMA was described as being an alternative way to obtain a hydrogel at low cost. Furthermore, the issue related to the combination of the hydrogel with the MPs was presented, and the results of its response to the magnetic field. We overcame the MPs instability in an aqueous environment by coating them with PET and as a result, we showed that they responded to the magnetic field even if they were submerged in the hydrogel. The as-prepared hydrogel, due to its UV sensitivity, enables formation of the meso-scale channel that guides the fluid, yet having from its other site of the wall the inkjet MPs. Thanks to these preliminary data, it is possible to progress toward developing the 3D-printable process with the adequate precision so as to design and build a soft actuator with the controlled working performance. The development of soft biocompatible materials with MPs for controlled actuation could lead to the creation of advanced prosthetics, minimally invasive surgical tools, and precise drug delivery systems, significantly improving patient outcomes and quality of life.

Acknowledgements

The Cooperative Laboratory Study Program (COLABS) enabled this work. https://www.insc.tohoku.ac.jp/english/exchange/colabs/. We express our gratitude to Prof. Fumio Narita for his support. We would like to thank Associate Prof. Hiroki Kurita and Senior Assistant Prof. Masashi Matsuura for providing FeCo and SmFeN particles.

References

[1] He et al; Magnetic hydrogel-based flexible actuators: A comprehensive review on design, properties, and applications, *Chemical Engineering Journal*, Vol. 462,2023,142193, ISSN 1385-8947.

[2] Haq et al. Mechanical properties of PNIPAM based hydrogels: A review*; Materials Science and Engineering: C, Vol. 70, Part 1, 2017, pages 842-855.*

DOI 10.5162/EUROSENSORS2025/MP60

Thin-Film Strain Gauge Sensor to determine the difference between infill cell designs for the sandwich beams

Rafał Trzeciakowski, Rafał Pawłowski, Karolina Laszczyk, Paweł Piórkowski*
Wroclaw University of Science and Technology, 27 Wybrzeże Stanisława Wyspiańskiego st.
50-370 Wrocław, Poland
**contact: karolina.laszczyk@pwr.edu.pl*

Summary:
This study investigates the utility of a thin-film strain gauge sensor for measuring axial stresses to determine the difference between various infill cell designs for 3D-printed sandwich beams. A dedicated measurement system was designed and implemented to do the measurements. Two designs were tested under three-point bending tests. The results confirmed that use of strain gauge measurements ato be used as one of the approaches to further optimize the 3D printed beams.

Keywords: 3D printing, sandwich beam, stress measurements, bending tests, strain gauge

Background, Motivation and Objective

The particularly promising area of research in 3D printing is the optimization of the models so as to get the more reliable and mechanically resilient structures. Previous research has emphasized the benefits of different core topologies in enhancing properties such as stiffness and energy absorption [1-2]. One of the methods to determine the printable structure mechanical stresses is to use strain gauges. The present study was conducted to confirm the use of strain gauges as a consistent and accurate tool for measuring mechanical stresses in 3D-printed beams with complex cell topologies as a possible approach to optimize their design. By applying strain gauges to the beams with various infills, it was possible to capture stresses along axes and determine differences between various infill cell designs. Establishing a systematic measurement approach can contribute to the method to optimize 3D-printed beams and other structures through the adequate infill cell design.

The materials and methods

The measurements were conducted on samples with two different cell topologies: Schwarz P and Star (Fig. 1a). The specimens, i.,e the beams, with dimensions of (63.2 × 6.3 × 6.6) mm³, were manufactured using vat-photopolymerization in a 3D printer Asiga MAX X35 (ASIGA, AU). Each beam infill cells were arranged in a particular configuration: 21 × 2 × 2. Before mounting the thin-film strain gauge, the surface of each specimen was cleaned with isopropyl alcohol (IPA) and then coated with a primer (Ataszek, PL). The strain gauge was precisely positioned in the central area of the beam surface and glued using a cyanoacrylate adhesive. Next, left for 15 minutes to ensure proper bonding between the components. A three-point bending test was performed on five specimens of each topology using the tensile testing machine CS2-1100 Chatillon (Ametek, US; Fig. 1b). The recorded force-deflection characteristics present the stiffness of each design by analyzing the linear region of the curve, followed by the calculation of Young's modulus based on a formula presented in [3]. The entire testing process was recorded using a digital camera to synchronize the data with strain gauge measurements. The strain gauge was integrated into a Wheatstone bridge circuit, and changes in the output voltage caused by the specimen's deflection were recorded using a digital multimeter 34461A (Keysight, US). From the measured voltage, the deflection of the specimen was determined. Hooke's law was applied within the elastic range of the sample to calculate stress, following the approach described in [4]. The collected data was analyzed to identify both the advantages and limitations of the performed measurements.

Results

The graph in Figure 1c presents the relationship between the average stress and the average deflections for both infill topologies. The noticeable difference in the slope of the lines indicates distinct mechanical properties of the structures. The Schwarz P topology achieved an average stress of (1.22±0.25) MPa at the average deflection of 1.7 mm, whereas the Star infill beams reached (0.94±0.25) MPa at the average deflection of 1.6 mm. The higher stress

value for Schwarz P suggested greater stiffness of the beam. At the same time, Young's modulus analysis showed that the Schwarz P topology resulted in Young's modulus value of (305.3±8.3) MPa. Meanwhile the Star topology resulted in slightly lower Young's modulus (236.2±30.0) MPa, indicating a higher ability to undergo the elastic deformation.

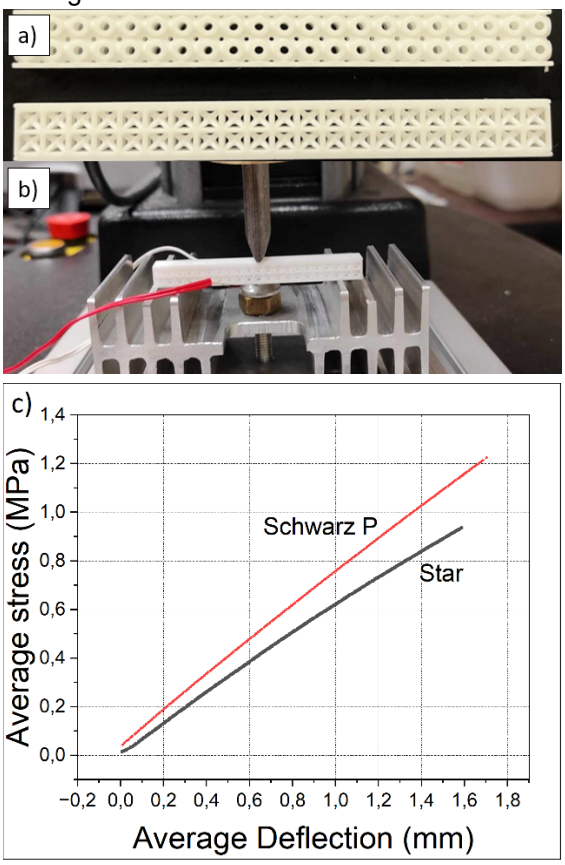


Fig. 1. The tested samples with the strain gauge: a and b photographs: of printed beams (a), with Schwarz P (top) or Star (bottom) topology and the three-point bending test (b); c) the graph: the averaged stress values as a function of the averaged deflection values for sandwich structures with the Schwarz P and Star topologies

Conclusions

The conducted measurements enabled the determination of axial stresses using the strain gauges. Based on the results, we confirmed the difference in the mechanical properties of the beams with different infill topologies. The Schwarz P topology made the beam stiffer, resulting in a higher average stress compared to the Star topology (about 23%). However, the analysis also highlighted the possible limitations of such approach excluding ist use in some engineering applications, e.g. in the health monitoring and the mechanical component testing. These applications are particularly sensitive to factors including temperature fluctuations, surface preparation quality, and the adhesive properties. Further studies should include fatigue analysis and the impact of various printing parameters on the mechanical properties. Additionally, the use of alternative measurement method, such as X-ray diffraction (XRD) should be considered to more accurately determine local stresses and deformations, allowing for design optimization. To precisely determine Young's modulus, the implementation of additional measurement techniques and analytical methods should be explored, especially if we would like to scale-down components for microsystems. The proposed future research directions include conducting tests under controlled conditions to maximize measurement repeatability and identify the influence of external factors on test results. It is also crucial to determine the exact Young's modulus value, for example, through computer simulations, which would enable more precise modeling of the analyzed structures' behavior and their practical engineering applications.

References

[1] N. Iranmanesh, H. Yazdani Sarvestani, B. Ashrafi, M. Hojjati, Beyond honeycombs: Core topology's role in 3D-printed sandwich panels, Materials Today Communications 37 (2023); doi: 10.1016/j.mtcomm.2023.107548

[2] M. Li, Z. Hu, B. Yan, J. Wang, H. Zhang, F. Ye, B. Sun, J. Liu, Y. Li, G. Ding, F. Zang, and Z. Yang, "A flexible resistive strain gauge with reduced temperature effect via thermal expansion anisotropic composite substrate,"Microsystems nanoengineering, vol. 10, p. 129, 09 (2024); doi: 10.1038/s41378-024-00762-w

[3] S.Z. Gebrehiwot, L.E. Leal, J.N. Eickhoff, L. Rechenberg, The influence of stiffener geometry on flexural properties of 3D printed polylactic acid (PLA) beams, Progress in Additive Manufacturing 6, 71–81 (2021); doi: 10.1007/s40964-020-00146-2

[4] D. Bajaj, I. Madhav, M. Juneja, R. Tuli, Methodology for stress measurement by transparent dental aligners using strain gauge, World Journal of Dentistry 9(1), 13–18 (2018); doi: 10.5005/jp-journals-10015-1499

Acknowledgements

This project has received funding from the European Union's Horizon 2020 research and innovation programme under the Marie Skłodowska-Curie grant agreement No 101007429. Project co-financed by the Polish Ministry of Education and Science under the program called International Co-financed Projects.

DOI 10.5162/EUROSENSORS2025/MP61

Detection of Electron Beam in Atmospheric Pressure Using CMOS Image Sensor

Michał Krysztof[1], Kamil Baranowski[1], Michał Zychla[1], Matthias Hausladen[2], Rupert Schreiner[2], Aleksandr Knápek[3]

[1] Faculty of Electronics, Photonics and Microsystems, Wroclaw University of Science and Technology, 11/17 Janiszewskiego St., 50-372 Wroclaw, Poland
[2] Faculty of Applied Natural Sciences and Cultural Studies, OTH Regensburg, D-93053 Regensburg, Germany
[3] Institute of Scientific Instruments of the Czech Academy of Sciences, Královopolská 147, 612 64 Brno, Czech Republic

Corresponding Author's e-mail address: michal.krysztof@pwr.edu.pl

Summary:
In the article, a new detection system that enables observation of the electron beam signal passing through a gas layer at atmospheric pressure is presented. An experimental setup consisting of an electron gun (electron emitter, extraction, and focus electrodes), silicon nitride membrane, and a CMOS image sensor is described, as well as first image of the electron beam spot after passing through 400 µm of air at atmospheric pressure is presented.

Keywords: electron detection, field emission, CMOS sensor, MEMS

Introduction

The theory of electron motion in gases dates to the beginning of the twentieth century, mainly due to the work of Townsend [1]. In the middle of the century, more accurate experiments on electron mobility and determination of electron drift velocity were carried out [2, 3]. Recently, new devices capable of mapping the complete spatial-temporal evolution of electron swarms have been reported [4, 5]. They allowed to determine several important parameters, i.e., drift velocity, longitudinal diffusion coefficient, and effective ionization coefficient.

The apparatus' mentioned in [2–5] that are capable of measuring electron swarms are large and complicated, similar to spectrometers. With the evolution of microelectronics and microsystem technologies, vacuum microelectronics systems are being miniaturized, for example, the miniature MEMS scanning electron microscope was developed at Wroclaw University of Science and Technology [6], where the atmospheric pressure electron detection method was developed. The described method shows that the electron signal that passes through silicon nitride membrane is not absorbed by air but can be collected at the anode, as the theory of electron motion in gas predicts. The measured electron signal depends on the gas type, pressure, and distance from the membrane to the detector. To find out how those parameters influence the electron beam in gas a new detection method using a CMOS image sensor needs to be developed to observe the electron swarm development in real time.

Recently, at Ostbayerische Technische Hochschule in Regensburg, Germany, an electron beam detection device was developed that uses the Raspberry Pi High Quality Camera [7]. Their research enables the emission current value to be linked to the signal intensity measured on the camera, so that the electron emission parameters can be measured in real time. The results are obtained in high vacuum.

This article presents the first results of using the CMOS image sensor electron detector developed at the OTH for investigation of electron beam measurements in atmospheric pressure.

Experimental Setup and Measurements

The experiment involves observing a beam of electrons that come out of a vacuum chamber through a silicon nitride membrane (1) mounted on top of a small vacuum chamber, propagating in a gas using a CMOS camera (2) (Fig. 1). Inside the vacuum chamber, a small electron gun, consisting of a silicon electron emitter covered with carbon nanotubes and extraction and focus electrodes, was mounted. The silicon membrane

was vacuum sealed to the vacuum flange with a 3 mm hole drilled through. The CMOS image sensor prepared at the OTH Regenburg was placed in front of the membrane.

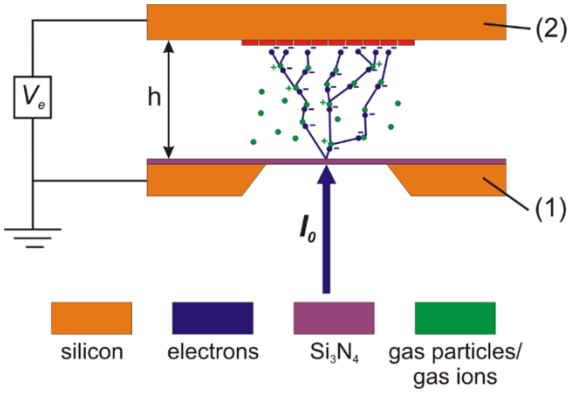


Fig. 1. Basic schematic of the MEMS/CMOS electron detection measurement system.

The experiment was carried out with 10^{-5} mbar vacuum inside the chamber. The emitter was supplied with –2 kV and the extraction voltage was set to –500 V to limit the emission current to limit the initial electron beam current to 1 µA. The voltage at the focus electrode (–2 kV) allowed focusing of the beam to be focused on the membrane. The effect of the electron beam passing through ~400 µm of gas was observed on the CMOS sensor (Fig. 2).

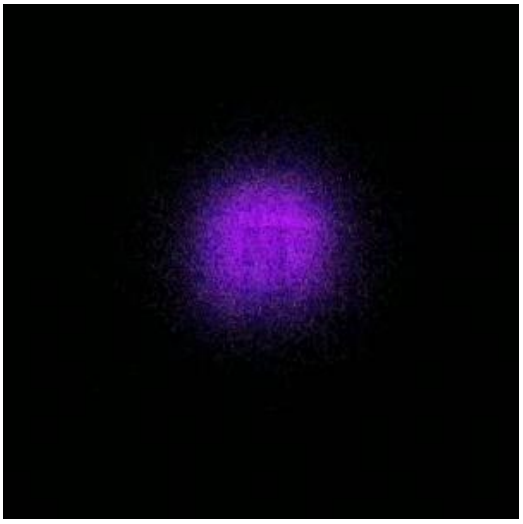


Fig. 2. Image of the electron beam spot taken with Raspberry Pi High Quality Camera.

Conclusions

The results show that it is possible to use the CMOS image sensor for electron beam observation under atmospheric pressure. The CMOS sensor was developed for electron beam current measurements in high vacuum. The sensor is suitable for registering the electron beam spot shape, from which one can observe if the electron emitter is symmetric, but also by calculating the image intensity, the emission current can be calculated.

Similarly, observing the electron beam spot after passing through a gas (Fig. 2) one can observe the diffusion of electrons in a gas, but for now it is not clear if it is possible to calculate the electron beam current from the image intensity. This will be done in the next step of the investigation. We will check what signal is actually detected by the CMOS sensor and how the parameters of the gas (i.e. gas type, gas pressure), and the detection setup (i.e. the distance from the membrane to the sensor) will influence the results.

References

[1] J. S. Townsend, H. T. Tizard, The Motion of Electrons in Gases, *Proceedings of the Royal Society of London. Series A, Containing Papers of a Mathematical and Physical Character*, 88 (604), 336-347 (1913), doi: 10.1098/rspa.1913.0034

[2] H. Ryżko, Drift velocity of electrons and ions in dry and humid air and in water vapour, *Proceedings of the Physical Society*, vol. 85, 1283-1295 (1965) doi: 10.1088/0370-1328/85/6/327

[3] J. A. Rees, Electron drift velocities in air, *Australian Journal of Physics*, 26, 427-431 (1973) doi: 10.1071/PH730427

[4] I. Korolov, M. Vass, Z. Dankó, Scanning drift tube measurements of electron transport parameters in different gases: argon, synthetic air, methane and deuterium, *Journal of Physics D: Applied Physics*, 49, 415203 (2016) doi: 10.1088/0022-3727/49/41/415203

[5] X. Chen, W. He, X. Du, X. Yuan, L. Lan, X. Wen, B. Wan, Electron swarm parameters and Townsend coefficients of atmospheric corona discharge plasmas by considering humidity, *Physics of Plasmas*, 25, 063525 (2018) doi: 10.1063/1.5025116

[6] M. Krysztof, M. Białas, T. Grzebyk, A. Gorecka-Drzazga, Atmospheric Pressure Electron Detection Method for MEMS Electron Microscope, *IEEE Electron Device Letters*, vol. 43, no. 5, pp. 813-815 (2022) doi: 10.1109/LED.2022.3162950.

[7] M. Hausladen, A. Schels, A. Asgharzade, P. Buchner, M. Bartl, D. Wohlfartsstätter, S. Edler, M. Bachmann, R. Schreiner, Investigation of Influencing Factors on the Measurement Signal of a CMOS Image Sensor for Measuring Field Emission Currents, *Sensors* 25(5):1529 (2025) doi: 10.3390/s25051529.

Acknowledgements

This research was funded in part by National Science Centre, Poland under the WEAVE-UNISONO project no. 2023/05/Y/ST7/00267.

DOI 10.5162/EUROSENSORS2025/MP62

Piezoresistive Pressure Sensors Based on ZrO_2 Substrate Fabricated by Photolithography and Inkjet Printing

Vojtěch Povolný[1], Alexandr Laposa[1], Jiří Kroutil[1]
[1] Czech Technical University in Prague, Department of Microelectronics, Technická 2, 16627 Praha 6, Czech Republic,
povolvoj@fel.cvut.cz

Summary:
This work compares piezoresistive pressure sensors fabricated on ZrO_2 substrates using two different manufacturing technologies: photolithography and inkjet printing. Both fabrication methods produced sensors with precise and reproducible dimensions, with initial tests showing clear differences in sensitivity and performance, highlighting the potential of each technology for specific applications.

Keywords: Piezoresistive sensor, Inkjet printing, Photolithography, Ceramic substrate, Pressure measurement

Background, Motivation and Objective

Piezoresistive pressure sensors using ceramic substrates are particularly suitable for harsh environments due to their excellent mechanical properties, chemical inertness, and thermal stability. Alumina (Al_2O_3) and zirconia (ZrO_2) are widely used ceramic materials. Al_2O_3 is primarily beneficial due to its high hardness and superior wear resistance, whereas ZrO_2 offers enhanced strength, improved fracture toughness, and a comparatively lower Young's modulus [1, 2].

Inkjet printing has recently emerged as an attractive alternative due to its precise deposition capabilities, design flexibility, and cost-effectiveness. In contrast, photolithography remains a benchmark technology known for high precision and reliability in sensor manufacturing. Understanding the comparative performance of these two distinct fabrication methods is critical for optimizing sensor development strategies [3].

The objective of this research is to fabricate and evaluate piezoresistive pressure sensors on ZrO_2 substrates separately using photolithography and inkjet printing to assess their respective strengths and limitations, ultimately providing guidance for selecting optimal fabrication approaches for specific sensor applications.

Description of the New Method or System

Two separate sets of piezoresistive pressure sensors were fabricated using 32 mm diameter ZrO_2 ceramic substrates. Each set featured membranes with a thickness of 600 µm, structured with meander-shaped metal strain gauges.

The first set of sensors was fabricated using traditional photolithography, utilizing precise metal patterning to form aluminum strain gauges. The second set of sensors employed DragonFly IV inkjet printing technology from NanoDimension, applying conductive silver nanoparticle inks. Structures fabricated by photolithography achieved linewidths around 40 µm, gaps of 80 µm, and a uniform thickness of approximately 50 nm. Inkjet-printed structures achieved linewidths around 72 µm, gaps of 110 µm, and a uniform thickness of approximately 1.6 µm (*Fig. 1.)*.

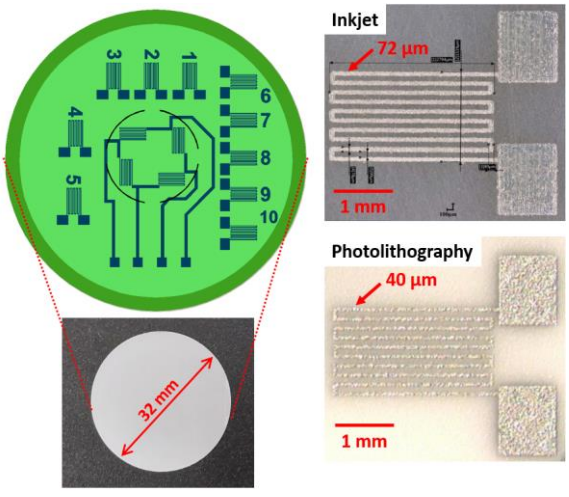


Fig. 1. Layout and details of test structures fabricated by inkjet printing and photolithography.

Results

Both manufacturing methods demonstrated excellent dimensional precision and repeatability. Pressure tests conducted at 27

kPa exhibited differences in sensitivity between the two technologies. The test rig (*Fig. 2.*) includes a custom 3D-printed fixture for mounting ceramic sensor samples, connected to a pneumatic pressure system. The sensors are secured using wing screws and contacted via probe wires for electrical measurements. The setup allows precise pressure application and real-time monitoring of resistance changes using a PC-connected interface. Electrical characterization revealed that sensors fabricated via photolithography exhibited resistance values around ~7 kΩ, which are suitable for conventional sensor applications. In contrast, inkjet-printed sensors showed significantly lower resistance values (~20 Ω), creating challenges for accurate resistance measurement and limiting their practical use in standard pressure sensing applications. The observed difference in resistance is primarily attributed to the disparity in the thickness of the deposited metallization layers between the two fabrication processes.

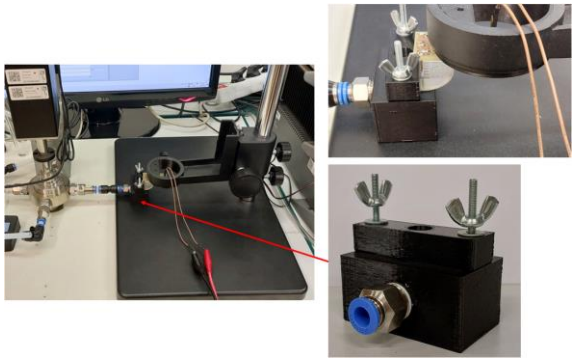


Fig. 2. Measurement setup for pressure sensors

Comparing both technologies, inkjet printing provides benefits including flexible design capabilities and reduced production complexity, while photolithography ensures highly precise patterns and reliable performance suitable for applications requiring stringent specifications.

Future work involves membrane thickness optimization for both methods, employing thinner membranes to enhance sensor sensitivity significantly. Additionally, exploring the integration of carbon-based inks for inkjet-printed sensors is planned, which could enhance performance through increased strain sensitivity and increased resistance.

References

[1] Shakir, R. A., & Géber, R. (2023). Structure and properties of ZrO_2–Al_2O_3–MgO porous ceramic for biomedical applications. Results in Engineering, 18, 101104; doi: 10.1016/j.rineng.2023.101104

[2] L. Zhao, J. Zuo, B. He, and Y. Jiang, “Properties of ceramic substrate materials for high-temperature pressure sensors for operation above 1000 °C,” Journal of Sensors, vol. 2018; doi.org/10.1155/2018/2317295

[3] J. Anglada, J. Molera, N. García, J.M. Colom, M. Pinyol, A. Duran, “Integration of conductive silver sensors on zirconia ceramics by screen-printing for monitoring strain under applied load,” Ceramics International, vol. 49, no. 5, pp. 7583–7590, 2023; doi.org/10.1016/j.ceramint.2022.12.005

Acknowledgements

This research has been supported by the Technology Agency of the Czech Republic under the project FEIM (No. TN02000067 “Future Electronics for Industry 4.0 and Medical 4.0” under the National Centre of Competence Programme. Special thanks go to ELCERAM a.s.,Czech Republic and Profactor GmbH, Austria for specimen manufacturing in the production facilities.

DOI 10.5162/EUROSENSORS2025/MP63

Elastomer-based flexible THz metasurfaces for sensing applications

Andras Kovacs[1], Przemyslaw Lopato[2], Michal Herbko[2], Julien Petit[1], Benjamin Sittkus[1], Volker Bucher[1], Ulrich Mescheder[1,3]
[1] Furtwangen University, Robert Gerwig-Platz 1, 78120 Furtwangen im Schwarzwald, Germany,
[2] West Pomeranian University of Technology, ul. Sikorskiego 37, 70-313 Szczecin, Poland,
[3] Associated to the Faculty of Engineering, University of Freiburg, Freiburg, Germany
Andras.Kovacs@hs-furtwangen.de

Summary:
For THz sensing systems, reconfigurable metasurface is a key issue for obtaining miniaturized, fast and cheap spectral scanning systems in the THz domain. This paper presents the manufacturing and characterization of flexible elastomer, PDMS (polydimethylsiloxane)-based THz metasurfaces. Numerical models were applied to analyze the system THz properties. Measurements proved the usability of proposed flexible THz sensors. For a 25% deformation, a decrease of resonant frequency by 8% (~ 20 GHz) was obtained.

Keywords: Terahertz; metasurface; flexible sensors; elastomer; PDMS;

Introduction

THz sensing has a great potential for many applications in wireless communication [1], imaging [2], material analysis [3], wearable sensors [4], and biomedical detection [5]. Active modulation of THz metamaterial (MM) devices can be achieved by mechanical, electrical, magnetic, and optical control [6]. Flexible substrates enable the effective tuning of the THz MM resonance frequency under various mechanical loads such as bending, folding, twisting, compressing and stretching without causing the system to degrade even under repeated multiple loading [7] where the materials and the device components must exhibit long-term stability, especially good adhesion and no layer wear or cracking. Often, rigid materials such as Au, Al, Mo, Ni, Ti, are used as a conductive layer [4] in combination with flexible materials such as polyvinyl alcohol (PVA), polyimide (PI), polydimethylsiloxane (PDMS), polyethylene glycol naphthalene dicarboxylate (PEN) [6].

Optimization of such flexible and tunable MM is obtained by (i) low permittivity of the substrate in order to maintain the resonance strength and hence the bandwidth of the MM and (ii) low loss (absorption coefficient), to maximize the transmission propagation through the substrate. Properties such as low Young's modulus ($7.5 \cdot 10^{4}$ GPa) and low absorption (13 cm^{-1} at 1 THz) are attributes that make elastomers (PDMS) suitable substrates choice for flexible, tunable MMs utilized as a filter or sensor.

Numerical Model

Numerical calculations were performed using the Finite Element Method (FEM) in Comsol Multiphysics software. The 3D-model geometry of a single element of the THz metasurface (MS) is shown in Fig. 1. $\varepsilon_r = 2$ was used for relative permittivity of PDMS. Numerical analysis was performed for a conductive layer with a thickness of 10 µm and conductivity of aluminum ($3.77 \cdot 10^{7}$ S/m). The application of periodic boundary conditions enables to perform analysis of the whole MS only with a single structural element with significant reduction of numerical analysis time [8].

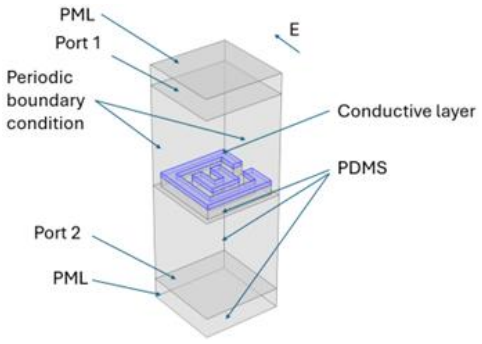


Fig. 1. Schematic view of the numerical model utilized in the simulation (MS element: double split ring resonator; PML: Perfectly Matched Layer).

Metasurface Fabrication

For the production, a silicon wafer was coated with 1.1 µm thick Parylene-C (temperature: 110 °C, pyrolysis at 740 °C, pressure at 3 Pa,

coating time: 1 h 26 min). To produce the elastomer, a PDMS spin-coating (10:1 base to agent, Sylgard 184 elastomer) was applied (400 rpm, 60 sec), followed by defoaming, curing (110°C for 30 min) and O_2 plasma flash activation (100 W, 30 sec). The thickness of the PDMS layer was approx. 165 µm. Al sputter coating (500 nm), and Al structuring with nLOF 2070 photoresist (7000 rpm, 60 sec, expose time: 5 sec, post bake: 115 °C, development time: 240 sec) was applied. Al was etched in a phosphoric acid etching mixture (PWS 80-16-4(65)) at 47 °C, the photoresist was removed and the flexible MS structure was peeled off (Fig. 2).

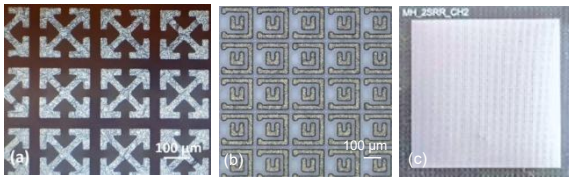


Fig. 2. (a), (b) Microscope pictures of Al coating on elastomer surface with various MS elements, and (c) full chip surface of 1.5 cm x 1.5 cm.

Results and Discussion

The results obtained for the double split ring resonator structure (experimental example in Fig. 2 (b)) using the numerical model are presented in Fig. 3. There are two major resonances for frequencies f_{r1} = 0.24 THz and f_{r2} = 0.71 THz as presented in Fig. 3(a). The numerical analysis indicates a strong effect of conductivity on the amplitudes of the transmission coefficient where for a pronounced resonance a conductivity of $\sigma > 1 \cdot 10^6$ S/cm is needed. Fig. 3(b) shows the dependance of transmission coefficient $|S_{21}|$ on conductivity for f_{r1} and f_{r2}. The highest amplitudes were obtained for the conductivity of Al $\sigma = 3.77 \cdot 10^7$ S/m.

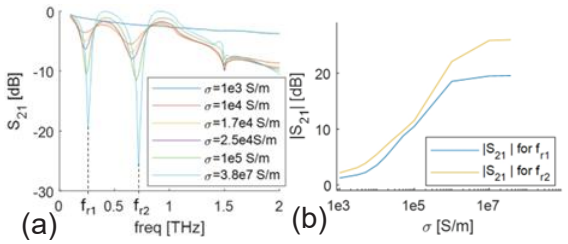


Fig. 3. Results of numerical simulations of double split ring resonator-based MS: (a) transmission coefficient $|S_{21}|$ frequency responses for various values of conductive layer electrical conductivity, (b) dependence of the resonant curve amplitude on conductive layer electrical conductivity.

For the proposed Al layer, the measured de-embedded frequency responses of MSs are presented in Fig. 4(a). The obtained resonant frequencies are in good agreement with the simulation results shown in Fig. 3(a). To prove the applicability of the actively configurable filter, an experiment was carried out in which the device was mechanically stretched by 25% (affecting e.g., gaps sizes in structural elements of MS). Fig. 4(b) shows a tuning of the primary resonance frequency (f_{r1}) of about 8% due to stretching of 25%.

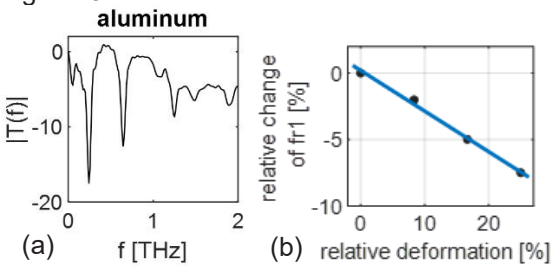


Fig. 4. (a) De-embedded measured transmission frequency responses of MS with conductive layers made of Al, and (b) results of sensor stretching experiment.

Conclusion

THz waves interact effectively with good conductors such as Al. Simulations were conducted to assess the impact of electrical conductivity on the transmission coefficient S_{21} of the THz MS. Performed measurements proved the usability of proposed flexible sensors. For 25% deformation, which is far below the maximum stretching of PDMS (ca. 60%) an 8% decrease of resonance frequency (~ 20 GHz) was observed.

References

[1] C. Chaccour et al., “Seven Defining Features of Terahertz (THz) Wireless Systems: A Fellowship of Communication and Sensing”, *IEEE Communications Surveys & Tutorials*, Vol. 24, No. 2, 967-993, 2022. DOI: 10.1109/COMST.2022.3143454

[2] X. Li et al., “High-throughput terahertz imaging: progress and challenges”, *Light: Science & Applications* 12:233, 2023. https://doi.org/10.1038/s41377-023-01278-0

[3] J. Jang et al., “Terahertz spectral analysis: An in-depth exploration of spectroscopy approaches for ultrafast dynamics”, *Current Applied Physics* 59 197–207, 2024. https://doi.org/10.1016/j.cap.2023.11.015

[4] Suzuki, D. et al., “A flexible and wearable terahertz scanner”, *Nature Photon* 10, 809–813, 2016. https://doi.org/10.1038/nphoton.2016.209

[5] Tian, J., Cao, W., “Reconfigurable flexible metasurfaces: from fundamentals towards biomedical applications”, *PhotoniX* 5, 2, 2024. https://doi.org/10.1186/s43074-023-00116-1

[6] J. Li et al., “A Review: Active Tunable Terahertz Metamaterials”, *Adv. Photonics Res.* 2300351, 2024. https://doi.org/10.1002/adpr.202300351

[7] J. Li et al., “Mechanically tunable terahertz metamaterials”, *Appl. Phys. Lett.* 102, 121101, 2013. https://doi.org/10.1063/1.4773238

[8] P. Lopato et al., “Influence of a thin dielectric layer on resonance frequencies of square SRR metasurface operating in THz band”, *Open Eng.* 13(1), 20220400, 2023. https://doi.org/10.1515/eng-2022-0400

DOI 10.5162/EUROSENSORS2025/MP64

GNPs-Based Strain Sensors Derived from Recycled Cellulose Acetate: Fabrication and Analysis

Pegah Zarafshani[1], Fabrizia Cilento[2], Flavio Esposito[1], Lucia Sansone[2], Stefania Campopiano[1], Muhammad Zahid[3], Abhishek Kumar[3], Agostino Iadicicco[1], Michele Giordano[2]
[1] Department of Engineering, University of Naples "Parthenope", 80143 Naples, Italy
[2] Institute for Polymers, Composites and Biomaterials, National Research Council of Italy (IPCB-CNR), 80055 Portici, Italy
[3] Quantum Technologies, Optronics and Material Laboratories, Leonardo SPA, 00195, Rome, Italy
Corresponding author: pegah.zarafshani001@studenti.uniparthenope.it

Summary:
Nanocomposites based on graphene nanoplatelets (GNP) were developed using recycled cellulose acetate from cigarette filters as the polymer matrix. Electrical conductivity measurements showed significant improvement with increasing GNP content, peaking at the saturation of the electrical network. The electromechanical performance of the sensors demonstrated a gauge factor (GF) near 20 at 3 wt% GNP content in the 0-2% strain range due to the tunneling effect. The new matrix ensures sensor sustainability and stability through cyclic testing.

Keywords: Recycled cellulose acetate, graphene nanoplatelets, strain sensor, nanocomposite, piezoresistive

Introduction

Strain sensors are essential for Structural Health Monitoring (SHM) in aerospace structures, providing real-time data on stress and deformation to ensure safety and integrity [1,2]. Carbon-based nanocomposites, particularly those doped with graphene nanoplatelets (GNPs), have shown great potential due to their high sensitivity and cost-effectiveness compared to traditional fiber optic sensors and strain gauges [3,4]. However, the increasing disposal of electronic sensors is leading to significant environmental problems due to the release of heavy metals and non-recyclable semiconductors, contributing to e-waste [5]. This issue has generated global interest in developing electronic sensors with longer lifespans and reduced e-waste. Numerous examples of electronic sensors with self-healing or recyclable properties have emerged in response to these concerns [6]. This study focuses on using recycled cellulose acetate (CA), derived from cigarette filters, as the polymer matrix for developing strain sensors based on graphene nanoplatelets (GNPs). The use of recycled materials helps reduce the demand for new raw materials and offers environmental benefits. The developed sensors, while innovative in their use of recycled polymer matrix, support green manufacturing pathways in response to environmental concerns.

Experimental Details

- Materials

The nanocomposites used GNPs incorporated into recycled cellulose acetate, which was processed from discarded cigarette butts [7]. GNP powder was supplied by NANESA, Arezzo, Italy, with an average thickness of 14 nm, an average lateral size of 30 μm, and electrical resistivity of 10^{-5} Ω·m. Acetone was used as solvent for GNP dispersion.

- Fabrication of Nanocomposites

Conductive mixtures of GNPs/CA with three different graphene contents (3, 6, and 15 wt%) were prepared as reported in Fig. 1: Graphene nanoplatelets were initially dispersed in acetone by magnetic stirring and sonication for 1 hour in an ice bath while being simultaneously stirred.

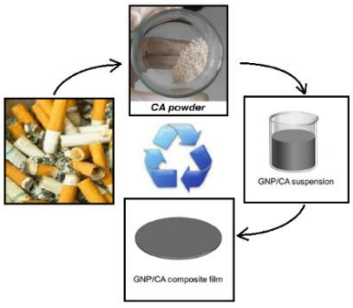


Fig. 1. Schematic illustration of the fabrication process.

The recycled CA was subsequently introduced into the solution under continuous stirring for 30 minutes at a controlled low speed. The final mixtures were then cast into molds and left at room temperature to completely evaporate the acetone and solidify.

Results and Discussion

- Electrical Properties

The electrical conductivity of GNP/CA nanocomposites was investigated using the two-point probe method. The 3 wt%, 6 wt%, and 15 wt% GNP/CA sheets had conductivities of 0.001, 0.005, and 0.142 S/m, respectively. As predicted, being in the region between the percolation threshold and saturation point [8], increasing the GNP content resulted in higher conductivity.

- Electromechanical properties

Tensile tests showed an increase in resistance with applied strain, confirming the piezoresistive nature of the sensors. Fig. 2 illustrates the relative resistance change over time as the sensor is stretched step by step and then released in the same increments. Each step corresponded to a 0.1% strain, up to a total strain of nearly 1%. The gauge factor (GF) of the sensors peaked at a value of approximately 20 for the 3 wt% GNP/CA content, while the 15 wt% GNP/CA content exhibited a GF of around 5 for strains up to nearly 2%.

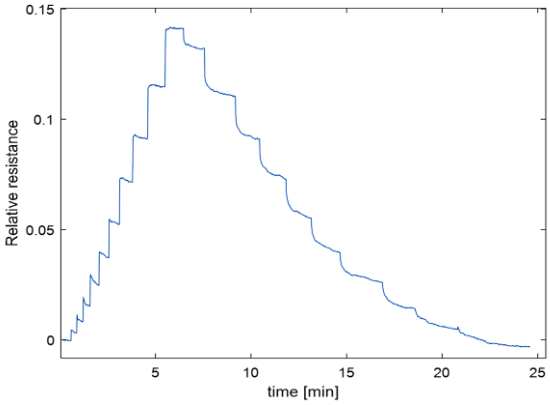


Fig. 2. Relative resistance changes of the sensor under strain for GNP/CA with 3 wt% graphene content (Each step: 0.1 % strain, totally 10 steps).

- Long-Term Stability

Cyclic tests (100 cycles, 1% strain) confirmed the robustness of the sensors, demonstrating high durability and stable electromechanical responses with minimal signal degradation. The use of recycled cellulose acetate as the matrix provided excellent stability and compatibility with the conductive GNP network and produced robust sensors suitable for long-term applications.

Conclusion

In summary, this study demonstrated the successful fabrication of GNP/CA nanocomposites using recycled cellulose acetate from cigarette butts. The sensors exhibited piezoresistive properties with gauge factors peaking at 20 for 3 wt% GNP/CA content. Despite lower conductivity compared to other polymer matrices, the sensors showed improved performance over previous work. Cyclic tests confirmed their robustness and long-term stability, highlighting the environmental benefits and potential applications.

References

[1] Y. Zhang, N. Anderson, S. Bland, S. Nutt, G. Jursich, S. Joshi, All-printed Strain Sensors: Building Blocks of the Aircraft Structural Health Monitoring System, *Sens. Actuators A Phys.* 253, (2016); doi: 10.1016/j.sna.2016.10.007.

[2] F. Yin, D. Ye, C. Zhu, L. Qiu, Y. Huang, Stretchable, Highly Durable Ternary Nanocomposite Strain Sensor for Structural Health Monitoring of Flexible Aircraft, *Sensors* 17, 2677 (2017); doi: 10.3390/s17112677.

[3] A. S. Fiorillo, C. D. Critello, A. S. Pullano, Theory, technology, and applications of piezoresistive sensors: a review, *Sens. Actuators A Phys.* 281, 156–175 (2018); doi: 10.1234/s10000.

[4] F. S. Irani, A. H. Shafaghi, M. C. Tasdelen, T. Delipinar, C. E. Kaya, G. G. Yapici, M. K. Yapici, Graphene as a Piezoresistive Material in Strain Sensing Applications, *Micromachines* 13, 119 (2022); doi: 10.3390/mi13010119.

[5] A. del Bosque, X. Fernández, A. Gómez, M. Sánchez, A. Ureña, Highly stretchable strain sensors based on graphene nanoplatelet-doped Ecoflex for biomedical purposes, *Sens. Actuators A Phys.* 353, 114249 (2023); doi: 10.1234/s10000.

[6] X. Tao, S. Liao, Y. Wang, Polymer-assisted fully recyclable flexible sensors, *EcoMat* 3, (2021); doi: 10.1002/eom2.12083.

[7] A. De Fenzo, M. Giordano, L. Sansone, A Clean Process for Obtaining High-Quality Cellulose Acetate from Cigarette Butts, *Materials* 13, 4710 (2020); doi: 10.3390/ma13214710.

[8] S. Lu, C. Tian, X. Wang, D. Chen, K. Ma, J. Leng, L. Zhang, Health monitoring for composite materials with high linear and sensitivity GnPs/epoxy flexible strain sensors, *Sens. Actuators A Phys.* 267, (2017); doi: 10.1234/s10000.

DOI 10.5162/EUROSENSORS2025/MP65

Development of a Ferrofluidic Inclinometer exploiting a Vision-based Readout Strategy

Bruno Andò, Danilo Greco, Salvatore Castorina, Alberto Campisi,
University of Catania (DIEEI), Catania, Italy;
danilo.greco@phd.unict.it

Summary:
This paper presents an innovative inclinometer exploiting ferrofluids as a seismic mass with tunable properties via an external magnetic field. Tilt readout is performed through a Vision-based technique, by tracking the ferrofluid displacement under the balance of magnetic and gravitational forces. The system features non-contact measurements, robustness against mechanical shocks and low-cost. Experimental results have shown an accuracy of ±0.39° and a resolution better than 0.08° over the operating range [0°, 16°].

Keywords: Ferrofluid, Inclinometer, Computer-Vision, Image processing, Contactless measurement.

Background, Motivation and Objective

Ferrofluids (FFs) are colloidal liquids consisting of nanoscale ferromagnetic particles coated with surfactants and dispersed in a carrier fluid. They exhibit super-paramagnetic behavior under a magnetic field while maintaining their fluidity [1]. Their physical properties, like volume and viscosity, can be modified by changing the magnetic field; this tunability allows ferrofluids to mimic spring-mass systems, enabling the development of advanced inertial sensors (such as accelerometers, inclinometers, and gyroscopes) with real-time adjustable performance [2].

FF-based inclinometers are more reliable and shock-resistant compared to traditional approaches because they employ a ferrofluidic aggregate as the seismic mass. In the event of mechanical shocks or extreme tilting, the ferrofluidic mass may exceed its displacement limit without incurring damage, and normal operation is restored when conditions return to their original state. Ferrofluidic inclinometers exploiting various electrical readout methods have already been demonstrated in [3], [4], and [5].

This paper presents a novel FF inclinometer that makes use of a Vision-based readout approach. Above already mentioned features, key advantages of this method include: *i)* the ability to tune properties and performance via an external magnetic field by using FF as the seismic mass; *ii)* a Vision-based readout that eliminates the need for physical contact and electrical connections with the sensing element; *iii)* a low-cost fabrication using cheap technologies and components.

Description of the New Method and System

The tilt sensor features a glass tube filled with a saturated solution of deionized water and sodium chloride (NaCl), and a ferrofluidic mass. The ferrofluid seismic mass has been realized by pouring 30 µl of Ferrotec® EFH3 ferrofluid into 15 ml of salt-saturated solution. This material was selected for its high saturation magnetization (65 mT) and low viscosity (12 mPa·s). A W-10-N neodymium magnet, mounted on a screw, generates the external tuning magnetic field which also give to the FF mass the characteristic spike-like shape. By adjusting the distance between the magnet and the glass pipe, the field intensity over the ferrofluid is varied. Magnetic field values over distance have been measured through an A1324 Hall-effect magnetic sensor, by Allegro Microsystem Inc.

The target tilt is detected by tracking the displacement of the ferrofluidic mass, which balances magnetic (retaining) and gravitational forces in a steady state. FF mass shift is monitored by a low-cost, embedded Vision system. The proposed readout approach is aimed at estimating the displacement of the FF mass from the rest position due to the target tilt, from an acquired image of the FF drop. Image acquisition and processing are carried out using a Pi Camera Module v2.1 connected to a Raspberry Pi 4 Model B.

A suitable experimental setup has been realized in order to assess the proposed measurement strategy. The following parts can be distinguished in Fig. 1-a, -b: *1)* glass vial containing the FF; *2)* ferrofluidic mass; *3)* magnet; *4)* magnetic field tuning screw; *5)* target tilt screw;

6) GY-521 module, featuring an InvenSense MPU-6050 inertial sensor, used as reference for tilt values.

Acquired images go through a sequence of digital filters aimed at improving the effectiveness of parameters estimation, as shown in Fig. 1c, including: *i)* image cropping to the region of interest; *ii)* conversion to grayscale; *iii)* image blurring through a Gaussian filter to reduce random noise and improve FF contour recognition; *iv)* thresholding: enhance the contrast in the image and improves FF recognition; *v)* identification of the bounding rectangle surrounding the FF shape. Then, the geometric quantities defined in Fig. 1-d, are evaluated in order to estimate the FF mass displacement: the dimensions of the bounding rectangle and its aspect ratio, W, H and W/H, respectively; the horizontal and vertical displacement of the FF center of mass (C) with respect to the vertex of the triangular reference marker (V), ΔX and ΔY, respectively; the distance of the mid-point of the FF shape base (M) to the vertex (V), ED. A dedicated study has demonstrated that ΔX shows the better correlation with tilt angle, with respect to other parameters. The above-mentioned quantities are natively estimated in pixels, thus in order to convert them to real dimensions, the pixels-to-millimeters conversion coefficient has been estimated by measuring the base and heigh of the reference marker. The estimated conversion coefficient value is $31.8\ 10^{-3}\ mm/px$.

Results

The system response has been investigated by estimating the geometric parameters at different tilt angles and for different values of the applied magnetic field. The operating range limit is represented by the tilt angle value that leads the FF mass escaping from the retaining force. For each magnetic field and tilt angle couple of values, 10 images have been acquired. Experimental results in terms of the mean value and standard deviation (error bars) of the parameter ΔX over 10 acquisitions, as a function of the tilt angle, θ, for different values of the magnetic fields are reported in Fig. 2. It can be observed that, as the magnetic field decreases, the system responsivity increases while the operating range narrows. The system response in case of 5.78 mT, which corresponds to a distance of 3.3 mm between the magnet and the glass vial, represents the better tradeoff between operating range, responsivity and accuracy values. By fitting experimental data with a 2nd-order polynomial, the following relation is achieved:

$$\theta = -0.048\Delta X^2 + 2.117\ \Delta X + 0.073$$

The estimated uncertainty in the 3σ-limit is 0.39°, while the resolution, reported on the right axis of Fig. 2, is 0.08° in the worst case.

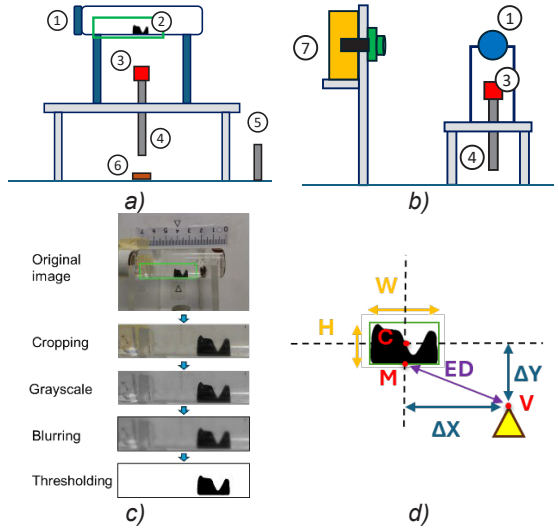


Fig. 1. Schematization of the experimental setup: a) front view; b) side view. c) Example of image processing d) graphical representation of the parameter.

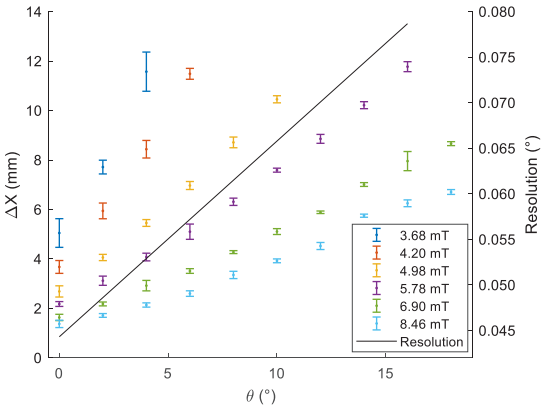


Fig. 2. Estimated value of ΔX vs tilt angle and applied magnetic field (left axis). Estimated resolution for the case 5.78 mT (right axis).

References

[1] W. Yang, Y. Zhang, X. Yang, C. Sun, Y. Chen, Systematic analysis of ferrofluid: a visualization review, advances engineering applications, and challenges. J Nanopart Res 24, 102 (2022).

[2] J. Popplewell and R. E. Rosensweig, "Magnetorheological fluid composites," J. Phys. D, Appl. Phys., vol. 29, no. 9, pp. 2297–2303, Jan. 1996.

[3] B. Ando, A. Ascia, S. Baglio and N. Savalli, "A Novel Ferrofluidic Inclinometer," IEEE Trans. Instrum. Meas., vol. 56, no. 4, pp. 1114-1123, Aug. 2007.

[4] B. Ando, A. Ascia and S. Baglio, "A Ferrofluidic Inclinometer in the Resonant Configuration," IEEE Trans. Instrum. Meas., vol. 59, no. 3, pp. 558-564, Mar. 2010.

[5] B. Andò, S. Baglio, A. Beninato, A Ferrofluid Inclinometer with a Time Domain Readout Strategy, Procedia Eng., vol. 47, 2012, pp 586-589.

DOI 10.5162/EUROSENSORS2025/MP66

A Calibration Method for Spatial Localization of OPM Sensors Based on a Rigid Coil Array Framework

Weinan Xu[1], Fuzhi Cao[2], Yong Li[3], Chunhui Wang[4], Xiaolin Ning[5]
[1,2,3,4,5] School of Instrumentation Science and Optoelectronic Engineering, Beihang University, Beijing 100191, China
lewin309@163.com

Summary:
A calibration method based on a rigid coil array framework was developed for spatially localizing Optically Pumped Magnetometer (OPM) sensors in wearable Magnetoencephalography (MEG) systems. The proposed framework integrates multiple coils into a fixed geometric configuration, enabling precise validation of sensor positioning and enhancing the front-end registration process. By incorporating the Structural Similarity Index Measure (SSIM) as an optimization objective, the method significantly improves localization accuracy compared to conventional approaches. Simulation results demonstrated that the localization error was maintained below 3 mm, meeting the precision requirements for OPM-MEG registration. The rigid coil array structure effectively reduced random errors introduced by manual operations and tracking systems, providing a stable reference framework for aligning sensor coordinates with anatomical brain data. This work advances both theoretical and practical aspects of OPM-MEG calibration, offering a robust solution for high-precision sensor localization.

Keywords: OPM-MEG; sensor localization; rigid coil array; Biot–Savart law; Structural Similarity Index Measure (SSIM); magnetic field fitting; registration accuracy; spatial positioning; least-squares optimization.

Title

A Calibration Method for Spatial Localization of OPM Sensors Based on a Rigid Coil Array Framework.

Headlines

This study presents the design of a rigid structure capable of supporting a coil array, incorporating data preprocessing and nonlinear multi-parameter minimization. By using the Structural Similarity Index Measure (SSIM) as the objective function, the system accurately determines the spatial positions and orientations of sensors in OPM-MEG. This work provides both theoretical and hardware support for the frontend of OPM-MEG registration.

Background

Calibration of spatial sensors is a critical component in the registration process of wearable OPM-MEG systems, enabling accurate alignment between the sensor coordinate system and the anatomical coordinate system of the brain. Conventional fixation methods often suffer from insufficient stability and are susceptible to human-induced random errors during initial measurements. To address this limitation, a rigid framework for the sensor array is proposed in this study, which significantly reduces random errors and provides a more stable and reliable solution for subsequent sensor localization [1].

Description of the New Method or System

In previous studies, the use of coils for MEG registration typically involved attaching three or more coils directly onto the scalp or forehead. After fixation, a position tracker was employed to digitize both the scalp surface and the coil locations, thereby determining the spatial relationship between the coils and the subject's head. However, this approach introduces substantial random errors, both during the coil attachment process and in the operation of the tracking system.To mitigate these sources of error, a 3D rigid support structure capable of holding an array of coils has been designed. This rigid coil array famework structure serves to fix all coils in a unified and stable configuration, providing a dedicated coordinate system for the coil array that supports more accurate and reliable MEG registration.

The rigid coil array framework structure is capable of accommodating up to 35 coils, with both the positions and magnetic moment orientations of the coils being fixed. The primary function of the helmet in this setup is to serve as a spatial reference. By rigidly attaching the helmet to the RCS, both the sensors and the coils are placed

within a unified coordinate system. This configuration allows the spatial relationships between the sensors and the coils to be predetermined, enabling consistent and accurate localization within the shared structural frame. The rigid helmet is capable of accommodating up to 85 sensors. For detailed specifications and configuration, please refer to the relevant literature [3].

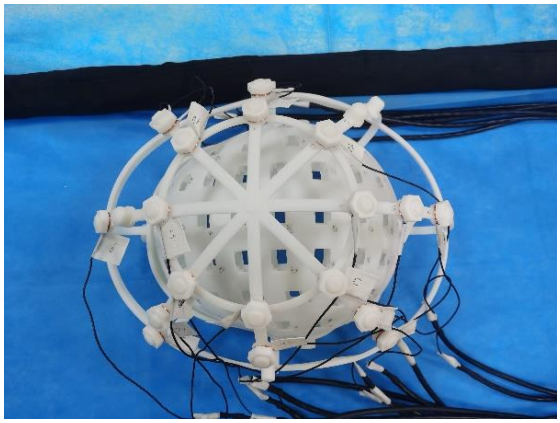


Fig. 1. Rigid Coil Array Framework Structure and rigid helmet

Results and conclusion

. Tab. 1: Experimental Results

Accuracy	Conventional	SSIM
1	2.96mm	2.21mm
2	2.79mm	2.53mm
3	2.12mm	1.99mm
4	2.79mm	2.13mm
5	2.94mm	2.58mm

In this experiment, 15 coils and 5 sensors were employed to evaluate the localization performance, with all procedures carried out under magnetically shielded conditions. As demonstrated in the corresponding figures and tables, the localization errors remained within 3 mm, thereby meeting the typical accuracy requirements for sensor-to-coil registration. Since the initial positions of the sensors were known a priori, all reported errors represent absolute deviations. The contribution of model-induced errors was negligible and therefore excluded from the analysis. Importantly, the use of SSIM as the objective function yielded consistently lower registration errors compared to those obtained using a conventional objective function, highlighting its effectiveness in improving localization accuracy.

Localization Principle

When the spatial extent of the current distribution is much smaller than the distance between the observation point and the current source, the Biot–Savart law can be approximated by the magnetic dipole model. This simplification is particularly useful for describing the far-field magnetic field generated by systems such as current loops or small permanent magnets. The magnetic field of a magnetic dipole at a point r\mathbf{r}r is given by eg. (1) [2].

$$B(\mathbf{r}) = \frac{\mu_0}{4\pi}\left[\frac{3(\mathbf{m}\cdot\hat{\mathbf{r}})\hat{\mathbf{r}} - \mathbf{m}}{|\mathbf{r}|^3}\right] \quad (1)$$

Where, $B(\mathbf{r})$ is the magnetic field at a position $\mathbf{r}$ （T） μ_0 is the permeability of free space； $\mathbf{m}$ is the magnetic dipole moment （A·m²） , defined as $\mathbf{m} = I\mathbf{A}$, with I denoting the current and $\mathbf{A}$ representing the vector area of the current loop; $\hat{\mathbf{r}} = \mathbf{r}/|\mathbf{r}|$ is the unit vector pointing from the dipole to the observation point; $r = |\mathbf{r}|$ is the distance from the dipole center to the field point.

$$f(\theta_s, \phi_s, x_s, y_s, z_s, k) = 1 - \mathrm{SSIM}(\mathbf{B}, \mathbf{B}^*) \quad (2)$$

Where, $\mathbf{B}$ denote the magnetic field computed from the model， $\mathbf{B}^*$ represent the magnetic field measured by the sensor. The position of the sensor is represented in Cartesian coordinates as $[x_s, y_s, z_s]$, The orientation of the sensor's sensitive axis is represented in spherical coordinates as (θ_s, ϕ_s) , θ_s is the polar angle measured from the positive zzz-axis, within the range [0,π]. ϕ_s is the azimuthal angle measured from the positive xxx-axis in the xyxyxy-plane, within the range [0,2π].

References

[1] C. Pfeiffer, L.M. Andersen, D. Lundqvist, M. Hämäläinen, J.F. Schneiderman, R. Oostenveld, Localizing on-scalp MEG sensors using an array of magnetic dipole coils, *PLoS ONE* 13, e0191111 (2018); doi: 10.1371/journal.pone.0191111

[2] V. Vivaldi, S. Sommariva, A. Sorrentino, A simplex method for the calibration of a MEG device, *Communications in Applied and Industrial Mathematics* 10, 35–46 (2019); doi: 10.2478/caim-2019-0005

[3] F. Cao, N. An, W. Xu, W. Wang, Y. Yang, M. Xiang, Y. Gao, X. Ning, Co-registration Comparison of On-Scalp Magnetoencephalography and Magnetic Resonance Imaging, *Frontiers in Neuroscience* 15, 706785 (2021); doi: 10.3389/fnins.2021.706785

DOI 10.5162/EUROSENSORS2025/MP67

Removal method of correlation artifact based on reference magnetic signal

Yong Li[1], Hao Lu[2], Fuzhi Cao[3], Dawei Wang[4], Chunhui Wang[5], Xiaolin Ning[6]
[1,2,3,5,6] School of Instrumentation Science and Optoelectronic Engineering, Beihang University, Beijing 100191, China
[4] Beijing Microelectronics Technology Institute, Beijing 100076, China
by2017335@buaa.edu.cn

Summary:
An OPMs-based hardware system has been constructed for the synchronous recording of magnetoencephalography (MEG) signals and reference magnetic signals of physiological artifacts such as eye blinks and cardiac magnetic fields. The randomized dependence coefficient (RDC) is used to evaluate the correlation between independent components and reference signals. Removing physiological artifacts according to the threshold of correlation can significantly improve the signal-to-noise ratio of MEG signals. In the calculation of RDC, the input features are standardized by Copula transform, and then high-dimensional features are constructed by random projection and activation function. Finally, the correlation is obtained by regularized canonical correlation analysis (RCCA).

Keywords: Optically pumped magnetometer, Magnetoencephalography, Physiological artifacts, Random correlation coefficient, Copula transform, Sensors, Independent component analysis.

Title

Removal method of correlation artifact based on reference magnetic signal.

Headlines

The paper outlines the existing physiological artifact removal methods, the OPM-MEG hardware system, data collection and preprocessing, correlation computation, and artifact removal evaluation metrics, highlighting the significance of reference-magnetic-signal-based correlation methods in advancing the field of automatic artifact removal.

Background and Motivation

The high spatiotemporal resolution of OPM makes it a valuable tool for brain functional imaging, as it can accurately capture neural activity in the brain. However, common physiological artifacts, such as eye blinks and cardiac signals, overlap with conventional neural source signals in the alpha, theta, and delta frequency bands (1 Hz–20 Hz), leading to signal contamination. This poses challenges for observing neural activity and studying brain-related disorders. Traditional approaches rely on expert visual inspection or EEG-based references, which are time-consuming or imprecise. Therefore, there is a need to develop a cost-effective, automated system for artifact recognition and removal based on reference magnetic signals.

Description of reference magnetic signal artifact recognition system

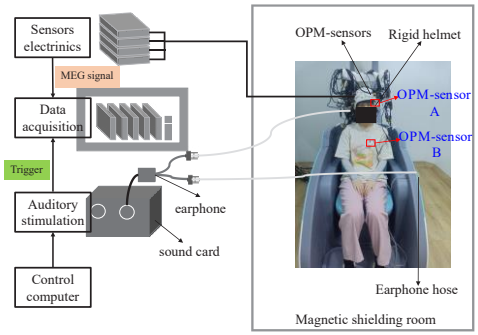


Fig. 1. Synchronous acquisition system of MEG and reference signal

The current approach primarily focuses on removing physiological artifacts using reference electrical signals [1], whereas this study enables artifact recognition and removal based on reference magnetic signals. A 34-channel OPMs hardware system was constructed for synchronous signal acquisition, in which two OPM sensors were placed near the eyes and chest to capture reference magnetic signals for eye-blink and cardiac artifacts, while the remaining 32 OPMs formed the OPM-MEG system to record neural activity in the brain. The sensor data from the OPM-MEG system were then decomposed using independent component analysis (ICA) to extract independent components. The randomized dependence coefficient (RDC) method [2] was

used to compute the correlation between each independent component and the reference signals. Artifacts were identified and removed based on correlation ranking and a defined threshold. Additionally, a beep-based auditory paradigm was used during data collection to stimulate the participants' brains.

Correlation calculation

The correlation between reference magnetic signals and artifact components was calculated using the randomized dependence coefficient (RDC) method, where the inputs are independent components of MEG and reference magnetic signals of physiological artifacts. The correlation score was obtained by optimizing Equation (4) using the regularized canonical correlation analysis (RCCA) method [3].

$$\mathrm{RDC}(X,Y) = \max_{\mathbf{a},\mathbf{b}} \frac{\mathrm{cov}(\mathbf{a}^{\mathrm{T}}\phi(X), \mathbf{b}^{\mathrm{T}}\phi(Y))}{\sqrt{\mathrm{var}(\mathbf{a}^{\mathrm{T}}\phi(X))\,\mathrm{var}(\mathbf{b}^{\mathrm{T}}\phi(Y))}}$$

Finally, components with the highest correlation ranking and a threshold greater than 0.3 were recognized as artifacts. Based on the recognized artifact component indices, the corresponding artifacts in the OPM-MEG signals were removed using the ICA component removal method.

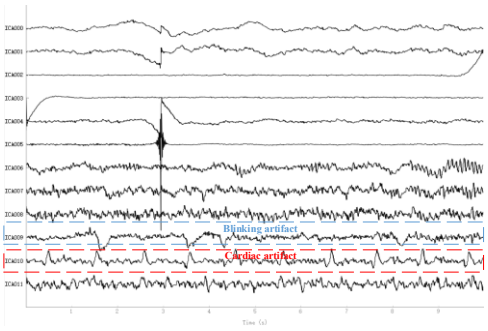


Fig. 2. Independent component analysis decomposition

Result

The correlation analysis results demonstrate that the Randomized Dependence Coefficient (RDC) can effectively evaluate the correlation between independent components and reference signals. After artifact removal based on correlation computation, the signal-to-noise ratio (SNR) of the OPM-MEG signals was calculated before and after artifact removal using the SNR evaluation method described in reference [4]. The results show that the proposed artifact identification method based on reference magnetic signal correlation significantly improves the quality of OPM-MEG signals. The RDC method effectively captures the nonlinear correlation between reference magnetic signals and artifact components, offering valuable insights into its potential applications in brain magnetic signal processing.

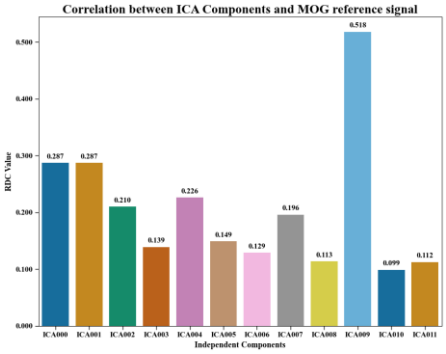


Fig. 3. Correlation result of blink artifacts

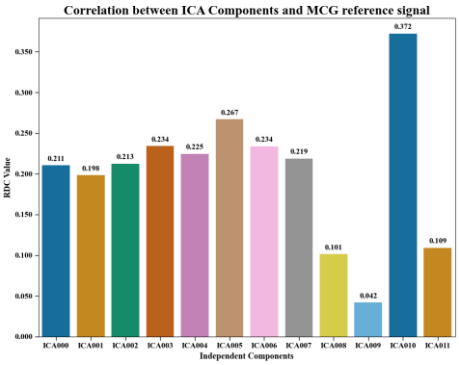


Fig. 4. Correlation result of cardiac artifacts

Tab. 1: Comparison of signal-to-noise ration

Participants	Before artifact removal	After artifacts removal
1	-0.72	8.24
2	3.18	11.31
3	1.86	9.17
4	1.94	9.15

References

[1] C. Zhang, L. Tong, Y. Zeng, J. Jiang, H. Bu, B. Yan, J. Li, Automatic artifact removal from electroencephalogram data based on a priori artifact information, Biomed Res Int 2015, 720450 (2015); doi: 10.1155/2015/720450

[2] D. Lopez-Paz, P. Hennig, B. Schölkopf, The randomized dependence coefficient, in: Advances in Neural Information Processing Systems 26 (NeurIPS 2013), 2013; doi: 10.48550/arXiv.1304.7717.

[3] H.D. Vinod, Canonical ridge and econometrics of joint production, J. Econometrics 4, 147–166 (1976); doi: 10.1016/0304-4076(76)90010-5.

[4] U. Marhl, T. Sander, V. Jazbinšek, Simulation Study of Different OPM-MEG Measurement Components, Sensors 22, 3184 (2022); doi: 10.3390/s22093184

DOI 10.5162/EUROSENSORS2025/MP68

Comprehensive Mass Resolution Model for 2D Nanomechanical Resonant Sensors

Timothy Platten[1], *Pengcheng Zhang*[1*] *and Christofer Hierold*[1]
[1] Department of Micro- and Nanosystems, ETH Zürich, 8006 Zürich, Switzerland
*Corresponding author: zpengchen@ethz.ch

Summary: Nanomechanical resonators have been explored as candidates for various sensing applications. Two-dimensional (2D) nanomechanical resonators are of particular interest due to their ultralow mass and large surface-to-volume ratio, which may enable high mass resolution under vacuum conditions. However, a comprehensive model for calculating dynamic range (DR) and mass resolution in 2D circular nanomechanical resonators is still lacking. In this work, we establish such a model by incorporating the effects of fringing fields and the Casimir effect. Our results indicate that fringing fields have significant impact on simulating device properties. The Casimir effect could be of relevance for low initial strain membranes and initial electrode gaps below 100 nm.

Keywords: Theoretical models, Nanomechanical resonant sensors, Dynamic range (DR), Mass resolution

Background, Motivation and Objective

Nanomechanical resonators have been investigated for sensing applications such as temperature, mass, and gas detection, due to their fast response and potential for high resolution in controlled environments like vacuum [1]. Mass changes, for example, are detected through shifts in resonance frequency [2], as illustrated in Fig. 1(c). Two-dimensional (2D) nanomechanical resonators are particularly interesting due to their ultralow mass and high surface-to-volume ratio, making them highly sensitive to external stimuli like strain, mass, light, and temperature [1]. For sensing applications, the frequency resolution (or equivalent mass resolution) is critical as it directly impacts the performance of the resonant sensor. The frequency resolution strongly depends on the dynamic range (DR), as a higher DR improves the signal-to-noise ratio (SNR) and thus allows the detection of smaller frequency shifts. In this work, we establish a comprehensive dynamic range model for circular 2D nanomechanical resonators by incorporating both the fringing fields and the Casimir effect. The model suggests that these effects may influence dynamic range and mass resolution, especially at high DC gate voltages. A parameter sweep of thickness, radius, and initial gap distance analyzes their impact, providing a framework for improved modeling of sensing performance and 2D resonant membrane design.

Theoretical Model

The resonant membrane, as seen in Fig. 1(a), is capacitively actuated by DC and AC voltages. Properties such as static center deflection (w_0), strain (ε), resonance frequency (f_0), and critical amplitude (a_c) are derived from the force balance, obtained by differentiating the total system

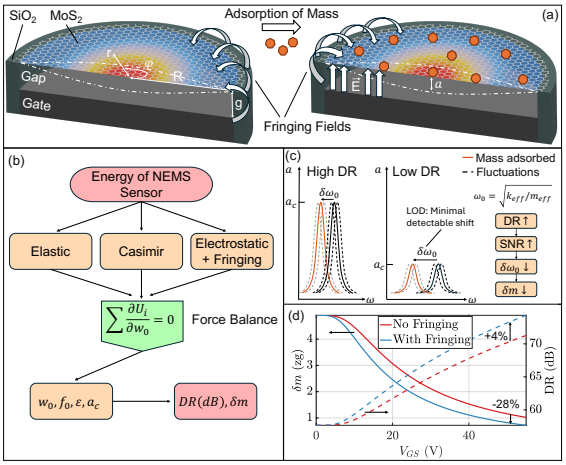


Fig. 1: (a) Schematic of mass adsorption on a resonant sensor. (b) Flowchart of the theoretical model. (c) Illustration of the minimal detectable frequency shift due to mass adsorption for sensors with low and high DR. (d) Impact of the fringing fields effect on mass resolution and DR as a function of applied gate voltage.

energy (Fig. 1(b)). The electrostatic energy (including fringing fields [3]) and Casimir energy [4] contributions are given by:

$$U_{es} = \frac{\pi\varepsilon_0 R^2}{2w_0} \ln\left(\frac{g}{g-w_0}\right) V_{GS}^2 A_f\,, \qquad (1)$$

$$A_f = 1 + c_1\frac{g}{R} + c_1\frac{g}{R}\ln(\frac{c_2 R}{g}), \qquad (2)$$

$$U_{cs} = \eta_0 \frac{\pi^3 \hbar c R^2}{1440 w_0}\left(\frac{1}{(g-w_0)^2} - \frac{1}{g^2}\right), \qquad (3)$$

where R is radius, g is gap distance, A_f is the fringing fields factor, c_1 and c_2 are fitting parameters, and η_0 is the Casimir factor (accounting for

the conductivity of the materials). From the derived properties, the DR and the mass resolution are determined by [5]:

$$\mathrm{DR} = 20\log\left(\frac{0.745a_c}{\sqrt{2S_{x,th}\Delta f}}\right), \tag{4}$$

$$\delta m \approx \frac{2m_{eff}}{Q} \times 10^{-\mathrm{DR\,(dB)}/20}, \tag{5}$$

where $S_{x,th}$ is thermomechanical noise, Δf is measurement bandwidth, m_{eff} is effective mass, and Q is quality factor. The DR describes the ratio between the maximum vibration amplitude and the noise floor, reflecting the signal-to-noise ratio. A higher DR thus enables the detection of smaller masses.

Results and Discussion

According to our model, the Casimir effect begins to influence the device properties only when the gap distance is below 100 nm, the initial strain is low, and the applied voltage is small or zero. In all other cases, its effect is negligible. To investigate the effect of fringing fields on resonant sensor performance, we sweep the DC gate voltage and evaluate the resulting dynamic range and mass resolution, as shown in Fig. 1(d). The calculated DR and mass resolution are higher when fringing fields are taken into account. Notably, the impact of the fringing fields effect is primarily governed by the device's radius-to-gap ratio (R/g), with the model showing a 4% increase in DR observed for R/g = 1 at 50 V, reaching up to 73 dB. This corresponds to an approximately 28% lower minimal detectable mass, reaching sub-zeptogram levels for a device with R=0.5μm and t=2nm. Moreover, at higher DC gate voltages, the difference between models with and without fringing fields becomes more pronounced.

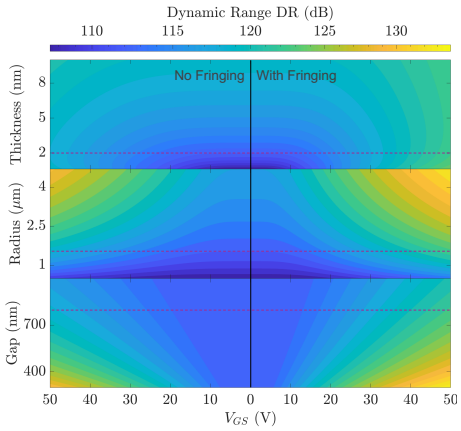


Fig. 2: Dynamic range as a function of varying geometric device parameters: (a) thickness, (b) radius, and (c) gap. The fringing fields effect is considered for the right side of the plot. The purple lines represent the fixed parameter values.

To better visualize how geometric device parameters influence the DR and how fringing fields affect it, Fig. 2 presents a parameter sweep with and without considering the fringing fields effect. We observe, that when fringing fields are considered the DR increases faster with applied gate voltage. Additionally, DR increases with increasing radius and decreasing gap distance, while an increase in thickness enhances DR at low voltages but reduces it at higher voltages. Similarly, Fig. 3 presents the parameter sweep for mass resolution. Since mass resolution is directly derived from the DR, it exhibits the same trends observed for DR.

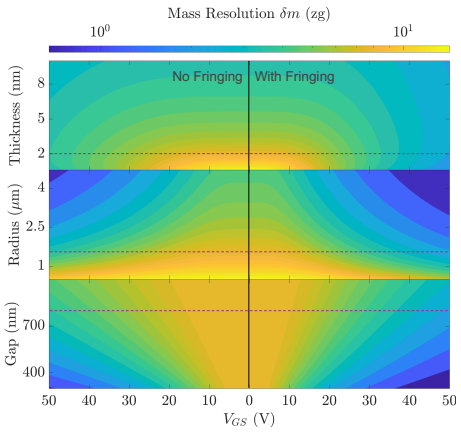


Fig. 3: Mass resolution as a function of varying geometric device parameters: (a) thickness, (b) radius, and (c) gap. The fringing fields effect is considered for the right side of the plot. The purple lines represent the fixed parameter values.

References

[1] B. Xu, P. Zhang, et al., Nanomechanical resonators: toward atomic scale, *ACS Nano* 16(10), 15545–15585 (2022); doi: 10.1021/acsnano.2c01673

[2] Y. T. Yang, C. Callegari, et al., Surface adsorbate fluctuations and noise in nanoelectromechanical systems, *Nano Letters* 11(4), 1753–1759 (2011); doi: 10.1021/nl2003158

[3] R. Maity, N. P. Maity, et al., Analysis of fringing capacitance effect on the performance of micro-electromechanical-system-based micromachined ultrasonic air transducer, *Micro & Nano Letters* 13(6), 872–877 (2018); doi: 10.1049/mnl.2017.0688

[4] G. L. Klimchitskaya, U. Mohideen, and V. M. Mostepanenko, The casimir force between real materials: experiment and theory, *Reviews of Modern Physics* 81(4), 1827–1885 (2009); doi: 10.1103/revmodphys.81.1827

[5] P. Zhang, Y. Jia, Z. Liu, and R. Yang, Strain-enhanced dynamic ranges in two-dimensional MoS_2 and $MoTe_2$ nanomechanical resonators, *Applied Physics Reviews* 11(1), (2024); doi: 10.1063/5.0167141

DOI 10.5162/EUROSENSORS2025/MP69

Simulation and Optimization of Magnetic Field Actuated MEMS-Based Metasurface for Terahertz Applications

Barbara Szymanik[1], Przemyslaw Lopato[1], Michal Herbko[1], Michal Maciusowicz[1], Grzegorz Psuj[1]
Pranesh Kondamarri[2], Julien Petit[2], Andras Kovacs[2], Ulrich Mescheder[2]
[1] West Pomeranian University of Technology, Szczecin, al. Piastow 17, Poland,
[2] Furtwangen University, Robert-Gerwig-Platz 1, 78120, Germany
Corresponding author: Przemyslaw Lopato[1] (plopato@zut.edu.pl)

Summary:
A device based on a terahertz metasurface built from a split ring resonator array is presented. In the proposed device, part of the structural element is anchored in a silicon substrate, while the other part is movable (cantilever) and can be deformed using an external magnetic field of various intensities. Such a MEMS system, due to its variable geometry, constitutes a reconfigurable resonant structure that can be utilized e.g., as a sensor, based on detecting changes in the refractive index. In this work, the geometry of such a device is proposed, analyzed using numerical modeling and optimized.

Keywords: FEM simulation, metasurface, terahertz frequency, MEMS, magnetic actuation

Introduction

Metamaterials (MM), due to the possibility of obtaining electromagnetic (EM) properties not found in nature, and unique possibilities of interaction with a propagating EM wave, constitute a very interesting and rapidly developing technology widely used in sensors. The two-dimensional version of MM, called metasurfaces (MS) is relatively easy to fabricate (compared to MMs) and can be realized by thin-film fabrication techniques like surface-micromachining.

Such MS find many various applications in fields like telecommunication, sensors, selective absorbing structures, polarizers, surface wave control devices, and imaging systems [1]. The usage of MS in sensing is based on detecting changes in the refractive index (n) of the analyte. MS, as a resonant structure, is affected by varying n in the vicinity of electric field concentration areas, e.g., in capacitive gaps between conductive parts of structural elements [2].

Magnetic Field Tunable THz Metasurface

In this study, we present a THz-MS built from a split ring resonator (SRR) array. In the proposed device, part of the structural element is anchored to a silicon substrate (Fig. 1), while the other part is movable (cantilever, CL) and can be deflected using an external magnetic field of different intensity (contrary to electric field driven solutions [2]). Such a system, due to its variable geometry, constitutes a reconfigurable resonant structure with variable electromagnetic parameters (for a propagating THz pulse), and has potential for sensing the dielectric properties of the analyte.

MEMS Design and Technology

Surface micromachining with sacrificial layer technique is used to realise the CLs. It consists of two layers: A high electrical conductivity (σ) layer (Aluminum (Al)) for THz-shielding and a high magnetic permeability (μ_r) layer for bending in applied magnetic field ($\vec{B}$). Spray coated iron (Fe), sputtered Fe and nickel were investigated. Spray coated Fe has low surface-uniformity due to particle cluster formation (Fig. 2a - inset) and high carbon and oxygen concentration and hence smaller μ_r than pure Fe (Fig. 2a). Sputtered Fe layers are uniform and homogeneous however, show oxidation (Fig 2b, c) which reduces μ_r. Additionally, with increasing CL film thickness, the intrinsic stress dominates resulting in CL deformation and crack generation. Hence, an optimized fabrication process to reduce oxidation, stress and achieve high μ_r and σ layers is required and will be presented.

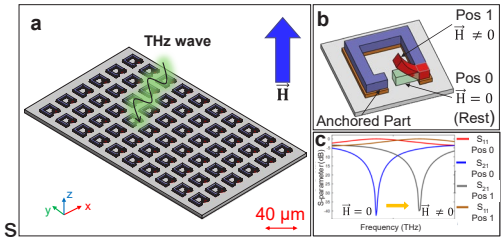


Fig. 1. Concept of MEMS metasurface actuated using magnetic field (a) SRR-based single structural element actuation (b), deflection caused resonant frequency shift (c).

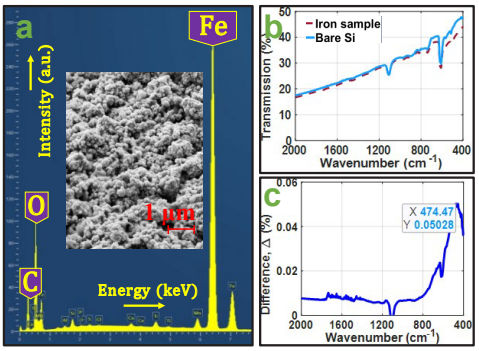


Fig. 2 a) EDX analysis spray coated Fe. The spectrum shows oxygen concentration at 27.22 Wt% and carbon at 22.1 Wt%. Cantilever surface with clusters (inset). b) FTIR transmittance: Fe sputtered silicon wafer (Si) and bare Si. c) The difference of both transmittances, Δ shows a peak at 474.47 cm^{-1} indicating iron oxide (Fe_2O_3) formed.

Numerical Model

For investigation of magnetic deflection of CL, a 2D-numerical model was developed. This model incorporated a permanent magnet (PM) and a CL in its vicinity, featuring fixed geometric and material parameters. Preliminary experiments indicated that a local $\vec{B}$ of approximately 0.1 T is necessary to induce a noticeable CL-deflection. Consequently, the remanence of the magnet was chosen to provide 0.1 T at the CL's.

The magneto-mechanical behavior was studied using the COMSOL software suite. The proposed model was employed to examine critical experimental parameters, including the CL's geometric dimensions, the type of magnetic material selected, its location relative to the magnet, and the material selected. Fig. 3 presents an exemplary result for the CL-deflection with fixed dimensions (length = 100 µm, thickness = 0.4 µm (Al: 0.3 µm, magnetic layer: 0.1 µm) with two different magnetic materials: soft iron (μ_r= 1000) and permalloy (μ_r = 10,000).

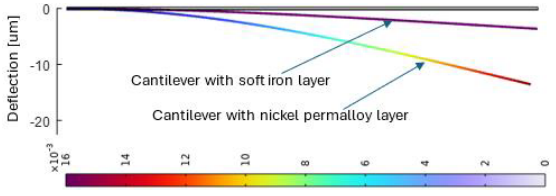


Fig. 3. The cantilever deflection in the magnetic field.

The CL with a soft iron layer achieved a maximum deflection of approximately 4.3 µm, whereas the CL with permalloy reached about 15.2 µm. This significant difference in bending can be attributed to the higher μ_r of permalloy, which enables a stronger magnetic response under the same excitation conditions.
The deformed geometry (shape of the CL profile) is then transferred to a 3D model, solving the high-frequency EM problem. The model uses periodic boundary conditions applied to the side walls to reduce computational complexity. This enables the analysis of just one element and obtaining the result for an infinite matrix of structural elements.

Results and Conclusions

An exemplary frequency response obtained for single CL-MS is shown in Fig. 4. Two resonances can be observed and utilized for sensing. The output of MS (a resonant sensor) will be the resonant frequency change (f_{R1} and f_{R2}) shown in Fig. 5 for single and double CL structures. Initially, f_{R1}, f_{R2} vary quasi-linearly and reach saturation at higher values. The magnetic field deformable metasurfaces can be utilized for reconfigurable sensors of thin film analytes. More results will be presented on the conference.

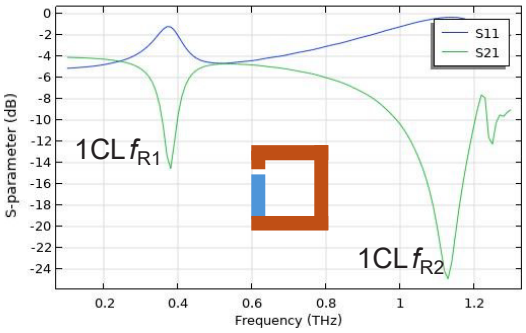


Fig. 4. Simulated Frequency response of single cantilever based metasurface (1CL) with two resonances (f_{R1} and f_{R2}); H=0.

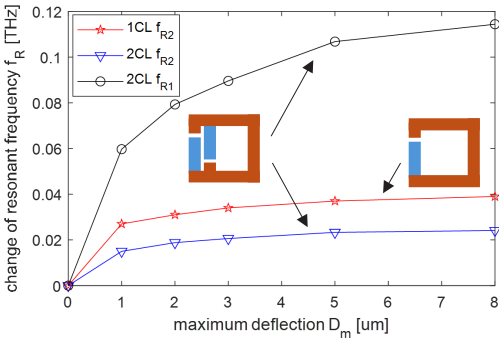


Fig.5 Change of resonant frequency caused by various levels of deflection by magnetic field for single and double cantilever structural elements.

References

[1] G. Oliveri, D. H. Werner, A. Massa, Reconfigurable electromagnetics through metamaterials—A review. *Proc. IEEE* 103, 1034–1056 (2015); doi: 10.1109/JPROC.2015.2394292

[2] S. Zahra et al, Electromagnetic Metasurfaces and Reconfigurable Metasurfaces: A Review, *Front. Phys.*, 8, 593411 (2021), doi: 10.3389/fphy.2020.593411

This work was funded by the National Science Centre (NCN, Poland) grant no. 2022/47/I/ST7/ 02055 and Deutsche Forschungsgemeinschaft (DFG, Germany), grant no. ME 2093/9-1.

DOI 10.5162/EUROSENSORS2025/MP70

Simulation Environment for Optimized Grating-Based Plasmon Couplers

Pongsak Sarapukee[1], Christian Spenner[1], Dirk Schulz[1], and Stefan Palzer[1],
[1]Department of Electrical Engineering and Information Technology, Technical University Dortmund, Otto-Hahn-Straße 8, 44227 Dortmund, Germany
stefan.palzer@tu-dortmund.de

Summary:
The properties of surface plasmons create the potential for sensitivity to nanoscale environmental changes and allows for practical applications including light guiding, nanomanipulation, biosensing, high-resolution imaging, and optical switching. Grating structures have emerged as a central tool enabling the design of dedicated systems for modulating light-matter interactions. This contribution presents a Finite-Difference Time-Domain (FDTD) method enhanced with the Drude model, Perfectly Matched Layer, Periodic Boundary Condition, and Total Field/Scattered Field-Method that form the basis a simulation environment for surface plasmon couplers. The simulations are able to cover a wide parameter space, aiding optimal design identification. Validation against experimental results on actual grating structures has been used to improve the model's accuracy and predictive capabilities. This iterative approach yields insights into efficient grating-based plasmon coupler designs thus contributing to plasmonics understanding and optimized applications.

Keywords: Surface Plasmon, Grating, Simulation, FDTD method

Introduction

Surface plasmons are coherent oscillations of electrons at the interface of a metal and a dielectric substance. They feature unique properties that have driven significant research and development in a multitude of sensing applications. Their high sensitivity in local environments at the nanoscale has enabled a wide range of practical applications. Among the various techniques to harness these properties, grating structures have emerged as a crucial tool for controlling and enhancing the interaction between light wave and matter. They are of particular interest when aiming at designing integrated microdevices and tailoring device performance to specific applications.

The performance of grating-based plasmon couplers crucially hinges on the excitation angle of plasmonic modes. Both the size and thickness of the grating elements are known to impact the excitation angle, affecting the coupling efficiency and overall device functionality [1]. The relationship between these parameters, the materials used in grating fabrication, and the resulting excitation angle is complex and requires a comprehensive understanding to design optimized plasmonic couplers.

The Finite-Difference Time-Domain (FDTD) method [3], which is a numerical simulation technique widely used to model electromagnetic wave propagation and interaction with complex structures is deployed to accomplish this task in an efficient manner. To achieve an accurate representation, the Drude model method, Perfectly Matched Layer (PML), Periodic Boundary Condition (PBC), and Total Field/Scattered Field-Method (TF/SF) are included into the simulation environment. This computational approach allows for rapid exploration of a wide parameter space, facilitating the identification of optimal grating designs for specific plasmonic applications [4].

Simulation Environment

The simulation environment has been designed to accurately predict the behaviour of actual grating structures with high efficacy at optimzed computational costs. To this end, appropiate adjustments and boundary conditions have been implemented. The model presented here has been used to guide and validated grating designs via comparison to experimental results using a silver-based grating coupler [5].

To derive the governing equations for the 2D case in the x-y-plane, only the TM mode with the electrical field components E_x, E_y, the magnetic field component H_z and polarization current density components J_x, J_y are considered. The approximation is formed at a location between the

neighbouring components but not at the location of the points themselves. This procedure is as well valid for the time derivatives for which the midpoint between the time steps n and $n+1$ is taken. The spatial discretization pattern is illustrated in Figure 1.

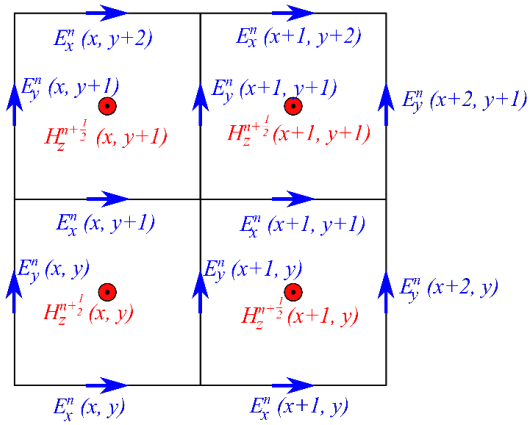


Figure 1: Representation of the Yee grid: The electric and magnetic field values are shifted against each other by half a time step in order to produce results that are possible physical solutions accurately describing the system behaviour.

For the analysis of the behavior of electromagnetic fields at thin metal layers, the Drude model is implemented and the excitation of the incident wave is performed using the Total Field/Scattered Field (TF/SF) method. 2D simulations with periodic boundary conditions are used to analyze the structure's behavior. The structure of the simulation area is shown in Figure 2.

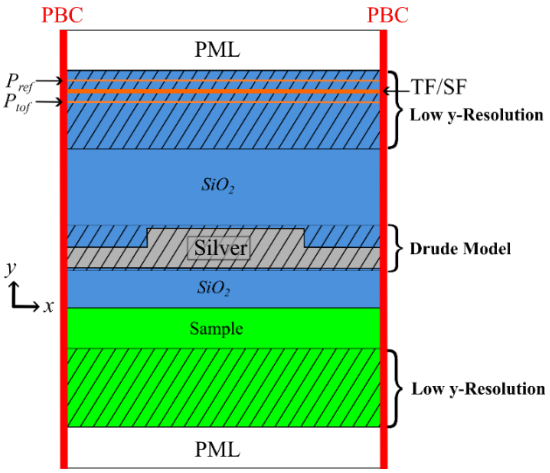


Figure 2: Structure for validating the chosen model indicating the areas of the PLM and periodic boundary condition as well as for the TF/SF method. The Drude model is implemented for the Plasmon excitation region, taking into account the realities of the fabrication process.

Results

The simulation model yields good agreement with experimental results. An exemplary analysis of the effect of changing the simulation resolution in the x-direction is investigated. For this purpose, reflectance spectra are calculated for different discretization widths Δx. The results are shown in Figure 3.

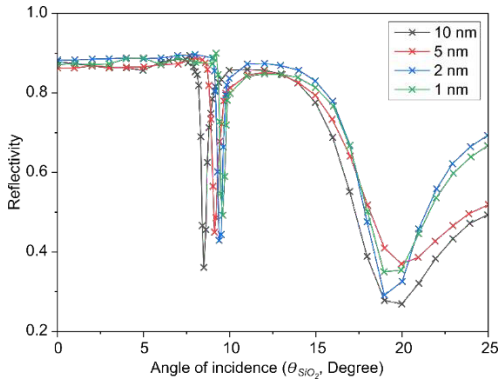


Figure 3: Simulation of the described structure under variation of the resolution in x-direction. The resolution in y-direction is 2 nm, the thickness of the dielectric layer is 1100 nm and the PML is 50 points wide. A pronounced influence on the accuracy of the simulated results with the simulation resolution may be appreciated.

References

[1] A. Sellai, "Effect of Grating Profile in a Surface Plasmon-Polariton Enhanced-Efficiency Schottky Photodetector," in *2008 3rd International Conference on Information and Communication Technologies: From Theory to Applications*, 2008, pp. 1–6.

[2] A. Meshalkin, V. Podlipnov, A. Ustinov, and E. Achimova, "Analysis of diffraction efficiency of phase gratings in dependence of duty cycle and depth," *Journal of Physics: Conference Series*, 2019. [Online].

[3] B. Archambeault, O. M. Ramahi, and C. Brench, "The Finite-Difference Time-Domain Method," in *EMI/EMC Computational Modeling Handbook*: Springer, Boston, MA, 1998, pp. 35–67. [Online].

[4] P. Sarapukdee, C. Spenner, D. Schulz, and S. Palzer, "Optimizing Stability and Performance of Silver-Based Grating Structures for Surface Plasmon Resonance Sensors," *Sensors*, vol. 23, no. 15, 2023, doi: 10.3390/s23156743.

[5] P. Sarapukdee, D. Schulz, and S. Palzer, "Concept, simulation, and fabrication of inverted grating structures for surface plasmon resonance sensors," *Journal of Sensors and Sensor Systems*, vol. 13, no. 2, pp. 157–166, 2024, doi: 10.5194/jsss-13-157-2024.

DOI 10.5162/EUROSENSORS2025/MP71

Time-integrated Sensing to Study Extreme Weather Events in Pulsed Pesticide Contamination

Namra Tariq[1], Chloe Martin[1], Fiona Regan[1], Hans-Jørgen Albrechtsen[2] and Karolina Barbara Milenko-Kuszewska[3]

[1] School of Chemical Sciences, DCU Water Institute, Dublin City University, Glasnevin, Dublin 9, Ireland,

[2] Denmark Technical University, Denmark,

[3] SINTEF, Norway

Corresponding Author's email: fiona.regan@dcu.ie

Summary:
This study highlights the impact of hydrometeorological extreme events on pesticide contamination in surface and groundwater resources in Ireland and Denmark. Using passive and grab sampling, the study compares pesticide levels before, during, and after such events. Solid-phase extraction (SPE) followed by LC-MS quantification will be used to analyze target pesticides. Passive sampling, a cost-effective and time-integrated technique, allows for better detection of episodic contamination events. The findings aim to improve understanding of how climate change-driven weather extremes influence pesticide loads in the water bodies. This research could enhance monitoring strategies for water quality management in the face of climate change.

Keywords: Climate Change, Pesticides, Passive Sampling, Liquid Chromatography-Mass-Spectrometry, Water Quality Assessment

Background, Motivation an Objective

Climate Change is acting as a driving force in the fundamental transformation of the hydrological systems across the globe, resulting in the exacerbation of water scarcity issue, degradation of water quality and causing an amplification in flood risks. The hydrological cycle greatly depends upon the fluctuations in the climatic variables especially Temperature and Precipitation [1].Torrential rainstorms and floods tend to increase the mobility of suspended solids, metallic substances, nutrients, plastics and agricultural pollutants into the water bodies resulting in severe contamination of the drinking water reservoirs [4]. The sudden surge in the levels of current and emerging contaminants in the water bodies has caused significant damage to the ecosystem health and sustainibility [5].

Passive sampling is an emerging technique for the preconcentration of pesticides from aquatic environments, achieved by deploying a sorbent-based device in situ for extended periods, typically ranging from 4 to 6 weeks. Despite its proven efficacy, the application of passive sampling for the screening and detection of priority pesticides in natural surface waters and groundwater remains relatively limited in the scientific literature. This method functions as a cost-effective, time-integrated sensor, capable of providing time-weighted average (TWA) concentrations of target analytes. Such an approach is particularly advantageous for capturing episodic contamination events and mitigating the limitations associated with conventional spot sampling, which often fails to detect transient pollutant occurrences.

The present study aims to investigate the intensification of pesticide contamination in surface and groundwater systems associated with the occurrence of hydrometeorological extreme events. This will be achieved through a comparative assessment of pesticide levels before, during, and after such events at selected sites in Ireland and Denmark, employing both passive sampling and grab sampling approaches. To isolate target analytes, water samples will undergo solid-phase extraction (SPE), followed by quantitative analysis using Liquid Chromatography coupled with Mass Spectrometry (LC-MS). This analytical workflow is designed to determine the concentrations of selected pesticides and assess temporal variations in contaminant loads in response to extreme weather conditions.

Description of the New Method or System

Passive Sampling is a cost-effective, time-saving, power-free and highly reliable method to accurately detect the pollution levels by determining the time weighted average (TWA) concentrations in an aquatic environment. Polar organic chemical integrative sampler (POCIS) and DGT passive samplers are highly robust and reliable passive samplers used for determining the levels of pesticides and pharmaceuticals in natural waters [2]. In the recent studies, use of Chemcatcher and LC/MS targeted analysis has been very helpful in quantifying 121 polar organic compounds in two sensitive rivers in UK, ranging in concentration <ng L^{-1} to >500 ng L^{-1} over a 12 month deployment period [3]. In the past, a wide range of passive samplers have been developed by using various sorbents and barriers in order to regularize the uptake rate. A recent study that compared three co-deployed passive samplers

(Speedisk, Hydrogel based passive sampler and POCIS) suggested that all samplers showed high accumulation of compounds with a consistent surface-specific uptake with a significant co-relation ($r \geq 0.76$) among all [6]. In the present study, different types of passive samplers shall be deployed at three locations in river Tolka (Ireland) and a water treatment plant in Denmark for the detection of contamination level of hazardous pesticides such as Clotrimazole, Thiamethoxam, Cypermethrin, Permethrin, Bifenthrin, Thiabendazole, Tebuconazole, Tetraconazole etc. in these drinking water resources. Moreover, the results obtained from passive sampling shall be compared with grab sampling in order to get a better image of the contamination levels of these substances. Furthermore, this shall be followed by the use of solid phase extraction and Liquid Chromatography Mass Spectrometry for identification and quantification of the targeted analytes. Moreover, these substances shall be regularly monitored for identifying the direct impact of torrential rains, flood and drought on their occurrence and prevalence.

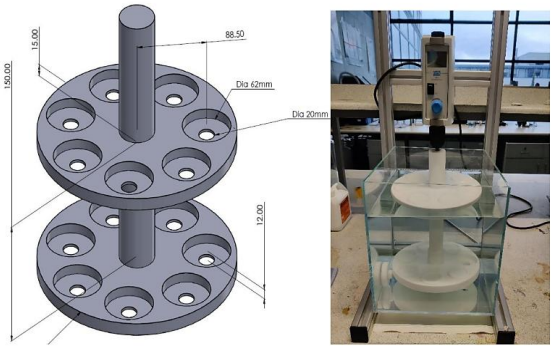


Fig. 2. PTFE Passive sampling carousel and dimensions

Results

A recent study at DCU was conducted on eleven selected pharmaceuticals highlighted that passive sampling showed higher number and concentration of these substances than grab sampling. This was due to the higher volumes of water gathered by passive samplers that would otherwise be overlooked by grab sampling. The presence of pharmaceuticals trimethoprim, diclofenac, clarithromycin, azithromycin, carbamazepine, venlafaxine, etc. were detected in river Liffey by passive sampling. The Chemcatcher device can measure the micropollutants in their freely dissolved concentration in the surface water bodies. Hence, the detection of pesticides by Passive Samplers is highly essential to reflect the bioavailability of these contaminants as well as their immediate impact on aquatic life. Current study shall focus on similar methodology to determine the pesticide contamination in selected sites by drawing a comparison between various passive samplers deployed in selected sites over a certain period.

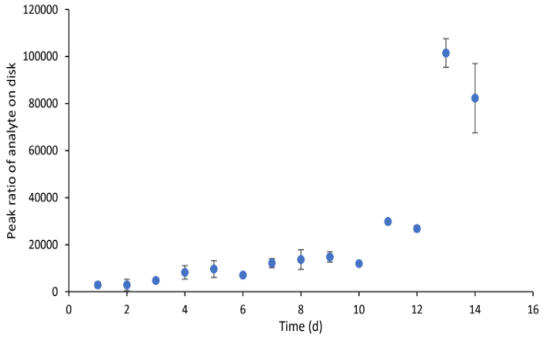


Fig. 2. Graph of Uptake of Trimethoprim in Chemcatcher HLB-L passive sampling disks during a 14-day exposure study at 1000 ng/L.

References

[1] S. Wang, L. Zhang, G. Wang, D. She, Q. Zhang, J. Xia, Y. Zhang, More intense and longer torrential rain and flood events during the recent past decade in Eurasia, *Water Resources Research* 59(8), e2022WR033314 (2023); doi: 10.1029/2022WR033314

[2] Y. Li, Z. Wang, X. Zhang, Z. Chen, Z. Zhao, X. Li, L. Wang, Application of passive sampling device for exploring the occurrence, distribution, and risk of pharmaceuticals and pesticides in surface water, *Science of the Total Environment* 901, 168393 (2023); doi: 10.1016/j.scitotenv.2023.168393

[3] R. F. Robinson, G. A. Mills, R. Grabic, A. Bořík, G. R. Fones, Quantification and risk assessment of polar organic contaminants in two chalk streams in Hampshire, UK using the Chemcatcher passive sampler, *Science of the Total Environment* 939, 173316 (2024); doi: 10.1016/j.scitotenv.2023.173316

[4] M. T. Van Vliet, J. Thorslund, M. Strokal, N. Hofstra, M. Flörke, H. Ehalt Macedo, ... & L. M. Mosley, Global river water quality under climate change and hydroclimatic extremes, *Nature Reviews Earth & Environment* 4(10), 687-702 (2023); doi: 10.1038/s41586-023-00669-6

[5] N. Ntsasa, A. Mkhohlakali, T. Mogashane, J. Tshilongo, M. R. Letsoalo, Trends in Systematic Techniques for Pollutants Monitoring in the Environmental Water Systems (2024); doi: 10.5772/intechopen.1007099

[6] P. Fialová, K. Šverclová, K. Grabicová, R. Grabic, H. Švecová, P. Nováková, B. Vrana, Performance comparison of three passive samplers for monitoring of polar organic contaminants in treated municipal wastewater, *Science of the Total Environment 908*, 168153 (2024); doi: 10.1016/j.scitotenv.2023.168153

Acknowledgements

The Authors would like to thank the European Commission and the Environmental Protection Agency for funding in the frame of the collaborative international consortium STARDUST financed under the 2022 Joint call of the European Partnership 101060874 - Water4All.

DOI 10.5162/EUROSENSORS2025/MP72

Establishing a Raman spectra database for the detection of Terbuthylazine metabolites using SERS-based optical sensors

Ioan-Alexandru Baragau[1], Oana Rasoga[1], Hans-Jørgen Albrechtsen[2], Konrad Gizynski[3], Karolina Milenko[4], Elizaveta Vereshchagina[4], Jesil Jose[4], Andreea Costas[1], Fiona Regan[5]
[1] National Institute of Materials Physics, 405 A, Atomistilor Street, P.O. Box M.G. 7, 077125 Magurele, Romania
[2] Department of Environmental and Resource Engineering - DTU Sustain, Technical University of Denmark, Bygningstorvet, Building 115, DK - 2800 Kgs. Lyngby, Denmark
[3] Institute of Physical Chemistry, Polish Academy of Sciences, Kasprzaka 44/52, 01-224 Warsaw, Poland
[4] SINTEF Microsystems and Nanotechnology, Gaustadalleen 23C, 0737 Oslo, Norway
[5] DCU Water Institute, School of Chemical Sciences, Dublin City University, Ireland
Corresponding Author's e-mail address: oana@infim.ro, hana@dtu.dk, kgizynski@ichf.edu.pl

Summary:
This study presents a comprehensive theoretical and experimental examination of Raman spectra for prevalent pesticide metabolites in Danish groundwater. The objective is to facilitate sensor development and enhance chemical identification processes by creating a database for the Raman spectra of terbuthylazine metabolites using three excitation wavelengths.

Keywords: groundwater, terbuthylazine, metabolites detection, Raman spectroscopy, Density Functional Theory.

Background, Motivation, and Objective

Climate change significantly impacts hydroclimatic events across Europe, leading to an increase in the frequency and intensity of extreme weather phenomena such as heavy rainfall, prolonged droughts, and heat waves. These hydroclimatic events play a crucial role in influencing the behavior and distribution of pesticides in the environment [1]. They can substantially affect the transport, degradation, and persistence of pesticides, often resulting in increased contamination levels in both surface water and groundwater. Understanding the relationship between hydroclimatic conditions and pesticide dynamics is essential, especially as climate change is expected to intensify extreme weather events. Many pesticides lack established Environmental Quality Standards (EQS) due to insufficient data on their concentrations and ecological effects. [2]. Collecting pesticide occurrence data will help standardize EQS and safeguard water quality within the EU's evolving regulatory frameworks. In Denmark, many banned or restricted pesticides still appear in groundwater, often exceeding the 0.1 µg/L threshold. For example, terbuthylazine, banned since 2008, has its breakdown products detected at frequencies up to 70% and concentrations ranging from 0.01 ng/L to 9.7 µg/L. The highest concentration was found for terbuthylazine-TP MT23 (LM5) while the lowest was for terbuthylazine-TP MT24 (LM1) [3]. This persistence underscores the need for improved detection methods.

Raman spectroscopy is an effective analytical technique for detecting pesticides, offering distinct spectra for identification and quantification. Its main advantage is efficiency, with analyses often completed in minutes, enabling rapid screening of large sample sets, crucial during contamination events or routine monitoring. Surface-Enhanced Raman Spectroscopy (SERS) has been effectively used to analyse different pesticide classes. Its miniaturization on a chip allows for compact sensors that enable sensitive on-site analysis [4]. This study examines the Raman spectra of common metabolites found in Danish groundwater. The objective is to facilitate sensor development and enhance chemical identification processes by creating a database for the terbuthylazine metabolites Raman spectra using three excitation wavelengths.

Simulation and detection

Density Functional Theory (DFT) calculations were carried out using Gaussian 16 to simulate the Raman spectra of the target compounds.

The calculated spectra were compared with experimental Raman data to validate the vibrational modes and identify characteristic peaks. Each prominent spectral feature was analyzed in terms of the corresponding vibrational motion and the specific part of the molecule responsible. Theoretical insights provided by the DFT simulations enhanced the interpretation of the experimental spectra, enabling accurate assignment of functional groups.

The samples of metabolites prepared for Raman analysis were created using gold-coated silicon substrates, which were structured with defined spotting areas to ensure structural integrity through the application of pressure-sensitive adhesive (PSA). Following the drop-casting of 7 µL of the metabolite solution, the samples were covered with a glass substrate to serve as a protective layer. The prepared solutions consisted of various terbuthylazine metabolites, which were diluted in water to concentrations of 10^{-3},10^{-4} mM, starting from a stock solution of 10 mM that was prepared in ethanol, which subsequently was evaporated, and the compounds were dissolved in distilled water.

Raman spectra for 532nm and 633nm were obtained utilizing a Horiba LabRAM HR Evolution Spectrometer, employing a 50x objective lens at maximum power (17 mW). The spectra were recorded by directing the laser through glass onto the metabolite crystallites present on the analyzed substrates, with an acquisition time of 5'' and 5 accumulations, with a total time of 4'56'' per sample. Raman spectra for 785nm excitation wavelength were collected using BWS465-785S i-Raman Plus spectrometer. The spectra were collected for 240'', 2 accumulations and 306mW of power.

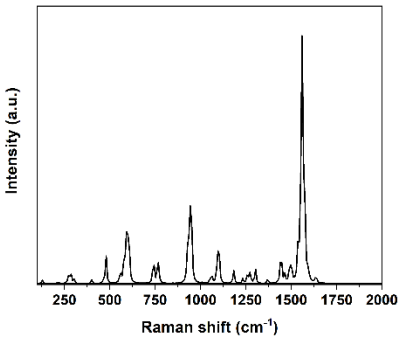


Fig.1. Terbuthylazine-TP MT23 (LM5) simulated Raman spectra using DFT calculation

Results

For all the involved metabolites, we extracted and compared the simulated spectra with the experimental Raman spectra. For instance, in the case of terbuthylazine-TP MT23 (LM5), which is the most abundant metabolite, the spectra are presented in Fig. 1 and 2. The experimental spectra have been normalized for better clarity. We chose the LM5 metabolite not only for its frequent detection but also because its spectra vary significantly with the excitation wavelength.

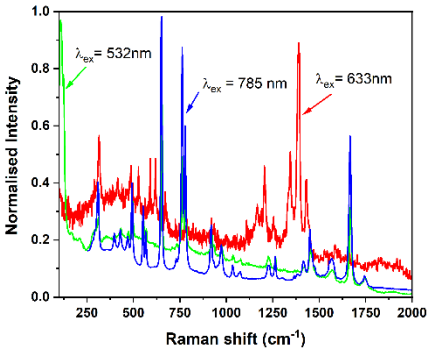


Fig.2. Terbuthylazine-TP MT23 (LM5) experimental Raman spectra

References

[1] Ma, CS., Zhang, W., Peng, Y. et al. Climate warming promotes pesticide resistance through expanding overwintering range of a global pest. Nat Commun 12, 5351 (2021). https://doi.org/10.1038/s41467-021-25505-7

[2] Thorling, L., Albers, C.N., Ditlefsen, D., Hansen, B., Johnsen, A.R., Kazmierczak, J., Mortensen, M.H. & Troldborg, L., "Grundvand. Status og udvikling 1989–2022". Teknisk rapport, GEUS 2024, https://doi.org/10.22008/gpub/38547

[3] Nanusha, M. Y., Frøkjær, E. E., Rüsz Hansen, H., Bonde Rasmussen, S., Bruun Nicolaisen, J., & Hansen, M. (2023)." Explorative Quantitative Nontarget Analysis Reveals Micropollutants in Danish Groundwater". ACS EST Water, 3(12), 3992-4003, https://doi.org/10.1021/acsestwater.3c00403

[4] E. Vereshchagina, K. Milenko and F. T. Dullo, "Microfluidic Surface-Enhanced Raman Scattering Sensors based on Nanoimprint Resist for Sensitive Detection of Pesticides in Water," IEEE SENSORS, Vienna, Austria, 2023, pp. 1-4, doi: 10.1109/SENSORS56945.2023.10324970.

Acknowledgements

The authors would like to thank the European Commission and the Research Council of Norway for funding in the frame of the collaborative international consortium STARDUST financed under the 2022 Joint call of the European Partnership 101060874 - Water4All. This work was supported by a grant from the Ministry of Research, Innovation and Digitization, CNCS/CCCDI – UEFISCDI, project number CO-FUND-WATER4ALL-STARDUST-1, within PNCDI IV. Project no. WATER4ALL/I/20/STARDUST/2024 is co-financed/financed by the National Centre for Research and Development under the Water4All Partnership Programme.

DOI 10.5162/EUROSENSORS2025/MP73

Optimization of Ultrasound Coupling for Clamp-on Flowmeters Using FEM Tools

Maximilian Schackmar[1], Achim Bittner[1], Alfons Dehé[1,2], Patrick Selle[1], Thilo Engel[3], Thomas Hahn-Jose[3], Axel Sikora[1,4]

[1] Hahn-Schickard-Gesellschaft für angewandte Forschung e.V., Wilhelm-Schickard-Str. 10, 78052 Villingen-Schwenningen, Germany

[2] Georg H. Endress Chair of Smart Systems Integration, Department of Microsystems Engineering – IMTEK, Albert-Ludwigs-Universität Freiburg, Georges-Köhler-Allee 103, 79110 Freiburg, Germany

[3] inoson GmbH, Sophie-Krämer-Straße 8, 66386 St. Ingbert

[4] Institute of Reliable Embedded Systems and Communication Electronics (ivESK), Offenburg University, Badstrasse 24, 77652 Offenburg, Germany

Maximilian.Schackmar@Hahn-Schickard.de

Summary:

Many state-of-the-art flowmeters are based on ultrasonic time-of-flight measurements. To enable an easy, fast and low-cost clamp-on mounting with an appropriate signal level, the materials and geometries must be tailored accordingly. Within this study, various materials for coupling wedges and matching-layers were evaluated with respect to acoustic impedance and transmission performance using the finite element method (FEM). Additionally, the incidence angle between the transducer and the fluid interface was optimized to maximize energy transfer and to minimize reflections. The simulation results were then compared with experimental measurements, showing improved signal quality and consistency across different setups. In future work these highly accurate measurements will be used for an AI-based leakage detection.

Keywords: Ultrasound coupling, FEM Simulation, clamp-on flowmeter, leakage detection, AI algorithm

Introduction

Ultrasonic (US) based flowmeters are state-of-the-art for accurate flow measurements [1]. Due to high impedance differences between solids and liquids, coupling conditions are critical for high-precision flow measurement, especially using clamp-on flowmeters. These systems can be based on externally mounted ultrasonic transducers transmitting acoustic waves through a coupling wedge, a matching-layer and finally the pipe wall into the fluid without direct contact to the fluid. Energy losses occur at interfaces between transducer, wedge, matching-layer, and the target fluid, primarily due to impedance mismatches and suboptimal geometrical alignment.

Within this study, several strategies for optimization of US coupling setups were investigated to overcome these limitations. The optimized setup will be used to develop an AI-based algorithm for leakage detection.

Simulation and Experimental Setup

The ultrasonic wave propagation in the clamp-on flowmeter setup is simulated using a two-dimensional finite element model in COMSOL Multiphysics. The simulation approach is based on a time-explicit transient analysis using the discontinuous Galerkin finite element method (dG-FEM). The elastic wave propagation in solids and acoustic wave propagation in fluids (water in this case) is modelled in a coupled framework. The dG-FEM is chosen due to its robustness and accuracy in handling material interfaces with high impedance contrasts - particularly critical at the solid-fluid boundary - and its suitability for transient high-frequency (MHz) simulations [2]. The 2D mode reduces the model size significantly and lowers calculation time while maintaining sufficient physical accuracy. The calculation time would be prohibitively high for full 3D simulations, especially for transient simulations in the MHz regime.

The geometry consists of two ceramic PZT (lead zirconate titanate) piezoelectric transducers, each of which is attached to a coupling wedge with a matching-layer, mounted on the same side of a water-filled pipe. The transducers, coupling wedges and matching layers are identical in size and are arranged in a mirror-symmetric configuration (see Figure 1).

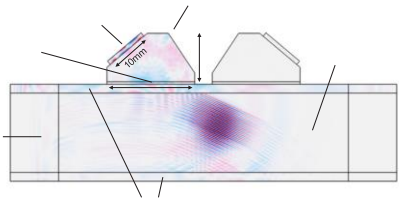


Figure 1: Geometry of the FEM model and a simulated pressure field (30 µs after excitation)

One transducer acts as the transmitter (Tx) and the other as the receiver (Rx). The acoustic waves emitted by the transmitter pass through the wedge and matching-layer into the fluid through the pipe wall. These waves then reflect off the lower wall and return on a mirrored path to be received by the Rx transducer. Additionally, structure-borne sound propagates directly through the pipe wall and reaches the receiving transducer before the fluid-borne reflection arrives. This early-arriving signal is relevant for the interpretation of the received waveform (cf. Figure 2). The coupling

wedge with the attached Rx transducer is always placed centrally at the point on the pipe where the impinging sound waves generate the highest acoustic pressure. To prevent reflections from the domain boundaries, absorbing layers were added to both pipe ends of the FEM model. Simulations were carried out on pipes made of steel, copper, and PVC, with outer diameters and wall thicknesses conforming to DIN 15 standards.

Various coupling wedge materials (e.g., PMMA, POM-C, PTFE) and matching-layer materials (e.g., PU-tape, silicone-tape, silicone grease) were tested. Simulations were carried out with various wedge geometries at different angles between the transducer and the pipe wall to determine the optimum angle of incidence at the matching-layer/pipe-wall interface for total internal reflection of longitudinal waves while maximising the coupling of transverse waves. Suppressing unwanted longitudinal modes prevents signal corruption and enhance primary shear wave transmission [3]. A unipolar square-wave burst of 10 pulses with an amplitude of 5 V, a duty cycle of 50 % and a frequency of 2 MHz is used as the excitation signal. For each case, the electrical voltage at the receiving transducer is evaluated to assess the efficiency of the ultrasound coupling.

Results

Figure 2 shows a direct comparison of simulated and measured waveforms. The shapes of the time-domain waveforms and their arrival times match closely, validating the simulation model. However, the simulated amplitudes are around 40 % smaller than the measured values. A possible explanation for this is that the literature values of the material damping ratios used in the simulation differ slightly from the actual damping ratios.

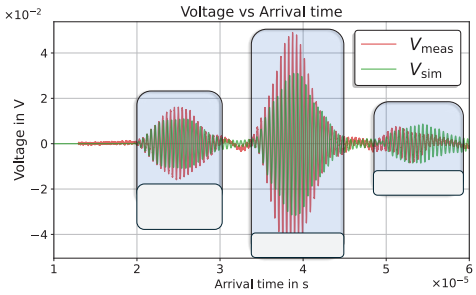
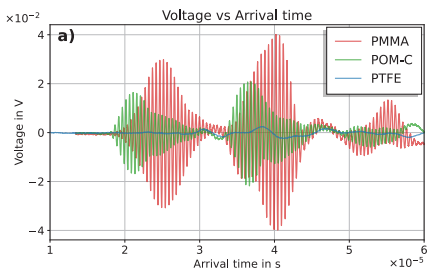


Figure 2: Comparison of simulated and measured time-domain voltage waveforms (DIN 15 steel pipe)

Figure 3 illustrates the experimentally determined waveforms, using different wedge- and matching-layer materials. Among all tested configurations, PMMA as the coupling wedge material combined with a silicone grease matching-layer yielded the highest received signal amplitude and -integrity.



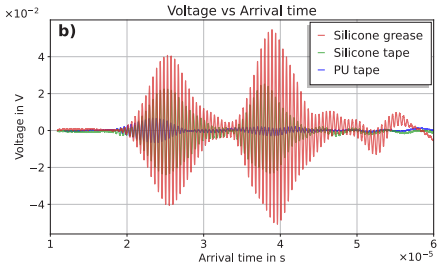


Figure 3: Measured waveforms for different wedge- (a) and matching-layer materials (b) (DIN 15 steel pipe)

Figure 4 presents the simulated waveforms at different incidence angles for a DIN 15 steel pipe. The best sensitivity and waveform integrity for the steel pipe is achieved at a coupling angle of 35°. For copper and PVC pipes of equivalent dimensions, the optimal angle shifts to 40°, where similar improvements in sensitivity and signal coherence are observed. These angles thus represent the optimal configurations for each pipe material and the given geometry.

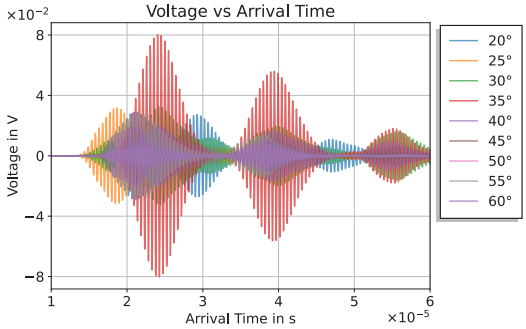


Figure 4: Simulated waveforms for different incidence angles (DIN 15 steel pipe)

Conclusions

This study shows the optimization of ultrasonic transmission of clamp-on transducers into liquid-filled pipe systems. Signal integrity and sensitivity can be significantly improved by optimizing the geometry and material configuration of coupling elements. Finite element simulations and measurements were conducted to evaluate various wedge and matching-layer materials, as well as to determine the optimal incidence angle for efficient energy transfer. The simulated waveforms closely match the experimental data, validating the model approach. The high-quality US measurement enables the application as leakage sensor. In further research an AI based algorithm will be developed to detect leakage in pipe systems.

References

[1] J. Senthil et al., A comprehensive review on accuracy in ultrasonic flow measurement using reconfigurable systems and deep learning approaches, *AIP Advances 10(10):105221 (2020);* doi: 10.1063/5.0022154

[2] J. D. Achenbach, Wave Propagation in Elastic Solids, *North-Holland*, (1973)

[3] W. Hu et al., Mode conversion and critical angle effects in ultrasonic flow sensors, *Proc. of ICISMME 2015 (Atlantis Press)*, pp. 1057–1060 (2015)

DOI 10.5162/EUROSENSORS2025/TP1

Nanowire Array Biosensor

Ashkhen Yesayan[1], *Aleksandr Grabski*[2]
[1] *Swiss Federal Institute of Technology in Lausanne, 1015 Lausanne, Switzerland.,*
[2] *MPSI, Paris-Saclay University, 91192 Gif-sur-Yvette, France*
ashkhen.yesayan@epfl.ch

Summary:
In this work, we performed analytical and numerical studies of a nanowire array field-effect biosensor. The concept of the electrical double layer is applyed in conjunction with a nanowire junctionless FET model. The model accounts for biosensing dynamics, and the sensor's sensitivity is evaluated for femtomolar variations of biomolecule concentration within the analyte solution. The signal-to-noise ratio (SNR) is also estimated, providing a lower bound on the detectable concentration.

Keywords: Nanowire array, biosensing, FET, sensitivity

Introduction

Nanowire (NW)-based biosensors have gained significant attention in recent years due to their exceptional sensitivity to low concentrations of biological analytes and the relative simplicity of their fabrication processes. For sensing applications, the surface of a semiconductor nanowire is usually functionalized with molecular receptors that are selectively designed to bind to target biomolecules. This surface modification enables the specific immobilization of biological entities—such as proteins, nucleic acids, or pathogens—onto the nanowire surface. These surface-bound biological charges then modulate the current through the NW FET; thereby, the biological event is converted into a measurable electrical signal. Understanding and simulating the complex physical and chemical interactions occurring in these biosensors is vital for improving their performance and optimizing their design.

Design-oriented analytical and numerical models have been developed for single-NW-based biochemical sensors [1,2]. The developed models predict sensor sensitivity even when the biomolecule concentration is in the femtomolar range. While single-NW devices offer simplicity and scalability, sensor architectures based on arrays of nanowires present distinct advantages. Specifically, NW array FET biosensors demonstrate enhanced sensitivity and improved signal stability [3]. This is largely due to the increased surface area for molecular binding and the statistical averaging effect provided by the multiple sensing elements within the array.

Methodology

In this work, we generalize the biosensor model from [2] and apply it to a silicon NW array biosensor. The system under study is illustrated in Fig. 1. The Si NW array is immersed in an analyte solution, which replaces the conventional metallic gate in NW FETs. The ‘gate voltage’ is applied via a reference electrode immersed in the solution. The source and drain potentials are applied directly to the bottom and top of the nanowires, as in regular FET devices (see Fig. 1a). We consider n-doped Si NWs covered with an array of y-shaped nanopillars designed to detect biomolecules (see Fig. 1b). Antibody-antigen binding is a spontaneous chemical reaction which is enthalpy driven, meaning that no external energy is required to enable the binding. The formation of paratope/epitope molecular interfaces results in a creation of a charged area very close to NW, which modulates NW FET current. The diffusion charge of ions in the solution is also considered. The concept of electric double layer is applied in the analyte solution and NW junctionless FET analytical model [4] is used to model the transducer part of the sensor. We assume that the functionalized layer on the NW has low permeability and that the ion partitioning from the solution is negligible. Under these conditions, the biological charges are separated from the NW surface by the insulating layer with (t_{eff}) thickness, see Fig. 1b, consisting of the functionalized layer and the oxide. Then we consider that each NW in a cylindrical volume is surrounded by an analyte solution of thickness (l), see Fig. 1b. The symmetry boundary

conditions are applied on the virtual surface of this cylindrical volume.

Results

To better understand how the spatial arrangement of nanowires influences sensing performance, we carried out a comprehensive analysis of the electric potential distribution in the surrounding analyte solution using COMSOL simulations (illustrated in Fig. 2). Since biological charge binding is a time-dependent process, the electric potential is plotted at different time points. These simulations help identify optimal nanowire placement strategies that maximize interaction with target molecules while minimizing noise.

A key metric in evaluating biosensor performance is the signal-to-noise ratio (SNR), which becomes especially critical when detecting extremely low analyte concentrations, such as those in the picomolar to femtomolar range. Our study includes an estimation of the SNR, showing reasonable values even at femtomolar concentrations.

References

[1] A. Yesayan, F. Jazaeri, and J. Sallese, Analytical modeling of double-gate and nanowire junctionless ISFETs, IEEE Trans. Electron Devices, 67 (3), 1157–1164, (2020). doi: 10.1109/TED.2020.2965167.

[2] A. Yesayan, A. Grabski, F. Jazaeri and J. -M. Sallese, Design-Oriented Analytical Model for Nanowire Biosensors Including Dynamic Aspects, IEEE Trans. Electron Devices, 72, (3), 1337-1344, (2025). doi: 10.1109/TED.2025.3526113

[3] Li X, Mo J, Fang J., et al., Vertical nanowire array-based biosensors: device design strategies and biomedical applications, Journal of Materials Chemistry B, 8, no. 34, 7609-7632, (2020). doi: 10.1039/D0TB00990C

[4] J.-M. Sallese, N. Chevillon, et al., Charge-based modeling of junctionless double-gate field-effect transistors, IEEE Trans. Electron Devices, 58 (8) 2628–2637, (2011).

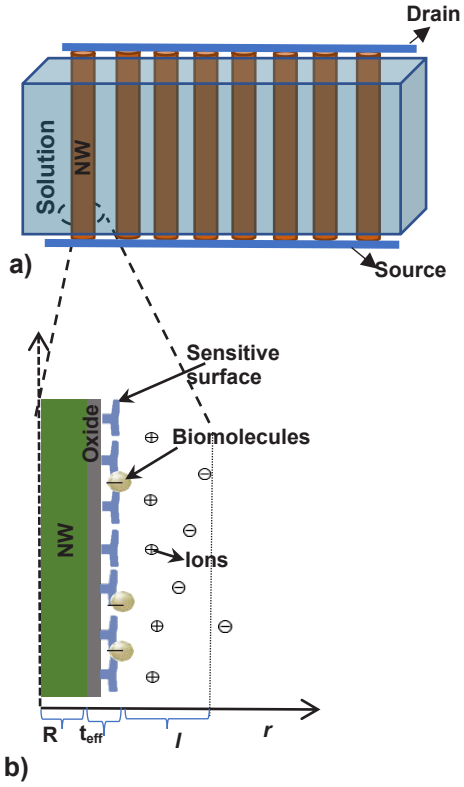


Fig. 1. a) Schematic structure of NW array biosensor, b) the surface coverage and surrounding solution of a single NW.

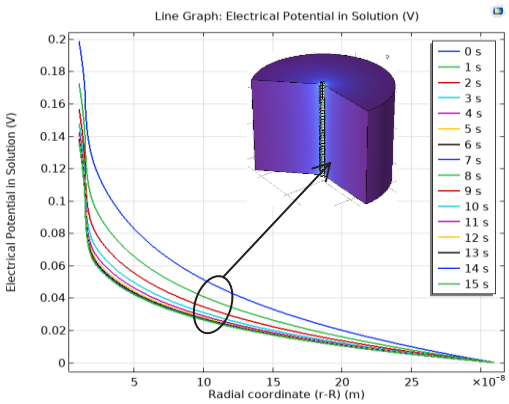


Fig. 2. Electrical potential distribution in analyte solution surrounding a single NW at different time slots.

DOI 10.5162/EUROSENSORS2025/TP2

Dopamine assessment on conductive polymers/gold NPs with appended metalloporphyrins composites

Tahereh Rohani Bastami [1,2], Francesco Pizzoli[1], Fabrizio Caroleo[1], Sara Nardis[1], Roberto Paolesse[1], and Larisa Lvova[1]

[1]Department of Chemical Sciences and Technology, University of Rome "Tor Vergata", Rome, 00133, Italy
[2]Department of Chemical Engineering, Faculty of Advanced Technologies, Quchan Univesity of Technology, Quchan 94771-77870, Iran
larisa.lvova@uniroma2.it

Summary:

The potential of gold nanoparticles with appended metalloporphyrin synthesized through one-pot sono-synthesis and incorporated in conductive PANI and PPy polymeric coatings deposited on SPEs for catalytic oxidative detection of dopamine (DA) has been evaluated. The CV and LSV studies of developed composite materials have demonstrated their specific response to DA n in 2.5×10^{-5} – 1.0×10^{-3} M concentration range. The morphology of electropolymerized PPy and PANI polymeric coatings bearing ZnTPP$(CO_3)_4$@AuNPs and ZnTPP$(SO_3)_4$@AuNPs were tested my SEM and spectroscopic methods.

Keywords: electrochemical dopamine detection; gold nanoparticles; porphyrin catalytic center; conductive PANI and PPy polymeric coatings; composite materials.

Background, Motivation and Objective

Dopamine (DA) is a primary neurotransmitter, synthesized in the brain and involved in many functions: it is responsible for feelings of pleasure, motivation, and gratification, and is also involved in processes such as movement, memory, and attention [1]. DA is one of the most important biomarkers of the brain diseases, its measurable changes in body fluids, as for instance in urine, may be associated with a physiological or pathophysiological processes [2]. Hence the development of analytical systems permitting the fast and effective DA levels control in biological liquids is a challenging task. Chemical sensors, and in particular electrochemical sensors based on electrocatalytically active nanohybrid materials have been reported for the oxidation of different biological materials, and for DA detection in particular [3-5].

In this work, 4 conductive PANI and PPy polymeric coatings obtained through co-polymerization with gold nanoparticles, AuNPs, with appended water-soluble Zn-porphyrin complexes synthesized through one-pot sono-synthesis were tested in comparison to non-modified PANI and PPY for catalytic dopamine assessment.

The coatings were obtained on carbon black SPE from with from aniline or pyrrole monomer solutions, and doped either with ZnTPP$(CO_3)_4$@AuNPs or with ZnTPP$(SO_3)_4$@AuNPs through Cyclic Voltammetry electropolymerization process in standard 3-electrode cell, with Pt wire counter and SCE reference, Table 1. Film electrolymerizations were run for 10-20 cycles, scanning the potential from -0.3 to 1.1 V range, with 100 mV/s scan rate. The water-soluble Zn(II) complexes of 5,10,15,20-tetraphenyl sulfonate, ZnTPP$(SO_3)_4$ or 5,10,15,20-tetraphenyl carboxylate appended on AuNPs and bearing negative charge served as counter-ions for positively charged PPy and PANI polymeric backbone upon electropolymerization. Further, the catalytic effect of AuNPs on DA oxidation was tested for obtained films in comparison to bare carbon black (CB) material of SPE working electrode, CB coated either with PPy (and ClO_4^- - counter anions), or PANI (Cl^- counter anions), and for CB/ZnTPP$(CO_3)_4$ @AuNPs coating.

Tab. 1: Composition of tested polymeric coatings for oxidative DA assessment.

N	Coating	Deposition solution
1	-	-
2	PPy	**Sol.1:** 0.15M pyrrole in ACN, 0.1M $TBClO_4$
3	PANI	**Sol.2:** 0.15M aniline in 1M HCl
4	PPy/ ZnTPP$(CO_3)_4$ @AuNPs	**Sol.1** : 5mM ZnTPP$(CO_3)_4$ @AuNPs = 1:1
5	PPy/ ZnTPP$(SO_3)_4$ @AuNPs	**Sol.1** : 5mM ZnTPP$(SO_3)_4$ @AuNPs = 1:1
6	PANI/ ZnTPP$(CO_3)_4$ @AuNPs	**Sol.2** : 5mM ZnTPP$(CO_3)_4$ @AuNPs = 1:1

7	PANI/ $ZnTPP(SO_3)_4$ @AuNPs	Sol.2 : 5mM $2ZnTPP(SO_3)_4$ @AuNPs = 1:1

Results

As it is shown in Figure 1 the higher currents indicating the formation of highly conjugated conductive coating were obtained for PANI films doped with $ZnTPP(SO_3)_4$@AuNPs served as counter-ions for positively charged PANI-backbone during electropolymerization.

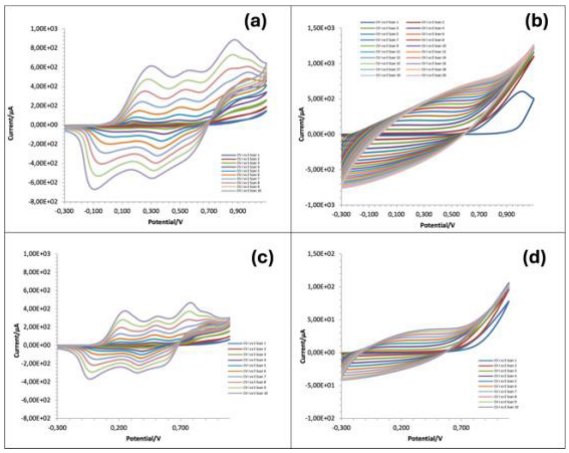


Fig. 1. CV electropolymerization of (a) PANI/ $ZnTPP(SO_3)_4$@AuNPs*, coating 7; (b)* PPy/$ZnTPP(SO_3)_4$ @AuNPs*, coating 5; (c)* PANI/$ZnTPP(CO_3)_4$@AuNPs*, coating 6; (d)* PPy/$ZnTPP(CO_3)_4$@AuNPs*, coating 4. CV 10-20 cycles from -0.3 to 1.1V, 100 mV/s scan rate.*

The morphology of electropolymerized PPy and PANI polymeric coatings bearing $ZnTPP(CO_3)_4$ @AuNPs and $ZnTPP(SO_3)_4$@AuNPs were tested by SEM microscopy and spectroscopic methods. As it may be seen from Figure 2(a) and magnified insert, the more uniform film with well distributed AuNPs was registered for coating 7: PANI/ $ZnTPP(SO_3)_4$@AuNPs.

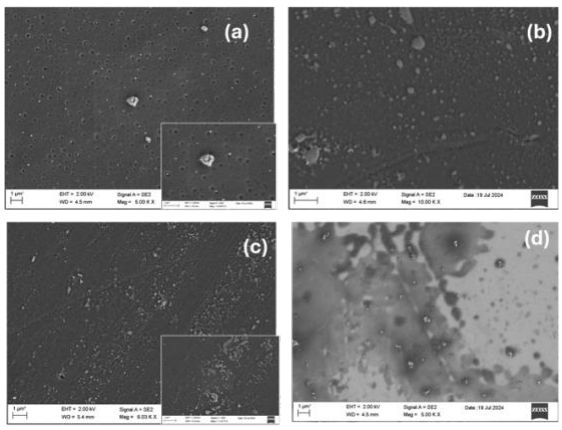


Fig. 2. SEM images of (a) PANI/ $ZnTPP(SO_3)_4$@AuNPs*, coating 7; (b)* PPy/$ZnTPP(SO_3)_4$ @AuNPs*, coating 5; (c)* PANI/$ZnTPP(CO_3)_4$@AuNPs*, coating 6; (d)* PPy/ $ZnTPP(CO_3)_4$@AuNPs*, coating 4.*

CV and LSV studies of developed composite materials have demonstrated the specific response to DA neurotransmitter in a 2.5×10^{-5} – 2.0×10^{-3} M concentration range, with LDL of 50 µM. The best performance have shown coating 7, based on PANI and doped with $ZnTPP(SO_3)_4$ @AuNPs, Fig. 3.

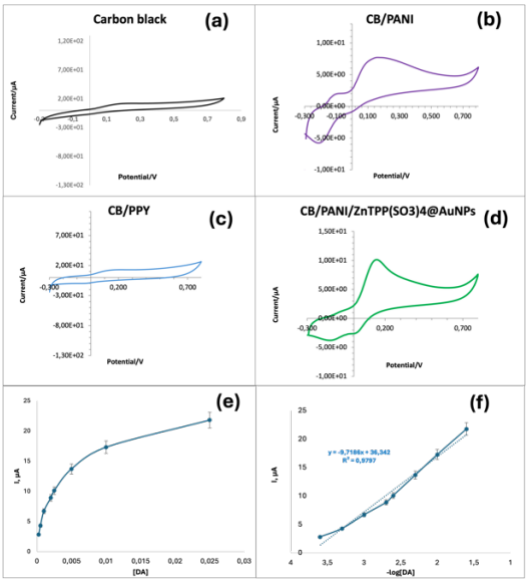


Fig. 3. (a) CV of DA detection at (a) CB; (b) CB/PANI; (c) CB/PPy; (d) PANI/ $ZnTPP(SO_3)_4$@AuNPs, coating 7. Calibration curves od DA response obtained for c PANI/ $ZnTPP(SO_3)_4$@AuNPs*, coating 7: (e) current vs DA cpncentartion, (d) – cyrrent vs -log[DA].*

The detailed discussion on influence of conductive polymeric matrix, AuNPs and metalloporphyrin complexes properties on sensitivity and selectivity properties of the composite materials, as well as examples of real samples analysis, will be provided in our presentation.

References

[1] Iversen, S.D.; Iversen, L.L. Trends Neurosci., 2007, 30, 188.
[2] An, M.; Gao, Y. Genomics Proteomics Bioinformatics, 2015, 13, 345.
[3] Kim, D.S.; Kang, E.S.; Baek, S. et al., Sci Rep, 2018, 8, 14049.
[4] Anuar, N.S.; Basirun, W.J.; Shalauddin, Md.; Akhter, S. RSC Adv., 2020,10, 17336.
[5] Lakard, S.; Pavel, I.A.; Lakard, B. Biosensors, 2021, 11, 179.

DOI 10.5162/EUROSENSORS2025/TP3

Benchmarking surface sensitivity of LSPR sensors: comparison of experimental methods

Rebeka Kovács[1,2], Tomáš Lednický[3], Mario Ziegler[3], Attila Bonyár[1,2],
[1] Department of Electronics Technology, Faculty of Electrical Engineering and Informatics, Budapest University of Technology and Economics, Budapest, Hungary
[2] Institute for Solid State Physics and Optics, HUN-REN Wigner Research Centre for Physics, Budapest, Hungary
[3] Leibniz Institute of Photonic Technology, Albert-Einstein-Str. 9, 07745 Jena, Germany
kovacsrebeka@edu.bme.hu

Summary:
Localized surface plasmon resonance (LSPR) principle-based biosensing methods enable the detection of various target molecules. When illuminated by a light source, oscillation of the free electrons occurs on the surface of the metal nanoparticles, thus enhancement of the scattering and absorption can be observed. The plasmon decay plays a major role in the signal enhancement from immobilized molecules. Therefore, estimating the field enhancement profile is the key to LSPR sensor benchmarking. Here, we compare two techniques utilizing Layer-by-Layer (LbL) and atomic layer deposition (ALD)

Keywords: localized surface plasmon resonance (LSPR), plasmonic nanostructure, refractive index sensing, plasmon decay length, layer-by-layer (LBL), atomic layer deposition (ALD)

Background, Motivation and Objective

LSPR sensors have been in the scientific focus, due to their great advantages, such as real-time monitoring of label-free molecular interactions, high sensitivity and selectivity. The detection of target molecules (e.g., proteins, DNA, etc.) can be estimated from the peak shift of the extinction spectra [1], which corresponds to changes of the refractive index surrounding plasmon nanoparticles. The scale of sensors' optical response depends greatly on the plasmonic structures and their field confinement and enhancement. Therefore, to maximize the performance and the signal, it is crucial to precisely define and control the size, shape, interparticle distance, and material properties with respect to the size of target molecules [2]. These properties affect the plasmon decay length of the metal nanoparticles, which helps us to define the effective sensing range of the sensors. For many nanoparticles with a diameter of 50–100 nm, their plasmon decay length can be observed in an exponential decay, around 5–10 nm, which can be compared to the size of protein molecules [3].

Mapping the field enhancement around the plasmonic nanoparticles is a crucial part in optimizing the performance of the sensors. Plasmon penetration depth can be studied in many ways: one research used a less invasive technique, applying biomolecules [4] on the gold nanoparticles.

However, one of the most frequently chosen methods for immobilization is the layer-by-layer (LBL) deposition method, which gives us an opportunity to precisely control the number of the layers and to characterize our sensors while offering a cost-effective, reliable solution. The layers are built from two different solutions (where one is positively charged, the other is negatively charged), which overlap one another at a molecular level, thus a homogenous optical material is created [5].

Another method to create precisely controlled conformal ultra-thin layers on the nanoparticles, is the atomic layer deposition (ALD) technique, which is a chemical synthesis process, where the gas-phase deposition is under high vacuum conditions [6]. Multiple self-terminating surface reactions are repeated precisely in order to grow the layers. ALD is particularly effective for modifying metallic surfaces; it can be used to funetune plasmonic characteristics, or to protect them from contamination and oxidation [7].

In this work, we study the effect of utilizing polyelectrolyte bilayers (created by LBL deposition) with different thicknesses on the target signal, to determine the signal's dependency on the distance from the particles. Furthermore, we compare the results to the measurements with ALD technique.

Description of the New Method or System

The samples containing the nanoparticles were created by annealing thin (8nm) Au film deposited by magnetron sputtering on a borosilicate glass wafer, which was followed by reactive ion

etching cut up to 12×7 mm sensors (Fig.1), which were oxygen plasma cleaned prior to use.



Fig. 1. The uniform thin film-based LSPR sensor on a glass wafer

LBL deposition was carried out by utilizing a microfluidic system, which enabled the control of the fluids during the experiment. Each additional layer on the gold nanoparticles caused a shift of the resonance peak positions that were detected by a spectrometer.

For the LBL deposition, 0.1mM polystyrene sulfonate (PSS) and 0.1 mM polyallylamine hydrochloride (PAH) were used in 0.1 M NaCl buffer. Both solutions were alternatively pumped over the chip, with water injection in between every step. The decay length (l_d) is calculated using the LSPR shift ($\Delta\lambda$) and the layer thickness (d). One bilayer of PAH/PSS is around ~4 nm, and the refractive index of n = 1.5. The measurements were carried out in a microfluidic chamber integrated into an LSPR experimental setup.

In the case of the ALD technique, trimethylaluminium (TMA) and oxygen were used as precursors. Growth per cycle (GPC) was 0.156 nm per cycle; the thickness of the film can be controlled by the number of cycles. The following Al_2O_3 layer thicknesses were applied on different chip samples: 1, 2, 4, 8, 16, 32, 64, 128 nm.

Results

The optical spectra of the sensors were taken in air (n=1) before and after ALD treatment. The layer thickness was measured with ellipsometry on a calibration piece of Si wafer. Figure 2. shows scanning electron microscope (SEM) images of selected nanoparticles.

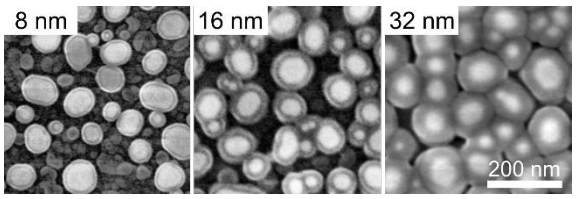


Fig. 2. SEM images of selected AuNPs covered by Al_2O_3 layers deposited by ALD.

The results of the ALD and LBL depositions and the peak shifts are presented in Figure 3. ALD offers a better solution for mapping the plasmon field around the nanoparticles, since the layer properties are more defined than in the case of LBL.

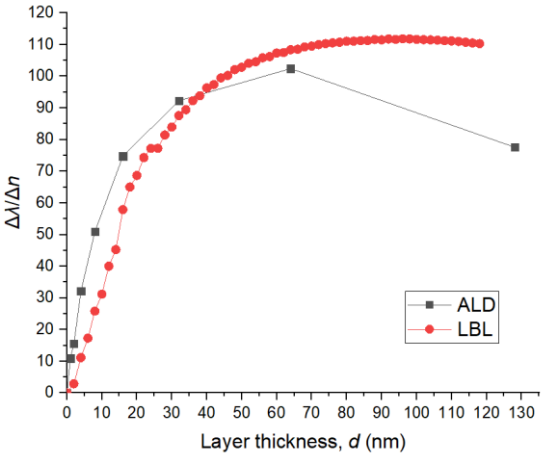


Fig. 3. Comparison of the ALD and LBL results.

References

[1] M. P. Mcoyi, K. T. Mpofu, M. Sekhwama, and P. Mthunzi-Kufa, Developments in Localized Surface Plasmon Resonance, *Plasmonics*, Nov. (2024); doi: 10.1007/s11468-024-02620-x.

[2] P. J. Rivero, J. Goicoechea, F. J. Arregui, P. J. Rivero, J. Goicoechea, and F. J. Arregui, Localized Surface Plasmon Resonance for Optical Fiber-Sensing Applications, in *Nanoplasmonics - Fundamentals and Applications*, IntechOpen, (2017); doi: 10.5772/67544.

[3] A. J. Haes, S. Zou, G. C. Schatz, and R. P. Van Duyne, A Nanoscale Optical Biosensor: The Long Range Distance Dependence of the Localized Surface Plasmon Resonance of Noble Metal Nanoparticles, *J. Phys. Chem. B*, vol. 108, no. 1, pp. 109–116, Jan.(2004) doi: 10.1021/jp0361327.

[4] T, Read, R, V, Olkhov. A, M. Shaw, Measurement of the localized plasmon penetration depth for gold nanoparticles using a non-invasive bio-stacking method. hys.Chem.Chem.Phys.,(2013) 15, 6122

[5] Choi, J.; Rubner, M. F. Influence of the degree of ionization on weak polyelectrolyte multilayer assembly. Macromolecules (2005), 38, 116-124.

[6] R. W. Johnson, A. Hultqvist, and S. F. Bent, A brief review of atomic layer deposition: from fundamentals to applications, *Materials Today*, vol. 17, no. 5, pp. 236–246, Jun. (2014) doi: 10.1016/j.mattod.2014.04.026.

[7] Im, H., Wittenberg, N. J., Lindquist, N. C., & Oh, S.-H. Atomic layer deposition: A versatile technique for plasmonics and nanobiotechnology. Journal of Materials Research, 27(04),(2012) 663–671. doi:10.1557/jmr.2011.434

Acknowledgements

This work was partially supported by Nanoplasmonic Laser Fusion Research Laboratory (NAPLIFE) project financed by the National Research and Innovation Office (2022-2.1.1-NL-2022-00002), Hungary. The research was also supported by the National Research and Innovation Office under project number: 2020-1.2.3-EUREKA-2022-00030. The project is also supported by the Doctoral Excellence Fellowship Programme (DCEP) is funded by the National Research Development and Innovation Fund of the Ministry of Culture and Innovation and the Budapest University of Technology and Economics, under a grant agreement with the National Research, Development and Innovation Office. Project no. 2024-2.1.1-EKÖP has been implemented with the support provided by the Ministry of Culture and Innovation of Hungary from the National Research, Development and Innovation Fund, financed under the EKÖP-24-3 funding scheme."

DOI 10.5162/EUROSENSORS2025/TP4

The Importance of Surface Sensitivity in the Optimization of Plasmonic Sensors

Attila Bonyár [1, 2], Rebeka Kovács[1], Nóra Tarpataki[1], Tomáš Lednický[3]
[1] Department of Electronics Technology, Faculty of Electrical Engineering and Informatics, Budapest University of Technology and Economics, Egry József street 18, H-1111, Budapest, Hungary
[2] Wigner Research Centre for Physics, Konkoly-Thege Miklós way 29-33, H-1121, Budapest, Hungary
[3] Leibniz Institute of Photonic Technology, Albert-Einstein-Str. 9, 07745 Jena, Germany
bonyar.attila@vik.bme.hu

Summary:
In this work the importance of optimizing the surface sensitivity of nanoplasmonic sensors is discussed. In localized surface plasmon resonance (LSPR) based sensing, the size, shape and arrangement of the used nanoparticles all affect their sensitivity. We will demonstrate that by careful design and near-field engineering, the plasmon decay length of nanoparticle-arrangements can be fine-tuned, taking into account the size of receptor and target molecules used in the different sensing scenarios. By optimizing the surface sensitivity of the sensors, their performance in small molecule detection can be maximized.

Keywords: Localized Surface Plasmon Resonance; Refractive Index Sensitivity; Surface Sensitivity; Modelling adsorption interfaces.

Background

One of the main challenges of fabricating plasmonic nanostructures for chemical and biosensing applications is optimization of the structures in order to maximize their sensitivity. The most widely used parameter for benchmarking the fabricated sensors is the bulk refractive index sensitivity (*RIS*), which relates the spectral response ($\Delta\lambda_p$) to the RI changes in the medium surrounding the nanoparticles (Δn_b), as defined in Eq. 1 [1].

$$RIS = \frac{\Delta\lambda_p}{\Delta n_b} \quad (1)$$

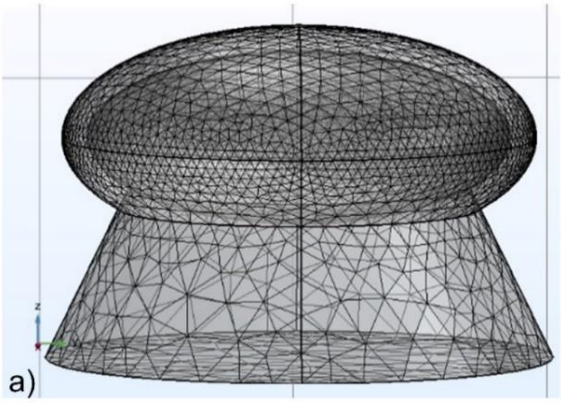
However, for small molecule sensing applications the surface sensitivity, that characterizes the spectral response in the function of the deposited layer thickness can be more meaningful. The surface sensitivity is usually evaluated by using Eq. 2, where nl and t are the refractive index and thickness of a deposited layer on the nanoparticle's surface, and ξ_D is the plasmon decay length [2].

$$\Delta\lambda_p = RIS(n_l - n_b)\left(1 - e^{\frac{-2t}{\xi_D}}\right) \quad (2)$$

Surface sensitivity is primarily depending on the plasmon decay length around the particles, affected by their size and shape and strongly influenced also by plasmonic coupling.

Description of the Used Methods

Surface sensitivity can be determined experimentally by using subsequential chemical deposition tools, such as the layer-by-layer (LbL) method, that uses positively and negatively charged molecules to create layers with increasing thickness and thus map the plasmon decay length of the particles. If the geometry of the used nanoparticles is known numerical simulations can also be used to map the response of the nanoparticles, as illustrated in Fig. 1.



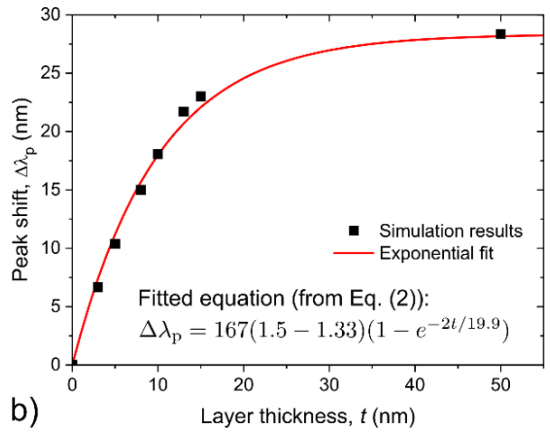


Fig. 1/a: The structure and mesh of the hexagonal (periodic) unit cell for modeling the response and surface sensitivity of densely-packed gold nanoparticle arrays. In the simulations a growing thickness of layers with known refractive index (n_l=1.5) is deposited onto the nanoparticles in water medium (n_b=1.33) [3]. b) The calculated peak shift values as a function of the deposited layer thickness. By fitting Eq. 2 on the dataset (with known RIS) the plasmon decay length of the structure can be obtained (19.9 nm in this case) [3].

Results

In this talk, the importance of optimizing the surface sensitivity of plasmonic nanostructures will be highlighted. It will be demonstrated through numerical simulations that if the size of the receptor-target molecules is known, the field decay length can be optimized to maximize the signal of target binding, through the interparticle gap engineering of densely-packed nanoparticle arrangements (see Fig. 2).

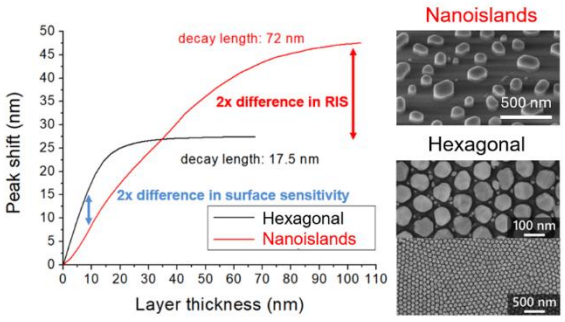


Fig. 2: Experimental comparison of the response of two realized nanoparticle arrangements. Top right, red: gold nanoislands on glass, created by sequential thin film deposition (sputtering) and solid-state dewetting. Bottom right, black: hexagonally arranged ellipsoidal gold nanoparticles, created by using a porous alumina template, thin film deposition and dewetting [4].

Fig. 2 demonstrates that while the gold nanoislands on glass (red curve) have a two-times higher bulk refractive index sensitivity compared to the hexagonally arranged gold nano-ellipsoids, the latter structures have significantly higher surface sensitivity. E.g. for binding a thin layer with only 10 nm thickness on the surface of the sensors, the hexagonal particle systems respond with a peak shift that is twice that of the nanoislands. This property is ultimately important for small molecule detection.

Two case studies will also be presented to illustrate the effect of layer formation on the interpreted signal during gas sensing and fluid refractive index sensing applications [3]. It will be demonstrated that during both gas sensing and fluid RI sensing, structures that have high surface sensitivity are increasingly affected by layer formation on their surface originating from the adsorption of gas molecules or ions (respectively for the different applications). Considering these layers during the sensing applications is essential for the correct interpretation of sensor signals.

References

[1] Z. A. Zaky, A. M. Ahmed, A. S. Shalaby, A. H. Aly, Refractive index gas sensor based on the Tamm state in a one-dimensional photonic crystal: Theoretical optimization. Scientific Reports 10, 9736 (2020); doi: 10.1038/s41598-020-66427-6

[2] Li, J.; Ye, J.; Chen, C.; Li, Y.; Verellen, N.; Moshchalkov, V. V.; Lagae, L.; Van Dorpe, P. Revisiting the Surface Sensitivity of Nanoplasmonic Biosensors. ACS Photonics 2015, 2 (3), 425–431. https://doi.org/10.1021/ph5004779.

[3] M. Proenca T. Lednický, D. I. Meira, M. S. Rodrigues, F. Vaz, J. Borges, A. Bonyár, LSPR gas sensitivity: Introducing a new parameter for benchmarking plasmonic gas sensors, through a case study of densely-packed Au nanoparticle layers, ACS Applied Materials & Interfaces, 16 (42), 57832-57842 (2024).

[4] T. Lednický, A. Bonyár, Large Scale Fabrication of Ordered Gold Nanoparticle–Epoxy Surface Nanocomposites and Their Application as Label-Free Plasmonic DNA Biosensors. ACS Applied Materials and Interfaces 12, 4, 4804–4814 (2020); doi: 10.1021/acsami.9b20907

Acknowledgements

The research was supported by the National Research and Innovation Office under project number 2020-1.2.3-EUREKA-2022-00030 and by the Nanoplasmonic Laser Fusion Research Laboratory project (2022-2.1.1-NL-2022-00002). Tomáš Lednický acknowledges CzechNanoLab Research Infra-structure supported by MEYS CR (LM2023051) and funding from the European Union's Horizon Europe research and innovation programme under grant agreement No 101109232).

DOI 10.5162/EUROSENSORS2025/TP5

Metal Oxide – Schiff Base Nanofibers as Novel Optical Sensors for Different Metal Ion Detection in Aquatic Environment

Debleena Mandal[1] ,Magdalena Barwiolek[1], Dominika Jankowska[1], Anna Kaczmarek-Kędziera[1], Tadeusz M. Muzioł[1], Iryna Tepliakova[2], Roman Viter[2]*
[1]Faculty of Chemistry, Nicolaus Copernicus University in Torun, Gagarina 7, 87-100 Torun, Poland,
[2] Faculty of Physics, Mathematics and Optometry, University of Latvia, 19 Raina Blvd., Riga, LV 1586, Latvia
mandaldebleena@doktorant.umk.pl

Summary:

Schiff base derivatives of 2,4-dihydroxybenzaldehyde and o-phenylenediamine are potential candidate for fluorescent chemosensors because their metal oxide – Schiff base composites can exhibit fluorescence properties and can be sensitive to the metal ions in the aquatic environment. The spectroscopic properties of the ligand crystalized in MeOH and ethyl acetate were investigated by ^{1}H, ^{13}C, $^{1}H^{13}C$ NMR, IR, UV-Vis, and fluorescent properties, along with sensitivity tests of its zinc(II) and copper(II) complexes. The morphology and composition of new materials were determined using SEM/EDS and AFM microscopy. The emission of new materials was noted.

Keywords: Schiff base, photoluminescence, chemosensors, ZnO composites, ESIPT.

Introduction

Many mental illnesses, including Alzheimer's disease, Parkinson's disease, epilepsy, etc., have been caused by the imbalance of Zinc ions[1]. Zinc ion causes severe environmental pollution due to their widespread use in electroplating [2]. Thus, a highly selective detection probe for zinc ions and other transition metal ions is needed. Schiff bases are a potential candidate due to their fluorescence properties, which can be used to detect metal ions[3-4]. Optical chemosensors caused a revolution in the sensing field due to their high specificity, sensitivity, and fast detection features. Optical sensors, based on absorbance and photoluminescence for metal ions detection, are simple, low cost, and can be integrated into one system. Optical SB sensors have shown good sensitivity to metal ions, such as Zn^{2+}, Al^{3+}, Cu^{2+}, etc. The change of optical properties of the SB after interaction with metal ions and the sensing mechanism is explained by the isomerization of chemical bonds (C=N, -CH=N, etc.) and donor-acceptor photo-induced electron transfer[9].

The new ligand **L1**, sensitive to various ions, was obtained. It also showed an excited-state intramolecular proton transfer (ESIPT) mechanism, which provides an attractive material platform for fabricating optoelectronic devices. **L1** was also coupled with ZnO tetrapods to enhance its sensitive properties. The ionosensor was also obtained from Zinc oxide (nf/tp) and Schiff bases, which were selective towards various metal ions.

Method

2,4 dihydroxybenzaldehyde (98%) and o-phenylenediamine (analytical grade) were purchased from Sigma Aldrich and used without further purification. **L1.MeOH** and **L1.EA** ligand was obtained and was analyzed for its sensor properties. (Fig.1)

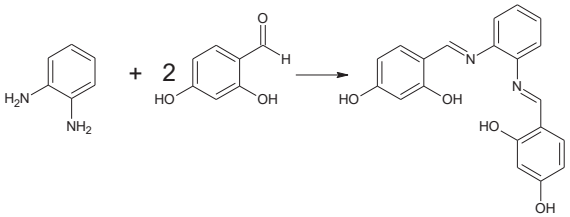


*Fig. 1. Scheme of synthesis of ligand **L1**.*

Results

Sensor tests of the ligand have been performed in ethanol. The sensitivity of the ligands was investigated by adding the metal ion probes to the ligand ethanol solution. Initially, the equilibrium of the intensity was achieved, and the probe was

added. Full PL spectra were measured before the injection and after setting the equilibrium between adsorption and desorption. The interactions of both the ligands **L1.MeOH** and **L1.EA** with various metal ions were studied. It was found that **L1.MeOH** was sensitive towards Zn^{2+},Cu^{2+},Al^{3+},Mg^{2+},Co^{2+} and Mn^{2+} ions, whereas **L1.EA** towards Zn^{2+}, Cu^{2+} and Al^{3+}.

The interaction between metal ions and the ligand in ethanol led to decreased photoluminescence intensity. The sensor's response time has been studied by measuring photoluminescence kinetics at fixed wavelengths (380 and 432 nm).

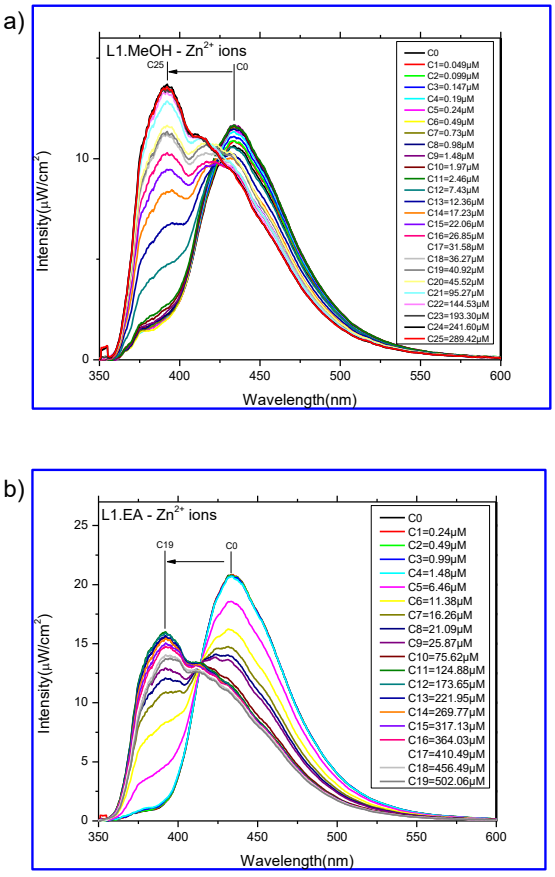


*Fig.2. The photoluminescence spectra of **L1.EA**. Each spectrum corresponds to the additional concentration of Zn2+ ions,(a) for ligand **L1.MeOH** (b) for ligand **L1.EA***

It was found that the sensor response to metal ions increased with the ion concentration (Fig.2). The changes in emission intensity upon the addition of metal ions can result from the photoinduced charge transfer mechanism (PCT). The intramolecular charge transfer (ICT) from the donor to the acceptor was observed upon excitation.

The ligand crystallized in two different forms, L1.MeOH has methanol and L1.EA has ethyl acetate in the crystal structure.

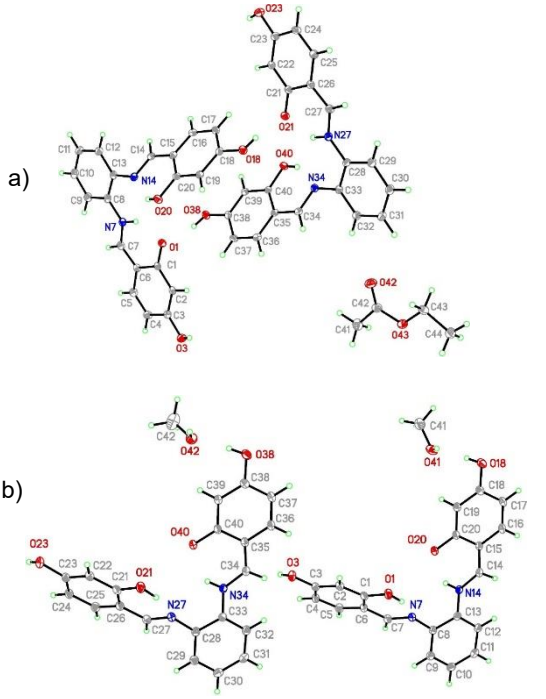


*Fig.3. ORTEP of a)**L1.EA** and b)**L1.MeOH** with two crystallographically independent Schiff bases in the asymmetric unit and molecule of solvent.*

References

[1] L. Yang, F. Wang, J. Zhao, X. Kong, K. Lu, M. Yang, J. Zhang, Z. Sun, J. You, Detection of metal ions using a fluorescence-based method, *Talanta* 221, 121477 (2021); doi: 10.1016/j.talanta.2020.121477

[2] S. Xue, P. Wang, K. Chen, Fluorescent sensor for metal ion recognition, *Spectrochimica Acta Part A: Molecular and Biomolecular Spectroscopy* 226, 117616 (2020); doi: 10.1016/j.saa.2019.117616

[3] G. Gümüşgöz Çelik, E. Şenkuytu, O. Şahin, S. Serin, Synthesis and characterization of new metal complexes, *Inorganica Chimica Acta* 527, 120556 (2021); doi: 10.1016/j.ica.2021.120556

[4] M. Kumar, A. Kumar, M.K. Singh, S.K. Sahu, R.P. John, A novel benzidine-based Schiff base “turn-on” fluorescent chemosensor for selective recognition of Zn^{2+}, *Sensors and Actuators B: Chemical* 241, 1218–1223 (2017); doi: 10.1016/j.snb.2016.10.102

Acknowledgments

The research was financed by grant4students IDUB project 20/2022 and Horizon Europe—the Framework Programme for Research and Innovation (2021-2027) HE-MCSA-RISE-2022, Sens4Corn, grant number 101086364.

DOI 10.5162/EUROSENSORS2025/TP6

Two-Step Nanostructuring of Carbon Electrodes for Multiplexed Electrochemical Sensing Using Off-Axis MPECVD and Laser Micropatterning

Mattia Pierpaoli[1], Iwona Kaczmarzyk[1], Adrian Olejnik[1], Robert Bogdanowicz[1]
[1] Faculty of Electronics, Telecommunications and Informatics, Gdansk University of Technology, 11/12 Gabriela Narutowicza Street, Gdansk, 80-233, Poland
matpierp@pg.edu.pl

Summary:

Graded carbon nanomaterials were synthesized using off-axis microwave plasma-enhanced chemical vapor deposition and patterned via laser direct writing to easily create multiplexed electrochemical sensors. These electrodes exhibit high sensitivity and selectivity for multiple analytes due to the gradient in structural and electronic properties across the active surface. The approach provides a scalable platform for integrated sensing systems with minimal cross-talk and enhanced electrochemical performance.

Keywords: carbon nanomaterials, electrochemical sensing, plasma deposition, laser patterning, multiplexed sensors

Background, Motivation and Objective

Electrochemical sensing platforms are increasingly demanded for rapid, low-cost, and multiplexed chemical detection in environmental and biomedical applications. Traditional fabrication approaches often struggle to provide both high spatial resolution and material diversity across sensor arrays. Carbon nanomaterials (CNMs) offer tunable electronic and surface properties beneficial for sensing, but uniform films limit functional diversity [1]. This work introduces a new strategy for creating graded carbon nanomaterials (GCNs) using off-axis microwave plasma-enhanced chemical vapor deposition (MPECVD), enabling spatially varying properties on a single substrate. Laser direct writing defines electrode geometries, creating a versatile, miniaturized sensor platform.

Description of the New Method or System

We report the synthesis of GCNs with a controlled gradient in nanostructure and composition across the substrate, achieved via off-axis MPECVD (SEKI Technotron AX5400S, 2.45 GHz, 1300 W) by modulating plasma-substrate interaction. These films are patterned into independent microelectrodes using laser direct writing (5W JPT Air-Cooled UV-Laser), enabling a multiplexed sensor array. This integrated method provides a scalable route for engineering spatially resolved electrochemical functionalities on a single chip.

Results

Carbon nanostructures synthesised by off-axis MPECVD exhibit pronounced morphological gradients that intensify with increasing angular displacement from the plasma centre (Fig. 1). Morphological analysis via scanning electron microscopy (SEM) revealed a distinct variation in nanostructure across the substrate.

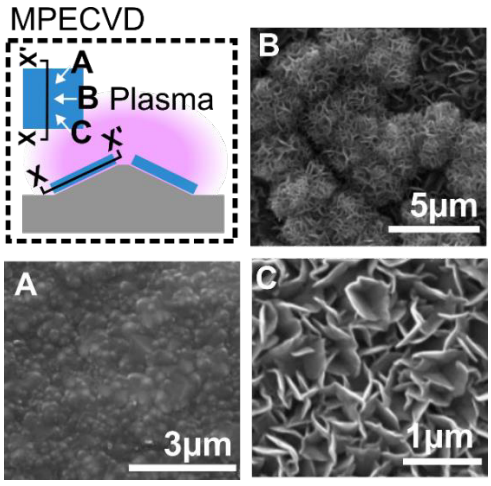


Fig. 1. Schematic representation of the off-axis synthesis process by MPECVD and corresponding SEM pictures of the different spots considered

The upper region (A) exhibited a uniform, flat, and regular surface morphology. In contrast, the middle region (B) displayed a heterogeneous distribution, characterized by both medium and small-sized overlapping nanowall-like structures. The lower region (C) consisted of homogenous nanowall-covered electrodes [2].

Electrochemical impedance spectroscopy (EIS) provided further insights into the structural diversity. While regions (A) and (C) showed spectra consistent with a single circuit element, the intermediate region (B) required a dual-element fit when using the ferri/ferrocyanide ($Fe(CN)_6^{3-/4-}$) redox couple, indicating structural and electrochemical heterogeneity (Fig. 2a).

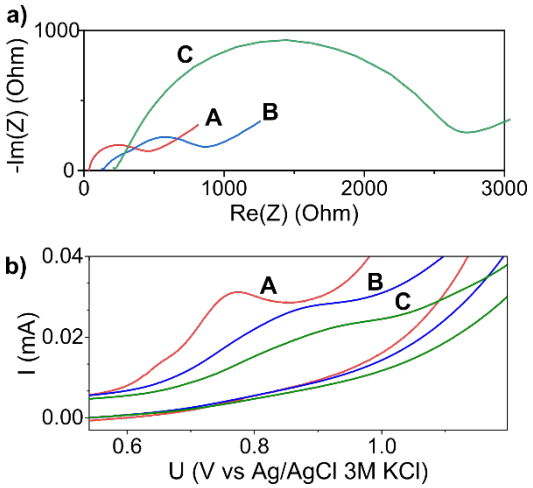


Fig. 2. (a) Nyquist plot of $Fe(CN)_6^{3-/4-}$ in 100mM PBS and (b) voltammograms of 100mg/l metoprolol in PBS for the three discretized single electrodes from the single synthesized off-axis sample

Interestingly, metoprolol detection by cyclic voltammetry (CV) shows that oxidation was most favorable on structure (A), as evidenced by a higher peak current and a lower oxidation potential (Fig. 2b). This trend was followed by structure (B), with structure (C) exhibiting the least favorable behavior despite its higher surface area. EIS measurements supported this observation, showing that structure (C), while presenting a dense structure of carbon nanowall, had a significantly higher charge transfer resistance (R_{ct}) compared to (A).

This spatial electrochemical fingerprinting technique enables high-throughput screening of nanocarbon libraries directly on-chip, facilitating the identification of the most electrochemically responsive nanostructures without requiring individual fabrication. The integration of SEM, EIS, and CV validates the graded nanocarbon platform as a versatile and efficient tool for the rapid evaluation of electrochemical materials, thereby accelerating the assessment of sensor batches.

References

List and number all bibliographical references at the end of the paper. When referenced within the text, enclose the citation number in square brackets, i.e. [1]

[1] M. Pierpaoli, P. Jakóbczyk, M. Ficek, B. Dec, J. Ryl, B. Rutkowski, A. Lewkowicz, R. Bogdanowicz, Tailoring Defects in B, N-Codoped Carbon Nanowalls for Direct Electrochemical Oxidation of Glyphosate and its Metabolites. *ACS Applied Materials & Interfaces*, 16(28) (2024); doi: 10.1021/acsami.4c04478

[2] M. Pierpaoli, M. Ficek, P. Jakóbczyk, J. Karczewski, R. Bogdanowicz Self-assembly of vertically orientated graphene nanostructures: Multivariate characterisation by Minkowski functionals and fractal geometry. *Acta Materialia*, 214 (2021) doi: 10.1016/j.actamat.2021.116989

Acknowledgements

Financial support of these studies from Gdańsk University of Technology by the DEC 8/1/2022/IDUB/I3b/Ag grant under the Argentum - 'Excellence Initiative - Research University' program is gratefully acknowledged.

DOI 10.5162/EUROSENSORS2025/TP7

Metasurface development for SERS-based optical sensors

Angela Mihaela Baracu[1], Adrian Dinescu[1], Karolina Milenko-Kuszewska[2], Oana Rasoga[3], Ioan-Alexandru Baragau[3]
[1] National Institute for Research and Development in Microtechnologies-IMT Bucharest, 126A, Erou Iancu Nicolae Street, 077190 Voluntari, Romania
[2] SINTEF Microsystems and Nanotechnology, Gaustadalleen 23C, 0737 Oslo, Norway
[3] National Institute of Materials Physics, 405 A Atomistilor Street, 077125 Magurele, Romania
Corresponding Authors: angela.baracu@imt.ro; oana.rasoga@infim.ro; karolina.milenko@sintef.no

Summary:
Using both numerical simulations and nano-fabrication techniques, we experimentally demonstrated the SERS functionality of a novel nanostructure by employing a drop-casted thiabendazole analyte. The nanostructure was specifically designed with tailored shapes and dimensions to achieve plasmon resonance within the visible range.

Keywords: Nanopatterning, SERS structures, pesticide detection.

Introduction

The advancement of nanotechnology has led to innovative nanomaterials and technological applications across a range of fields, including electronics and sensing [1-2]. Surface-enhanced Raman spectroscopy (SERS) is an effective method for detecting ultra-low concentrations of analytes, enabling detailed structural and molecular identification. Nanotechnology offers a wide array of plasmonic nanostructures, such as gold nanoparticles (AuNPs), silver nanoparticles (AgNPs), and 3D plasmonic substrates, that significantly enhance SERS performance [3]. The efficiency of SERS sensors relies on the manufacturing of complex nanostructured architectures, which enhance the electromagnetic field, amplifying the Raman scattering signals.

This paper presents the simulation results, the manufacturing process, and the Raman characterization of metasurfaces used for SERS applications.

Optical Design and Simulations

The nanostructures were designed with specific C shapes, arranged in a lattice, with sizes of 80 nm width and 430 nm diameter to achieve plasmon resonance within the 650-750 nm wavelength range, considering electron-beam lithography (EBL) as fabrication technology. This wavelength range was chosen to enhance the Raman peaks of pesticide Thiabendazole (TBZ), which exhibit significant vibrations when using a 633 nm excitation wavelength. However, it is important to note that most pesticides will have Raman peaks in a similar wavelength range. The simulations were conducted using the Finite-Difference Time-Domain (FDTD) method, implemented in Ansys Lumerical commercial software. The simulations include full 3D model of the nanostructures: C-shape particles (60 nm hight), Au layer (40 nm thickness) and Si substrate (Fig. 1a). Three C-shaped structures were included in a rectangular simulation volume, with the perfectly matched layer (PML) boundary conditions in the X direction (the propagation direction) and periodic boundary conditions in the Y and Z directions. The substrate was illuminated from the top by a broadband plane wave. The reflected intensity was measured above the substrate, while the electric field distribution was recorded at the gold–air interface.

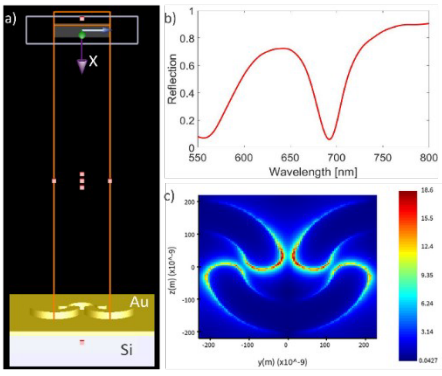


Fig. 1. a) Cross-section of the simulation model; b) Simulated reflection; c) Simulated electric field distribution

The simulated reflection with strong resonance around 691 nm wavelength is presented in Fig. 1b, while the electric field distribution around the nanostructures is presented in Fig. 1c.

Metasurface fabrication and SERS detection

The metasurface manufacturing process started with the spin-coating at 2500 (rpm) of a thin polymer film (polymethyl methacrylate: PMMA 950k A4), followed by a thermal treatment on a hot plate performed at a temperature of 160°C for 3 minutes. The pattern transfer was carried out via electron beam exposure using the dedicated RAITH e_Line system, with the following parameters: acceleration voltage – 30 kV, beam current – 200 pA, and a clearing dose of 300 μC/cm². Proximity effect correction was applied using the PECS software module.

The subsequent step consisted in the structures developing by immersing the wafers in a solution of methyl isobutyl ketone (MIBK) and isopropyl alcohol (IPA) in a 1:3 ratio at 22°C for 60 seconds. A thin Au film with a thickness of 60 nm was then deposited using the electron beam (e-beam) vacuum evaporation method, performed with the TEMESCAL FC-2000 system, which provides high-quality deposition suitable for the lift-off process.

The following step in the fabrication process involved selective metal removal by dissolving the polymer together with the Au film on its surface (lift-off technique). The scanning electron microscopy (SEM) image illustrated in Fig. 2 reveals the nanopatterned C shapes on the silicon substrate. The patterned area was 250μ×250 square micrometres. In the end, the metasurfaces were covered with 40 nm thickness Au to generate the plasmonic effect.

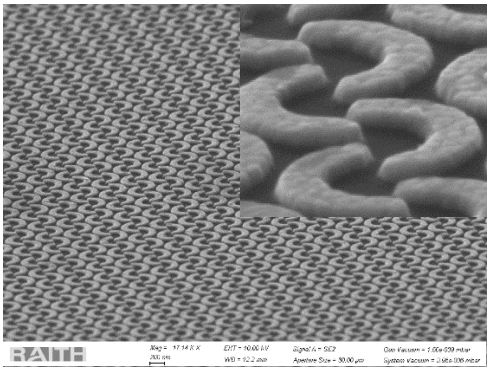


Fig. 2. Side-view SEM micrograph of the nanopatterned metasurfaces on Si substrate (a) and detail of an area containing the nanopatterned C shapes.

SERS investigation

To test the SERS functionality, Raman measurements of the patterned and un-patterned areas using the thiabendazole as an analyte were performed. 5 μl from a stock solution of 10 mM thiabendazole dissolved in ethanol were drop-casted onto the Au-SERS (patterned) surface and Au area (un-patterned). Raman spectra were measured with a Horiba LabRAM HR Evolution Spectrometer. The samples were excited with a 633 nm wavelength using 50x objective and 25% of the maximum power (17mW). The spectra were recorded, focusing the laser on the thiabendazole crystallites found on the analysed substrates with 10 s of acquisition time and 10 accumulations. The differences in the Raman spectra for the needle-like filament crystallites formed onto the Au-SERS and un-patterned gold area are illustrated in Fig.3.

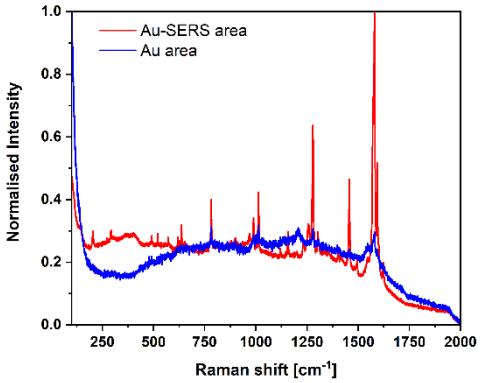


Fig. 3. The normalized Raman spectra of the thiabendazole films

Conclusions

We developed a novel SERS nanostructure obtained by using numerical simulations and EBL fabrication technique. We demonstrated the SERS functionality using thiabendazole as an analyte. Further SERS investigations will be carried out to explore the pesticide sensing performances.

References

[1] N. N. Nguyen, N. T. Nguyen, P. T. Nguyen, Q. N. Phan, T. L. Le, and H. D. K. Do, “Current and emerging nanotechnology for sustainable development of agriculture: Implementation design strategy and application,” *Heliyon*, vol. 10, no. 10, p. e31503, May 2024, doi: 10.1016/j.heliyon.2024.e31503.

[2] R. K. Gangwar et al., “Optical fiber SERS sensors: Unveiling advances, challenges, and applications in a miniaturized technology,” *Coord Chem Rev*, vol. 510, p. 215861, Jul. 2024, doi: 10.1016/j.ccr.2024.215861.

[3] X. Tang et al., “Advancements and challenges on SERS-based multimodal biosensors for biotoxin detection,” *Trends Food Sci Technol*, vol. 152, p. 104672, Oct. 2024, doi: 10.1016/j.tifs.2024.104672.

Acknowledgements

This work was supported by a grant of the Ministry of Research, Innovation and Digitalization, CNCS/CCCDI-UEFISCDI, project number CO-FUND-WATER4ALL-STARDUST-2, whithin PNCDI IV and core program: PN 2307 - μNanoEl, Contract No. 8N/03.01.2023, “Advanced research in micro-nano electronic and photonic devices, sensors and microsystems for societal applications” μNanoEl within PNCDI IV (2022–2027).

DOI 10.5162/EUROSENSORS2025/TP8

Hydrogen Sensors for Oxygen-Free Ambient

Nan Ma[1], Zhifu Liu[1], Yunsong Li[1], Alexey Vasiliev[2,3], Oleg Kul[3], Alexey Shaposhnik[4], Mikhail Yablokov[5]
[1]Shanghai institute of ceramics, Heshuo Road, 585, 2001899, Shanghai, P.R. China
[2] Dubna State University, Universitetskaya str,19, Dubna, 141980, Russia
[3] LLC "C-Component", Tushinskaya str., 17, 125362, Moscow, Russia
[4] Voronezh State Agrarian University, Michurin str., 1, 394087, Voronezh, Russia
[5] Enikolopov Institute of Synthetic Polymeric Materials, 117393, Moscow, Profsoyuznaya 70
Corresponding Author's e-mail address: A-A-Vasiliev@yandex.ru

Summary:
Hydrogen sensors for oxygen-free atmosphere are special branch of sensors characterized by another sensing mechanism different from usual devices operating in air. These sensors are specially interesting because it is necessary to monitor the state of the lithium ion batteries, transformers, technological gases. We consider the application of hydrogen adsorbing films, field effect transistors, metal oxide sensors, and percolation effect sensors for such applications. It was demonstrated that Ag and Cu doped Pd film can detect low concentrations of hydrogen in inert gas on ppm level.

Keywords: hydrogen sensor, inert and oxygen-free atmosphere, oil

Introduction

The main part of usual gas sensors is designed for the application in normal O_2 containing atmosphere. For example, the sensitivity mechanism of metal oxide gas sensors involves the chemisorption of oxygen on the surface of *n*-type semiconductor nanoparticles in ionic form. At working temperature of the sensor, oxygen ions interact with reducing gases, this leads to the oxidation of H_2, CH_4, VOC, etc. and to the injection of electrons to the conductance band of semiconductor. A similar but opposite mechanism is valid as in the case of the application of p-type semiconductors and at the detection of oxidizing gases.

However, the gas sensors of different types can be used also in oxygen-free ambient: in vacuum, inert atmosphere, even in liquids like transformer oil. It is notable that the very first metal oxide sensors were investigated since 1955 in vacuum. The detection of gases and, in particular, hydrogen in inert ambient is important in many applications: in the monitoring of Li-ion batteries, H_2 fuel cells, nuclear power stations, oil filled power transformers, etc.

The sensors, which can be used in inert atmosphere, are metal oxide semiconductor sensors, Pd-film resistive sensors, MIS structures with Pd film gate and the sensors based on percolation effect based on Pd nanoparticles dispersed in polymer matrices.

The sensors based on Pd-Ni thin film is used as a detector of H_2 dissolved in transformer oil in a Vaisala MHT410 instrument. The saturation of thin Pd-Ni film with H_2 dissolved in oil leads to an increase in film resistance. Typical sensitivity of such film is of about 1 % of resistance change per 1 % of hydrogen in gas atmosphere. Of course such sensor operating at near room temperature is slow, characteristic time of the sensor response is of about 1 hour.

Field effect devices with Pd gate can be used not only for the detection of H_2 in gas, but also in oil [1]. The sensor immersed to the oil is characterized by a detection limit of about 10 ppm and rather long response time of several hours. This is not a big disadvantage for the oil monitoring, because the degradation processes in a transformer are relatively slow.

Metal oxide sensors based, first, on ZnO can be used for the detection of active gases in inert atmosphere and in vacuum [2]. The mechanism of the detection of H_2 in this case is very simple, this is just dissociative adsorption of hydrogen in ionized form, and this gives a square root dependence of sensor conductivity as a function of H_2 concentration.

Experiment

In the experiment we applied gas sensors based on pure SnO_2 fabricated using thick film technology. The working temperature of the sensor was fixed at 350ºC, the specific surface area of the sensing material was of about 50 m^2/g. The experimental installation made of stainless steel was equipped with oxygen measuring instrument "Zirkon" based on solid elec-

trolyte gas sensor. It enabled the measurement of O_2 concentration with detection limit of 0.1 ppm. The tubes of the installation were purged by pure Ar with residual concentration of O_2 of <1 ppm for 5 hours to get the concentration of O_2 in gas of about 1 ppm. After this, we introduced H_2 using mass flow controller.

Thin films of Pd-Ag and Pd-Ag/Cu were deposited on Al_2O_3 substrates via magnetron sputtering using Pd, Ag, and Cu targets. The choice of the sensing material was motivated to avoid the phase transition in pure palladium at the saturation with hydrogen. For example, it is shown in [3] that the saturation of one side of Pd plate with hydrogen leads to the bending of the plate. Evidently, periodic saturation of the film leads finally to the peeling of the Pd film from the substrate. The application of dopant (Ag, Ru, Cu) blocks this process. The Pd-Ag film was prepared by sputtering Pd at 75 W and Ag at 10 W for 45 s. In contrast, the Pd-Ag/Cu film was deposited under identical conditions for Pd and Ag, with a concurrent Cu deposition at 25 W for 15 s. The hydrogen response of these films was evaluated at room temperature using H_2 concentrations ranging from 50 ppm to 20000 ppm in an N_2 background. The sensor response was defined as $R=(R_{H2}–R_{N2})/R_{N2}$, where R_{H2} and R_{N2} denote the resistance in the H_2/N_2 mixture and pure N_2, respectively.

The application of Pd/polymer composite also permits the minimization of the peeling effects of H_2 in the film. When Pd concentration in amorphous polymer is near percolation threshold, the conductivity of sensor drops with hydrogen pressure, detection limit reaches 10 ppt. The gas-sensitivity properties of polymer composite coatings were found to be directly related to their morphology.

Results and Discussion

It was shown that the tin dioxide based gas sensor is characterized by a strong response to hydrogen in oxygen-free atmosphere. The threshold level of oxygen changing completely the sensor response is a concentration compatible with the concentration of H_2. at this concentration the mechanism involving the catalytic oxidation of hydrogen is substituted by direct dissociative ionosorption of H_2. Thus, if O_2 concentration exceeds H_2 concentration (we deal with ppm level concentrations), the response time of the sensor has usual order of magnitude of few seconds. In opposite case, the H_2 response increases by approximately one order of magnitude, and the response and recovery time increases up to ~ 1000 s.

As shown in Fig. 1, the response of the Pd-Ag film saturates and even decreases at H_2 concentrations above 5 000 ppm, likely due to the α-PdHx to β-PdHx phase transition. In contrast, the response of the Pd-Ag/Cu film increases steadily as the H_2 concentration rises from 50 ppm to 20 000 ppm, reaching 5.5% at 20 000 ppm. Moreover, the Pd-Ag/Cu film exhibits excellent response and recovery behaviors, with both response and recovery times decreasing with increasing H_2 concentration, achieving 69 s and 492 s at 20 000 ppm H_2, respectively.

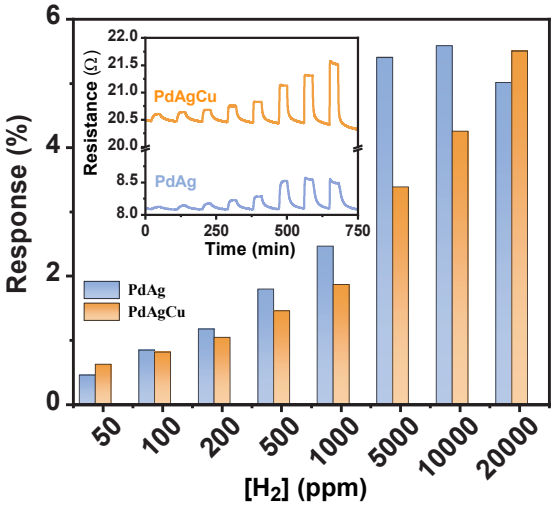


Fig.1 Response of Pd-Ag and Pd-Ag/Cu to H_2 concentrations from 50 ppm to 20000 ppm.

Therefore, the sensor based on the Pd-Ag/Cu film demonstrates outstanding H_2 sensing performance in an oxygen-free environment.

Conclusion

We analyzed the application of different gas sensors for the discovery of hydrogen in oxygen-free ambient: in inert atmosphere and in liquids. It was demonstrated that the thin resistive Pd-Ag/Cu film can be used for the detection of hydrogen with high sensitivity of about 5.5 % (change of resistance) per 2 % of H_2 in gas. The sensor based on SnO_2 demonstrates response time of about 20 min and detection limit of about 1 ppm.

References

[1] A.Litvinov, N.Samotaev, M.Etrekova, A.Ivanova, D.Filipchuk, Yu.Klishin. Using Field-Effect Gas Sensors for Monitoring H_2 in Transformer Oil. MATEC Web of Conferences 327, 01005 (2020). https://doi.org/10.1051/matecconf/202032701005

[2] E.E.Gutman. Space and Aircraft Sensors. Sensors and Actuators B, 18, 22-27 (1994). htpps://doi.org/10.1016/0925-4005(94)87050-0

[3] E. N. Lyubimenko, M.V.Goltsova. The Form Changing of Palladium Plate Induced by Small One-Side Hydrogen Impacts. Metallofiz. Noveishie Tekhnol. 2014, v. 36, # 2, p. 247—258. DOI: 10.15407/mfint.36.02.0247

DOI 10.5162/EUROSENSORS2025/TP9

Electronic Circuit for Temperature and Humidity measurements for the purpose of the Mini Robot Caterpillar

Katarzyna Wilczewska, Alicja Musiał, Marcin Flak, Karolina Laszczyk
Politechnika Wrocławska, Wybrzeże Stanisława Wyspiańskiego 27, 50-370 Wrocław, Poland
m3@pwr.edu.pl, karolina.laszczyk@pwr.edu.pl

Summary:
The paper presents the design of an electronic circuit for temperature and humidity measurements for a Mini Robot Caterpillar. There are two types of circuits proposed: wired and wireless. The preliminary results of the integration of the thermoresistor into the 3D-printable body of the robot is presented, i.e. opportunities and limitations in the context of integrating a sensor with a 3D-printed movable structure. Additionally, the possible ways for miniaturizing the measuring system are discussed.

Keywords: thermoresistor, 3D printing, humidity sensor, circuit, wireless communication

Introduction

The goal of the Mini Robot Caterpillar is the environmental monitoring in hard to reach places like ventilation shafts or fallen buildings. We were inspired by the other research of meso- or micro-scale soft robots that mimicked nature, such as a bioinspired footed robot [1] or a shape-changing crawling robot [2]. The robot, we aimed to develop, must fulfill the following restrictions: 1) to be 10 mm long so that its body can fit in tiny spaces, 2) to measure temperature in the range of 20-200°C. Its movement is based on the remote thermal actuation. For this, the body of the caterpillar was 3D-printed in a hybrid form from a developed composite and the commercial UV-sensitive resin. By incorporating, e.g. temperature or gas sensor, the robot could ensure safety of workers and rescuers.



Fig. 1. The schematic illustration of the Mini Robot Caterpillar.

Except for the electronic circuit to serve for temperature measurements, the assembly trials were conducted to integrate the thermoresistor into the 3D-printable component similarly to work reported in [3], where embedding components using an additive process was demonstrated on a 0201 LED. In this paper, we propose designs of two circuit types - wired and wireless with the latest being expanded about wireless communication.

Circuits for temperature measurements

For the wired circuit, its control was provided by the microcontroller raspberry pi pico (Raspberry Pi Foundation, UK). As the sensor we chose a thermoresistor PT-1000 (RS PRO, PL), with a 4-wire connection eliminating measurement error that comes from the wire resistance, as presented in Fig.2b-c. In order to confirm the wired circuit functionality, a reference PT-500 was connected to a digital multimeter SDM3045Xl (SIGLENT Technologies, CPR). Both sensors were put on a hot plate, in the ambient air, hence they were simultaneously exposed to set different temperatures (23°C, 100°C, 150°C and 200°C). Figure 2a presents the results of the measured temperature by the sensors in the wired circuit. There is a linear dependency, as expected, and a slight difference in acquired temperatures, for 150°C. and 200°C.

For the wireless version, a two in one digital sensor was selected, i.e. measuring the humidity and the temperature, DHT11 (D-Robotics UK). The circuit also included the transponder. It consisted of a transmit antenna module RF 433 MHz and a microcontroller Arduino UNO R3 module that was programmed in the ArduinoIDE. Meanwhile, the receiver was composed of a microcontroller Arduino Nano, a receiving antenna module and an LCD display. The measurement data was superimposed on the carrier wave using amplitude-shift keying (ASK). The ASK signal was then transmitted via a 433 MHz electromagnetic wave. The signal in the receiver was then demodulated, filtered and amplified, resulting in data being converted into a readable format. The information was then

displayed on the LCD screen as presented in Fig. 2d.

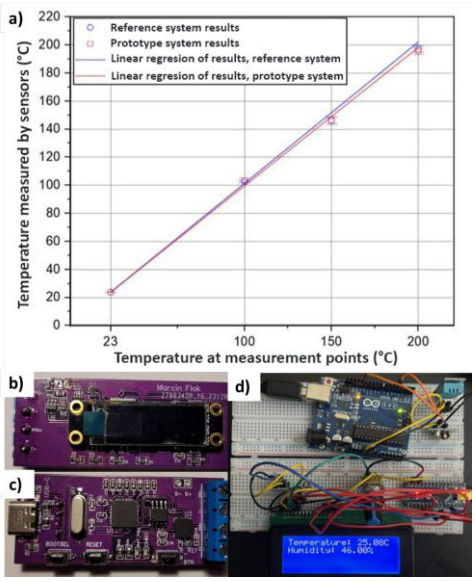


Fig. 2. The temperature measurements: a) the graph of the reference temperature vs. the temp. measurements received by the wired circuit; b-d) the digital photographs of the PCB circuits of the wired version - top (b) and bottom (c) views, respectively, and the wireless version (d);

Assembly of the sensors with the 3D printable component

The Mini Robot Caterpillar was designed based on the preliminary study of the 3D-printed hybrid composite structure, i.e. the cantilever. To conduct trials to assemble the sensor to the 3D printed cantilever, its design was modified; inside lengthwise the cantilever the channels (dia. 350 µm) were included through which copper wires (dia. 50 µm) were interwoven. Next, the PT-1000 sensor was soldered (Fig.3a).

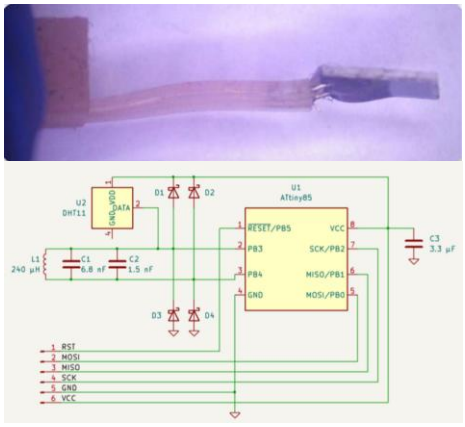


Fig. 3. The further development proof-of-concept for the Mini Robot Caterpillar: a) a digital photography showing the integration of the temperature sensor in the 3D-printed structure b) the miniaturized transponder circuit.

The result of combining the sensor with the cantilever raised questions about its compatibility; the structure was bent due to the gravitational force. This significantly disrupts the bending of the cantilever, hence the movement of the Mini Robot. Because of the incompatibility in size between the transponder and the Mini Robot, a radio transmission with a dedicated LC circuit was proposed. Figure 3b presents the scheme of the circuit. Here, the Arduino module was replaced by a smaller ATtiny85 microcontroller (Atmel Corporation, USA). As a result, this transponder could also work as a passive power supply making the Mini Robot to be driven autonomously.

Conclusions and Perspectives

We present the work related to the project of the remotely actuated Mini Robot Caterpillar. Our aim is to integrate with the Robot the temperature and humidity sensors. Two circuit types to enable sensor measurements and suitable for the Mini Robot Caterpillar were presented - a wired version and a wireless alternative. Moreover, for future development, it is necessary to challenge two issues: 1) a mismatch in size of the transponder and the mini robot, and 2) the sensor's integration with the Robot's body. For this, a dedicated LC circuit was proposed that is lighter and scaled down in size. This opens a new perspective in the integration of the sensors with the 3D-printed robot.

Acknowledgements

The work was released by the Student Science Club - Microengineering, Microelectronics and Microsystems (M3)." within frame of the project „Miniature crawler robot for measuring ambient temperature in hard-to-reach places” financed by the programme “Student Science Clubs create innovations” financed by the Ministry of Science and Higher Education

References

[1] X. Wang et al. “Bioinspired footed soft robot with unidirectional all-terrain mobility.”, Materials Today 35 (2020): 42-49.
[2] B. A. Trimmer, V. Vishesh, P. Templeton, “Design and control of a soft, shape-changing, crawling robot.”, arXiv:1509.07569.
[3] S. Lüngen, T. Tiedje, K. Meier, K. Nieweglowski and K. Bock, "Reliability of 3D additive manufactured packages," 2018 7th Electronic System-Integration Technology Conference (ESTC), Dresden, Germany, 2018, pp. 1-5, doi: 10.1109/ESTC.2018.8546417.

DOI 10.5162/EUROSENSORS2025/TP10

Colorimetric Detection of Cortisol Using an Alginate-Based Biosystem

Sepideh Izaddoust[1,2], Lourdes Basabe-Desmonts[2,3], Fernando Benito-Lopez[2],

[1]Microfluidics Cluster UPV/EHU, Analytical Microsystems & Materials for Lab-on-a-Chip Group, Analytical Chemistry Department, University of the Basque Country UPV/EHU, Leioa, Spain

[2]Microfluidics Cluster UPV/EHU, BIOMICs microfluidics Group, Lascaray Research Centre, University of the Basque Country UPV/EHU, Vitoria-Gasteiz, Spain

[3]IKERBASQUE, Basque Foundation for Science, Bilbao, Spain

fernando.benito@ehu.eus

Summary:

This study highlights an alginate-based biosystem tailored for colorimetric cortisol detection, a vital biomarker in stress and health analysis. By integrating alginate beads with blue tetrazolium, the biosystem exhibits a visually detectable colour shift across cortisol concentrations ranging from 10 to 240 µg dL^{-1}. Calibration demonstrates 30 min as the optimal detection time with the highest accuracy. However, the system shows a slight decrease in accuracy for longer detection times, indicating partial instability over time. This innovation shows significant potential for clinical diagnostics and research applications in endocrine health.

Keywords: Lab-on-a-chip, Alginate hydrogel, Cortisol hormone, Colorimetric sensing assay, Microfluidics

Background, Motivation an Objective

Biocompatible alginate bead biosystems, incorporating enzymatic reactions, have been developed for rapids, colorimetric detection of glucose in sweat, achieving detection times of 13 min [1]. Alginate hydrogels are created by cross-linking linear polysaccharide chains, forming a 3D network that can retain a significant amount of water. Cross-linking can occur through physical and ionic methods using divalent cations like Ca^{2+} and Ba^{2+}. These methods enable the encapsulation of reagents within the alginate scaffold [2].

Cortisol, known as a stress biomarker, is a steroid hormone that partakes in many of the body processes such as regulating blood pressure, blood sugar and helping a correct immunological response are some of its main functions. In a healthy patient, the release of cortisol follows a well-defined circadian rhythm, modulated by the allostatic response to external stimulus. However, exposure to a chronic stress condition can lead to a higher-level of cortisol in the blood serum (> 25 µg dL^{-1}) which is known as Cushing syndrome and necessitate the early-stage detection of this syndrome.

To meet this purpose, we present an alginate-based scaffold that has been functionalized with specific chemical reagents to enable the rapid detection of cortisol. This system is meticulously designed to detect cortisol concentrations within the physiological and pathological (elevated) range found in blood by providing a reliable and efficient method for cortisol measurement, this technology holds significant promise for various applications in clinical diagnostics.

Description of the New Method or System

The colorimetric sensor was composed of alginate combined with blue tetrazolium (2.7 mM in methanol) and exposed to 1 M NaOH. Its functionality relied on the diffusion of components from within the alginate bead to the surrounding medium. To create the biosystem, alginate was dripped into a blue tetrazolium/calcium chloride solution (9:1) for 10 min. When NaOH and cortisol solutions were introduced, the blue tetrazolium diffused outward from the bead, reacting with cortisol in the NaOH environment. This reaction reduced blue tetrazolium to formazan, producing a colour change from transparent to purple. The colour intensity, measurable at 510 nm [3], directly corresponded to cortisol concentration (see Fig.1).

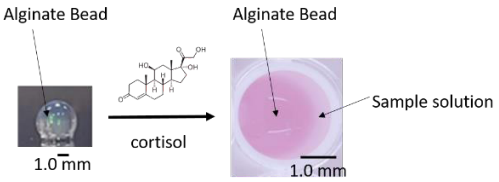


Fig. 1. Schematic representation of the performance of de alginate based biosensor.

Results

The colorimetric assay was fabricated by dripping 20 µL of alginate into a 9:1 solution of blue tetrazolium and 400 mM $CaCl_2$ using a syringe pump. Beads, left in the solution for 10 min, were spherical with an average diameter of 2.0 ± 0.3 mm. The obtained transparent alginate beads showed a pale-yellow colour demonstrating the entrapment of blue tetrazolium inside the beads. After rinsing with methanol and distilled water, the beads were transferred to a 96-well plate. NaOH (10 µL) and cortisol samples (150 µL) were added, and colour changes were recorded every 10 min for 90 min (see Fig.2). The evolution of the reaction between cortisol and blue tetrazolium over 90 min was observed for various cortisol concentrations (10-240 µg dL^{-1}). Results indicate a decreasing reaction rate over time due to the complete release of blue tetrazolium and the completion of the reaction.

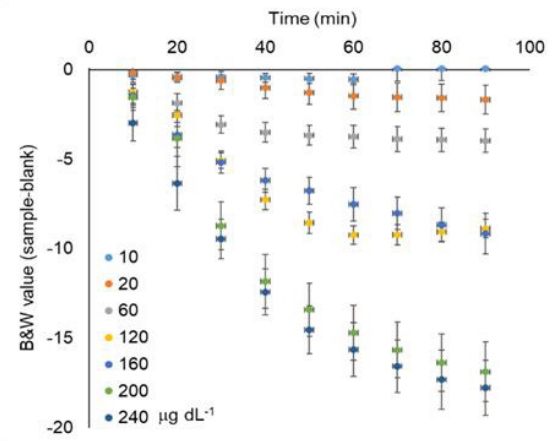


Fig. 2. Reaction of cortisol with blue tetrazolium using the alginate bead over 90 min for a range of concentrations 10-240 µg dL^{-1}. Error: (SD, n = 8).

The results demonstrated that a specific cortisol concentration produced a characteristic colour intensity at a defined time interval (see Fig.3).

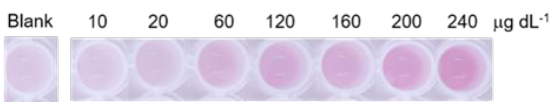


Fig. 3. Picture of the 96-well plate with alginate bead at different concentrations of cortisol, after 60 min reaction.

Calibration curves were constructed by subtracting blank values, enabling evaluation of biosystem efficiency for detecting cortisol across physiological and Cushing syndrome ranges. The optimal detection time was determined to be 30 min, yielding the highest accuracy. However, at longer detection times, a partial decrease in accuracy was observed, indicating potential biosystem instability (see Fig.4).

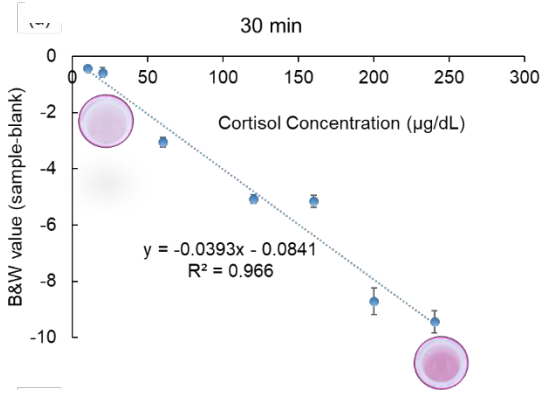


Fig. 4. Calibration curve for cortisol samples 10-240 µg dL^{-1} reacting with blue tetrazolium entrapped in alginate beads a) at 30 min. Error: (SD, n = 8).

Conclusions

This study explored a novel method for colorimetric cortisol detection. The feasibility of using blue tetrazolium as a chromophore for quantifying low concentrations of cortisol was assessed, and its integration into an alginate-based bead matrix was developed. In the near future, this biosystem can be used for the early detection and monitoring of endocrine disorders, as well as for assessing stress levels in patients.

Acknowledgements

We acknowledge funding support from Basque Government, under Grupos Consolidados with Grant No. IT1633-22 and Proyecto de Investigación Fundamental Colaborativa – Investigación Fundamental ELKARTEK: KK-2023/00070.

References

[1] Garcia-Rey S, Gil-Hernandez E, Basabe-Desmonts L, Benito-Lopez F. Colorimetric Determination of Glucose in Sweat Using an Alginate-Based Biosystem. Polymers (Basel) 2023;15:1–13. https://doi.org/10.3390/polym15051218.

[2] Lee KY, Mooney DJ. Alginate: Properties and biomedical applications. Progress in Polymer Science (Oxford) 2012;37:106–26. https://doi.org/10.1016/j.progpolymsci.2011.06.003.

[3] Tu E, Pearlmutter P, Tiangco M, Derose G, Begdache L, Koh A. Comparison of Colorimetric Analyses to Determine Cortisol in Human Sweat. ACS Omega 2020;5:8211–8. https://doi.org/10.1021/acsomega.0c00498.

DOI 10.5162/EUROSENSORS2025/TP11

Direct-printed amiodarone electrochemical sensor. Identification of DNA based bioreceptor

Marcin Urbanowicz[1], Magdalena Urbanowicz[2], Agnieszka Paziewska-Nowak[1], Kornelia Bobrowska[1], Anna Sołdatowska[1], Marek Dawgul[1], Dorota G. Pijanowska[1]
[1] Nalecz Institute of Biocybernetics and Biomedical Engineering, Polish Academy of Sciences, Ks. Trojdena 4 St., 02-109 Warsaw, Poland,
[2] Falsified Medicines and Medical Materials Department, National Medicines Institute, Chełmska 30/34 St., 00–725 Warsaw, Poland

Summary: This study focuses on the electrochemical behaviour of amiodarone, a widely used antiarrhythmic drug, to develop a direct-printed electrochemical sensor. The oxidation of amiodarone was confirmed via voltammetric techniques. A comparative analysis of graphite electrodes fabricated using direct printing (DPE) and screen printing (SPE) technologies revealed the superior performance of DPE sensors, with a sensitivity of 1.403 µA/µM – nearly twice that of SPE-based sensors. In the second part of the study, we screened for double-stranded DNA sequences capable of forming complexes with amiodarone. High-performance liquid chromatography (HPLC) identified the 5'-AGCTATAAAT-3' sequence as a promising bioreceptor. The interaction between amiodarone and DNA was further confirmed by NMR spectroscopy, based on diffusion coefficient measurements and chemical shift changes observed in NOESY and TOCSY spectra. These findings demonstrate the potential of integrating printed sensor technologies with molecular interaction studies for drug screening and biosensing applications.

Keywords: Amiodarone, Direct printing, DNA, Interaction analysis

Introduction

Amiodarone is one of the primary drugs used in the treatment of cardiac arrhythmias. However, its use is associated with many adverse effects, including pulmonary toxicity, liver damage, thyroid dysfunction, and visual disturbances. Therefore, the ability to personalize therapeutic dosing remains a significant clinical challenge. Biosensors offer a convenient tool for monitoring drug concentrations in patients, though their effectiveness relies heavily on high sensitivity and selectivity. This is particularly important for amiodarone, which has a narrow therapeutic window ranging from 0.5 to 2.5 µg/mL depending on individual patient characteristics. Reports of its potential genotoxicity suggest that amiodarone may strongly interact with DNA [1], making DNA a potential component for molecular recognition in biosensor applications [2].

Methods

Commercially available screen-printed graphite electrodes (SPE) and directly printed electrodes (DPE), fabricated using a programmable microdispensing robot, were used for sensor construction (diameter 1.6 mm). The redox behaviour of amiodarone was studied using glassy carbon electrodes (GCE) and cyclic voltammetry (CV) at a scan rate of 50 mV/s. Calibration curves were obtained using differential pulse voltammetry (DPV) with a pulse amplitude of 100 mV, a pulse duration of 0.005 s, and a scan rate of 20 mV/s. All electrochemical measurements were conducted in PBS buffer (pH 6.0).

For DNA interaction studies, 30 double-stranded DNA sequences (10 base pairs each) were screened to identify potential binding motifs. HPLC analysis was performed using a Phenomenex Gemini 5 µm NX-C18 column (250 mm × 4.6 mm) with a gradient of mobile phases: (A) 1 mM NH_4COOH (pH 6) and (B) acetonitrile. The gradient program ranged from 5–15% B (0–8 min), 15–90% B (8–18 min), held at 90% B (to 32 min), and returned to 5% B (50–60 min), with a flow rate of 1 mL/min and UV detection from 190–900 nm. NMR studies were conducted in D_2O buffer (25 mM NaCl / 25 mM K_3PO_4) with TSPA-d_4 as an internal standard. Standard pulse sequences were used for 1D and 2D experiments. DOSY was performed with 1024 transients, diffusion time 150–220 ms, and gradient strength ranging from 6 to 50 G/cm. TOCSY and NOESY spectra were acquired with a spectral width of 5000 Hz, 1024 × 512 complex points, 64 scans, and relaxation delays of 1 s. TOCSY spin-lock time was 80 ms; NOESY mixing time was 200 ms.

Results

In the first stage, measurement conditions, such as pH, ionic strength, and voltammetric parameters were optimized. The electrochemical activity of amiodarone was then investigated. The results confirmed that amiodarone undergoes an irreversible electrochemical oxidation at a potential of 850 mV (Fig. 1).

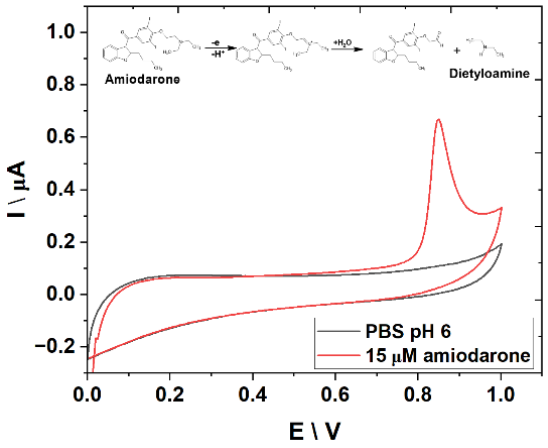


Fig. 1. GCE: redox mechanism of amiodarone.

Subsequently, calibration curves for graphite SPE and DPE electrodes were obtained using the DPV technique, as shown in Fig. 2. For electrodes of identical diameter, the DPE sensors demonstrated significantly higher sensitivity and a broader linear range compared to SPE.

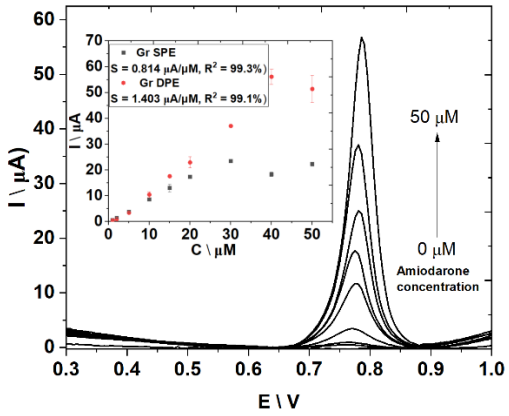


Fig. 2. Differential pulse voltammograms for Gr DPE with various concentrations of amiodarone. Inset: calibration curves for Gr-SPE (black markers) and DPE (red markers).

The second part of the study focused on identifying a DNA sequence capable of forming a complex with amiodarone. HPLC analysis (Fig. 3) of the drug's interaction with 30 different double-stranded DNA sequences revealed that the greatest decrease (by 53%) in free DNA absorbance was observed for the sequence 5'-AGCTATAAAT-3'. Additionally, a new peak at retention time (RT) = 1.909 min suggests the formation of a DNA-amiodarone complex.

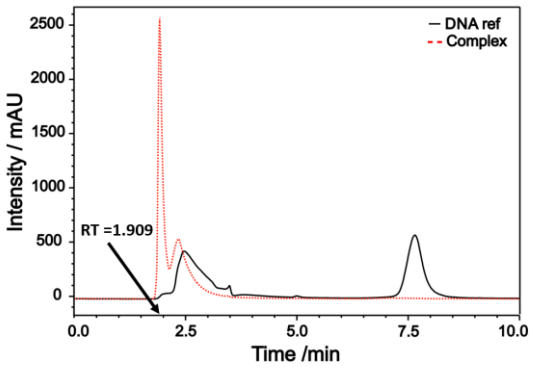


Fig. 3. HPLC chromatogram of 5'-AGCTATAAAT-3' dsDNA and complex of this DNA with amiodarone.

The interaction was further confirmed using NMR spectroscopy. Diffusion coefficient values enabled the calculation of the association constant (K_a = 2.12 M^{-1}) and dissociation constant (K_d = 0.47 M). Moreover, TOCSY (Fig. 4) showed chemical shift changes of approximately 0.06 ppm, providing strong evidence for specific binding between amiodarone and the selected DNA sequence and further confirming complex formation.

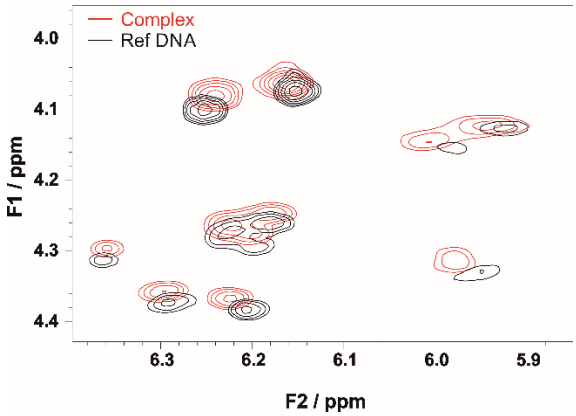


Fig. 4. TOCSY spectra of amiodarone-DNA complex after 2 h incubation.

The results provide a foundation for using the identified DNA sequence as a bioreceptor for amiodarone, enabling the development of a selective biosensor for clinical application.

References

[1] M.R. Almeida, et. all, Genotoxic studies in hypertensive and normotensive rats treated with amiodarone, Mutat. Res. Toxicol. Environ. Mutagen. 657, 155 (2008). doi: 10.1016/j.mrgentox.2008.09.005.

[2] M. Urbanowicz, et. all, A novel dsDNA decamer-based electrochemical biosensor for selective determination of irinotecan active metabolite - SN38, Sensors Actuators B Chem. 397, 134701 (2023). https://doi: 10.1016/j.snb.2023.134701.

Acknowledgements

The studies were financially supported by the IBBE PAS statutory project 225.

DOI 10.5162/EUROSENSORS2025/TP12

Sensitive cell identification in impedance flow cytometry using optimized dielectric buffer properties and low cost microchannels

M. Favrod-Coune[1,2], O. Guenat[3] and P. Eberle[1]
[1] Lucerne University of Applied Sciences, Switzerland
[2] Graduate School for Cellular and Biomedical Sciences, University of Bern, Switzerland
[3] University of Bern, ARTORG Center, Switzerland
patric.eberle@hslu.ch

Summary: Impedance flow cytometry is a promising technique to identify cells label-free. In this study, dielectric properties of buffer solutions are examined together with 3D focusing to achieve sensitive cell identification using low-cost microfluidic chips based on co-planar electrodes and wide channels. The efficiency for identification of polystyrene beads and HEK, C28, and C2C12 cells under various buffers and sheath flow conditions is analyzed.

Keywords: Impedance flow cytometry, cell identification, label-free, co-planar electrodes, 3D flow focusing

Background

Isolating and sorting single cells is of critical importance in biology, biotechnology, precision medicine [1] and point-of-care diagnostics [2]. Fluorescence-activated cell sorting (FACS) and magnetic-activated cell sorting (MACS) are well-established, commercially available methods. Although these conventional techniques offer high-throughput and are widely used [3], they have significant drawbacks, including expensive markers, time-consuming labeling [4], and the absence of specific markers for certain cells [4], limiting their use for cell therapy [5]. These limitations have motivated research toward non-invasive, label-free alternatives such as impedance flow cytometry, which identifies cells based on their impedance at different frequencies. However, impedance measurements depend not only on the cells but also on the buffer, electrode configuration, channel geometry and cell-to-electrode distance. Developing a system that provides reproducible signals for identical cells while sensitively differentiating distinct cell types remains challenging. A key approach is to match the electrode volume as closely as possible to the cell volume [6] maximizing electric field perturbation and impedance change. In addition, with a channel size comparable to the cell size, cell positioning becomes more consistent, removing variation in the signal due to position changes. On the other hand, a smaller channel increases the risk of clogging, as well as the fabrication complexity and costs. Innovative ideas were implemented to address this issue, like modifying the electrode configuration [7], using a channel constriction [8] or using an insulating sheath fluid [6], [9].

Theory

When a cell or particle passes through the electric field between two electrodes, the electrical current changes, corresponding to an impedance change. An effective way to reduce the noise of the signal and eliminate the impedance of the buffer impedance is to use a differential electrode configuration, with the current change due to the cell in the first electrode pair compared to a second empty electrode pair. As a cell passes over the first electrode pair, the difference of the measured currents of both electrode pairs is proportional to the difference of the inverse of the both impedances:

$$\frac{1}{Z_{\text{CiB}}(f)} - \frac{1}{Z_{\text{B}}(f)} = \frac{i_1(f)}{V} - \frac{i_2(f)}{V} = \frac{\Delta i(f)}{V} \quad (1)$$

where i_1 and i_2 are the two measured currents of each electrode pair at frequency f for a chosen voltage V, and $Z_{\text{CiB}}, Z_{\text{B}}$ are the impedances of the cell in buffer and of the buffer. The cell identification is maximized when two different cells produce the largest difference in differential current Δi. This is ideally achieved when the buffer has a larger impedance compared to the cell $Z_{\text{B}}(f) \gg Z_{\text{CiB}}(f)$. However, this is challenging to achieve: since the cell is itself surrounded by buffer, increasing the buffer's impedance also increases the one of the cell in buffer, and especially if the channel's cross-section is large compared to the cell (which is economical and robust against clogging). Δi should also be significantly larger than the minimal resolvable current of the instrument to ensure trustworthy results. One approach to solve this problem is to use two buffers: a conductive buffer close to the cell and an isolating buffer used as a sheath flow. Both buffers should have similar osmotic pressure as the cells. With its high conductivity (1.6 S/m), phosphate-buffered saline (PBS) is ideal for a conductive buffer. In theory, a solution of 10g sucrose into 100mL of deionized water achieves

the same osmotic pressure as PBS, with a very low conductivity (1e-3 S/m).

Methods

Here, the validity of the presented theory was tested using a custom-built trans-impedance amplifier FGPA-based, with a wide (180um x 80um) and inexpensive microfluidic chip mounted on co-planar electrodes. A 3D printed mold was used to cast the PDMS microfluidic chip. The cell is focused in the center of the channel using hydrodynamic 3D focusing, with a sheath fluid, allowing a reproducible position of the particle. Polystyrene beads and several cells lines (HEK, C28, C2C12) were measured for several sheath and core buffers of specific conductivities, using PBS, a 10% sucrose solution and mixes of both. The differential current Δi, the noise and the signal-to-noise ratio (SNR) were compared. The impact of the buffer configuration on cell discrimination was studied using support vector machine (SVM), which finds the hyperplan that separates best all cell populations.

Results

When the core and sheath buffers are similar, Δi increased with conductivity, and the noise remained constant. In such configuration, as the channel is much larger than the particle, using PBS as the core and sheath fluids seems to provide the largest signals. Cells and beads lead to different conclusions when the conductivity of the sheath fluid was reduced while keeping a core of PBS. For beads, the signal intensity linearly decreased, whereas for the cells, different behavior were observed for different cells. Figure 1 illustrates changes of current produced by HEK cells in a PBS core, with different sheath fluids. The imaginary part remained constant, but the real part was reduced, leading to a lower amplitude. For C28, the amplitude remained constant but the similar phase shift was observed. The size difference between both cell types could explain this behavior. In all cases, the lowest noise was observed with a PBS core and sucrose as sheath fluid, leading in fine to a higher SNR. Interestingly and surprisingly, SVM accurately identified all cell populations in nearly all configurations, and no general ideal configuration could be identified. Only the identification of beads size was proved more successful when both the core and the sheath fluids were the most conductive. Our results suggest that 3D focusing in combination with co-planar electrodes can be used to identify cells sensitively in a wide microfluidic chip.

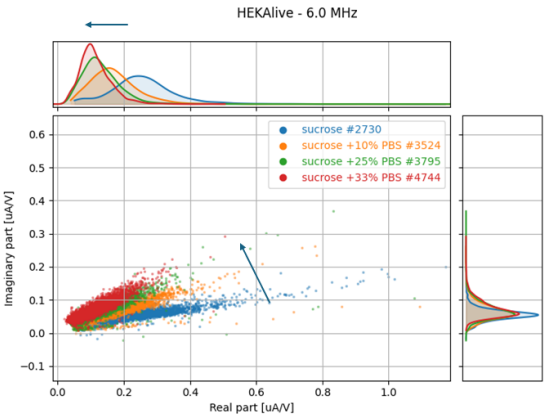


Fig. 1: HEK cells in a core of PBS surrounded by various sheath fluids, at 6 MHz, (#nb of cells)

References

[1] C. Wyatt Shields IV, C. D. Reyes, and G. P. López, "Microfluidic cell sorting: a review of the advances in the separation of cells from debulking to rare cell isolation," *Lab Chip*, vol. 15, pp. 1230–1249, 2015.

[2] C. Honrado, P. Bisegna, N. S. Swami, and F. Caselli, "Single-cell microfluidic impedance cytometry: from raw signals to cell phenotypes using data analytics," *Lab Chip*, vol. 21, pp. 22–54, 2021.

[3] K. de Wijs, C. Liu, A. Dusa, D. Vercruysse, B. Majeed, D. S. Tezcan, K. Blaszkiewicz, J. Loo, and L. Lagae, "Micro vapor bubble jet flow for safe and high-rate fluorescence-activated cell sorting," *Lab Chip*, vol. 17, pp. 1287–1296, 2017.

[4] M. Xavier, R. O. Oreffo, and H. Morgan, "Skeletal stem cell isolation: A review on the state-of-the-art microfluidic label-free sorting techniques," *Biotechnology Advances*, vol. 34, no. 5, pp. 908–923, 2016.

[5] C. A. Lazarski and P. J. Hanley, "Review of flow cytometry as a tool for cell and gene therapy," *Cytotherapy*, vol. 26, pp. 103–112, Feb. 2024.

[6] C. Bernabini, D. Holmes, and H. Morgan, "Micro-impedance cytometry for detection and analysis of micron-sized particles and bacteria," *Lab Chip*, vol. 11, pp. 407–412, Feb. 2011.

[7] F. Caselli and P. Bisegna, "Simulation and performance analysis of a novel high-accuracy sheathless microfluidic impedance cytometer with coplanar electrode layout," *Medical Engineering & Physics*, vol. 48, pp. 81–89, 2017.

[8] D. Yang, Y. Zhou, Y. Zhou, J. Han, and Y. Ai, "Biophysical phenotyping of single cells using a differential multiconstriction microfluidic device with self-aligned 3d electrodes," *Biosensors and Bioelectronics*, vol. 133, pp. 16–23, 2019.

[9] X. Xie, M. Gong, Z. Zhang, X. Dou, W. Zhou, J. Li, M. Zhu, Y. Du, and X. Xu, "Optimization of an electrical impedance flow cytometry system and analysis of submicron particles and bacteria," *Sensors and Actuators B: Chemical*, vol. 360, p. 131432, 2022.

DOI 10.5162/EUROSENSORS2025/TP13

Lens-free Microscope for Portable Pollen Grains Imaging System

Agus Budi Dharmawan[1,2], Georg Schöttler[1,2], Andreas Waag[1,2], J. Daniel Prades[1,2]
[1] Institute of Semiconductor Technology, Technische Universität Braunschweig, Hans-Sommer-Str. 66, 38106 Braunschweig, Germany
[2] Laboratory for Emerging Nanometrology (LENA), Technische Universität Braunschweig, Langer Kamp 6 a/b, 38106 Braunschweig, Germany

Summary:
The developed lens-free microscope is a compact, portable system capable of real-time, high-resolution pollen imaging. It accurately reconstructs pollen morphology comparable to a conventional lens-based microscope, while offering a larger field of view and simplified design. With its small size and fast processing, it holds strong potential as a ubiquitous microscopy platform in diverse environment.

Keywords: Holography, Lens-free microscope, Image reconstruction, Pollen, Real-time measurement

Background

Pollen allergies tend to peak during the flowering season, often leading to significant health concerns. Recent estimates suggest that between 1% and 40% of the European population is affected by allergic rhinitis, with a gradual upward trend being observed [1]. Although pollen monitoring and counting systems are widely used, they still face challenges in accurately distinguishing pollen grains from other similarly sized particles. Therefore, imaging-based approaches using microscopes remain essential for reliable identification and improved detection accuracy.

Different approaches—such as laser-based systems with lens-focused beams[2], imaging using inverted microscopes[3], and setups employing three-wavelength laser illumination[4]—have been developed for pollen imaging system. However, these methods convey particular complexities like relying heavily on laser-based illumination and multiple optical lenses in their configurations. This limits their massive applicability in harsh or outdoor environments, where compact, robust and low-cost setups are required.

In this work, we present the development of a compact, lightweight, and portable lens-free microscope for pollen imaging system. By eliminating traditional lenses, the system significantly reduces complexity and costs, while enhancing performance.

Material and Method

The lens-free microscope used in this study is based on the principle of in-line holography. The system consists of only three main components: a light source, a CMOS image sensor, and a sample placed between them. The light source is specifically designed to possess an optimal level of coherence, which is critical for generating clear interference patterns.

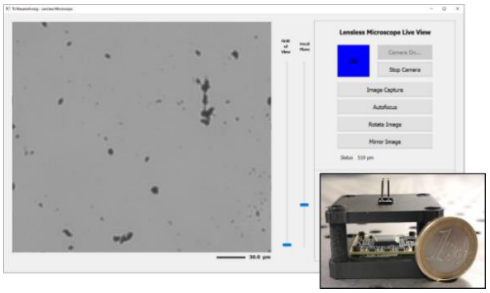


Fig. 1. Graphical user interface of the lens-free apps. Inset: 4 cm × 4 cm × 3 cm the lens-free microscope setup

To meet these requirements, a custom-fabricated 10 µm GaN-based micro-LED with a peak wavelength of 450 nm was developed in our cleanroom facility. The use of a micro-LED in this setup not only enhances spatial coherence and energy efficiency, but also simplifies the system design and minimizes the risk of damage to both the sample and the sensor. For image acquisition, a 5-megapixel MT9P031 CMOS sensor is used to record the light intensity across the sensing surface. To facilitate system control and real-time image capture, a custom graphical user interface (GUI) application was developed in-house. This software enables users to perform live image acquisition and provides cloud connectivity, allowing remote monitoring and data access from virtually any location. Fig. 1 shows a screenshot of the GUI and an image of the microscope prototype fabricated.

Due to the high spatial coherency of the micro-LED illumination, this simple design is effective in generating distinct interference patterns forming a raw image, from which 3D image information with higher spatial resolution can be extracted. For this, a reconstruction algorithm based on the Fourier Transform has been integrated into the system. The reconstruction process works by back propagating the pattern in the frequency domain to reconstruct the optical field in the object plane. The reconstruction process implemented in this system is mathematically represented the equation bellow:

$$U(x,y,z_{target}) = \frac{1}{N_x N_y} \sum_{n_x=0}^{N_x-1} \sum_{n_y=0}^{N_y-1} f(n_x,n_y) e^{ik_z z} e^{2\pi i \frac{x n_x}{N_x}} e^{2\pi i \frac{y n_y}{N_y}}$$

Results and discussion

We tested the system using pollen grains collected directly from flower samples. The sample is prepared by applying a droplet containing pollen onto a glass slide, followed by direct observation using the lens-free microscope. For comparison, the same samples are also examined using a conventional Leica DM2700 M lens-based microscope.

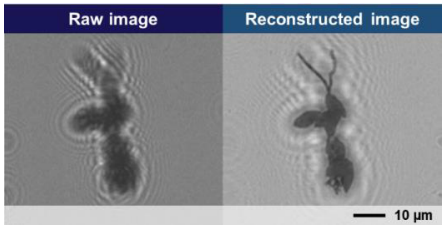


Fig. 2. The comparison between the raw and reconstructed images generated by lens-free microscope.

The initial test involved live image acquisition and reconstruction of pollen images using the lens-free microscope. The results demonstrated that the system is capable of accurately reconstructing images with high resolution and sharpness (Fig. 2). Moreover, the reconstruction algorithm is completed in under one second, enabling real-time image processing. The reconstructed images were then compared to those captured with the lens-based microscope (Fig. 3). The comparison showed that the lens-free microscope could reconstruct pollen morphology with a quality comparable to the images produced by the conventional much more complex and much more expensive system.

These results confirm that our lens-free microscope can achieve a resolution high enough for analyzing pollen. Additionally, the wide active area of the CMOS sensor (5.7 mm × 4.28 mm) allows the system to capture images with a large field of view while maintaining high resolution—an achievement that is challenging for traditional lens-based microscopes. With a resolution of down to 700 nm, this system opens the door to further developments, such as pattern recognition for shape classification and spectral analysis, for identifying unique characteristics of various pollen types and enabling more precise and comprehensive analysis.

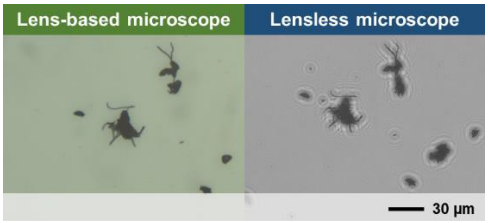


Fig. 3. The evaluation of the images captured by lens-based microscope and lens-free microscope.

With compact dimensions of just 4 cm × 4 cm × 3 cm (Fig. 1 inset), the lens-free microscope not only serves as an effective tool for pollen imaging, but also demonstrates strong potential as a point-of-care device and a ubiquitous microscopy platform, facilitating on-demand observations in diverse environment. Moreover, its compact and lightweight design enables to be used in extreme conditions, such as outer space.

References

[1] M. Sofiev et al., “European pollen reanalysis, 1980–2022, for alder, birch, and olive,” Scientific Data, vol. 11, no. 1, Oct. 2024, doi: 10.1038/s41597-024-03686-2.

[2] J. A. Grant-Jacob, et al., “Single-frame 3D lensless microscopic imaging via deep learning,” Optics Express, vol. 30, no. 18, p. 32621, Jun. 2022, doi: 10.1364/oe.464678

[3] S. Rawat, J. T. Béjar, and A. Wang, “Characterization of optical, thermal, and viscoelastic properties of pollenkitt in angiosperm pollen using In-Line digital holographic microscopy,” ACS Applied Bio Materials, vol. 7, no. 6, pp. 4029–4038, May 2024, doi: 10.1021/acsabm.4c00367.

[4] J. A. Grant-Jacob, et al., “Lensless imaging of pollen grains at three-wavelengths using deep learning,” Environmental Research Communications, vol. 2, no. 7, p. 075005, Jul. 2020, doi: 10.1088/2515-7620/aba6d1

Acknowledgements

This project is support from the sponsorship of the Alexander von Humboldt Professorship of the Humboldt Foundation and the Federal Ministry for Education and Research (Germany), partially funded by Zukunft Niedersachsen of the Lower Saxony Ministry for Science and Culture and the Volkswagen Foundation (Germany), and the Ministry of Science and Culture of the state of Niedersachsen in the frame of the QVLS Q1 research project (Germany).

DOI 10.5162/EUROSENSORS2025/TP14

Recent Advances in Multiparameter 2D Chemical Imaging of Environmental Samples with Optical Sensors (Optodes)

Andrey V. Kalinichev[1,2], *Martin R. Rasmussen*[1], *Klaus Koren*[1]
[1] *Aarhus University, Department of Biology, Ny Munkegade 116, 8000 Aarhus C, Denmark,*
[2] *Aarhus University, Aarhus Institute of Advanced Studies, Høegh-Guldbergs Gade 6B, 8000 Aarhus C, Denmark*
akalinichev@aias.au.dk

Summary:
We review recent advancements in multiparameter chemical imaging with optodes. Our focus is on the latest developments in 2D optical chemical imaging using dual-emission and grid-based optodes. These novel sensor designs allow for the simultaneous mapping of essential environmental parameters, including oxygen, temperature, and pH. Applications in soil and marine sediments demonstrate the robustness, accuracy, and versatility of these sensors. Our findings emphasize the potential of multiparameter optodes for detailed analysis of biogeochemical processes in complex environments.

Keywords: optical sensors, imaging, multiparameter measurements, 2D visualization, chemical gradients

Background, Motivation, and Objective

Understanding chemical gradients and heterogeneities is crucial for monitoring and interpreting processes in natural and engineered environments. Optical sensors (optodes) have significantly advanced environmental monitoring by enabling non-invasive, real-time visualization of chemical gradients in two dimensions (2D) [1]. Recent research has focused on integrating multiple sensing functionalities into single sensing platforms, enabling comprehensive multiparameter imaging (e.g., O_2, temperature, pH).

Despite substantial progress, challenges remain regarding sensor calibration, integration, and practical implementation. Multiparameter imaging is essential for revealing interactions within environmental samples such as sediments, soils, and aquatic ecosystems.

The objective of this research is to address the existing challenges by introducing recent developments in polymer-based optode designs. Here, we summarize recent progress, outline remaining challenges, and illustrate the applicability of multiparameter 2D optical chemical imaging for improved understanding of complex environmental processes.

Description of the New Method

We present recent advances in multiparameter optical chemical imaging by developing and optimizing novel optode designs based on two approaches:

(i) Advanced dual-emission luminescent optodes [2]. This approach utilizes newly synthesized luminescent indicator dyes exhibiting dual-emission properties, combining thermally activated delayed fluorescence (TADF) and phosphorescence signals. Such optodes enable precise and reliable two-dimensional imaging of oxygen (O_2) and temperature distributions.

(ii) Grid-based optode arrays [3]. Building upon previously demonstrated sensor array concepts, we have developed innovative grid optode designs. These sensors consist of a regular array of sensing spots, each containing a defined chemical composition printed onto a transparent substrate. The layout resembles a checkerboard pattern where each spot functions as a discrete chemical sensor, enabling 2D mapping through spatially resolved optical readout. This approach facilitates the simultaneous mapping of various chemical parameters with high spatial resolution.

Results

Our results demonstrate successful applications of multiparameter optodes in 2D imaging of environmental samples. We highlight examples, including:

(i) Simultaneous imaging of O_2 and temperature distributions in heterogeneous soil.

We successfully visualized two-dimensional oxygen and temperature gradients in soil containing a water pipe system, which mimicked underground heat exchange conditions (see Fig. 1).

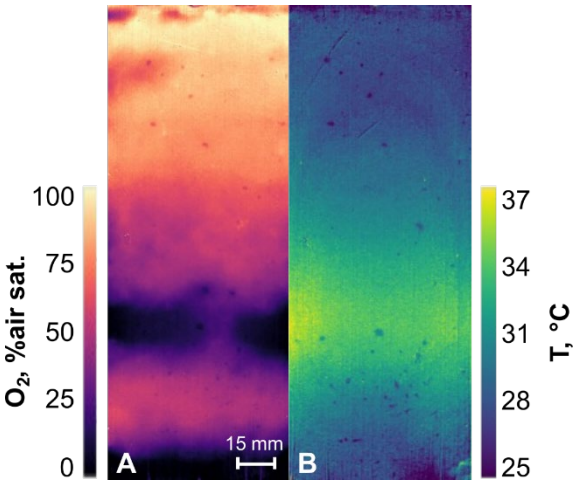


Fig. 1. 2D visualization of oxygen concentration (A) and thermal imaging (B) of heat transfer in soil with a heated water pipe [2].

The dual-emission mechanism significantly simplifies calibration, enhances measurement accuracy, and provides robust performance for rapid multiparameter imaging with minimal cross-interference.

(ii) Grid-based optode arrays for O_2 and pH mapping in marine sediments.

The developed grid optodes effectively mapped spatially resolved O_2 and pH gradients simultaneously within sulfidic marine sediments (see Fig. 2). These measurements provided detailed insights into sediment biogeochemical processes, highlighting the strengths of grid-based approaches for precise, spatially discrete multiparameter imaging in complex marine systems.

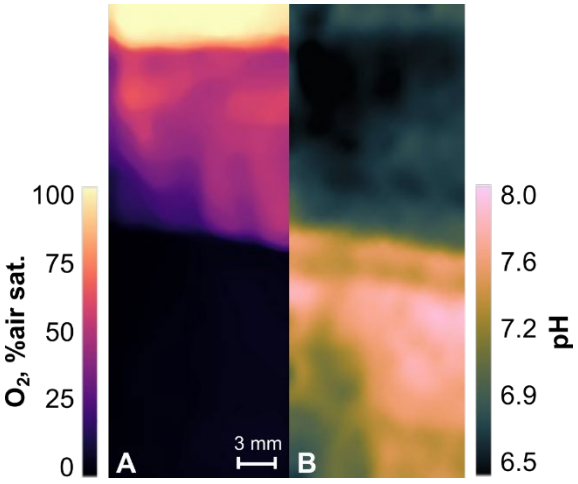


Fig. 2. (A) Oxygen concentration and (B) pH distribution image measured in sulfidic sediment using grid optodes [3].

Conclusions

Our results demonstrate the versatility and strong potential of multiparameter optical sensors for environmental applications. These recent developments significantly expand the analytical capabilities of optodes and pave the way for their broader use in monitoring, particularly for studying dynamic biogeochemical processes in heterogeneous samples.

References

[1] A.V. Kalinichev, S.E. Zieger, K. Koren, Optical sensors (optodes) for multiparameter chemical imaging: classification, challenges, and prospects, *Analyst* 149, 29–45 (2024); doi: 10.1039/D3AN01725D

[2] G. Schwendt, A.V. Kalinichev, S.M. Borisov, K. Koren, Simultaneous Imaging of Temperature and Oxygen by Utilizing Thermally Activated Delayed Fluorescence and Phosphorescence of a Single Indicator, *ACS Meas. Sci. Au.* 4, 568–576 (2024); doi: 10.1021/acsmeasuresciau.4c00040

[3] A.V. Kalinichev, M. Rasmussen, F.L. Hoch, Z. Parnicka, J. Fiutowski, K. Koren, C. Kunstmann, Simultaneous multiparameter 2D imaging with grid optodes: a 3D-printed sensor array approach with interpolation-based reconstruction; *in prep.*

Acknowledgements

This research was supported by the Aarhus Institute of Advanced Studies (AIAS).

DOI 10.5162/EUROSENSORS2025/TP15

Fabrication of modified α-Fe_2O_3 NPs on ZnO NRs/Ni-foam nanocomposite as electrode for electrochemical detection of arsenic in drinking water

Sreymean Ngok[1], Rem Yann[1,4], Chan Oeurn Chey[3], Xianjie Liu[2], Magnus Willander [1], Omer Nur [1]*
[1] Department of Science and Technology, Physics Electronics and Mathematics, Linköping University, SE-601 74 Norrköping, Sweden
[2] Laboratory of Organic Electronics, ITN, Linköping University, SE-60174, Norrköping, Sweden
[3] Graduate School of Science, Royal University of Phnom Penh, Phnom Penh, Cambodia.
[4] Department of Physics, Faculty of Science, Royal University of Phnom Penh, Phnom Penh, Cambodia.
[*] Correspondence: sreymean.ngok@liu.se ; Tel: (+46 11 36 32 19)

Highlights:

- Modification of α-Fe_2O_3 NPs on ZnO NRs/Ni-foam nanocomposite have been successfully synthesized.
- ZnO NRs/Ni-foam/ α-Fe_2O_3 NPs nanocomposite was synthesized by hydrothermal and dip coating method using ZnO nanorods and α-Fe_2O_3 nanoparticles.
- Optimum of conditions for As (V) detection by ZnO NRs/Ni-foam/ α-Fe_2O_3 NPs electrode was determined.

Keywords: nanoparticles synthesis, hydrothermal synthesis, electrochemical sensor, arsenic detection, nanocomposite metal oxide

Abstract

Arsenic (As) is a highly toxic contamination element which is especially found in drinking water[1]. Arsenic exposure to drinking water is a major concern due to environmental pollution and health hazards[2,3]. Arsenic detection in drinking water is analyzed by fabrication of an efficient electrode for demonstrating an electrochemical sensor. The electrode is based on a modified surface of the ZnO nanorods (NRs) synthesized on Ni-foam substrate by depositing α-Fe_2O_3 nanoparticles (NPs) to detect the contamination of arsenic(V) in drinking water. This electrode is synthesized through two separate growth steps which are the hydrothermal (ZnO NRs) step followed by the dip coating method (α-Fe_2O_3 NPs). The dip coating method was repeated for different dipping cycles, 2 times (ZNF-2), 3 times (ZNF- 3) and 4 times (ZNF- 4) in order to achieve a uniform coverage of the ZnO NRs surface. Through different dip coatings, the ZNF-3 samples indicated that uniform and homogeneous morphology was observed from the SEM images accompanied by the highest oxidation current. The electrodes were characterized by XRD, XPS, SEM and UV-vis spectroscopy. In this study, we analyzed the electrode by the electrochemical performance of sensor electrode in a wide range of arsenic(V) concentrations from 0 to 50 ppb and was monitored by cyclic voltammetry. This study has shown a calibration plot that is linear over a concentration range of 0-50 ppb of arsenic(V), and the regression equation extracted from the calibration curve was found to be y = 0.003x -0.6271 (with R^2 = 0.991). The limit of detection (LOD) and limit of quantification (LOQ) were found to be 4.12 ppb and 13.74 ppb, respectively, which are lower than the maximum allowed value recommended by the World Health Organization (WHO) for arsenic in drinking water. This reasonable performance of the ZnO NRs/Ni-foam/α-Fe_2O_3NPs nanocomposite electrode can be further developed and utilized toward efficient arsenic(V) detection in drinking water. Future work will expand the development of efficiency for electrochemical detection of arsenic(V) in drinking water in real samples.

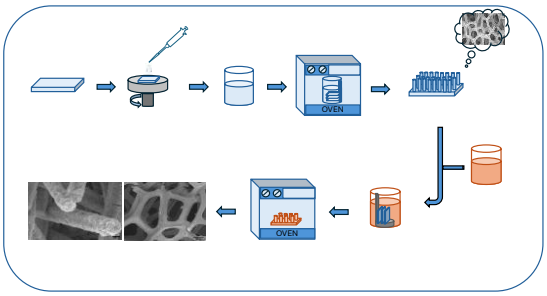


Fig 1: Schematic diagram showing the process for synthesis of the ZnO NRs/Ni-foam/α-Fe_2O_3NPs nanocomposite electrode.

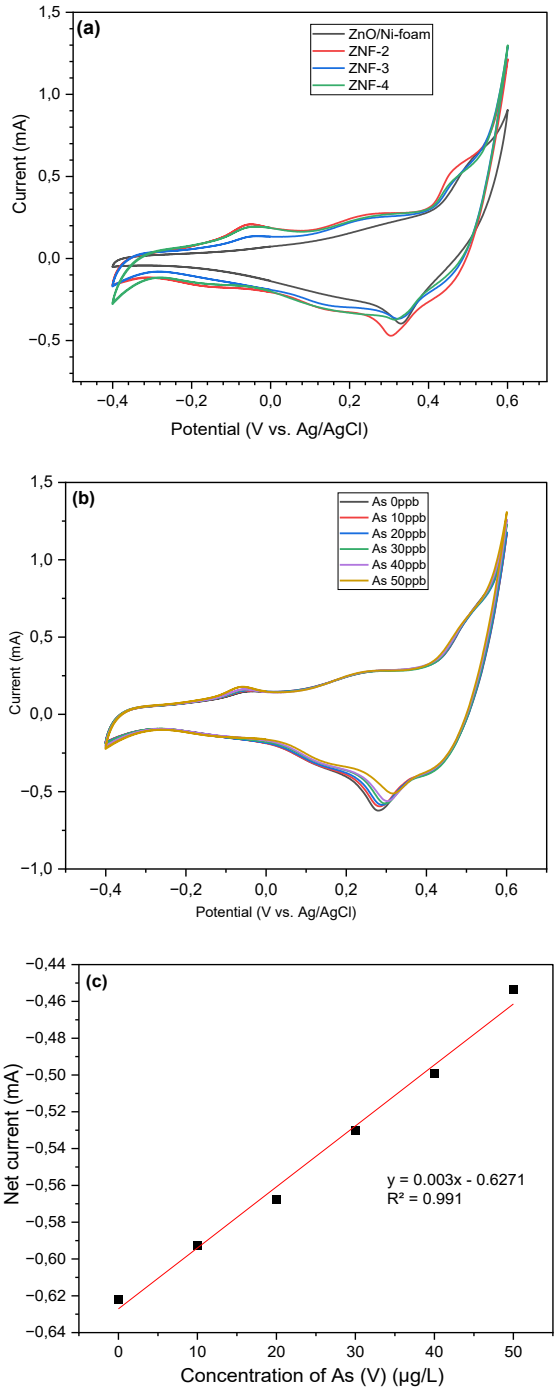


Fig 2: Cyclic voltammetry curves of (a). ZnONRs/Ni-foam, (ZNF- 2), (ZNF- 3) and (ZNF- 4) electrode in 1M KOH electrolyte (b). ZNF-3 electrode at different concentrations of arsenic(V) at potential scan from -0.4 to 0.6 V, and scan rate 100 mV/s. (c) the corresponding linear calibration plots of the net current against arsenic(V) concentrations.

References

[1] J.H.T. Luong, E. Lam, K.B. Male, Recent advances in electrochemical detection of arsenic in drinking and ground waters, Anal. Methods. 6 (2014) 6157–6169. https://doi.org/10.1039/c4ay00817k.

[2] W.R. Cullen, K.J. Reimer, Arsenic Speciation in the Environment, Chem. Rev. 89 (1989) 713–764. https://doi.org/10.1021/cr00094a002.

[3] S. Nellaiappan, K.C. Pillai, A.S. Kumar, Flow-injection analysis coupled with electrochemical detection of poisonous inorganic arsenic(III) species using a gold nanoparticle/carbon nanofiber/chitosan chemically modified carbon screen printed electrode in neutral pH solution, Anal. Methods. 10 (2018) 799–808. https://doi.org/10.1039/c7ay02655b.

Acknowledgements

Authors acknowledge the financial support from the Department of Science and Technology (ITN), Linköping University as well as ISP and SIDA, Sweden.

DOI 10.5162/EUROSENSORS2025/TP16

Influences on the Sensitivity of Camera-Based Colorimetric Gas Sensors Systems

Sonja Hoffmann[1,2], Sabine Trupp[2]
[1] Fraunhofer EMFT, Hansastrasse 27d, 80686 Munich, Germany
[2] Bundeswehr University Munich, Institute of Physics, Werner-Heisenberg-Weg 39, 85577 Neubiberg, Germany
sonja.hoffmann@emft.fraunhofer.de

Summary:
Colorimetric gas sensors detect analytes through a color-changing reaction of a sensor material. This work shows how light sources and image formats affect the sensitivity of camera-based colorimetric sensor. For this work, bromocresol green was embedded in polyvinyl chloride for NH_3 detection. Three white LEDs with different color temperatures were tested, revealing that the neutral white LED exhibited the highest sensitivity. Furthermore, RAW image data provided the best results due to its higher bit depth compared to JPG and PNG formats, significantly enhancing sensor system sensitivity.

Keywords: Colorimetric gas sensor, Raspberry Pi camera, light source, pH indicator, data format

Background, Motivation and Objective

Colorimetric gas sensors identify analyte gases by causing a visible color change in a gas-sensitive material, known as the sensor material. These sensors provide several benefits, such as cost efficiency and operation at room temperature. A colorimetric sensor consists of three key components: a sensor material, a light source, and a detector that measures the color change [1]. The impact of the sensor material on the sensitivity of the gas sensors, e.g. examining the effects of the sensor dye, the matrix material, and the plasticizer has been investigated by previous studies [2]. This work concentrates on the impact of the light source and the image data format on the results provided by the sensor system. Therefore, a well-known sensor dye bromocresol green in polyvinyl chloride (PVC) as the polymer matrix is used as sensor material for the detection of the gas NH_3. When exposed to NH_3, a pH reaction occurs resulting in a color change of the sensor dye from orange to blue. As a detector for the colorimetric gas sensor a Raspberry Pi Camera v1 is applied. The sensor material was directly applied on the camera pixels to produce the gas sensitive camera sensor. To investigate the impact of the light source three different types of white LEDs with different color temperatures were tested: a warm white (WW, 3000 K), a cold white (CW, 11 000 K) and a neutral white (NW, 5000 K) LED. The camera records images in 10 bit RAW format or processed as 8 bit images e.g., in a PNG or JPG format. In order to investigate the impact of the data format the sensitivity to NH_3 is compared for RAW, PNG and JPG images.

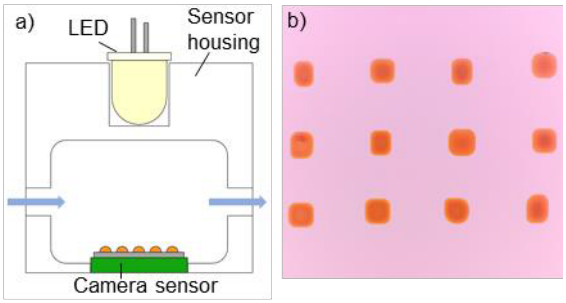


Fig. 1. Schematic drawing of the sensor set-up (a) and JPG image recorded by the camera sensor illuminated by NW LED (b).

Design of the colorimetric gas sensor

The setup of the test system includes a Raspberry Pi Camera v1 as the detector (Figure 1a). The housing and optics were removed and the blank camera sensor is directly functionalized with the sensor material using a 0.5 µl syringe. The sensor material consisted of BCG (70 mmol/l) and PVC (7.5 w%) diluted in benzoic acid methyl ester and ethanol (3/1). 0.05 µl of the sensor material solution was dispensed on the camera in a 4x3 grid with a spot size of 200–300 µm. The functionalized camera sensor was placed inside a white plastic housing. The camera sensor was illuminated by a white LED through the white plastic chamber and was placed on top of the camera sensor. The white LEDs have uniform light intensity and beam angle. The current was set to 3 mA with a fixed shutter time of the camera of 200 µs. The sensor

response is the change of the red, green and blue (RGB) color values upon NH_3 exposure. Therefore, an image series was recorded in JPG, PNG and RAW data format (Figure 1b). The images are processed to extract the color values by superimposing a 4x3 grid on each image, and averaging the RGB values over a circular region with a diameter of 30 pixels at the center of each sensor spot.

Results

The reaction of the sensor material with NH_3 leads to changes in the color values R, G and B, and is exemplarily demonstrated for the R value (ΔR) in the following. ΔR Is calculated by the difference of R value before and during NH_3 exposure and is averaged over the sensor spots. The spectrum of the light source influences the sensitivity and reproducibility of the camera based colorimetric gas sensor as exemplified by the JPG images (Figure 2). The sensor material shows the highest sensitivity upon NH_3 illuminated by NW light, followed by CW light. The lowest sensitivity is obtained with the WW LED.

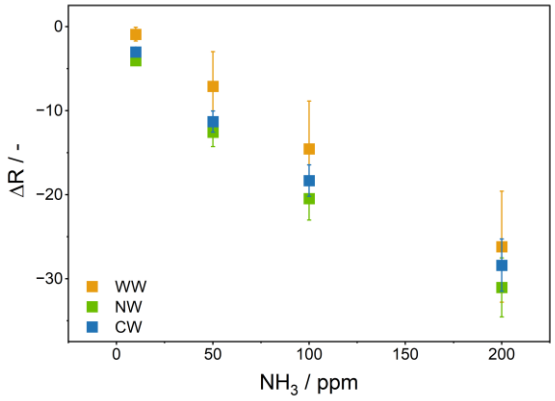


Fig. 2. Change in the R color value (ΔR) upon exposure to 10, 50, 100 and 200 ppm of NH_3 at 55% r.H., 25°C, and 1013 mbar using the WW;NW and CW LED.

The WW LED has the highest proportion of red light among the selected LEDs. This leads to an oversaturation of the R value, requiring higher concentrations of NH_3 to cause a visible color change. The standard deviation of ΔR is significantly higher than for NW and CW LED. The variation in the response of the sensor spots illuminated by the WW LED is significantly higher. This can be related to an inhomogeneous illumination of the camera sensor. Consequently, the WW LED is considered as unsuitable, whereas the NW LED is identified as the best light source for this set-up.

Furthermore, the data format of images does impact the sensor's sensitivity, shown for the NW LED as the light source (Figure 3). Using RAW images leads to higher sensitivity for the sensor system than JPG and PNG images. There is no significant difference in sensor response between PNG and JPG images.

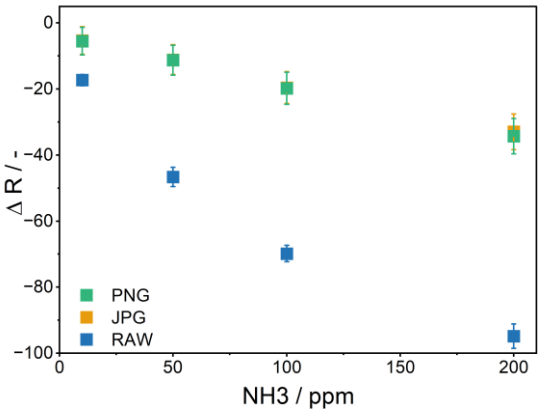


Fig. 3. Change in the R color value (ΔR) upon exposure to 10, 50, 100 and 200 ppm of NH_3 at 55% r.H., 25°C and 1013 mbar, comparing different data formats illuminated by the NW LED.

The significantly higher sensitivity of the RAW image is caused by its higher bit depth. 8 bit images can display a total number of 256 color values per color channel, while 10 bit images display 1024 color values. Thus, the higher color depth and finer gradation of colors with 10 bit compared to 8 bit images lead to higher sensitivity of the sensor.

Conclusion

The performance of camera-based colorimetric gas sensors can be significantly enhanced by selecting the appropriate light source and image data format. In this setup, the highest sensitivity was achieved using the neutral white NW LED, which resulted in improved sensitivity. Additionally, recording images in RAW data format further increased the sensitivity.

References

[1] K.S Suslick, N.A Rakow, A. Sen, Colorimetric sensor arrays for molecular recognition. *Tetrahedron*, *60*, 11133–11138 (2004), doi: 0.1016/j.tet.2004.09.007

[2] J. Courbat, D. Briand, J. Damon-Lacoste, J. Wöllenstein, N.F. de Rooij, Evaluation of pH indicator-based colorimetric films for ammonia detection using optical waveguides. *Sensors and Actuators B: Chemical*, *143*, 62–70, (2009) doi:10.1016/j.snb.2009.08.049

Acknowledgements

We would like to thank our colleagues from UniBW and Fraunhofer EMFT for their support throughout this research. The project was conducted within the initiative "Biogenic Value Creation and Smart Farming" of the Fraunhofer-Gesellschaft funded by the German federal government and the German state.

DOI 10.5162/EUROSENSORS2025/TP17

Noble Metal Decorated Graphene Sensor for Detecting Hydrogen at Room Temperature

Padmanathan Karthick Kannan[1], Martin Tyler[2], Julian W. Gardner[1]
[1] School of Engineering, University of Warwick, Coventry CV4 7AL, United Kingdom
[2] Paragraf, 7-8 West Newlands, Somersham, Cambridgeshire, England, PE28 3EB, United Kingdom
Corresponding author's e-mail address: J.W.Gardner@warwick.ac.uk

Summary:
This study reports the development of a Pd functionalized graphene-based chemiresistor device for the detection of hydrogen at room temperature. This low-cost graphene device can operate and detect hydrogen efficiently at room temperature and hence has a very low power unlike pellistor-based sensors. Our preliminary data clearly reveal that the sensor can detect hydrogen at concentrations ranging from 0.01 % to 1 % hydrogen in air. This shows the potential of a graphene chemiresistor to be used for detection of hydrogen leaks in, for example H_2-based cars emerging to replace combustion engines.

Keywords: Gas chemiresistor, graphene, hydrogen sensor, chemical sensor.

Background, Motivation an Objective

With the rapid development of diverse technologies, the world is currently experiencing a severe energy crisis. Though non-renewable energy sources are utilized to solve energy shortages, there is an urgent need for green energy to promote the development of a more sustainable environment [1]. Hydrogen is one among the three major energy sources along with solar and nuclear, and it helps to reduce air pollution and global warming due to its zero-emission nature. Furthermore, due to its high abundance and recyclable nature, hydrogen has always been a suitable option for the global green energy system. Although hydrogen has numerous advantages in energy development and other industrial applications such as fuels, transportation, storage, its colourless and odourless properties along with its asphyxiating nature make it extremely difficult for humans to detect leaks. The lower explosive limit (LEL) is 4% hydrogen in air and so is a major fire hazard. Therefore, retaining hydrogen safety as primary consideration, it is very important to design gas sensors with high sensitivity and rapid response time to assure human safety. A plethora of materials have been investigated for the development of hydrogen sensors including nano metal oxides, conducting polymers, carbon nanotubes, graphene and hybrid materials based on combinations of the aforementioned components [2]. Among these materials, metal oxides semiconductors and Pt pellistors are commonly used as the active material in the fabrication of resistive and thermal hydrogen sensors and have been shown to exhibit enhanced sensitivity with a very short response time. However, the main disadvantage is that they can only operate at high temperatures and so require high power consumption. One of the most important considerations in the practical use of hydrogen sensors is that it should be able to function at a possible low temperature to avoid explosions. Recently, graphene-based sensors have grown in popularity for detecting harmful and toxic gases at room temperature because of their ultra-high surface to volume ratio and superior physisorption [3]. Traditionally scalable production of large area graphene devices requires transfer from a copper growth substrate to the product substrate. This process can lead to cracks in the graphene film and can lead to metal and organic residues which damage device performance and increase variability. Paragraf's devices are made from directly deposited graphene. This results in no contamination from polymers or catalysts, and high quality graphene material. However, pristine graphene has been shown to have poor response, but the nanoparticle loaded graphene has shown an enhanced response with excellent sensitivity due to catalytic effect [4]. Here, we investigate the response of a graphene chemiresistor functionalized with a thin layer of palladium (Pd) against a reference uncoated graphene chemiresistor.

Description of the New Method or System

Graphene devices were produced at Paragraf Ltd using proprietary techniques for deposition of graphene directly onto a metal oxide substrate. The graphene was patterned to produce a 94 µm channel contacted through passivated metal

tracks. Dies were cleaved and mounted onto a bespoke PCB with epoxy coated wirebonds contacting the device. For hydrogen sensing studies, pristine and palladium loaded graphene (deposited via e-beam evaporation, 1Å/s, 1 nm) chemiresistor devices were compared

Fig. 1 shows a photograph of the graphene chemiresistor device attached to a small PCB and the pads wire-bonded via an ultrasonic wedge bonder.



Fig. 1. Functionalized graphene chemiresistor *mounted on a carrier PCB for sensor response measurements*

The graphene sensors were placed in a customized chamber, which passes constant current through the source-drain channel to measure its resistance. Up to 8 devices can be tested simultaneously in the automated gas test station, under the control of a National Instruments LabVIEW Virtual Instrument. Graphene resistances were measured using an NI USB 6343 data acquisition system (DAQ) and standard PC computer.

Results

The sensing performance of both pristine and Pd decorated graphene was investigated in the concentration range of 0.01 % to 1 % of hydrogen at RT (Figures 2a and 2b). The response data show that pristine graphene has shown no response to hydrogen in all the concentration range, while the Pd decorated one responded very well in the measured range. The exposure time of hydrogen was set to 5 minutes. The sensor response is defined using the following equation.

$$Response\ (\%) = \left[\frac{R_g - R_a}{R_a}\right] \times 100 \qquad (1)$$

Where R_a is the resistance value measured in air and R_g is the resistance measured in the gas.

The resistance of the Pd decorated graphene sample was found to increase with an increase non-linearly in hydrogen (see Fig 2c). Further studies on the effect of humidity and interfering gases on the sensing response of Pd decorated graphene towards hydrogen are in progress and will be presented in the conference.

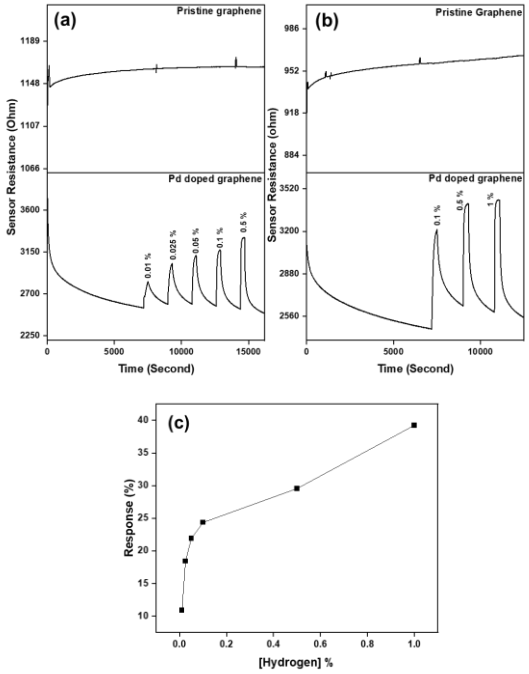


Fig. 2. Time series resistance plots of pristine and Pd decorated graphene at (a) low concentrations (b) high concentrations (c) Plot of sensor response (%) versus % concentration of hydrogen at RT.

References

[1] Md M. H. Bhuiyan, Z. Siddique, Hydrogen as an alternative fuel: A comprehensive review of challenges and opportunities in production, storage, and transportation, International Journal of Hydrogen Energy 102, 1026-1044 (2025); doi: 10.1016/j.ijhydene.2025.01.033

[2] M. Choudhary, A. Shrivastav, A.K. Sinha, A.K. Chawla, D.K. Avasthi, K. Saravanan, S. Krishnamurthy, R. Chandra and S. Wadhwa, Emerging Nanomaterials for hydrogen sensing: Mechanisms and prospects, International Journal of Hydrogen Energy 77, 557-574 (2024); doi: 10.1016/j.ijhydene.2024.06.149

[3] P. Recum, T. Hirsch, Graphene based Chemiresistive gas sensors, Nanoscale Advances 6, 11-31 (2024); doi: 10.1039/D3NA00423F

[4] A.V. Singhal, H. Charaya, I. Lahiri, Noble Metal Decorated Graphene-Based Gas Sensors and Their Fabrication: A Review, Critical Reviews in Solid State and Materials Sciences 42, 499-526 (2017); doi: 10.1080/10408436.2016.1244656

Acknowledgements

This research was supported by the Engineering and Physical Sciences Research Council grant EP/W024284/1.

DOI 10.5162/EUROSENSORS2025/TP18

Al-doped ZnO Gas Sensors Toward Safe and Effective Monitoring in Protected Environments

Emanuela Tavaglione[1], *Arianna Rossi*[1], *Matteo Ferroni*[2], *Vincenzo Guidi*[1], *Barbara Fabbri*[1]
[1] *Department of Physics and Earth Science, University of Ferrara, Via Giuseppe Saragat 1/C, 44122 Ferrara, Italy*
[2] *Institute for Microelectronics and Microsystems IMM-CNR, Via Gobetti 101, 40129 Bologna, Italy*
Corresponding Author's e-mail address: emanuela.tavaglione@unife.it

Summary:
In environmentally fragile settings, harmful gases may put both human health and sensitive materials at risk. Indeed, effective monitoring of hazardous compounds must be conducted without affecting the surroundings. In these circumstances, visible-light photoactivated metal-oxide semiconductor gas sensors are a suitable alternative to their thermoactivated counterparts. Al-doped ZnO emerges as a promising material for more sustainable gas sensors in such applications.

Keywords: chemoresistive gas sensors, photo-activation, cultural heritage, aluminum metal doping, environmental monitoring

Introduction

Atmospheric pollutants have been demonstrated not only to compromise human health, but also to negatively affect the permanence and integrity of materials, especially in environmentally fragile sites, such as museums [1]. In these settings, objects, staff, and visitors must be protected against the presence of hazardous gases. This highlights the necessity of new gas sensing technologies, which must be portable, user-friendly and non-invasive, hence able to discriminate analytes without compromising the space. Nowadays, sustainability is another crucial concern. In this context, it refers to both the synthesis of the sensing materials and how they operate, with the use of abundant and low-toxic elements, and employing sensors with low energy consumption. To this end, visible-light photoactivated metal-oxide semiconductor (SMOXs) gas sensors represent a viable alternative to their well-established thermally activated counterparts, which involve high temperatures (200-500°C). However, their performance tends to be inadequate, due to low response values, slow kinetics, and non-reversibility of the signal, also caused by a lack of knowledge on the gas sensing mechanism in this regime [2]. Furthermore, as wide-bandgap semiconductors, most SMOX materials require UV light for photoactivation, making it the most used source despite its low efficiency, high energy consumption and potential destruction of analytes. In this framework, ZnO is a widely studied material both in thermo- and photoactivation, typically functionalized with noble metals [2] in order to enhance and tune the material sensing properties. ZnO functionalization by innovative metal doping, such as aluminum, could enable the generation of inter-gap states [3], making this SMOX a good candidate for a visible-light activated sensor. Additionally, aluminum is an abundant and safe element, making it a more sustainable choice for the development of efficient and environmentally friendly gas sensors.

Materials and methods

For this purpose, aluminum doped zinc oxide (Al:ZnO) was synthesized by a sol-gel approach. It was prepared with two different molar concentrations of Al (3% and 5%) and each of them was calcined at three different temperatures, namely 450, 500 (Fig.1), and 600 °C.

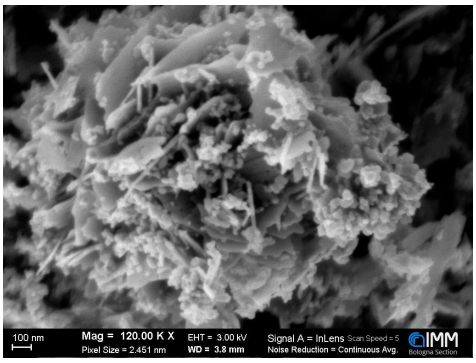


Fig. 1. Scanning Electron Microscopy (SEM) image of Al:ZnO, 5% of Al concentration, calcined at 500 °C.

Results and further perspectives

The sensors have been studied in dry air condition, and then were tested with NO_2, toluene, benzene, NH_3, acetaldehyde, and acetone, analytes of particular relevance in museums and archives [1]. The tests were carried at three different operating temperatures, namely 200, 300, and 400 °C. The sensors exhibited a selectivity based on the operating temperature, as presented in Tab.1.

Tab. 1: Best sensor responses (R) obtained for each gas at 300, 400, and 600 °C. For each operating temperature, the best-performing sensor among the tested is reported.

Gas	*R* at 200°C	*R* at 300°C	*R* at 400°C
NO_2	5.5 Al5%600°C	0.6 Al5%500°C	0.3 Al5%500°C
Toluene	none	8.5 Al3%500°C	saturated
Benzene	0.1 Al3%600°C	1.2 Al5%500°C	3.7 Al5%500°C
NH_3	1.6 Al3%600°C	3.9 Al5%600°C	saturated
Acetald.	none	saturated	9 Al5%500°C
Acetone	12 Al5%600°C	saturated	saturated

In preliminary investigations, under blue-light activation (468 nm) at room temperature (RT) in dry air, the most promising sensor was Al:ZnO with 5% of aluminum, calcinated at 500°C. As shown in Fig. 2, the sensor exhibited fast response and recovery kinetics, with a response time of 2 min to 0.1 ppm of NO_2 and a recovery time, from the injection of 0.2 ppm of NO_2, of 9 min.

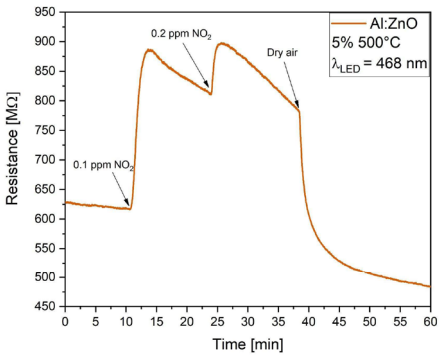


Fig. 2. Electrical resistance of Al:ZnO sensor (5% Al, calcinated at 500 °C) under blue-light activation (468 nm) at RT in dry air, exposed to 0.1 and 0.2 ppm of NO_2.

This study demonstrates the potential of combining material sustainability with technological advancements in gas sensors, paving the way for applications in protected environments, such as cultural heritage sites. Further studies will be conducted on the performance and the gas sensing mechanism in thermo- and photoactivation regime, through the *Operando Diffuse Reflectance Infrared Fourier Transform* spectroscopy apparatus at disposal of the University of Ferrara.

References

[1] A. Fenech et al., *Volatile aldehydes in libraries and archives*, Atmospheric Environment 44, 2067–2073 (2010); doi: 10.1016/j.atmosenv.2010.03.021

[2] A. Gaiardo et al., *ZnO and Au/ZnO thin films: Room-temperature chemoresistive properties for gas sensing applications*, Sensors and Actuators B 237, 1085–1094 (2016); doi: 10.1016/j.snb.2016.07.134A.

[3] R. Dhahri et al., *Gas sensing properties of Al-doped ZnO for UV-activated CO detection*, Journal of Physics D: Applied Physics 49, 135502 (2016); doi: 10.1088/0022-3727/49/13/135502

Acknowledgements

E. Tavaglione scholarship in Physics is funded by the D.M. n. 118/2023, supported by PNRR - funded by the UE - NextGenerationEU - Mission 4 “Education and Research” - Component 1 “Strengthening the offer of educational services: from nursery schools to university” - Investment 4.1 PNRR scholarships for Cultural Heritage.

DOI 10.5162/EUROSENSORS2025/TP19

Field Calibration Strategies for Methane Monitoring with Electronic Noses

Guillem Domènech-Gil[1], Daniel Montecinos[2], Kalpana Munnuru Singamshetty[1], David Bastviken[1]
[1] Department of Thematic Studies and Environmental Change, TEMA M, Linköping university, Sweden
[2] Current address: Department of community planning and Air Quality Unit, Swedish Meteorological, Hydrological Institute SMHI, Sweden.
guillem.domenech-gil@liu.se

Summary:
The practical application of chemoresistive gas sensors is hindered by expensive calibration equipment and uncertainty about their performance under non-steady-state conditions outside laboratory facilities. To address this situation, we have developed a calibration method that reduces costs and, tailored for field applications, reports concentration with low error measures. We focus on methane case studies, although the method can be extrapolated to other scenarios, detailing how the type and amount of available data affect outcomes and reliability.

Keywords: field calibration, chemical sensors, metal oxide, electronic nose, machine learning

Headlines

Chemoresistive sensors can monitor specific gases thanks to advanced data processing techniques. However, these techniques usually rely on laboratory calibrations under controlled conditions, which can be quite different from real-world scenarios. This mismatch poses a challenge for users who need reliable sensor performance in everyday situations. To tackle this, we have developed a new method that cuts down on calibration costs while ensuring the sensors work well in the field, even under varying conditions.

Background, Motivation and Objective

In recent years, we have seen an increase in the use of machine learning to solve problems that would otherwise be practically impossible. One of these problems is the cross-sensitivity of chemoresistive sensors, which is their major drawback. It has been shown that these sensors can achieve high selectivity if an extensive number of calibration measurements are carried out followed by intensive data processing tailored to the needs of the studied case [1]. Most of these measurements are done in laboratories, under steady-state conditions and controlled atmospheres, what cannot guarantee their performance in practical cases under dynamic conditions and uncontrolled atmospheres. Moreover, despite the low cost of chemoresistive sensors, the equipment needed to carry out these calibrations is very expensive, which unfortunately hinders the widespread use of these sensors.

The few studies that consider using the sensors for field applications mainly find two solutions: (1) assume the concentration(s) will be correctly predicted [3]; or (2) conduct a study of e.g. odours [4] when individual gas concentrations are not necessary. With our method we present another option that can reduce the costly laboratory calibration and decrease the computational power from high to middle values, that can enable portable microcontrollers to support such models in real-time.

Description of the New Method

Low-cost sensor systems, presented in detail elsewhere [5], were equipped with an in-house C code, a tailor-made printed circuit board that powered and controlled four TGS Figaro sensors, and a pressure, temperature, and humidity BME680 sensor. The sensor system housing allowed direct exposure to air through different openings and convective air circulation to ensure the correct exposure to gases. Approximately 20 of these electronic noses where calibrated in situ under different field and weather conditions to evaluate the amount of data necessary to obtain well-performing models. The calibration process allowed tracking the concentration of the target gas in the relevant measurement atmospheric gas mixture without the need of the typical gas mixing systems available in laboratories, equipped with mass flow controllers, regulators,

gas standards, safety cabinets, and test chambers. Thus, the cost is considerably lower. More importantly, this opens for the possibility of performing initial field calibrations adapted to the case studied ensuring better final performance and allows periodical reviews on-site to ensure long-term reliability. After the field calibration, the data collected from different sensors goes through a process of pre-processing, feature extraction, and consequent multivariate statistics quantification technique, what reports methane concentrations between atmospheric values and up to two orders of magnitude higher without the need of computational power-hungry algorithms such as neural network or support vector regression. This range of concentrations covers most practical cases where sources of methane emission have been tedious to evaluate until now but can be easily adapted to the needs of other cases.

Results

As a representative example, the concentration of methane predicted from our model for unseen data including certain variety of concentration ranges is shown in Figure 1 together with the data from a reference system. We can observe that for both atmospheric and much higher concentration values the trends agree. Figure 2 shows how the error evolves with points and highlights that after certain amount of time, the RMSE converges to a stable value. Additionally, results from the different systems and the evolution of the mean absolute error, mean absolute percent error, root mean squared error (RMSE) metrics as a function of the number and type of points used will be presented.

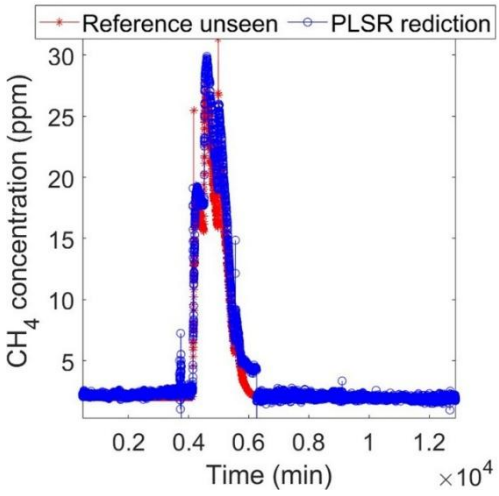


Fig. 1. Unseen concentration as a function of time reported by a reference system and the results of the partial least squares regression performed with data from our electronic nose using a novel field calibration strategy.

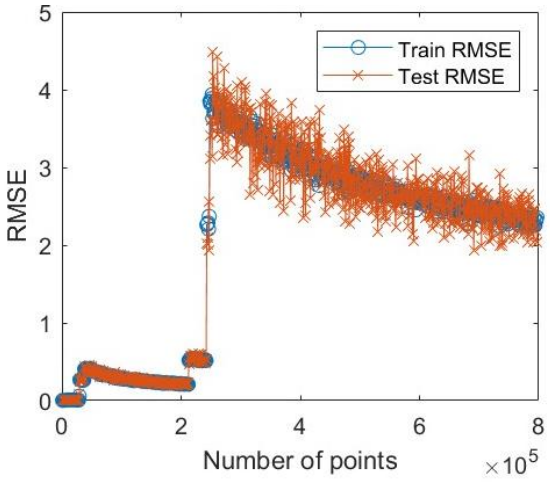


Fig. 2. Evolution of root mean squared error as a function of number of points.

References

[1] Y. Ma, X. Qiu, Z. Duan, L. Liu, J. Li, Y. Wu, Z. Yuan, Y. Jiang, H.Tai, A Novel Calibration Scheme of Gas Sensor Array for a More Accurate Measurement Model of Mixed Gases, *ACS Sens.* 9, 11, 6022-6031, (2024); doi: 10.1021/acssensors.4c01867.

[2] J. Fonollosa, S. Sheik, R. Huerta, S. Marco, Reservoir computing compensates slow response of chemosensor arrays exposed to fast varying gas concentrations in continuous monitoring, *Sens. Act. B Chem.* 215, 618-629 (2015); doi: 10.1016/j.snb.2015.03.028.

[3] I. Shtepliuk, G. Domènech-Gil, V. Almqvist, A.H. Kautto, I. Vågsholm, S. Boqvist, J. Eriksson, D. Puglisi, Electronic nose and machine learning for modern meat inspection, *J. Big Data* 12, 96 (2025); doi: 10.1186/s40537-025-01151-4.

[4] G. Domènech-Gil, N.T. Duc, J.J. Wikner, J. Eriksson, S.N. Påledal, D. Puglisi, D. Bastviken, Electronic Nose for Improved Environmental Methane Monitoring, Environ. Sci. Technol. 58, 352-361 (2024); doi: 10.1021/acs.est.3c06945.

Acknowledgements

This work has been financially supported by the Horizon Europe's grant agreement no.101120651, Next-2Digits, Formas grant 2018-01794, and Swedish Research Council grant 2016-04829.

DOI 10.5162/EUROSENSORS2025/TP20

Rapid detection of olive oil markers using a gas chromatography sensor system

Omar Tarek Penagos Carrascal[1,3], Jan Bröckelmann[2], Tilman Sauerwald[1,3], Mark Bücking[2], Gina Zeh[1]
[1] Fraunhofer Institute for Process Engineering and Packaging IVV, Department of Sensory Analytics and Technologies, Giggenhauser Strasse 35, 85354, Freising, Germany
[2]Fraunhofer Institute for Molecular Biology and Applied Ecology IME, Auf dem Aberg 1, 57392 Schmallenberg, Germany
[3] Saarland University, Campus A5.1, 66123 Saarbrücken, Germany
omar.tarek.penagos.carrascal@ivv.fraunhofer.de

Summary:
A gas chromatography (GC) sensor system is proposed for the rapid analysis of olive oil. Alterations of olive oil were analyzed, with hexanal, *E*-2-hexenal, *E*-3-hexenyl acetate, and nonanal being identified as key marker compounds for its quality. These four key markers were successfully separated on a 3 m semi-polar GC column in 1 min. The sensor (SGP40, Sensirion AG), coupled to a polar GC column, showed good reactivity towards the four identified marker compounds, although with considerable tailing (peak tailing factor ~4.3), which can be mitigated by applying the first derivative to the sensor signal.

Keywords: Olive oil, gas chromatography, sensor system, quality control

Introduction

Olive oil is a food of great nutritional value due to its high content of mono- and polyunsaturated fatty acids, in addition to being a source of vitamins. The price of olive oil has experienced an increasing trend due to its demand and a harvest shortage. This makes it vulnerable to adulteration, whereby fractions of high-quality olive oil are mixed with lower quality oils. It is therefore crucial to detect counterfeit products to protect its market and the general public [1], [2].

Several analytical methods exist for evaluating olive oil. Gas chromatography-mass spectrometry (GC-MS) is the best known and most robust, especially for determining the origin of the oil [1]. However, instruments are expensive and must be operated by qualified personnel. To make such analyses, less expensive, and easier to perform a gas chromatography sensor system is proposed, with acceptable losses in performance.

Defining which substances are target markers and or interferents is essential as it helps the scope of the system being developed to be determined. Within this scope, the detection capability of the sensor and the resolution of the chromatography must be finely tuned to achieve the fastest and most reliable measurements.

Some of the results obtained during the conceptualization and demonstration of the proposed system are shown in this paper.

Materials and results

A baseline measurement was carried out to identify the main markers of olive oil using a commercial product as standard in a dynamic headspace-thermal desorption-GC measurement with a semi-polar Rtx-1701 GC column (L: 30 m, ID: 0.25 mm, coating: 0.25 µm). Based on this measurement, hexanal, *E*-2-hexenal, *E*-3-hexenyl acetate and nonanal were chosen as reference markers for the subsequent steps of the study.

In a second step, solid-phase microextraction (SPME) GC-MS measurements of the identified marker compounds dissolved in sunflower oil were performed. These were carried out on a semi-polar column (OV-1701, L: 3 m, ID: 0.1 mm, coating: 0.1 µm) to determine the time range that an olive oil measurement could take on a column with these characteristics. The results are shown in Figure 1. Two temperature programs were used:

- Fast program: 35 °C held for 0.35 min, then heated up to 200°C at 100°C/min with 1 mL/min helium carrier gas.
- Slow program: 35°C held for 2 min, then heated up to 100°C at 5°C/min, then up to 250°C at 25°C/min with 0.25 mL/min helium carrier gas.

These measurements showed that the separation would take between 1 min (fast program) and 7 min (slow program). The shortest difference in retention times in both programs is 11 s between *E*-3-hexenyl acetate

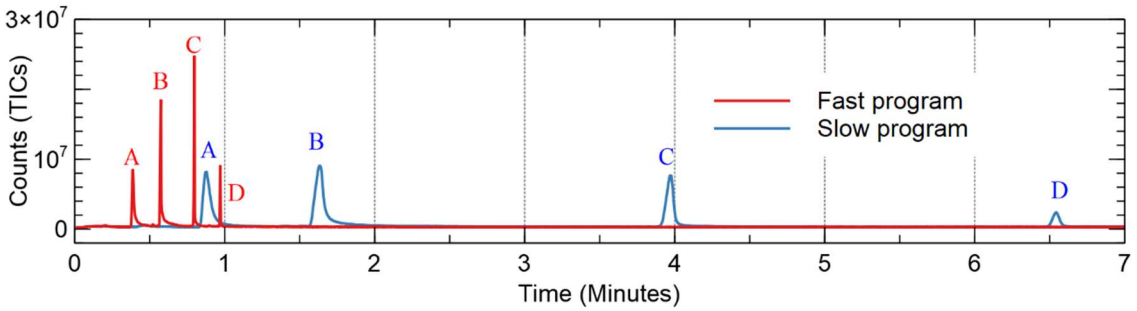


Figure 1: comparison between fast and slow programs for SPME-GC-MS with a 3 m GC column. A: hexanal, B: E 2 hexenal, C: E 3 hexenyl acetate, D: nonanal.

and nonanal for the fast program and around 45 s between hexanal and *E*-2-hexenal for the slow program.

Figure 2 shows the results of a SPME-GC-SOMSA (Selective Odorant Measurement by Sensor Array) [3], (polar column, DB-FFAP, L: 15 m, ID: 0.25 mm, coating: 0.25 µm) measurement of a spiked solution of the four previously identified markers in sunflower oil. The Sensirion SGP40 sensor showed good reactivity to the selected markers, emitting signals at similar times to those shown by the GC-MS. Considerable tailing (peak tailing factor around 4.3, peak full width at half maximum FWHM: 26-30 s) can be observed in the raw data. After performing a first derivative of the sensor signal, the peaks become more recognizable (FWHM: 3-5 s).

The peak widths of the derived signals are significantly narrower than the distance between the two closest peaks, even in the 1-minute GC run. This suggests that a GC-MOS sensor system may be able to perform quality control measurements of olive oil within one minute. However, further evaluation is needed to determine whether the derivative-based signal processing method remains effective when peaks partially overlap.

Outlook

The sampling method is currently under investigation as it has a direct impact on the analysis time and the quality of the results. To achieve fast and satisfactory measurements, a balance must be found between reduced sampling times and reduced peak intensities.

Next steps include the evaluation of sensors integrated with the optimized short GC column and method (cf. Figure 1).

References

[1] E. Kakouri, P.-K. Revelou, C. Kanakis, D. Daferera, C. S. Pappas, and P. A. Tarantilis, *Foods*, vol. 10, no. 7, Art. no. 7, Jul. 2021, doi: 10.3390/foods10071565.

[2] “Olive oil - European Commission.” Accessed: Apr. 08, 2025. [Online]. Available: https://agriculture.ec.europa.eu/data-and-analysis/markets/price-data/price-monitoring-sector/olive-oil_en

[3] M. Koehne, O. T. P. Carrascal, T. Sauerwald, and G. Zeh, *Vorträge*, pp. 230–235, Jun. 2024, doi: 10.5162/sensoren2024/C2.3.

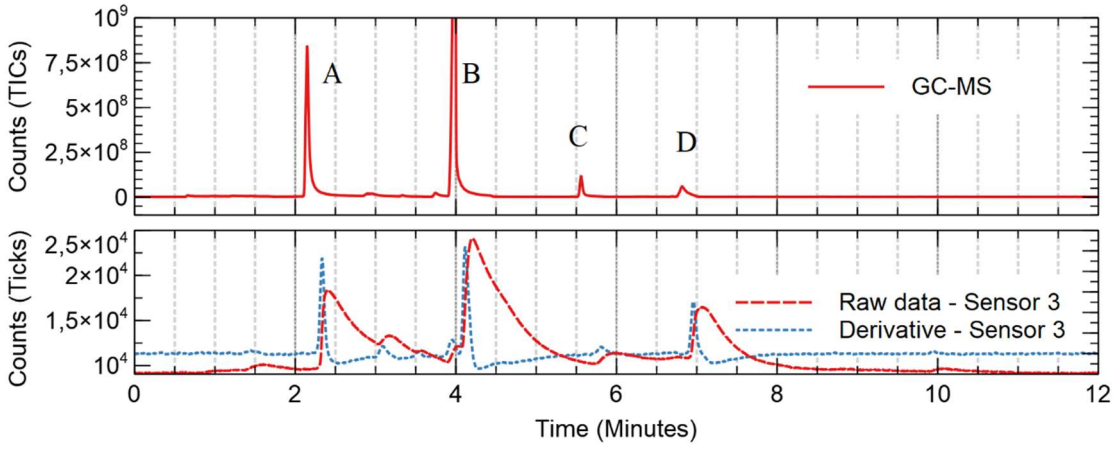


Figure 2: Measurement of the four identified markers in sunflower oil by GC-SOMSA. Top: Signal provided by GC-MS, Bottom: Signal provided by layer 3 of SGP40 (300°C) and derivative of signal. A: Hexanal (200 µg/mL), B: E-2-Hexenal (400 µg/mL), C: E-3-Hexenyl acetate (20 µg/mL) and D: Nonanal (5 µg/mL)

DOI 10.5162/EUROSENSORS2025/TP21

Optimizing AC Excitation Frequency for Linear Complex Impedance Response in Metal Oxide Semiconductor Gas Sensing

Hamza Ali Imran[1] , *Oliver Brieger*[1], *Christian Bur*[1] *and Andreas Schütze*[1]
[1]Lab for Measurement Technology, Saarland University, Saarbrücken, ermany
Corresponding Author's e-mail address: h.imran@lmt.uni-saarland.de

Summary: Metal Oxide Semiconductor (MOS) gas sensors are of high interest in gas detection applications due to their high sensitivity and low cost. However, conventional read-out methods based on resistive measurements often exhibit a highly nonlinear response to gas concentration, limiting their effectiveness for accurate quantification. In this study, we present an alternative approach that leverages impedance spectroscopy to identify an optimal excitation frequency at which the imaginary component of the impedance (Z'') exhibits a highly linear correlation with gas concentration. As a case study, we evaluate the AS-MLV-P2 sensor under varying concentrations of ethanol gas. The proposed method demonstrates strong linearity, achieving an R^2 value of 98.26 % for a linear fit between the mean of Z'' over 35 frequency sweeps and Ethanol concentrations ranging from 1000 ppb to 8000 ppb, at an excitation frequency of 3.568 MHz.

Keywords: Metal Oxide Gas Sensors Systems, Electrical Impedance Spectroscopy, Complex Response

Introduction

Metal Oxide Semiconductor (MOS) gas sensors are widely used, especially for the detection of Volatile Organic Compounds (VOCs) in applications such as environmental monitoring, indoor air quality, clinical diagnostics, and food spoilage [1, 2, 3]. These sensors typically rely on DC resistance measurements, where gas exposure causes changes in the resistance of the functionalized metal oxide layers. However, the resistive response is highly nonlinear, especially at higher concentrations. Achieving linearity in MOS gas sensors enhances sensitivity across a wide concentration range, reduces the need for complex calibration, and extends the dynamic range of detection. It also improves baseline stability and minimizes the impact of humidity and temperature, all while using standard commercial sensing elements — making the approach both accurate and practical [4].

On the other hand, exciting these sensors with an alternating voltage and analyzing their impedance response opens the possibility of identifying a frequency at which the imaginary component of the impedance (Z'') exhibits a linear relationship with gas concentration. This behavior was first reported by [4], where a linear Z'' response to methane concentration was observed using the thick-film sensor TGS2611. In the present study, we extend this concept by investigating the AS-MLV-P2 thin-film sensor exposed to ethanol gas. We not only validate the linear response of Z'' under specific excitation frequencies but also introduce a methodology for identifying the optimal frequency at which the sensor demonstrates the highest linearity between Z'' and gas concentration.

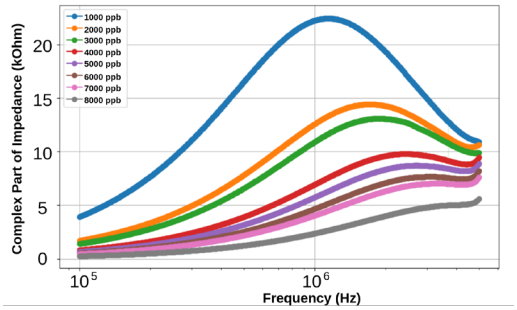


Fig. 1: Mean curve of (Z'') over 100 kHz to 5 MHz for ethanol concentrations of 1000–8000 ppb (35 sweeps, concentration step: 1000 ppb, temperature: 150 °C, relative humidity: 50 % at room temperature.

Methodology

We performed Electrical Impedance Spectroscopy (EIS) [5, 6] on the AS-MLV-P2 sensor exposed to ethanol gas concentrations ranging from 1000 ppb to 8000 ppb at 50% relative humidity, using zero air as the carrier gas. Impedance data were acquired with an Agilent 4292A Impedance Analyzer over the 100 kHz to 5 MHz frequency range. The sensor was maintained at 150 °C using a PID-controlled feedback loop connected to its heater resistor.

Recordings were taken under steady-state conditions using predefined sensor settings and an automated analyzer. Each *recording session* consisted of 35 frequency sweeps and required approximately 300 seconds. After each session, a 10-minute interval was maintained at constant temperature and gas exposure. For each ethanol concentration, 18 such recordings were

DOI 10.5162/EUROSENSORS2025/TP21

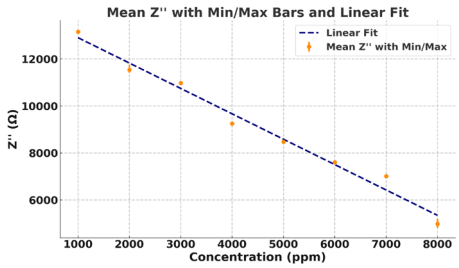


Fig. 2: Mean imaginary impedance (Z'') with Min-Max bars for ethanol concentrations from 1000 ppb to 8000 ppb at the optimal excitation frequency (3.568 MHz).

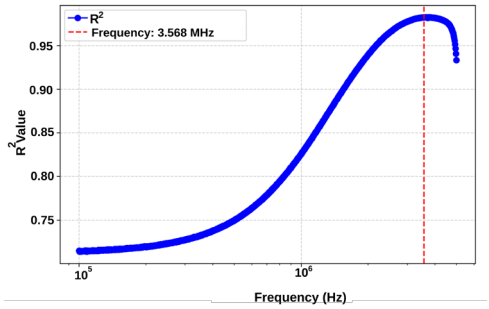


Fig. 3: Coefficient of determination (R^2) for linear fit between Z'' for frequencies 100 kHz to 5 MHz. Peak at 3.568 MHz indicates optimal excitation frequency.

conducted. Bode plot analysis showed that the sensor stabilized by the 10th session; however, the 18th (final) session was used for comparison across concentrations.

To compare Z'' across concentrations and identify the optimal operating frequency, we computed the mean over all sweeps in each recording. Figure 1 shows the mean curve of Z'' across the frequency range for each concentration over 35 sweeps, illustrating the impedance behavior. The mini-max spread of Z'' was within $\pm 100\,\Omega$ which confirms the mean as a reliable representation. This data was provided to Algorithm 1, which returned the frequency corresponding to the maximum R^2 value.

By applying Algorithm 1, we identified the optimal frequency of 3.568 MHz, at which the coefficient of determination R^2 reached 98.26%. Figure 2 shows the mean values of the imaginary impedance component Z''_{Mean} and also the minimum-maximum bars across different gas concentrations. Moreover, the R^2 curve for the entire frequency sweep is shown in 3.

Conclusions and Future Directions

We are investigating how operating temperature affects sensor behavior in the EIS setup and its response to various gas mixtures. The goal is to enhance selectivity and sensitivity by optimizing both operating frequency and temperature.

Algorithm 1 Optimal Frequency Selection via Linearity of Z''

Input: $D = \{(f_i, c_j, Z''_{ij})\}$
Output: Optimal freq. f^* maximizing linearity of Z'' vs. $concentration$
$R^2_{\text{best}} \leftarrow 0$, $f^* \leftarrow \emptyset$
for all $f \in$ UniqueFrequencies(D) **do**
  $D_f \leftarrow \{(c_j, Z''_{ij}) \mid f_i = f\}$
  if $|D_f| \geq 2$ **then**
    Fit linear model: $Z'' = \alpha c + \beta$
    Compute R^2_f
    if $R^2_f > R^2_{\text{best}}$ **then**
      $R^2_{\text{best}} \leftarrow R^2_f$, $f^* \leftarrow f$
      Store regression model and D_f
    end if
  end if
end for
Save D_{f^*} and its linear fit
return f^*, R^2_{best}

References

[1] A. Schütze, T. Baur, M. Leidinger, W. Reimringer, R. Jung, T. Conrad, and T. Sauerwald, "Highly sensitive and selective voc sensor systems based on semiconductor gas sensors: how to?," *Environments*, vol. 4, no. 1, p. 20, 2017.

[2] A. H. Alinoori and S. Masoum, "Multicapillary gas chromatography—temperature modulated metal oxide semiconductor sensors array detector for monitoring of volatile organic compounds in closed atmosphere using gaussian apodization factor analysis," *Analytical chemistry*, vol. 90, no. 11, pp. 6635–6642, 2018.

[3] H. A. Imran, B. Ersöz, R. Fix, C. Bur, and A. Schütze, "Metal oxide semiconductor gas sensor systems for food freshness detection: A review of recent studies," in *Proceedings of the 17. Dresdner Sensor-Symposium 2024*, AMA Service GmbH, 2024.

[4] R. A. Potyrailo *et al.*, "Extraordinary performance of semiconducting metal oxide gas sensors using dielectric excitation," *Nature Electronics*, vol. 3, no. 5, pp. 280–289, 2020.

[5] A. C. Lazanas and M. I. Prodromidis, "Electrochemical impedance spectroscopy a tutorial," *ACS measurement science au*, vol. 3, no. 3, pp. 162–193, 2023.

[6] M. Schüler, T. Sauerwald, and A. Schütze, "Metal oxide semiconductor gas sensor self-test using fourier-based impedance spectroscopy," *Journal of Sensors and Sensor Systems*, vol. 3, no. 2, pp. 213–221, 2014.

Acknowledgements

Funded by the European Union

This work is part of the EU-funded SERENADE Project under Horizon Europe MSCA-DN (Grant No. 101072846).

DOI 10.5162/EUROSENSORS2025/TP22

Novel Pyridinium Luminophores for Optical Ammonia Detection

Viktor Zabolotnii[1], Roman Viter[1], Matis Martins Drava[1], Artis Kinens[1]
[1] University of Latvia, 19 Raina Blvd., Riga, LV 1586, Latvia
viktor.zabolotnii@lu.lv

Summary:
Ammonia detection is one of the actual problems in food packaging applications. This paper presents the results of the study of optical sensors of ammonia vapor based on novel organic pyridine luminophores modified with acids. Optical, structural properties of luminophores at room temperature were investigated. The sensitivity of the luminophores to ammonia vapor in the 20-700 ppm concentration range was investigated.

Keywords: optical sensors, ammonia, pyridinium luminophores, optical sensors, biogenic amines, food safety, photoluminescence, volatile organic compounds.

Introduction:
Biogenic amines, such as ammonia, detection is one of the actual problems in food packaging applications. Classical methods of food quality control are time consuming, including expensive materials and technics [2]. Optical sensors for the detection of biogenic amines are becoming a real challenge for industrial and food safety applications [1,2]. This is due to their simplicity, low-cost production technology, and ability to operate outside of laboratory conditions. Pyridinium luminophores are promising materials for application in the field of optical sensors, which demonstrate highly intensive photoluminescence with high quantum yield at room temperature. These organic structures could be easily chemically tuned according to industry needs. One of the methods of improving sensitivity to ammonia is the treatment of luminophore with acids. As a base for the future sensors were used 1-(2-(9H-carbazol-9-yl)benzyl)pyridin-1-ium-4-carboxylate (mmd93), chemical structure of luminophore shown in Figure 1, modified with hydrochloric acid (mmd93-HCl) and trifluoroacetic acid (mmd93-TFA).

Experimental part:
Synthesis of mmd93 was performed by following the experimental procedure reported by Leduskrasts et al. [3] For modification two portions of mmd93 each were mixed with of HCl and TFA respectively and dried in the furnace overnight.
Sensor tests with ammonia vapors were provided in a specially designed chamber.

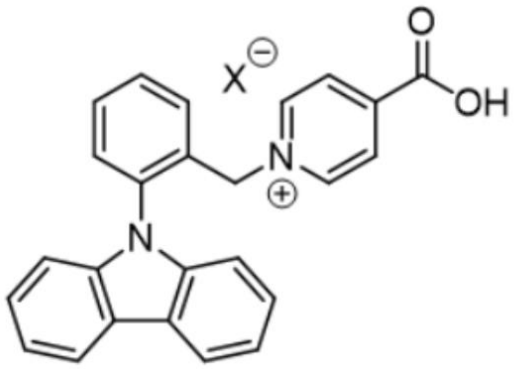


Figure 1. Chemical structure of mmd93 modified with acid.

The chamber (V_c=7.7 l) isolated from the environment, equipped with ventilator, sample holder, quartz window, inlet and outlet. The probe consists of precisely measured volume of ammonia saturated vapors (V_a<<V_c) injected inside with a syringe. Photoluminescence (PL) was initiated with portable light source (UV LED, 325 nm, 0.05 mW). During the sensor testing full PL spectra was recorded before and after injection of each probe. Kinetics was recorded for pre-selected wavelengths.

Results and Discussion:
From FT-IR spectroscopy (Figure 2) we can observe changes in spectra for all the samples in 1500 – 750 cm^{-1}. That could be explained by the interactions between luminophore and introduced acids with formulation of new carboxylic groups. Diffuse reflectance spectroscopy shown red shift of the peak of absorption for modified

with acids mmd93 (Figure 3).

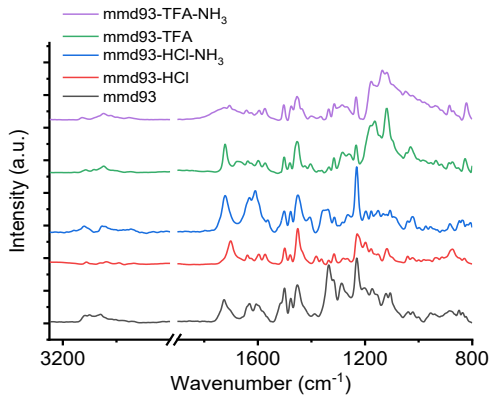


Figure 2. FT-IR of pure and modified mmd93.

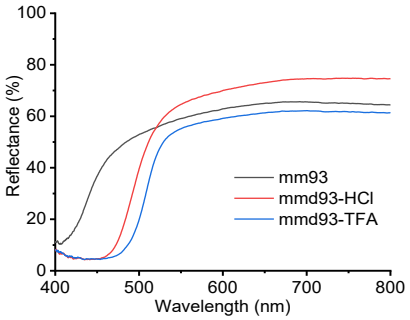


Figure 3. Diffuse reflectance spectroscopy of pure and modified mmd93.

Results of sensor testing of mmd93-HCl and mmd93-TFA against ammonia vapors are presented in Figure 2 and Figure 3 respectively. Intensity of PL decreases for both samples during the experiments upon the interaction of ammonia vapors.

For mmd93-HCl measurements were provided in the range of the concentrations of ammonia vapors between 20 ppm and 200 ppm. For mmd93-TFA sensor testing were performed in the range of concentration 50 – 700 ppm of ammonia vapors.

As we can observe interaction with ammonia vapors for each compound results in different form of kinetic curve and reaction initiates with different vapors concentrations.

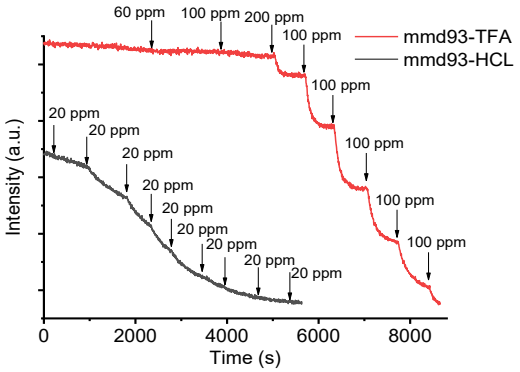


Figure 4. Kinetics of sensor response of modified compounds for ammonia vapors.

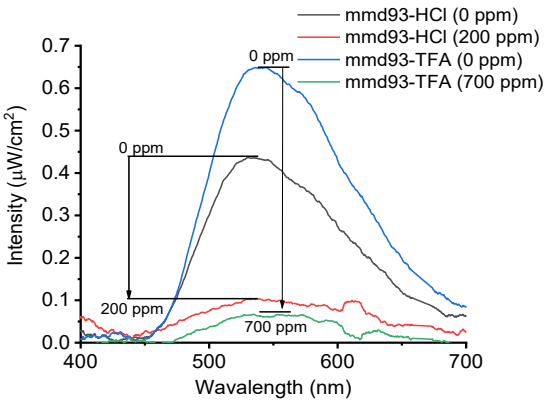


Figure 5. Full spectra of modified compounds before and after interaction with ammonia.

Conclusions:

Investigated compounds show PL response for ammonia. Sensor range, senor response time calculated for interaction with ammonia vapors. Compounds show promising results for detection of ammonia vapors at room temperature, what is applicable for food packaging applications. Further studies will be provided to optimize the sensor performances (sensitivity, selectivity, limit of detection).

References:

[1] H. Vasconcelos, J.M.M.M. de Almeida, A. Matias, C. Saraiva, P.A.S. Jorge, L.C.C. Coelho, Detection of biogenic amines in several foods with different sample treatments: An overview, Trends Food Sci Technol 113 (2021) 86–96. https://doi.org/10.1016/J.TIFS.2021.04.043.

[2] A. Verma, R. Gupta, A.S. Verma, T. Kumar, A review of composite conducting polymer-based sensors for detection of industrial waste gases, Sensors and Actuators Reports 5 (2023) 100143. https://doi.org/10.1016/J.SNR.2023.100143.

[3] K. Leduskrasts, A. Kinens, E. Suna, The emission efficiency of cationic solid state luminophores is directly proportional to the intermolecular charge transfer intensity, Chemical Communications 59 (2023) 6905–6908. https://doi.org/10.1039/D3CC01674A.

Acknowledgements:

We acknowledge the project *'Design of pyridinium luminophore structural and optical properties for tailored sensor response', LU-BA-PA-2024/1-0040.* The research is financed by the Recovery and Resilience Facility project "Internal and External Consolidation of the University of Latvia" (No.5.2.1.1.i.0/2/24/I/CFLA/007).

DOI 10.5162/EUROSENSORS2025/TP23

A Novel IoT System for Highly-specific Gas Sensing Applied to Health Monitoring at Home

Ismael Benito-Altamirano[1,2], Omar Romera-Aller[1], María González-Gómez[1], Miquel Alfaras[3], Zouhair Haddi[3], Anaïs Espinoso[3], José A. Sáez[4] and Cristian Fàbrega[1]
[1] IN2UB, Department of Electronic and Biomedical Engineering, Universitat de Barcelona, 08028 Barcelona, Spain,
[2] e-Health Center, Faculty of Computer Science, Multimedia and Telecommunications, Universitat Oberta de Catalunya, 08018 Barcelona, Spain
[3] NVISION Systems and Technologies SL, 08028 Barcelona, Spain
[4] Sensing&Control SL, 08028 Barcelona, Spain
ismael.benito@ub.edu, ibenitoal@uoc.edu

Summary:
We introduce a novel low-power IoT system for highly-specific gas sensing applied to home health monitoring. The system integrates environmental sensors and one-pixel colorimetric gas sensors to detect indoor pollutants like CO2 and formaldehyde. These colorimetric sensors, based on dyes, enable precise gas measurements. The system offers real-time data collection and transmission, providing a scalable, non-intrusive solution for continuous monitoring. Although focused on health applications, the system's design is versatile, allowing integration into a variety of IoT-based contexts.

Keywords: IoT system, colorimetric sensors, gas sensing, low-power, home health monitoring

Introduction

In this work, we introduce a low-power IoT system designed for highly-specific gas sensing applied to home health monitoring. We leveraged compact, energy-efficient components, including one-pixel colorimetric gas sensors, environmental sensors, and an ESP32 microcontroller. Our system aimed to provide continuous real-time monitoring of indoor pollutants, such as CO2 and formaldehyde, to assist healthcare providers in remote health assessments[1]. We focused on minimizing power consumption while ensuring precise and reliable measurements, making the system suitable for deployment in home environments.

System Architecture

Our system was built around the MAX86916 OnePixel sensors, which are photo-diode sensors with red, green, blue, and infrared LED illuminations. Such photonic devices had provided good results for the colorimetric readout of gasometric dyes[2] in the past [3]. These sensors were paired with the well-known BME680 sensors, capable of measuring air quality, temperature, humidity, and pressure. Following these, our system integrated several key components, mainly the ESP32 microcontroller, a low-power, dual-core microcontroller with integrated Wi-Fi and Bluetooth capabilities. Next, we used the CP2102N USB-to-UART controller for USB communication and the MCP73831T lithium-ion battery charging IC for battery management. For data storage, we incorporated a standard microSD card slot. Time synchronization and accurate time-keeping were handled by the PCF8523TS RTC module. The device also featured a RPi A-compliant socket for connecting a screen, enabling user interaction and feedback. To ensure optimal gasflow near to the colirimetric dyes, the system included MAX6650 IC-based fan control circuitry. Fig. 1 shows the designed placement for the system in a board. Finally, the system was designed to connected by a REST API to a health monitoring at home cloud [4].

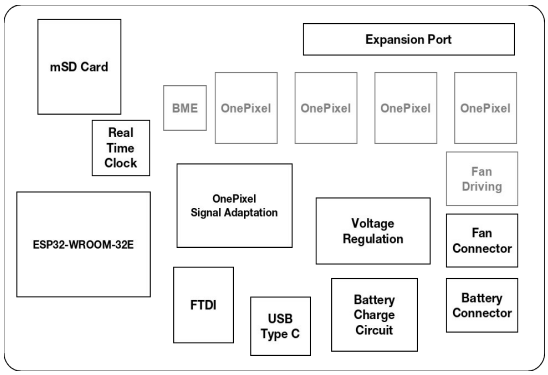


Fig. 1. The design of our IoT-system for highly-specific gas sensing. Black/gray colors represent different layers of PCB placement.

Results

We iterated the board design twice, addressing specific design improvements with each version. Fig. 2 and Fig. 3 presents a Dolfins Board (rev1.1) from the last fabrication batch, which is the size of a credit card, e.g. 3+3⁄8 in × 2+1⁄8 in, or approx. 8.5 cm × 5.4 cm.

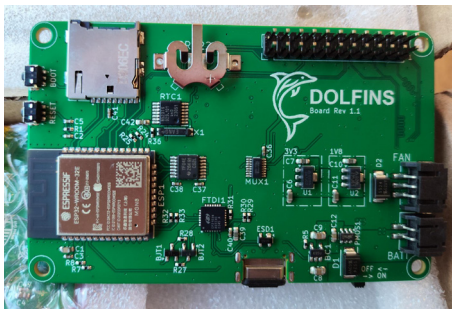


Fig. 2. Front of the fabricated board of the system (DOLFINS Board rev1.1), displaying several components of the board, such as the ESP32 microcontroller, the SD card, the RTC subsystem and all the power and communication subsystems.

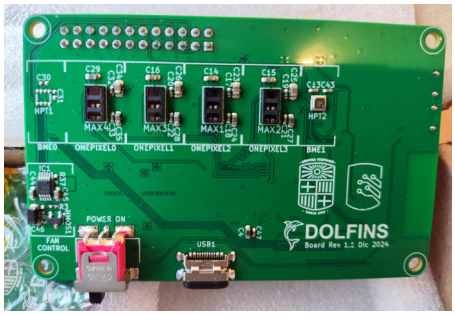


Fig. 3. Back of the fabricated board of the system (DOLFINS Board rev1.1), displaying several components of the board, such as the four MAX86916 One-Pixel sensors, one soldered BME680 environmental sensor and the fan control subsystem.

As power consumption was a key focus for us, over these last version of our system boards we measured the system's power draw in various operating modes, including sensor readings, Wi-Fi transmission, and idle states. The results, shown in the provided power consumption graph (Fig. 4), demonstrated the system's ability to operate efficiently with minimal energy. The minimal consume was found, as expected, when the device was configured in an IDLE state, a wake-up by RTC stage, where the device presented only a consumption around 100mW. Environmental and optical sensors displayed a consumption in the range of 300-400mW. Finally, usage during sensor and Wi-Fi communication activities revealed distinct peaks, around 750mW, when the device is communicating, but returning to the 350mW expected for working mode of the device, indicating efficient power management. Measurements were performed using a Dolfins 1.1 board powered by an Agilent B2912A SMU, which also recorded current and voltage through SCPI-controlled Python scripts. Instantaneous power was calculated and averaged with a 100-point rolling mean, synchronizing device activity using a custom firmware fork to isolate each functional mode.

All in all, the system has demonstrated a cost-effective, low-consumption approach for gas sensing at home. Further results will include obtaining laboratory data from the gasometric dyes in lab environments [2] and 'real data' in a simulated home environment with actors performing routine actions simulating a home-living scenario.

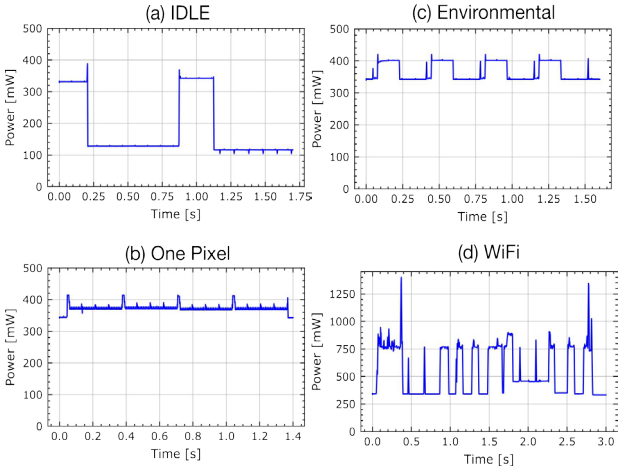


Fig. 4. Power consumption profiles for the Dolfins Board (rev1.1) under different operational modes: (a) Idle mode, (b) One-pixel sensor activity, (c) Environmental sensor activity, (d) Wi-Fi communication. The plots show the variation in power consumption over time for each mode.

References

[1] Eurostat. Ageing Europe — Looking at the Lives of Older People in the EU. Publications Office of the European Union, Luxembourg, 2020 edition, 2020. Manuscript completed in September 2020.

[2] M. González-Gómez et al., "Ultra Low-Cost and Selective Water-Based Colorimetric Ink for Indoor CO2 Monitoring," IEEE Sensors Journal, vol. 25, no. 8, 2025.

[3] C. Driau, et al., "How to implement a selective colorimetric gas sensor with off-the-shelf components," Sensors and Actuators B: Chemical, 293:41–44, 2019.

[4] I. Benito-Altamirano, et al., "When Colorimetry Meets the Cloud: IoT-Enabled Health Monitoring at Home via Highly-Specific Gas Sensing," in Advanced Information Networking and Applications, Springer Nature, Cham, 2025, pp. 1–11.

Acknowledgements

Authors acknowledge the support from ACCIO (Innotec 2021 ACE034/21/000057). I.Benito-Altamirano acknowledges the support from MCIN (PID2022-138721NB-I00) Spain.

DOI 10.5162/EUROSENSORS2025/TP24

Development of wafer singulation technique for MEMS and MOX gas sensors using 355 nm UV laser ablation process

Serguei Stoukatch, Francois Dupont, Jean-Michel Redouté
Microsys lab, Department of Electrical Engineering and Computer Science,
Liege University, Allée de la Découverte 10, 4000 Liège, Belgium,
Corresponding Author's e-mail address: serguei.stoukatch@uliege.be

Summary:
This work presents a 355 nm UV laser ablation process for singulation of silicon wafers. The process may be suitable for singulation of wafers that are sensitive to water and particle contamination such as specific MEMS and MOX micro-hotplate gas sensors. Conventional dicing using a rotating blade and constant water flow can damage and contaminate delicate structures and functional layers. In contrast, the proposed UV laser method requires no liquids, minimizes particle generation near the dicing street, and offers a cleaner, safer alternative for singulating sensitive wafers.

Keywords: UV laser ablation, laser micro-processing, wafer singulation technique, MEMS and metal-oxide (MOX) micro-hotplates gas analyzer, assembly gas sensors, alternative wafer singulation technique.

Introduction

A large majority of silicon wafers [1] are singulated using a sawing process that consists in mechanical cutting of the silicon wafer by a diamond blade rotating typically from 30,000 to 60,000 rpm, and with a feeding speed between 1 and 100 mm/s. The width of the dicing blade usually ranges between 20 and 200 µm, defining the width of the dicing kerf. This mechanical cutting process generates silicon dust and employs a high-pressure water flow directed into the dicing area to remove said dust while simultaneously cooling down the blade and the wafer. The process works very well on the majority of CMOS ICs and is successfully extended to MEMS-wafers. However, the presence of high-pressure water and the unavoidable occurrence of silicon dust generated during sawing imposes additional limitations on this process' applicability. For example, the high-pressure water can mechanically damage movable parts of MEMS devices such as beams, micro-mirrors, RF switches and micro-heaters of metal-oxide (MOX) micro-hotplates gas analyzers. Additionally, silicon dust can contaminate the micro-features of these components. Specifically, in the case of MOX-gas sensors, the sensing materials deposited on the micro-hotplate can be also affected by water and silicon dust. It has been previously shown [2] that silicon wafers can be ablated using various laser techniques, but extensive research is needed to adapt the process to specific applications. In this paper, we investigate the feasibility of singulating silicon wafers using a direct ablation process using a 355nm UV laser.

Materials and methods

The study was carried out on a polished silicon wafer with a diameter of 100 mm, a standard thickness of 525 ± 25µm, crystal orientation (111), N-type, and a resistivity of 0.0020–0.0045 Ohm.cm. We performed the study using a WS Flex optomechanical system from Optec. It is equipped with a Talon 355-12 W (Spectra Physics) 12 W Nb: YAG Q-switched DPSS laser, with a wavelength of 355 nm (UV). The laser beam spot size diameter at target is 8 µm. The laser has several parameters that can be adjusted within the operating range (laser repetition rate, laser spot speed, laser pulse energy, number of repetitions, etc.), however some of them are interdependent. We adjusted the laser speed to obtain a 50% diameter overlap between successive laser spots, as well as other parameters to obtain maximum laser fluence [3]. The variable parameter during the study was the number passes or repetitions, which is the number of times the laser beam moves through the programmed pattern. The chosen pattern is a 5 mm x 5 mm square, which is a typical size for a silicon die or MEMS device. We explored the impact of the number of repetitions starting from 1 to 5,000 (0, 10, 20, 50, 100, 500, 1000, 2000, 5000 and 10000). Using 1000 or more repetitions, a complete cut of a 525 µm thick silicon wafer was achieved.

Results

We performed the analysis and characterization of the laser ablation process. We investigated singulated dies and areas of the wafer in proximity of the laser cut by means of optical inspection

using a visible light optical micro-scope Leica Z6APO and performed profilometric scanning using a stylus type profilometer DektakXT from Bruker. The kerf width is about 30-40 µm and the area near to the kerf has specific features originated by the laser processing. They have distinct hard ridges with an average height of 5-7 µm, and a width (a1 and a2) extending up to 10 µm (Fig.1).

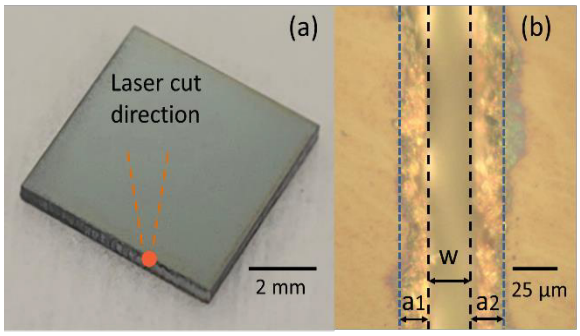


Fig. 1. An individual singulated die (a), a top sideview of the laser cut and area affected by the laser processing (b), where w is the kerf width, and a1 and a2 are the widths of the left and right area affected by the laser processing.

Outside of this area, the surface remains smooth with average roughness of 0.02 µm, which is typical for an unprocessed wafer. The nature of these ridges remains to be studied, but they are likely formed from silicon evaporating during laser ablation and re-depositing on the surface. The more laser passes, the wider the area next to the laser kerf affected by the laser processing. Remarkably, we did not detect any chipping near the laser cut, which typically occurs during a conventional saw dicing process.

We have also analyzed the sidewall of singulated silicon dies, presented in Fig.2.

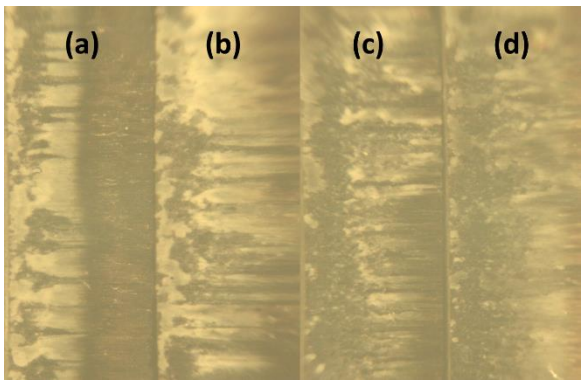


Fig. 2. Sidewall microscopic observation of laser ablated wafers using 1000 (a), 2000 (b), 5000 (c) and 10000 (d) passes. Laser cut direction from right to left.

We characterized the sidewall roughness in terms of R_a and R_q (roughness average and root mean square roughness correspondingly). The results are presented in Table 1.

Tab. 1: Sidewall roughness versus number passes.

Passes	# *10^3	1	2	5	10
Rough-ness	R_a, µm	0.45	0.85	1.49	1.84
	R_q, µm	0.54	0.99	1.74	2.14

The roughness variation is most likely due to the laser induced damage along the cut sur-face. The more laser passes, the rougher sur-face of the sidewall. Despite this, the sidewall surface is smoother than that obtained by the saw dicing process and does not exhibit chipping (neither topside nor back-side chipping), which is typically around 5 - 10 µm under optimized saw dicing process parameters with a dicing kerf of 50-60 µm wide.

In our study, we demonstrated that it is possible to singulate a silicon wafer into individual dies using a UV laser. The 1000 laser passes (repetitions) allow to obtain a repeatable and good quality full through-cut on a 525 µm thick silicon wafer. This results in less damage (sidewall and area near the laser cut) compared to a conventional saw dicing technique, and a smaller kerf width. Meanwhile, various technical challenges remain to be solved. The laser dicing process must be further optimized to increase processing speed and reduce material redeposition.

References

[1] S. Stoukatch, F. Dupont and J. -M. Redouté, Advanced Wafer Singulation Techniques for Miniaturized Metal-oxide (MOX) Micro-hotplates Based Gas Analyzer,2024 IEEE 10th Electronics System-Integration Technology Conference (ESTC), Berlin, Germany, 2024, pp. 1-8, doi: 10.1109/ESTC60143.2024.10712018.

[2] M. R. Marks, K.Y. Cheong, Z. Hassan, A review of laser ablation and dicing of Si wafers, PrecisionEngineering,73,377-408, 2022, doi: 10.1016/j.precisioneng.2021.10.001.

[3] F. Dupont, S. Stoukatch, P. Laurent, S. Dricot, M. Kraft, 355 nm UV laser patterning and post-processing of FR4 PCB for fine pitch components integration, Optics and Lasers in Engineering, 100C (2018) pp. 186-194.; doi: 10.1016/j.optlaseng.2017.08.014.

Acknowledgements

The work was fully funded by the European framework program HORIZON-CL4-2023-RESILIENCE-01-33 - Smart sensors for the Electronic Appliances market (RIA), 101130159 – AMUSENS. This research paper was inspired by consortium members during the preparation and implementation of the AMUSENS project.

DOI 10.5162/EUROSENSORS2025/TP25

Response of Silicon Nanowire Arrays to Humidity and Ammonia

M.T. Sultan[1], E. Fakhri[1], P. Powroznik[2], A. Kazmierczak-Balata[2], W. Jakubik[2], A. Manolescu[1], and H.G. Svavarsson[1]
[1] Department of Engineering, Reykjavik University, 102 Reykjavik, Iceland
[2] Institute of Physics CSE, Silesian University of Technology, Konarskiego 22B, 44-100 Gliwice, Poland
Corresponding Author's e-mail: muhammads@ru.is, Anna.Kazmierczak-Balata@polsl.pl

Summary: Ammonia (NH_3) is a corrosive gas that can pose significant risks to human health, even at low concentrations. Its presence in exhaled breath can also serve as an indicator of various health conditions. This study demonstrates that silicon nanowires (SiNWs) exhibit high sensitivity to NH_3, with notably improved performance in humid environments. Incorporation of tungsten trioxide (WO_3) nanoparticles further enhances the sensor's sensitivity and accelerates its response time under a range of humidity conditions. These findings advance the development of robust, simple, and efficient NH_3 sensors, with potential applications in both environmental monitoring and medical diagnostics.

Keywords: SiNW, gas sensing, ammonia, humidity

Background, Motivation and Objective

Silicon nanowires (SiNWs) have gained significant interest in gas sensing due to their high surface-to-volume ratio, excellent electrical properties, and straightforward fabrication process. Their unique nanoscale structure enhances interaction with target gases, making SiNWs ideal candidates for the development of sensitive and selective sensors[1].

Ammonia(NH_3) is a toxic reducing gas, and prolonged exposure can pose serious health risks. Additionally, it is recognized as a potential biomarker for specific diseases when detected in exhaled breath. Despite their promise, developing highly sensitive and selective NH_3 sensors that perform efficiently in humid environments remains a significant challenge. Humidity plays a crucial role in sensor performance, as moisture can substantially affect the adsorption and desorption of gas molecules on the sensing surface.

In this work, we investigate the gas-sensing behavior of SiNWs in response to NH_3. The fabricated SiNW structures exhibit a strong response to NH_3, with notable improvements in sensitivity under humid conditions. Furthermore, we have demostrated the humidity sensing performance of SiNWs decorated with tungsten trioxide (WO_3) nanoparticles. This modification resulted in a promising response, particularly under varying humidity levels. The findings presented in this study contribute to the ongoing development of highly efficient ammonia sensors, with potential applications in both environmental monitoring and medical diagnostics.

Description of the New Method or System

The silicon nanowires (SiNWs) were fabricated using a metal-assisted chemical etching (MACE) method, which relies on highly anisotropic etching of silicon wafers in contact with metallic nanoparticles, specifically silver (Ag) in this case. An array of Ag nanoparticles is first formed by immersing a *p*-type silicon wafer in an $AgNO_3$ solution. Following deposition, immersing in a solution of hydrofluoric acid (HF) and hydrogen peroxide (H_2O_2), which facilitates the etching process, at regions where the surface is in contact with the Ag nanoparticles. After a predetermined etching time, the process is terminated by transferring the wafer into DI-water to stop the reaction. Remaining Ag residues are removed by subsequent treatment in HNO_3.

This technique produces vertically aligned nanowires with a high surface area, a key feature for gas sensing applications. In our approach, the bare SiNWs were also functionalized with WO_3 nanoparticles for improving humidity sensing. The resulting structure demonstrates exceptional performance, particularly in high-humidity environments. Our findings suggest that this design will not only enhances sensitivity but also maintains reliable functionality under humid conditions, making it a promising tool for the detection of diseases and the monitoring air pollution.

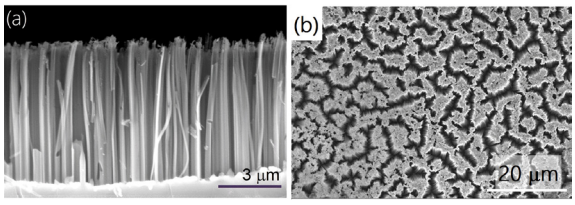


Fig. 1: (a) Cross-sectional, and (b) top-view SEM microgrpaphs of the SiNWs structure before incorporation of WO_3.

DOI 10.5162/EUROSENSORS2025/TP25

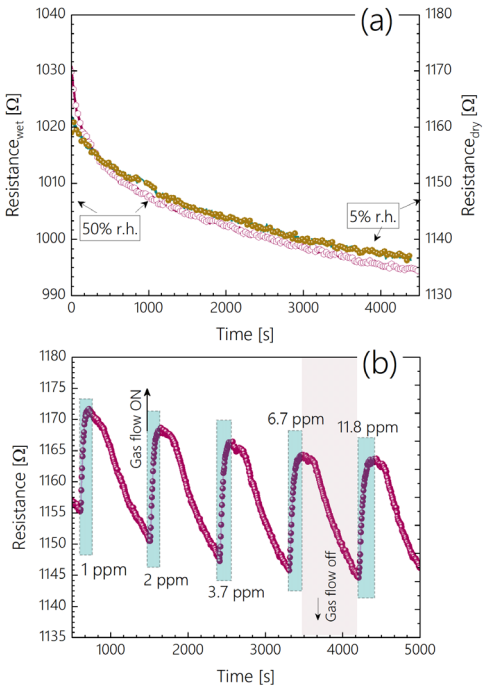


Fig. 2: Results for p-type SiNW response to (a) 5% and 50% r.h. and (b) to NH_3 measured at room temperature in carrier air with 50% r.h.

Results

A cross-sectional and top-view scanning electron microscope (SEM) image of the SiNW sample (Figure 1), shows that the nanowires are approximately 7 μm in length and 50 to 80 nm in diameter. Due to capillary effects and their high aspect ratio, the nanowires tend to bend and bundle together.

The electrical response of a *p*-type SiNW sensor, measured as resistance over time, is shown in Figure 2. Initial tests under varying relative humidity (r.h.) conditions at room temperature demonstrated no significant response to humidity before exposure to NH_3 gas (Figure 2(a)), confirming that humidity does not affect the sensor's baseline performance. Figure 2(b) presents the sensor's response to NH_3 at different concentrations (1 ppm, 2 ppm, 3.7 ppm, 6.7 ppm, and 11.8 ppm) under 50% relative humidity. A stable and pronounced increase in resistance was observed under 50% r.h. humidity. This change in resistance is attributed to the sensing mechanism, where the accumulation of holes at the SiNW surface decreases upon exposure to the reducing gas NH_3. A detailed description of ammonia sensing mechanism can be found elsewhere [2].

After the incorporation of WO nanoparticles, the SiNW sensor, which previously exhibited no response to humidity at both 5% and 50% r.h., became sensitive to moisture. This modification fundamentally altered the sensor's response

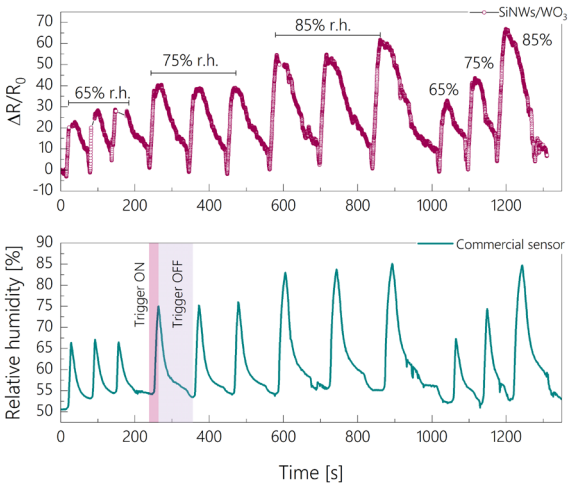


Fig. 3: Relative humidity monitored by commercial humidity sensor HTU21D (bottom plot) and the corresponding change in resistance measured over SiNWs/WO_3 structure (upper plot).

characteristics, enabling independent detection of both humidity and NH_3. Compared to previously reported structures, such as Si/WO and SiNWs/WO_3 [3, 4], the our structure demonstrate enhanced sensitivity and faster response times. Figure 3 illustrates the resistance over time for these modified structures. Current efforts are focused on optimizing the distribution of the nanoparticles to prevent agglomeration, which could negatively impact sensor performance. Once uniform nanoparticle distribution is achieved, the sensing capabilities will be systematically evaluated across a range of concentrations, underscoring the potential of these sensors for NH_3 detection in humid environments, with applications in medical diagnostics and air quality monitoring.

References

[1] M. Akbari-Saatlu, M. Procek, C. Mattsson, G. Thungström, H.-E. Nilsson, W. Xiong, B. Xu, Y. Li, and H. H. Radamson, "Silicon Nanowires for Gas Sensing: A Review," *Nanomaterials*, vol. 10, no. 11, p. 2215, 2020.

[2] M. T. Sultan, E. Fakhri, P. Powroznik, A. Manolescu, W. Jakubik, A. Kazmierczak-Balata, and H. G. Svavarsson, "Silicon nanowire-based ammonia gas sensor with enhanced response at elevated humidity levels," *Semiconductor Science and Technology*, vol. 40, no. 3, p. 035011, 2025.

[3] H. Mhamdi, R. Zaghouani, and T. e. a. Fiorido, "Study of n-WO_3/p-porous silicon structures for gas-sensing applications," *J Mater Sci: Mater Electron*, vol. 31, pp. 7862–7870, 2020.

[4] Y. F. Dong, L. Y. Li, W. F. Jiang, H. Y. Wang, and X. J. Li, "Capacitive humidity-sensing properties of electron-beam-evaporated nanophased WO_3 film on silicon nanoporous pillar array," *Physica E: Low-dimensional Systems and Nanostructures*, vol. 41, no. 4, pp. 711–714, 2009.

DOI 10.5162/EUROSENSORS2025/TP26

Vacancy-Engineered MoS_2 for Selective CO Sensing: A DFT Perspective on Intercalation

Dominik Florjan [1], Piotr Radomski[2] and Maciej J. Szary[1]
[1] Institute of Physics, Poznan University of Technology, ul. Piotrowo 3, 61-138 Poznan, Poland
[2] Institute of Materials Research and Quantum Engineering, Poznan University of Technology, ul. Piotrowo 3, 61-138 Poznan, Poland
dominik.florjan@doctorate.put.poznan.pl

Summary: Molecular intercalation holds significant implications for utilizing 2D materials in applications like gas detection and catalysis, yet it remains unexplored. Using density functional theory (DFT), this study investigates the intercalation of CO and CO_2 into MoS_2 and the role of sulfur vacancies. CO intercalation is unfavorable in pristine MoS_2, while CO_2 intercalation is marginally favorable at high coverages. Sulfur vacancies enable selective CO intercalation by incorporating CO into vacancy sites, facilitating catalytic CO-to-CO_2 conversion without affecting CO_2 intercalation. This highlights the potential of defect engineering in MoS_2 for gas detection and catalytic applications.

Keywords: Carbon monoxide conversion, CO, CO_2, Single-atom vacancy doping, Density functional theory

Introduction

The strategic manipulation of interlayer spaces in two-dimensional (2D) materials via molecular intercalation offers compelling routes for tailoring electronic, catalytic, and sensing properties [1, 2, 3]. Molybdenum disulfide (MoS_2), a prototypical transition metal dichalcogenide, stands as a prime candidate for such functionalization, particularly concerning interactions with small gas molecules relevant to environmental monitoring and catalysis, such as carbon monoxide (CO) and carbon dioxide (CO_2). However, a fundamental understanding of the thermodynamics governing intercalation and the influence of intrinsic defects remains crucial for realizing practical applications.

Methodology

This study investigates the intercalation of carbon monoxide (CO) and carbon dioxide (CO_2) into bilayer molybdenum disulfide (MoS_2) using first-principles Density Functional Theory (DFT) simulations within the QUANTUM ESPRESSO framework. The calculations employed the projector augmented-wave (PAW) method with the Perdew-Burke-Ernzerhof (PBE) exchange-correlation functional, incorporating Grimme's D3 van der Waals corrections (PBE+D3) to accurately describe weak interactions. Bilayer MoS_2 models were constructed using 3×3, 4×4, and 5×5 supercells to examine a range of molecular coverages (0.462 to 10.272 molecules/nm^2). Both pristine MoS_2 bilayers and systems containing single-atom sulfur vacancies were simulated to assess the impact of defects.

Results

This contribution presents a comprehensive theoretical investigation, into the intercalation behavior of CO and CO_2 within bilayer MoS_2. We systematically evaluate the energetic favorability of intercalation for both molecules in pristine MoS_2 structures and, critically, assess the impact of introducing sulfur vacancies on this process.

Our calculations reveal distinct behaviors for CO and CO_2 in pristine MoS_2. Intercalation of CO is found to be energetically unfavorable across the range of molecular coverages studied, suggesting limited interaction within the van der Waals gap of defect-free bilayers. In contrast, CO_2 intercalation demonstrates marginal thermodynamic favorability, but only becomes notable at higher molecular concentrations within the interlayer region.

The introduction of sulfur vacancies introduces a profound selectivity into the system. We demonstrate that vacancies act as potent facilitators for CO intercalation, significantly lowering the intercalation energy, rendering the process energetically favorable, as seen in Figure 1a. The mechanism involves the incorporation of a CO molecule directly into the vacancy site within one of the MoS_2 layers, which significantly lowers the system's energy and renders the overall intercalation process favorable. Furthermore, our results suggest a potential pathway for vacancy-enabled catalytic conversion of CO to CO_2 within the intercalated structure (Figure 2e). Strikingly, the presence of these same sulfur vacancies has a negligible effect on the thermodynamics of CO_2 intercalation compared to the pristine system.

These findings highlight the pivotal role of defect engineering in modulating the gas interaction properties of MoS_2. The demonstrated ability of sulfur vacancies to selectively promote CO intercalation, while remaining relatively inert towards CO_2, offers significant implications for the development of advanced MoS_2-based materials. Potential applications include enhanced sensitivity and selectivity in combustion gas sensors,

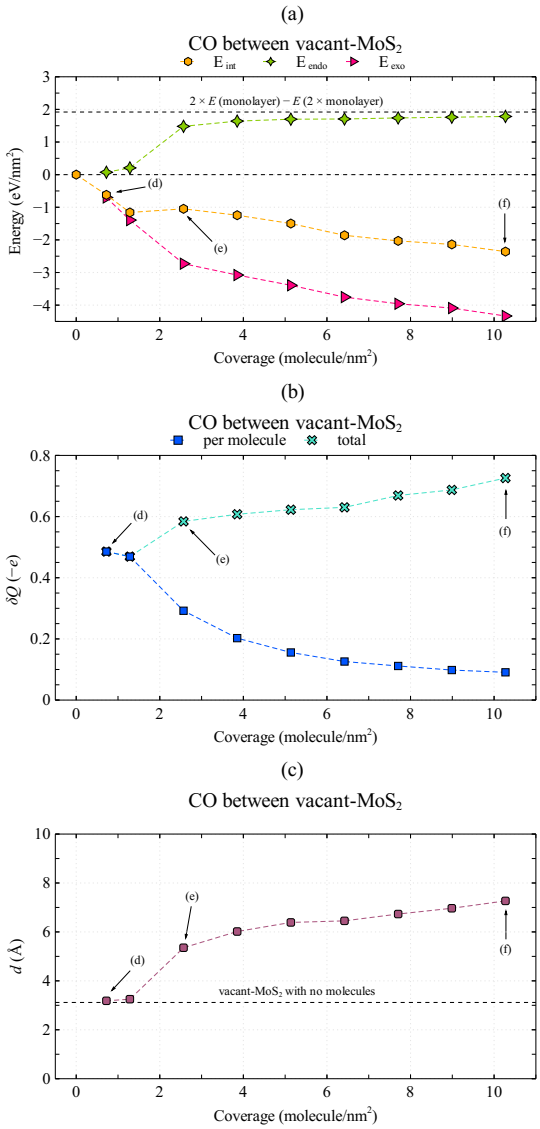


Fig. 1: Graphs characterizing CO intercalated between one pristine and one vacancy-doped MoS_2 monolayer: (a) intercalation energy with endothermic and exothermic contributions, (b) total charge transfer and charge transfer averaged per molecule, (c) distance between relaxed layers, all plotted as a function of sheet coverage.

targeted CO capture systems, and novel catalytic platforms. This work underscores the potential of leveraging intrinsic defects as a design parameter for fine-tuning the functionality of 2D materials for specific molecular interactions.

Acknowledgments

This work was funded by the Ministry of Education and Science in Poland within the project ”Perły Nauki” under Grant No. PN/01/0058/2022. Calculations reported in this work have been performed at the Interdisciplinary Center for Mathematical and Computational Modeling (ICM) of the University of Warsaw under Grant No. G96-1893.

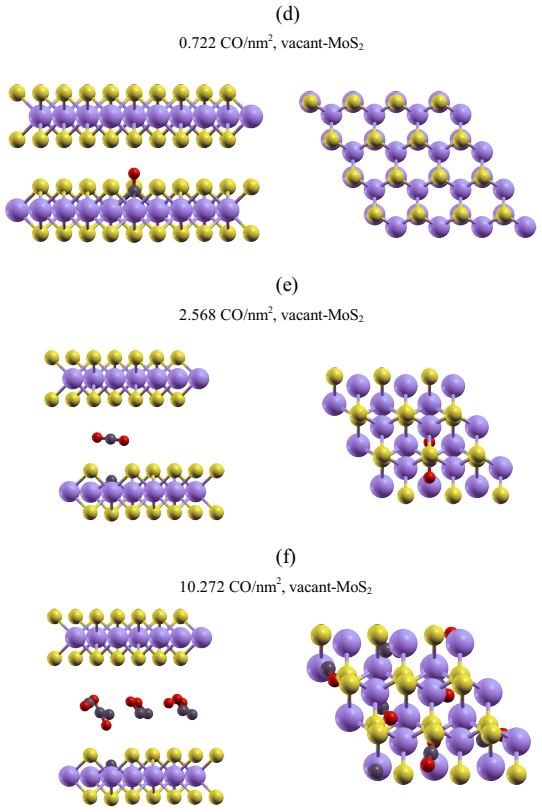


Fig. 2: Subfigures (d), (e), and (f) contain selected relaxed configurations, corresponding to the points marked with arrows in Figure 1.

References

[1] J. Wan, S. D. Lacey, J. Dai, W. Bao, M. S. Fuhrer, and L. Hu, “Tuning two-dimensional nanomaterials by intercalation: materials, properties and applications,” *Chemical Society Reviews*, vol. 45, no. 24, pp. 6742–6765, 2016.

[2] I. V. Chepkasov, M. Ghorbani-Asl, Z. I. Popov, J. H. Smet, and A. V. Krasheninnikov, “Alkali metals inside bi-layer graphene and mos2: Insights from first-principles calculations,” *Nano Energy*, vol. 75, p. 104927, 2020.

[3] A. Nijamudheen, D. Sarbapalli, J. Hui, J. Rodríguez-López, and J. L. Mendoza-Cortes, “Impact of surface modification on the lithium, sodium, and potassium intercalation efficiency and capacity of few-layer graphene electrodes,” *ACS applied materials & interfaces*, vol. 12, no. 17, pp. 19393–19401, 2020.

DOI 10.5162/EUROSENSORS2025/TP27

On the design of a magnetically driven quasi-static MEMS micromirror

Perla Malagò[1], Clement Fleury[1], Stefano Lumetti[1], Luiz Enger[1], Sara Guerreiro[1], Adrien Piot[1], Anton Lagosh[1]
[1] Silicon Austria Labs GmbH, Europastrasse 12, 9504 Villach, Austria
perla.malago@silicon-austria.com

Summary:
This paper focuses on the design of a magnetic MEMS micromirror featuring linear and non-contact actuation, low-power, and compact size with respect to state-of-the-art magnetic micromirrors. The proposed device operates in the low-frequency regime and finds application in satellite and optical communications. The results show that it is possible to realize a compact micromirror exhibiting performance surpassing the state-of-the-art micromirrors employed in similar application fields.

Keywords: Magnetic MEMS, micromirrors, fast prototyping, satellite communications, quasi-static applications

Introduction and motivation

Nowadays, magnetic MEMS are used for a wide range of applications, including micromirrors, accelerometers, gyroscopes, torsion sensors and gradiometers [1, 2]. Usually, magnetic MEMS including permanent magnets and micro-coils offer functionalities like sensing, actuation and energy harvesting and are employed in several application fields such as automotive, biomedical, space, and IoT [3-4]. This work focuses on the design of a magnetic MEMS micromirror. On one hand, state-of-the-art magnetic MEMS micromirrors feature low power consumption, fast response times and large scan angles. On the other hand, the integration of permanent micromagnets suitable to produce the magnetic fields required for the generation of large electromagnetic actuation forces remains a critical challenge that makes most of the magnetic MEMS micromirrors bulky and expensive compared with their counterparts based on piezoelectric, electrostatic and thermoacoustic transduction mechanisms [5]. Here, the Authors propose a magnetic micromirror featuring low power consumption, large scan angles, downscaled size, and highly linear response. Such a device is suitable for space applications like optical or satellite communications, where state-of-the-art micromirrors rely on bulky structures and an actuation mechanism based on high-power electric motors.

System description

The system includes an array of permanent magnets as well as micro-coils fabricated on the suspended micromirror plate around the reflective area (see Fig. 1).

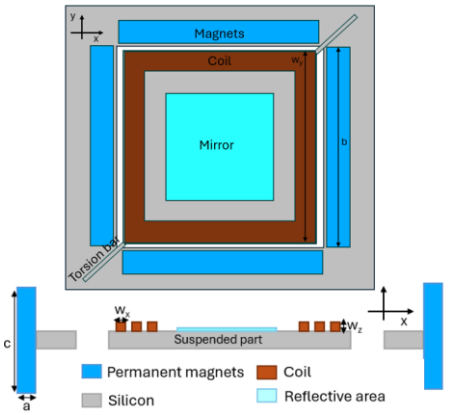


Fig. 1. Schematic representation of the magnetic MEMS micromirror together with its critical components and the corresponding cross-section.

The MEMS micromirror exploits the Lorentz force arising from the interaction of the electrical current through the micro-coils with the magnetic field generated by the permanent magnets to actuate and control the motion of the suspended region. The system and its critical components are described by the following parameters: magnet width (a), length (b) and thickness (c), and magnetization vector (m_x, m_y, m_z); number coil turns (n_w), coil wire thickness (w_z), width (w_x) and length (w_y), electric current flowing across the coils (i). For the envisioned application, the reflective area has in-plane dimensions of 5 x 5 mm^2 while the size of the entire suspended region including the coil system is 9 x 9 mm^2. The system is designed to fulfill the following target

specifications: power losses (PL) < 400 mW, field of view (FoV) of ±15°, and low-frequency operation (< 100 Hz).

Methods

The design of the magnetic MEMS micromirror is carried out by combining two different approaches: finite-element methods for mechanical simulations and analytical calculations for the design of the magnet-coil system. Mechanical simulations are performed using the COMSOL Multiphysics software [6] to determine the minimum pressure required to achieve FoV = ±15°. Electromagnetic simulations are based on the open-source Python package "Magpylib-force" that allows for fast (microsecond) computation of magnetic fields and electromagnetic force between magnets and current-carrying wires [7], thereby enabling to the time-efficient investigation of a wide range of system parameters.

Design and simulation: results

The results of the mechanical simulations show that a pressure P_t = 150 N/m^2 on the micromirror plate is required to achieve FoV = ±15°. Several system parameter sets (*a*, *c* and *i*) satisfying the target requirements and enabling the generation of an electromagnetic actuation force corresponding to the required P_t are identified via electromagnetic simulations: the results are summarized in Fig. 2(a) and (b) for a fixed coil design having n_w = 24, w_z = 20 µm, w_x = 20 µm and w_y = 8 mm corresponding to a total resistance R = 33.1 Ω.

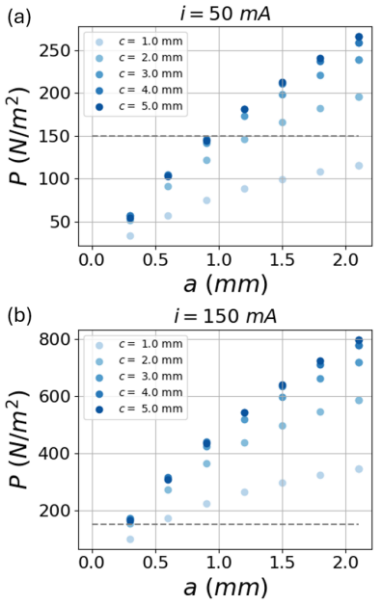


Fig. 2. Pressure as a function of the magnet width (a) for different magnet height (c) for an electrical current flowing in the coil of (a) i = 50 mA and (b) i = 150 mA. The dashed grey lines indicate P_t.

Fig. 2(a) shows that, for *i* = 50 mA and PL = 40 mW, it is possible to achieve P > P_t by adopting system designs where *a* > 1 mm and *c* > 2 mm. Fig. 2(b) demonstrates that, by increasing the coil current to *i* = 150 mA (PL = 370 mW), P_t can be achieved by reducing the permanent magnet size to *a* > 0.5 mm and *c* > 1 mm, which opens the possibility of realizing a more compact micromirror with equal performances.

Conclusions

This paper shows that it is possible to design a compact magnetic MEMS micromirror for low-frequency applications by combining mm-size permanent magnets and micro-coils. Sets of system parameters fulfilling the target performance requirements are determined. Future work will be devoted to microfabricating the magnetic micromirror and to testing its performance as well as to including magnetic field sensors suitable for closed-loop device operation.

References

[1] D. Niarchos, Magnetic MEMS: key issues and some applications, *Sensors and Actuators A: Physical*, 109 1–2, 166-173 (2003); doi: 10.1016/j.sna.2003.09.010

[2] O. Cugat, J. Delamare, G. Reyne, Magnetic microactuators and systems, *IEEE Transactions on magnetics* 39.6: 3607-3612 (2003); doi:10.1109/TMAG.2003.816763

[3] S. Lumetti, P. Malagò, D. Spitzer, S. Zaruba, M. Ortner, Computationally Efficient Magnetic Position System Calibration, *Engineering Proceedings*, 2(1), 72 (2020); doi: 10.3390/ecsa-7-08219

[4] J. Yunas, B. Mulyanti, I. Hamidah, M. Mohd Said, R. E. Pawinanto, W. A. F. Wan Ali, ... & Yeop Majlis, B. Polymer-Based MEMS Electromagnetic Actuator for Biomedical Application: A Review, *Polymers*, 12(5), 1184 (2020); doi: 10.3390/polym12051184

[5] M Ahmad, M Bahri, M Sawan, MEMS Micromirror Actuation Techniques: A Comprehensive Review of Trends, Innovations, and Future Prospects, *Micromachines*, 15.10: 1233 (2024); doi: 10.3390/mi15101233

[6] https://www.comsol.com/, accessed 12.03.2025

[7] P. Malagò, F. Slanovc, M. Ortner, L. Enger, M. Montagnese, P. Smaliukas, J. Bardong, I. Shishkin, C. Novotny, S. Horvath, A. Rusconi and S. Lumetti, Design of magnetic MEMS micro-speakers, *Journal of Physics: Conference Proceedings*, (2025).

Acknowledgements

This work has been supported by Silicon Austria Labs (SAL), owned by the Republic of Austria, the Styrian Business Promotion Agency (SFG), the federal state of Carinthia, the Upper Austrian Research (UAR), and the Austrian Association for the Electric and Electronics Industry (FEEI).

DOI 10.5162/EUROSENSORS2025/TP28

Design and Fabrication of Carbon Black Polymer Composite Based Pressure Sensor Array

Mohammad Ariful Islam Bhuyan, Md Mayen Uddin, Hyeon Cheol Kim
University of Ulsan, Ulsan, South Korea,
hckim08@mail.ulsan.ac.kr

Abstract:
In this paper, we present the unique design, fabrication, and performance analysis of a flexible pressure sensor based on a composite of carbon black and polydimethylsiloxane (PDMS). This proposed sensor is capable of detecting localized pressure with little amount of deformation. It is fabricated using a simple and cost-effective method by dispersing carbon black particles into a PDMS matrix to form a conductive elastomer. The resulting composite exhibits excellent flexibility, mechanical durability, and piezoresistive behavior under varying pressure loads.

Keywords: Flexible, Pressure, Polymer, Piezoresistive, Sensor.

Background, Motivation and Objective

Flexible pressure sensors have garnered significant attention for application in wearable electronics, soft robotics, artificial skin, and health monitoring systems due to their ability to detect subtle mechanical stimuli while maintaining flexibility, durability, and sensitivity. Piezoresistive sensors are especially attractive owing to their simple design, ease of fabrication, and straightforward signal processing.

PDMS is widely employed as a flexible substrate for such sensors due to its favorable mechanical and chemical properties [1]. When combined with conductive fillers like carbon-based materials, PDMS can form piezoresistive composites that effectively convert mechanical deformation into electrical signals. Carbon black (CB), in particular, is a low-cost, conductive filler with high surface area and good compatibility with PDMS, making it a practical alternative to more complex nanomaterials [2][3].

This study presents the design, fabrication, and performance evaluation of a carbon black–PDMS composite pressure sensor array.

Description of the Method

The sensor fabrication process involved mixing the Silicone elastomer base and Curing agent at a 10:1 weight ratio to create a PDMS-based composite. Dimethylsiloxane was used as a base material, combined with a crosslinking agent, methyltrichlorosilane, to enable curing. The mixture was subjected to mechanical shear mixing for approximately 10-15 minutes to ensure uniform dispersion of the crosslinker throughout the matrix. Degassing step lasting 1 hour to remove any trapped air bubbles. This process was repeated to prepare multiple PDMS composite with varying CB content ranging from 5% to 20% by volume. Among these, the composite with 15% of CB exhibited the best performance in terms of piezoresistive response and mechanical integrity.

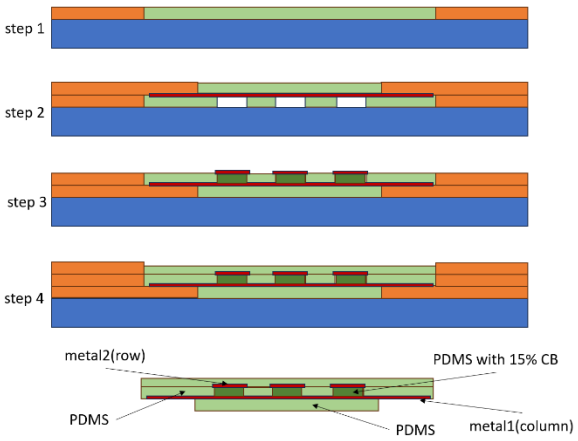


Fig. 1. Fabrication process of the sensor

We followed the proposed sensor fabrication process shown in Fig. 1. After each step, the sample was cured at 100 °C for 1 hour. Fig. 2 shows the fabricated sensor and its bending test. The sensing composite element has a cylindrical shape with a diameter of 3 mm and a thickness of 1 mm. Flexible copper strips were used as metal electrodes.

Results

The fabricated sensor was tested under various applied pressure levels. A cell evaluated at different pressure levels, as shown in Fig. 3. As the

applied pressure increased, the sensor's resistance decreased due to the reduced distance between CB particles caused by the deformation of the PDMS matrix.

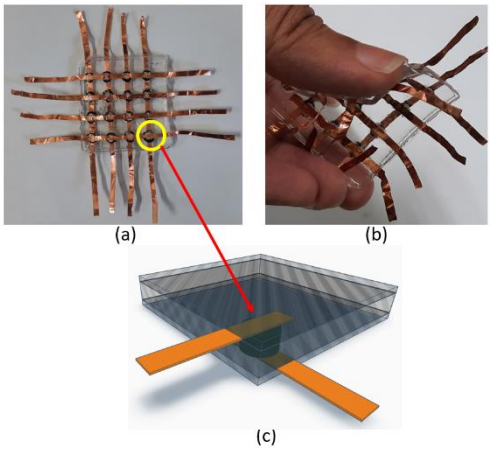


Fig. 2. (a) Fabricated polymer based pressure sensor. (b) Bending test of sensor. (c) Piezoresistive sensor cell.

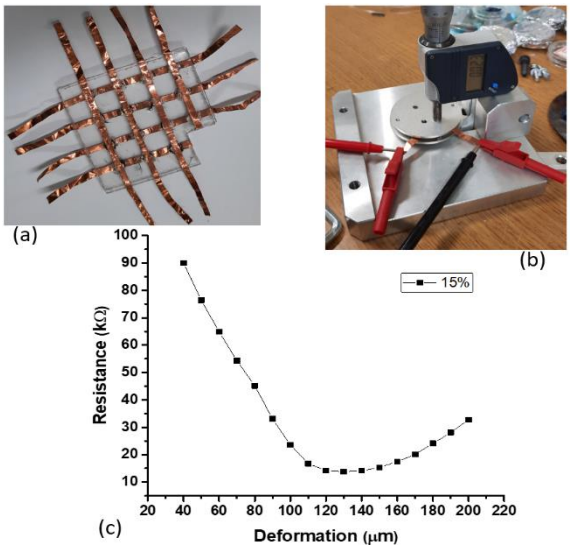


Fig. 3. (a) Sensor cell removed for individual test. (b) Cell test platform with pressure mechanism. (c) Resistance changes because of deformation.

However, beyond a certain pressure threshold, the resistance began to increase. This is attributed to excessive pressure causing particle displacement and strain-induced microstructural changes that disrupt conductive pathways.

Tab. 1: Weight list for sensor testing.

Obs.	Objects Name	Total weight (g)
(a)	Small metal balls	13
(b)	Glue stick	27
(c)	Hollow cylinder	34
(d)	Metal plate	150
(e)	Glass bottle	195
(f)	Orange	270

The entire sensor array was tested under different weight induced pressure levels. The list of applied weights is provided in Table 1, and the electronic setup along with the $\Delta I/I_0$ (%) response results are shown in Fig. 4.

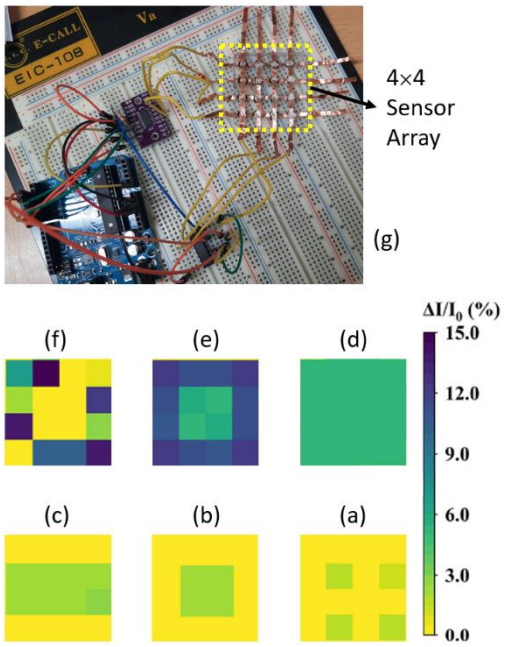


Fig. 4. (a)-(f): $\Delta I/I_0(\%)$ response test under different loading conditions. Loading details shown in Table.1 (g) Sensor testing platform with electronics.

Conclusion

At higher pressure levels, a slight increase in resistance was observed, likely due to particle displacement and structural strain within the matrix. The sensor array demonstrated good sensitivity, repeatability, and stability across a range of pressure conditions.

Acknowledgement

This work was financially supported by Aiobio Co., Ltd. The authors gratefully acknowledge the company's support and contribution to the successful completion of this study.

References

[1] J. Chen *et al.*, "Polydimethylsiloxane (PDMS)-based flexible resistive strain sensors for wearable applications," 2018. doi: 10.3390/app8030345.

[2] Y. Q. Gill, M. S. Irfan, F. U. H. Khan, F. Saeed, H. Ehsan, and A. Shakoor, "Carbon black/nickel hybrid filler reinforced conductive polypropylene composites," *Mater Res Express*, vol. 6, no. 8, 2019, doi: 10.1088/2053-1591/ab1a5d.

[3] D. Ahn, H. J. Choi, H. dong Kim, and S. Y. Yeo, "Properties of conductive polyacrylonitrile fibers prepared by using benzoxazine modified carbon black," *Polymers (Basel)*, vol. 12, no. 1, 2020, doi: 10.3390/polym12010179.

DOI 10.5162/EUROSENSORS2025/TP29

Comprehensive correlative study of post-treated vertically grown ZnO nanowires

Tanisha Bhadauria[1,2], Nicolas Guillaume[1], Celine Ternon[2], Gustavo Ardila[1]
[1]Univ. Grenoble Alpes, Univ. Savoie Mont Blanc, CNRS, Grenoble INP, CROMA, F-38000 Grenoble, France.
[2]Univ. Grenoble Alpes, CNRS, Grenoble INP, LMGP, F-38000 Grenoble, France.
Corresponding Author's e-mail address: gustavo-adolfo.ardila-rodriguez@grenoble-inp.fr

Summary:

This paper presents the fabrication of vertically oriented zinc oxide nanowires (NWs) grown by Chemical Bath Deposition (CBD) and conduct different structural and electrical measurements such as AFM (PFM, SMIM and KPFM) on them. Moreover, we will present the first ever SMIM measurements on ZnO NWs. The correlation of these measurements will provide important information about their performance in piezoelectric transducing applications. **Keywords:** ZnO, piezoelectricity, nanowires, VING, AFM

Background, Motivation an Objective

Emerging energy transducers can gather energy from the surroundings. Solar, thermal, and mechanical energy can be converted into electricity in order to power electronic devices [1]. Mechanical energy is present in our everyday surroundings, such as airflow, noises, and human activity and can be converted into electricity using the piezoelectric effect [2]. The vertical integration of these NWs (also known as VING) is one of the most studied. This structure can also be used in mechanical sensing applications [3]. Vertically grown ZnO NWs as part of the VING structure will be examined in this study.

Novelty

The vertically oriented NWs will undergo different post treatment methods and then multiple AFM, XRD and PL measurements will be conducted on the same sample and correlated, providing important information for structural and piezoelectric properties for piezoelectric transducing applications. AFM measurements include Piezoresponse Force Microscopy (PFM) [4] and Kelvin Probe Force Microscopy (KPFM). In particular, Scanning Microwave Impedance Microscopy (SMIM) measurements will be performed, which have never been done before in this kind of structure. We will also present the study of the effect of different treatments (annealing among others) on these NWs.

A Si wafer covered with a thin layer of Si_3N_4 was used as substrate for the growth of ZnO NWs. A 10 nm layer of chromium followed by 200nm of gold were deposited on the substrate using electron beam evaporation. This is used as bottom electrode in the final device. Then, a texturized film of ZnO (seed layer) was deposited by sol-gel. XRD was conducted to check the correct texturization of the seed Layer. The growth of NWs was carried out using the CBD method at 90 ℃ for 2 hours [5]. The average length of the NWs was 800 nm and the average diameter was 82 nm (See Fig. 1). The as-grown NWs underwent post-treatment processes, which involved vacuum annealing at different temperatures and oxygen plasma exposure for varying durations, followed by subsequent structural and electrical characterization.

Results

To analyse the structural properties of ZnO NWs, XRD was recorded as depicted in Fig. 2. (a) It confirmed the texturization of about 92.3% for the NWs which supports the verticality of ZnO NWs. Defect studies were done using photoluminescence (see Fig. 2b). It shows that in comparison to the as-grown NWs, there was a decrease in the surface defects post-treatment. Local characterization of the NWs was performed using an AFM Icon (BRUKER) in DataCube and PeakForce modes. These modes allow periodic contact measurements with withdrawn in between, enabling contact mode measurements on non-planar materials. DataCube PFM provided the phase and the mechanical displacement of the NWs under electrical stress at 5V and 12kHz. Fig. 3. shows histogram PFM amplitude results extracted from a single NW. From the histrograms, the d_{33} coefficient is evaluated as **4.98 pm/V** for as grown ZnO NWs, **2.82 pm/V** for O_2 Plasma treatment and **4.25 pm/V** for annealing at 300 °C. Preliminary KPFM results can be found in the Fig. 4. The variation of the potential

between NWs could be linked to a non-uniformity of the doping in different NWs. These initial measurements will be compared with results obtained on the samples after different treatments, possibly modifying their doping concentrations. This will provide insight on the piezoelectric performance in correlation to their semiconductor properties. While an enhancement in piezoelectric performance after post-treatment was expected, the present findings indicate a different trend. This could be due to an increase of doping concentration or decrease in surface trap density. The KPFM study indicated significant variances in work function across the samples, supporting the possibility of alterations in both doping and surface conditions. Additional exploration utilizing SMIM could provide more insights in understanding these results.

Illustrations, Graphs, and Photographs

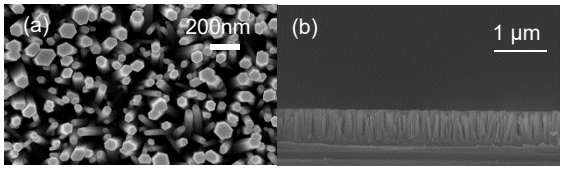


Figure.1. SEM Images of ZnO NWs on Au/Cr/Si_3N_4/Si Substrate (a) Top View (b)Cross Section

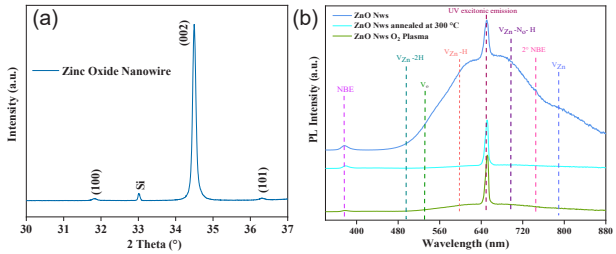


Figure. 2. (a) XRD measurements of as-grown ZnO NWs (b). PL measurements of as-grown and post-treated ZnO NWs

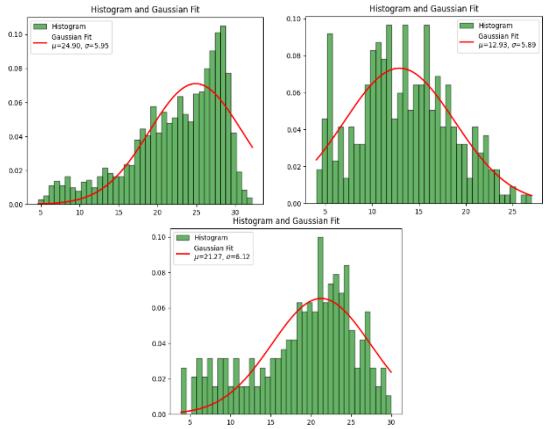


Figure.3. DataCube PFM of NWs (Histogram and gaussian fit of the PFM amplitude on a single NW of (a) of as-grown sample (b) O_2 Plasma treatment, (c) annealing at 300 °C

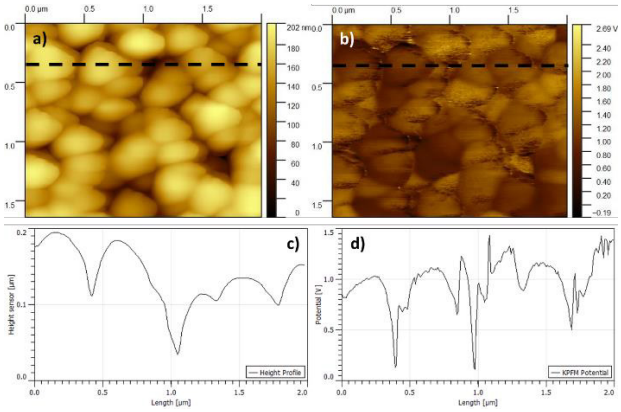


Figure.4. KPFM measurements of NWs (a) Topography (b) Potential (contact potential difference) (c) Cross section of the topography located on the black dash line (d) Cross section of the potential located on the black dash line

References

[1] R. Tao, R. Hinchet, G. Ardila, L. Montès, and M. Mouis, *PRIME 2014: 10th Conference on Ph. D. Research in Microelectronics and Electronics: conference proceedings: June 29th - July 3rd, 2014, Grenoble, France*. IEEE, 2014.

[2] Y. Hu, Y. Zhang, C. Xu, L. Lin, R. L. Snyder, and Z. L. Wang, "Self-powered system with wireless data transmission," *Nano Lett*, vol. 11, no. 6, pp. 2572–2577, Jun. 2011, doi: 10.1021/nl201505c.

[3] S. Lee *et al.*, "Ultrathin nanogenerators as self-powered/active skin sensors for tracking eye ball motion," *Adv Funct Mater*, vol. 24, no. 8, pp. 1163–1168, Feb. 2014, doi: 10.1002/adfm.201301971.

[4] T. Jalabert, M. Pusty, M. Mouis, and G. Ardila, "Investigation of the diameter-dependent piezoelectric response of semiconducting ZnO nanowires by Piezoresponse Force Microscopy and FEM simulations," *Nanotechnology*, vol. 34, no. 11, Mar. 2023, doi: 10.1088/1361-6528/acac35.

[5] T. Demes, C. Ternon, D. Riassetto, V. Stambouli, and M. Langlet, "Comprehensive study of hydrothermally grown ZnO nanowires," *J Mater Sci*, vol. 51, no. 23, pp. 10652–10661, Dec. 2016, doi: 10.1007/s10853-016-0287-8.

Acknowledgements

This work has been supported by the ANR projects LATINO (under grant agreement ANR-21-CE50- 0026) from the French Ministry of Rese

DOI 10.5162/EUROSENSORS2025/TP30

Sputter deposited aluminum nitride for an efficient manufacturing of piezoelectric folded MEMS membranes

Maria-Theresia Becker[1], Dennis Becker[1], Achim Bittner[1], Alfons Dehé[1,2]
[1] Hahn-Schickard-Gesellschaft für angewandte Forschung e.V., Wilhelm-Schickard-Str. 10, 78052 Villingen-Schwenningen, Germany
[2] Georg H. Endress Chair of Smart Systems Integration, Department of Microsystems Engineering – IMTEK, Albert-Ludwigs-Universität Freiburg, Georges-Köhler-Allee 103, 79110 Freiburg, Germany
Maria-Theresia.Becker@Hahn-Schickard.de

Summary:
Folded membranes with high aspect ratio features and vertical sidewalls utilize conformal aluminum nitride (AlN) layers to maximize the active area of MEMS transducer chips [1,2]. This work studies the possibilities and limitations of efficient sputtering to replace the currently used atomic layer deposition (ALD) by a denser, crystalline and faster deposited thin film. Scanning electron microscopy (SEM) analysis of test structures show the successful coverage of features with aspect ratios of up to 12:1 by variation of process parameters such as the working distance and the nitrogen to argon gas flow ratio.

Keywords: 3D membranes; high aspect ratio features; piezoelectric aluminum nitride; reactive magnetron sputtering; MEMS transducer

Introduction

In terms of miniaturization of MEMS devices, a MEMS transducer design with a folded membrane structure was introduced [1,2]. Chip area is used efficiently by lateral actuation of the vertical side walls (SW) of high aspect ratio features. For manufacturing, conformal CVD-processes were used to deposit the mechanical carrier layers, as well as the electrodes and the piezoelectric aluminum nitride (AlN) thin film. The latter is currently deposited by atomic layer deposition (ALD) as it can cover high aspect ratio (AR) trenches with constant film thicknesses [2]. Compared to sputtering, ALD-AlN exhibits a different microstructure leading to less dense and less crystalline films [3,4]. The piezoelectric response of aluminum nitride depends on the crystallinity of the layer [5] and the deposition rate of ALD-ALN is very low [6], this work aims to replace the ALD layer by a more efficient sputtered aluminum nitride. AlN sputtering on vertical SWs has been discussed in literature for free standing structures or edges [7]. In this work sputtering into deep features with high ARs is investigated.

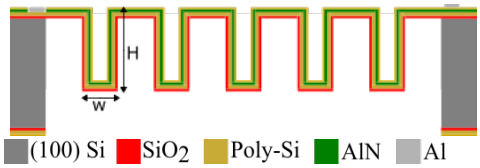


Fig. 1. Folded membrane structure with a conformal piezoelectric layer [2];

Experimental details

For the experimental analysis, trenches with different aspect ratios (AR) from AR1:1 to AR 12:1 are etched into the silicon (Si) (100) substrates with deep reactive ion etching (DRIE). The AR is defined by the height (H) to width (w) of a trench (*Figure 1)*. The structure is covered with 1 µm of n-doped Poly-Silicon (Poly-Si) via low-pressure chemical vapor deposition (LPCVD). AlN layers are deposited in the sputtering device CS730S from von Ardenne. Sputtering parameters for the sputter clean and the deposition process are summarized in Table 1. For the scanning electron microscopy (SEM) analysis, samples are cleaved and film thicknesses at different positions are measured with a Zeiss Crossbeam 550L Scanning electron microscope.

Tab. 1: Sputtering parameters, constant parameters: power = 800 W, pressure = 4 µbar; ISE Sputter Clean at same conditions but in pure Argon

Sample	Working distance in mm	Nitrogen content in %
AlN 1	71	22.2
AlN 2	78	22.2
AlN 3	85	22.2
AlN 4	71	47.2
AlN 5	71	73.6

Results and discussion

This work evaluates the possibilities of a conventional sputtering system to cover the sidewalls of

high aspect ratio features with AlN. Process parameters from Tab.1 are chosen to find the main trends and levers to achieve that. Figure 2(a) and Figure 2(b) show the dependency of the WD and the nitrogen to argon gas flow ratio on the film thickness at the bottom of the horizontal side wall relative to the film thickness at the top of the SW. The main levers for enhanced sidewall coverage are found to be minimizing the working distance (WD) and maximizing the nitrogen to argon gas flow ratio. This matches the expectation from literature, as both parameters are increasing the amount of ionized sputter atoms within the plasma [8].

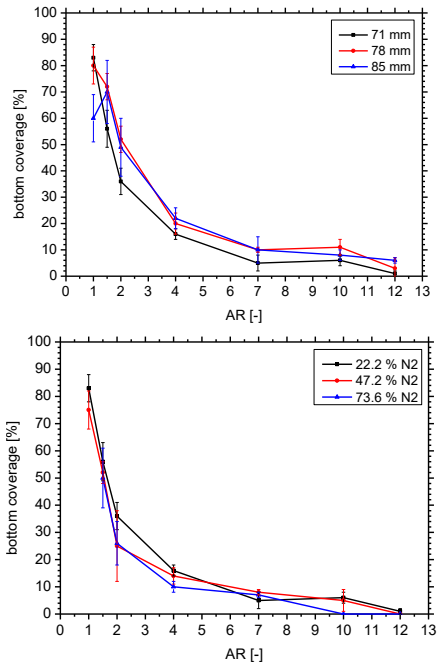


Fig. 2. Dependence of the WD (a) and the nitrogen content (b) on the AR-dependent SW coverage

A maximum AR of 12:1 was covered at the highest WD and lowest nitrogen content. SEM images also reveal the grain structure tilt at the SW. *Figure 3* shows the tilting of the grains across the edge of a trench by 56°. Independent from the AR, the film thickness at the surface is approximately three times the film thickness at the top of the vertical SW. Along the SW, it decreases until the bottom of the trench is reached or no layer is left.

Summary and Outlook

In this work the possibilities and limitations of a conventional sputtering system were evaluated and it was achieved to cover structures with a maximum AR of 12:1 with AlN. The main levers for an enhanced SW coverage of high aspect ratio features are minimizing the working distance and maximizing the nitrogen to argon gas flow ratio. The final paper will investigate the grain structures at the SW and thinning profiles for different aspect ratios and parameter combinations. Influences on the microstructure will be analyzed e.g. through XRD analysis. Prospectively, influences on the behavior of a folded MEMS membrane will be investigated and discussed.

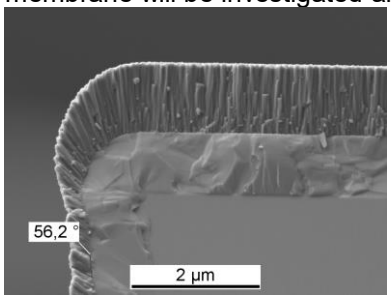


Fig. 3. SEM image of the edge of an AR with elongated grains perpendicular to the surface at the horizontal surface, and tilted grains at the vertical SW.

References

[1] D. Becker, A. Bittner and A. Dehé, Three-dimensional folded MEMS manufacturing for an efficient use of area, MikroSystemTechnik *Kongress 2023,* 307-310 (2023)

[2] D. Becker, R. Scharf, T. Leonhard, A. Merz, A. Bittner, A. Dehé, Meander-Shaped Piezoelectric Mems Loudspeaker with Maximized Area Efficiency for In-Ear Applications, Sensors and Actuators Reports 2024, SNR 5th Anniversary (2024), doi: 10.2139/ssrn.5098652

[3] P. Sippola, A. Perros, O.Ylivaara, H. Ronkainen, J. Julin, X. Liu, T. Sajavaara, J. Etula, H. Lipsanen, R.Puurunen, Comparison of mechanical properties and composition of magnetron sputter and plasma enhanced atomic layer deposition aluminum nitride films, *Journal of Vacuum Science & Technology A1 36, 051508 (*2018), doi: 10.1116/1.5038856

[4] L. Yu, B. Shkondin, A. Lavrinenko, O. Takayama, Thickness-dependent optical properties of aluminum nitride films for mid-infrared wavelengths, *Journal of Vacuum Science & Technology A1 39,* 043408 (2021), doi: 10.1116/6.0000884

[5] T. Kamohara, M. Akiyama, N. Kuwano, Influence of polar distribution on piezoelectric response of aluminum nitride thin films, *Applied Physics Letters* 3, 92 (2008), doi: 10.1063/1.2892041

[6] J. Oke, T.J. Jen, Atomic layer deposition and other thin film deposition techniques: from principles to film properties, *Journal of Materials Research and Technology 21*, 2481-2514 (2022), doi: 10.1016/j.jmrt.2022.10.064

[7] M. Ramezani, V. V. Felmetsger, N. G. Rudawski and R. Tabrizian, Growth of C-Axis Textured AlN Films on Vertical Sidewalls of Silicon Microfins, *IEEE Transactions on Ultrasonics, Ferroelectrics, and Frequency Control 68/3, 753-759* (2021) doi: 10.1109/TUFFC.2020.3013111K.

[8] Sarakinos, L. Martinu in D. Lundin, T. Minea, J. Gudmundsson, High Power Impulse Magnetron Sputtering, Elsevier, 333-374 (2020), doi: 10.1016/B978-0-12-812454-3.00013-9

DOI 10.5162/EUROSENSORS2025/TP31

Modelling and Characterization of PZT-based High Performance PMUTs for In-Air Applications

Andreas Vogl[1], Guido Sordo[1], Ludvik Lidicky[2]
[1] SINTEF Digital, Dep. Smart sensors and microsystems, Gaustadalléen 23c, 0373 Oslo, Norway,
[2] Elliptic Laboratories ASA, Hausmannsgate 21, 0182 Oslo, Norway
Corresponding author: Andreas.Vogl@sintef.no

Summary:
Micro-Electromechanical systems (MEMS) structures using piezoelectric thin films have often delicate mechanical structures (e.g. membranes) combined with a thin-film stack consisting of electrodes, the piezoelectric material and other materials such as stress compensation layers. Analytical models have been developed for the design of a membrane structure that is used as piezoelectric micromachined ultrasound transducers (PMUT). The validity of this models has been checked with measurements of the devices. An example of a sensing application is presented.

Keywords: piezoMEMS, PZT, modeling, PMUT, ultrasound

Background

piezoMEMS – MEMS including piezoelectric thin-films for actuation and/or sensing - is a technology which is already wide-spread used in e.g. RF-filters or ink jet print heads. The potential for applications is, however, much bigger and piezoelectric miniaturized ultrasound transducers (PMUT) are an emerging technology e.g. for applications in air [1]. Such devices can be used as arrays and enable e.g. activity detection. These industrial devices are based on thin-film AlN, but higher performance for actuation can be achieved with thin-film PZT due to its ca. 6 times higher piezoelectric coefficient $e_{31,f}$ [2]. To unlock the full design potential good models are necessary. We present here an analytical modelling framework and the validation of it with measurements on manufactured devices.

Analytical modelling framework

Fig. 1 shows a schematic cross-section of multilayered membrane structure consisting of silicon, silicon dioxide, a Pt bottom electrode (which is very thin, therefore, not visible in the figure), the PZT layer and the gold top electrode. This is circular structure and therefore the polar coordinate system and the radius of the inner electrode r_1 and membrane radius r_2. To describe flexural rigidity D_m of this multilayered structure with materials of different mechanical properties one must calculate the z-coordinate of the neutral plane z_n (Eq. (1)) including the thicknesses t_i, the Young's modulus E_i and the Poisson ratio v_i of the *i*th layer.

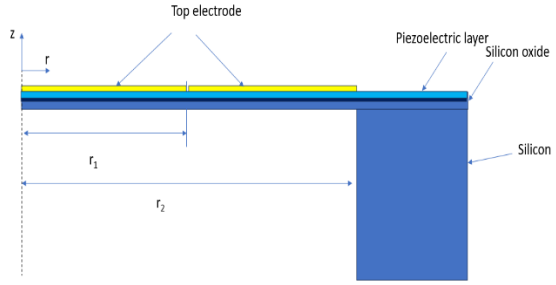


Fig. 1. Cross-section of a circular multilayered

$$z_n = \frac{\frac{E_1}{1-v_1^2}\frac{t_1^2}{2}+\sum_{i=2}^{n}\frac{E_i}{1-v_i^2}\left[\left(\sum_{j=1}^{i-1}t_j\right)+\frac{t_i}{2}\right]}{\sum_{i=1}^{n}\frac{E_i}{1-v_i^2}t_i} \quad (1)$$

We calculate the flexural rigidity D_m (2) of the multimorph structure taking also into account the flexural rigidity for one single layer $D_i = E_i t_i^3/12(1-v_i^2)$ using Steiner's theorem

$$D_m = \frac{E_1}{1-v_1^2}\left[\frac{t_1^3}{12}+t_1\left(\frac{t_1}{2}-z_n\right)^2\right]+\sum_{i=2}^{n}\frac{E_i}{1-v_i^2}\left\{\frac{t_i^3}{12}+t_i\left[\left(\sum_{j=1}^{i-1}t_j\right)+\frac{t_i}{2}\right]-z_n^2\right\} \quad (2)$$

The areal mass density μ_{weigh} can be calculated using the mass density ρ_i:

$$\mu_{weight} = \sum_{i=1}^{n}\rho_i t_i \quad (3)$$

The frequency of the first eigenmode can be calculated with the following [3]:

$$f_{eigen} = \frac{3.19^2}{2\pi r_2^2}\sqrt{\frac{D_m}{\mu_{weight}}} \quad (4$$

Results

PMUT devices were designed and manufactured according to specifications to have a resonance at 50kHz. Due to uncertainties in the manufacturing process (residual stress, underetch) different device layer thicknesses of the used silicon on insulator (SOI) wafers and membrane radii were applied (version AA: r_2 =650 µm, BB: r_2 = 680 µm, CC: 620 µm). A photograph of a manufactured PMUT including a 2µm PZT layer and gold electrodes on top is shown in Fig 2.

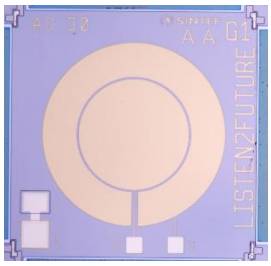


Fig. 2. PMUT design AA fabricated

The fabricated samples were characterized by their frequency of the first mechanical eigenmode.

Tab. 1:Measured resonant frequency and its std deviation of the different PMUT design,

Chip design	Device layer thickness [µm]	Resonance frequency [kHz] (first eigenmode)	
		Analytical model	Measured
BB	6	52	48 +/- 1.1
CC	6	53	57.5 +/- 1.5
AA	5	49	45,2 +/- 1,3
BB	5	45	41.3 +/- 1.9
CC	5	53	49.0 +/- 1.4

Tab1. shows that the multilayered analytical model delivers results quite close to the actual values. The actual values are deviating mostly due to manufacturing effects such as residual stress in the different thin-film layers as well as non-ideal etching profiles.

The functionality for the intended application for activity detection was tested with a set-up to detect a moving hand using the PMUTs as transmitters.

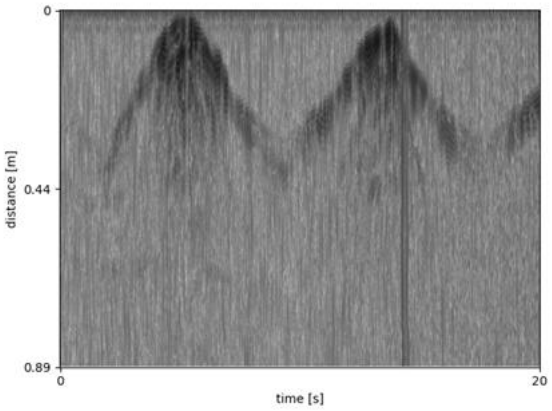


Fig. 3. Echoes from a hand moving at a varying distance.

Conclusions

We have shown a powerful analytical model for multilayered mechanical structures, which was applied to design PMUT devices. The PMUT devices were successfully manufactured using a thin-film PZT based piezoMEMS process using silicon on insulator wafers and release of the membrane by bulk-micromachining. The validity of the analytical model was verified by measurements on the finalized devices.

The functionality of the devices for the intended use in the field of activity detection was tested successfully by using them as transmitters in a set-up for echo detection.

References

[1] https://invensense.tdk.com/de/smartsonic/

[2] Muralt P, Kholkin M, Kohli M and Maeder T, Piezoelectric actuation of PZT thin-film diaphragms at static and resonant conditions, Sensors Actuators A 53 398–404, 199

[3] M. H. Bao, Micro mechanical transducers – Pressure sensors, accelerometers and gyroscopes, Elsevier, Amsterdam, 2000

Acknowledgements

This work has been financed by the Listen2Future project. Under grant 101096884, Listen2Future is co-funded by the European Union. Views and opinions expressed are however those of the author(s) only and do not necessarily reflect those of the European Union or Chips Joint Undertaking. Neither the European Union nor the granting authority can be held responsible for them. The project is supported by the Chips Joint Undertaking and its members (including top-up funding by Austria, Belgium, Czechia, Germany, Netherlands, Norway, and Spain).

DOI 10.5162/EUROSENSORS2025/TP32

Study of the possibility to add piezoelectric sensors on boat hulls and investigation of shear stress caused by drag

Guillaume Cayla[1], Peter D. Folkow[1],
Vincent Udén[2], Henrik Staaf[2], Cristina Rusu[2], Alex A. Shiri[3] and Michael.Leer-Andersen[3]
[1] Chalmers University of Technology, Hörsalsvägen 7, 412 58 Göteborg, Sweden,
[2] Research institute of Sweden, Lindholmsallén 10, 417 55 Göteborg, Sweden
[3] SSPA Sweden AB, Chalmers Tvärgata 10, 400 22 Göteborg, Sweden
henrik.staaf@ri.se

Summary:
Reducing flow resistance of underwater vehicles is of great importance to reduce energy consumption in maritime transportation. In this paper, we present numerical simulations and experimental methods for structural health monitoring of boat hulls, using self-powered piezoelectric sensors to assess shear/drag forces. The studies are based on drag tests on an immersed plate using piezoelectric sensors placed in different locations. Simulations are done using COMSOL Multiphysics. The numerical results show good agreement with experimental sensors' voltage output measured at various speeds.

Keywords: Piezoelectricity, Structural health monitoring (SHM), Fluid-Structure interaction (FSI), Strain, MEMS

Introduction

Marine structures sustain various mechanical loads from solid-fluid interactions of different types, which usually have negative impact on the structural performance. For a ship hull, loads like drag force induce vibrations that may lead to fatigue or even structural failure of the hull. Monitoring stress and strain, especially in vulnerable zones, remains essential for durability and safety for maritime applications. In addition, there is an increasing demand for research and solutions for the reduction of emissions from the shipping sector. In 2023 the International Maritime Organization introduced mandatory reductions levels in carbon emissions for new and existing ships, by stating energy efficiency indicators [1]. One effective means is the implementation of drag reduction methodologies, e.g. by introduction of air lubrification [2]. Therefore, understanding and minimizing the drag forces are key factors for lower emissions. Such studies are part of the goals of the current EU project REFEST for fishing fleets [3].

Strain gauges and piezoresistive sensors are commonly used for measuring strain/stress. However, strain gauges require an external power source, whereas piezoelectric sensors are self-powered, i.e. generate voltage when exposed to mechanical deformations. Piezoelectric transducers are typically used in boat's hull monitoring as ultrasonic sensing to create surface acoustic waves [4]. In this study, we use flexible piezoelectric sensors to measure dynamically the strain/ stress induced by water friction / resistance.

Piezoelectric sensors

For this study, we use commercial sensors, Micro Fiber Composite™ (MFC) that consists of rectangular piezoceramic rods, sandwiched between layers of adhesive, electrodes, and polyamide film [5]. The dimensions are 28mm x 14mm x 0.3mm with polarization in d31 mode and placed at different positions on the metal plate structure of 7m x 1m x 0.05m (Figure 1).

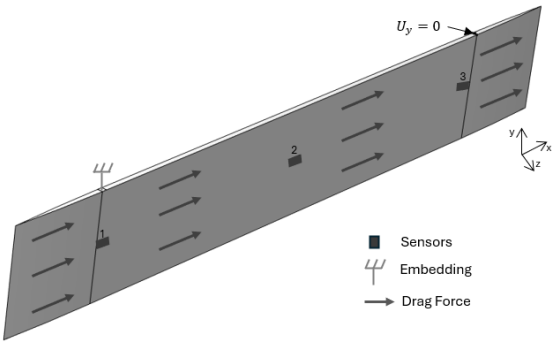


Fig. 1. Mounting of piezoelectric sensors on the plate that is tested under water (1:Front, 2:Middle, 3:Rear).

The sensors are mounted with thin adhesive and waterproof insulation. The plate was driven underwater at speeds from 1m/s to 5m/s. Special control and reading electronics were developed for real-time data acquisition (not shown here as well as the experimental part).

Simulation

The plate is supported by a rigid connector at the front and a chain at the back. This plate was simulated using *COMSOL Multiphysics 6.2*. Due to complexities when modelling the fluid-structure interaction (FSI), simplifications were made such as applying harmonic loading along the plate, corresponding to drag forces from turbulent flow. In this way, we can model the vibrations induced by fluid–structure interaction. In terms of boundary conditions, as seen in Figure 1, all the displacements are prescribed in the front of the plate and only displacements along the Y axis are prescribed at the back end of the plate, corresponding to the plate, being hold by the loose chain, if we assume small displacement hypothesis. These simplifications in the simulation allow to focus on electro-mechanical coupling of piezoelectric sensors and the strain from water resistance. Piezoelectric sensors are simulated with solid elements, with the same dimensions as sensors used during experiments. We coupled sensors with the plate, assuming a perfect interface with a flexible attachment to allow strain transmission.

Results

The voltage output from the piezoelectric sensors was analysed through both simulation and experimental measurements at flow velocities ranging from 1 to 5 m/s.

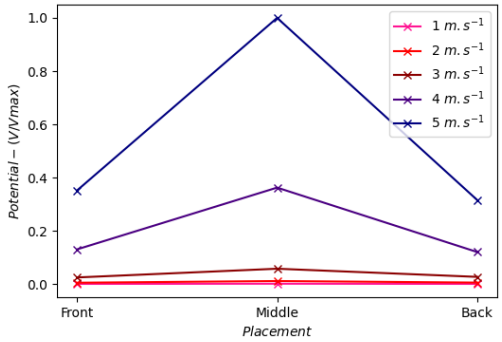


Fig. 2. Numerical output voltage for Smart Material-P2 along the plate [5].

As shown in Figure 2, the simulated results (normalized to the maximum value) indicate a distinct increase in voltage with higher fluid velocity, with the middle position consistently showing the highest output.

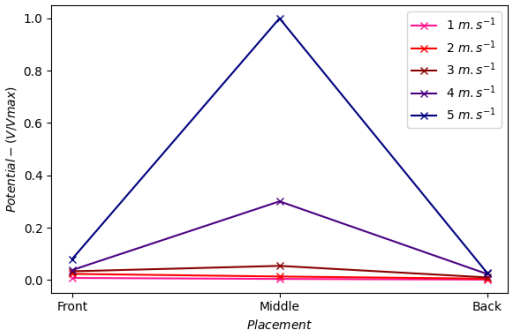


Fig. 3. Experimental output voltage for Smart Material-P2 sensors along the plate [5].

The measured data, presented in Figure 3, shows the same trend: The voltage output increases with velocity and peaks in the middle sensor placement. While absolute value differs due to normalization in the simulation and "real-world" effects in the measurement, the overall trend shows strong agreement.

Conclusion

This study demonstrates the potential of flexible piezoelectric sensors for monitoring strain caused by drag on submerged structures. The comparison between simulation and experimental data demonstrates that the developed model captures the key behaviour of strain distribution induced by hydrodynamic drag. They both shows that the middle region of the plate experiences the highest voltage output, indicating a stress concentration in this area. This correlation is validated by the numerical model. Future work will aim to refine the model to incorporate more realistic flow behaviour and test sensor response under more dynamic and realistic marine conditions.

References

[1] IMO, 2023. IMO strategy on reduction of GHG emissions from ships. MEPC 377 (80), 2023.
[2] https://www.scribd.com/document/486376944/SSPA-Hull-air-lubrication-future-and-challenges
[3] https://www.refest-project.eu/
[4] Lu Zhang et al 2019 IOP Conf. Ser.: Mater. Sci. Eng. 531 012090.
[5] https://www.smart-material.com/MFC-product-main

Polymer MEMS Microcantilever-Integrated Microfluidic System for Biochemical Sensing

Pooja P. Kanade[1], Paul T. Baine[2], Robert M. Bowman[1]
[1] *School of Mathematics and Physics, Queen's University Belfast, Belfast BT7 1NN, United Kingdom*
[2] *School of Electronics, Electrical Engineering and Computer Science, Queen's University Belfast, Belfast BT7 1NN, United Kingdom*
p.kanade@qub.ac.uk

Polymer MEMS Microcantilever-Integrated Microfluidic System for Biochemical Sensing

Pooja P. Kanade[1], Paul T. Baine[2], Robert M. Bowman[1]
[1] *School of Mathematics and Physics, Queen's University Belfast, Belfast BT7 1NN, United Kingdom*
[2] *School of Electronics, Electrical Engineering and Computer Science, Queen's University Belfast, Belfast BT7 1NN, United Kingdom*
p.kanade@qub.ac.uk

DOI 10.5162/EUROSENSORS2025/TP33

Snap-through Mode Shape Reconstruction of Bistable PiezoMEMS Membranes through Parametric Exploration

Mahdi Mortada [1, 2], Matthias Schlögl [1], Ulrich Schmid [1], Michael Schneider [1, 2]
[1] Institute of Sensor and Actuator Systems, TU Wien
[2] Christian Doppler Laboratory for Piezoelectric Silicon MEMS with Enhanced Sensitivity and Responsivity, Institute of Sensor and Actuator Systems, TU Wien
Gußhausstraße 27-29, 1040, Vienna, Austria
mahdi.mortada@tuwien.ac.at

Summary: In this work, snap-through modes shapes of bistable piezoelectric micro-electromechanical devices are presented based on a prior investigation of its parametric behavior. These devices make use of compressive aluminium nitride thin film in order to achieve bistability, hence the ability of switching between two ground states.

Keywords: Snap-through, Resonance mode, PiezoMEMS, Bistability, Aluminium nitride

Background

Typically, resonance modes of resonators are investigated using sweep measurements, which mainly involve low-amplitude chirp signals. While effective for characterizing linear behavior, this approach only reveals the device's response under small excitation conditions. When subjected to high-amplitude excitations, the device response deviates significantly, exhibiting nonlinear behavior. In our PiezoMEMS devices, characterized by its bistability, such nonlinear effects become prominent, making it insufficient to rely solely on traditional linear analysis. Previous work, such as [1], has explored this nonlinear behavior, but their analysis did not relate the observed response to the broader parametric behavior of the device, an important step for distinguishing between linear and nonlinear regimes. In our work, we aim to bridge this gap by combining the approach from [1] with the method used in [2], providing a more comprehensive understanding of the behavior of bistable membranes.

Method

In this work, we have emploied a hybrid static–dynamic approach to reconstruct the shape of the snap-through, following the methodology in [1]. The process begins with a static analysis using white light interferometry (WLI, Polytec MSA400), generating an 11×11 mesh that captures the surface topography of our piezoMEMS device of 800 μm diameter. The dynamic analysis is performed using laser Doppler vibrometry (LDV). Selecting the point of interest requires prior parametric studies to ensure relevance, hence the implementation of correlation maps to assure that all measurements done for the full 11x11 mesh have similar profile. To this end, we adopt the method introduced in [2] to construct a parameter space that characterizes the snap-through behavior, specifically a systematic variation of the applied electrical signals, namely voltage and frequency, to map out the parameter space.

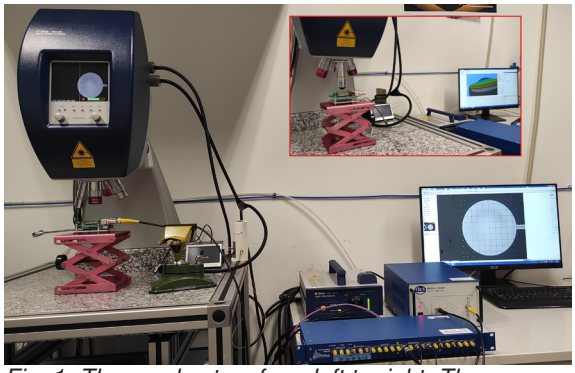


Fig. 1: The used setup, from left to right: The MSA400 system used for LDV and WLI outputs, the bistable device under the lens, MLA3 as the DAQ unit, voltage amplifier of fixed gain x50, and finally PC screen showing the built 11x11 mesh. In the center, the WLI scanning of the used device is done.

Results

The results exhibit similarities to those reported in [2], particularly in the appearance of complex fractal patterns. In our case, we applied nearly double the voltage levels used in previous work. As a result, a new fractal region was observed at approximately half the frequency of the original fractal region, which was located near the first linear natural mode at 105 kHz, see Figure 2.

To explore this further, we extended the voltage range up to 165 volts to better reveal the newly developed fractal region. We conducted 8 repeated measurements within the newly observed region. This repetition enabled us to correlate velocity data across different excitation conditions as shown in Figure 2. As a result, we identified highly correlated regions, from which points of interest were selected for the subsequent snap-through shape reconstruction mea-

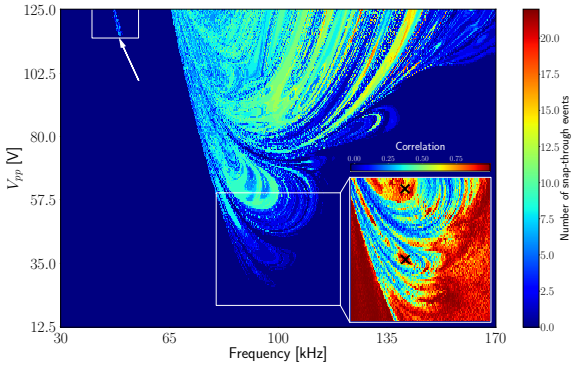


Fig. 2: The built parameter space made up of voltage and frequency variation. To the lower right cornerm correlation maps for the region of interest is shown. Selected points of interest are of (96 kHz, 37.5 V) and (95 kHz, 57.5 V). In the upper left, the subharmonic region starts to show up which is extended in Figure 3

surements. Similar step was done for the correlated region in Figure 1.

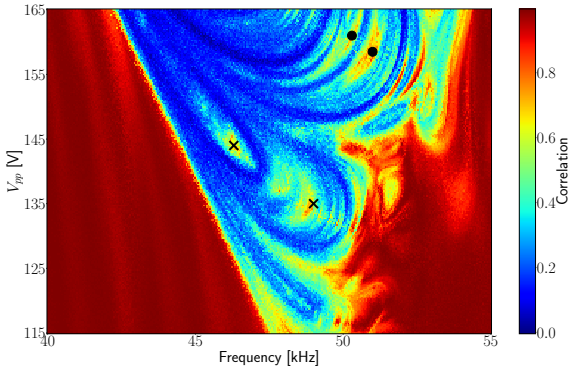


Fig. 3: The correlation map of the second fractal region. The selected points are (46.3 kHz, 144 V) and (49 kHz, 135 V)

From the selected points in both regions, as seen in Figure 4, it is evident that the bistable device undergoes a transitional mode of 11 during its snap-through behavior. A clear similarity is observed between the two modes generated from the distinct regions, the subharmonic fractal region shows a 90-degree shift in the radial nodal line, suggesting similarity to degenerate modes.

We also examined points of interest at higher voltage levels, around 160 volts, within the subharmonic fractal region denoted by • in Figure 3. These measurements revealed a noisier representation of the snap-through behavior. It is likely that, at these specific points, the device exhibits different snap-through patterns, as the high-energy, nonlinear dynamics become too complex to be accurately captured using simple correlation maps based solely on the center point velocity of the membrane. As a direction for future work, exploring alternative materials such as ScAlN may help reduce the required voltage to access this region. This study highlights the importance of combining the methods from [1] and

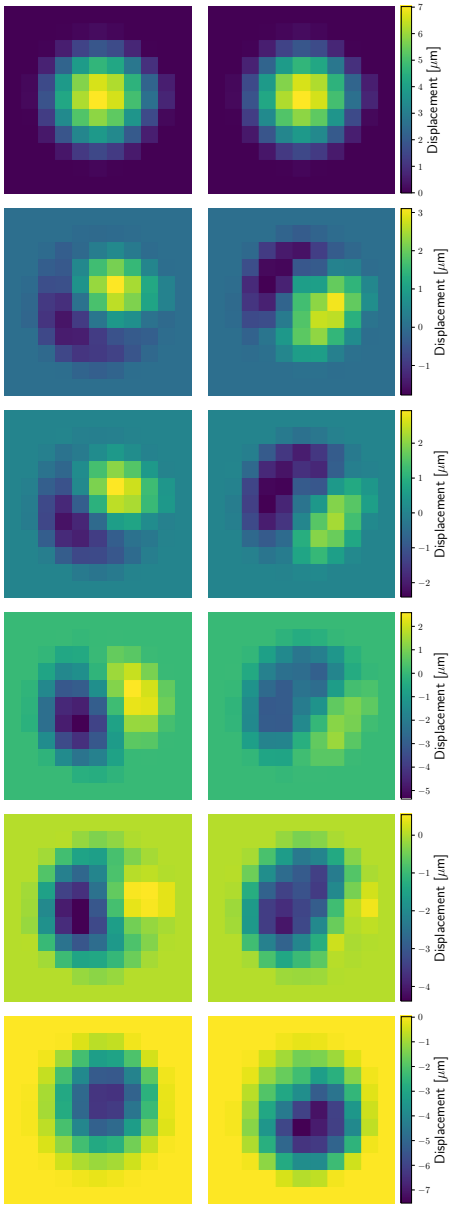


Fig. 4: Different snap-through snippets taken at different times from time = 0 until the first snap-through. First column represents points taken from the fundamental mode fractal region, Figure 2, and second column represents points taken from the subharmonic fractal region, Figure 3.

[2], particularly for such devices that exhibit nonlinear behavior.

References

[1] M. Dorfmeister, M. Schneider, and U. Schmid, “3d characterisation of piezoelectric bistable mems membranes during switching,” *Sensors and Actuators A: Physical*, vol. 298, p. 111576, 2019.

[2] M. Mortada, P. T. Das, U. Schmid, and M. Schneider, “High-resolution parametric characterization of snap-through behaviour in bistable piezomems membranes,” *Sensors and Actuators A: Physical*, p. 116548, 2025.

DOI 10.5162/EUROSENSORS2025/TP34

Ultra-Stable Few-Layer Black Phosphorus UV Detector Encapsulated in Nitrocellulose

Michał Suplewski [1], Małgorzata Szczerska [1], Paweł Jakóbczyk [1]*
[1] Department of Metrology and Optoelectronics, Faculty of Electronics, Telecommunications and Informatics, Gdansk University of Technology, Gabriela Narutowicza 11/12, 80-233 Gdansk, Poland,
* corresponding author, pawel.jakobczyk@pg.edu.pl (Paweł Jakóbczyk), Phone: +48 58 347 19 76

Summary:
We present a novel UV photodetector based on few-layer black phosphorus (FLBP) encapsulated in nitrocellulose, which enhances material stability while preserving intrinsic electronic properties. The detector operates in the solar-blind UV region (205-285 nm), exhibiting a clear resonance shift in response to UV light. With no need for external optical filters, this flexible device can be integrated into wearable and portable sensor platforms. The nitrocellulose coating significantly mitigates environmental degradation, marking a step forward in phosphorene-based optoelectronics.

Keywords: black phosphorus, UV photodetector, nitrocellulose, solar-blind, environmental stability

Introduction

Phosphorene, a two-dimensional allotrope of black phosphorus, possesses exceptional optoelectronic properties, including a tunable bandgap and high carrier mobility, making it a promising material for photodetection applications. However, its practical implementation has been severely limited by its rapid degradation under ambient conditions [1–3].

We present a novel UV photodetector composed of a few layers of black phosphorus encapsulated in nitrocellulose, a protective matrix that enhances stability while preserving the intrinsic electronic properties of the material. Our device exhibits a distinctive resonance shift in response to UV light (205-285 nm), driven by the interplay between the anisotropic band structure of the phosphor and the strain-modulated encapsulation environment. Notably, this detector operates in the solar blind region without the need for additional optical filters, and its flexible structure enables seamless integration into wearable and portable sensor platforms. The nitrocellulose coating significantly mitigates environmental degradation, exceeding previous stability benchmarks for black phosphorus-based devices.

Our research represents a significant step towards the commercialisation of phosphorene-based optoelectronics, paving the way for highly stable UV photodetectors with applications in environmental monitoring, biomedical diagnostics and industrial safety.

FLBP/nitrocellulose photodetector fabrication

FLBP was synthesized via liquid-phase exfoliation of commercially available black phosphorus crystals (Smart Elements). In this process, 38 mg of pre-ground BP crystals were dispersed in 8 mL of argon-purged 95% ethanol (Sigma-Aldrich), resulting in a concentration of 4.75 mg/mL. The mixture was then subjected to controlled ultrasonication using a Bandelin Sonopuls HD2200 probe system operating at a frequency of 20 kHz and a power setting of 40 W, with a pulsed 0.5-second ON/OFF cycle. To minimize degradation, the reaction vessel was kept at a temperature of 0–3°C using an ice bath, while continuous argon gas purging (Air Liquide) was maintained throughout the 4-hour exfoliation process. The fabrication procedure for FLBP suspension followed established protocols from the literature [4]. The FLBP/nitrocellulose photodetector was fabricated by first creating a thin FLBP layer through drop-casting 5 µL of FLBP suspension onto interdigital electrodes, repeating the process five times to ensure adequate coverage. All steps of the FLBP film fabrication were carried out in a glove box under an argon atmosphere to prevent degradation. After each deposition, the sample was left to dry at room temperature for 30 minutes inside the glove box. Once the final FLBP layer was completed, a protective nitrocellulose coating was applied by drop-casting from an ethanol solution. The resulting FLBP/nitrocellulose (FLBP/NC) composite film was first dried under argon at room temperature for 24 hours, followed by an additional drying step under reduced pressure for 2 hours.

Mesurement system

We connected to the sample via two gold probe needles using a FormFactor Cascade MPS150 probe station. Resistance measurements were performed using a KEITHLEY 2450 SourceMeter. To ensure measurement stability and minimize electromagnetic interference, all tests were conducted inside a grounded Faraday cage (FormFactor Cascade ShieldEnclosure), mounted on a vibration-isolated FormFactor Cascade table. A distinct change in resistance is observed upon activation of the 1.2 mW LED source, confirming the functionality of the detector in the deep-UV region.

Results

The performance of the developed UV photodetector based on few-layer black phosphorus (FLBP) encapsulated in nitrocellulose was verified through resistance measurements under deep-UV illumination. As shown in Fig. 1, the device demonstrates a clear change in resistance upon exposure to a 265 nm LED source at 1.2 mW power for 1620 s.

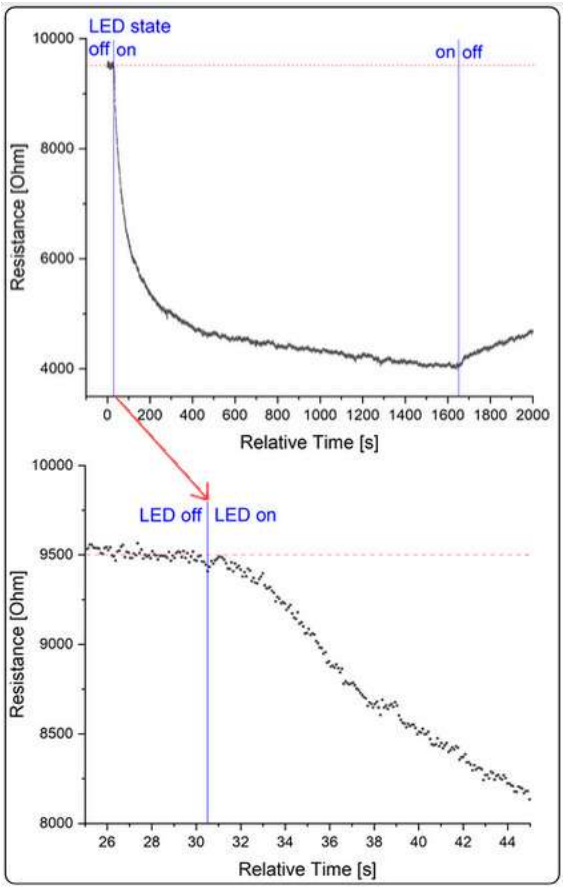


Fig. 1. Time-dependent resistance of the FLBP sample measured with and without illumination with a 265 nm LED diode. Changes in resistance are observed after switching on the 1.2 [mW] LED.

On a flat FLBP/NC surface kept in the dark at room temperature, the average surface resistance is approximately 9 kΩ. When the 265 nm LED source is switched on, the FLBP/NC material absorbs the incoming photons, causing electrons to be excited from the valence band to the conduction band, thereby generating electron-hole pairs. This process increases the number of charge carriers, resulting in a decrease in the material's resistance. As a result, the average surface resistance rapidly drops to 4.1 kΩ. When the light is switched off, the electron-hole pairs recombine, and the average surface resistance begins to increase again (Fig. 1).

This measurable and reversible change in resistance confirms the detector's sensitivity to UV light and demonstrates its solar-blind UV performance without the need for external filtering. Moreover, the observed reversibility indicates that the nitrocellulose encapsulation effectively preserves the functional properties of FLBP during prolonged exposure to ambient conditions.

References

[1] D. Roy, P. Pal, T. Pal, and R.-A. Doong, "Advancement in phosphorene: Synthesis, properties, and applications," Applied Materials Today 35, 101944 (2023).

[2] W. Li, Z. Wang, F. Zhao, M. Li, X. Gao, Y. Zhao, J. Wang, J. Zhou, Y. Hu, Q. Xiao, X. Cui, M. J. Eslamibidgoli, Michael. H. Eikerling, R. Li, F. Brandys, R. Divigalpitiya, T.-K. Sham, and X. Sun, "Phosphorene Degradation: Visualization and Quantification of Nanoscale Phase Evolution by Scanning Transmission X-ray Microscopy," Chem. Mater. 32, 1272–1280 (2020).

[3] L. Peng, N. Abbasi, Y. Xiao, and Z. Xie, "Black Phosphorus: Degradation Mechanism, Passivation Method, and Application for In Situ Tissue Regeneration," Adv Materials Inter. 7, 2001538 (2020).

[4] M. Szczerska, M. Kosowska, J. Gierowski, M. Cieślik, M. Sawczak, P. Jakóbczyk, „Investigation of the Few-Layer Black Phosphorus Degradation by the Photonic Measurements", Adv. Materials Inter. 10, 2202289 (2023)

Acknowledgements

This study was supported as a project funded by the Ministry of Science and Higher Education of the Republic of Poland under agreement no. MNiSW/2024/DPI/433.

DOI 10.5162/EUROSENSORS2025/TP35

Orthogonality characterization of 3D Helmholtz coil fields

Peter Leitner[1], Florian Slanovc[1], Luiz Enger[1], Michael Ortner[1], Stephan Leisenheimer[2], Cristina-Georgia Iot[3], Catalina-Petruta Juglan[3], Mihai Iatco[3], Mihai Muntean[3]
[1] Silicon Austria Labs GmbH, Sandgasse 34, 8010 Graz, Austria
[2] Infineon Technologies AG Neubiberg, Am Campeon 1-15, 85579 Neubiberg, Germany
[3] Infineon Technologies Romania, Novo Park, Bulevardul Dimitrie Pompeiu 6, București 020335

Summary:
We present a new method for the characterization of 3D Helmholtz coils with respect to their field orthogonality errors. It is based on 3D field sensing inside the homogeneity region using conventional 3D Hall sensors that need to be precisely orthogonality calibrated in a first step. Repeated measurements with different such sensors are used to confirm the algorithmically determined 3D coil field tolerances. Upon finding discrepancies, we discovered environmental influences affecting the determination of the coil orthogonality angle errors and propose means to minimize their impact.

Keywords: Helmholtz coil characterization; 3D Hall sensors; Hall sensor tolerances; Helmholtz coil magnetic field tolerances; piezo-Hall effect

Introduction

The magnetic field generated by a system of Helmholtz coils is subject to mechanical manufacturing tolerances, in case of a 3D system in particular the alignment of the three coil pairs relative to each other. Similarly, also multi-axis sensor systems need a precise assembly of three orthogonally placed Hall plates, each measuring the perpendicular field projection. Any angle deviations from orthogonality of Hall plates or coil arrangements lead to incorrectly measured or generated magnetic fields. As we show below, neither topic should be considered isolated from the other as discrepancies in orthogonality of coils can be determined from precisely calibrated sensors and vice versa.

A Helmholtz coil is made of a co-axial pair of air coils, separated by precisely the radius of the respective coils generating a homogeneous field in their center. An arbitrary field orientation is achieved by superposition of three such fields from three orthogonally placed pairs of coils.

Instead of conducting a magnetic field inversion, typically having many degrees of freedom to determine the coil assembly orientation from multiple simultaneous field measurements and to potentially correct for coil misalginments, we rather aim at a coil field characterization in terms of its orthogonality errors, irrespective of the particular mechanical tolerances in the three-axis coil assembly responsible (e.g. by angular deviation or center offsets either of the coil pairs themselves or between those pairs). An alternative rigorous treatment of the field of 3D coil systems considering its source with the intricate details down to the level even of the geometry of conducting elements for specific winding technologies has been elaborated in [1].

In [2] a calibration scheme for a three-axis Helmholtz coil via optical methods by gauging the assembly with a laser tracking routine is presented. [3] describe the calibration of a triaxial Helmholtz coil via a rotating magnetic field scheme using a minimization procedure for an objective orthogonality angle deviation function. A calibration method for a planar sensor array in a 3D Helmholtz coil system using machine learning based sensor vector correction is presented in [4]. We on the other hand use a single 3D sensor per measurement and relate the Hall plate sensor output to the three coil field components in our calibration such that the field generated in the coil system can be corrected for the coil misalignment by adjusting the nominal currents applied to the three coils.

Methods

Our scheme allows for arbitrary orientational placement of a 3D Hall sensor into the homogeneity region of the coil system. It requires priorly determined 3D sensor orthogonality angle errors or equivalently, the Hall plate orientations $\boldsymbol{n}_1$, $\boldsymbol{n}_2$ and $\boldsymbol{n}_3$ and sensitivities as input into the algorithm. Supplying current to each of the coils separately and measuring the sensor outputs on the three Hall plates, we obtain a signal matrix $O_{ij} = \boldsymbol{n}_i \cdot \boldsymbol{B}_j$, $(i, j) = 1,2,3$ for the projection of each coil field onto each of the Hall plates. The background field and sensor offsets are corrected for in the signal matrix, recorded a couple of thousand times to average out sensor noise. We

solve for the three coil fields in the relation between fields and Hall plate signals,

$$\begin{pmatrix} n_{xx} & n_{xy} & n_{xz} & 0 & 0 & 0 & 0 & 0 & 0 \\ n_{yx} & n_{yy} & n_{yz} & 0 & 0 & 0 & 0 & 0 & 0 \\ n_{zx} & n_{zy} & n_{zz} & 0 & 0 & 0 & 0 & 0 & 0 \\ 0 & 0 & 0 & n_{xx} & n_{xy} & n_{xz} & 0 & 0 & 0 \\ 0 & 0 & 0 & n_{yx} & n_{yy} & n_{yz} & 0 & 0 & 0 \\ 0 & 0 & 0 & n_{zx} & n_{zy} & n_{zz} & 0 & 0 & 0 \\ 0 & 0 & 0 & 0 & 0 & 0 & n_{xx} & n_{xy} & n_{xz} \\ 0 & 0 & 0 & 0 & 0 & 0 & n_{yx} & n_{yy} & n_{yz} \\ 0 & 0 & 0 & 0 & 0 & 0 & n_{zx} & n_{zy} & n_{zz} \end{pmatrix} \begin{pmatrix} B_{xx} \\ B_{xy} \\ B_{xz} \\ B_{yx} \\ B_{yy} \\ B_{yz} \\ B_{zx} \\ B_{zy} \\ B_{zz} \end{pmatrix} = \begin{pmatrix} O_{xx} \\ O_{yx} \\ O_{zx} \\ O_{xy} \\ O_{yy} \\ O_{zy} \\ O_{xz} \\ O_{yz} \\ O_{zz} \end{pmatrix}$$

and obtain angles $\alpha = \angle(\boldsymbol{B}_x, \boldsymbol{B}_z)$, $\beta = \angle(\boldsymbol{B}_x, \boldsymbol{B}_y)$ and $\gamma = \angle(\boldsymbol{B}_y, \boldsymbol{B}_z)$, specifying the deviation from orthogonality. Different sensors, each calibrated for their own orthogonality errors are used to re-evaluate the coil orthogonality and provide an average and spread of the coil calibration results.

Results: Humidity and temperature effect on the sensor orthogonality

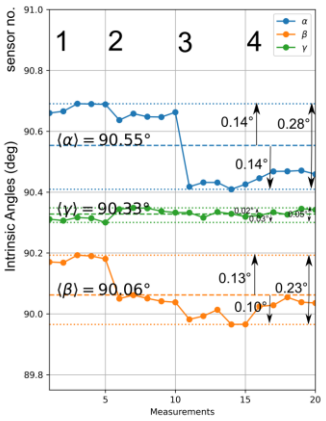


Figure 1: Orthogonality error results based on 5 measurements with 4 different 3D Hall sensors.

Substantial deviations from orthogonality of $\sim 1°$ between results obtained from different sensors were found in attempts to calibrate several coil systems, indicating a systematic error in the procedure. While repeated calibrations with one sensor confirmed the previous outcomes, the results of different sensors did not match with one another. When therefore repeating the sensor calibration in a precalibrated Helmholtz coil system (specified with an orthogonality accuracy $< 0.1°$) based on a computation scheme like the one described above but swapped roles of known coil field orientations and yet to be determined Hall plate orientations), we found those sensor calibration measurements to vary from day to day by as much as $\sim 1°$ with fluctuating environmental parameters of humidity and temperature. We addressed the issue with repeated sensor calibrations in varying environmental conditions to generate a table of calibration measurements depending on temperature and humidity. When performing the actual coil orthogonality characterization, values for sensor orientations $\boldsymbol{n}_i$ were determined from a 2D interpolation of our sensor calibration table, representation plate orientations as to be expected in those specific humidity and temperature conditions. With the corrected imputs, the coil orthogonality could be significantly improved and specified within a range of $\pm 0.15°$ around the average based on the results from all the different sensors used, see Fig. 1.

Discussion

An algorithm and measurement procedure for the orthogonality calibration of a 3-axis Helmholtz coil were discussed. The procedure is statistical only in the way that measurements are to be repeated to minimize the impact of sensor noise on the signal, while the fields are computed in a deterministic way.

A major realization was the impact of humidity and temperature on the sensors via mechanical stresses onto the sensing element packages. The effect of mechanical stresses on the accuracy of 3D Hall sensors and a means of compensation via a cointegrated piezoresisitive stress sensors was reported only recently in 2024 [5] and provides an alternative to our interpolation scheme, once this sensor technology becomes commercially available.

References

[1] P. Beran, Identifizierung und Kalibrierung der Orthogonalitätsfehler von mehrachsigen Spulen- und Sensorsystemen zur Erzeugung und Messung von Magnetfeldern, *PhD thesis*, Technische Universität Braunschweig 2021

[2] A. Fontanet, J. Marcos, Ll. Ribó, V. Massana, J. Campmany, Design and construction of 3D Helmholtz coil system to calibrate 3D Hall probes, *10th International Particle Accelerator Conference 1350*, (2019), doi:10.1088/1742-6596/1350/1/012167

[3] L. Yue, D. Cheng, Y. Wang, M. Wang, J. Zhao; A comprehensive calibration method for non-orthogonal error and scale factor error of triaxial Helmholtz coil. *Rev. Sci. Instrum.* 1 August 2021; 92 (8): 085105. https://doi.org/10.1063/5.0049784

[4] S. Zhang, C. Li, Design of a three-axis Helmholtz coil for magnetic sensor calibration, *Academic Journal of Science and Technology*, Vol. 5, No. 1, 2023

[5] A. Fleck, M. Cornils, L. Osberger, O. Paul: Effective Compensation of the Piezo-Hall Effect in CMOS-integrated 3D Hall Sensors, *2024 IEEE Sensors, Kobe, Japan, 2024*, doi: 10.1109/SENSORS60989.2024.10784587

Acknowledgements

This work has been jointly supported by Infineon Technologies AG and by Silicon Austria Labs (SAL), owned by the Republic of Austria, the Styrian Business Promotion Agency (SFG), the federal state of Carinthia, the Upper Austrian Research (UAR), and the Austrian Association for the Electric and Electronics Industry (FEEI).

DOI 10.5162/EUROSENSORS2025/TP36

A lightweight Method for Interconnecting Sensors via Power Line Communication

Martin Brandl, Karlheinz Kellner
Department for Integrated Sensor Systems, University for Continuing Education Krems, 3500 Krems, Austria
Martin.Brandl@donau-uni.ac.at

Summary:
As a wireless connection of sensor systems is not always possible, a modem for powerline communication (PLC) was developed for the wired connection of sensor systems. Especially for retrofitting components in vehicles, for example, a data connection via the existing cable network is advantageous and no additional new cables need to be installed. For this purpose, a small and cost-effective PLC modem was developed that can be operated with the modulation formats BPSK and DSSS-BPSK in order to transmit sensor data at 19.2kBit/s via cable harnesses. The performance of the PLC modem in terms of channel noise and single tone interference was examined and discussed.

Keywords: Sensor interconnection, Power line communication, Automotive, Sensor retrofit, Data communication.

Introduction

Nowadays a large number of sensors are used to measure a wide range of parameters for different purposes. In order to be able to process the sensor data, the sensors are connected to a data processing unit by cable or wirelessly. A wireless connection is usually very easy to establish, whereas a wired connection of sensors is often associated with considerable effort. However, if there are already cables between the planned location of the sensor and the data processing unit (e.g. power cables), these can be used for data transmission with Power Line Communication (PLC). PLC describes a method in which the data to be transmitted is modulated onto one or more high-frequency carriers and the connecting cable is used as the transmission medium. However, the connecting cables are usually only optimized for energy transmission and not for data transmission. For example, the cables are not shielded against electromagnetic interferences and the available transmission bandwidth is only a few MHz. The modulation methods for PLC must therefore have a very limited bandwidth and a high resistance to electromagnetic interference. In addition, the PLC modem must be highly cost-efficient for use with simple sensor systems.

Methods

Two PLC modems with different data transmission methods were investigated [1]-[3]. The transmission methods investigated were Binary Phase Shift Keying (BPSK) and BPSK combined with Direct Sequence Spread Spectrum (DSSS). The data was modulated onto a carrier at 8 MHz with a data rate of 19.2kbit/s. The DSSS method uses a 7-bit Barker code for spreading. The PLC modems were implemented on the basis of a low-cost microcontroller from RENESAS R5F10 (R5F10: multi-chip package solutions with a RL78 16-bit microcontroller and a LIN system basic chip), whereby the number of additional electronic components was optimized and minimized. The PCB board of the realized PLC modem is shown in Fig. 1. The modem was optimized for networking sensors in the automotive sector and therefore designed for a supply voltage of 12V.

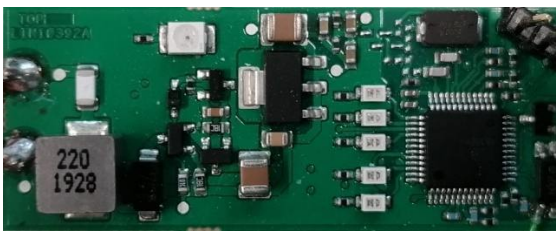


Fig. 1. Full functional board of the PLC-modem for BPSK or DSSS-BPSK (on the left edge: pads for connecting the power lines).

Results

The properties of a PLC modem with the modulation formats BPSK and DSSS-BPSK with data rate of 19.2kBit/s were investigated using

MATLAB simulations. A channel model representative of automotive cable harnesses with a typical delay spread of 0.8µs was used for the simulation [4]. A direct path and two reflections after 0.25µs (-10dB) and 0.5µs (-20dB) were used for the channel model of the cable harness. The carrier was selected at f_c=8.064MHz (420*19.2kHz) and the sampling frequency at 64.512MSample/s (3,360*19.2kHz). White noise limited by the sampling frequency and a sinusoidal interference signal with $f_0=f_c$+5kHz were used as interference signals. The bit error rates (BER) measured at the receiver as a function of the power of the interference signals on the transmission channel (SNR - Signal to Noise Ratio and SIR - Signal to Interference Ratio) were evaluated and compared for the modulation formats BPSK (Fig. 2) and DSSS-BPSK (Fig. 3), whereby the theoretical spreading gain of DSSS-BPSK compared to BPSK is $10*\log_{10}(N_{Barker})$=8.4dB. This spreading gain could also be demonstrated for single tone interference in the simulation (Fig. 4).

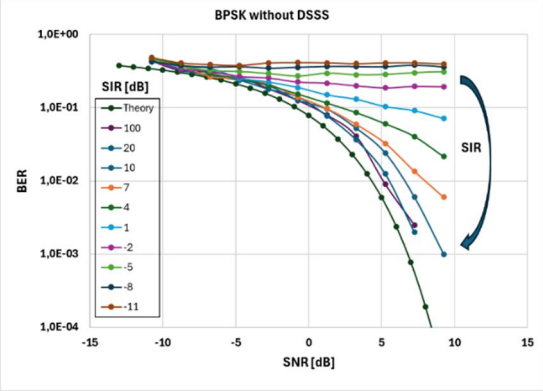


Fig. 2. Bit error rate (BER) in dependency of white noise (SNR) and a single tone interferer (SIR) of a PLC-modem with BPSK and without DSSS.

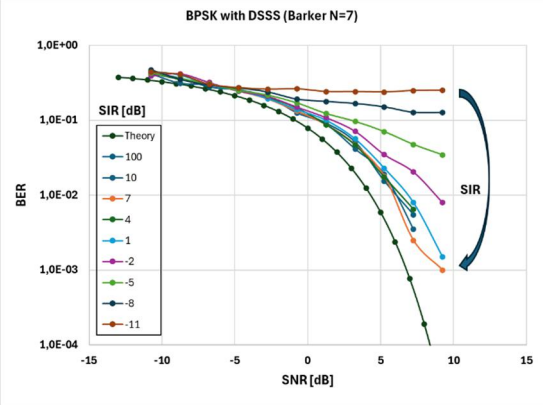


Fig. 3. Bit error rate (BER) in dependency of white noise (SNR) and a single tone interferer (SIR) of a PLC-modem with BPSK and with DSSS (N_{Barker}=7).

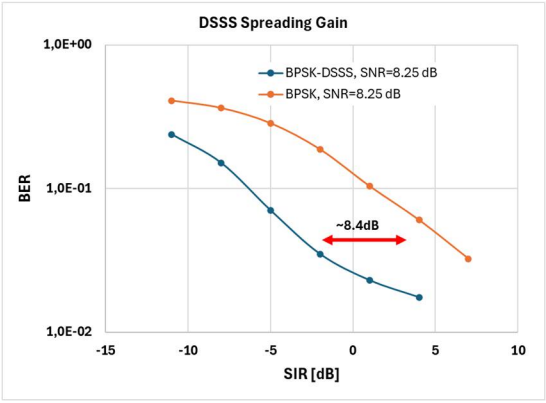


Fig. 4. Achieved compression gain of about 8.4dB by use of DSSS in case of a single tone interferer. The data rate was 19.2kBit/s and the channel SNR=8.25dB.

Conclusions

An integrated modem for powerline communication was developed to network sensors via an existing wired connection. The properties of the BPSK and DSSS-BPSK modulation formats used were investigated with regard to their immunity to white noise and single tone interference. It was shown that the use of DSSS with a 7-bit Barker code can achieve the theoretical compression gain of 8.4 dB to reduce single tone interference. Another advantage of using DSSS is that the transmission power can be higher by the spreading factor than with BPSK if the maximum transmission power (EMC limits) is specified. The PLC system shown uses a very cost-effective µC with few additional components and has been optimized for networking sensors in automotive applications.

References

[1] A.G. Bolaji, T. Shongwe, Performance comparison of Modified BPSK-OFDM and QFSK-OFDM in PLC Channel noise. *Int. Journal of Electronics and Telecommunications*, 66 (2020).

[2] P. Kiedrowski, T. Marciniak, Z. Lutowski, L. Zabłudowski, Effectiveness of BPSK modulation with peak noise avoidance algorithm in smart street lighting communications based on PLC. *Image Processing & Communications*, 23(1), 5-10 (2018).

[3] M. Brandl, K. Kellner, Performance evaluation of power-line communication systems for lin-bus based data transmission. *Electronics*, 10(1), 85 (2021).

[4] M. Lienard, M.O. Carrion, V. Degardin, P. Degauque, Modeling and analysis of in-vehicle power line communication channels. *IEEE Transactions on Vehicular Technology*, 57(2), 670-679 (2008).

DOI 10.5162/EUROSENSORS2025/TP37

Tracking Fish Trajectories through Dynamic Pressure Signals: A Dual-Sensor System for Hydrodynamic Cues Monitoring

C. Porcon[1], B. Lagneaux[1], F. Razan[1], G. Jodin[1]
[1]Univ Rennes, ENS Rennes, CNRS, IETR - UMR 6164, F-35000 Rennes, France
Corresponding authors: [corentin.porcon; bastien.lagneaux; gurvan.jodin]@ens-rennes.fr

Summary: Accurate characterization of hydrodynamic cues produced during fish locomotion is essential for understanding behavioral dynamics. In this work, a novel pressure sensor system is presented to isolate the dynamic pressure components associated with fish movements, while compensating for wave induced pressure. The system combines a differential pressure sensor and a water level sensor. Its accuracy has been demonstrated through experimental validation against a classical potential flow model around a cylinder, confirming the robustness and effectiveness of the proposed approach.

Keywords: Sensors, dynamic pressure, instrumentation, wave, hydrodynamic model, embedded systems

Introduction

Understanding the social behaviors and navigation strategies of fish has long been recognized as a significant challenge in marine ethology, and bio-inspired engineering [1]. During locomotion, fish are known to generate complex hydrodynamic signatures composed of vortices and persistent pressure fluctuations [2]. These flow-induced cues can offer valuable insight into their orientation strategies.

Traditionally, such phenomena have been studied using optical techniques like Particle Image Velocimetry and Laser Doppler Velocimetry. Although these methods are highly accurate, they typically involve complex instrumentation, invasive setup, and limited deployability in naturalistic environments. Moreover, their intrusive nature may interfere with the spontaneous behavior of the observed animals.

To address these limitations, pressure-based sensing has emerged as a promising alternative. However, in aquatic environments, pressure recordings often conflate dynamic contributions from fish movements with hydrostatic components induced by surface wave fluctuations [3]. Disentangling these overlapping signals remains a major technical bottleneck.

To overcome this, a sensor system has been developed to isolate the dynamic pressure component, while filtering out wave-induced hydrostatic disturbances. The device integrates a differential pressure transducer and a water-level sensing module. Its performance has been experimentally evaluated and benchmarked against a theoretical model: the potential flow around a rigid cylinder [4].

Materials and Methods

Dynamic pressure measurement system

An experimental device was developed, consisting of two complementary sensors designed to isolate the dynamic pressure component (P_{dyn}) generated by swimming fish, while compensating for hydrostatic fluctuations (P_{wave}) induced by surface waves.

The primary sensor was implemented as a high-sensitivity piezoresistive differential transducer. It measured the pressure difference between a measurement point, subjected to both P_{dyn} and P_{wave}, and a reference point located inside a submerged cavity. This cavity, being shielded from dynamic flow effects, allowed for the measurement of only the static pressure (P_{stat}), comprising atmospheric pressure and hydrostatic pressure at rest. The resulting signal was expressed as:

$$\Delta P = P_{\mathrm{mes}} - P_{\mathrm{ref}} = (P_{\mathrm{dyn}} + P_{\mathrm{wave}} + P_{\mathrm{stat}}) - P_{\mathrm{stat}},$$

The sensing element was composed of a membrane coupled with a strain gauge, offering a resolution of 0.2Pa and a bandwidth of 1kHz [5].

To estimate hydrostatic fluctuations, a secondary sensor was used to continuously monitor the instantaneous free-surface elevation $h(t)$. The sensor operated via impedance measurement in an AC oscillator circuit connected to submerged electrodes, thereby avoiding polarization effects and long-term electrochemical drift [6].

This formulation assumes shallow water conditions, where wave-induced pressure variations are approximately hydrostatic and do not decay significantly with depth [7].

The two sensors were interfaced with an ESP32 microcontroller, which ensured synchronized signal acquisition at 125 Hz. The dynamic pressure component was then obtained by subtracting the estimated hydrostatic pressure:

$$P_{\mathrm{dyn}} = \Delta P - P_{\mathrm{wave}}, \quad \text{with} \quad P_{\mathrm{wave}} = \rho\, g\, h(t).$$

where ρ is the water density and g is the gravitational acceleration.

Experimental validation setup

To evaluate the accuracy and robustness of the proposed system, an experimental validation was conducted using a classical hydrodynamic benchmark [4]. The experiments were carried out in a laboratory water tank equipped with a motorized mechanism for translating a rigid cylinder (diameter: 5 cm) at a constant velocity of 0.13 m/s. The pressure sensor was positioned 5 cm from the centerline of the cylinder. The experiments was repeated 12 times to ensure measurement repeatability.

Figure 1 presents the sensor (a), the experimental setup (b), and the block diagram of the data acquisition board (c).

The raw dataset and analytical tools were made publicly accessible via GitHub [8].

Results and Discussion

Comparison with theoretical reference case

To assess the system's ability to isolate dynamic pressure, the corrected experimental measurements were compared to analytical predictions derived from potential flow theory around a cylinder [4]. As illustrated in Figure 2(a), the differential pressure signal ($P_{\mathrm{dyn}} + P_{\mathrm{wave}}$) and the wave-induced pressure signal (P_{wave}). This representation highlights the contribution of hydrostatic disturbances to the total measured signal. Figure 2(b) presents the dynamic pressure signal compared to the theoretical

DOI 10.5162/EUROSENSORS2025/TP37

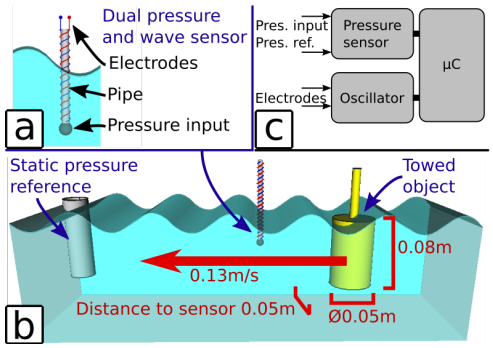


Fig. 1: (a) Dual pressure and wave sensor, (b) Experimental setup, (c) Block diagram of the electronic board.

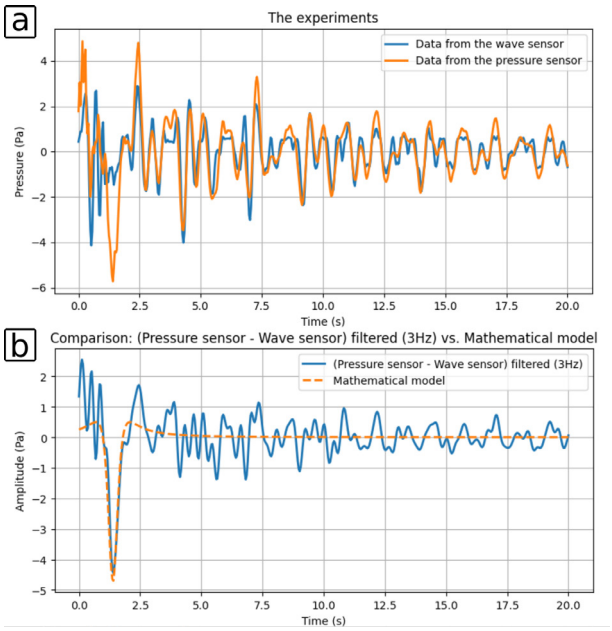


Fig. 2: (a) Raw differential pressure signal ($P_{\mathrm{dyn}} + P_{\mathrm{wave}}$) and wave-induced component (P_{wave}), (b) Corrected dynamic pressure compared with the theoretical model.

prediction. The experimental results show excellent agreement with the analytical model in both amplitude and temporal evolution, confirming the system's ability to accurately extract key hydrodynamic features.

The analytical model used for validation is publicly available in an open-source repository [8].

Discussion and practical implications

The sensor successfully captured the dynamic pressure generated by the moving body while significantly attenuating wave-induced perturbations. Although some residual noise remains, its amplitude was reduced by approximately a factor of four. The proposed system enables direct and non-invasive measurement of dynamic pressure fields, offering data well suited for trajectory estimation and flow analysis. In contrast to optical systems, it is easy to deploy, and does not require tracers or external illumination, making it ideal for experimental and semi-natural environments.

Conclusion

A dual-sensor system was designed and experimentally validated to isolate the dynamic pressure component from wave-induced hydrostatic fluctuations in aquatic environments. The device combines a differential pressure sensor with a water level sensor and enables correction of pressure signals.

The system was evaluated under controlled conditions using a benchmark case based on potential flow theory. The comparison with theoretical predictions confirmed the accuracy and robustness of the proposed approach.

Owing to its compactness, the system represents a valuable alternative to conventional optical techniques. Ongoing developments aim to extend the system into sensor arrays capable of reconstructing pressure and velocity fields for advanced hydrodynamic analysis in biological, without being invasive to aquatic organisms.

Future work will focus on deploying a network of these sensors to generate spatially resolved pressure maps. These maps will allow for the reconstruction of velocity fields and enable a more detailed analysis of wake structures and hydrodynamic cues.

Acknowledgment

This work was supported by a Research Grant RGY0059/2022 from HFSP [9].

References

[1] J. C. Liao, "A review of fish swimming mechanics and behaviour in altered flows," *Philosophical Transactions of the Royal Society B: Biological Sciences*, vol. 362, no. 1487, pp. 1973–1993, 2007.

[2] W. Hanke, C. Brücker, and H. Bleckmann, "The ageing of the low-frequency water disturbances caused by swimming goldfish and its possible relevance to prey detection," *Journal of Experimental Biology*, vol. 203, no. 7, pp. 1193–1200, 2000.

[3] F. Zonta and M. Onorato, "Growth and spectra of gravity–capillary waves in countercurrent air/water turbulent flow," *Journal of Fluid Mechanics*, vol. 777, pp. 245–259, 2015.

[4] E. Guyon, J.-P. Hulin, and L. Petit, *Hydrodynamique Physique*. Paris: CNRS Éditions, 2001.

[5] C. Porcon, B. Lagneaux, G. Jodin, F. Razan, and B. Sun, "Experimental system of synchronized pressure sensors for hydrodynamic measurements," tech. rep., IETR, ENS Rennes and Westlake University, 2024. Technical Report.

[6] N. Liu, R. Wei, P. Zhang, Y. Sun, and Z. Li, "Design and test of large-range wave height sensor based on water resistance measurement and fuzzy system," *Personal and Ubiquitous Computing*, vol. 25, pp. 457–465, 2021.

[7] J. Bosboom and M. J. F. Stive, "Coastal hydrodynamics," 2022. `https://geo.libretexts.org/Bookshelves/Oceanography/Coastal_Dynamics_(Bosboom_and_Stive)/5.04\%3A_Wave_orbital_velocity_pressure_and_bed_shear_stress/5.4.2\%3A_Dynamic_Pressure`.

[8] C. Porcon, "Hydrodynamic model – experimental data and code." `https://github.com/41PortCom/Model_Hydrodynamics/`. GitHub repository.

[9] HFSP, "Human frontier science program research grant rgy0059/2022." `https://doi.org/10.52044/HFSP.RGY00592022.pc.gr.153593`, 2022.

Modelling and Experimental Validation of PZT-based Spring Terminated Micro-Actuator

Ismaeel Shah [2], *Aron Michael*[2]
[1,2] UNSW, Kensington, NSW, Australia
a.michael@unsw.edu.au

Modelling and Experimental Validation of PZT-based Spring Terminated Micro-Actuator

Ismaeel Shah [2], *Aron Michael*[2]
[1,2] UNSW, Kensington, NSW, Australia
a.michael@unsw.edu.au

Modelling and Experimental Validation of PZT-based Spring Terminated Micro-Actuator

Ismaeel Shah [2], *Aron Michael*[2]
[1,2] UNSW, Kensington, NSW, Australia
a.michael@unsw.edu.au

DOI 10.5162/EUROSENSORS2025/TP38

Enhancing Stability of Few-Layer Black Phosphorus via Nitrocellulose Encapsulation for Optoelectronic Applications

Jakub Gierowski[1], Michał Suplewski[1], Paweł Jakóbczyk[1], Małgorzata Szczerska[1]*
[1] Department of Metrology and Optoelectronics, Faculty of Electronics, Telecommunications and Informatics, Gdansk University of Technology, Gabriela Narutowicza 11/12, 80-233 Gdansk, Poland,
** corresponding author, malszcze@pg.edu.pl (Małgorzata Szczerska), Phone: +48 58 347 13 61*

Summary:

Few-layer black phosphorus (FLBP) degrades rapidly in ambient conditions, hindering its practical applications. We demonstrate that a nitrocellulose encapsulation film enables real-time optical monitoring of FLBP while protecting it from degradation. Optical transmission measurements performed over 3 hours confirm the stability of encapsulated samples compared to unprotected references. This approach enables the integration of FLBP in photonic devices under ambient conditions.

Keywords: black phosphorus, nitrocellulose encapsulation, optical stability, degradation, fiber-optic interferometer

Introduction

Few-layer black phosphorus (FLBP) is a promising 2D material with strong potential for optoelectronic applications due to its anisotropic optical response and broadband absorption [1,]. However, its practical implementation is hindered by rapid degradation under ambient conditions, where oxygen and moisture induce chemical breakdown and surface roughening [2].

To address this limitation, we propose an encapsulation strategy based on nitrocellulose protective films. These transparent films not only shield FLBP from air and humidity but also enable real-time optical measurements to be performed directly on the protected material. The primary aim of this study is to evaluate the efficiency of this encapsulation in maintaining optical stability over time and to explore its feasibility for use in practical photonic platforms.

FLBP-nitrocellulose film preparation

FLBP was prepared by liquid-phase exfoliation of black phosphorus crystals (Smart Elements). 38 mg of ground BP was dispersed in 8 mL of argon-purged 95% ethanol (Sigma-Aldrich) and next the mixture was ultrasonicated using a Bandelin Sonopuls HD2200 (20 kHz, 40 W, 0.5 s ON/OFF pulses) for 4 hours at 0–3 °C under continuous argon flow. This method followed established literature protocols [3]. To fabricate the FLBP-nitrocellulose film, 5 µL of FLBP suspension was drop-cast onto interdigital electrodes five times in an argon-filled glove box, with 30-minute drying intervals at room temperature. A protective nitrocellulose layer was then applied from an ethanol solution. The composite film was dried under argon for 24 hours, then under reduced pressure for 2 hours.

Optical Measurements

The interference spectra were recorded by the Optical Spectrum Analyzer. A measurement setup consists of a 1320 nm light source, a fiber coupler, a sample, and a spectrum analyzer. The light emitted from the source is coupled into the fiber and directed towards the sample. The resulting signal observed in the analyzer displays an interference spectrum. The optical analysis was conducted on two samples, with spectra being recorded immediately after sample preparation (0 hours), as well as after 1 hour, 2 hours, and 3 hours. By measuring at different time intervals, it becomes possible to observe changes in the optical properties resulting from the degradation process of the samples. In this case significant difference between successive measurement from unprotected samples can be observed. On the other hand, as one can note the optical spectra have not changed after measuring time, which can mean that the process of degradation did not occur and did not influence the optical spectra of the measured signal.

Measurement Results

The optical stability of FLBP was evaluated by monitoring interference spectra over time using a fiber-optic setup and an optical spectrum analyzer. Two sets of samples: one encapsulated with nitrocellulose nitrate and one left unprotected were analyzed immediately after

preparation (0 h), and subsequently at 1 h, 2 h, and 3 h intervals.The results, shown in Fig. 1, reveal a clear difference in the behavior of protected versus unprotected FLBP. For unprotected samples, significant spectral changes occurred within the first hour, including a reduction in fringe visibility and a shift in baseline intensity, both of which indicate rapid degradation of the material due to environmental exposure.

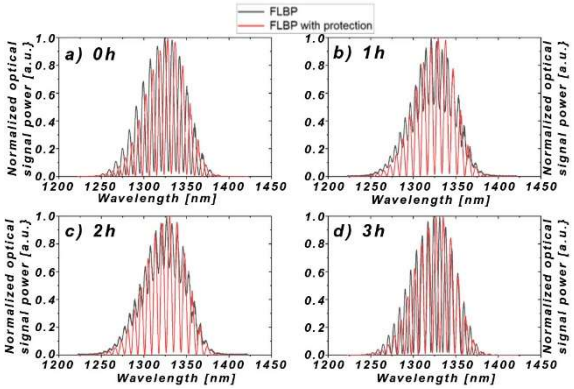


Fig. 1. Optical spectra of the samples of unprotected and protected with nitrocellulose FLBP, after a) 0h b) 1h, c) 2h and d) 3h.

In contrast, the encapsulated samples maintained stable interference patterns over the entire measurement period. No measurable spectral shifts or amplitude variations were detected, suggesting that the nitrocellulose nitrate layer effectively prevents oxidation and moisture-induced damage. This confirms the suitability of the encapsulation for maintaining long-term optical performance of FLBP under ambient conditions.

Simulation results

Parameters for simulation with nitrocellulose setup were as follows, note that this was setup consisting of 3 layers with different refractive index (n) and thickness (l): n_0=1.47 (fiber core); n_1=1 (air), l_1=100 μm (distance from the sample); n_2=1.46 (FLBP), l_2=5*10 μm (FLBP thickness) ; n_3=2.5 (nitrocellulose), l_3=1280 μm (nitrocellulose thickness). To compare the results with or without nitrocellulose parameter n_2 was simply set to 1. Fig Y shows compared results for setup with FLBP and FLBP covered with nitrocellulose.

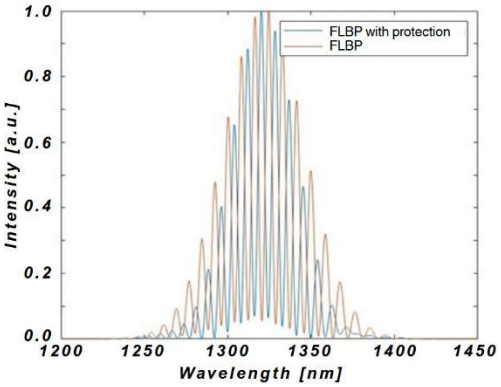


Fig. 2 Simulation results for setup with FLBP and FLBP covered with nitrocellulose (protected).

As can be observed on Fig. Y similar phase shift as on measurement results can be seen. This proves that additional layer of nitrocellulose is responsible for phase shift. This proves that addition of nitrocellulose film did not affect optical properties of FLBP. Nitrocellulose, as demonstrated here, provides a straightforward and effective means to overcome the primary barrier to FLBP's technological adoption, paving the way for its use in advanced optoelectronic and photonic systems.

References

[1] M. Buscema, D.J. Groenendijk, S.I. Blanter, G.A. Steele, S.J van der Zant, A. Castellanos-Gomez, „Fast and Broadband Photoresponse of Few - Layer Black Phosphorus Field-Effect Transistors“, Nano Letters 14, 3347-3352 (2014)

[2] W. Li, Z. Wang, F. Zhao, M. Li, X. Gao, Y. Zha, J. Wang, J. Zhou, Y. Hu, Q. Xiao, X. Cui, M. J. Eslamibidgoli, M. H. Eikerling, R. Li, F. Brandys, R. Divigalpitiya, T.-K. Sham, X. Sun*, „Quantification of Nanoscale Phase Evolution by Scanning Transmission X-ray Microscopy“, Chem. Mater. 32, 1272-1280 (2020)

[3] M. Szczerska, M. Kosowska, J. Gierowski, M. Cieślik, M. Sawczak, P. Jakóbczyk, „Investigation of the Few-Layer Black Phosphorus Degradation by the Photonic Measurements”, Adv. Materials Inter. 10, 2202289 (2023)

Acknowledgements

This study was supported as a project funded by the Ministry of Science and Higher Education of the Republic of Poland under agreement no. MNiSW/2024/DPI/433.

DOI 10.5162/EUROSENSORS2025/TP39

Nanoimprint lithography for multiple cavity height Fabry-Perrot filter array from two-level master

Clement Fleury[1], Benjamin Kalas[1], Bernardo Realista-Ferreira[1], Raveendra Nallagatla[1], Munir Azeem[1], Patrick Schuster[2], Marco Preuß[2], Vivien Lingel[2], Manu Garg[1], Bharathkumar Mareddi[1], Thang Duy Dao[1],
[1] Silicon Austria Labs GmbH, Sandgasse 34, 8010 Graz, Austria,
[2] EV Group E. Thallner GmbH, DI Erich Thallner Str. 1, 4782 St. Florian am Inn, Austria
clement.fleury@silicon-austria.com

Summary:
We demonstrate the design, fabrication and testing of a Fabry-Perrot filter array that can be adapted as an optical element in front of a sensor array. The technique uses nanoimprint lithography with a simple two-level master. The thickness of resin needed for each cavity is designed to match the resonant wavelength. Leveraging the local resin volume conservation, a modulation of the residual layer thickness is obtained by fill-factor engineering. The device is validated by transmission spectroscopy across the visible range.

Keywords: Optical filter array, Fabry-Perrot, Nanoimprint lithography, Fill-factor engineering

Introduction

Optical spectroscopy is widely used for sensing various species of interest whose spectral fingerprints are well known. Besides FTIR, that uses one single detector, common spectroscopy separates light into bins and uses a sensor array (CMOS or else) to record the intensity in each. The use of gratings is precise but requires space. Depending on the application, the most convenient, lightest and most compact solution is to directly insert a filter array right in front of the detector, ideally performed at wafer level [1]. Tuning a different filter for each pixel can be challenging. RGB filter arrays traditionally make use of one material per band, but it does not provide solutions for many narrow bands. Fabry Perrot (FP) filters, instead, can make use of one material to obtain narrow band filters that are tuned by the height of the cavity. Traditional additive manufacturing requires many alignment procedures and depositions to achieve the right height for each pixel. The present article shows a convenient solution making use of the properties of nanoimprint lithography (NIL).

Description of the New Method

The FP filters have been designed using an optical transfer matrix approach. The resin that was used for NIL spans a refractive index of 1.46 to 1.52 in the visible range, with sub 10^{-5} extinction coefficient, both extracted from spectroscopic ellipsometry. The mirrors that were considered are 60 nm silver layers deposited with the EVATEC BPME. The optical constants of silver used for simulation were taken from the literature [3]. The starting master design was a checkerboard of 800 by 800 pixels of size 20 µm where the black squares were etched by 418 nm (step value). This design was modified in such a way that the fill-factor was modulated from .125 to .875 along the diagonal direction of the array. Applying the conservation of volume during NIL imprint [2] and assuming no flow in the mm range, it was predicted that the residual layer thickness RLT (i.e. the low level after imprint) would be the base line – i.e. the average level - minus the local fill factor times the step, and the high level a step above that. This horizontal modulation of the fill factor therefore translates into a cavity thickness tuning in the NIL imprint across the array. The master mold was fabricated accordingly, and the NIL imprint was made using an EVG 7200 with a resin thickness matching the height of the silicon master. This imprint was performed on a 60-nm-thick Ag film deposited on a borosilicate wafer, followed by the deposition of an additional 60-nm-thick Ag mirror that was then deposited on top, creating the FP cavity array. The resulting wafer is shown in Fig. 2c.

The fabricated device was characterized by using a spectroscopic ellipsometer Semilab SE-2000 in transmission mode, with the FP filter placed at the focal spot of the focusing lenses. The spot is 300 µm wide and captures a weighted sum of the high-level and low-level cavities, with a small range of fill-factors broadening the peaks.

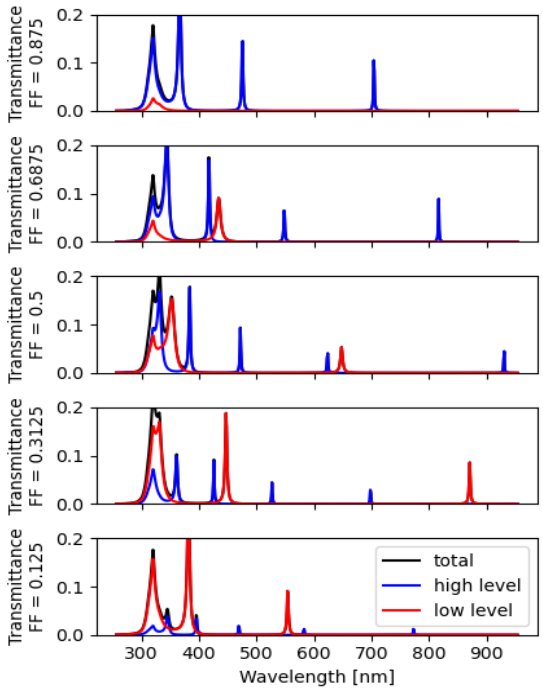


Fig. 1: Simulated response for variable fill-factors

Results

Fig. 1 shows the result of the optical simulation for five fill-factor values, where the contributions of high and low level are separated. With increasing fill-factors the peaks shift to lower wavelengths, as the cavities shrink. The decrease of the low-level peaks intensity as fill factor increases is due to their loss of weight in the signal to the profit of high-level peaks. The peaks at the UV side are due to the low extinction coefficient of Silver near its inter-band transition edge (~3.8 eV) [3], leading to near-zero permittivity.

The corresponding experimental values are shown in Fig. 2a where the positions of the spot and its area are shown as an overlay on the structure mask layout. Arrows show the shifts with fill-factor. The peaks are broader in the range of 10 nm, but part of this can be attributed to the spot size integrating a range of fill-factors together. The results show similar trends as the simulation, although not all peaks are matching, probably due to deviation between the expected and obtained RLT due to the flow of the resin. Additional modelling needs to be done to compensate for these effects.

Conclusions

Using NIL, we have demonstrated the fabrication of a Fabry Perrot filter array from a simple 2-level master by pre-tuning the fill-factor across the array. The process will further be developed to combine multilevel master with the presented technique so the fill-factor needed range can be limited to around 10% for fine tuning, and the peak intensity variation be less affected.

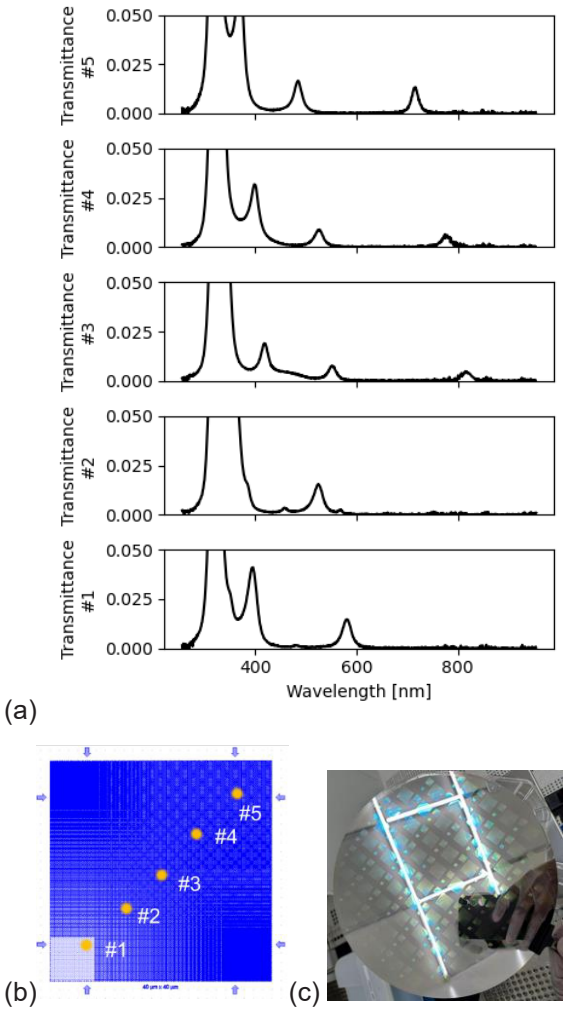


Fig. 2. (a) Measured response at (b) measurement sites, (c) wafer with filter arrays

References

[1] M.S. Cano-Velázquez *et al*, Optical Sensing with Picometer-level Precision using an Integrated Multispectral Chip, *Proceedings of Eurosensors XXXVI*, DOI 10.5162/EUROSENSORSXXXVI/OT7.37

[2] S Landis *et al,* Stamp design effect on 100 nm feature size for 8 inch NanoImprint lithography, 2006 *Nanotechnology* 17 2701, DOI 10.1088/0957-4484/17/10/043

[3] P. B. Johnson and R. W. Christy. Optical constants of the noble metals. Phys. Rev. B 6, 4370-4379 (1972)

Acknowledgements

This work has been supported by Silicon Austria Labs (SAL), owned by the Republic of Austria, the Styrian Business Promotion Agency (SFG), the federal state of Carinthia, the Upper Austrian Research (UAR), and the Austrian Association for the Electric and Electronics Industry (FEEI).

Printed Paper-Based Thermal Devices Using a Custom CB/rGO Ink for Sensing and Heating

Dimitris Barmpakos[1], Apostolos Apostolakis[1], Vassiliki Belessi[2], Vasilios Georgakilas[3], Grigoris Kaltsas[1]

[1] microSENSES Laboratory, Department of Electrical and Electronics Engineering, University of West Attica, Athens, Greece

[2] Department of Graphic Design and Visual Communication, University of West Attica, Athens, Greece

[3] Department of Materials Science, University of Patras, Rio, Greece

Corresponding Author's e-mail address: g.kaltsas@uniwa.gr

Printed Paper-Based Thermal Devices Using a Custom CB/rGO Ink for Sensing and Heating

Dimitris Barmpakos[1], Apostolos Apostolakis[1], Vassiliki Belessi[2], Vasilios Georgakilas[3], Grigoris Kaltsas[1]

[1] microSENSES Laboratory, Department of Electrical and Electronics Engineering, University of West Attica, Athens, Greece

[2] Department of Graphic Design and Visual Communication, University of West Attica, Athens, Greece

[3] Department of Materials Science, University of Patras, Rio, Greece

Corresponding Author's e-mail address: g.kaltsas@uniwa.gr

DOI 10.5162/EUROSENSORS2025/TP40

Detection of Butyric Acid Concentration in Aqueous Solution Towards Intraruminal Volatile Fatty Acid Measurement

Jarred Fastier-Wooller[1], *Daiki Yamaguchi*[1], *Shun Muramatsu*[1], *Michitaka Yamamoto*[1], *Toshihiro Itoh*[1]
[1] *Dept. Precision Engineering, Graduate School of Engineering, The University of Tokyo, 7-3-1 Hongo, Bunkyo-ku, 113-8656, Tokyo, Japan*
jarredfw@g.ecc.u-tokyo.ac.jp

Summary:
The use of polybutadiene thin-film coating on quartz crystal microbalance sensors is explored for measuring butyric acid concentration in an aqueous solution. Experiments show polybutadiene has a higher absorption rate of butyric acid. The fabricated sensor demonstrates an insensitivity to acetic acid and a low sensitivity to propionic acid. Therefore, progress is made towards selectively measuring butyric acid in aqueous solutions containing volatile fatty acids.

Keywords: QCM sensor, liquid sensing, butyric acid, rumen monitoring

Introduction

Methane (CH_4) is a well-known greenhouse gas with a reported potency of 20-85 times greater than carbon dioxide (CO_2). The impact of dairy, non-dairy, and other bovine species are the source of ≈22% of all global CH_4 emissions [1]. Using well-established systems, such as GreenFeed or respiration chambers, the CO_2 and CH_4 emissions can be measured. However, these external measurements don't provide complex information on the health status of the cattle. Measuring the concentration of volatile fatty acids (VFAs) in the rumen is of interest as it can be correlated to the production of CH_4, provide more comprehensive health statistics of the animal, and assist in preventing acidosis [2, 3].

Of the VFAs, acetic, propionic, and butyric acids are of most interest. However, these VFAs have similar molecular structures and are notoriously difficult to differentiate. We aim to measure these three acids in a small formfactor device capable of being swallowed by the cattle. Towards this goal we have implemented a quartz crystal microbalance (QCM) sensor. A QCM is a small and cost-effective resonator capable of measuring incredibly small quantities of molecules. By applying a thin film to the surface of a QCM, it is possible to capture molecules of interest and measure the change in mass on the surface of the sensor [4].

Materials and Methods

Prior to sensor fabrication, the presence of polybutadiene (BR) in aqueous solutions containing VFAs is investigated. Each sample has 0.05 M of a single VFA in DI water. "VFA + BR" samples have 0.8 g of BR beads per 5 ml of solution. Measured molar concentrations of VFA samples are measured by liquid chromatography after 2 hours (Table 1).

Tab. 1: Butyric acid (Bu), Propionic acid (Pr), and Acetic Acid (Ac) molar concentration in samples.

Sample	Bu [M]	Pr [M]	Ac [M]
VFA #1	0.052	0.046	0.045
VFA #2	0.052	0.046	0.045
VFA + BR #1	0.042	0.045	0.045
VFA + BR #2	0.042	0.045	0.045

Samples with BR present show a higher absorption of butyric acid compared to the other VFAs. From this result we believe that BR coating may provide a higher selectivity to butyric acid.

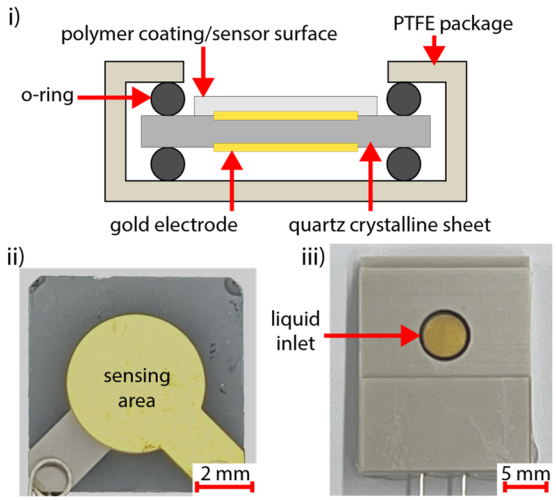


Fig. 1. i) structure of device with the positioning and composition of sensor and polytetrafluoroethylene (PTFE) packaging. ii) 20 MHz resonant QCM sensor with a ⌀ 5 mm sensing area. iii) packaged sensor.

The sensor is prepared by dissolving a solution of BR (3 wt%) and tetralin (97 wt%) and applying it to the surface of a commercial 20 MHz resonant QCM by spin coating (3000 rpm). The coated sensor is dried in a vacuum chamber at 60°C for 12 hours. The sensor is inserted into an airtight polytetrafluoroethylene (PTFE) package with the coated side of the sensor open (Fig. 1).

Experimental testing is performed inside a constant temperature chamber at 25°C. The sensor is suspended in a beaker with a magnetic stirrer to rapidly homogenize the solution (Fig. 2). Measurements were performed using a vector network analyzer (VNA) from Keysight (FieldFox n9923a).

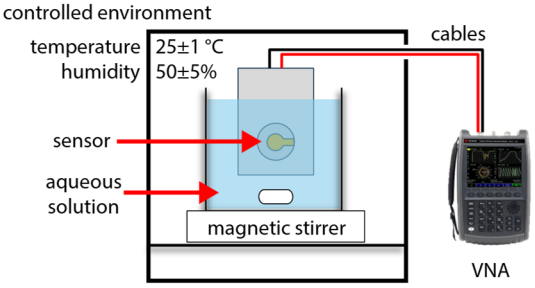


Fig. 2. Diagram of the experimental setup.

Results and Discussion

The sensor was submersed in DI water and the response to the addition of 0.05 mol/L of acetic, propionic, and butyric acids were tested.

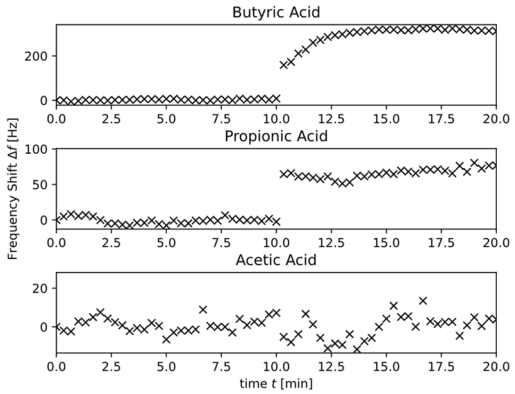


Fig. 3. Measured results from butyric, propionic, and acetic acid sample solutions. The VFA is added at 10 minutes.

The response of the sensor shows a 300 Hz change to butyric acid and a relatively insensitive response to the other VFAs of <80 Hz and <20 Hz (Fig. 3). The response to butyric acid is rapid at under 2.5 minutes and is stable after 5 minutes. The step response of butyric acid was also tested in 0.02 mol/L increments. The linear relationship between butyric acid concentration in aqueous solution can be seen in Fig. 4.

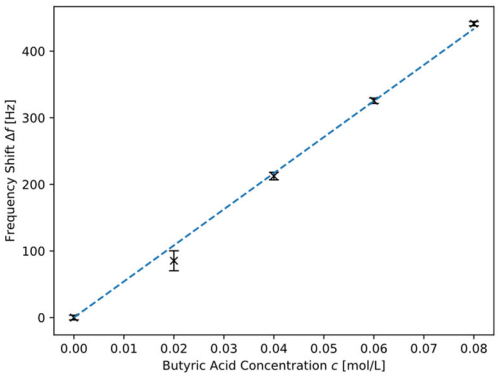


Fig. 4. Step response to butyric acid. Error bars represent standard deviation between measurements.

Systematic and human error are likely the cause of discrepancy in fig. 4. Further testing for repeatability is underway. However, these results demonstrate that a BR coated QCM is capable of selectively measuring butyric acid concentration in an aqueous solution.

Materials and Methods

A BR coated QCM is fabricated and used to measure the concentration of butyric acid in an aqueous solution. The sensor is shown to be less sensitive to propionic and acetic acid, allowing the differentiation of VFAs, a function which is not yet reliably available in such a small form-factor.

References

[1] Z. Lei, et al., A 130-year global inventory of methane emissions from livestock: Trends, patterns, and drivers, *Global Change Biology* 28(17), 5142-5158 (2022); doi: 10.1111/gcb.16280

[2] N. Stepanchenko, et al., Microbial composition, rumen fermentation parameters, enteric methane emissions, and lactational performance of phenotypically high and low methane-emitting dairy cows, *Journal of dairy science* 106(9), 6146-6170 (2023); doi: 10.3168/jds.2022-23190

[3] Y. Yusuke, et al., Comparative Studies on Electrodes for Rumen Bacteria Microbial Fuel Cells, *Sensors* 23(8), 4162 (2023); doi: 10.3390/s23084162

[4] N. Alanazi, et al., A review of quartz crystal microbalance for chemical and biological sensing applications, *Sensing and Imaging* 24(1), 10 (2023); doi: 10.1007/s11220-023-00413-w

Acknowledgements

A part of this work was supported by the Cabinet Office, Government of Japan, Cross-ministerial Moonshot Agriculture, Forestry and Fisheries Research and Development Program, “Technologies for Smart Bio-industry and Agriculture” (funding agency: Bio-oriented Technology Research Advancement Institution) (grant number: JPJ009237).

DOI 10.5162/EUROSENSORS2025/TP41

Flip Chip bonding of bare die on a flexible PET substrate with ablated copper.

Muhammad *Hassan Malik*[1], *Asaf Levy*[4], *Emily Bezerra*[1,2], *Carolin Kollegger*[3], *Sabine Lengger*[1], *Thomas Herndl*[3], *Effi Dvash*[4], *Mani Teja Vijjapu*[1]
[1] *Silicon Austria Labs, Europastrasse 12, A-9524 Villach, Austria,*
[2]*Laboratory of Bio/CMOS Interfaces, École Polytechnique Fédérale de Lausanne (EPFL), Neuchâtel, Switzerland*
[3] *Infineon Technologies Austria AG, Babenbergerstraße 10, A-8020 Graz, Austria*
[4] *KLA Corporation, P.O. Box 215, Yavne 81101, Israel*
muhammad-hassan.malik@silicon-austria.com

Summary:
The use of low-cost materials such as PET, paper, and unpackaged bare dies has become critical for cost-effective mass production, as demand for flexible hybrid electronics has skyrocketed, particularly for internet of things (IoT), electronic skin, and wearable applications. The advantages of this design include the sustainable use of resources, such as low-cost, readily accessible, and biologically degradable raw materials, and their suitability for printed electronics applications has been well researched. Mostly printed silver and sputtered silver has covered this market but has its own shortcomings. Combining this with techniques such as flip chip bonding and subtractive laser ablation provides us with the opportunity of fast fabrication and smaller size which can cater for new applications. In this study, we look at the flip chip bonding bare die to ablated copper on a PET substrate aided with anisotropic conductive paste. Furthermore, we investigate its reliability by performing bending tests.

Keywords: Ultra-thin dies; Hybrid integration; Printed electronics; Anisotropic conductive adhesives, (ACA); Anisotropic conductive paste (ACP); Polyethylene-terephthalate (PET); Chip on flex (COF); flexible electronics; laser ablation

Introduction

The implementation of devices based on low-cost materials such as PET, paper, and unpackaged bare dies has become crucial for economical mass production, as the demand for flexible hybrid electronics has increased extensively, specifically for the internet of things (IoT), electronic skin, and wearables applications [1]. Because standard wire bonding techniques are limited in their ability to accommodate flexible substrates, flip chip bindings are an important bonding technology for integration on them. Flip chip applications on flexible substrates have increased significantly, including Smart Cards, paging devices, disk drives, and LCD driver chips. These products are designed for large volume, low-cost, high-density assembly, compact and thin packaging, and low power consumption applications. [2][3]. In the past flip chip bonding on PET based substrates with printed silver circuitry has shown promising results but investigation on copper-based substrates is really limited. In this work, we bond bare dies to PET substrate with ablated copper circuitry. Moreover, to improve the reliability of the die it was encapsulated by a UV cured epoxy. In this research we investigate the possibility of flip chip bonding bare die to copper coated on PET substrate. The test vehicle consists of an NFC tag which can be used as a readout circuit.

Methods and materials

A 100µm PET substrate, coated with 500 nm of copper via physical vapor deposition, was utilized as the substrate. The circuitry design was created using commercial CAD software. A pulsed UV laser (Explorer One; 355 nm; 50KHz) was employed to ablate the copper surface, effectively removing the copper to achieve the desired electrical pattern. This laser system enables the ablation of relatively large patterns with high precision and resolution.

A die-bonder (Fineplacer, Finetech GmbH) was used to bond the ultra-thin dies to the ACA flip-chip. The system comprises of a heatable die handling tool and a separate heated stage. The bonding settings were calibrated so that the stage and tool temperatures were 135°C. A modest bonding force (30 N) was used to minimize any damage to the thinned dies. Planarization of the surfaces is crucial in this procedure; thus, the picking tool and stage were accurately adjusted using a pressure-sensitive foil, resulting in a perfect planer chip orientation. This is a two-step

method that begins with dispensing the ACP and then applies pressure and temperature. ACP provides electrical connections at fine-pitches and gives mechanical stability to the joint by acting as an underfill. A schematic of the final sample is shown in Fig.1 with the red arrow shows the conductive path.

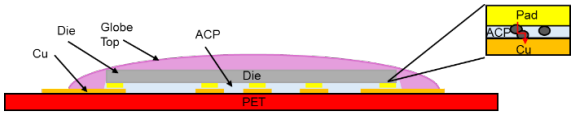


Fig. 1. Bonded sample

The bonded region was eventually covered by glob top dispensing. In the instance of Glob-top, a single component UV curable epoxy glue (OG116-31, Epotec, USA) was dispensed and cured by both UV irradiation and heated to 70°C. After fabrication, the samples were electrically evaluated at bending diameters ranging from 5 to 50 mm with a vernier caliper. The change in voltage was specified as the criteria to identify whether bending had any influence on the die's electrical interconnections. Optical images of the NFC tags can be seen in Fig .2.



Fig. 2. Optical images of NFC tag while bending

Results

After fabrication, the samples were electrically evaluated at bending diameters ranging from 50 to 30 mm with a vernier caliper. 50mm is the length of the sample when not bended. Three NFC tags were used in the experiment to make a quantitative analysis. Three diodes on the die were selected for the test. For the reference, diode voltages were measured on a rigid PCB board. These values are denoted by (x) in Fig 3. As we can see in Figure 3, the voltage increases as the bending diameter decreases.

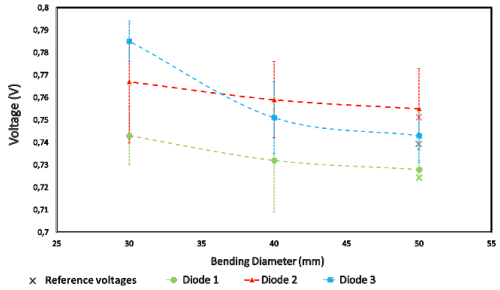


Fig. 3. Electrical characterization of the fabricated samples at different loop diameters.

Till 40mm, all three diodes indicate a little rise ~0.08V. The rise in electrical resistance of the bonded stack during the bending test can be attributed to the loss of contact between the conductive particles in the adhesive and the pads on the substrate or die. We also observe diode 3 shows a significant increase in the voltage ~0.04V bending from 40mm to 30mm compared to ~0.01V when bending from 50mm to 40mm.This can be attributed to the delamination of the chip edge from the substrate. Thus, we may conclude that this flip chip technique can be employed for bonding on flexible substrate fabricated and patterned by laser ablation, which can serve as an alternative to printed silver. This also opens further possibilities if silver cannot meet the application's demands.

References

[1] Muhammad Hassan Malik, Giovanna Grosso, Hubert Zangl, Alfred Binder, Ali Roshanghias, "Flip Chip integration of ultra-thinned dies in low-cost flexible printed electronics; the effects of die thickness, encapsulation and conductive adhesives," Microelectronics Reliability, vol. 123, 2021. https://doi.org/10.1016/j.microrel.2021.114204

[2] R. Aschenbrenner, R. Miessner and H. Reichl, "Adhesive flip chip bonding on flexible substrates," Proceedings. The First IEEE International Symposium on Polymeric Electronics Packaging, PEP '97 (Cat. No.97TH8268), Norrkoping, Sweden, 1997, pp. 86-94, doi: 10.1109/PEP.1997.656478.

[3] Muhammad Hassan Malik, Jaroslaw Kaczynski, Hubert Zangl and Ali Roshanghias, "Flip Chip Bonding on Stretchable Printed Substrates; The Effects of Stretchable Material and Chip Encapsulation," Flexible and Printed Electronics, 2023. doi: 10.1088/2058-8585/acb2d9

Acknowledgements

This work has been jointly funded by the EECONE project, supported by the Chips Joint Undertaking and its members, including the top-up funding by National Funding Authorities under grant agreement no. 101112065 and by Silicon Austria Labs (SAL), owned by the Republic of Austria, the Styrian Business Promotion Agency (SFG), the federal state of Carinthia, the Upper Austrian Research (UAR), and the Austrian Association for the Electric and Electronics Industry (FEEI).

DOI 10.5162/EUROSENSORS2025/TP42

Biological transistor (bioFET) for the specific and label-free sensing of CRP in unprocessed blood

Shubham Babbar[*1], Avital Eisenberg-Lerner[2], Ziv Rotfogel[2,3], Evgeny Pikhay[4], Inna Shehter[4], Ayala Elkayam[4], Muhammad Y. Bashouti[5], Barak Akabayov[6], Izhar Ron[1], Guy Hazan[7,8], Yakov Roizin[4], Gil Shalev[1,5]

[1] School of Electrical Engineering, Ben-Gurion University of the Negev, Israel.
[2] Ophthalmology Research Laboratory, Kaplan Medical Center, Rehovot, Israel.
[3] Faculty of Medicine, Hadassah Medical School, The Hebrew University of Jerusalem, Jerusalem, Israel.
[4] Tower Semiconductor, PO Box 619, Migdal Haemek, Israel
[5] The Ilse-Katz Institute for Nanoscale Science and Technology, Ben-Gurion University of the Negev, POB 653, Beer-Sheva 8410501, Israel.
[6] Department of Chemistry and Data Science Research Center, Ben-Gurion University of the Negev, 8410501, Beer-Sheva, Israel.
[7] School of Medicine, Faculty of Health Sciences, Ben-Gurion University of the Negev, Beer-Sheva, Israel.
[8] Pediatric Department D, Soroka University, Medical Center, Beer-Sheva, Israel.
*Presenting author: shubham@post.bgu.ac.il
Corresponding author: glshalev@bgu.ac.il

Abstract: Point-of-care (POC) diagnostic technologies are essential for timely clinical decision-making, significantly improving patient outcomes. However, the widespread adoption of POC diagnostics is hindered by the lack of technological methods that combine miniaturization, accuracy, multiplex sensing from ultra-small samples, and cost-effectiveness. Traditional diagnostic methods, such as Enzyme-Linked Immunosorbent Assay (ELISA), are unsuitable for POC applications due to their complexity, high cost, and reliance on labeling techniques, which can alter molecular interactions and lead to non-specific signals. Transistor-based diagnostic technologies offer a promising alternative, with the potential for extreme miniaturization, robustness, and high sensitivity. Despite ongoing efforts over the past four decades, no transistor-based technology has yet achieved specific and label-free sensing for medical diagnostics.

In this study, we introduce the Meta-Nano-Channel biological field-effect transistor (MNC bioFET), a novel device that addresses the challenges of the solution-solid interface in transistor-based diagnostics. The MNC bioFET's multi-gate design enables selective excitation of conducting channels with varied coupling to surface potential variations induced by molecular interactions, allowing for highly sensitive, specific, and label-free detection. We demonstrate the MNC bioFET's capability by detecting C-Reactive Protein (CRP), a critical biomarker for inflammation and tissue damage. The MNC bioFET, manufactured using standard CMOS processes, offers significant advantages for POC diagnostics, including stability, robustness, and the potential for mass production. This technology represents a significant step forward in the development of practical, high-performance POC diagnostic tools.

DOI 10.5162/EUROSENSORS2025/TP43

Novel gating mechanism employed on nano bio-FET towards real-time, point-of-care diagnostics in human whole blood

Vijay Garika[1#], Shankar Bhattarai[8], Sherina Harilal[2], Avital Eisenberg-Lerner[3], Ziv Rotfogel[3,4], Evgeny Pikhay[5], Inna Shehter[5], Ayala Elkayam[5], Muhammad Y. Bashouti[2,6], Barak Akabayov[7], Izhar Ron[1], Yakov Roizin[5], Vladimir Bamm[8], Melanie Wills[8], Gil Shalev[1,6]*

[1] *School of Electrical Engineering, Ben-Gurion University of the Negev, Israel.*
[2] *Department of Solar Energy and Environmental Physics, Swiss Institute for Dryland Environmental and Energy Research, J. Blaustein Institutes for Desert Research, Ben-Gurion University of the Negev, Midreshet Ben-Gurion 8499000, Israel.*
[3] *Ophthalmology Research Laboratory, Kaplan Medical Center, Rehovot, Israel.*
[4] *Faculty of Medicine, Hadassah Medical School, The Hebrew University of Jerusalem, Jerusalem, Israel.*
[5] *Tower Semiconductor, PO Box 619, Migdal Haemek, Israel*
[6] *The Ilse-Katz Institute for Nanoscale Science and Technology, Ben-Gurion University of the Negev, POB 653, Beer-Sheva 8410501, Israel.*
[7] *Department of Chemistry and Data Science Research Center, Ben-Gurion University of the Negev, 8410501, Beer-Sheva, Israel.*
[8] *Department of Molecular and Cellular Biology, University of Guelph, 50 Stone Road East, Guelph, Ontario, Canada.*

***Principle/Presenting author**: garika@post.bgu.ac.il.*
* ***Corresponding author**: glshalev@bgu.ac.il.*

Abstract: Lyme disease, a pathogenic illness caused by *Borrelia* bacteria in North America and various other areas, poses a considerable clinical diagnostic challenge. The prevailing technique for Lyme disease testing involves the detection of host immune antibodies against the pathogen as opposed to detecting the pathogen itself. The difficulty in early identification stems from the host antibody reactivity that emerges several weeks post-infection. A biologically modified field-effect transistor (BioFET) promises a potential platform to directly detect pathogens but is limited by the detection of faint responses generated from the lowest concentrations due to the nonuniform and random distribution of binding interactions on the sensing area. We have unveiled a novel asymmetrical switching gated BioFET that enables electrostatic manipulation of the conducting channel's dimension, configuration, and position, thereby enhancing the coupling of localized electrostatics of biological events and the electrodynamics of the nano conducting channel underneath. In the current study, we report a specific and label-free detection of outer source protein A (OspA), the causative factor of Lyme disease, ranging from 1 fg/mL to 1 µg/mL in ultra-small 0.5 µL drops of human whole blood. By tuning the nano conduction channel with asymmetrical gating, we demonstrated the remarkable lowest limit-of-detection (LOD) of 1 fg/mL and an excellent dynamic range of 6 orders with a linearity of 0.97. We report extensive control measurements that validate the reliability and specificity of the sensor's signals, quantifying the non-specific response. Furthermore, numerical simulations are performed to validate the potential detection of weak localised binding responses with asymmetric gating. Our technique is readily applicable to a diverse array of biomarkers, suggesting significant potential for numerous low-cost, real-time, biomedical applications.

DOI 10.5162/EUROSENSORS2025/TP44

Approximation of temperature characteristics of Seebeck coefficients for CuNi-Ag and $Ca_3Co_4O_9$-Ag thermopiles

Szymon Wójcik, Andrzej Dziedzic
Wrocław University of Science and Technology, Wrocław, Poland

Summary:

Determining the approximation for CuNi-Ag and $Ca_3Co_4O_9$-Ag thermopiles based on real measurements to allow prediction of Seebeck coefficient values against temperature.

Keywords: energy harvesting, thermoelectricity, thick film, thermocouple, thermoelectric microgenerator

Motivation and description of work

Thermoelectric microgenerators are one of the promising directions in the field of energy harvesting from a temperature gradient. Their operation is based on the thermoelectric phenomenon, in which the electric power is generated as a result of the temperature difference between two junctions of different materials. Such devices, due to their small scale, can be used in a wide range of applications, from powering sensors in Internet of Things (IoT) devices to industrial and medical applications, where small size and ability to operate in extreme temperature conditions are important. A key parameter characterizing thermoelectric materials is the Seebeck coefficient, which describes a material's ability to generate thermoelectric force under a temperature gradient. Optimization of this coefficient for thermoelectric microgenerators makes it possible to increase their efficiency and performance.

As part of the research, the Seebeck coefficient was modeled as a function of operating temperature, based on actual measurements. The structures that were modeled were fabricated in the form of thermopiles from pairs of CuNi-Ag materials on an LTCC substrate and $Ca_3Co_4O_9$-Ag on an alumina substrate [1]. For these structures, voltage and resistance were measured as a function of temperature, from -40°C to about 160°C, cooling or heating the junction area of the structure. On this basis, the low-gradient (differential) Seebeck coefficient was determined as a function of temperature was calculated. The selected structures were aged by placing them sequentially at 150°C, 250°C and 350°C for 100 hours. After each aging step, the above-mentioned measurements were repeated.

Results

Due to the fact that the value of the Seebeck coefficient depends on the temperature, it was decided to approximate its characteristic with a third-degree polynomial and compare experimental values with least squares approximations. The approximating function took the form presented in Eq. (1).

$$S(T) = a_3 \cdot (T - 273.15)^3 + a_2 \cdot (T - 273.15)^2 + a_1 \cdot (T - 273.15) + a_0 \quad (1)$$

Table 1. Approximation parameters for as-fired and thermally aged CuNi-Ag and Ca349-Ag thermopiles.

Parameter	T-type thermo-couple	CuNi-Ag on LTCC				Ca349-Ag on alumina			
		As-fired	150°C (423 K)	250°C (523 K)	350°C (623 K)	As-fired	150°C (423 K)	250°C (523 K)	350°C (623 K)
a_3 [μV/K⁴]	-5.95E-08	-7.82E-07	-1.09E-06	7.18E-07	-1.24E-06	-1.31E-05	-3.66E-06	-6.94E-06	-4.54E-06
a_2 [μV/K³]	-6.65E-05	3.45E-04	3.30E-04	8.55E-05	4.67E-04	2.47E-03	1.51E-03	1.67E-03	1.18E-03
a_1 [μV/K²]	8.93E-02	-5.79E-03	1.33E-02	1.16E-02	-4.64E-03	-1.02E-01	-1.31E-01	-1.27E-01	-8.88E-02
a_0 [μV/K]	3.82E+01	4.08E+01	3.93E+01	4.15E+01	4.02E+01	1.10E+02	1.12E+02	1.12E+02	1.11E+02

Based on the determined approximations, the accuracy of the approximations was determined using Eq. (2), (3) and (4).

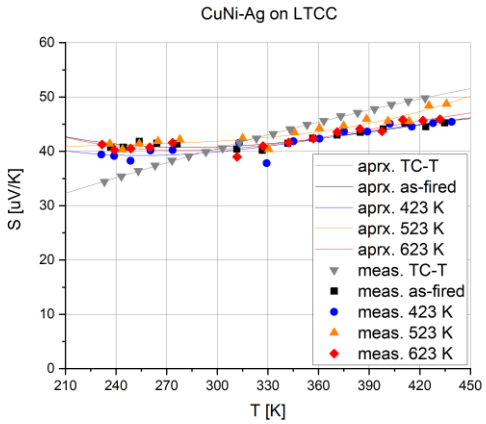
$$R^2 = 1 - \frac{\sum_{i=1}^{n} (S_i - \hat{S}_i)^2}{\sum_{i=1}^{n} (S_i - \bar{S})^2} \quad (2)$$

$$MSE = \frac{1}{n}\sum_{i=1}^{n}\left(S_i - \hat{S}_i\right)^2 \quad (3)$$

$$RMSE = \sqrt{MSE} \quad (4)$$

where: $S_i - measured\ value, \hat{S}_i - value\ predicted\ by\ the\ model;\ \bar{S} - average\ value\ and\ n - number\ of\ measurements.$

a)



b)

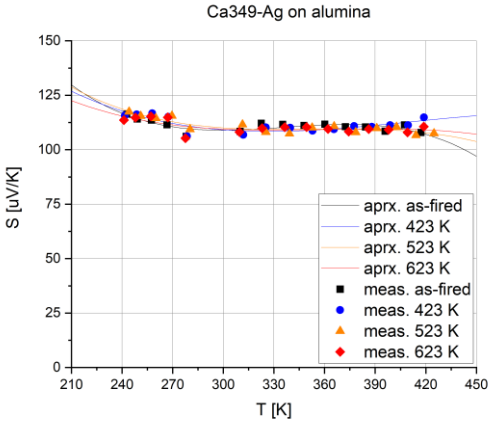


Fig.1. Approximations with distribution of real values for (a) CuNi-Ag on LTCC; (b) Ca349-Ag on alumina

Table 2. Quality of approximation for as-fired and thermally aged CuNi-Ag and Ca349-Ag thermopiles.

Parameter	T-type thermocouple	CuNi-Ag on LTCC				Ca349-Ag on alumina			
		As-fired	150°C (423 K)	250°C (523 K)	350°C (623 K)	As-fired	150°C (423 K)	250°C (523 K)	350°C (623 K)
$\bar{S}$ [μV/K]	42.62	42.44	41.89	43.78	42.47	111.03	111.60	110.83	110.50
R^2 [-]	0.999	0.997	0.991	0.995	0.996	0.997	0.995	0.997	0.995
MSE [(μV/K)^2]	0.006	0.338	1.005	0.656	0.454	2.355	3.605	2.104	3.958
RMSE [μV/K]	0.078	0.581	1.003	0.810	0.674	1.535	1.899	1.451	1.989

The approximations obtained from the measurements are acceptable, although they show weaker fit than the reference values for the T-type thermocouple (standardized Cu-CuNi wire thermocouple). Determination coefficients R^2 of about 0.99 show the good quality of the models' fit and confirm their ability to predict actual values. The RMSE index indicates how much, on average, the values predicted by the model can differ from the actual values. The higher RMSE values for the Ca349-Ag system are due to the wider range of data, where the average Seebeck coefficient is about 110.99 μV/K, while for CuNi-Ag it is about 42.64 μV/K (based on all measurement series).
The results obtained for CuNi-Ag, can be related to the standard T-type thermocouple. The approximation determined in the same way has an R^2 of 0.999 and an RMSE of 0.078 μV/K. The average Seebeck coefficient for the T-type thermocouple in the analyzed temperature range is equal to 42.62 μV/K.
The results show that the Seebeck coefficient approximation is a reasonable solution, but it should be taken into account that the third-degree polynomial is not always able to perfectly predict the results. Increasing the degree of the polynomial in the equation could allow a more accurate match between predicted and actual results. However, it can be concluded that in many applications the third-degree approximation works well for simple calculations.

References

[1] A. Dziedzic, S. Wójcik, M. Gierczak, S. Bernik, N. Brguljan, K. Reinhardt, S. Körner; Planar Thermoelectric Microgenerators in Application to Power RFID Tags, Sensors 2024, 24, 1646; doi: 10.3390/s24051646

DOI 10.5162/EUROSENSORS2025/TP45

MEMS Based Field Mill for Measuring Hybrid Electric Fields

Wilfried Hortschitz [1], *Gabor Kovacs*[1] *and Franz Keplinger*[2]
[1] Department for Integrated Sensor Systems, University for Continuing Education Krems, Viktor Kaplan Str. 2E, A2700 Wiener Neustadt
[2] Institute of Sensor and Actuator Systems, Technische Universität Wien, Gusshausstrasse 27-29, A1040 Vienna
wilfried.hortschitz@donau-uni.ac.at

Summary: In this paper we report a microsystem-based sensor system allowing measurement of static and low-frequency electric fields. The micro-electro-mechanical system is electrostatically actuated in-plane. A microcontroller unit is incorporated for generating signals for excitation but also to evaluate the signal after amplification via a digital lock-in amplifier. It is successfully shown that the system can measure DC and AC electric fields.

Keywords: MEMS, electric-field, AC+DC, hybrid field, measurement

Introduction

The measurement of electric fields has been a subject of interest for many decades, with various methods developed to quantify static fields. However, the increasing complexity of modern energy systems, which are progressively transitioning to hybrid configurations due to the integration of renewable energy sources and the need for long-distance transmission, has created a demand for more versatile measurement systems. Traditional electric field mills are typically limited to static field measurements, which constrains their applicability in these evolving energy landscapes [1]. In response to this need, we present a micro-electro-mechanical system (MEMS)-based measurement system designed to measure both static (DC) and low frequency, dynamic (AC) components of electric fields. This MEMS-based Field Mill (MEMS-EFM) [3] uses silicon-on-insulator (SOI) technology and is electrostatically actuated in-plane. The system incorporates a microcontroller unit (MCU) for signal generation and evaluation, utilising a digital lock-in amplifier to enhance the accuracy and reliability of the measurement.

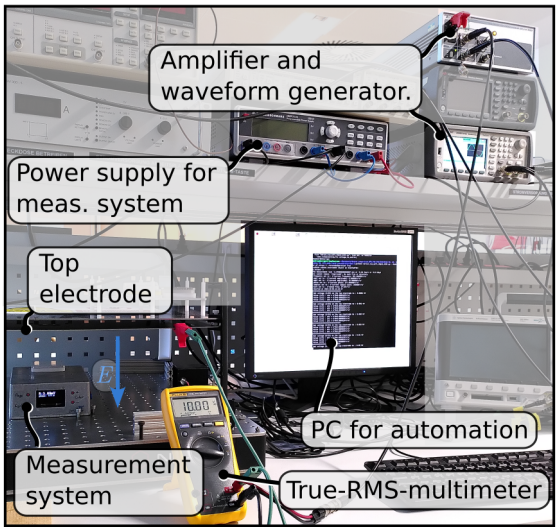


Fig. 1: Fully automated measurement set-up: The outer electric field E is created by applying the hybrid voltage from the high voltage amplifier to the top electrode above the measurement system which is positioned on a grounded plane.

Motivation

There are many ways to measure electric fields, but until now no compact system is available to measure reliable AC and DC [1]. This paper focuses not on improved sensitivity of the MEMS-EFM for DC such as done in [3] but on additional possibilities by the lock-in to measure also low-frequency components of the electric field.

Measurement Set-up

The sensor system, which provides cover for the fragile microsystem. The MEMS is located below an insulated floating electrode. The electronic circuitry for supplying the electrostatic actuation and amplifying the induced currents to voltage to be read by the ADC of the MCU is shown in Fig. 2. The amplification of the transimpedance amplifiers used to convert the currents generated by the MEMS is 100 MΩ. Both electrostatic drives were supplied with peak to peak voltages of $\leq$15 Vpp at 382 Hz which is the half of the resonance frequency of the MEMS. The hybrid voltage for the electric field was generated by a high-voltage amplifier (9200A, Tabor Electronics) while the amplifier input signal was provided by a waveform generator (Keysight 33500B). The voltage was applied to a electrode of 50 cm $\times$ 50 cm size made of stainless steel. The distance between the electrode that holds the voltage and a grounded sensor system is 0.125 m. A true RMS multimeter was used to

measure the resulting values of the AC and DC components. The insulator around the MEMS is of 6 mm height and is produced by rapid prototyping. The MEMS is located below the rectangular part on top of a white insulator. This metal part is electrically floating and was machined from aluminum and acts also as field concentrator, increasing the field in an area of approximately 20 mm^2 above the MEMS.

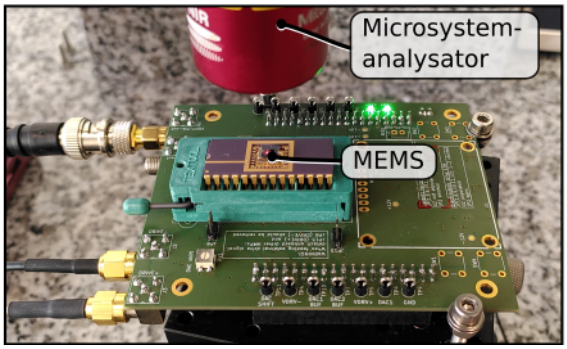


Fig. 2: Evaluation PCB with an electric field sensor in a ceramic package below Micro-System-Analyzer. All in- and outputs were supplied via lab equipment.

MEMS

The micro-systems were processed from custom designed layouts in the clean-room of ISAS-TUWIEN. The improved designs are based on the best prior chip-layouts where especially drive- and/or sensing electrodes were enhanced. The chips were wire-bonded into ceramic dual line standard packages enabling simple exchange in combination with a universal DIP sockets (Textool) as part of the actuation and evaluation circuit. Figure 3. depicts exemplary layout-data and the SEM image of a fabricated micro-sensor. Figure 4 shows the results of a measurement with hybrid electric field. At higher AC-fields of more than 1200 VRMS/m the amplifier saturates. In the lower-left part of the diagram, at low values of the external field, the deviation from the fitted slope is visible. This is due to resolution limit which is estimated to be 80 VRMS/m for AC fields of 50 Hz.

Conclusion

The results show that it is possible to measure DC and AC components of the electrostatic field using one single sensor system. The discussed system, which is incorporating a micro-controller for signal generation, acquisition and evaluation is a complete stand-alone device which can be used battery-powered. The signal evaluation at DC or at a given low frequency is implemented via a digital lock-in with adaptable demodulation frequency. The resolution limit was determined to be 80 VRMS/m.

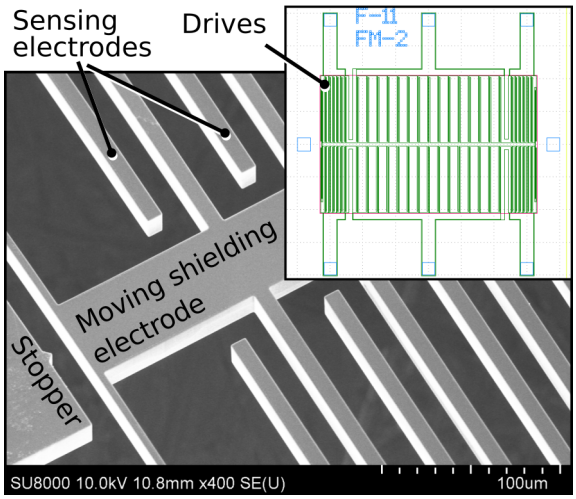


Fig. 3: SEM picture of a fabricated structure. The complete structure was etched into the 20 µm thick device layer of an SOI-wafer. The inset show a MEMS example layout. Side length of a single chip is 5 mm.

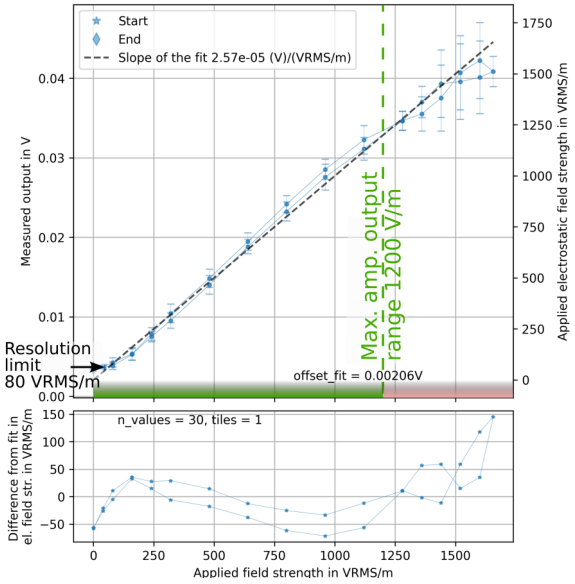


Fig. 4: Measured results for the MEMS supplied with different AC-fields of 50 Hz super-imposed on a DC-field of 400 V/m.

References

[1] W. Hortschitz, et al. *Measurement Science and Technology*, 35, 5, 052001, (2024), IOP Publishing; doi: 10.1088/1361-6501/ad243a

[2] Chen, T., et al. (2024). DC electric field sensor in a grounded enclosure with height adjustable pin., *Journal of Electrostatics*, 129, 103936; doi: https://doi.org/10.1016/j.elstat.2024.103936

[3] Wang, G., et al. (2024). A Review on Resonant MEMS Electric Field Sensors. *Micromachines*, 15(11), 1333.; doi: 10.3390/mi15111333

DOI 10.5162/EUROSENSORS2025/TP46

A High-Sensitivity Co-Oscillating Electrochemical Vector Hydrophone Based on Micron-Scale Controllable Microelectrodes

Honghao Zhang[1,2], Junbo Wang[1,2], Deyong chen[1,2], Yulan Lu[1,2]
[1] Aerospace Information Research Institute, Chinese Academy of Sciences, Beijing 100190, CHINA
[2] University of Chinese Academy of Sciences, Beijing 100049, CHINA
luyl@aircas.ac.cn

Summary:
This paper reports a novel co-oscillating electrochemical vector hydrophone with ~5 times higher sensitivity than that of current best levels (peak sensitivity -166.36dB vs. -180.10dB REF 0dB=1V/μPa) within 1Hz~ 1000Hz. This considerable improvement was due to the novel MEMS microelectrodes which featured with a micron-scale controllable spacing between the anode and cathode and larger cathode area.

Keywords: MEMS, electrochemical, co-oscillating vector hydrophone, microelectrodes, micron-scale controllable.

Background, Motivation an Objective

Vector hydrophones act as important parts in underwater acoustic detections and target reignitions. With the development of shock absorption and noise reduction technologies, the radiation noise of underwater targets has been reduced. However, very low-frequency noise (such as blade frequency and shaft frequency) cannot be eliminated. Current hydrophones still have limitations in low-frequency sensitivity [1]. Although we have accumulated some technical expertise [2-3], there remains room for improvement in this field.

Description of the New Method or System

Figure 1 shows the new type vector hydrophones based on co-oscillating electrochemical principles. This sensor composes of protective shell, electrolyte, and proposed micron-scale controllable microelectrodes. In operation, the external underwater sound distributions change the active ion concentrations around the two cathodes, and then unbalance the REDOX reactions ($3I^- - 2e^- = I_3^-$ and $I_3^- + 2e^- = 3I^-$) occurred on microelectrodes. Finally, the differential voltage is output.

Figure 2 (a) shows proposed novel micron-scale controllable microelectrodes. Smaller spacing between anode and cathode and lager cathode area are definitively conducive to improve sensitivity. In this paper, a micron-scale controllable insulation ring structure is designed to realize smaller distance between anode and cathode. Meanwhile, the area of the anode and cathode spacing on the surface is reduced, which is conducive to the distribution of more vias, so as to have a larger cathode area on the sidewall of vias. The micron-scale controllable insulation ring structure is achieved by using aluminum as sacrifice layer for lift-off. Figure 2 (b) shows the MEMS process flow of the microelectrodes. Before etching vias, the circular aluminum sacrificial layer for lift-off was made as the anode and cathode spacing. After deep reactive ion etching the vias and depositing electrode metal Ti/ Pt by sputtering, selectively removing aluminum sacrificial layer in 85 wt% phosphoric acid.

Results

The watertight encapsulated co-oscillating electrochemical vector hydrophone was tested with a vibration table and a standing-wave tube. Figure 3 (a) shows its sensitivity curve. Its peak sensitivity reaches -166.36dB @ 20Hz (REF 0dB=1V/μPa). Figure 3 (b) shows the noise level, with a lower level than shallow sea state zero between 1-200Hz. Figure 3 (c) shows its directivity curve @ 200Hz, with a smooth and symmetrical shape of “8”, and the pit depth reached -47.6dB. Compared with the existing devices, the results are shown in Table 1. The vector hydrophone described in this paper has higher sensitivity and deeper pit point. The above good performance shows excellent application prospect of proposed vector hydrophone in very low-frequency.

Figures

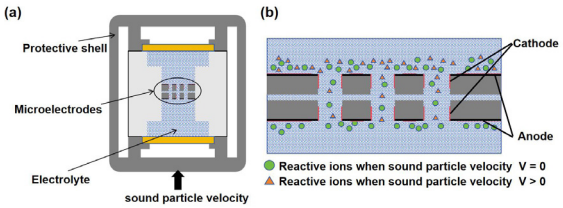


Fig. 1. *Schematic diagram of MEMS co-oscillating electrochemical vector hydrophone (a) Structure diagram (b) Working principle*

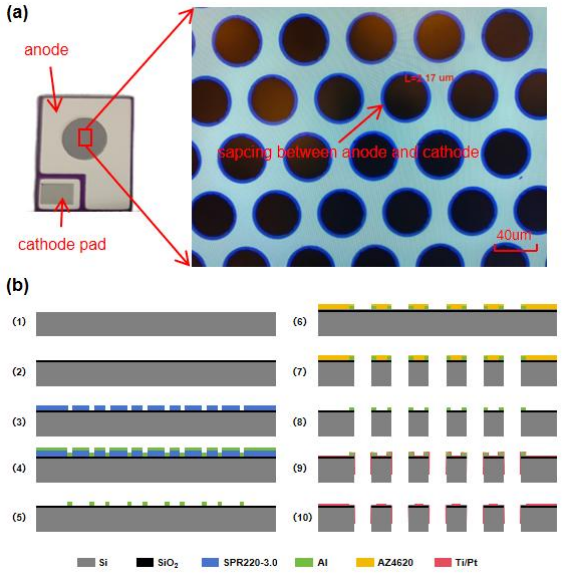


Fig. 2. (a) *Proposed microelectrodes image* (b) *MEMS process flow chart*

Tables

Tab.1: *Performance comparison of different devices*

"dB" of sensitivity REF 0dB=1V/μPa;

"dB" of pit depth is relative amplitude.

Device	Peak sensitivity	Pit depth
[2]	-188.86dB	/
[3]	-180.10dB	-40.8dB
This study	-166.36dB	-47.6dB

ACKNOWLEDGMENTS

This work was supported in part by the National Natural Science Foundation of China under Grant62201549, Grant 52335012 and Grant U23A20362, in part by Beijing Natural Science Foundation under Grant 4242012, in part by the Youth Innovation Pro-motion Association CAS under Grant 2023134, in part by the Strategic Priority Research Program (B) of the Chinese Academy of Sciences under Grant XDB1110201.

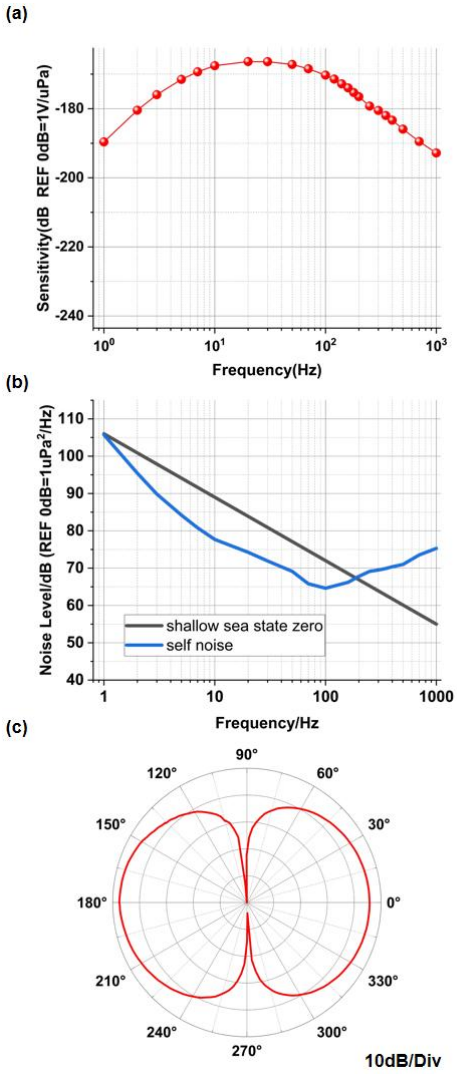


Fig. 3. *Experimental results (a) Sensitivity curve (b) Noise level (c) Directivity curve @200Hz*

Reference

[1] H. Saheban, Z. Kordrostami,Hydrophones, fundamental features, design considerations, and various structures: A review, Sensors and Actuators A: Physical 329, 112790(2021); doi:10.1016/j.sna.2021.112790

[2] A. Zhong, M. Chen, A MEMS-Based Co-Oscillating Electrochemical Vector Hydrophone, *Micromachines 13*, 143-153 (2022); doi: 10.3390/mi13010143

[3] L. Hu, T. Liang, A Three-axis Co-Oscillating Vector Hydrophone Based on MEMS Electrochemistry, *22nd International Conference on SolidState Sensors, Actuators and Microsystems*, 1567-1570 (2023).

DOI 10.5162/EUROSENSORS2025/TP47

Performance Improvement of Resonant Absolute Pressure Sensors Based on Topology Optimization and Suspension Design

*Xiaohan Liu[1,2], Bo Xie[1,2**], Junbo Wang[1,2], Deyong Chen[1,2],Yulan Lu[1,2],Bowen Tan[1,2], Xingyu Li[1,2], Zhaoyaun Tan[1,2]*

[1] State Key Laboratory of Transducer Technology, Aerospace Information Research Institute, Chinese Academy of Sciences, Beijing 100049, China，

[2] School of Electronic, Electrical and Communication Engineering, University of Chinese Academy of Sciences; Beijing 100049, China

***Bo Xie[1,2], Email: xiabo@aircas.ac.cn*

Summary:

This paper proposes an innovative solution that combines topology optimization and suspension design to meet the aerospace industry's demands for high reliability, lightweight, and environmental adaptability in resonant absolute pressure sensors. Experimental and simulation result demonstrate that the temperature infection is reduced by 75% in harsh environments. The optimized sensor achieves an accuracy of 0.01% FS within a 140 kPa range under harsh temperatures (−50°C to 85°C).

Keywords: Suspension Design, Topology Optimization, Resonant Pressure Sensor, temperature-insensitive, High Accuracy

Introduction

In the aerospace field, precise absolute pressure measurement is crucial for the control systems of aircraft. Resonant pressure sensors offer excellent measurement accuracy and response speed, making them ideal pressure sensors [1]. However, traditional design methods often suffer from issues such as error accumulation under harsh conditions like environmental temperature changes, and environmental pressure changes [2]. topology optimization and Suspension design, as advanced structural design techniques, can effectively enhance the performance of sensors. This study combines both approaches and proposes a new sensor design method.

Suspension Design and Topology Optimization

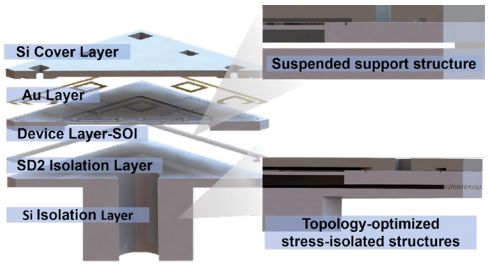


Fig. 1. Sensor Structure.

In sensor design, the commonly used GOS (glass on silicon) stress isolation structure with a "high thickness ratio" is employed to reduce the propagation of assembly stress [3] (Fig. 1).

However, due to material property variations and process defects, temperature changes induce thermal stress in the isolation structure itself, leading to frequency shifts. Based on the Principal Stress Line topology optimization method, the optimized structure ensures the device's stiffness while reducing mass by 50%. Based on the actual process flow, three types of isolation structures are derived from the optimized isolation structure (Fig. 2).

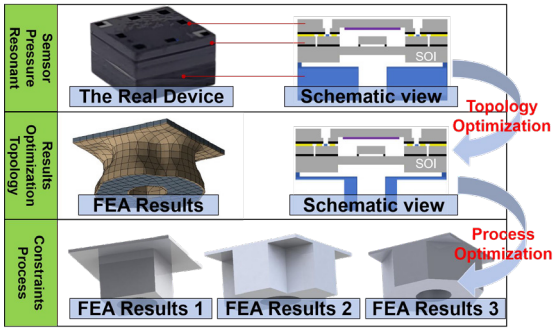


Fig. 2. The Process of Isolation Structure Topology Optimization.

After performing finite element verification of the three structures, it is found that, within the temperature range of −55°C to 85°C, the first structure exhibits the least sensitivity to thermal

stress and the strongest anti-interference capability: 6.3Hz/°C and 9.9Hz/°C (Fig. 3)

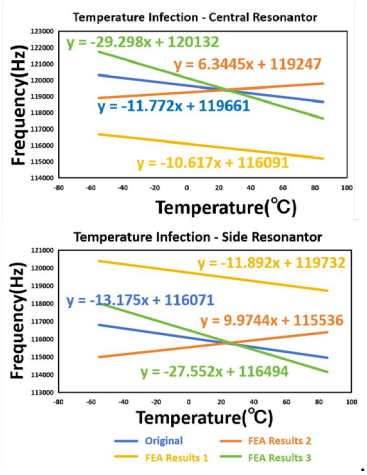


Fig. 3. The impact of temperature changes on the original structure and the three optimized structures.

In the absolute pressure sensor, the SD2 Layer in the isolation structure is visualized to achieve a suspended design, lengthening the stress transmission chain from the isolation structure to the sensor, reducing the stress experienced by the device itself, and minimizing the impact on the frequency (Fig. 4).

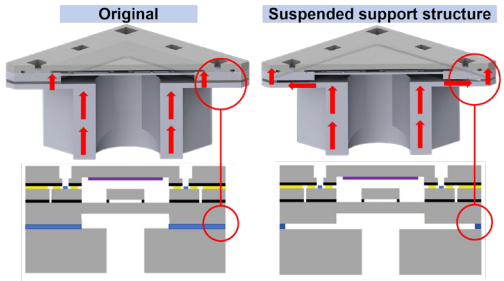


Fig. 4. Schematic diagram of the suspended structure design. The structure marked in red is SD2. And,the stress transmission chain and processing schematic diagram.

Through finite element simulation, stress is applied to devices with and without the support structure under the same conditions, verifying that the suspended support structure reduces the impact of environmental stress on the resonant frequency by 75% (Fig. 5).

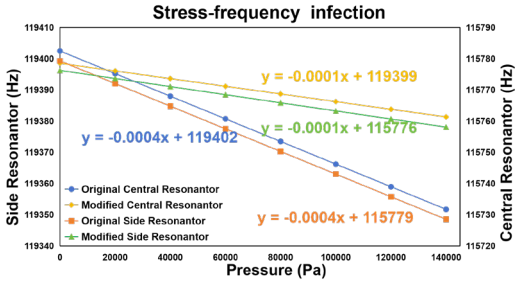


Fig. 5. The impact of environmental stress on frequency.

Results

Compared to traditional designs, the use of a suspension system effectively isolates external vibration interference and temperature changes, ensuring the sensor's stability. Experimental results show that after three temperature cycles (−55°C to 85°C), the device still maintains an accuracy of 0.01% FS (Fig. 6). The resonant absolute pressure sensor proposed in this paper, based on topology optimization and suspension design, offers significant advantages in performance, particularly in improving sensor stability and anti-interference capabilities.

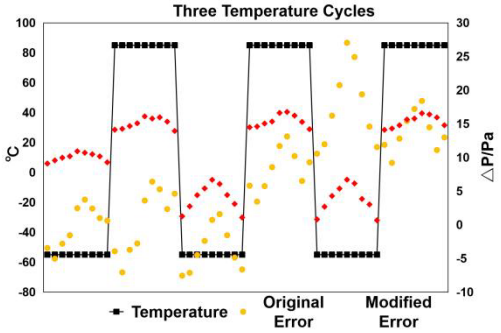


Fig. 6. Sensor Accuracy Under Four Temperature Cycles

References

[1] CJ Welham, J Greenwood, MM Bertioli, A High Accuracy Resonant Pressure Sensor by Fusion Bonding and Trench Etching. Sensors and Actuators A: Physical. 1999, 76, 298–304; doi: 10.1016/s0924-4247(99)00065-5

[2] X.Y, Li, H, Xue, Y.L, Lu, et al, Integrated Isolation Structure for Reducing Thermal Stresses of Resonant Pressure Microsensor, IEEE Sensors Journal, VOL. 24, NO. 23, 1 DECEMBER 2024; doi: 10.1109/jsen.2024.3476 478

[3] S.Y, Chen, J.X Qin, Y.L, Lu, et al, An All-Silicon Resonant Pressure Microsensor Based on Eutectic Bonding, *Micromachines* 2023, 14(2), 441; doi:10.3390/mi14020441

Acknowledgements

National Key Research and Development Program of China：2022YFB3204901

National Natural Science Foundation of China：62121003

DOI 10.5162/EUROSENSORS2025/TP48

Novel Acoustic Method for Detecting Fluid Phase Boundaries

Marcel Kamrad [1], *Jens Rautenberg* [2], *Leonhard Reindl* [1], *Katrin Schmitt* [1] *and Jürgen Wöllenstein* [1]

[1] University of Freiburg, Department of Microsystems Engineering - IMTEK, Georges-Köhler-Allee 102, 79110 Freiburg Germany
[2] Endress+Hauser Flow Deutschland GmbH, Rosenauer Str. 27, 96450 Coburg, Germany
marcel.kamrad@imtek.uni-freiburg.de

Summary: This work presents a novel, non-invasive sensing approach based on leaky lamb wave for detecting phase boundaries between immiscible fluids. The development of this approach is ongoing and utilizes the sensitivity of quasi-guided waves to fluid-specific properties such as density and speed of sound. Variations in these properties influence wave attenuation and time-of-flight characteristics. By analyzing these characteristics, the system enables precise and contactless localization of fluid interfaces.

Keywords: Phase Boundary Detection, Leaky Lamb Waves, Acoustic Sensing, Fluid Density, Speed of Sound, Non-Invasive Measurement

Introduction

Accurate detection of phase boundaries between immiscible fluids with differing physical properties - such as density and speed of sound - is crucial across a broad spectrum of industrial processes. These include chemical and petrochemical production, phase separation systems, and the monitoring of liquid-liquid or liquid-gas interfaces within storage tanks and process vessels [1]. Conventional sensing methods, such as invasive probes, optical sensors, and radiation-based systems, often suffer from significant limitations. These include fouling, mechanical wear, complex safety requirements, and sensitivity to contamination. Such constraints can compromise long-term reliability and operational efficiency [2]. To overcome these limitations, we propose a novel, non-invasive sensing method based on the excitation and analysis of quasi-guided surface acoustic waves. This technique enables precise and contactless detection of fluid interfaces through the walls of containers (e.g., pipes or tanks), without direct exposure to the process media.

Sensor Concept and Operating Principle

The proposed sensing concept utilizes leaky Lamb waves that are excited in the walls of fluid-containing structures, such as tanks or pipes, as illustrated in Fig. 1. These quasi-guided waves propagate along the solid boundary, while part of their energy leaks into the adjacent fluid at a defined angle - known as the coincidence angle - which depends on the phase velocity of the Lamb waves and the speed of sound of the fluid. The radiated acoustic energy travels across the fluid, interacts with the opposite wall of the tank, and re-couples into the structure where it again leaks into the fluid, forming distinct propagation paths (e.g., direct path, l-path, V-path) [3]. These wave groups are received by dedicated transducers, and variations in signal characteristics are analyzed to infer the position of the fluid interface.

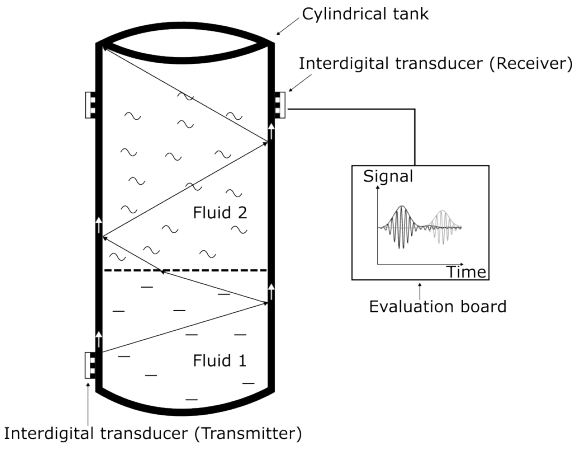


Fig. 1: Sensor concept and operating principle.

The detection mechanism is sensitive to the acoustic properties of the fluids, as described for a homogeneous fluid system in [4]. Variations in density and sound velocity affect both the coincidence angle and wave attenuation. At the interface between two immiscible fluids, partial reflection, transmission, and refraction occur, governed by Snell's Law. These interactions are characterized by acoustic impedance mismatches and also result in measurable changes in amplitude and propagation time.

Results

The characteristics of wave propagation under fluid loading were characterized by solving the dispersion relations of Lamb waves, incorporating the complex wavenumber to account for attenuation effects [4]. The analysis focused on the fundamental symmetric and antisymmetric modes in a stainless steel plate (material properties: $c_p = 5750\,\mathrm{m/s}$, $c_s = 3150\,\mathrm{m/s}$, $\rho = 7950\,\mathrm{kg/m^3}$) loaded on one side with two representative process fluids: water ($\rho = 1000\,\mathrm{kg/m^3}$, $c = 1500\,\mathrm{m/s}$) and oil ($\rho = 800\,\mathrm{kg/m^3}$, $c = 1250\,\mathrm{m/s}$). The resulting coincidence angles and attenuation coefficients for both fluid cases are depicted in Fig. 2.

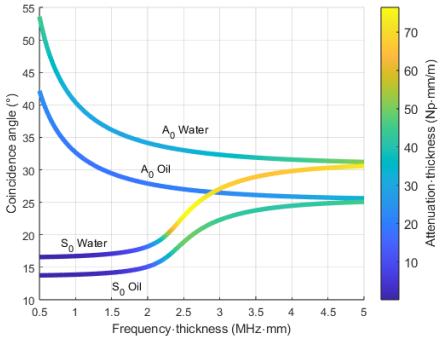


Fig. 2: Coincidence angle and attenuation for a one-sided fluid-loaded stainless steel plate with fundamental Lamb-wave modes.

A two-dimensional model was implemented, consisting of two parallel plates separated by a distance of $h = 2\,\mathrm{cm}$, with a transmitter–receiver distance of $D = 7\,\mathrm{cm}$. The fundamental antisymmetric A_0 mode was excited at a frequency–thickness product of $1\,\mathrm{MHz \cdot mm}$. The propagation time of I-path signal was evaluated for various fluid configurations and different positions of the phase boundary, as shown in Fig. 3. The corresponding relative signal amplitudes for both the direct path (on the transmitting plate) and the I-path (on the receiving plate) are presented in Fig. 4 for water and oil. An exponential decay of the direct path amplitude is observed, which results from the continuous leakage of energy into the adjacent fluid medium. Simultaneously, the amplitude of the signal on the receiving plate increases due to energy radiation from the transmitting plate and subsequently undergoes exponential attenuation along the I-path.

Conclusion and Outlook

We have introduced a non-invasive sensing technique based on the excitation of leaky Lamb waves for detecting phase boundaries between immiscible fluids. The presented sensitivity study promises accurate interface localization without direct fluid contact, offering substantial advantages over conventional methods.

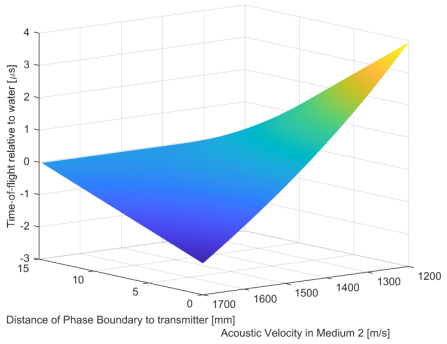


Fig. 3: Time-of-flight for the I-Path relative to water for different acoustic velocities for the second fluid and different phase boundary positions.

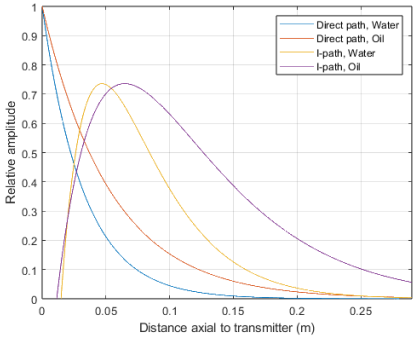


Fig. 4: Relative amplitudes for direct path and I-path for water and oil.

Future work will focus on improving system accuracy. In particular, the influence of temperature on the signal will be examined. Finally, extensive comparisons between simulations and experimental data will be conducted to validate the proposed sensing concept.

References

[1] G. Lu, et al., A new-type sensor for monitoring oil-water interface level and oil level, *2009 9th International Conference on Electronic Measurement & Instruments*, Beijing, China, 2009, pp. 2-981–2-983; doi: 10.1109/ICEMI.2009.5274393

[2] S. Hassani, U. Dackermann, A Systematic Review of Advanced Sensor Technologies for Non-Destructive Testing and Structural Health Monitoring, *Sensors* 23, 2204 (2023); doi: 10.3390/s23042204

[3] G. Lindner, et al., Wave Propagation in an Acoustic Wave Guide Sensor for Liquids Driven by Pulsed Excitation of Surface Acoustic Waves, *IEEE Frequency Control Symposium*, Honolulu, HI, USA, 2008, pp. 39-43, doi: 10.1109/FREQ.2008.4622952

[4] J. Rautenberg, et al., Utilizing Leaky Lamb Waves in an Acoustic Waveguide for the Measurement of Liquid Properties, *Proceedings SENSOR 2013*, 74–79; doi: 10.5162/sensor2013/A3.3

DOI 10.5162/EUROSENSORS2025/TP49

Measurement of Vacuum Pressure with Resonators in the Closed-Loop Configuration

Jiaxin Qin[1,2], Xiaohan Liu[1,2], Junbo Wang[1,2], Deyong Chen[1,2], Bo Xie[1,2], Yulan Lu[1,2], Xiaoye Huo[1,2]
[1] Aerospace Information Research Institute, Chinese Academy of Sciences, Beijing, 100094, China
[2] School of Electronic, Electrical and Communication Engineering, University of Chinese Academy of Sciences, Beijing, 100049, China
jbwang@mail.ie.ac.cn

Summary:
This paper proposes a vacuum resonant pressure sensor that is operated in the closed-loop configuration. The damping of MEMS resonator is related to its environment pressure, so the vacuum pressure sensor can be measured by the quality factor or vibration amplitude of resonator. In order to extend the lower limit, a comb-finger actuator is applied to drive the resonator. To enhance the performance, the resonator is operated in closed-loop and the amplitude ratio of detecting and driving signals are used as the output metric. The results show that the sensor can measure the pressure covers from 3.5E−4 Pa to 10 Pa with a repeatability error of ±1.2% RD.

Keywords: Vacuum pressure sensor, damping of MEMS resonator, closed-loop control, piezoresistive strain gauge

Background, Motivation an Objective

Vacuum gauge is widely used in various industrial equipment to monitor the process pressure. The most famous sensor used for high- and medium-vacuum measurement is ionization gauge, and measurement error is about 10% RD. Besides, the volume of their sensing elements is quite large, usually several micrometers, so they are influenced by the direction of installation.

MEMS sensors are famous for their small volume, and a few efforts have been done to achieve the measurement. However, most sensors can only measure low to medium vacuum pressure. For example, Chen et al. have proposed a sensor based on coupled resonators, which can measure the pressure from 9E-5 Pa to 1 Pa. However, the structure is complicated and the sensor is operated in the open-loop configuration, so the accuracy is limited.

In this paper, a simplified resonator is applied and operated in closed-loop configuration. The lower limit and accuracy are optimized with the applied driving / detecting structure and the output metric of amplitude ratio.

Description of the New Method or System

The governing equation is expressed as (1), where ω and x are frequency and the maximum amplitude of the resonator. In addition, F and Q are the driving force and quality factor of the resonator. Since damping monotonically increases with the environment pressure, if F is constant, pressure can be quantified by x. Furthermore, x changes monotonically with F, so if the ratio of x and F is used as the output signal of the sensor, the influence of the fluctuation of detecting and driving signals can be reduced.

$$x = \frac{F}{Q}\sin(\omega t) \Rightarrow \frac{x}{F} = \frac{1}{Q}\sin(\omega t) \qquad (1)$$

The structure of the resonator and closed-loop configuration are shown in Fig. 1. The resonator is a H-type double-ended tuning fork (H-DETF), and works at out-of-phase modes. It is driven by comb-finger actuator to reduce the damping so that Q and x is sensitivity to pressure only when the pressure is small enough. The amplitude is detected by a pair of piezoresistive strain gauge, which has a higher signal-to-noise ratio than capacitive pickup, so it is helpful to obtain a stable signal x_o [2].

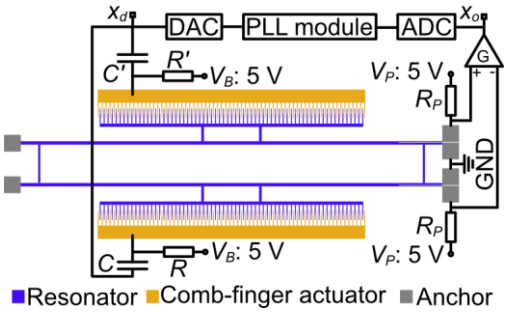


Fig. 1. Structure of the MEMS resonator.

The detecting signal is transformed to digital signal by ADC, then the phase-locked loop (PLL)

calculates the frequency and phase, and then the driving signal is generated and transformed to analog signal x_d by DAC. The key point is that the amplitude of the driving signal from DAC is constant. Therefore, the amplitude ratio of x_o and x_d can qualify the pressure according to (1).

Results

The testing was conducted at 25±0.5 ℃ and the amplitude ratio against pressure is shown in Fig. 2. The relationship between ratio and pressure is nonlinear which is similar to previous studies [1], and the maximum sensitivity is obtained from 0.1 Pa to 10 Pa, which is about 0.7 /Dec. The singularity around 2 Pa is due to reference gauge is changed from hot ionization gauge to capacitive diaphragm gauge, but they have different zeros. The subgraph shows that it can distinguish the pressure down to approximately 3.5E−4 Pa.

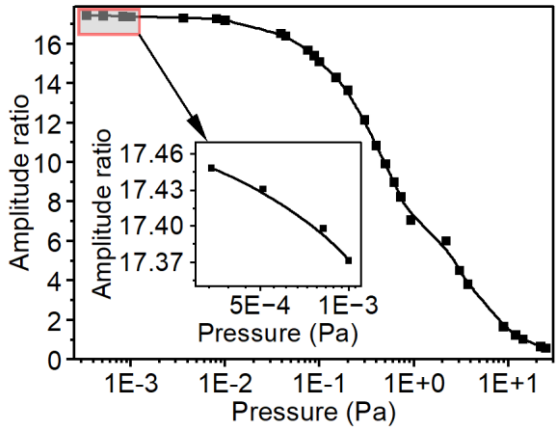


Fig. 2. Sensitivity of the proposed sensor.

The repeatability error was measured at zero pressure, during which the pressure was increased to the upper limit and then down to zero pressure for five times. As shown in Fig. 3, the absolute error is 0.2 and the relative error is calculated as ±1.2% RD.

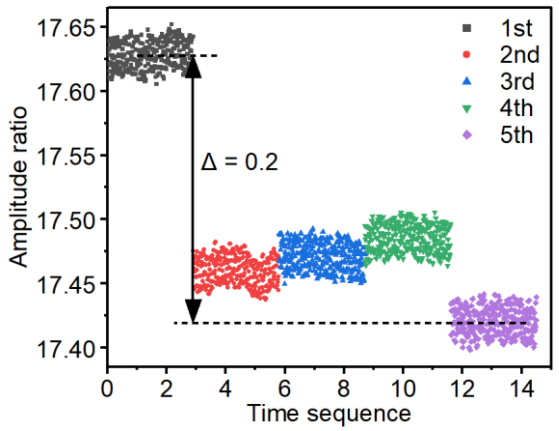


Fig. 3. The repeatability error of the sensor at zero.

The zero drift is continuously monitored for 38 hours, as shown in Fig. 4. The amplitude ratio signals generally show a decrease across the period, which is due to the stress relive and aging. The total variation is about 3% RD, so the drifting rate is about 0.08% RD every day.

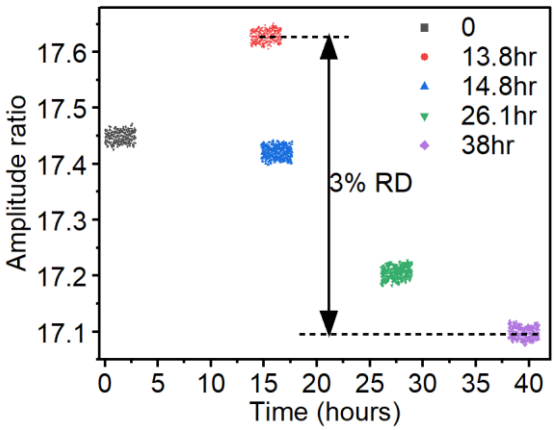


Fig. 4. The zero drift of the sensor.

The results are compared with previous studies as shown in Tab. 1, which shows that it has the advantage of simple structure and low repeatability error.

Tab. 1: Comparison with previous arts

	Principle	Range	Error
Ref. [1]	Damp of coupled resonator/open-loop	9E−5 Pa to 1 Pa	20% RD
Ref. [3]	Damp of diaphragm vibration/open-loop	6E−5 Pa to 11 Pa	<10 % RD
This work	Damp of H-DETF with comb-finger actuator/closed-loop	3.5E−4 Pa to 10 Pa	~1.2 %RD

References

[1] X. Chen, Z. Hou, et al., A MEMS resonant vacuum gauge for high vacuum measurement, *Vacuum* 228, 113513 (2024); doi: 10.1016/j.vacuum.2024.113513

[2] F. Giacci, S. Dellea, et al., Capacitive vs piezoresistive MEMS gyroscopes: a theoretical and experimental noise comparison, *Procedia Engineering* 120, 406-409 (2015); doi: 10.1016/j.proeng.2015.08.652

[3] T. Kim, J. Ko, et al., Self-assembled silicon membrane resonator for high vacuum pressure sensing, *Vacuum* 201, 111101 (2022); doi: 10.1016/j.vacuum.2022.111101

Acknowledgements

This work was supported in part by the National Key R&D Program of China Grant 2023YFC2410600, in part by National Natural Science Foundation of China Grant 62121003.

DOI 10.5162/EUROSENSORS2025/TP50

Wearable Multi-Modal Sensor Array with Wireless Communication for Monitoring Medical Bandage Condition

István Bársony[1], János Bozorádi[1], Ferenc Braun[1], Gábor Battistig[1], Péter Földesy[2], Péter Fürjes[1]
[1] HUN-REN Centre for Energy Research, Konkoly-Thege str. 29-33., H-1121 Budapest, Hungary,
[2] HUN-REN SZTAKI, Kende u. 13-17., H-1111 Budapest, Hungary
furjes.peter@ek.hun-ren.hu

Summary:
A portable bandage monitoring device was developed consisting a flexible, multimodal sensor system integrated with the preliminary signal readout and processing electronics. The sensing part of the device is designed to be bendable and compatible with bandage environment. The rigid part of the electronics is dedicated to collect the sensor's data streams and to communicate with the driving PC or mobile device via Bluetooth protocol. Via this wireless communication, the computer can receive the data flow and evaluate to visualise the bandage condition. Calibration and preliminary functional validation was elaborated to verify its capability of the device for measuring temperature, moisture and pressure distribution under the bandage. Android based application was also developed for processing and visualizing the characteristic parameters of the bandage to provide comprehensive information or warning signal for the doctors during remote supervision and home care.

Keywords: wearable, multi-modal, sensor array, smart bandage, wireless, wound monitoring

Introduction

In clinical practice, the proper use of bandages and care of wounds has primary importance in case of treatment postoperative and ulcerative injuries or varicose veins. Accordingly, to get continuous or regular information on the bandage condition without removal or remotely could decrease the required intervention time and improve the success of cure. [1] In case of homecare of the patient the remote monitoring of significant physico-chemical parameters of the bandage or wound could be crucial. The "intelligent bond" is to facilitate the work of the physician and the cure of the patient by monitoring the process of healing.

On that score "smart" bandage monitoring sensor array was developed with low power consumption readout, signal processing and communication electronics to facilitate continuous supervision by mobile device. [2] The intelligent system enable to provide continuous multimodal information of bandage parameters as temperature, moisture and local tightness / pressure of the bandage. In case of an emergency it could immediately warn the user and the physician about the need for checking or replacing the bandage.

Materials and Methods

The integrated wireless monitoring system consists of a rigid and a flexible part as demonstrated in Fig. 1. The flexible PCB contains all the sensors in an adequate geometry for measuring the local compression (five FSR pressure sensors), temperature and moisture (SI7021 sensor hub) under the bandage. The applied multiple pressure sensors are able to measure the inhomogeneous, perimeter dependent pressure distribution. It has a biocompatible coverage ensuring moisture intake.



Fig. 1. Bandage monitoring system with the flexible sensing and the rigid signal processing / communication part.

The rigid part (Fig. 2) contains an EFM32 with an ARM Cortex M0+ core and 32 kB flash memory with the advantage of energy efficient operation with several energy modes. Analogue modules include ADCs, DACs, operational amplifiers, and analogue comparators. It also contains an RF module – RFD22301 Arduino based Bluetooth low energy MCU for wireless communication. This device can operate also in low energy modes (BLE – Bluetooth Low Energy). To connect flexible and rigid part USB C connector was applied.

Data processing and visualisation software was also developed. For testing the proper functionality of the sensor system, as well as their influence on the operation behaviour various tests and calibrations were elaborated by using different bandages applied in medical practice.

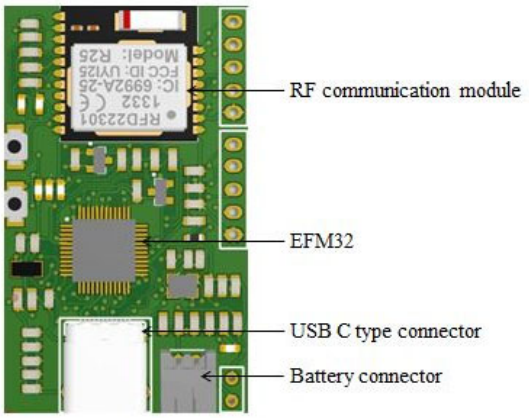


Fig. 2. Schematic architecture of the signal processing / communication electronics.

Results

To verify the applicability and reliability of the sensor system the physical parameters of different compression bandages / stockings were monitored during wearing in normal conditions for one hour. Two types of medical aids were tested as summarized in Table 1.

Table 1. Applied compression stockings

Type	*Compression range*	*Sizes*
Elastostar	*II.* *23-32 Hgmm*	*S-M-L*
Pharmatextil Elastobar	*III.* *34-46 Hgmm*	*S-M-L*

The local pressure values were collected, filtered and analysed. The compression of the stockings decreased from the ankle (F4 position) to the knee (F0 position) as expected and demonstrated in Fig. 3 and 4 in case different types of aids. The difference between the II. and III. types of stocking is also verified clearly, although the measured pressures were experienced higher than defined. Therefore, the adequate setting, wearing conditions and position of the patient were considered. As Fig. 5 demonstrates the pressure values are almost invariable near the knees, however increased notably near the ankle comparing standing and sitting positions.

Acknowledgements

The authors thank the supportive work of Nóra Orsolya Nyirfás and Miklós Szappanos.

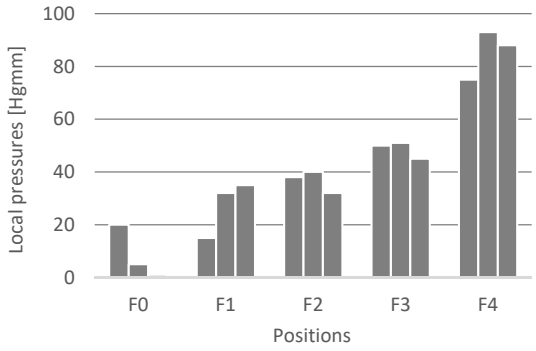


Fig. 3. Pressure distribution along the lower leg from the knee (F0) to the ankle (F4) wearing Type II compression stocking.

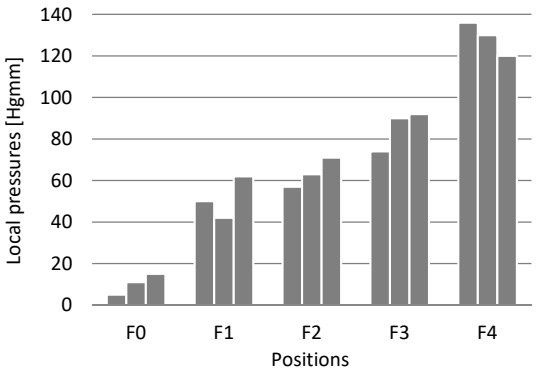


Fig. 4. Pressure distribution along the lower leg from the knee (F0) to the ankle (F4) wearing Type III compression stocking.

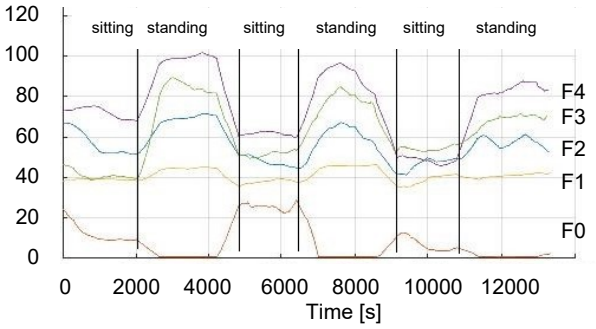


Fig. 5. Pressure values measured in different positions (pressure 1: ankle – pressure 5: knee) along the lower leg in case standing and sitting patient.

References

[1] Tim R. Dargaville, Brooke L. Farrugia, James A. Broadbent, Stephanie Pace, Zee Upton, Nicolas H. Voelcker, Sensors and imaging for wound healing: A review, Biosensors and Bioelectronics 41 (2013) 30–42

[2] Tim R. Dargaville, Brooke L. Farrugia, James A. Broadbent, Stephanie Pace, Zee Upton, Nicolas H. Voelcker, Sensors and imaging for wound healing: A review, Biosensors and Bioelectronics 41 (2013) 30–42

DOI 10.5162/EUROSENSORS2025/TP51

Integrating Carbon Nanotube Strain Gauges onto Stretchable PDMS Patches for Respiration Activity Sensing

Stefanie Jucker[1], Morten Vollmann[1], Cosmin Roman[1], Signe Lin Vehusheia[1], Mainak Basu[1], Christofer Hierold[1]
[1] ETH Zurich, Tannenstrasse 3, 8092 Zürich, Switzerland
croman@ethz.ch

Summary:
In this work we demonstrate the integration of a solid-state carbon nanotube strain gauge onto a soft, stretchable PDMS patch. We have designed, simulated and characterized the mechanical response of these devices. White-light interferometry is utilized to characterize the mechanical deformation suffered upon assembling the strain gauges onto the patches, and to determine key parameters such as the leverage factor η (1.25 nm/µm) which captures the strain transfer from the patch to the individual carbon nanotube strain gauge. Simulations show that η can be tuned by design for customizable sensitivity.

Keywords: Carbon nanotubes, PDMS, Stretchable patches, Strain sensing, Wearable sensors

Background and Motivation

Piezoresistive sensors based on individual carbon nanotubes (CNTs) have demonstrated excellent gauge-factors, ultra-low power consumption and very small footprints [1]. These features are promising for wearable biomedical devices. Also, the tiny mass of CNTs makes them insensitive to body motion artifacts. Several groups have developed stretchable strain sensors based on CNT-containing films. For instance, layers containing CNTs have been printed onto PDMS substrates, achieving up to 45% stretchability with gauge factors (GF) ~36 for wearable strain sensors [2]. Such devices are low-cost and achieve excellent stretchability. Their GFs are typically <100, but only at very large strains. On the other hand, individual carbon nanotubes could exceed GFs >1000 at large strains, and >100 at low strains [1]. Besides lower power consumption, strain gauges based on individual-CNTs, having a larger GF at low strain levels, could be employed in applications where strains are not that large, e.g. on the thorax.

Description of the New Method

In this work we present a new respiration activity patch (RAP) concept based on individual-CNT strain gauges. The concept shown in Fig. 1 consists of a MEMS device with two movable sides connected by springs, and two CNT strain gauges. The MEMS device is adhered to a stretchable PDMS patch and connected electrically to two flat flexible cables (FFCs). Details on the fabrication process of the MEMS device and the CNT dry-transfer are given in [3].

The MEMS devices suffer distortions upon transfer onto the soft PDMS substrate. As exemplified

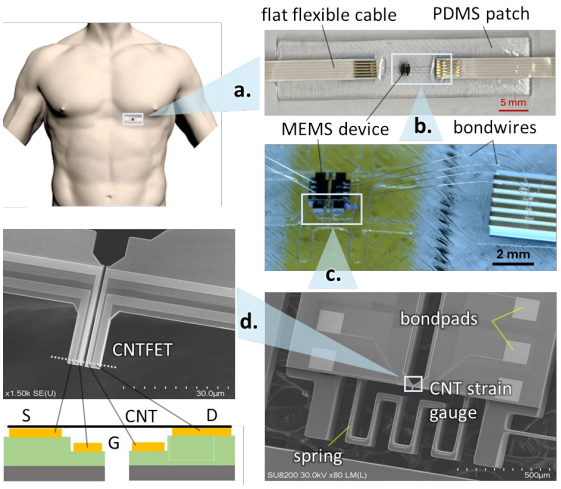


Fig. 1. Overview of the respiratory activity patch (RAP), from thorax placement (top-left) to schematic representation of the carbon nanotube (CNT) strain gauge (bottom-left). (a,b) Optical, (c,d) SEM images of the MEMS device and the CNT field effect transistor (CNTFET). (a-d) Images from different samples.

in Fig. 2 this leads to sloping and offsets between the two sides of the MEMS, which increases the CNT dry-transfer difficulty. However, white light interferometer (WLI) images are useful to select devices for further CNT transfer that show minimal deformations.

A key figure of the RAP mechanical behavior is the leverage factor η, defined as the ratio of the CNT elongation δl to the PDMS patch deformation ΔL (between FFCs). Its value was determined in two ways. First, η was extracted from Comsol Multiphysics simulations. This was necessary because the soft-hard PDMS-silicon interfaces result in non-trivial deformation fields, making an analytical derivation of η impossible.

Second, η was determined experimentally with a dedicated straining setup with piezoelectric actuation that fits under the WLI.

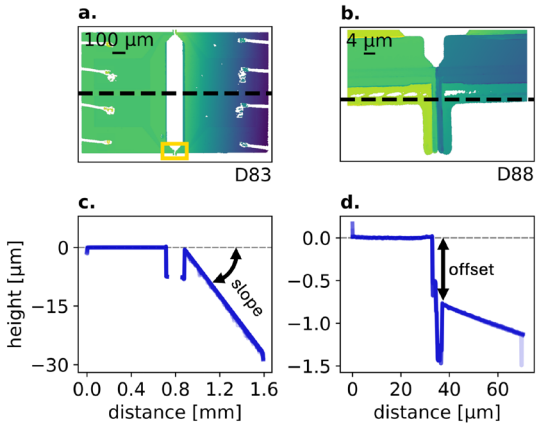


Fig. 2. WLI analysis of two different RAP devices. (a,c) Whole MEMS chip area and (b,d) close-up to the CNT electrode region. (a,b) Top-view WLI images and (c,d) slice plots at dashed lines in (a,b) respectively.

Results

In Fig. 3 a typical simulated mechanical deformation of a uniaxially strained RAP is shown for a MEMS device with a 3-fold spring design. The values of η extracted from simulation vary depending on the spring design (3 vs 5-fold), patch thickness (1.3 vs 2.2 mm) and PDMS E-modulus (1.5 vs 4.5 MPa), in the range 1.5-6.64 nm/µm. This range can be exploited in the future for customizing the sensitivity of the RAP to a specific use-case. Two measured devices are shown in Fig. 3.b. One of the two devices shows an η value of 1.25 nm/µm (3-fold spring) and the other

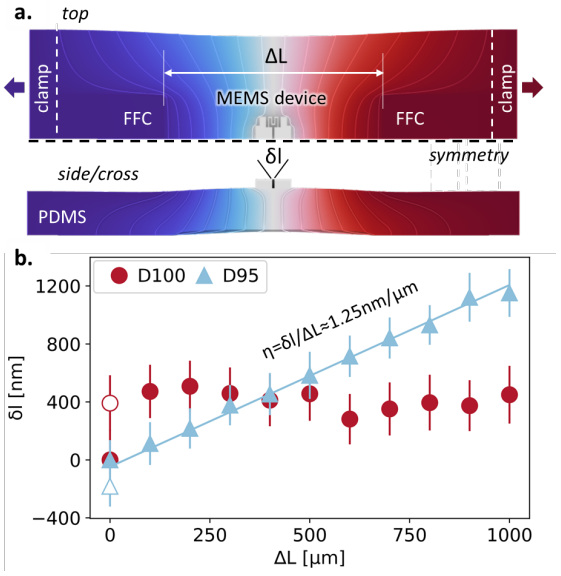


Fig. 3. Determination of the leverage factor η, via (a) Comsol mechanics simulations of the RAP deformation and (b) WLI imaging of two different RAPs characterized mechanically in a piezo-actuated setup.

(1-fold spring) shows no discernable response. Simulations and experiments agree about the order of magnitude of η. Future improvements in the placement precision of the MEMS devices onto the PDMS, and PDMS thickness control should improve the agreement. Fig. 4. shows additional analysis based on WLI of the evolution of the slope and the electrode vertical offset during straining. While large offsets could lead to CNT shorts to the gate electrode, the slope might influence strain levels and sensitivity. Besides revealing the complex mechanical interaction between the MEMS device and the PDMS support, these results suggest that pre-straining the patches can remove undesired initial slopes and offsets.

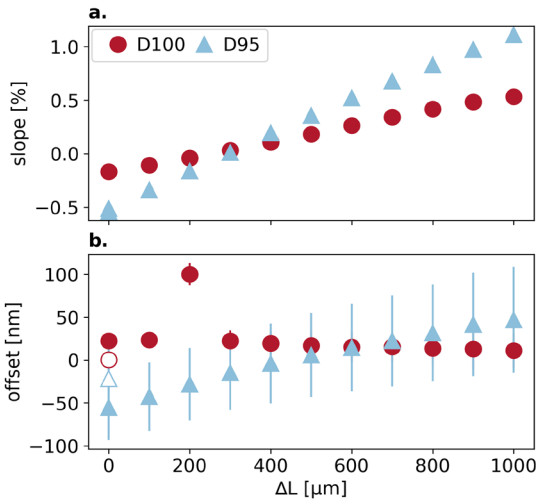


Fig. 4. Experimental determination from WLI images of the evolution of (a) slope and (b) offset mechanical distortions during uniaxial straining of the patch.

This work is a first demonstration of integrating a solid-state CNT strain gauge onto a soft, stretchable PDMS patch, and overcoming challenges stemming from hard-soft material interfaces.

References

[1] T. Helbling, C. Roman, L. Durrer, C. Stampfer, and C. Hierold, *IEEE TED* 58, 4053-4060 (2011); doi: 10.1109/TED.2011.2165544

[2] X. Wang, J .Li, H. Song, H. Huang, and J. Gou, *ACS Appl. Mats. & Interfaces* 10, 7371-7380 (2018); doi: 10.1021/acsami.7b17766

[3] M. Vollmann, C. Roman, M. Haluska, and C. Hierold, *IEEE MEMS Conference 2023*; doi: 10.1109/MEMS49605.2023.10052187

Acknowledgements

We thank the BRNC, CMi and First-CLA Cleanrooms, and in particular U. Drechsler, M. Haluska, H. ben Lakhdar, L. Maini for their help and support. This work has been supported by the European Union's Horizon 2020 research and innovation program under grant agreement no. 101017915 (DIGIPREDICT).

DOI 10.5162/EUROSENSORS2025/TP52

Dielectric Mass Concentration and Moisture Sensing of Organic Powders in Industrial Sensors

T. Schwar[1], *M. Neumayer*[1], *T. Suppan*[1], *J. Dornhofer*[1], *T. Bretterklieber*[1]
H. Wegleiter[1], C. Feilmayr[2] and S. Schuster[2]
[1] Institute of Electrical Measurement and Sensor Systems, Inffeldgasse 23/II, A-8010 Graz, Austria
[2] voestalpine Stahl GmbH, voestalpine-Straße 3, Linz, 4020, Austria. thomas.schwar@tugraz.at

Summary: Capacitive measurement has been determined as a suitable sensing technology for flow measurement in pneumatic conveying. In a typical sensor setup, electrodes are attached to the circumference of a non-conductive pipe. The flow rate can be determined from the capacitive signals. A known drawback of capacitive sensing technology is its cross-sensitivity to moisture. Recently, a dielectric material model for pulverized organic materials has been proposed that allows the simultaneous determination of the mass concentration and the moisture from dielectric measurements. This provides a potential approach for a moisture compensation option. In this work, the sensing effect within an industrial process sensor is investigated to examine the feasibility of the approach in industrial applications.

Keywords: dielectric sensing, mass flow metering, pneumatic conveying, moisture

Introduction

Accurate mass flow metering for pneumatically conveyed powder materials is relevant for various industries. Commonly used sensing principles for this measurement are differential pressure sensors, acoustic sensors, impact sensors, microwave sensors, etc. The determination of the mass flow rate from the sensing signals is then often established from calibration measurements. Also, capacitive sensing is a possible sensing strategy. Hereby, a capacitive sensor is formed by placing electrodes around the conveying pipe as depicted in Figure 1. The capacitances of the sensors are influenced by the transport goods. The mass flow rate can then be determined from the capacitive measurement signals, e.g. using calibration-based approaches, but also with model-based techniques. E.g. recent research has shown the application of electrical capacitance tomography (ECT) [1] for this task. The principal signal processing scheme of ECT is illustrated by the block diagram included in Figure 1, which comprises the determination of the spatial relative permittivity distribution ε_r and the velocity profile v. The spatial mass concentration β_s in $\mathrm{kg/m^3}$ can be evaluated from the relative permittivity ε_r utilizing a material model to compute the mass flow rate $\dot{m}$. A relevant aspect in the application of capacitive sensing is the cross-sensitivity towards moisture. For the stated measurement problem and the sensing principle, variations in the humidity affect the capacitances and subsequently lead to measurement errors. A compensation strategy is therefore required. In [2], a material model for organic pulverized material (coal) was presented, which describes the relation between the spatial mass concentration β_s, the humidity ψ, as well as the relative permittivity ε_r and the conductivity σ. With this approach, a compensation method can potentially be realized through an impedance measurement. The approach could also be used for moisture sensing, e.g. for agricultural goods for food products, and is therefore of high interest. However, the results in [2] did not address the applicability of the process within an industrial sensor, i.e. a sensor where the electrodes for the impedance measurements are mounted on the outside of a pipe as sketched in Figure 1.

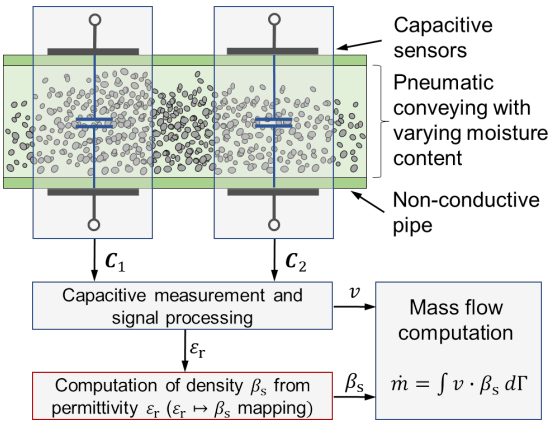


Fig. 1: Scheme of a capacitive mass flow measurement for a pneumatic conveying.

In addition, the analysis in [2] was carried out for a frequency range of several $10\,\mathrm{MHz}$. Here, a realization with an integrated impedance analyzer such as the AD5933 [3], which has an upper measurement frequency of $100\,\mathrm{kHz}$, would be preferable.

In this work, we investigate the feasibility of the proposed approach with a low-cost measure-

ment IC for a process sensor. The analysis is carried out for pulverized coal as used in [2], and the sensor application is taken from [1].

Measurements, Modeling and Results

The analysis comprises two parts. First, the dielectric material model is characterized, afterwards, the expected impedance in a process sensor can be determined. Following [2], the conductivity σ and the relative permittivity ε_r of pulverized coal can be modeled by

$$\sigma = ((a_0 + a_1\psi)\beta_\mathrm{s})^2 \quad (1)$$

$$\varepsilon_\mathrm{r} = ((b_0 + b_1\psi)\beta_\mathrm{s})^3 \quad (2)$$

Figure 2 shows the results of a dielectric characterization of the used coal for a frequency of $85\,\mathrm{kHz}$, which lies well within the frequency range of the AD5933. The experiments have been performed following the procedure described in [2, 4], for a moisture variation between $0\,\%$ and $2.5\,\%$. The mass concentration has been varied between $\beta_\mathrm{s} = 600\,\mathrm{kg/m^3}$ and $\beta_\mathrm{s} = 700\,\mathrm{kg/m^3}$. Figure 2 depicts the probe and measurement electronics used. The probe was also used in [2]. The black dots mark the measurements. The blue and red lines are computed using the parameterized model Equations (1) and (2), respectively. As proposed, the material model provides a unique relation between the dielectric material properties, the mass concentration and the moisture concentration.

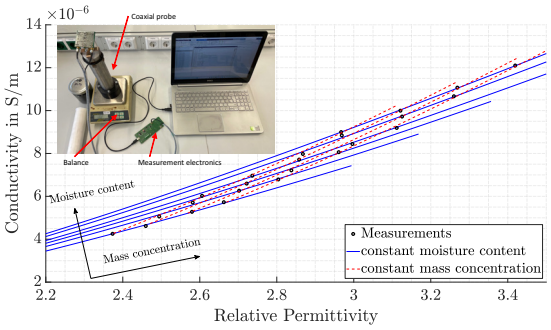


Fig. 2: Dielectric characterization of coal for different mass concentrations and different moisture content.

The parameterized material model for the relative permittivity and the conductivity is then used to evaluate the expected behaviour of the measurement impedance $\underline{Z}$. This part of the work was carried out by means of a COMSOL simulation for the sensor geometry of the sensor presented in [1]. Figure 3 depicts the behaviour of the impedance. The model is also included in the figure. Two electrodes are placed at the bottom side of the sensor pipe, and the entire pipe is filled with coal. Due to the non-conductive pipe, as depicted in Figure 1, the impedance between the electrodes is capacitive. Yet the result shows a significant variation of the conductivity and the phase for the simulated variation of the mass concentration β_s and the moisture ψ, which are well within the measurement range of the AD5933. The results therefore show that the mass concentration β_s and the humidity ψ can be sensed using an impedance measurement in an industrial sensor setup.

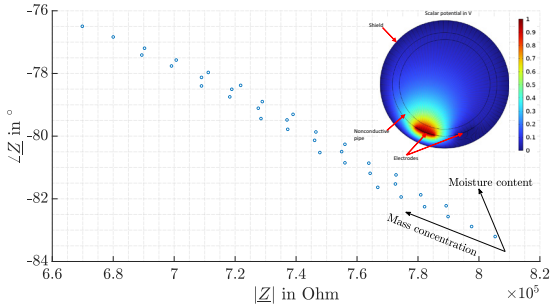


Fig. 3: Simulated impedance $\underline{Z}$ for an industrial sensor setup with the determined dielectric material model.

Conclusion

In this work, the feasibility of joint mass concentration and moisture sensing of coal powders in industrial sensors was presented. The final paper will include a more detailed analysis of the approach, a discussion of the determination of β_s and ψ from the impedance and an uncertainty analysis.

Acknowledgment

The financial support by the Austrian Federal Ministry for Digital and Economic Affairs, the National Foundation for Research, Technology and Development, and the Christian Doppler Research Association is gratefully acknowledged.

References

[1] M. Neumayer, T. Bretterklieber, T. Suppan, H. Wegleiter, C. Feilmayr, S. Schuster, and S. Puttinger, “Ect in a large scale industrial pneumatic conveying system,” *Measurement Science and Technology*, vol. 35, p. 096002, jun 2024.

[2] T. Suppan, M. Neumayer, T. Bretterklieber, C. Feilmayr, S. Schuster, and H. Wegleiter, “Dielectric sensing of mass concentration and moisture in coal powders,” *IEEE Sensors Letters*, vol. 7, no. 8, pp. 1–4, 2023.

[3] I. Analog Devices, *AD5933: 1 MSPS, 12-Bit Impedance Converter, Network Analyzer*, 2020. Accessed: 2025-04-02.

[4] T. Suppan, M. Neumayer, T. Bretterklieber, P. Stefan, and H. Wegleiter, “Measurement methodology to characterize permittivity-mass concentration relations of aerated bulk materials,” in *2021 IEEE International Instrumentation and Measurement Technology Conference (I2MTC)*, IEEE Xplore, July 2021.

A New Sensor Effect for Nuclear Process Control

Siya Lozanova[1], Avgust Ivanov[1], Chavdar Roumenin[1],

[1]Instutute of Robotics at Bulgarian Academy of Sciences, Sofia 1113 "Acad. G. Bonchev" Str. Bl. 2, Bulgaria,

Corresponding Author's e-mail: roumenin@abv.bg

A New Sensor Effect for Nuclear Process Control

Siya Lozanova[1], Avgust Ivanov[1], Chavdar Roumenin[1],
[1]Instutute of Robotics at Bulgarian Academy of Sciences, Sofia 1113 "Acad. G. Bonchev" Str. Bl. 2, Bulgaria,
Corresponding Author's e-mail: roumenin@abv.bg

DOI 10.5162/EUROSENSORS2025/TP53

A Shunt Based Low Frequency Current Sensing Approach at an Earthing Switch for Power Grid Applications

A. Elsässer [1], *M. Neumayer* [1], *B. Schweighofer* [1], *T. Bretterklieber* [1], *F. Grubinger* [1], P. Schachinger [2] and H. Wegleiter[1]
[1] Institute of Electrical Measurement and Sensor Systems, Inffeldgasse 23/II, A-8010 Graz, Austria
[2] Austrian Power Grid AG, Wagramerstraße 19, A-1220 Vienna, Austria
a.elsaesser@tugraz.at

Summary: Low frequency currents (LFCs) in the power grid, typically caused by geomagnetic disturbances or man-made sources, can lead to transformer saturation and grid instabilities. This work presents a shunt based measurement approach using an existing earthing switch as a sensing element. Due to the low and temperature-dependent resistance of the switch, an inline calibration method is introduced to determine the shunt sensitivity during operation. A custom test bench simulates realistic current signals and validates the concept. The resulting system achieves an estimated measurement uncertainty of $20\ \mathrm{mA}$, primarily limited by thermoelectric effects. This approach offers a robust and low-complexity alternative for monitoring LFCs in high-voltage environments.

Keywords: low frequency currents, quasi-DC, shunt based measurement, inline calibration, earthing switch

LFC Currents and Measurement Approaches

The power grid, a backbone of modern infrastructure, carries not only the expected 50 Hz current but also low-frequency quasi-DC currents. These low frequency currents (LFCs), typically in the range of 0.1 mHz to 0.1 Hz [1], are gaining importance due to increasing grid utilization. They are usually caused by geomagnetic disturbances such as solar flares and coronal mass ejections, but also by man-made sources like public transportation systems [2]. LFCs can lead to half-cycle saturation of transformers, resulting in harmonic generation, elevated reactive power demand, and voltage instabilities [1, 2]. Reported measurement systems mostly use closed-loop zero flux current transducers to measure LFCs [3]. However, this method comes with disadvantages such as: nonlinearities of the magnetic approach, requirement of offset compensation in regular, frequent intervals and it is also unclear wether they can withstand a short circuit event. In this work we introduce the shunt based LFC measurement approach, which is depicted in figure 1, as well as concepts that deal with the challenges involved.

Shunt Based Measurement Approach

Figure 1 illustrates the proposed shunt based measurement concept, where the existing earthing switch connecting the transformer neutral point to ground is used as a shunt. The main current components flowing through the switch are:

- i_{ac}: residual 50 Hz current, typically a few hundred mA,
- I_{lfc}: usually below 1 A, up to 330 A globally [4],
- i_{ref}: a low frequency sinusoidal reference signal with no DC or LFC components, amplitude up to a few amperes. This current is required for the inline calibration method, which is introduced later in this work.

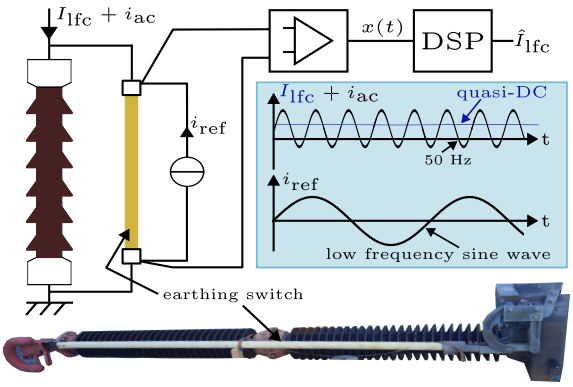


Fig. 1: Shunt based LFC measurement with schematic illustration of the three current components

The voltage signal across the switch is measured using 4-wire-technique and amplified to obtain the signal $x(t)$. While this approach is conceptually simple, it introduces several practical challenges:

- low, temperature-dependent shunt resistance,
- thermoelectric voltages at junctions,
- offset voltages from electronic components,
- electrical noise, particularly at low frequencies.

The first major challenge is the low resistance of the earthing switch, typically around $500\ \mu\Omega$, which varies depending on the switch design, mechanical connections and environmental factors such as temperature. To compensate for this, we introduce an inline calibration method

that determines the shunt sensitivity ($S(\theta)$) during operation. The LFC current is then calculated using the DC component of the spectral analysis of x(t) and the calibrated sensitivity $S(\theta)$. Thermoelectric voltages pose the most significant source of uncertainty. For example, assuming a maximum temperature gradient of 30 °C and a measurement accuracy of 10 %, the resulting discrepancy is 3 °C. Considering a Cu–Al junction with a Seebeck coefficient of approximately 3 µV / K, this yields a thermoelectric voltage of 9 µV, equivalent to about 18 mA of LFC current. Offset voltages, from electronic components are less critical, as they can largely be eliminated by performing a baseline measurement with the circuit disconnected from the shunt. The remaining contribution is about 0.5 µV. Overall, the total uncertainty in the LFC measurement is around 20 mA. To reduce noise, a zero-drift amplifier without 1/f noise was used. Remaining white noise is minimized through signal averaging.

Test Bench PCB and Measurement Setup

To validate the shunt based measurement, a dedicated test bench PCB was developed. The circuit simulates the relevant current components flowing through the earthing switch. A summing amplifier combines three input voltages u_{i1}, u_{i2}, and u_{i3}, corresponding to i_{ac}, I_{lfc}, and i_{ref}. This signal is fed into a power amplifier. By placing the shunt resistor R_f in the feedback path, the amplifier operates as a current source and generates the combined current $I_{out} = i_{ac} + I_{lfc} + i_{ref}$. The resulting voltage drop across the earthing switch is amplified to form the signal $x(t)$, which is captured using a Picoscope, while the current signals are measured with a current clamp.

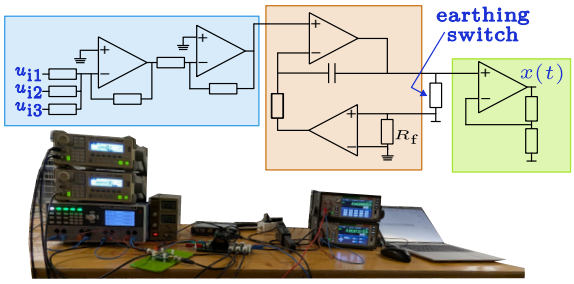


Fig. 2: Schematic of the test bench PCB and photograph of the measurement setup.

Results and Inline Calibration

To obtain the LFC value ($\hat{I}_{lfc}$) the shunt sensitivity $S(\theta)$ must be known, which can be achieved by applying the inline calibration method: Therefore, i_{ref} is introduced into the system, whose value is obtained from the current clamp signal by extracting its spectral component at 3 Hz. To determine $S(\theta)$, the amplitude of the 3 Hz reference component in $X(f)$ is used combined with the known i_{ref}. Since i_{ref} contains no DC components, both offset voltages and thermoelectric contributions do not affect the calibration and can be neglected. For accurate calibration, i_{ref} must remain stable and its amplitude precisely known. Once $S(\theta)$ is determined, the LFC current $\hat{I}_{lfc}$ is calculated by dividing the DC component of $X(f)$ by the calibrated sensitivity. A small peak at 50 Hz, caused by i_{ac}, is also visible but does not influence the LFC estimation.

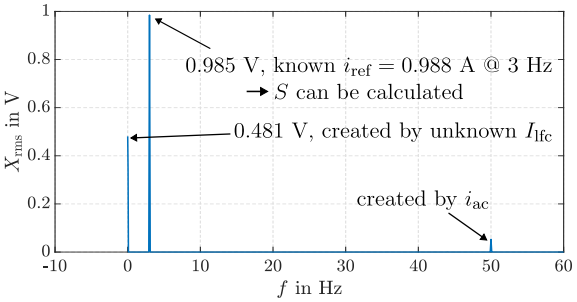


Fig. 3: Spectral analysis of $x(t)$ showing reference signal, DC component, and residual 50 Hz peak.

Conclusion

This work demonstrated the feasibility of a shunt based approach for measuring LFC in power grid applications and addressed key challenges such as temperature-dependent sensitivity and thermoelectric effects. By applying an inline calibration method, the LFC current can be determined with an estimated uncertainty of 20 mA, primarily due by thermoelectric voltages. The full paper will provide a detailed uncertainty analysis.

Acknowledgement

The financial support by the Austrian Federal Ministry for Digital and Economic Affairs, the National Foundation for Research, Technology and Development, and the Christian Doppler Research Association is gratefully acknowledged.

References

[1] "Geomagnetic Disturbances: Their Impact on the Power Grid," *IEEE Power and Energy Magazine*, vol. 11, no. 4, pp. 71-78, July-Aug. 2013, doi: 10.1109/MPE.2013.2256651.

[2] P. Schachinger, D. Albert and H. Renner, "Low Frequency Currents Source Identification," *2022 20th International Conference on Harmonics & Quality of Power (ICHQP)*, Naples, Italy, 2022, pp. 1-6, doi: 10.1109/ICHQP53011.2022.9808423

[3] D. Albert, P. Schachinger, R. L. Bailey, H. Renner and G. Achleitner (2022). Analysis of long-term GIC measurements in transformers in Austria. *Space Weather*, 20, e2021SW002912. doi: 10.1029/2021SW002912

[4] Wik, M., Pirjola, R., Lundstedt, H., Viljanen, A., Wintoft, P., and Pulkkinen, A.: Space weather events in July 1982 and October 2003 and the effects of geomagnetically induced currents on Swedish technical systems, Ann. Geophys., 27, 1775–1787, doi: 10.5194/angeo-27-1775-2009, 2009

DOI 10.5162/EUROSENSORS2025/TP54

Low Cost Level Sensing for Receivers in Small Sized Refrigeration Systems with Natural Refrigerants

M. Neumayer [1], G. Pertiller [2], F. Eder [2], R. Rieberer [2]

[1] Institute of Electrical Measurement and Sensor Systems, Graz University of Technology, Inffeldgasse 23/II, A-8010 Graz, Austria

[2] Institute of Thermal Engineering, Graz University of Technology, Inffeldgasse 25B, A-8010 Graz, Austria

neumayer@tugraz.at

Summary: Natural refrigerants, such as porpane (R290), are increasingly being used in refrigeration systems and heat pumps due to their positive environmental properties in comparison to other refrigerants. This applies in particular to small refrigeration systems. Due to the flammability potential, sensors that monitor the refrigerant charge are of interest. In this work we study the feasibility of low cost level switch using ultra sound transducers. The detection of the refrigerant is based on a de-tuning effect, which allows a low cost implementation.

Keywords:
level sensing, vessel, natural refrigerants, refrigeration systems, heat pumps

Introduction

Compression refrigeration systems and heat pumps have become a main system component for the cooling and heating of buildings [1]. Due to their environmental impact and international regulations, previously used refrigerants such as hydrofluorocarbons (HFCs) should no longer be used in new systems. To replace these conventional refrigerants, natural refrigerants such as hydrocarbons, e.g. R290 (propane), or R717 (ammonia), are to be used [2]. Due to the potential flammability of some of these refrigerants, new regulations have been introduced for their application [3], e.g. a maximum refrigerant charge. Therefore, the use of natural refrigerants is particularly relevant in small refrigeration systems. To minimize the risks due to the refrigerants, leakage detection systems are also of interest. In the case of small refrigeration systems, the implementation of a leak detection system is of further interest, as it is able to detect minor losses of refrigerant before they compromise the system's efficiency.

The need for such sensors either level sensors, or level switches, has been addressed by various researchers [3, 4]. In this work we investigate the feasibility of low cost ultrasound (US) level sensing based on a de-tuning effect of small vessels. Figure 1 sketches the scheme. A US transducer is mounted on the outside of the refrigerante receiver. A photography of a typical refrigerante receiver is depicted in the small inset in Figure 1. For the sensing task a pulse signal is used as excitation signal for the US transducer. The resonance behavior of the transducer is influenced by the refrigerant level within the refrigerante receiver, where the presence of a liquid refrigerant will lead to a dampening effect for the oscillation of the transducer. A simple way to sense this is evaluating the peak magnitude of the oscillation after the excitation. In the following procedure, a test bed and measurements are presented to show the feasibility of the approach.

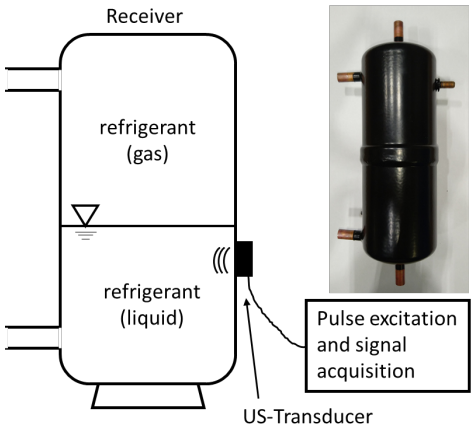


Fig. 1: Photography of an receiver for small compression refrigeration systems and sketch of the proposed level sensing approach using an US transducer.

Test Bed and Measurements

In this section, the test bed for the experiments and the proposed measurement procedure are addressed and results are presented. Figure 2 shows a photography of a test bed for the evaluation of the proposed sensing approach. It consists of a receiver and a second tank to adjust the fill level via height adjustment. For reference measurements a sight glass is installed. The experiments are performed with propane (R290) as refrigerant.

To test the proposed sensing principle a US-transducer was mounted on the wall of the receiver. Figure 3 depicts two measured signals

DOI 10.5162/EUROSENSORS2025/TP54

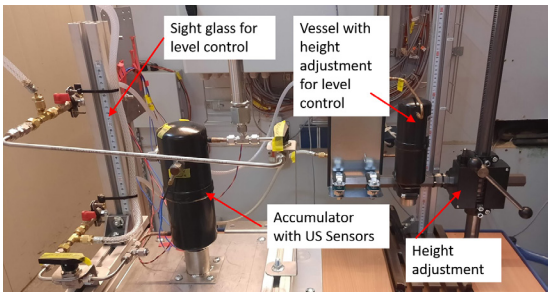


Fig. 2: Test bed for the evaluation of the sensing approach. The central element of the test bed is an refrigerant receiver, where the US transducers are applied. The level of the refrigerant is controlled by the height of a second vessel. A sight glass is used for the level control.

and a sketch of the measurement circuitry to apply a high voltage pulse to the transducer. The voltage signals show the pulse excitation at $t = 10\,\mu s$, which are followed by some oscillations with a high frequency, which are due to electrical parasitics. Afterwards, at about $t = 15\,\mu s$, the voltage signal is dominated by the mechanical oscillations of the transducer, which are influenced by the liquid level of the refrigerant. For the sensing of the refrigerant, the negative peak of the transducer signal is evaluated as marked in Figure 3.

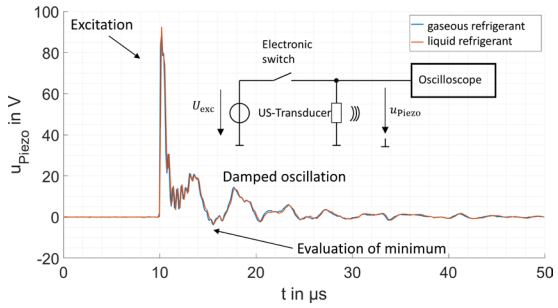


Fig. 3: Scheme of the measurement circuitry and measurement signals from the US transducer with gaseous refrigerant (blue) and liquid refrigerant (red).

Figure 4 depicts a statistical evaluation of the minimum voltage level of the oscillation over a series of experiments. The inset inside the figure shows the relevant sequence of the signal. The evaluation of the signals shows a separation of the minimum values, which can be used to detect the liquid refrigerant in the vessel. In the presence of the liquid refrigerant at sensor hight, the negative peak value is smaller, which corresponds to the increased dampening due to the liquid fluid inside the vessel. The raw data shows an overlap between the states. Here, detection can be improved by averaging [5]. While all experiments have been performed with lab equipment, the procedure can be realized with low hardware effort.

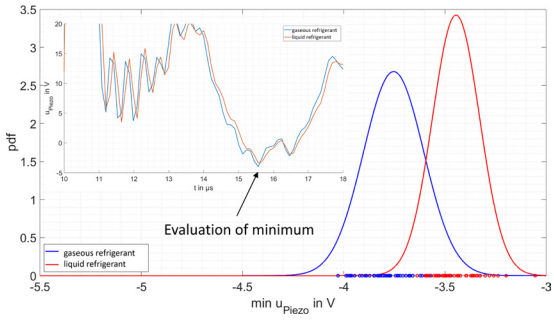


Fig. 4: Statistical evaluation of the minimum voltage level of the US resonance with gaseous refrigerant (blue) and liquid refrigerant (red).

Conclusion

In this work the feasibility of a low cost ultrasound (US) based level sensing based on a de-tuning effect on small refrigerant vessels was demonstrated. The final paper will include a more detailed study, addressing application specific details and an analysis of cross sensitivities.

Acknowledgment

This work is based on the contents of the FFG project “CLEAR - Create an additional way to extract information from a refrigerant circuit” (FFG project no.: FO999914926) and is funded by the Federal Ministry for Climate Action, Environment, Energy, Mobility, Innovation and Technology, (BMK) and carried out as part of the Energy Research Program 2023

References

[1] A. S. Gaur, D. Z. Fitiwi, and J. Curtis, “Heat pumps and our low-carbon future: A comprehensive review,” *Energy Research Social Science*, vol. 71, p. 101764, 2021.

[2] G. Mathur, “Using natural refrigerants propane (R290) carbon dioxide (R744) as direct or indirect heat pump systems to address pfas issue,” 04 2024.

[3] A. A. Bani Issa, C. Liang, E. A. Groll, and D. Ziviani, “Residential heat pump and air conditioning systems with propane (R290) refrigerant: Technology review and future perspectives,” *Applied Thermal Engineering*, vol. 266, p. 125560, 2025.

[4] T. Klebig, L. Hummel, P. Ostmann, J. Klingebiel, C. Vering, and D. Mueller, “Leckagedetektion mit Vibrationssensoren: Good Vibes für Wärmepumpen,” DKV-Tagung, Dresden, 11 2024.

[5] S. Kay, *Fundamentals of Statistical Signal Processing: Detection theory*. Fundamentals of Statistical Signal Processing, Prentice-Hall PTR, 1998.

DOI 10.5162/EUROSENSORS2025/TP55

Limitations of LWIR Cameras for Industrial Air Leak Detection

Klaus Lex [1,2], Thilo Sauter[1,2] and Hubert Brückl[1]
[1] Department of Integrated Sensor Systems, University of Continuing Education Krems, Viktor Kaplan Straße 2 - Bauteil E, 2700 Wiener Neustadt, Austria
[2] TU Wien, Karlsplatz 13, 1040 Vienna, Austria klaus.lex@donau-uni.ac.at

Summary: Infrared (IR) cameras have seen increasing applications such as autonomous driving, healthcare, surveillance, condition monitoring within the industry, and many more. This work explores the possibility of using an unfiltered, uncooled VOx long-wave infrared (LWIR) detector to detect compressed air leaks. By loosening a fitting and comparing the minimum temperature within the area of the leak from a series of thermal images to the theoretical temperature drop expected from the expanded gas, we demonstrate limitations that these types of cameras are not generally suitable by themselves for detecting compressed air leaks within the industrial landscape.

Keywords: VOx, long-wave infrared, gas sensors, leak detection, compressed air

Introduction

Whether it is health hazards due to harmful substances, risk of explosion, machine failure, greenhouse gases, or increased energy consumption, detecting gas leaks has been a crucial process within the industry since the first industrial revolution. Starting with a steel wheel and a flint to create sparks to detect a firedamp, to the development of safety lamps [1], detecting gas leaks has since moved from contact-based methods, such as spray-on solutions, fixed sensor installations of ultrasonic transducers, accelerometers [3], or pressure transducers [4], to remote sensing solutions, such as vision-based approaches found in OGI cameras that make use of different IR regions to detect common industrial gases [2]. With OGI cameras that use varying detectors to cover different regions in the infrared spectrum, they are all fixed in what gases they can detect, and as seen in [2], none of them can detect compressed air. This raises the question whether LWIR cameras can also be used to detect compressed air leaks.

Methodology

First, a baseline for the expected temperature difference due to the expanding air needs to be established for comparison with the LWIR camera.

Knowing that Joule-Thomson expansion is an isenthalpic process, the expected temperature drop at room temperature ($22\ ^\circ\mathrm{C}$) can be calculated with Eq. 1 for air compressed to relative pressures in the range of 1 to 8 bar, which should cover most industrial systems.

$$\Delta T = \mu_{JT} \cdot \Delta P \quad \text{with} \quad \mu_{JT} = 0.3°C/atm \quad (1)$$

For this, a Joule-Thomson coefficient of $0.3\ ^\circ\mathrm{C/atm}$ from [5] for air at $20\ ^\circ\mathrm{C}$ is used and should be sufficiently close to the ambient temperature of $22\ ^\circ\mathrm{C}$.

Experimentally, a copper pipe was pressurized with air at a series of relative pressures between 1-8 bar and then released into the atmosphere through an artificial leak created from loosening the threaded connection between a tee-fitting and a coupling, connected to a globe valve.

A Hikvision DS-2TD2637T-10/P was used to record images from the LWIR and visible (VIS) spectrum [6]. Since the camera lacks the ability to manually set temperature limits, a black body of type HT40B [7] set to $22\ ^\circ\mathrm{C}$ was used. Then, for each pressure level, 60 raw thermal and VIS frames were collected at approximately 1 s intervals when the artificial leak was supplied with air from the position seen in Fig. 1.

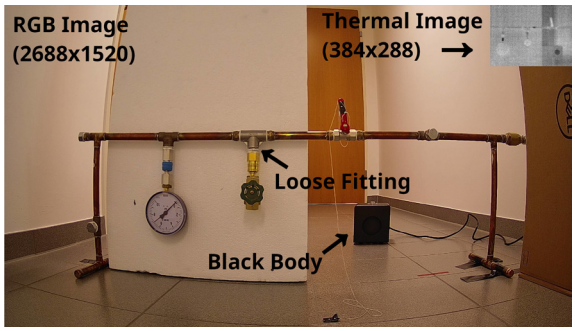


Fig. 1: Unprocessed images for LWIR and VIS

After calibrating the camera and performing stereo rectification (Fig. 2), a mask was created for the tee fitting (Fig. 3) where the artificial leak is located in the VIS image using the Meta Segment Anything 2 Model (SAM 2) [8]. This mask was then applied to the thermal image after performing non-local means denoising and temperature correction to find the pixel with the minimum measured temperature as seen in Fig. 4.

Without manual non-uniformity correction (NUC) available, the median of all pixel intensities within the black body reference circle (Fig. 4) was computed and the difference from the set temperature of $22\ ^{\circ}\mathrm{C}$ was subtracted from each pixel of the thermal image to correct measurements.

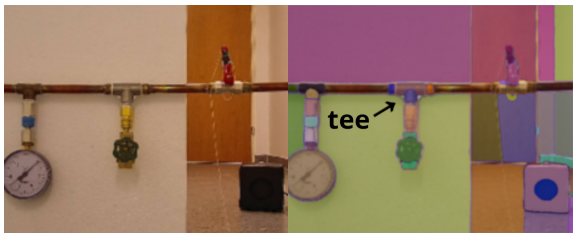


Fig. 2: VIS rectified

Fig. 3: VIS segmented

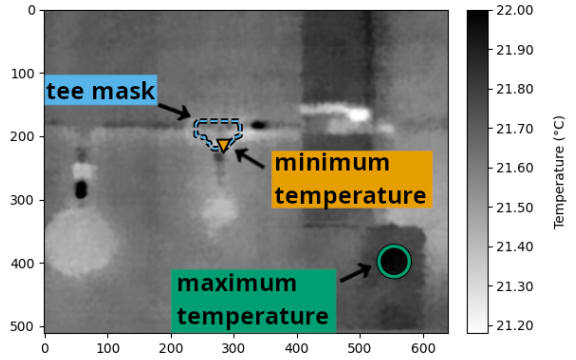


Fig. 4: LWIR rectified with temperature ROIs

Results

The distribution of the corrected minimum temperature differences measured at different compression levels compared to the theoretical temperature drop is shown in Fig. 5.

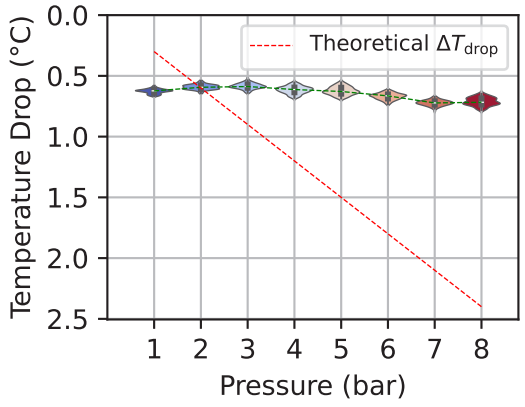


Fig. 5: Temperature drop for compressed air at 22 ℃

Compared to the expected linear temperature drop, the measured temperature differences remain almost constant. Although the color bar as seen in Fig. 4 suggests that the theoretical temperature differences should be detectable, the thermal conductivity of the copper pipe seems to prohibit such a small local temperature difference to persist long enough.

Conclusion

In this work, a LWIR camera was used to explore whether a leak of compressed air could be detected in an industrial setting. The results show that even with the use of a black body reference, a LWIR camera experiences limitations to detect compressed air leaks at the tested location, leaving room for future exploration of different pipe materials or as a supporting modality for other sensors.

Acknowledgement

The financial support by the Austrian Federal Ministry of Climate Action, Environment, Energy, Mobility, Innovation and Technology (BMK) via the Austrian Research Promotion Agency (FFG) in the AI-RoboSens project #899918 is gratefully acknowledged.

References

[1] D. Humphry, I. On the fire-damp of coal mines, and on methods of lighting the mines so as to prevent its explosion, *Philosophical Transactions of the Royal Society of London* Volume 106, 1-22 (1816); doi:10.1098/rstl.1816.0001

[2] Teledyne FLIR, "What Types of Gases Can You See With an OGI Camera?", *FLIR.eu*, Accessed: Apr. 9, 2025. [Online.] Available: https://www.flir.eu/products/g306

[3] S. Yin, Y. Liu, W. Han, Single-point location algorithm based on an acceleration sensor for pipeline leak detection, *Measurement* Volume 163, 108021 (2020); doi.org/10.1016/j.measurement.2020.108021

[4] J. Li, Q. Zheng, Z. Qian, A novel location algorithm for pipeline leakage based on the attenuation of negative pressure wave, *Process Safety and Environmental Protection* Volume 123, 309-316 (2019); doi.org/10.1016/j.psep.2019.01.010

[5] R. T. Balmer, Chapter 14 - Vapor and Gas Refrigeration Cycles, *Modern Engineering Thermodynamics*, Academic Press, 535-590 (2011); 10.1016/B978-0-12-374996-3.00014-2

[6] Hikvision, "DS-2TD2637T-10/P", *hikvision.com*, Accessed: Apr. 25, 2025. [Online.] Available: https://www.hikvision.com/en/products/Thermal-Products/Thermography-thermal-cameras/Bullet-series/ds-2td2637t-10-p/

[7] IRtech, "Black Body (HT40B)", *dalithermal.com*, Accessed: Apr. 25, 2025. [Online.] Available: https://www.dalithermal.com/productinfo/769148.html

[8] N. Ravi, V. Gabeur, Y.-T. Hu, R. Hu, C. Ryali, T. Ma, H. Khedr, R. Rädle, C. Rolland, L. Gustafson, E. Mintun, J. Pan, K.V. Alwala, N. Carion, C.-Y. Wu, R. Girshick, P. Dollár, C. Feichtenhofer, SAM 2: Segment Anything in Images and Videos, *arXiv preprint* (2024); arXiv:2408.00714

DOI 10.5162/EUROSENSORS2025/TP56

Experimental Analysis of Flat Spot-Induced Vibrations Using Piezoelectric IEPE-Accelerometers

Philipp Kersten[1], *Christian Engel*[1], *Soeren Hirsch*[1]
[1] *University of Applied Sciences Brandenburg, Magdeburger Straße 50, 14770 Brandenburg an der Havel, Deutschland,*
philipp.kersten@th-brandenburg.de

Summary:

This work presents an experimental approach to investigate and classify material vibrations induced by flat spots on train wheels. The simplified test setup intentionally omits spring elements, while vibration data is acquired using integrated electronics piezo-electric (IEPE) accelerometers. Both time-domain and frequency-domain analyses are applied to comprehensively evaluate the vibrational behaviour. The results offer valuable insights into the dynamic effects of flat spots, paving the way for implementing diagnostic sensor networks in railway systems.

Keywords: Railway, Flat Spot, IEPE Accelerometers, Vibration Analysis, Predictive Maintenance

Introduction

Railway maintenance is increasingly shifting from time- and usage-based strategies toward condition monitoring and predictive maintenance. In predictive maintenance, accurate data analysis is crucial for estimating a component's lifespan, making it essential to classify and investigate critical failure modes [1]. One such failure mode is the development of flat spots on train wheels. These flat spots result from wheel wear caused, for example, by emergency braking or delayed brake release during acceleration and generate periodic impact forces during rotation, ultimately damaging both the wheel and the infrastructure. [2]. In addition to the detection of flat spots, a well-designed sensor network also enables the monitoring of relevant environmental factors, which can be of decisive importance for the precise estimation of component service life. Our approach aims to improve fault diagnosis and contribute to more effective predictive maintenance strategies in railway operations.

Experimental Details and Theory

To investigate wheel-induced excitations under controlled conditions, a scaled test rig equipped with IEPE-accelerometers was designed specifically for detecting flat spots on train wheels. To ensure a realistic representation of the railway system, a scale conversion of approximately 1:4.6 was determined based on the ratio between an actual railway wheel and the acquired flange rollers. The experimental setup includes four rail flange rollers, that are rigidly connected via a steel plate and run on rails without any additional suspension or damping elements. This direct, rigid coupling ensures that any impulsive excitation - such as that produced by a flat spot on a wheel - is transmitted almost immediately and uniformly to the entire system. A USB-Signal Conditioner is recognized as a microphone, enabling straightforward data logging with just a few lines of code. Four predefined measurement positions mounts (denoted as M_n) are distributed along the structure to allow comparison of vibration responses between the different wheels. When a flat spot contacts the rail, it generates a transient impulsive force $F(t)$, which results in a measurable acceleration response along the vertical z-axis [3]. The coordinate system and sensor positions on the model are illustrated in Figure 1.

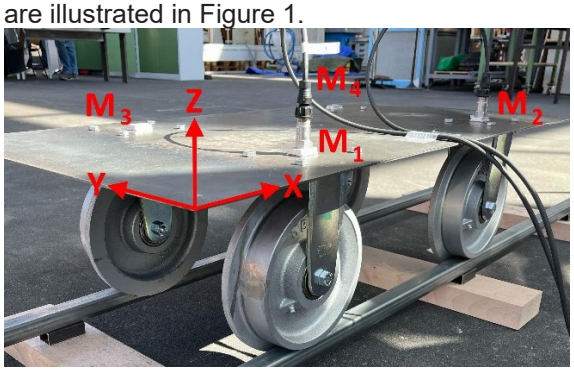


Fig. 1. Experimental Setup

Assuming that the system behaves like a single-degree-of-freedom damped oscillator, the dynamic response shown in figure 2 is described by the equation of motion (1) [4].

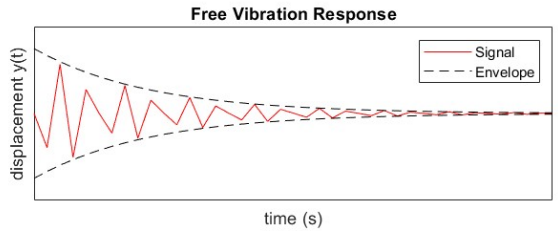


Fig. 2. Damped sinusoidal oscillation

$$\boldsymbol{F(t) = m\ddot{y}(t) + c\dot{y}(t) + ky(t)} \qquad (1)$$

Where m is the effective mass of the system, c is the damping coefficient, k is the effective stiffness of the rigid connection and $y(t)$ represents the displacement response. Equation (2) gives the free vibration response (assuming underdamped conditions, $0 < \zeta < 10$) for the case where the impulsive force can be approximated as an instantaneous excitation.

$$\boldsymbol{y(t) = Ae^{-\zeta\omega_n t}sin(\omega_d t + \phi)} \qquad (2)$$

A being the initial amplitude determined by the impulse magnitude, ζ the damping factor, w_n the natural frequency, w_d the damped natural frequency, and ϕ a phase constant determined by the initial conditions [4].

Results and Discussion

Figure 3 illustrates a one-shot measurement of the flat spot hitting the rail while comparing two measuring points M_1 and M_2. Overall, the measurement confirms the theory of a damped sine wave with its decaying oscillatory behaviour. For better comparison we added envelope curves in both figures 2 and 3.

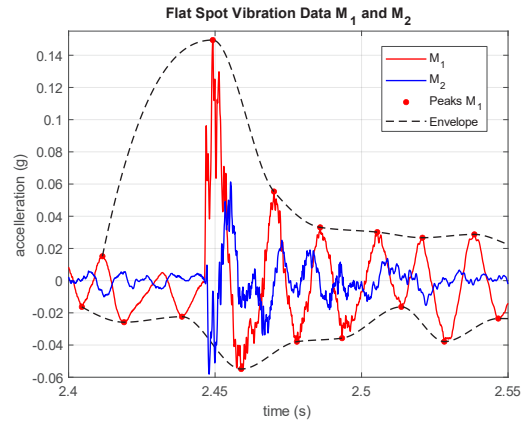


Fig. 3. Comparison of theoretical and measured flat spot signals.

While M_1 gets the higher peak values, because its sensor is placed directly over the wheel with the flat spot, placing M_2 over one of the rear wheels results in a more damped and phase shifted response of M_1. This implies that, based on the system's damping characteristics and the materials and weight distribution used, the sensor node for detecting flat spots can be placed farther from the excitation source. The temporal shift of the signal peaks suggests that a simple time-of-flight analysis could be sufficient to determine the exact location of the flat spot. However, when sensors are installed on both axle A and axle B, there is a risk that the flat spot signal may be detected at the alternate location. This makes it crucial - especially for pattern recognition and peak detection - to develop a sensor network that can unambiguously determine the origin of each flat spot. The frequency analysis of the measurement data shows that the dominant vibration modes lie in a clearly defined frequency range between 20 Hz and 100 Hz.

Conclusion and Outlook

This study demonstrates the feasibility of using piezoelectric accelerometers in a scaled test setup to detect flat spots on train wheels. The setup replicates the impulsive excitations from wheel defects and allows analysis of vibration responses across multiple sensor positions, confirming the behaviour of a damped single-degree-of-freedom system and providing insights into spatial excitation propagation. In future, the system will be optimized with a custom sensor network for both flat spot detection and continuous environmental monitoring to more precisely assess external influences on service life. Additionally, a motor-driven test rig is under development to enable controlled wheel rotation, facilitating the analysis of periodic impact responses at varying speeds. This will help to better understand the frequency content of flat spot signatures and the influence of speed, ultimately supporting the design of robust, speed-invariant detection algorithms for real-world predictive maintenance in railway systems.

References

[1] A. Murtaza, A. Saher, M. Zafar,S. Moosavi, M. Aftab, Paradigm shift for predictive maintenance and condition monitoring from Industry 4.0 to Industry 5.0: A systematic review, challenges and case study, *Results in Engineering* Volume 24, https://doi.org/10.1016/j.rineng.2024.102935

[2] L. Pan, B. Lu, C. Yang, L. Chen, Y. Song, T. Zhang, The Impact of Wheel Flat on Traction Drive System of Electric Locomotives, *IET Electrical Systems in Transportation* Volume 2024, Issue 1, doi: 10.1049/2024/2889871

[3] A. Sharma, V. R. Reddy, "Wireless sensor networks for condition monitoring in the railway industry: A review," *Sensors*, vol. 20, no. 21, p. 6239, Oct. 2020

[4] C.M. Harris, A.G. Piersol, *Harris' Shock and Vibration Handbook*, 5th ed. (McGraw-Hill, New York, 2002); doi: 10.1121/1.397223

DOI 10.5162/EUROSENSORS2025/TP57

Blind Prediction of Odor Concentration in Deodorization Process in Wastewater Treatment Plant Using E-nose and Dynamic Olfactometry

Isabelle Crosnier[1], Assia Nevers[1], Fida Maalem[1], Madani Diallo[1], Fabien Siinoa[1], Vincent Bourges[1], Fatma Ayouni[2], Jean-Christophe Mifsud[2] Ivan Romanytsia[2]
[1,]SIAAP Direction des Laboratoires et de l'Environnement, Service Environnement
[2] ELLONA SAS 3 Avenue Didier Daurat, 31400 Toulouse, France
isabelle.crosnier@siaap.fr, fatma.ayouni@ellona.io

Summary:
In response to the perennial challenge of mitigating odorous emissions from wastewater treatment processes, this project focuses on the innovative utilization of electronic noses (e-noses) for accurate odor concentration predictions. Undertaken at the SIAAP wastewater treatment plant, where the treatment of 2,600,000 m^3/day of wastewater generates persistent olfactory nuisances for nearby residents, this study addresses the pressing need for advanced monitoring solutions, compliant with regular audits using reference method as dynamic olfactometry)

Keywords: E-nose, odor unit, dynamic olfactometry, wastewater treatment, emission

Background

The SIAAP, since its establishment in 1970, has grappled with the olfactory consequences of treating wastewater laden with organic matter. The evolving nature of odorous compounds necessitated a progressive redesign of the existing measurement network. Traditional sulfur compounds are no longer sole indicators, prompting the quest for sensors that not only monitor odor emissions effectively but also present a cost-effective alternative to current systems.

Description of System

In pursuit of a viable solution, the study identified the Ellona Watch Tower (WT1) electronic noses coupled with the Ellona dryer as a promising technology for real time analysis to quantify odors and gas emissions in unstable environmental conditions. Two of these electronic noses were strategically deployed at the Seine Aval site, equipped with specialized hardware to meet SIAAP's stringent requirements for monitoring channeled sources. The deployment involved a meticulous training phase spanning three months, utilizing dynamic olfactometry data to optimize the e-noses for real-world scenarios.

Results

The results demonstrate a commendable success rate, with the optimized e-nose training achieving a remarkable 90% accuracy in predicting odor levels from blind samples. The linear regression model (PLS) built on multivariate statistics yielded calibration curves with an R^2 exceeding 0.93, showcasing a robust correlation between the electronic noses and olfactometry scores. The Ellona WT1 IOMS devices, equipped with Metal Oxide sensors and electrochemical sensors, not only quantified odors but also measured gases such as ammonia, VOCs, hydrogen sulfide, and mercaptans.

These devices, less expensive to purchase and maintain than traditional systems, offered a lower quantification threshold. Their successful deployment enabled the monitoring of atmospheric emissions from key odorous compounds, revealing concentrations below 500 EOU/m3, indicative of proper functioning deodorization facilities. Moreover, ongoing applications showcase the potential of the WT1 IOMS devices for real-time odor concentration monitoring and instantaneously displaying odor plumes in the SYPROS modeling tool from SIAAP.

Conclusions

This project not only addresses the inherent challenges of persistent odorous emissions in wastewater treatment but also presents a practical solution in the form of Ellona WT1 IOMS devices. Their versatility, robustness, and cost-effectiveness position them as valuable assets in the continuous improvement of environmental monitoring at the SIAAP wastewater treatment plant. This research contributes significantly to the ongoing pursuit of "zero nuisance" and enhances our understanding of odor emissions.

DOI 10.5162/EUROSENSORS2025/TP58

A Novel Surface Recognition System Using an Artificial Finger

Alireza Abbasimoshaei[1], Alhussein Mohamed Hazem Osman[1], Fady Youssef[1], Thorsten A. Kern[1]
[1] Hamburg University of Technology, Institute for Mechatronics in Mechanics, Hamburg, Germany
Al.abbasimoshaei@tuhh.de

Summary:
This paper presents a method for an interactive surface recognition system using a robot and a vibrotactile sensor. The robot was equipped with an artificial finger made of metal to which a three-axis accelerometer was attached. The robot interacted with 10 different surfaces by performing scratching movements on each of them. Random Forest is used as the surface classification algorithm by extracting statistical features of the vibrations detected by the accelerometer. By using only one accelerometer as the main measurement feedback, the results show that it has acceptable classification accuracy.

Keywords: Surface Recognition, Vibrotactile Sensing, Robot Perception, Accelerometer, Random Forest Classification

Background, Motivation an Objective

The sense of touch is important for humans to recognize and experience the properties of everyday objects. For instance, when we run our finger over an unfamiliar object, we can detect the texture. Therefore, there is a growing interest in the development of algorithms and sensors that allow robots to use and interpret tactile feedback while manipulating objects [1].

There are several approaches to surface detection and identification systems [2]. Previous research has differed in terms of the sensors used and the surface texture information extracted from the objects. Acoustic signals generated by friction have been used for material identification [3]. In [4], an artificial finger equipped with a microphone (i.e., a dynamic touch sensor) is used to detect friction noise, which is mapped into the frequency domain using the Fast Fourier Transform (FFT) to detect different textures.

Compared to previous studies, this work proposes a simpler and more efficient approach to material classification by capturing the vibrotactile feedback generated during interaction with each material surface using just a 3-axis accelerometer. In addition, a classification algorithm was presented. There have been some studies involving tactile texture recognition with the use of deep learning methods, such as [6]. However, in contrast to these studies, this work uses only a single modality and a less costly tactile sensor, showing that similar results can be achieved with a simpler setup and data processing methods.

Experimental Setup

The robot used in the experiments and the entire experimental setup is shown in Fig. 1. The robot model is a universal robot (UR10e) developed by Universal Robotics. A metal rod simulating a finger is attached as the end effector of the robot, to which a 3-axis accelerometer is mounted. The robot was controlled by a series of commands to perform a scratching behavior.

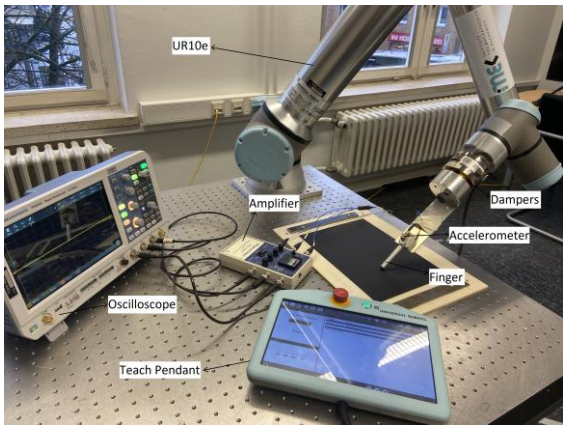


Fig. 1. Experimental setup

The measurement data is recorded during the sliding motion of the robot finger over the material surface at a rate of about 8.33 KHz in a time window of 1.2s. An example of the measurement is shown in Fig. 2.

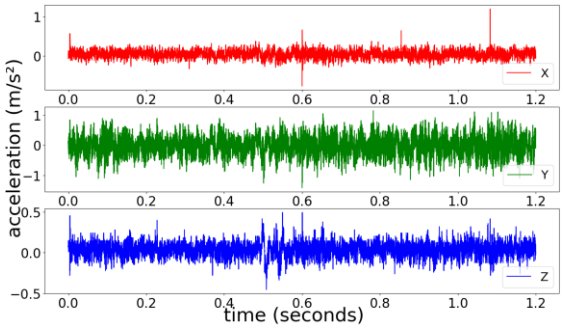


Fig. 2. Sample of a measurement recording

The scratching behavior was performed by sliding the robotic fingertip at a speed of 20 mm/s over a distance of 200 mm over the respective material surface in x direction. For this study, ten surfaces are used for classification and are shown in Fig. 3. The scratching behavior was performed 25 times on each surface resulting in 250 trials.



Fig. 3. Ten surfaces examined by the system

Results

The main objective of this study was to achieve high surface recognition rate by a random forest classification model and check this possibility. Fig. 4 shows the confusion matrix of this random forest classification model and it gives us predictions in 7.83 MS and an accuracy of 91.5%.

Conclusion and Further Improvements

Surface recognition systems play a crucial role in many fields such as biometrics, robotics, and security. The ability to accurately identify and distinguish between different materials based on their physical properties provides a reliable and efficient method for identifying and authenticating objects and their surroundings. One of the main results of this study is to investigate how combination of robotics and machine learning can improve the surface recognition task in industry. In this work, results have shown that this combination can give us good result and for future using more materials and testing other machine learning algorithms can give us a better vision.

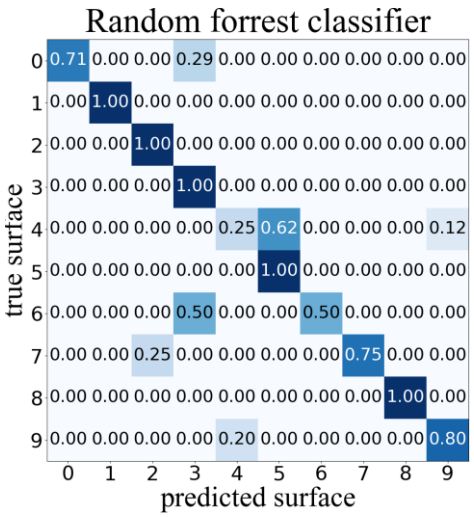


Fig. 4. Confusion matrix of the classifier

References

[1] R. S. Dahiya, G. Metta, M. Valle, G. Sandini, Tactile sensing—from humans to humanoids, IEEE Transactions on Robotics 26, 1-20 (2009); doi: 10.1109/TRO.2009.2033617

[2] S. Luo, J. Bimbo, R. Dahiya, H. Liu, Robotic tactile perception of object properties: A review, Mechatronics 48, 54-67 (2017); doi: 10.1016/j.mechatronics.2017.07.009

[3] S. Luo, L. Zhu, K. Althoefer, H. Liu, Knock-knock: acoustic object recognition by using stacked denoising autoencoders, Neurocomputing 267, 18-24 (2017); doi: 10.1016/j.neucom.2017.05.048

[4] J. Edwards, J. Lawry, J. Rossiter, C. Melhuish, Extracting textural features from tactile sensors, Bioinspiration & Biomimetics 3, 035002 (2008); doi: 10.1088/1748-3182/3/3/035002

[5] T. Taunyazov, Y. Chua, R. Gao, H. Soh, Y. Wu, Fast texture classification using tactile neural coding and spiking neural network, in 2020 IEEE/RSJ International Conference on Intelligent Robots and Systems (IROS), IEEE, 2020, 9890-9895; doi: 10.1109/IROS45743.2020.9341720

Acknowledgements

This research was funded under the Program ”Innovative Hochschule” (innovative university) by the Federal Ministry for Education and Research (BMBF) of Germany (Grant No. 13IHS232C) and the City of Hamburg.

DOI 10.5162/EUROSENSORS2025/TP57

Adaptive algorithm for microsensor in sustainable environmental monitoring

Nursultan Daupayev[1], Christian Engel[2], Ricky Bendyk[2], Prof. Dr.-Ing. Sören Hirsch[1]
[1] Brandenburg University of Applied Science, Department of Engineering, Magdeburger Str. 50, 14770 Brandenburg/Havel, Germany
Corresponding Author's e-mail address: nursultan.daupayev@th-brandenburg.de

Summary: Traditional data collection from sensors produce a lot of data, which lead to constant power consumption and require more storage space. This study proposes an algorithm for a data acquisition and processing method based on Fourier transform (DFT), which extracts dominant frequency components using harmonic analysis (HA) to identify frequency peaks. This algorithm allows sensors to activate only when an event occurs, while preserving critical information for detecting defects, such as those in the surface structures of buildings and ensuring accuracy for further predictions.

Keywords: Microsensor, data reduction, anomaly detection, fourier transform, harmonic analysis

Introduction

Continuous collection of environmental data in sensors plays an important role for example for anomaly detection in building structures [1]. However, regular data collection results in high energy consumption and data redundancy, where it is necessary to either optimize data in the hardware storage or delete them, which leads to a loss of data quality [2].

Description of the method

Within the scope of applying the algorithm, we collected different parameters including carbon dioxide (CO_2), humidity (H) and temperature (T) from a micro multivariate sensor, shown in Fig. 1, installed on the surface of the wall inside the building's room.

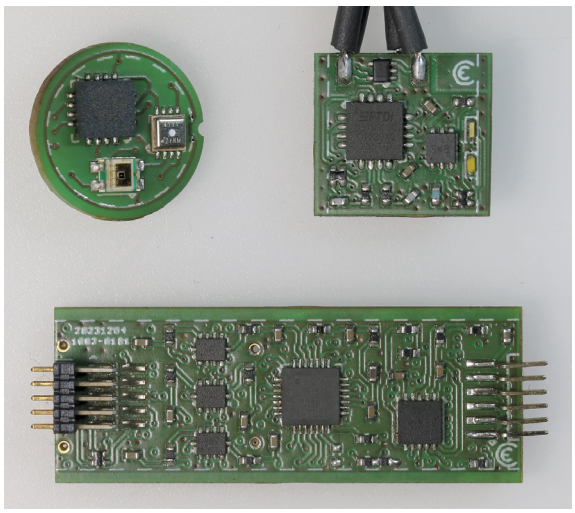


Fig. 1: Multivariate Microsensor

Initially, the algorithm analyses the data behaviour and it can be represented as a time series graph for CO_2, T, H (Fig. 2) and simulation (Fig. 3) for CO_2 based on 24-hour measurements with an interval of 15 minutes. In this study, we focus only on the CO_2, since the application of the method on all parameters is similar.

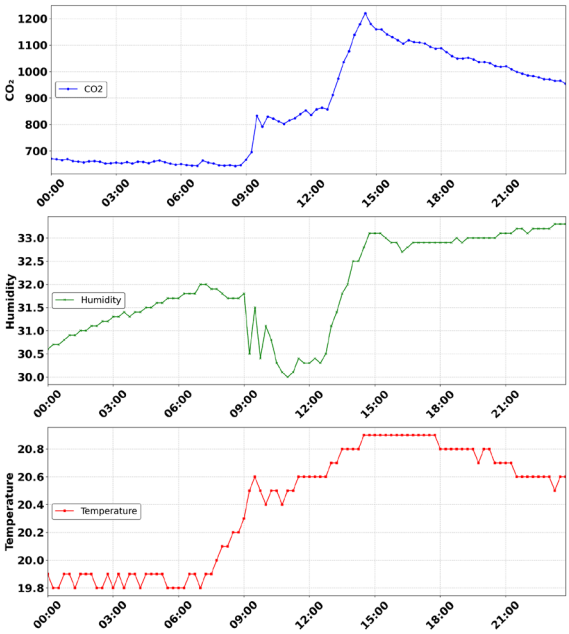


Fig. 2: Microsensor Measurements

Following this, the developed algorithm is aimed at reducing the number of measurements by finding important peaks and excluding insignificant measurement points. To achieve this, by applying Fast Fourier Transform (FFT), algorithm transforms the data from the time domain to the

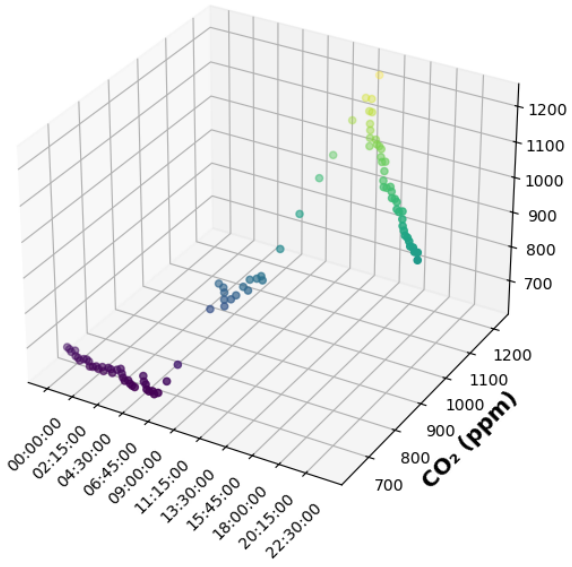


Fig. 3: CO_2 Modeling

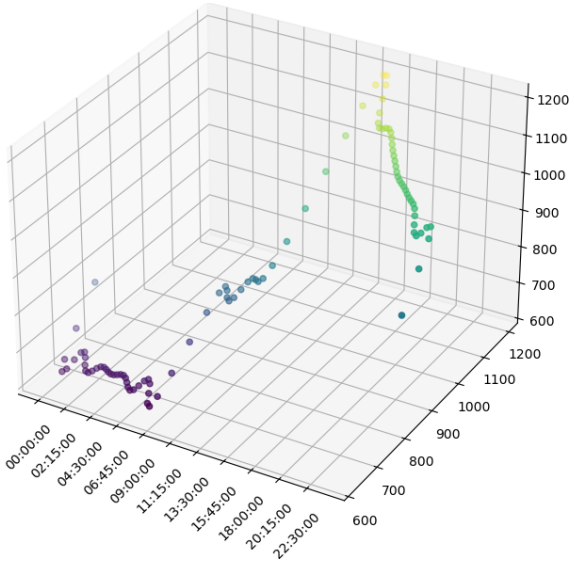


Fig. 4: Reconstructed CO_2 Signal

frequency domain, which made it possible to identify the periodic characteristics of the sensor signals:

$$X[k] = \sum_{n=0}^{N-1} x[n] e^{-j\frac{2\pi}{N}kn}, \quad k = 0, 1, \ldots, N-1. \tag{1}$$

Then, it determines the optimal number of harmonics to achieve a reduction in sensor measurement, where the optimal number of harmonics is selected. In this case, there are 26 optimal harmonics:

$$A[k] = |X[k]| = \sqrt{(\mathrm{Re}\{X[k]\})^2 + (\mathrm{Im}\{X[k]\})^2} \tag{2}$$

After selecting the optimal harmonics, an algorithm uses an inverse fast Fourier transform (IFFT) to reconstruct the signal (Fig 4.). It is expected to be close to the original data, showing minor deviations from them:

$$x[n] = \frac{1}{N} \sum_{k=0}^{N-1} X[k] e^{j\frac{2\pi}{N}kn} \tag{3}$$

In addition, we are also aim to save energy by preserving at least 50% of the total signal energy (in current data measurements), while minimizing the amount of data by eliminating unimportant harmonics and saving the main signal trends:

$$\sum_{k=0}^{K_{\text{opt}}} |X[k]|^2 \geq 0.5 \sum_{k=0}^{N-1} |X[k]|^2 \tag{4}$$

Results

As a result, the necessary points for sensor activation were obtained by applying the DFT and HA, that allowed to reduce the number of measurements, while saving important frequency characteristics of the signal (Fig.5).

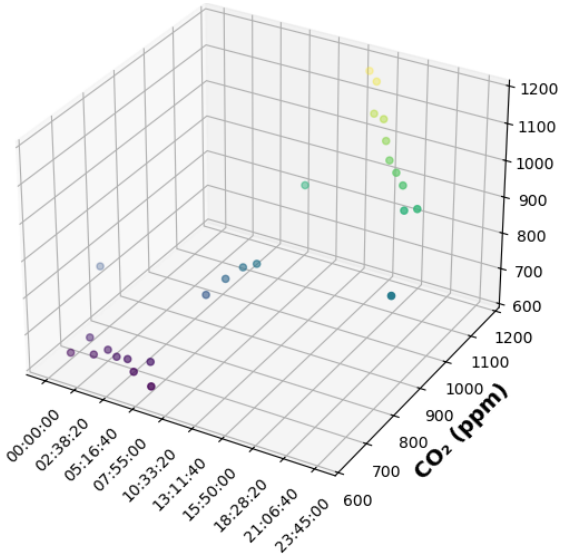


Fig. 5: Microsensor activation time for CO_2

References

[1] L. Liu, R. Song, Q. Wei, Event-Triggered Energy Optimization of Wireless Sensor Networks, *IEEE International Conference on Networking, Sensing and Control (ICNSC)*, Shanghai, China, 2022, pp. 1–6; doi: 10.1109/ICNSC55942.2022.10004164.

[2] S. N. Ahsan, M. Aureli, Three-dimensional analysis of hydrodynamic forces and power dissipation in shape-morphing cantilevers oscillating in viscous fluids, *International Journal of Mechanical Sciences* **149**, 436–451 (2018); doi: 10.1016/j.ijmecsci.2017.09.034.

DOI 10.5162/EUROSENSORS2025/TP60

Sensor Density Optimization of Active Magnetic Shielding System based on Monte Carlo Simulation

Haofan Wang[1,3], Yuning Wu[1,3], Daiyong Chen[2], Rui Feng[1,3], Bangcheng Han[1,3]
[1] School of Instrumentation and Optoelectronic Engineering, Beihang University, Beijing,100191, China
[2]Institute of Large-scale Scientific Facility and Centre for Zero Magnetic Field Science, Beihang University, Beijing 100191, China
[3] Hangzhou Institute of Extremely-Weak Magnetic Field Major National Science and Technology Infrastructure, Hangzhou, 310028, China
hanbangcheng@buaa.edu.cn

Summary:
Active Magnetic Shielding (AMS) systems have become a key component in ensuring near-zero magnetic environments. However, there is still a lack of clear mechanisms for feedback sensor density, layout, and compensation effects in the region of interest (ROI). In this article, the Tikhonov regularization compensation algorithm is employed to analyse the dependency by Monte Carlo simulation. Results indicate a declining compensation error in any layout conditions as the sensor density increases. Therefore a sensor density optimization method based on the threshold compensation error is proposed.

Keywords: Active Magnetic Shielding, Sensor Network, Monte Carlo Simulation, Tikhonov Regularization, Statistical Analysis

Introduction

AMS systems, employing perimeter sensor networks and triaxial coils, play a critical role in ultra-low-field environments for precision experiments such as neutron electric dipole moment (nEDM) measurements and magnetoencephalography (MEG)[1,2]. Conventional approaches either address sensor placement through system ill-conditioning analysis or co-optimize layouts with compensation targets under restrictive zero-field compensation target constraints at sensor locations, faceing inherent limitations due to the coupled optimization[3,4]. This work resolves these limitations by introducing a probabilistic Monte Carlo (MC) framework, establishing quantitative relationships between sensor density, spatial distribution, and shielding efficacy, which can guide the optimization of sensor density in AMS systems.

Analysis Object

Our Investigation is based on an AMS configuration comprising a triaxial Merritt coils (four independently controlled windings per axis, 2.0 m × 1.8 m × 1.6 m) and a fluxgate magnetometer network (2-10 sensors) deployed between coil boundaries and a 5×5×5 grid ROI, which satisfies the assumption that excitation current and magnetic field response in region of interest ROI of coil exhibiting a linear or approximately linear relationship $\boldsymbol{B} = A\boldsymbol{I}$, corresponding to coil constant matrix A.

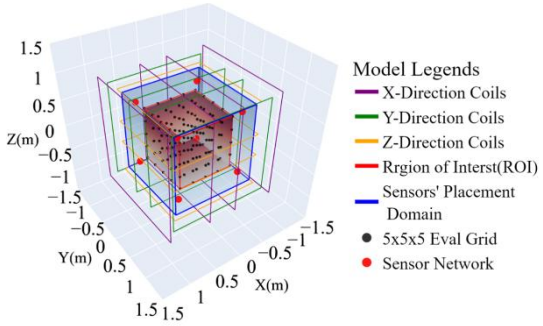


Fig. 1. Relative positions of sensor network and ROI evaluation points in AMS system

Tikhonov Regularization Compensation

A fluctuation term is introduced to the Tikhonov regularization compensation (TRC) cost function J(Δ**I**) to overcome the compensation instability in linear feedback caused by ill-posed problems of response matrix A correspond to sensor layout and coil structrue:

$$J(\Delta \boldsymbol{I}) := \frac{1}{2} \| A\Delta \boldsymbol{I} - B \|^2 + \frac{\alpha}{2} \| \Delta \boldsymbol{I} \|^2 \qquad (1)$$

Together, the linear compensation algorithom is shown as follows:

$$\Delta \boldsymbol{I}_r = A_r^+ \boldsymbol{B} \tag{2}$$

$$A_r^+ = V \Sigma_r^{-1} U^T \tag{3}$$

where $A = U\Sigma V^T, \Sigma_r^{-1} = diag\left(\frac{\sigma_{ii}}{\sigma_{ii}^2 + \alpha^2}\right)$.

In following MC simulations, for each different layout, an optimal transfer regularization parameter α for balancing compensation error and resolving fluctuations through grid search method is applied to ensure that TRC works in the best condition.

Density-compensation analysis based on Monte Carlo Simulation

Operating in an inhomogeneous magnetic environment $\mathbf{B}_{init}$ and $\mathbf{B}_{ext}$, the methodology integrates Monte Carlo sampling of 10,000 coil current vectors **I** and sensor layouts P with Tikhonov-regularized compensation (TRC) loops. E_{vec} and E_{sca} quantify vector and scalar relative errors between residuals across the ROI and field distribution generated from **I**, $\mathbf{B}_{init}$, $\mathbf{B}_{ext}$ after 10 control iterations under each layout P. The simulation process are as follows:

(1) Generate background magnetic field at sensors $\mathbf{B}_{init}$ and at ROI evaluation points $\mathbf{B}_{ext}$;
(2) Uniformly sampling generate different sensor layouts P and final control state defined by steady-state current **I**;
(3) Uniformly sampling 5 × 5 × 5 evaluation point grid within ROI for characterizing its magnetic field distribution and calculate:
Operating point of TRC : $\boldsymbol{B}_{set} = \boldsymbol{B}_{init} + A_P \boldsymbol{I}$

Ideal distribution in ROI : $\boldsymbol{B}_{ideal} = \boldsymbol{B}_{ext} + A_{ROI} \boldsymbol{I}$;
(4) The TRC is driven at each sensor layout P in 10 iterations of compensation, thereby computing the set of scalar and vector deviations, E_{sca} and E_{vec} between the magnetic field distribution $\mathbf{B}_{comp}$ within the ROI at steady state and $\mathbf{B}_{ideal}$;
(5) Repeat simulation for all sensor density N.

Results and Conclusions

Run MC simulation for N=2~10 under 100-sized sampled **P** and **I** in each turn: As sensor density N increases, 95% percentile of errors E_{vec} declines from 369.17% to 8.49%, while for E_{sca} is 55.1% to 1.77%, revealing a more and more significant statistical decoupling between sensor layout and TRC compensation performance in ROI.

The optimization framework can be formally described as follows. First, compute the 95th percentile $Q_{0.95}(E)$,(E= $E_{vec,}$ or E_{sca}) across all simulation scenarios to establish a conservative upper bound for the probability estimation error. Subsequently, determine the minimum sensor density N that satisfies the constraint where error ``metric remains within the predefined maximum tolerance threshold E_{max}. This constrained optimization problem can be mathematically formulated as:

$$\begin{cases} N = argmin\left(Q_{0.95}(E)\right) \\ s.t. E < E_{\max} \end{cases} \tag{4}$$

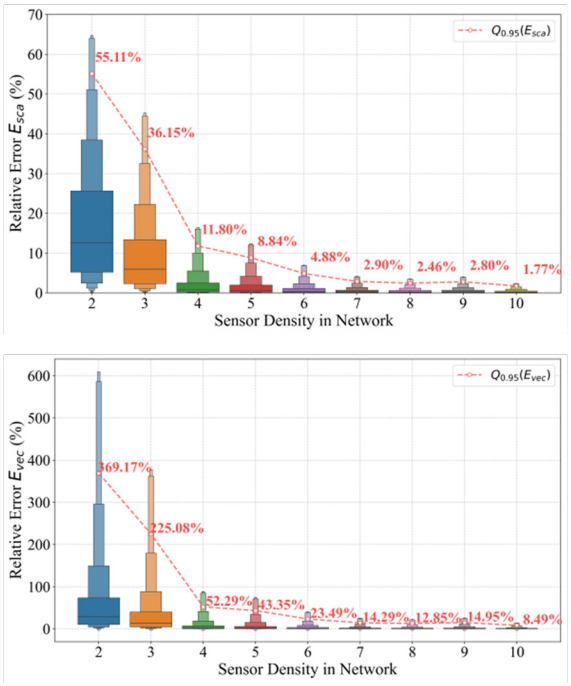


Fig. 2. Distribution and 95% percentile value of E_{sca} and E_{vec}.

In addition, with proper sensor density, the sensor layout and compensation performance can be successively optimized independently, where the latter has a potential improvement by tuning the AMS operate points via operating points based on target field method.

References

[1] G.W. Ski, Development of mangetic field control systems in the nEDM experiment (2016).

[2] Y.Y. Ma, Y. Gao, H.Q. Wu, et al. OPM-MEG Measuring Phase Synchronization on Source Time Series: Application in Rhythmic Median Nerve Stimulation. *IEEE Transactions on Neural Systems and Rehabilitation Engineering*, 32, 1426-1434 (2024); doi: 10.1109/TNSRE.2024.3381173.

[3] C. Abel, N.J. Ayres, G. Ban, et al. A large 'Active Magnetic Shield' for a high-precision experiment: nEDM collaboration. *The European Physical Journal C*, 83(11), 1061 (2023), doi: 10.1140/epjc/s10052-023-12225-z.

[4] T. Lins. High Precision Physics in Low Magnetic Fields: Implementation of a Sub-Nanotesla Field with Femtotesla Temporal Stability (2016).

DOI 10.5162/EUROSENSORS2025/TP61

Selective Breath Acetone Detection for Metabolic Health Monitoring

Jaehyun Ko[1], *Andreas Güntner*[1]
[1] *Human-centered Sensing Lab, Department for Mechanical and Process Engineering, ETH Zürich, Switzerland*
jaehko@hsl.ethz.ch

Summary:
Breath acetone is a promising non-invasive biomarker for monitoring lipolysis and ketosis. We developed a chemiresistive sensor combining WO_3 nanoparticles and Pt–Al_2O_3 catalytic filters for selective, low-ppb acetone detection. This device correlates strongly with clinical reference methods and allows real-time tracking of metabolic states in both humans and animals under fasting, exercise, or pathological conditions.

Keywords: breath analysis, chemiresistive gas sensor, acetone, metabolic monitoring, catalytic filter

Background, Motivation an Objective

Non-invasive breath analysis is increasingly recognized as a valuable tool for metabolic health monitoring. Among volatile organic compounds (VOCs) in exhaled breath, acetone is a robust biomarker for fat metabolism, offering diagnostic insights into states such as fasting, exercise-induced lipolysis, or diabetic ketosis [1–4]. Conventional detection methods like gas chromatography-mass spectrometry (GC-MS) are sensitive but unsuitable for point-of-care or field applications due to their complexity and cost.

In this work, we present a cost-effective gas sensor system using WO_3 nanoparticles for chemiresistive acetone detection, with selectivity enhanced with a Pt–Al_2O_3 catalytic filter. This configuration suppresses common breath interferents such as ethanol and isoprene, improving selectivity. The sensor's performance was validated under controlled metabolic interventions and against established blood ketone biomarkers, highlighting its clinical and veterinary relevance.

Description of the New Method or System

The sensing layer consists of flame spray–synthesized WO_3 nanoparticles deposited on a microheater platform. To mitigate interference from non-ketonic VOCs, a porous Pt–Al_2O_3 catalytic layer is placed upstream, oxidizing competing compounds at low temperatures (<150 °C) while preserving acetone. The sensor operates at ~300 °C and detects acetone in the low ppb–ppm range with minimal cross-sensitivity.

This configuration allows operation in ambient air without pre-conditioning, making it suitable for mobile breath diagnostic devices. The system's temporal resolution enables dynamic profiling of metabolic shifts.

Results

The sensor exhibited excellent linearity and sensitivity to acetone with negligible response to ethanol and isoprene. In animal studies, breath acetone levels increased significantly with different status of the animals, in line with known lipolytic dynamics [2,3]. These signals showed strong correlation ($R^2 > 0.9$) with blood β-hydroxybutyrate concentrations measured concurrently.

References

[1] Güntner, A. T. et al. Monitoring Rapid Metabolic Changes in Health and Type-1 Diabetes with Breath Acetone Sensors. *Sens. Actuators B Chem.* 367, 132182 (2022); doi.org/10.1016/j.snb.2022.132182

[2] Königstein, K. et al. Breath Acetone Change during Aerobic Exercise Is Moderated by Cardiorespiratory Fitness. Small Sci. 1, 2100004 (2021); https://doi.org/10.1002/smsc.202100004

[3] Weber, I. C. et al. Monitoring Lipolysis by Sensing Breath Acetone Down to Parts-per-Billion. *J. Breath Res.* 15, 016006 (2021); doi.org/10.1088/1752-7163/abca2b

[4] Güntner, A. T. et al. Noninvasive Body Fat Burn Monitoring from Exhaled Acetone with Si-Doped WO_3-Sensing Nanoparticles. *Anal. Chem.* 89, 10578–10584 (2017); doi.org/10.1021/acs.analchem.7b02666

DOI 10.5162/EUROSENSORS2025/TP62

Rapid and Sensitive MiRNA Detection in Biofluids Using Ultra Microelectrode Sensors.

[1]Marcello Valente, Md. A. Ridwan, [2]John Browne, [1]Javier Higes Marques [2,3]K. G, Meade, [1]A. O'Riordan

1 Tyndall National institute, UCC, Cork, Ireland

2 UCD School of Agriculture and Food Science, University College Dublin, Belfield, D04 V1W8, Dublin, Ireland.

3 UCD Conway Institute of Biomolecular and Biomedical Research, University College Dublin, Belfield, D04 V1W8, Dublin, Ireland.

Summary:

MiRNA are short nucleic acids sequences that are correlated to many important genetic cascades response, immune response being among one of the most important. Our previous sensors, able to detect DNA, is now used not only to detect miRNA sequences in plasma but it's also adapted to work with a portable potentiostat, making the aim of an electrochemical sensor on field more realistic.

Keywords: #miRNA #Bovinehealth #electrochemestry #microelectrode #IDE

Headlines

.

Background, Motivation an Objective

MiRNA, despite their limited dimension once matured compared to the average mRNA, are oligonucleotide sequences that help to regulated different genetic signals cascades and some of them are considered potential new biomarker for different pathologies, miRNA21 being among them one of the most studied [1]

As proved by our comparison with the gold standard for miRNA study, qPCR, we noticed the difficulties in using this techniques to discriminate between miRNA21 different threshold of concentration related to immunoresponse [2], consequentially we used a previous work done on our chip sensor [3] to be readapted to a microarray-like structure mediated by chitosan and glutaraldeide on the working electrode, we tested spiked solution of plasma both using commercial potentiostat and our prototype developed from the schematics of Dr. Aidan Murphy thesis [4]

Description of the New Method or System

The comparison with qPCR using the same spiked plasma samples has let focused on the large range possible, this is related to the limits of both techniques since qPCR has shown a still superior quality, it' unable to detect the metabolic threshold related to immune-response, this is even more improved by the use of portable prototype (Fig.2)

Results

We have been able to cover a large range of Molarity specific for miRNA21, resulting in a R^2 of 0.98, with a portable system that have the potential to be cheaper

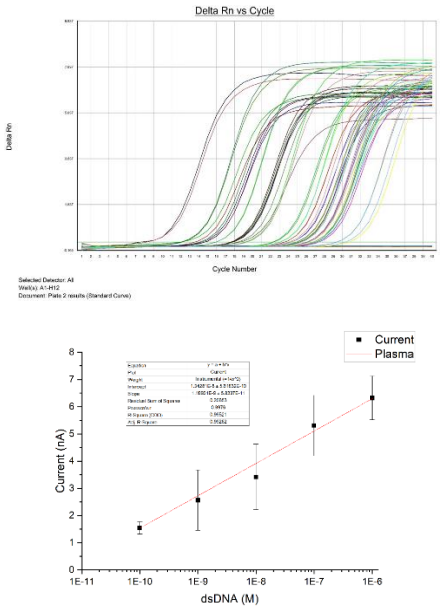


Fig. 1. Comparison between qPCR and our methods.

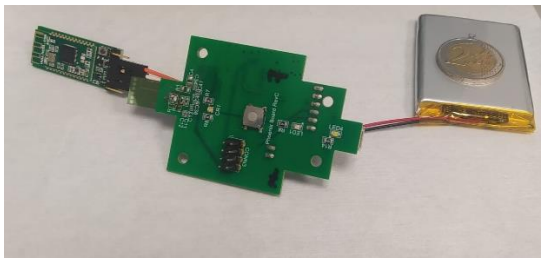


Fig. 2. Architecture of prototype and sensor chip

Acknowledgements

This field is to thank the institution financing the research and colleagues for their contribution to the preparation of the article.

References

[1] L. F. R. Gebert and I. J. MacRae, ‘Regulation of microRNA function in animals’, *Nat. Rev. Mol. Cell Biol.*, vol. 20, no. 1, pp. 21–37, Jan. 2019, doi: 10.1038/s41580-018-0045-7.

[2] W. Jin, E. M. Ibeagha-Awemu, G. Liang, F. Beaudoin, X. Zhao, and L. L. Guan, ‘Transcriptome microRNA profiling of bovine mammary epithelial cells challenged with Escherichia coli or Staphylococcus aureusbacteria reveals pathogen directed microRNA expression profiles’, *BMC Genomics*, vol. 15, no. 1, p. 181, Dec. 2014, doi: 10.1186/1471-2164-15-181.

[3] I. Seymour, B. O’Sullivan, P. Lovera, J. F. Rohan, and A. O’Riordan, ‘Removal of Dissolved Oxygen Interference in the Amperometric Detection of Monochloramine Using a pH Control Method’, in *2019 IEEE SENSORS*, Montreal, QC, Canada: IEEE, Oct. 2019, pp. 1–4. doi: 10.1109/SENSORS43011.2019.8956674.

[4] A. Murphy, ‘Murphy, A. 2023. Electrochemical sensor interface. PhD Thesis, University College Cork.’, UCC. [Online]. Available: https://hdl.handle.net/10468/14984

DOI 10.5162/EUROSENSORS2025/TP63

Direct-printed, solid-contact pH sensor for clinical applications: Challenges of non-specific adsorption

Marcin Urbanowicz[1], *Agnieszka Paziewska-Nowak*[1], *Kornelia Bobrowska*[1], *Anna Sołdatowska*[1], *Marek Dawgul*[1], *Marcin Ekman*[2], *Dorota G. Pijanowska*[1]
[1] *Nalecz Institute of Biocybernetics and Biomedical Engineering, Polish Academy of Sciences, Ks. Trojdena 4 St., 02-109 Warsaw, Poland,*
[2] *Department of Surgical Oncology, Transplant Surgery and General Surgery, Medical University of Gdańsk, Poland*

Summary: We present a solid-contact pH sensor based on an hydrogen ion-selective membrane (ISM). The sensor substrate was fabricated using direct printing technology. A conducting polymer, polyazulene (pAz), was applied as an ion-to-electron transducer layer. Metrological characterization demonstrated that the sensor operates over a wide range of hydrogen ion concentrations, exhibiting a fast Nernstian response. Additionally, surface plasmon resonance (SPR) was employed to study the non-specific adsorption of organic molecules on the ISM-coated gold chip. Studies have shown that for proteins, the non-specific adsorption to ISM is dependent on the isoelectric point. In the case of drugs, it was shown that the non-specific adsorption of ibuprofen is much higher than that of acetaminophen.

Keywords: pH sensor, Direct printing, Potentiometry, Non-specific adsorption

Introduction

pH sensors based on ion-selective membranes are leading analytical tools for determining hydrogen ion concentration in clinical applications. Their ability to provide reliable and rapid measurements makes them indispensable in pH monitoring in body fluids. However, one of the major challenges in the practical application of these potentiometric sensors is the non-specific adsorption of various organic compounds on the sensor surface, which can lead to signal drift and reduced performance over time. Therefore, research focused on enhancing sensor sensitivity and improving resistance to non-specific adsorption is essential. Advances in these areas are critical for the further development of potentiometric sensor technology, enabling their broader applications in continuous monitoring and clinical diagnostics.

Methods

Electrodes were manufactured using direct printing technology. The direct printing was processed using a programmable microdispensing robot. The basic structures of the electrode were fabricated on a nonconductive polyester foil, with consecutively deposited silver paste, carbon paste, and insulating layers [1]. Electroconducting polymer (ECP), polyazulene (pAz), was deposited onto the graphite direct-printed electrode by cyclic voltammetry technique [2]. Modified electrodes were covered with an hydrogen ion-selective membrane (ISM) cocktail. The cocktail was composed of 0.5 wt.% potassium tetrakis(*p*-chlorophenyl)borate, 1 wt.% tridodecylamine, 65.5 wt.% bis-(2-ethylhexyl)-sebacate, and 33 wt.% polyvinyl chloride. Surface plasmon resonance (SPR) was used as a technique for monitoring the non-specific adsorption of various organic compounds to ISM. The ISM was deposited onto the surface of a gold SPR chip using the spin-coating technique. The non-specific adsorption was studied for selected organic molecules, including proteins: lactoferrin (Lf), fibrinogen (Fib), bovine serum albumin (BSA); amino acids: phenylalanine (Phe), methionine (Met), alanine (Ala), lysine (Lys), nucleic acids (calf thymus DNA); small biomolecules: glucose (Glu); and commonly used drugs: ibuprofen (Ibu), acetaminophen (Acph). The applied concentrations reflect typical clinical and physiological ranges.

Results

The pH sensors featuring a pAz transducer layer were characterized in terms of metrological parameter and response (Table 1 and Fig. 1).

Table 1 Metrological parameters of pH sensor based on pAz.

S \ mV/dec	pH range	$T_{95\%}$ \ s
55.4±0.1	2-10	7

The selectivity coefficients determined for the pH sensors (Table 2) confirmed their suitability for pH measurements in complex matrices, including human plasma.

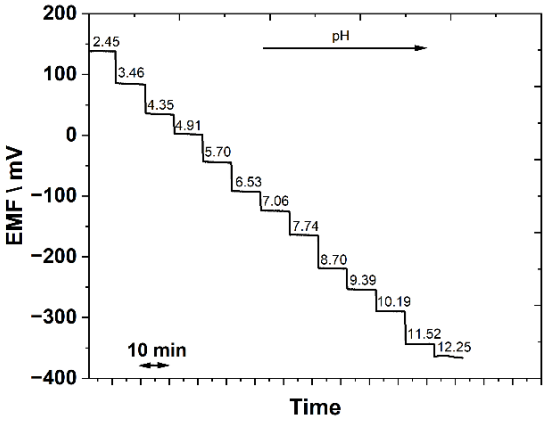


Fig. 1. Response of a direct-printed pH sensor to changes H^+ concentration.

Table 2: Selectivity coefficients $K_{H,j}$, required (req.) and experimentally estimated (exp.) values for constructed pH sensor determined using fix interference method (FIM) recommended by IUPAC.

interfering ions (j)	C_{phys} \ mM	$\log(K_{H,j})_{req.}$	$\log(K_{H,j})_{exp.}$
Na^+	150	-7.8	-9.7
K^+	5	-6.4	-8.3
NH_4^+	0.05	-4.4	-7.2
Ca^{2+}	2	-6.7	-8.8
Mg^{2+}	2	-8.2	-8.8

To investigate the non-specific adsorption, the ISM used in the sensor was deposited onto a gold SPR chip using the spin-coating technique. A series of organic compounds (Lf, Fib, BSA, DNA, Phe, Met, Ala, Lis, Glu, Ibu, Acph) were dissolved in a phosphate buffered saline solution (PBS, pH = 7.4), and their non-specific interactions with the ISM were monitored using SPR apparatus (Fig. 2. A). The surface loading density of these molecules on the membrane was quantified (Fig. 2. B). The results indicate that the level of membrane loading under constant environmental conditions varied depending on the type of organic compound. In the case of proteins, adsorption was strongly influenced by their isoelectric point (pI), with Lf (pI = 8.7, MW = 80 kDa) adsorbing at levels exceeding 3 ng/mm², Fib (pI = 7.4, MW = 340 kDa) reaching approximately 1.5 ng/mm², and BSA (pI = 4.5, MW = 66 kDa) showing minimal adsorption below 0.5 ng/mm². In contrast, small amino acids did not display a clear dependence on pI, suggesting that alternative mechanisms, such as hydrophobic interactions, may govern their adsorption behaviour. Furthermore, Ibu, one of the tested drugs, demonstrated non-specific binding to the ISM, in contrast to Acph, which exhibited negligible adsorption. Notably, the hydrophobic character of the ISM and near neutral pH of the PBS solution likely played a significant role in mediating these non-specific interactions. Collectively, these findings highlight that membrane hydrophobicity, the pH of the surrounding environment, and the isoelectric point of the organic molecules are key factors influencing non-specific adsorption onto ISM.

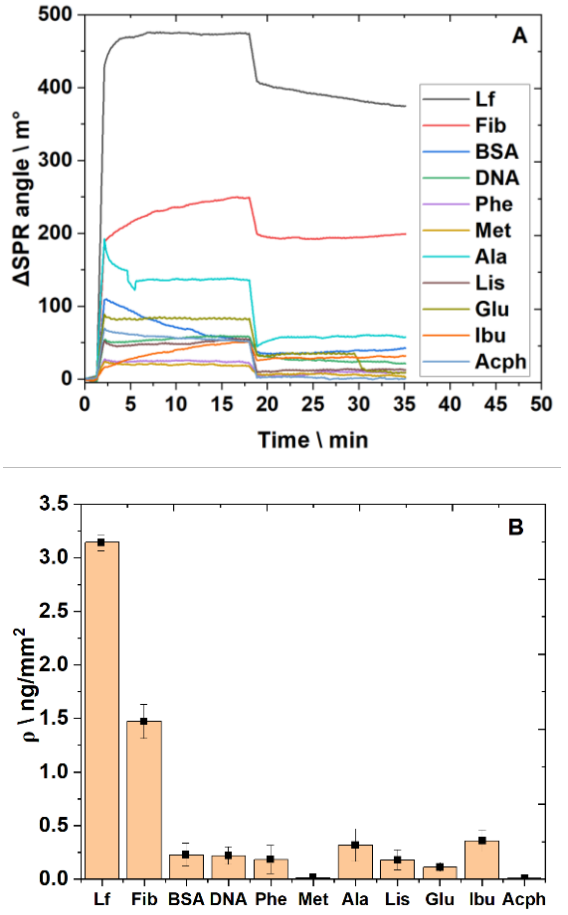


Fig. 2. A. Sensorgrams of non-specific adsorption of organic compounds onto the ISM; B. The loading density of the ISM with the applied organic molecules.

References

[1] M. Urbanowicz, M. Dawgul, D. Pijanowska, Planarna mikroelektroda jonoselektywna oraz sposób jej wytwarzania. Patent application 2024:WIPO ST 10/C PL448894.

[2] M. Urbanowicz, K. Sadowska, A. Paziewska-Nowak, A. Sołdatowska, D.G. Pijanowska, Highly Stable Potentiometric (Bio)Sensor for Urea and Urease Activity Determination, Membranes (Basel) 11, 898 (2021). doi: 10.3390/membranes11110898.

Acknowledgements

The studies were financially supported by the project KPOD.07.07-IW.07-0115/24 funded by the Medical Research Agency (ABM), Poland, and IBBE PAS statutory project 225.

DOI 10.5162/EUROSENSORS2025/TP64

DNA-6MP interactions for electrochemical biosensor development

Anna Sołdatowska[1], Marcin Urbanowicz[1], Magdalena Urbanowicz[2], Kamila Sadowska[1], Dorota G. Pijanowska[1]
[1] Nalecz Institute of Biocybernetics and Biomedical Engineering, Polish Academy of Sciences, Ks. Trojdena 4 St., 02-109 Warsaw, Poland,
[2] Falsified Medicines and Medical Materials Department, National Medicines Institute, Chełmska 30/34 St., 00-725 Warsaw, Poland
asoldatowska@ibib.waw.pl

Summary: This study presents a novel analytical tool for the detection of 6-mercaptopurine (6MP) through the development of a DNA-based electrochemical biosensor. A specific double-stranded DNA sequence (5′-GGCAGGACGGAG-3′) was identified for its ability to selectively bind 6MP, with an affinity constant of 2.52 × 10^3 M^{-1}, as confirmed by DOSY NMR. Selectivity was further verified by HPLC analysis in the presence of common metabolites and co-administrated drugs. When immobilized on the electrode surface, this DNA-based bioreceptor offers a rapid, cost-effective, and easy-to-use alternative to conventional analytical tools, with promising applications in therapeutic drug monitoring and personalized medicine.

Keywords: 6-mercaptopurine, DNA-drug interaction, selective bioreceptor, electrochemical biosensor, short double-stranded DNA

Introduction

The development of selective bioreceptors remains a key challenge in designing effective DNA-based biosensors for small-molecule drugs. Most current systems rely on isolated DNA fragments, which often lack the specificity required to distinguish the target compound from similar metabolites or co-administered drugs. To address this limitation, this study focused on the use of a specifically selected double-stranded DNA sequence as a bioreceptor for the detection of 6-mercaptopurine (6MP), an active form of an immunosuppressive drug, with the aim of improving both the accuracy and reliability of DNA-type biosensors.

Methods

Custom-synthesized DNA with the sequence 5′-GGCAGGACGGAG-3′ was purchased in double-stranded (*ds*DNA) form. This sequence represents a variant of others previously reported in the literature [1]. To evaluate its potential as a bioreceptor for 6-mercaptopurine, diffusion-ordered spectroscopy (DOSY) NMR was employed. Since the diffusion coefficient (D) value depends on the molecular size—being greater for small molecules such as 6MP and lower for larger molecules such as DNA—binding causes a noticeable shift in D. By comparing the diffusion coefficients of free and bound forms, the binding constant can be determined. For the tested DNA sequence, selectivity studies were conducted via high-performance liquid chromatography. Eleven molecules were chosen as potential interferents: typical metabolites, such as urea, uric acid, glucose, and ascorbic acid; pain killers; nonsteroidal anti-inflammatory drugs, such as acetaminophen, ibuprofen, diclofenac and mesalazine; and two antibiotics, ciprofloxacin, and metronidazole, which are frequently used for the prevention of postoperative recurrence of Crohn's disease. Additionally, metformin, an antidiabetic medication, was included, reflecting its widespread use among the growing population of diabetes patients.

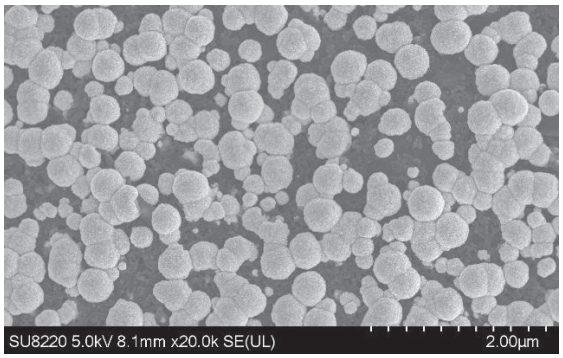


Fig. 1. SEM image of GSPE/Pt.

The developed biosensor employs a graphite screen-printed electrode (GSPE) modified with platinum nanoparticles (PtNPs) to enhance sensitivity via their strong electrocatalytic properties. PtNPs were electrodeposited by Cyclic Voltammetry (CV) technique, from 3 mM H_2PtCl_6 in a

0.5 M H_2SO_4 solution at a scan rate of 50 mV/sec. Figure 1 presents an SEM image of a GSPE with deposited PtNPs. A linear linker, cysteamine (Cys), was used to covalently attach a carboxyl-terminated double-stranded DNA sequence, forming a stable and functional recognition layer.

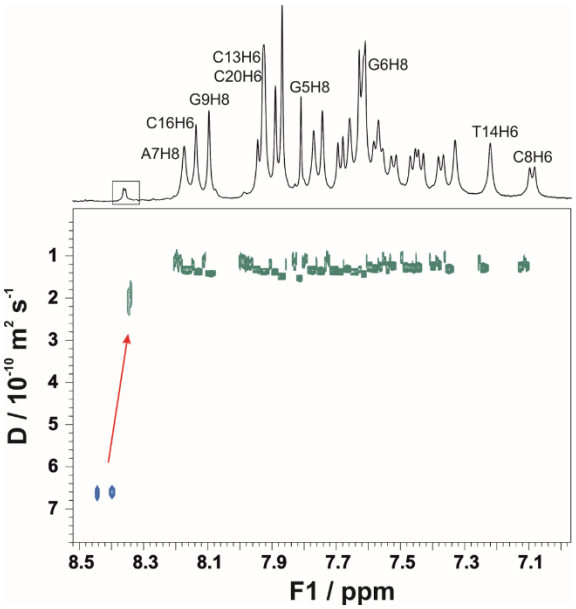


Fig. 2. NMR DOSY spectra of 6MP (blue) and dsDNA (GGCAGGACGGAG)+6MP (green) at a concentration ratio 4 : 1 respectively.

Results

The DOSY NMR spectra of 6MP and its complex with *ds*DNA GGCAGGACGGAG are shown in Figure 2. On the basis of the diffusion coefficient changes upon complex formation, the K_a binding constant was calculated, with a value of $2.52 \cdot 10^3$ M^{-1}. The HPLC results, interpreted as the selectivity of the bioreceptor, summarized in Table 1, reveal different patterns of interference across the various molecules and tested DNA. For comparison, the obtained value for 6MP–27% confirmed strong complex formation with the selected DNA strand, as only 27% of the free DNA remained in the tested solution. Metabolites such as urea, uric acid, etc., and painkillers, with calculated values of approximately 80%, showcase their limited interactions with DNA. Medications such as ciprofloxacin, diclofenac, mesalazine, metformin, and metronidazole also exhibit weak interactions with the studied DNA sequence [2].

*Tab. 1: HPLC selectivity studies presented as the percentage of peak area from the DNA complex (*the error of the analytical procedure is ±2%).*

percentage of peaks area from the DNA complex vs unbound DNA (%)	
6-Mercaptopurine	27
Urea	80
Uric acid	78
Glucose	79
Ascorbic acid	79
Acetaminophen	78
Ibuprofen	80
Ciprofloxacin	79
Diclofenac	101*
Mesalazine	102*
Metformine	80
Metronidazole	100

Voltammetric measurements with the designed biosensor confirmed the presence of DNA on the electrode surfaces, as the oxidation signals of guanine and adenine were recorded. Notably, a significant decrease in the adenine signal was observed following incubation with 6-mercaptopurine, indicating that analyte detection can be achieved indirectly by monitoring this decrease. The developed biosensor exhibited a linear response from 2 to 75 nM (Figure 3), which allows accurate quantification in potential real samples through appropriate dilution, as physiological concentrations typically exceed this range.

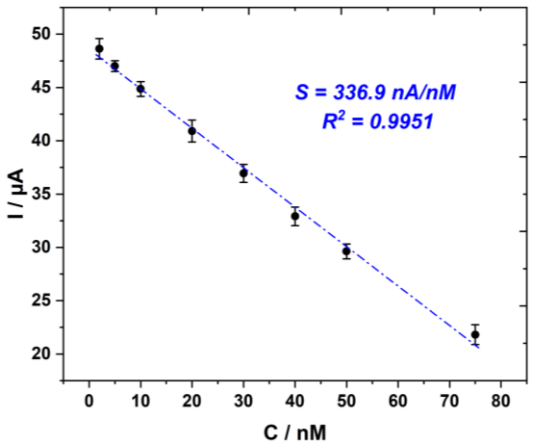


Fig. 3. Calibration curve for 6MP determination on GSPE/Pt -Cys-dsDNA.

References

[1] S.U. Rehman, et al., Interaction of 6 Mercaptopurine with Calf Thymus DNA – Deciphering the Binding Mode and Photoinduced DNA Damage, *PLoS One* 9, e93913 (2014); doi: 10.1371/journal.pone.0093913.

[2] A. Sołdatowska, et al., Exploring DNA-6MP interactions to develop a receptor with selective binding properties, *Int. J. Biol. Macromol.* 305 (Pt 1):140910 (2025); doi: 10.1016/j.ijbiomac.2025.140910

Acknowledgements

The studies were financially supported by the project 2019/35/O/ST5/01886 funded by the National Science Centre (NCN), and Minigrant FBW/1.1/21 from the IBBE PAS, Warsaw PL.

DOI 10.5162/EUROSENSORS2025/TP65

Electrochemical detection of cortisol using carbon nanotubes (CNT) modified with a pyrene derivative

Ana R. Santos[1], Fátima Bento[2], Bruno Faria[1], Maria C. Paiva[1], Alexandre F. Silva[3], Júlio C. Viana[1]
[1] IPC – Institute for Polymers and Composites, University of Minho, Campus de Azurém, 4800-058 Guimarães, Portugal
[2] CQ-UM – Chemistry Research Centre of the University of Minho, Campus de Gualtar, 4710-057 Braga, Portugal
[3] CMEMS – Center for Microelectromechanical Systems, University of Minho, Campus de Azurém, 4800-058 Guimarães, Portugal
id10233@alunos.uminho.pt

Summary:
Constant high cortisol levels resulting from chronic stress impair mental health and performance, yet real-time monitoring remains challenging. For non-invasive analysis, an electrochemical cortisol sensor was developed using carbon nanotubes (CNTs) non-covalently functionalized with pyrene derivatives (PY). Functionalized CNTs enabled cortisol interaction, with sensitivity and dynamic range evaluated through differential pulse voltammetry (DPV). Molecular dynamics (MD) simulations further clarified cortisol–pyrene interactions. This approach lays the groundwork for simple, non-invasive stress monitoring.

Keywords: Carbon nanotubes, Pyrene derivatives, Electrochemical sensing, Cortisol detection, Molecular dynamics

Introduction

Mental health has become a major concern in recent decades, with chronic workplace stress recognized as a significant issue worldwide. This condition adversely affects work performance and overall well-being. Continuous monitoring of stress biomarkers—particularly cortisol, a well-established indicator of chronic stress—provides a promising approach to mitigating these effects. Consequently, there is a growing demand for accessible, non-invasive cortisol monitoring biofluids, such as saliva and sweat [1].

Electrochemical biosensors employing antibodies, aptamers, or molecularly imprinted polymers (MIPs) have been extensively studied [2,3]. For antibody immobilization, materials such as ZnO, molybdenum disulfide (MoS_2), gold nanoparticles (AuNP), silver oxide (Ag/AgO), and reduced graphene oxide (rGO) have been explored. Aptamer-based systems have used platinum/graphene and screen-printed graphene electrodes (SPGE), magnetic beads (MBs), and graphene quantum dots (GQD). MIP-based sensors offer a lower cost alternative, with materials such as AuNP-doped poly-o-PD, indium oxide (In_2O_3), and polydimethylsiloxane (PDMS)/carbon nanotube-cellulose nanocrystal (CNT-CNC). Although they offer varying sensitivity and detection ranges, the limitations persist: antibody instability and use of animal hosts, aptamer biodegradation, costly and time-consuming production, complex MIP optimization, and secondary probes. While more straightforward approaches using CNT showed significant potential in biosensing applications (e.g., metalloporphyrin-CNT electrodes), they often require complex chemistry and high costs.

Here, we demonstrate a CNT-based cortisol sensor exploiting the intrinsic properties of pyrene derivatives [4] for selective detection. This approach eliminates expensive biorecognition molecules and complex chemical modifications, with the potential for real-time stress monitoring in wearable devices.

Results

Commercial screen-printed carbon electrodes (SPCEs) were modified with carbon nanotubes non-covalently functionalized with pyrene derivatives (CNT-PY) via drop-casting. The sensor response to cortisol solutions (µM range) was evaluated by differential pulse voltammetry (DPV) (Fig. 1). The pyrene derivative (PY) exhibited characteristic electrochemical behavior with a distinct reduction peak at -1.1 V in cortisol-free solution. Increasing cortisol concentrations caused partial inhibition of this peak's intensity (Fig. 1). A calibration curve for the CNT-PY sensor (Fig. 2) was established across a cortisol concentration range of 10-760 µM. The sensor demonstrated good sensitivity to cortisol (3.85

μA/log[CORT] μM) with a determination coefficient (R^2) of 0.948.

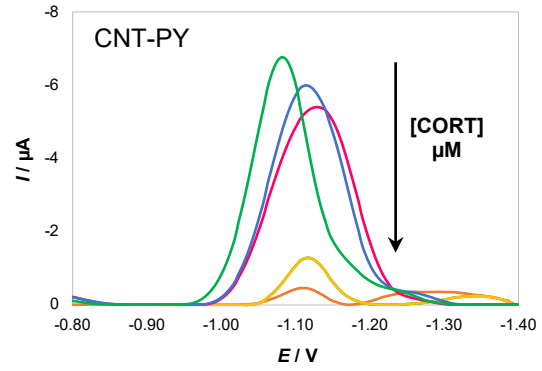


Fig. 1. DPV obtained for CNT-PY sensor in response to a range of μM cortisol concentration solutions.

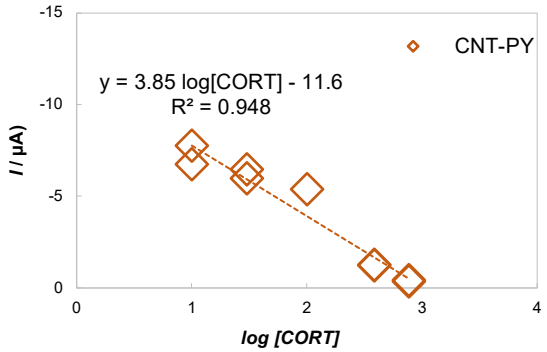


Fig. 2. CNT-PY sensor calibration curve for different cortisol concentrations using DPV.

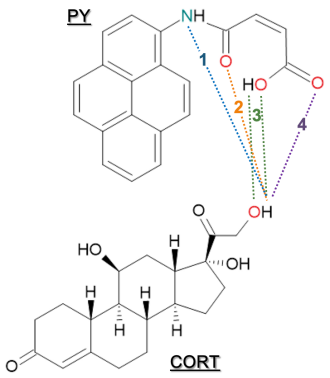


Fig. 3. Schematics of most frequent PY and cortisol interactions.

Tab. 1: Hydrogen bond analysis results of MD simulations.

HBond Type	HBond/ CORT	% CORT	**Occupancy max %**
1	0.8	40	0.17
2	1.1	80	0.28
3	1.8	70	0.09
4	1.8	80	0.11

To clarify the interaction mechanism between PY and cortisol, molecular dynamics (MD) simulations were performed using LAMMPS software. The modeled systems contained 4000 ethanol molecules, 20 PY molecules, and 10 cortisol molecules. Ethanol was modeled using the OPLS-AA force field, while the rest of the system followed the GROMOS54A7 force field, with parameters obtained from the ATB database. For the NPT ensemble, the temperature was maintained at 300 K using a Nosé-Hoover thermostat. Visual Molecular Dynamics (VMD) software was used to perform hydrogen bond (HBond) analysis between specific PY and cortisol functional groups (Fig. 3).

Table 1 summarizes the HBond analysis results. HBond type 4 (see Figure 3) showed the highest HBond frequency per cortisol molecule (HBond/CORT) and involved the highest percentage of cortisol molecules (% CORT) in PY interactions. Overall, the maximum occupancy (HBond persistence over time) remained low, consistent with the system's high dynamics. These results suggest that PY-cortisol interactions occur primarily through the chemical groups involved in HBond type 4. This non-covalent interaction between the two molecules could explain the partial passivation of PY´s electroactive site due to cortisol presence, which accounts for the observed inhibition of its reduction peak at −1.1 V.

Acknowledgments

This work was carried out within the scope of the individual PhD scholarship reference 2021.07771.BD, exclusively funded by FCT—Fundação para a Ciência e a Tecnologia.

References

[1] A. Kaushik, A. Vasudev, S.K. Arya, S.K. Pasha, S. Bhansali, Recent advances in cortisol sensing technologies for point-of-care application, Biosens Bioelectron 53 (2014) 499–512. https://doi.org/10.1016/j.bios.2013.09.060.

[2] A.N. Naeem, S. Guldin, S.S. Ghoreishizadeh, Electrochemical Sensors for Cortisol: A Review, IEEE Sens J 24 (2024) 5746–5758. https://doi.org/10.1109/JSEN.2023.3349293.

[3] G. Karuppaiah, M.H. Lee, S. Bhansali, P. Manickam, Electrochemical sensors for cortisol detection: Principles, designs, fabrication, and characterisation, Biosens Bioelectron 239 (2023). https://doi.org/10.1016/j.bios.2023.115600.

[4] E. Cunha, M.F. Proença, M.G. Pereira, M.J. Fernandes, R.J. Young, K. Strutyński, M. Melle-Franco, M. Gonzalez-Debs, P.E. Lopes, M. Da Conceição Paiva, Water Dispersible Few-Layer Graphene Stabilized by a Novel Pyrene Derivative at Micromolar Concentration, Nanomaterials 8 (2018). https://doi.org/10.3390/nano8090675.

DOI 10.5162/EUROSENSORS2025/TP65

Force measurement in Laparoscopic Stapler for Ex-Vivo Tissue Characterization

János Márk Bozorádi[1,2], Zsófia Sz Bérces[1], Géza Papp[3], Maria Berkes Maros[2], Péter Fürjes[1]
[1] Microsystems Lab., Inst. of Technical Physics and Materials Science, HUN-REN Centre for Energy Research, Budapest, Hungary
[2] Óbuda University Doctoral School on Materials Sciences and Technologies, Budapest, Hungary
[3] Uzsoki Hospital, Budapest, Hungary
Corresponding Author's e-mail address: bozoradi.janos@ek.hun-ren.hu

Summary:
Minimally invasive surgical (MIS) procedures of the gastric tract often involve resection of tissues such as the bowel, colon or part of the stomach. Modern surgical trends point toward surgical robotics being more and more widely applied, but manual laparoscopy is still prevalent. We believe that gathering large quantities of mechanical data through tissue characterization is fundamental for the improvement of laparoscopic tools and procedures. A crucial feature of small-scale integrated measurement systems is the coverage of the sensor and the accompanying readout electronics. In our work we intended to test our proprietary MEMS force sensor developed by HUN-REN CER's Microsystems Lab for in-situ tissue characterization by integrating it into a stapler currently used in medical practice. Using a flexible printed circuit board (PCB) carrier and customized 3D printed enclosures, a series of stapler-compatible sensor casings were developed. These were tested both with hard cover used in our tabletop measurement system [1] as well as combining with polydimethylsiloxane (PDMS) to evaluate its effectiveness as a biocompatible sensor encapsulation.

Keywords: tissue; biomechanics; compression; MEMS force sensor; encapsulation; PDMS;

MEMS force sensor for MIS application

During MIS the palpation of tissues is done via miniature grippers which give surgeons an indirect tactile sense. This feeling of stiffness which correlates to elasticity is essential in decision making during surgeries. Grippers used for tissue palpation have a touch area of roughly 5 × 15 millimeters, while staplers cover about 10 × 60 millimeters. Due to the developed piezoresistive MEMS force transducer has a lateral dimension of 2 × 2 millimeters, its form factor is optimal to integrate into the staple cartridge of a laparoscopic stapler currently used in MIS procedures. This allows us to measure the forces exerted on the tissue at the moment of stapling as well as testing the effects of tissue deformation caused by the non-parallel operation of the stapler jaws by placing multiple sensors along the staple surface.

Biocompatible sensor encapsulation

Whether used in ex-vivo tissue measurements or integrated into the prototype of a smart laparoscope the sensor needs adequate encapsulation because the end goal is to make in-vivo application possible. Before such a device can even be considered for FDA or MDR qualification biocompatibility and the sterilizability must be validated. The use of electronics means that the system must be hermetically sealed since most of the electrical components are not trivially biocompatible. This includes the sensor, the printed circuit board (PCB), the electrical components and of course their soldering materials.

Ex-vivo measurements on resected samples allowed us to test the sensor without any encapsulation utilizing its full sensitivity. In this tabletop measurement system, a metal disc cover was used on the sensor's force transmission rod to adequately transfer tactile force onto the deforming membrane. [1] Moreover in the case of a previous ENIAC INCITE project [2], the sensor system was installed into a 3D printed PLA (later changed to SLM stainless steel) laparoscope tip and covered with PDMS. According to recent literature, the most practical material to use for sensor integration in biomedical applications is still PDMS. Among the advantages of using PDMS the most notable for our application are physiological indifference, biocompatibility, resistance to biodegradation while it also has good mechanical properties and is relatively easy to fabricate in the desired geometry. [3] It is popular in the fabrication of novel sensing techniques for

wearable electronics, but also in the development of mechanical sensors. PDMS's elasticity is also well programable by simply increasing or decreasing the amount of curing agent during mixing. [4] Although this encapsulation can significantly modify the sensing characteristics of the integrated device.



Figure 1. 3D printed stapler cartridge with the integrated MEMS force sensor

Results

A pair of special stapler cartridges were designed, fabricated and implemented with high integrability, equipped with piezoresistive force sensors (see Fig. 1). The cartridge case was modeled and 3D printed to fit into a laparoscopic stapler currently being in medical use. For easy insertion and to reduce size, a flexible polyimide-based PCB carrier was designed to fit into the cartridge. In the previous designs the sensor was still wire bonded to the PCB [1], while this newer type of sensor works as a surface mounted component. The base cover of the sensor was still a metal disc manufactured from Ni stencil material.

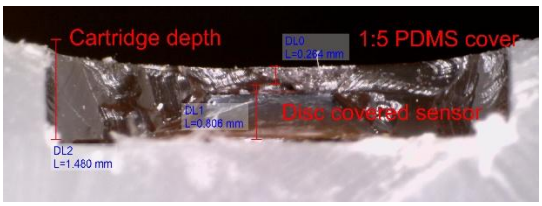


Figure 2. Cutaway view of the finished cartridge

After mounting the sensor in the cartridge, it was filled with de-gassed PDMS characterized with 1:5 curing agent-elastomer ratio as demonstrated in Fig. 2. The complete cartridge was cured on 65°C for 1.5 hours. This ratio was chosen to ensure optimal mechanical transfer considering the PDMS elasticity analyzed by our previous tests.

The sensor was calibrated before and after the cartridge was filled up with PDMS. The resulting force dependent output voltage response curves in Fig. 3 suggest that, both the sensitivity and the linearity of the force sensor is affected by the encapsulation. The flexibility and the viscoelasticity of the PDMS cover material has to be taken into account.

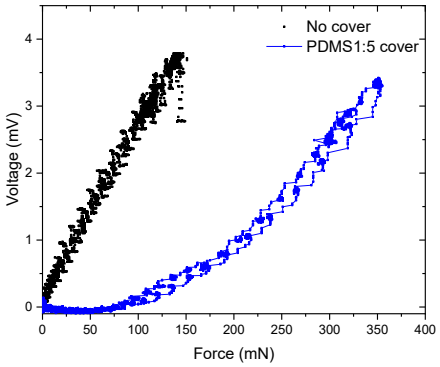


Figure 3. Voltage vs. force calibration curves of the original bare sensor and the encapsulated one embedded in the 1.5 mm deep trench of the cartridge

Our work supports the identification of optimal geometry and material composition for elastic coverage of highly sensitive mechanical transducers and testing them on practice models as well as ex-vivo tissue samples. Although for better comprehension of the material effects of elastic coverage, a larger series of sensor-enhanced cartridges must be fabricated and characterized.

References

[1] J. M. Bozorádi, Z. Sz Bérces, P. Fürjes, and G. Papp, "PT4.238 - Characterization of Gastric Tissue Samples with MEMS Force Sensor Based Indentation method," in *Poster*, Debrecen (Hungary): AMA Service GmbH, Von-Münchhausen-Str. 49, 31515 Wunstorf, 2024, pp. 317–318. doi: 10.5162/EUROSENSORSXXXVI/PT4.238.

[2] J. Radó *et al.*, "3D force sensors for laparoscopic surgery tool," *Microsyst. Technol.*, vol. 24, no. 1, pp. 519–525, Jan. 2018, doi: 10.1007/s00542-017-3443-4.

[3] Nanbakhsh, K., Shah Idil, A., Lamont, C. *et al.* On the longevity and inherent hermeticity of silicon-ICs: evaluation of bare-die and PDMS-coated ICs after accelerated aging and implantation studies. Nat Commun 16, 12 (2025). doi: 10.1038/s41467-024-55298-4

[4] I. Miranda *et al.*, "Properties and Applications of PDMS for Biomedical Engineering: A Review," *J. Funct. Biomater.*, vol. 13, no. 1, p. 2, Dec. 2021, doi: 10.3390/jfb13010002.

Acknowledgements

The work was supported by the National Research, Development and Innovation Fund (NKFIA) via INBIOM TKP2021-EGA-04 grant.

DOI 10.5162/EUROSENSORS2025/TP67

Design of Soft and Fast Nanocantilever for High-Speed Atomic Force Microscopy

Eying Sim Wong[1], Aron Michael[1], Hemanshu Pota[2], Chee Yee Kwok[1]
[1] UNSW Sydney, High St, Kensington, Sydney NSW, Australia,
[2] UNSW Canberra, Northcott Drive, Campbell ACT, Australia
e.simwong@unsw.edu.au

Summary:
The key to enhance the imaging rate without damaging delicate biological samples in life science applications is to design a cantilever probe with low spring constant but high resonance frequency. Achieving these two key mechanical characteristics is challenging due to their direct proportional relationship. Here, we report a silicon dioxide-based cantilever design that enabled low spring constant while ensuring high resonance frequency. In comparison to the existing cantilevers for HS-AFM for life science applications, this cantilever demonstrated the lowest spring constant with the highest resonance frequency to spring constant ratio and addressed the challenge.

Keywords: Low spring constant, HS-AFM, Tapered HS-AFM, High resonance frequency, tapered beam, grey-scale lithography

Motivation and Objective

Due to the high demands in life science applications, designing a cantilever with a low spring constant is essential for ensuring safe scanning of soft samples. On the other hand, to capture their dynamic behavior, a high resonance frequency cantilever is needed for enabling fast imaging rate [1]. To this end, various cantilever designs for such applications have been reported. Nanoworld produces a 7 µm × 2 µm × 0.08 µm ultrashort cantilever for life science applications [2]. This cantilever exhibits a resonance frequency of 1.2 MHz and a spring constant of 0.15 N/m and has been used to study the effect of host defense peptides on cell wall synthesis at 0.5 – 2 frames per second (fps), facilitating the development of superior drug discovery [2]. Fantner et al. were able to measure the kinetics of pre-death activity of antimicrobial peptides using silicon nitride-based cantilevers that has a low spring constant of 0.3 – 1 N/m. Although the cantilever exhibits one of the lowest spring constants available amongst the cantilevers, the resonance frequency (355 kHz in air) of the cantilever was so low that it was not possible to detect biological reactions that occur at sub-second time scale or even faster [3]. Most commercially available HS-AFM cantilevers exhibit a spring constant of 0.15 – 0.7 N/m and resonance frequency of 0.2 – 1.3 MHz, making them unsuitable for imaging dynamic interactions in nanoscale and soft biological samples simultaneously. Most of the reported cantilevers are silicon nitride-based due to its large Young's Modulus suited for high resonance frequency applications. However, it has the disadvantage of yielding stiff cantilevers. In this work, the design of the lowest spring constant cantilever that also exhibit high resonance frequency comparable to previously reported cantilever probes for HS-AFM application is reported.

Methodology

The unique design features of the soft and fast cantilever design are: (a) linear tapering in the xz plane as illustrated in Fig. 1(a). The linear profile is defined by $Q_0 = (u_0, w_0) = (0, w_0)$ and $Q_1 = (u_1, w_1) = (L, w_1)$ and described by Eq. (1); (b) Bézier parabolic tapering in the xy plane as illustrated in Fig, 1(b). The tapering is defined by three points $P_0 = (0, 0)$, $P_1 = (0, y_1)$ and $P_2 = (L, y_2)$ and described by Eq. (2); (c) made from a silicon dioxide, SiO_2 thin film as opposed to silicon or silicon nitride, SiN in previous reports.

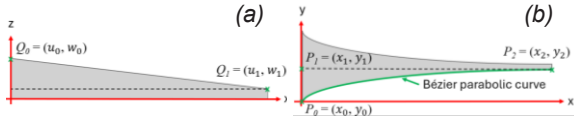


Fig. 1. (a) Vertically linear tapered profile in the xz plane; (b) Bézier parabolic tapering profile in the xy plane

$$\boldsymbol{H(x) = \frac{w_1 - w_0}{u_1 - u_0} x + w_0 = \frac{w_1 - w_0}{L} x + w_0} \quad (1)$$

$$\boldsymbol{f(x) = (y_2 - 2y_1)\left(\frac{\sqrt{4x_2(x)}}{2x_2}\right)^2 \pm 2y_1\left(\frac{\sqrt{4x_2(x)}}{2x_2}\right)} \quad (2)$$

Results and Discussions

The methodology is applied to a typical rectangular cantilever with 7 μm × 0.7 μm × 0.27 μm overall dimension. The cantilever has 5 MHz resonance frequency and 0.7 N/m spring constant - resulting in a figure of merit (FoM), which is the ratio of resonance frequency to spring constant, of 7.14 (MHz.m/N). When the Bézier parabolic profile is introduced to the rectangular cantilever, its resonance frequency increases by 80 % to 8.5 MHz and its spring constant is reduced by 57.14 % to 0.5 N/m as seen from Fig. 2. The resonance frequency further increases by 9 MHz and the spring constant reduces to 0.3 N/m by 40 % as the control point P_1 moves away along the y axis from P_0. The effect of introducing the linear vertical tapering on the resonance frequency and spring constant is studied as function of thickness at the free end and compared to the rectangular cantilever in Fig. 3. The resonance frequency is increased by as much as 2 MHz to 7 MHz and the spring constant is reduced significantly to 0.15 N/m. When both the linear tapering and the Bézier parabolic tapering profile are introduced, the resonance frequency is more than doubled to 10.5 MHz while the spring constant is reduced by a factor of 70 to 0.01 N/m as shown in Fig. 4(a). In comparison to the typical SiN cantilevers, significant reduction in spring constant while yielding similar resonance frequency has been demonstrated by the proposed SiO_2 based cantilever design, leading to the softest cantilever with and the highest FoM of 300 to our knowledge as can be seen from Fig. 4(b).

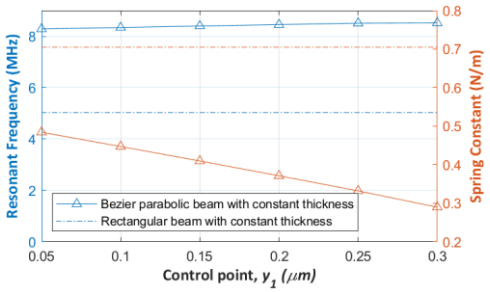


Fig. 2. Effect of Bézier parabolic profile on the resonance frequency and spring constant of SiO_2 beam

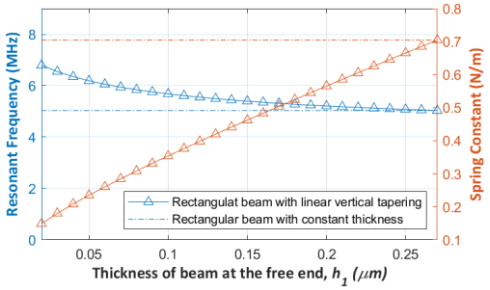


Fig. 3. Effect of vertically linear tapering on the resonance frequency and spring constant of SiO_2 beam

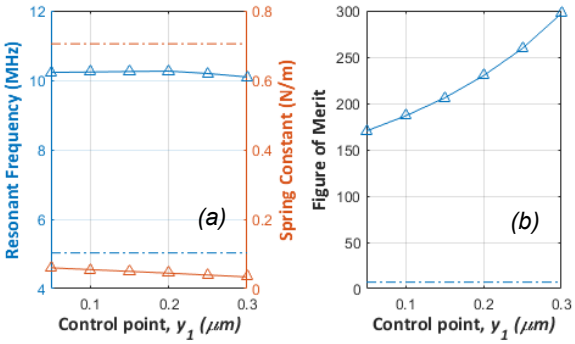


Fig. 4. (a) Effect of double-axis tapering on the resonance frequency and spring constant of SiO_2 beam; (b) Effect of double-axis tapering on the figure of merit

The designed cantilever has been fabricated and characterized, substantiating the design approach. The SEM image of fabricated cantilever is shown in Fig. 5.

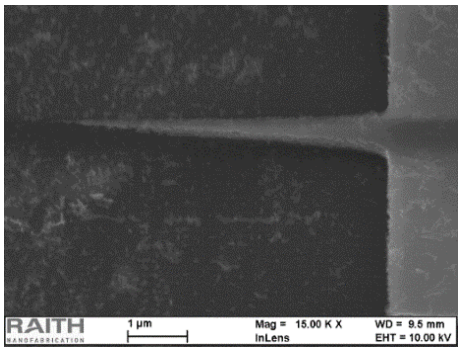


Fig. 5. SEM image of released cantilever

References

[1] T. Ando, High speed atomic force microscopy coming of age, *Nanotechnology*, 23 (2012); doi: 10.1088/0957-4484/23/6/062001

[2] USC-F1.2-K0.15 - NanoWorld® (2025) NanoWorld. Available at: https://www.nanoworld.com/Ultra-Short-Cantilevers-USC-F1.2-k0.15 (Accessed: 25 April 2025)

[3] S. Jekhmane, M. G. Derks, S. Maity, C. J. Slingerland, K. H. Tehrani, J. Medeiros-Silva, V. Charitou, D. Ammerlaan, C. Fetz, N. A. Consoli, et al., Host defence peptide plectasin targets bacterial cell wall precursor lipid ii by a calcium-sensitive supramolecular mechanism, *Nature microbiolgy*, 9(7):1778–1791; doi: 10.1038/s41564-024-01696-9

[4] G. E. Fantner, R. J. Barbero, D. S. Gray, and A. M. Belcher, Kinetics of antimicrobial peptide activity measured on individual bacterial cells using high-speed atomic force microscopy, *Nature nanotechnology 5*, 280–285 (2010); doi: 10.1038/nnano.2010.29

DOI 10.5162/EUROSENSORS2025/TP68

Microphysiological analytical chip with non-invasive Raman microspectroscopy analysis of epithelial permeability and inflammatory biomarkers

Calogiuri A.[1], Bellisario D.[1], Sciurti E.[1], Blasi L.[1], Esposito V.[1], Casino, F.[1], Siciliano P.[1], Francioso L.[1]*

[1]Institute for Microelectronics and Microsystems IMM-CNR, Via per Monteroni "Campus Ecotekne", 73100 Lecce, Italy

lucanunzio.francioso@cnr.it

Summary:

The presented work reports the non-invasive detection of multiple biomarkers in a custom microphysiological chip, designed for co-culture tissues and organ-on-chip investigations. The proposed SERS-on-chip detection system is optimized for the specific detection of two colorectal cancer biomarkers at physiological concentrations, the Oncostatin M and TNF-α. Under optimized pH conditions, tuned on-board, the ML algorithm in F12K medium achieved 99 % accuracy for Oncostatin M detection and 92 % accuracy vs TNF-α detection.

Keywords: Microphysiological chip, biomarkers chemical sensing, lab-on-chip, organ-on-chip, Raman sensing

Background, Motivation an Objective

The need for a rapid, specific and sensitive diagnostic system to identify unique antigens biomarkers, such as those associated with inflammation or cancer is crucial in modern biomedical research. The detection of these markers in complex matrices like body fluids or cell culture media is particularly challenging due to their low concentration, as well as the presence of multiple interfering components. SERS-enhanced detection combines high sensitivity and potential specificity with the added advantages of water non-interference and compatibility with transparent polymeric materials, making it a perfect fit for organ-on-chip non-invasive diagnostic methods[1-3].

Description of the New Method or System

The presented work reports the non-invasive detection of multiple biomarkers in a custom microphysiological platform, designed for co-culture tissues. However, one of the main limitations of SERS method lies in spectral overlap, which results from the binding of multiple analytes to the substrate. The proposed algorithm approaches this limitation by functionalizing the surface of a miniature SERS substrate integrated in a measurement chamber of the chip with a self-assembled monolayer (SAM) of 3-mercaptopropionic acid (3-MPA). Due to the pH modification of the cell culture medium vs the target protein isoelectric points, the carboxylic groups of 3-MPA can interact in a more selective way with a reduced number of molecules (target/acid protonation status modification), enhancing the Machine Learning (ML) classification performance. The proposed SERS-on-chip detection system was optimized for the specific detection of two colorectal cancer biomarkers at physiological concentrations, the Oncostatin M and TNF-α.

Results

The pH modulation is managed at chip level with an embedded microfluidic mixer, without affecting the cell culture chamber and acquiring the Raman spectra through the chip lid (Fig. 1). The obtained Raman spectra (500-2000 cm^{-1}, 632.8 nm laser, 1800 gr/mm grating, 20x objective) collected on a microfluidic chip onto a 37°C stage were analyzed using a supervised Machine Learning approach and then correlated with standard TEER measurements of epithelial permeability in order to classify the different junctions damages (T0, T2h, T4h of exposure the

chelating agent) in a non-destructive way. This approach allows to detect TJ status at different agent exposure time with a validation accuracy of 82% and a test accuracy of 96%. Raman microspectroscopy, combined with support vector machines algorithm, represents a promising method for improving the diagnostic precision of microphysiological platforms. Furthermore, this tool represents a non-destructive and promising method for disease prediction, physiological parameters monitoring and drugs PK/PD screening. Under optimized pH conditions, the ML algorithm in F12K medium achieved 99 % accuracy for Oncostatin M detection and 92 % accuracy vs TNF-α detection (Fig. 2). A complementary proposed study was focused to analyse with same setup the structural and biochemical changes in a Caco-2 intestinal epithelial model before and after treatment with a calcium chelating agent. Two different data-splitting approaches, “sample-based” and “spectra-based,” were also compared. Raman microspectroscopy results were confirmed by TEER measurements and immunofluorescence staining.

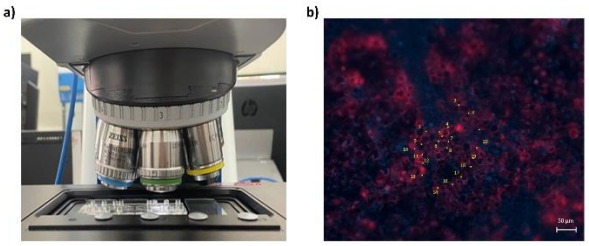


Fig.1 a) MicroRaman Microscope with motorized stage for 2D cell culture mapping; b) Immunofluorescent staining of Caco-2 cells intestinal epithelium, marked with 20 points from inter-cellular junctions analyzed with Raman spectroscopy (Red e-cadherins on tight junctions, Blue nuclei).

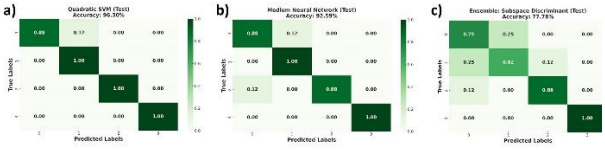


Fig.2 Heatmap of the test accuracy across four classes, corresponding to different EGTA exposure times (T0, T2h, T4h and empty membrane) of Quadratic SVM (A), Medium Neural Network (B) and Ensemble (C) algorithms.

References

[1] Zbinden, A.; Marzi, J.; Schlünder, K.; Probst, C.; Urbanczyk, M.; Black, S.; Brauchle, E.M.; Layland, S.L.; Kraushaar, U.; Duffy, G.; Schenke-Layland, K.; Loskill, P. Non-invasive marker-independent high content analysis of a microphysiological human pancreas-on-a-chip model. In *Matrix Biology*, Schenke-Layland, K., 2020; Volumes 85-86,. 205–220.

[2] Beton-Mysur, K.; Brozek-Pluska, B. Raman Spectroscopy and Imaging Studies of Human Digestive Tract Cells and Tissues-Impact of Vitamin C and E Supplementation. *Molecules* , **2023**, 28,137.

[3] Popp, J.; Schie, I.W. Ashort guide for Raman Spectroscopy of Eukaryotic Cells. Spectroscopy online. 2019; Volume 34, Issue 8,. 18-22.

DOI 10.5162/EUROSENSORS2025/TP69

Fully Integrated Sensor Platform for Remote Respiratory Biomarker Monitoring

Simon Schlapansky[1], Federico Burisch[1], Ryan Rusch[1], Andreas Güntner[1]
[1]Human-centered Sensing Laboratory, Department of Mechanical and Process Engineering, ETH Zürich, Switzerland
schlsimo@ethz.ch

Summary:
Space exposes astronauts to extreme environmental conditions, which can induce significant physiological changes. While current systems primarily track basic vital signs, prolonged missions will necessitate monitoring complex physiological changes. This work introduces a fully integrated sensor platform for selective detection of molecular breath biomarkers. Depositing highly sensitive porous nanoparticle gas sensing films directly onto microelectronic circuitry provides access to low power, miniaturized sensor systems suitable for portable or wearable applications.

Keywords: Astronaut health monitoring, Breath analysis, Wearables, Chemoresistive sensors, Nanoparticles

Background, Motivation and Objective

Astronauts face extreme environmental stressors in space, including microgravity, radiation, disrupted circadian rhythms, and altered diets. [1] These factors induce significant physiological changes, affecting metabolism [2], the microbiome [3] and the musculoskeletal system [4]. Current health monitoring aboard the ISS relies on intermittent, crew-intensive sampling methods (e.g. blood tests, microbiome swabs), which are unsuitable for long-duration missions.

To address this, real-time, non-invasive monitoring technologies are needed. [5] Wearable sensors offer continuous, autonomous tracking but are currently limited to basic vitals. [6] Extending this to molecular level biomarkers, however, requires novel sensor platforms. Breath analysis offers a unique, non-invasive approach to access real-time information of metabolic, musculoskeletal and microbiome-related changes.[7]

While past technologies like NASA's PUMA [8] and ESA's RSS [9] focus on basic gases (CO_2, O_2), breath contains a vast array of informative volatile organic compounds (VOCs) in the ppb–ppt range. Acetone, for instance, reflects fat metabolism and nutritional state [10]; isoprene correlates with muscle activity and circadian rhythm. [2,4] Commercial sensors, however, often lack the necessary selectivity to detect these analytes.

Recent advances in nanotechnology, on novel semiconducting metal-oxide (SMOx) sensors, such as silicon-doped WO_3 and palladium-doped SnO_2, allow sensitive, and selective detection of acetone and isoprene in breath at ppb levels. [10,11] To realize their potential for space applications, further system integration into portable, low-power platforms is needed.

Description of the New Method or System

Results

In this work, we present a miniaturized chemoresistive sensor platform incorporating molecule-selective sensors fabricated via flame aerosol deposition. This approach enables the formation of nanoparticle-based sensing films directly on commercial micro-hotplate substrates with high spatial precision.

The sensing films are deposited within the active area of the interdigitated electrodes (d = 300 µm), as verified by SEM imaging (Figure 1b). A shadow mask is employed to shield the contact and heater pads, ensuring clean deposition exclusively in the sensing region. Flame aerosol deposition, driven by thermophoresis, results in the formation of highly porous, nanostructured films. These structures are subsequently mechanically stabilized through post-deposition annealing and wire-bonded onto leadless chip carriers.

The employed micro-substrates consist of a suspended membrane with an integrated microheater that precisely controls the temperature of the sensing film. Thanks to an optimized chip design, the heaters maintain high thermal efficiency, operating at temperatures up to 300 °C with a power consumption of only ~60 mW.

A custom-designed circuit board has been developed to interface with the sensors, enabling precise control and readout of their electrical response. Sensor performance is evaluated under well-controlled exposure to gas mixtures with variable relative humidity levels using a calibrated gas mixing setup. The test conditions are tailored to mimic exhaled breath under different physiological states. This allows us to assess sensor selectivity, sensitivity, and stability toward key breath biomarkers under realistic conditions.

Such a miniaturized sensor platform has the potential to not only transform health management in space but also on earth by enabling continuous, non-invasive and decentralized monitoring of biochemical markers with molecular precision.

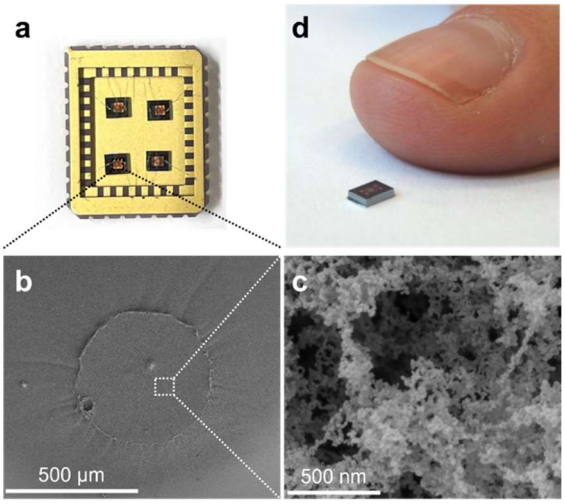


Figure 1. (a) Sensor package wire-bonded to a chip carrier after deposition of a flame-made and in situ annealed Pd-doped SnO_2 film. SEM confirms (b) the accurate sensing film deposition onto the designated area with interdigitated electrodes and indicates (c) the highly porous film architecture. (d) The total size of one microsensor is around 2x2 mm. Figure reproduced from [12].

References

[1] Ying Xuan Chua C. et al., Advanced material technologies for space and terrestrial medicine, *Nat. Rev. Mater*. 9, 808-821 (2024); doi: 0.1038/s41578-024-00691-0

[2] Barger L. K. et al. Prevalence of sleep deficiency and use of hypnotic drugs in astronauts before, during, and after spaceflight: an observational study, *Lancet Neurol*. 13, 904-912 (2014); doi: 10.1016/S1474-4422(14)70122-X

[3] Mortazavi S. M. J. et al. How the adaptation of the human microbiome to harsh space environment can determine the chances of success for a space mission to Mars and beyond, *Front. Microbiol*. 14 (2024); doi: 10.1016/j.actaastro.2006.09.026

[4] Chang D. G. et al. Lumbar Spine Paraspinal Muscle and Intervertebral Disc Height Changes in Astronauts After Long-Duration Spaceflight on the International Space Station, *Spine* 41, 1917-1924 (2016); doi: 10.1097/BRS.0000000000001873

[5] T. Elias Abi-Ramia Silva et al. Gas sensing for space: Health and environmental monitoring *Trends in Analytical Chemistry* 177, 117790 (2024); doi: 10.1016/j.trac.2024.117790

[6] Agency, C. S. Bio-Monitor: Keeping an eye on astronauts' vital signs. Canadian Space Agency https://www.asc-csa.gc.ca/eng/sciences/bio-monitor.asp (2014).

[7] Güntner A.T. et al. Breath Sensors for Health Monitoring *ACS Sens*. 4, 2, 268–280, (2019); doi: 10.1021/acssensors.8b00937

[8] Dietrich, D. L. et al. Portable Unit for Metabolic Analysis. US-Patent-10,076,268 (2018).

[9] Hoffmann, U., Dräger, T., Baumann, R. & Fasoulas, S. Development and application of a miniaturised sensors system for respiratory investigations (MAP-RSS). *Proc. Life in Space for Life on Earth Symposium* 553, 102 (2008).

[10] Weber, I. C. et al. Monitoring Lipolysis by Sensing Breath Acetone down to Parts-per-Billion. *Small Sci*. 1, 2100004 (2021); doi: 10.1002/smsc.202100004

[11] van den Broek, J. et al. Selective monitoring of breath isoprene by a portable detector during exercise and at rest. *Sens. Actuators B Chem*. 357, 131444 (2022); doi: 10.1016/j.snb.2022.131444

[12] Güntner A.T. et al. E-Nose Sensing of Low-ppb Formaldehyde in Gas Mixtures at High Relative Humidity for Breath Screening of Lung Cancer? *ACS Sens.* 1, 5, 528–535 (2016); doi: 10.1021/acssensors.6b00008

Acknowledgements

This study was financially supported by the European Space Agency via the Discovery Programme (Contract No. 4000144484).

DOI 10.5162/EUROSENSORS2025/T4.3.2

A low-power wireless sensor platform for real-time monitoring of pH and nitrate in the soil

Célia Boko[1], Elise Saoutieff[1], Paul Fourcade[1], Vincent Elhorga[1], Arthur Ohl[1], Iris Vogeler[2], Henk Smit[2], Nivedha Surendran[3], Axel Wille[3], Han Shao[4], Alan O'Riordan[4], Lukasz Kulas[5], Patryk Kalkowski[5], Henrique Trindade[6], Lukas Kohl[7], Safi Ullah[7]
[1] Univ. Grenoble Alpes, CEA, Leti, Grenoble, France
[2] Christian-Albrechts-Universität, Kiel, Germany
[3] Fraunhofer Institute for Electronic Microsystems and Solid State Technologies, Munich, Germany
[4] Nanotechnology Group, Tyndall National Institute, Cork, Ireland
[5] Gdansk University of Technology, Gdansk, Poland
[6] University of Trás os Montes e Alto Douro, Quinta de Prados, Portugal
[7] University of Eastern Finland, Kuopio, Finland
celia.boko@cea.fr

Summary:
The low-power sensing platform proposed by the FAMOSOS project is intended to be a wireless, low-power and multifunctional system for real-time soil monitoring. We developed a cost-effective *in situ* sensing system for nitrate concentrations in the soil solution along with soil moisture, pH and temperature. Soil water samples are collected through a porous ceramic probe with a piezoelectric micropump, analysed through on-chip electrochemical measurements, communicating with a LoRa-based underground network. This paper presents the system design as well as the results from the first field test.

Keywords: soil monitoring, innovative sensors, low-power, real-time, wireless underground sensor network.

FAMOSOS Background, Motivation and Objective

Soil is essential to human health, the economy, and environment, playing a crucial role in the water, nutrients, and carbon cycles. However, soil degradation is a growing concern, with significant implications for climate change, agriculture, and biodiversity. In response, the European Soil Strategy 2030 aims to restore and protect soil by 2050 through targeted actions and the proposed Soil Monitoring Law [1]. One of the main challenges in soil management today is the lack of real-time, *in situ* technologies for effective soil monitoring. The FAMOSOS (Farm Monitoring via Real-time SOil Sensing) [2] project addresses this challenge by developing a low-cost, real-time electronic system designed to help farmers optimise fertiliser use, reduce greenhouse gas emissions, and minimize water pollution. The system aligns with EU objectives for sustainable soil health and would equip farmers with essential tools to make informed decisions.

FAMOSOS System

FAMOSOS introduces an innovative IoT-based electrochemical sensor platform, known as the "beta system", designed for real-time, *in situ* data acquisition. This system consists of:

- an electrochemical sensor composed of gold and platinum nanowires with various electrodeposited overlayers, enabling selective and multiplexed detection of multiple analytes (NO_3^-, pH)
- a temperature and moisture sensor (TEROS 54, METER Group) for monitoring soil environmental conditions
- a porous ceramic probe combined with a piezoelectric micropump for extracting soil solution
- a low-power electronic board integrating an Analog Front End (AFE) for driving electrochemical and moisture/temperature sensors
- an antenna for wireless LoRa data transmission
- an SD card for storing sensor data

A schematic view of the FAMOSOS system, specifically the electronic architecture and its interface with other components, is shown in Fig. 1.

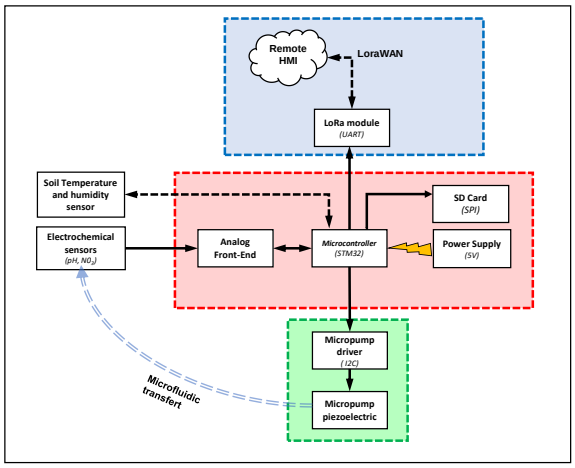


Fig. 1. Schematic beta-system design

AFE Electronic

The previous architecture features an Analog Front End (AFE) that integrates an STM32 microcontroller unit (MCU) and a portable potentiostat from CH Instruments. It was designed to support both innovative analog sensors (pH, NO_3^-) and commercial digital sensors (temperature and moisture) while also controlling the micropump. The electronic board enables sensor data acquisition, local data storage on an SD card, and LoRa-based data transmission. Fig. 1. highlights the board (indicated by the red rectangle), including its power management circuit for IoT and other connectable components. The beta system, embedded in a watertight casing and designed for outdoor field testing is shown in Fig.2.

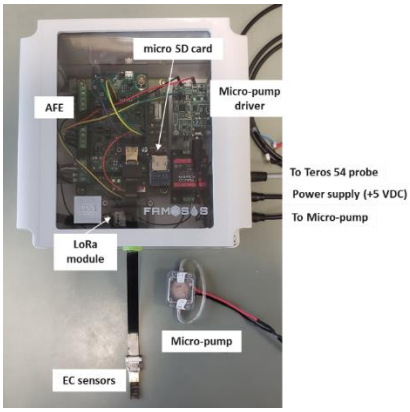


Fig. 2. watertight casing for beta-system electronic board

The AFE collects raw sensor data, which is then converted into physical values by the microcontroller. The data is formatted using a custom protocol and transmitted to the cloud via LoRa. The wireless system includes underground base stations and end devices. To minimize power consumption, sensors and peripherals remain in standby mode and wake up only when data transmission is required.

Results

The FAMOSOS concept was demonstrated through initial successful laboratory tests, followed by the beginning of the beta-system deployment in the field. Subsequent trials are being conducted on a site in Portugal, involving different crop rotations and various N fertilization levels.



Fig. 3. Beta-system in Portugal test field

By developing a tool which provides farmers with real-time information on the soil N status, FAMOSOS will make a significantly contribution to enhancing soil understanding to improve management practices such as optimizing N fertilization strategies. This will enable more sustainable agricultural production through increased nitrogen use efficiency and supporting environmental health by decreasing N leaching and N_2O emissions

References

[1] EU Soil Health: [Online]. Available: https://environment.ec.europa.eu/topics/soil-health_en (accessed: Apr. 15 2025)

[2] E. Saoutieff, P. Fourcade, C. Boko, V. Elhorga, S. Boisseau, I.Vogeler et al., « Advanced sensor system dedicated to real-time soil monitoring», EUROSENSORS XXXVI 2024, pp 269-270

Acknowledgements

The project is funded as an EJP-SOIL external project by the French National Research Agency (ANR) under grant ANR-23-SOIL-0002-04, the Irish Department of Agriculture, Food and the Marine under grant agreement No. 2022EJPSOIL202, the Finnish Ministry of Agriculture (4400T-0569), and the German Federal Ministry of Education and Research BMBF under grant number 031B1377B.